

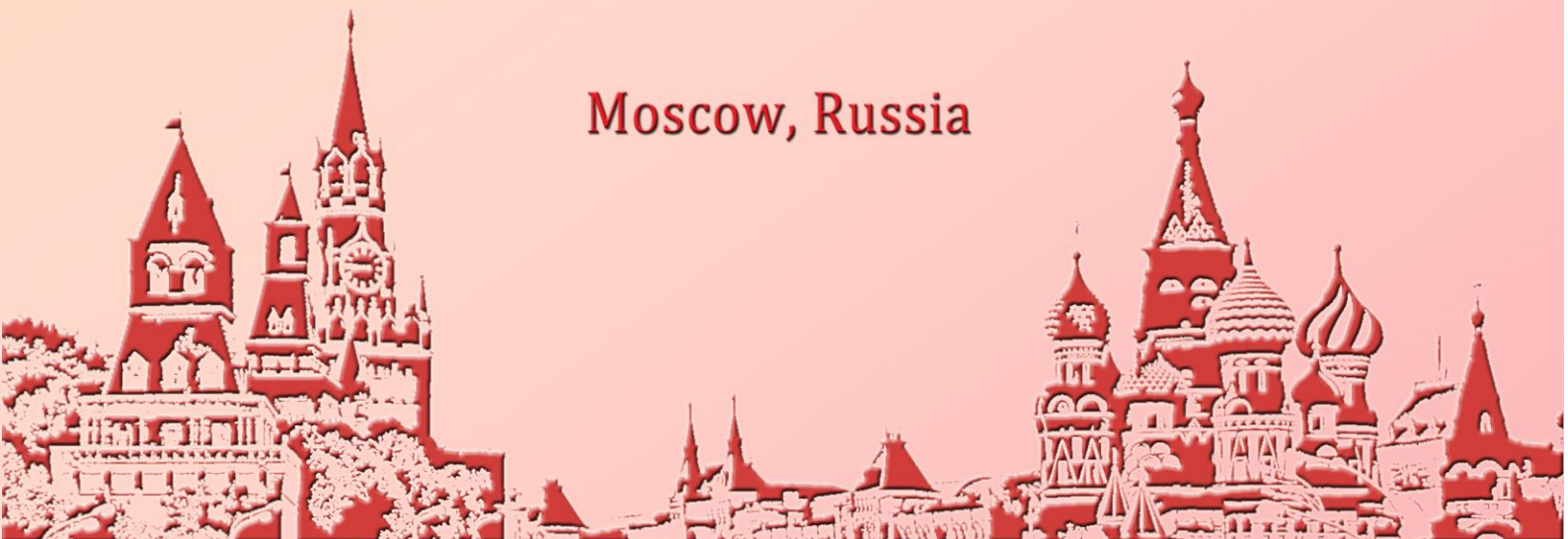
A graphic element for the SHS 2019 logo, featuring a vertical stack of horizontal bars in shades of orange, yellow, and red, topped with a crown-like shape.

# SHS 2019

## **XV International Symposium on Self-Propagating High-Temperature Synthesis**

**September, 16-20, 2019**

**Moscow, Russia**



**XV International Symposium on Self-Propagating High-Temperature Synthesis** — Chernogolovka: IPCP RAS, 2019. 594 p.

eISBN 978-5-6040595-4-8

ISBN 978-5-6040595-4-8



9 785604 059548

© IPCP RAS, 2019

## *Organizers*

National University of Science and Technology MISIS  
(NUST MISIS), Moscow, Russia

Merzhanov Institute of Structural Macrokinetics and Materials Science,  
Russian Academy of Sciences (ISMAN)  
Chernogolovka, Russia

## *Symposium Committees*

### **SYMPOSIUM CO-CHAIRMEN:**

E.A. Levashov (Russia)

M.I. Alymov (Russia)

### **INTERNATIONAL COORDINATORS:**

Yu.S. Pogozhev (Russia)

V.N. Sanin (Russia)

### **LOCAL ORGANIZING COMMITTEE:**

A.M. Alymova (Russia)

O.V. Amelina (Russia)

O. A. Golosova (Russia)

V.V. Kurbatkina (Russia)

O.O. Likhanova (Russia)

O.S. Manakova (Russia)

A.Yu. Potanin (Russia)

D.A. Sidorenko (Russia)

A.E. Sytshev (Russia)

M.K. Melkonyan (Russia)

### **PROGRAM COMMITTEE:**

A.S. Mukasyan (USA) – chair

A.S. Rogachev (Russia) – vice chair

F. Baras (France)

E. Dreizin (USA)

Z. Fu (China)

K. Manukyan (USA)

H. Nersisyan (Korea)

R. Orru (Italy)

J. Puszynski (USA)

S.A. Rogachev (Russia)

D.V. Shtansky (Russia)

D. Vrel (France)

T. Weihs (USA)

### **INTERNATIONAL**

### **ADVISORY BOARD:**

A.A. Chernikova (Russia) – chair

S.M. Aldoshin (Russia)

N.P. Aleshin (Russia)

I. Agote (Spain)

M.I. Alymov (Russia)

A.P. Amosov (Russia)

S.T. Aruna (India)

T. Babul (Poland)

O.A. Bannykh (Russia)

V.V. Boldyrev (Russia)

F. Bernard (France)

V.M. Buznik (Russia)

G. Cao (Italy)

B. Derin (Turkey)

M.R. Filonov (Russia)

F.V. Grechnikov (Russia)

E. Gutmanas (Israel)

V.M. Ievlev (Russia)

A.F. Ilyushchenko (Belarus)

E.N. Kablov (Russia)

M.I. Karpov (Russia)

A. Kawasaki (Japan)

S. Kharatyan (Armenia)

V.S. Komlev (Russia)

M.N. Krasnyanskii (Russia)

N.T. Kuznetsov (Russia)

S.A. Kuznetsov (Russia)

E.A. Levashov (Russia)

J. Lis (Poland)

N.Z. Lyakhov (Russia)

V.I. Lysak (Russia)

Yu.M. Maksimov (Russia)

Z. Mansurov (Kazakhstan)

R. Mendes (Portugal)

A.S. Mukasyan (USA)

O. Odawara (Japan)

S.A. Oglezneva (Russia)

M. Ohyanagi (Japan)

G. Oniashvili (Georgia)

M. Rodriguez (Spain)

A.S. Rogachev (Russia)

A.I. Rudskoy (Russia)

V.N. Sanin (Russia)

V.I. Sergienko (Russia)

V.Ya. Shevchenko (Russia)

A.E. Sytshev (Russia)

G.F. Tavazde (Georgia)

A.Yu. Tsivadze (Russia)

P. Vincenzini (Italy)

G. Xanthopoulou (Greece)

O. Yücel (Turkey)

V.I. Yukhvid (Russia)

## *Acknowledgments*

Symposium is carried out under the support of

The Russian Foundation for Basic Research (Project 19-08-20051)

The Ministry of Science and Higher Education of the Russian Federation (Program of increasing the competitiveness of the National University of Science and Technology MISIS among leading world scientific-and-educational centers 5-100)

The Russian Academy of Sciences

## Contents

|  |    |
|--|----|
| SH-SYNTHESIS OF POWDERS BASED ON TRANSITION METAL BORIDES<br>R. G. Abdulkarimova, A. J. Seidualiyeva, K. Kamunur .....   | 1  |
| RAPID-HEATING-TYPE COMBUSTION SYNTHESIS OF METALLIC IRON: EFFECTS<br>OF TEMPERATURE AND ATMOSPHERE<br>K. Abe, A. Kurniawan, M. Sanada, T. Nomura, T. Akiyama.....  | 4  |
| SELF-PROPAGATING HIGH-TEMPERATURE SYNTHESIS OF $Fe_2VAl$ -BASED<br>THERMOELECTRIC MATERIALS<br>K. Abe, N. Okinaka, T. Akiyama.....   | 7  |
| REACTIVE FLASH SPARK PLASMA SINTERING OF ALUMINA REINFORCED BY<br>SILICON CARBIDE NANOCOMPOSITES: PHYSICOCHEMICAL STUDY<br>M. Abedi, D. O. Moskovskikh, A. S. Mukasyan .....   | 10 |
| STRUCTURE AND PHASE FORMATION IN ALUMINUM OXYNITRIDE DURING<br>SELF-PROPAGATING HIGH-TEMPERATURE SYNTHESIS<br>T. G. Akopdzhanyan, A. A. Kondakov, N. A. Kochetov, S. I. Rupasov, A. P. Kozlova,<br>A. V. Bondarev..... | 12 |
| ISMAN: NEW RESULTS AND ACHIEVEMENTS<br>M. I. Alymov, O. K. Kamynina .....  | 13 |
| KINETIC MEASUREMENTS FOR SOLUTION COMBUSTION SYNTHESIS<br>PROCESSES<br>N. Amirkhanyan, S. L. Kharatyan, K. V. Manukyan.....  | 15 |
| APPLICATION OF SHS FOR FABRICATION OF ALUMINUM-MATRIX<br>NANOCOMPOSITES (REVIEW)<br>A. P. Amosov, E. I. Latukhin, A. R. Luts, Yu. V. Titova, A. A. Kuzina, D. A. Maidan.....   | 17 |
| FORMATION OF $Mo/Nb/Si/B$ CAST COMPOSITE BY SHS IN CONDITIONS OF<br>ARTIFICIAL GRAVITY<br>D. E. Andreev, Yu. S. Vdovin, V. I. Yukhvid .....  | 22 |
| GRAVITY-ASSISTED METALLOTHERMIC SHS OF COMPOSITES BASED ON<br>$Mo-Ti-Cr-Ni$<br>D. E. Andreev, K. V. Zakharov, D. M. Ikornikov, V. I. Yukhvid, N. Yu. Khomenko.....   | 25 |
| ADAPTIVE COATINGS FOR HIGH TEMPERATURE APPLICATIONS<br>S. M. Aouadi .....  | 27 |
| THE KEY ROLE OF STRUCTURAL AND PHASE COMPOSITION FOR FORMATION<br>GRADED MATERIALS BY SHS-COMPACTION TECHNOLOGY<br>Z. Aslamazashvili, G. Oniashvili, G. Zakharov, G. Tavadze, M. Chikhradze.....                       | 30 |
| PRODUCTION OF ULTRAFINE-GRAINED POWDER COMPOSITES IN $BN$ , $B_4C$ , AND<br>$B_xC_yN_z$ SYSTEMS BY SHS METHOD<br>Z. Aslamazashvili, G. Zakharov, G. Mikaberidze, M. Chikhradze, G. Tavadze,<br>G. Oniashvili .....     | 33 |
| HEAT-RESISTANT COATINGS FORMED FROM SHS POWDER OF THE<br>$ZrSi_2-MoSi_2-ZrB_2$ SYSTEM FOR CARBON COMPOSITES<br>A. N. Astapov, E. A. Levashov, I. P. Lifanov, Yu. S. Pogozhev, A. Yu. Potanin,<br>M. V. Prokofiev.....  | 36 |
| HARDMETALS WITH HIERARCHICAL AND EXTRA HOMOGENEOUS STRUCTURE<br>FOR A NEW GENERATION MINING TOOLS<br>E. N. Avdeenko, A. A. Zaitsev, I. Konyashin, E. A. Levashov, D. A. Sidorenko.....                                 | 40 |
| EXPERIMENTAL STUDY OF THE EFFECT OF ATTACKING METAL PARTICLES ON<br>MAGNESIUM, BORON, ALUMINUM, MOLYBDENUM OXIDES<br>A. N. Baideldinova, S. Tolendiuly, L. V. Mukhina, G. I. Ksandopulo.....                           | 42 |

|   |    |
|---|----|
| THE EFFECT OF MAGNESIUM ON THE COMBUSTION PROCESS OF GAS GENERATOR MIXTURES   |    |
| A. Ye. Bakkara, N. N. Mofa, B. S. Sadykov, Z. L. Sultanova, Z. A. Mansurov .....                                      | 45 |
| AN OVERVIEW OF ATOMISTIC APPROACHES IN SHS PROCESSES  |    |
| F. Baras, O. Politano, A. Fourmont, S. Le Gallet, A. Nepapushev, A. Sedegov, S. Vadchenko, A. Rogachev .....          | 49 |
| PRODUCTION OF LAYERED COMPOSITE MATERIALS BASED ON TITANIUM BORIDES   |    |
| P. M. Bazhin, A. M. Stolin, A. S. Konstantinov, A. P. Chizhikov, A. D. Prokopets .....                                | 52 |
| VOLUME COMBUSTION SYNTHESIS OF $Li_4SiO_4$  |    |
| K. Benzeşik, A. Turan, O. Yücel .....   | 54 |
| GAS ENVIRONMENT INFLUENCED TRIBOLOGICAL BEHAVIOR OF TMD COATINGS  |    |
| A. V. Bondarev, T. Polcar .....   | 58 |
| NANOCOMPOSITE $Si-Ta-C-N-(Ag)$ COATINGS FOR WIDE TEMPERATURE RANGE APPLICATIONS                                       |    |
| A. V. Bondarev, A. N. Sheveyko, M. N. Antonyuk, T. Polcar, E. A. Levashov, D. V. Shtansky .....                       | 59 |
| SUPPORTED CATALYSTS OF DEEP OXIDATION AND HYDROGENATION BY SELF-PROPAGATING SURFACE SYNTHESIS                         |    |
| V. N. Borshch, I. M. Dement'eva .....   | 61 |
| METALLOTHERMIC PRODUCTION OF $FeCo$   |    |
| M. Bugdayci, A. Turan .....   | 64 |
| SPARK PLASMA SINTERING AND SELF-PROPAGATING HIGH-TEMPERATURE SYNTHESIS OF ULTRA-HIGH TEMPERATURE CERAMICS $Hf-C-N$    |    |
| V. S. Buinevich, A. A. Nepapushev, G. V. Trusov, D. O. Moskovskikh, A. S. Rogachev, A. S. Mukasyan .....              | 67 |
| THERMAL EXPLOSION IN THE $2Co-Ti-Al$ SYSTEM: COMBUSTION, PHASE FORMATION AND PROPERTIES                               |    |
| M. L. Busurina, A. E. Sytshev, D. Yu. Kovalev, N. V. Sachkova, A. V. Karpov, A. N. Gryadunov, V. A. Shcherbakov ..... | 69 |
| THERMITE SYNTHESIS OF NANOCOMPOSITE $Co-In_2O_3$ AND $Fe-In_2O_3$ FILMS   |    |
| L. E. Bykova, V. G. Myagkov, V. S. Zhigalov, A. A. Matsynin .....   | 72 |
| PREPARATION OF POROUS NIOBIUM-ALUMINUM INTERMETALLIC BY COMBUSTION SYNTHESIS IN THERMAL EXPLOSION MODE                |    |
| X. Cai, P. Feng .....   | 74 |
| COMBUSTION SYNTHESIZED MATERIALS FOR ELECTROCHEMICAL APPLICATIONS   |    |
| K.-Y. Chan, A. A. Voskanyan, C.-K. Ho, L. Wang, W. Y. Lam, C.-Y. V. Li, B. Qin .....                                  | 78 |
| SOLUTION COMBUSTION SYNTHESIS OF CARBON-BASED POROUS NANOMATERIALS FOR EFFICIENT ELECTROCHEMICAL APPLICATIONS         |    |
| P. W. Chen, C. X. Xu, K. Y. Liu, X. Gao .....   | 80 |
| SELF-PROPAGATING HIGH-TEMPERATURE SYNTHESIS AND SPARK PLASMA SINTERING OF TUNGSTEN ALLOYS FOR FUSION APPLICATIONS     |    |
| S. Dine, E. Bernard, C. Grisolia, N. Herlin, D. Vrel .....  | 82 |
| SHS AND SPS CONSOLIDATION OF COMPLEX COMPOSITIONAL REFRACTORY ALLOYS  |    |
| S. Dine, V. Kentheswaran, G. Dirras, D. Vrel .....  | 84 |

|  |     |
|--|-----|
| NEW MATERIALS PREPARED BY ARRESTED REACTIVE MILLING AND MECHANISMS OF THEIR IGNITION AND COMBUSTION  |     |
| E. L. Dreizin, M. Schoenitz, K. L. Chintersingh, M. Mursalat, S. K. Valluri, D. Hastings .....   | 85  |
| EFFECT OF DOPING ON THE ALLOY CHEMISTRY OF NICKEL BASED SUPERALLOYS FROM COUPLING FIRST PRINCIPLES CALCULATIONS AND ADVANCED CHARACTERIZATIONS   |     |
| J. Du .....  | 88  |
| Fe, Ti, AND Ni ALUMINIDS FOR MODIFICATION OF POWDER ANTIFRICTION MATERIALS   |     |
| L. N. Dyachkova, A. Ph. Ilyushenko, L. Ya. Voronetskaya, N. M. Parnitsky .....   | 92  |
| STRUCTURE AND PROPERTIES OF BORON CARBIDE PRODUCED BY SHS AND MECHANOCHEMICAL SYNTHESIS: A COMPARATIVE STUDY   |     |
| Zh. V. Ereemeeva, S. Vorotilo, V. S. Panov, L. V. Myakisheva, A. I. Lizunov, A. A. Nepapushev, D. A. Sidorenko, D. Y. Mishunin .....   | 96  |
| SELF-PROPAGATING HIGH-TEMPERATURE SYNTHESIS OF TITANIUM CARBIDE  |     |
| T. Ergul, U. Cinarli, M. Bugdayci, A. Turan .....  | 99  |
| STRUCTURAL-PHASE TRANSFORMATIONS IN LOCALIZATION ZONES OF PLASTIC DEFORMATION OF Ti–Al COMPOSITE   |     |
| T. V. Fadeev, A. K. Abkaryan, G. M. Zeer, M. N. Volochaev, I. V. Nemtsev, L. I. Kveglis.....   | 102 |
| VIBROACOUSTIC MONITORING OF THE INTERMETALLIC PHASES FORMATION IN SURFACE ALLOYING USING ELECTRON-BEAM TECHNOLOGY  |     |
| S. V. Fedorov, M. P. Kozochkin, Thein Htoo Maung, and Min Htet Swe .....   | 105 |
| TRENDS OF MATERIALS RESEARCH   |     |
| R. Fellenberg .....  | 109 |
| POROUS INTERMETALLICS PREPARED BY THERMAL EXPLOSION  |     |
| P. Feng, X. Cai, X. Jiao, Z. Li, C. Sang .....   | 112 |
| THE PROCESSES OF STRUCTURE FORMATION IN THE MECHANICALLY ACTIVATED POWDER MIXTURE Ti + Al SUBJECTED TO $\gamma$ -IRRADIATION   |     |
| V. Yu. Filimonov, M. V. Loginova, S. G. Ivanov, A. A. Sitnikov, V. I. Yakovlev, A. V. Sobachkin, A. Z. Negodyaev, A. Yu. Myasnikov, A. V. Gradoboev, B. P. Tolochko, M. R. Sharafutdinov ..... | 116 |
| CHARACTERISTICS OF THE CAPILLARY SPREADING OF COPPER ON THE POROUS FRAMEWORK OF THE PRODUCTS OF THE SHS MIXTURE OF Ni–Al   |     |
| R. M. Gabbasov, A. M. Shulpekoy, V. D. Kitler .....  | 119 |
| HIGH TEMPERATURE GAS EXTRUSION OF POWDER MIXTURE Ni + Al   |     |
| F. F. Galiev, I. V. Saikov, M. I. Alymov, V. D. Berbentsev, A. V. Gulyutin, V. I. Bugakov, N. V. Sachkova, and S. V. Konovalikhin .....  | 122 |
| THE MECHANICAL ACTIVATION OF METALLIC POWDER, AN ESSENTIAL ROUTE TO PREPARE DENSE NANOSTRUCTURED MATERIALS BY SPS  |     |
| S. Le Gallet, F. Bernard.....  | 124 |
| SYNTHESIS OF MAX PHASE Ti <sub>2</sub> AlN BY SPARK PLASMA SINTERING OF Ti/AlN COMPOSITE POWDERS OBTAINED BY MECHANICAL ACTIVATION   |     |
| V. G. Gilev, M. N. Kachenyuk, A. A. Smetkin, S. A. Oglezneva .....   | 126 |
| GENERATION OF SELF-PROPAGATING HIGH-TEMPERATURE SYNTHESIS ON THE SURFACE OF SINTERED TITANIUM SPONGE POROUS SAMPLES IN A THIN LAYER BY ELECTRIC IMPULSE  |     |
| R. P. Golodok, V. V. Savich, S. V. Poberezhny, O. O. Kuznechik, E. G. Grigoriev .....  | 129 |

|   |     |
|---|-----|
| SHS OF TITANIUM–CHROMIUM CARBIDES: INFLUENCE OF GREEN COMPOSITION   |     |
| O. A. Golosova, P. A. Miloserdov, V. A. Gorshkov, O. M. Miloserdova .....   | 134 |
| HIGH-TEMPERAURE SYNTHESIS OF CAST CERAMIC MATERIALS BASED ON Cr <sub>2</sub> AlC MAX PHASE IN LAYERED AND MIXED SYSTEMS   |     |
| V. A. Gorshkov, P. A. Miloserdov, V. I. Yukhvid, N. Yu. Khomenko, N. V. Sachkova.....   | 136 |
| REACTIVE FORGING – PROCESSING OF DENSE MATERIALS AND PARTS WITH FINE MICROSTRUCTURE BY PRESSURE ASSISTED SHS  |     |
| E. Y. Gutmanas, I. Gotman .....   | 139 |
| MILL SCALE WASTE REPROCESSING BY CENTRIFUGAL METALLOTHERMIC SHS FOR PRODUCTION OF CAST FERROALLOYS Fe–(Si; Si–Al; B; B–Al)  |     |
| D. M. Ikornikov, V. N. Sanin, D. E. Andreev, V. I. Yukhvid.....   | 140 |
| SHS POWDERS FOR THERMAL SPRAY COATINGS  |     |
| A. Ph. Ilyushenko, P. A. Vityaz, T. L. Talako, A. I. Letsko .....   | 144 |
| STUDIES ON THE PORE FORMATION MECHANISM OF POROUS TiAl <sub>3</sub> INTERMETALLICS BY COMBUSTION SYNTHESIS  |     |
| X. Jiao, P. Feng .....  | 146 |
| Ta-CONTAINING MATERIALS BY SHS  |     |
| O. K. Kamynina, S. G. Vadchenko, A. S. Shchukin, V. G. Salamatov .....  | 150 |
| PRODUCTION OF SPHERICAL MICROPOWDER OF THE HIGH-TEMPERATURE STRENGHT NiAl-BASED ALLOY USING COMBUSION SYNTHESIS AND THEIR APPLICATION IN THE SELECTIVE LASER MELTING TECHNOLOGY |     |
| Yu. Yu. Kaplanskii, E. A. Levashov, Zh. A. Sentyurina, P. A. Loginov, A. V. Korotitskiy, E. I. Patsera.....   | 153 |
| INFLUENCE OF ADDITIVES ON PHYSICO-MECHANICAL PROPERTIES OF HIGH STRENGTH ALUMINOSILICATE REFRACTORY SHS MATERIALS   |     |
| R. D. Kapustin.....   | 156 |
| SHS OF Al <sub>x</sub> CoCrFeNi HIGH-ENTROPY ALLOYS   |     |
| F. Kaya, B. Derin.....  | 158 |
| HISTORY AND DEVELOPMENT PROSPECTS OF THE KAZAKHSTAN SCHOOL OF CHEMICAL PHYSICS  |     |
| T. A. Ketegenov .....   | 160 |
| MULTIFUNCTIONAL BORON NANOPARTICLS: AN ECOLOGICAL METHOD OF PRODUCTION, PROPERTIES  |     |
| P. A. Khaptakhanova, S. A. Uspenskii, T. S. Kurkin, A. N. Zelenetskii, S. Yu. Taskaev.....  | 162 |
| PREPARATION OF Mo–Cu PSEUDOALLOY FROM CuMoO <sub>4</sub> PRECURSOR BY COMBINING SOL-GEL METHOD AND SHS  |     |
| H. Kirakosyan, K. Nazaretyan.....   | 165 |
| PLASMA-CHEMICAL ACTIVATION OF SHS IN EXTERNAL ELECTRIC FIELDS   |     |
| A. I. Kirdyashkin, R. M. Gabbasov .....   | 169 |
| THE Cr–B–C–N FILMS PRODUCED BY PULSED CATHODE-ARC EVAPORATION (P-CAE) OF THE CrB <sub>2</sub> ROD MANUFACTURED USING SHS-COMPACTING   |     |
| Ph. V. Kiryukhantsev-Korneev .....  | 173 |
| STRUCTURE AND PROPERTIES OF h-ZrB <sub>2</sub> AND h-ZrB <sub>2</sub> /a-BN COATINGS DEPOSITED BY MAGNETRON SPUTTERING OF THE SHS-TARGETS                                       |     |
| Ph. V. Kiryukhantsev-Korneev, A. Kozlova, N. S. Kozlova, E. A. Levashov .....   | 174 |



|  |     |
|--|-----|
| HIGH-TEMPERATURE Mo–(Zr,Hf)–Si–B COATINGS DEPOSITED USING SHS-PRECURSORS   |     |
| Ph. V. Kiryukhantsev-Korneev, T. A. Sviridova, N. V. Shvindina, E. A. Levashov .....   | 175 |
| MECHANICAL ALLOYING WITH PARTIAL AMORPHIZATION OF Fe–Cr–Co–Ni–Mn MULTICOMPONENT POWDER MIXTURE AND ITS SPARK PLASMA SINTERING FOR COMPACT HIGH-ENTROPY MATERIAL PRODUCTION |     |
| N. A. Kochetov, A. S. Rogachev, A. S. Shchukin, S. G. Vadchenko, I. D. Kovalev .....   | 176 |
| PREPARATION OF CHROMIUM POWDER AND ITS COMPOSITE WITH TUNGSTEN FROM COMPLEX OXIDES BY MAGNESIUM VAPOURS REDUCTION  |     |
| V. N. Kolosov, M. N. Miroshnichenko, T. Yu. Prokhorova .....   | 178 |
| REDUCTION OF OXIDE COMPOUNDS OF TUNGSTEN AND MOLYBDENUM BY CALCIUM VAPOURS   |     |
| V. N. Kolosov, V. M. Orlov, M. N. Miroshnichenko .....   | 182 |
| AN X-RAY POWDER DIFFRACTION STUDY OF NEW CRYSTAL Ni <sub>3.35</sub> W <sub>9.65</sub> C <sub>4</sub>   |     |
| S. V. Konovalikhin, N. Yu. Khomenko, I. I. Chuev, S. A. Guda, S. L. Silyakov, D. Yu. Kovalev .....   | 187 |
| NONSTATIONARY COMBUSTION OF LAYERED HETEROGENEOUS SYSTEMS  |     |
| S. V. Kostin, P. M. Krishenik, S. A. Rogachev, A. E. Sytshev .....   | 189 |
| SYNTHESIS OF NEW MIXED NIOBIUM–TUNGSTEN OXIDE BRONZES  |     |
| M. K. Kotvanova, I. A. Sologubova .....  | 193 |
| SYNTHESIS OF METAL OXIDE RADICALS IN ROTATING REACTOR WITH ALUMINOTHERMIC FLAME  |     |
| G. I. Ksandopulo .....   | 195 |
| APPLICATION OF SHS-ELECTRODE MATERIALS IN PULSED ELECTROSPARK DEPOSITION TECHNOLOGY  |     |
| A. E. Kudryashov, E. A. Levashov .....   | 199 |
| FEATURES OF DEPOSITION, STRUCTURE AND PROPERTIES OF ELECTROSPARK COATINGS OF Cr–Al–B–Si, Mo–Si–B AND Zr–Si–B ON NICKEL ALLOY   |     |
| A. E. Kudryashov, E. A. Levashov, Ph. V. Kiryukhantsev-Korneev, A. N. Sheveiko .....   | 202 |
| APPLICATION OF SHS-ELECTRODE MATERIALS IN METALLURGY   |     |
| A. E. Kudryashov, A. V. Makarov, N. I. Repnikov, E. M. Martynov .....  | 206 |
| DEVELOPMENT OF FUNCTIONALLY GRADED WEAR-RESISTANT WC/a-C COATINGS BY A COMBINATION OF PULSED ARC EVAPORATION AND ELECTROSPARK DEPOSITION                                   |     |
| K. A. Kuptsov, A. N. Sheveyko, D. A. Sidorenko, D. V. Shtansky .....   | 208 |
| ADVANCED ULTRA-HIGH-TEMPERATURE COMPOSITES BASED ON SHS-SINGLE PHASE SOLID SOLUTION (Hf,Ta)B <sub>2</sub>  |     |
| V. V. Kurbatkina, E. I. Patsera, E. A. Levashov .....  | 209 |
| FABRICATION OF Al–AlN NANOCOMPOSITE BY POWDER METALLURGY METHOD USING AlN NANOPOWDER OF SHS-AZ BRAND   |     |
| A. A. Kuzina, A. P. Amosov, D. A. Zakharov, Yu. V. Titova .....  | 211 |
| SYNTHESIS OF METAL-LIKE REFRACTORY COMPOUNDS AND ULTRA-HIGH-TEMPERATURE MATERIALS IN MOLTEN SALTS  |     |
| S. A. Kuznetsov, V. S. Dolmatov, A. R. Dubrovskiy, Yu. V. Stulov .....   | 215 |
| FILTRATION COMBUSTION OF SiF <sub>4</sub> AND CaH <sub>2</sub> IN VERTICAL FLOW REACTOR  |     |
| A. Yu. Lashkov, A. D. Bulanov, O. Yu. Troshin .....  | 218 |

|  |     |
|--|-----|
| COMBUSTION SYNTHESIS AND CONSOLIDATION OF (Zr/Hf)B <sub>2</sub> –(Zr/Hf)Si <sub>2</sub> –MoSi <sub>2</sub><br>POWDER CERAMICS FOR HIGH-TEMPERATURE PROTECTIVE COATINGS |     |
| M. V. Lemesheva, Yu. S. Pogozhev, A. Yu. Potanin, S. I. Rupasov, V. I. Vershinnikov,<br>E. A. Levashov .....   | 220 |
| NON-ISOTHERMAL SYNTHESIS OF NANOLAMINATES  |     |
| O. K. Lepakova, N. I. Afanasyev, A. M. Shulpekov,<br>V. D. Kitler.....   | 223 |
| RECENT ADVANCES AND APPROACHES IN SHS OF HIGH-TEMPERATURE<br>MATERIALS (OVERVIEW)  |     |
| E. A. Levashov .....   | 227 |
| SOLUTION COMBUSTION SYNTHESIS OF N-DOPED NiO/Ni@C COMPOSITE<br>NANOMATERIALS AND ITS ELECTROCHEMICAL PERFORMANCE AS ANODE<br>MATERIAL OF LITHIUM/SODIUM ION BATTERIES  |     |
| Y. Y. Li, C. X. Xu, K. Y. Liu, P. W. Chen .....  | 231 |
| LASER TECHNOLOGY IN SYNTHESIS AND PROCESSING OF SHS DERIVED MAX<br>MATERIALS   |     |
| J. Lis, P. Rutkowski, D. Kata, L. Chlubny, D. Sala .....   | 233 |
| FABRICATION OF TiC–TiB <sub>2</sub> COMPOSITE CERAMIC BY SELF-PROPAGATING<br>HIGH-TEMPERATURE SYNTHESIS  |     |
| K. Y. Liu, Y. Y. Li, P. W. Chen.....   | 235 |
| PROPERTIES AND CHARACTERISTICS OF UFG OF NICKEL FOR DIFFUSION WELDING OF<br>HETEROGENEOUS MATERIALS  |     |
| A. V. Liushinskii .....  | 236 |
| MECHANICAL AND ADHESIVE PROPERTIES OF TITANIUM DOPED Fe–Co–Ni<br>BINDER FOR DIAMOND CUTTING TOOL   |     |
| P. A. Loginov, D. A. Sidorenko, E. A. Levashov .....   | 239 |
| STRUCTURE AND PROPERTIES OF ALLOYED COMPOSITES Al–TiC FABRICATED<br>BY SHS METHOD  |     |
| A. R. Lutz, A. P. Amosov, E. I. Latukhin, A. D. Rybakov, S. I. Shipilov .....  | 242 |
| MA SHS AS A KINETIC PHENOMENON   |     |
| N. Lyakhov, T. Grigorieva, M. Korchagin.....   | 246 |
| COMBUSTION IN OILY COPPER WASTE–NiO–NH <sub>4</sub> NO <sub>3</sub> SYSTEM & SYNTHESIS OF<br>Cu–Ni ALLOY   |     |
| H. A. Mahmoudi, L. S. Abovyan, V. V. Vardapetyan,<br>S. L. Kharatyan.....  | 247 |
| COMBUSTION OF TiO <sub>2</sub> /ZrO <sub>2</sub> –Ca THERMITE MIXTURES IN NITROGEN   |     |
| Yu. M. Maksimov, A. N. Avramchik, B. Sh. Braverman,<br>A. M. Shulpekov .....   | 250 |
| OBTAINING OF COMPOSITE MATERIALS BY SHOCK-WAVE TREATMENT AND<br>SHS  |     |
| A. Yu. Malakhov, I. V. Saikov, V. G. Salamatov,<br>S. A. Seropyan.....   | 252 |
| KINETIC FEATURES OF NICKEL OXIDE REDUCTION BY METHANE AT NON<br>ISOTHERMAL CONDITIONS  |     |
| S. Mamyán, H. A. Chatilyan, S. L. Kharatyan .....  | 254 |
| MULTILAYER TiN <sub>2</sub> C COATINGS PRODUCED BY A COMBINATION OF PULSED<br>ARC EVAPORATION AND ELECTRO-SPARK DEPOSITION IN VACUUM                                   |     |
| O. S. Manakova, K. A. Kuptsov, A. N. Sheveyko, D. V. Shtansky,<br>D. A. Sidorenko.....   | 257 |

|  |     |
|--|-----|
| THE ROLE OF MECHANOCHEMICAL TREATMENT IN THE DEVELOPMENT OF SH-SYNTHESIS AND OBTAINING COMPOSITION SYSTEMS OF DIFFERENT PURPOSES               |     |
| Z. A. Mansurov, N. N. Mofa, B. S. Sadykov, A. Ye. Bakkara .....  | 259 |
| CURRENT STATE AND FUTURE PROSPECTS OF SOLUTION COMBUSTION SYNTHESIS  |     |
| Kh. Manukyan.....  | 263 |
| SHS OF MACROPOROUS NiAl ALLOYS USED IN ADVANCED RADIANT BURNERS  |     |
| A. Maznoy, A. Kirdyashkin, V. Kitler, N. Pichugin,<br>V. Salamatov .....   | 264 |
| SYNTHESIS OF COMPOSITE MATERIALS IN THE Ti–Cr–B SYSTEM FROM MIXTURES BASED ON CALCIUM CHROMATES  |     |
| P. A. Miloserdov, V. A. Gorshkov, O. M. Miloserdova, O. A. Golosova .....  | 269 |
| YESTERDAY, TODAY AND TOMORROW CHALLENGES FOR SHS   |     |
| Y. Miyamoto .....  | 272 |
| SH-SYNTHESIS OF CERAMIC MATERIALS BASED ON PRE-ACTIVATED AND MODIFIED SYSTEMS  |     |
| N. N. Mofa, B. S. Sadykov, G. Kaiypbek, T. B. Osserov, D. Shaltykova .....   | 274 |
| EVALUATION OF THE HOMOGENEITY OF POWDER COMPOSITIONS FOR SELF-PROPAGATING HIGH-TEMPERATURE SYNTHESIS USING SPECTRAL ANALYSIS METHODS           |     |
| V. V. Mokrushin, O. Yu. Zabrodina, A. A. Potekhin, I. A. Tsareva, A. Yu. Postnikov,<br>M. V. Tsarev, P. G. Berezhko .....                      | 278 |
| REACTION SPARK PLASMA SINTERING OF BINARY AND HIGH-ENTROPY CARBIDES  |     |
| D. O. Moskovskikh, A. S. Mukasyan .....  | 281 |
| ELIMINATION OF SURFACE DEFECTS OF SLM PRODUCTS DUE TO A SYNTHESIS OF NiAl INTERMETALLIC AT ELECTRO-SPARK DEPOSITION OF Al-CONTAINING PRECURSOR |     |
| S. K. Mukanov, M. I. Petrzhik, A. E. Kudryashov, E. A. Levashov .....  | 282 |
| SHS CERAMICS: HISTORY AND RECENT ADVANCES  |     |
| A. S. Mukasyan.....  | 287 |
| THE EXCLUSIVE ROLE OF THE INITIATION TEMPERATURE IN THE START OF NANOSCALE SOLID-STATE REACTIONS   |     |
| V. G. Myagkov.....   | 292 |
| THE INITIATION TEMPERATURES IN NANOTHERMITE REACTIONS  |     |
| V. G. Myagkov.....   | 294 |
| REACTIVE ROUNDED Ti/Al COMPOSITE POWDERS PRODUCED BY HIGH-ENERGY BALL MILLING FOR SELECTIVE LASER MELTING TECHNOLOGY                           |     |
| A. A. Nepapushev, D. O. Moskovskikh, V. S. Buinevich, S. G. Vadchenko,<br>A. S. Rogachev.....  | 296 |
| MORPHOLOGICAL DIVERSITY OF METAL NITRIDES CRYSTALS: SYNTHESIS, CHARACTERIZATION AND THEORETICAL MODELING                                       |     |
| H. H. Nersisyan, W. B. Kim, J. H. Lee .....  | 299 |
| STRUCTURE AND PHASE COMPOSITION OF Nb–Si–C-BASED COMPOSITES PREPARED BY SHS METHOD   |     |
| R. M. Nikonova, N. S. Larionova, V. I. Lad’yanov, B. E. Pushkarev,<br>A. V. Panteleyeva.....   | 301 |
| SHS IN A MELT OF Al–TiC(B) COMPOSITES  |     |
| R. M. Nikonova, A. V. Panteleyeva, V. I. Lad’yanov .....   | 304 |

|   |     |
|---|-----|
| ADVANCED COMBUSTION SYNTHESIS FOR HIGH PERFORMANCE MATERIALS AND POWER SYSTEMS DEVELOPMENTS   |     |
| O. Odawara.....   | 307 |
| FORMATION OF STRUCTURE OF SHS- AND MA-POWDERS $Ti_3SiC_2$ BY SPS  |     |
| S. A. Oglezneva, T. L. Talako, A. A. Smetkin, A. I. Letsko,<br>M. N. Kachenyuk .....  | 310 |
| EXOTHERMIC HYDROGENATION KINETICS OF MG WITH CATALYTIC DISSOCIATION OF MOLECULAR HYDROGEN   |     |
| M. Ohyanagi, Y. Shimizu, M. Otowaki, K. Shirai.....   | 312 |
| CAPACITOR GRADE POWDERS FROM SCRAP OF TANTALUM CAPACITORS PRODUCTS  |     |
| V. M. Orlov, T. Yu. Prokhorova, E. N. Kiselev.....  | 314 |
| COMBINATION OF SHS AND SPS PROCESSING ROUTES FOR ADVANCED CERAMICS  |     |
| R. Orrù, G. Tallarita, R. Licheri, G. Cao.....  | 317 |
| HEAT-RESISTANT PHOSPHATE MATERIALS IN SELF-PROPAGATING EXOTHERMIC SYNTHESIS MODE  |     |
| Ch. G. Pak, V. M. Batrashov, G. A. Koshkin,<br>K. V. Sokolova .....   | 320 |
| PRODUCTION OF ULTRA-REFRACTORY CARBIDES OF VARIOUS STOICHIOMETRIES IN THE SYSTEMS Ta–Zr–C, Ta–Hf–C BY SHS                             |     |
| E. I. Patsera, S. A. Vorotilo, V. V. Kurbatkina, E. A. Levashov .....   | 322 |
| CHEVREL PHASE COMPOUND NANOMATERIALS SYNTHESIS VIA ULTRA-FAST SELF-PROPAGATING HIGH TEMPERATURE SYNTHESIS REACTION                    |     |
| M. Pawar, P. Gouma .....  | 325 |
| CONSOLIDATION OF SHS DERIVED SiC BASED COMPOSITES   |     |
| Z. Pędzich, K. Wojteczko, A. Wojteczko, A. Gubernat,<br>M. M. Bućko .....   | 327 |
| APPLICATION OF HARDMETAL ELECTRODE MATERIALS IN PULSED ELECTROSPARK DEPOSITION TECHNOLOGY   |     |
| T. G. Penyashki, M. I. Petrzhhik, A. E. Kudryashov .....  | 329 |
| RARE EARTH OXIDES TRANSPARENT CERAMICS BASED ON THE SHS-DERIVED POWDERS   |     |
| D. A. Permin, S. S. Balabanov, E. M. Gavrishchuk, A. V. Novikova, Ye. E. Rostokina,<br>S. V. Filofeev, V. A. Koshkin .....            | 332 |
| SHOCK COMPACTION AND SINTERING OF Ni POWDERS: INFLUENCE OF $Y_2O_3$ –CoO CONTAINING OXIDE FILMS                                       |     |
| O. L. Pervukhina, A. S. Shishkina.....  | 334 |
| INVESTIGATION OF THE EFFECT OF METAL POWDERS ON THE SURFACE OF THE TARGET SUBJECTED TO HIGH ENERGY TREATMENT                          |     |
| E. V. Petrov, V. S. Trofimov.....   | 336 |
| REACTIVE PHASE FORMATION BY ELECTROSPARK DEPOSITION   |     |
| M. I. Petrzhhik, A. E. Kudryashov, E. I. Zamulaeva .....  | 339 |
| HIERARCHICALLY-STRUCTURED HIGH-TEMPERATURE $ZrB_2$ –MoB–MoSi <sub>2</sub> CERAMICS PRODUCED BY DIFFERENT SHS ROUTES AND SUBSEQUENT HP |     |
| Yu. S. Pogozhev, M. V. Lemesheva, A. Yu. Potanin, S. I. Rupasov, V. I. Vershinnikov,<br>E. A. Levashov .....                          | 340 |
| MILLION-ATOM MOLECULAR DYNAMICS SIMULATIONS OF EXPLOSIVE CRYSTALLIZATION IN AMORPHOUS CuTi THIN FILMS                                 |     |
| O. Politano, S. A. Rogachev, F. Baras, A. S. Rogachev .....   | 344 |

|   |     |
|---|-----|
| STRUCTURE FORMATION AT CONSECUTIVE PORTION PACKING OF MONODISPERSED GRANULES IN SQUARE MATRICES WITH SMOOTH AND PROFILED BOTTOM                                     |     |
| M. A. Ponomarev, V. E. Loryan .....   | 347 |
| SYNTHESIS OF POROUS MATERIAL FROM MIXTURES OF BORON, TITANIUM, AND NICKEL-CLAD ALUMINUM COMPOSITE POWDERS (NPA75-80)  |     |
| M. A. Ponomarev, V. E. Loryan .....   | 351 |
| ANTIBACTERIAL PROPERTIES OF TiCaPCON COATING DOPED WITH Pt AND Fe DEPOSITED USING SHS TARGETS   |     |
| V. A. Ponomarev, A. N. Sheveyko, S. G. Ignatov, J. Polčák, D. V. Shtansky .....   | 355 |
| APPLICATION OF SHS FOR PRODUCTION OF COMPOSITE CERAMIC CATHODES FOR PVD OF HIGH-TEMPERATURE PROTECTIVE Mo–(Hf/Zr)–Si–B COATINGS                                     |     |
| A. Yu. Potanin, Ph. V. Kiryukhantsev-Korneev, S. I. Rupasov, Yu. S. Pogozhev, E. A. Levashov .....  | 357 |
| THE KINETICS AND MECHANISMS OF HIGH-TEMPERATURE OXIDATION OF HEAT-RESISTANT MoSi <sub>2</sub> –MoB–HfB <sub>2</sub> CERAMICS PRODUCED BY HYBRID SHS + HP TECHNOLOGY |     |
| A. Yu. Potanin, S. Vorotilo, Yu. S. Pogozhev, P. V. Loginov, E. A. Levashov .....   | 359 |
| SELF-PROPAGATING HIGH-TEMPERATURE SYNTHESIS OF METAL MATRIX COMPOSITE POWDERS FROM MECHANOACTIVATED POWDER MIXTURES   |     |
| G. A. Pribytkov, A. V. Baranovskii, M. G. Krinitsyn, V. V. Korzhova, E. N. Korosteleva .....  | 362 |
| SYNTHESIS AND APPLICATION OF SHS COMPOSITE POWDERS OF THE TITANIUM BORIDE–TITANIUM SYSTEM   |     |
| G. A. Pribytkov, M. G. Krinitsyn, V. V. Korzhova, I. A. Firsina .....   | 364 |
| 2D DISCRETE MODEL OF THE MULTICOMPONENT SHS PROCESS   |     |
| V. G. Prokof'ev .....   | 368 |
| EFFECT OF THERMOCAPILLARY FLOW OF MELT ON COMBUSTION OF A BINARY GASLESS MIXTURE  |     |
| V. G. Prokof'ev, A. I. Kirdyashkin, V. D. Kitler, O. V. Lapshin .....   | 372 |
| SELF-SUSTAINING REACTIONS AT NANOSCALE  |     |
| J. A. Puszynski .....   | 374 |
| HIGH ENERGY BALL MILLING OF SHS MIXTURES: MECHANISMS AND OPPORTUNITIES  |     |
| A. S. Rogachev, S. G. Vadchenko, N. A. Nepapushev, D. O. Moskovskikh .....  | 375 |
| MOLECULAR DYNAMICS SIMULATION OF REFRACTORY COMPOUNDS AND METHODS OF THEIR SYNTHESIS  |     |
| S. A. Rogachev .....  | 377 |
| THE ROLE OF MICROWAVES IN THE IGNITION OF LOW-EXOTHERMIC SYSTEMS: THE CASE OF Ni–Ti INTERMETALLICS  |     |
| R. Rosa, L. Trombi, C. Milioli, F. Cugini, A. Casagrande, C. Leonelli, P. Veronesi .....  | 378 |
| SOLUTION COMBUSTION SYNTHESIS OF NANOSTRUCTURED METASTABLE NITRIDES AND INTERMETALLICS  |     |
| S. I. Roslyakov, A. S. Mukasyan, Kh. V. Manukyan .....  | 380 |
| ENERGY INTENSITY OF SOLID FUEL SYSTEMS WITH MECHANICALLY ACTIVATED ALUMINUM   |     |
| B. S. Sadykov, A. Ye. Bakkara, L. Galfetti, K. S. Zhamanbalinova, N. Meirbekov, N. N. Mofa .....  | 383 |

|  |     |
|--|-----|
| <b>SHOCK-WAVE TREATMENT OF REACTIVE POWDERS</b>  |     |
| I. V. Saikov, S. G. Vadchenko, I. D. Kovalev, M. I. Alymov.....  | 387 |
| <b>TEMPERATURE MEASUREMENTS OF THE COMBUSTION WAVE BY DYNAMIC SPECTROMETRY</b>   |     |
| V. G. Salamatov, A. I. Kirdyashkin, V. D. Kitler .....   | 390 |
| <b>CENTRIFUGAL ASSISTED SHS SURFACING OF CoCrFeNiMnAl<sub>x</sub> HIGH ENTROPY ALLOY ON Ti ALLOY SUBSTRATE</b>   |     |
| V. N. Sanin, D. M. Ikornikov, O. A. Golosova, D. E. Andreev,<br>V. I. Yuxhvid.....   | 391 |
| <b>CENTRIFUGAL CASTING–SHS PROCESS OF THE CAST CoCrFeNiMn-TYPE HIGH-ENTROPY ALLOY HARDENED BY THERMOMECHANICAL TREATMENT AND THE INTRODUCTION OF SILICON–BORIDE HARDENERS</b>  |     |
| V. N. Sanin, D. M. Ikornikov, O. A. Golosova, D. E. Andreev, V. I. Yuxhvid,<br>S. V. Zherebtsov .....  | 394 |
| <b>COMBINED METHOD OF PRODUCING AN ALLOY OF IMMISCIBLE ELEMENTS Cu<sub>70</sub>Fe<sub>30</sub> WITH SUBMICRON STRUCTURAL COMPONENTS</b>  |     |
| V. V. Sanin, M. R. Filonov, Yu. A. Anikin, E. V. Kosticina, V. I. Yuxhvid,<br>D. M. Ikornikov.....   | 398 |
| <b>SHS BORON-CONTAINING LIGATURES, INTRODUCTION INTO THE MELT AND THE RESEARCH OF INFLUENCE ON THE PROPERTIES OF THE RESULTING ALUMINUM-MATRIX COMPOSITES</b>  |     |
| V. V. Sanin, M. R. Filonov, Yu. A. Anikin, V. I. Yuxhvid, D. M. Ikornikov .....  | 402 |
| <b>INTEGRATED PROCESS SHS-REMELTING-PREP FLOW SHEET PRODUCTION OF NiAl–Fe COMPOSITE MICROGRANULES FOR THE ADDITIVE TECHNOLOGY</b>  |     |
| V. V. Sanin, M. R. Filonov, E. A. Levashov, V. I. Yuxhvid, Zh. A. Sentyurina,<br>A. I. Logacheva .....   | 405 |
| <b>SOLUTION COMBUSTION SYNTHESIS OF DOPED Ca<sub>2</sub>AlMnO<sub>5</sub> AS A NEW OXYGEN STORAGE MATERIAL</b>   |     |
| A. Sato, G. Saito, K. Abe, T. Nomura, T. Akiyama.....  | 408 |
| <b>THE STUDY OF HIGH-ENTROPY CERAMICS Hf<sub>0.2</sub>Ta<sub>0.2</sub>Ti<sub>0.2</sub>Nb<sub>0.2</sub>Mo<sub>0.2</sub>C AND Hf<sub>0.2</sub>Ta<sub>0.2</sub>Ti<sub>0.2</sub>Nb<sub>0.2</sub>Zr<sub>0.2</sub>C OBTAINED BY SHS AND SPARK PLASMA SINTERING</b> |     |
| A. Sedegov, S. Vorotilo, V. Tsybulin, K. Kuskov, D. Moscovskikh, S. Vadchenko,<br>A. Mukasyan .....  | 412 |
| <b>PEROVSKITE-LIKE MATRIX FOR IMMOBILIZATION OF HIGH-LEVEL RADIOACTIVE WASTE PRODUCED BY SHS METHOD</b>  |     |
| A. O. Semenov, M. S. Kuznetsov, O. Yu. Dolmatov.....   | 415 |
| <b>THERMALLY COUPLED PROCESSES IN A COMPOSITE GRANULAR MIXTURE (Ni + Al)–(Ti + C)</b>  |     |
| B. S. Seplyarskii, R. A. Kochetkov, T. G. Lisina, N. I. Abzalov .....  | 418 |
| <b>THE IMPLEMENTATION OF THE CONVECTIVE MODE OF COMBUSTION FOR GRANULAR MIXTURES OF Ti + xC</b>  |     |
| B. S. Seplyarskii, R. A. Kochetkov, T. G. Lisina, M. I. Alymov.....  | 421 |
| <b>NI–AL BASED REACTIVE MATERIAL: MECHANICAL PROPERTIES AND FEATURES OF COMBUSTION</b>   |     |
| S. A. Seropyan, I. V. Saikov, V. G. Salamatov, M. I. Alymov, A. V. Dolmatov,<br>P. Yu. Gulyaev .....   | 424 |
| <b>EXOTHERMIC SYNTHESIS AND CONSOLIDATION OF Ta<sub>4</sub>ZrC<sub>5</sub> COMPOSITE</b>   |     |
| V. A. Shcherbakov, A. N. Gryadunov, S. G. Vadchenko, M. I. Alymov .....  | 426 |
| <b>BEHAVIOURS OF ELECTROTHERMAL EXPLOSION OF TITANIUM–CARBON BLACK MIXTURE UNDER QUASI-ISOSTATIC COMPRESSION</b>   |     |
| V. A. Shcherbakov, A. V. Shcherbakov.....  | 429 |

|  |     |
|--|-----|
| THE METASTABLE PHASE COMPOSITION OF FeTiB FILMS PRODUCED BY MAGNETRON SPUTTERING   |     |
| E. N. Sheftel, Ph. V. Kiryukhantsev-Korneev, V. A. Tedzhetov, E. V. Harin, G. Sh. Usmanova.....  | 432 |
| FORMATION OF TiC/C LAYER ON Ti ALLOYS BY A SIMULTANEOUS ELECTRO-SPARK AND ARC EVAPORATION TREATMENT WITH GRAPHITE ELECTRODE  |     |
| A. N. Sheveyko, K. A. Kuptsov, A. E. Kudryashov, D. V. Shtansky.....   | 434 |
| EVOLUTION OF THE STRUCTURAL CONDITION OF REACTION POWDER MIXTURES OF THE Ti–Ni SYSTEM UNDER MECHANICAL ACTIVATION. THEORETICAL ESTIMATES BASED ON EXPERIMENTAL STUDIES |     |
| O. A. Shkoda, O. V. Lapshin .....  | 435 |
| STRUCTURAL EVOLUTION AND MAGNETIC PROPERTIES OF HIGH ENTROPY CuCrFeTiNi ALLOYS PREPARED BY MECHANICAL ALLOYING AND SPS   |     |
| N. F. Shkodich, M. Spasova, M. Farle, D. Yu. Kovalev, A. A. Nepapushev, K. V. Kuskov, Yu. S. Vergunova, Yu. B. Scheck, A. S. Rogachev .....                            | 438 |
| SHS IN SURFACE ENGINEERING   |     |
| D. V. Shtansky .....   | 440 |
| SELF-PROPAGATING HIGH-TEMPERATURE SYNTHESIS OF HEAT-RESISTANT ELECTRICALLY CONDUCTIVE COATINGS BASED ON Ni–Al AND Ti–Al–C SYSTEM COMPOUNDS                             |     |
| A. M. Shulpekov, R. M. Gabbasov, O. K. Lepakova.....   | 443 |
| MODIFYING OF THE STAINLESS STEEL POROUS SURFACE BY NANOSTRUCTURED ALUMINA  |     |
| V. V. Shustov, V. A. Zelensky, A. B. Ankudinov .....   | 446 |
| HYBRID POWDER BINDERS FOR EXTRA WEAR RESISTANT DIAMOND CUTTING TOOLS   |     |
| D. A. Sidorenko, P. A. Loginov, E. A. Levashov .....   | 449 |
| SHS METALLURGY OF THE HARD ALLOY ON THE BASIS OF TUNGSTEN CARBIDE WITH THE NICKEL BOND   |     |
| S. L. Silyakov, V. I. Yukhvid, N. Yu. Khomenko, T. I. Ignat'eva, N. V. Sachkova.....   | 450 |
| FEATURES OF GRAIN STRUCTURE AT SHS EXTRUSION FOR MATERIAL BASED ON TiC + Co  |     |
| L. S. Stelmakh, A. M. Stolin, P. M. Bazhin .....   | 454 |
| PRODUCTION OF COMPOSITE CERAMIC MATERIALS AND PRODUCTS BY COMBINED USE OF SHS AND HIGH-TEMPERATURE SHEAR DEFORMATION   |     |
| A. M. Stolin.....  | 457 |
| FILTRATION COMBUSTION OF TITANIUM–ALUMINUM–NITROGEN TERNARY SYSTEM IN FLOW-TYPE REACTOR  |     |
| I. A. Studenikin, A. V. Linde, A. A. Kondakov, V. V. Grachev .....   | 458 |
| HIGH THERMOELECTRIC PERFORMANCE OF p-BiSbTe COMPOUNDS PREPARED BY ULTRA-FAST THERMALLY INDUCED REACTION  |     |
| X. Su, Y. Yan, X. Tang .....   | 462 |
| PUBLISHER SUPPORTS TRANSFER FROM RESEARCH TO APPLICATION   |     |
| R. Suchentrunk .....   | 463 |
| COMBUSTION SYNTHESIS AND STRUCTURE FORMATION IN Ni–Al–C SYSTEM   |     |
| A. E. Sytshev, N. A. Kochetov, A. S. Shchukin, M. L. Busurina, A. V. Aborkin.....  | 464 |
| SHS SYNTHESIS OF THERMOELECTRIC MATERIALS: THERMODYNAMIC CRITERION FOR COMBUSTION SYNTHESIS  |     |
| X. Tang, X. Su, Y. Yan .....   | 467 |

|   |     |
|---|-----|
| <b>PECULIARITIES OF TECHNOLOGICAL PARAMETERS OF SHS-ELECTRICAL ROLLING</b>  |     |
| G. Tavadze, T. Namicheishvili, G. Oniashvili, A. Tutberidze, Z. Aslamazashvili, G. Zakharov .....   | 468 |
| <b>SHS OF CERAMIC NITRIDE–CARBIDE NANOPOWDER COMPOSITIONS OF <math>\text{Si}_3\text{N}_4</math>–<math>\text{SiC}</math> AND <math>\text{AlN}</math>–<math>\text{SiC}</math> WITH THE USE OF SODIUM AZIDE AND HALIDE SALTS</b> |     |
| Yu. V. Titova, A. P. Amosov, D. A. Maidan, G. S. Belova, I. A. Uvarova .....  | 471 |
| <b>SHS OF BN NANOPOWDER USING BORON-CONTAINING COMPOUNDS AND SODIUM AZIDE</b>   |     |
| Yu. V. Titova, A. P. Amosov, D. A. Maidan, D. R. Safaeva, M. V. Suslov, D. V. Ostroukhov .....  | 475 |
| <b>MICROWAVE ASSISTED COMBUSTION SYNTHESIS OF <math>\text{AlFe}_2\text{B}_2</math></b>  |     |
| L. Trombi, F. Cugini, R. Rosa, P. Veronesi, M. Solzi, C. Leonelli .....   | 479 |
| <b>METAL FOAMS FABRICATED BY SPRAY SOLUTION COMBUSTION SYNTHESIS AND SPARK PLASMA SINTERING</b>   |     |
| G. V. Trusov, A. B. Tarasov, D. O. Moskovskih, A. S. Rogachev, A. S. Mukasyan .....   | 480 |
| <b>APPLICATION OF RESISTOMETRY AND IMPEDANCE SPECTROSCOPY METHODS TO STUDY MIXING OF POWDER MIXTURES FOR SHS</b>  |     |
| M. V. Tsarev, V. V. Mokrushin, K. V. Korshunov, A. M. Shapovalov, A. Yu. Postnikov, I. A. Tsareva, O. Yu. Zabrodina, D. G. Ivanov, Ye. V. Zabavin, A. Ye. Kanunov .....   | 482 |
| <b>Ni–Cr–Al–Mg CATALYSTS PREPARED BY SOLUTION COMBUSTION SYNTHESIS FOR CATALYTIC REFORMING OF METHANE INTO SYNTHESIS GAS</b>  |     |
| S. A. Tungatarova, G. Xanthopoulou, G. N. Kaumenova, T. S. Baizhumanova .....   | 486 |
| <b>FABRICATION OF ALUMINUM-CERAMIC SKELETON COMPOSITES BASED ON TITANIUM ALUMINIDE CARBIDE USING SHS PROCESS</b>  |     |
| E. R. Umerov, A. P. Amosov, E. I. Latukhin, P. E. Kichaev, V. A. Novikov .....  | 489 |
| <b>MAGNETIC PROPERTIES OF POWDER <math>\text{Fe-30Cr-(8-16)Co}</math> ALLOYS OBTAINED BY LOW-TEMPERATURE SINTERING</b>  |     |
| A. S. Ustyukhin, V. A. Zelenskii, I. M. Milyaev, M. I. Alymov, S. F. Zabelin .....  | 493 |
| <b>SYNTHESIS OF SHS MEMBRANES BASED ON MICA-LIKE STRUCTURE MATERIALS FOR LIQUID AND GAS FILTRATION</b>  |     |
| V. I. Uvarov, A. R. Kachin, V. E. Loryan, V. S. Shustov, M. V. Tsodikov .....   | 496 |
| <b>CLAD POWDERS BY COMBINED USE OF METAL REDUCTION AND HIGH-ENERGY BALL MILLING IN SALT SOLUTIONS: THEIR PREPARATION AND IGNITION</b>   |     |
| S. G. Vadchenko .....   | 499 |
| <b>EXPERIMENTAL 2D MODEL OF HETEROGENEOUS COMBUSTION</b>  |     |
| S. G. Vadchenko, E. V. Suvorova, A. S. Rogachev .....   | 501 |
| <b>SYNTHESIS OF THE <math>\text{Ti}_2\text{AlC}</math> AND <math>\text{Ti}_3\text{AlC}_2</math> MAX PHASE WITH A REDUCTION STEP VIA COMBUSTION OF A <math>\text{TiO}_2 + \text{Mg} + \text{Al} + \text{C}</math> MIXTURE</b>  |     |
| V. I. Vershinnikov, D. Yu. Kovalev .....  | 504 |
| <b>HYBRID SURFACE ENGINEERING TECHNOLOGIES FOR SELF-ADAPTIVE FRICTION AND WEAR BEHAVIOR IN EXTREME ENVIRONMENTS</b>   |     |
| A. A. Voevodin .....  | 508 |



|  |     |
|--|-----|
| <b>SYNTHESIS AND CHARACTERIZATION OF BN/Pt AND BN/Au NANOHYBRIDS AS PERSPECTIVE CATALYSTS</b>  |     |
| I. N. Volkov, A. M. Kovalkii, D. V. Shtansky.....  | 513 |
| <b>SHS OF SOLID SOLUTIONS IN Ta–Zr–C SYSTEM: MACROKINETIC FEATURES, PHASE/STRUCTURE FORMATION, AND PHASE STABILITY</b>   |     |
| S. Vorotilo, E. A. Levashov, K. Sidnov, E. I. Patsera.....   | 515 |
| <b>ULTRAFINE-GRAINED BORON CARBIDE CERAMICS FABRICATED VIA ULTRAFAST SHS-QP SINTERING ASSISTED BY HIGH-ENERGY BALL MILLING</b>   |     |
| W. Wang, Z. Zhang, Z. Fu, H. Wang, J. Zhang, W. Ji.....  | 517 |
| <b>PIONEER RESEARCH AND BREAKTHROUGHS CPI IN THE FIELD OF SHS CATALYSTS, PIGMENTS AND TPS FOR SPACE APPLICATION THAT INITIATED NEW COMBUSTION SYNTHESIS RESEARCH DIRECTIONS IN THE WORLD</b>                                       |     |
| G. Xanthopoulou, G. Ksandopulo.....  | 520 |
| <b>DENDRIC 3-DIMENTIONAL STRUCTURE COMBUSTION, FLAME BIFURCATION IN REPETITIVE EXTINCTION-IGNITION DYNAMICS, LIQUID PHASE SINTERING - A NEW COMPREHENSIVE REACTION MECHANISM FOR SCS IN CONDITIONS OF NANO-SCALE HETEROGENEITY</b> |     |
| G. Xanthopoulou, O. Thoda, S. Roslyakov, E. Levashov, G. Vekinis .....   | 525 |
| <b>ONE-STEP ULTRA-RAPID FABRICATION OF BULK THERMOELECTRIC MATERIALS VIA SELF-PROPAGATING HIGH-TEMPERATURE SYNTHESIS COMBINED WITH IN-SITU QUICK PRESSING</b>  |     |
| Y. Yan, T. Hu, X. Su, W. Liu, X. Tang .....  | 529 |
| <b>SOLID SOLUTION PRECIPITATION MECHANISM AND MICROSTRUCTURE EVOLUTION OF Al<sub>2</sub>O<sub>3</sub>/ZrO<sub>2</sub> NANOCOMPOSITE CERAMICS</b>   |     |
| Y. Yu, Y. Zheng, W. Yu, X. Su, B. Liu, F. Lin .....  | 530 |
| <b>PRODUCTION OF METALS AND ALLOYS THROUGH VACUUM METALLOTHERMIC PROCESS</b>   |     |
| O. Yucel, K. C. Tasyurek, M. Bugdayci, A. Turan.....   | 532 |
| <b>SHS METALLURGY OF COMPOSITE MATERIALS BASED ON REFRACTORY METALS</b>  |     |
| V. I. Yuxhvid, D. E. Andreev, Yu. S. Vdovin, S. L. Silyakov, N. V. Sachkova, I. D. Kovalev .....   | 537 |
| <b>NEAR-NANO AND COARSE-GRAIN WC POWDERS OBTAINED BY THE SHS AND CEMENTED CARBIDES ON THEIR BASIS</b>  |     |
| A. A. Zaitsev, E. A. Levashov, V. I. Vershinnikov, I. Konyashin, E. I. Patsera.....  | 540 |
| <b>W–Ag NANOCOMPOSITE PREPARATION BY COMBINING SCS AND SHS</b>   |     |
| M. K. Zakaryan, A. A. Baldryan, S. L. Kharatyan.....   | 543 |
| <b>JOINT REDUCTION OF NiO + WO<sub>3</sub> OXIDES BY COMBINED Mg/C REDUCER. SYNERGETIC EFFECT</b>  |     |
| M. K. Zakaryan, Kh. T. Nazaretyan, S. V. Aydinyan, S. L. Kharatyan.....  | 546 |
| <b>COMPARISON OF THE INFLUENCE OF VIBRATION AND CENTRIFUGAL FORCES FOR THE FORMATION OF HARD ALLOYS</b>  |     |
| G. Zakharov, Z. Aslamazashvili, G. Tavadze, G. Oniashvili, T. Batsikadze, D. Kvashkvadze .....   | 549 |
| <b>METALLOTHERMIC SHS OF ALLOYED COMPOSITES BASED ON Co</b>  |     |
| K. V. Zakharov, D. E. Andreev, V. I. Yuxhvid, N. V. Sachkova, N. Yu. Khomenko .....  | 552 |
| <b>SELF-PROPAGATING HIGH-TEMPERATURE SYNTHESIS OF α-Si<sub>3</sub>N<sub>4</sub> WITH PARTICIPATION OF SODIUM HALOGENIDES</b>   |     |
| V. V. Zakorzhevsky, N. I. Mukhina, I. D. Kovalev .....   | 553 |

|  |     |
|--|-----|
| STRUCTURE AND PROPERTIES OF ANTIBACTERIAL YET BIOCOMPATIBLE<br>Ag-DOPED MULTICOMPONENT COATINGS OBTAINED BY PULSED<br>ELECTROSPARK DEPOSITION USING SHS-ELECTRODES ..... | 556 |
| E. I. Zamulaeva, A. Yu. Potanin, A. N. Sheveyko, N. A. Gloushankova, N. V. Shvindina,<br>S. G. Ignatov, E. A. Levashov, D. V. Shtansky .....                             | 556 |
| HARD-MAGNETIC MATERIAL FROM A MECHANOACTIVATED SPHERICAL<br>POWDER OF THE ALLOY 25XK15ЮБ   |     |
| V. A. Zelensky, V. S. Shustov, A. B. Ankudinov, I. M. Milyaev, M. I. Alymov.....   | 558 |
| SOLID-STATE REACTIONS IN Al-BASED MULTILAYER NANOSYSTEMS   |     |
| S. M. Zharkov, R. R. Altunin, E. T. Moiseenko .....  | 561 |
| COMBUSTION SYNTHESIS OF COMPOSITION ALLOYS   |     |
| M. Kh. Ziatdinov .....   | 563 |
| OBTAINING CARBON-CONTAINING COMPOSITES BASED ON ILMENITE AND<br>CHROME CONCENTRATE BY SHS  |     |
| S. Tolendiuly, S. M. Fomenko, A. Akishev, N. Rakhym, D. Kashkynbai.....  | 565 |
| APPLICATION of MICROVAWE RADIATION IN HETEROGENEOUS CATALYSIS  |     |
| A. Zurnachyan, D. Davtyan, E. Karakhanov, A. Akopyan, R. Mnatsakanyana.....  | 568 |
| <br>   |     |
| <i>Author Index</i> .....  | 570 |

## SH-SYNTHESIS OF POWDERS BASED ON TRANSITION METAL BORIDES

R. G. Abdulkarimova<sup>\*a</sup>, A. J. Seidualiyeva<sup>a</sup>, and K. Kamunur<sup>a</sup><sup>a</sup>Al-Farabi Kazakh National University, Almaty, 050038 Kazakhstan

\*e-mail: abdulkarimovaroza@mail.ru

DOI: 10.24411/9999-0014A-2019-10001

New materials creation with different properties and level of quality based on widely used raw materials, including man-made, is currently determined by the tasks of scientific and technological progress. One of the main sources of boron ores in Kazakhstan are borates from the Inder deposit. These wide available raw materials can be used to obtain boron-containing refractory powder materials [1–3]. Popular methods of producing such materials are characterized by high energy consumption and high labor intensity. The use of self-propagating high-temperature synthesis (SHS) is currently one of the most effective approaches for creating new materials. An important role in obtaining materials in SHS mode is played by preliminary mechanochemical activation (MA), which allows achieving a high degree of particle dispersion and changing the structure, energy intensity, and high reactivity of the material [4].

To obtain samples of refractory powders of transition metal borides were prepared from a mixture containing powdered titanium dioxide, chromium oxide, enriched borate ore from the Inder deposit (boron oxide content up to 40%), and magnesium powder. Preliminary mechanical activation of samples was carried out in a Pulverisette 5 high-energy planetary-centrifugal mill. Green mixtures were prepared with a stoichiometric ratio of components.

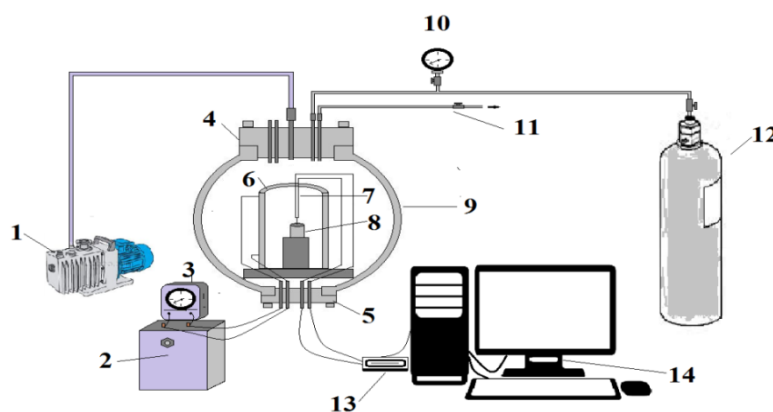
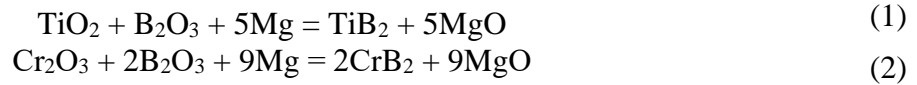


Fig. 1. High pressure reactor: 1 vacuum pump, 2 transformer, 3 ammeter, 4 upper reactor lid, 5 lower reactor lid, 6 tubular heating furnace, 7 thermocouple, 8 sample, 9 reactor vessel, 10 pressure gauge, 11 exhaust valves, 12 balloon with argon, 13 data acquisition system block LTR U 1, 14 computer.

To carry out SH-synthesis in order to obtain refractory powders of titanium and chromium borides, the systems  $\text{TiO}_2\text{--B}_2\text{O}_3(\text{ore})\text{--Mg}$  and  $\text{Cr}_2\text{O}_3\text{--B}_2\text{O}_3(\text{ore})\text{--Mg}$  were selected. Experiments were performed in a high-pressure reactor (Fig. 1). After SH-synthesis, the obtained powders were leached with hydrochloric acid and washed with distilled water. X-ray phase analysis of samples was performed by a DRON-4M diffractometer using  $\text{CoK}$  radiation in the interval  $2\theta = 10^\circ\text{--}70^\circ$ . The morphology of the obtained samples was studied by scanning electron microscopy (QUANTA 3D 200i, FEI, USA).

The synthesis of titanium and chromium diborides took place in the following reactions in the combustion wave:



The preliminary MA mixture was used. It is known that MA in a high-energy planetary mill contributes to a decrease in the powder particle size and an increase in the reactivity of components during SHS [3]. The phase composition of titanium products and chromiferous systems after SHS process and treatment with hydrochloric acid was investigated.

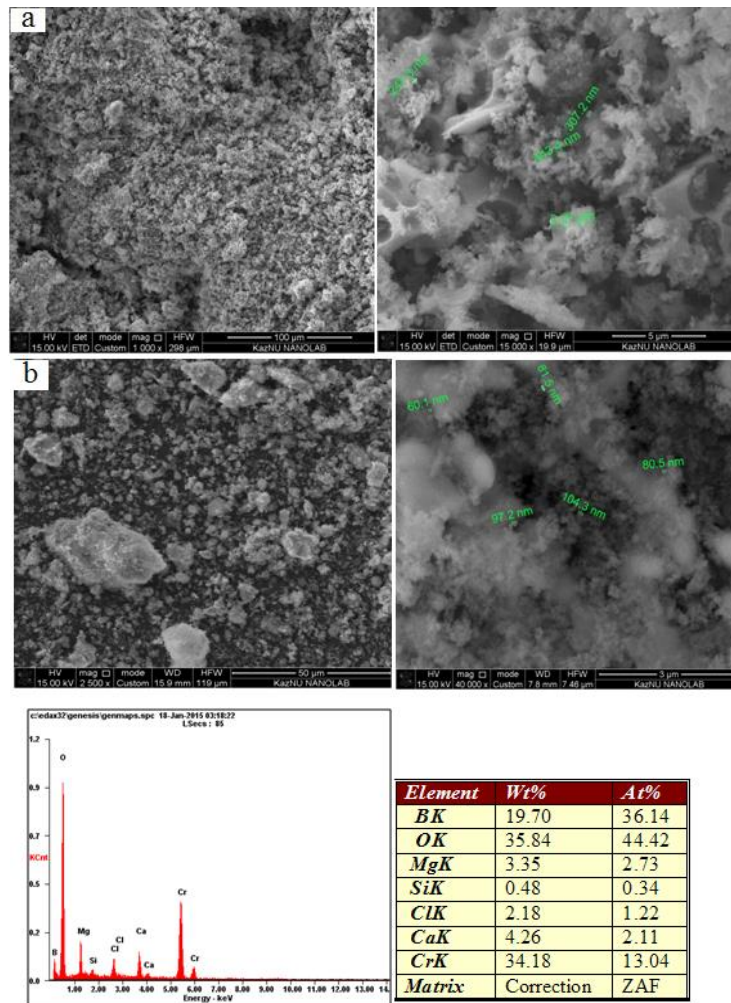


Fig. 2. Microstructure of SHS products of the  $\text{Cr}_2\text{O}_3\text{--B}_2\text{O}_3(\text{ore})\text{--Mg}$  system: (a) without MA, (b) MA for 5 min.

SEM studies showed the formation of crystal phases of combustion products of the  $\text{Cr}_2\text{O}_3\text{--B}_2\text{O}_3\text{--Mg}$  system (Fig. 2) without and with MA (nanoparticles). Similar results were obtained for the system  $\text{TiO}_2 + \text{B}_2\text{O}_3(\text{ore}) + \text{Mg}$ .

Thus, it is shown that the combined use of MA and SHS makes it possible to obtain submicron and nano-sized powder of titanium diboride (up to 98.2%), chromium diboride (up to 98.6%).

It is established that the use of MA contributes to the formation of nanoscale particles of refractory powders of titanium and chromium borides.

1. D.S. Raimkhanova, R.G. Abdulkarimova, Z.A. Mansurov, Research of nanostructure formation during SHS of boride containing composite materials, *J. Mater. Sci. Chem. Eng.*, 2014, vol. 2, pp. 66–69.
2. R.G. Abdulkarimova, S.M. Fomenko, S. Tolendiuly, et al, SH-synthesis of boron-containing multifunctional composite materials, *J. Combust. Plasma Chem.*, 2016, vol. 14, no. 4, pp. 310–319.
3. M.D. Diyarov, D.A. Kalicheva, S.V. Meshcheryakov, The natural wealth of Inder and their use, Alma–Ata: Science, 1981, 102 p.
4. A.E. Sytshev, A.G. Merzhanov, Self-propagating high-temperature synthesis of nanomaterials, *Successes Chem.*, 2004, vol. 73, no. 2, pp. 157–170.

## RAPID-HEATING-TYPE COMBUSTION SYNTHESIS OF METALLIC IRON: EFFECTS OF TEMPERATURE AND ATMOSPHERE

K. Abe<sup>\*a</sup>, A. Kurniawan<sup>a</sup>, M. Sanada<sup>a</sup>, T. Nomura<sup>a</sup>, and T. Akiyama<sup>a</sup>

<sup>a</sup>Hokkaido University, Sapporo, Hokkaido, 060-8628, Japan

\*e-mail: k\_abe@eng.hokudai.ac.jp

DOI: 10.24411/9999-0014A-2019-10002

### INTRODUCTION

CO<sub>2</sub> emission from the iron and steel industry accounts for around 9% of total CO<sub>2</sub> emission in the world [1]. Direct ironmaking method using carbon-infiltrated iron oxides has been focused on to reduce the amount of CO<sub>2</sub> emission from the industry [2]. For reduction of the carbon-infiltrated goethite ore, the distance between iron ore and carbon is important; closer contact makes the reduction faster.

Goethite ( $\alpha$ -FeOOH) based iron ore has been utilized as an alternative raw material to high-grade iron ore in the iron and steel industry. It is decomposed to Fe<sub>2</sub>O<sub>3</sub> and H<sub>2</sub>O by mild calcination, and interestingly, nanopores form in the product Fe<sub>2</sub>O<sub>3</sub> [3]. Carbon-infiltrated goethite ore has been prepared using tar vapor as a carbon source [4]. The ore was reduced at lower temperatures because carbon was deposited through the nanopores of the ore and close (nano-order) contact between ore and carbon was achieved [5].

Combustion synthesis (CS) is a simple and short-time method to synthesize a product using combustion reaction. We have already reported that carbon-infiltrated goethite ore had been obtained by tar impregnation/carbonization method and that metallic iron had generated from the carbon-infiltrated goethite ore after rapid-heatig-type CS experiment in an oxygen flow [6]. Metallic iron was partially obtained by the short-time experiments, however, the reduction degree is still not so high. The effects of temperature and oxygen concentration in the CS experiments on reduction degree were investigated in this study.

### EXPERIMENTAL

Goethite-based iron ore (particle size: 1–2 mm, total Fe: 57 mass%, combined water: 8.8 mass%) was firstly calcined at 573 K for 24 h in a muffle furnace in air. Liquid carbon source was prepared from coal-tar (fixed carbon: 32 mass%, ash: 0.04 mass%, moisture: 0.15 mass%) and reagent toluene (99.5%). The coal tar and the toluene (1:1 in weight) were well-mixed using magnetic stirrer at 323 K for 1 h to make tar solution. The calcined goethite ore (3.0 g) and the tar solution (6.0 g) were put in an alumina crucible and it was heated at 773 K for 1 h under an Ar flow (0.5 L min<sup>-1</sup>) to get carbon-infiltrated goethite ore. After that, it was crushed into original ore size: 1–2 mm.

100 mg of the obtained carbon-infiltrated goethite ore were charged into a quartz tube ( $\phi$  6) [6]. The ore was rapidly heated up to 973–1173 K at a heating rate of 20 K s<sup>-1</sup> and was held at the temperatures for 10 s. O<sub>2</sub>/Ar gases (total flow rate; 1 L min<sup>-1</sup>, oxygen concentration; 15–100 vol %) were flowed from the top of the tube during the heating. The gas flow was immediately changed to Ar after the finish of the heating process.

Phase identification of the samples was conducted using X-ray diffractometry (XRD; Miniflex, Rigaku, Tokyo, Japan). The surface and the cross-section of the samples were observed by scanning electron microscopy (SEM; JSM-7001FA, JEOL, Tokyo, Japan) with energy dispersive X-ray spectroscopy (EDS).

## RESULTS AND DISCUSSIONS

Figure 1 shows the cross-sectional SEM and EDS observations of the carbon-infiltrated goethite ore. Carbon-infiltrated goethite ore with a thick carbon layer at the surface of the ore was successfully obtained by the tar treatment. Figure 2 shows the XRD patterns of the carbon-infiltrated goethite ores after the CS experiments at different heating temperatures. Despite the total heating time in the CS experiments was below one minute, reduction partially proceeded to metallic iron. Metallic iron was observed at all heating temperatures, and the reduction degree was the highest in the sample which was heated at 1073 K. Figure 3 shows the temperature changes during the CS experiments. Measurements of temperature changes during the experiments were conducted by an R-type thermocouple placed directly over the ore-bed. The temperatures measured during the experiments were much higher than the setting ones at every holding temperature. This meant carbon combustion successfully occurred at the surface of the ores. Combustion of the surface carbon started at around 973 K; sudden temperature increases were observed near the temperature. When the holding temperature was higher (1123 or 1173 K), carbon combustion started before the temperature holding and was completed before the heating process finished. This meant that almost all of the surface carbon disappeared during heating and ore-surface was exposed to oxygen, causing re-oxidation of the reduced ore at high holding temperatures. At 973 K, the temperature continued to increase until the end of the heating process, meaning carbon combustion was not completed during the experiment. Re-oxidation was ignored at this condition, however, reduction was not proceeded because the maximum temperature (1164 K) was much lower than the other conditions. At 1073 K, surface carbon remained during the experiment and the reached temperature was very high, resulting in the highest reduction degree.

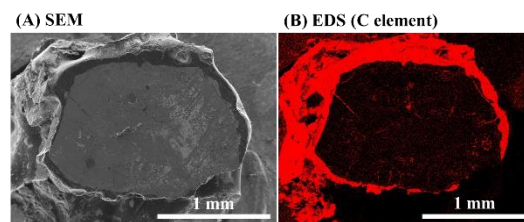


Fig. 1. SEM-EDS images of the cross-section of the obtained carbon-infiltrated goethite ore.

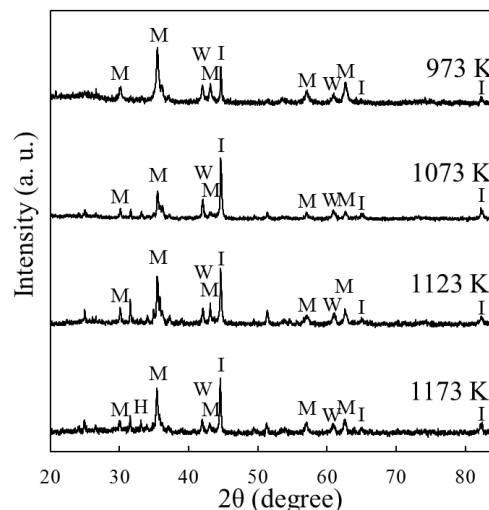


Fig. 2. XRD patterns of the carbon-infiltrated goethite ore after the rapid-heating-type CS experiments at different temperatures.

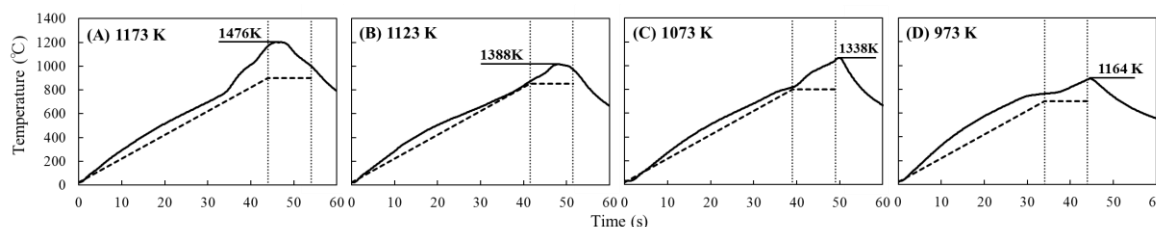


Fig. 3. Temperature changes during the rapid-heating-type CS experiments. The dotted lines mean setting temperatures and the solid lines mean the measured temperatures.

Figure 4 shows the XRD patterns of the carbon-infiltrated goethite ores after the CS experiments at different oxygen concentrations. Metallic iron was not observed when the flowed gases had higher oxygen concentrations (50 and 100 vol % O<sub>2</sub>). Carbon combustion

completed in a moment at high oxygen concentration and iron ore was easily exposed to oxygen, resulting in the lower reduction degree. At lower oxygen concentrations, carbon combustion reaction continued until heating process finished. The iron ore was effectively reduced without re-oxidation at lower oxygen concentrations.

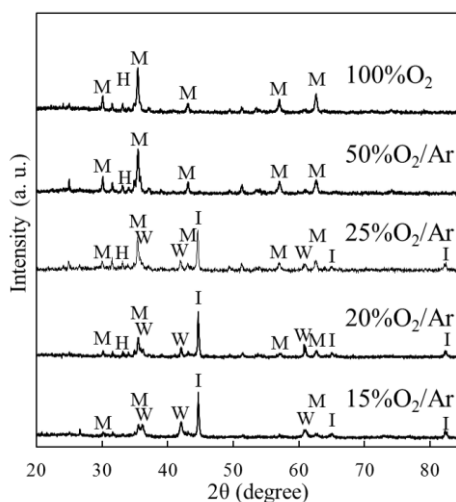


Fig. 4. XRD patterns of the carbon-infiltrated goethite ore after the rapid-heating-type CS experiments flowing 15–100 vol % O<sub>2</sub>/Ar gases.

## CONCLUSIONS

In this study, carbon-infiltrated goethite ore was produced by tar impregnation/carbonization method, and it was reduced via rapid-heating-type combustion synthesis process flowing oxygen gas. The surface carbon of the goethite ore worked not only as heat source for reduction of the ore but also as protective coat against oxidation. At higher temperatures and higher oxygen concentrations, carbon combustion completed early and oxidation of the ore by the flowing oxygen could not be prevented, resulting in lower reduction degree. At optimum condition, carbon combustion effectively promoted reduction of the ore and all of the surface carbon did not disappear, resulting in higher reduction degree.

1. International Energy Agency (IEA), CO<sub>2</sub> emissions from fuel combustion, 2016.
2. C. Xu, D. Cang, A brief overview of low CO<sub>2</sub> emission technologies for iron and steel making, *J. Iron Steel Res. Int.*, 2010, vol. 17, no. 3, pp. 1–7.
3. H. Naono, R. Fujiwara, Micropore formation due to thermal decomposition of acicular microcrystals of  $\alpha$ -FeOOH, *J. Colloid Interface Sci.*, 1980, vol. 73, no. 2, pp. 406–415.
4. Y. Hata, H. Purwanto, S. Hosokai, J. Hayashi, Y. Kashiwaya, T. Akiyama, Biotar ironmaking using wooden biomass and nanoporous iron ore, *Energy Fuels*, 2009, vol. 23, no. 2, pp. 1128–1131.
5. S. Hosokai, K. Matsui, N. Okinaka, K. Ohno, M. Shimizu, T. Akiyama, kinetic study on the reduction reaction of biomass-tar-infiltrated iron ore, *Energy Fuels*, 2012, vol. 26, no. 12, pp. 7274–7279.
6. K. Abe, A. Kurniawan, K. Ohashi, T. Nomura, T. Akiyama, ultrafast iron-making method: carbon combustion synthesis from carbon-infiltrated goethite ore, *ACS Omega*, 2018, vol. 3, no. 6, pp. 6151–6157.



## SELF-PROPAGATING HIGH-TEMPERATURE SYNTHESIS OF Fe<sub>2</sub>VAl-BASED THERMOELECTRIC MATERIALS

K. Abe<sup>\*a</sup>, N. Okinaka<sup>a</sup>, and T. Akiyama<sup>a</sup>

<sup>a</sup>Hokkaido University, Sapporo, Hokkaido, 060-8628, Japan

\*e-mail: k\_abe@eng.hokudai.ac.jp

DOI: 10.24411/9999-0014A-2019-10003

### INTRODUCTION

Thermoelectric conversion is a promising candidate among various heat recovery methods for the next generation. Thermoelectric materials have been recently focused for direct conversion from thermal energy to electric one by Seebeck effect. Thermoelectric properties are commonly evaluated using the dimensionless figure of merit  $ZT$ :

$$ZT = S^2T/\rho\kappa \quad (1)$$

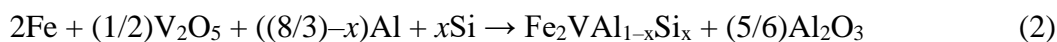
where  $Z$  is the figure of merit ( $K^{-1}$ ),  $S$  is the Seebeck coefficient ( $VK^{-1}$ ),  $T$  is the absolute temperature (K),  $\rho$  is the electric resistivity ( $\Omega m$ ), and  $\kappa$  is the thermal conductivity ( $Wm^{-1}K^{-1}$ ). To improve the thermoelectric properties, higher Seebeck coefficient (absolute value), and lower electrical resistivity and thermal conductivity are needed.

Fe<sub>2</sub>VAl has been focused as environment-friendly-material because it contains relatively plentiful and non-toxic elements. Theoretically, SHS method to produce Fe<sub>2</sub>VAl is much better than a conventional one because of lower energy consumption [1]. We already reported the possibility of producing Fe<sub>2</sub>VAl using self-propagating high-temperature synthesis (SHS) [2]. During SHS, the products melted and macroscopically separated into two parts (Fe<sub>2</sub>VAl and Al<sub>2</sub>O<sub>3</sub>) due to gravity [2]. To improve its thermoelectric properties of the SHSed Fe<sub>2</sub>VAl, ball-milling treatment and substitution of fourth element can be the effective ways. This is because after ball-milling and sintering, the grain size decreases and the thermal conductivity decreases by the effect of phonon scattering. Substitution of a fourth element such as Si significantly increases its Seebeck coefficient.

The purpose of this study is to improve the thermoelectric properties of SHSed Fe<sub>2</sub>VAl by substitution of Si to Al-site and post-treatment of ball-milling and SPS.

### EXPERIMENTAL

The following thermite reaction was used for SHS in this study:



Here,  $x$  is molar substitution ratio of Si to Al site ( $x = 0-0.10$ ).

Commercially available powders of Fe (3–5  $\mu m$ ), V<sub>2</sub>O<sub>5</sub> (75  $\mu m$ ), Al (3  $\mu m$ ), and Si (45  $\mu m$ ) were weighed and then they were well mixed for 1 h before the SHS experiment. Next, the resulting mixture was placed in a vertically-placed graphite crucible and a carbon foil igniter was put on the powders. The powders were electrically flashed at a room temperature in an argon atmosphere, as shown in Fig. 1.

The products were fragmented to particles below 300  $\mu m$  and then the particles were milled with a planetary ball-milling system using stainless balls in a stainless pot at a ball-to-sample mass ratio of 10:1. The ball-milling was conducted for 12 h at 350 rpm. The milled samples

were finally SPSeD at 1273 K for 1 min in vacuum at a uniaxial pressure of 25 MPa. Thermoelectric properties were evaluated using a Seebeck coefficient/electrical resistance measurement system (ZEM-3, ULVAC-RIKO, Yokohama, Japan) and a laser flash thermal constant analyzer (TC-7000, ULVAC-RIKO, Yokohama, Japan).

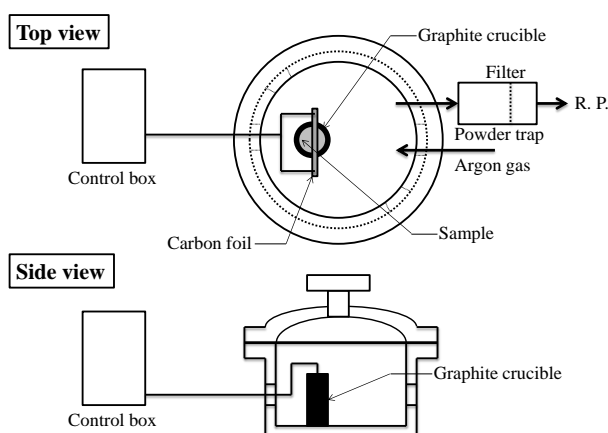


Fig. 1 Schematic image of the SHS apparatus.

## RESULTS AND DISCUSSIONS

The calculated adiabatic flame temperatures for Eq. (2) were 2327 K at every  $x$  value. This temperature corresponds to the melting point of  $\text{Al}_2\text{O}_3$ , meaning that  $\text{Al}_2\text{O}_3$  was partially molten during SHS. The melting point of  $\text{Fe}_2\text{VAl}$  is around 1800 K, implying all  $\text{Fe}_2\text{VAl}_{1-x}\text{Si}_x$  products were molten during SHS.

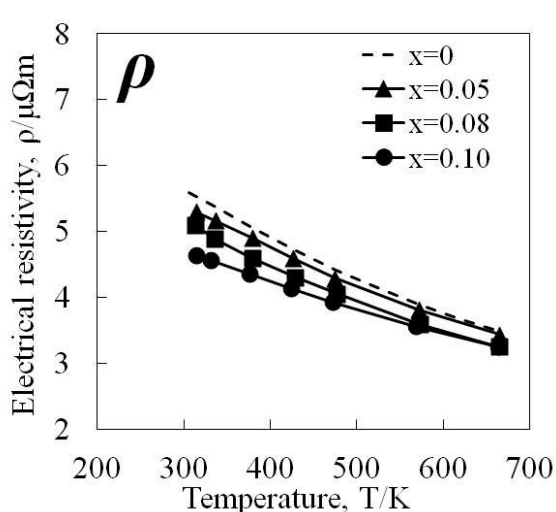


Fig. 2. Electrical resistivity ( $\rho$ ) of the SHSed  $\text{Fe}_2\text{VAl}_{1-x}\text{Si}_x$ .

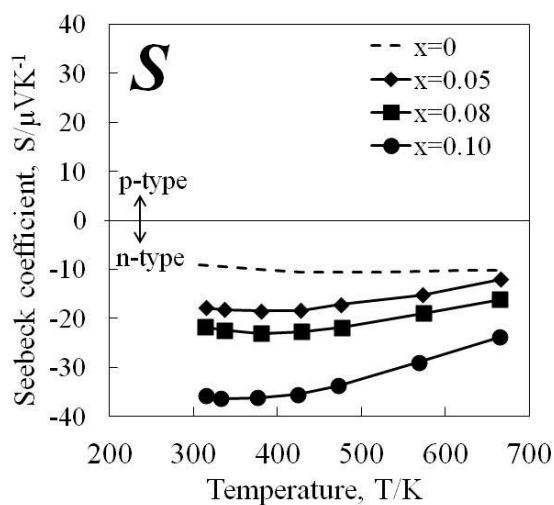


Fig. 3 Seebeck coefficient ( $S$ ) of the SHSed  $\text{Fe}_2\text{VAl}_{1-x}\text{Si}_x$ .

Figure 2 shows the temperature dependence of the electrical resistivity of SHSed  $\text{Fe}_2\text{VAl}_{1-x}\text{Si}_x$ . The electrical resistivity decreased with temperature increasing because of its semiconductor-like tendency. When the fraction of Si increased, the electrical resistivity decreased. In  $\text{Fe}_2\text{VAl}_{1-x}\text{Si}_x$ , the dominant carrier is electron and substitution of Si to the Al position increased the number of carrier because Si has four and Al has three valence electrons. The electrical resistivity is inversely proportional to the carrier concentration, so the electrical resistivity decreased as  $x$  value increased.

Figure 3 shows the temperature dependence of the Seebeck coefficient of SHSed  $\text{Fe}_2\text{VAl}_{1-x}\text{Si}_x$ . Generally, Si-substituted  $\text{Fe}_2\text{VAl}_{1-x}\text{Si}_x$  is n-type (negative Seebeck coefficient)

thermoelectric material [3]. Every  $\text{Fe}_2\text{VAl}_{1-x}\text{Si}_x$  sample successfully showed a negative Seebeck coefficient. In addition, the absolute value of the Seebeck coefficient was much higher in Si-substituted  $\text{Fe}_2\text{VAl}_{1-x}\text{Si}_x$  compared to  $\text{Fe}_2\text{VAl}$  ( $x = 0$ ). It is said that the Fermi level in  $\text{Fe}_2\text{VAl}$  is located at the valley of pseudogap [4, 5] and the Seebeck coefficient is easily increased by substitution of small amount of a fourth element such as Si. Figure 4 shows the temperature dependence of the thermal conductivity of SHSed  $\text{Fe}_2\text{VAl}_{1-x}\text{Si}_x$ . The thermal conductivity was reduced as the Si amounts in  $\text{Fe}_2\text{VAl}_{1-x}\text{Si}_x$  was increased. When Si is substituted in  $\text{Fe}_2\text{VAl}$ , lattice strain resulting from the difference in crystal radius between Al (0.53 Å) and Si (0.40 Å) is introduced. Phonon scattering at the crystal lattice was more encouraged than that of stoichiometric  $\text{Fe}_2\text{VAl}$ , resulting in the lower thermal conductivity. In this study, we succeeded to produce Si-substituted  $\text{Fe}_2\text{VAl}_{1-x}\text{Si}_x$  and the thermoelectric properties were improved by the Si substitution. However, the thermoelectric properties of  $\text{Fe}_2\text{VAl}_{1-x}\text{Si}_x$ , which was produced by conventional arc-melting method or mechanical alloying method, is much better than those of SHSed  $\text{Fe}_2\text{VAl}_{1-x}\text{Si}_x$ . We already found  $\text{Al}_2\text{O}_3$  was still left in the alloy part [2] and it might be the cause of the different thermoelectric properties.

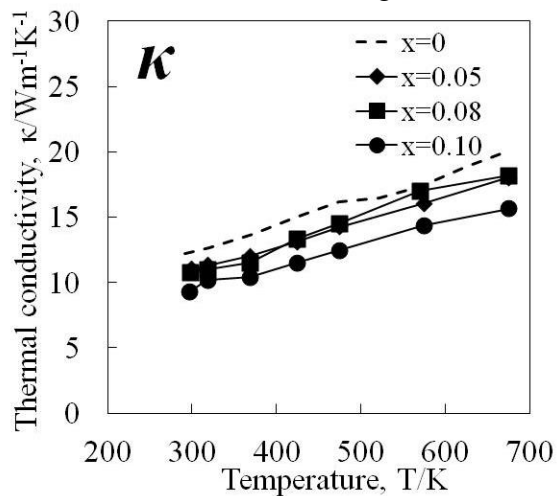


Fig. 4. Thermal conductivity ( $\kappa$ ) of the SHSed  $\text{Fe}_2\text{VAl}_{1-x}\text{Si}_x$ .

## CONCLUSIONS

Si-substituted  $\text{Fe}_2\text{VAl}$  were synthesized via SHS, planetary ball milling, and SPS. The electrical resistivity was decreased as the amount of fourth-element substitution due to the increase in the number of dominant carrier.  $\text{Fe}_2\text{VAl}_{1-x}\text{Si}_x$  showed higher negative Seebeck coefficient values than stoichiometric  $\text{Fe}_2\text{VAl}$ . The thermal conductivity of  $\text{Fe}_2\text{VAl}_{1-x}\text{Si}_x$  was decreased as the amount of fourth-element substitution because the phonon scattering was increased by the introduction of lattice strain which was caused by the difference in atomic radius between Al and Si.

1. A. Kikuchi, N. Okinaka, T. Akiyama, Thermodynamic analysis of thermite synthesis for thermoelectric  $\text{Fe}_2\text{VAl}$ , *Appl. Therm. Eng.*, 2004, vol. 70, no. 3, pp. 876–883.
2. K. Abe, A. Kikuchi, N. Okinaka, T. Akiyama, Single thermite-type combustion synthesis of  $\text{Fe}_2\text{VAl}$  for thermoelectric applications from Fe,  $\text{V}_2\text{O}_5$  and Al powders, *J. Alloys Compd.*, 2014, vol. 611, pp. 319–323.
3. M. Mikami, A. Matsumoto, K. Kobayashi, Synthesis and thermoelectric properties of microstructural Heusler  $\text{Fe}_2\text{VAl}$  alloy, *J. Alloys Compd.*, 2008, vol. 461, nos. 1–2, pp. 423–426.
4. G. Y. Guo, G.A. Botton, Y. Nishino, Electronic structure of possible 3d ‘heavy-fermion’ compound  $\text{Fe}_2\text{VAl}$ , *J. Phys.: Condens. Matter*, 1998, vol. 10, no. 8, L119.
5. D. J. Singh, I. I. Mazin, Electronic structure, local moments, and transport in  $\text{Fe}_2\text{VAl}$ , *Phys. Rev. B*, 1998, vol. 57, no. 22, pp. 14352–14356.

## REACTIVE FLASH SPARK PLASMA SINTERING OF ALUMINA REINFORCED BY SILICON CARBIDE NANOCOMPOSITES: PHYSICOCHEMICAL STUDY

**M. Abedi<sup>\*a</sup>, D. O. Moskovskikh<sup>a</sup>, and A. S. Mukasyan<sup>b</sup>**

<sup>a</sup>National University of Science and Technology MISiS, Moscow, 119049 Russia

<sup>b</sup>Department of Chemical and Biomolecular Engineering, University of Notre Dame, Notre Dame, IN, 46556 USA

\*e-mail: abedi@edu.misis.ru

DOI: 10.24411/9999-0014A-2019-10004

Possessing numerous excellent properties such as high hardness, excellent oxidation resistance, remarkable chemical stability, noticeable wear resistance and great thermal shock resistance of alumina-based composites have attracted the attention of researchers since the last few decades. However, due to the fact that the mechanical properties of strength and fracture toughness of Al<sub>2</sub>O<sub>3</sub> are relatively low, application of these types of ceramics is subject to limitations [1]. In order to overcome this obstacle, strengthening and toughening of ceramics by the dispersion of the second phase as a reinforcement of ceramic matrix has been utilized.

It has been demonstrated in the previous studies that the addition of SiC as a reinforcement particle in the alumina matrix increases the strength, wear and creep resistance, as well as fracture toughness of the ceramic. The addition of SiC particles to alumina-based composites led to a change in fracture mechanism from intergranular to transgranular [2].

Previously, the Al<sub>2</sub>O<sub>3</sub>/SiC composites have been fabricated by hot pressing, as well as spark plasma sintering (SPS). Recently, a novel method of sintering has been developed which is known as flash sintering which is capable of the fully densifying different type of material less than one minute [3]. This method is based on applying a very high electrical power to the sample which extremely accelerated the consolidation process of the materials. Although this method initially was developed for materials with negative temperature coefficient for electrical resistivity, it has been shown that this technique has the ability to sinter materials with all range of electrical conductivity including metallic conductors, ionic conductors, semiconductors and room temperature insulators. Furthermore, other methods of flash sintering were developed by inspiring of the basic model. One of these techniques is flash spark plasma sintering (FSPS), which works by a modification of tooling setups of conventional SPS [4].

In this work, we applied a novel consolidation method, so-called, reactive flash spark plasma sintering (RFSPS). RFSPS comprises the application of FSPS conditions to the Al<sub>2</sub>O<sub>3</sub>-Si/C powder mixture, which contains reactive nanostructured Si/C particles prepared by high-energy ball milling technique. The SiC phase content varies in the range 0–20 wt % and Al<sub>2</sub>O<sub>3</sub> powder with particles of less than 60 nm is used. Alumina reinforced by SiC nanocomposites are produced by SPS, FSPS, and RFSPS techniques and their properties are compared. Specifically, the dependence of final materials' density versus carbide amount is explored. Furthermore, the mechanical properties of obtained ceramics including the fracture toughness and Vickers hardness are measured and analyzed. It is found that the hardness and fracture toughness of obtained nanocomposites grow by increasing reinforcement content.

The authors gratefully acknowledge the financial support of the Ministry of Science and Higher Education of the Russian Federation in the framework of Increase Competitiveness Program of MISiS (Support project for young research engineers)

1. B.-K. Jang, et al., Fracture behaviour and toughening of alumina-based composites fabricated by microstructural control, in fracture mechanics of ceramics: fatigue, composites, and high-temperature behavior, R.C. Bradt, et al., Editors. 1996, Springer US: Boston, MA. p. 371–382.
2. S. Gustafsson, et al., Pressureless sintered Al<sub>2</sub>O<sub>3</sub>–SiC nanocomposites, *Ceram. Int.*, 2008, vol. 34, no. 7, pp. 1609–1615.
3. M. Cologna, B. Rashkova, R. Raj, Flash sintering of nanograin zirconia in < 5 s at 850°C, *J. Am. Ceram. Soc.*, 2010, vol. 93, no. 11, pp. 3556–3559.
4. C. Manière, G. Lee, E.A. Olevsky, All-materials-inclusive flash spark plasma sintering, *Sci. Rep.*, 2017, vol. 7, no. 1, 15071.

## STRUCTURE AND PHASE FORMATION IN ALUMINUM OXYNITRIDE DURING SELF-PROPAGATING HIGH-TEMPERATURE SYNTHESIS

**T. G. Akopdzhanyan<sup>\*a</sup>, A. A. Kondakov<sup>a</sup>, N. A. Kochetov<sup>a</sup>, S. I. Rupasov<sup>b</sup>,  
A. P. Kozlova<sup>b</sup>, and A. V. Bondarev<sup>b</sup>**

<sup>a</sup>Merzhanov Institute of Structural Macrokinetics and Materials Science, Russian Academy of Sciences, Chernogolovka, Moscow, 142432 Russia

<sup>b</sup>National University of Science and Technology MISiS, Moscow, 119049 Russia

\*e-mail: tigran@ism.ac.ru

DOI: 10.24411/9999-0014A-2019-10005

Nowadays high-temperature nitride and oxide ceramics takes one of the leading places among novel materials for various industries: electronics, radio, aircraft and space engineering, nuclear industry.

One of the most promising materials for creating polycrystalline ceramics with high mechanical and unique physicochemical properties is aluminum oxynitride with a cubic crystal structure ( $\gamma$ -AION). AION ceramics is well known due to its excellent optical and mechanical properties and could be used in various application fields. To obtain high-quality polycrystalline AION ceramics it is necessary to ensure high purity AION powders with narrow particle distribution.

The main synthesis methods of AION powder are solid state reaction of AlN and Al<sub>2</sub>O<sub>3</sub> and carbothermal reduction of Al<sub>2</sub>O<sub>3</sub> at temperatures higher than 1700°C for a few hours. Recently, a lot of other methods such as plasma arc melting, nitriding of a precursor derived from aluminum–glycine gel method, etc. were developed. These methods have some disadvantages such as high cost of initial materials (for example AlN), carbon impurities (which cause pores in sintered ceramics), low energy efficiency and complexity of the technology. Self-propagating high-temperature synthesis (SHS) is a highly efficient method to produce powders and ceramics, especially nitride ceramics.

Earlier, we showed the possibility of obtaining pure aluminum oxynitride for ceramics, including optical ceramics. In this work, the possibility of controlling the structure and phase formation in AION is investigated. The effect of initial components of green mixture on the structure and phase composition of AION is also studied. The possibility of obtaining a bimodal structure is studied, which will make it possible to obtain a bimodal distribution of particles in powders. The influence of oxides of rare-earth metals on the phase composition and structure of the material is also studied.

The work was funded by RFBR (project no.19-08-00655).

## ISMAN: NEW RESULTS AND ACHIEVEMENTS

M. I. Alymov\*<sup>a</sup> and O. K. Kamynina<sup>a</sup>

<sup>a</sup>Merzhanov Institute of Structural Macrokinetics and Materials Science, Russian Academy of Sciences, Chernogolovka, 142432 Russia

\*e-mail: alymov@ism.ac.ru

DOI: 10.24411/9999-0014A-2019-10006

Merzhanov Institute of Structural Macrokinetics and Materials Science, Russian Academy of Sciences (Russian acronym ISMAN) was founded in 1987. The purpose and scope of Institute activities are to carry out fundamental, research, and applied scientific studies in the field of physics and chemistry of combustion and explosion processes, including self-propagating high-temperature synthesis, physicochemical transformations of substances under high temperatures and pressures, and materials science.

The following are some important results obtained at the Institute in recent years.

In the framework of the macrokinetic approach, analytical and numerical methods were used to study the thermal conditions of passivation of pyrophoric nanopowders at lower initial temperature of layer. It was shown that a decrease in initial temperature of nanopowder leads to a transition from layer-by-layer to volume passivation. It made it possible to control the permissible level of heating during passivation even at high concentration of oxidizing agent in the gas. Analytical expressions for determining the conditions for layer-by-layer and volume passivation, which were confirmed by numerical calculations, were obtained [1].

Experimental and theoretical method for the calculation of gas flow parameters at which a slow conductive mode of combustion of granular mixtures transforms into a fast convective one was developed. Dependence of the burning velocity on the gas flow in the convective mode was determined. The results can be used to explain and predict the occurrence of fast-moving forest fires [2].

Propagation of solid flame over a combustible wire placed at the axis of cylindrical mirror was studied by mathematical modeling. The use of mirror for return of radiant losses was found to significantly expand the limits of combustion in linear systems. Even in case of non-ideal reflection, the combustion temperature and burning velocity can be expected to attain their superadiabatic values. [3].

$(\text{Zr}_x\text{Ti}_{1-x})_3\text{AlC}_2$  MAX phase was prepared by SHS method. X-ray diffraction analysis of the  $(\text{Zr}_x\text{Ti}_{1-x})_3\text{AlC}_2$  ( $0 < x < 1$ ) crystals made it possible to more accurately determine the composition of a new MAX phase prepared by SHS:  $(\text{Ti}_{0.67}\text{Zr}_{0.33})_3\text{AlC}_2$ . Density functional theory calculation results suggested that the formation of crystals with this composition is energetically favorable. The arrangement of the Zr and Ti atoms in the metal-carbon layer was shown to be disordered [4].

$\text{Ta}_4\text{ZrC}_5$  и  $\text{WC-W}_2\text{C}$  composites with melting point above  $4000^\circ\text{C}$  were first synthesized by electro thermal explosion (ETE) under pressure.  $\text{WC-W}_2\text{C}$  composite has a density of  $12.5 \text{ g/cm}^3$  and microhardness of 16–21 GPa. High physical and mechanical characteristics were explained by the presence of needle-like  $\text{W}_2\text{C}$  particles in  $\text{WC-W}_2\text{C}$  composite [5].

The influence of additives of sodium halides on the structure formation in the system  $\text{Si} + \text{Si}_3\text{N}_4$  during nitriding in the combustion mode was studied. It was found that the use of sodium halide additives makes it possible to form the  $\alpha$  silicon nitride phase of different morphology. Combustion mode for obtaining the equiaxed  $\alpha$  silicon nitride phase was

developed. Silicon nitride samples prepared with mean diameter of particles of 1.2–1.5  $\mu\text{m}$  possess specific surface area of 5–6  $\text{m}^2/\text{g}$  [6].

Electrically conducting composite ceramic materials based on Al–AlN–TiB<sub>2</sub>, BN–TiN–AlN–TiB<sub>2</sub>, and MAX phases Cr<sub>2</sub>AlC and Ti<sub>2</sub>AlN prepared by SHS were investigated. [7].

The gravity-assisted combustion synthesis of  $\gamma$ -TiAl from TiO<sub>2</sub> as a raw material in the presence of mixed Al–Ca reductant was explored. The use of Al–Ca reductant was found to markedly increase the yield of TiAl and decrease the amount of residual contaminants (such as oxygen, nitrogen, carbon) in target product [8].

Mn, Co, and Ni/ZSM-5 catalysts were first produced by low-temperature combustion synthesis. The physicochemical and catalytic properties of the catalysts were studied during deep oxidation and hydrogenation of CO<sub>2</sub> [9].

SHS technology was developed for nitriding a vanadium–aluminum alloy containing 15–20 mass % nitrogen. Successful tests of nitrated vanadium–aluminum alloy as a nitriding component for the production of vanadium–aluminum–nitrogen master alloy were carried out. The method of obtaining the master alloy has already been implemented at Uralredmet Ltd. [10].

These results offer important opportunities for further basic research in the field of SHS, materials science, and novel industrial developments.

1. B.S. Seplyarskii, N.M. Rubtsov, T.P. Ivleva, M.I. Alymov, Influence of the initial temperature on the passivation of pyrophoric nanopowders (macrokinetic approach), *Dokl. Academ. Nauk*, 2019, vol. 484, no. 2, pp. 48–52.
2. B.S. Seplyarskii, R.A. Kochetkov, T.G. Lisina, Experimental and theoretical method for calculating the conditions of convective combustion mode, *Chem. Phys.*, 2019, vol. 38, no. 3.
3. A.P. Aldushin, Propagation of SHS wave along a wire in conditions of saved radiant losses, *Int. J. Self-Propag. High-Temp. Synth.*, 2018, vol. 27, no. 2, pp. 69–71.
4. S.V. Konovalikhin, S.A. Guda, D.Yu. Kovalev, Composition and structure of (Zr<sub>0.37</sub>Ti<sub>0.63</sub>)<sub>3</sub>AlC<sub>2</sub> MAX phase crystals prepared by self-propagating high-temperature synthesis, *Inorg. Mater.*, 2018, vol. 54, no. 9, pp. 953–956.
5. V.T. Telepa, M.I. Alymov, V.A. Shcherbakov, A.V. Shcherbakov, V.I. Vershinnikov, Synthesis of the WC–W<sub>2</sub>C composite by electro-thermal explosion under pressure, *Lett. Mater.*, 2018, vol. 8, no. 2, pp. 119–122.
6. V.V. Zakorzhevskii, Effect of oxygen impurities and synthesis temperature on the phase composition of the products of self-propagating high-temperature synthesis of Si<sub>3</sub>N<sub>4</sub>, *Inorg. Mater.*, 2018, vol. 54, no. 4, pp. 349–353.
7. A.V. Karpov, D.Yu. Kovalev, I.P. Borovinskaya, A.E. Sytshev, Electrically conducting ceramics based on Al–AlN–TiB<sub>2</sub>, *High Temp.*, 2018, vol. 56, no. 4, pp. 527–531.
8. D.E. Andreev, V.I. Yukhvid, D.M. Ikornikov, V.N. Sanin, T.I. Ignat'eva, Gravity-assisted metallothermic SHS of titanium aluminide with Al–Ca mixture as a reducing agent, *Int. J. Self-Propag. High-Temp. Synth.*, 2018, vol. 27, no. 2, pp. 89–91.
9. V.N. Borshch, S.Ya. Zhuk, N.V. Sachkova, Activation of the surface of polymetallic carries by the formation of intermediate intermetallic phases, *Kinetics and Catalysis*, 2018, vol. 59, no. 3, pp. 386–391.
10. V.V. Zakorzhevsky, I.P. Borovinskaya, et al, A method for producing a nitrogen-containing material based on metal nitrides for master alloys of titanium alloys, Patent no. 2422246, 2011 (in Russ.).



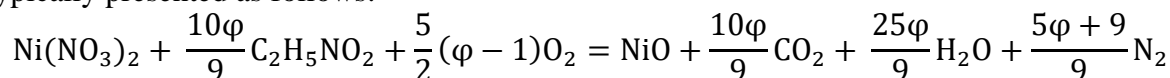
## KINETIC MEASUREMENTS FOR SOLUTION COMBUSTION SYNTHESIS PROCESSES

N. Amirkhanyan<sup>\*a</sup>, S. L. Kharatyan<sup>a,b</sup>, and K. V. Manukyan<sup>c</sup><sup>a</sup>Laboratory of Kinetics of SHS Processes, Institute of Chemical Physics NAS of Armenia, Yerevan 0014, Armenia<sup>b</sup>Department of Chemistry, Yerevan State University, Yerevan 0025, Armenia<sup>c</sup>Nuclear Science Laboratory, Department of Physics, University of Notre Dame, Notre Dame, Indiana 46556, United States

\*e-mail: narine21-am@rambler.ru

DOI: 10.24411/9999-0014A-2019-10007

Solution combustion synthesis (SCS) is a unique approach for the fabrication of nanoscale materials and thin films for applications ranging from electronics to biomaterials [1]. This method of materials' synthesis involves self-sustained non-catalytic heterogeneous reactions. Because SCS is a self-sustained thermal process where the primary source of heat comes from combustion reactions, it can be considered as a specific type of self-propagating high-temperature synthesis (SHS) or combustion synthesis (CS). In SCS processes, two main features—reaction duration and temperature—define the products' morphology, structure, and composition. Therefore, it is critical to control the reaction conditions and obtain knowledge on the kinetics for the SCS processes to control the properties of the resulting materials. SCS reactions between metal nitrates, such as Ni(NO<sub>3</sub>)<sub>2</sub> and fuel (e.g., glycine, C<sub>2</sub>H<sub>5</sub>NO<sub>2</sub>) can be typically presented as follows:



where  $\varphi$  is the fuel-to-oxidizer ratio,  $\varphi = 1$  implies that all oxygen required for complete combustion of fuel derives from the oxidizer, while  $\varphi > 1$  ( $< 1$ ) implies fuel-rich (or lean) conditions.

The chemical mechanism of these reactions is complex. Therefore, obtaining kinetic data that describes the rate of individual chemical reactions is difficult. Thermal analysis methods (e.g., differential thermal analysis, DTA) were used to extract kinetic parameters of some SCS reactions. For example, for the nickel nitrate–urea system, the obtained apparent activation energy using the Kissinger method was reported to be  $\sim 180$  kJ/mol [2]. DTA analysis of nickel nitrate–glycine system with excessive amounts of glycine fuel revealed a two-step process with different activation energies [3]. It was speculated that the first process with an activation energy of  $\sim 123$  kJ/mol corresponds to the reaction between NH<sub>3</sub> and HNO<sub>3</sub>, which forms during decomposition of glycine and nickel nitrate, respectively. The second reaction may be related to the reduction of NiO by hydrogen. The activation energy of this reaction is lower ( $\sim 111$  kJ/mol) and within values for hydrogen reduction (85–110 kJ/mol) reported elsewhere. Thermal analysis methods, however, are limited to low heating rates (0.2–1 K/s). In typical SCS reactions, the heating rates can be as high as 500–1000 K/s. Therefore, the application of real-time combustion diagnostic tools to determine the kinetic parameters is of practical interest.

In this work, we use rapid micro-thermocouple measurements to record time–temperature profiles and determine front propagation velocities in the Ni(NO<sub>3</sub>)<sub>2</sub> + C<sub>2</sub>H<sub>5</sub>NO<sub>2</sub> system to extract apparent activation energy of the processes. The measured parameters were treated using the theory proposed by Zeldovich and Frank–Kamenetskii [4], according to which the

combustion front propagation velocity ( $V$ ), maximum temperature ( $T$ ), and apparent activation energy ( $E_a$ ) of the processes are related by the following equation:

$$\ln\left(\frac{V}{T}\right) = \text{const} - \frac{E_a}{2RT}$$

where  $R$  is the gas constant and equals to  $8.314 \text{ J}\cdot\text{K}^{-1}\cdot\text{mol}^{-1}$ .

In a typical experiment, reactive solutions were prepared first by dissolving an oxidizer, such as nickel nitrate hydrate ( $\text{Ni}(\text{NO}_3)_2\cdot 6\text{H}_2\text{O}$ ) and fuels (glycine, methenamine, citric acid) with  $\phi$  ratio in deionized water and thoroughly stirred. The obtained solutions were poured into a boat (50 mm in length, 10 mm width, and 10 mm height) and dried at 373 K for the different durations to evaporate the solvent and produce reactive gels. The SCS reaction was initiated by the local preheating (spot of  $\sim 1 \text{ mm}^3$ ) of gels in the air by a resistively heated tungsten wire. After initiation, the chemical reaction propagates through the gels in the form of a moving combustion wave. The time–temperature profiles (Fig. 1a) of the process is recorded by two 100  $\mu\text{m}$  K-type thermocouples inserted inside the reactive gels. Multiple runs were used to measure the average combustion temperatures. The front propagation velocities were determined by dividing the distance between thermocouples ( $D$ ) by temporal distance between thermocouple signals ( $\tau$ ). A typical Arrhenius-type plot of  $\ln(V/T)$  against the reciprocal temperature for  $\text{Ni}(\text{NO}_3)_2 + \text{C}_2\text{H}_5\text{NO}_2$  ( $\phi = 0.75$ ) is shown in Fig. 1b. Linear fitting of the data points permits to extract apparent activation energies of  $84 \pm 8 \text{ kJ}\cdot\text{mol}^{-1}$ . We can suggest that such measurements based on real-time combustion diagnostic methods provide more reliable estimation of the apparent activation energies. Other examples of such measurements involving different systems will also be outlined during the presentation. The role of different fuels, solvents and other reaction conditions will be presented and discussed.

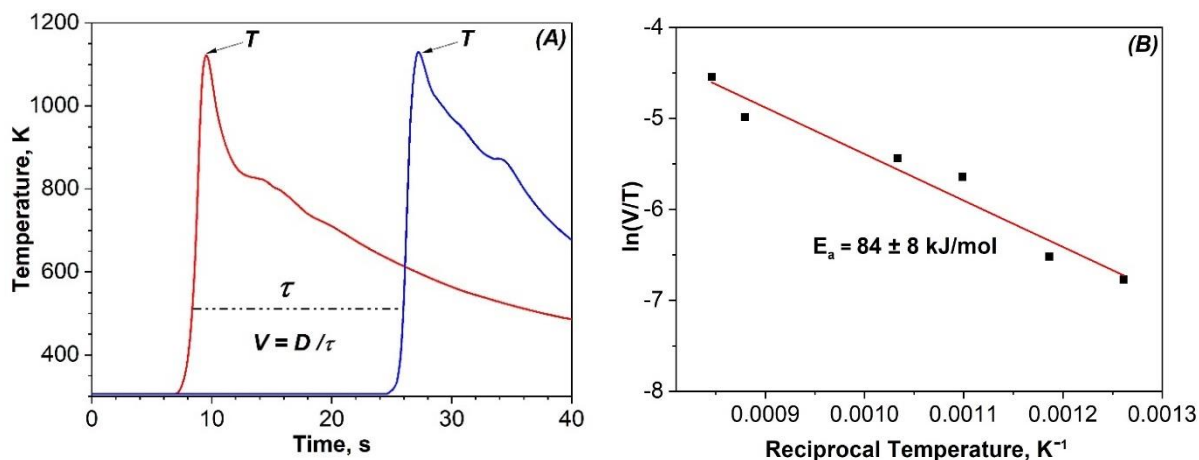


Fig. 1. (a) Typical time–temperature profiles for  $\text{Ni}(\text{NO}_3)_2 + \text{C}_2\text{H}_5\text{NO}_2$  system to extract maximum combustion temperature,  $T$ , and combustion front propagation velocity,  $V$ , where  $D$  is the distance between thermocouples in cm and  $\tau$  is the temporal distance of thermocouple signals in seconds. (b) Linear fitting of the  $\ln(V/T)$  against the reciprocal temperature to extract apparent activation energy ( $E_a$ ) for NiO formation in fuel-lean conditions.

1. A. Varma, A.S. Mukasyan, A.S. Rogachev, K.V. Manukyan, Solution combustion synthesis of nanoscale materials, *Chem. Rev.*, 2016, vol. 116, pp. 14493–14586.
2. L.S. González-Cortés, F.E. Imbert, Fundamentals, properties and applications of solid catalysts prepared by solution combustion synthesis (SCS), *Appl. Catal., A*, 2013, vol. 452, pp. 117–131.
3. A. Kumar, E.E. Wolf, A.S. Mukasyan, Solution combustion synthesis of metal nanopowders: Nickel-reaction pathways, *AIChE J.*, 2011, vol. 57, pp. 2207–2213.
4. Y.B. Zeldovich, D.A. Frank–Kamenetskii, Theory of thermal flame propagation (in Russian), *J Phys Chem*, 1938, vol. 12, pp. 100–105.

## APPLICATION OF SHS FOR FABRICATION OF ALUMINUM-MATRIX NANOCOMPOSITES (REVIEW)

**A. P. Amosov\*<sup>a</sup>, E. I. Latukhin<sup>a</sup>, A. R. Luts<sup>a</sup>, Yu. V. Titova<sup>a</sup>, A. A. Kuzina<sup>a</sup>,  
and D. A. Maidan<sup>a</sup>**

<sup>a</sup>Samara State Technical University, Samara, 443100 Russia  
e-mail: egundor@yandex.ru

DOI: 10.24411/9999-0014A-2019-10008

The first place in the production of composites with a metal matrix is occupied by aluminum-matrix composites (AMCs), due to their low weight, high specific strength, wear resistance, corrosion resistance, a fairly wide temperature range of operation, good technological properties [1–3]. The greatest volume of their application falls on road transport, where they are used for engine parts and brakes. Because of the scarcity of fibers, their high cost and complex manufacturing technology, the AMCs, discretely strengthened with ceramic particles  $\text{Al}_2\text{O}_3$ , SiC, TiC,  $\text{TiB}_2$ ,  $\text{Si}_3\text{N}_4$ , AlN, etc., are more affordable and widely used. The presence of such refractory, high-strength and high-modulus ceramic particles in the matrix of aluminum alloys, which do not dissolve in the matrix, causes a significant improvement in mechanical properties including at elevated temperatures while maintaining a small specific gravity and other properties of aluminum.

However, the wider use of AMCs is constrained by a number of unresolved issues. It is necessary to increase the level of strength properties of AMCs as it is often insufficient especially at elevated temperatures. But the increase in strength due to the increase in the volume fraction of ceramic particles of micrometer size from 0.5 to 50  $\mu\text{m}$  along with positive effects leads to such disadvantages as low crack resistance, low hardness and strength at elevated temperatures, poor mechanical machinability [4]. Much more promising is another direction of increasing the strength of AMCs - reducing the size of the reinforcing particles, the transition to the use of nanoparticles (from 1 to 100 nm) instead of micrometer-sized particles. With such a decrease in the size, other strengthening mechanisms begin to work, and a significant change in the properties of aluminum-matrix composites is achieved with a significantly lower content of the reinforcing phase, and, as a consequence, maintaining high ductility, which is very important to overcome such lacks of AMCs as low ductility and crack resistance with increased strength [5, 6]. In dispersion-strengthened nanocomposites, the matrix bears the main part of the external load, and the effective resistance to the displacement of dislocations in the body of the metal matrix is created by ceramic nanoparticles (Orowan mechanism), grain boundaries (Hall–Petch mechanism), the mismatch of elastic modules (EM) and coefficients of thermal expansion (CTE) of the matrix and nanoparticles. The greater the resistance, the higher the degree of strengthening of the material. Calculations show that the most significant contributions to strengthening are created by the mismatch of CTE, as well as by Orowan mechanism, especially when the particle diameter does not exceed 50 nm with the content of nanoparticles up to 15 vol %.

However, it should be borne in mind that the results of calculations are valid for a perfectly uniform distribution of reinforcing particles over the matrix body with a perfectly continuous contact and a strong adhesion bond between the particles and the matrix. Therefore, in order to realize the large potential of strengthening the AMCs due to the reinforcement by nanoparticles, it is necessary that the technologies for manufacturing such AMCs provide a uniform distribution of nanoparticles over the matrix and a strong adhesive interfacial bond. The

fulfillment of these requirements is a big technological problem since usually nanoparticles are poorly wetted by the matrix material and are prone to the formation of agglomerates from nanoparticles due to interparticle adhesive forces, the value of which increases sharply with decreasing particle size [4–6]. For uniform distribution of nanoparticles, it is necessary to overcome the forces of their adhesion and destroy agglomerates, as well as to ensure wettability of nanoparticles by the matrix material.

Numerous solid-phase and liquid-phase methods of manufacturing the nanoparticle-reinforced AMCs, which are divided into ex-situ and in-situ methods, have been developed. In the case of ex-situ methods, previously prepared reinforcing nanoparticles in powder form are introduced into AMCs and mixed with the matrix metal in solid or liquid state, and in the case of in-situ methods, the reinforcing particles are synthesized directly during the manufacture of AMCs by chemical reactions in the body of solid or liquid matrix metal.

Solid-phase methods (powder metallurgy, mechanical alloying, friction with mixing) in comparison with liquid-phase methods allow to use relatively large volumes of the reinforcing phase, which can also be poorly wetted with aluminum melt, to avoid the formation of undesirable brittle phases in the reaction of the filler with the melt, to achieve a uniform distribution of reinforcing nanoparticles over the matrix, but these methods have a noticeable residual porosity of composites and low adhesion of the matrix with nanoparticles. The use of solid-phase methods is currently limited both by the high cost associated mainly with the multistage and energy consumption of the process of manufacturing blanks from dispersed-hardened AMCs, and by the simple shapes of these blanks, which must be further machined to make the component of desired shape and size [4–6]. But for the sake of justice, it should be emphasized that among the AMCs reinforced with nanoparticles, only the nanocomposites of the SAP brand (Al–Al<sub>2</sub>O<sub>3</sub>) and Al–Al<sub>4</sub>C<sub>3</sub> with the content of the reinforcing nanoparticles of Al<sub>2</sub>O<sub>3</sub> and Al<sub>4</sub>C<sub>3</sub> up to 22% and with the unique mechanical properties up to 500°C made by solid-phase methods have so far found industrial production and application.

Liquid-phase methods are more cost-effective for industrial production due to the possibility of using the available low-cost equipment for foundry production and fabrication of castings and components of complex shape, however, with a limited amount of reinforcing phase in composites, since the melt loses its fluidity at a high content of the reinforcing phase. However, such a simple and economical ex-situ method as mechanical stirring the reinforcing nanopowders in bulk with the melt of aluminum or its alloys does not lead to success, since nanopowders do not sink in the melt, are not absorbed by the melt. In this regard, to ensure the introduction of nanopowders, it is necessary to use special ex-situ methods for the introduction of nanopowders: mixing in the semi-solid state of the matrix metal, spraying or spinning the melt, physical effects on the melt, primarily by ultrasound and others [4–6]. Technologies based on these methods are complex, require special equipment, inefficient, energy consumption. More simple technology based on the use of a variety of nanopowdery pseudo-master alloys (mixtures of nanopowders with metal powders-carriers, often in the form of pressed briquettes), is limited by the possibility of dissolution of the briquettes in the aluminum melt. The content of the reinforcing ceramic powder in the pseudo-master alloy usually does not exceed several percent, and therefore the content of the nanoscale reinforcing phase in the thus obtained nanostructured cast AMCs is usually small and does not exceed 0.1%.

In the case of in-situ methods, when carrying out chemical synthesis reactions of reinforcing particles directly in the melt, the increased content of the reinforcing phase is provided at a lower cost compared to the expensive separately synthesized nanopowders, as well as a high thermodynamic stability, a more intimate contact and a good bond (adhesion) between the phases of the composite, as the reinforcing phase is not introduced from the outside with the particle surface usually contaminated by oxides and adsorbed gases and moisture, but these particles are formed directly in the body of the melt, are not in contact with the atmosphere, do not contain moisture and have fresh clean surfaces [7]. However, in-situ methods have such

disadvantages as noticeable residual porosity of AMCs, uneven distribution of synthesized reinforcing particles over the matrix, which usually form clusters and agglomerates along the grain boundaries of the matrix alloy. To overcome the last drawback, such methods as ultrasonic treatment of the melt in the synthesis of AMCs or subsequent plastic deformation of the resulting composite ingot (forging or rolling, especially at different speeds of rotation of the rolls) are used [8, 9].

To date, the technological problems of manufacturing the AMCs by liquid-phase methods with a high content (up to 15 vol %) and the uniform distribution of nanoparticles over the matrix are unresolved, what is necessary for the implementation of large potential opportunities for strengthening the AMCs due to reinforcement by nanoparticles, and there are no economically viable technologies for the industrial production of cast aluminum-matrix composites reinforced with nanoparticles.

A significant contribution to the solution of the above problems can be made by using the achievements of a simple energy-saving powder technology of self-propagating high-temperature synthesis (SHS) of solid chemical compounds (carbides, borides, nitrides, oxides, etc.) and materials based on them [10]. SHS process can be used in solid-phase and liquid-phase methods of manufacturing the dispersion-strengthened AMCs [11]. In the case of development of cast aluminum-matrix composites, discontinuously reinforced with nano-sized ceramic particles, the application of SHS process is possible in three directions: (1) synthesis of inexpensive ceramic nanopowders for their subsequent introduction into the matrix melt (ex-situ); (2) introduction of the previously prepared ceramic nanoparticles into the matrix melt (ex-situ) with the use of SHS process, creating a large gradient of temperature and chemical potential, what promotes wetting and uniform distribution of nanoparticles; and (3) synthesis of inexpensive reinforcing ceramic nanoparticles directly in the aluminum melt (in-situ) with ensuring their good adhesion to the matrix [12].

On the market abroad and in Russia, there are mainly ceramic nanopowders of plasma chemical synthesis, the prices of which (nitrides, carbides and borides) are from 1000 to 3000 euros per 1 kg [13]. Such high prices of nanopowders largely prevent their use for reinforcement of AMCs and the organization of economically valid industrial production of AMCs, dispersion-strengthened by nanoparticles. The analysis shows that the price of SHS nanopowders, in particular, nitrides of azide technology of SHS, can be an order of magnitude less, so the use of SHS nanopowders for reinforcing the aluminum alloys in all three of the above directions is promising [12, 14–19]. The first direction is represented by the results of the successful application of nanopowder products of azide SHS technology for reinforcing the aluminum alloys with a reinforcing phase content of up to 4%, using various ex-situ methods of introducing the nanopowders into the melt of aluminum (or its alloys): in the form of nanopowdery pseudo-master alloys (pressed briquettes of mixtures of nanopowders with metal powders-carriers), in the form of composite master alloys obtained by fusion of flux carnallite  $KCl \cdot MgCl_2$  with nanopowders, by mixing nanopowders into an aluminum alloy in a semi-solid state [14, 15]. In the second direction, ex-situ injection of 7.7% aluminum nitride nanopowder, previously obtained by the azide SHS technology, into the melt of aluminum was carried out in a mixture with a charge Ti + C, leading to the implementation of SHS process of reinforcing phase TiC in the aluminum melt (in-situ) [16]. The third direction of the synthesis of reinforcing ceramic nanoparticles directly in the aluminum melt (in-situ) was carried out in the fabrication of aluminum-matrix composite Al–10% TiC by introducing a charge Ti + C into the melt [12, 17]. Dilution of the SHS charge with inert additives, replacement of the initial powders of pure elements with their precursors, i.e. chemical compounds, the use of fluxes made it possible to achieve the nanolevel of the dispersed reinforcing phase TiC in this composite. In the synthesis of the reinforcing phase by SHS method, the alloying of the aluminum matrix by various elements can also play an important role in increasing the mechanical properties of AMCs [18, 19]. For example, nanocomposite Al–5%Cu–0.5%TiC, obtained by dissolving in

the Al–5%Cu melt of the Al–TiC master nanocomposite, previously synthesized by burning a mixture of Al and Ti powders with carbon nanotubes in vacuum, showed along with increased strength of 540 MPa unique ductility  $\delta = 19\%$ , which was almost 3 times higher than the original matrix alloy Al–5% Cu with 485 MPa and 6.6%, respectively.

1. M.K. Surappa, Aluminium matrix composites: Challenges and opportunities, *Sadhana*, 2003, vol. 28, parts 1&2, pp. 319–334.
2. A.A. Adebisi, M.A. Maleque, M.M. Rahman, Metal matrix composite brake rotor: historical development and product life cycle analysis, *Int. J. of Autom. & Mech. Eng.*, 2011, vol. 4, pp. 471–480.
3. R.S. Rana, R. Purohit, S. Das, Review of recent studies in Al matrix composites, *Int. J. of Sci. & Eng. Research*, 2012, vol. 3, no. 6, pp. 1–16.
4. C. Borgonovo, D. Apelian, Manufacture of aluminum nanocomposites: A critical review, *Mater. Sci. Forum*, 2011, vol. 678, pp. 1–22.
5. F. He, Ceramic nanoparticles in metal matrix composites, *Ceramic Nanocomposites: A volume in Woodhead Publishing Series in Composites Science and Engineering*, 2013, pp. 185–207.
6. R. Casati, M. Vedani, Metal matrix composites reinforced by nano-particles - A review, *Metals*, 2014, no. 4, pp. 65–83.
7. S.L. Pramod, S.R. Bakshi, B.S. Murty, Aluminum-based cast in situ composites: A review, *J. Mater. Eng. Perform.*, 2015, vol. 24, no. 6, pp. 2185–2207.
8. W.J. Kim, S.I. Hong, J.M. Lee, S.H. Kim, Dispersion of TiC particles in an in situ aluminum matrix composite by shear plastic flow during high-ratio differential speed rolling, *Mater. Sci. Eng.*, 2013, vol. A559, no. 1, pp. 325–332.
9. R.N. Rai, R.A.K. Prasado, G.L. Dutta, M. Chakraborty, Forming behavior of Al–TiC in-situ composites, *Mater. Sci. Forum*, 2013, vol. 765, pp. 418–422.
10. E.A. Levashov, A.S. Mukasyan, A.S. Rogachev, D.V. Shtansky, Self-propagating high-temperature synthesis of advanced materials and coatings, *Int. Mater. Reviews*, 2016, DOI: 10.1080/09506608.2016.1243291.
11. H. Nath, A.P. Amosov, SHS amidst other new processes for in-situ synthesis of Al-matrix composites: A review, *Int. J. Self-Propag. High-Temp. Synth.*, 2016, vol. 25, no. 1, pp. 50–58.
12. A.P. Amosov, A.R. Luts, E.I. Latukhin, A.A. Ermoshkin, Application of SHS processes for in situ preparation of alumomatrix composite materials discretely reinforced by nanodimensional titanium carbide particles (Review), *Russ. J. Non-Ferr. Met.*, 2016, vol. 57, no. 2, pp. 117–123.
13. *Nanomaterials and related products: catalogue and price list*, [http://www.plasmachem.com/download/PlasmaChem-General\\_Catalogue](http://www.plasmachem.com/download/PlasmaChem-General_Catalogue) Nanomaterials 2019.
14. A.P. Amosov, Y.V. Titova, D.A. Maidan, A.A. Ermoshkin, I.Y. Timoshkin, Application of the nanopowder production of azide SHS technology for the reinforcement and modification of aluminum alloys, *Russ. J. Non-Ferr. Met.*, 2015, vol. 56, no. 2, pp. 222–228.
15. A.P. Amosov, A.R. Luts, Yu.V. Titova. Aluminum matrix composites reinforced with SHS nanoparticles, *Int. Conf. Dedicated to the 50th Anniversary of Self-Propag. High-Temp. Synth. (SHS-50)*, 2017, Chernogolovka, Russia.
16. A.P. Amosov, Y.V. Titova, D.A. Maidan, E.I. Latukhin, Application of SHS auxiliary reaction of titanium carbide for introduction of AlN nanoparticles into aluminum melt, *J. Phys.: Conf. Series*, 2018, vol. 1115, no. 4, 042001.
17. L. Peijie, E.G. Kandalova, V.I. Nikitin, A.G. Makarenko, A.R. Luts, Zh. Yanfei, Preparation of Al–TiC composites by self-propagating high-temperature synthesis, *Scr. Mater.*, 2003, vol. 49, no. 7, pp. 699–703.

18. A.P. Amosov, A.R. Luts, E.I. Latukhin, A.D. Rybakov, V.A. Novikov, S.I. Shipilov, Effect of alloying on structure and properties of particle — reinforced aluminum matrix composites Al/TiC produced by SHS in aluminum melt, *J. Phys.: Conf. Series*, 2018, vol. 1115, no. 4, 042002.
19. D. Zhou, F. Qiu, Q. Jiang, The nano-sized TiC particle reinforced Al–Cu matrix composite with superior tensile ductility, *Mater. Sci. Eng.*, 2015, vol. A622, pp. 189–193.

## FORMATION OF Mo/Nb/Si/B CAST COMPOSITE BY SHS IN CONDITIONS OF ARTIFICIAL GRAVITY

**D. E. Andreev<sup>a</sup>, Yu. S. Vdovin<sup>\*a</sup>, and V. I. Yukhvid<sup>a</sup>**

<sup>a</sup>Merzhanov Institute of Structural Macrokinetics and Materials Science, Russian Academy of Sciences, Chernogolovka, Moscow, 142432 Russia

\*e-mail: vdovin-us@ism.ac.ru

DOI: 10.24411/9999-0014A-2019-10009

Mo–Si-based composition materials (CMs) have great potential for realization in industry [1]. The introduction of boron into Mo–Nb–Si allows to form dense borosilicate glass, which protect CMs from oxidization [1, 2]. CMs based on Mo/Nb/Si/B and related parts are produced by casting, powder metallurgy, and additive technologies. In this paper, the cast Mo/Nb/Si/B-based composites produced by SHS in conditions of artificial gravity are studied.

In experiments, the combustion rate ( $u$ ), the material loss during combustion ( $\eta_1$ ), and the yield of the “metal” phase into ingot ( $\eta_2$ ) were determined in the experiments:

$$u = h/t$$

$$\eta_1 = [(m_1 - m_2)/m_1] \times 100\%$$

$$\eta_2 = (m_3/m_1) \times 100\%$$

where  $m_1$  is the mass of green mixture,  $m_2$  is the mass of combustion product, and  $m_3$  is the mass of target metallic ingot. SHS-prepared ingots were characterized by analytical chemistry, X-ray diffraction analysis, and scanning electron microscopy.

Mo–Nb–Si–B composites were synthesized from green mixture consisting of high exothermic mixture MoO<sub>3</sub>/Nb<sub>2</sub>O<sub>5</sub>/Al/Si/B and low exothermic mixture Mo/Nb/Si/B (Table 1).

Table. 1. Green mixture used in experiments.

|           | Mo   | Si  | Nb  | B   | MoO <sub>3</sub> | Nb <sub>2</sub> O <sub>5</sub> | Al   |
|-----------|------|-----|-----|-----|------------------|--------------------------------|------|
| Mixture 1 | –    | 1.5 | –   | 0.5 | 68.9             | 2.4                            | 26.7 |
| Mixture 2 | 92.5 | 3.0 | 3.4 | 1.1 | –                | –                              | –    |

40 g of the prepared mixtures were placed in quartz shells with an internal diameter of 25 mm and a height of 70 mm. According to thermodynamic calculation in a wide range of ratios of compositions ( $\alpha$ ), the combustion temperature exceeds 3000 K. The combustion products contain considerable amounts of gaseous products (metal vapor and suboxides). In order to suppress the sputtering of the mixture during combustion, experiments were carried out under the action of gravity forces  $a = 1\text{--}400\text{ g}$ . As a result, the combustion products are separated into two layers: Mo–Nb–Si–B target product and Al<sub>2</sub>O<sub>3</sub> oxide layer (slag product). It was found that  $\eta_1$  decreases and  $\eta_2$  increases within the range  $\alpha = 0\text{--}40\text{ wt \%}$  weight. At  $\alpha > 60\%$ , the completeness of the target product yield into ingot decreases sharply and at  $\alpha = 70$  reaches zero (the limit of gravitational separation is reached). At  $\alpha = 80\%$  combustion stopped.

The influence of the ratio of compositions 1 and 2 in the green mixture ( $\alpha$ ) on the chemical composition of cast CM is shown in Fig. 1. With increasing  $\alpha$  from 0 to 40 % Mo content varies slightly, boron is almost unchanged (1 wt %). Content of Si, Al, and O decreases. It should be noted that for small  $\alpha$ , Si content is significantly greater than the calculated value. The appearance of excess Si in combustion products is apparently associated with the melting of the



surface layer of the quartz cup and with the transition of Si into the composition of CM. With an increase in  $a/g$  from 1 to 400, a weak increase in the Mo content and a weak drop in all other elements take place.

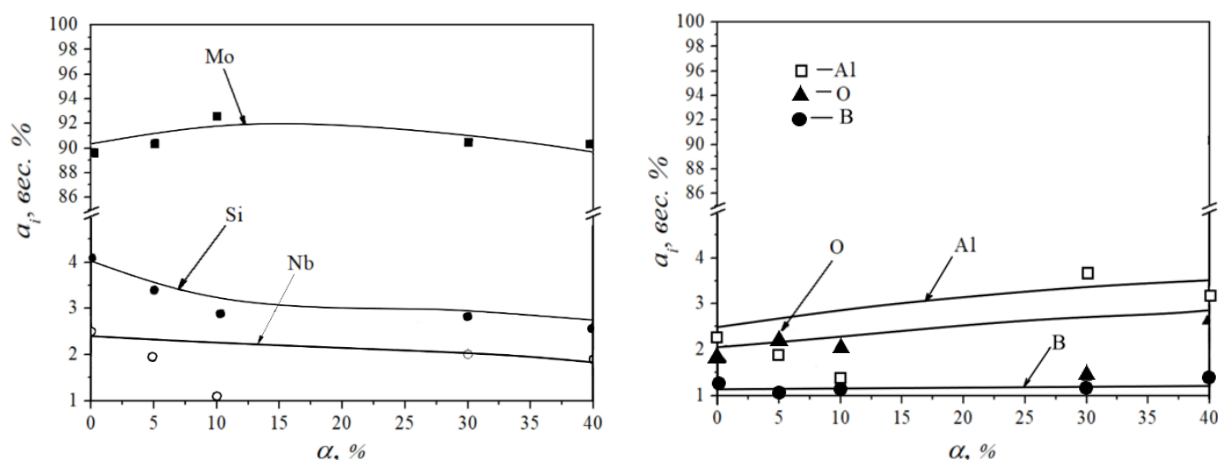


Fig. 1. The influence of the ratio of compositions 1 and 2 in the green mixture ( $\alpha$ ) on the chemical composition of cast CM,  $a = 40$  g.

XRD pattern of cast CM is seen in Fig. 2 to contain 3 phases: Mo(Nb),  $(\text{Mo, Nb})_5\text{SiB}_2$ , and  $(\text{Mo, Nb})_3\text{Si}$ . XRD analysis and SEM studies (Fig. 3) showed that the basis of CM is a solution of niobium in molybdenum, in which the strengthening phases are distributed.

The studies revealed the following sequence of processes occurring after ignition of a mixture of high-exothermic ( $\text{MoO}_3/\text{Nb}_2\text{O}_5/\text{Al}/\text{Si}/\text{B}$ ) and low-exothermic ( $\text{Mo}/\text{Nb}/\text{Si}/\text{B}$ ) compositions. A combustion front is formed, which spreads through the mixture. In the combustion front, the chemical transformation of the initial mixture into final products takes place. The high combustion temperature of the mixtures leads to melting of the initial reagents and combustion products. Under the influence of gravity forces, melts of metal and oxide phases of combustion products are separated. At the final stage there is a cooling of the two-phase melt, the formation of the phase composition and structure of the CM and slag layer occurs.

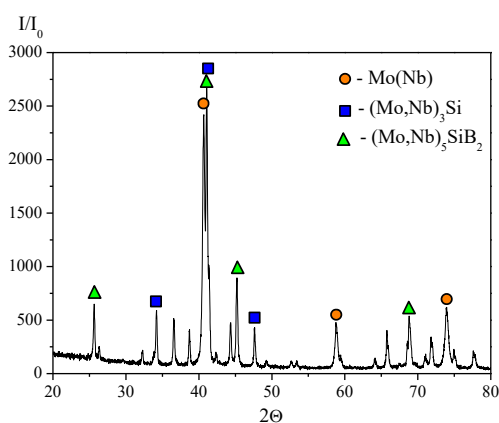


Fig. 2. XRD pattern of cast Mo/Nb/Si/B composite ( $a = 40$  g).

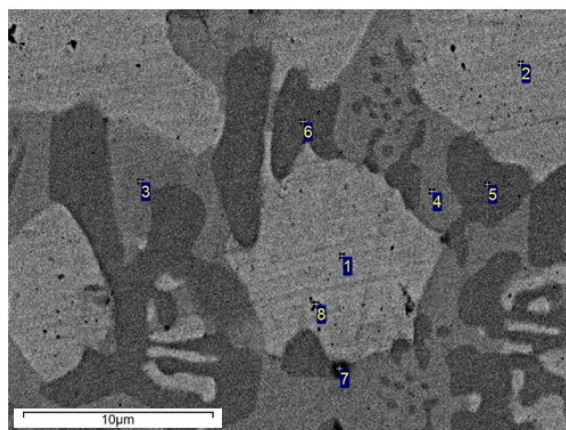


Fig. 3. Microstructure of cast Mo/Nb/Si/B composite ( $a = 40$  g).

Analysis of the processes occurring at the stage of combustion makes it possible to present the following model of combustion of a mixture of  $n(\text{MoO}_3/\text{Nb}_2\text{O}_5/\text{Al}/\text{Si}/\text{B}) + m(\text{Mo}/\text{Nb}/\text{Si}/\text{B})$ . According to thermodynamic calculations and experimental results obtained in a wide range of ratios  $\text{MoO}_3/\text{Nb}_2\text{O}_5/\text{Al}/\text{Si}/\text{B}$  and  $\text{Mo}/\text{Nb}/\text{Si}/\text{B}$ , the combustion temperature exceeds 3000 K. In

this case, in the zone of heating the combustion wave, the components of the mixture undergo the following transformations:

- melting of  $\text{MoO}_3$  at  $T = 1070$  K and subsequent boiling (without decomposition) at  $T = 1480$  K;
- a vapour of  $\text{MoO}_3$  is filtered into the zone of chemical transformations;
- at 2300 K, after melting of protective film ( $\text{Al}_2\text{O}_3$ ) on the surface of Al particles, ignition followed by combustion of Al occur;
- high-temperature combustion products enter into heat and mass transfer with other “cold” components of the mixture, which after heating enter into chemical interactions.

The scheme of transformations in reaction cells can be represented as:



The work was supported by RFBR (project no.18-08-00228).

1. S. Drawin, J.F. Justin, Advanced lightweight silicide and nitride based materials for turbo-engine applications, *AerospaceLab*, 2011, no. 3, pp. 1–13
2. H.-P. Martinz, B. Nigg, J. Matej, M. Sulik, H. Larcher, A. Hoffmann, Properties of the sisor oxidation protective coating on refractory metal alloys. *Int. J. Refract. Met. Hard Mater.*, 2006, vol. 24, pp. 283–291.

## GRAVITY-ASSISTED METALLOTHERMIC SHS OF COMPOSITES BASED ON Mo–Ti–Cr–Ni

**D. E. Andreev<sup>\*a</sup>, K. V. Zakharov<sup>a</sup>, D. M. Ikornikov<sup>a</sup>, V. I. Yukhvid<sup>a</sup>,  
and N. Yu. Khomenko<sup>a</sup>**

<sup>a</sup>Merzhanov Institute of Structural Macrokinetics and Materials Science, Russian Academy of Sciences, Chernogolovka, Moscow, 142432 Russia

\*e-mail: ade@ism.ac.ru

DOI: 10.24411/9999-0014A-2019-10010

Centrifugal overloading is an efficient way to influence thermite mixture combustion with liquid-phase chemical conversion products and combustion regularities: gravity separation of metallic and oxide phases of combustion products, formation of chemical and phase compositions, and structure. Foundations of centrifugal SHS metallurgy of cast ceramics, alloys and composite materials, centrifugal SHS welding on steel substrates, etc. were developed on the base of the basic research results [1–4]. Production technologies for such materials often do not allow achieving the required set of properties and, in addition, are complex multi-step energy-intensive methods. One of the efficient directions in solving the problem of guaranteed increase product quality of these materials while reducing the energy and material manufacture-related costs is the development of a comprehensive technology for the production of Mo-based cast materials.

It is possible to create new functional gradient materials (FGM) and coatings by material-forming combustion processes (self-propagating high-temperature synthesis – SHS). The proposed project is part of the research on the SHS problem of new composite materials. Along with experimental studies, it is planned to simulate the processes of high-temperature synthesis in mixed systems under the action of gravity forces, taking into account the thermal heterogeneity of the mixture.

The development and modeling of the process of creating new FGM and hard alloys, as well as new methods for applying protective coatings to machine parts and mechanisms, are the most effective directions for creating new machinery, increasing the life of machines and mechanisms operating under conditions of intense wear, temperature. The novelty of the work is the development of scientific foundations of a new technology for the production of composite tubular products by the method of centrifugal surfacing of hard alloys with dispersive hardening of compounds based on MAX phases ( $\text{Mo}_2\text{TiAlC}_2$ ,  $\text{Mo}_2\text{Ti}_2\text{AlC}_3$ ,  $\text{Ti}_2\text{AlC}$ , and  $\text{Ti}_3\text{AlC}_2$ ) generated during the synthesis on steel substrates and mathematical modeling parallel to physical experiments. In the framework of the formation in the synthesis of phase transition in the melt observed in the experiments, it is supposed to take into account the mathematical models of mobility of the liquid phase and to provide the influence of the convective motion of gravity forces on the structure and velocity of the synthesis front.

In the research, experimental equipment and methods for conducting experiments will be developed; regularities and mechanism of gravity-assisted metallothemic SHS of a non-tungsten solid alloy (Mo–Ti–Cr–Ni–Al–C with alloying additives B, O etc.) will be established; the regularities and mechanism of gravity-assisted SHS-surfacing of the free-base solid alloy Mo–Ti–Cr–Ni–Al–C with alloying additives B, O etc. on the inner surface of steel pipes will be established. The expected results will expand the possibilities of managing the material-forming combustion processes and will allow them to be used to produce composite tubes with a gradient structure and will also have the prospect of using them to create new machinery, increase the life of machines and mechanisms operating under conditions of intense wear,

aggressive environments, and high temperatures. In parallel with the formulation and conduct of physical experiments, mathematical models of frontal regimes of exothermic chemical transformation of mixed compounds will be developed. Within the framework of this direction, information will be collected on the features of macrokinetics and on the mathematical modeling of high-temperature synthesis in mixed formulations. From the proposed number of models, the main, as well as effective methods for their numerical solution and corresponding programs for computers will be selected. The results of numerical experiments will be compared with the results of physical experiments.

The research was supported by the Russian Foundation for Basic Research (project no. 19-03-00088).

1. V.I. Yuxhvid, Modification of SHS-processes, *Pure Appl. Chem.*, 1992, vol. 64, no. 7, pp. 977–988.
2. V.I. Yuxhvid, D.E. Andreev, V.N. Sanin, N.V. Sachkova, Energy stimulation of autowave synthesis of hafnium aluminides, *Russ. J. Phys. Chem. B*, 2017, vol. 11, no. 5, pp. 815–819.
3. D.E. Andreev, D.M. Ikornikov, V.I. Yuxhvid, V.N. Sanin, Combustion of a high-calorific thermite mixture on the surface of a titanium substrate, *Combust. Explos. Shock Waves*, 2017, vol. 53, no. 5, pp. 574–579.
4. V.I. Yuxhvid, D.E. Andreev, V.N. Sanin, N.V. Sachkova, Autowave chemical transformations of highly exothermic mixtures based on niobium oxide with aluminum, *Combust. Explos. Shock Waves*, 2017, vol. 53, no. 5, pp. 580–584.

## ADAPTIVE COATINGS FOR HIGH TEMPERATURE APPLICATIONS

S. M. Aouadi

Department of Materials Science and Engineering, The University of North Texas,  
Denton, TX 76203, USA  
e-mail: samir.aouadi@unt.edu

DOI: 10.24411/9999-0014A-2019-10011

**Abstract.** This talk will provide an overview of the latest research developments in the design and exploration of ceramics with high temperature adaptive behavior. The adaptive behavior, triggered by thermal or thermo-mechanical stimulus, may be used to create smart surfaces such that change their chemistry and structure depending, to achieve a desired functionality. The initial focus of the talk will be on understanding the major mechanisms that lead to a reduction in friction and/or wear in high temperature lubricious materials. Adaptive mechanisms will be discussed and will include metal diffusion and formation of lubricant phases at worn surfaces, thermally- and mechanically-induced phase transitions in hexagonal solids, contact surface tribo-chemical evolutions to form phases with low melting point, and formation of easy to shear solid oxides. The second focus of this talk will be on self-healing ceramics and how thermal stimulus may trigger the migration and/or formation of a new phase to heal cracks that may have initiated as a result of repeated mechanical stimuli. Specific examples will be provided for applications that pertain to thermal barrier coatings. Changes in the structural and chemical properties of these materials as a function of temperature will be correlated to their performance using a range of experimental tools in addition to simulations based on *ab initio* and molecular dynamics calculations. This review also includes a discussion of the industrial applications of these materials as well as of potential design improvements and other anticipated future developments.

The quickly emerging need to finish surfaces of additive manufactured parts in addition to parts produced using more traditional techniques requires the use of materials with adaptive surfaces that automatically adjust their properties in response to external stimuli via interaction with both the ambient environment and contact with the parts. The new design requires a surface that satisfies a specific protective functionality that will enable the main part to last longer. Most protective surface finishes require the use of ceramics in pure or composite form that may be produced using a variety of techniques that include but are not limited to physical vapor deposition, chemical vapor deposition, laser cladding, plasma spray, and cold spray. Functional ceramics are prone to cracking as a result of external mechanical stimuli, which are further exacerbated by thermal stimuli. Once cracks have formed within a ceramic, the integrity of the protective surface is significantly compromised. A potential solution would be to resort to the self-healing/surface reconstruction concept in the design of next-generation protective surfaces, which would significantly increase the lifetime and reliability of materials and would drastically reduce replacement costs.

Surface reconstruction (self-organization) during sliding contact has received less attention so far but has the potential to create self-healing and self-lubricating materials that are crucial for environmentally-friendly tribological applications. Friction and wear are usually viewed as irreversible processes that lead to energy dissipation (friction) and material deterioration (wear). These adverse effects can be mitigated using solid lubricants that are able to self-organize on sliding surfaces to minimize friction and/or wear. The formation of an optimum solid lubricant at the interface between sliding surfaces is crucial to the efficiency and lifetime of applications,

especially when operating in harsh environments. For example, ternary oxides that contain a noble metal were recently shown to shear easily at elevated temperatures and to exhibit extremely low friction coefficients ( $< 0.2$ ) when tested at temperatures that exceed  $T > 500^\circ\text{C}$  [1]. These oxides were also successfully incorporated into the design of an adaptive coating, whereby multiple lubricious phases and a hard phase are combined to form a composite material that reduces both friction and wear over a broad temperature range [2]. The most promising high-temperature solid lubricant that has been reported in the literature is silver tantalate ( $\text{AgTaO}_3$ ) [3]. In these studies, the measured coefficient of friction (COF) was found to vary with load and values as low as 0.04 were reported when tested at  $750^\circ\text{C}$  using a 1 N load. More recently, the author investigated surface reconstruction mechanisms that result from thermal and mechanical stimuli during high temperature sliding for Nb-based surfaces (Figs. 1 and 2) [4] and for self-healing thermal barrier coatings (Fig. 3) [5].

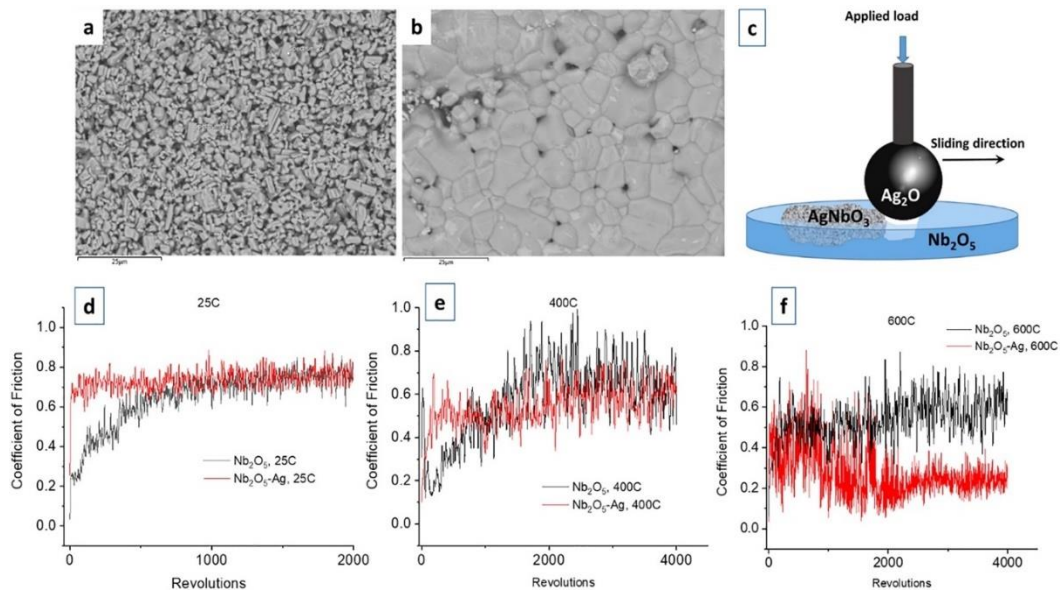


Fig. 1. Preparation of the bulk niobium oxide sample by (a) pressing and (b) sintering the pellet. The sample was further tested for the tribological performance (c). Tribology test of  $\text{Nb}_2\text{O}_5$  with and without the presence of Ag at (d)  $25^\circ\text{C}$ , (e)  $400^\circ\text{C}$ , and (f)  $600^\circ\text{C}$ . Results indicate a reduction in the coefficient of friction in case of silver presence at  $600^\circ\text{C}$  (f).

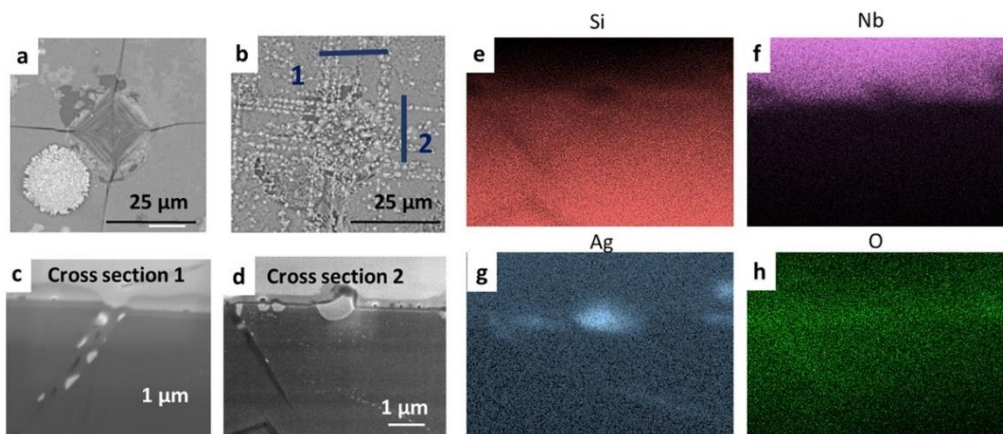


Fig. 2. (a) Cracks formed during the indentation test on the  $\text{Nb}_2\text{O}_5/\text{Ag}_2\text{O}/\text{Nb}_2\text{O}_5$  sample; (b) after annealing the cracks became invisible; Cross-sectional micrograph of (c) region 1 and (d) region 2; EDS analysis of cross section 2 for (e) Si, (f) Nb, (g) Ag, and (h) O, indicating a larger content of silver and oxygen at the crack site.

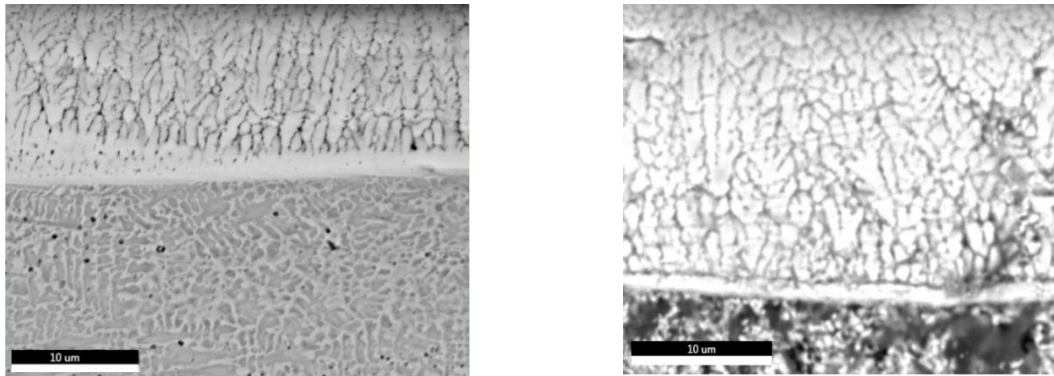


Fig. 3. Cross-sectional SEM micrographs of: (a) laser-processed YSZ coating, (b) annealed YSZ coating, (c) laser-processed YSZ–Al<sub>2</sub>O<sub>3</sub>–TiC coating, and (d) annealed YSZ–Al<sub>2</sub>O<sub>3</sub>–TiC coating. Processing Power = 800 W.

The research was supported by the Army Research Laboratory.

1. S.M. Aouadi, H. Gao, A. Martini, T.W. Scharf, C. Muratore, Lubricious oxide coatings for extreme temperature applications: a review, *Surf. Coat. Technol.*, 2014, vol. 257, pp. 266–277.
2. S.M. Aouadi, D.P. Singh, D. Stone, K. Polychronopoulou, F. Nahif, C. Rebholz, C. Muratore, A.A. Voevodin, Adaptive VN/Ag nanocomposite coatings with lubricious behavior from 25 to 1000°C, *Acta Mater.*, 2010, vol. 58, pp. 5326–5331.
3. A. Martini, T. Scharf, S.M. Aouadi, Load-dependent high temperature tribological properties of silver tantalate coatings, *Surf. Coat. Technol.*, 2014, vol. 244, pp. 37–44.
4. A. Shirani, J. Gu, B. Wei, J. Lee, S.M. Aouadi, D. Berman, Tribologically enhanced self-healing of niobium oxide surfaces, *Surf. Coat. Technol.*, 2019, vol. 364, pp. 273–278.
5. J.J. Gu, S.S. Joshi, Y.-S. Ho, B.W. Wei, T.Y. Hung, Y.Y. Liu, N.B. Dahotre, S.M. Aouadi, Tunable self-healing YSZ–Al<sub>2</sub>O<sub>3</sub>–TiC laser processed thermal barrier coatings, *Surf. Coat. Technol.* (in press).

## THE KEY ROLE OF STRUCTURAL AND PHASE COMPOSITION FOR FORMATION GRADED MATERIALS BY SHS-COMPACTION TECHNOLOGY

Z. Aslamazashvili<sup>\*a</sup>, G. Oniashvili<sup>a</sup>, G. Zakharov<sup>a</sup>, G. Tavadze<sup>a</sup>, and M. Chikhradze<sup>a</sup>

<sup>a</sup>Tavadze Metallurgy and Materials Science Institute, Tbilisi, 0186 Georgia

\*e-mail: oniash@gtu.ge

DOI: 10.24411/9999-0014A-2019-10012

The goal of the work is to define key aspects of structure and phase composition for obtaining graded materials by self-propagating high-temperature synthesis (SHS)-compaction technology, working under high dynamic loadings, where the adhesion strength between the layers is not worse than the strength of its ceramic and metal-ceramic layers [1, 2].

In order to have good adhesion between the layers it is necessary not to have sharp border between them and to have smooth transformation. For the realization of above said, diffusion process is necessary. For the process high temperature and time are necessary. Proceeding from the peculiarity of SHS-compaction high temperatures are generated, but at the same time process is very rapid and there is no enough time for diffusion process. Form obtaining well consolidated samples by mentioned technology, it is necessary to have maximal velocity of the synthesis front.

Based on results of experiments carried out in Ti–B, Ti–B–N, Ti–B–N–C, Ti–C, and Ti–Cr–C systems, the following peculiarities of structure and phase composition of layers were defined [3]:

- The neighboring ceramic or metal-ceramic layers of graded material should contain at least one or more similar phases;
- In transient zone, brittle low-strength chemical compounds must not form;
- The metal layer, if it exists, must comply with the following requirements: we should select the compound, where wetting angle with ceramic or metal-ceramic material must be no more than 90°;
- Metal layer should have the same content as ceramic layer or metal components in metal-ceramic layer;
- Metal layer should have the same content as metal alloy included in metal-ceramic layer;
- When obtaining the graded material, the synthesis velocities of exothermic layers are the same;

The analysis of experiments showed that if one of the above listed conditions is realized, we can obtain graded material with smooth transient zone and good adhesion.

Graded material 1 (Fig. 1): one of the layers is synthetic composite ceramic material (SCCM-1) based on Ti–B–N system. The second layer is Ti–B–C–N-based SCCM-2. The SCCM-1 consists of the following phases: TiB, TiN (small amount), and Ti<sub>2</sub>N. The second layer SCCM-2 consists of the following phases: TiB, TiCN (small amount), Ti<sub>2</sub>CN, and TiB<sub>2</sub>.

Graded material 2 (Fig. 2): the first layer is SCCM-1 based on Ti–B–N system, the second layer is metal-ceramic material TiB<sub>0.6</sub> based on Ti–B system. SCCM-1 consists of TiB<sub>2</sub> (small amount), TiB, TiN (small amount), and Ti<sub>2</sub>N. TiB<sub>0.6</sub> layer consists of TiB and Ti. Those 2 layers have one common phase TiB. As a result, the graded material is obtained. The outer surfaces have different properties, but the transition layer from one to another is smooth. Therefore, the material is characterized by high adhesion strength between the layers.



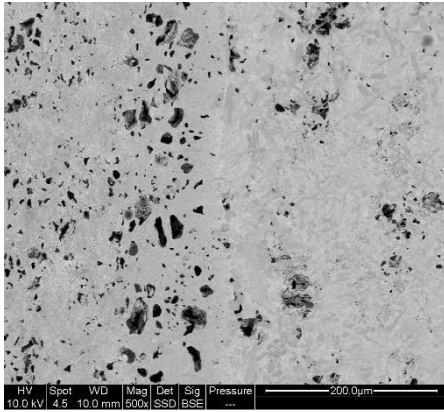


Fig. 1. Microstructure of transient zone of graded material between SCCM-1 and SCCM-2.

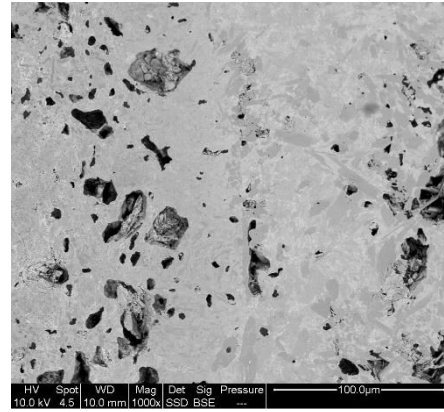


Fig. 2. Microstructure of transient zone of graded material between SCCM-1 and  $TiB_{0.6}$ .

Graded material 3 (Fig. 3): the first layer is SCCM-2 based on Ti–B–N–C system, the second layer is metal-ceramic  $TiB_{0.6}$  based on Ti–B system. SCCM-2 contains TiB, TiCN (small amount),  $Ti_2CN$ , and  $TiB_2$ . The second layer consists of TiB and Ti. Those 2 layers have one common phase TiB. As a result, the graded material is obtained. The outer surfaces have different properties, but the transition layer from one to another is smooth. Therefore, the material is characterized by high adhesion strength between the layers.

Graded material 4: the first layer is SCCM-1 based on Ti–B–N system, the second layer is metallic Ti (Fig.4.). One of the components of the SCCM-1 layer of initial chasm is Ti, and after the synthesis it consists of the phases: TiB,  $Ti_2N$ ,  $TiB_2$  (small amount), and TiN (small amount). Both layers have Ti as one of the components in initial chasm, as a result the graded material whose outer surfaces have different properties is obtained. The transition between the layers is smooth. The material is characterized by good adhesion between the layers.

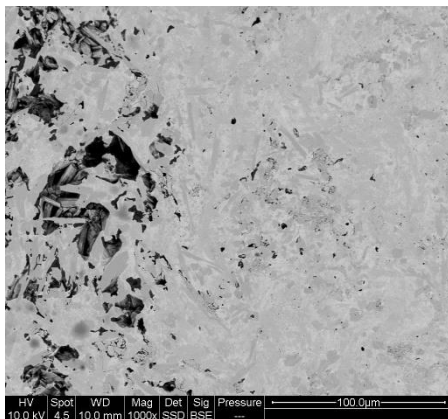


Fig. 3. Microstructure of transient zone of graded material between SCCM-2 and  $TiB_{0.6}$ .

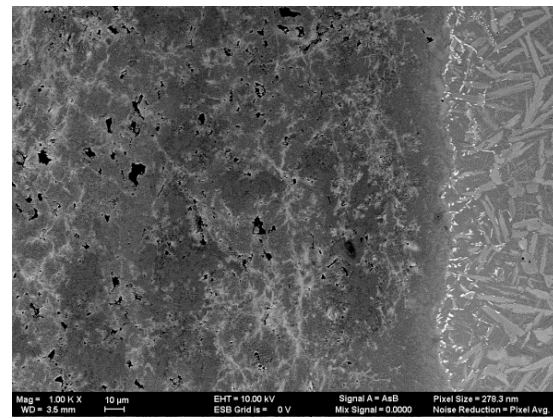


Fig. 4. Microstructure of transient zone of graded material between SCCM-1 and Ti.

Graded material 5 consists of SCCM-2 based on Ti–B–N–C system and metallic Ti. Both layers have Ti as one of the components in initial chasm, as a result the graded material whose outer surfaces have different properties is obtained. The transition between the layers is smooth. The material is characterized by good adhesion between the layers.

Graded material 6: the first layer is SCCM-1 based on Ti–B–N system, the second is metallic-ceramic TiC-based layer. SCCM-1 consists of  $TiB_2$  (small amount), TiB, TiN (small amount), and  $Ti_2N$ . In this layer the velocity of synthesis front  $V$  is  $\sim 10$  mm/s. The second layer consists of the following phases: TiC and metal phase, which can be Ni, Fe or steel, for example,

X18H15. Those 2 layers do not have any common or similar phases, but the velocity of the synthesis front is same ( $V \sim 10$  mm/s). As a result, the graded material is obtained. The outer layers have different properties, but the similarity of synthesis velocity provides good mixing and combination of components on the border. The transition between the layers is smooth, which provides the high adhesion strength between the layers. Figure 5 shows the microstructure of transient zone of material 6.

Graded material 7: one of the layers contains the phases TiC, Cr<sub>3</sub>C<sub>2</sub>, and metallic phase which may be Ni, Co or TiC, Cr<sub>3</sub>C<sub>2</sub>, Cr<sub>23-x</sub>Fe<sub>x</sub>C<sub>6</sub>, and metallic phase which can be Fe or steel (X18H15). In this layer the velocity of synthesis front is  $V \sim 18$  mm/s. The other layer is metal-ceramic phase consisting of TiC and metal phase (Ni, Fe, and steel X18H15). Those 2 layers have common phases and at the same time the velocities of synthesis front in both layers are the same  $V \sim 18$  mm/s. As a result, graded material is obtained. The outer layers have different properties, but the similarity of synthesis velocity provides good mixing and combination of components on the border. The transition between the layers is smooth, which provides the high adhesion strength between the layers. Figure 6 shows the microstructure of transient zone of graded material between TiC/Cr<sub>3</sub>C<sub>2</sub>-X18H15 and TiC-X18H15.

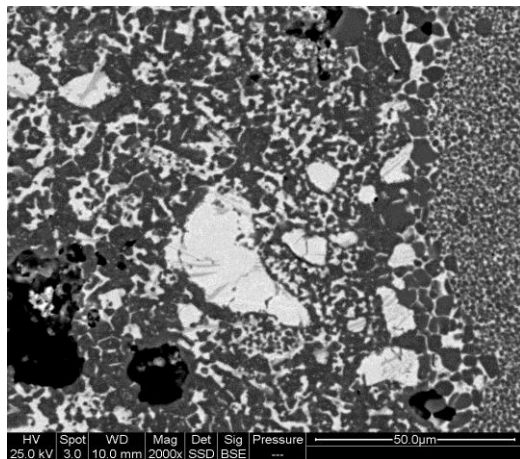


Fig. 5. Microstructure of transient zone between SCCM-1 and metal-ceramic TiC-Steel (X18H15).

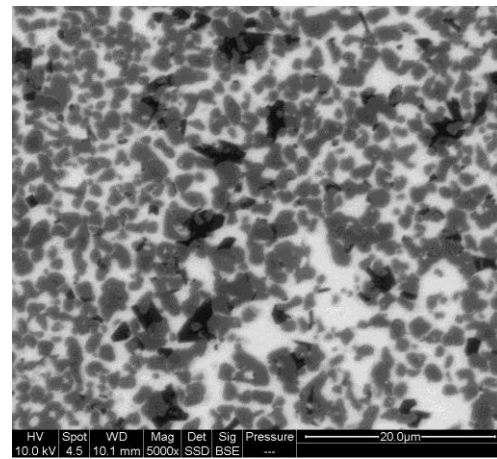


Fig. 6. Microstructure of transient zone of graded material between metal-ceramic TiC/Cr<sub>3</sub>C<sub>2</sub>-X18H15 and TiC-X18H15.

1. Z. Aslamazashvili, G. Zakharov, G. Oniashvili, G. Urushadze, G. Mikaberidze, G. Tavadze, M. Chikhradze, Microstructure peculiarities of metal-ceramic materialz of Ti-Cr-C system by SHS-compaction, Book of Abstracts SHS, 2017, p. 37.
2. Z. Aslamazashvili, G. Zakharov, G. Oniashvili, N. Aslamazashvili, G. Mikaberidze, M. Chikhradze, G. Tavadze, Peculiarities of microstructure of ceramic materials in obtained in Ti-B-C-N system by SHS, p. 42.
3. Patent: AP 2017 14618, Saqpatenti, Georgia, 2017.

## PRODUCTION OF ULTRAFINE-GRAINED POWDER COMPOSITES IN BN, B<sub>4</sub>C, AND B<sub>x</sub>C<sub>y</sub>N<sub>z</sub> SYSTEMS BY SHS METHOD

**Z. Aslamazashvili<sup>a\*</sup>, G. Zakharov<sup>a</sup>, G. Mikaberidze<sup>a</sup>, M. Chikhradze<sup>a</sup>, G. Tavadze<sup>a</sup>,  
and G. Oniashvili<sup>a</sup>**

<sup>a</sup>Tavadze Metallurgy and Materials Science Institute, Tbilisi, 0186 Georgia

\*e-mail: zuraaslamazashvili@yahoo.com

DOI: 10.24411/9999-0014A-2019-10013

One of the main aims of modern scientific researches is to focus the production of energy and resource-saving ecologically safe technologies and their realization. In this point one of the prospective directions is self-propagating high-temperature synthesis (SHS). The main idea of the work is to study the possibility to fabricate radiation resistant and radiation protective ceramic materials from <sup>10</sup>B and <sup>11</sup>B containing raw material (B<sub>2</sub>O<sub>3</sub>). At the first stage, this leads to elaboration of technology for production fine-grained powder composites BN, B<sub>4</sub>C, and B<sub>x</sub>C<sub>y</sub>N<sub>z</sub> in B–C–N system by using effective SHS technologies. At the second stage, Ti–B–C–N ceramic materials will be elaborated using fine-grained BN, B<sub>4</sub>C, and B<sub>x</sub>C<sub>y</sub>N<sub>z</sub> composites [1–4]. Experiments were carried out in high pressure reactors in order to obtain powder composite from the cheap raw material B<sub>2</sub>O<sub>3</sub> produced in Turkey. The boron carbide was obtained in SHS reactor in argon atmosphere, the carbon was added in form of synthetic graphite (model: KS15) and in form of soot (Model: II803). For production of BN nitrogen was used under a pressure of 5–10 MPa; synthetic graphite KS15, soot, and nitrogen were used for production of B<sub>x</sub>C<sub>y</sub>N<sub>z</sub>. In all cases Mg was used as reductant metal. For the production of ultrafine powders, 10 wt % final product and 20 wt % NaCl were added in initial chasm. The experiment includes drying of initial components, dosing, mixing, and synthesis under 2–10 MPa. The standard chemical treatment was also applied for materials obtained in SHS reactor.

Table 1.

|   | Content of initial chasm and possible reactions of SHS processes   | Process implementation conditions                                     | Result of experiment  | Grain size of product, nm |
|---|--|---|---|---------------------------|
| 1 | B <sub>2</sub> O <sub>3</sub> (98%) and synthetic graphite KS15:<br>2B <sub>2</sub> O <sub>3</sub> + 6Mg + C = B <sub>4</sub> C + 6MgO<br>B <sub>2</sub> O <sub>3</sub> = 47.3; Mg = 48.65; C = 4.05 | P <sub>0</sub> = 0.5 MPa,<br>P <sub>f</sub> = 2.0 MPa,<br>Argon       | Wash by HCl,<br>efficiency:<br>η <sub>t</sub> = 18.92%; η <sub>exp</sub><br>= 18.5% | 78–360                    |
| 2 | B <sub>2</sub> O <sub>3</sub> (98%) and soot II803:<br>2B <sub>2</sub> O <sub>3</sub> + 6Mg + C = B <sub>4</sub> C + 6MgO<br>B <sub>2</sub> O <sub>3</sub> = 47.3; Mg = 48.65; C = 4.05              | P <sub>0</sub> = 0.5 MPa,<br>P <sub>f</sub> = 1.5 MPa,<br>Argon       | Wash by HCl,<br>efficiency:<br>η <sub>t</sub> = 18.92%;<br>η <sub>exp</sub> = 18.2% | 78–350                    |
| 3 | B <sub>2</sub> O <sub>3</sub> (98%):<br>B <sub>2</sub> O <sub>3</sub> + 3Mg + N <sub>2</sub> = 2BN + 3MgO<br>B <sub>2</sub> O <sub>3</sub> = 41.18; Mg = 42.35; N <sub>2</sub> = 16.47               | P <sub>0</sub> = 5–10 MPa,<br>P <sub>f</sub> = 10–15 MPa,<br>Nitrogen | Wash by HCl,<br>efficiency:<br>η <sub>t</sub> = 29,41%;<br>η <sub>exp</sub> = 29%   | 50–60                     |
| 4 | B <sub>2</sub> O <sub>3</sub> (98%) and synthetic graphite KS15:<br>B <sub>2</sub> O <sub>3</sub> + Mg + C + N = B <sub>x</sub> C <sub>y</sub> N <sub>z</sub> + MgO                                  | P <sub>0</sub> = 5–10 MPa,<br>P <sub>f</sub> = 10–15 MPa,<br>Nitrogen | Wash by HCl,<br>efficiency:<br>η <sub>t</sub> = 25.64%; η <sub>exp</sub><br>= 25,3% | 95–350                    |
| 5 | B <sub>2</sub> O <sub>3</sub> (98%) and soot II803:<br>B <sub>2</sub> O <sub>3</sub> + Mg + C + N = B <sub>x</sub> C <sub>y</sub> N <sub>z</sub> + MgO   | P <sub>0</sub> = 5–10 MPa,<br>P <sub>f</sub> = 10–15 MPa,<br>Nitrogen | Wash by HCl,<br>efficiency:<br>η <sub>t</sub> = 25.64%;<br>η <sub>exp</sub> = 25.2% | 95–350                    |

Table 1 shows the content of initial chasm and possible reactions of SHS processes and experimental results for obtaining boron carbide, boron nitride, boron carbo-nitride from cheap raw materials produces in Turkey. The investigations of elemental content of  $B_xC_yN_z$  using analyzer "EXSPERT" showed that when the initial pressure in SHS reactor is 5 MPa, the final product of boron carbo-nitride contains 8.5 wt % nitrogen, while an increase in the pressure up to 9–10 MPa gives 18–18.5 wt % content of nitrogen in final product. By changing the pressure, it is easy to change the chemical composition of final product. The final products BN,  $B_4C$ , and  $B_xC_yN_z$  were studied using micro analyzer to define granulometry and chemical content. Figure 1 shows the microstructure of boron carbide, which gives possibility to define grain sizes. Figures 2–4 presents the microstructure and chemical contents of boron carbide, boron nitride, and boron carbo-nitride in relevant points.

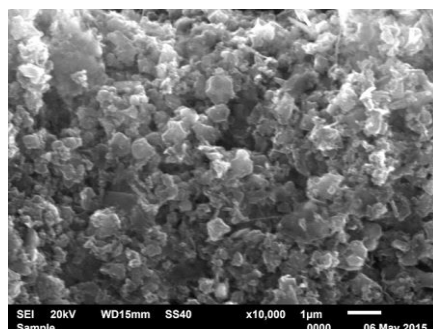
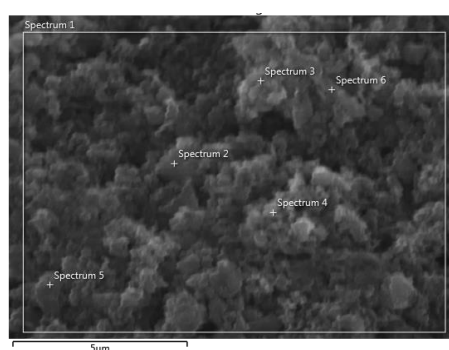
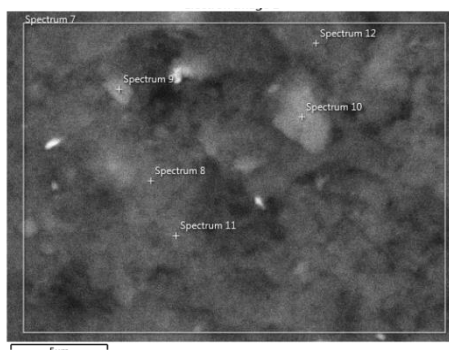


Fig. 1. Microstructure of  $B_4C$ .



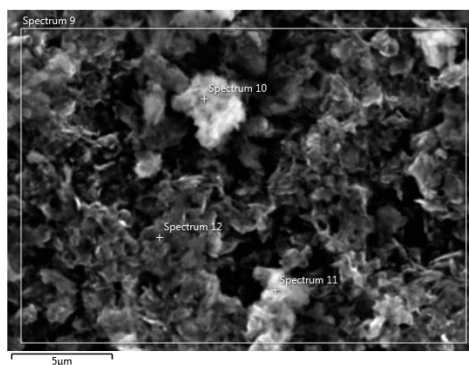
|   | Spectrum 6 | Spectrum 1 | Spectrum 2 | Spectrum 3 | Spectrum 4 | Spectrum 5 |
|---|------------|------------|------------|------------|------------|------------|
| B | 55.68      | 56.18      | 62.36      | 51.89      | 53.67      | 58.01      |
| C | 39.00      | 35.65      | 31.97      | 43.22      | 37.45      | 33.59      |

Fig. 2. Microstructure of  $B_4C$  and chemical compositions in marked points (wt %).



|   | Spectrum 7 | Spectrum 8 | Spectrum 9 | Spectrum 10 | Spectrum 11 | Spectrum 12 |
|---|------------|------------|------------|-------------|-------------|-------------|
| B | 32.51      | 56.77      | 33.35      | 39.63       | 56.24       | 64.19       |
| C | 0.80       |            |            |             |             |             |
| N | 50.53      | 33.93      | 46.84      | 40.67       | 36.44       | 29.37       |

Fig. 3. Microstructure of BN and chemical compositions in marked points (wt %).



|   | Spectrum 9 | Spectrum 10 | Spectrum 11 | Spectrum 12 |
|---|------------|-------------|-------------|-------------|
| B | 60.46      | 61.61       | 58.06       | 60.00       |
| C | 9.82       | 8.27        | 9.97        | 9.15        |
| N | 27.33      | 29.74       | 28.70       | 28.18       |

Fig. 4. Microstructure of  $B_xC_yN_z$  and chemical compositions in marked points (wt %).

Using the installation ELTRA-CS-800 the general content of carbon in  $B_4C$  and  $B_xC_yN_z$  was defined (Table 2).

Table 2.

| Material    | Sample | Carbon content, wt % |
|-------------|--------|----------------------|
| $B_4C$      | 1      | 24.36                |
|             |        | 24.45                |
| $B_4C$      | 2      | 24.05                |
|             |        | 24.02                |
| $B_xC_yN_z$ | 3      | 13.06                |
|             |        | 13.28                |
| $B_4C$      | 59     | 24.8                 |
|             |        | 24.65                |
| $B_4C$      | 64     | 26.87                |
|             |        | 26.93                |

## Conclusions

- (1) Experiments showed that it is possible to obtain fine-grained  $B_4C$ , BN,  $B_xC_yN_z$  from boron oxide  $B_2O_3$  produced in Turkey.
- (2) By changing the pressure of nitrogen in SHS reactor it is possible to change the content of BN and  $B_xC_yN_z$ .
- (3) Structural and spectral analysis showed that it is possible to obtain fine-grained  $B_4C$  and  $B_xC_yN_z$  in the range of 500–200 nm and BN with size less than 100 nm.
- (4) In  $B_4C$  and  $B_xC_yN_z$ , the total content of carbon is 24 and 13 wt %, respectively.

1. R.A. Murgatroyd, B.T. Kelly, Technology and assessment of neutron absorbing materials, *At. Energ. Rev.*, 1977, vol. 15, no. 1.
2. J.C. Marra, Thermal stresses in  $B_4C$  pellets – due to inadvertent irradiation of rod, *Eng. Comput.*, 1991, vol. 25.
3. J.C. Marra, Materials and mechanical design analysis of boron carbide reactor safety rods, Task technical and QA Plan, Task Number 91-047-1, 1991.
4. Concept of development of SHS: publishing house “Teoria”, 2003.

HEAT-RESISTANT COATINGS FORMED FROM SHS POWDER OF THE  $ZrSi_2$ – $MoSi_2$ – $ZrB_2$  SYSTEM FOR CARBON COMPOSITES

A. N. Astapov<sup>a</sup>, E. A. Levashov<sup>b</sup>, I. P. Lifanov<sup>a</sup>, Yu. S. Pogochev<sup>b</sup>, A. Yu. Potanin<sup>b</sup>, and M. V. Prokofiev<sup>a</sup>

<sup>a</sup>Moscow Aviation Institute (National Research University), Moscow, 125993 Russia

<sup>b</sup>National University of Science and Technology MISiS, Moscow, 119049 Russia  
e-mail: Lexxa1985@inbox.ru

DOI: 10.24411/9999-0014A-2019-10014

Composite materials based on  $C_f/C$  and  $C_f/SiC$  classes are among the most promising heat-resistant materials with unique properties [1], the combination of which determines the priority of their use in heat-stressed structural elements of rocket and space technology products. However, in oxygen-containing environments, their use is limited by the tendency of carbon to oxidize, starting at temperatures of 400–450°C, and the insufficient heat resistance of the SiC matrix, which causes the materials to lose mechanical properties. In high-velocity, high-enthalpy flows of oxygen-containing gases, the degradation of the structure of composites is significantly aggravated as a result of the simultaneous course of thermochemical processes (oxidation, catalysis) and mechanical entrainment (erosion). The expansion of the temperature–time intervals of operability of  $C_f/C$  and  $C_f/SiC$  composites is the exceedingly actual task of modern materials science. The research is carried out in several directions [2, 3]: modifying of composites matrixes, applying of protective coatings to reinforcing fibers, but the most effective is the application of heat-resistant coatings on the working surfaces of parts in contact with oxidizing media.

Currently the main objects of interest are coatings with the main structural component of ultra-high-temperature ceramics based on super-high-melting transition metal borides ( $ZrB_2$ ,  $HfB_2$ ,  $TiB_2$ ) with the addition of carbides (SiC, ZrC, HfC, TiC, TaC) and silicides ( $MoSi_2$ ,  $TiSi_2$ ,  $ZrSi_2$ ,  $TaSi_2$ ,  $WSi_2$ ). The report presents the current results of ongoing theoretical and applied research in the direction of creating heat-resistant coatings based on the  $ZrSi_2$ – $MoSi_2$ – $ZrB_2$  system. Materials of this system fully meet the requirements of the physicochemical model of the operation of a heat-resistant coating as a part of the structural wall of heat-resistant materials in hypersonic high-enthalpy flows of oxidizing gases [4]. The model provides the formation of a branched microcomposite structure in the form of a refractory dendritic-cellular type of heat-resistant phases ( $MoSi_2$ ,  $ZrB_2$ ) with the presence of relatively low-melting phases ( $ZrSi_2$ ) in its cells. The framework provides material resistance to erosion entrainment, and the low-melting phase provides self-healing effect and accelerated formation of a protective oxide film through the liquid phase. The compositions of the studied material in the  $ZrSi_2$ – $MoSi_2$ – $ZrB_2$  system were selected based on the results of oxidation in air at 1650°C for 5 h of compacts obtained from the corresponding powders by hot pressing [5].

To obtain the composite ceramic powders based on the  $ZrSi_2$ – $MoSi_2$ – $ZrB_2$  system, a magnesium thermal synthesis scheme with a reduction stage was used [6]. The starting components for the preparation of the reaction mixtures were analytically pure powders of silica  $SiO_2$ , zirconia  $ZrO_2$ , and molybdenum oxide  $MoO_3$  with a content of the main substance of 98.0–99.5% in its composition. As a source of boron, granulated coarse-grained powder of boric anhydride  $B_2O_3$  with a content of the main substance of not less than 99.0% was used, which was preliminarily milled in a ball rotating mill (BRM) (ISMAN, Chernogolovka) with a mass ratio of powder and grinding bodies of 1:5, and then sieved to separate the fraction with a particle size less than 100  $\mu m$ . Pure magnesium powder MPF-3 with an active component

content of 98.5–99.5% and an average particle size of 100–150  $\mu\text{m}$  was used as a reducing agent, which was introduced into the reaction mixtures with some excess, which provided the maximum degree of reduction of oxide components.

The powders were mixed in BRM in sealed steel drums using cylindrical carbide grinding bodies at a ratio of 1:6. The synthesis of final reaction mixtures was carried out in a universal SHS reactor of the brand SHS-8 (ISMAN, Chernogolovka) with a reaction chamber volume of 8 liters. The reaction mixture was loaded into a graphite container by free filling. The combustion process was initiated using a tungsten coil, which was placed in such a way that it touched the surface of the mixture. The synthesis was carried out in argon with pressure excess of 3 MPa. The combustion process was monitored by a manometer recording the pressure inside the reaction chamber of the SHS reactor.

This intermediate product consisting of composite particles containing the target phase and magnesium oxide MgO was crushed in a jaw crusher, and then crushed in BRM. To remove MgO, as well as excess of unreacted magnesium and extraction of ceramic powders, chemical (acid) enrichment in an aqueous solution of hydrochloric acid (HCl of chemical purity) was used. The resulting precipitate of the target product was filtered, washed with water and dried at 100°C, and then grinded in BRM and sieved through a sieve with a cell size of 63  $\mu\text{m}$ . To deagglomerate the particles of the obtained powder, the powder was subjected to grinding in a planetary centrifugal mill (PCM) of the MPP-1 brand (Technics and Disintegration Technology LLC, St. Petersburg). X-ray phase analysis (XRD) was performed on an ARL X'tra diffractometer (Thermo Fisher Scientific, Switzerland) with a Cu  $K\alpha$  copper anode. The phase composition of the synthesized powders includes zirconium diboride ZrB<sub>2</sub>, disilicides ZrSi<sub>2</sub>, MoSi<sub>2</sub>, as well as minor amounts of elemental Si and monosilicide ZrSi.

Coatings were formed by the method of slip-firing fusion. Square samples with a side of 20 mm and a thickness of 8 mm made of C<sub>f</sub>/C and C<sub>f</sub>/SiC composites were used as substrates. A solution of colloxylin in amyl acetate and diethyl oxalate was used as a binder in the slip suspension and powders of the ZrSi<sub>2</sub>–MoSi<sub>2</sub>–ZrB<sub>2</sub> system with a dispersion rate of < 10  $\mu\text{m}$  were used as the filler. The ratio of binder and powder in the composition was 1:1. Slip layers were applied with a brush on all surfaces and edges of the samples. Drying was performed in an oven at 80°C for 30 min. The firing was carried out in a shaft-type SSHVE-1.2.5/25 I2 vacuum furnace (LLC «OZ VNIETO», Russia) in a high purity argon (grade 4.8) atmosphere at an operating pressure in the chamber of 0.1–0.2 Pa. A rational temperature–time firing parameters was established: heating to 180°C at a rate of 10°C/min, then to 800°C at a rate of 30°C/min with intermediate 10-min isothermal exposures at 180 and 700°C, and further up to 1660–1680°C with a rate of 50–55°C/min.

Microstructural studies were performed using a scanning electron microscope (SEM) EVO-40 (Carl Zeiss, Germany) equipped with an X-ray energy dispersive spectrometer (EDS) (Oxford Instruments, United Kingdom). Samples for metallography were obtained with precision equipment of the Struers company (Denmark).

By means of XRD, SEM and EDS, it was established that the structure of the formed coatings is represented mainly by the same components as in the initial powder - the ZrSi<sub>2</sub> matrix with uniformly distributed MoSi<sub>2</sub> and ZrB<sub>2</sub> particles in it. In addition to these compounds, there is also a significant amount of highly dispersed ZrC particles with a linear size in the range of 1–3  $\mu\text{m}$  (the result of the reduction of silicon from ZrSi<sub>2</sub> by the reaction  $\text{C} + \text{ZrSi}_2 \rightarrow \text{ZrC} + 2\text{Si}$ ) and a small amount of SiC particles (the result of the interaction of silicon with carbon formed during binder decomposition in the process of coating firing). The formation of an intermediate layer between the substrate and the main coating layer with a thickness of 2–3  $\mu\text{m}$  represented by SiC is observed during the formation of coatings on samples of C<sub>f</sub>/C composite. Typical microstructures of coatings on C<sub>f</sub>/SiC and C<sub>f</sub>/C samples are shown in Fig. 1. The ability of the liquid phase to heal defects in the protected material in particular discontinuities and very deep cracks in the SiC layer has been established.

To compensate the loss of silicon as a result of sublimation under conditions of high-temperature vacuum firing, additional studies have been carried out on applying a thin layer of slurry made of elemental silicon powder over the layer of the base material slip. A typical microstructure of slip coating obtained with the use of an additional layer of silicon slip is shown in Fig. 2. A characteristic distinguishing feature of these coatings is the presence in their structure, along with the above-mentioned constituent elements of elemental silicon and interlayers of highly dispersed  $ZrSi_2$  particles in a matrix of silicon, resembling a structure of eutectic type. According to the data of high-quality XRD, the coating includes four phases:  $ZrB_2$ ,  $MoSi_2$ ,  $ZrSi_2$ , and Si.

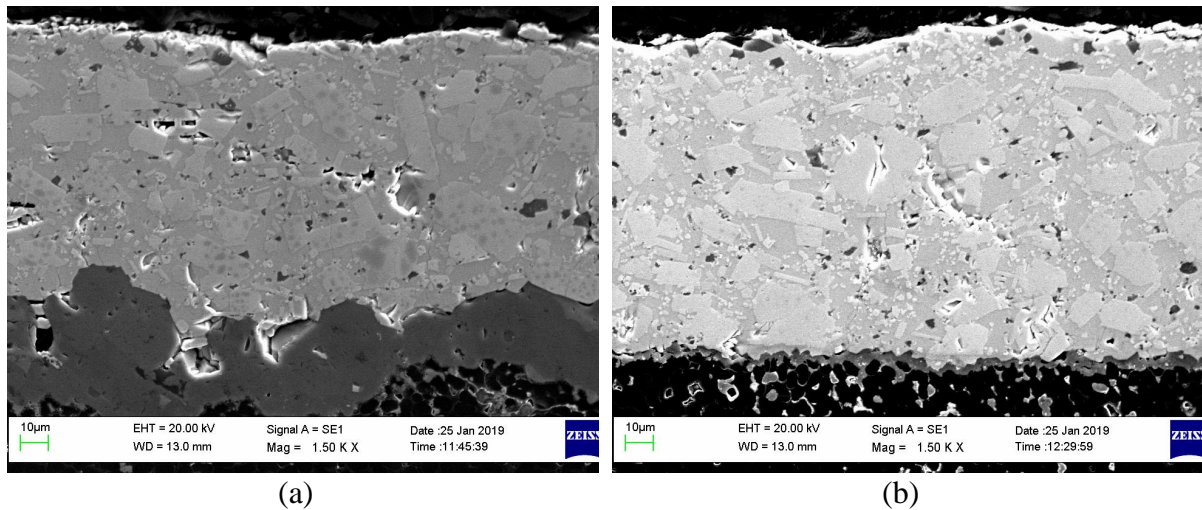


Fig. 1. Microstructure of slip coating formed from  $ZrSi_2$ – $MoSi_2$ – $ZrB_2$  powders on (a)  $C_f/SiC$  and (b)  $C_f/C$  composite samples.

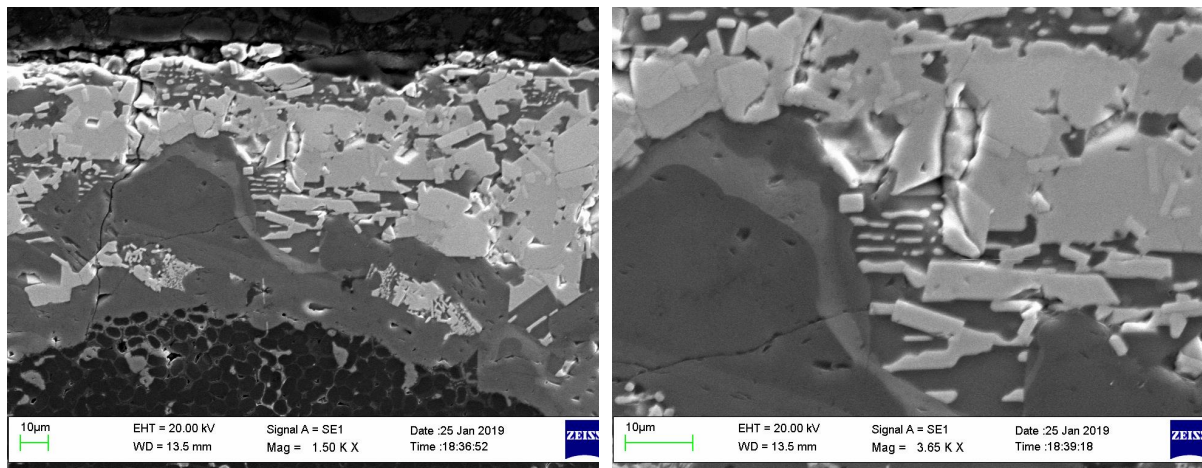


Fig. 2. Microstructure of slip coating formed from  $ZrSi_2$ – $MoSi_2$ – $ZrB_2$  powders with an additional layer of silicon slip on samples of  $C_f/SiC$  composite.

At present, experimental samples with coatings for heat resistance tests under static oxidation conditions in chamber furnaces and for gas-dynamic bench tests under conditions of thermochemical interaction with high-velocity, high-enthalpy oxygen-containing plasma flows have been prepared.

This work was carried out with the financial support from the Ministry of Science and Higher Education of the Russian Federation within the State Assignment (no. 9.1077.2017/PCh).



1. S. Zhang, Y. Zhang, A. Li, Q. Chen, X. Shi, J. Huang, Z. Hu, Carbon composites, In: Composite materials engineering, vol. 2 / Yi X.-S., Du S., Zhang L. (eds.), Singapore: Springer, 2018, pp. 531–617.
2. X. Jin, X. Fan, C. Lu, T. Wang, Advances in oxidation and ablation resistance of high and ultra-high temperature ceramics modified or coated carbon/carbon composites, *J. Eur. Ceram. Soc.*, 2018, vol. 38, no. 1, pp. 1–28.
3. A.A. Yurishcheva, A.N. Astapov, I.P. Lifanov, L.N. Rabinskiy, High temperature coatings for oxidation and erosion protection of heat-resistant carbonaceous materials in high-speed flows, *Key Eng. Mater.*, 2018, vol. 771, pp. 103–117.
4. V.S. Terentieva, A.N. Astapov, Conceptual protection model for especially heat-proof materials in hypersonic oxidizing gas flows, *Russ. J. Non-Ferr. Met.*, 2018, vol. 59, no. 6, pp. 709–718.
5. A.N. Astapov, Yu.S. Pogozhev, M.V. Prokofiev, I.P. Lifanov, A.Yu. Potanin, E.A. Levashov, V.I. Vershinnikov, Kinetics and mechanism of high-temperature oxidation of the heterophase  $ZrSi_2$ – $MoSi_2$ – $ZrB_2$  ceramics, *Ceram. Int.*, 2019, vol. 45, no. 5, pp. 6392–6404.
6. I.P. Borovinskaya, A.A. Gromov, E.A. Levashov, Y.M. Maksimov, A.S. Mukasyan, A.S. Rogachev, Concise encyclopedia of self-propagating high-temperature synthesis: History, theory, technology, and products, Elsevier Science, 2017, p. 466.

## HARDMETALS WITH HIERARCHICAL AND EXTRA HOMOGENEOUS STRUCTURE FOR A NEW GENERATION MINING TOOLS

E. N. Avdeenko<sup>\*a</sup>, A. A. Zaitsev<sup>a</sup>, I. Konyashin<sup>a</sup>, E. A. Levashov<sup>a</sup>, and D. A. Sidorenko<sup>a</sup><sup>a</sup>National University of Science and Technology MISiS, Moscow, 119049 Russia

\*e-mail: avdeenko.misis@mail.ru

DOI: 10.24411/9999-0014A-2019-10015

Development of promised mining tools with improved performance and properties is an important task. In addition to large reserves of oil and gas in the Arctic region there are about 10% world reserves of nickel, about 19% world reserves of the platinum group metals, 10% world reserves of titanium and more than 3% world reserves of zinc, cobalt, gold and silver. Climate conditions in the Arctic region are very tough. This causes a reduction in the ductility and fracture toughness of hardmetals and also excludes the use of water cooling. Mining tools are subjected to severe fatigue, compressive and bending loads, and intense abrasive wear. Therefore, increasing the mechanical and performance properties of the tools is a task of great importance, especially in the Arctic region. Mechanical and performance properties of hardmetals can be varied over a wide range either by changing the cobalt content or by affecting the grain size of the carbide phase. However, these approaches do not allow a simultaneous increase of the wear-resistance and fracture toughness of WC–Co hardmetals.

A promising approach allowing one to improve the mechanical properties of coarse-grained hardmetals is the nano-modification of the binder phase due to the decomposition of the supersaturated solid solution of tungsten and other refractory metals in the binder phase. The solubility of TaC and WC in cobalt is similar and decreases when decreasing the temperature, which allows one to expect that it is possible to form dispersed tantalum-containing precipitates (e.g.  $\text{Co}_3\text{Ta}$ ,  $\text{Co}_3(\text{W}, \text{Ta})$  or  $\text{Co}_3(\text{W}, \text{Ta})_3\text{C}$  phases) in the binder phase upon cooling from sintering temperatures, in analogy with the formation of nanoparticles in heat-treated WC–Co hardmetals with low carbon contents and consequently high concentrations of tungsten dissolved in the Co-based binder [1–5]. The proposed hypothesis was partially confirmed in the work [6] in which calculations by the electron-density functional method for the Co–Ta system was performed. The growth of fracture toughness and strength of hardmetals can also be achieved by obtaining hardmetals with a narrow WC grain distribution [7].

In this work, WC40 grade powder with an average particle size of 40  $\mu\text{m}$  was used to obtain a narrow fractional WC powder with a grain size of 5–15  $\mu\text{m}$  [8]. The narrow fractional WC powder was mixed with a Co powder (extrafine grade, Umicore, Belgium) and a TaC powder (HGS grade, H.C. Starck, Germany) in a ball mill. Sintering was carried out in a Sinter-HIP furnace at a maximum temperature of 1420°C. The hardmetals obtained from the narrow fractional WC powder have a very uniform microstructure and comprise rounded tungsten carbide grains in the microstructure (Fig. 1b) as compared to the traditional coarse-grained hardmetals (Fig. 1a). It was established by transmission electron microscopy (TEM) and high resolution TEM (HRTEM) that the cobalt binder of a hardmetal sample comprises nanocrystalline precipitates consisting of  $(\text{Ta}_x\text{W}_y\text{Co}_z)\text{C}_k$  with a mean size of around 5 nm (Fig. 2). The binder nano-hardness of the hardmetals with the hierarchical structure is found to be  $7.5 \pm 0.2$  GPa, while the binder nano-hardness of conventional coarse-grained hardmetals is less than roughly 5 GPa. The hardmetals with hierarchical and ultra-uniform microstructure are characterized by a unique combination of transverse rupture strength (2490 MPa), hardness ( $\text{HV} = 11.7$  GPa) and fracture toughness ( $K_{1C} = 15.9$  MPa·m<sup>1/2</sup>).

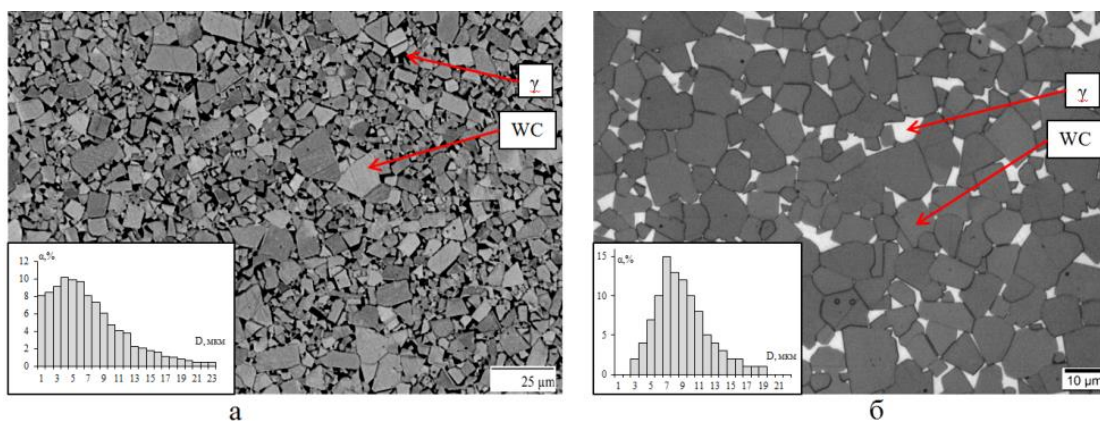


Fig. 1. Microstructures of coarse-grained hardmetals obtained from a conventional coarse-grain WC powder (a) and using the narrow fractional WC powder (b).

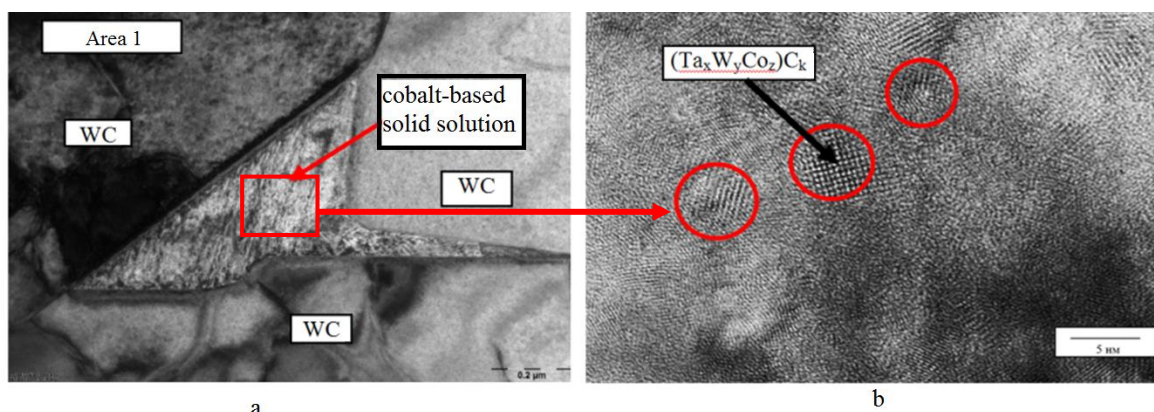


Fig. 2. Structure of the binder phase of a hardmetal sample: (a) TEM image and (b) HRTEM image.

This work was supported by the Ministry of Science and Higher Education of the Russian Federation in the frame of the Federal Target Program «Investigations and Developments over Priority Directions of the Scientific and Technology Complex of Russia for 2014–2020», agreement no. 14.575.21.0156, project RFMEFI57517X0156.

1. H. Suzuki, H. Kubota, The influence of binder phase composition on the properties of WC–Co cemented carbides, *Plnaseberichte für Pulvermetallurgie*, 1966, vol. 14, pp. 96–109.
2. H. Jonsson, Studies of the binder phase in WC–Co cemented carbides heat-treated at 650°C, *Pow. Met.*, 1972, vol. 15, pp. 1–10.
3. H. Jonsson, Studies of the binder phase in WC–Co cemented carbides heat-treated at 950°C, *Planseeberichte für Pulvermetallurgie*, 1975, vol. 23, pp. 37–55.
4. I. Konyashin, F. Lachmann, B. Ries, A.A. Mazilkin, B.B. Straumal, Chr. Kübel, L. Llanes, B. Baretzky, Strengthening zones in the Co matrix of WC–Co cemented carbides, *Scr. Mater.*, 2014, vol. 83, pp. 17–20.
5. I. Konyashin, B. Ries, F. Lachmann, R. Cooper, A. Mazilkin, B. Straumal, A. Aretz, V. Babaev, Hardmetals with nanograin reinforced binder: Binder fine structure and hardness, *Int. J. Refract. Met. Hard Mater.*, 2008, vol. 26, pp. 583–588.
6. S. Kirklin, J.E. Saal, V.I. Hegde, C. Wolverton, High-throughput computational search for strengthening precipitates in alloys, *Acta Mater.*, 2016, vol. 102, pp. 125–135.
7. R.P. Herber, W.D. Schubert, B. Lux, Hardmetals with «rounded» WC grains, *Int. J. Refract. Met. Hard Mater.*, 2006, vol. 24, pp. 360–364.
8. E.N. Avdeenko, E.I. Zamulaeva, A.A. Zaitsev, Investigation of ball milling and classification of coarse-grained tungsten carbide powders, *Tsvetnye Metally*, 2018, no. 8, pp. 90–96.

## EXPERIMENTAL STUDY OF THE EFFECT OF ATTACKING METAL PARTICLES ON MAGNESIUM, BORON, ALUMINUM, MOLYBDENUM OXIDES

A. N. Baideldinova<sup>a</sup>, S. Tolendiuly<sup>a</sup>, L. V. Mukhina<sup>\*a</sup>, and G. I. Ksandopulo<sup>a</sup>

<sup>a</sup>Institute of Combustion Problems, Almaty, 050012 Kazakhstan

\*e-mail: milabrega@yandex.ru

DOI: 10.24411/9999-0014A-2019-10016

SHS in powder metal oxide systems carried out under rotating conditions allows to obtain a number of nontrivial substances with free valency. During transition of the combustion wave to a superadiabatic mode and "freezing" of high-temperature intermediate states of matter, nonequilibrium phases stable in time are formed.

### 1. The attacked layer based on magnesium oxide

In a two-layer system (CuO + Al) + MgO, defective aluminomagnesium spinel  $\text{Mg}_{0.388}\text{Al}_{2.408}\text{O}_4$  (38.5 % wt) was obtained which proved to be effective in catalytic processes. To increase the yield of this material, a four-layer system (CuO + Al)–MgO–(CuO + Al)–MgO was developed. In this system, the substance  $\text{Mg}_{0.388}\text{Al}_{2.408}\text{O}_4$  was obtained almost in pure form – 93.5% by weight.

The binding energy between magnesium and oxygen atoms in the MgO molecule has a high value of 570 kJ/mol. In order to break this bond between atoms and to allow magnesium interact with copper or aluminum in the four-layer system, the rotation speed was increased from 1500 to 2500 rpm, this corresponding to an increase in centrifugal acceleration at the boundary between the first attacker and the attacked layers from 377 to 1048 g. The increased energy potential of the reaction radically changed the picture of the process, resulting in formation of magnesium and copper aluminates ( $\text{Mg}_2\text{Al}_3$  and  $\text{Cu}_9\text{Al}_4$ ). Due to a successful combination of strength, plasticity, corrosion resistance, the both obtained phases are of interest for further study as modifying additives.

Spinel  $\text{Al}_2\text{MgO}_4$  and copper oxide were formed under the action of the mixture based on copper oxide and aluminum attacking magnesium oxide in the presence of boron (CuO + Al) + (Mg + B). Aluminocobalt spinel  $\text{Al}_{0.27}\text{Co}_{0.73}(\text{Al}_{0.73}\text{Co}_{1.27})$  and  $\text{O}_4\text{Al}_{0.27}\text{Co}_{0.73}(\text{Al}_{0.73}\text{Co}_{1.27})\text{O}_4$  which is also of interest, and noble spinel  $\text{MgAl}_2\text{O}_4$  of high purity (close to 100 %) were obtained under the action of cobalt clusters ( $\text{Co}_3\text{O}_4$  + Al) + MgO on the layer of magnesium oxide.

### 2. The attacked layer based on boron oxide

Interesting results were obtained for four attacking systems – those of copper, molybdenum, tungsten and titanium.

#### 2.1. The active layer generating copper clusters

The system (CuO + Al) – ( $\text{B}_2\text{O}_3$  + Al) with a screen made of quartzite grains allowed to obtain a significant (13.4%) amount of non-equilibrium copper silicide  $\text{Cu}_{0.83}\text{Si}_{0.17}$  and the compound  $\text{Al}_{20}\text{B}_4\text{O}_{36}$  in the amount of 3.4%. In the four-component system (CuO + Al)–( $\text{B}_2\text{O}_3$  + Al)–(CuO + Al)–( $\text{B}_2\text{O}_3$  + Al), a promising monovalent copper metaborate  $\text{CuBO}_2$  was obtained in the amount of 17.7%. Under other conditions, an intermetallic compound  $\text{Cu}_9\text{Al}_{14}$  and a modifier  $\text{Al}_{20}\text{B}_4\text{O}_{36}$  were obtained in this system. According to EPR data, the products of each of the described systems contain substances with free valency.

#### 2.2. The active layer generating molybdenum clusters

A two-layer system ( $\text{MoO}_3$  + Al)–( $\text{B}_2\text{O}_3$  + Al) made it possible to obtain compounds of boron with molybdenum  $\text{MoB}_2$  (0.4%),  $\text{B}_2\text{Mo}_5\text{Si}$  (24.6%), and the intermetallid  $\text{Al}_3\text{Mo}$  (5.9%). In one

of these samples, without the use of a quartzite filter, a foamed amorphous mass containing  $\text{Mo}_3\text{Si}$  molybdenum silicide and cristobalite in small amounts was obtained.

In the system of pure boron oxide ( $\text{MoO}_3 + \text{Al}$ )– $\text{B}_2\text{O}_3$ , the substance  $\text{Al}_{20}\text{B}_4\text{O}_{36}$  was obtained in an amount of 3.8%, which is 0.4% more than in the copper-based system. The increase in the output of  $\text{Al}_{20}\text{B}_4\text{O}_{36}$  in the course of transition from copper (density  $8.94 \text{ g/cm}^3$ ) to molybdenum (density  $10.3 \text{ g/cm}^3$ ) allows to suppose that when increasing the weight of clusters of the attacking metal, the output of the modifier will increase by a more significant amount. This assumption was confirmed by experiments on the attack of boron-containing layers by systems based on tungsten (density  $19.3 \text{ g/cm}^3$ ).

Table 1. Initial compositions, the arrangement of layers, phase composition and ESR spectra of the products of the systems  $(\text{MeO} + \text{Al})\text{--}\gamma\text{-Al}_2\text{O}_3$  for various metals.

| Layers  | X-ray phase analysis   |        | EPR spectra |
|---|--|--------|-------------|
|   | Formula  | % mass |             |
| $\text{Co}_2\text{O}_3 + \text{Al}$                     | $\text{Al}_2\text{O}_3$  | 39.7   |             |
| $\text{Co}_2\text{O}_3 + \text{Al} + 40\%$              | $\text{Al}_{2.427}\text{O}_{3.64}$   | 34.5   |             |
| $\text{Al}_2\text{O}_3$                                 | $\text{Al}_{2.66}\text{O}_4$   | 25.8   |             |
| $\text{SiO}_2$  |  |        |             |
| $\gamma\text{-Al}_2\text{O}_3$                          |  |        |             |
| $\text{NiO} + \text{Al}$                                | $\text{Al}_2\text{O}_3$  | 57.2   |             |
| $\text{NiO} + \text{Al} + 35\% \text{ Al}_2\text{O}_3$  | $\text{Al}_{2.66}\text{O}_4$   | 28.5   |             |
| $\text{NiO} + \text{Al}$                                | $\text{SiO}_2$   | 10.9   |             |
| $\gamma\text{-Al}_2\text{O}_3$                          | Ni   | 3.5    |             |
| $\text{CuO} + \text{Al}$                                | $\text{Al}_2\text{O}_3$  | 74.8   |             |
| $\text{CuO} + \text{Al} + 40\% \text{ Al}_2\text{O}_3$  | $\text{Al}_{2.427}\text{O}_{3.64}$   | 11.3   |             |
| $\gamma\text{-Al}_2\text{O}_3$                          | $\delta\text{-Al}_2\text{O}_3$   | 8.3    |             |
| $\text{SiO}_2$  | Cu   | 1.6    |             |
|   | $\text{SiO}_2$   | 1.5    |             |
|   | $\text{Ca}_{2.25}(\text{Si}_3\text{O}_{7.5}(\text{OH})_{1.5})(\text{H}_2\text{O})$ | 1.3    |             |
|   | $\text{Cu}_2\text{O}$  | 1.2    |             |
| $\text{MoO}_3 + \text{Al}$                              | $\text{Al}_2\text{O}_3$  | 73.4   |             |
| $\text{MoO}_3 + \text{Al} + 30\%$                       | $\text{Al}_{7.7}\text{Mo}_{30}\text{Si}_{3.3}$                                     | 21.5   |             |
| $\text{Al}_2\text{O}_3$                                 | Mo   | 5.1    |             |
| $\text{MoO}_3 + \text{Al} + 40\%$                       | $\text{Al}_2\text{O}_3$  | 73.7   |             |
| $\text{Al}_2\text{O}_3$                                 | $\text{Al}_{7.7}\text{Mo}_{30}\text{Si}_{3.3}$                                     | 12.6   |             |
| $\text{MoO}_3 + \text{Al}$                              | $\text{MoO}_2$   | 9.8    |             |
| $\gamma\text{-Al}_2\text{O}_3$                          | Mo   | 2.6    |             |
|   | $\text{SiO}_2$   | 1.3    |             |
| $\text{WO}_3 + \text{Al}$                               | $\text{CaAl}_4\text{O}_7$  | 66.8   |             |
| $\text{WO}_3 + \text{Al} + 40\% \text{ Al}_2\text{O}_3$ | $\text{Al}_{2.427}\text{O}_{3.64}$   | 18.4   |             |
| $\text{CaO}\cdot\text{WO}_3 + \text{Al}$                | $\text{Al}_{2.66}\text{O}_4$   | 11.7   |             |
| $\gamma\text{-Al}_2\text{O}_3$                          | W  | 3.2    |             |

### 2.3. The attacking layer generating tungsten clusters

Two-layer systems  $(\text{WO}_3 + \text{Al})\text{--}(\text{B}_2\text{O}_3 + \text{Al})$  have been developed to produce  $\text{Al}_{20}\text{B}_4\text{O}_{36}$ . The output of  $\text{Al}_{20}\text{B}_4\text{O}_{36}$  was equal to 34%. Comparison of the results of experiments with attacking layers based on copper and molybdenum confirmed the fact that the density of the attacking metal plays a crucial role. To study the possibility of obtaining light metal borides, a

two-layer system  $(\text{WO}_3 + \text{Al})-(\text{SiO}_2 + \text{B}_2\text{O}_3 + \text{Al})$  was developed in which titanium boride was obtained.

### 3. The attacked layer based on aluminum oxide

To study the effect of metal clusters on the attacked layers of aluminum oxide being attacked  $\gamma\text{-Al}_2\text{O}_3$  was used due its increased chemical activity with respect to  $\alpha\text{-Al}_2\text{O}_3$ . Table 1 shows EPR spectra of products of layer systems  $(\text{MeO} + \text{Al})-\gamma\text{-Al}_2\text{O}_3$ . In all cases, there is a signal from free radicals between the third and fourth components of the  $\text{Mn}^{2+}$  standard.

The nonlinear dependence of the relative intensity of the free radical signal on the density of the attacking metal is presented in Table 2. According to EPR spectra, the heaviest metal–tungsten shows a significant advantage, as in the case of the attack of boron oxide layers (point 2).

Table 2. Metal density and the ratio of the height of the free valency peak to the height of the standard peak.

| Metal | Density, g/cm <sup>3</sup> | The relative intensity of the peak |
|-------|----------------------------|------------------------------------|
| Co    | 8.90                       | 0.18                               |
| Ni    | 8.90                       | 2.16                               |
| Cu    | 8.94                       | 0.23                               |
| Mo    | 10.30                      | 2.07                               |
| W     | 19.30                      | 4.42                               |

### 4. The attacked layer based on molybdenum oxide

In a two-layer system  $(\text{CuO} + \text{Al})-(\text{MoO}_3 + \text{Al})$ , with the separation of the attacking and attacked layers by a filter of quartzite grains, a nontrivial substance  $\text{Cu}_{64}\text{O}$  was obtained in a small amount (1% by weight). With an increase in the flow rate of copper clusters, in the product there is no molybdenum in the amount available for X-ray analysis. This means that the layer being attacked has been heated by the released energy to 1000–1260°C. As is known, in this temperature range there takes place sublimation of molybdenum trioxide, the process on which production of  $\text{MoO}_3$  from ash is based. This is also confirmed by the appearance in the product of a significant amount (38.2%) of mullite  $3\text{Al}_2\text{O}_3 \cdot 2\text{SiO}_2$ , the formation of which occurs in the temperature range of 1100–1200°C.

The removal of a quartzite filter from the initial layer system and a direct attack of the layer  $(\text{MoO}_3 + \text{Al})$  by copper clusters led to reduction of molybdenum from molybdenum trioxide. This indicates the fact that, firstly, the power of the flow was sufficient to initiate chemical reactions in the attacked layer. Secondly, the speed of the combustion wave front and the heating of the stoichiometric mixture of molybdenum oxide with aluminum exceeded the rate of trioxide sublimation, allowing it to react with the reducing agent. An important fact is also detection, using X-ray phase analysis, of cristobalite – a high-temperature phase of aluminum silicate, which is stable under equilibrium conditions in the temperature range from 1470°C to the melting point at 1728°C. The presence of cristobalite in the synthesis products indicates their rapid cooling and only a partial transition of the high-temperature phase to low-temperature one (mullite).

- 1 G.I. Ksandopulo, A.N. Baideldinova, The SHS process in the layered systems, SHS-composite materials: Multi-authored monograph, ed. by prof. Z.A. Mansurov, Almaty: Qazaq University, 2017, pp. 33–84.
- 2 G. Ksandopulo, A. Baideldinova, Y. Riabikin, L. Mukhina, E. Ponomareva, N. Vasilieva, Research of products of high temperature synthesis flowing in the rotation conditions, *IOP Conf. Ser.: Mater. Sci. Eng.*, 2017, vol. 175, 012037.

## THE EFFECT OF MAGNESIUM ON THE COMBUSTION PROCESS OF GAS GENERATOR MIXTURES

A. Ye. Bakkara<sup>\*a,b</sup>, N. N. Mofa<sup>a</sup>, B. S. Sadykov<sup>a,b</sup>, Z. L. Sultanova<sup>b</sup>,  
and Z. A. Mansurov<sup>a,b</sup>

<sup>a</sup>Institute of Combustion Problems, Almaty, 050012, Kazakhstan

<sup>b</sup>Al-Farabi Kazakh National University, Almaty, 050040, Kazakhstan

\*e-mail: bakkara\_ayagoz@mail.ru

DOI: 10.24411/9999-0014A-2019-10017

Metal powders are one of the most important components of combustible compositions of different composition and purpose. Their use is primarily due to the high thermal effect of metal oxidation, as well as a decrease in the average molecular weight of gaseous combustion products as a result of the deoxidation of H<sub>2</sub>O and CO<sub>2</sub> during their interaction with the metal [1]. This is especially important for hydro-responsive fuel systems, in which the metal contains up to 80%, and it is the main fuel [2–4]. The most common and fairly energy-consuming metal fuel for fuel systems for different purposes is aluminum. In some fuels, primarily ballistic, aluminum particles due to the low oxidative activity of oxygen-containing combustion products ignite with a long time delay. In such cases, use is made of magnesium or its alloys with aluminum, the particles of which ignite faster than aluminum and burn completely [1, 3]. The most important characteristic of metal powders when used in combustible mixtures is the content of active (non-oxidized) metal, as well as the size and shape of particles. To obtain highly dispersed metal particles of magnesium with a modified surface of the particles, it is important to choose the optimal conditions of MCT for a specific modifying additive. This article presents the results and a comparative analysis of the studies on magnesium MCT in the presence of graphite. For the experiments, MPF-3 grade magnesium powder was used. The microstructure of the starting magnesium powder particles was investigated. The results of the microstructural analysis of the initial MPF-3 magnesium powder showed (Fig. 1) that the magnesium particles have a flaky shape and the average particle size of the sample exceeds 200 μm, while the thickness of the flakes is about 20 μm. The specific surface of such samples, according to the results of the BET method, is 0.181 m<sup>2</sup>/g. The results of the EDX analysis showed the presence of 2.26% oxygen in magnesium, i.e. the presence on the surface of the particles of the oxide film. However, X-ray phase analysis of the original magnesium brand MPF-3 showed that 9.6% Mg(OH)<sub>2</sub> is present in its composition, i.e. the surface of the particles is covered with a hydroxide film.

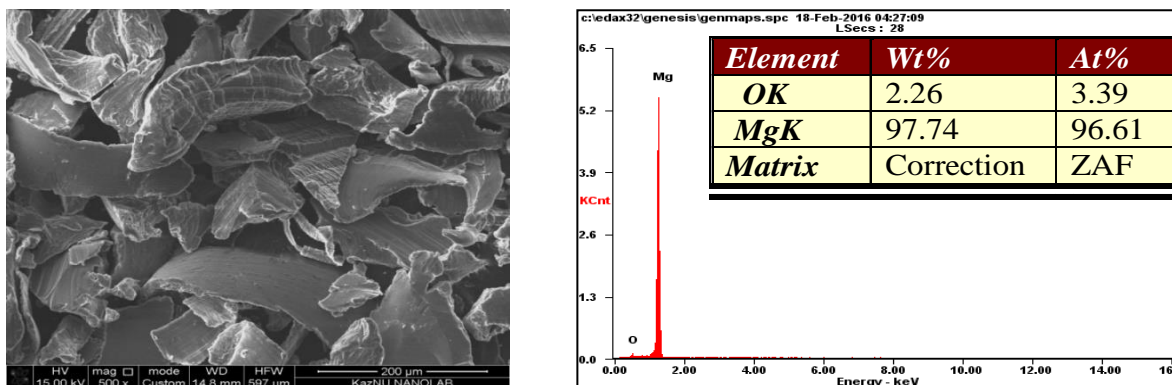


Fig. 1. Electron microscopic image, energy dispersive spectrum and mass fraction of elements of original magnesium powder brand MPF-3.

Mechanochemical processing (MCT) of powders was carried out in the pulverisette 5 centrifugal planetary mill (manufactured by FRITSCH) with a volume of each working chamber of 500 mm<sup>3</sup>, a platform rotation speed of 400 rpm, an acceleration of grinding balls 40g, power consumption 1, 5 kW/h. The MCT was performed in an air atmosphere with a powder/ball ratio ( $M_P/M_{b,r}$ ) = 1/4. During grinding, the amount of modifying additive introduced is different (5–20%).

The processing time was no more than 20 min to exclude self-ignition. The choice of the optimal time of the MCT was determined by the results of previous studies. In order to prevent the particles from oxidizing by atmospheric oxygen after the MCT and to estimate the changes actually associated with the mechanical action, the samples of the dispersed mixture were passaged with hexane (C<sub>6</sub>H<sub>14</sub>).

As a result, magnesium oxide with graphite particles retain a lamellar form. The specific surface for the composite particles (Mg 80% + C 20%) rises to 16.383 m<sup>2</sup>/g. The results of the EDX analysis of the elemental composition of the Mg–C composite particles showed that after the MCT the mass fraction of oxygen atoms increases, so for (Mg 80% + C 20%) it is more than 6% (Fig. 2).

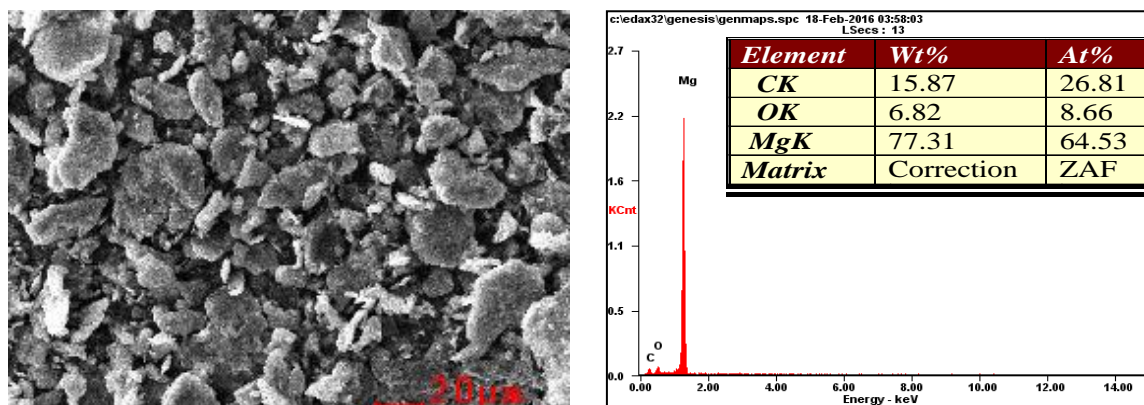


Fig. 2. Electron microscopic image, energy dispersion spectrum and mass fraction of elements in the composite (Mg 80% + C 20%) after 20-min MCT.

Consequently, on the surface of the magnesium particles after MCT, the thickness of the oxide layer increases. However, according to the results of X-ray phase analysis, no oxides are formed on the surface of the particles, and hydroxides, the amount of which can reach 15%.

To estimate the substructural features of aluminum particles after MCT, crystallite sizes were studied by XRD in the Mg/C composites obtained. According to the results of the analysis, in the process of mechanochemical processing, the size of the crystallites changes from the amount of the modifier used (Table 1).

Table 1. The size of the crystallites of magnesium after 20 min of the MCT with graphite

| Graphite content in composites | Crystallite size L, Å |
|--------------------------------|-----------------------|
| –                              | 580                   |
| 5% C                           | 600                   |
| 10% C                          | 770                   |
| 15% C                          | 590                   |
| 20% C                          | 520                   |

In the case of magnesium oxide with graphite, crystallites first grow, and when the carbon content is 15–20%, the crystallite size decreases, i.e. more intensive accumulation of defects in the volume of grains. The surface film of magnesium particles is destroyed (loosened) and saturated with highly dispersed carbon particles. Thus, the use of graphite with magnesium oxide according to all analyzed characteristics contributes to a change in the morphology and



structure of the particles during the formation of metal/carbon composites. The observed changes in the size of the magnesium particles modified by the organic additive (graphite) in MCT are due to the fact that carbon, which is also dispersible in the MCT process, plays a significant role in the formation of the surface layer of the particles in all the cases considered.

Silicon dioxide in this case is used in an inactivated state. The mixtures were prepared with a stoichiometric ratio of components: Mg 44% + SiO<sub>2</sub> 56%. For a mixture of quartz and composite (Mg/C) after the MCT, the induction period of ignition also decreases and the temperature and duration of combustion of mixtures with SiO<sub>2</sub> increase (Fig. 3).

Table 2 shows the indicators of the main characteristics of the combustion process and the strength of the synthesized samples. This is probably due to the optimal ratio of the particle size of the components of the mixture, and accordingly with an increase in the packing density, which ensures the density of contact between the oxidizer and the fuel.

The products of technological combustion of samples whose combustible component is a composite (Mg/C) have a low indicator of strength characteristics due to the porous, loose structure of the samples (Fig. 4). This is due to the fact that combustion proceeds in layers and in a large amount of gaseous products of synthesis are formed.

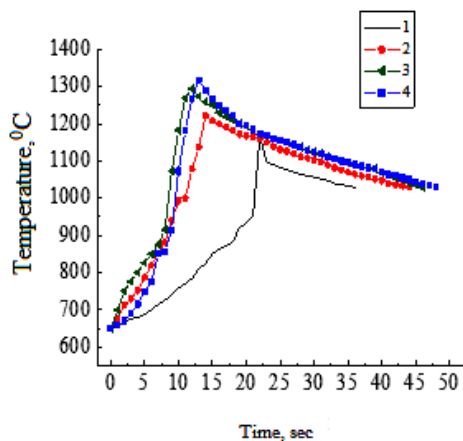


Fig. 3. Thermograms of combustion systems (SiO<sub>2</sub> + Mg) with magnesium in the initial state and after 20-min MCT with different amounts of graphite: 1 Me init.; 2 to 5%; 3 10%; 4 20% C.



Fig. 4. Fracture and external appearance of SHS samples obtained with magnesium modified at MCT with a content of 20% C.

Table 2. Approximate maximum temperature, burning rate of SiO<sub>2</sub> mixtures with modified magnesium, and strength characteristics of the synthesized samples.

| Composition                 | $T_{max}$ , °C | Burning rate, deg/s | $\sigma$ , MPa |
|-----------------------------|----------------|---------------------|----------------|
| Mg init. + SiO <sub>2</sub> | 1170           | 23.6                | 50             |
| Mg + 5%C                    | 1295           | 40.9                | 5.8            |
| Mg + 10%C                   | 1318           | 58.6                | 1              |
| Mg + 20%C                   | 1223           | 51.4                | 1              |

The results of combustion of mixtures, in which aluminum and magnesium were used as a fuel component after MCT in the presence of graphite, showed the effectiveness of this method for improving the thermo-kinetic characteristics of the combustion process, and also determined the conditions for the preparation of combustible material and the combustion process. The latter fact is important when using the obtained nanostructured Mg/C composites as part of combustible systems, for example, for gas generators or for puffing up and producing porous systems of a specific purpose. Such compositions, as a rule, are heterogeneous condensed systems.

1. V.N. Alikin, A.V. Vakhrushev, A.S. Yermilov, A.M. Lipanov, S.Yu. Serebrennikov, Solid fuels of jets. Thom. IV. Topлива Charges. Engines. Mechanical engineering, Moscow, 2010. (In Russian)
2. L.F. Pokhil, A.F. Belyaev, Yu.V. Frolov, Combustion of powdery metals in the fissile environments. Science, Moscow, 1972. (In Russian)
3. A.E. Sheyndlin, E.I. Shkol'nikov, A.V. Parmuzina, S.A. Tarasova, S.A. Yanushko, A.V. Grigorenko, Mikrogeneratory Hydrogenium on an aluminum oxidation basis water for portable sources of current. News of RAS. Power engineering, 2008. (In Russian)
4. Ya.M. Paushkin, Liquid and solid rocket fuels. Science, Moscow, 1978. (In Russian)

## AN OVERVIEW OF ATOMISTIC APPROACHES IN SHS PROCESSES

F. Baras<sup>\*a</sup>, O. Politano<sup>a</sup>, A. Fourmont<sup>a</sup>, S. Le Gallet<sup>a</sup>, A. Nepapushev<sup>b</sup>, A. Sedegov<sup>b</sup>,  
S. Vadchenko<sup>c</sup>, and A. Rogachev<sup>b,c</sup>

<sup>a</sup>Laboratoire ICB, CNRS/Université Bourgogne Franche Comté, Dijon, France

<sup>b</sup>Center of Functional Nano-Ceramics, National University of Science and Technology  
MISiS, Moscow, 119049 Russia

<sup>c</sup>Merzhanov Institute of Structural Macrokinetics and Material Science, Russian Academy of  
Sciences, Chernogolovka, Moscow, 142432 Russia

\*e-mail: fbaras@u-bourgogne.fr

DOI: 10.24411/9999-0014A-2019-10018

Since the discovery of SHS by A. Merzhanov and I.P. Borovinskaya, the topic attracts interest both from the experimental and theoretical point of view. The "Concise Encyclopedia of SHS" [1] demonstrates the wide range of theoretical interests in SHS processes including combustion theory, thermal explosion, auto-oscillations, reaction-diffusion, dissolution-precipitation, grain growth, spin combustion, heterogeneous kinetics, phase transformations, and non-equilibrium systems. The understanding the SHS processes relies on the study of reactions kinetics, heat and mass transfer, as well as the dynamics of structural transformations. Besides the usual multi-physics description, the atomistic approach provided by Molecular Dynamics simulations (MDS) becomes a useful tool in describing SHS processes. MDS indeed give the basic atomistic steps leading to observed microstructure beyond any thermodynamic or kinetic modeling. MDS can be considered as a modeling that offers a counterpart to in-situ experiments to explore elemental mechanisms. In addition, MDS allow us to calculate most of the parameters that are used in numerical modeling at the macroscopic scale. This approach thus offers a self-consistent multi-scale modeling that provides a powerful tool for the interpretation of experimental results.

In the case of SHS in nanometric metallic multilayers, MDS prove to be a very appropriate method for numerical studies, as the accessible time and length scales are in the same range of magnitude as in "real" experiments. During this talk, we will briefly review the main features of SHS in nanofoils considering Ni/Al as a model system [2]. We will show how modeling and experiments are complementary approaches in order to detect intrinsic behaviors and reactive mechanisms (see Fig. 1).

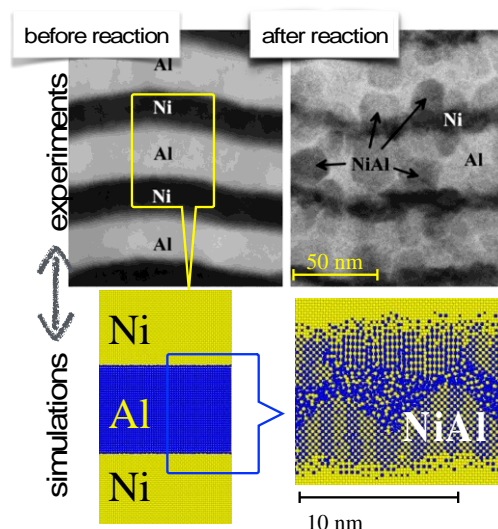


Fig. 1. Comparative study of MDS and experiments in the case of SHS in Ni/Al nanofoils.

Next, an overview of recent achievements will be reported, including crystal growth, nucleation, and SHS propagation in complex systems.

Crystal growth in the case of self-propagating reactions in Ni-Al nanofoils was also investigated by means of MDS [3]. We studied the heteroepitaxial growth of NiAl on Ni during mixing and alloying at interfaces (see Fig. 2). The microstructure evolution was tracked along with grain orientation dynamics. For the different orientations of the Ni interface, a simple geometric construction based on the relationship between unit cells of Ni and NiAl explains crystal growth specificities. The nucleation process and growth kinetics were also investigated. This study proves that crystal growth varies considerably, in relation to Ni orientation. The influence of composition gradient on the crystal nucleation of the NiAl intermetallic was considered in [4].

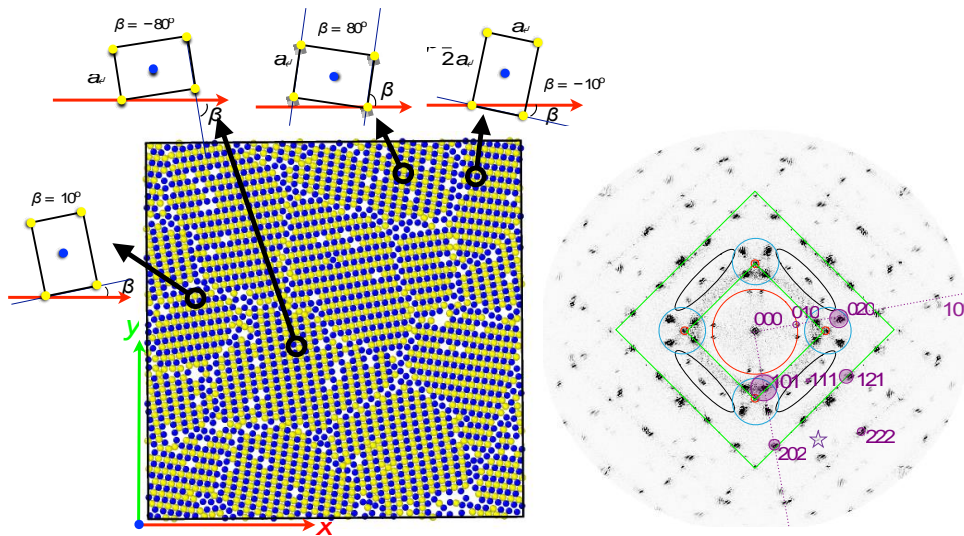


Fig. 2. Snapshot of a (001)-slice across the NiAl phase, parallel to the interface, and corresponding virtual diffraction (SAED) pattern. The Al and Ni atoms are shown as blue (dark grey) and yellow (light grey) spheres, respectively.

Thanks to the progress in computing facilities and the set up of large-scale MDS, more and more complex systems can be considered in order to understand the role of defects or intricate microstructure in nanostructured samples. For instance, the influence of defect concentration on the combustion of reactive Ni/Al nanofoils was considered in [5] as well as the grain size effects in [6]. As shown in Fig. 3, the SHS propagation can also be studied in the case of disordered nanostructured grains.



Fig. 3. Snapshot of SHS propagation in a sample with 80 disoriented 15 nm-grains. Each grain has a layered structure.

In the last part of the talk, we will focus on the case of reactive composite particles Ni/Al and Ti/Al. In parallel to experimental investigations for producing highly reactive particles for

additive technologies, MD simulations [10] are developed in order to follow the elemental mechanisms governing the kinetics aspects at the microscopic level, such as friction between metallic particles, diffusion, creation of defects, local ordering, precipitation, local stress and reactive behavior due to laser initiation. Figure 4 shows the thermal response of a Ni/Al reactive particle pre-heated at 600K.

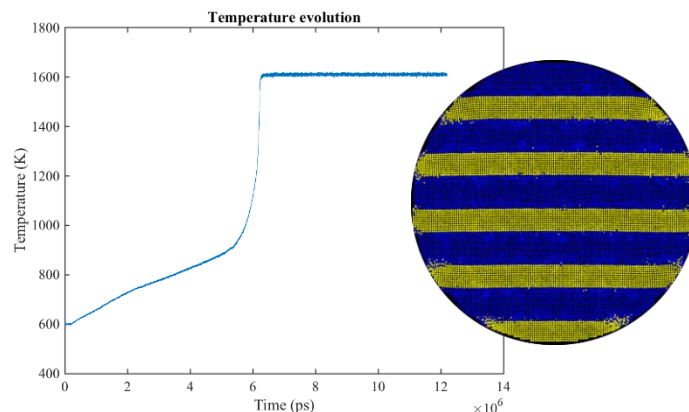


Fig. 4. Thermal behavior of a reactive particle and initial configuration of the reactive particle ( $d = 24\text{nm}$ ).

In summary, molecular dynamics approaches allow us to elucidate the mechanisms of nonisothermal processes such as phase transformations and self-propagation reactions. The atomistic-level understanding obtained from MDS can help interpret and guide experimental work in SHS.

Part of this work is supported by the International Russian-French PHC Kolmogorov "RECIPES" (no. 41144SG), the Ministry of Science and Higher Education of the Russian Federation in the framework of the Federal Target Program "Research and Development on Priority Directions of the Scientific and Production Complex of Russia for 2014–2020", agreement no. 14.587.21.0051, project RFMEFI58718X0051.

1. I.P. Borovinskaya, A.A. Gromov, E.A. Levachov, Y.M. Maksimov, A.S. Mukasyan, A.S. Rogachev, Concise Encyclopedia of Self-Propagating High-Temperature Synthesis: History, Theory, Technology, and Products, Elsevier Pbl., 2011.
2. F. Baras, V. Turlo, O. Politano, S.G. Vadchenko, A.S. Rogachev, A.S. Mukasyan, SHS in Ni/Al Nanofolds: A Review of Experiments and Molecular Dynamics Simulations, *Adv. Eng. Mater.*, 2018, vol. 20, pp. 1–20.
3. F. Baras, O. Politano, Epitaxial growth of the intermetallic compound NiAl on low-index Ni surfaces in Ni/Al reactive multilayer nanofolds, *Acta Mater.*, 2018, vol. 148, pp. 133–146.
4. P. Yi, M.L. Falk, T.P. Weihs, Suppression of homogeneous crystal nucleation of the NiAl intermetallic by a composition gradient: A molecular dynamics study, *J. Appl. Phys.*, 2017, vol. 146, 184501.
5. B. Witbeck, J. Sink, D.E. Spearot, Influence of vacancy defect concentration on the combustion of reactive Ni/Al nanolaminates, *J. Appl Phys.*, 2018, vol. 124, 045105–9.
6. B. Witbeck, D.E. Spearot, Grain size effects on Ni/Al nanolaminate combustion, *J. Mater. Res.*, 2019, vol. 23, pp. 1–10.

## PRODUCTION OF LAYERED COMPOSITE MATERIALS BASED ON TITANIUM BORIDES

P. M. Bazhin<sup>\*a</sup>, A. M. Stolin<sup>a</sup>, A. S. Konstantinov<sup>a</sup>, A. P. Chizhikov<sup>a</sup>,  
and A. D. Prokopets<sup>a</sup>

<sup>a</sup>Merzhanov Institute of Structural Macrokinetics and Materials Science Russian Academy of Sciences, Chernogolovka, Russia  
e-mail: bazhin@ism.ac.ru

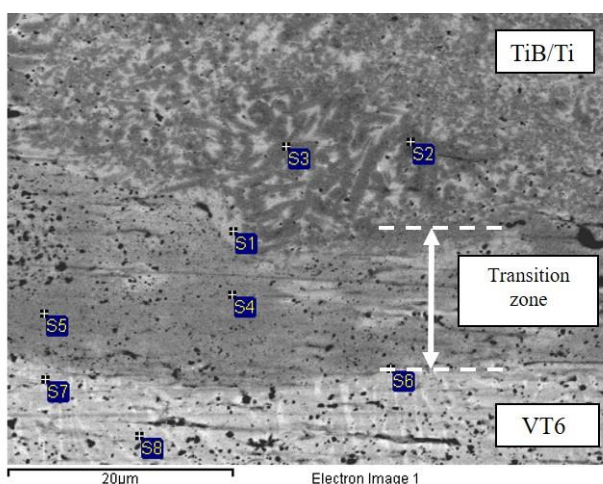
DOI: 10.24411/9999-0014A-2019-10019

Composite materials possessing higher strength and fracture toughness as compared to traditional homogeneous materials are widely used in industry. Among them, layered metal–intermetallic (or ceramic) composite materials (LCMs) are of great interest [1].

Free SHS compression is a promising method combining the production with consolidation of macrolayers in a single cycle for tens of second [2]. This method includes compaction and formation of synthesized material under the action of constant low pressure (~ 10–50 MPa).

Powders of titanium (PTS grade, 45  $\mu\text{m}$ , 87 wt %) and amorphous black boron (B-99A grade, 1  $\mu\text{m}$ , 13 wt %) were used as starting reagents to prepare TiB with 30 wt % titanium binder. VT6 alloy with a size of 30  $\times$  30 mm and a thickness of 7 mm was chosen as a substrate.

As a result, LCMs with 5-mm TiB-based ceramic material were prepared. During free SHS compression, the melting of surface layer of titanium alloy occurs; the combustion temperature of this composition was 1800°C. Under the action of external pressure after passage of combustion wave through the sample, the molten titanium and aluminum are mixed with synthesized ceramic composite at the interface (spectra 1, 4, and 5; Fig. 1). In this case, a transition zone 10–20  $\mu\text{m}$  thick is formed. The presence of transition zone favors an improvement in the adhesive strength between the layers. The transition zone is followed by ceramic composite consisting of titanium monoboride whiskers (spectra 2 and 3) with a size up to 15  $\mu\text{m}$  and initial titanium diboride grains less than 1  $\mu\text{m}$  in diameter, located in the titanium matrix.



| Spectrum | B    | Al   | Si   | Ti    | V    |
|----------|------|------|------|-------|------|
| S1       |      | 2.98 | 0.55 | 96.47 |      |
| S2       | 4.55 |      |      | 95.45 |      |
| S3       | 7.21 | 0.65 | 0.61 | 91.53 |      |
| S4       | 0.91 | 1.01 | 4.44 | 93.64 |      |
| S5       |      | 1.06 |      | 98.94 |      |
| S6       |      | 5.23 | 0.97 | 90.42 | 3.38 |
| S7       |      | 6.36 | 1.08 | 90.69 | 1.86 |
| S8       |      | 6.58 |      | 89.28 | 4.14 |

Fig. 1. SEM image and EDS data of transition zone of LCM.

These results showed the possibility of obtaining layered ceramic composites by combined use of SHS and high-temperature deformation.

This work was supported by the Russian Science Foundation (project no. 18-79-10254).

1. S.A. Zelepugin, Synthesis of the metal–intermetallic layered composite material of the Ti–TiAl<sub>3</sub> system by various methods, M.: VIAM, 2016.
2. A.M. Stolin, P.M. Bazhin, A.S. Konstantinov, M.I. Alymov, Production of large compact plates from ceramic powder materials by free SHS compaction, *Dokl. Chem.*, 2018, vol. 480, pp. 136–138.

VOLUME COMBUSTION SYNTHESIS OF  $\text{Li}_4\text{SiO}_4$ K. Benzeşik<sup>a</sup>, A. Turan<sup>\*b</sup>, and O. Yücel<sup>a</sup><sup>a</sup>Istanbul Technical University, Metallurgical and Materials Eng. Dpt., Istanbul, 34469 Turkey<sup>b</sup>Yalova University, Faculty of Engineering, Chemical and Process Engineering Dpt., Yalova, 77200 Turkey

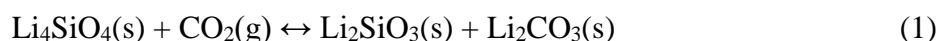
\*e-mail: aturan@yalova.edu.tr

DOI: 10.24411/9999-0014A-2019-10020

The huge  $\text{CO}_2$  emission emitted by human activities, including the combustion of fossil fuels, have been recognized as one of main contributors to climate change, with the atmospheric  $\text{CO}_2$  concentration increasing by 40% since the industrial revolution. To address this global problem, carbon dioxide capture and storage (CCS) technologies including oxy-combustion, pre-combustion and post-combustion carbon capture have been developed.

One of the most promising techniques for  $\text{CO}_2$  capture consists in its separation by the reversible reaction with a sorbent (post-combustion). Three suitable materials are known to have good capacities for the sorption of  $\text{CO}_2$  at high temperatures: CaO-based materials, hydrotalcites (HT) and lithium-based materials. Activated carbons and zeolites have been widely used, though the low equilibrium temperature for adsorption (25–150°C) limits their application at high temperature.

The lithium-based ceramics such as lithium oxide ( $\text{Li}_2\text{O}$ ), lithium zirconate ( $\text{Li}_2\text{ZrO}_3$ ), lithium orthosilicate ( $\text{Li}_4\text{SiO}_4$ ), lithium aluminate ( $\text{Li}_5\text{AlO}_4$ ), lithium ferrite ( $\text{LiFeO}_2$ ) and lithium titanate ( $\text{Li}_4\text{TiO}_4$ ) have been used for  $\text{CO}_2$  capture. Among the lithium-based compounds,  $\text{Li}_4\text{SiO}_4$  is a candidate material for  $\text{CO}_2$  capture at high temperatures. The reaction of this solid is attributed to the mechanism by which the  $\text{Li}_2\text{O}$  within the crystal structure of  $\text{Li}_4\text{SiO}_4$  reversibly reacts with  $\text{CO}_2$ , as given by Eq. (1).



The advantages of this solid include a relatively high capture capacity (theoretical value of 36.7 wt %) at temperatures of 450–700°C, fast kinetics of carbonation/decarbonation, good mechanical properties and also the possibility of use in repeated carbonation/decarbonation cycles. Although there are some ongoing studies about the regeneration potential of this material, the main features of regeneration mechanism could not have been introduced yet.

Conventionally and commercially  $\text{Li}_4\text{SiO}_4$  is synthesized via solid-state synthesis. This technique requires very high energy consumption to heat up the reactant materials ( $\text{Li}_2\text{CO}_3$  and  $\text{SiO}_2$ ) at about 950°C resulting in synthesized powders having very large particle size and crystallite size. Combustion synthesis methods provide synthesized ceramic powders with low energy requirement and in nano-size.

With this study, it is aimed to optimize the volume combustion synthesis conditions of the  $\text{Li}_4\text{SiO}_4$  and for this purpose; present study was conducted in two main stages: volume combustion synthesis experiments and characterization of synthesized powders. In the experimental series, the starting materials were technical grade lithium carbonate ( $\text{Li}_2\text{CO}_3$ , min. 99% by mass) as lithium source and high-quality silicon (Si, min. 99.5% by mass, -325 mesh) powder. The volume combustion synthesis process took place according to Eq. (2).





Since the specific heat value of the above reaction was calculated as 3295.9 J/g by means of FactSage 7.1 thermo-chemical simulation software, it was predicted that a combustion synthesis technique could be applicable for synthesis of  $\text{Li}_4\text{SiO}_4$ . Indeed, a SHS process was tried to carry out by using stoichiometric mixture in Eq. 2 before VCS experiments, but the reaction was not self-sustainable due to low volume of Si powders in initial powder mixture. The authors, therefore, designed experimental series by using VCS principles. Before VCS experiments, the initial powders were mixed by a turbula mixer for 15 min in order to obtain homogeneous mixtures. Then, the powders were put into alumina boats which have  $100 \times 30 \times 12$  mm dimensions as it is seen in Fig. 1.

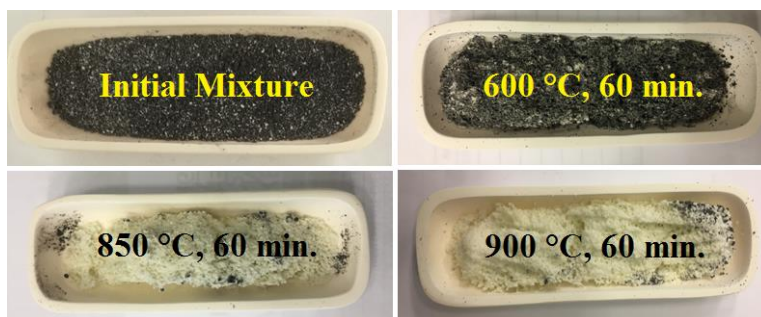


Fig. 1. Initial powder mixture and selected products.

Samples were put in the muffle furnace in order to conduct the volume combustion synthesis reaction. At the beginning, furnace temperature was at room temperature and heated up to 500, 550, 600, 650, 700, 750, 800, 850 and 900°C to optimize the reaction temperature with the holding duration of 60 minutes. Once the temperature was optimized, 75 min of holding duration was also studied for the temperatures which have resulted in higher weight loss. Also, in Fig. 1, the photographs of selected reaction products were given.

Theoretical weight loss of the reaction given in Eq. 2 is 31.85%, so the remaining solid ratio is 68.15%. It can indicate the degree of reaction conversion rate. In Fig. 2, remaining solid ratios of reaction products are given. At the temperatures equal and greater than 650°C, remaining product ratio started to remarkably decrease from approximately 90% to the values closer to 68.15% which is the calculated-theoretical value. The change between 700 and 900°C was very low in the experiments carried out for 60 min. However, in the experiments conducted for 75 min, remaining product ratio was almost same as the theoretical value at the temperatures equal and greater than 800°C. Thus, it was clear to see the reaction reaches equilibrium at 800°C for reaction duration of 75 min.

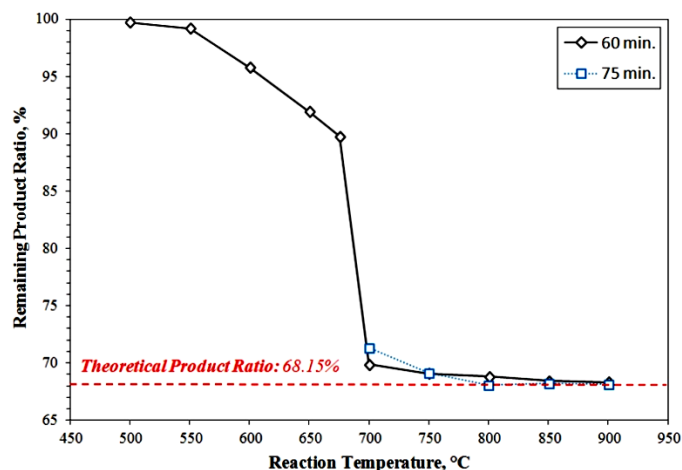


Fig. 2. Change of remaining product ratio with increasing reaction temperature and duration.

XRD patterns of synthesized powders were given in Figs. 3, 4 and 5. Patterns indicate the formation  $\text{Li}_4\text{SiO}_4$  phase with increasing process temperature and duration successfully. From 500 to 675°C for 60 min, formation of  $\text{Li}_4\text{SiO}_4$  occurred. But at 675°C there were still unreacted and other phases such as  $\text{Li}_2\text{CO}_3$ , Si and  $\text{SiO}_2$  (Fig. 3). In the experiments conducted for 60 min, intensity of  $\text{Li}_4\text{SiO}_4$  peaks remarkably increased with the increase of temperature, particularly at the temperatures equal to and greater than 700°C. In the experiment conducted at 900°C, the product consisted of mainly  $\text{Li}_4\text{SiO}_4$  and slight amounts of  $\text{Li}_2\text{CO}_3$  and  $\text{SiO}_2$  (Fig. 4). When the reaction duration increased to 75 min, the amount of formed  $\text{Li}_4\text{SiO}_4$  phase slightly increased (Fig. 5).

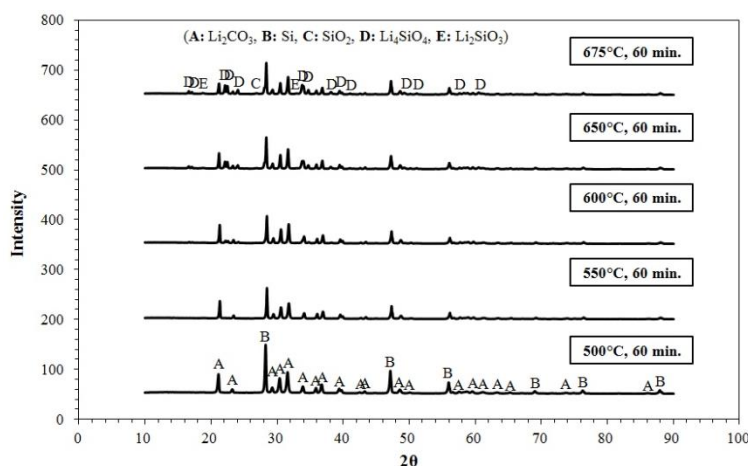


Fig. 3. XRD patterns of reaction products from 500 to 675°C for 60 min.

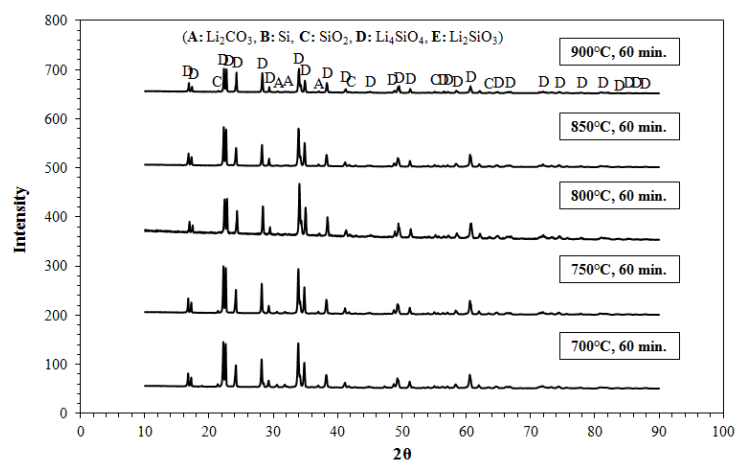


Fig. 4. XRD patterns of reaction products from 700 to 900°C for 60 min.

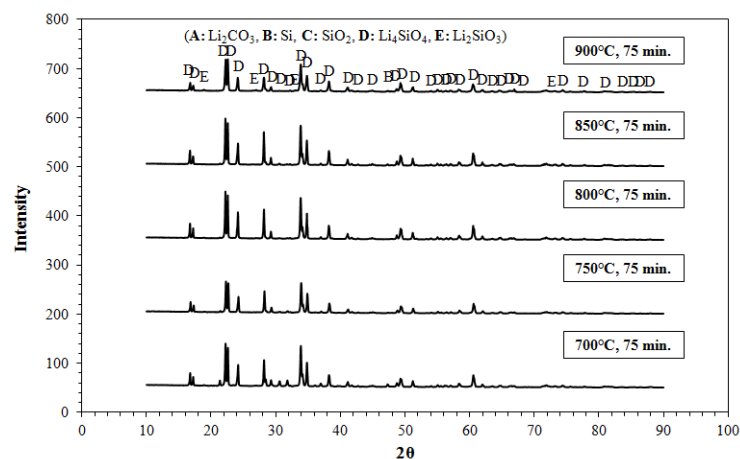


Fig. 5. XRD patterns of reaction products from 700 to 900°C for 75 min.

In the present study, the synthesis of  $\text{Li}_4\text{SiO}_4$ , through VCS method, was achieved with high conversion rate at the temperatures lower than that of solid-state synthesis technique. This study is an ongoing work and planned further studies were shared below.

- Optimization of  $\text{Li}_2\text{CO}_3$  stoichiometry;
- Particle size and SEM-EDS characterizations of synthesized powders;
- $\text{CO}_2$  capture tests of synthesized powders from experiments with high conversion rate.

1. Zubbri et al., Parametric study and effect of calcination and carbonation conditions on the  $\text{CO}_2$  capture performance of lithium orthosilicate sorbent, *Chin. J. Chem. Eng.*, 2018, vol. 26, pp. 631–641.
2. R.H.R.H. Moss, J.A.J.A. Edmonds, K.A.K.A. Hibbard, M.R. Manning, S.K.S.K. Rose, D.P.D.P. van Vuuren, T.R.T.R. Carter, S. Emori, M. Kainuma, T. Kram, et al., The next generation of scenarios for climate change research and assessment, *Nature*, 2010, vol. 463, pp. 747–756.
3. IEA - International Energy Agency, Redrawing the Energy–climate Map: World Energy Outlook Special Report, 2013.
4. H. Yang, Z. Xu, M. Fan, R. Gupta, R.B. Slimane, A.E. Bland, I. Wright, Progress in carbon dioxide separation and capture: a review, *J. Environ. Sci.*, 2008, vol. 20, pp. 14–27.
5. J.C.M. Pires, F.G. Martins, M.C.M. Alvim-Ferraz, M. Simões, Recent developments on carbon capture and storage: an overview, *Chem. Eng. Res. Des.*, 2011, vol. 89, pp. 1446–1460.
6. Suélen M. Amorim, Michele D. Domenico, Tirzhá L.P. Dantas, Humberto J. José, Regina F.P.M. Moreira, Lithium orthosilicate for  $\text{CO}_2$  capture with high regeneration capacity: Kinetic study and modeling of carbonation and decarbonation reactions, *Chem. Eng. J.*, 2016, vol. 283, pp. 388–396.
7. A.S. Mukasyan, P. Dinka, Novel approaches to solution–combustion synthesis of nanomaterials, *Int. J. Self-Propag. High-Temp. Synth.*, 2007, vol. 16, no. 1, pp. 23–35.
8. A. Varma, A.S. Rogachev, A.S. Mukasyan, S. Hwang, Combustion synthesis of advanced materials: principles and applications, *Adv. Chem Eng.*, 1998, vol. 24, pp. 79–226.
9. M.T. Izquierdo, A. Turan, S. Garcia, M.M. Maroto-Valer, Optimization of  $\text{Li}_4\text{SiO}_4$  synthesis conditions by a solid state method for maximum  $\text{CO}_2$  capture at high temperature, *J. Mater. Chem. A*, 2018, vol. 6, 3249–3257.

## GAS ENVIRONMENT INFLUENCED TRIBOLOGICAL BEHAVIOR OF TMD COATINGS

**A. V. Bondarev<sup>\*a</sup> and T. Polcar<sup>a</sup>**

<sup>a</sup>Czech Technical University in Prague, Karlovo náměstí 13, 121 35, Prague, Czech Republic

\*e-mail: andrei.bondarev@fel.cvut.cz

DOI: 10.24411/9999-0014A-2019-10021

Transition metal dichalcogenides (TMDs) are intrinsic solid lubricants with hexagonal layered structure and weak Van der Waals bonding between basal planes in crystallographic lattice, which provide low shear stress values under sliding conditions and associated with a low friction coefficient. Since friction and wear processes are mostly depends on surface properties, the TMDs can be considered as a surface modifier for tailoring of optimal tribological performance by deposition of thin coatings. The TMD coatings have been widely used in tribological applications where low friction coefficient is highly desirable, meanwhile presence of oxygen or/and water vapors in the ambient environment significantly reduce their tribological performance. In addition, low load-bearing capacity of pure TMDs coatings can cause their failure during operations. Subsequently, to produce coatings with enhanced mechanical and tribological properties TMDs have been combined with different additives to obtain composite structure, for instance with Ti, Zr, Cr, Au, and Pb, as well as non-metallic compounds, such as polymers C, N and F or even with multicomponent systems. While mechanical properties go up when nanocomposite structure is formed, the sensitivity to environment is also can be reduced but it is still the problem even for complex compositions of coatings. For tribotesting in controlled environment, air with different humidity, dry argon, dry nitrogen or even vacuum were utilized mostly. But published results indicate that still there are splits in over leading factor affects degradation of TMDs lubricity, it is ambient moisture-sulfur bonding or oxidation process. Behind this discussion about reasons of TMDs degradation exposed to different environment one more curious observation was misplayed - it was found that friction behavior of Mo–Se–C coatings in even oxygen and moisture free environments can be influenced by inert atmosphere. This phenomenon was also detected for carbon-based coatings and, moreover, it was reported that friction coefficient in vacuum was higher in comparison with inert gas atmosphere, which means physisorption and chemisorption processes, changes in surface energy or even intercalation of gas atoms in material structure have measurable impact on friction processes. Another point is that gas atoms can be located in cages in the amorphous TMD coatings and their release in molecular form during friction test also influence on tribological properties. But gas-involved tribological processes are still almost fully under-explored field of material science and goal of present work is to uncover phenomena occuder in different environments during friction of TMD-based coatings using advanced characterization and simulation methods. The TMD-based coatings were deposited by RF magnetron sputtering in Ar and in Ar + N<sub>2</sub> atmosphere. Pin-on-disk tribological tests were performed in ambient air, vacuum, argon and nitrogen environment. For characterization of coatings, wear tracks and wear debris SEM, XRD, TEM, Raman and XPS were utilized, MD simulations were performed to highlight interaction of gases and solid lubricants during friction processes.

## NANOCOMPOSITE Si-Ta-C-N-(Ag) COATINGS FOR WIDE TEMPERATURE RANGE APPLICATIONS

A. V. Bondarev<sup>\*a</sup>, A. N. Sheveyko<sup>b</sup>, M. N. Antonyuk<sup>b</sup>, T. Polcar<sup>a</sup>, E. A. Levashov<sup>b</sup>, and D. V. Shtansky<sup>b</sup><sup>a</sup>Czech Technical University in Prague, Prague, 12135 Czech Republic<sup>b</sup>National University of Science and Technology MISIS, Moscow, 119049 Russia

\*e-mail: andrei.bondarev@fel.cvut.cz

DOI: 10.24411/9999-0014A-2019-10022

New challenges related to the application of coatings at high temperatures in aggressive media require the development of novel coatings with combination of high hardness and fracture toughness, low coefficient of friction, stable elemental and phase compositions, high oxidation resistance. Among ceramics, the SiC- or Si<sub>3</sub>N<sub>4</sub>-based coatings demonstrate high hardness and thermal stability, good tribological properties, but the minor point is that these compounds are brittle and have poor crack resistance. Solution can be found in composition and structure tailoring. Silicon-based ceramics is very flexible in contexts of structure, it can possess crystalline, crystalline + amorphous or fully amorphous structure. Also, it can be easily modified by transition metals addition (Ti, Mo, Ta) and in this way the structure becomes more complex and multiphase. For the tribological applications in wide temperature range Ta-doped coatings are in the focus because of lubricious properties of tantalum oxides which can be formed at elevated temperatures and can be combined with low friction properties of SiO<sub>x</sub> [1]. Soft component addition with zero solubility in silicon-based phases can significantly increase the crack resistance with compromising decrease in hardness [2], in addition soft metals like silver improve tribological performance of coatings as well [3, 4]. The goal of present study was to fabricate Si-based coatings with different design and to investigate structure-properties relationships with special focus on tribological performance. The Si-(Ta)-C-N-(Ag) coatings were deposited by magnetron of multicomponent targets fabricated using SHS powders [5, 6] and in case of silver co-deposition the metallic Ag target was employed. It was shown, that depending on deposition conditions the coatings consisted of crystalline (*fcc* Ta(Si,C,N), Ta<sub>5</sub>Si<sub>3</sub>) or amorphous or nanocomposite structure with nanocrystallites 3 nm in size, embedded in an amorphous matrix. The coatings were characterized by high thermal stability and oxidation resistance at temperatures below 800°C. The coefficient of friction of Si-Ta-C-(N) coatings decreased with temperature from 0.38 (25°C) to 0.28 (600°C) and 0.23 (800°C), while their wear resistance increased. The addition of silver provides a positive effect on mechanical properties of coatings but enchantment of tribological properties was contradictory due to lamination of oxide top layers and Ag that cause adhesion failure. In Ag-free coatings a thin (~ 100 nm) oxide layer and TaSi<sub>x</sub>O<sub>y</sub> microfibers formed during the tests at elevated temperatures played a key role in enhanced tribological behavior, reducing the coefficient of friction and wear due to rolling/sliding friction. Depending on the elemental composition, hardness and Young's modulus of the coatings were 16–26 GPa and 155–268 GPa, respectively.

1. Q. Zeng, T. Chen, Superlow friction and oxidation analysis of hydrogenated amorphous silicon films under high temperature, *J. Non-Cryst. Solids*, 2018, vol. 493, pp. 73–81.
2. A.V. Bondarev, M. Golizadeh, N.V. Shvyndina, I.V. Shchetinin, D.V. Shtansky, Microstructure, mechanical, and tribological properties of Ag-free and Ag-doped VCN coatings, *Surf. Coat. Technol.*, 2017, vol. 331, pp. 77–84.

3. A.V. Bondarev, P.V. Kiryukhantsev-Korneev, E.A. Levashov, D.V. Shtansky, Tribological behavior and self-healing functionality of TiNbCN–Ag coatings in wide temperature range, *Appl. Surf. Sci.*, 2017, vol. 396, pp. 110–120.
4. A.V. Bondarev, D.G. Kvashnin, I. V. Shchetinin, D.V. Shtansky, Temperature-dependent structural transformation and friction behavior of nanocomposite VCN–(Ag) coatings, *Mater. Des.*, 2018, vol. 160.
5. A.V. Bondarev, S. Vorotilo, I.V. Shchetinin, E.A. Levashov, D.V. Shtansky, Fabrication of Ta–Si–C targets and their utilization for deposition of low friction wear resistant nanocomposite Si–Ta–C–(N) coatings intended for wide temperature range tribological applications, *Surf. Coat. Technol.*, 2019, vol. 359, pp. 342–353.
6. S. Vorotilo, E.A. Levashov, V.V. Kurbatkina, D.Yu. Kovalev, N.A. Kochetov, Self-propagating high-temperature synthesis of nanocomposite ceramics TaSi<sub>2</sub>–SiC with hierarchical structure and superior properties, *J. Eur. Ceram. Soc.*, 2018, vol. 38, pp. 433–443.

## SUPPORTED CATALYSTS OF DEEP OXIDATION AND HYDROGENATION BY SELF-PROPAGATING SURFACE SYNTHESIS

V. N. Borshch\*<sup>a</sup> and I. M. Dement'eva<sup>a</sup>

<sup>a</sup>Merzhanov Institute of Structural Macrokinetics and Materials Science, RAS,  
Chernogolovka, Moscow, 142432 Russia  
e-mail: borsch@ism.ac.ru

DOI: 10.24411/9999-0014A-2019-10023

Supported catalysts are used in a wide variety of heterogeneous catalytic processes. Most of the work in modern catalytic literature is devoted to their development and research. Such interest is justified by the substantial advantages of this type of catalysts consisting of two components: the active phase (AP), which determines the catalytic properties, and the support, which is mainly responsible for the physical and mechanical properties of the catalyst (hardness, wear resistance, heat resistance). As a rule, the support has a well-developed surface and maintains the AP's highly dispersed state, which is virtually impossible to use in catalysis without fixation. Physicochemically, supports often increase the activity and selectivity of the AP both by influence on its electronic structure and the morphology of microparticles through chemical bonds and by a number of auxiliary reactions on a support. Moreover, a support improves the stability of AP particles by preventing their destruction or excessive growth because of migration of AP atoms. However, this separation of functions complicates the process of catalyst synthesis, especially the deposition and formation of AP on the surface of the support. As a rule, it is a multistage and energy-consuming technology. One of the approaches to significantly simplify this stage and reduce energy costs may be the process of self-propagating surface synthesis. The essence of this method is to initiate burning on the surface of the pores of a dry support impregnated with a mixture of solutions of an oxidizing agent (nitrates of catalytically active metals) and a reducing agent (fuel). AP of such catalysts is a mixture of metals and their oxides, the ratio of which depends on the composition of the impregnating solutions and the type of support. In the present work, nitrates of Mn, Co, and Ni were used as oxidants; urea, citric acid, sucrose, and sorbitol were used as fuel. The application was carried out on a wide range of supports, as with high Lewis acidity ( $\gamma$ -Al<sub>2</sub>O<sub>3</sub>), medium acidity (zeolites such as NaA, NaX and ZSM-5) and almost neutral (silica gel). In addition, deposition was carried out on ready-made Fe–Ni–Co–Mn polymetallic catalysts of deep oxidation (DOC), i.e. there was a modification of their surface. The content of AP on the supports varied within 5–15% wt in terms of metals. The deposition was limited in order to prevent excessively intense combustion and high process temperature, which could lead to AP sintering and loss of its activity. To stabilize the metal component of the AP, we proposed a method for processing the newly obtained catalysts with a solution of hydrogen peroxide in an inert atmosphere. The process consists in applying a thin protective film of oxygen on the surface of the AP during the decomposition of H<sub>2</sub>O<sub>2</sub>. This approach allows to obtain catalysts that are stable even in the process of deep oxidation at elevated temperatures.

Combustion was initiated by heating of sample in a quartz reactor in argon. Figure 1 represents the typical thermograms of the process. When using urea as a fuel, there is a clearly marked onset of burning and a sharp temperature rise ( $T_{\max} = 305^{\circ}\text{C}$ ) in the visually observable combustion wave. In the case of sucrose, the combustion process is slow, the ignition is weak and starts at a lower temperature ( $T_{\text{ignit}} = 48^{\circ}\text{C}$ ).

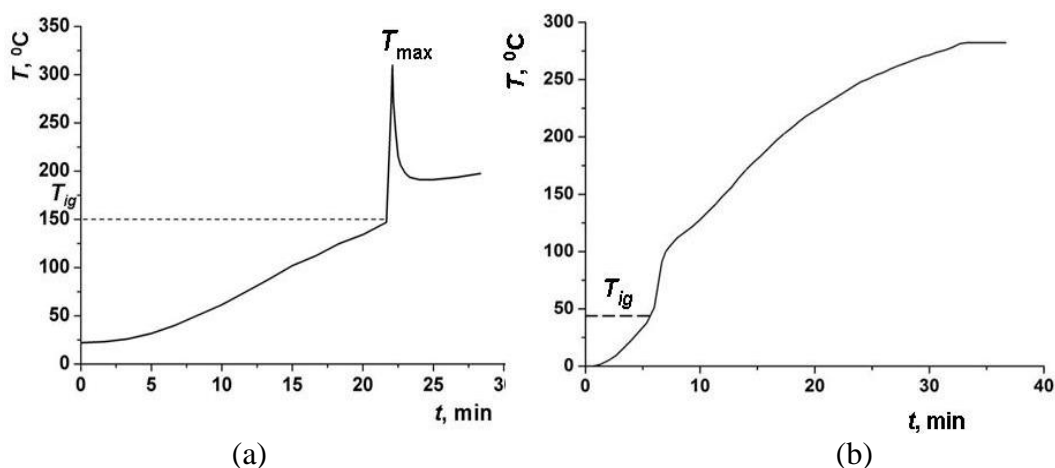


Fig.1. Thermograms of synthesis process of the catalyst 5%Co–5%Mn/ $\gamma$ -Al<sub>2</sub>O<sub>3</sub> when using (a) urea and (b) sucrose as a fuel. Ignition temperatures are marked.

The XRD patterns of the catalysts obtained have a high level of noise, which indicates a highly defective, largely amorphous AP structure. The AP peaks, especially when its content is low, are masked by support peaks (Fig. 2).

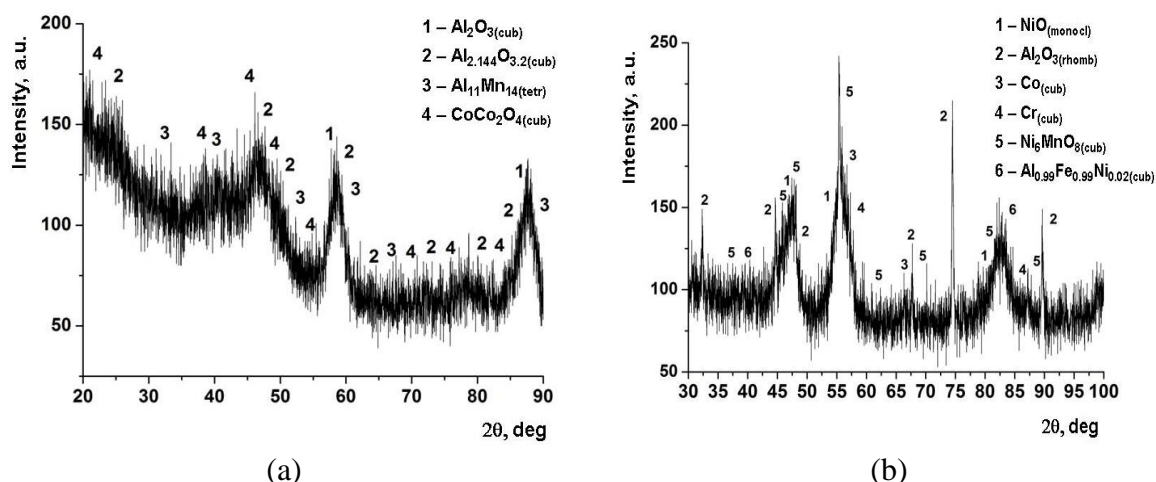


Fig. 2. XRD patterns of the catalysts: (a) 5%Co–5%Mn/ $\gamma$ -Al<sub>2</sub>O<sub>3</sub> obtained with sucrose as a fuel and (b) 5%Co–5%Cr/DOC obtained with urea as a fuel.

The AP obtained by this method has a high dispersion, however, in the case of using carriers with a large specific surface (more than 100 m<sup>2</sup>g<sup>-1</sup>), this dispersion turns out to be insufficient. After the formation of AP, the specific surface of the catalysts on these supports decreases. These conclusions can be made as a result of the analysis of Table 1.

Table 1. Specific surface of some supports and catalysts on these supports.

|   | Zeolite<br>NaA | 10%Co–<br>5%Mn/<br>NaA | $\gamma$ -Al <sub>2</sub> O <sub>3</sub> | 10%Co–5%Mn/<br>$\gamma$ -Al <sub>2</sub> O <sub>3</sub> | Zeolite<br>ZSM-5 | 5%Co–<br>5%Mn/<br>ZSM-5 | 5%Co–5%Ni/<br>ZSM-5 |
|---|----------------|------------------------|--|---|------------------|-------------------------|---------------------|
| $S_{sp}$ , m <sup>2</sup> g <sup>-1</sup> | 74.9           | 79.0                   | 180.0                                    | 155.9   | 560              | 188                     | 235                 |

The surface of the obtained catalysts is coated with nanofomers, the shape of which is determined by the composition of AP. In turn, the size and shape of the pores are determined by the used carrier. This effect can be observed in Fig. 3.



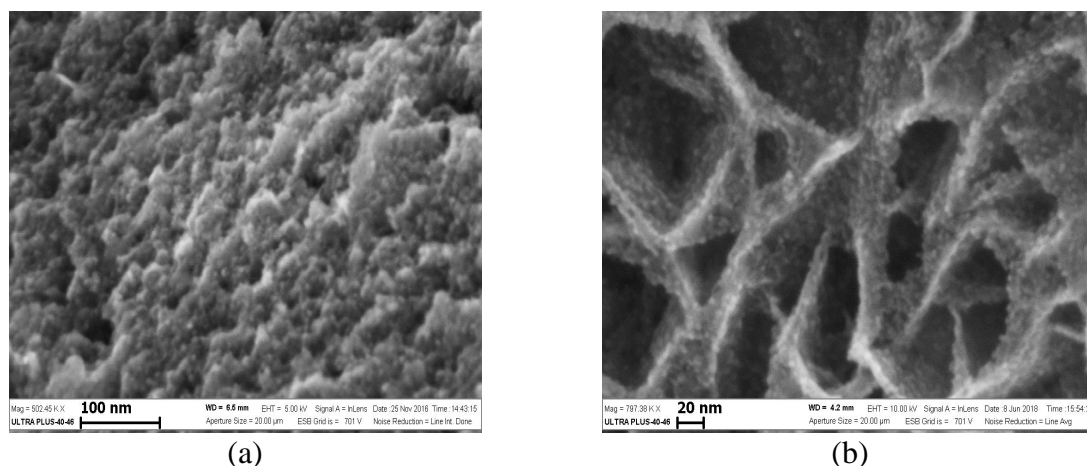


Fig. 3. SEM micrograph of AP of (a) catalyst 10%Co–10%Ni/silica gel and (b) catalyst 5%Mn/DOC.

All the catalysts obtained were tested in the processes of deep oxidation of CO and propane, and hydrogenation of CO<sub>2</sub>. The composition of the gas mixture in the process of deep oxidation: 0.2% vol propane, 0.7% vol CO, 2% vol O<sub>2</sub>, N<sub>2</sub> up to 100%, gas hour space velocity, GHSV = 120,000 h<sup>-1</sup>. In the process of hydrogenation, the mixture consisted of the following gases: 2.7% vol CO<sub>2</sub>, 10.8% vol H<sub>2</sub>, He up to 100%, GHSV = 3000 h<sup>-1</sup>. The results are shown in Fig. 4. As can be seen in Fig. 4a, during the deep oxidation process, the catalyst showed high activity. CO oxidation begins already at a temperature of 100°C, and at 150°C its conversion exceeds 80%. Almost complete propane conversion is achieved at a temperature of 350°C. After 7 experiments, the drop of propane conversion at 350°C on this catalyst did not exceed 2%. The complete hydrogenation of CO<sub>2</sub> on a cobalt–nickel catalyst supported by ZSM-5 occurs at 350°C with a selectivity of 100% for methane (Fig. 4b).

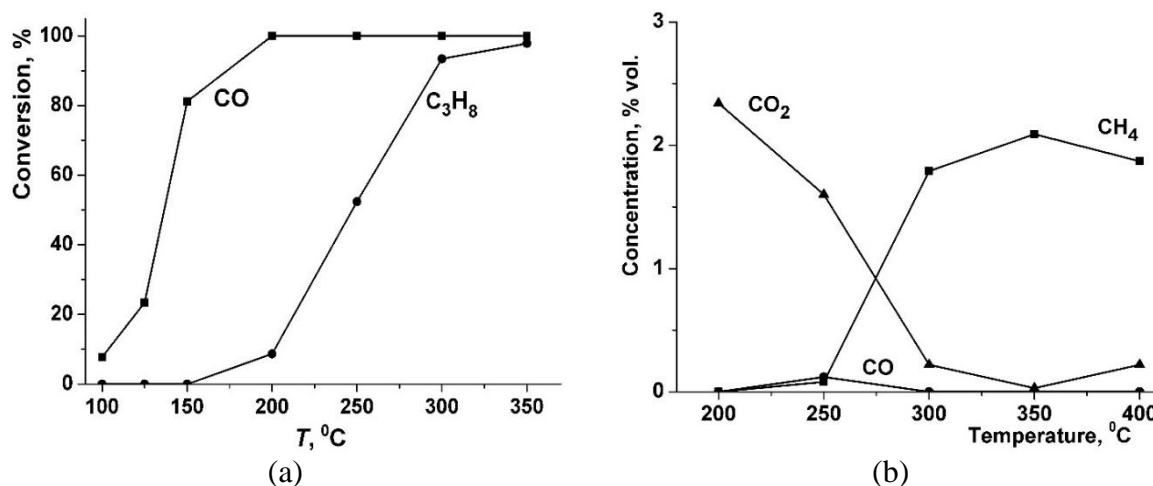


Fig. 4. (a) Conversion of CO and propane vs temperature on 10%Co–5%Mn/γ-Al<sub>2</sub>O<sub>3</sub> catalyst in deep oxidation process; (b) hydrogenation of CO<sub>2</sub> on 10%Co–10%Ni/ZSM-5 catalyst.

Thus, self-propagating surface synthesis is promising method to produce catalysts with multicomponent AP on a wide range of supports, possessing high activity and stability in oxidizing and reducing processes.

## METALLOTHERMIC PRODUCTION OF FeCo

M. Bugdayci<sup>\*a</sup> and A. Turan<sup>a</sup><sup>a</sup>Chemical and Process Engineering Department, Faculty of Engineering, Yalova University, Yalova, 77200 Turkey

\*e-mail: mehmet.bugdayci@yalova.edu.tr

DOI: 10.24411/9999-0014A-2019-10024

In high power applications, engines and generators in aviation industry, the use of soft magnetic materials with high mechanical strength is a necessity. Research on these high strength soft magnetic materials has been intensified in recent years and consequently significant improvements have been achieved. In these studies, it is shown that Fe–Co alloy is candidate material due to high Curie temperature, low magneto-crystal anisotropic property, high strength, and excellent magnetic properties for the applications. FeCo alloy containing 50% Fe and 50% Co is very difficult to shape due to its very brittle nature. The positive effects of vanadium or chromium addition on the composition to remove the fragility of the alloy appear in the literature. FeCo alloys are produced with high energy melting systems, in this study, they will be produced by reducing the oxides of their components by aluminothermic and magnesiothermic methods, which producing their own energy without the need any external energy. Magnetite ( $\text{Fe}_3\text{O}_4$ ) and mill scale as oxidic iron raw materials,  $\text{Co}_2\text{O}_3$  as cobalt source will be used. In order to remove the fragility of the alloy, a stoichiometric 2% vanadium addition will be carried out and  $\text{V}_2\text{O}_5$  will be used as a vanadium source. In experiments performed to synthesize FeCo, magnetite is as a source of iron,  $\text{Co}_3\text{O}_4$  is as a cobalt source, and aluminum was used as the reductant, and the effects of the change in aluminum stoichiometry on FeCo recovery efficiencies were investigated. Permendur 24 production of the target set of samples in the 90-95-100-110-120% of the samples containing stoichiometric Al weighing, weighing 100 g, mixed, then kept at 105°C for 40 min at ETÜV dehumidification. The dried mixture was charged to the copper crucible in which the metalothermic reduction was carried out, and the reaction was carried out by means of a variant. Metallic samples and slag obtained from the experiment were analyzed by XRF and AAS techniques and consistent results were observed. The results of chemical analysis of metal and slag are given in Table 1. The metal yields obtained from these results are as in Fig. 1. When Table 1 and Fig. 1 were examined, Fe and Co yield in the 90% stoichiometric composition was determined as 70.94 and 59.45%, respectively, while these values reached 92.89 and 77.50% when Al stoichiometry increased to 105%. After this value, it was determined that the added aluminum had a tendency to self-reduce by lowering the reaction temperature and reduced the yield of metal.

Table 1. Results of chemical analysis of the metal obtained as a result of the experiments performed for FeCo production.

| Stoichiometry | Fe    | Co    | Al    |
|---------------|-------|-------|-------|
| %90           | 53.92 | 14.27 | 30.81 |
| %95           | 57.28 | 15.09 | 27.37 |
| %100          | 62.33 | 18.48 | 19.19 |
| %105          | 70.6  | 18.6  | 10.4  |
| %110          | 68.04 | 18.2  | 13.1  |
| %115          | 65.08 | 17.34 | 16.58 |
| %120          | 64.95 | 16.25 | 18.2  |

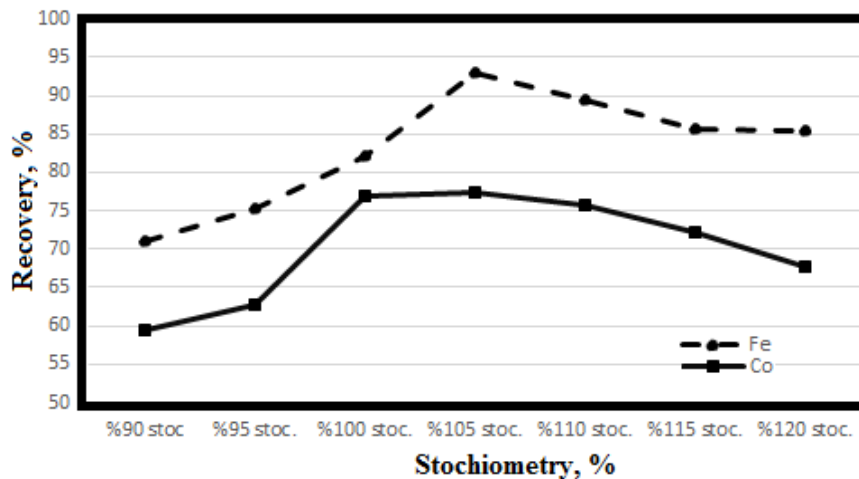


Fig. 1. Metal yields obtained by changing Al stoichiometry in experiments for FeCo production.

Simultaneously with the experiments conducted for the production of Permendur 24 and Permendur 49, thermodynamic examination of the system was carried out with the help of FactSage 7.1 program. The adiabatic temperature is an important parameter for the reaction to start and self-progress and must be a minimum of 1527°C. Figure 2 shows an adiabatic temperature graph drawn for the production of Permendur 24. When the graph is examined, it is seen that the adiabatic temperature of the system increased up to a certain point with the addition of increasing Al (2910°C) and then fell. This temperature is higher than 1527°C and is sufficient to start the reaction. This explains the reduction of metal recovery efficiencies after adding 105% stoichiometric Al in the experiments.

After determining the adiabatic temperature of the system, with the aluminum stoichiometry, the possible phases to be formed in the alloy are modeled. At this stage, FactSage program, the Gibbs free energy minimizer working with the logic of the equilibrium mode was used. The program shows the stable phases that can occur at simulated pressure and temperature values. The results obtained from the FeCo system are given in Fig. 3.

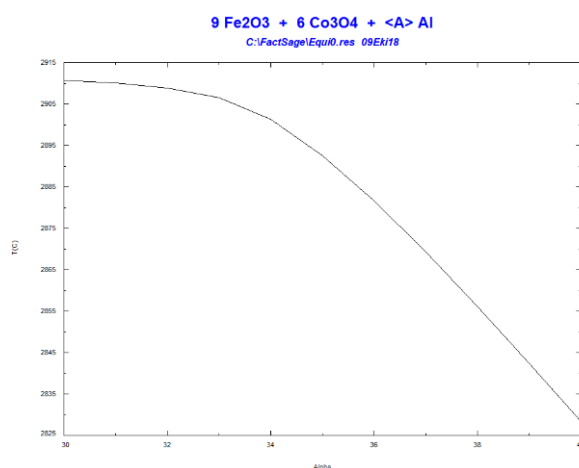


Fig. 2. Adiabatic temperature values with Al stoichiometry in FeCo production.

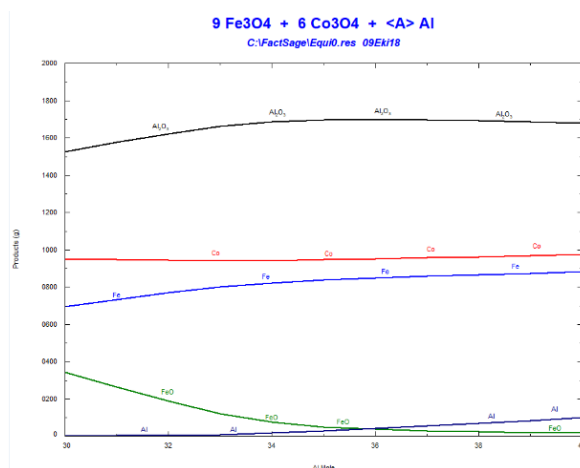


Fig. 3. Possible phases obtained by Al stoichiometry in FeCo production.

This work was supported by research grants from the Yalova University scientific research project unit (BAP) (project no. 2018/AP/0002). The authors are deeply grateful to the Yalova University BAP.

1. M. Yang, C. Wang, S. Yang, C. Wu, D. Chen, Z. Shi, X. Liu, Study of phase equilibria, diagrams and transformations in the Fe–Co–Si ternary system, *Mater. Chem. Phys.*, 2017, vol. 201, pp. 180–188.
2. R.S. Sundar, S.C. Deevi, Soft magnetic FeCo alloys: alloy development, processing, and properties, *Int. Mater. Rev.*, 2005, vol. 50, no. 3, pp. 157–192.
3. J.H. White, C.V. Wah, Workable magnetic compositions containing principally iron and cobalt, US Patent 1 862 559, 1932.
4. M.S. Masteller, D.W. Dietrich, Process for improving magnetic performance in a freemachining ferritic stainless steel, US Patent US05501747, 1996.
5. A.A. Couto, P.I. Ferreira, Phase transformations and properties of Fe–Co alloys, *J. Mater. Eng.*, 1989, vol. 11, no. 1, pp. 31–36.
6. K. Kawahara, Structures and mechanical properties of an FeCo–2V alloy, *J. Mater. Sci.*, 1983, vol. 18, pp. 3427–3436.
7. Z. Zhu, C. Ji, L. Zhong, S. Liu, F. Cui, H. Sun, W. Wang, Magnetic Fe–Co crystal doped hierarchal porous carbon fibers for removal of organic pollutants, *J. Mater. Chem. A*, 2017, vol. 5, is. 34, pp. 18071–18080.

## SPARK PLASMA SINTERING AND SELF-PROPAGATING HIGH-TEMPERATURE SYNTHESIS OF ULTRA-HIGH TEMPERATURE CERAMICS Hf–C–N

V. S. Buinevich<sup>\*a</sup>, A. A. Nepapushev<sup>a</sup>, G. V. Trusov<sup>a</sup>, D. O. Moskovskikh<sup>a</sup>,  
A. S. Rogachev<sup>b</sup>, and A. S. Mukasyan<sup>c</sup>

<sup>a</sup>National University of Science and Technology MISiS, Moscow, 119049 Russia

<sup>b</sup>Merzhanov Institute of Structural Macrokinetics and Materials Science, Russian Academy of Sciences, Chernogolovka, Moscow, 142432 Russia

<sup>c</sup>Department of Chemical and Biomolecular Engineering, University of Notre Dame, Notre Dame, IN, 46556 USA

\*e-mail: buynevich.vs@misis.ru

DOI: 10.24411/9999-0014A-2019-10025

The future of the aerospace industry is directly related to the development and modernization of the heat-loaded components of hypersonic aircraft: jet engines, nose tips and sharp leading edges of the wings, which are required to withstand ultrahigh temperatures (above 2000°C) caused by aerodynamic heating. The greatest practical interest for the aerospace industry is centered around ultra-high temperature ceramics based on borides, nitrides, carbides, carbonitrides and double transition metal carbides [1–4]. These materials have unique physical and chemical properties. They are characterized by unparalleled combination of heat resistance, thermal conductivity, refractoriness (melting points above 3000°C), hardness, as well as electrical and thermal properties close to those of metals [5–9]. According to recent publications, hafnium carbonitride of optimum composition not only has good mechanical properties and high thermal conductivity, but also is believed to have the highest melting point (above 4200°C) among all currently existing systems. This peak refractoriness is explained by several factors affecting the melting point: the presence of point defects in the crystal lattice and strong covalent and ionic bonds in the system.

Synthesis of carbonitrides with optimal composition is complicated by the high melting points of the main components and the difficulty of controlling the carbon–nitrogen ratio in the compound. Traditional methods of production, such as high-temperature diffusion saturation, require extensive and expensive high-temperature annealings. Moreover, the resulting carbonitrides often deviate from the composition with the maximum melting point (HfC<sub>0.3</sub>N<sub>0.5</sub>). Alternative “nonequilibrium” synthesis methods include mechanochemical synthesis and self-propagating high-temperature synthesis (SHS). These approaches allow one to obtain the material of the desired composition in a short period of time. Correspondingly, the purpose of this work was to obtain a new promising ultrahigh-temperature ceramic material based on hafnium carbonitride powders produced by the mechanochemical synthesis or SHS, followed by spark plasma sintering (SPS).

The synthesis of carbonitride was carried out according to the following schemes:

a) mechanochemical processing of powders of hafnium and graphite in a nitrogen atmosphere in a planetary ball mill (PBM) "Activator 2S" during 30 min at a jar gas pressure of 0.4 MPa;

b) mechanical activation of mixture of hafnium and graphite in PBM for 5 min, followed by SHS in a laboratory reactor at a nitrogen pressure of 0.8 MPa.

Ball milling was carried out at a 20:1 ball-to-mixture mass ratio, rotation frequency 694 rpm and rotation ratio  $k = 1.0$ . The synthesized powders were studied by X-ray phase analysis (XRD)

and scanning electron microscopy (SEM). Sintering was carried out on a Spark Plasma Sintering Labox 650 unit at a 100°C/min heating ratio in temperature range 1900–2200°C, with a dwelling time 0–10 min at a pressure of 50 MPa. As a result, hafnium carbonitride powders of different composition were obtained and sintered into dense ceramics. The maximum density (98.7%) was observed in the sample obtained using the SHS method, along with the highest hardness (21.3 GPa) and crack resistance (4.7 MPa m<sup>1/2</sup>) among all samples.

1. I.G. Talmy, J.A. Zaykoski, M.M. Opeka, High-temperature chemistry and oxidation of ZrB<sub>2</sub> ceramics containing SiC, Si<sub>3</sub>N<sub>4</sub>, Ta<sub>5</sub>Si<sub>3</sub> and TaSi<sub>2</sub>, *J. Am. Ceram. Soc.*, 2008, vol. 91, pp. 2250–2257.
2. D. Sciti, V. Medri, L. Silvestroni, Oxidation behaviour of HfB<sub>2</sub>–15 vol % TaSi<sub>2</sub> at low, intermediate and high temperatures, *Scr. Mater.*, 2010, vol. 63, pp. 601–604.
3. M. Balaceanu, T. Petreus, V. Braic, Characterization of Zr-based hard coatings for medical implant applications, *Surf. Coat. Technol.*, 2010, vol. 204, pp. 2046–2050.
4. S.R. Levine, E.J. Opila, R.C. Robinson, Characterization of an ultra-high temperature ceramic composite, *NASA TM*, 2004, 213085, pp. 1–26.
5. M.J. Gasch, D.T. Ellerby, S.M. Johnson, Ultra high temperature ceramic composites, *Handbook of Ceramic Composites* (Ed.: N.P. Bansal), Kluwer Academic Publishers, NY, USA, 2005, pp. 197–224.
6. S.M. Scala, L.M. Gilbert, Theory of hypersonic laminar stagnation region heat transfer in dissociating gases, *NASA Tech Note*, 1963, 71-70918.
7. L. Lees, On the boundary layer equations in hypersonic flow and their approximate solutions, *J. Aero. Sci.*, 1953, vol. 20, pp. 143–145.
8. E.V. Zoby, Empirical stagnation-point heat-transfer relation in several gas mixtures at high enthalpy levels, *NASA Tech Note*, 1968, 4799.
9. Q. Hong, A. Walle, Prediction of the material with highest known melting point from ab initio molecular dynamics calculations, *Phys. Rev.*, 2015, vol. 92.

## THERMAL EXPLOSION IN THE 2Co–Ti–Al SYSTEM: COMBUSTION, PHASE FORMATION AND PROPERTIES

**M. L. Busurina<sup>\*a</sup>, A. E. Sytshev<sup>a</sup>, D. Yu. Kovalev<sup>a</sup>, N. V. Sachkova<sup>a</sup>, A. V. Karpov<sup>a</sup>,  
A. N. Gryadunov<sup>a</sup>, and V. A. Shcherbakov<sup>a</sup>**

<sup>a</sup>Merzhanov Institute of Structural Macrokinetics and Materials Science, Russian Academy of Sciences, Chernogolovka, Moscow, 142432 Russia

\*e-mail: busurina@ism.ac.ru

DOI: 10.24411/9999-0014A-2019-10026

Investigation of structural materials in Ni–Al and Ti–Al binary and Ti–Al–Me (Me = Ni, Fe, Co, Cu) ternary systems and their functional dependence on the chemical composition, properties and structure is a promising task for modern electronics [1, 2]. Ternary intermetallic compounds  $X_2YZ$  where X and Y are the transition metals, Z is the element of III–IV groups belong to the alloys of Heusler. These alloys have very attractive properties (shape memory, super elasticity, magneto-optical and magnetocaloric properties) and can be controlled by a magnetic field. One of the promising compounds based on the ternary intermetallic system Co–Ti–Al is the Heusler alloy  $Co_2TiAl$ .

Compounds based on Co–Ti–Al system are produced in various ways: arc melting, shock wave synthesis, spark plasma sintering. In the practice of creation of intermetallic materials by the method of self-propagating high-temperature synthesis (SHS), the question of obtaining intermetallic compounds of both binary and ternary systems is widely investigated. The purpose of this work is to study the features of the structure and phase formation in intermetallic material based on the  $Co_2AlTi$  (Heusler phase) synthesized by SHS. Synthesis was carried out both in vacuum under a pressure of  $13.3 \cdot 10^{-2}$  Pa and in argon ( $\sim 10^5$  Pa). The synthesis of 2Co–Ti–Al samples occurs in the thermal explosion mode. The reaction simultaneously takes place in the entire volume of the sample with the maximum rate of temperature rise reached  $3500^\circ\text{C}/\text{s}$ . Initial temperature of SHS reaction in vacuum (Fig. 1) is  $565^\circ\text{C}$ , which is almost  $100^\circ\text{C}$  below the Al melting point and indicates the beginning of a solid-phase reaction. The maximum temperature of SHS reaction in a vacuum is  $1470^\circ\text{C}$ . The ignition temperature in the argon is  $690^\circ\text{C}$ . The cooling rate of the samples in the argon is also higher than in vacuum, which is explained by a higher heat sink. The maximum combustion temperature in the argon is  $1476^\circ\text{C}$  and is very close to the melting temperature of Co ( $1494^\circ\text{C}$ ).

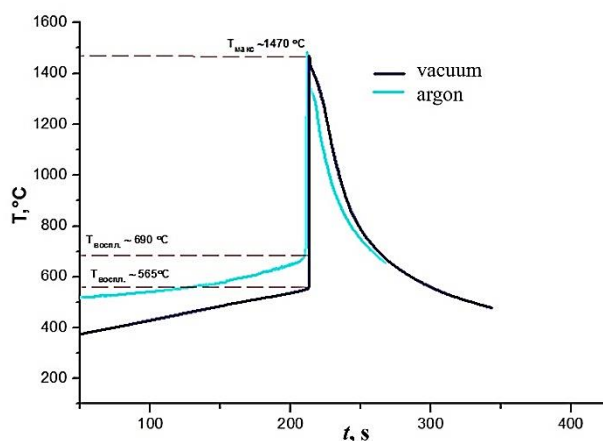


Fig. 1. Temperature profiles of SHS reaction for 2Co–Ti–Al system in vacuum and argon.

X-ray phase analysis (Fig. 2) showed the formation of  $\text{Co}_2\text{AlTi}$  phase (Heusler phase), the mass content of which is equal to 99 mass %. The total content of secondary phases ( $\text{Co}_3\text{Ti}$ ,  $\text{Co}_2\text{Ti}$ ) does not exceed 1 wt %. The unit cell parameter of  $\text{Co}_2\text{TiAl}$  is  $a = 5.8433 \pm 0.0002 \text{ \AA}$ . The compound has a face-centered cubic lattice (Fm3m) and is a structural prototype of  $\text{AlCu}_2\text{Mn}$ .

Combustion product has a homogeneous microstructure (Fig. 3) consisting of rounded  $\text{Co}_2\text{TiAl}$ -phase grains with an average size of  $20 \mu\text{m}$ . The EDA results confirmed the chemical composition of the main  $\text{Co}_2\text{TiAl}$  phase. However, there are areas where the  $\text{Co}_2\text{AlTi}$  grains are separated by the layer based on intermetallic compound of variable composition  $\text{TiCo}_x$  with a thickness of  $10 \mu\text{m}$ . The density of the material was  $5.9 \text{ g/cm}^3$ , which is lower than the theoretical density of  $6.4 \text{ g/cm}^3$ . This is due to the porosity of the sample. The pore size reaches  $50\text{--}100 \mu\text{m}$ .

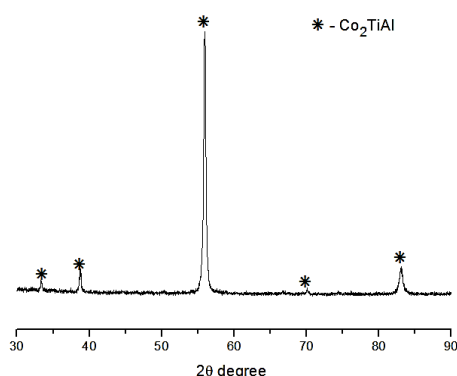


Fig. 2. XRD pattern of combustion product in 2Co-Ti-Al system.

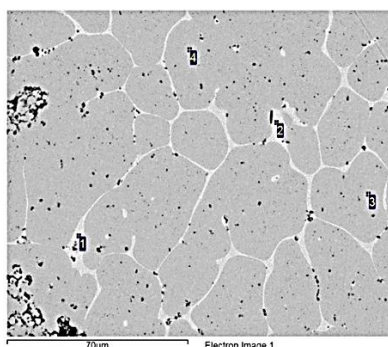


Fig. 3. SEM of combustion product in 2Co-Ti-Al system.

| Spectrum | Al    | Ti    | Co    |
|----------|-------|-------|-------|
| 1        | 2.31  | 18.00 | 79.69 |
| 2        | 1.54  | 24.58 | 73.88 |
| 3        | 15.86 | 22.74 | 61.40 |
| 4        | 15.23 | 23.63 | 61.13 |

Time-resolving X-ray diffraction data [3] showed that the phase formation goes through several successive stages (Fig. 4). Only lines of initial reagents Ti, Al and Co of cubic and hexagonal modification are observed on the diffraction field when heated from room temperature to the ignition temperature. In an exothermic reaction, which was initiated at a temperature close to the melting point of Al, the lines of the initial reagents disappear in a time not exceeding 1 s. Lines 200 and 220 corresponding to the  $\text{Co}_2\text{TiAl}$  phase appeared after the disappearance of lines of initial components. There is a sharp shift of these lines in the region of large angles due to the cooling of the sample after the reaction and intense heat losses. In 9 seconds after ignition, the weak diffraction lines appear on the diffraction field. They identified as lines 111 and 114 of the intermetallic compounds  $\text{Co}_3\text{Ti}$  and  $\text{Co}_2\text{Ti}$ , respectively. XRD of the surface of the synthesized product showed that the main phase is the  $\text{Co}_2\text{TiAl}$  phase (72 mass %). The contents of  $\text{Al}_3\text{Ti}$ ,  $\text{Co}_2\text{Ti}$ , and  $\text{Al}_2\text{O}_3$  secondary phases were 2, 10, and 16 mass %, respectively.

For electromagnetic studies, a non-porous dense samples were produced by SHS densification. The synthesized material showed the presence of ferromagnetic hysteresis loops (Fig. 5a). The maximum value of specific saturation magnetization at room temperature was  $1.64 \text{ am}^2/\text{kg}$ . Electrical resistivity (at room temperature) is  $1.35 \mu\Omega\text{m}$  (Fig.5 b). Resistivity  $\rho$  increases monotonically with increasing temperature.

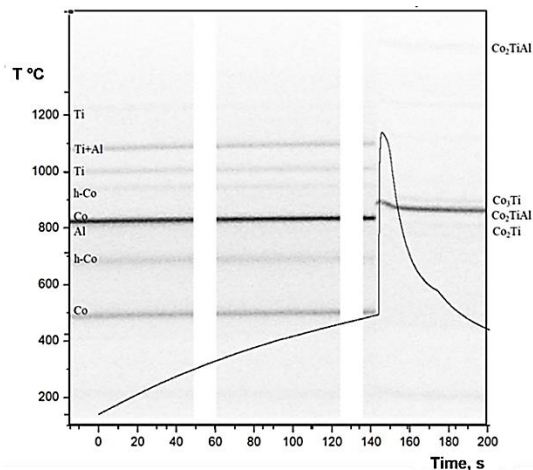


Fig. 4. Time-resolved X-ray analysis of phase transformations in the 2Co-Ti-Al system during SHS.



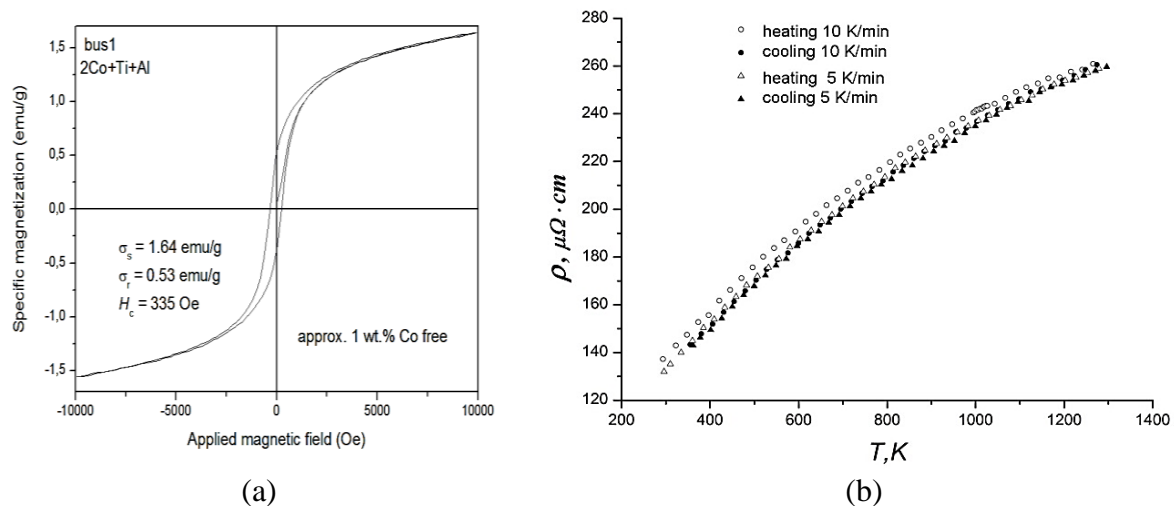


Fig. 5. Magnetic and electrical properties of synthesized product  $\text{Co}_2\text{TiAl}$ .

Resistivity  $\rho$  shows the metallic character of conduction being  $\rho = 1.35 \mu\Omega\text{m}$  at  $T = 293 \text{ K}$  and increases with increasing temperature. Electrical conductivity depends mainly on the relative densification of matrix and conductive phases.

At the beginning of the SHS reaction the nucleation of the  $\text{TiAl}_3$  grains by diffusion of Al atoms from the melt into the Ti lattice takes place. Taking into account that the diffusion coefficient of Al in  $\alpha\text{-Ti}$  is about  $5 \cdot 10^{-18} \text{ m}^2/\text{s}$ , and in  $\beta\text{-Ti}$  is  $3 \cdot 10^{-14} \text{ m}^2/\text{s}$ , it can be concluded that the leading mechanism of SHS reaction is diffusion of Al in  $\beta\text{-Ti}$ . Cobalt decreases the beta transus temperature ( $\alpha\text{-Ti} \rightarrow \beta\text{-Ti}$ ) from  $885^\circ\text{C}$  to  $758\text{--}806^\circ\text{C}$ . The solubility of Co into Al at eutectic temperature does not exceed 0.009 at %. Solubility of Al in  $\epsilon\text{-Co}$  is also practically zero. The solubility of Co into  $\text{AlTi}_x$  intermetallic is quite high (2.3–9.6 at %). The solubility of Al in  $\text{TiCo}_s$  intermetallics, as well as in Co and Ti is 6.8–13.7 at %. The solubility of Co into Ti is 10.3 at % and of Ti in Co is 8.5 at %. Therefore, it can be assumed that the formation of  $\text{Co}_2\text{AlTi}$  occurs due to the dissolution of Co atoms in the melt Ti–Al.

1. R. De Groot, F. Mueller, P. Engen, K. Buschow, New class of materials: Half-metallic ferromagnets, *Phys. Rev. Lett.*, 1983. vol. 50, no. 25, pp. 2024–2027.
2. T. Graf, C. Felser, S. Parkin, Simple rules for understanding of Heusler compounds, *Prog. Solid State Chem.*, 2011, vol. 39, pp. 1–50.
3. D. Yu. Kovalev, V.I. Ponomarev, Time-resolved x-ray diffraction in SHS research and related areas: An overview, *Int. J. Self-Propag. High-Temp. Synth.*, 2019, vol. 28, no. 2 (in press).
4. E.B. Pismenskaya, A.S. Rogachev, V.I. Ponomarev, I.O. Khomenko, Evolution of the phases during gasless thermal explosion in the systems Ni–Al and Ti–Al, *Int. J. Self-Propag. High-Temp. Synth.*, 1997, vol. 6, p. 47.
5. M. Yin, S. Chen, P. Nash, Enthalpies of formation of selected  $\text{Co}_2\text{YZ}$  Heusler compounds, *J. Alloys Compd.*, 2013, vol. 577, pp. 46–56.
6. Y. Mishin, Chr. Herzig, Diffusion in the Ti–Al system, *Acta Mater.*, 2000, vol. 48, pp. 589–623.
7. C. Leyens, M. Peters, Titanium and titanium alloys: Fundamentals and applications, WILEY-VCH Verlag GmbH & Co. KGaA, Weinheim, 2003.
8. K.A. Fomina, V.V. Marchenkov, E.I. Shreder, H.W. Weber, Electrical and optical properties of  $\text{X}_2\text{YZ}$  ( $\text{X} = \text{Co}, \text{Fe}$ ;  $\text{Y} = \text{Cr}, \text{Mn}, \text{Ti}$ ;  $\text{Z} = \text{Ga}, \text{Al}, \text{Si}$ ) Heusler alloys, *Solid State Phenom.*, 2011, vol.168, pp. 545–548.
9. I.P. Borovinskaya, A.N. Pityulin, SHS-produced hard alloys. In: Self-propagating high-temperature synthesis of materials. Combustion science technology series, vol. 5, New York: Taylor & Francis, 2002, pp. 270–291.

## THERMITE SYNTHESIS OF NANOCOMPOSITE Co–In<sub>2</sub>O<sub>3</sub> AND Fe–In<sub>2</sub>O<sub>3</sub> FILMS

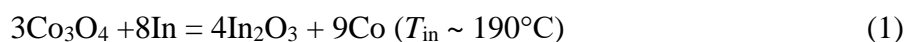
L. E. Bykova<sup>\*a</sup>, V. G. Myagkov<sup>a</sup>, V. S. Zhigalov<sup>a</sup>, and A. A. Matsynin<sup>a</sup>

<sup>a</sup>Kirensky Institute of Physics, Federal Research Center KSC SB RAS, Krasnoyarsk, 660036 Russia

\*e-mail: lebyk@iph.krasn.ru

DOI: 10.24411/9999-0014A-2019-10027

Granular nanocomposites consisting of ferromagnetic nanoparticles embedded in semiconductor (In<sub>2</sub>O<sub>3</sub>, TiO<sub>2</sub>, ZnO, and SnO<sub>2</sub>) or dielectric (SiO<sub>2</sub>, Al<sub>2</sub>O<sub>3</sub>, MgO, and ZrO<sub>2</sub>) matrices have been intensively studied as objects interesting both for fundamental research and application. The most common methods for synthesizing magnetic nanocomposites and hybrid materials use wet chemistry; these include sol-gel methods, solvothermal methods, sonochemical synthesis, thermal decomposition, chemical reduction, and radiolysis [1, 2]. After wet chemistry, the next most important method of obtaining functional magnetic nanocomposites is the formation of magnetic granular films created from a joint deposition of metal and an insulator [3, 4]. The search for new methods to create ferromagnetic nanocomposite films is relevant. This paper discusses the synthesis of ferromagnetic nanocomposite film materials on the basis of solid-state thermite reactions between layers of oxides of 3d metals (Co<sub>3</sub>O<sub>4</sub> and Fe<sub>2</sub>O<sub>3</sub>) and the metal In. Ferromagnetic nanocomposite Co–In<sub>2</sub>O<sub>3</sub> thin films were synthesized using thermite reactions between layers of In and Co<sub>3</sub>O<sub>4</sub> (1) by vacuum annealing of In/Co<sub>3</sub>O<sub>4</sub> film bilayers.



Ferromagnetic nanocomposite Fe–In<sub>2</sub>O<sub>3</sub> thin films were synthesized using thermite reactions between layers of In and Fe<sub>2</sub>O<sub>3</sub> (2) by vacuum annealing of In/Fe<sub>2</sub>O<sub>3</sub> film bilayers.

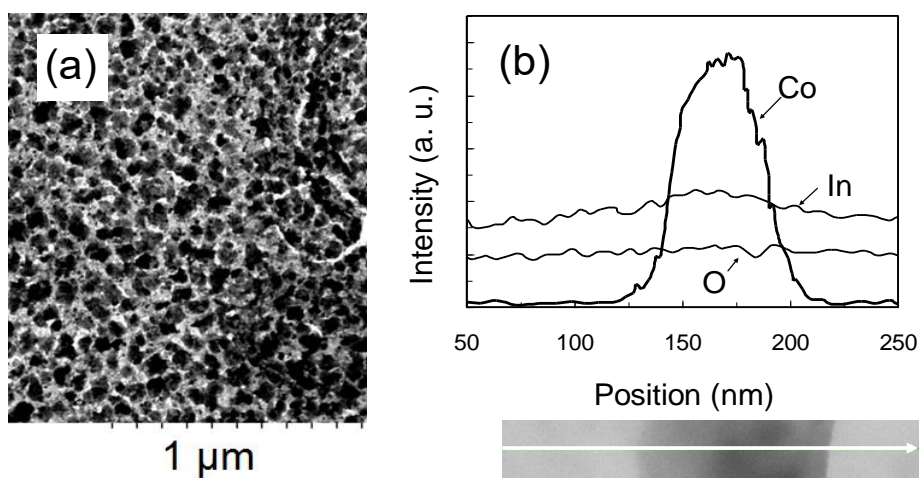
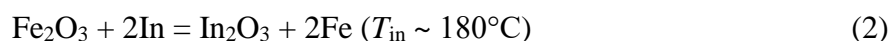


Fig. 1. (a) Electron microscopy image and (b) elemental composition of the Co–In<sub>2</sub>O<sub>3</sub> nanocomposite film.

The initiation temperature of reactions ( $T_{in}$ ) and the structural and magnetic properties of the nanocomposite films were identified. Electron-microscopic study of films showed the creation of Co, Fe (60–100 nm) nanoclusters surrounded by a layer of  $In_2O_3$  over a large area (Figs. 1, 2). Thus, the termite method is promising for synthesizing ferromagnetic nanocomposite thin films consisting of ferromagnetic clusters embedded in oxide matrices and characterized by the high magnetization and chemical stability.

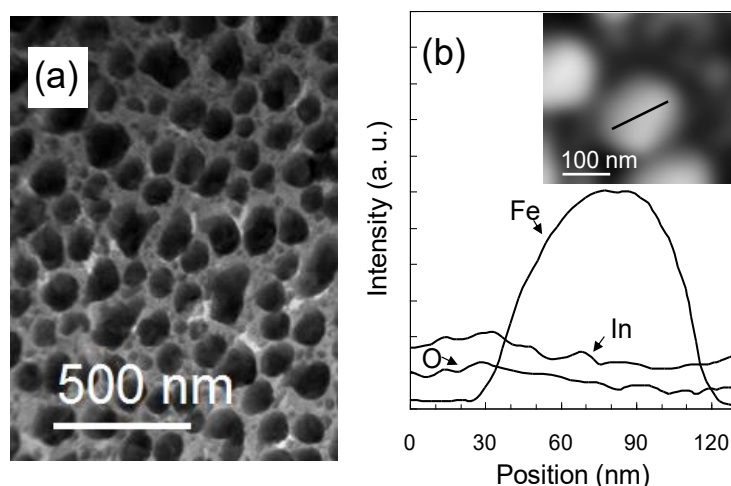


Fig. 2. (a) Electron microscopy image and (b) elemental composition of the Fe- $In_2O_3$  nanocomposite film.

The research was supported by RFBR together with the Government of the Krasnoyarsk Territory, the Krasnoyarsk Regional Fund of Science (project no. 18-42-243009r\_mol\_a).

1. S. Wei, Q. Wang, J. Zhu, L. Sun, H. Line, Z. Guo, Multifunctional composite core-shell nanoparticles, *Nanoscale*, 2011, vol. 3, pp. 4474–4502.
2. R.G. Chaudhuri, S. Paria, Core/shell Nanoparticles: Classes, Properties, Synthesis Mechanisms, Characterization, and applications, *Chem. Rev.*, 2012, vol. 112, pp. 2373–2433.
3. S. Mann, Self-assembly and transformation of hybrid nano-objects and nanostructures under equilibrium and non-equilibrium conditions, *Nat. Mater.*, 2009, vol. 8, pp. 781–792.
4. K. Sato, M. Mizuguchi, R. Tang, J.-G. Kang, M. Ishimaru, K. Takanashi, T. J. Konno, Direct imaging of atomic clusters in an amorphous matrix: A Co-C granular thin film, *Appl. Phys. Lett.*, 2012, vol. 101, pp. 191902-1–191902-3.

## PREPARATION OF POROUS NIOBIUM–ALUMINUM INTERMETALLIC BY COMBUSTION SYNTHESIS IN THERMAL EXPLOSION MODE

X. Cai<sup>a</sup> and P. Feng<sup>\*a</sup><sup>a</sup>School of Materials Science and Engineering, China University of Mining and Technology, Xuzhou, 221116 P. R. China

\*e-mail: pzfeng@cumt.edu.cn

DOI: 10.24411/9999-0014A-2019-10028

**Abstract.** Porous Nb–Al intermetallic was prepared by thermal explosion (TE) mode of combustion synthesis (CS). The temperature profile, phase composition, open porosity, and oxidation resistance of Nb–Al compact were investigated. The results showed that the significant exothermic reaction occurs, which means that an obvious TE appears during heating process. The volume expansion of 190% was observed in product, and the heated sample exhibited interconnected pores with a high open porosity of 65.7%. The porous NbAl<sub>3</sub> intermetallic show ‘pest’ oxidation in the temperature range of 500–600°C, and follow parabolic oxidation law at 400°C. Moreover, the highly porous structure makes this material have great potential for separation and heat insulation applications at medium temperature range from room temperature to 400°C.

**Keywords:** Niobium–aluminum; Intermetallics; Thermal explosion; Sintering

Figure 1 shows the temperature evolution profiles and DSC curves of NbAl samples at a linear heating rate of 10°C/min. As shown in Fig. 1a, the temperature of the sample slowly increases with the furnace temperature at a constant rate. Then, a noticeable temperature change occurs at 669°C: the temperature stops increasing and reaches a plateau for 236 s. During this time of plateau, the heating is continued, and the temperature increases again at the end of this plateau due to the temperature gradient between the sample (669°C) and the furnace (713°C). When the temperature reaches 791°C, the curve shifts upward and increases to maximum deviation of 925°C. Subsequently, the temperature increases slowly and tends to the furnace temperature (dotted line). From the DSC curve (Fig. 1b), it can be inferred that temperature plateau at 669°C corresponds to the melting of Al, and the profile show a single, sharp exothermic peak at 931°C, resulting in the temperature of the sample climbed continually, which is indicative of the TE reaction. Moreover, the ignition point of exothermic peak in DSC is consistent with the temperature curve increased markedly at 791°C.

An interesting feature of Nb–Al system is that TE occurs there at a temperature almost 130°C higher than the melting point of Al (660°C), which is distinct from most other TE reaction system, for instance, Fe–Al [1–5] and Ti–Al [6–11]. Previous study shows that the combustion reaction of Nb–Al is triggered by the dissolution-precipitation process. However, according to the Nb–Al phase diagram, the solubility of Nb in Al is almost near zero and is very limited even in liquid Al. And from the published data, the solubility of Nb in liquid Al is about 0.02 wt % at 700°C, increasing to 0.06 wt % at 800°C. These data indicate that the higher temperature will be required for the ignition of thermal explosion in Nb–Al system. Moreover, the difficulty in wetting the Nb particle surface by liquid Al could be other factor hinder the reaction.

The green compact was characterized by the silver-gray luster of metals, indicates that the Al and Nb powders become a compact with certain strength by the uniaxially pressed process, as shown in Fig. 2a. After sintering, compare with the green compact, the volume of the sintered disc increased significantly (Fig. 2b) and the expansion ratio were measured to 190%, meanwhile, the sample kept in original shape without deformation, crack and losing angle.

Figure 2c shows the XRD patterns of the green compact and as prepared products. Peaks of the pure crystalline Nb and Al are detected in the green compact, and for the sample heated to 1000°C for 1 h, single phase and well crystallized tetragonal NbAl<sub>3</sub> (JCPDS no. 13-0146) with the major peaks at  $2\theta = 20.59, 25.35, 39.17, 41.95, 47.31, 65.03^\circ$  corresponding to the diffraction of the (002), (101), (112), (004), (200), and (204) planes are synthesized.

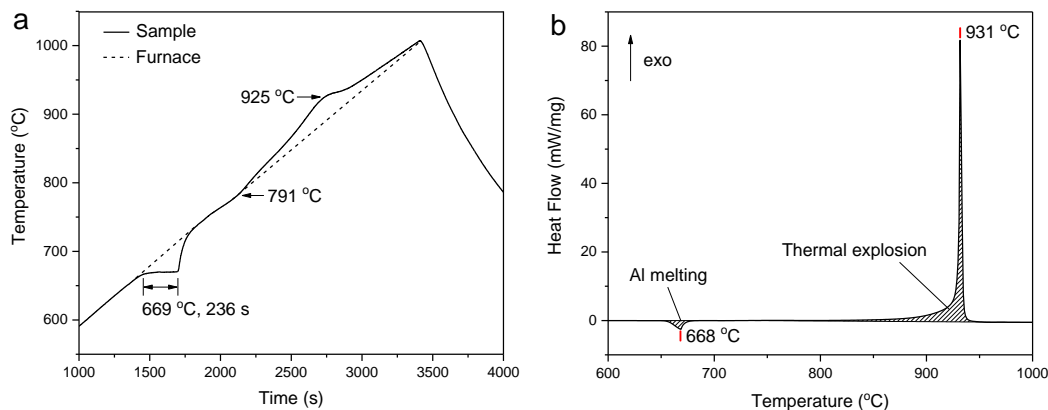


Fig. 1. (a) Temperature–time profile and (b) DSC plot of Nb–Al compact heated to 1000°C with a heating rate of 10 °C/min.

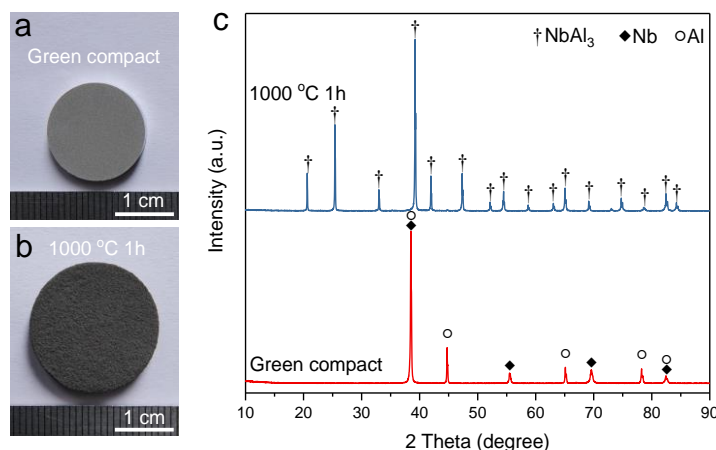


Fig. 2. Macroscopic image and XRD patterns: (a) green compact, (b) sample heated to 1000°C for 1 h, (c) XRD patterns of green compact and product.

Figure 3a shows the secondary electron image of the fracture surface of sample heated to 1000°C for 1 h. A sponge-like and highly porous structure consisting of a large number of agglomerated particles was obtained. Moreover, the enlarged image (Fig. 3b) shows the neighboring particles with size about 3–6 μm are connected through necks (marked by white arrows), indicating the initial stage of sintering in the sample. The open porosity of the sintered specimen was measured to be 65.7%, which is higher than that of the green compact (19.4%). Besides, the density of the sample is about 1.56 g·cm<sup>-3</sup> and lower than the theoretical density of NbAl<sub>3</sub> (4.54 g·cm<sup>-3</sup>) due to the highly porous structure of the product. Figure 3c shows the EPMA mapping results of as prepared porous intermetallic. As can be seen from the back-scattering electron (BSE) image, single-phase structure was obtained, which is in good agreement with the XRD patterns. The element mapping shows that Nb and Al are homogeneously distributed in the final products, furthering confirmed that each single particle is composed of NbAl<sub>3</sub> phases. Furthermore, during the process of sample preparation for EPMA, the specimen was immersed in an uncured epoxy resin, then the resin was cured. After polishing, it was found that the pores were filled with the resin, showed the feature of interconnected pores (open pores).

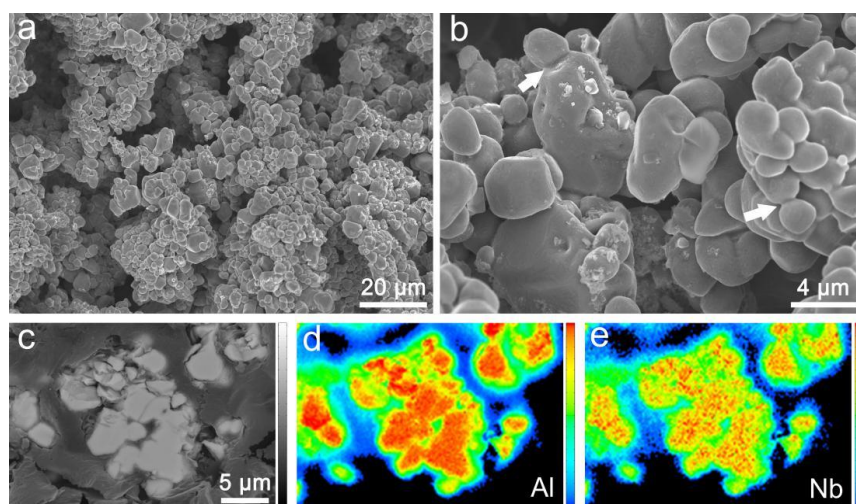


Fig. 3. (a, b) SEM image of porous NbAl<sub>3</sub> intermetallic. (c–e) EPMA mapping results of synthesized porous NbAl<sub>3</sub>.

To investigate the high-temperature oxidation behavior of porous Nb–Al intermetallic, the mass gain (%) was measured as a function of the oxidation time at 400, 500, 550, and 600°C and plotted in Fig. 4a. The sample has almost no change in mass gain when oxidized at 400°C, as can be seen from the enlarged curve (Fig. 4b), during the oxidation experiments at 400°C, the mass gain of samples shows a continuous increase with the exposure time. In the initial period (I), the weight increases significantly, indicating a higher oxidation rate. In the subsequent stage (II), the oxidation rate decreases and the mass gains of the porous Nb–Al intermetallic are found to follow the parabolic oxidation rate law. The mass gain was only 0.19% when oxidation was for 144 h. However, for the sample oxidized at 500, 550, and 600 °C, the mass gain is two orders of magnitude higher than that of sample oxidized at 400°C, which means that the oxide scale was not protective. Moreover, at the end of oxidation experiments, it was found that the sample was complete disintegration into a powder. The accelerated oxidation of porous Nb–Al intermetallic at 500–600°C can be well interpreted by the ‘pest’ or catastrophic oxidation: grain-boundary and non-selective oxidation, does not form the protective alumina scale in the sample and producing cracks due to the mismatch in volume expansion between the formed oxide and the base alloy, which causes complete disintegration of monolithic samples into powder. This phenomenon not only had been detected in Nb and its alloys, but also revealed in MoSi<sub>2</sub> and high-entropy alloys. In order to improve the oxidation resistance of such materials with ‘pest’, alloying and coating are effective means for the formation of an adhesive, dense, protective scale on the surface of material.

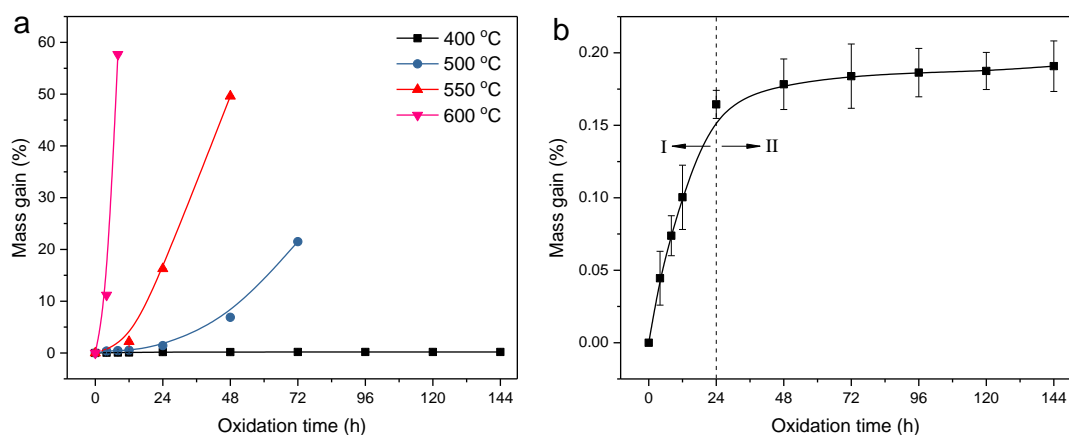


Fig. 4. Mass gain vs. time plot of porous NbAl<sub>3</sub> intermetallic after oxidation: (a) 400°C, 500, 550, and 600°C for 144 h, (b) enlarged plot of 400°C in (a).

This work was supported by National Natural Science Foundation of China (51574241).

1. Y.N. Liu, X.P. Cai, Z. Sun, H.Z. Zhang, F. Akhtar, T. Czujko, P.Z. Feng, Fabrication and characterization of highly porous FeAl-based intermetallics by thermal explosion reaction, *Adv. Eng. Mater.*, 2019.
2. X.P. Cai, Y.N. Liu, P.Z. Feng, X.Y. Jiao, L.Q. Zhang, J.Z. Wang, Fe–Al intermetallic foam with porosity above 60% prepared by thermal explosion, *J. Alloys Compd.*, 2018, vol. 732, pp. 443–447.
3. Y.N. Liu, X.P. Cai, Z. Sun, X.Y. Jiao, F. Akhtar, J.Z. Wang, P.Z. Feng, A novel fabrication strategy for highly porous FeAl/Al<sub>2</sub>O<sub>3</sub> composite by thermal explosion in vacuum, *Vacuum*, 2018, vol. 149, pp. 225–230.
4. X.P. Cai, Y.N. Liu, X.H. Wang, X.Y. Jiao, J.Z. Wang, F. Akhtar, P.Z. Feng, Oxidation resistance of highly porous FeAl foams prepared by thermal explosion, *Metall. Mater. Trans. A.*, 2018, vol. 49, no. 8, pp. 3683–3691.
5. Y.N. Liu, Z. Sun, X.P. Cai, X.Y. Jiao, P.Z. Feng, Fabrication of porous FeAl-based intermetallics via thermal explosion, *Trans. Non-Ferr. Met. Soc. China*, 2018, vol. 28, pp. 1141–1148.
6. X.Y. Jiao, X.R. Ren, X.H. Wang, S.G. Wang, P.Z. Feng, J.Z. Wang, Porous TiAl<sub>3</sub> intermetallics with symmetrical graded pore-structure fabricated by leaching space holder and thermal explosion process, *Intermetal.*, 2018, vol. 95, pp. 144–149.
7. X.Y. Jiao, X.H. Wang, P.Z. Feng, Y.N. Liu, L.Q. Zhang, F. Akhtar, Microstructure evolution and pore formation mechanism of porous TiAl<sub>3</sub> intermetallics via reactive sintering, *Acta Metall Sin-Engl*, 2018, vol. 31, no. 4, pp. 440–448.
8. X.Y. Jiao, P.Z. Feng, Y.N. Liu, X.P. Cai, J.Z. Wang, T. Czujko, Fabrication of highly porous TiAl<sub>3</sub> intermetallics using titanium hydride as a reactant in thermal explosion reaction, *J. Mater. Res.*, 2018, vol. 33, no. 18, pp. 2680–2688.
9. X.Y. Jiao, X.H. Wang, X.Q. Kang, P.Z. Feng, L.Q. Zhang, F. Akhtar, Effect of heating rate on porous TiAl-based intermetallics synthesized by thermal explosion, *Mater. Manuf. Processes*, 2017, vol. 32, no. 5, pp. 489–494.
10. Z. Wang, X.Y. Jiao, P.Z. Feng, X.H. Wang, Z.S. Liu, F. Akhtar, Highly porous open cellular TiAl-based intermetallics fabricated by thermal explosion with space holder process, *Intermetal.*, 2016, vol. 68, pp. 95–100.
11. X.Y. Jiao, X.H. Wang, X.Q. Kang, P.Z. Feng, L.Q. Zhang, J.Z. Wang, F. Akhtar, Hierarchical porous TiAl<sub>3</sub> intermetallics synthesized by thermal explosion with a leachable space-holder material, *Mater. Lett.*, 2016, vol. 181, pp. 261–264.

## COMBUSTION SYNTHESIZED MATERIALS FOR ELECTROCHEMICAL APPLICATIONS

**K.-Y. Chan<sup>\*a</sup>, A. A. Voskanyan<sup>a</sup>, C.-K. Ho<sup>a</sup>, L. Wang<sup>a,b</sup>, W. Y. Lam<sup>a</sup>,  
C.-Y. V. Li<sup>a</sup>, and B. Qin<sup>a</sup>**

<sup>a</sup>Department of Chemistry, The University of Hong Kong, Pokfulam Road, Hong Kong SAR

<sup>b</sup>Department of Chemistry, Nankai University, China

\*e-mail: hrsckky@hku.hk

DOI: 10.24411/9999-0014A-2019-10029

There are immense interests in exploring electrochemical power systems, such as metal-ion, metal-air, and flow batteries, to meet the growing demand in large scale energy storage. Reported high performance electrodes of these devices are usually composed of advanced nanostructured materials which cannot be synthesized economically in large scale. Combustion synthesis is attractive for its relatively low capital costs and minimum energy demand. Compositions of metal/metal oxides mixtures can be conveniently controlled with precursors atomically mixed in solution combustion. Porosity is created by gas evolution during combustion and the temperature profile favors particles of well-developed crystallinity. A large range of product composition and structural properties can be tuned by amounts and choices of precursors, fuels, oxidants, solvents, and inert additives.

We discuss here a few recent investigations of applying combustion synthesized metal/metal oxides to electrochemical devices.

Manganese dioxide was synthesized with manganese nitrate and glycine precursors using a previously reported colloidal solution combustion synthesis (CSCS) method, [1] in which 22 nm colloidal SiO<sub>2</sub> particles are added before combustion and removed from the product by etching after combustion. The manganese dioxide synthesized has uniform pores of 29 nm dia., 120 m<sup>2</sup>/g surface area, 0.35 mL/g pore volume, and is composed of 2–3 nm  $\delta$ -phase crystals ( $\delta$ -MnO<sub>2</sub>). [2] Electrochemical studies of the CSCS synthesized MnO<sub>2</sub> show excellent performance as an anode in a lithium-ion battery (LIB) and better than most MnO<sub>2</sub> electrodes reported in literature [2].

The overlapping redox peaks after the 1<sup>st</sup> cycle in Fig. 1a show good reversibility in discharge (lithiation) and charge (delithiation) processes. Figure 1b shows charge/discharge profiles at different rates compared with a commercial  $\beta$ -MnO<sub>2</sub> (CommMnO<sub>2</sub>). Besides high rate capability, CSCS-MnO<sub>2</sub> showed excellent cyclability and was able to maintain a high capacity of 320 mAh/g on average for 160 cycles. The SEM image of Fig. 1c after 200 cycles also verifies the preservation of the uniform pore structure.

In another example, high quality palladium thin film was deposited via a one-step aqueous combustion process onto glassy carbon as shown in Fig. 2a with a relatively low deposition temperature of 250°C [3]. Excellent catalytic property and stability are shown in Fig. 2b for electrooxidation of ethanol in alkaline solution. Electrochemical oxygen reduction in a rotating disk operation is shown in Fig. 2c with corresponding kinetics shown in the Koutechy-Levich plot of Fig. 2d.

We also discuss other recent investigations of combustion synthesized materials for applications in electrochemical devices which include the positive electrode (cathode) of lithium-ion battery and negative electrode(anode) of sodium-ion battery.



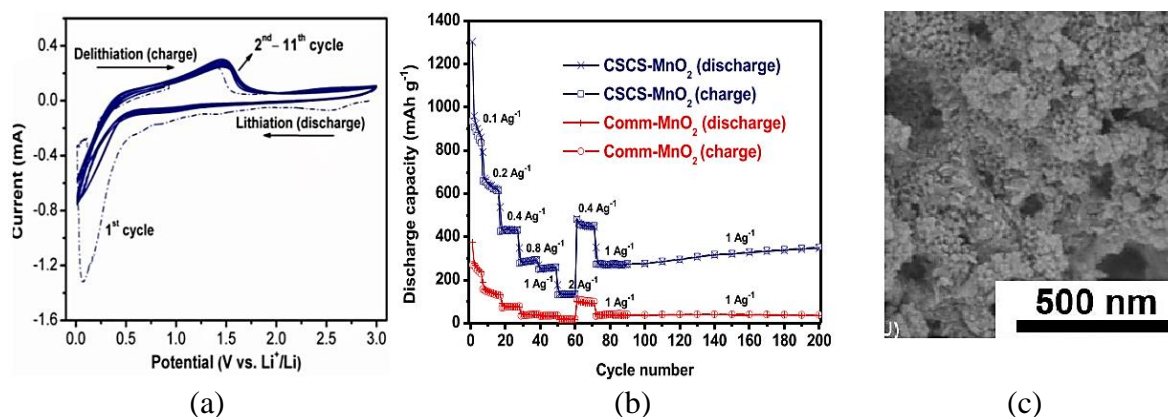


Fig. 1. (a) CV curves of CSCS synthesized  $\delta$ -MnO<sub>2</sub> at 0.2 mV/s performed in a lithium-ion coin cell with lithium foil counter electrode, at 1 M LiPF<sub>6</sub> in 1:1:1 ethyl carbonate/dimethyl carbonate/ethylmethyl carbonate solution. (b) The rate performance of CSCS synthesized  $\delta$ -MnO<sub>2</sub> and commercial  $\beta$ -MnO<sub>2</sub> as well as cycling performance at high current density of 1 A g<sup>-1</sup>; (c) SEM image of CSCS  $\delta$ -MnO<sub>2</sub> anode demonstrating well-preserved mesoporous structure after 200 cycles at 1 A g<sup>-1</sup> current density.

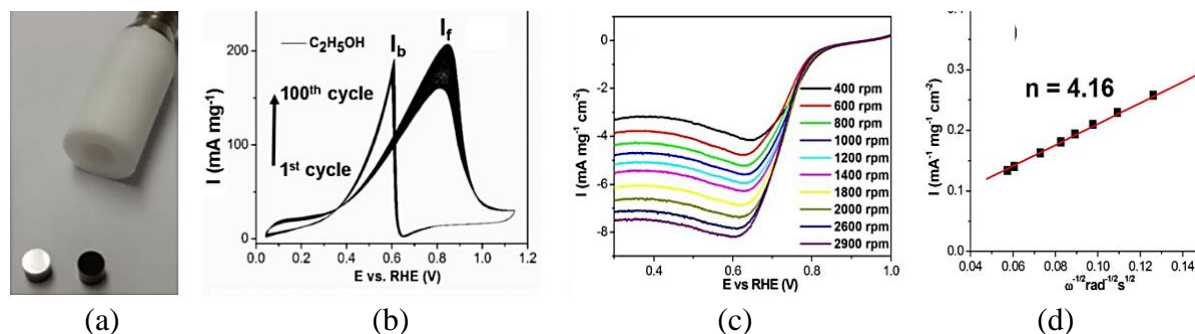


Fig. 2. (a) Detachable glassy carbon electrode before and after deposition of Pd film by combustion; (b) Cyclic voltammograms in 0.5 M NaOH + 0.5 M ethanol; (c) Oxygen reduction polarization curves at different rotation speeds for Pd film in an oxygen saturated 0.1 M NaOH solution at a scan rate of 10 mV s<sup>-1</sup>; and (d) Koutecky-Levich plot of  $I^{-1}$  versus  $\omega^{-1/2}$  at 0.3 V vs RHE.

This work was fully supported by a grant from the Research Grant Council of the Hong Kong Special Administrative Region, China (Project no. T23-601/17-R).

1. A.A. Voskanyan, K.Y. Chan, C.Y.V. Li, Colloidal solution combustion synthesis: toward mass production of a crystalline uniform mesoporous CeO<sub>2</sub> catalyst with tunable porosity, *Chem. Mater.*, 2016, vol. 28, no. 8, pp. 2768–2775.
2. A.A. Voskanyan, C.K. Ho, K.Y. Chan, 3D  $\delta$ -MnO<sub>2</sub> nanostructure with ultralarge mesopores as high-performance lithium-ion battery anode fabricated via colloidal solution combustion synthesis, *J. Power Sources*, 2019, vol. 421, no. 1, pp. 162–168.
3. A.A. Voskanyan, C.Y.V. Li, K.Y. Chan, Catalytic palladium film deposited by scalable low-temperature aqueous combustion, *ACS Appl. Mater. Interfaces*, 2017, vol. 38, no. 9, pp. 33298–33307.

## SOLUTION COMBUSTION SYNTHESIS OF CARBON-BASED POROUS NANOMATERIALS FOR EFFICIENT ELECTROCHEMICAL APPLICATIONS

P. W. Chen<sup>\*a</sup>, C. X. Xu<sup>a,b</sup>, K. Y. Liu<sup>a</sup>, and X. Gao<sup>a,c</sup><sup>a</sup>State Key Laboratory of Explosion Science and Technology, Beijing Institute of Technology, Beijing, 100081 China<sup>b</sup>Aerospace Institute of Advanced Materials & Processing Technology, Beijing, 100074 China<sup>c</sup>Institute of Pulsed Power Science, Kumamoto University, Kumamoto, 8608555 Japan

\*e-mail: pwchen@bit.edu.cn

DOI: 10.24411/9999-0014A-2019-10030

Fabricating advanced functional material for excellent energy conversion and storage performance has great importance for solving global energy issues. Porous materials are an ideal choice to improve the mass transport and interface charge transfer in energy devices such as Li-ion batteries and fuel cell, owing to their large surface area and abundant channels. On the other hand, carbon is recognized as a leading electrode material of the above-mentioned applications. Therefore, it is of great interest to develop novel and efficient synthesis strategies to produce porous carbon-based functional materials. Solution combustion is an exciting phenomenon, which involves propagation of self-sustained exothermic reactions along an aqueous or sol-gel media and allows for the synthesis of a variety of nanoscale materials. Through solution combustion method, the reactions of the reductant liquid and oxidant additive was utilized as energy source and carbon source for the formation of different carbon-based porous nanomaterials. These as-prepared nanomaterials were characterized via various techniques, exhibiting different outstanding electrochemical properties and high potential applications in Li-ion battery. Firstly, N-doped carbon nanofoam (Fig. 1a) was synthesized via the combustion of hydrazine hydrate ( $\text{N}_2\text{H}_4 \cdot \text{H}_2\text{O}$ ) absorbing carbon dioxide ( $\text{CO}_2$ ) and magnesium powder. Firstly, the dry ice was added into hydrazine hydrate to form  $\text{NH}_2\text{NHCOO}^-$  ions as reductant, carbon source and nitrogen source. Subsequently, the magnesium powder was added into the solvent and ignited via a tungsten heating wire. After combustion, the products were recovered and characterized to be N-doped carbon nanofoam, exhibiting efficient electrochemistry performance toward Li-ion battery and oxygen reduction reaction. Moreover, N-doped carbon nanomesh sheets (Fig. 1b) were synthesized through the combustion of ethanol amine absorbing  $\text{CO}_2$  and magnesium powder along the same procedure. The as-prepared N-doped carbon nanomesh sheets with well-formed one- to four-atom-thick sheet structure possess multiple outstanding properties, such as superior half-wave potential (0.81 V vs RHE), stable oxygen reduction reaction in alkaline medium.

Secondly, using glucose ( $\text{C}_6\text{H}_{12}\text{O}_6$ ) and copper nitrate ( $\text{Cu}(\text{NO}_3)_2$ ) as fuel and oxidizing agent respectively,  $\text{CuO}/\text{Cu}_2\text{O}/\text{C}$  composites (Fig. 2a) with different carbon contents were prepared by the solution combustion synthesis method. The as-obtained  $\text{CuO}/\text{Cu}_2\text{O}$  nanoparticles exhibit uniform spherical morphology and were well distributed in the *in-situ* synthesized carbon with a content ranging from 3–36 wt %. An anode for Li-ion battery was prepared using this  $\text{CuO}/\text{Cu}_2\text{O}/\text{C}$  composite for the investigation of its electrochemical performance via various techniques. The results reveal its high potential applications with multiple properties, such as  $> 400 \text{ mAh/g}$  capacity at  $20 \text{ mA g}^{-1}$  current density and highly stable cycling performance with capacity  $260 \text{ mA h g}^{-1}$  after 600 cycles at a current density  $0.2 \text{ A g}^{-1}$ . This performance is attributed to the synergistic effect of anodes porous structure, conducting carbon coating and two-component  $\text{CuO}/\text{Cu}_2\text{O}$  structure.

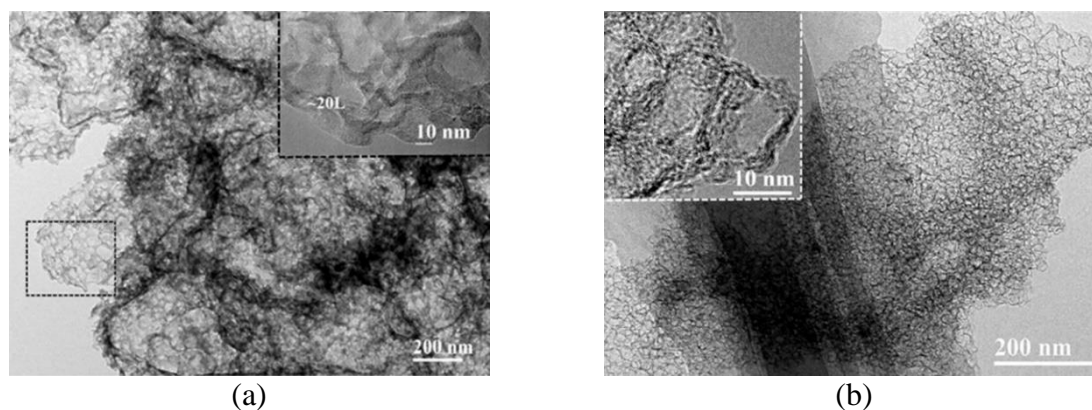


Fig. 1. TEM images of solution combustion synthesized (a) N-doped carbon nanofoam and (b) N-doped carbon nanomesh sheets.

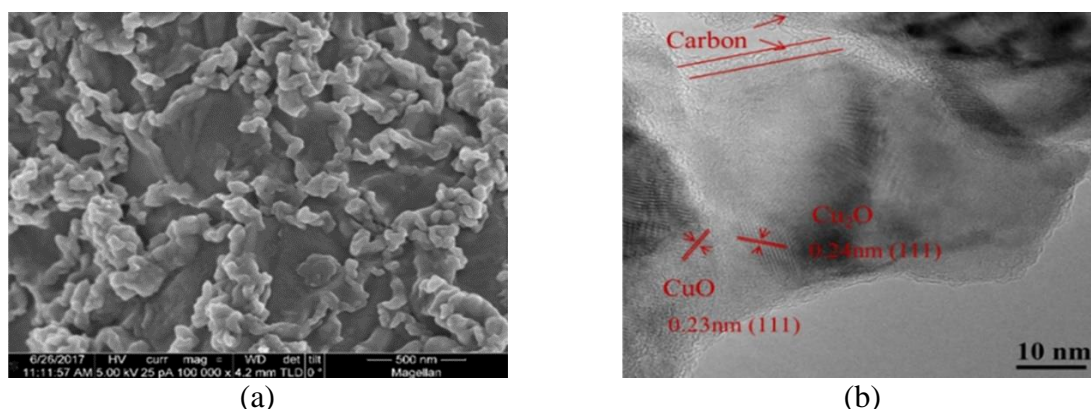


Fig. 2. (a) SEM image and (b) TEM image of as-obtained CuO/Cu<sub>2</sub>O/C composites.

Our studies introduce a general solution that can further integrate various additives dissolved homogeneously, thus opening a new avenue of constructing carbon-based functional materials with controlled morphology and modified electrochemical properties.

## SELF-PROPAGATING HIGH-TEMPERATURE SYNTHESIS AND SPARK PLASMA SINTERING OF TUNGSTEN ALLOYS FOR FUSION APPLICATIONS

S. Dine<sup>\*a</sup>, E. Bernard<sup>b</sup>, C. Grisolia<sup>b</sup>, N. Herlin<sup>c</sup>, and D. Vrel<sup>a</sup>

<sup>a</sup>LSPM, UPR 3407 CNRS, Villetaneuse, 93430 France

<sup>b</sup>CEA, IRFM, Saint Paul lez Durance, 13108 France

<sup>c</sup>CEA, IRAMIS, Gif-sur-Yvette Cedex, 91191 France.

\*e-mail: sarah.dine@lspm.cnrs.fr

DOI: 10.24411/9999-0014A-2019-10031

Since tungsten has been chosen as the reference material for the ITER divertor, extensive research has been conducted in order to improve some key properties for whose pure, commercial grade tungsten, present some limitations. Among these, one can find mechanical properties at room temperature, where the brittleness of tungsten reduces its machinability, but also resistance to blistering linked to hydrogen implantation [1], and to corrosion at high temperatures.

Recent studies have shown that low grain sizes, under 700 nm could induce a sharp decrease of the ductile to brittle transition temperature (DBTT), down to cryogenic temperatures [2]; it is also believed that nanostructured bulk tungsten, with an enhanced grain boundaries network would also be favourable to back-diffusion of implanted hydrogen atoms. On the other hand, chromium and vanadium alloying elements are believed to improve corrosion resistance (as in stainless steels) and to limit grain growth during heat treatments.

However, current production routes are not suitable for the fabrication of large bulk nanostructured tungsten samples.

In this work, we propose a novel methodology based on self-propagating high-temperature synthesis (SHS) to obtain partially alloyed nanometric powders in the 20–150 nm range (Fig. 1) [3]. These powders were then sintered by spark plasma sintering (SPS), and mechanical tests were performed. Our SHS reactor is able to synthesize up to 500 g of powder in a reproducible way.

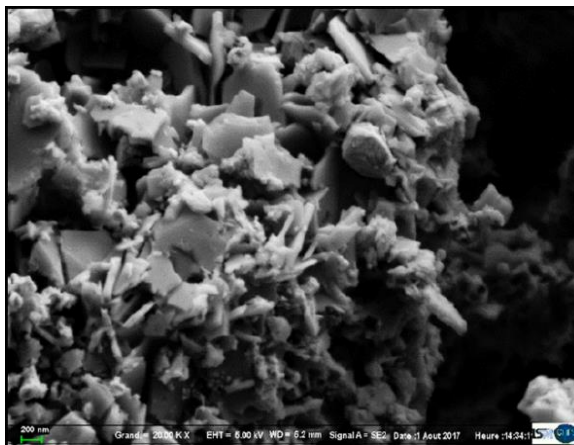


Fig. 1. SEM image of tungsten powders developed by SHS reactor.

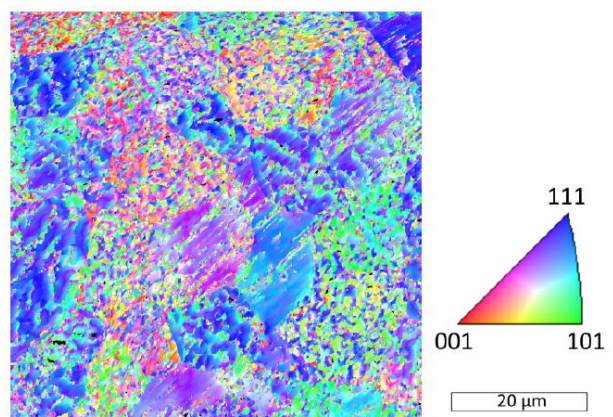


Fig. 2. EBSD mapping giving the crystallographic orientation of the grains on the sample W-2000°C-5'.

Results obtained from SEM, EDX, EBSD and XRD observations on sintered samples show that full tungsten densification may be obtained at a temperature lower than 1800°C and that the resulting morphology, keeping a partial nanostructure inherited from the synthesized powders (Fig. 2), seems indeed favorable to the use of these materials in fusion environments. Hardness measurements were performed and show a systematic increase proportional to the amount of alloying element. Compressive tests show also a significant increase in elastic limit, up to 1 GPa, depending on the nature and the amount of alloying elements (up to 6 wt %). Nevertheless, our samples are not brittle and show a plastic deformation of up to 40% before fracture.

1. K. Ouaras, M. Redolfi, D. Vrel, C. Quiros, G. Lombardi, X. Bonnin, K. Hassouni, *J. Fusion Energ.*, 2018, vol. 37, pp. 37–46.
2. A.A.N. Németh, J. Reiser, D.E.J. Armstrong, M. Rieth, *Int. J. Refract. Met. Hard Mater.*, 2015, vol. 50, pp. 9–15.
3. S. Dine, E. Bernard, N.H. Boime, C. Grisolia, D. Tingaud, D. Vrel, SHS synthesis and SPS densification of nanometric tungsten, *Adv. Eng. Mate.*, 2018, 1701138.

## SHS AND SPS CONSOLIDATION OF COMPLEX COMPOSITIONAL REFRACTORY ALLOYS

**S. Dine<sup>a</sup>, V. Kentheswaran<sup>a</sup>, G. Dirras<sup>a</sup>, and D. Vrel<sup>\*a</sup>**

<sup>a</sup>LSPM, UPR 3407 CNRS, Villetaneuse, 93430 France

\*e-mail: dominique.vrel@lspm.cnrs.fr

DOI: 10.24411/9999-0014A-2019-10032

Complex compositional alloys (CCAs) are a recent breakthrough in material science. Classical metallurgy indeed focuses on alloys made of a single main element, to which different alloying elements may be added in small proportions; in addition, binary phase diagrams have been extensively studied, but the practical use of alloys rich in at least 2 elements is mainly focused on specific compositions such as eutectics or intermetallics. In sharp contrast, CCAs, often called high entropy alloys when, depending on the author, 4 or 5 (or more) elements are considered, are made with compositions where all the elements can be considered as principal, with an atomic content of each element ranging from 5 to 30%.

Following our researches on tungsten (S. Dine *et al.*, this conference), we have thus been studying the synthesis of refractory CCAs, by co-reducing various oxides of metals, including WO<sub>3</sub>, Ta<sub>2</sub>O<sub>5</sub>, MoO<sub>3</sub>, Nb<sub>2</sub>O<sub>5</sub>, Cr<sub>2</sub>O<sub>3</sub>, and V<sub>2</sub>O<sub>5</sub>, to produce binary, ternary or quaternary solid solutions, all these elements having a *bcc* crystal structure.

Mixtures of these oxides, magnesium and a moderator (NaCl or MgO), for a total mass sample of up to 1.2 kg were ignited after a thorough mixing, using a newly developed water cooled SHS reactor. The resulting products, made of metallic alloys, magnesia and possibly salt were then lixiviated in a hydrochloric acid solution to dissolve salt and magnesia, then filtered. To insure the purity of the final product, this step has been repeated, and a third filtering finally performed after rinsing. The resulting powders are then dried, softly grinded, and then densified using spark plasma sintering.

Results concerning binary, ternary and quaternary alloys will be presented, with a description of the influence of the size of the sample on the purity, the microstructure and the crystal structure of the resulting products. Finally, a methodology for the optimisation of the composition of the alloys and resulting preliminary results will also be presented.

## NEW MATERIALS PREPARED BY ARRESTED REACTIVE MILLING AND MECHANISMS OF THEIR IGNITION AND COMBUSTION

**E. L. Dreizin<sup>\*a,b</sup>, M. Schoenitz<sup>a</sup>, K. L. Chintersingh<sup>a</sup>, M. Mursalat<sup>a</sup>,  
S. K. Valluri<sup>a</sup>, and D. Hastings<sup>a</sup>**

<sup>a</sup>New Jersey Institute of Technology, Newark, NJ, 07102 USA

<sup>b</sup>Tomsk State University, Tomsk, 634050 Russia

\*e-mail: dreizin@njit.edu

DOI: 10.24411/9999-0014A-2019-10033

Arrested reactive milling (ARM) uses high-energy ball milling to prepare nanocomposite powders of reactive materials [1]. Starting components capable of highly exothermic reactions are combined in each powder particle; the particle sizes are typically varied in the range of 1–100  $\mu\text{m}$ . Metal–metal, metal–metalloid, and metal–metal oxide composites were prepared previously and have demonstrated attractive ignition and combustion characteristics [2]. This talk will discuss several new materials prepared by ARM.

Previously, it was shown that mechanically alloyed Al·Ti powders burn faster than pure Al [3]; however, it was difficult to adjust the particle sizes of the milled powders to match those of a fine aluminum powder commonly used in energetic formulations. In this work, aluminum-rich Al·Ti composite powders with controllable particle size distributions were prepared by staged mechanical milling using liquid polar and nonpolar organic process control agents (PCAs). In the first milling stage, when a non-polar liquid, hexane, served as PCA, a composite powder was formed. The powder particle sizes were reduced in the second stage, using acetonitrile, a polar PCA. The prepared finely dispersed particles had lower onset temperatures for intermetallic formation reactions and lower ignition temperatures compared with the powder prepared in one stage using hexane as PCA. Combustion rates for all composites were greater than for reference aluminum, while net energy release remained comparable. The results suggest that staged milling with PCAs of different polarity is a viable method to control particle size distributions and ignition behavior in mechanically milled, metal-based reactive composite powders while maintaining the energy content. Particle size control is critical for adopting such materials in practical systems.

It was found recently that high energy milling can modify boron powders to improve their combustion characteristics. In particular, boron doped with iron was prepared and shown to have improved ignition kinetics and burn rates [4, 5]. Similar boron-based powders doped with other metals, including Co, Ni, Zr, and Hf, were prepared. Additionally, boron doped with iron prepared by ARM was compared to a similar compound, where iron coating was applied to boron powders using precipitation of iron pentacarbonyl,  $\text{Fe}(\text{CO})_5$ . For all prepared materials, thermo-analytical measurements were performed to quantify their oxidation behavior. Ignition temperatures were measured using a heated filament ignition experiment and particles were burned in air and in the products of a hydrocarbon flame. The results describing oxidation, ignition, and combustion of these materials will be presented and discussed. It is observed that iron is the most attractive dopant improving overall ignition and combustion characteristics of boron.

The most common application of ARM was to prepare thermite compositions, such as Al· $\text{MoO}_3$  [6–8], Al·CuO [9–11], etc. Recently, analogous reactive materials were prepared where instead of metal oxides, metal fluorides served as oxidizers for metals or metalloids [12, 13]. Both Al- and B-based composites with  $\text{CoF}_2$ ,  $\text{BiF}_3$ , and  $\text{NiF}_2$  as oxidizers were prepared, and their ignition and combustion behaviors were characterized. It was observed

that composites containing metal fluoride oxidizers were readily ignited thermally; however, unlike similar thermites, they were insensitive to initiation by electrostatic discharge. This could be due to a high ionic conductivity of the fluorides, reducing the heat release caused by the discharge's current. In combustion, metal fluoride containing reactive powders release substantial amounts of gas products, which is expected to be beneficial for propellants and explosives. The burn rates of the prepared aluminum and boron-based composites in air are enhanced compared to those of elemental aluminum and boron powders, respectively. In the flames with CO, CO<sub>2</sub>, and H<sub>2</sub>O as main oxidizing species, the burn rates of the metal-metal fluoride composites are comparable to those of elemental metals.

Finally, new spherical powders were prepared by ARM using thermites and other reactive material compositions when milling was performed in presence of two immiscible fluids serving as PCA. Similar spherical powders were prepared milling individual powders of elemental metals and metal oxides. Spherical powders with dimensions varied from tens to hundreds of  $\mu\text{m}$  were obtained with Al·CuO thermites as well as with pure Al, B, Ti, Al·B composites and with other materials. The spherical powder particles were filled to a relatively high density, although certain porosity remained. In experiments, it was observed that the sizes of formed spheres decreased at longer milling times. The filling density of the spherical powder particles increased respectively. Although the mechanism of formation of these spherical powders is not understood, it is hypothesized that such powders were formed from Pickering emulsions produced by the PCA components interacting with the suspended powder. Spherical powders formed only for specific milling conditions and after certain milling times. Enhanced flowability of spherical powders makes them easy to handle, mix with other components, and attractive for additive manufacturing.

For all prepared powders, a suite of experimental techniques illustrated in Fig. 1 is used to characterize their behavior. These techniques are supplemented by detailed thermo-analytical measurements and by characterizing particle sizes and shapes for the prepared powders.

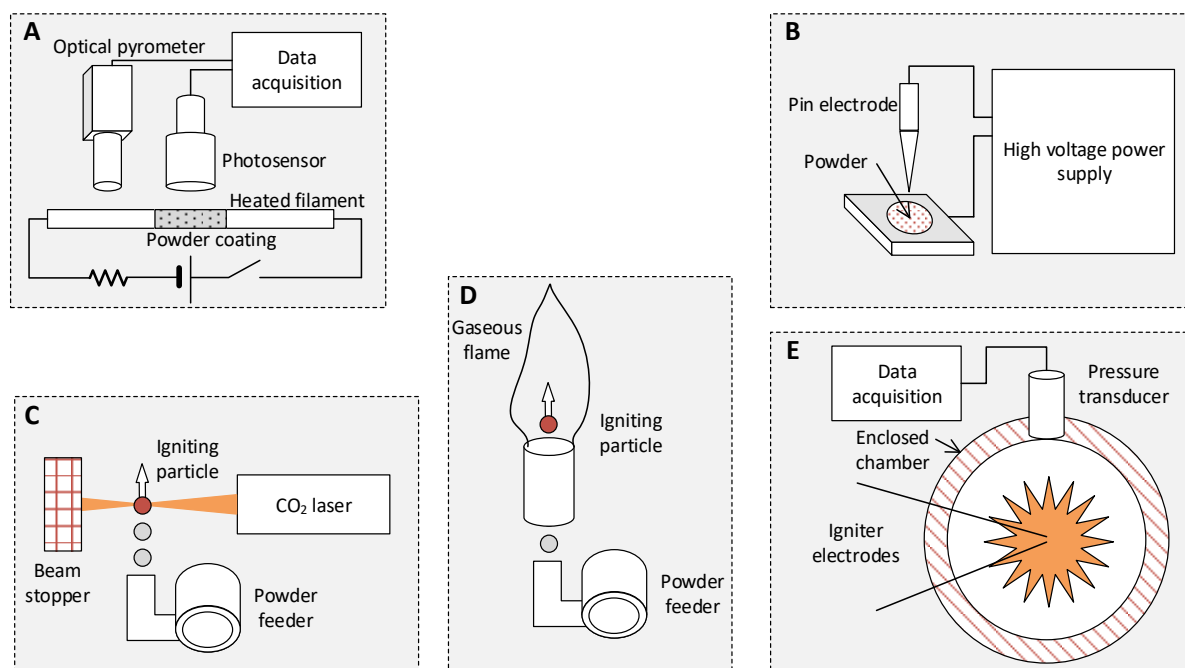


Fig. 1. Experimental techniques used to characterize ignition and combustion of powders prepared by ARM: A. Powder ignition using an electrically heated filament; B. Powder ignition by electrostatic discharge; C. Powder ignition by a CO<sub>2</sub> laser beam and combustion in air; D. Powder combustion in products of a gaseous flame; E. Constant volume explosion experiment.



1. E.L. Dreizin, M. Schoenitz, Nano-composite energetic powders prepared by arrested reactive milling, US Patent 7.524.355, 2009.
2. E.L. Dreizin, M. Schoenitz, Mechanochemically prepared reactive and energetic materials: a review, *J. Mater. Sci.*, 2017, vol. 52, pp. 11789–11809.
3. Y. Shoshin, E.L. Dreizin, Laminar lifted flame speed measurements for aerosols of metals and mechanical alloys, *AIAA Journal*, 2004, vol. 42, pp. 1416–1426.
4. K.L. Chintersingh, M. Schoenitz, E.L. Dreizin, Combustion of boron and boron–iron composite particles in different oxidizers, *Combust. Flame*, 2018, vol. 192, pp. 44–58.
5. K.L. Chintersingh, M. Schoenitz, E.L. Dreizin, Boron doped with iron: Preparation and combustion in air, *Combust. Flame*, 2019, pp. 286–295.
6. D. Stamatis, E.L. Dreizin, K. Higa, Thermal initiation of Al–MoO<sub>3</sub> nanocomposite materials prepared by different methods, *J. Propul. Power*, 2011, vol. 27, pp. 1079–1087.
7. S.M. Umbrajkar, S. Seshadri, M. Schoenitz, V.K. Hoffmann, E.L. Dreizin, Aluminum-rich Al–MoO<sub>3</sub> nanocomposite powders prepared by arrested reactive milling, *J. Propul. Power*, 2008, vol. 24, pp. 192–198.
8. R.A. Williams, M. Schoenitz, A. Ermoline, E.L. Dreizin, Low-temperature exothermic reactions in fully-dense Al/MoO<sub>3</sub> nanocomposite powders, *Thermochim. Acta*, 2014, vol. 594, pp. 1–10.
9. A. Ermoline, D. Stamatis, E.L. Dreizin, Low-temperature exothermic reactions in fully dense Al–CuO nanocomposite powders, *Thermochim. Acta*, 2012, vol. 527, pp. 52–58.
10. D. Stamatis, Z. Jiang, V.K. Hoffmann, M. Schoenitz, E.L. Dreizin, Fully dense, aluminum-rich Al–CuO nanocomposite powders for energetic formulations, *Combust. Sci. Technol.*, 2009, vol. 181, pp. 97–116.
11. S.M. Umbrajkar, M. Schoenitz, E.L. Dreizin, Exothermic reactions in Al–CuO nanocomposites, *Thermochim. Acta*, 2006, vol. 451, pp. 34–43.
12. S.K. Valluri, I. Monk, M. Schoenitz, E. Dreizin, Fuel-rich aluminum–metal fluoride thermites, *Int. J. Energ. Mater. Chem. Propul.*, 2017, vol. 16, pp. 81–101.
13. S.K. Valluri, M. Schoenitz, E.L. Dreizin, Boron–Metal fluoride reactive composites, MRS Fall Meeting, MRS, Boston, MA, 2017.

## EFFECT OF DOPING ON THE ALLOY CHEMISTRY OF NICKEL BASED SUPERALLOYS FROM COUPLING FIRST PRINCIPLES CALCULATIONS AND ADVANCED CHARACTERIZATIONS

**J. Du**

Department of Materials Science and Engineering, the University of North Texas,  
Denton, TX, 76203 USA  
e-mail: jincheng.du@unt.edu

DOI: 10.24411/9999-0014A-2019-10034

**Abstract.** Transition-metal dopants play a critical role in the high-temperature mechanical strength and corrosion resistance of nickel-based superalloys. In this talk, I will present an integrated computational and experimental study of the site occupancy behavior of common alloying elements such as chromium and cobalt in the  $\gamma'$ -Ni<sub>3</sub>Al phase by using *ab initio* density functional theory (DFT) calculations together with three-dimensional (3D) atom probe and high-resolution transmission electron microscopy characterization. The 3D atom probe data show a clear preference of chromium on the aluminum sublattice over the nickel sublattice in Rene88 super alloys. First-principles DFT total energy calculations were performed to understand the site occupancy of chromium in the L<sub>12</sub> structured  $\gamma'$ -Ni<sub>3</sub>Al. The obtained chromium site preference energies have been compared using the anti-site and vacancy based substitution formation mechanism, as well as using the standard defect formation formalism. It was found that chromium prefers aluminum site, consistent with the 3D atom probe result. In addition, interaction energies between two chromium atoms have also been determined from first-principles calculations. Chromium atoms were found to prefer close by on either nickel or aluminum sublattices or on a nickel–aluminum mixed lattice, suggesting a potential tendency of chromium segregation in the phase. The results show an integrated computational materials engineering (ICME) approach from combined computational and experimental effort can provide insights on the alloy chemistry and future design of nickel based super alloys.

Nickel based superalloys are used in jet engine and industrial gas turbines for the aerospace and power industries. Precipitation strengthened nickel-base superalloys consists of the gamma ( $\gamma$ ) matrix with the intermetallic  $\gamma'$  precipitates [1]. The  $\gamma$ -phase is a solid solution with a face-centered crystal lattice and randomly distributed different species of atoms. Ni<sub>3</sub>(Al,Ti), also called gamma prime ( $\gamma'$ ), acts as the primary strengthening phase with an ordered L<sub>12</sub> crystal structure. The  $\gamma'$ -Ni<sub>3</sub>Al compound has also a significant technological importance due to the positive temperature-dependence of its yield strength as well as its good high temperature oxidation resistance which makes Ni base superalloys ideal for high temperature applications.

Integrated computational materials engineering (ICME) is a new materials research approach that can expedite the development materials for various functional and structural applications by integrating advanced simulation and modeling methodologies and characterizations methods [2, 3]. In this talk, I will present our recent study of the dopant effect on the alloy chemistry of nickel based super alloys by using density functional theory (DFT) based first principles calculations and advanced characterizations using high resolution TEM and atom probe tomography.

The misfit between the matrix and  $\gamma'$  impacts the mechanical properties of the alloys, and specific elements are often added to modify the resulting strains and affect the physical properties at the atomic level. In fact, various studies using both experimental and computational methods have investigated to understand the partitioning of transition metal

elements (such as Cr, Co, W, Ta) between  $\gamma$  and  $\gamma'$ . Several researchers have concluded that Cr occupies the Al sublattice in  $\gamma'$ -Ni<sub>3</sub>Al by using atom-probe tomography (APT), scanning electron microscopy (SEM), atom location by channeling enhanced microanalysis (ALCHEMI) technique. Site preference of  $\gamma$  partitioning atoms like Co has been studied by atom probe field ion microscopy (APFIM) by several researchers. Site preference for different elements in Ni<sub>3</sub>Al has been calculated by a variety of computational techniques including *ab initio* based, first principles method, EAM potential based and cluster variation methods. In this work, we have combined experimental characterization and DFT based first principles calculations to understand the doping elements such as chromium and cobalt on the stability of the  $\gamma'$  phase and the overall alloy chemistry.

We have performed characterizations of nickel-based alloys by using high resolution TEM and atom probe tomography (APT) [3]. Carefully coupled TEM and APT experiments provide direct experimental evidence of site preference of the alloying elements. Figure 1a shows an EFTEM micrograph exhibiting a bimodal size distribution of  $\gamma'$  precipitates. As Cr is depleted in the  $\gamma'$  precipitates, it exhibits a darker contrast with respect to the surrounding matrix region. The precipitate-free depletion zones around the larger primary  $\gamma'$  precipitates are clearly visible. Figure 1a also shows a section of the APT reconstruction (where only Al atoms are shown) with the  $\gamma'$  regions exhibiting a higher Al concentration. Figure 1b–d shows 1D composition plots of different alloying elements present in the Rene88 alloy. The composition profiles for Ni and Al exhibit periodic modulations, as shown in Figure 1b where the peaks of Ni align with the troughs of Al and vice versa, proving the presence of alternating Ni and 50% Ni–50% Al sublattices sites along the  $\langle 001 \rangle$  direction of  $\gamma'$ . Similar composition profiles for Al and Ti have been plotted in Fig. 1c.

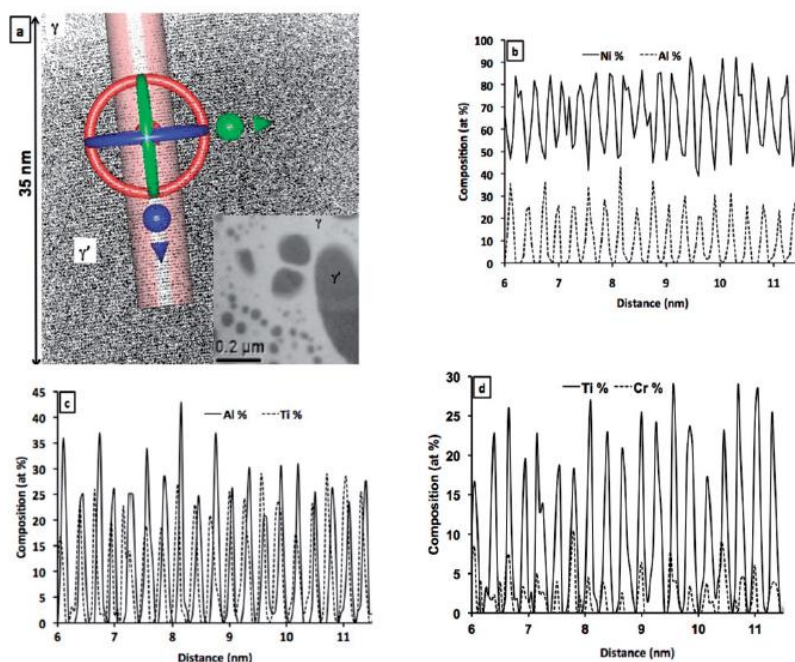


Fig. 1. Results from local electrode atom probe (LEAP) tomography and transmission electron microscope: (a) data region for the LEAP data collection, inset shows an energy-filtered TEM image of  $\gamma$  (lighter) and  $\gamma'$  (darker) phases; (b) plot of Ni and Al at % compositions from LEAP; (c) plot of Al and Ti at % compositions from APT; and (d) plot of Ti and Cr at % compositions from APT [3].

At the same time, plane wave based DFT calculations were performed to obtain total energies of the perfect and defect included  $\gamma'$ -Ni<sub>3</sub>Al super cells [4–6]. Different defect formation mechanisms can be used to determine the site preference

energies based the results from DFT calculations. Table 1 shows defect formation energies of Cr substitution on the Al and Ni sub-lattices by using different formalisms. It can be seen that the vacancy and antisite based mechanism both predict that Cr preference of the Al sublattice, while the standard defect formation energy calculations predict positive formation energies. It was also shown that the super cell size used in the calculations has an effect on the energies. Figure 2a shows the pair distribution function in substituted  $\gamma'$ -Ni<sub>3</sub>Al where a Cr atom substitutes an Al atom. After the substitution, the surrounding Ni atom move toward the substitution site that led to a decrease of Cr–Ni bond distance. This due to the strong electronic interaction and charge transfer revealed by Fig. 2b charge density difference plot.

Table 1. Site preference energies (eV) calculated from the standard defect formalism, antisite, and vacancy mechanism with different supercell sizes [4].

|   | This study            |                       | Other studies         |                   |
|---|-----------------------|-----------------------|-----------------------|-------------------|
|   | $2 \times 2 \times 2$ | $3 \times 3 \times 3$ | Booth-Morrison et al. | Jiang and Gleeson |
| Standard defect formation formalism – Cr          |                       |                       |                       |                   |
| $E_{\text{Cr}}^{\text{Al}}$                       | 1.193                 | 1.363                 | 0.565                 | 1.33              |
| $E_{\text{Cr}}^{\text{Ni}}$                       | 0.946                 | 1.212                 | 0.648                 | 1.29              |
| Anti-site based formalism – Cr                    |                       |                       |                       |                   |
| $E_{\text{Cr}}^{\text{Ni} \rightarrow \text{Al}}$ | -0.810                | -0.917                | 0.695                 | -0.50             |
| Vacancy-based formalism – Cr                      |                       |                       |                       |                   |
| $E_{\text{Cr}}^{\text{Ni} \rightarrow \text{Al}}$ | -1.580                | -1.585                |                       |                   |

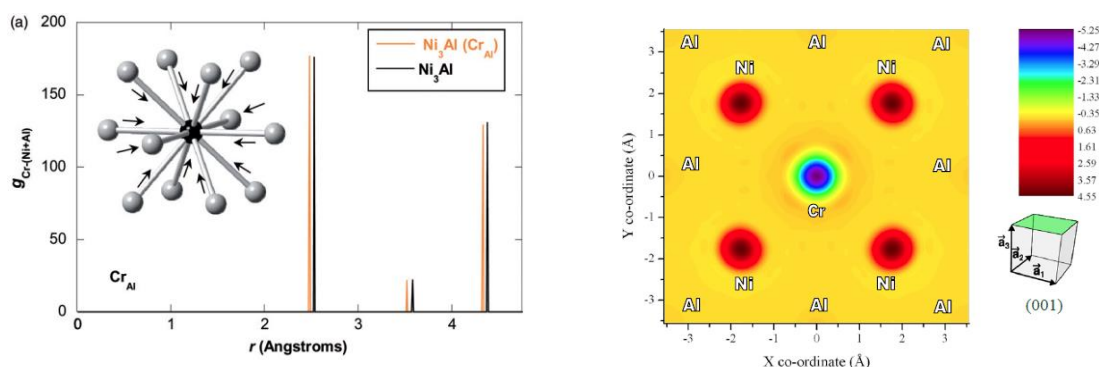


Fig. 2. (a) Comparison of radial distribution function of Cr substitution on Al site in  $\gamma'$ -Ni<sub>3</sub>Al and in perfect  $\gamma'$ -Ni<sub>3</sub>Al from plane wave DFT calculations. Inset: schematic figure showing the movement of atom positions after substitution. Center black ball: Cr, large grey ball: Ni [4]. (b) Difference charge density plot after Cr substitution an Al atom. The color scheme shows the level of charge transfer between different atoms.

In summary, we have investigated the site preference and interactions of doping transition metal elements in the ordered  $\gamma'$ -Ni<sub>3</sub>Al phase in nickel-based superalloys by combining 3D atom probe, TEM, and first-principles DFT calculations. It is found that the chromium atoms have a strong preference for the aluminum sublattice as evidenced from atom probe data and as confirmed using first-principles DFT calculations based on both the vacancy and anti-site-mediated substitution mechanisms. The interactions between chromium atoms have also been studied using DFT calculations. The results show that chromium atoms favor being close to each other, either in the nickel, aluminum, or mixed sublattices, suggesting potential local segregation of chromium in the ordered  $\gamma'$ -Ni<sub>3</sub>Al phase.

1. M.J. Donachie, S.J. Donachie, *Superalloys: A Technical Guide*, 2nd ed., ASM International, Materials Park, OH, 2002.
2. J.H. Panchal, R.K. Surya, D.L. McDowell, Key computational modeling issues in integrated

- computational materials engineering, *Comp. Aided Des.*, 2013, vol. 45, no. 1, pp. 4–25.
3. J. Du, J. Rimsza, Atomistic computer simulations of water interactions and dissolution of inorganic glasses, *npj Mater. Degrad.*, 2017, vol. 16, pp. 1–12.
  4. M. Chaudhari, A. Singh, P. Gopal, S. Nag, G.B. Viswanathan, J. Tiley, R. Banerjee, J. Du, Site occupancy of chromium in the  $\gamma'$ -Ni<sub>3</sub>Al phase of nickel-based superalloys: a combined 3D atom probe and first-principles study, *Philos. Mag. Lett.*, 2012, vol. 92, pp. 495–506.
  5. M. Chaudhari, J. Tiley, R. Banerjee, J. Du, Site preference and interaction energies of Co and Cr in gamma prime Ni<sub>3</sub>Al: a first-principles study, *Modell. Simul. Mater. Sci. Eng.*, 2013, vol. 21, 055006.
  6. M. Chaudhari, J. Du, J. Tiley, R. Banerjee, Density functional theory based calculations of site occupancy in the gamma prime Ni<sub>3</sub>Al phase of nickel based super alloys, Proceeding of 1st World Congress on Integrated Computational Materials Engineering (ICME), 2011, pp. 151–158.

## Fe, Ti, AND Ni ALUMINIDS FOR MODIFICATION OF POWDER ANTI-FRICTION MATERIALS

L. N. Dyachkova<sup>\*a</sup>, A. Ph. Ilyushenko<sup>a</sup>, L. Ya. Voronetskaya<sup>a</sup>, and N. M. Parnitsky<sup>a</sup><sup>a</sup>O.V. Roman Powder Metallurgy Institute, Minsk, 220005, Republic of Belarus

\*e-mail: dyachkova@tut.by

DOI: 10.24411/9999-0014A-2019-10035

At the present time, powder anti-friction materials based on iron and copper have found the widest application for parts of friction units, since the technology of powder metallurgy makes it possible to most fully realize the basic conditions for creating wear-resistant materials with a pronounced heterogeneous structure due to the introduction of various kinds of additives, both interacting and not interacting with the base metal. Due to the great possibilities in varying the chemical and phase composition, powder materials have a wide range of tribotechnical properties and can be used for light, medium and heavy loaded working conditions.

Iron graphite materials are most known among iron-based anti-friction materials, in which graphite is partially dissolved in iron, while strengthening it, and the remaining part plays the role of solid lubricant [1].

Numerous additives in different concentrations and different dispersion are introduced into powder materials to increase the mechanical and tribotechnical properties. Improving tribotechnical properties of powder materials based on iron is achieved by the introduction of solid lubricants (sulfides, selenides, tin, lead), solid inclusions in the form of oxides, borides, carbides, intermetallides [2–5].

The properties of powder materials, including anti-friction materials, are determined by the phase composition and morphology of the structure, which are formed during sintering and depend on the composition of the base and introduced additives. In this regard, the effect of the introduction of additives of ultrafine intermetallide powders of different phase composition produced by the method of mechanically activated self-propagating high-temperature synthesis (MASHS) [6] on the structure and properties of powder materials based on iron and copper was investigated.

Powders of aluminides of nickel, titanium, and iron of the following chemical and phase composition were used as additives in the anti-friction material based on iron: Ni–14 wt % Al (Ni<sub>3</sub>Al); Ni–50 wt % Al (Ni<sub>5</sub>Al<sub>3</sub>–NiAl); Ti–21.5 wt % Al (Ti<sub>3</sub>Al); Ti–57.5 wt % Al (TiAl<sub>2</sub>–TiAl<sub>3</sub>); Fe–17 wt % Al (Fe<sub>3</sub>Al); Fe–57 wt % Al (Fe<sub>2</sub>Al<sub>5</sub>, FeAl<sub>3</sub>).

Intermetallide powders were introduced in the amount of 0.2; 0.5; 1 wt % when mixed with iron powders and 0.6% graphite. Samples for the research were pressed at a pressure of 500 MPa to a relative density of 83–85% and were sintered in a protective-reducing atmosphere of endogas for 1 h at a temperature of 1100°C.

Three-point bending tests were performed on a Tinius Olsen testing machine (England) at a loading rate of 2 mm/min. The structure was studied on a MEF-3 metallographic microscope (Austria) and an electron scanning microscope “Mira” of Tescan Company (Czech Republic) with an X-ray microscope attachment “Oxford Instruments” (United Kingdom).

Studies have shown that the introduction of nickel-based intermetallides strengthens powder steel more effectively than titanium-based ones (Fig. 1). Strength improvement occurs only with the introduction of 0.2–0.5% and is 1.5–2 times compared with the strength of steel powder without an additive – 280 MPa. The increase in strength is explained not only by the modifying effect, but also by alloying the iron base with nickel formed during the decomposition of the intermetallide or in the elemental form in the intermetallide. This was confirmed by the X-ray

microanalysis. The nickel content gradually decreases from maximum in the center of the intermetallide particle to zero in the base. The absence of aluminum in the structure is probably due to a small amount of it.

The greatest strengthening occurs with the introduction of intermetallides having a lower melting point or polymorphic transformation –  $\text{Ni}_3\text{Al}$  and  $\text{TiAl}_2\text{–TiAl}_3$ . Hardness is higher for materials with the introduction of  $\text{TiAl}_3$  intermetallide, and unlike strength, the hardness increases with an increase in the amount of intermetallide additive up to 1 wt %.

The study of the structure showed that the degree of structure modification of powder steel depends on the composition of aluminide and its content (Fig. 2). With an increase in the amount of additive, its modifying effect occurs to a greater extent, regardless of the composition. This explains the increase in hardness of the material.

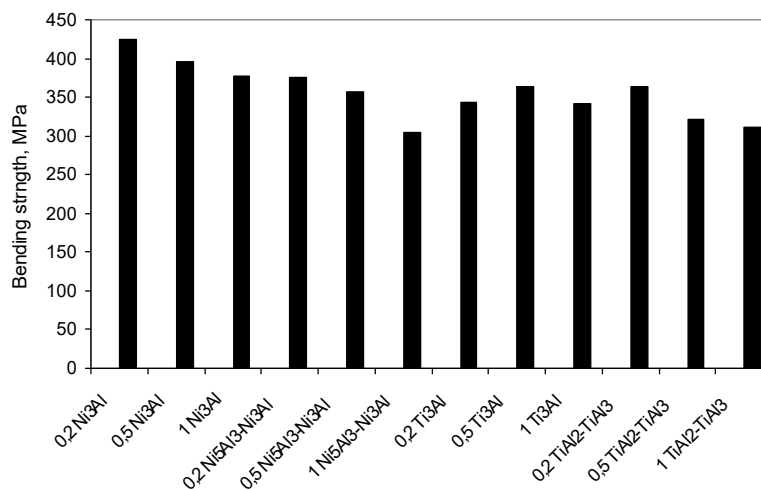


Fig. 1. The effect of the content of the aluminide additive on the strength of powder steel FeGr0.6.

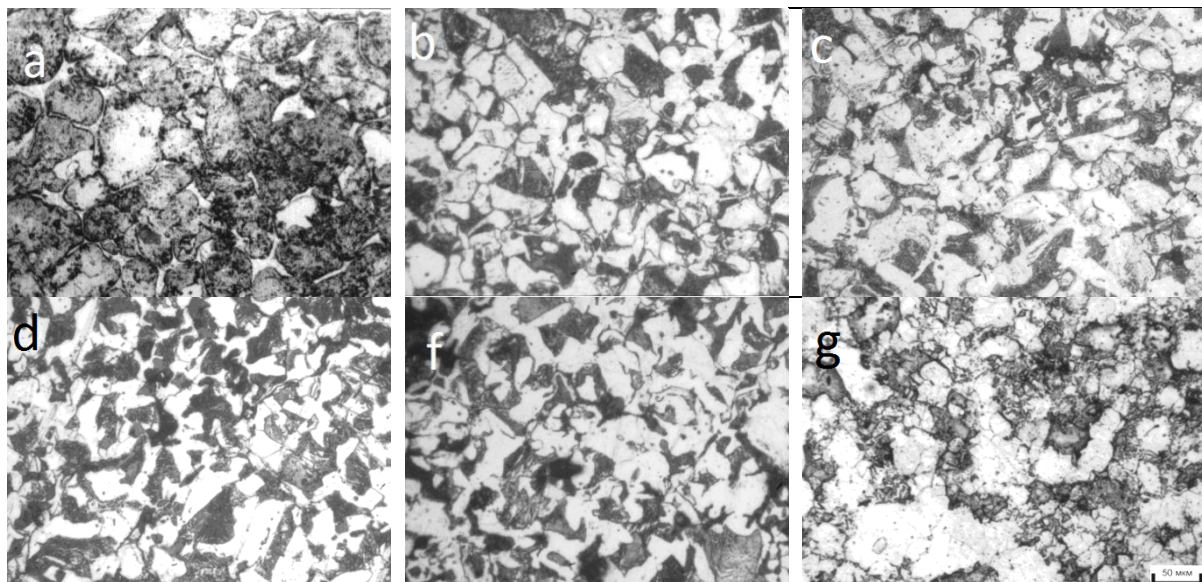


Fig. 2. The microstructure of powder steel PK50 with the introduction of 1% aluminide. (a) without additive; (b)  $\text{NiAl}_3$ ; (c)  $\text{Ni}_5\text{Al}_3\text{–Ni}_3\text{Al}$ ; (d)  $\text{Ti}_3\text{Al}$ ; (f)  $\text{TiAl}_2\text{–TiAl}_3$ ; (g)  $\text{Fe}_3\text{Al}$ .

The reduction in grain size, as a rule, has a positive effect on the strength of the material, but with the introduction of 1% aluminide, regardless of its composition, the strength of powder steel decreases. This is explained by the fact that with an increase in the content of the additive, particles of aluminides, which are located mainly along the grain boundaries of iron phase, lead

to their weakening. In addition, the decrease in strength is also due to the fact that aluminide powders have a high content of oxides. The presence of oxides leads to a decrease in the carbon content in steel, which is spent on their recovery. This occurs especially with the introduction of titanium aluminides, in which the oxygen content is higher than in nickel aluminides due to the higher sensitivity of titanium for oxygen.

X-ray microscopic analysis of steel powder with the additive of nickel aluminide of the  $\text{Ni}_5\text{Al}_3$ – $\text{Ni}_3\text{Al}$  phase composition revealed that, like in the single-phase  $\text{Ni}_3\text{Al}$  intermetallide, in this case there is a coherent bond of intermetallide with the base. In the border region with the intermetallide, the presence of nickel in the amount of 0.6–1.4% and aluminum in the amount of 2–5.5% is identified.

The complex intermetallide is heterogeneous in composition. It contains regions with increased (up to 70–75%) nickel content and increased (28–34%) aluminum content, and nickel and aluminum content gradually decreases in the border region with iron base.

The greater alloying of the base with the introduction of single-phase intermetallide compared to two-phase one explains the greater strength of the material. The diffusion of nickel from the intermetallide into the iron base leads to the fact that the nickel content in the central region of the intermetallide is much higher than in the border region.

Titanium aluminide  $\text{Ti}_3\text{Al}$  is also coherently bound to the iron base. The coherent bond of the intermetallide with the base is also confirmed by the fact that a transition layer is formed in the region of the intermetallide particle bordering the iron base. Its composition differs from that of the intermetallide. The titanium content in the center of the intermetallide particle is 11–17%, aluminum is 10–17%, the content of titanium and aluminum is 8 and 17% at the border with the base, respectively. Titanium content is 2–3%, aluminum is 5–6% in the base directly at the border with the inclusion of intermetallide. Further, titanium content is gradually reduced up to 0.3% and titanium is not identified after 20  $\mu\text{m}$ , aluminum is not identified after 10–15  $\mu\text{m}$ . This suggests that the diffusion of titanium into the iron base is much greater than aluminum.

Two phase titanium aluminide  $\text{TiAl}_2$ – $\text{TiAl}_3$  is heterogeneous in composition. Titanium content in the particle varies from 9 to 30%, aluminum changes from 8 to 21%. With the introduction of this aluminide, alloying of the iron base with titanium occurs to a lesser extent than with the introduction of the single-phase  $\text{Ti}_3\text{Al}$  intermetallide. This explains the lower strength and hardness of the material.

The dependence of the strength of powder steel on the amount of iron aluminide additive is presented in Fig. 3. Increasing the amount of the additive up to 0.5 wt % leads to an increase in strength of 20–30 MPa; up to 1 wt %, to a slight decrease in strength with the addition of single-phase iron aluminide, and 60–65 MPa – with the addition of two-phase one. It should be noted that the addition of iron aluminide provides higher strength of powder steel than nickel and titanium aluminides.

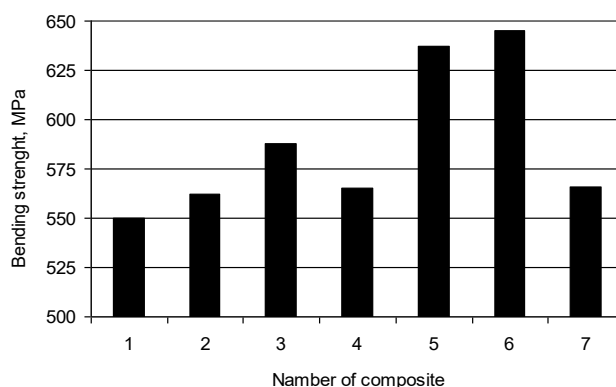


Fig. 3. The effect of the content of iron aluminide additive on the strength of powder steel PK50. 1 without additive; 2 0.2%  $\text{Fe}_3\text{Al}$ ; 3 0.5%  $\text{Fe}_3\text{Al}$ ; 4 1%  $\text{Fe}_3\text{Al}$ ; 5 0.2%  $\text{Fe}_2\text{Al}_5$ – $\text{FeAl}_3$ ; 6 0.5%  $\text{Fe}_2\text{Al}_5$ – $\text{FeAl}_3$ ; 7 1%  $\text{Fe}_2\text{Al}_5$ – $\text{FeAl}_3$ .



1. I.M. Fedorchenko, I.N. Frantsevich, I.D. Radomyselsky, et. al., Powder metallurgy, materials, technology, properties, fields of application, Kiev: Naukova Dumka, 1985, p. 624.
2. L.N. Dyachkova, I.N. Letsko, Study of the process of improving the mechanical and tribotechnical properties of iron-based powder materials by the introduction of ultrafine additives, *Vesti of NASB. Ser. Phys. Tech. Sci.*, 2007, no. 3, pp. 21–26.
3. P.A. Vityaz, V.I. Zhornik, et. al., Modification of materials and coatings with nano-sized diamond-containing additives, Minsk: Belarusian science, 2011, p. 527.
4. F.A. Sadykov, N.P. Barykin, I.R. Aslanyan, Wear of copper and its alloys with submicrocrystalline structure, *Wear*, 1999, vol. 225–229, pp. 649–655.
5. L.N. Dyachkova, I.N. Letsko, The effect of dispersed additives of chromium borides on the structure and properties of powder carbon steel, *Powder Metall. Minsk*, 2007, no. 30, pp. 67–70.
6. M.A. Korchagin, T.F. Grigorieva, B. B. Bokhonov, M. R. Sharafutdinov, A. P. Barinova, N. Z. Lyakhov, Solid-phase combustion mode in mechanically activated SHS systems. I. The effect of the duration of mechanical activation on the characteristics of the process and the composition of the combustion products, *FGV*, 2003, vol. 39, no. 1, pp. 51–59.

## STRUCTURE AND PROPERTIES OF BORON CARBIDE PRODUCED BY SHS AND MECHANOCHEMICAL SYNTHESIS: A COMPARATIVE STUDY

Zh. V. Eremeeva<sup>a</sup>, S. Vorotilo<sup>a</sup>, V. S. Panov<sup>a</sup>, L. V. Myakisheva<sup>a</sup>, A. I. Lizunov<sup>a</sup>, A. A. Nepapushev<sup>a</sup>, D. A. Sidorenko<sup>a</sup>, and D. Y. Mishunin<sup>a</sup>

<sup>a</sup>National University of Science and Technology MISiS, Moscow, 119049 Russia

DOI: 10.24411/9999-0014A-2019-10036

High requirements are looked for the absorbing components of modern nuclear reactors. These requirements determine different properties of regulatory bodies, such as: high efficiency of neutron absorption, low burning rate of absorbing isotopes during the exploitation of the reactor, high resistance to radiation damages, volume stability at normal-operating temperatures and overheat. The usage of the boron carbide in absorbing components is determined by the special physical properties of the <sup>10</sup>B isotope – the effective capture cross-section of thermal neutrons as well as high mechanical properties at high temperatures.

It has been established, that the application of nanostructured boron carbide ceramics allows one to receive improved physical-mechanical properties as compared with coarse-grained ceramics. In the case of materials which are used in the nuclear and space fields, the application of the boron carbide in the nanocrystalline state will reduce the negative effect of radiation on these materials i.e. reducing of radiation swelling and embrittlement.

The object of this research were boron carbide (B<sub>4</sub>C) powders produced received by the two methods: (a) mechanical synthesis (MCS) of a mixture of the soot PM-15 and grade A amorphous boron (splintered particles of 5–20 μm), and (b) self-propagating high-temperature synthesis (SHS) method (flaky particles of 7–28 μm).

Figure 1 shows microstructures of the boron carbide powder particles.

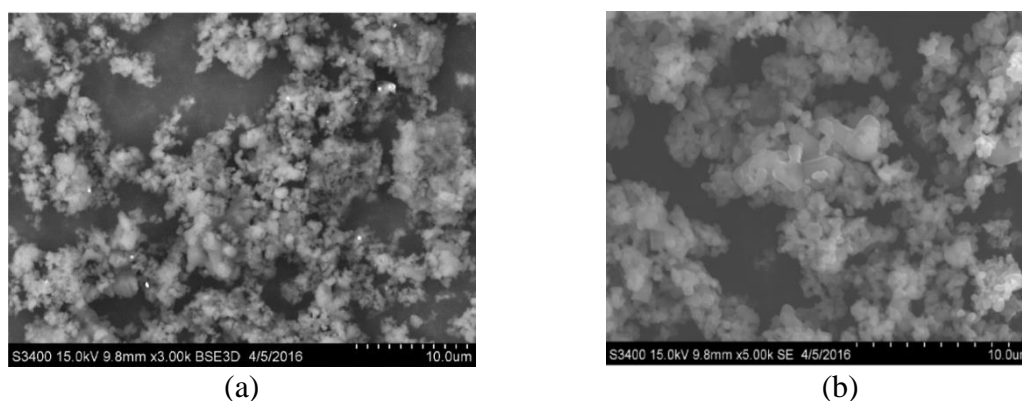


Fig. 1. SEM images of boron carbide powder prepared by (a) mechanosynthesis and (b) SHS.

Mechanochemical synthesis (MCS) was carried out in the planetary mill "Activator 2S" with planetary disk rotation speed 600 to 900 rpm and drum rotation speed 1000–1800 rpm. The "balls/charge" ratio is 30÷45:1, argon pressure in drums is 3–5 atm, treatment duration is 5 to 120 min.

Hot pressing was carried out using special hydraulic press DSP-515 SA (Dr. Fritsch Sondermaschinen GmbH, Germany) which is equipped with the temperature control system.

The determination of the specific area of initial powders and obtained boron carbide powders was carried out using the analyzer of the specific surface and porosity NOVA 1200e (USA) by the method of low-temperature nitrogen adsorption (BET-method). The universal laser device FRITSCH ANALYSETTE 22 MicroTec plus was used for determination of grain-size composition of boron carbide powder obtained by the SHS-method. The submicron particle analyzer Beckman COULTER No. 5 was used for determination of grain-size composition of amorphous nano-sized boron carbide powder obtained by mechanosynthesis according to GOST 19440-94.

X-ray analysis of compounds obtained was carried out using DRON-2.0 X-ray diffractometer (copper  $K\alpha$  irradiation, diffraction angle range  $10^\circ$  to  $130^\circ$ ). The Raman spectra were measured on a Horiba Jobin Yvon T64000 Raman spectrometer.

Analytical electron microscope JEM-2100 was used to obtain electron microscopic images and electron diffraction patterns. The content of impurities was determined by the atomic absorption and the emission spectral analysis.

Based on grain-size composition and SEM-data it was established that boron carbide powders synthesized by mechanical synthesis are nanoscale particles of unequal shape with diameters of 50–500 nm, combined into agglomerates.

Table 1 shows some properties of boron carbide powders.

Table 1. Properties of boron carbide powders.

| B <sub>4</sub> C | Flow rate, s | Bulk density, g/cm <sup>3</sup> | Specific area, m <sup>2</sup> /g | Average size of agglomerates, $\mu\text{m}$ | Particle size, nm |
|------------------|--------------|---------------------------------|----------------------------------|---|-------------------|
| mechanosynthesis | No           | 1.195                           | 16–24                            | 5–10  | 100–300           |
| SHS              | No           | 1.25                            | 18–32                            | 5–25  | 200–500           |

The compactibility of boron carbide powders obtained was investigated. It was established that the SHS B<sub>4</sub>C-powder and MCS-B<sub>4</sub>C-powder are densified quite well in the pressure range 200 to 900 MPa, and have density of 2.85 and 2.9 g/cm<sup>3</sup> at 600 MPa respectively, which is significantly higher than the one for standard boron carbide powder obtained by carbothermic method.

Hot pressing of these powders was carried out using the following regime: total duration 200 min, isothermal holding 60 min, the rate of temperature rises  $10^\circ\text{C}/\text{min}$ , the temperature of hot pressing 2000 to  $2150^\circ\text{C}$ .

Figure 2 shows the dependence of the sample relative density for boron carbide powders obtained by various methods on the hot pressing temperature.

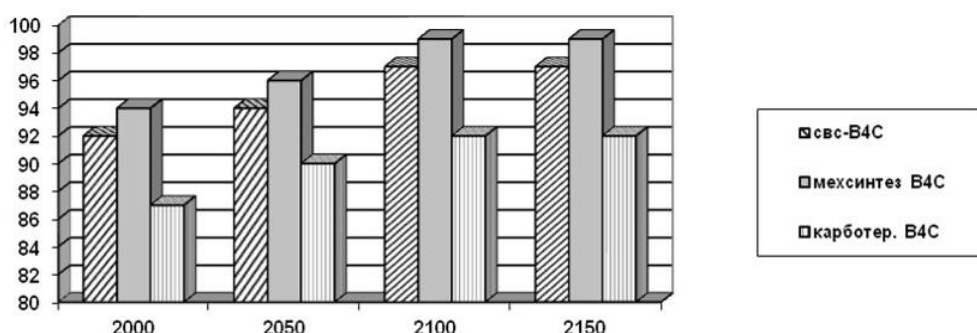


Fig. 2.

Figure 3 shows the structure of hot-pressed samples for boron carbide powders obtained by various methods.

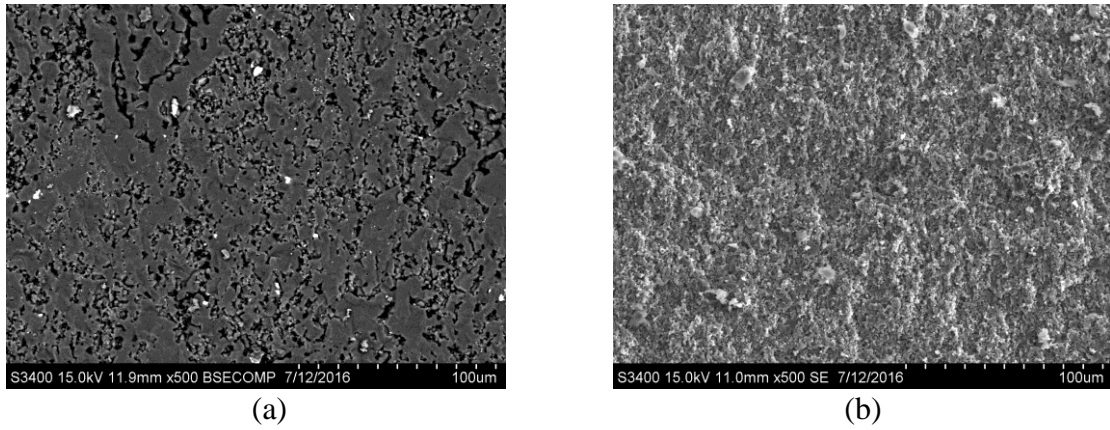


Fig. 3. SEM images of hot-pressed samples of boron carbide powders prepared by (a) SHS and (b) MCS.

The experiments carried out showed the possibility of the obtaining of nanosized boron carbide powders by mechanochemical synthesis of soot and amorphous boron and obtaining the theoretical density of boron carbide after hot pressing.

The work was supported by RFBR, project no. 17-08-00204.

## SELF-PROPAGATING HIGH-TEMPERATURE SYNTHESIS OF TITANIUM CARBIDE

**T. Ergul<sup>a</sup>, U. Cinarli<sup>a</sup>, M. Bugdayci<sup>\*b</sup>, and A. Turan<sup>b</sup>**

<sup>a</sup>Chemical and Process Engineering Department, Institute of Science, Yalova University,  
Yalova, 77200 Turkey

<sup>b</sup>Chemical and Process Engineering Department, Faculty of Engineering, Yalova University,  
Yalova, 77200 Turkey

\*e-mail: mehmet.bugdayci@yalova.edu.tr

DOI: 10.24411/9999-0014A-2019-10037

Titanium carbide synthesis was first performed by Moissan in an electric arc furnace. TiC, which is between the refractory carbides, has become a highly studied material over the last decades because of its perfect combination of high hardness, high melting temperature, good thermal and electrical conductivity. Titanium carbide has a B1 type face centered cubic (FCC) crystal structure. The cage parameter of TiC is 0.432 nm.

TiC shows wide composition range from TiC<sub>0.47</sub> to TiC with respect to the Ti/C ratio without changing the structure of FCC. However, its properties change according to Ti/C ratio. In the Ti–C binary phase diagram, hexagonal  $\alpha$ -Ti, at low temperatures, and FCC  $\beta$ -Ti at elevated temperatures can dissolve a limited amount of C. TiC has a melting temperature of 3067°C.

Titanium carbide is a ceramic powder which is one of the hardest natural carbides and, it is used in cermets and advanced ceramic tools. Titanium carbide is produced through carbothermic reduction, chemical vapor deposition, direct carburization, mechanical alloying, and self-propagating high temperature synthesis (SHS) methods. Between the methods in question, SHS results in the formation of high purity and nano-size products because of extremely short reaction times. In this process, TiC is produced with less external energy requirement.

In this study, TiC was produced by using SHS method from TiO<sub>2</sub>, Mg, and C raw materials with respect to Eq. 1. Raw materials were mixed at different stoichiometric ratios as 1.0x and 1.1x for C and from 0.9x to 1.2x for Mg. Powder mixtures were put in a copper crucible. Reactions were started by means of a metal wire which the electricity was passed through. Reactions lasted very fast as a result of the nature of metallothermic reactions. SHS experiments were carried out under air atmosphere.



Before the experimental studies, thermochemical simulation studies were carried out by means of HSC Chemistry 6.1 software. Some calculated thermodynamical data (for Eq. 1) can be seen in Table 1. For metallothermic reactions, specific heat is an important parameter showing the self-propagation of reactions. The specific heat value of the reaction (Eq. 1) was calculated as 3152.9 J/g and, it is greater than 2250 j/g. Therefore, it was enough for self-sustainable reaction conditions.

Table 1. Calculated thermodynamical data for Eq.1 (HSC Chemistry 6.1).

|                                      |          |
|--------------------------------------|----------|
| $\Delta H_{\text{rxn}}$ , kJ/mol     | –442.95  |
| $\Sigma_{\text{reactant}} M$ , g/mol | 140.49   |
| Specific heat, J/g                   | –3152.92 |

After SHS experiments, an HCl leaching step was conducted to purify TiC and to extract Mg-based impurities of the products out. Following leaching conditions were applied: solid weight of 10 g, solid/liquid ratio of 1/10 and duration of 60 minutes at room temperature. Liquid phase consisted of 23 mL distilled water and 77 mL 37% HCl. Filter cakes were dried at 105 °C for 150 minutes. Dried filter cakes were weighed and, mass loss values, after leaching, were recorded. Weight loss values (with respect to leached solid weights) were given in Fig. 1 for SHS experiments carried out under air atmosphere. As stated in the literature, TiC is not dissolved in HCl acid. Therefore, it was expected to solve all compounds without TiC in products through applied HCl leaching step. For the SHS products of experiments conducted with 1.1x C stoichiometry, filter cake weight were very similar in the experiments carried out with 1.1x and 1.2x Mg stoichiometric ratios. But for 1.0x C stoichiometric ratios, solid weight values decreased with increasing Mg stoichiometric ratios.

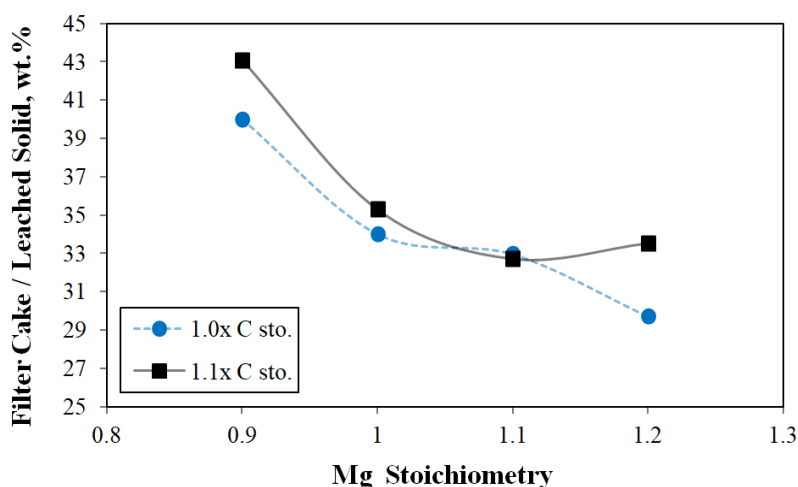


Fig. 1. Weight change of filter cakes after HCl leaching in the SHS experiments conducted under air atmosphere.

After SHS and following leaching experiments obtained powders were characterized by using XRD technique. Bruker D8 Advance X-ray diffractometer was used to examine phases formed in powders. These analyses were performed in XRD apparatus at 35 kV and 40 mA conditions,  $\text{CuK}\alpha$  radiation (1.54060 Å) in the range of 10°–90°. Figures 2 and 3 show XRD patterns of selected SHS products in the experiments carried out under air atmosphere. In both patterns, TiC phases were detected after leaching. It was predicted that amount of TiC phase will be enhanced in the experiments which will be carried out under Ar atmosphere to prevent further oxidation

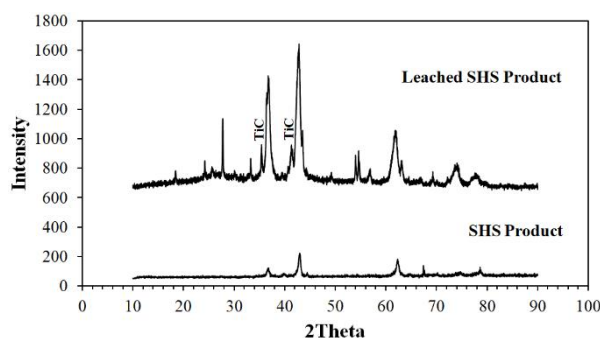


Fig. 2. XRD patterns of products in the experiment ( $\text{TiO}_2\text{:C:Mg}$ , 1.0-1.0-1.1) under air atmosphere before and after HCl leaching.

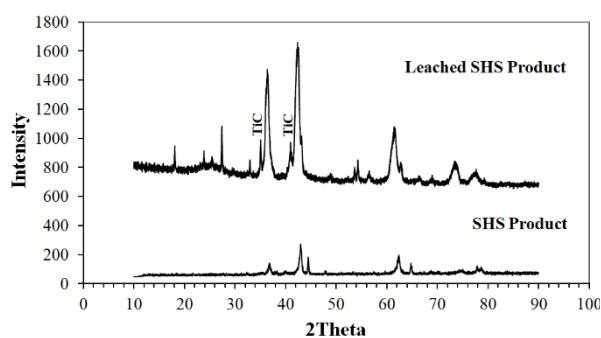


Fig. 3. XRD patterns of products in the experiment ( $\text{TiO}_2\text{:C:Mg}$ , 1.0-1.1-1.1) under air atmosphere before and after HCl leaching.

The present study is an on-going work. Following further studies were planned: SHS experiments under argon atmosphere, optimization of leaching conditions and investigation of effects of mechanical activation on synthesized powders.

1. P. Schwarzkopf, R. Kieffer, Refractory Hard Metals – Borides, Carbides, Nitrides and Silicides, Macmillan, New York, 1953.
2. F. Habashi, Handbook of extractive metallurgy, Wiley-VCH, 1997.
3. A. Turan, M. Bugdayci, O. Yucel, Self-propagating high temperature synthesis of TiB<sub>2</sub>, *High Temp. Mater. Processes*, 2015, vol. 34, no. 2, pp. 185–193.
4. O. Yucel, B. Derin, İ.Z. Kol, M. Alkan, Production of TiB<sub>2</sub> powder via magnesiothermic process, 2008, project no. 105M339. 99.
5. Q. Yuan, Y. Zheng, H. Yu, Mechanism of synthesizing nanocrystalline TiC in different milling atmospheres, *Int. J. Refract. Met. Hard Mater.*, 2009, vol. 27, no. 4, pp. 696–700.

## STRUCTURAL-PHASE TRANSFORMATIONS IN LOCALIZATION ZONES OF PLASTIC DEFORMATION OF Ti–Al COMPOSITE

T. V. Fadeev<sup>\*a</sup>, A. K. Abkaryan<sup>a</sup>, G. M. Zeer<sup>a</sup>, M. N. Volochaev<sup>a</sup>,  
I. V. Nemtsev<sup>a</sup>, and L. I. Kveglis<sup>a</sup>

<sup>a</sup>Siberian State University, Institute of Non-Ferrous Metals and Materials Science,  
Krasnoyarsk, 660025 Russia

\*e-mail: timur.fadeev.96@mail.ru

DOI: 10.24411/9999-0014A-2019-10038

The work is devoted to the study of physicochemical processes caused by the localization of plastic deformation, initiated by the dynamic load of the titanium-aluminum composite material. It is shown that a high concentration of tension during high-speed loading can cause the movement of plastic deformation waves and the solid-phase synthesis of Al<sub>3</sub>Ti intermetallic phases, when different types of structures can coexist within the same formula unit.

This study can contribute to the development of composite materials based on Ti–Al, which are used for the manufacture of gas turbine blades, hollow and ribbed welded structures for the aviation industry, etc. An important advantage of the materials used in aircraft, is their low density. It allows to obtain composites with a high level of specific strength. The Ti–Al system has been extensively studied. However, a number of unclear questions remain, namely: what intermetallic phases can form during plastic deformation; what are the conditions for the formation of Ti–Al intermetallic phases: Al<sub>5</sub>Ti<sub>2</sub>, Al<sub>11</sub>Ti<sub>5</sub>, Al<sub>2</sub>Ti, AlTi<sub>3</sub>, Al<sub>3</sub>Ti, among which various types of structures (stable, metastable, virtual) can be realized within one formula unit?

Samples were obtained using standard equipment at the Lavrent'ev Institute of Hydrodynamics, SB, RAS. To study the structure of transition zones between titanium and aluminum, scanning electron microscopes with microprobe TM-3000 and JEOL 7000LV were used. Phase analysis was performed on a Bruker X-ray diffractometer in copper radiation.

Figure 1 shows (a) image of a template cut from composite Ti–Al sample after punching by a bullet and (b) SEM image of the zone of shear line (area 3). The interpretation of the diffraction spectrum showed that the differences between the experimental values of the interplanar distances  $d$  from the tabulated distances are 0.75% for Ti and 0.37% for Al. The chemical composition was controlled using a JEOL7001F scanning electron microscope with microanalysis. Figure 3 shows the SEM image of the site where the solid-phase reaction took place. The results of microanalysis are shown in Table 1.

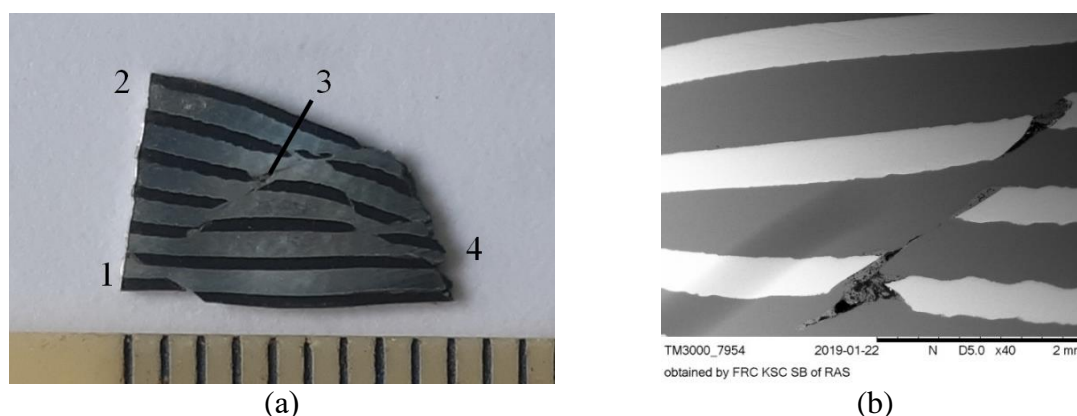


Fig. 1. (a) Image of template cut from composite Ti–Al sample after punching by bullet; (b) SEM image of the zone of shear line (area 3).



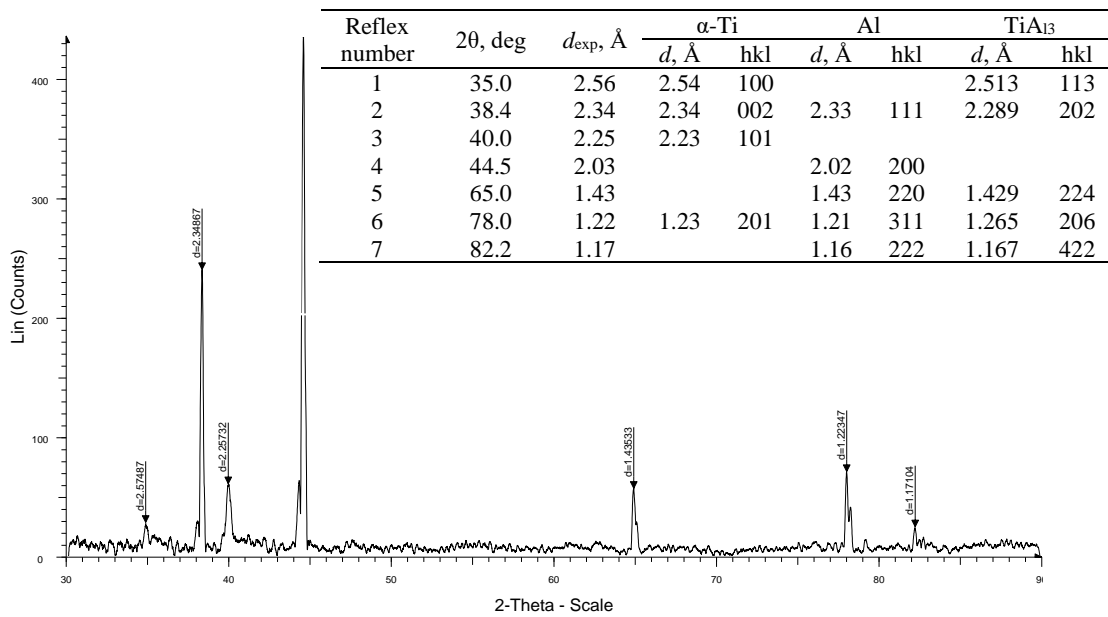


Fig. 2. X-ray diffraction pattern of the zone shown in Fig.1b.

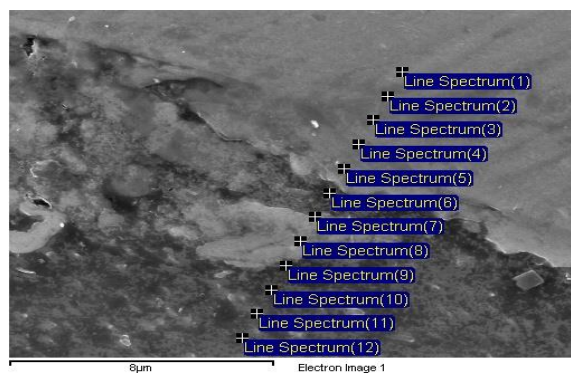


Fig. 3. SEM image of the site where the solid-phase reaction took place.

Table 1. Elemental composition (wt %) corresponding to Fig. 3.

| Spectrum | Al     | Ti    |
|----------|--------|-------|
| (1)      | 0.62   | 99.38 |
| (2)      | 0.77   | 99.23 |
| (3)      | 1.24   | 98.76 |
| (4)      | 14.89  | 85.11 |
| (5)      | 30.23  | 69.77 |
| (6)      | 76.67  | 23.33 |
| (7)      | 64.88  | 35.12 |
| (8)      | 52.87  | 47.13 |
| (9)      | 88.23  | 11.77 |
| (10)     | 98.63  | 1.37  |
| (11)     | 100.00 |       |
| (12)     | 100.00 |       |
| (13)     | 100.00 |       |

The elemental composition of the solid phase reaction zone indicates the absence of other elements besides titanium and aluminum. The mixing zone is about 10  $\mu\text{m}$ . According to the XRD pattern, Al<sub>3</sub>Ti intermetallic compounds with different crystal lattices are formed in the

mixing zone [1, 2] Such polymorphism is realized due to small atomic shifts in the bending zones of the crystal lattice [3].

In the zone of stress concentration during high-speed loading, high pressures develop. As a result, the strength properties of metals become insignificant. It is known [4] that upon welding waves with regular sinusoidal shape are formed on the contact surfaces, sometimes with vortex zones. We see such sinusoids in the zone of plastic shear in Fig. 1b.

For most solids, the shear modulus decreases beyond the limit of elasticity, and in rods of such materials, at sufficiently large deformations, not shock waves, but plastic waves arise.

According to [5], the relationship between the pressure difference  $P$  and the mass transfer rate  $V$  is the ratio obtained for plane elastic waves in the contact zone of various media:  $\Delta P = \rho Vc$ , where  $\rho$  is the density of material;  $V$  is the speed of interacting elements;  $c$  is the speed of sound in the medium.

For Ti, the speed of sound is 4140 m/s, the density is 4.500 kg/m<sup>3</sup>, and the speed of a bullet flying through it is 735 m/s.

The pressure developing in the rupture zone under the action of a bullet is 13.7 GPa. This is the minimum load that can develop in the areas of localization of plastic deformation of our composite sample. For plastic deformation waves, this value is quite acceptable. Thus, we observe solid-phase synthesis with the formation of the TiAl<sub>3</sub> phase in various structural modifications precisely in the zone of the shear band crossing the entire thickness of the sample. In addition to the product of a mechanochemical reaction, we see the excitation of plastic deformation waves in the stress concentration zone.

1. The structure and phase composition of the titanium–aluminum composite in the zone of plastic strain localization after high-speed dynamic loading are investigated.

2. Considerable crystal lattice distortions were found: shifts and bends, texture formation due to grain reorientation, as well as changes in Ti lattice parameters by 0.75%, for Al by 0.37%

3. The products of solid-phase synthesis with the formation of the phase TiAl<sub>3</sub> in various structural modifications were found precisely in the zone of the shear band crossing the entire thickness of the sample. The emergence of polymorphism due to the curvature of the crystal lattice

4. On the interface of dissimilar metals, plastic deformation waves were detected in stress concentration zones.

The authors thank V.I. Mali (Lavrent'ev Institute of Hydrodynamics, SB, RAS) for providing the samples.

1. G. Ghosh, M. Asta, First-principles calculation of structural energetics of Al–TM (TM = Ti, Zr, Hf) intermetallics, *Acta Mater.*, 2005, vol. 53.
2. Z.L. Wu, D.P. Pope, L1<sub>2</sub> Al<sub>3</sub>Ti-based alloys with Al<sub>2</sub>Ti precipitates—I. Structure and stability of the precipitates, *Acta Metall.*, 1994, vol. 42, pp. 509–518
3. V.E. Panin, The Fundamental role of the local curvature of a crystal structure in the nonlinear behavior of solids in fields of external effects, *Phys. Mesomech.*, 2013, vol. 16, no. 3, pp. 5–6.
4. M.A. Lavrentiev, B.V. Shabat, Problems of hydrodynamics and their mathematical models, Main editors of the physical and mathematical literature of the publishing house "Science", 1973.
5. G. Kolsky, Voltage waves in solids, M.: Foreign Literature, 1955.

## VIBROACOUSTIC MONITORING OF THE INTERMETALLIC PHASES FORMATION IN SURFACE ALLOYING USING ELECTRON-BEAM TECHNOLOGY

S. V. Fedorov<sup>\*a</sup>, M. P. Kozochkin<sup>a</sup>, Thein Htoo Maung<sup>a</sup>, and Min Htet Swe<sup>a</sup>

<sup>a</sup>Moscow State Technical University STANKIN, Moscow, 127994 Russia

\*e-mail: sv.fedorov@icloud.ru

DOI: 10.24411/9999-0014A-2019-10039

Among the many ways to modify the surface of machine parts and tools the most common methods of chemical and thermal treatment, involving in most cases, the diffusion saturation of alloying elements with the possibility of formation of reinforcing phases in the near-surface layer. The same methods include technologies of self-propagating high-temperature synthesis (SHS) based on the use of internal energy of the chemical interaction of the initial reagents [1].

This paper presents experiments on the hardening of the aluminum alloy (1.3% Cu, 0.26% Fe) surface by intermetallic phases of the NiAl system. The aluminum plate was coated with a thickness of about 0.2  $\mu\text{m}$  of heat-resistant nickel alloy NiCr20TiAl. The use of various fillers or diluents instead of pure nickel, even those involved in the synthesis as reaction by-products, is not a limitation for the creation of a SHS system.

Subsequently, the plate with a metal coating applied to it was exposed to a series of pulses of a wide-aperture low-energy high-current electron beam with a duration of about 5  $\mu\text{s}$ . Chemical reactions between the metal film and the aluminum base were initiated.

Processing was carried out in the installation RITM-SP, which is a combination of a source of low-energy high-current electron beams RITM and two magnetron sputtering systems on a single vacuum chamber [2]. The installation allows to obtain a beam of microsecond duration with a current density of up to 10.000 A/cm<sup>2</sup> at an accelerating voltage of 15–30 kV. The area of one-time processing is about 50 cm<sup>2</sup>. The operating pulses were given at the generator charging voltage values from 18 to 24 kV, which corresponded to the irradiation energy density from 4.2 to 6 J/cm<sup>2</sup>.

The formation of the structure in the near-surface layer of the material is largely due to the pulsed nature of the action in the microsecond range. Here, the main factors of the surface alloying process are the energy of the electron beam, which depends on the accelerating voltage and the thickness of the deposited thin film. The dependence of the modified layer thickness on the accelerating voltage has a pronounced extreme character. Irradiation with insufficient energy in the beam is not able to initiate the SHS process, and its excess leads to evaporation of most of the film.

However, the control of the surface electron-beam alloying process of significantly complicates the instability of the electron beam pulse parameters and the process of its interaction with the processed material, which leads to some random changes in quality indicators that occur spontaneously, regardless of the control system. In this situation, it is proposed to use the acoustic emission method to monitor the process.

The pulsed action of the electron beam on the sample causes a vibroacoustic wave associated with the effect of thermoelasticity in a thin surface layer heated to the evaporation temperature of the substance in the vacuum. The recoil impulse due to the evaporation of the material in the irradiation zone also contributes. The high vibroacoustic activity of the resulting process is shown experimentally.

To register the vibroacoustic signal generated during the technological process, the plate was connected to the accelerometer using a waveguide in the form of a copper wire with a cross section of  $2.5 \text{ mm}^2$ . The channel diagram is shown in Fig. 1. The use of a wire waveguide made it possible to have the recording equipment at a distance from sources of electromagnetic interference.

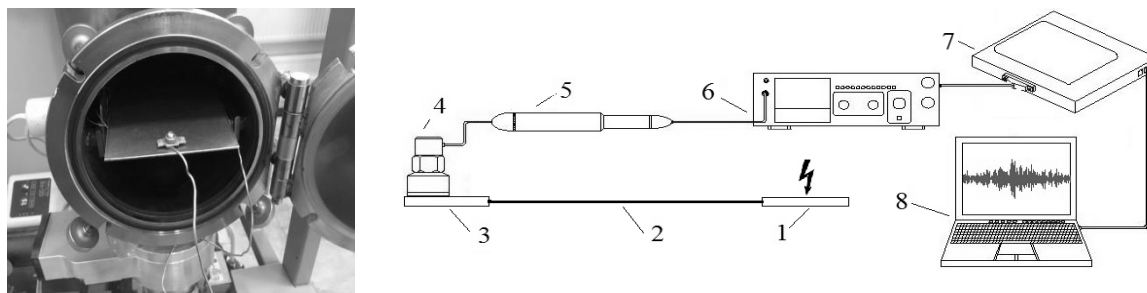


Fig. 1. Experimental setup: the sample placed in the RITM-SP unit for surface alloying and the scheme for vibroacoustic signals recording; 1 sample; 2 wire waveguide; 3 receiving plate; 4 KD-35 accelerometer; 5 PM-3 preamplifier; 6 VSV-003 amplifier; 7 E440 ADC; 8 registering computer.

The initial signal, passing through the elastic system, undergoes transformations in accordance with the amplitude-frequency characteristic of the observation channel. Experiments have shown that in this case, the components in the frequency range up to 40 kHz stand out against the background of noise. Low-frequency components up to 1 kHz, including all kinds of noise caused by the operation of the units of the RITM-SP unit, were also excluded from consideration. To obtain information about the processes occurring on the irradiated sample, the recorded vibroacoustic signal was subjected to time and frequency analysis. Effective (mean square) values of the amplitude of these signals filtered in different frequency ranges were taken as parameters of the vibroacoustic signal reflecting the kinetics of the processes on the workpiece surface.

The width of the analyzed frequency bands approximately corresponded to the width of the octave band. Due to the discreteness of the spectra obtained, the analysis in narrower frequency ranges could have a significant spread associated with energy fluctuations in the electron beam and some variability of the amplitude-frequency characteristic of the elastic system.

It is observed that the amplitude of the vibroacoustic signal for the case of a coated sample increases significantly, starting from the third-fourth pulse. Analysis of optical images confirmed that the formation of intermetallic phases on the surface of the aluminum plate under irradiation by the first pulse, as a rule, does not occur. The film is partly evaporated and partly mixed with the base and crystallizes in the form of long dendrite crystals (Fig. 2b). With further irradiation, in place of these crystals appear intermetallic phase inclusions up to several microns in size (Fig. 2c).

Figure 3 shows the recording of vibroacoustic signal and the effective values of its amplitude in octaves 32, 16, and 2–4 kHz, the irradiation of plates of pure aluminum (Figs. 3a, 3c) and coated (Figs. 3b, 3d). The main signal energy was released in the first 40 ms. In Fig. 4, the signal spectra for (a) low and (b) high frequencies are shown.

It is seen that in the presence of an alloying coating in the processes of changing the structure of the sample surface, short discrete pulses prevail, giving a contribution to energy at higher frequencies, which is in good agreement with [3, 4]. The growth of high-frequency energy in the spectrum of the vibroacoustic signal is accompanied by an increase in the content of the intermetallic phase.

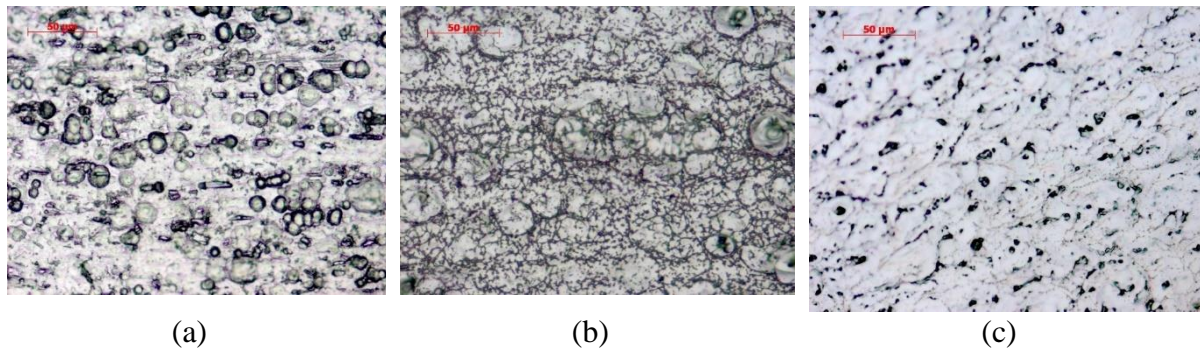


Fig. 2. The structure of the metal film of NiCr20TiAl alloy: (a) before the action of the electron beam; (b) after the action of the first pulse of the electron beam; (c) after irradiation with five pulses.

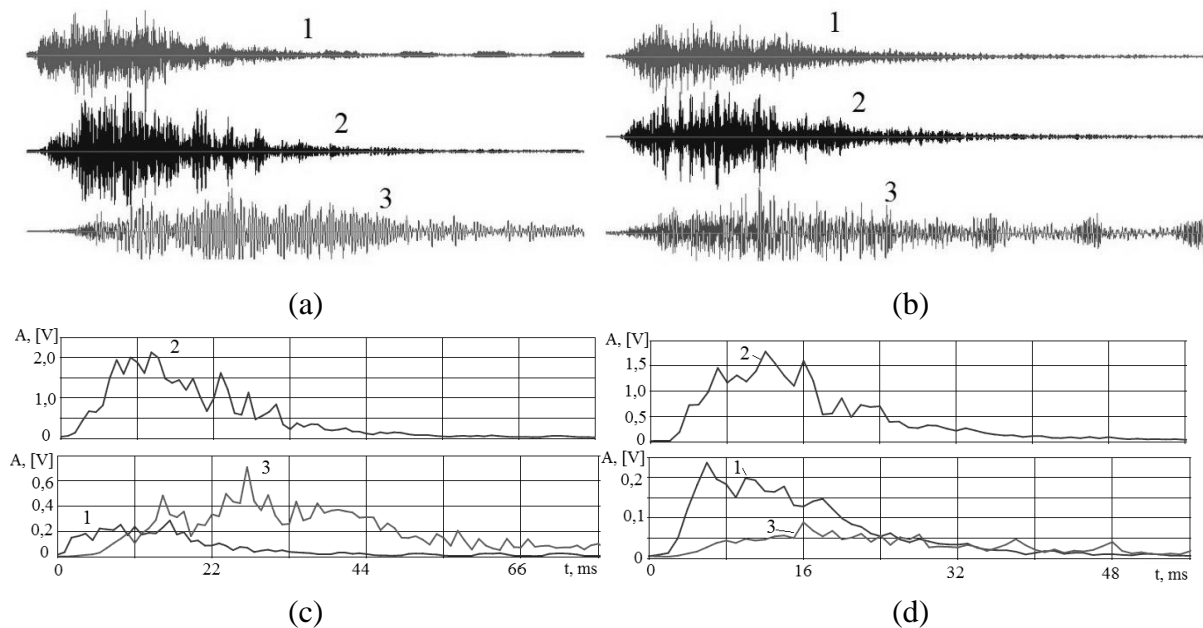


Fig. 3. Records of vibroacoustic signal and effective values of its amplitude in octaves 1 32, 2 16, and 3 2–4 kHz at irradiation of pure aluminum plates (a, c) and plates coated with NiCr20TiAl alloy (b, d) at the time of intermetallic phase formation.

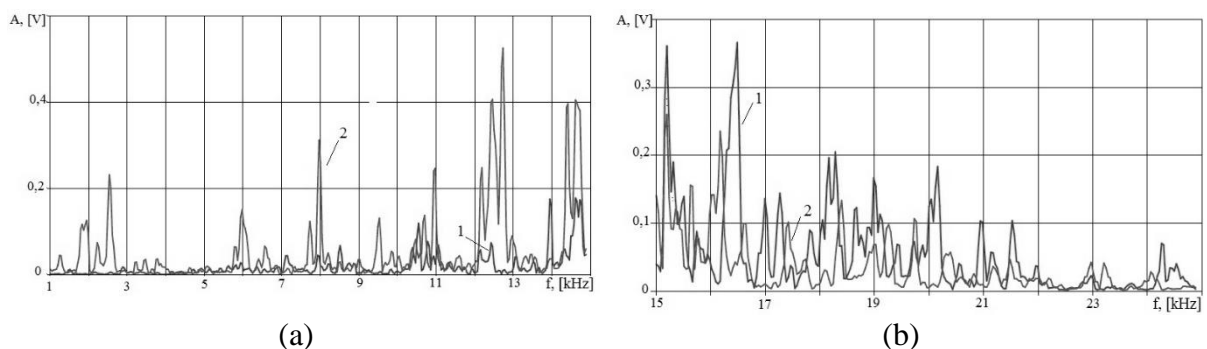


Fig. 4. The comparison of the amplitude spectra of the vibroacoustic signal during the pulse exposure in the range (a) 1–15 kHz and (b) 15–25 kHz for 1 coated plate and 2 uncoated inserts.

When irradiating an aluminum alloy without coating, there is a clear predominance of low-frequency energy. On records of effective values of signal amplitude in the range of 2–4 kHz (Figs. 3c, 3d) it can be seen that the irradiation of the plate without coating gives an amplitude

eight times greater. This suggests that the process of formation of the intermetallic phase takes place without the "rough" pulses that accompany the processes of melting and recrystallization in aluminum. Vibroacoustic signals accompanying the processes in materials subjected to electron beam effects have a complex varies spectrum. To effectively control the results of irradiation of various materials in an automated mode, a deterministic algorithm for processing vibroacoustic information is required, which allows to evaluate the quality of the results in real time. In this case, quite a limited set of diagnostic parameters, the digital values of which allow you to monitor the quality of the process and decide on its repetition or change of the initial parameters.

For example, the analysis of vibroacoustic signals during irradiation of coated plates and a clean plate in the coordinates  $E$  (coefficient of kurtosis) -  $Alf/Ahf$  (the ratio of amplitudes in the bands of low and high frequencies in the neighborhood of the maximum signal in an octave of 16 kHz) makes it possible to unambiguously judge the passage of the reaction of intermetallic compounds (Fig. 5). Due to the change in the nature of the vibroacoustic signal on the chart, clusters of points are formed that are distinguishable in these coordinates. The oval shows a cluster of pulsed electron-beam effects, where the successful passage of the synthesis was recorded.

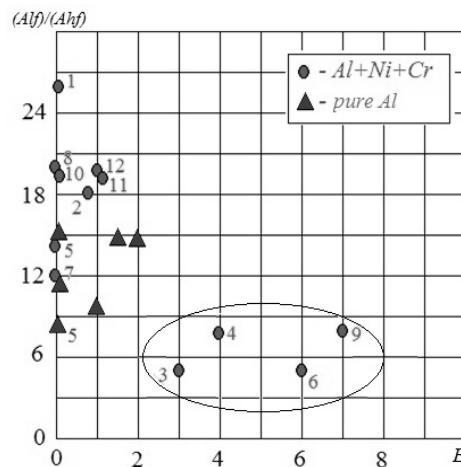


Fig. 5. Graphical representation of the results of the analysis of vibroacoustic signals in the coordinates  $E$  (coefficient of kurtosis)/ $Alf/Ahf$  (the ratio of the amplitudes in the low frequency band to the amplitudes in the high frequency band in the neighborhood of the maximum signal in octave 16 kHz); number near the point means a sequence of pulses with a charging voltage of 20 kV.

The financial support provided by the Ministry of Education and Science of the Russian Federation, in the framework of the state task in the field of scientific activity of MSTU "STANKIN" (no. 11.1817.2017/4.6).

1. A.S. Mukasyan, C.E. Shuck, Kinetics of SHS Reactions: A Review, *Int. J. Self-Propag. High-Temp. Synth.*, 2017, vol. 26, no. 3, pp. 145–165.
2. A.B. Markov, E.V. Yakovlev, V.I. Petrov, Formation of surface alloys with a low-energy high-current electron beam for improving high-voltage hold-off of copper electrodes *IEEE Tran. Plasma Sci.*, 2013, vol. 41, pp. 2177–2182.
3. R.M. Gabbasov, A.I. Kirdyashkin, V.G. Salamatov, Acoustic emission during combustion of Ni–Al composites, *IOP Conf. Series: J. Phys.*, 2018, vol. 1115, 042025.
4. P. Gulyaev, Temperature hysteresis in the unstable combustion mode of SHS: experiment with high-speed micro-pyrometry, *IOP Conf. Series: J. Phys.*, 2018, vol. 1115, 042025.

## TRENDS OF MATERIALS RESEARCH

**R. Fellenberg**VDI Technologiezentrum GmbH, Duesseldorf, 40468 Germany  
e-mail: fellenberg@vdi.de

DOI: 10.24411/9999-0014A-2019-10040

Materials play a key role in all industrial branches and are of high economic relevance. New materials help to increase the efficiency of solar cells and power plants, enable green cars and electric mobility or offer improved medical care by means of new diagnostic and therapeutical methods. Successful innovations in material science require cooperation of different disciplines and a high degree of networking between industrial and academic expertise. This is supported by a targeted funding of the Federal Ministry of Education and Research [1].

New materials and materials are enormously important for the innovative power of modern economies. Up to 70% of all new products are estimated to be based on new materials today. The market value of new and advanced materials will increase to \$ 230 billion by 2030, according to the European Commission. The resulting value creation potential for a variety of products exceeds the sum many times over. The importance of materials as a cost factor is also increasing in Germany: material costs now account for approx. 43% of the gross production value of all manufactured goods. It is therefore important to improve raw material and material efficiency as well as to develop efficient substitution materials and recycling processes in order to reduce material costs and dependence on critical raw materials. Material research is of immense importance for the expansion of the international competitiveness of our country.

Materials and materials are inconspicuous to many people. They often perform their importance unnoticed in many products. However, new materials are indispensable for solving concrete technological, ecological and social problems.

Some exemplary highlights illustrate the social significance of materials research [2]:

- Clean water through high-tech materials
- Materials for energy storage
- Hygiene through innovative materials
- Future houses - intelligent, comfortable, affordable
- Materials for 3D printing
- New materials from the virtual world

### Materials for 3D printing

Today's manufacturing processes have a high resource requirement. For example, in material-removing processes such as turning or milling, up to 90% of the starting materials are produced as production waste. In addition, during the manufacturing processes, these wastes are contaminated with secondary substances such as lubricants, which recycling is associated with high costs, especially in the case of expensive raw materials. With current methods only comparatively simple components can be produced cost-effectively, which are then joined together to form more complex structures. Due to this complex final assembly, these products often only become profitable in large quantities. Generative manufacturing processes or additive manufacturing such as 3D printing or laser sintering, build production parts directly from informal materials such as liquids or powders. In this way, the material efficiency is increased and waste by waste avoided. These resource-saving processes allow the production of components with variable material properties or the production of products made of different

materials. With generative processes, complex products with integrated functions can be produced cost-effectively even in small quantities. Especially with lightweight components and medical devices, the material potential can be used effectively [3].

#### New materials from the virtual world

The special properties of a material are determined by its atomic and molecular structures. With the help of combined simulation methods on the computer, new materials can already be designed at the atomic level. With so-called multi-scale simulations, components from the atomic to the macroscopic level can be fully developed, optimized and virtually tested. Here complex mathematical equations, the exact knowledge of atomic bonds as well as suitable material models help to network simulation experts and material developers interdisciplinary and to develop components completely on the computer. Particularly interesting are new materials with extreme properties, such as high strength, corrosion resistance or an exceptional temperature resistance, for example, to improve superalloys for energy technology or to develop hybrid materials for lightweight construction. The complete simulation of materials and their properties on the computer can shorten the laborious development work that has taken years in the lab to date, reduce development costs and help to find new materials [3].

#### Digitalization

Digitalization of the whole society is running or growing up in most industrial countries. This is also a big trend (or more) in materials science. A basis is a comparison of experimental and simulated data as well as to make the data pool for different materials and applications. A so called digital twin can be formed. But there are some uncertainties in using this data basis like

- Are there enough data for the description?
- What is the error of the used data (experimental, simulated) and the error of the achieved model? (backup of data)
- How is the availability and the exchange?
- Who is the owner of the data?

One example is the American Materials Genome Initiative [4] a government-based initiative which is running since 2011. The aim is to push the development of new materials to the production and application. Digitizing material data and make them available and searchable in big databases is the central point.

#### Surface technologies

Mostly material properties were determined by surfaces. Surfaces create mostly the resulting materials properties. That's why surface engineering is a key technology in industry. Today such processes are widespread in many industrial branches. For example, the economic significance is shown by the fact that the worldwide market for protective coatings (mostly corrosion resistant) for 2016 is estimated at around \$ 18 billion at an annual growth of 4 percent. In addition to classic surface technologies such as electroplating, physical and chemical vapor deposition as well as dipping, spraying and spraying processes play innovative process developments such as self-organization and self-healing processes, ultra short pulse lasers or atomic layer deposition as well as further developments of the modeling and simulation techniques an increasing role. A further growth is limited by costs and a qualification deficiency.

#### Biologization of technology [5]

Based on the key technologies, the "biologization of technology" aims to integrate biology and technology in order to make knowledge at the interface between the two areas usable for the sustainable strengthening of the competitiveness of German companies as well as for the benefit of the citizens.

Nature fascinates and inspires with a multitude of specialized individual and system biological solutions that have adapted to the surrounding environment in a biological evolution that has been going on for millions of years. In the course of their development, living organisms have succeeded in reducing their energy and resource requirements, developing



intelligent information processing and recycling strategies, and optimally coordinating metabolic reactions in a confined space. The basis for this capability of biological systems are highly parallelized and at the same time running precise synthesis and decomposition processes, self-learning and energy-efficient systems, specifically switchable mechanisms for e. g. regulation and information transport and a high degree of crosslinking independent modules in a fault-tolerant overall system. The development and understanding of these biological systems has been largely driven by technological advances in key technologies. Developments in materials research, photonics, production research, process development, and new approaches to nanotechnology, which include e. g. the introduction of high-resolution imaging techniques, miniaturized tools for cell manipulation or new technical solutions for filters and membranes have enabled / accelerated this. Based on innovation in key technologies, e. g. biological and biochemical findings and processes are commercialized in the context of industrial / white biotechnology while bionic approaches have broadened the spectrum of technical solutions.

Despite these important achievements, it remains to be noted that only a small fraction of nature's know-how is currently being used for technological purposes. A next logical step for new innovations, therefore, is the further transfer of fundamental processes and principles of biology to technology.

Possible research goals are:

- the use / adaptation of existing technical solutions to biological questions
- bio-inspired technical solutions
- a technology-bio-interaction through the use of biological materials, processes and principles for technical issues

1. <https://www.werkstofftechnologien.de/en/>.
2. [https://www.bmbf.de/pub/Vom\\_Material\\_zur\\_Innovation.pdf](https://www.bmbf.de/pub/Vom_Material_zur_Innovation.pdf).
3. <https://www.werkstofftechnologien.de/>.
4. <https://www.mgi.gov/>
5. <https://m.vdi.de/technik/fachthemen/technologies-of-life-sciences/artikel/innovationspotenziale-an-der-schnittstelle-biologie-und-technik-1/>.

## POROUS INTERMETALLICS PREPARED BY THERMAL EXPLOSION

P. Feng<sup>\*a</sup>, X. Cai<sup>a</sup>, X. Jiao<sup>a</sup>, Z. Li<sup>a</sup>, and C. Sang<sup>a</sup><sup>a</sup>School of Materials Science and Engineering, China University of Mining and Technology, Xuzhou, 221116 P. R. China

\*e-mail: pzfeng@cumt.edu.cn; fengroad@163.com

DOI: 10.24411/9999-0014A-2019-10041

**Abstract.** The intermetallic compounds based on the high aluminum activity have very attractive properties, such as low density, high melting temperature, high thermal conductivity, high elastic modulus, high specific strength, specific stiffness and good high-temperature oxidation resistance, which have been regard as a novel inorganic porous material and been playing an active role for the application in high temperature and corrosive environments. Tremendous efforts have been devoted for the researches on innovative processing technologies of porous intermetallic compounds in recent year, resulting in better control of the porous structures and substantial improvements of the properties. This paper intends to give a comprehensive review about the most recent progresses in preparation, microstructure and properties of porous Fe–Al, Ti–Al and Ni–Al intermetallic compounds, as well as their potential applications in application prospect. The preparation methods for porous intermetallic compounds mainly including chemical element reaction synthesis, pore forming additive, combustion synthesis, and impregnation method are discussed. In particular, the fast preparing highly porous intermetallic compounds with near-net-shape by thermal explosion reaction are exposed in detail, which is a simultaneous reaction that involves a whole model of the combustion synthesis. Finally, to facilitate further research and development, the present problems and the technical challenges are discussed, and several future research directions are also suggested in this review.

**Keywords:** intermetallic compound; Fe–Al; Ti–Al; Ni–Al; porous material; preparation

### 1. Fe–Al

The combustion images recorded from the powder compacts with the nominal composition of Fe–50 at % Al are illustrated in Fig. 1a. It can be seen from the various steps of the thermal explosion that the sample keeps the original cylindrical shape until the sample locally self-ignites and then a combustion front instantaneously propagates along the sample similar to a combustion wave.

The microstructure of sample sintered at 1000°C for 1 h is presented in Fig. 1b, the white irregular are the skeletons and the black regions represent pores. And the pores are connected with each other to form an interconnected channel, which has great potential in the application of multi medium filtration system due to the high filtering precision. In addition, the pores and particles characteristics of porous FeAl were observed obviously by the SEM (Fig. 1c), pores are distributed evenly on the fracture surface of the sample, further magnification can be seen that the particles are connected with each other to form a spatial skeleton. The open porosity of final product was measured to 61 vol %.

To investigate the effects of Al content and phase composition on the high-temperature oxidation behavior of Fe–Al intermetallic foams, the mass gain ( $\text{g cm}^{-2}$ ) was measured as a function of the oxidation time at 650°C and plotted in Fig. 1d. During the oxidation experiments, the mass gain of all samples shows a continuous increase with the exposure time. In the initial stage (I), the weight increases significantly, indicating a higher oxidation rate. In the subsequent stage (II), the oxidation rate decreases and the mass gains of the Fe–Al foams are found to

follow the parabolic oxidation rate law. As can be seen in Fig. 1d, the Fe–Al foam that underwent homogenization heat treatment (sintering at 1000°C for 1 h) exhibits a better oxidation resistance than the Fe–Al foam sintered at 700°C for 30 min. Moreover, higher Al contents were found to have a beneficial effect on the oxidation resistance of Fe–Al foams.

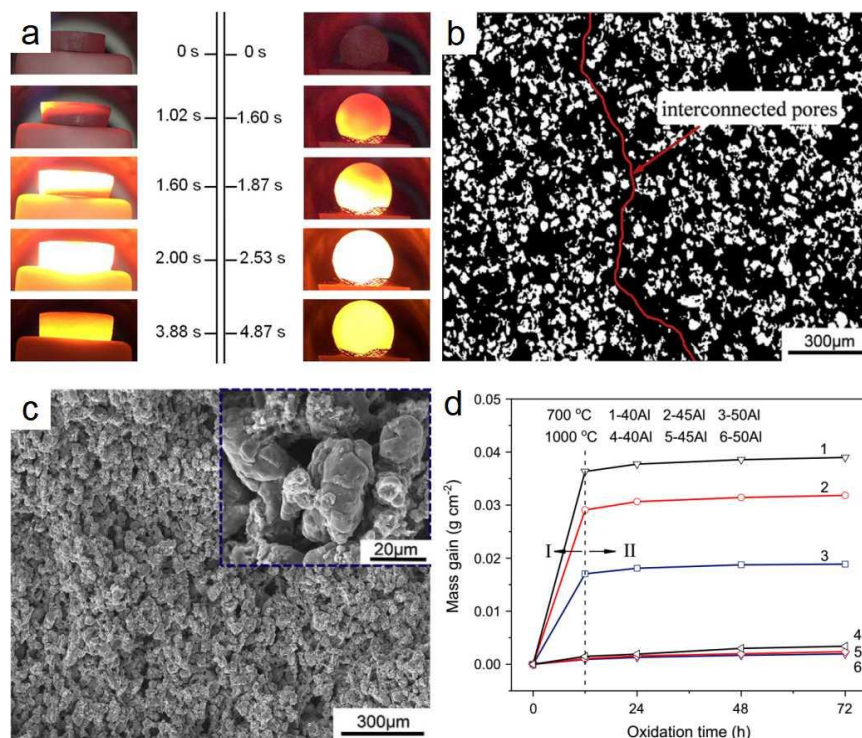


Fig. 1. Preparation, microstructure and properties of porous Fe–Al intermetallic compounds. (a) Combustion synthesis images of Fe–50Al powder compacts. (b) Optical micrograph and (c) SEM images. (d) Mass gain of Fe–Al foams oxidized at 650°C for 72 h in air [1–5].

## 2. Ti–Al

Highly porous TiAl<sub>3</sub> intermetallics with interconnected structures were successfully prepared by a novel processing of TE reaction with leachable NaCl space holder material.

Figures 2a–2f show SEM micrographs of sintered specimens with 0, 50, and 70 vol % NaCl, and lots of small pores (< 80 μm) were found among the sponge-like skeletons due to the violent TE reaction. Apart from that, large pores were evenly distributed on the skeletons and marked with red circles (Figs. 2c–2f), the pore size were about 250–550 μm, which apparently originates from the removed NaCl particles (200–500 μm). Meanwhile, it is obvious that the number of pores significantly increased with the increase in the NaCl content, from 0 to 70 vol % NaCl. Therefore, it is reasonable to conclude that the pore size and porosity can be tailored by adding NaCl particles. Figures 2g and 2h show the macrographs of green compacts after NaCl dissolution and sintered porous TiAl<sub>3</sub> by adding 0, 50, 60, 65, and 70 vol % NaCl. The green compacts kept the integrated body after leaching process, and pores can be found on the surface of specimens by naked eye (Fig. 2g). After sintering, there had been an obvious expansion phenomenon and the volume expansion ratios were measured to 48.8, 121.2, 99.8, 93.2, and 91.8%, corresponding to 0, 50, 60, 65, and 70 vol % NaCl, respectively. Whereas, the specimens after vacuum sintering maintained the original cylindrical shape, no deformation and cracking were observed (Fig. 2h), revealing that the vacuum atmosphere have a positive effect on the integrity of samples. In addition, the open porosity was measured to 56.3, 80.4, 84.8, 85.7, and 86.3%. It was apparent that porous TiAl<sub>3</sub> intermetallics with high open porosity (> 80%) were successfully obtained by adding NaCl above 50 vol %.

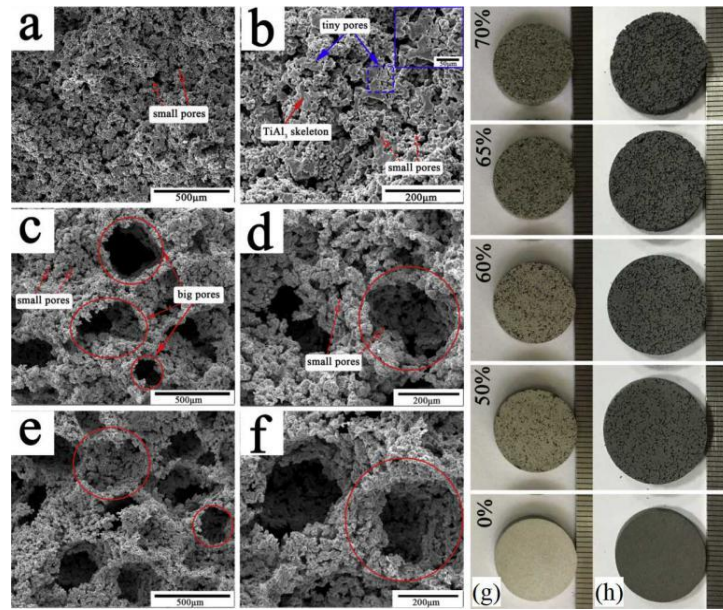


Fig. 2. SEM photographs of sintered specimens of (a, b) 0 vol % NaCl, (c, d) 50 vol % NaCl, and (e, f) 70 vol % NaCl with different magnification; (g) and (h) shows the macrographs of green compacts after NaCl dissolution and sintered  $\text{TiAl}_3$  discs [6–11].

### 3. Ni–Al

Figures 3a–3f show SEM micrographs of the sintered  $\text{Ni}_3\text{Al}$  (N3A),  $\text{NiAl}$  (NA), and  $\text{NiAl}_3$  (NA3) specimen cross-sections. The gray regions are the skeletons, and the black parts represent pores. For N3A (Figs. 3a, 3b), the pores varied in shape and size, oval-shaped pores (30–50  $\mu\text{m}$ ) and narrow pores (50–100  $\mu\text{m}$  in length, 20  $\mu\text{m}$  in wide) irregularly distributed in the specimens, while some spherical small pores (< 3  $\mu\text{m}$ , marked with blue arrows) existed in the skeletons of the porous monoliths (Fig. 3b). The pores in NA (Figs. 3c, 3d) were nearly circular, as marked on the figure with red circles. In addition, some small spherical pores (< 5  $\mu\text{m}$ ) shown by red arrows were precipitated from the skeletons. The pores in NA3 (Figs. 3e, 3f) are irregular and the pore size is around 10–50  $\mu\text{m}$ .

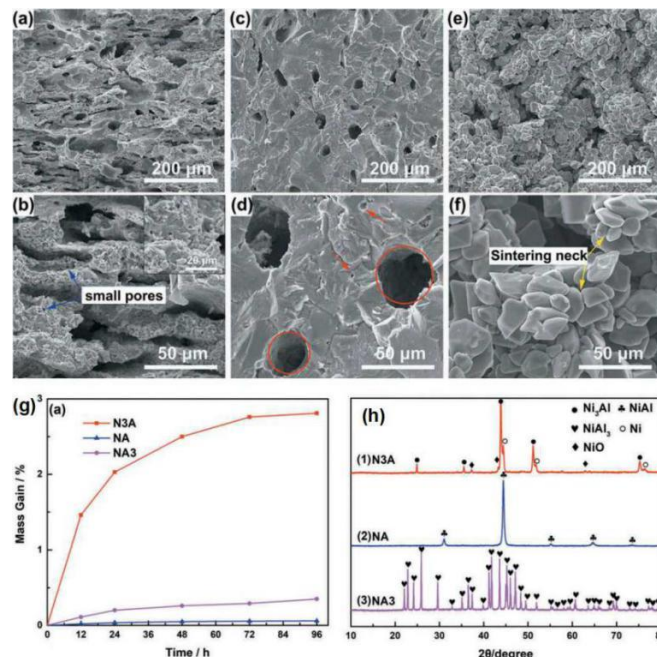


Fig. 3. SEM images of sintered specimens of (a, b) N3A, (c, d) NA, and (e, f) NA3 with different magnification; The oxidation behavior of  $\text{Ni}_3\text{Al}$ ,  $\text{NiAl}$ , and  $\text{NiAl}_3$ : (g) Mass gain, (h) XRD patterns after oxidation at 650°C for 96 h in air [12].

1. Y.N. Liu, X.P. Cai, Zhi Sun\*, H.Z. Zhang, F. Akhtar, T. Czujko, P.Z. Feng, Fabrication and characterization of highly porous FeAl-based intermetallics by thermal explosion reaction, *Adv. Eng. Mater.*, 2019.
2. X.P. Cai, Y.N. Liu, P.Z. Feng, X.Y. Jiao, L.Q. Zhang, J.Z. Wang, Fe–Al intermetallic foam with porosity above 60% prepared by thermal explosion, *J. Alloys Compd.*, 2018, vol. 732, pp. 443–447.
3. Y.N. Liu, X.P. Cai, Z. Sun, X.Y. Jiao, F. Akhtar, J.Z. Wang, P.Z. Feng, A novel fabrication strategy for highly porous FeAl/Al<sub>2</sub>O<sub>3</sub> composite by thermal explosion in vacuum, *Vacuum*, 2018, vol. 149, pp. 225–230.
4. X.P. Cai, Y.N. Liu, X.H. Wang, X.Y. Jiao, J.Z. Wang, F. Akhtar, P.Z. Feng, Oxidation resistance of highly porous FeAl foams prepared by thermal explosion, *Metall. Mater. Trans. A.*, 2018, vol. 49, no. 8, pp. 3683–3691.
5. Y.N. Liu, Z. Sun, X.P. Cai, X.Y. Jiao, P.Z. Feng\*, Fabrication of porous FeAl-based intermetallics via thermal explosion, *Trans. NonFerr Met. Soc. China*, 2018, vol. 28, pp. 1141–1148.
6. X.Y. Jiao, X.R. Ren, X.H. Wang, S.G. Wang, P.Z. Feng, J.Z. Wang, Porous TiAl<sub>3</sub> intermetallics with symmetrical graded pore-structure fabricated by leaching space holder and thermal explosion process, *Intermetallics*, 2018, vol. 95, pp. 144–149.
7. X.Y. Jiao, X.H. Wang, P.Z. Feng, Y.N. Liu, L.Q. Zhang, F. Akhtar, Microstructure evolution and pore formation mechanism of porous TiAl<sub>3</sub> intermetallics via reactive sintering, *Acta Metall Sin-Engl*, 2018, vol. 31, no. 4, pp. 440–448.
8. X.Y. Jiao, P.Z. Feng, Y.N. Liu, X.P. Cai, J.Z. Wang, T. Czujko, Fabrication of highly porous TiAl<sub>3</sub> intermetallics using titanium hydride as a reactant in thermal explosion reaction, *J. Mater. Res.*, 2018, vol. 33, no. 18, pp. 2680–2688.
9. X.Y. Jiao, X.H. Wang, X.Q. Kang, P.Z. Feng, L.Q. Zhang, F. Akhtar, Effect of heating rate on porous TiAl-based intermetallics synthesized by thermal explosion, *Mater. Manuf. Processes*, 2017, vol. 32, no. 5, pp. 489–494.
10. Z. Wang, X.Y. Jiao, P.Z. Feng, X.H. Wang, Z.S. Liu, F. Akhtar, Highly porous open cellular TiAl-based intermetallics fabricated by thermal explosion with space holder process, *Intermetallics*, 2016, vol. 68, pp. 95–100.
11. X.Y. Jiao, X.H. Wang, X.Q. Kang, P.Z. Feng, L.Q. Zhang, J.Z. Wang, F. Akhtar, Hierarchical porous TiAl<sub>3</sub> intermetallics synthesized by thermal explosion with a leachable space-holder material, *Mater. Lett.*, 2016, vol. 181, pp. 261–264.
12. Z.J. Li, Rapid preparation of porous Ni–Al intermetallics by thermal explosion, *Combust. Sci. Technol.*, 2019.

THE PROCESSES OF STRUCTURE FORMATION IN THE MECHANICALLY ACTIVATED POWDER MIXTURE Ti + Al SUBJECTED TO  $\gamma$ -IRRADIATION

V. Yu. Filimonov<sup>\*a</sup>, M. V. Loginova<sup>a</sup>, S. G. Ivanov<sup>a</sup>, A. A. Sitnikov<sup>a</sup>, V. I. Yakovlev<sup>a</sup>, A. V. Sobachkin<sup>a</sup>, A. Z. Negodyaev<sup>a</sup>, A. Yu. Myasnikov<sup>a</sup>, A. V. Gradoboev<sup>b</sup>, B. P. Tolochko<sup>c</sup>, and M. R. Sharafutdinov<sup>c</sup>

<sup>a</sup>Altai State Technical University, Barnaul, 656038 Russia

<sup>b</sup>Tomsk Polytechnic University, Tomsk, 634050 Russia

<sup>c</sup>Institute of Solid State Chemistry and Mechanochemistry, SB, RAS, Novosibirsk, 630128 Russia

\*e-mail: vyfilimonov@rambler.ru

DOI: 10.24411/9999-0014A-2019-10042

It is known that the high temperature synthesis in preliminary mechanically activated powder mixtures (MASHS) has several advantages over traditional high-temperature synthesis (SHS) [1]. These advantages include: the formation of almost ideal contact of reactants in the solid phase; cleaning of reagent surfaces from oxides and impurities; formation of non-equilibrium defects, amorphous phases and disordered structures during mechanical activation (MA). All these factors greatly facilitate the processes of solid-phase diffusion and make possible the realization of true solid-phase combustion. However, the processes of structure formation in solids have a number of differences from similar processes in liquids or gases which associated primarily with low diffusion rate. The hierarchy of structural inhomogeneities (which are determined by a different scale of heterogeneity in the volume of a mechanocomposite [2]) leads to the multistep chemical transformations and to formation of a multiphase synthesis product which is distributed unevenly in the sample volume. This is extremely undesirable from point of view of practical materials science.

It can be assumed that  $\gamma$ -irradiation can be used to implement the "soft" structure management of activated mixtures. Indeed, during gamma irradiation, the concomitant processes of radiation-stimulated diffusion could contribute to the processes of dissolution and homogenization, changes in the boundaries of homogeneity of the phases and solid solutions, creating the favorable conditions for interdiffusion at interphase boundaries [3]

In the present investigation, the experimental study of the effect of gamma radiation on the microstructure of activated Ti + Al powder mixture and on the dynamics of the phase formation processes for irradiated mixture was carried out. The high-temperature synthesis was realized in a thermal explosion mode. The study consisted of several stages: (1) Mechanical activation of powder mixture Ti + Al. Mechanical milling was performed in the AGO-2 planetary ball mill with two vials. The volume of the vial was 160 cm<sup>3</sup>, the ball diameter was 8 mm, the powder mass in each vial was 10 g, the mass of the balls was 200 g. The centrifugal acceleration of balls was 400 ms<sup>-2</sup> (40 g). In order to prevent oxidation, the vials were vacuum pumped and then filled with argon up to a pressure of 0.3 MPa. The milling time was 7 min. (2)  $\gamma$ -irradiation. The irradiation processes were conducted on a certified stationary setup "Researcher" (<sup>60</sup>Co isotope, RISD, Tomsk). The intensity of  $\gamma$ -irradiation doses was 98 Gy/s. The level of exposure to  $\gamma$ -quanta (with energy of 1.17 MeV) was determined by absorbed doses of D $\gamma$  [Gy], which were: 1·10<sup>3</sup> Gy (exposure time 22 min), 5·10<sup>3</sup> Gy (exposure time 1 h 51 min), 2·10<sup>4</sup> Gy (7 h 28 min), and 5·10<sup>4</sup> Gy (exposure time 18 h 41 min). (3) Microstructural and elemental analysis of irradiated samples. The microstructure of the initial mixture and synthesis products was studied on microsections using a Tescan MIRA scanning electron microscope equipped

with an EDS X-Act microanalyzer (Oxford Instruments) with a Si-drift detector. The device allows the analysis of elements ranging from boron to uranium. (4) The synthesis in the thermal explosion mode was carried out using microwave radiation according to the method described in [4]. To study the phase formation dynamics, we used radiation from the electron storage ring of VEPP-3 station 5b "Diffraction cinema" at the Institute of Nuclear Physics, SB, RAS (Novosibirsk). A continuous frame shooting of diffraction patterns was carried out using monochromatic radiation with a wavelength  $\lambda = 1.505 \text{ \AA}$ , in the range of scanning angles of  $36^\circ$ – $68^\circ$ . The frame rate was varied from 0.3 to 1 frame/s.

The microstructural analysis of the samples cross sections made it possible to establish that two types of heterogeneous microstructures are formed during MA. The first structure is characterized by large spheroid inclusions (tens of microns) of titanium particles in aluminum matrix. The second structure is characterized by a submicron scale of heterogeneity. It was established that the diffusion zone with dimensions of several micrometers is formed at the boundaries of the contact of large inclusions of titanium and aluminum matrix during the activation. The increase of the radiation dose up to the maximal leads to expansion of the diffusion zone by 3–4 times. Wherein, the small titanium inclusions disappear. This confirms the stated hypothesis of increasing the degree of homogenization under the influence of radiation.

Figure 1 shows the dependence of the components content on time for the unirradiated sample (a) and the sample irradiated at the maximal dose ( $5 \cdot 10^4 \text{ Gy}$ ) (b) during thermal explosion. As follows from the figure, the kinetics of the primary phase formation processes for the irradiated and unirradiated sample is different. Both in the irradiated and in the non-irradiated mixture, already in the process of preliminary heating (up to  $600^\circ\text{C}$ ), the significant amount of reaction products is formed. Along with the unreacted starting components, the compounds  $\text{TiAl}$ ,  $\text{TiAl}_3$  are present in the mixtures. Insignificant amount of  $\text{Ti}_3\text{Al}$  compound is present in the irradiated sample. In the process of rapid self-heating, the content of the  $\text{TiAl}$  compound increases in the unirradiated mixture while the titanium content decreases. The content of the  $\text{TiAl}_3$  phase varies slightly. In the irradiated mixture, the content of  $\text{Ti}_3\text{Al}$  compound almost does not change but it decomposes at the certain temperature. The rapid increase in the content of the  $\text{TiAl}$  phase is accompanied by a decrease in the content of the  $\text{TiAl}_3$  compound (in contrast to the unirradiated mixture).

Figure 2 shows the X-ray diffraction patterns of the quenched samples at various high temperature annealing times (the heat source did not turn off).

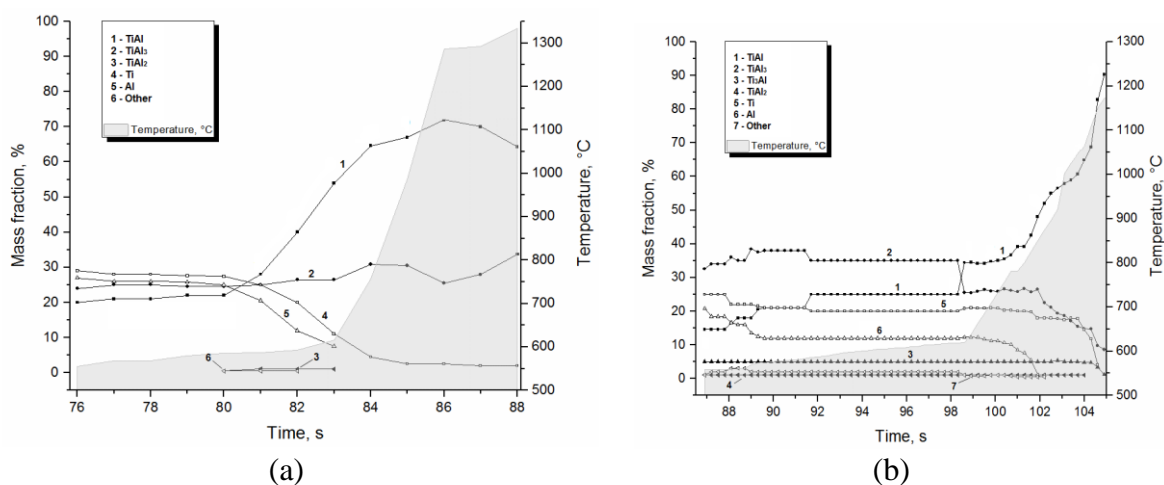


Fig. 1. Dynamics of phase formation during thermal explosion for (a) unirradiated and (b) irradiated ( $5 \cdot 10^4 \text{ Gy}$ ) mixtures.

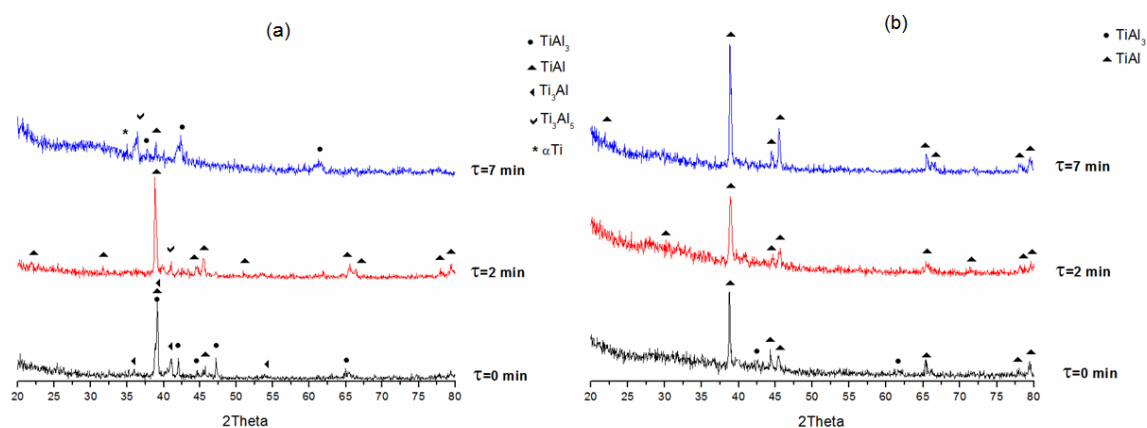


Fig. 2. XRD patterns of the quenched samples at various high temperature (1200°C) annealing times: (a) unirradiated sample; (b) irradiated sample.

In both irradiated and non-irradiated samples, the single-phase compound TiAl is formed after 2 min of annealing. However, in the unirradiated sample, the decomposition and recrystallization of the TiAl phase occurs up to 7 min of annealing. This process is accompanied by formation of  $\alpha$ -Ti and TiAl<sub>3</sub> compound. In the irradiated sample, the composition of the product does not change. Moreover, with an increase in the annealing time, the structure stabilizes that is determined by increase in the intensity of the diffraction peaks and decrease in their width.

Based on the above, it can be assumed that the irradiation of mechanically activated Ti + Al mixture contributes to the processes of solid-phase dissolution of the components and the homogenization of the system. As a result, the reaction paths in the irradiated and unirradiated mixture are different. The reaction product which synthesized in the irradiated mixture is more resistant to thermal effects.

1. A.S. Rogachev, A.S. Mukasyan. Combustion for material synthesis, CRS Press, Taylor & Francis Group, 2015.
2. K.V. Manukyan, B.A. Mason, L.J. Groven, Ya-Cheng Lin, M. Cherukara, S.F. Son, A. Strachan, A.S. Mukasyan, Tailored reactivity of Ni + Al nanocomposites: Microstructural Correlations, *J. Phys. Chem. C.*, 2012, vol. 116, pp. 21027–21038.
3. A.C. Damask, Studies in radiation effects on solids (vol. 2), Gordon and Breach, 1967.
4. V.Yu. Filimonov, A.A. Sitnikov, A.V. Afanas'ev, M.V. Loginova, V.I. Yakovlev, A.Z. Negodyaev, D.V. Schreifer, V.A. Solov'ev, Microwave assisted combustion synthesis in mechanically activated 3Ti + Al powder mixtures: Structure formation, *Int. J. Self-Propag. High-Temp. Synth.*, 2015, vol. 24, no. 4, pp. 210–214.



## CHARACTERISTICS OF THE CAPILLARY SPREADING OF COPPER ON THE POROUS FRAMEWORK OF THE PRODUCTS OF THE SHS MIXTURE OF Ni–Al

R. M. Gabbasov<sup>\*a</sup>, A. M. Shulpekova, and V. D. Kitler<sup>a</sup>

<sup>a</sup>Tomsk Scientific Center, SB, RAS, Tomsk, 634055 Russia.

\*e-mail: ramilus@yandex.ru

DOI: 10.24411/9999-0014A-2019-10043

The use of technological combustion for synthesis of high-temperature cermet materials is hampered by insufficient knowledge of the physicochemical processes in the high-temperature synthesis wave. The effect of capillary metal melt flows on non-isothermal spatial waves of chemical transformation in porous heterogeneous systems has been studied even less. A review of the existing literature shows that the description of heat and mass transfer in a porous medium remains fragmentary for a number of practically important applications [1]. The classical analysis of the kinetics of the impregnation of porous bodies with melts encounters considerable difficulties with intensive heating, changing the particle size of the porous medium and the course of a chemical reaction [2]. Melting the reagents and wetting the more refractory components of the mixture with the melt increases the heat release rate in the heterogeneous reaction and, accordingly, increases the temperature in the zone of chemical transformation. At the same time, the rate of thermocapillary flow and convective heat transfer increase. The mechanism for the implementation of thermocapillary convection - the Marangoni effect in a heterogeneous reaction medium has not been studied enough. The results of the study, on the one hand, are of great fundamental importance for the development of the theory of nonlinear wave processes in heterogeneous systems, and on the other, practical for the development of technologies for the synthesis of metal-ceramic and composite materials. In the above works it was assumed that the impregnation material and the carcass material do not interact with each other and can be considered as independent phases. However, as was shown by the authors on the example of the combustion of Ti–Si–C systems with nickel and copper, the impregnation material interacts with the framework material, which leads to a change in the phase composition of the material [3, 4]. In this paper, as an extreme case, the Ni–Al–Cu system was taken for the study, in which we initially assumed a strong chemical interaction between the components. Due to the proximity of the atomic radii of Ni and Cu in this binary system, a continuous series of solid solutions is formed. Therefore, we assumed that the process of formation of a porous skeleton and its impregnation can proceed simultaneously.

The aim of the work was to study the processes occurring during SHS of Ni–Al system while simultaneously interacting with copper wire, as well as the macro- and microstructure, phase composition of the samples.

For the study, Ni (PNC1-L7) and Al (ASD-4) powders were used. The powders were mixed in a ratio of 68.5 wt % Ni and 31.5 wt % Al (NiAl stoichiometry). The resulting mixture was held for 3 h in a vacuum furnace at a temperature of 200°C. The mixture was pressed into a cylinder with a diameter of 15 mm. The relative density of the samples, depending on the pressing force, was in the range of 0.4–0.6. In a series of experiments, a copper wire 1 mm in diameter was placed along the sample axis. The initiation of the reaction was performed using a tablet of a mixture of 70 wt % Ti with 30 wt % B, which was heated by an electric spiral. The experimental setup is shown in Fig. 1. To record thermograms, thermocouples of the brand WRe 5/20 were connected to an ADC and a personal computer. The speed of propagation of

the combustion wave front was determined using a high-speed Motion ProX-3 video camera. The phase composition of the synthesis products was determined on a portable tabletop X-ray device RIKOR ( $\text{CoK}_\alpha$  radiation) at the Tomsk common use center (SB, RAS). Microstructural studies were performed using an optical microscope (Axiovert 200M, Karl Zeiss). The copper concentration in the samples was determined using local X-ray microanalysis (EDAX).

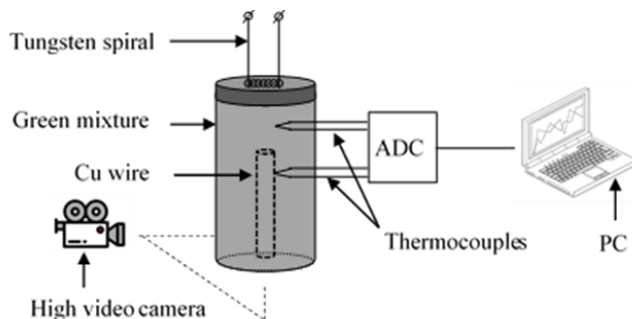


Fig. 1. Experimental setup.

The dependence of relative density on the pressing force consists of three sections with different inclinations relative to the  $x$  axis (Fig. 2a). This may indicate the existence of three different macrostructures in the powder mixture. The front propagation velocity monotonously increases with an increase in the relative density of the sample, while the dependence of the maximum temperature has a maximum at a relative density of 0.43 (Fig. 2b).

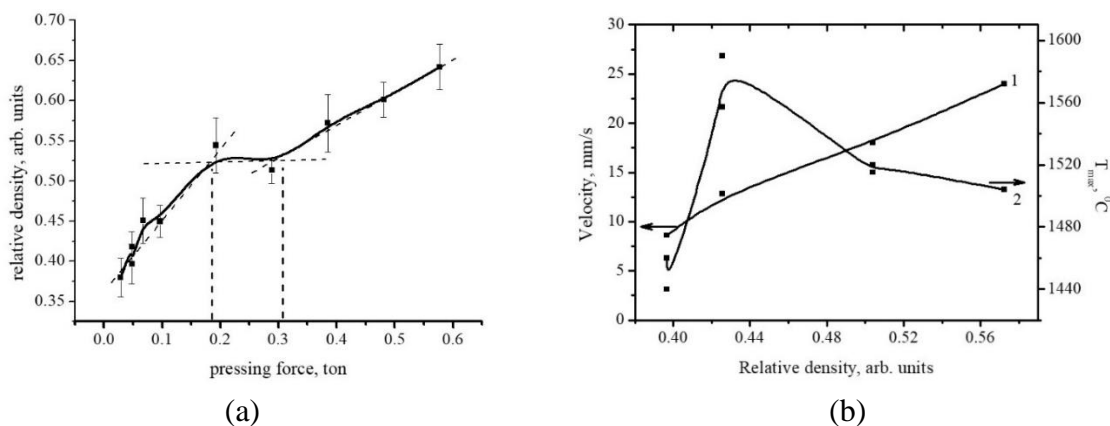


Fig. 2. (a) Relative density of samples at different pressing forces, (b) speed (curve 1) and maximum temperature of the combustion wave front (curve 2).

The distribution of copper in the radial direction from the center of the sample was studied by the method of local X-ray microanalysis. The sample in this case was a cylinder made of a pressed mixture of Ni and Al with a diameter of 15 mm and a height of 10–12 mm with copper wire 1 mm in diameter located along its axis. After synthesis, on all samples except one with a density of 0.4, a cylindrical cavity with a diameter of about 1 mm is formed in place of the copper wire. Copper is redistributed in the radial direction, and its concentration decreases from the center to the edge of the sample (Fig. 3a). And the depth of its penetration into the sample increases with an increase in the relative density of the sample (Fig. 3b). Figure 4a shows a thermogram for a sample with pressed copper wire, the thermocouple in this case was located so that the junction was in direct contact with the copper wire. The initial temperature surge is associated with a higher thermal conductivity of copper relative to the thermal conductivity of the original mixture. The temperature minimum following it coincides with the melting point of copper ( $T = 1080^\circ\text{C}$ ). A smooth rise in temperature is probably due to the interaction of the copper melt with the porous NiAl framework. The above assumptions are confirmed by high-

speed video. According to X-ray powder diffraction data, a solid solution of copper in NiAl is formed in the area of copper spreading, which confirms the interaction of copper and NiAl.

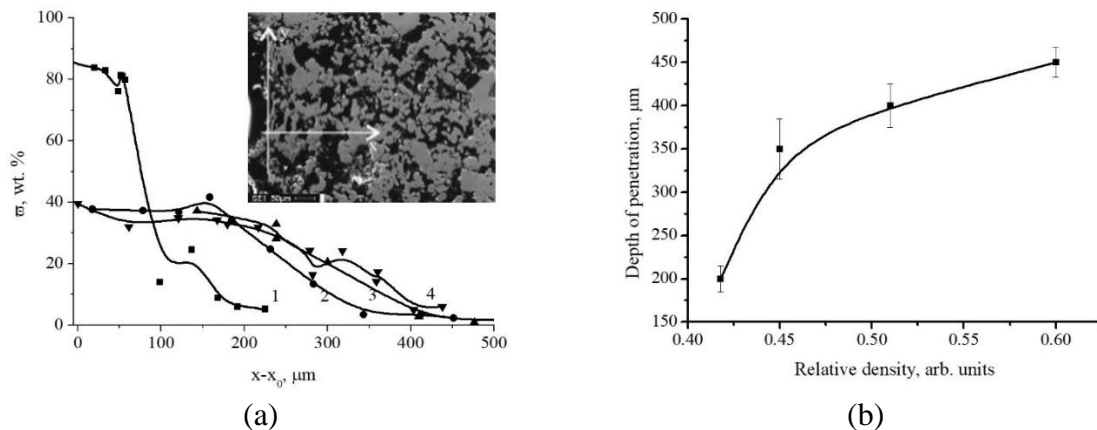


Fig. 3 (a) The distribution of copper along the radial axis of the sample, (b) the depth of penetration of copper depending on the relative density of the sample: 1 0.4; 2 0.47; 3 0.51; and 4 0.57.

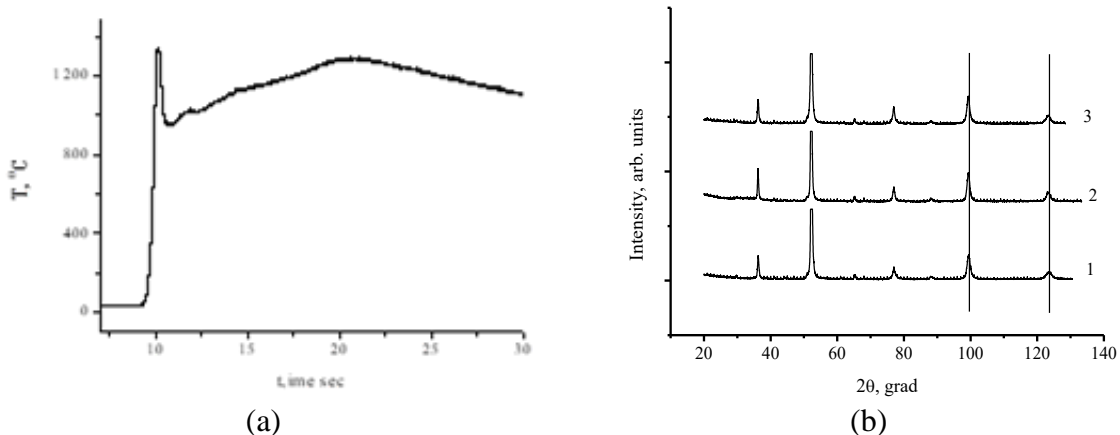


Fig. 4. (a) Changes in temperature in the copper wire, (b) XRD patterns of samples with different contents of copper powder in the mixture.

Thus, it was found that with an increase in the relative density in the range of 0.4–0.6, the depth of penetration of copper increases. The capillary spreading of copper over the porous NiAl framework is carried out by melting copper and the interaction of the melt with the forming porous framework with the formation of a solid solution of copper in NiAl.

This work was supported by the Russian Foundation for Basic Research (project no. 19-03-00081) and as part of a state assignment for the Tomsk Scientific Center of the Siberian Branch of the Russian Academy of Sciences (project no. 0365-2019-0004).

1. K. Vafai, Handbook of porous media, Third Edition, New York: Taylor and Francis Group, 2015, 959 p.
2. S.I. Popel, Surface phenomena in melts, M.: Metallurgy, 1994, 432 p.
3. E.I. Latukhin, A.P. Amosov, D.V. Borisov, A.M. Ryabov, A.Yu. Illarionov, The interaction of the porous MAX-phase of carbosilicide titanias with nickel melt in the conditions of the SHS process, *Bull. Samara State Tech. Univ. Ser. Tech. Sci.*, 2017, vol. 53, no. 1, pp. 143–151.
4. A.P. Amosov, E.I. Latukhin, A.M. Ryabov, E.R. Umerov, V.A. Novikov, The application of the SHS process for the manufacture of copper–titanium silicon carbide composite (Cu–Ti<sub>3</sub>SiC<sub>2</sub>), *IOP Conf. Ser.*, 2018, vol. 1115.

## HIGH TEMPERATURE GAS EXTRUSION OF POWDER MIXTURE Ni + Al

**F. F. Galiev<sup>\*a</sup>, I. V. Saikov<sup>a</sup>, M. I. Alymov<sup>a</sup>, V. D. Berbentsev<sup>b</sup>, A. V. Gulyutin<sup>b</sup>,  
V. I. Bugakov<sup>b</sup>, N. V. Sachkova<sup>a</sup>, and S. V. Konovalikhin<sup>a</sup>**

<sup>a</sup>Merzhanov Institute of Structural Macrokinetics and Materials Science, Russian Academy of Sciences, Chernogolovka, Moscow, 142432 Russia

<sup>b</sup>Vereshchagin Institute for High Pressure Physics, Russian Academy of Sciences, Troitsk, Moscow, 142190 Russia

\*e-mail: fanis.galiev@mail.ru

DOI: 10.24411/9999-0014A-2019-10044

The method of high-temperature gas extrusion (HTGE) is one of the methods of metal forming, in which the material is subjected to severe plastic deformation by extrusion under high hydrostatic pressure of an inert gas. This method involves local heating in the deformation zone. HTGE also allows to change the temperature and pressure during extrusion, which in turn allows to adjust the rate of deformation. As noted in [1], this method can be used to process brittle metals, powder and composite materials. Powder materials are treated with high-temperature gas extrusion in 2 ways. The first method includes pre-pressing, sintering, and extrusion. The second is placing the powder into a thin-walled metal tube, the ends of the tube are sealed and extruded together with a powder mixture [1]. This research is devoted to the combination of SHS and HTGE to obtain long-dimensional intermetallic and cermet rods during extrusion of reactive powder mixtures. The second method of extrusion of the powder mixture [1] was used in the experiments. The mixture of Ni–Al with stoichiometric ratio of 68.5:31.5 was taken as the model system. Steel rod 10 mm in a diameter with a drilled blind hole was used as a shell, which was filled with pre-compressed tablets of the powder mixture. The scheme of the installation of high-temperature gas extrusion is shown in Fig. 1.

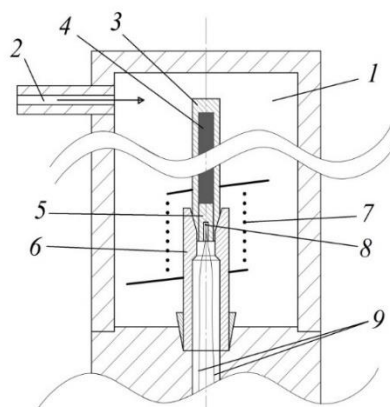


Fig. 1. The scheme of the installation of high-temperature gas extrusion. 1 high pressure vessel, 2 inlet gas pipeline, 3 sample for extrusion, 4 Ni–Al compacted powder, 5 plug with axial drilling for thermocouple, 6 gas extrusion matrix, 7 heater, 8 thermocouple, 9 pins for temperature measurement.

HTGE was carried out in the following mode: gas pressure 200 MPa, the temperature of the beginning of extrusion 780°C. The diameter of the matrix was 6 mm. Thus, the degree of deformation was 64%.

The image of the polished sample of the resulting rod is shown in Fig. 2a. The obtained samples were characterized by X-ray phase analysis using a Dron-3M diffractometer ( $\text{CuK}\alpha$  radiation) with an angle step of  $0.02^\circ$  and an exposure time for 1 s. The microstructure was studied using optical microscope and Zeiss Ultra plus Field Emission scanning electron microscope equipped with an INCA 350 Oxford Instruments X-ray microanalyzer. Quantitative X-ray phase analysis (according to the Rietveld Method) shows that the sample subjected to gas extrusion consists of about 50% NiAl intermetallic,  $\text{Ni}_3\text{Al}$ , and  $\text{Ni}_2\text{Al}_3$ . No spectra of Ni and Al were detected. The microhardness of the sample ranged from 585 to 1150  $\text{HV}_{0.1}$ , depending on the indentation zone. The SEM studies showed that the structure of the synthesized sample is heterogeneous and consists of zones with different chemical compositions. According to the Ni–Al phase diagram [2], such zones correspond to various intermetallic compounds ( $\text{Ni}_2\text{Al}_3$ , NiAl,  $\text{Ni}_5\text{Al}_3$ ,  $\text{Ni}_3\text{Al}$ ) and Al solid solution in pure Ni. The heterogeneity of the phase composition is associated with incomplete reaction of components. The microstructure of the sample is shown in the Fig.2 b.

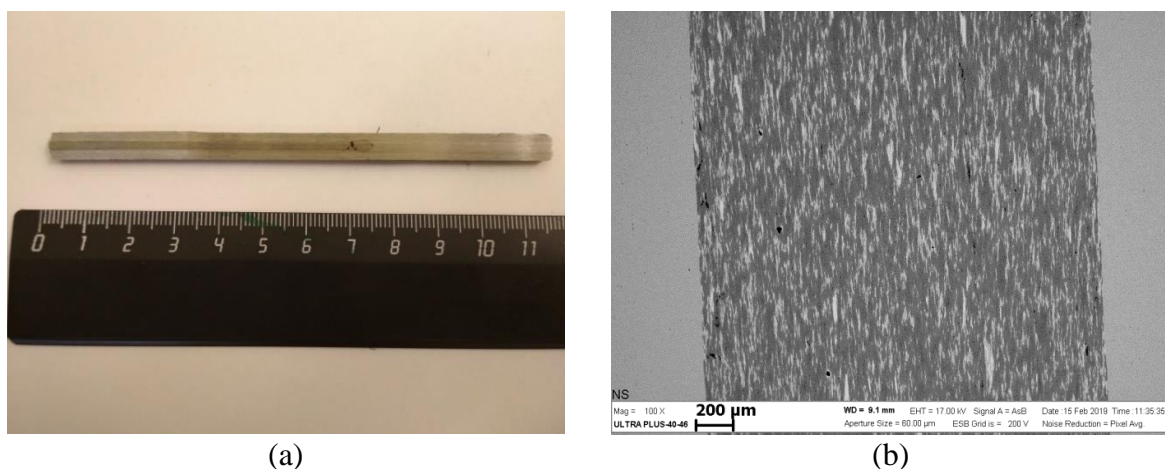


Fig. 2. (a) Overall view and (b) microstructure of produced sample.

Thus, a high-temperature gas extrusion of reactive powder mixture was carried out on the Ni–Al model system, and long cylindrical rods of Ni–Al intermetallic in a steel shell were obtained.

1. V.D. Berbentcev, M.I. Alymov, S.S. Bedov, Consolidation of nanopowders by gas extrusion, *Russ. Nanotech.*, 2007, vol. 2, nos. 7–8, pp. 116–120.
2. N.P. Lyakishev, State diagrams of double metal systems, M.: Engineering, 1996, vol. 1, 992 p.

## THE MECHANICAL ACTIVATION OF METALLIC POWDER, AN ESSENTIAL ROUTE TO PREPARE DENSE NANOSTRUCTURED MATERIALS BY SPS

S. Le Gallet<sup>a</sup> and F. Bernard<sup>\*a</sup>

<sup>a</sup>Lab. ICB UMR 6303 CNRS/UBFC, Dijon, 21078 France

\*e-mail: fbernard@u-bourgogne.fr

DOI: 10.24411/9999-0014A-2019-10045

The fabrication of dense nanostructured materials is a main challenge of many researchers. Indeed, it is often reported an enhancement of mechanical properties versus the grain size. However, the number of processes to produce them is not large [1]. It is well known the powder metallurgy is an interesting route to produce dense nanostructured materials starting from nanopowders or from nanostructured powders [1]. These latter were obtained according to different routes: (i) from individual nanopowders prepared from chemical processes (i.e. sol-gel, hydrothermal method), (ii) from nanostructured powders prepared by ball milling (i.e. planetary ball mill, attritor). The main difficulty with the use of ultra-fine powders concerns the management of the oxygen contamination (i.e. the highly reactivity) at the surface of the metallic powders. One solution to limit such reactivity is the use of ball milling process.

The main interest of the ball milling process is to form large agglomerates with a micrometric size composed of nanocrystallites. Such a microstructure is obtained after repeated fracture/welding processes induced during the milling (Fig. 1).

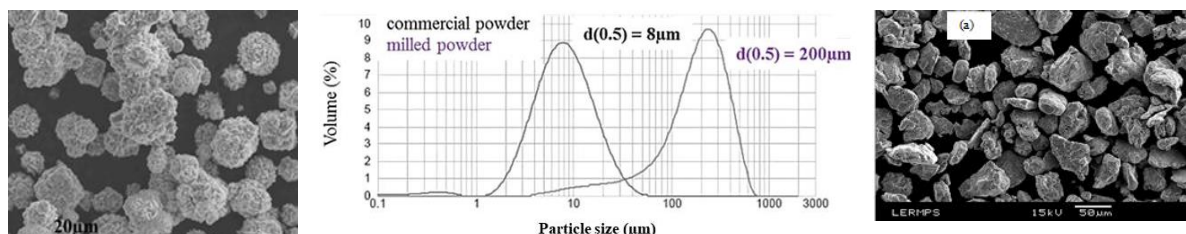


Fig. 1. SEM observations of Ni commercial powder (left part) and the same powders after a ball milling (right) showing the agglomeration process (central part) [2].

Consequently, a non-equilibrium stage is obtained because of the reduction of the crystallite size and the multiplication of structural defects such as stacking faults, twins or dislocations (Fig. 2).

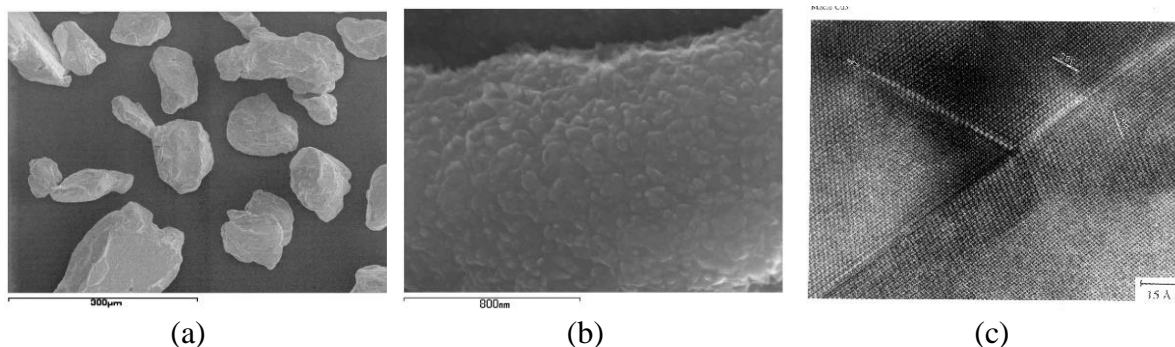


Fig. 2. SEM observation of Cu milled powder, (a) large view, (b) zoom on one Cu agglomerate and (c) TEM observation on Cu milled powder showing twins [3].

The main interest of such a situation is to modify the heat treatment conditions like a reduction of SHS ignition or the sintering temperatures, an increasing of the sintering reactivity and, then it is possible to limit the grain growth without reducing the densification stage using especially the SPS (spark plasma sintering) technology in which an electric current is used to heat rapidly the powder by Joule effect.

In this work, two solutions using sequential mechanical and field activations will be investigated to:

(i) synthesize and simultaneously densify nanostructured powder mixture [3, 4]. It concerns the production of intermetallics by reactive sintering including an SHS reaction. As an example, solid reactants (Mo and Si) in a stoichiometric ratio are milled for producing mechanically activated agglomerates composed of Mo and Si nanocrystallites. The green body is then exposed to a temperature (i.e. the current) at which the reaction occurs and, to a uniaxial pressure to consolidate the product. Thus, the control of SPS processing parameters allowed obtaining dense nano-organized  $\text{MoSi}_2$  compounds. Specifically, an increase of the heating rate makes it possible to control the chemical composition by avoiding the formation of secondary phases such as  $\text{Mo}_5\text{Si}_3$ .

(ii) consolidate different nanostructured metallic powders prepared by ball milling for enhanced mechanical properties [5, 6]. The rapidity of the SPS process leads to a limited grain growth. A mechanical activation on commercial Ni powders was accomplished by high energy planetary mill in order to reduce the crystallite size and to increase structural defects. Consequently, a dense nanostructured Ni with an  $R_p0.2\%$  of 498 MPa and an elongation of 28% was obtained whereas a dense microstructured Ni with a true elongation of 42% and yield strength of 230 MPa has been produced. Finally, from a best control of the ball milling conditions, it is possible to manage the best compromise between yield strength and ductility.

1. E. Gaffet, F. Bernard, J.C. Niepce, F. Charlot, C. Gras, G. Le Caer, J.L. Guichard, P. Delcroix, A. Mocellin, O. Tillement, Some recent developments in mechanical activation and mecanosynthesis, *J. Mater. Chem.*, 1999, vol. 9, pp. 305–314.
2. O. Boytsov, E. Gaffet, F. Bernard, A. Ustinov, Correlation between milling parameters and microstructure characteristics of nanocrystalline copper powder prepared via a high energy planetary ball mill. *J. Alloys Compd.*, 2007, vol. 432, pp. 103–110.
3. Z.A. Munir, E. Gaffet, F. Charlot, F. Bernard, One-step synthesis and consolidation of nano-phase materials, US Patent N°6 200 515 B1, 13 Mars 2001.
4. G. Cabouro, S. Chevalier, S. Le Gallet, E. Gaffet, Yu. Grin, F. Bernard, Dense  $\text{MoSi}_2$  produced by reactive flash sintering: control of Mo/Si agglomerates prepared by high energy ball milling, *Powder Technol.*, 2011, vol. 208, pp. 526–531.
5. C. Wolff, S. Mercier, H. Couque, A. Molinari, F. Naimi, F. Bernard, Thermal-electrical-mechanical simulation of the nickel densification by SPS. Comparison with experiment, *Mech. Mater.*, 2016, vol. 100, pp. 126–147.
6. F. Naimi, L. Minier, S. Le Gallet, H. Couque, F. Bernard, Dense nanostructured nickel produced by SPS from mechanically activated powders: enhancement of mechanical properties. *J. Nanomater.*, 2013, ID 674843.

## SYNTHESIS OF MAX PHASE $Ti_2AlN$ BY SPARK PLASMA SINTERING OF $Ti/AlN$ COMPOSITE POWDERS OBTAINED BY MECHANICAL ACTIVATION

V. G. Gilev<sup>\*a</sup>, M. N. Kachenyuk<sup>a</sup>, A. A. Smetkin<sup>a</sup>, and S. A. Oglezneva<sup>a</sup>

<sup>a</sup>Perm National Research Polytechnic University, Perm, 614990 Russia

\*e-mail: xray@pm.pstu.ac.ru

DOI: 10.24411/9999-0014A-2019-10046

The compound  $Ti_2AlN$  belongs to the class of refractory materials having a layered structure and is described in general form by the formula  $M_n + 1AX_n$ , where M is a transition metal, A is an element of group IIIA or IVA of the periodic system, and X is carbon or nitrogen. Various methods are used for the synthesis [1–3].

The starting materials for the synthesis of  $Ti_2AlN$  were titanium powder TPP-7 with a fraction less than 325  $\mu m$  and two different AlN powders: AlN -1 ( $< 58 \mu m$ ,  $d(4/3) = 11.46 \mu m$ ,  $d50 = 8 \mu m$ ) and AlN- 2 ( $< 69 \mu m$ ,  $d(4/3) = 20.7 \mu m$ ,  $d50 = 17.2 \mu m$ ). Mechanical activation (MA) of the powder mixtures was carried out using a SAND planetary mill at a mill drum rotation frequency of 280  $min^{-1}$  in a vacuum ( $P < 10 Pa$ ) for 0.667, 2, and 3 h. The mass ratio of the grinding bodies and the material being processed corresponded to 7.5:1. To exclude contamination of the material during MA a tooling made of titanium was used.

Spark plasma sintering of powder compositions was carried out using a Sinter SPS-1050b equipment in a graphite mold with a graphite foil shell under a pressure of 30 MPa. The temperature was varied in the range of 900–1400°C; the isothermal aging was carried out in vacuum for 5 min; and the average heating rate was 80°C/min. The results of determining the chemical composition of aluminum nitride powders are given in Table 1.

Table 1. EDS data of AlN powders.

| Powders | Chemical composition, wt % |      |      |      |      |      |      |      |      |      |      |
|---------|----------------------------|------|------|------|------|------|------|------|------|------|------|
|         | Al                         | Ti   | Fe   | Cr   | Mn   | Cu   | Ni   | Zn   | Mo   | Zr   | Rb   |
| AlN -1  | 99.31                      | –    | 0.54 | 0.06 | 0.05 | 0.03 | 0.02 | –    | –    | –    | –    |
| AlN -2  | 98.02                      | 1.22 | 0.44 | 0.06 | 0.08 | 0.02 | –    | 0.04 | 0.03 | 0.02 | 0.01 |

In the AlN-1 powder, the main phase was the hexagonal phase P63mc (space group 186), as well as 7 wt % Al impurity. In addition, according to the XRD analysis, the initial AlN-1 powder has about 7% bayerite  $Al(OH)_3$  as an impurity (space group 14). In the AlN-2 powder, there were no these impurities (Al and its hydroxide). The presence of oxygen in powders and mixtures after MA was assessed using a scanning electron microscope (Table 2). It can be seen that the oxygen content is lower in AlN-2 powder and related mixture than in AlN-1 and Ti/AlN-1.

Table 2. EDS data of AlN powders and mixtures after MA for 3h.

| Sample   | Number of measurements | Ti   | Al   | N    | O    |
|----------|------------------------|------|------|------|------|
| AlN-1    | 6                      | –    | 61.0 | 22.1 | 17.1 |
| AlN-2    | 7                      | –    | 63.7 | 35.9 | 0.67 |
| Ti/AlN-1 | 5                      | 47.8 | 27.5 | 7.7  | 16.1 |
| Ti/AlN-2 | 4                      | 54.1 | 31.8 | 13.7 | 0.91 |



The degree of homogenization of the Ti/AlN mixture during mechanical activation can be estimated from the results of X-ray phase analysis [3]. When using Cu  $K\alpha$  radiation with a wavelength of 0.154 nm and an energy of 8051 eV, the depth of penetration into Ti and AlN differs by about 7 times. As the MA time increases from 40 to 180 min, the intensity of the Ti lines increases and of the AlN lines decreases. The AlN-1/Ti ratio determined by the method of full-profile analysis decreases with increasing  $\tau_{MA}$  and as the composition of the formed composite particles is homogenized. After 3-h MA, this value is 0.56, which is close to the value of 0.428 calculated for the initial composition of the mixture (Table 3).

Table 3. Phase content (wt %) and AlN/Ti ratio in Ti/AlN mixtures after MA.

| Duration of MA, h              | Mixture with AlN-1 |      |        | Mixture with AlN-2 |      |        |
|--------------------------------|--------------------|------|--------|--------------------|------|--------|
|                                | AlN-1              | Ti   | AlN/Ti | AlN-2              | Ti   | AlN/Ti |
| 0.667                          | 64.4               | 35.6 | 1.78   | —                  | —    | —      |
| 2.0                            | 47.9               | 52.1 | 0.77   | —                  | —    | —      |
| 3.0                            | 36.7               | 65.3 | 0.56   | 41.3               | 58.7 | 0.70   |
| Calculation of the composition | 30                 | 70   | 0.428  | 30                 | 70   | 0.428  |

The quality of MA mixture with AlN-2 is worse possibly due to the larger particle size. Similar results were obtained for MA Ti/SiC mixtures [4].

Changes in shrinkage rate and vacuum pressure for samples with two types of AlN powder during SPS are shown in Fig. 1.

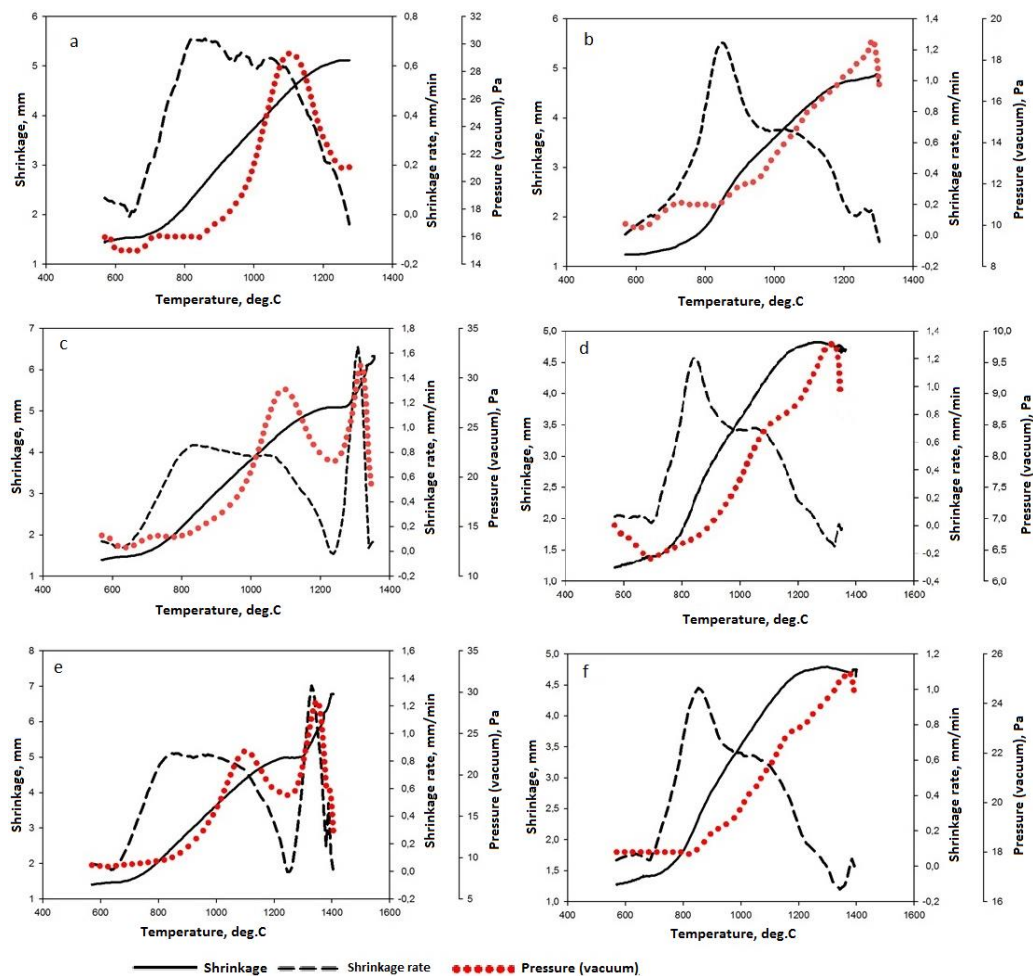


Fig. 1. Changes in shrinkage, shrinkage rate and vacuum pressure during SPS at (a, b) 1300°C, (c, d) 1350°C, and (e, f) 1400°C for samples with (a, c, e) AlN-1 and (b, d, f) AlN-2.

The presence of aluminum impurities in the composition with AlN-1 leads to an earlier onset of shrinkage. This composition is characterized by the presence of pressure peak in the region of 1100°C, as well as peaks of pressure and shrinkage rates in the region of 1350 and about 1400°C, associated with the decomposition of Ti<sub>2</sub>AlN. The sample with AlN-2 during SPS at 1350 and 1400°C has only a weak peak on the shrinkage rate curve near 1350 and 1400°C, respectively.

Table 4 presents data on the mass loss of the samples during the SPS ( $\Delta m$ ), density and open porosity ( $P_o$ ), determined by hydrostatic weighing after boiling in water, microhardness and the MAX phase portion in the composition.

Table 4. The results of the synthesis of Ti<sub>2</sub>AlN samples at different temperatures of SPS.

| $T_{SPS}, ^\circ C$ | Samples with AlN-1 powder |                |           |                        |                     | Samples with AlN-2 powder |                |           |                        |                     |
|---------------------|---------------------------|----------------|-----------|------------------------|---------------------|---------------------------|----------------|-----------|------------------------|---------------------|
|                     | $\Delta m, \%$            | $\rho, g/cm^3$ | $P_o, \%$ | HV <sub>50</sub> , GPa | Ti <sub>2</sub> AlN | $\Delta m, \%$            | $\rho, g/cm^3$ | $P_o, \%$ | HV <sub>50</sub> , GPa | Ti <sub>2</sub> AlN |
| 900                 | 0                         | 3.29           | 16.2      |                        | 18                  | 0                         | 3.45           |           |                        | 20                  |
| 1000                | 0                         | 3.69           | 10.7      |                        | 40                  | 0                         | 3.66           | 12.4      |                        | 52                  |
| 1100                | -1.1                      | 4.10           | 2.4       |                        | 64                  | 0                         | 4.13           | 1.07      |                        | 69                  |
| 1200                | -4.1                      | 4.24           | 1.9       | 6.8±1.1                | 89                  | -1                        | 4.27           | 0.05      | 6.8±0.8                | 91                  |
| 1250                |                           |                |           |                        |                     |                           | 4.33           | 0.09      |                        |                     |
| 1300                | -5.6                      | 4.26           | 1.9       | 6.7±0.7                | 90                  |                           | 4.336          | 0.01      | 4.7±0.3                | 97±1                |
| 1350                | -25.4                     | 4.30           | 2.5       |                        | 88                  | -3                        | 4.358          | 0.15      |                        | 92                  |
| 1400                | -34.7                     | 4.36           | 2.8       |                        | 75                  | -5.3                      | 4.33           | 0.48      |                        | 89                  |

As can be seen in Table 4, the use of more pure AlN powder made it possible to obtain a more pure product, up to 97–98 wt % at 1300°C and a non-porous state. When the temperature rises to 1350–1400°C, a decrease in the proportion of Ti<sub>2</sub>AlN is observed, which is a consequence of the decomposition of Ti<sub>2</sub>AlN with the formation of TiN, weight loss and the appearance of porosity. The latter is less pronounced when using AlN-2 powder.

This work was supported by the Ministry of Education and Science of the Russian Federation in the framework of the implementation of the basic part of the state task (no. 11.8353.2017/8.9).

1. D.Yu. Kovalev, M.A. Luginina, A.E. Sytshev, Reaction synthesis of the Ti<sub>2</sub>AlN MAX-phase, *Russ. J. Non-Ferr. Met.*, 2017, vol. 58, no. 3, pp. 303–307.
2. A.A. Kondakov, A.V. Linde, I.A. Studenikin, V.V. Grachev, Synthesis and decomposition of max phase Ti<sub>2</sub>AlN in the mode of filtration combustion, *XIV Int. Symp. Self-Propag. High-Temp. Synth.: Book of Abstracts*, 2017, pp. 84–86.
3. V.G. Gilev, M.N. Kachenjuk, Fazoobrazovaniye pri sinteze Ti<sub>2</sub>AlN plazmenno iskrovym spekaniyem v sisteme Ti/AlN (Phase formation at the Ti<sub>2</sub>AlN under the spark-plasma sintering in the Ti/AlN system), *Novye ognepory (New refractories)*, 2018, no. 12, pp. 49–53.
4. M.N. Kachenjuk, V.G. Gilev, A.A. Smetkin, Effect of mechanical activation on a mixture for synthesizing titanium silicon carbide, *Refract. Ind. Ceram.*, 2018, vol. 59, no. 3, pp. 257–261.

# GENERATION OF SELF-PROPAGATING HIGH-TEMPERATURE SYNTHESIS ON THE SURFACE OF SINTERED TITANIUM SPONGE POROUS SAMPLES IN A THIN LAYER BY ELECTRIC IMPULSE

**R. P. Golodok\*, V. V. Savich, S. V. Poberezhny, O. O. Kuznechik, and E. G. Grigoriev**

<sup>a</sup>O.V. Roman Powder Metallurgy Institute, Minsk, 220005 Belarus

<sup>b</sup>Merzhanov Institute of Structural Macrokinetics and Materials Science, Russian Academy of Sciences, Chernogolovka, Moscow, 142432 Russia

\*e-mail: robertgolodok@mail.ru

DOI: 10.24411/9999-0014A-2019-10047

It is shown that an electric impulse generates self-propagating high-temperature synthesis on the surface of molded porous permeable materials by electro-impulse sintering of titanium sponge powders. It is localized in the surface layer (from 100  $\mu\text{m}$  for titanium sponge powders with a particle size of 0.63–1.00 mm, up to 400  $\mu\text{m}$  for powders with a particle size of 1.00–3.2 mm). The results of structure and strength properties of the produced samples showed that they are porous, permeable, forming a two-phase system: thin surface oxide-nitride (ceramic) layer–titanium (metal) base.

## Introduction

Porous permeable materials of a two-phase thin surface ceramic layer–metal base system produced from titanium powders are promising for the manufacture of filter elements or catalytic systems used in fuel systems of heat engines, technological cycles of chemical industry enterprises, and in power industry [1, 2]. The development and improvement of technologies for producing such materials is a currently important task for powder metallurgy. Practical experience in the research of electro-impulse sintering of titanium sponge powders can be used in order to solve this task [3]. Air generation on the surface of sintered porous permeable materials of self-propagating high-temperature synthesis and the study of the structure and physicomaterial properties of such materials was the objective of this work.

## Experimental

Titanium sponge powders were used as initial material for producing experimental samples. Their fractional (particle size distribution) and chemical composition are presented in Table 1.

Magnetic-impulse welding equipment Impuls BM was used for sintering of experimental samples. It ensured the conversion of a high-voltage discharge (1.5–2.0 kV) of a capacitor (1200–1500  $\mu\text{F}$ ) into an impulse current [2] flowing through titanium sponge powder in a dielectric matrix, and being compressed by electrodes-punches. The modes of electro-impulse effect were chosen in such a way that the used electrodes-punches and dielectric matrix ensured the preparation of experimental samples from initial powders in the form of porous thin-walled (1.5–2.0 mm) rings 25–26 mm in height and 18–20 mm in outer diameter.

Table 1. Chemical composition of titanium sponge powders TU 1715-449-05785388-99

| Grade | Fraction, mm | Mass fraction, minimum | Chemical composition, % |                             |          |          |
|-------|--------------|------------------------|-------------------------|-----------------------------|----------|----------|
|       |              |                        | Titanium                | Mass fraction of impurities |          |          |
|       |              |                        |                         | Iron                        | Nitrogen | Chlorine |
| TPP-2 | -3.2+1.0     | 80                     | Base                    | 1.8                         | 0.3      | 0.3      |
| TPP-5 | -1.0+0.63    | 70                     |                         | 0.5                         | 0.15     | 0.15     |

An electric impulse created by the thyristor contactor KT-07 of the resistance spot welding machine MT2201 was used to generate self-propagating high-temperature synthesis on the surface of the molded experimental samples. The resistance welding regulator RKS-801 allowed changing parameters of the electro-impulse effects that were selected in such a way as to provide electrodes-punches with necessary for the generation of self-propagating high-temperature synthesis electrothermal contact with the end faces of the experimental samples.

The surface and structure of the initial powder, as well as the surface structure of the sintered experimental samples were investigated using a Mira scanning electron microscope (Tescan, Czech Republic) and a MeF-3 optical microscope (Reichert-Jung Optische Werke, Austria). The phase composition of the chemical elements of these surfaces was investigated using an INCA Energy 350 X-ray micro analyzer (Oxford Instruments Analytical, United Kingdom).

The permeable properties of experimental samples were investigated on test facility for porous permeable materials [4, 5], and the strength properties were investigated using a Instron 1196 universal test machine (USA).

### Results and discussion

SEM images of particles of titanium sponge powders are shown in Fig. 1.

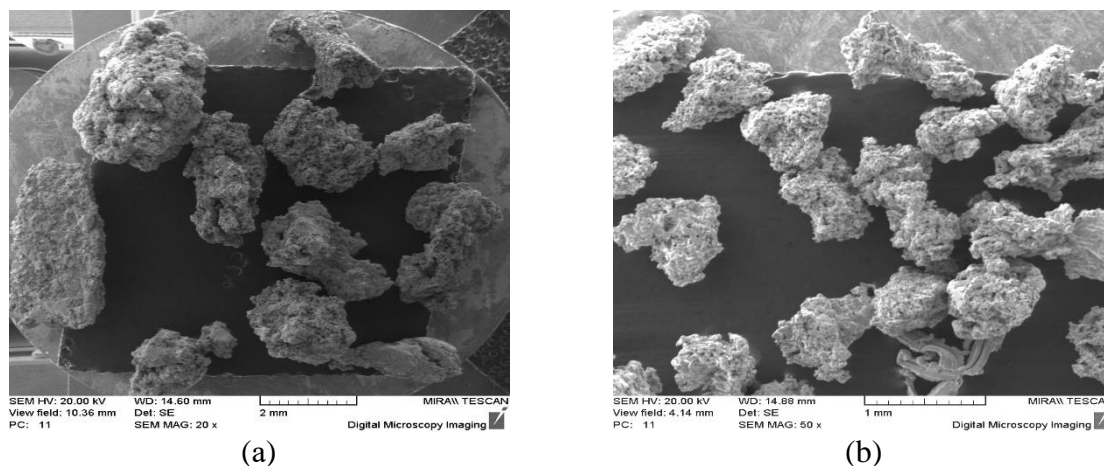


Fig. 1. Particles of the initial titanium sponge powder: (a) TPP-2; (b) TPP-5.

After electro-impulse sintering of titanium sponge powders, experimental samples were produced (Fig. 2a), which were in the form of rings (Fig. 2b) and had a gray metallic color and a porous surface.

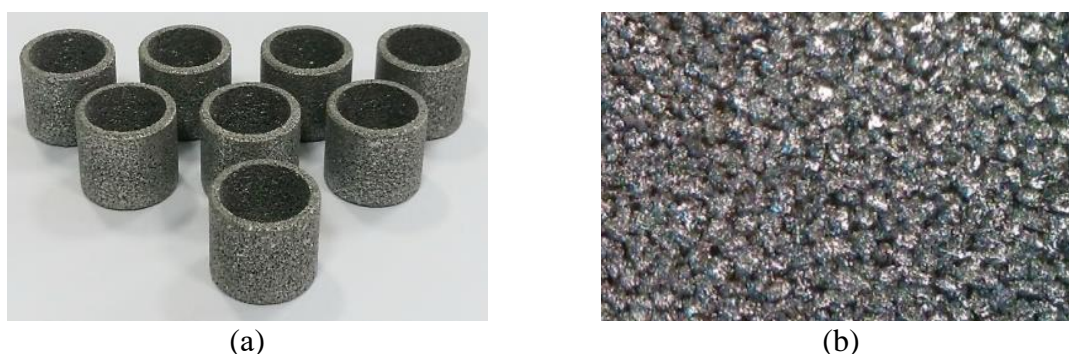


Fig. 2. (a) Experimental samples and (b) state of their surfaces after electro-impulse sintering of titanium sponge powders.

During the electro-impulse effect, the color of the surface changed on the sintered experimental samples from gray to dark gray and then from crimson to bright orange. After the end of the electro-impulse effect on the experimental samples, the appearance of two burning

fronts, having bright yellow and turning white in the contact zones of their end surfaces with electrodes-punches. These fronts moved towards each other from end surface to end surface through the sample.

After the cessation of burning, the experimental samples retained their original shape and their surfaces had a predominantly white-orange color (Fig. 3). The color change indicated the formation of a new substance phase on the surface of the coating.



Fig. 3. (a) Experimental sample and (b) state of its surface after the generation of self-propagating high-temperature synthesis.

A new phase formed after the end of self-propagating high-temperature synthesis in the surface layer and its interface with the primary one (the lower part of Fig. 4c) are clearly visible in Fig. 4b and in the upper part of Fig. 4c. The results of the study using micro X-ray spectral analysis of surface layers to a depth of 1.8 mm of experimental samples (Fig. 5) have showed that the layer of the new phase can reach a thickness of 100  $\mu\text{m}$  for samples from powder TPP-5 and up to 400  $\mu\text{m}$  for powder TPP-2 consisting of such chemical elements as titanium, oxygen and nitrogen. Thus, a thin layer of new formed phase after self-propagating high-temperature synthesis can be considered as oxide-nitride ceramics.

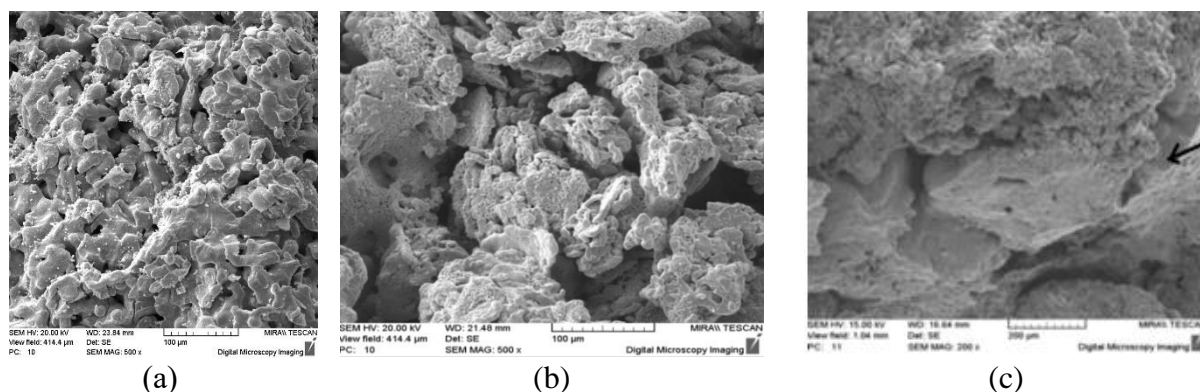


Fig. 4. The appearance of the surface of the original sample (a) and the new phase formed in the surface layer (b) and its interface (c) with the primary one (shown by arrow).

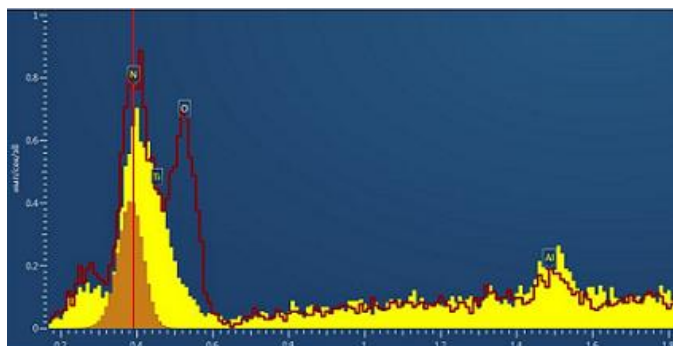


Fig. 5. Aliasing of the micro X-ray spectral analysis of the studied surfaces: brown and yellow colors correspond to the initial state of the surface, and the red line corresponds to the final state.

The results of the study of permeability and strength properties of experimental samples are presented in Table 2.

Table 2 – Permeability and strength properties of the studied materials

| Type of titanium sponge powder                    | Pore size, $\mu\text{m}$ |                      | Coefficient of permeability $\text{K} \cdot 10^{13}, \text{m}^2$ | Porosity, % | Compressive strength, MPa |
|---|--------------------------|----------------------|--|-------------|---------------------------|
|   | $D_{\text{max}}$         | $D_{\text{average}}$ |  |             |                           |
| After electro-impulse sintering                   |                          |                      |  |             |                           |
| TPP-2   | 317–318                  | 219–220              | 720–722  | 53–56       | 100–103                   |
| TPP-5   | 174–175                  | 128–130              | 369–371  | 45–47       | 118–120                   |
| After self-propagating high-temperature synthesis |                          |                      |  |             |                           |
| TPP-2   | 309–312                  | 213–215              | 680–684  | 48–50       | 112–115                   |
| TPP-5   | 165–168                  | 115–117              | 330–334  | 41–43       | 126–130                   |

Research results in Table 2 showed that the used modes of electro-impulse sintering of titanium sponge powders had provided porous permeable materials, which can be used [4, 5] due to their characteristics for the manufacture of promising filter elements of pneumatic and hydraulic drive systems. The use of an electric impulse to generate self-propagating high-temperature synthesis on the surface of sintered samples leads to a decrease in their permeability properties by 14–16% while simultaneously increasing the strength properties by the same amount. The microstructure of materials presented in Figs. 3–5 is a two-phase system, where a thin outer surface layer is represented as nitride oxide ceramics, and the internal volume, including interparticle contacts, remains metallic titanium. As follows from the analysis of references [1, 2], such materials can be used to manufacture elements of filtering or catalytic systems used in fuel systems of heat engines, in technological cycles of chemical industry enterprises, and in power industry.

### Conclusions

1. The use of electro-impulse sintering of titanium sponge powders and an electric impulse to generate self-propagating high-temperature synthesis on the surface makes it possible to produce porous permeable composite materials of a two-phase system, where a thin (up to 400  $\mu\text{m}$ ) surface layer is represented as nitride oxide ceramics, and the metal base is sponge titanium. The strength and permeability properties of these materials depend not only on the modes of electric impulse effect, but also on the fractional composition of the initial powders.
2. Using electro-impulse sintering of titanium sponge powders with particle sizes of 1.0–3.2 mm and self-propagating high-temperature synthesis in a thin layer of a porous sample, the following properties are achieved: average pore size is 219–220  $\mu\text{m}$ , coefficient of permeability is (680–684)  $\text{K} \cdot 10^{13} \text{m}^2$ , porosity is 48–50%, and compressive strength is 112–115 MPa.
3. Using electro-impulse sintering of titanium sponge powders with particle sizes of 0.63–1.0 mm and self-propagating high-temperature synthesis in a thin layer of a porous sample, the following properties are achieved: average pore size is 128–130  $\mu\text{m}$ , coefficient of permeability is (330–334)  $\text{K} \cdot 10^{13} \text{m}^2$ , porosity is 41–43%, and compressive strength is 126–130 MPa.
4. According to permeability and strength properties, these materials are promising for the production of filter elements or catalytic systems used in the fuel systems of heat engines, in the technological cycles of chemical industry enterprises, and in power industry.

1. V.V. Savich, A.M. Andreev, O.O. Kuznechik, R.P. Golodok, The state and prospects for the development of hydrogen energy and the role of catalyst support materials and getter

- materials used in it, New materials and technologies: powder metallurgy, composite materials, protective coatings, welding: materials of the 12th International Scientific and Technical Conference, Minsk: Navukovaya Dumka, 2016. pp. 289–293.
2. A.M. Taraykovich, G.A. Sheko, O.O. Kuznechik, R.P. Golodok, V.E. Romanenkov, T.E. Eutukhova, Production of a promising catalyst support for high-temperature catalytic reforming from titanium sponge powders by electro-impulse sintering and plasma-chemical synthesis, *Powder Metall.: Inter-Republican Interdepartmental Collection of Scientific Papers*, 2016, no. 39, pp. 77–81.
  3. R.P. Golodok, V.V. Savich, A.M. Taraykovich, S.V. Coast, OO Grasshopper, A.O. Konakov, T.N. Vorobyov, Production of permeable materials from titanium sponge with their subsequent surface modification for use in catalytic processes under highly-concentrated flows of electro-impulse energy in air, *Powder Metall.: Inter-Republican Interdepartmental Collection of Scientific Papers*, 2017, no. 40, pp. 118–124.
  4. V.M. Kaptsevich, New filtering materials and prospects for their use, Minsk: Belarusian State Agrarian Technical University, 2008, p. 232.
  5. L.P. Pilinevich, Porous powder materials with an anisotropic structure for filtering liquids and gases, Minsk: Tonpiq, 2005, p. 252.

## SHS OF TITANIUM–CHROMIUM CARBIDES: INFLUENCE OF GREEN COMPOSITION

O. A. Golosova<sup>\*a</sup>, P. A. Miloserdov<sup>a</sup>, V. A. Gorshkov<sup>a</sup>, and O. M. Miloserdova<sup>a</sup>

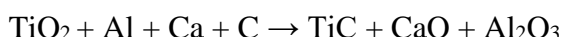
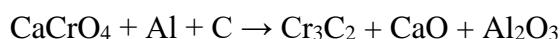
<sup>a</sup>Merzhanov Institute of Structural Macrokinetics and Materials Science, Russian Academy of Sciences, Chernogolovka, Moscow, 142432 Russia

\*e-mail: golosova@ism.ac.ru

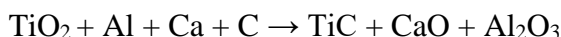
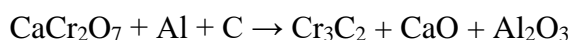
DOI: 10.24411/9999-0014A-2019-10048

In the paper, the effect of green mixture composition on combustion parameters and composition of SHS Cr–Ti–C products was studied. In order to prepare titanium–chromium carbides by SHS process, a mixture of chromium oxides  $\text{CrO}_3$  and  $\text{Cr}_2\text{O}_3$  was previously used. However,  $\text{CrO}_3$  is toxic and low technologic. Therefore, calcium chromates  $\text{CaCrO}_4$  and  $\text{CaCr}_2\text{O}_7$ , which are  $\text{CrO}_3$  stabilized by calcium oxide, were chosen as a chromium-containing additive.

We studied systems based on  $\text{CaCrO}_4$ :



and based on  $\text{CaCr}_2\text{O}_7$ :



In experiments, replacing aluminum with calcium for more complete reduction of titanium oxide was carried out.

Calculation of combustion temperature of mixtures depending on the titanium oxide content showed that the combustion temperature of mixture 2 (Fig. 1b) is higher than that of mixture 1 (Fig. 1a). Mixture 2 is also characterized by higher amount of gaseous products. The calculated yield of target product remains practically unchanged.

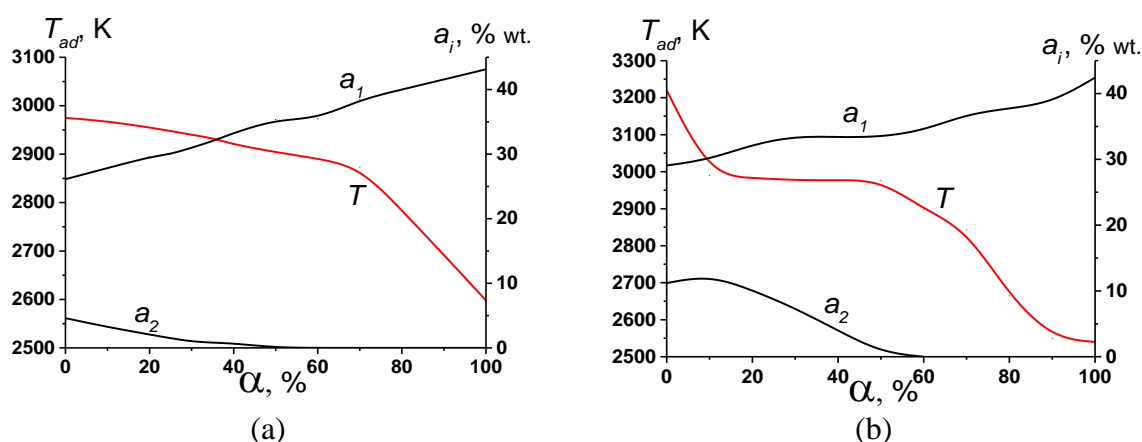


Fig. 1. Calculated adiabatic combustion temperature ( $T_{ad}$ ), mass fraction of metallic ( $a_1$ ) and gaseous ( $a_2$ ) reaction products as a function of  $\alpha$ . (a) System 1, (b) system 2.

$\alpha = (M_2 / (M_1 + M_2)) \times 100\%$ , where  $M_1$  is the mass of mixture based on (a)  $\text{CaCrO}_4$  and (b)  $\text{CaCr}_2\text{O}_7$ ,  $M_2$  is the mass of  $\text{CaCr}_2\text{O}_7$ .



Experiments were carried out using a reactor with  $V = 3.5$  l under an overpressure of argon of 5 MPa. Mixtures were placed in graphite container 40 mm in diameter. Mixture mass was 50 g. Results are presented in Fig. 2.

It is seen that an increase in the titanium oxide fraction leads to a decrease in the burning velocity. The material loss caused by sputtering decreases from 5.8 to 3.5%. The separation of target product from oxide layer in  $\text{CaCrO}_4$ -based mixtures occurs up to  $\alpha = 10\%$  (Fig. 2a). To expand the phase separation limit, 20 wt % highly exothermic  $\text{CaO}_2 + \text{Al}$  additive was added into the mixture. This made it possible to prepare cast product up to  $\alpha = 30\%$ . In the case of mixtures based on  $\text{CaCr}_2\text{O}_7$  (Fig. 2b), cast product is obtained up to  $\alpha = 40\%$  without the use of highly exothermic additive. The material loss caused by sputtering is slightly reduced from 12 to 10%.

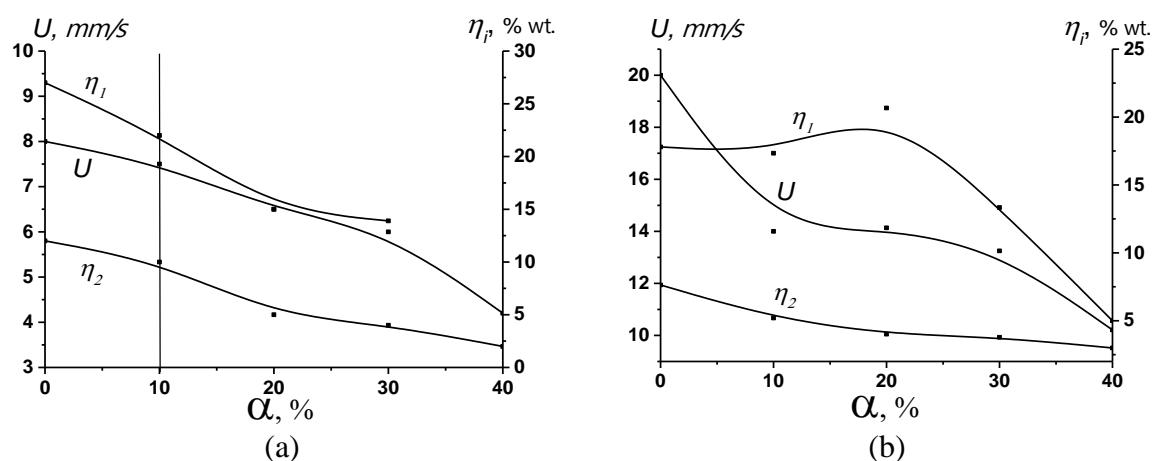


Fig. 2. Measured values of burning velocity ( $U$ ), yield of target product ( $\eta_1$ ), and material loss caused by sputtering ( $\eta_2$ ) as a function  $\alpha$ .

### Conclusions

The use of mixtures based on calcium dichromate improves reaction parameters and phase separation. For mixtures based on calcium chromate, it is necessary to use a highly exothermic additive.

The research was supported by the Russian Foundation for Basic Research (project no. 18-08-00804).

HIGH-TEMPERAURE SYNTHESIS OF CAST CERAMIC MATERIALS BASED ON Cr<sub>2</sub>AlC MAX PHASE IN LAYERED AND MIXED SYSTEMS

V. A. Gorshkov<sup>\*a</sup>, P. A. Miloserdov<sup>a</sup>, V. I. Yuxhvid<sup>a</sup>, N. Yu. Khomenko<sup>a</sup>,  
and N. V. Sachkova<sup>a</sup>

<sup>a</sup>Merzhanov Institute of Structural Macrokinetics and Materials Science, Russian Academy of Sciences, Chernogolovka, Moscow, 142432 Russia

\*e-mail: gorsh@ism.ac.ru

DOI: 10.24411/9999-0014A-2019-10049

Recently in Russia and abroad there has been a great scientific and practical interest in ceramic materials based on MAX phases of carbide and nitride compounds. MAX phases have a layered structure in which layers of transition metal carbides alternate with aluminum. They attract considerable attention because of the unusual combination of properties that make them promising to work in extreme conditions and have great potential for use in the aerospace, automotive and industrial fields, because they have a unique combination of features like metals and ceramics with excellent mechanical, chemical, thermal, and electrical properties [1, 2].

Of the methods for producing ceramic materials based on MAX phase Cr<sub>2</sub>AlC, the most well-known methods of hot pressing, sintering spark plasma (SPS Spark Plasma Sintering) and in the thermal explosion mode are in the literature. Using these methods, small samples are obtained, and the processes are carried out at high pressure and on complex equipment [3, 4]. These methods are inefficient and energy intensive. The most promising way to obtain such materials is the self-propagating high-temperature synthesis (SHS) [5]. One of the directions of this method is metallothermic SHS using initial mixtures consisting of metal oxides, a reducing metal (aluminum), and a non-metal (carbon, boron, silicon). The burning temperatures of such mixtures exceed, as a rule, the melting points of the final products obtained in the combustion wave in a liquid-phase (cast) state. Cast materials with various contents of the MAX phase Cr<sub>2</sub>AlC [6, 7] were obtained by metallothermic SHS. In these studies, the authors used initial mixtures containing chromic anhydride (CrO<sub>3</sub>), which is hygroscopic and thermally unstable, to obtain the desired products, which limits the practical implementation of the method.

In this work, we studied the patterns of high-temperature synthesis of cast ceramic materials based on Cr<sub>2</sub>AlC MAX phase in layered and mixed systems containing thermally stable and non-hygroscopic reagents. The synthesis process (Fig. 1) was carried out on the basis of chemically (I) and thermally (II) coupled reactions:

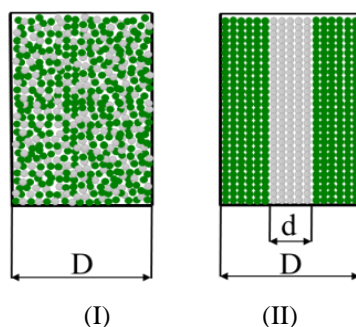
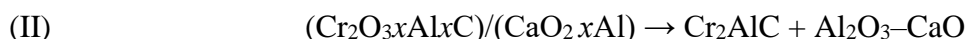
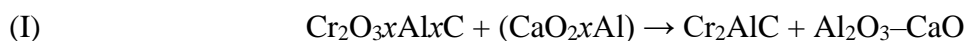


Fig. 1. Schemes of the organization of the synthesis process. (I) based on chemically coupled reactions; (II) based on thermally coupled reactions.

The finished mixture was placed in a transparent quartz cups with a diameter of 15–25 mm and a height of 50–60 mm. Syntheses were carried out in a SHS reactor with a volume of 3 l under an initial excess pressure of argon of 5 MPa. In the experiments, the burning rate, the yield of the metal phase into the ingot, and the mass loss of the mixture during combustion were determined. The phase composition of the combustion products was determined by X-ray phase analysis and electron microscopy. X-ray phase analysis was performed using a DRON-3M diffractometer. Quantitative analysis was performed according to the Rietveld method. The study of the microstructure and elemental composition of the samples was carried out using an ULTRA plus Zeiss ultra-high-resolution field-emission scanning electron microscope equipped with an INCA 350 Oxford Instruments microanalysis system.

In the experiments carried out according to scheme (I), the ratios between the masses  $M_2/(M_1 + M_2)$  of the weakly exothermic  $\text{Cr}_2\text{O}_3x\text{Al}_x\text{C}$  ( $M_1$ ) and highly exothermic  $\text{CaO}_2x\text{Al}$  ( $M_2$ ) mixtures were varied.

It was found that with an increase in the ratio  $M_2/(M_1 + M_2)$  from 0.1 to 0.4, the burning rate monotonically increases from 1.3 to 3.4 cm/s, the yield of the target product in the ingot relative to the mass of the charge increases from 27 to 38% and reaches a maximum (38%) at a ratio of 0.3, and then decreases to 31%. In this case, the mass loss of the mixture is 0.6–4.5%.

In the experiments carried out according to scheme (II), the ratios between the layers  $(D - d)/d$  of weakly exothermic  $\text{Cr}_2\text{O}_3x\text{Al}_x\text{C}$  (1) and highly exothermic  $\text{CaO}_2x\text{Al}$  (2) mixtures were varied. It was found that with an increase in the ratio  $(D - d)/d$  from 1/3 to 3/2, the yield of the target product in the ingot increases and reaches a maximum (35%) at a ratio of 1/1, and then decreases. The mass loss of the mixture is 0.8–5.6%.

It should be noted that the combustion of the weakly exothermic  $\text{Cr}_2\text{O}_3x\text{Al}_x\text{C}$  mixture in both cases failed.

The analysis of the obtained ingots showed that when organizing the process according to scheme (I), they are composite materials based on MAX phase  $\text{Cr}_2\text{AlC}$  (from 53 to 67%), carbides ( $\text{Cr}_3\text{C}_2$ ,  $\text{Cr}_7\text{C}_3$ ) and aluminides ( $\text{Al}_8\text{Cr}_5$ ) of chromium, and during synthesis on based on thermally coupled reactions (II), the target products are composite materials based on MAX phase  $\text{Cr}_2\text{AlC}$  (from 50 to 65%), carbides ( $\text{Cr}_3\text{C}_2$ ,  $\text{Cr}_7\text{C}_3$ ) and aluminides ( $\text{Al}_8\text{Cr}_5$ ) chromium. The highest content of the MAX phase  $\text{Cr}_2\text{AlC}$  is in the samples obtained in experiments conducted according to scheme (I), with the ratio  $M_2/(M_1 + M_2) = 0.3$ , and in the samples obtained in experiments conducted according to scheme (II), the ratio between the layers  $(D - d)/d = 1/1$ .

The diffraction lines of MAX  $\text{Cr}_2\text{AlC}$  phase are narrow, which indicates a high degree of perfection of its crystal structure. At the same time, there is a nanolaminate structure with a layer thickness of several nanometers.

The research was supported by the Russian Foundation for Basic Research (project no. 19-08-00053).

1. M.W. Barsoum, T. El-Raghy, The MAX phases: unique new carbide and nitride materials, *Amer. Sci.*, 2001, vol. 89, no.4, pp. 336–345.
2. J.D. Hettinger, S.E. Lofland, P. Finkel, T. Meehan, J. Palma, K. Harrell, S.Gupta, A. Ganguly, T. El-Raghy, M.W. Barsoum, Electrical transport, thermal transport, and elastic properties of  $\text{M}_2\text{AlC}$  ( $M = \text{Ti}, \text{Cr}, \text{Nb}, \text{and V}$ ), *Phys. Rev. B*, 2005, vol. 72, pp. 115–120.
3. S.B. Li, W.B. Yu, H.X. Zhai, G.M. Song, W.G. Sloof, S.Z. waag, Mechanical properties of low temperature synthesized dense and fine-grained  $\text{Cr}_2\text{AlC}$  ceramics, *J. Eur. Ceram. Soc.*, 2011, no. 31, pp. 217–224.
4. X. Duan, L. Shen, D. Jia, Y. Zhou, S. Zwaag, W.G. Sloof, Synthesis of high-purity, isotropic or textured  $\text{Cr}_2\text{AlC}$  bulk ceramics by spark plasma sintering of pressure-less sintered powders, *J. Eur. Ceram. Soc.*, 2015, vol. 35, pp. 1393–1400.

5. E.A. Levashov, A.S. Mukasyan, A.S. Rogachev, D.V. Shtansky, Self-propagating high-temperature synthesis of advanced materials and coatings, *Int. Mater. Rev.*, 2017, vol. 62, no. 4, pp. 203–239.
6. V.A. Gorshkov, P.A. Miloserdov, M.A. Luginina, N.V. Sachkova, A.F. Belikova, High-temperature synthesis of a cast material with a maximum content of the MAX phase Cr<sub>2</sub>AlC, *Inorg.Mater.*, 2017, vol. 53, no. 3, pp. 271–277.
7. V.A. Gorshkov, P.A. Miloserdov, N.V. Sachkova, M.A. Luginina, V.I. Yukhvid, SHS metallurgy of Cr<sub>2</sub>AlC MAX phase-based cast materials, *Russ. J. Non-Ferr. Met.*, 2018, vol. 59, no. 5, pp. 570–575.

## REACTIVE FORGING – PROCESSING OF DENSE MATERIALS AND PARTS WITH FINE MICROSTRUCTURE BY PRESSURE ASSISTED SHS

E. Y. Gutmanas\*<sup>a</sup> and I. Gotman<sup>b</sup><sup>a</sup>Technion-Israel Institute of Technology, Department of Materials Science and Engineering, Haifa, 32000 Israel<sup>b</sup>Department of Mechanical Engineering, ORT Braude College, Karmiel, 21982 Israel  
e-mail: gutmanas@technion.ac.il

DOI: 10.24411/9999-0014A-2019-10050

Exothermic reactions between components of reactive materials result in pronounced evolution of energy in short period of time. In the last decade a gradual shift to applied research has led to the development of a number of unconventional processes based on exothermic reactions that allow simultaneous synthesis and consolidation of porous combustion products. Pressure assisted thermal explosion, TE, mode of self-propagating high-temperature synthesis, SHS, results in dense products in cases when the heat evolved during TE and pressure applied are sufficient for consolidation.

SHS/TE-based reactive forging (RF) has been developed: self-sustained reaction is ignited by rapid heat transfer from preheated press rams to the exothermic blend, and uniaxial pressure is applied. Combined with short distance infiltration (SDI) approach, RF provides conditions for fabrication of interpenetrating phase *in situ* composites with binary or ternary ceramics, intermetallics, intermetallic–ceramic, and metal–ceramic composites [1–5]. Compared to traditional melt infiltration, SDI has the advantage of the considerably shorter infiltration distances ( $\mu\text{m}$  vs.  $\text{mm/cm}$ ).

The RF-SDI approach has also been successful in fabrication ceramic matrix–diamond grinding wheels, ceramics nozzles, light armor tiles, sputtering targets. Nanostructuring of powder blends results in lower ignition temperatures,  $T_{\text{ig}}$ , and can be used for ignition of high  $T_{\text{ig}}$  blends and thus for fabrication of multicomponent materials. RF approach employing exothermic inserts and “chemical furnace” approach can be used for consolidation of refractory materials. Shape charge liners (SCL) based on use of reactive materials and especially those with high specific weight can improve the performance of shape charge liners.

Simultaneous synthesis and consolidation of reaction products employing pressure assisted SHS is a “green”, cost effective and thus perspective fabrication route of structural parts.

1. I. Gotman, E.Y. Gutmanas, N. Travitzky, Dense *in-situ*  $\text{TiB}_2/\text{TiN}$  and  $\text{TiB}_2/\text{TiC}$  CMCs: reactive synthesis and properties, *Mater. Sci. Eng.*, 1998, vol. 244, pp. 127–137.
2. E.Y. Gutmanas, I. Gotman, Dense high temperature by thermal explosion under pressure, *J. Eur. Ceram. Soc.*, 1999, vol. 19, pp. 2381–2393.
3. D. Horvitz, I. Gotman, E.Y. Gutmanas, N. Claussen, *In situ* processing of dense  $\text{Al}_2\text{O}_3$ –Ti aluminide interpenetrating phase composites, *J. Eur. Ceram. Soc.*, 2002, vol. 22, pp. 947–954.
4. Y. Khoptiar, I. Gotman, E.Y. Gutmanas, Pressure assisted combustion synthesis of dense layered  $\text{Ti}_3\text{AlC}_2$  carbide and its mechanical properties, *J. Amer. Ceram. Soc.*, 2005, vol. 88, pp. 28–33.
5. I. Gotman, E.Y. Gutmanas, Reactive forging - pressure assisted thermal explosion mode of shs for processing dense *in situ* composites and structural parts: a review; *Adv. Eng. Mater.*, 2018, vol. 20, no. 8, 1800376.

## MILL SCALE WASTE REPROCESSING BY CENTRIFUGAL METALLOTHERMIC SHS FOR PRODUCTION OF CAST FERROALLOYS Fe–(Si; Si–Al; B; B–Al)

**D. M. Ikornikov<sup>\*a</sup>, V. N. Sanin<sup>a</sup>, D. E. Andreev<sup>a</sup>, and V. I. Yuxhvid<sup>a</sup>**

<sup>a</sup>Merzhanov Institute of Structural Macrokinetics and Materials Science, Russian Academy of Sciences, Chernogolovka, Moscow, 142432 Russia

\*e-mail: denis-ikornikov@yandex.ru

DOI: 10.24411/9999-0014A-2019-10051

The management of wastes generated by hot metal and steel has become an important issue due to ever-tightening environment regulations. Furthermore, the depletion of iron ores necessitates extensive research work to reuse the secondary raw materials produced as a by-product in steel companies and considered as waste materials. The metallurgical industry is one of the most massive material-forming industries. In several iron and steel making processes, about 500 kg/ton of solid wastes of different nature are generated; one of these wastes is the mill scale which represents about 2% of steel produced [1].

During hot rolling of steel, iron oxides form on the surface of the metal as scales. The scale is accumulated as waste material in all steel companies. Mill scale, often called as scale, is the flaky surface consisting of the iron oxides iron (II) oxide (FeO), iron (III) oxide (Fe<sub>2</sub>O<sub>3</sub>), and iron (II,III) oxide (Fe<sub>3</sub>O<sub>4</sub>, magnetite). It can be considered as a valuable metallurgical raw material for iron and steel making industry [2]. In an integrated steel plant, portion of mill scale, the large size one, was recycled in sintering plants. But a study on recycling mill scale of steel in the sintering process showed that the sinter productivity decreased with the increase in mill scale addition due to a decrease in sinter bed permeability [2].

In the past years, steelmakers used this mill scale as oxidizer in conventional electric arc furnace steelmaking process. However, the modern electric arc furnaces are equipped with oxygen lancing system to enhance melting and oxidation processes with higher efficiency than mill scale practice [2]. A small portion of mill scale has been used by cement plants. However, the mill scale does not uniformly blend with the other feed stock materials due to its higher density than any of the blend components and thus causes a greater variation in the blend of the kiln feed. At the same time, the amount of mill scale used by cement plants, as a raw material in the manufacturing of clinker, is still rather little.

A study on laboratory scale was made to use mill scale waste to prepare iron powder. The authors used CO followed by H<sub>2</sub> as a reducing gas. When the reduction was carried out by carbon monoxide the maximum iron content (98.40 wt % Fe) in the iron powder was obtained at 1050°C for 180 min. A reduction annealing under hydrogen makes it possible to decrease carbon and oxygen contents of the reduced iron powder up to acceptable values, 0.23 and 0.28%, respectively. A recent study was made of the reduction of mill scale to sponge iron using coke at different temperatures and times. Sponge iron was successfully produced for reuse in electric furnaces as part of the metallic charge or as a raw material in the production of iron-based powder metallurgy parts.

Unfortunately, no technology has been implemented, in mass, to recover and use such materials. In some steel manufacturing companies, the bulk of mill scale waste was dumped in landfills and resulted in leaching of some percentages of heavy metals into soil and groundwater, thus threatening the environment. The continuous demand for more landfills and bad effect on the environment highlight the need for more effective methods of productive utilization of mill scale. Accordingly, most used route to recycle the iron content wastes,

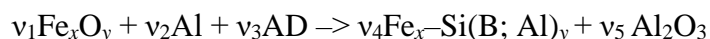
briquettes are charged into blast furnace due to its reducing atmosphere or into the electric arc furnace (EAF) during the melting of stainless steel scrap [2]. These processes allow the processing of mill scale in the metal product, but the economic efficiency remains at a sufficiently low level.

In this study, we investigated the feasibility of centrifugal metallothermic SHS to produce valuable products: cast ferroalloys Fe–(Si; Si–Al; B; B–Al) using iron oxide mill scale ( $\text{Fe}_x\text{O}_y$ ) and recycled aluminum as the components of aluminothermic mixture for obtaining the cast ferroalloys as master alloys for following use in steel making industry. A promissory route to production of cast different composition ferroalloys is using technique, which was called the SHS-technology of high temperature melts or the SHS-metallurgy [3]. This is an energy-saving technique due to the use of internal energy released in high-caloric combustion reactions. Early, the possibility of preparation on cast ceramic coatings inside metallic pipes firstly was demonstrated by reprocessing of mill scale [4].

This study involved three stages:

- (i) the preliminary investigation of the starting reagents (industrial mill scale) and the selection of optimal modes of their heat treatment for purification;
- (ii) the study of mutual relationship the initial mixture compositions and final composition of the ferroalloys (ferrosilicon, ferrosilicoaluminum and ferroboration)
- (iii) the phase and chemical composition investigations of synthesized ferroalloys and the study of experimental condition effect on formation of final compositions

The overall scheme of reaction taking place in graphite crucible can be written in the form:



where AD stands for some alloying additive such as Si,  $\text{SiO}_2$ , B, and  $\text{B}_2\text{O}_3$ .

Mill scales generated in the hot rolling step of steel, together with reducing agent (recycled aluminum powder) and some alloying additive (AD) were used as raw materials. Sieve analysis, chemical composition, and XRD examination of mill scale were carried out. The mill scale is not sorted by the requirements of the standard for chemical products. So preliminary analysis of the mill scale revealed that the main pollution source of the initial SHS mixture is the presence of the organic component (this is due to the specifics of the rolling production and surface treatment during the hot rolling of steel billets). In order to remove the organic wests, we calcined the scales in shallow trays and found out that the optimal conditions of such a thermal treatment were 300–350°C for 2–3 h. After calcining, the scales were ground down to a particle size of below 400  $\mu\text{m}$ .

For each experimental run, the amount of the reducing agent, AD and mill scale was calculated according to the material balance. Combustion was carried out in graphite molds 80 mm in diameter. The inner surface of the graphite molds was laminated with Al oxide ( $\text{Al}_2\text{O}_3$ ) to ensure minimal reactive interaction between the form material and metal melt. Because the attained temperatures (up to 3000°C) are well above the m.p. of reaction products, the melt represents a mixture of mutually insoluble metallic (alloy) and oxide ( $\text{Al}_2\text{O}_3$ ) phases. Due to strongly different specific weights, these phases undergo gravity-assisted phase separation and subsequent crystallization. As the result the lower layer is target material (ferroalloys) while the upper one,  $\text{Al}_2\text{O}_3$ .

Our previous studies have demonstrated that the SHS process carried out under high gravity conditions affords the best separation of the target product (ingot) from the slag ( $\text{Al}_2\text{O}_3$ ) and convective mixing of all alloy components, which becomes especially important with an increase in the number and concentration for alloys with an increased number of components and their concentration of components in the alloy. Therefore, the synthesis of the as cast alloy under study was carried out in a centrifugal SHS setup [4].

The investigation is a universal axial centrifugal installation with the possibility of forming the necessary synthesis conditions in a broad range of specified overloads. Its main feature of the SHS installation included systems for initiating the reaction mixture, controlling the rotation velocity of the samples, and measuring the sample temperature after synthesis (at the cooling stage). To calculate the ratio of the starting components, we should know the mutual concentration of iron and oxygen in the scale (values  $x$  and  $y$ ) exactly. The chemical and the phase analyses of two studied scale compositions (Table 1), which were supplied from different plants, revealed the difference in the mutual relationship of iron oxides.

Table 1. Main characteristics of the scale types.

| Sample no. | FeO : Fe <sub>2</sub> O <sub>3</sub> , wt % | Particle size, mm | Impurities, wt % |
|------------|---|-------------------|------------------|
| 1          | 46 : 48                                     | 1–5               | 6                |
| 2          | 68 : 28                                     | 0.5–10            | 4                |

The first party contained a larger amount of Fe<sub>2</sub>O<sub>3</sub> (48 wt %), while the second one, on the contrary, preferentially consisted of FeO. The size of scale particles was from 0.5 to 10 mm. Both compositions had impurities, which included inclusions of iron, silicon oxide, alumina, and organic compounds (oil, paraffin, etc.). The presence of the latter can substantially affect the flow character of the SHS process due to intense gas liberation (gasifying the impurities) and lead to the complete or the partial emission of reaction products in the course of combustion. Therefore, it became necessary to organize preliminary scale calcination. The use of various thermal treatment modes and the subsequent analysis of the composition of the processes scale allowed us to reveal the optimal temperature range for calcination, which was  $T = 300\text{--}350^\circ\text{C}$  for 2–3 h (in the plane bottom plates). Calcination at  $T < 300^\circ\text{C}$  led to an essential increase in the calcination time (up to 10 h), and at  $T < 200^\circ\text{C}$  it led only to the partial gasifying of organic impurities. The performance of annealing at  $T > 400^\circ\text{C}$  is undesirable because the self-ignition of the evaporating gases occurring in some cases. After calcination and cooling, the scale was subjected to mechanical milling. It was found experimentally that the optimal particle size should be smaller than 400  $\mu\text{m}$ . It should be noted that the most expensive component of the starting mixture is the aluminum powder. According to our analysis, it was established that the substitution of chemically pure aluminum (brand PA-4) by a secondary one (the worked scrap) allowed us to decrease the cost of the starting mixture by more than 25%. However, the processed aluminum mostly contains impurities, the basic ones being iron (up to 5 wt %) and silicon (up to 1 wt %). It should be noted that these impurities cannot be attributed to “harmful” from the viewpoint of implementation of the SHS process. It even seems likely that their presence is desirable, since makes it possible to somewhat reduce the synthesis temperature, while the presence of silicon promotes the formation of target product (ferrosilicon and ferrosilicoaluminum). It well known that complete melting of system components is a prerequisite for good sensitivity of the process to gravity forces [5, 6]. The investigation on III stage (the effect of experimental condition on formation of final compositions) revealed that the burning velocity ( $U$ ) going up with increasing  $a/g$  (overload). The effect is most pronounced within the range  $a = 10\text{--}200$  g. Strong influence of mass forces on burning velocity was associated with intensification of convection and deformation within the reaction zone, which improves the completeness of combustion reaction. An increase in  $a/g$  (where  $a$  is the artificial gravity,  $g$  is the earth gravity) is also accompanied by a decrease in material loss ( $\eta_{\text{sput}}$ ) and an increase in the yield of target product ( $\eta_{\text{ngot}}$ ). Above 60( $\pm 5$ ) g, the  $\eta_{\text{ingot}}$  values get close to theoretical ones. The results revealed that 3 synthesized ferrosilicoaluminum alloys can be obtained within a wide range of parameters  $\alpha$  Si (the mass fraction of Si and Al in final ingot). Thus, prepared ferrosilicon samples exhibited no residual porosity, that is, had a character of cast materials, with a small contraction cavity at the center. An increase in  $\alpha$ Si was found to have slight influence on  $U$  it decreased from 4 to 3 cm/s.



The XRD data in Fig. 1 suggest that cast ferrosilicon is formed by three ( $\text{Fe}_2\text{Si}$ ,  $\text{FeSi}$ ,  $\text{FeSi}_2$ ). The incising of  $\alpha\text{Si}$  in initial mixture leads to formation of high concentrated ferrosilicon phases ( $\text{FeSi}_2$ ). Figures 2 and 3 illustrate composition and the microstructure of SHS produced as-cast ferro alloys by reprocessing of mill scale wastes.

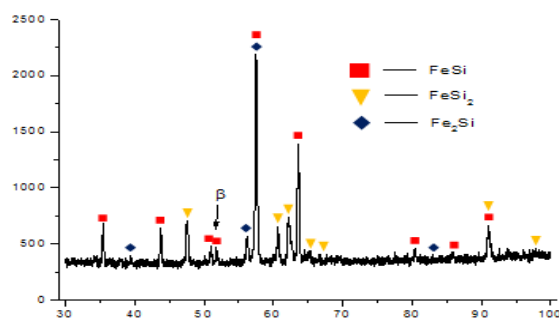
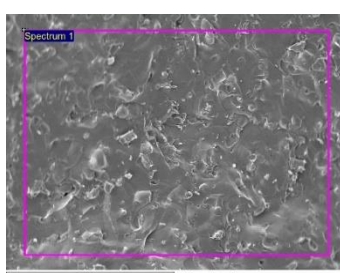
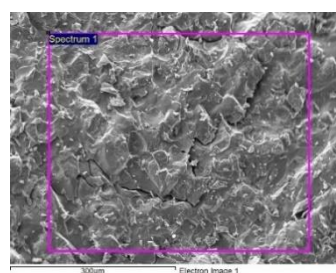


Fig. 1. Typical diffraction pattern of Fe-40Si cast ferrosilicon synthesized by SHS.



| Al  | Si   | Mn  | Fe   |
|-----|------|-----|------|
| 4.3 | 23.2 | 0.6 | 71.9 |

Fig. 2. The microstructure (fissure) and chemical composition of synthesized cast ferroalloy Fe-Si-Al.



| Al  | Si   | Cr  | Mn  | Fe   |
|-----|------|-----|-----|------|
| 4.0 | 20.0 | 3.4 | 4.8 | 67.8 |

Fig. 3. The microstructure (fissure) and chemical composition of synthesized cast ferro alloys Fe-Si-Al(Cr, Mn).

The analysis of the obtained data allows drawing a conclusion about the prospects of the materials under investigation and the method of their production for the formation of volumetric materials for steel making industry. The production of complex alloyed ferroalloys can be realized in combustion mode (SHS) for powder mixtures based on scale. The process of obtaining high-alloy ferroalloys is completely energy independent, which makes it attractive for practical realization.

The work was supported by the Program of Fundamental Research of the Presidium RAS no. 15.

1. T. Umadevi, A. Brahmacharyulu, P. Karthik, P. C. Mahapatra, M. Prabhu, M. Ranjan, Recycling of steel plant mill scale via iron ore sintering plant, *Ironmaking Steelmaking*, 2012, vol. 39, no. 3, pp. 222–227.
2. R. Farahat, M. Eissa, G. Megahed, and A. Baraka, Reduction of mill scale generated by steel processing, *Steel Grips*, 2010, vol. 8, pp. 88–92.
3. V.N. Sanin., D.M. Ikornikov, D.E Andreev., V.I. Yuxhvid, Centrifugal SHS metallurgy of nickel aluminate based eutectic alloys, *Russ. J. Non-Ferr. Met.*, 2014, vol. 55, no. 6, pp. 613–619.
4. V.N. Sanin, D. E. Andreev and V. I. Yuxhvid. Self-Propagating High-Temperature Synthesis Metallurgy of Pipes with Wear-Resistant Protective Coating with the Use of Industrial Wastes of Metallurgy Production. *Russian Journal of Non-Ferrous Metals*, 2013, Vol. 54, No. 3, pp. 274–279.

## SHS POWDERS FOR THERMAL SPRAY COATINGS

**A. Ph. Ilyushenko<sup>\*a</sup>, P. A. Vityaz<sup>a</sup>, T. L. Talako<sup>a</sup>, and A. I. Letsko<sup>a</sup>**<sup>a</sup>O.V. Roman Powder Metallurgy Institute, Minsk, 220005 Republic of Belarus

\*e-mail: alexil@mail.belpak.by

DOI: 10.24411/9999-0014A-2019-10052

Modern industrial technologies require development of novel materials with improved properties and lower cost. Surface engineering attempting to create functional layers is obviously the most economical way to provide high performance of machinery and equipment. Among the wide range of available methods, thermal spray (TS) coatings offer the most versatile solutions. Demand characteristics of thermal sprayed powders can be very different, depending on the spraying process, operating conditions, desired properties of final coatings, etc. Besides the intrinsic materials properties, technical requirements for TS feedstock powders include good flowability and sprayability. They are greatly affected by the particle shape and morphology as well as particle size distribution. That is why thermal spray feedstock powder production technology must be reliable, flexible, and inexpensive, if possible.

The prospects of manufacturing advanced powders for thermal spray coatings by the self-propagating high-temperature synthesis (SHS) have been discussed. Apart from important economical benefits, SHS allows production of powders with improved or unique structure and properties in size ranges and with an external morphology suitable for different thermal spray processes. With SHS, it is possible to manufacture composites via single-stage process even in systems of materials with significantly different properties (melting temperatures, etc.) as well as compositions that cannot be formed by the other methods. Different kinds of reaction mixtures and SHS processes activation play an important role in structure and phase formation mechanisms, providing good flexibility and reliability even for industrial-scale production.

At present, hundreds of different SHS powders have been investigated as feedstock materials for TS-coatings. Different methods of plasma spraying (air plasma spraying (APS), supersonic air plasma spraying (SAPS), low-pressure plasma spraying (LPPS), underwater plasma spraying (UPS)), detonation spraying (DS), flame spraying (FS), as well as high-velocity oxygen-fuel spraying (HVOF) have been approved for depositing protective coatings from SHS powders. The compositions of the most widely reported thermal sprayed SHS powders as well as methods of their deposition and properties of the coatings are presented.

SHS powders of carbides, nitrides and silicides have been endorsed for wear-resistant and high-temperature TS-coatings. Composite of type “refractory compound/metallic binder” are among the most widely used for thermal spraying SHS powders. The most popular compositions becoming widespread for thermal spray applications are titanium- and chromium carbide-based powders as well as titanium diboride-containing composites. Iron, nickel, cobalt, aluminium, copper and their alloys are usually used as binders. A big progress was achieved with composites having complex binders or solid lubricant phases. Principal advantages of the synthesized composite powders include fine distribution of carbide grains in the material volume and high cohesive bond strength between the components. These favor good coating properties. In general, deposition efficiency, density, hardness and wear resistance of TS-coatings from the composite SHS powders were better than that from similar plated or agglomerated ones.

Intermetallics, nickel, iron and titanium aluminides-based powders are currently used for thermal spray protective coatings. There is much interest in depositing thick ferrite and composite ceramic coatings for electromagnetic applications.

Some examples of original powders developed at the O.V. Roman Powder Metallurgy Institute are presented. The industrial-scale production of SHS powders has been established in the institute with good reproducibility of powders properties. Since 1996 O.V. Roman Powder Metallurgy Institute has been supplying SHS-powders under the contract to different thermal spray companies in USA, Sweden, Germany, India, Poland and etc.

STUDIES ON THE PORE FORMATION MECHANISM OF POROUS  $\text{TiAl}_3$  INTERMETALLICS BY COMBUSTION SYNTHESISX. Jiao<sup>a,b</sup> and P. Feng<sup>\*a</sup><sup>a</sup>School of Materials Science and Engineering, China University of Mining and Technology, Xuzhou, 221116 P. R. China<sup>b</sup>School of Chemical Engineering and Technology, China University of Mining and Technology, Xuzhou, 221116 P. R. China

\*e-mail: pzfeng@cumt.edu.cn

DOI: 10.24411/9999-0014A-2019-10053

Porous Al-based intermetallics have been widely investigated as potential functional materials due to their excellent properties such as low density, good oxidation resistance as well as the controllable porosity and permeability, which enabled their applications to be greatly developed in the area of filtration, catalytic carrier and heat insulation [1, 2]. Combustion synthesis (CS) is the typical sintering process for preparing porous intermetallic compounds and this process has the advantages of low-energy consumption, fast production and simple equipment [3, 4]. In the CS process, the sample is ignited and a strong exothermic reaction propagates as a combustion wave through the entire reactant without any other energy supply [3].

CS can be divided into two different modes depending on the heating procedure: (1) self-propagating high temperature synthesis (SHS) refers that the sample is ignited by localized heating and then quickly propagated to the other end of the sample and (2) thermal explosion (TE) mode means that the whole sample is heated at a constant heating rate until combustion behavior occurred [5, 6]. Chen [7] have studied the appearance of FeAl sintered discs and the sample was easy to crack at the edges on account of the uneven heating of powder compact. Gao [8] have fabricated porous FeAl intermetallics by SHS and step sintering, while the sample occurred deformation and presented the oval shape after SHS sintering.

Several porous Al-based intermetallics (Cu–Al, Fe–Al, Ni–Al, Cr–Al, and Ti–Al) have been successfully fabricated by thermal explosion reaction in our research group [9, 10]. The final sintered sample can maintain the original cylindrical shape and avoid the deformation and crack phenomenon after TE process on account of even heating of the powder compact. In this experiment, elemental Ti and Al powders were mixed with Ti/Al molar ration of 1:3 and then experienced a compaction process under 300MPa. The prepared compact was heated to 600, 650, 670, 675, 680, 690, and 700°C with the heating rate of 10°C/min in a high vacuum furnace (OTF-1200,  $5.7 \times 10^{-3}$  MPa).

The present paper aims to explore the influence of sintering temperature on exothermic reaction behavior through visual presentation, temperature–time curve and the change of sample appearance. Finally, the variation of pore structures and reaction mechanism of TE will be explained. The visual presentation and various steps of exothermic state can be clearly seen in Fig. 1 that recorded the whole sintering process. Taking the axial direction as an example (Fig. 1a), the sample initially turned to jacinth (1.17 s) and became red hot (1.30 s), then rapidly presented bright white (1.31 s) leading to the completion of combustion reaction. The whole TE process only lasted 1.4 s (from green compact to sintered sample) and therefore exhibited that the sample was ignited by overall heating, instantaneous reaction and rapid cooling, which was considered as an important characteristic of TE mode. Meanwhile, the sample kept the integrated shape after TE sintering.

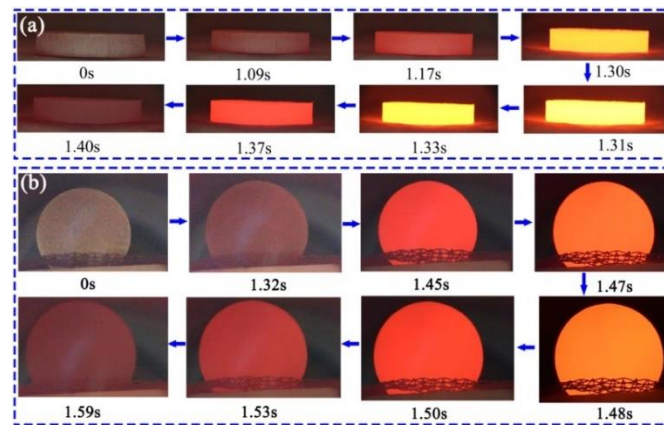


Fig. 1. Visual presentation of  $\text{TiAl}_3$  powder compact during sintering process from (a) axial and (b) radial directions.

When the furnace temperature rises directly to  $700^\circ\text{C}$  as shown in Fig. 2a, the sample temperature kept on a modest increase to the point C according to the heating rate of  $10^\circ\text{C}/\text{min}$  and appeared platform at CD stage, which can be considered as an incubation period. The point C measured to  $672^\circ\text{C}$  and slightly above the melting point of aluminum ( $666^\circ\text{C}$ ). It should be noted that the specimen was ignited when the temperature reached ignition temperature of point D ( $T_{\text{ig}}$ ,  $677^\circ\text{C}$ ) with large amounts of heat released, resulting in a sharp rise in sample temperature and climbing to the combustion temperature of point E ( $T_{\text{cs}}$ ,  $1148^\circ\text{C}$ ). It indicates that TE reaction appeared at stage DE and then cooled down to the furnace temperature. Careful observation revealed that AC period can be divided into rising stage along with furnace temperature (AB) and the sample temperature was slightly above the furnace temperature (BC). Additionally, the furnace temperature (marked by green font) was  $685^\circ\text{C}$  when the sample was ignited. Similar variation trend was also obtained in the case of the continuous heating to  $690$ ,  $680$ , and  $675^\circ\text{C}$ ,  $T_{\text{ig}}$  of samples were both  $677^\circ\text{C}$  while the  $T_{\text{cs}}$  measured to  $1130$ ,  $1110$ , and  $1022^\circ\text{C}$  respectively, as presented in Figs. 2b–2d. The macroscopic images inserted into the temperature-time curves indicate that the silver wires pressed into the surface of the sample before sintering were disappeared after TE. This phenomenon was attributed to the combustion temperature ( $T_{\text{cs}}$ ) was much higher than the melting point of silver ( $962^\circ\text{C}$ ). Figure 2e shows the highest sample temperature only reached  $672^\circ\text{C}$  when the furnace temperature set at  $670^\circ\text{C}$ , the released heat cannot induced TE reaction and the silver wires were merely partial melting. The reaction heat between solid titanium and aluminum described in Fig. 2f was  $631 \text{ J/g}$  under an adiabatic condition, therefore the diffusion reaction happens at  $T_0$  ( $627^\circ\text{C}$ ). The diffusion rate of atoms in the liquid is much faster than in the solid, which greatly promotes the reaction between solid titanium and liquid aluminum and induced a violent exothermic reaction.

Figure 3a shows the DSC result and reveals the thermal response during the whole sintering process. There were two exothermic peaks, one is the gentle exothermic phenomenon (marked by red dashed line) before the endothermic peak of melting aluminum, another violent exothermic peak (about  $672^\circ\text{C}$ ) represents the solid-liquid reaction. Pure  $\text{TiAl}_3$  phase dominated the Ti–Al system when the furnace temperature set at  $675$  and  $700^\circ\text{C}$ . Figures 3c and 3d show the expansion ratio and porosity of sintered discs when sintering at  $600$ – $700^\circ\text{C}$ . The sample experienced great volume expansion effect from  $15.7$  to  $88.4\%$  and open porosity increased from  $24.8$  to  $58.7\%$  with the increasing temperature from  $670$  to  $675^\circ\text{C}$ .

Pore structures of sintered samples can be reflected by SEM images, as shown in Fig. 4. The fracture morphology depicted in Figs. 4a–4d indicates that there is only powder metallurgy sintering between the particles and no visible pores were observed. While the sintering temperature was set at  $670^\circ\text{C}$ , some honeycomb structures have appeared and pore walls present smooth characteristic, which were marked by red dotted circles in Figs. 4e and 4f. EDS analysis was used to explain the composition of these special products, the blue part in Fig. 5a was

amplified and the elemental analysis reveals that the hollow areas were aluminum element, which were also shown in Figs. 5b–5d. This proves that aluminum experienced melting at this sintering temperature and then cooled down without having enough time and temperature to react with titanium element.

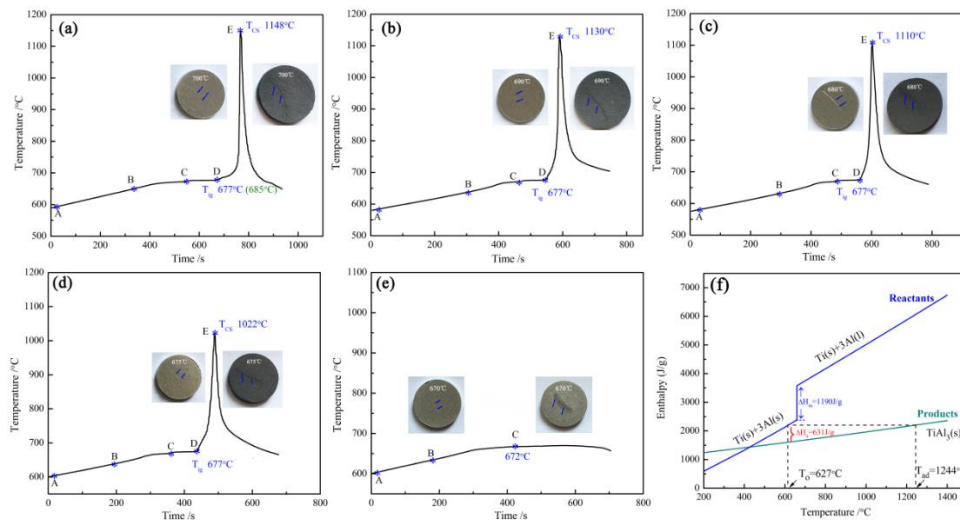


Fig. 2. Temperature–time curves during the continuous heating to (a) 700°C, (b) 690°C, (c) 680°C, (d) 675°C, (e) 670°C and (f) thermodynamic analysis of the reaction between Ti and Al in Ti–75 at % Al compacts.

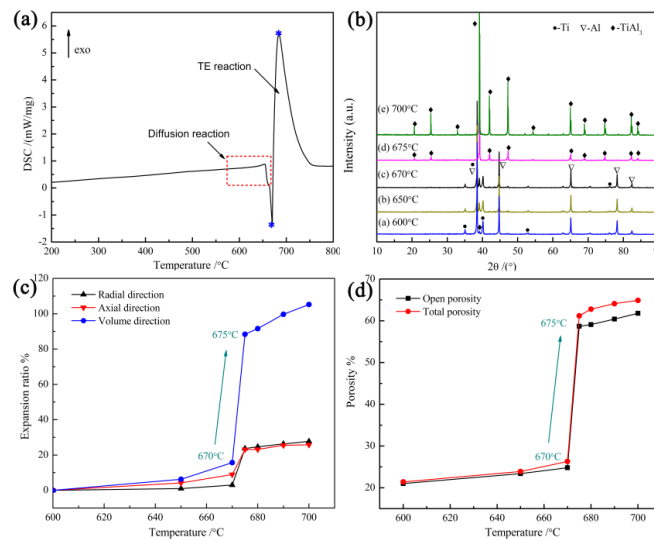


Fig. 3. DSC curve of Ti–75Al at % compact with the heating rate of 10°C/min (a); XRD patterns (b), expansion ratio (c) and porosity (d) sintering at 600–700°C.

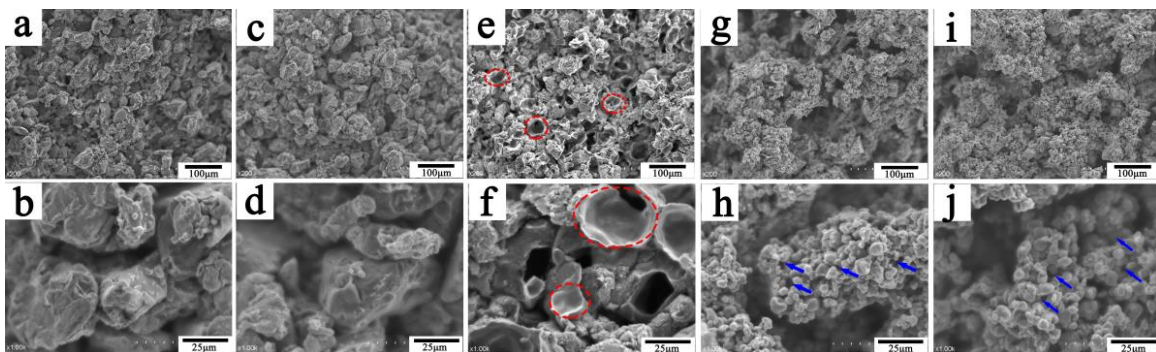


Fig. 4. Fracture morphology of Ti–75Al at % compact sintered at (a) 600°C, (b) 650°C, (c) 670°C, (d) 675°C, (e) 700°C and (f–j) with different magnification.

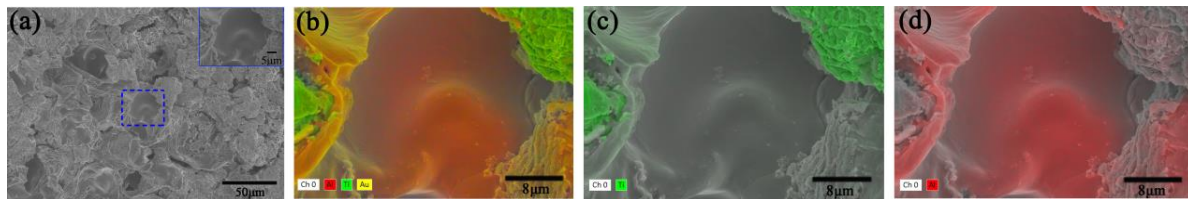


Fig. 5. EDS analysis of the Ti–75Al at % compact sintered at 670°C.

This work was supported by National Natural Science Foundation of China (51574241).

1. X.Y. Jiao, P.Z. Feng, Fabrication of highly porous TiAl<sub>3</sub> intermetallics using titanium hydride as a reactant in the thermal explosion reaction, *J. Mater. Res.*, 2018, vol. 33, pp. 2680–2688.
2. Y.N. Liu, X.P. Cai, A novel fabrication strategy for highly porous FeAl/Al<sub>2</sub>O<sub>3</sub> composite by thermal explosion in vacuum, *Vacuum*, 2018, vol. 149, pp. 225–230.
3. X.P. Cai, Y.N. Liu, Oxidation resistance of highly porous Fe–Al foams prepared by thermal explosion, *Metall. Mater. Trans. A*, 2018, vol. 49, pp. 3683–3691.
4. Y.M. Shu, A. Suzuki, Fabrication of porous NiAl intermetallic compounds with a hierarchical open-cell structure by combustion synthesis reaction and space holder method, *J. Mater. Process. Technol.*, 2019, vol. 264, pp. 182–189.
5. H. Sina, S. Iyengar, Reactive synthesis and characterization of titanium aluminides produced from elemental powder mixtures, *J. Therm. Anal. Calorim.*, 2015, vol. 122, pp. 689–698.
6. X.Y. Jiao, X.R. Xuan, X.H. Xiao, Porous TiAl<sub>3</sub> intermetallics with symmetrical graded pore-structure fabricated by leaching space holder and thermal explosion process, *Intermetallics*, 2018, vol. 95, pp. 144–149.
7. G. Chen, P. Cao, Y.H. He, Effect of aluminium evaporation loss on pore characteristics of porous FeAl alloys produced by vacuum sintering, *J. Mater. Sci.*, 2012, vol. 47, pp. 1244–1250.
8. H.Y. Gao, Y.H. He, P.Z. Shen, Porous FeAl intermetallics fabricated by elemental powder reactive synthesis, *Intermetallics*, 2009, vol. 17, pp. 1041–1046.
9. X.P. Cai, Y.N. Liu, Fabrication of highly porous CuAl intermetallic by thermal explosion using NaCl space holder, *JOM*, 2018, vol. 70, pp. 2173–2178.
10. X.Y. Jiao, X.H. Wang, Effect of heating rate on porous TiAl-based intermetallics synthesized by thermal explosion, *Mater. Manuf. Processes*, 2017, vol. 32, pp. 489–494.

## Ta-CONTAINING MATERIALS BY SHS

O. K. Kamynina<sup>\*a</sup>, S. G. Vadchenko<sup>a</sup>, A. S. Shchukin<sup>a</sup>, and V. G. Salamatov<sup>a</sup><sup>a</sup>Merzhanov Institute of Structural Macrokinetics and Materials Science, Russian Academy of Sciences, Chernogolovka, Moscow, 142432 Russia

\*e-mail: sci-secretary@ism.ac.ru

DOI: 10.24411/9999-0014A-2019-10054

As is known, tantalum exhibits a number of unique properties such as high melting point (2996°C), good ductility, hardness, heat resistance, and exceedingly high corrosion resistance in aggressive media. Moreover, tantalum as a biocompatible metal that does not cause irritation of living tissues and is inert toward long-term exposure to the liquid medium of human body. In view of this, Ta is getting more and more widely used in implant surgery to replace damaged bones and stitch nerves or tendons. The unique properties of tantalum afford for its various industrial applications in mechanical engineering, electronics, aerospace industry, nuclear power engineering, and medicine [1, 2]. However, the use of ductile tantalum as a structural and functional material is restricted by its large density and high production cost. Basic intention of this work was the SHS-assisted design of light-weight and inexpensive Ta-based materials whose service parameters would be close to those of modern structural and functional materials. In contrast to earlier attempts [3–5] to SHS produce Ta-based ceramic materials, we explored the preparation of Ti–Ta–Al intermetallics and sandwich-like Ta–(Ti + 0.65C)–(5Ti + 3Si)–Ta layered structures.

One of task objectives was the preparation Ti–Ta–Al alloys by SHS method in a mode of thermal explosion, with special emphasis on the influence of particle size/morphology of starting blends and their mechanical activation.

In a study on joining Ta foil with ceramics, we used commercial powders of Ti (PTS brand), carbon black (P804T), and Si ( $d < 10 \mu\text{m}$ , 99.4% pure) to prepare the  $30 \times 12 \times 5.5 \text{ mm}$  pellets of Ti + 0.65C and 5Ti + 3Si blends. Combustion experiments under 1 atm of Ar were performed in the geometry schematically presented in Fig. 1. Tantalum foils *1* used as substrates were 100  $\mu\text{m}$  thick. Prior to ignition with coil *7*, the assembly was uniformly warmed up to 700°C with heaters *4*. Load *6* was placed on firebrick *5*. The combustion process was video filmed with a MIRO M310 camcorder (5000 frames per second).

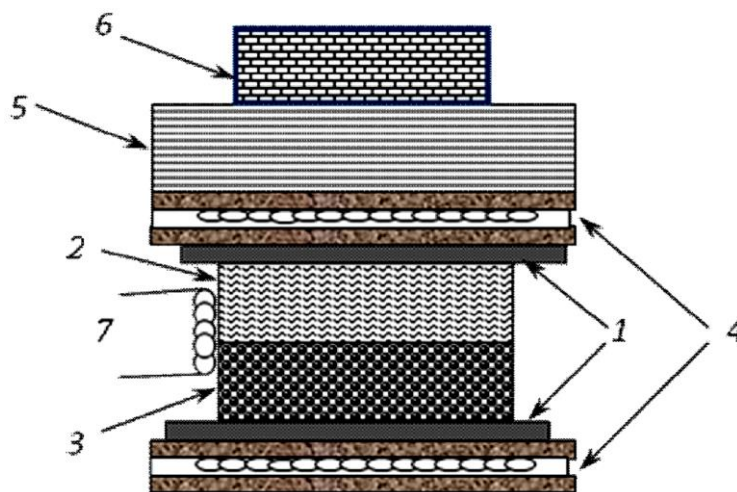


Fig. 1. Experimental setup: *1* Ta foils, *2* pellet of Ti + 0.65C blend, *3* pellet of 5Ti + 3Si blend, *4* electric heaters, *5* chamotte brick, *6* load (1240 g), and *7* igniting coil.



Burned samples were characterized by SEM/EDS (Carl Zeiss ULTRA Plus microscope equipped with EDS accessory INCA 350 Oxford Instruments) and three point bend testing (Instron-1195 machine).

Figure 2 presents still frames of combustion at different time moments. As could be expected, burning velocity (11 cm/s) in the Ti–C system (pellet 2 in Fig. 1) was higher (see Fig. 2) than that (7.5 cm/s) in the Ti–Si system (pellet 3 in Fig. 1). Formation of the liquid phase during combustion is evidenced by marked shrinkage of burned samples, down to about  $32 \times 14.5 \times 6$  mm.



Fig. 2. Still frames of combustion taken at different time moments (indicated).

Strong joining was observed between Ta (upper foil 1) and burned pellet 2, as well as between burned pellets 2 and 3. No joining happened at the interface between pellet 3 and lower Ta foil 1. This can be explained by a lower combustion temperature at the sample bottom:  $T_{ad} = 2130^{\circ}\text{C}$  for  $5\text{Ti} + 3\text{Si}$  and  $2240^{\circ}\text{C}$  for  $\text{Ti} + 0.6\text{C}$  mixture.

In this work, the possibility of producing Ti–Ta–Al based materials in SHS mode was demonstrated. We studied the dependence of product structure on the green mixture composition and the effect of preliminary mechanical activation. In the experiments, it was shown that formation of  $\text{TaAl}_2$  phase begins during mechanical activation. The Ta–Ti and Ta–Ti–C layers formed on the Ta substrate can be regarded as multifunctional coatings. The materials based on  $(\text{Ta},\text{Ti})\text{C}$  and  $\text{TaC}_x$  known for their high-temperature strength, corrosion resistance, and hardness are recommended for use as protective coatings onto the items operating in extreme conditions (above  $1500^{\circ}\text{C}$ , in aggressive media, etc.).

Our results open up new horizons for further studies and fabrication of materials based on Ta alloys with desired structure and properties.

1. W. Kock, P. Paschen, Tantalum: Processing, properties and applications, *J. Miner. Met. Mater. Soc.*, 1989, vol. 41, no. 10, pp. 33–39.
2. R.W. Buckman, New applications for tantalum and tantalum alloys, *J. Miner. Met. Mater. Soc.*, 2000, vol. 52, no. 3, pp. 40–41.
3. A.V. Bondarev, S. Vorotilo, I.V. Shchetinin, E.A. Levashov, D.V. Shtansky, Fabrication of Ta–Si–C targets and their utilization for deposition of low friction wear resistant nanocomposite Si–Ta–C–(N) coatings intended for wide temperature range tribological applications, *Surf. Coat. Technol.*, 2019, vol. 359, pp. 342–353.

4. V.V. Kurbatkina, E.I. Patsera, E.A. Levashov, Combustion synthesis of ultra-high-temperature materials based on (Hf,Ta)B<sub>2</sub>. Part 1: The mechanisms of combustion and structure formation, *Ceram. Int.*, 2019, vol. 45, no. 3, pp. 4067–4075.
5. V.V. Kurbatkina, E.I. Patsera, D.V. Smirnov, E.A. Levashov, S. Vorotilo, A.N. Timofeev, Part 2: Structure, mechanical and thermophysical properties of consolidated ceramics based on (Hf,Ta)B<sub>2</sub>, *Ceram. Int.*, 2019, vol. 45, no. 3, pp. 4076–4083.

## PRODUCTION OF SPHERICAL MICROPOWDER OF THE HIGH-TEMPERATURE STRENGTH NiAl-BASED ALLOY USING COMBUSTION SYNTHESIS AND THEIR APPLICATION IN THE SELECTIVE LASER MELTING TECHNOLOGY

**Yu. Yu. Kaplanskii<sup>\*a</sup>, E. A. Levashov<sup>a</sup>, Zh. A. Sentyurina<sup>a,b</sup>, P. A. Loginov<sup>a</sup>,  
A. V. Korotitskiy<sup>a</sup>, and E. I. Patsera<sup>a</sup>**

<sup>a</sup>National University of Science and Technology MISiS, Moscow, 119049 Russia

<sup>b</sup>JSC Kompozit, Korolev, 141070 Russia

\*e-mail: ykaplansky@gmail.com

DOI: 10.24411/9999-0014A-2019-10055

Currently, an increased attention is dedicated to the development of gas-turbine engines with enhanced performance via the application of novel heat-resistant materials and topologically optimized structures. One of the most prospective materials with high potential for application in the aerospace industry are NiAl-based heterophase alloys due to their high specific heat resistance, chemical stability, and creep resistance. Manufacturing of the heat-loaded parts (blades for rotors and impaler, burners, etc.) of gas-turbine engine from these particular alloys will increase its performance considerably. However, NiAl-based alloys are exceedingly brittle at room temperature (plasticity 3–6%), precluding their mechanical treatment and wide-scale industrial implementation. The technological breakthrough in the industrial implementation of NiAl-based alloys for aerospace industry will allow the creation of complex-shaped parts via additive manufacturing technologies. Currently, the most prospective additive manufacturing technology is selective laser melting (SLM) of powders of metals and alloys, which is being actively implemented at the advanced aerospace enterprises for the one-step manufacturing of complex-shaped parts. Implementation of this technology, however, requires spherical powders with close-cut and regulated particles size distribution (10–45  $\mu\text{m}$ ) and uniform chemical composition.

In this work, a universal technology for the production of chemically and structurally homogeneous NiAl-based spherical powders, based on the exothermic SHS reaction in mechanically activated mixture of the elemental powders. The developed technology includes the following operations: (1) preparation of the MA-mixtures in planetary ball mill (PBM); (2) pressing of MA mixtures up to  $\sim 40\%$  green body density; (3) SHS of the alloy in the water-cooled reactor under constant argon pressure (alloy is produced in a form of porous sinter cake); (3) milling of the sinter cakes in jaw crusher and PBM to a particle size smaller than 100  $\mu\text{m}$ ; (4) air separation of the target phase to 20–45  $\mu\text{m}$  and (5) plasma-assisted spheroidization of SHS powder.

According to this technology, spherical powders of novel prospective heat-resistant alloy NiAl–12Cr–6Co–0.25Hf, at % (designated CompoNiAl-M5-3) 20–45  $\mu\text{m}$  in size were produced [1]. The synthesized powders had a faceted shape and a bimodal distribution of particle size in the range of 10–87  $\mu\text{m}$  at  $D_{50} = 47 \mu\text{m}$ , flowability of 38 s and low bulk density of 2.35  $\text{g}/\text{cm}^3$ . Relatively high flowability of SHS powders is a result of absence of submicron particles.

The research into the spheroidization of SHS powders was conducted on the plasma device with an electro-discharge DC plasmatron. Ar + 17 vol % H<sub>2</sub> mixture was used as the plasma-forming gas. Investigation revealed that the optimal powder plasma treatment regime ensures the increase in the bulk density up to 3.95  $\text{g}/\text{cm}^3$  and flowability up to 19 s due to the

spheroidization of the particles. Spheroidization degree was up to 95% at particles size of 5–77  $\mu\text{m}$  and  $D_{50} = 43.1 \mu\text{m}$ , with no satellite particles. According to the chemical analysis, the content of oxygen and nitrogen impurities was below 0.12 and 0.0017 wt %, respectively.

SEM, TEM, and EDS studies of the spherical powders (Fig. 1) revealed a dendritic grain structure with degraded  $\text{Cr}(\text{Co})_e$  eutectic along the grain boundaries, interspersed with strengthening Hf nanoparticles ( $< 100 \text{ nm}$ ). Dendritic cells were 1–6  $\mu\text{m}$  in size. ICP-MS analysis of SHS powders before and after the spheroidization showed that the plasma treatment does not lead to the deviations in chemical composition.

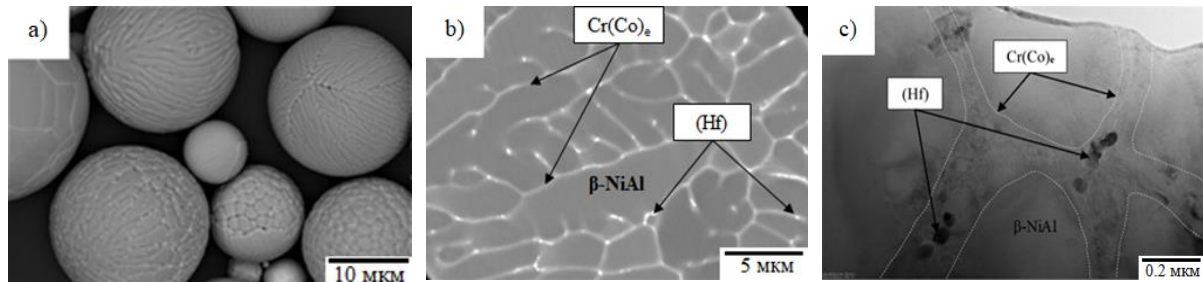


Fig. 1. (a) Morphology and (b, c) microstructure of spheroidized SHS-powders of ComoNiAl-M5-3alloy.

Spheroidized SHS powders with particle size of 20–45  $\mu\text{m}$  were sintered by hot isostatic pressing (HIP) and selective laser melting (SLM). Optimal HIP regime provided a dense material with the following mechanical properties: tensile strength ( $\sigma_b$ ) 2870 MPa; yield strength ( $\sigma_{0.2}$ ) 1131 MPa; and plasticity ( $\epsilon$ ) 16.87%. High-resolution TEM demonstrated that nano-sized particles of  $\text{Ni}_2\text{AlHf}$  Heysler phase are formed along the grain boundaries and within the NiAl matrix, which is caused by a decrease in the interface energy. Hf nanoparticles were observed only within the  $\alpha$ -Cr phase. SLM 280 installation (SLM Solution) was employed for the optimization of additive manufacturing of cubic samples and models of the blade of gas-turbine engine with a residual porosity below 0.2% (Fig. 2). Subsequent HIP treatment of SLM samples ensured a further enhancement of mechanical properties.



Fig. 2. SLM model of the blades of gas-turbine engine made of spherical CompoNiAl-M5-3 powders.

Two CompoNiAl-M5-3 alloy specimens manufactured by HIP, SLM + HT (850°C for 2 h), and SLM + HT + HIP were subjected to the thermomechanical testing to ascertain the temperature and load limits for the sustainable performance of the alloy. Young's modulus and yield strength at 850 °C and a loading rate of  $\sim 0.01 \text{ s}^{-1}$  were: 137.8 GPa and 455 MPa for HIP samples; 58 GPa and 334 MPa for SLM + HT samples; 75 GPa and 495 MPa for SLM + HT + HIP samples. Figure 3 reveals that the HIP of SLM samples ensures the considerable increase in the deformation resistance of the investigated NiAl-based alloy. Therefore, additional HIP treatment of complex-shaped SLM parts is necessary to reinforce the high-temperature strength of nickel aluminide-based alloys.

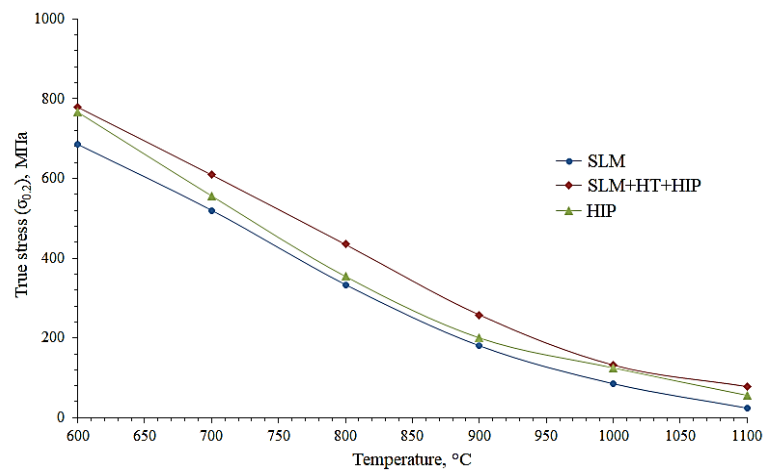


Fig. 3. Temperature dependence of the yield strength of CompoNiAl-M5-3 after HIP, SLM, and SLM+HIP.

The authors gratefully acknowledge support from Russian Science Foundation (project no. 19-79-10226).

1. Yu.Yu. Kaplanskii, A.V. Korotitskiy, E.A. Levashov, Zh.A. Sentyurina, P.A. Loginova, A.V. Samokhin, I.A. Logacheva, Microstructure and thermomechanical behavior of Heusler phase Ni<sub>2</sub>AlHf-strengthened NiAl–Cr(Co) alloy produced by HIP of plasma-spheroidized powder, *Mater. Sci. Eng. A*, 2018, vol. 729, pp. 398–410.

## INFLUENCE OF ADDITIVES ON PHYSICO-MECHANICAL PROPERTIES OF HIGH STRENGTH ALUMINOSILICATE REFRACTORY SHS MATERIALS

**R. D. Kapustin**

Merzhanov Institute of Structural Macrokinetics and Materials Science, Russian Academy of Sciences, Chernogolovka, Moscow, 142432 Russia

\*e-mail: kapustin-roman@mail.ru

DOI: 10.24411/9999-0014A-2019-10056

Currently, there are the following major global trends in the production of refractory materials:

- increasing requirements for quality and durability of materials;
- the use of highly pure and synthetic raw materials;
- an increase in the share of unburned unshaped refractories in the total volume of production (up to 50% of the total production of refractories and more) which reduces the complexity of work and reduces the cost of repairs;
- development of new materials and technologies for their production to increase the life of thermal units and reduce the cost of repair work.

This paper is devoted to the study of physicochemical properties and refractoriness of new modifications of unshaped refractory materials with improved physicochemical, mechanical and performance characteristics. The purpose of the work is to determine the properties of new refractory materials and to identify the most promising of them for the manufacture of products exposed to direct exposure to ultra-high temperatures, torch torches, etc. based on experimental studies. Obtaining refractories with higher characteristics and higher temperature of application will significantly increase the resistance of such problematic elements of furnaces as burner stones, baffles, and beams. The experimental research method involved the preparation of samples from refractory ceramic materials, their firing up to  $T = 1600^{\circ}\text{C}$ , followed by the study of their physicochemical characteristics and structural changes.

At the first stage of the experiments, corundum materials were investigated, including using electrowelled corundum and high-purity  $\text{Al}_2\text{O}_3$ . Samples were also made of tabular corundum, which is coarse-grained granules calcined at  $1950^{\circ}\text{C}$ . Such corundum is called “tabular” (lamellar), since its crystals have a lamellar form and size from 50 to 150  $\mu\text{m}$ . In addition, samples were made of electrocorundum with microfiber additives: basalt and carbon. At the second stage of the experiments corundum materials with the addition of periclase ( $\text{MgO}$ ) were investigated. These samples were also subjected to heat treatment at a maximum temperature of  $1600^{\circ}\text{C}$  (Fig. 1).

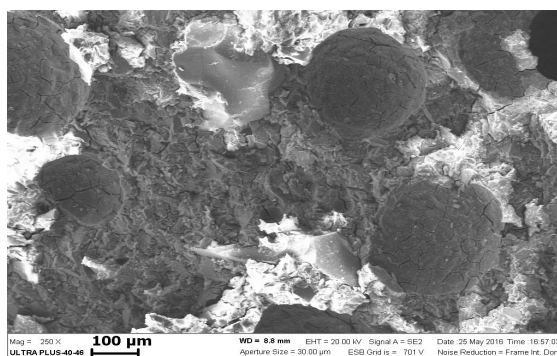


Fig. 1. Microstructure of unshaped corundum refractory material after heat treatment at  $1600^{\circ}\text{C}$ .

As part of the work, the evaluation of the strength properties of all the materials under investigation, including after heat treatment at various temperatures, was carried out. Changes in the structure of materials when exposed to different temperatures were also investigated.

As a result of experimental studies of the samples it was found:

- products from unshaped refractory materials based on  $\text{Al}_2\text{O}_3$  (electrocorundum) are able to work at temperatures of at least  $1600^\circ\text{C}$  without melting and destruction. Moreover, as a result of exposure at high temperatures and synthesis of new compounds, their strength properties and wear resistance are significantly increased;

- linear thermal shrinkage of corundum unshaped refractories (tabular, electrofused or ultrapure corundum) at temperatures up to  $1600^\circ\text{C}$  is about 6–7%;

- the introduction of carbon microfiber allows to reduce the mass and density of corundum refractories, but at the same time there is an increase in linear thermal shrinkage up to 9% at  $1600^\circ\text{C}$  due to fiber burnout;

- the introduction of periclase into corundum refractories of about 5–10 wt % allows to reduce the linear thermal shrinkage at  $1600^\circ\text{C}$  to 2%;

- the strength of corundum and corundum-periclase refractories after heat treatment at  $1600^\circ\text{C}$ , as a rule, increases by 35–50%. In addition, a significant increase in wear resistance and resistance to mechanical stress.

SHS OF  $\text{Al}_x\text{CoCrFeNi}$  HIGH-ENTROPY ALLOYS

 F. Kaya<sup>a</sup> and B. Derin<sup>\*a</sup>
<sup>a</sup>Istanbul Technical University, Metallurgical and Materials Engineering Department, Maslak, Istanbul, 34469 Turkey

\*e-mail: bderin@itu.edu.tr

DOI: 10.24411/9999-0014A-2019-10057

High-entropy alloys (HEAs) are new advanced materials group with properties that can meet the demands of the contemporary engineering disciplines. HEAs are simply defined as solid solution alloys containing more than four principal elements in equal or near-equal molar proportions and each principal element having a molar concentration between 5 and 35 at % [1, 2].  $\text{Al}_x\text{CoCrFeNi}$  system is one of the mostly studied HEAs which has excellent mechanical and chemical properties such as hardness, corrosion resistance, compressive strength, and abrasion resistance at both low and high temperatures [1–5].  $\text{Al}_x\text{CoCrFeNi}$  alloys could be potentially used for many application areas such as jet/turbine engine components, gear parts and hard facing applications; piping, pumps, mixing equipment for excessive corrosive chemical plants sea-based maritime structures as well as catalysts applications [1, 2, 6, 7].

$\text{Al}_x\text{CoCrFeNi}$  HEAs are usually produced by two different production methods: arc melting and mechanical alloying which are laboratory scale production methods rather than a mass production method and performed by using expensive metallic raw materials in a very long process time [1, 2]. In order for HEAs to replace the contemporary engineering materials, they are needed to be produced by cheaper, faster and easier techniques such as SHS method.

In the present paper,  $\text{Al}_x\text{CoCrFeNi}$  alloys were produced by aluminothermic type synthesis method from their oxides (i.e.  $\text{Co}_3\text{O}_4$ ,  $\text{Cr}_2\text{O}_3$ ,  $\text{NiO}$ ,  $\text{Fe}_2\text{O}_3$ ). Prior to the experiments, some thermochemical modelling studies were done to estimate the required amounts of the input materials, the adiabatic temperature of the SHS reactions, as well as the phase diagrams of HEAs by FactSage<sup>TM</sup> (Fig. 1).

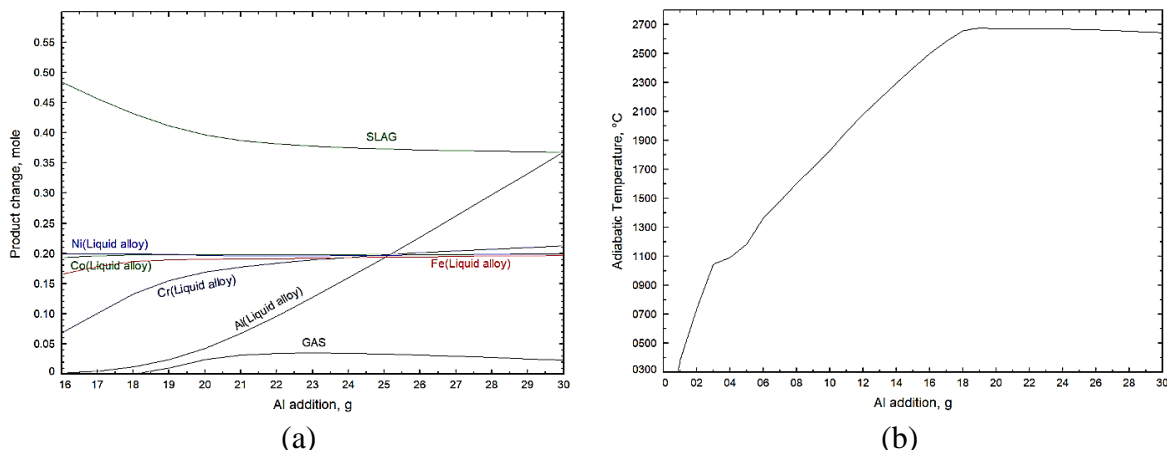


Fig. 1. Thermochemical calculations of a SHS thermite type reaction for (a) the product change and (b) the adiabatic temperature change by Al addition.

After thermochemical modelling, the oxide materials and reductant Al were dried and mixed for 60 min. After realizing the SHS experiments in Cu crucibles, the samples were remelted in a vacuum arc melter for homogenizing and rod casting (Fig. 2a). X-ray diffraction analysis



(XRD) was carried out using  $\text{CuK}\alpha$  radiation in order to determine the crystalline phases (Fig. 2b). It was seen that the sample was crystalline, having (110), (200), and (211) diffraction peaks of a BCC phase. Therefore, it was concluded that the as-received sample was a BCC solid solution, which was in accordance with literature findings.

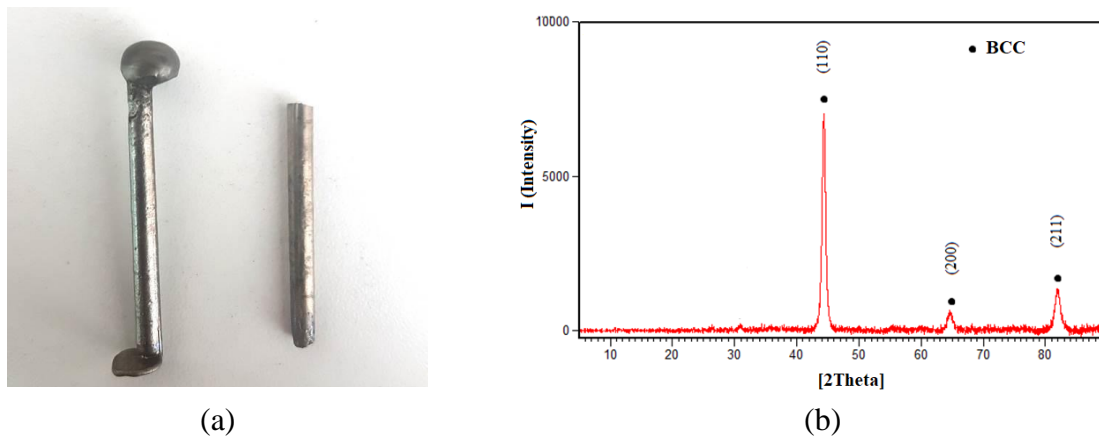


Fig. 2. (a) Rod casted sample of AlCoCrFeNi HEA, (b) XRD spectrum of the sample.

XRD results were also compared with thermochemical calculations. Table 1 shows that one selected composition scenario by model calculations agreed with experimental result and thus, an equimolar AlCoCrFeNi HEA was produced successfully.

Table 1. Chemical analysis of the sample.

|                   | Al    | Co    | Cr    | Fe    | Ni    |
|-------------------|-------|-------|-------|-------|-------|
| FactSage™ (mol %) | 20.86 | 19.52 | 20.36 | 19.47 | 19.77 |
| FactSage™ (wt %)  | 11    | 22    | 21    | 21    | 23    |
| XRD (wt %)        | 11.70 | 23.05 | 21.04 | 21.38 | 22.80 |

The research was supported by the Scientific and Technological Research Council of Turkey (TUBITAK, project no. 119M086).

1. B. Murty, J.W. Yeh, S. Ranganathan, High-Entropy Alloys (1<sup>st</sup> Edition): Butterworth-Heinemann, 2014.
2. Y. Zhang, T.T. Zuo, Z. Tang, M.C. Gao, K.A. Dahmen, P.K. Liaw, Z.P. Lu, Microstructures and properties of high-entropy alloys, *Prog. Mater. Sci.*, 2014, vol. 61, pp. 1–93.
3. Y.-F. Kao, T.-J. Chen, S.-K. Chen, J.-W. Yeh, Microstructure and mechanical property of as-cast, -homogenized, and -deformed  $\text{Al}_x\text{CoCrFeNi}$  ( $0 \leq x \leq 2$ ) high-entropy alloys, *J. Alloys Compd.*, 2009, vol. 488, no. 1, pp. 57–64.
4. W.-R. Wang, W.-L. Wang, J.-W. Yeh, Phases, microstructure and mechanical properties of  $\text{Al}_x\text{CoCrFeNi}$  high-entropy alloys at elevated temperature, *J. Alloys Compd.*, 2014, vol. 589, pp. 143–152.
5. Q.H. Li, T.M. Yue, Z.N. Guo, X. Lin, Microstructure and corrosion properties of AlCoCrFeNi high entropy alloy coatings deposited on AISI 1045 steel by the electrospark process, *Metall. Mater. Trans. A*, 2013, vol. 44, no. 4, pp. 1767–1778.
6. Z.Y. Lv, X.J. Liu, B. Jia, H. Wang, Y. Wu, Z.P. Lu, Development of a novel high-entropy alloy with eminent efficiency of degrading azo dye solutions, *Sci. Rep.*, 2016, vol. 6, 34213.
7. Y. Zhang, B. Zhang, K. Li, G.-L. Zhao, S.M. Guo, Electromagnetic interference shielding effectiveness of high entropy AlCoCrFeNi alloy powder laden composites, *J. Alloys Compd.*, 2018, vol. 734, pp. 220–228.

## HISTORY AND DEVELOPMENT PROSPECTS OF THE KAZAKHSTAN SCHOOL OF CHEMICAL PHYSICS

**T. A. Ketegenov**

Al-Farabi Kazakh National University, The Institute of Combustion Problems,  
Almaty, Kazakhstan  
e-mail: tlek58@mail.ru

DOI: 10.24411/9999-0014A-2019-10058

In 1988, there was established Kazakh Interdisciplinary Scientific and Technical Center of SHS on the basis of Chemical Kinetics and Combustion Department of Kazakh State University, reorganized later into the Institute of Combustion Problems (hereinafter IPG) by the Decision of the Council of Ministers of Kazakh SSR, no. 295, dated July 24, 1990.

Ksandopulo G. I. is the Academician of the Russian academy of technical sciences, professor. He was the first director of the Institute of Combustion Problems. The First International Symposium on SHS in 1991 (Almaty city) which gathered leading scientists from leading scientific centers was hold by him. This allowed for further raising investigations in the field of SHS technology to a higher level within the shortest possible time in Kazakhstan.

In the period of 1979-1983, the staff of the Institute was engaged in studying of combustible mixtures. According to the request of Moscow side had been organized the project "Pyrotechnic gas generator for emergency pressurization of automobile airbags with nitrogen". Hot nitrogen was produced in combustion mode of sodium azide with the various oxides. Stoichiometric mixture was compressed into tablets form, the burning of tablet was carried out in vacuum environment with the direct measurement of temperature and burning rate, a composition of generated gas (nitrogen with possible impurities) was determined by using chromatograph. A solid residue which sometimes was in the form of powder or in the form of melted mass, but sometimes in the form of microporous ceramics was studied, as well as the density of original tablet. The ceramics were synthesized in such manner seemed unusual, it is of great interest, the initial problem of synthesis, not hot nitrogen has been a secondary concern. The origin of obtained ceramics, as well as some features of combustion of investigated system, was difficult to explain from the perspective of classical concepts of inorganic chemistry. These questions stimulated work in two directions: firstly, the search for new types of ceramics that synthesized in combustion mode, and secondly, the combustion chemistry which consistently explains the totality of experimental data.

A unique technology has been developed in the field of SHS. It is also the world's first production of high-temperature welding compounds - "Furnon" that is for refractory and ceramics. This technology has been using at 120 large metallurgical and cement enterprises after successful tests at enterprises in Germany, Spain, Great Britain, Cuba and China. The ceramic electric heaters, chemical resistant coatings on metal as well as SHS catalysts and pigments were obtained by SHS method. There was developed and created an equipment for processing line, the production of rare ferroalloys (molybdenum, tungsten, vanadium) by using SHS method under pressure. Applied researches were also conducted in "Flyuga" company which was created by Ksandopulo G. I. The works on the analysis of physico-chemical properties of refractory SHS materials at operating temperatures, ceramic and abrasive materials, combustion regularities of  $V_2O_5$ -Al and  $Cr_2O_3$ -Al systems and other oxide systems with aluminum were investigated.

Professor Ksandopulo G. I. is the creator of the first production of aluminum powder and aluminum grains for SHS technology and mining in Kazakhstan. The priority of technical

developments conducted under the guidance of Professor Ksandopulo G. I. is proven by more than 170 patents and copyright certificates.

Nowadays, Professor Ksandopulo G. I. has proposed the theory of flame front bifurcation process. It is important when this occurring emergency situation in combustion chambers of rocket engine fuel and etc. It is planning to create the first Kazakhstan rocket fuel, which is free from harmful effects of bifurcation factor based on established regularities.

**The Institute of Combustion Problems focuses on the following priorities:**

- (a) a creation of new nanomaterials with targeted properties;
- (b) an obtaining of pure materials and alloys with desired properties and structure;
- (c) the fundamental principles of reclamation development and complex processing of mineral raw materials resulting in products with high marketability.

The main scientific direction of the Institute of Combustion Problems in the field of fundamental and applied researches is the study of chemistry and physics of combustion processes in gas and condensed phases:

- a study of gaseous flames structure;
- a study of self-propagating high-temperature synthesis problems in order to create new and improve the traditionally produced materials; the synthesis of high-temperature electrically conducting ceramic materials; study of regularities in order to obtain composite ceramics based on carbides, silicides, transition metal borides under SHS conditions;

At present time, key attention is paid to new problems on combustion theory and formation mechanism of abruption in flame front and its connection with variables such as C, T, P, investigation of auto-wave mode in larger dimensional combustion chambers like hydrodynamics with intermittency in concentration and temperature within various types of combustion, the kinetics of acoustic wave's interaction with a matter, as well as the effect of acoustic waves on the structure of mono and bifronts. The properties of bifront would be as fresh position in the view of knocking in internal combustion engines, and destructive vibration in liquid-fuel rocket engines.

**Publication activity**

Institute of Combustion Problems has been publishing a quarterly International journal "Eurasian Chemico-Technological Journal" (Eurasian Chemical Technology Journal) since 1999. This journal is refereed and covers all areas of chemistry and chemical technology. This is only one journal in Kazakhstan, which is published exclusively in English and included in Scopus database, Elsevier B.V publishing house.

Since 2003, Institute of Combustion Problems in cooperation with the Scientific Council on Combustion and Explosion at the Presidium of the Russian Academy of Sciences, publishes the International Scientific Quarterly Journal "Combustion and Plasmochemistry", which is registered in the Ministry of Culture, Information and Public of the Republic of Kazakhstan (certificate no. 2658-Zh, dated 07.02.2002). The scientific journal "Combustion and Plasmochemistry" is included to the list for publications of main scientific results for dissertations in chemical sciences by decision of the Committee for control of Education and Science of the MES of Kazakhstan (protocol number 7, 28.08.2007).

## MULTIFUNCTIONAL BORON NANOPARTICLES: AN ECOLOGICAL METHOD OF PRODUCTION, PROPERTIES

**P. A. Khaptakhanova<sup>\*a</sup>, S. A. Uspenskii<sup>a,b</sup>, T. S. Kurkin<sup>a</sup>, A. N. Zelenetskii<sup>a</sup>,  
and S. Yu. Taskaev<sup>b</sup>**

<sup>a</sup>Enikolopov Institute of Synthetic Polymeric Materials, Russian Academy of Sciences, Moscow, 117393 Russia

<sup>b</sup>Budker Institute of Nuclear Physics, Siberian Branch, Russian Academy of Sciences, Novosibirsk, 630090 Russia

\*e-mail: khaptakhanova@ispm.ru

DOI: 10.24411/9999-0014A-2019-10059

In recent years, there has been considerable interest in using biofuels as alternative energy sources. Moreover, many types of biofuels have a low energy density compared to energy resources sold, such as gasoline or kerosene. Therefore, a lot of research is currently carried out in the field of changing energy parameters of biofuels by adding various additives with a higher energy density.

Nanoscale powders are attractive as potential fuel additives because of their high energy density combined with high specific surface area. Furthermore, nanodispersions have a lower flash point than micron-sized particles. The main requirements for nanofillers as an additive to the fuel are as follows: the average size of nanodispersions should be from 5 to 20 nm, there should be no oxide layer on the surface of particles, the concentration of nanoparticles should not exceed 10 vol % [1].

Materials based on boron nanoparticles have a wide range of application as semiconductors such as protective coatings for increasing mechanical wear resistance, drugs for treating oncological diseases, and are also used in various combinations, including combustible nanofluids, gel rocket fuels, solid rocket fuels, and also as high density fuel additives.

Elemental boron has the largest volumetric heat of reaction with oxygen (138 kJ/cm<sup>3</sup>), compared to other elements. However, its ignition is greatly hindered by the presence of a B<sub>2</sub>O<sub>3</sub> oxide layer on the surface of the particles, the ignition temperature of which in an oxygen-containing medium is 1500–1950 K, regardless of the particle size. Moreover, the energy release from boron particles is significantly limited by the diffusion of elemental boron through the molten shell of the oxide layer, as well as during combustion in gases containing hydrogen, due to the formation of metastable HBO<sub>2</sub> particles [2]. The removal of the oxide layer occurs by evaporation, which is a slow process, accounting for a significant proportion of the total particle burning time. All these difficulties limit the scope of boron. The presence of an oxide layer on the surface of the nanodispersion of particles is due to technological methods of their preparation.

In general, methods of producing elemental boron nanoparticles implemented in technological practice are the methods of chemical deposition from the gas phase or methods of CDGP. There are many ways to implement CDGP, that are fundamentally different among themselves in the ways of launching chemical reactions and the conditions of the process. For example, there are electron-beam, laser, plasma, arc evaporation methods, or combinations thereof [3].

The exclusive advantages of the CDGP methods are tonnage, high yield of the target product (close to 98%) and high purity of elemental boron (99.6–99.9%).

One of the disadvantages of the above methods of obtaining is the fact that such methods allow to obtain crystalline powders of elemental boron, in which micron-sized particles

predominate in the powder as a result of the sintering process. Also on the surface of the particles obtained using the CDGP method, there is a layer of boron oxide, which makes it difficult to use them as an additive to biofuels.

Ultrasonic technology is a new approach to the improvement of the implemented methods of deposition from the gas phase, namely the dispersion of the sintered powder with micron particles to nanoscale. The proposed method is economical and technically easy to implement. By using this method it is possible to obtain a sufficient amount of boron nanoparticles within a short period of time. With ultrasonic dispersion, acoustic cavitation is the main factor of destruction, which is an effective energy concentration mechanism. The total energy of a collapsing bubble has a small energy value, however, the spherical convergence of the bubble leads to the formation of very large local energy densities, and therefore, high temperatures (5000–25000 K) and pressures (100 MPa) [4]. Under the influence of such loads, micron boron is crushed.

The line of dispersions of particles less than 100 nm was obtained with the use of prolonged exposure to ultrasound and cascade fractionation. When ultrasound was applied to the 80 nm fraction, particles smaller than 20 nm were obtained, plus there was a tendency to their decrease in size and their ovalization (Table 1). Data on the characteristics and parameters of the developed method of ultrasonic dispersion for boron nanoparticles, namely – data from dynamic light scattering devices and an electron microscope are presented in Table 1.

Table 1. Parameters and conditions for obtaining nanoparticles of elemental boron by method of ultrasonic dispersion.

| №  | Concentration of boron nanoparticles, mg/ml H <sub>2</sub> O | Particle size BEFORE ultrasonic treatment, nm | Ultrasonic processing time, min | Particle shape AFTER ultrasonic treatment | The size diapason of the obtained nanoparticles, nm |
|--|--|---|---------------------------------|---|---|
| Crystal elemental boron                    |  |   |                                 |   |   |
| Ultrasonic generator power – 0.6 ± 0.03 kW |  |   |                                 |   |   |
| 1  | 30 mg/ml H <sub>2</sub> O                                    | Diapason:<br>1000–2000                        | 25–30                           | Irregularly shaped<br>with sharp edges    | 350±100   |
| 2  |  |   | 50–60                           |   | 200±50  |
| 3  |  |   | 80–90                           |   | 80±10   |
| 4  |  |   | 115–120                         |   | 50±20   |
| 5  |  |   | 250–270                         | Spherical                                 | 20±15   |
| 6  |  |   | 300–320                         |   | 5±3   |

To assess the effect of ultrasound on the crystal structure of elemental boron, X-ray structural analysis was used. Under the influence of ultrasound, the monolithic crystal structures degrade over the crystallographic planes of their contact, i.e. the dispersion of the original micron boron powder increases to nanoscale size. The initial sample of boron on the diffractogram revealed a peak at 28°, which corresponds to crystalline boron oxide on the surface of microdispersion. Upon long-term treatment of micron boron with ultrasound, on the diffractogram of the nanosample the boron oxide reflex was not detected. Thus, the composition of the boron nanoparticles powder is itself a pure elemental boron.

Thus, ultrasonic dispersion allows obtaining of nanodispersed boron particles with a size less than 20 nm. During the process of ultrasonic treatment, their monodispersity increases and the oxide layer disappears from the surface, which leads to increase in the potential of their use as a fuel additive. At the same time, elemental boron nanoparticles obtained by the new technological method represent promising material for further scientific research in various fields of technology.

This work was supported by Russian Science Foundation (grant no. 19-72-30005). Electron Microscopy Studies were performed with the financial support from Ministry of Science and Higher Education of the Russian Federation. X-ray analysis and dynamic light scattering research were performed with the financial support from Ministry of Science and Higher Education of the Russian Federation using the equipment of Collaborative Access Center «Center for Polymer Research» of ISPM RAS.

1. D. Sandaram, V. Young, V.E. Zarko, Combustion of aluminum nanoparticles (review), *Russ. J. Phys. Combust. Explos.*, 2015, vol. 55, no. 2, pp. 37–63.
2. S. Karmakar, N. Wang, S. Acharya, K. Dooley, Effect of rare-earth oxide catalyst on the ignition and combustion characteristics of boron nanoparticles, *US J. Combust. Flame*, 2013, vol. 3, no. 6, pp. 1–11.
3. A.A. Lipeshev, A.V. Ushakov, I.V. Karpov, Plasma-chemical synthesis of nanodispersed powders and polymer nanocomposites, Russ. Sib. Feder. University, 2012, 328 p.
4. O.L. Khasanov, E.S. Dvilis, V.V. Polisadova, Effects of powerful ultrasound effects on the structure and properties of nanomaterials, Tomsk: Publishing house of Tomsk Polytechnic University, 2008, 139 p.

PREPARATION OF Mo–Cu PSEUDOALLOY FROM  $\text{CuMoO}_4$  PRECURSOR BY COMBINING SOL-GEL METHOD AND SHSH. Kirakosyan<sup>\*a</sup> and K. Nazaretyan<sup>a</sup><sup>a</sup>Nalbandyan Institute of Chemical Physics NAS RA, Yerevan, 0014 Armenia

\*e-mail: hasmik-kirakosyan@list.ru

DOI: 10.24411/9999-0014A-2019-10060

Mo–Cu pseudoalloys successfully combine the both metal's properties, such as high thermal and electrical conductivity, low and alterable thermal expansion coefficient, low weight and well high-temperature behavior rendering their widespread application in heavy-duty electronic contacts, welding electrodes, vacuum technology, military fields, aeronautics and some other advanced fields [1]. The Mo–Cu alloy has lower density than other Cu-refractory metal alloys and more suitable for spaceflight and navigation industries. Mo–Cu alloys are also easy to machine. Due to the controllable expansion of composite matrix, superior material stability and uniform thermal expansion characteristics, Mo–Cu alloys may withstand to critical thermal conditions as heat sink materials and spreaders, portable apparatus, rocket parts, etc. [2].

There are many methods for the synthesis of Mo–Cu pseudoalloys (mechanical alloying, mechano-chemical synthesis, electroless plating of appropriate salts, gel reduction, reduction with hydrogen from oxygenous compounds of copper and molybdenum, etc). The energy and time consumption, low efficiency and low productivity, the complexity of regulation of homogeneity, microstructure and porosity necessitates to bring a new and reliable pathway for powder synthesis.

In this work it was suggested a new simple and effective approach based on energy-saving combustion synthesis processes for the preparation of Mo–Cu pseudoalloys [3, 4]. The advantage of the method to prepare Mo–Cu is that firstly copper molybdate was obtained as a result of sol-gel process. In  $\text{CuMoO}_4$  molybdenum and copper are chemically bonded in the same crystal structure. The formation of a homogeneous composite is more preferable when salt is reduced, rather than metal oxides. By changing the ratios of the reducers (Mg, C) at stage II will provide the ability to control the thermal regime of the combustion process and therefore, the phase composition and microstructure of the product. For preparation of  $\text{CuMoO}_4$  precursor  $(\text{NH}_4)_6\text{Mo}_7\text{O}_{24}\cdot 4\text{H}_2\text{O}$  and  $\text{Cu}(\text{NO}_3)_2$  were used as initial reagents, and citric acid (CA) as complexing and reducing agent. A citric acid solution was added to a stoichiometric solution of ammonium molybdate and copper salt ( $\text{Mo}/\text{Cu} = 1$ ) in a proportion  $\text{CA}/\text{Cu}^{2+} = 3$ . Stoichiometric quantities of these substances were initially dissolved in deionized water to obtain saturated solutions and then the solutions were mixed. The obtained blue transparent solution was evaporated in a glassy beaker on the electric fryer at  $80^\circ\text{C}$  up to the gel state. The gel was dried at  $120^\circ\text{C}$  for 24 h, then pre-calcined at  $420^\circ\text{C}$  for 2 h. The procedure is shown in schematic diagram (Fig. 1). The composition of the sol-gel product was ascertained by the XRD and FT-IR analyses (Fig. 2). After the drying process, the sol-gel product was mixed with magnesium and carbon in a ceramic mortar and prepared cylindrical samples were ignited with an electrically heated tungsten coil in nitrogen atmosphere. Combustion parameters were measured by thermocouples: the results are presented in Fig. 3. Based on our previous experience with similar system [5], magnesium amount was changed from 1.2 to 1.4 mol. The addition of even 0.5 mol amount of carbon (2.3 wt %) in the  $\text{CuMoO}_4 + 1.2\text{Mg}$  green mixture, causes combustion velocity to decrease more than 5 times. The further increase of carbon amount continues to reduce the combustion velocity. In the entire range of change of carbon amount, the temperature decreases gradually.

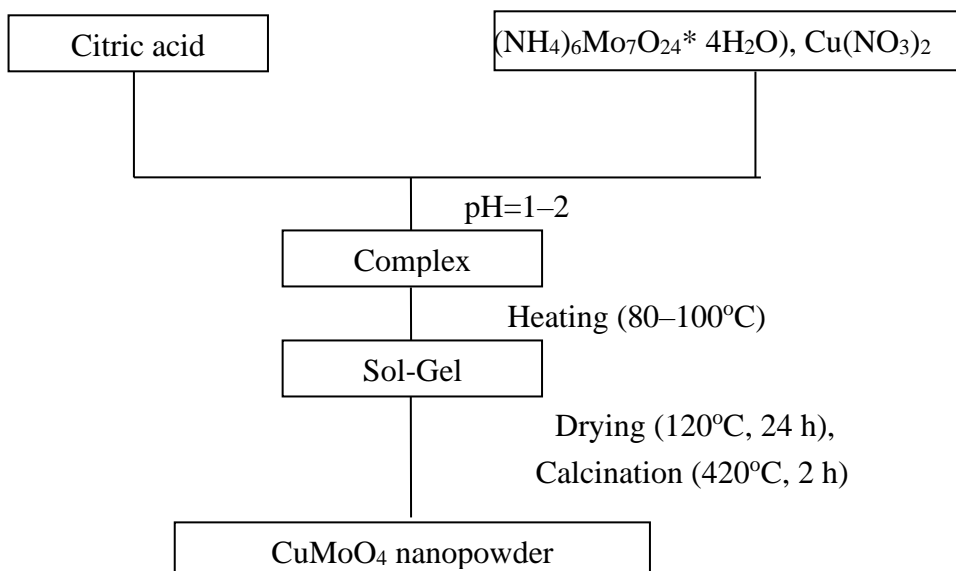


Fig. 1. Schematic diagram for preparation of  $\text{CuMoO}_4$  by sol-gel method.

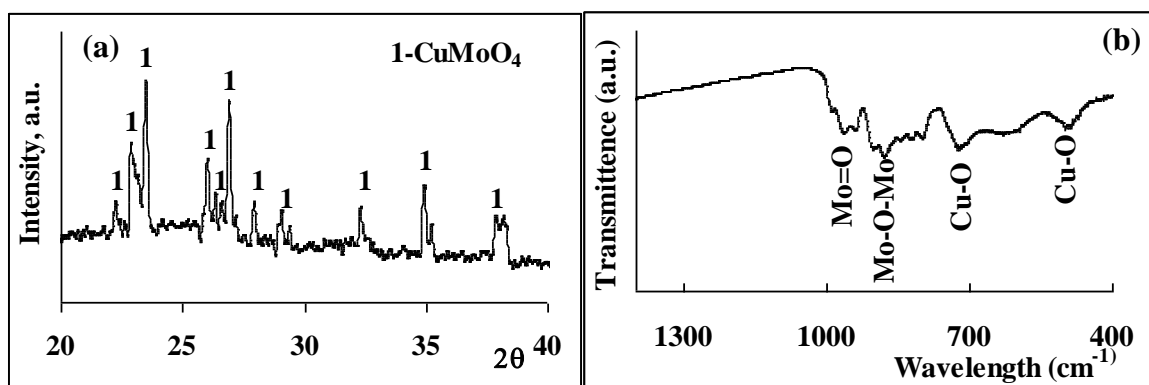


Fig. 2. (a) XRD pattern and (b) FT-IR spectrum of  $\text{CuMoO}_4$  obtained by sol-gel method.

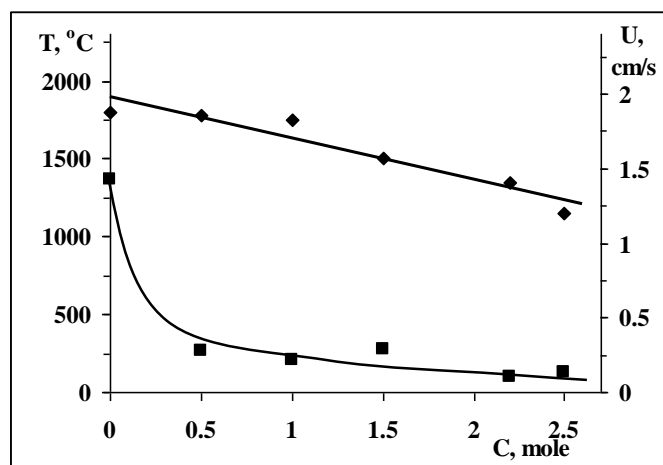


Fig. 3. Combustion temperature and velocity vs carbon amount for the  $\text{CuMoO}_4\text{-1.2Mg-xC}$  system,  $P = 0.3$  MPa.

Combustion products were subjected to XRD examinations (Fig. 4). It was revealed that at small amount of carbon only the reduction of copper occurs ( $\text{MoO}_2\cdot\text{MgO}$ , Cu). The increase in carbon amount leads to reduction of molybdenum. However, 1.2 mol of magnesium was insufficient for the complete reduction of the both metals in whole range of change of carbon amount. Further experiments were conducted with the mixtures containing 1.4 mol Mg. Based



on the results of combustion experiments and XRD analysis of the combustion products the mixture containing 1.4 moles magnesium and 2.7 moles carbon was sufficient for the complete reduction of metals and were selected as optimal to obtain Mo–Cu composite powders.

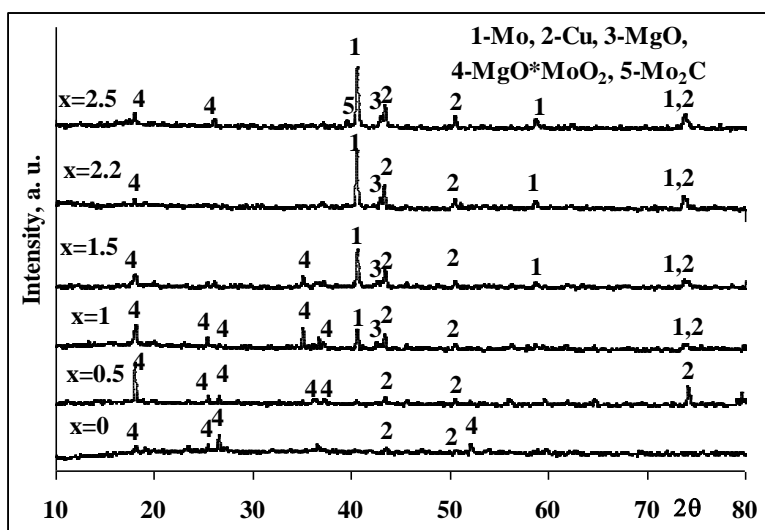


Fig. 4. XRD patterns of combustion products of the  $\text{CuMoO}_4-1.2\text{Mg}-x\text{C}$  mixtures.

After acid treatment (10% HCl) and removal of magnesia, the XRD pattern comprises only characteristic lines of molybdenum and copper (Fig. 5).

The presented approach outlines a pathway for the preparation of Mo–Cu nanocomposite by the combining energy-efficient sol-gel method and self-propagating high-temperature synthesis.

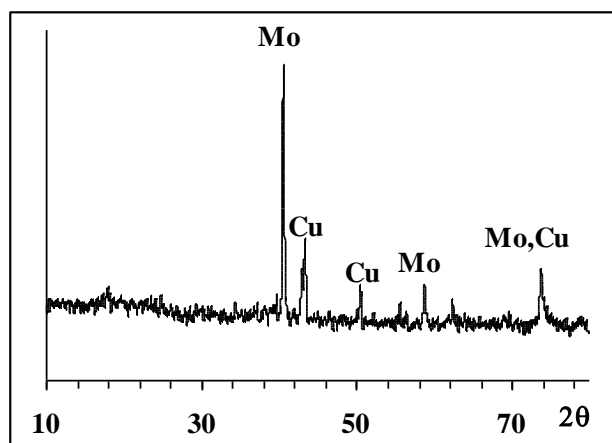


Fig. 5. XRD pattern of combustion products of the  $\text{CuMoO}_4-1.4\text{Mg}-2.7\text{C}$  mixture.

This work was supported by the Enterprise Incubator Foundation PhD Support Program (Hasmik Kirakosyan).

1. G. Chen, G. Wu, L. Jiang, D. Zhu, D. Sun, Microstructure and mechanical properties of high densification Mo/Cu composites, *Key Eng. Mater.*, 2007, pp. 2883–2886.
2. B.Q. Hu, P.K. Bai, J. Cheng, Preparation of low quality fraction Mo–Cu alloy by mechanical alloying process, *J. Funct. Mater.*, 2010, vol. 41, no. 5, pp. 837–843.
3. Y. Li, D. Wang, A. Sun, Preparation and characterization of Mo–Cu nanocomposite powders by chemical liquid reduction process. *J Cent South Univ*, 2013, vol. 20, pp. 587–591.

4. M.K. Zakaryan, H.V. Kirakosyan, L.S. Abovyan, S.V. Aydinyan, S.L. Kharatyan, Magnesian-carbothermal reduction of  $\text{CuWO}_4/\text{MeO}$  nanostructured precursors & synthesis of W/Cu composite materials, *Chem. J. Armenia*, 2017, vol. 70, no. 4, pp 450–461.
5. T. Minasyan, H. Kirakosyan, S. Aydinyan, L. Liu, S. Kharatyan, I. Hussainova, Mo–Cu pseudoalloys by combustion synthesis and spark plasma sintering, *J. Mater. Sci.*, 2018, vol. 53, pp. 1–11.

## PLASMA-CHEMICAL ACTIVATION OF SHS IN EXTERNAL ELECTRIC FIELDS

A. I. Kirdyashkin\*<sup>a</sup> and R. M. Gabbasov<sup>a</sup><sup>a</sup>Tomsk Scientific Center SB RAS, Tomsk, 634055 Russia

\*e-mail: kirdyashkin\_a@mail.ru

DOI: 10.24411/9999-0014A-2019-10061

Application of external electric field refers to known methods for controlling the combustion dynamics of gas and condensed systems. Field effects are provided by its (i) thermal and (ii) nonthermal factors: (i) the temperature acceleration due to Joule heating and (ii) direct effect on kinetics of heat and mass transfer and chemical reactions [1]. Nonthermal factors in gas systems are realizing during electric discharge in flame through an ionic wind and the generation of active chemical centers (radicals, ions, etc.).

For the combustion synthesis of inorganic materials, the thermal fields effects are caused by the electric current through bound particles skeleton of the green components and reaction products [2, 3]. In order to realize this effect in practice, it is required the Joule heading up to  $100\div 300\text{ W/cm}^3$ . Last condition is technically difficult to perform in a large volume of a mixture. It is important to implement less energy-consuming nonthermal field factors which are not fully studied for combustion synthesis.

The purpose of this work is to investigate nonthermal field effects on the ignition and combustion of metal-containing powder systems by the examples Ni–Al and Mo–Ti–B mixtures.

*Research methods and materials*

Powders Ni, Al, Mo, B, and Ti presented in Table 1 were used as initial reagents. Composition of the mixtures Ni + (13.3÷31.5) wt % Al and Mo + 12.1 wt % B + 6.5 wt % Ti was chosen in such a way to conduct the exothermic synthesis of condensed nickel aluminides, molybdenum and titanium borides, according to the brutto-reaction schemes:  $\text{Ni} + \alpha\text{Al} \rightarrow 0.5(3\alpha-1)\text{NiAl} + 0.5(1-\alpha)\text{Ni}_3\text{Al}$ ;  $\text{Mo} + \beta\text{B} + \gamma\text{Ti} \rightarrow \text{MoB} + \gamma\text{TiB}_2$ , where  $\alpha = 0.33\div 1.00$ ,  $\beta = 1.32$ ,  $\gamma = 0.16$  are the mole stoichiometric coefficients.

The mixtures were pressed into cylindrical briquettes ( $d = 20\text{ mm}$ ,  $h = 10\text{ mm}$ ) or placed inside the quartz tube ( $d = 11\text{ mm}$ ,  $h = 40\text{ mm}$ ). The relative density of the mixtures was  $\rho_r = 0.20\div 0.55$ . Field effects were studied in the processes described below.

A. Propagation of combustion in mixtures inside a quartz tube (Fig. 1a). From various sources, constant, alternating and unipolar pulse voltages were applied to the ends of the sample. Constant voltage:  $0.1\div 4.5\text{ kV}$ . Alternating voltage  $0.5\div 4.5\text{ kV}$ , frequency of  $1\div 200\text{ kHz}$ . Pulse voltage: pulse amplitude  $1\div 25\text{ kV}$ , pulse duration  $0.005\div 3\ \mu\text{s}$  and pulse frequency  $1\text{ kHz}$ . The constant and alternating voltage were applied through the circuit: «sample - ballast resistance - reference resistance». Pulse voltage was applied directly to the mixture. The dynamics of the combustion was controlled with a video camera. Gas medium: Ar, 100 kPa.

B. Ignition of the pressed powder compact with an electro-spiral through a gap of 3 mm (Fig. 1b). The direct voltage of  $\pm 650\text{ V}$  was applied to the electrical circuit «sample - spiral - ballast resistance - reference resistance» with the realization of self-sustained glow discharge between the spiral and the sample. The temperature dynamics was controlled by the C-type thermocouple. The latter was pressed into the near-surface layer of the sample. Gas medium: Ar, 100 Pa.

C. Ignition of one briquette of a mixture on another - translation of burning through a gap of

2.5 mm (Fig. 1c). The direct voltage of  $\pm 100\div 500$  V was applied to the electrical circuit «sample 1 - sample 2 - ballast resistance - reference resistance». Gas medium: Ar, 100 Pa.

Voltage ( $V$ ), current ( $i$ ) in electrical circuits was measured by the voltage across the reference resistances. In all cases, except for using pulse voltage, current was specially limited within 20 mA by selecting appropriate ballast resistance. For the case A, the average rate of temperature rise did not exceed 2.5 K/s. Taking into account the heat capacity of the substances and the volume of the samples, this fact means that Joule heating is within  $10 \text{ W/cm}^3$ .

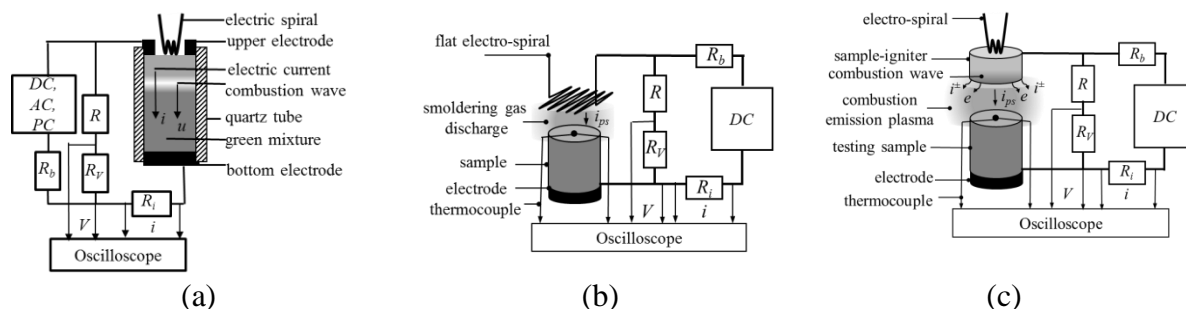


Fig. 1. Experimental setup for the study of non-thermal effects of electric fields on combustion (a) and ignition (b, c) of powder systems Ni–Al, Ti–Mo–B.

DC, AC, PC are sources of constant, alternating and pulsed voltage, respectively;  $R_s$ ,  $R_v$  are reference resistances.  $R_b = 200\div 230 \text{ k}\Omega$  is the ballast resistance.

Table 1. Mixture components.

| Powders | Trademark | $C$ , wt.% | $d$ , $\mu\text{m}$ |
|---------|-----------|------------|---------------------|
| Ni      | PNK-L5    | 99.9       | < 20                |
| Al      | ASD-4     | 99.7       | < 10                |
| Al      | ALEX      | 96.5       | 0.1                 |
| Mo      | MP        | 99.6       | < 5                 |
| B       | 99A       | 99.5       | < 0.5               |
| Ti      | PTM1      | 99,0       | < 45                |

$C$  is the component concentration;  $d$  is the particle diameter.

### Results and Discussion

Processes A. According to the data obtained, direct electric field has no effect on the dynamics of combustion. In alternating and pulse field, an average combustion rate may increase by a factor of two, with the effect amplified with increasing amplitude and frequency of oscillations and decreasing the duration of pulses of applied voltage. The effect of the field decreases with increasing a relative density and electrical conductivity of the mixture, increases together with the dispersity of initial particles, and depends nonlinearly on the chemical composition of samples. During combustion, the effect of the field has a cumulative nature. Electric field, starting from the ignition of the mixture, accelerates gradually the movement of reaction wave. Switching off the voltage during combustion leads to the monotonous deceleration of wave to its initial value. Preliminary treatment of mixtures by applying voltage for  $10\div 15$  s (maximum combustion duration for the samples used), followed by switching off voltage before ignition does not have a significant effect on combustion (Fig. 2). The effect of the field increases the degree of chemical conversions of condensed combustion products (Table 2).

Processes B. When a potential of the sample is positive, the ignition temperature decreases by 20%, and the ignition delay time decreases by 30% in comparison with ignition without voltage. For a negative potential, an increase in these parameters is observed (Table 3).

Processes C. The voltage in the gas layer between the samples of Ni + 31.5 wt % Al leads to the discharge induced by emissive combustion plasma of the sample 1. This is confirmed by the occurrence of current in the electrical circuit in the time interval between the completion of

combustion in the sample 1 and the ignition of the sample 2. The supply of a positive potential to sample 2 makes it possible to reduce the delay time of its ignition by more than an order of magnitude. Negative potential provides less effect (Table 4).

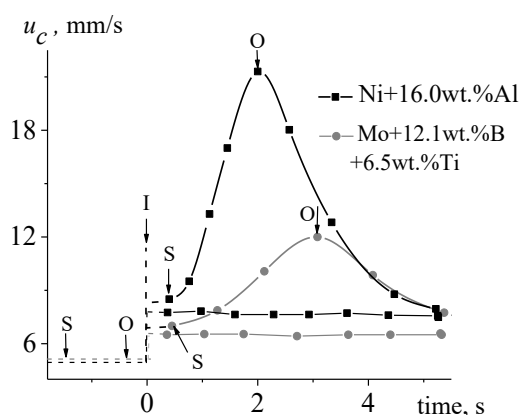


Fig. 2. Changes in the current combustion rate ( $u_c$ ) when alternating voltage is switch on and off at various times.  $V = 4\text{kV}$ ,  $125\text{kHz}$ . S is the voltage switching-on; O is the voltage outage; I is the ignition.

Table 2. Phase composition of combustion products.

| Green mixtures         | Normal conditions                       | Alternating voltage:<br>4 kV, 125 kHz       |
|------------------------|---|---|
| Ni+14wt.%Al            | Ni, NiAl                                | Ni <sub>3</sub> Al, Ni↓, NiAl↓              |
| Mo+12.1wt.%B+6.5wt.%Ti | Mo, MoB, Ti <sub>3</sub> B <sub>4</sub> | Mo, MoB ↑, Ti <sub>3</sub> B <sub>4</sub> ↓ |

Table 3. The effect of a constant electric field on the ignition of a Ni + 31.5 wt % Al mixture from an electrospiral. Al–ASD4,  $\rho_r = 0.52$ .

| Voltage, V | Power of electric spiral, W |             |           |           |           |           |
|------------|-----------------------------|-------------|-----------|-----------|-----------|-----------|
|            | 0                           |             | 1000      |           | 2200      |           |
|            | $T_i$ , K                   | $t_i$ , s   | $T_i$ , K | $t_i$ , s | $T_i$ , K | $t_i$ , s |
| 0          | –                           | –           | 1033      | 6.4       | 1183      | 2.1       |
| 650        | 448                         | 44          | 873       | 4.5       | 923       | 1.5       |
| -650       | no ignition                 | no ignition | 1343      | 9.3       | 1433      | 3.0       |

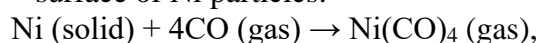
$t_i$  is the ignition delay time;  $T_i$  is the ignition temperature

Table 4. The effect of a constant electric field on the ignition of one sample of a mixture of Ni + 31.5 wt % Al from another. Al–ASD4,  $\rho_r = 0.52$

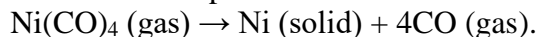
| Voltage, V | 0   | +120 | +140 | +200 | -400 |
|------------|-----|------|------|------|------|
| $t_i$ , s  | 1.7 | 1.0  | 0.6  | 0.1  | 1.0  |

The field effect on the ignition of the mixture with a positive potential is explained by the acceleration of reactions on the surface of Ni and Al powders exposed to negatively charged plasma particles of gas discharge (electrons and negative ions). This effect is known in a wide range of topochemical reactions on the solid surface of various metals that form volatile products [4]. The structure of the Ni + 31.5 wt % Al mixture which formed after a short treatment of the sample with the radiant heat of electric spiral was studied. It was found that for the sample with a positive potential, thin Ni coatings were formed on the surface of Al particles. Probable cause of Ni deposition is topochemical reactions induced by discharge:

– surface of Ni particles:



– surface of Al particles:



The source of CO is impurities of the initial Ni powder. The described processes provide the gas-phase transport of Ni and, as a consequence, the acceleration of chemical interaction between Ni and Al powders.

A similar plasma-chemical effect, apparently, accelerates combustion in alternating and pulse fields. This effect is caused by gas discharge in the porous space of the mixture, which induces the topochemical reactions before the combustion wave. The condition for discharge is met for highly porous mixtures in the case of comparable values of the specific electrical conductivity for the bound skeleton from mixture particles and plasma inside pores. Electro-transport through the porous space of the mixture confirms the presence of asymmetric electric current in the sample during combustion. Such current is typical for gas plasma. The increase in the combustion rate together with the frequency of the voltage is explained by improvement in the uniformity of discharge in the porous space. Diffuse discharge in gases takes place at a pressure of 100 kPa and, as a rule, at sufficiently high frequency and the short duration of pulsations of the electric fields [1].

*Concluding Remarks.*

- Gas-discharge plasma in direct electric field with the Joule heading up to 5 W/cm<sup>2</sup> decreases the ignition temperature by 20÷24% and significantly reduces the ignition delay time of the Ni–Al mixture.

- Alternating and pulse electric fields with Joule heating of less than 10 W/cm<sup>3</sup> accelerate the combustion of highly porous Ni–Al, Mo–B–Ti powders mixture up to 250% and increase the degree of chemical conversions in combustion products.

- Changes in the characteristics of combustion are explained by the plasma-chemical effect of gas discharge in the peripheral porous space of powder mixtures. The effect provides the acceleration of gas-phase transport of the mixture components due to activation of the reactions on the particles surface.

This work was carried out within the state task for TSC SB RAS (no. 0365-2019-0004) and supported by RFBR (project no. 18-48-700037).

1. S.M. Starikovskaia, Plasma assisted ignition and combustion, *J. Phys. D: Appl. Phys.*, 2006, vol. 39, no. 16, pp. 265–299.
2. I.A. Filimonov, N. Kidin, Thermal Effect of an External Electric Field, *Int. J. Self-Propag. High-Temp. Synth.*, 2004, vol. 13, no. 4, pp. 263–284.
3. Z.A. Munir, Field effects in Self-propagating solid-state synthesis reactions, *Solid State Ionics*, 1997, vol. 101, pp. 991–1001.
4. A.N. Magunov. Heat transfer of a nonequilibrium plasma with a surface – in Russian, 2005, p. 312.

## THE Cr–B–C–N FILMS PRODUCED BY PULSED CATHODE-ARC EVAPORATION (P-CAE) OF THE CrB<sub>2</sub> ROD MANUFACTURED USING SHS-COMPACTING

**Ph. V. Kiryukhantsev-Korneev**

National University of Science and Technology MISiS, Moscow, 119049 Russia  
e-mail: kiruhancev-korneev@yandex.ru

DOI: 10.24411/9999-0014A-2019-10062

Hard films in Cr–B–C–N system were deposited by pulsed cathode-arc evaporation (P-CAE) [1] of the CrB<sub>2</sub> target in Ar, N<sub>2</sub>, and C<sub>2</sub>H<sub>4</sub>. The target was manufactured by means of self-propagating high-temperature synthesis. The structure, chemical and phase composition of films were studied by high resolution transmission and scanning electron microscopy, X-ray diffraction, X-ray photoelectron spectroscopy, Raman spectroscopy, energy-dispersive analysis, and glow discharge optical emission spectroscopy. The films were characterised in terms of their hardness, elastic modulus, elastic recovery, friction coefficient, and wear rate. To evaluate the oxidation resistance, diffusion-barrier properties, and thermal stability, films were annealed in air atmosphere at temperatures between 600 and 1000°C.

The coatings had a structure typical for the CAE deposited coatings, with a significant proportion of condensed droplet phase, but the formation of unfavorable columnar morphology was eliminated. The coatings contained crystallites of h-CrB<sub>2</sub> and c-CrN phases, as well as a large amount of amorphous phase, the composition of which varied depending on the type of working medium. The coatings obtained in argon showed the highest hardness of 12 GPa, while the coatings obtained in C<sub>2</sub>H<sub>4</sub> medium were characterized by the highest elastic-plastic properties (72% of elastic recovery). The coefficient of friction of coatings applied in Ar, N<sub>2</sub>, and C<sub>2</sub>H<sub>4</sub> was 0.7, 0.4 and 0.3, respectively. The phase of diamond-like carbon in the latter case led to a decrease in the coefficient of friction due to the high proportion of sp<sup>2</sup>-bound carbon, which acts as a solid lubricant. Coatings of optimal composition had high resistance to high-temperature oxidation in the temperature range of 600–1000°C. At high temperatures, the oxidation process was accompanied by intense diffusion of boron atoms deep into the substrate.

This research was funded by the Ministry of Education and Science of Russia (State Assignment no. 11.7172.2017/8.9).

1. Ph.V. Kiryukhantsev-Korneev, A.N. Sheveyko, K.A. Kuptsov, A.V. Novikov, D.V. Shtansk, Ti–Cr–B–N coatings prepared by pulsed cathodic-arc evaporation of ceramic TiCrB target produced by SHS, *Prot. Met. Phys. Chem. Surf.*, 2013, vol. 49, no. 6, pp. 677–681.

## STRUCTURE AND PROPERTIES OF h-ZrB<sub>2</sub> AND h-ZrB<sub>2</sub>/a-BN COATINGS DEPOSITED BY MAGNETRON SPUTTERING OF THE SHS-TARGETS

Ph. V. Kiryukhantsev-Korneev<sup>\*a</sup>, A. Kozlova<sup>a</sup>, N. S. Kozlova<sup>a</sup>, and E. A. Levashov<sup>a</sup>

<sup>a</sup>National University of Science and Technology MISiS, Moscow, 119049 Russia

\*e-mail: kiruhancev-korneev@yandex.ru

DOI: 10.24411/9999-0014A-2019-10063

Hard Zr–B–(N) films were deposited by DC magnetron sputtering of the ZrB<sub>2</sub> target in Ar + N<sub>2</sub> (0, 10, 15, 25, and 100% N<sub>2</sub>). The target was manufactured by means of self-propagating high-temperature synthesis. The structure, chemical and phase composition of films were studied by high resolution transmission and scanning electron microscopy, X-ray diffraction, X-ray photoelectron spectroscopy, Raman and infrared spectroscopy, energy-dispersive analysis, and glow discharge optical emission spectroscopy. The films were characterised in terms of their hardness, elastic modulus, elastic recovery, resistance to cyclic impact loading, friction coefficient, and wear rate. Optical and electrical properties of films were also examined. To evaluate the short- and long-time oxidation resistance, diffusion-barrier properties, resistance to the thermo-cycling, and thermal stability, films were annealed in air atmosphere at temperatures between 500 and 800°C.

Results obtained show that films deposited at low nitrogen partial pressure consist of nanocrystallites of hexagonal ZrB<sub>2</sub>-phase, 8 nm in size and amorphous regions. N-rich films exhibit fully amorphous structure. Specific optical properties observed for these Zr–B–(N) coatings. The refraction index, coefficients of transmittance and reflectance were measured for wavelength diapason from 200 to 2500 nm. The maximum hardness of 37 GPa, Young's modulus of 400 GPa, and elastic recovery of 73% were determined for films deposited in Ar. The addition of nitrogen significantly increased wear resistance in sliding and impact conditions as well as optical transparency. Films showed good oxidation resistance at 600°C. Mechanical properties remained stable (37–41 GPa) up to 1200°C.

The work was supported by the Russian Foundation for Basic Research (Agreement no. 19-08-00187/19).

1. I.V. Iatsyuk, M.V. Lemesheva, Ph.V. Kiryukhantsev-Korneev, E.A. Levashov, Structure and properties of ZrB<sub>2</sub>, ZrSiB and ZrAlSiB cathode materials and coatings obtained by their magnetron sputtering, *IOP Conf. Ser.: Mater. Sci. Eng.*, 2018, vol. 347, 012028.
2. Ph.V. Kiryukhantsev-Korneev, M.V. Lemesheva, N.V. Shvyndina, E.A. Levashov, A.Yu. Potanin, Structure, mechanical properties, and oxidation resistance of ZrB<sub>2</sub>, ZrSiB, and ZrSiB/SiBC coatings, *Prot. Met. Phys. Chem. Surf.*, 2018, vol. 54, no. 6, pp. 1147–1156.



## HIGH-TEMPERATURE Mo–(Zr,Hf)–Si–B COATINGS DEPOSITED USING SHS-PRECURSORS

Ph. V. Kiryukhantsev-Korneev<sup>\*a</sup>, T. A. Sviridova<sup>a</sup>, N. V. Shvindina<sup>a</sup>,  
and E. A. Levashov<sup>a</sup>

<sup>a</sup>National University of Science and Technology MISiS, Moscow, 119049 Russia

\*e-mail: kiruhancev-korneev@yandex.ru

DOI: 10.24411/9999-0014A-2019-10064

Nanocomposite Mo–Si–B, Mo–Zr–Si–B, and Mo–Hf–Si–B coatings were deposited by direct current (DCMS) and pulsed magnetron sputtering (PMS) of the MoSiB, MoZrSiB, and MoHfSiB composite targets, correspondingly. Targets were fabricated via hot pressing of the precursors by the self-propagating high-temperature synthesis method. The structure, element and phase composition of coatings were studied by means of scanning and transmission electron microscopy, X-ray diffraction, X-ray photoelectron spectroscopy, energy-dispersive spectroscopy, Raman, and glow discharge optical emission spectroscopy. The films were characterised in terms of their adhesion, hardness, elastic modulus, elastic recovery, fatigue strength, and fracture toughness. To evaluate oxidation resistance, the coatings were annealed in air in the temperature range of 600–1500°C during different time expositions between 10 min and 5 h.

The results obtained demonstrate that the Mo–Si–B coatings possess higher hardness of 30 GPa, improved oxidation resistance and better thermal stability compared with their Mo–Zr–Si–B and Mo–Hf–Si–B counterparts. The 14 μm thick Mo–Si–B coatings were shown to withstand successfully oxidation during short-time exposure for 10 min at temperature as high as 1500°C due to the formation of protective silica scale. The oxidation of Mo–Hf–Si–B coatings was accompanied by the diffusion of hafnium to the coating surfaces and the formation of SiO<sub>2</sub>/HfO<sub>2</sub>/SiO<sub>2</sub> top-layer structure which were less protective against oxidation. Formation of Al<sub>2</sub>O<sub>3</sub>–SiO<sub>2</sub> and HfO<sub>2</sub> layers on the boundary with the substrate was also revealed in case of Mo–Hf–Si–B films. The complex layer structure SiO<sub>2</sub>/SiO<sub>2</sub> + ZrO<sub>2</sub>/MoZrSiB/SiO<sub>2</sub> was formed during high-temperature heating of MoZrSiB coatings. Other hand doping with hafnium and zirconium exclude the complete destruction of MoSiB coatings after annealing at 600°C due to silicide pest effect.

The work was supported by the Russian Science Foundation (Agreement no. 19-19-00117).

1. Ph.V. Kiryukhantsev-Korneev, I.V. Iatsyuk, N.V. Shvindina, E.A. Levashov, D.V. Shtansky, Comparative investigation of structure, mechanical properties, and oxidation resistance of Mo–Si–B and Mo–Al–Si–B coatings, *Corros. Sci.*, 2017, vol. 123, pp. 319–327.
2. Ph.V. Kiryukhantsev-Korneev, A.Yu. Potanin, Structure, mechanical properties, and oxidation resistance of MoSi<sub>2</sub>, MoSiB, and MoSiB/SiBC coatings, *Russ. J. Non-Ferr. Met.*, 2018, vol. 59, no. 6, pp. 698–708.
3. Ph.V. Kiryukhantsev-Korneev, A.V. Bondarev, D.V. Shtansky, E.A. Levashov, Structure and properties of nanocomposite Mo–Si–B–(N) coatings, *Prot. Met. Phys. Chem. Surf.*, 2015, vol. 51, no. 5, pp. 794–802.

# MECHANICAL ALLOYING WITH PARTIAL AMORPHIZATION OF Fe–Cr–Co–Ni–Mn MULTICOMPONENT POWDER MIXTURE AND ITS SPARK PLASMA SINTERING FOR COMPACT HIGH-ENTROPY MATERIAL PRODUCTION

N. A. Kochetov<sup>\*a</sup>, A. S. Rogachev<sup>a</sup>, A. S. Shchukin<sup>a</sup>, S. G. Vadchenko<sup>a</sup>,  
and I. D. Kovalev<sup>a</sup>

<sup>a</sup>Merzhanov Institute of Structural Macrokinetics and Materials Science, Russian Academy of Sciences, Chernogolovka, Moscow, 142432 Russia

\*e-mail: kolyan\_kochetov@mail.ru

DOI: 10.24411/9999-0014A-2019-10065

This paper presents the results of studying the mechanical alloying (MA) effect on the surface morphology, microstructure, and atomic-crystal structure of multicomponent Fe–Cr–Co–Ni–Mn powder mixture particles. The following materials were used as initial components: radio-engineering carbonyl iron powder (R-10 with an average particle size  $d = 3.5 \mu\text{m}$ ), nickel powder (NPE-1,  $d = 150 \mu\text{m}$ ), cobalt powder (PK-1u,  $d < 71 \mu\text{m}$ ), chromium powder (PH-1M,  $d < 125 \mu\text{m}$ ), and manganese powder (MR0,  $d < 400 \mu\text{m}$ ) were used. MA of the prepared mixture was carried out in the AGO-2 water-cooled mechanical activator using 9-mm steel balls with an acceleration of 90 g in air [1–3]. Alloying time varied between 5 and 90 min. The ratio of ball mass to the mass of the mixture was 20 : 1. XRD patterns of the initial and alloyed mixtures and the sample obtained by sintering were made using a DRON 3M diffractometer in  $\text{FeK}\alpha$  radiation in the range of angles  $2\theta = 30^\circ\div 100^\circ$ . The microstructure of mixtures and compact sample section after sintering was studied by scanning electron microscopy. It is found that no peaks of the initial components are present in the XRD pattern of the mixture after 90 min of mechanical activation, but there are peaks corresponding to the  $\gamma$ -Fe-based solid solution phase having a face-centered crystal lattice with an amorphous phase content increased by 20% (Fig. 1).

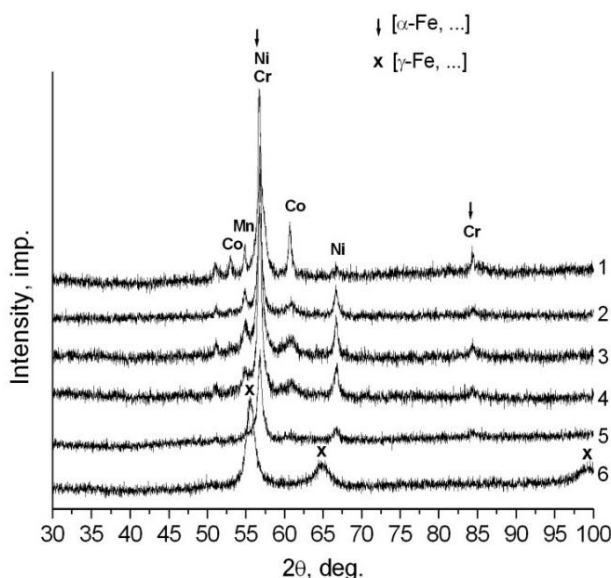


Fig. 1. XRD patterns of the initial mixture (1), and mixtures after MA: (2) for 5 min, (3) for 10 min, (4) for 15 min, (5) for 60 min, (6) for 90 min.

A compact single-phase material was obtained by spark plasma sintering at 800°C for 10 min from the mixture after 90-min alloying. Figures 2 and 3 show the XRD pattern and overall view of compact sample, respectively.

Material density was 7.49 kg/cm<sup>3</sup>, specific electrical resistivity was  $0.94 \pm 0.96 \cdot 10^{-6}$  Ohm·m, microhardness was 306–328 kg/mm<sup>2</sup>, and the phase was distributed uniformly throughout the volume (Fig. 4).

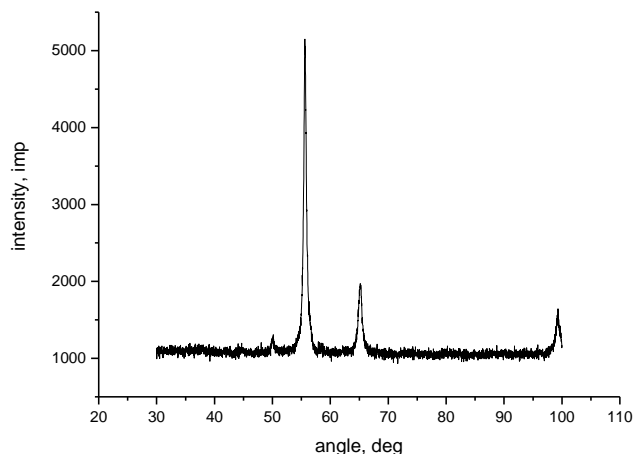


Fig. 2. XRD pattern of the compact material sample obtained by SPS from the mixture after 90 min alloying.

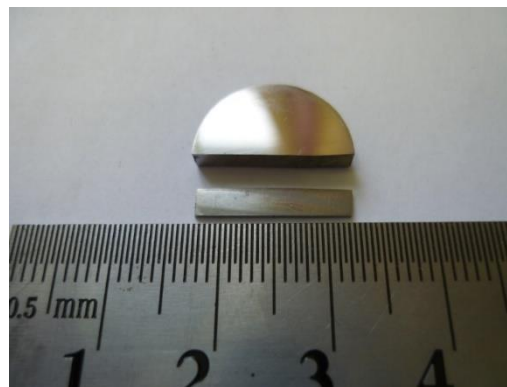


Fig. 3. Overall view of compact material sample obtained by SPS from the mixture after 90 min alloying.

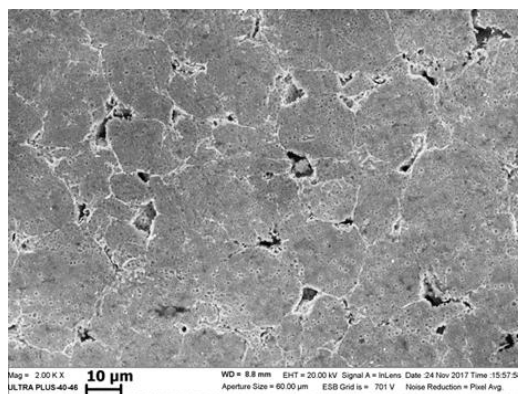


Fig. 4. Microstructure of compact sample section after etching in the HCl + HNO<sub>3</sub> mixture.

This work was supported by Russian Foundation for Basic Research, project no. 18-53-15006 (in the frames of International Russian–French Program RFBR-CNRS).

1. N.A. Kochetov, Combustion and characteristics of mechanically activated Ni + Al mixture: Effects of the weight and size of the milling balls, *Russ. J. Phys. Chem. B.*, 2016, vol. 10, no. 4, pp. 639–643.
2. I.D. Kovalev, N.A. Kochetov, Mechanical activation-induced structural changes in a 5Ti + 3Si mixture, *Inorg. Mater.*, 2017, vol. 53, no. 4, pp. 447–450.
3. N.A. Kochetov, S.G. Vadchenko, Mechanically activated SHS of NiAl: effect of Ni morphology and mechanoactivation conditions, *Int. J. Self-Propag. High-Temp. Synth.*, 2012, vol. 21, no. 1, pp. 55–58.

## PREPARATION OF CHROMIUM POWDER AND ITS COMPOSITE WITH TUNGSTEN FROM COMPLEX OXIDES BY MAGNESIUM VAPOURS REDUCTION

V. N. Kolosov<sup>\*a</sup>, M. N. Miroschnichenko<sup>a</sup>, and T. Yu. Prokhorova<sup>a</sup>

<sup>a</sup>Tananaev Institute of Chemistry - Subdivision of the Federal Research Centre Kola Science Centre of the Russian Academy of Sciences, Apatity, 184209 Russia

\*e-mail: tantal@chemy.kolasc.net.ru

DOI: 10.24411/9999-0014A-2019-10066

Chromium powder is widely used for the production of high-temperature cermets, which are composites having high electrical conductivity, thermal stability, and corrosion resistance [1]. Along with chromium, tungsten is also often regarded as a high-temperature structural material. However, its use is largely limited by susceptibility to oxidation at moderate temperatures. One of the effective ways to suppress the oxidation of tungsten at high temperatures is doping with chromium [2]. The use of chromium as an anticorrosive element is due to the fact that W–Cr alloy is an isomorphous system, and the Gibbs free energy of Cr<sub>2</sub>O<sub>3</sub> formation is more negative than the energy of WO<sub>3</sub> formation [3]. Therefore, chromium is preferentially oxidized as compared to tungsten in the W–Cr alloy. If chromium activity in the alloy is high enough, then a stoichiometric and continuous protective oxide film Cr<sub>2</sub>O<sub>3</sub> is formed. However, the consolidation of the alloy W–Cr is very difficult, because in this system there is a low interdiffusion of the components, even at high temperatures [4]. When sintering powders W and Cr, an activator element is usually added to their mixture. It allows to improve the sintering but has a negative impact on the performance properties of the material. At the same time, powders with high surface area provide a large driving force for sintering due to availability of abundant surface energy and results in dense compacts with significantly improved properties.

Production of chromium powder usually involves two main stages: metallothermic or electrolytic (extraction) reduction and mechanical milling [5, 6]. The milling process is energy-intensive and it also involves the risk of contamination of the powder by constituents from air and the mill tools material [7]. In addition, the crushed powder usually has a wide range of particle sizes. To obtain tungsten powders the most widely used method is hydrogen reduction. Thus, ammonium paratungstate or oxide WO<sub>3</sub> typically use as precursors. Reduction of precursors to metal includes several stages, which are performed at different temperatures. At the same time, the thermodynamic conditions of metal formation are very unfavorable, which necessitates the use of almost tenfold excess hydrogen during the reduction.

Previously, it was found that the reduction of double tungsten and molybdenum oxides containing MgO or CaO in their composition by magnesium vapor allows obtaining powders of these metals with a specific surface area of up to 20 m<sup>2</sup>·g<sup>-1</sup> [8, 9]. In this paper, the possibility of obtaining chromium powder and its composite with tungsten by reducing double Cr and W oxides with magnesium vapor is investigated.

As precursor for the preparation of chromium powder, chromite MgCr<sub>2</sub>O<sub>4</sub> was used. For comparison, Cr<sub>2</sub>O<sub>3</sub> oxide was reduced under similar conditions. To obtain a chromium–tungsten composite, a mixture of double CaCrO<sub>4</sub>–CaWO<sub>4</sub> oxides was used. The process occurred under an atmosphere of magnesium vapor and argon. A container with magnesium was mounted on the bottom of a reaction vessel. Weighed amounts (5 g) of precursor were loaded into metallic crucibles, which were placed over the magnesium-containing container. A shield was placed over the crucibles. The separation between the surface of the precursor and the shield was 27–30 mm. The assembly was mounted in stainless

steel retort, which was hermetically sealed, pumped down, filled with an inert gas, and heated to a required temperature. The reaction vessel was kept closed to avoid magnesium losses. The reduction process was in the temperature range 700–800°C under a residual argon pressure in the range of 5–15 kPa. The apparatus, methods of synthesis of double oxides and reduction are basically similar to those used earlier [8, 10]. The phase composition of the powders was determined by X-ray diffraction analysis using a Shimadzu XRD-6000 X-ray diffractometer ( $\text{CuK}\alpha$  radiation). The specific surface area and porosity of the powders were determined by BET and BJH measurements using a TriStar II 3020 VI.03 analyzer. The study of the morphology of the powders was carried out using a SEM LEO 420 scanning electron microscope. The reduction of chromium compounds takes place according to the reactions (1), (2) and in the selected temperature range is accompanied by a significant decrease in Gibbs energy (Table 1).

Table 1. Thermodynamic characteristics of reactions of chromium oxide compounds reduction by magnesium vapor.

| No | Reaction  | $-\Delta H_r,$<br>$\text{kJ}\cdot\text{mol}^{-1}$ | $\Delta S_r,$<br>$\text{J}\cdot(\text{mol}\cdot\text{K})^{-1}$ | $-\Delta G_{973},$<br>$\text{kJ}\cdot\text{mol}^{-1}$ | $-\Delta G_{1073},$<br>$\text{kJ}\cdot\text{mol}^{-1}$ |
|----|---|---|--|---|--|
| 1  | $\text{Cr}_2\text{O}_3 + 3\text{Mg} = 2\text{Cr} + 3\text{MgO}$   | 1049  | -445   | 615   | 571  |
| 2  | $\text{MgCr}_2\text{O}_4 + 3\text{Mg} = 2\text{Cr} + 4\text{MgO}$ | 1004  | -443   | 573   | 528  |

Crucibles with reaction products and corresponding shields after reduction of  $\text{Cr}_2\text{O}_3$  and  $\text{MgCr}_2\text{O}_4$  compounds are shown in Fig. 1. It can be seen that after the reduction of  $\text{Cr}_2\text{O}_3$  deposits of a white substance were found on the surfaces of the reaction product and the shield, while after the reduction of  $\text{MgCr}_2\text{O}_4$  under the same conditions, these surfaces are black.

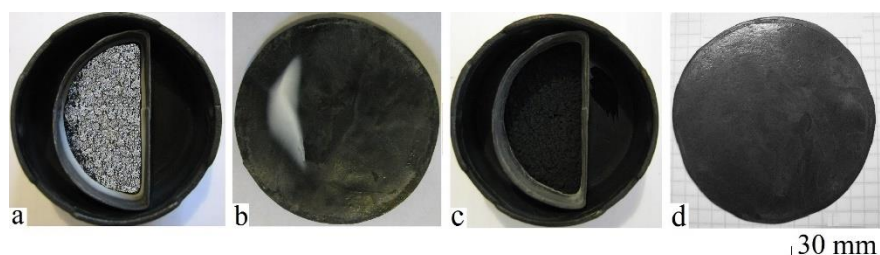


Fig. 1. Crucibles with reaction products (a, c) and corresponding shields (b, d) after reduction; precursors:  $\text{Cr}_2\text{O}_3$  (a),  $\text{MgCr}_2\text{O}_4$  (c); temperature in the reactor of 750°C, pressure of 10 kPa.

According to XRD data, the crust of the white substance on the surface of the reaction product and on shield after  $\text{Cr}_2\text{O}_3$  reduction is pure magnesium oxide. Under the crust there is chromium powder. After  $\text{MgCr}_2\text{O}_4$  reduction under the same conditions, the reaction product is chromium powder with MgO content corresponding to its fraction according to the reaction 2 (Table 1). When magnesium vapor reduction of  $\text{Cr}_2\text{O}_3$  specific surface area of chromium powders is 4–5  $\text{m}^2\cdot\text{g}^{-1}$ , while the reduction of  $\text{MgCr}_2\text{O}_4$  surface area reaches 15–33  $\text{m}^2\cdot\text{g}^{-1}$ . The specific surface area of chromium powders obtained by  $\text{MgCr}_2\text{O}_4$  reduction corresponds to the calculated average particle size of 25–50 nm. However, as can be estimated from the SEM image of the powder with a specific surface area of 33  $\text{m}^2\cdot\text{g}^{-1}$  (Fig. 2), the powder is represented by coarser particles with an average size of at least 200 nm.

According to the previously proposed model of powder particle formation during the reduction of oxide compounds of refractory metals by magnesium vapor, the high specific surface area of the powder is a consequence of its nanoporous structure [11]. For the obtained chromium powders, this is confirmed by the results of porosity measurement. The total surface area of the powder is almost equal to the total surface area of the pores (Fig. 3).

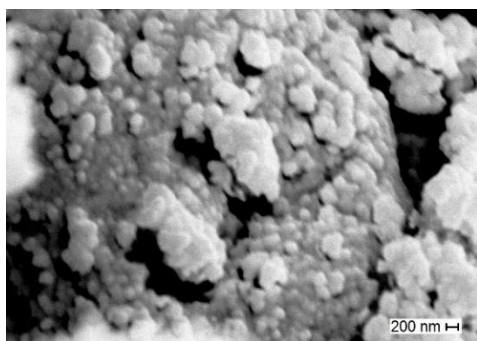


Fig. 2. SEM image of the chromium powder with specific surface area of  $33 \text{ m}^2 \cdot \text{g}^{-1}$ .

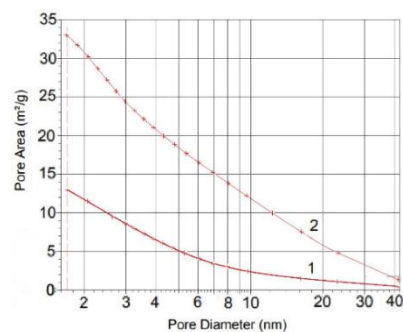


Fig. 3. Cumulative distribution curves of the pore area of chromium powders, specific surface area of powder: 1 13; 2  $33 \text{ m}^2 \cdot \text{g}^{-1}$ .

View of the precursor, crucible with the reaction product and the shield after reduction of the mixture  $\text{CaCrO}_4\text{--CaWO}_4$  shown in Fig. 4. It can be seen that the surface of the reaction product is mainly dark with small white inclusions. At the same time, there is white sediment in the central part of the shield, on the side facing the precursor. According to XRD data, it is a pure magnesium oxide (Fig. 5a). The reaction product consisted of tungsten, chromium and calcium and magnesium oxides (Fig. 5b). The washed powder contains only a mechanical mixture of Cr and W (Fig. 5c). The formation of the alloy during the reduction of compounds is difficult for the following reasons. First, mutual diffusion and atomic mobility in the Cr–W system are low even at higher temperatures [4]. In addition, the layers of MgO and CaO formed as a result of the reduction of oxide compounds serve as a diffusion barrier between metals.

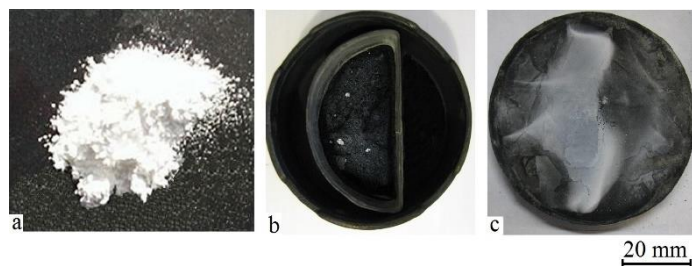


Fig. 4. View of the precursor (a), crucible with reaction product (b) and shield (c) after reduction  $\text{CaCrO}_4\text{--CaWO}_4$ ; temperature in the reactor of  $750^\circ\text{C}$ , pressure of 10 kPa.

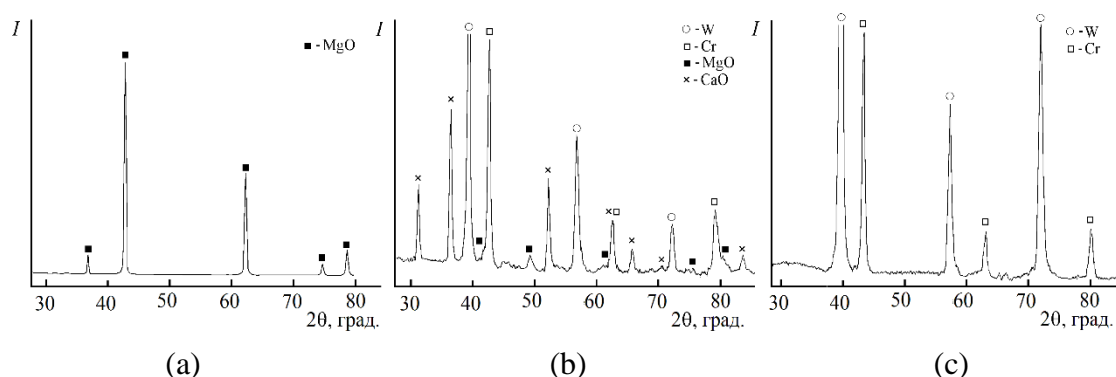


Fig. 5. XRD patterns of the white matter from the screen (a), the reaction product (b) and the washed powder (c) after reduction of the mixture  $\text{CaCrO}_4\text{--CaWO}_4$ .  $T = 750^\circ\text{C}$ ,  $P = 10 \text{ kPa}$ .

The specific surface area of the Cr–W powder mixture, depending on the reduction conditions, was  $24\text{--}34 \text{ m}^2 \cdot \text{g}^{-1}$ . The type of adsorption-desorption isotherms of these powders corresponds to type IV according to IUPAC classification, which is typical for mesoporous powders (Fig. 6).

Thus, the study confirms the previously established possibility for tungsten and molybdenum of increasing the specific surface area of powders obtained by the magnesium vapor reduction using compounds having refractory oxides in their composition as a precursor. By the reduction of such compound powders of chromium and Cr–W composite with tungsten with a specific surface area of 15–34 m<sup>2</sup>·g<sup>-1</sup> were produced, which one is 3–6 times higher than that for powders obtained by reduction in similar oxides Cr<sub>2</sub>O<sub>3</sub> and WO<sub>3</sub>.

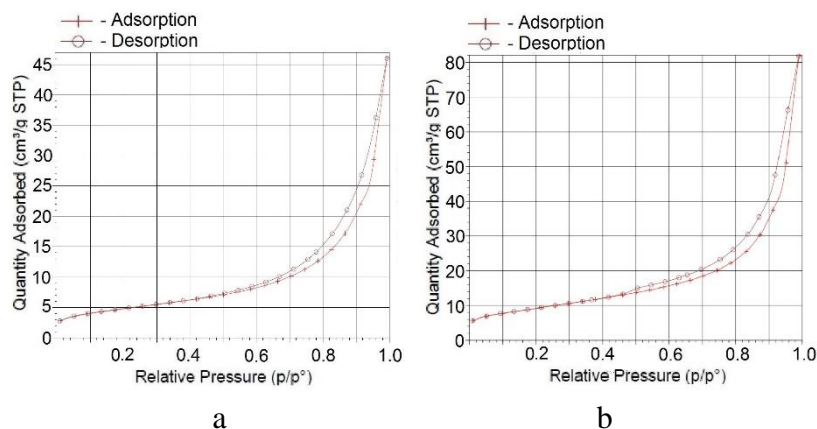


Fig. 6. Adsorption–desorption isotherms of nitrogen for chromium powders obtained from CaCrO<sub>4</sub>–CaWO<sub>4</sub> at 800°C (a), 720°C (b); specific surface area of powders, m<sup>2</sup>·g<sup>-1</sup>: (a) 24; (b) 34.

The research was supported by the Russian Foundation for Basic Research, (project no. 18-03-00248).

1. W. Schatt, K.-P. Wieters, Powder Metallurgy—Processing and Materials, European Powder Metallurgy Association, Shrewsbury, 1997.
2. S. Telu, A. Patra, M. Sankaranarayana, R. Mitra, S.K. Pabi, Microstructure and cyclic oxidation behavior of W–Cr alloys prepared by sintering of mechanically alloyed nanocrystalline powders, *Int. J. Refract. Met. Hard Mat.*, 2013, vol. 36, no. 1, pp. 191–203.
3. Barin, G. Platzki, Thermochemical Data of Pure Substances, New York: VCH, Weinheim, 1995.
4. F.J.A. Den Broeder, Interface reaction and a special form of grain boundary diffusion in the Cr–W system, *Acta Metall.*, 1972, vol. 20, pp. 319–332.
5. Handbook of Extractive Metallurgy, F. Habashi, ed., Wiley-VCH, Weinheim, 1997, vol. IV, pp. 1761–1811.
6. N.P. Lyakishev, M.I. Gasik, Metallurgy of Chromium, Allerton Press, NY, 1998.
7. W. Abdul-Razaq, M. Seehra, Observation of oxidation and mechanical strain in Cr nanoparticles produced by ball milling, *Phys. Stat. Sol.(a)*, 2002, vol. 193, pp. 94–102.
8. V.N. Kolosov, M.N. Miroshnichenko, V.M. Orlov, Influence of the chemical composition of precursors and reduction conditions on the properties of magnesiothermic tungsten powders, *Inorg. Mater.*, 2016, vol. 52, no. 8, pp. 783–790.
9. V.N. Kolosov, M.N. Miroshnichenko, V.M. Orlov, Influence of the composition of precursors and reduction conditions on the properties of magnesiothermic molybdenum powders, *Inorg. Mater.*, 2017, vol. 53, no. 10, pp. 1058–1063.
10. M.N. Miroshnichenko, V.N. Kolosov, T.I. Makarova, V.M. Orlov, Synthesis of molybdates and tungstanates of calcium and magnesium, *Isvestija S.-PbGTI(TU)*, 2017, no.38, pp. 44–47.
11. V.M. Orlov, M.V. Kryzhanov, V.T. Kalinnikov, Magnesium reduction of tantalum oxide compounds, *Dokl. Chem.*, 2014, vol. 457, part 1, pp. 161–163.

## REDUCTION OF OXIDE COMPOUNDS OF TUNGSTEN AND MOLYBDENUM BY CALCIUM VAPOURS

V. N. Kolosov<sup>\*a</sup>, V. M. Orlov<sup>a</sup>, and M. N. Miroshnichenko<sup>a</sup><sup>a</sup>Tananaev Institute of Chemistry - Subdivision of the Federal Research Centre Kola Science Centre of the Russian Academy of Sciences, Apatity, 184209 Russia

\*e-mail: tantal@chemy.kolasc.net.ru

DOI: 10.24411/9999-0014A-2019-10067

Tungsten and molybdenum are produced on an industrial scale only by powder metallurgy [1]. At the same time, the existing technologies are complex and have a limitation on the specific surface area of the obtained powders. The disadvantages of traditional technologies contribute to the search for alternative methods of production [2–5]. Earlier, it was shown that powders of tungsten and molybdenum with a specific surface area of up to  $20 \text{ m}^2 \cdot \text{g}^{-1}$  can be obtained by reduction their oxygen compounds with magnesium vapor and then leaching MgO with solutions of mineral acids [6, 7].

The purpose of this work was to study the characteristics of tungsten and molybdenum powders obtained by reduction its oxide compounds with calcium vapors. As a reductant, calcium has a stronger affinity for oxygen than magnesium.

MgWO<sub>4</sub>, CaWO<sub>4</sub>, Ca<sub>3</sub>WO<sub>6</sub>, MgMoO<sub>4</sub>, and CaMoO<sub>4</sub> were used as precursors, which were synthesized by the method [8]. The apparatus and techniques used to prepare and investigate tungsten and molybdenum powders were similar to those described previously [6]. The process was run under an atmosphere of calcium vapor and argon. A vessel containing calcium was mounted on the bottom of a reaction beaker. Weighed amounts (5 g) of precursors were loaded into metallic crucibles, which were placed over the calcium-containing vessel. Protective shields were placed over the crucibles. The space between the surface of the precursor and the shield was 27–30 mm. The reaction beaker was covered with a lid, which had an orifice in its center for the thermocouple sheath. The assembly was mounted in a stainless steel retort, which was hermetically sealed, pumped down, filled with an inert gas, and heated to a required temperature. The reaction beaker was kept closed to avoid calcium losses. The reduction process was run in the temperature range 800–860°C at a residual argon pressure in the range 5–10 kPa. The specific feature of the interaction of complex oxides of tungsten and molybdenum with calcium is the high thermal effect of the reactions (Table 1). The calcium vapor reduction of oxides makes it possible to control the rate of metal reductant delivery to the reaction zone, thereby maintaining the required process temperature.

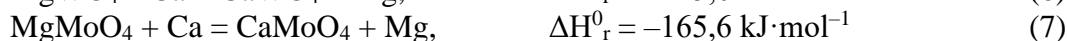
Table 1. Thermodynamic characteristics of calcium reduction reactions of complex tungsten and molybdenum oxides.

| № | Reaction  | $-\Delta H_r^0$<br>kJ·mol <sup>-1</sup> | $-\Delta S_r^0$ , J·(mol·K) <sup>-1</sup> | $\Delta Q_r$ ,<br>kJ·kg <sup>-1</sup> |
|---|---|---|---|---------------------------------------|
| 1 | MgWO <sub>4</sub> + 3 Ca = W + MgO + 3CaO         | 1519                                    | 37  | 3875                                  |
| 2 | CaWO <sub>4</sub> + 3 Ca = W + 4CaO               | 1351                                    | 12  | 3313                                  |
| 3 | Ca <sub>3</sub> WO <sub>6</sub> + 3 Ca = W + 6CaO | 1279                                    | 15  | 2458                                  |
| 4 | MgMoO <sub>4</sub> + 3Ca = Mo + MgO + 3CaO        | 1563                                    | 38  | 5138                                  |
| 5 | CaMoO <sub>4</sub> + 3Ca = Mo + 4CaO              | 1455                                    | 14  | 4545                                  |

Crucibles with reaction products and corresponding shields after the reduction of MgMoO<sub>4</sub> and MgWO<sub>4</sub> by calcium vapors are shown in Fig. 1. Also, as in the recovery of these compounds



by magnesium vapor [5, 6], white matter deposits are clearly observed on the surface of the reaction mass, on the walls of the crucible above the load level and on the shield surface. According to X-ray diffraction data, the white substance on the inner walls of the crucible and on the shield surface is pure calcium oxide (Figs. 2b, 3b). At the same time, white crusts on the surface of the reaction mass after the reduction of  $\text{MgWO}_4$  and  $\text{MgMoO}_4$ , were a mixture of  $\text{CaO}$  and  $\text{MgO}$  approximately in an equal mass ratio (Figs. 2c, 3c). Under the crust there was a homogeneous black powder,  $\text{Mo}$  or  $\text{W}$  with a small admixture of  $\text{CaO}$  and  $\text{MgO}$  (Figs. 2d, 3d). The presence of a significant amount magnesium oxide in the crust on the surface of the reaction mass is apparently due to the fact that the reaction of  $\text{MgMoO}_4$  and  $\text{MgWO}_4$  with calcium vapors involves the following exchange reactions:



This is confirmed by the X-ray diffraction data of intermediate products of reactions (1) and (4), since the  $\text{CaMoO}_4$  and  $\text{CaWO}_4$  compounds are absent in the initial reagents (Figs. 2e, 3e). The magnesium metal forming in the course of reactions (6) and (7) is vaporized from the reaction mass, is deposited on its surface, and is involved in the electronically mediated reaction [9]. Therefore, the oxide layer on the surface of the reaction mass contains magnesium oxide, along with calcium oxide.

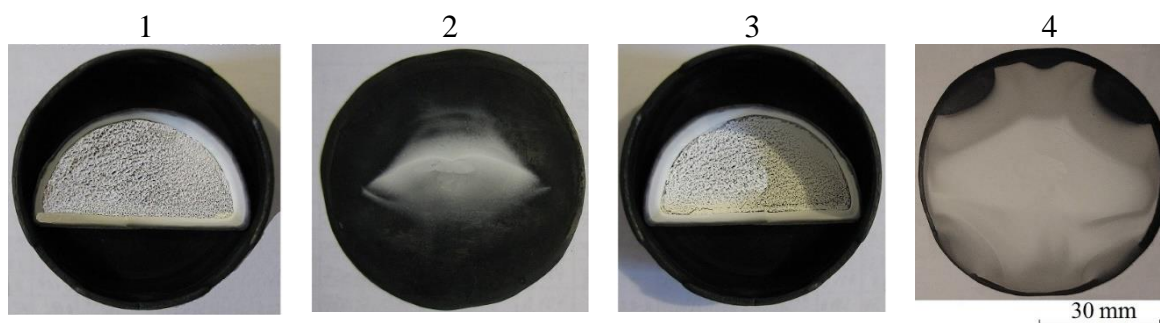


Fig. 1. (1, 3) Crucibles with reaction products and (2, 4) corresponding shields after reduction by calcium vapors; precursors: (1)  $\text{MgWO}_4$ , (3)  $\text{MgMoO}_4$ . Reduction temperature  $860^\circ\text{C}$ , residual pressure in the reactor 10 kPa.

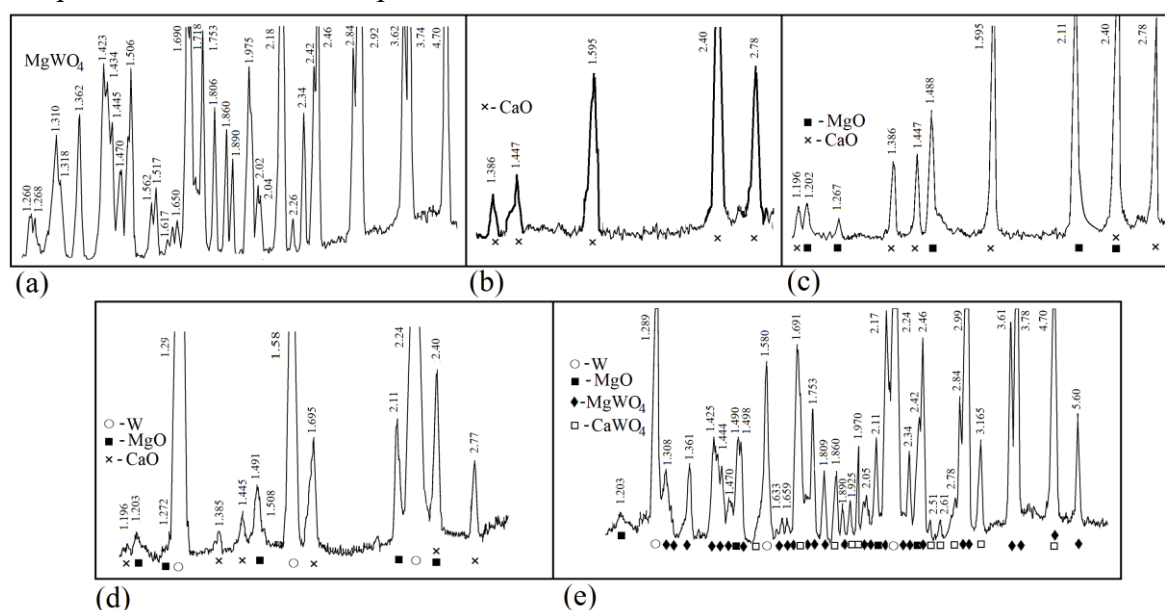


Fig. 2. X-ray powder diffraction patterns of (a)  $\text{MgWO}_4$  and (b–e) its reduction products. The residual pressure in the reactor was 10 kPa, and the reduction time was (b–d) 5 h and (e) 1 h.

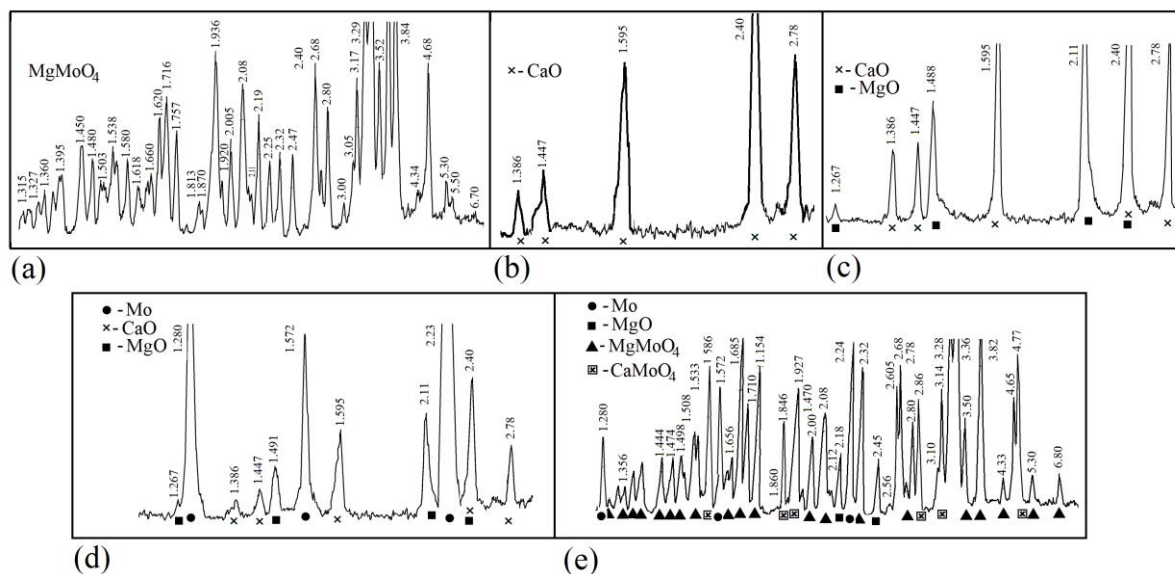


Fig. 3. X-ray powder diffraction patterns of (a)  $\text{MgMoO}_4$  and (b–e) its reduction products. The residual pressure in the reactor was 10 kPa, and the reduction time was (b–d) 5 h and (e) 1 h.

Crucibles with reaction products and corresponding shields after the reduction of  $\text{CaMoO}_4$ ,  $\text{CaWO}_4$ , and  $\text{Ca}_3\text{WO}_6$  by calcium vapors are shown in Figure 4. After the reduction of  $\text{CaMoO}_4$  on the part of the shield surface, on the walls of the crucible and on the surface of the reaction mass, white matter deposits are visible, which are pure calcium oxide (Fig. 5b). Under the CaO layer there is a homogeneous black molybdenum powder with a small amount of CaO impurity (Fig. 5c). At the same time, after the reduction of  $\text{CaWO}_4$  and  $\text{Ca}_3\text{WO}_6$ , the exfoliation of the components of the reaction products did not occur. The reaction mass is a homogeneous dark powder containing tungsten and calcium oxide in a stoichiometric ratio of the corresponding reaction (Fig. 5e).

In the reduction of double oxides of tungsten and molybdenum by calcium vapors, the specific surface of powders was  $14\text{--}20\text{ m}^2\cdot\text{g}^{-1}$ . The study of the porous structure of the powder showed that the specific surface is almost completely determined by the surface of the pores. Powder adsorption curves correspond to IUPAC type IV (Fig. 6). They are distinguished by the presence of a hysteresis loop and are characteristic of materials with a mesoporous structure.

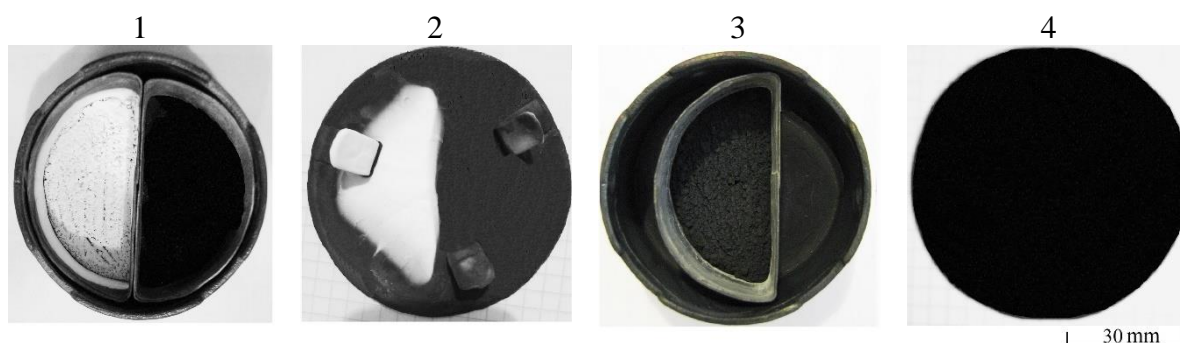


Fig. 4. (1, 3) Crucibles with reaction products and (2, 4) corresponding shields after reduction by calcium vapors; precursors: (1) (left crucible)  $\text{CaMoO}_4$ , (1) (right crucible)  $\text{CaWO}_4$ , (3)  $\text{Ca}_3\text{WO}_6$ . Reduction temperature  $860^\circ\text{C}$ , residual pressure in the reactor 10 kPa.

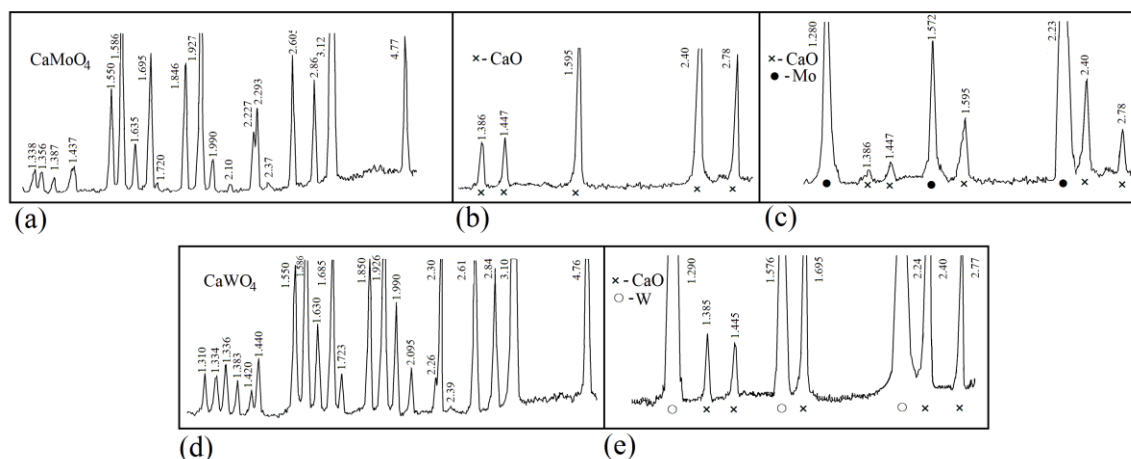


Fig. 5. X-ray powder diffraction patterns of (a)  $\text{CaMoO}_4$ , (d)  $\text{CaWO}_4$ , and (b, c, e) its reduction products. The residual pressure in the reactor was 5 kPa.

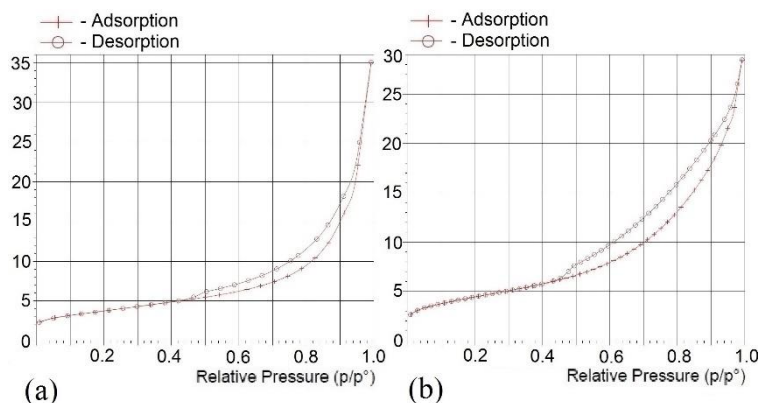


Fig. 6. Nitrogen adsorption–desorption isotherms for tungsten powders obtained by reduction (a)  $\text{MgWO}_4$  and (b)  $\text{CaWO}_4$  by calcium vapor; powder surface: (a) 14 and (b)  $16 \text{ m}^2 \cdot \text{g}^{-1}$ .

Thus, the results of the studies performed showed the possibility of obtaining mesoporous powders of tungsten and molybdenum with a high specific surface by reduction their complex oxide compounds. At the same time magnesium or calcium can be used as a reductant.

1. R.U. Kalamazov, Yu.V. Tsvetkov, A.A. Kal'kov, *Vysokodispersnye poroshki vol'frama i molibdena (Fine Tungsten and Molybdenum Powders)*, Moscow: Metallurgiya, 1988.
2. J.H. Lee, J.C. Jung, I.P. Borovinskaya, V.I. Vershinnikov, C.W. Won, Preparation of tungsten powder by the combustion of  $\text{CaWO}_4/\text{Mg}$ , *Met. Mater.*, 2000, vol. 6, no. 1, pp. 73–80.
3. S. Zhang, Y. Wen, H. Zhang, Low temperature preparation of tungsten nanoparticles from molten salt, *Powder Technol.*, 2014, vol. 253, no. 2, pp. 464–466.
4. H.H. Nersisyan, J.H. Lee, C.W. Won, The synthesis of nanostructured molybdenum under self-propagating high-temperature synthesis mode, *Mater. Chem. Phys.*, 2005, vol. 89, nos. 2–3, pp. 283–288.
5. H. Zhong, L. Jianghao, D. Xiangong, Low temperature molten salt preparation of molybdenum nanoparticles, *Int. J. Refract. Met. Hard Mater.*, 2016, vol. 54, no. 1, pp. 315–321.
6. V.N. Kolosov, M.N. Miroshnichenko, V.M. Orlov, Influence of the chemical composition of precursors and reduction conditions on the properties of magnesiothermic tungsten powders, *Inorg. Mater.*, 2016, vol. 52, no. 8, pp. 783–790.
7. V.N. Kolosov, M.N. Miroshnichenko, V.M. Orlov, Influence of the composition of

- precursors and reduction conditions on the properties of magnesiothermic molybdenum powders, *Inorg. Mater.*, 2017, vol. 53, no. 10, pp. 1058–1063.
8. M.N. Miroshnichenko, V.N. Kolosov, T.I. Makarova, V.M. Orlov, Synthesis of molybdates and tungstanates of calcium and magnesium, *Isvestija S.-PbGTI(TU)*, 2017, no.38, pp. 44–47.
  9. V.N. Kolosov, V.M. Orlov, Electronically mediated reactions in metal thermal reduction of molybdenum and tungsten oxide compounds, *Dokl. Phys. Chem.*, 2019, vol. 484, part 2, pp. 28–31.

AN X-RAY POWDER DIFFRACTION STUDY OF NEW CRYSTAL  
 $\text{Ni}_{3.35}\text{W}_{9.65}\text{C}_4$ S. V. Konovalikhin<sup>\*a</sup>, N. Yu. Khomenko<sup>a</sup>, I. I. Chuev<sup>a</sup>, S. A. Guda<sup>b</sup>, S. L. Silyakov<sup>a</sup>,  
and D. Yu. Kovalev<sup>a</sup><sup>a</sup>Merzhanov Institute of Structural Macrokinetics and Materials Science, Russian Academy of Sciences, Chernogolovka, Moscow, 142432 Russia<sup>b</sup>Southern Federal University, Rostov-on-Don, 344090 Russia

\*e-mail: ksv17@ism.ac.ru

DOI: 10.24411/9999-0014A-2019-10068

Unknown reflections in XRD patterns of SHS products of  $\text{WO}_3$  (59%) + NiO (12%) + Al (10%) + Ca (13%) + C (6%) mixture were found. XRD analysis showed that the unknown phase is  $\gamma$  phase ( $\text{Ni}_3\text{W}_9\text{C}_4$ ) or  $\kappa$  phase ( $\text{Ni}_3\text{W}_{10}\text{C}_{3.4}$ ). There are no structural data in PDF-2 and ICSD databases. The aim of this paper is to establish the crystal structure of this phase. XRD study, DFT calculation, and crystal chemical simulations were carried out. Comparison of results revealed the composition and structure of the new compound.

XRD study analysis was performed using a DRON-3M diffractometer in  $\text{CuK}\alpha$  radiation and in the range of  $2\theta = 20^\circ\text{--}80^\circ$  with a step of  $0.02^\circ$  and a time per step of 2 s. Composition and cell parameters were determined by Rietveld method. Profile refinement of reflections was made by Pseudo-Voigt. Texture, thermal parameters, and coordinates of atoms were fixed. Occupation of  $2a$  position by atoms W and Ni was refined in the latter stages. The weighed and profile  $R$  factors (experiment quality characteristics) calculated in the refinement process are:  $R_{\text{wp}} = 11.4\%$ ,  $R_p = 8.9\%$ ,  $R_e = 26.55\%$ ,  $\text{Goff} = 0.43$ . Theoretical XRD patterns were made by Mercury 3.5.1 package.

DFT calculations were carried out using a VASP 5.0 program on supercomputer «Blokhin» of Southern Federal University. PBE pseudopotential and generalized gradient approximations (GGA) were used. K-point mesh of  $3 \times 3 \times 3$  was applied for electronic optimization. The mesh size was chosen by the trial-and-error method. We considered three meshes of  $2 \times 2 \times 2$ ,  $3 \times 3 \times 3$ , and  $4 \times 4 \times 4$  and the one with the lowest total crystal energy turned out to be preferable.

Composition of the reaction products was the following: WC (82 %),  $\text{W}_2\text{C}$  (3.5%), and  $\text{Ni}_3\text{W}_x\text{C}_y$  (14.5%) (Fig. 1). It was shown that structures of  $\gamma$  and  $\kappa$  phase have different occupation ( $\mu$ ) of metal atoms ( $2a$ ) and C ( $2c$ ) [1, 2]. Comparison of XRD data for  $\text{Ni}_3\text{W}_9\text{C}_4$  and  $\text{Ni}_3\text{W}_{10}\text{C}_{3.4}$  crystals showed the difference in the intensity of 002 reflections ( $I_{002}$ ).  $I_{002}$  in  $\text{Ni}_3\text{W}_9\text{C}_4$  crystals is 10 times larger than in  $\text{Ni}_3\text{W}_{10}\text{C}_{3.4}$  (Fig. 2). The XRD data showed that in new crystals 002 reflections are absent (Fig. 1). Therefore, for the new phase the composition of  $\text{Ni}_3\text{W}_{10}\text{C}_{3.4}$  was chosen.

Analysis of XRD patterns showed that  $I_{301}$  ( $2\theta \approx 41.5^\circ$ ) is larger than  $I_{3-12}$  ( $2\theta \approx 42.1^\circ$ ) (Fig. 1), though there is an opposite ration in theoretical patterns of  $\text{Ni}_3\text{W}_{10}\text{C}_{3.4}$  crystal ( $I_{302} < I_{3-12}$ ) (Fig. 2). Crystal chemical simulation was made to get a perfect correspondence with XRD data. It was proposed a partial occupation of Ni atoms in position  $2a$  (composition of  $\text{Ni}_{3.5}\text{W}_{9.5}\text{C}_4$ ) or in 12k (structure  $\text{Ni}_6\text{W}_7\text{C}_4$ ) Ni atoms, or in both positions simultaneously (composition  $\text{Ni}_{6.5}\text{W}_{6.5}\text{C}_4$ ).

DFT calculation showed that structures of  $\text{Ni}_6\text{W}_7\text{C}_4$  and  $\text{Ni}_{6.5}\text{W}_{6.5}\text{C}_4$  are energetically less favorably (Table 1), furthermore,  $a < c$  for these compounds in contradiction of XRD data. The only structure with a partial occupation of Ni in position  $2a$  is in good correspondence with experimental data ( $I_{002} \approx 0$ ,  $I_{302} > I_{3-12}$ ,  $a > c$ ).

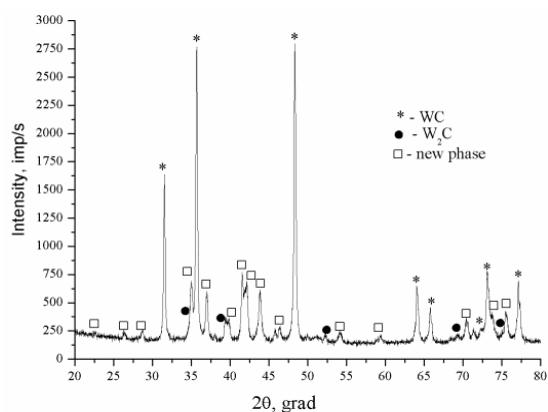


Fig. 1. XRD pattern of product SHS reaction.

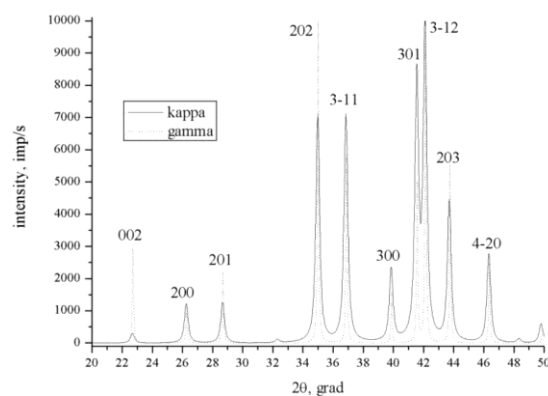


Fig. 2. Theoretical XRD patterns  $\gamma$ -phase crystals  $\text{Ni}_3\text{W}_9\text{C}_4$  and  $\kappa$ -phase  $\text{Ni}_3\text{W}_{10}\text{C}_{3.4}$ .

Table 1. The results of the XRD study and DFT calculation of crystals  $\text{Ni}_3\text{W}_{10}\text{C}_{3.4}$  and  $\text{Ni}_3\text{W}_9\text{C}_4$ .

| Phase                                       | $a$ , Å   | $c$ , Å   | $V$ , Å <sup>3</sup> | $N$ | $\epsilon_{\text{total}}$ , eV/mol | $\epsilon$ , eV/mol |
|---|-----------|-----------|----------------------|-----|------------------------------------|---------------------|
| $\text{Ni}_3\text{W}_9\text{C}_4$           | 7.6595    | 7.7102    | 391.5                | 236 | -321.736                           | -1.363              |
| $\text{Ni}_3\text{W}_{10}\text{C}_{3.4}$    | 7.8358    | 7.8472    | 417.3                | 208 | -359.926                           | -1.730              |
| $\text{Ni}_{3.5}\text{W}_{9.5}\text{C}_4$   | 7.8247    | 7.7881    | 413.0                | 216 | -361.227                           | -1.672              |
| $\text{Ni}_{3.5}\text{W}_{9.5}\text{C}_4^*$ | 7.8344(4) | 7.8048(7) | 414.87(7)            |     |                                    |                     |
| $\text{Ni}_6\text{W}_7\text{C}_4$           | 7.6540    | 7.8359    | 397.6                | 236 | -318.7857                          | -1.350              |
| $\text{Ni}_{6.5}\text{W}_{6.5}\text{C}_4$   | 7.6858    | 7.7744    | 397.2                | 240 | -311.2943                          | -1.297              |

\* XRD experiment.

The population of 0.65 for W atom and of 0.35 for Ni atom was found by Rietveld method. The final composition is  $\text{Ni}_{3.35}\text{W}_{9.65}\text{C}_4$ . Figure 3 shows the crystal structure. The cell parameters are listed in Table 1.

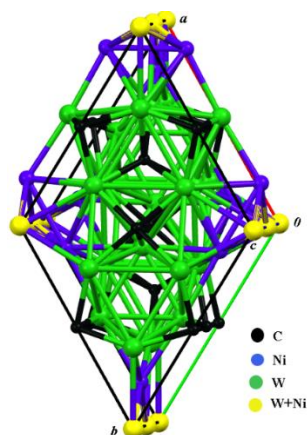


Fig. 3. Crystal structure of  $\text{Ni}_{3.35}\text{W}_{9.65}\text{C}_4$ .

## Conclusions.

The new phase of Ni–W–C system was synthesized by SHS method. Its composition ( $\text{Ni}_{3.35}\text{W}_{9.65}\text{C}_4$ ) was determined by XRD analysis, DFT calculation, and crystal chemistry simulation.

1. A. Harsta, T. Johansson, S. Rundqvist, J.O. Thomas, A neutron powder diffraction study of the  $\kappa$ -phase in the Co–W–C system, *Acta Chem. Scand. A*, 1977, vol. 31, no. 4, pp. 260–264.
2. M. Schonenberg, The structure of the  $\text{Co}_3\text{W}_3\text{C}_4$  phase, *Acta Metall.*, 1954, vol. 2, pp. 837–839.

# NONSTATIONARY COMBUSTION OF LAYERED HETEROGENEOUS SYSTEMS

S. V. Kostin<sup>a</sup>, P. M. Krishenik<sup>\*a</sup>, S. A. Rogachev<sup>a</sup>, and A. E. Sytshev<sup>a</sup>

<sup>a</sup>Merzhanov Institute of Structural Macrokinetics and Materials Science, Russian Academy of Sciences, Chernogolovka, Moscow, 142432 Russia  
\*e-mail: petr@ism.ac.ru

DOI: 10.24411/9999-0014A-2019-10069

The stability of combustion wave passing through the interface between two different SHS systems [1–4] is also of current importance in the task objective of reliable SHS joining of dissimilar materials [5]. Transition of combustion wave from one burning material to another is normally accompanied by transient phenomena such as pulsations of combustion temperature and burning velocity, which may affect the quality of SHS joining. Recent experiments [5] on SHS joining in  $(\text{Ti} + y\text{Si})/(\text{Ti} + x\text{C})$  sandwiches were successful and showed the formation of  $\text{Ti}_3\text{SiC}_2$  grains within the transition layer. Capillary fluid dynamic phenomena at the interface between two reactive systems were analyzed in [6, 7]. In this work, we numerically investigated combustion in two-layer SHS systems with special emphasis on thermal conditions at their interface caused by the presence of clearance gap. We consider the propagation of combustion wave over a two-layer sandwich—such as  $(\text{Ti} + y\text{Si})/(\text{Ti} + x\text{C})$  [5]—depicted in Fig. 1. The combustion wave initiated in reactive layer 1 (of thickness  $l_1$ ) moves downward and then ignites reactive layer 2 (with thickness  $L - l_2$ ) through a gaseous gap of thickness  $\Delta$  (Fig. 1). The problem is essentially 1D and there is no heat sink through the side surfaces. When the combustion wave initiated in layer 1 approaches to gap  $\Delta$  (Fig. 1), it can ignite layer 2 in a mode depending on the critical conditions for ignition formulated in [8]. Let us consider the transient phenomena taking place in the vicinity of gap  $\Delta$  in more detail.

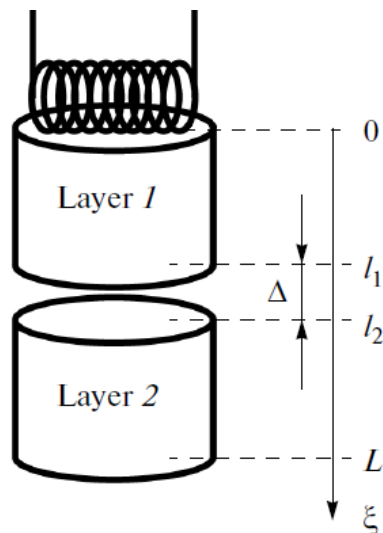


Fig. 1. Two-layer system under consideration.

## Close contact between the layers ( $\Delta \rightarrow 0$ ).

In analysis we used our previous results [1, 2]. It is assumed that (a) both reactions are gasless and (b) during the reactions there is no change in thermophysical parameters and sample dimensions. In vicinity of the interface, the heat flux into layer 2 (Fig. 1) depends on mutual relationship  $b$  between thermophysical parameters of layers 1 and 2:  $b = \sqrt{(\lambda_1 c_1 \rho_1) / (\lambda_2 c_2 \rho_2)}$ . The combustion temperature and burning velocity tend to grow upon approaching to layer 2 when  $b > 1$ , and to decrease if  $b < 1$ . And at some critical value  $b_c < 1$ , the flameout takes place. The induction ignition is observed when  $\Delta H_1 > \Delta H_2$  and the mode of burning when  $\Delta H_1 < \Delta H_2$ . It was received the time evolution of temperature profiles for  $b > 1$  and different thermal conductivity and density of layers 1 and 2:  $\lambda_1 \neq \lambda_2$ ,  $\rho_1 \neq \rho_2$ . The temperature spike at the interface is observed at within the warm up zone where  $v$  is the velocity of combustion wave propagation in layer 1. The temperature at the interface is given by the expression

$T_{st} \approx t_0 + \frac{2b}{1+b}(T_1 - T_0)$ , where  $T_1 = T_0 + Q_1/c_1$ . The temperature spike can be associated with heat accumulation at the interface:  $b = \sqrt{\lambda_1 c_1 \rho_1 / \lambda_2 c_2 \rho_2} \approx 1.6$ , which corresponds to the (Ti + ySi)/(Ti + xC) system taken as an example.

For  $b < 1$ , the values of  $T$  and  $v$  were found to sharply drop on approaching to the interface (Fig. 2).

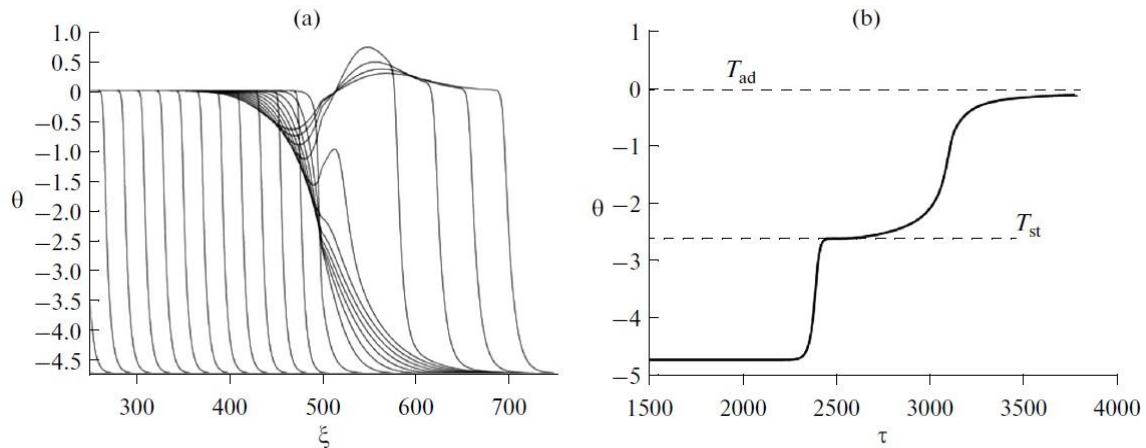


Fig. 2. (a) Time evolution of temperature profiles and (b) temperature profile at the interface,  $b \approx 0.6$ , where  $\theta$  and  $\tau$  are dimensionless temperature and time.

After long period of depression, the temperature restores to a level of  $T_{st} \approx T_0 + \frac{2b}{1+b}(T_1 - T_0)$ , just as upon ignition with an incandescent body [9].

Heat transfer from layer 1 to layer 2 actually obeys the laws of inert heat exchange. After warm-up to a sufficiently large depth, the established steady-state temperature,  $T_{st}$  is markedly lower than  $T_{ad}$  for layer 1. In case of inert heating, the reaction heat in layer 2 is negligibly small. But the latter becomes important when chemical reaction takes place in warmed up layer 2. The heat flux through the interface changes its sign, which gives rise to heat sink from the reacting volume. As a result, superadiabatic temperatures are attained within the bulk of layer 2, the maximal temperature at the interface being close to  $T_{ad}$ . The above results quantitative agree with experiment [3].

#### No contact between the layers ( $\Delta > 0$ ).

According to [10], radiative heat transfer from a burning layer through a gap is commensurable with heat transfer by thermal conduction. In case of layered systems with a ‘thin’ gap [ $\Delta < (\lambda_1/c_1\rho_1/v)$ ], one can use an effective heat transfer coefficient. Due to strong difference in thermophysical parameters of solids and gas, the combustion temperature in the vicinity of the gap gradually ‘takes off’ from  $T_{ad}$ . The initial temperature spike is followed by the stage of inert heating of layer 2 via the gap. A relatively long period of inert heating is followed by a shorter period of heat release from chemical reaction in the warmed up layer, and this gives rise to the backward heat flux toward the interface.

In contrast to close contact, the superadiabatic temperatures are attained in both reactive layers. It can be expected that in real conditions of SHS joining the process of heat/mass exchange between the dissimilar materials to be joined will be still more intensive.



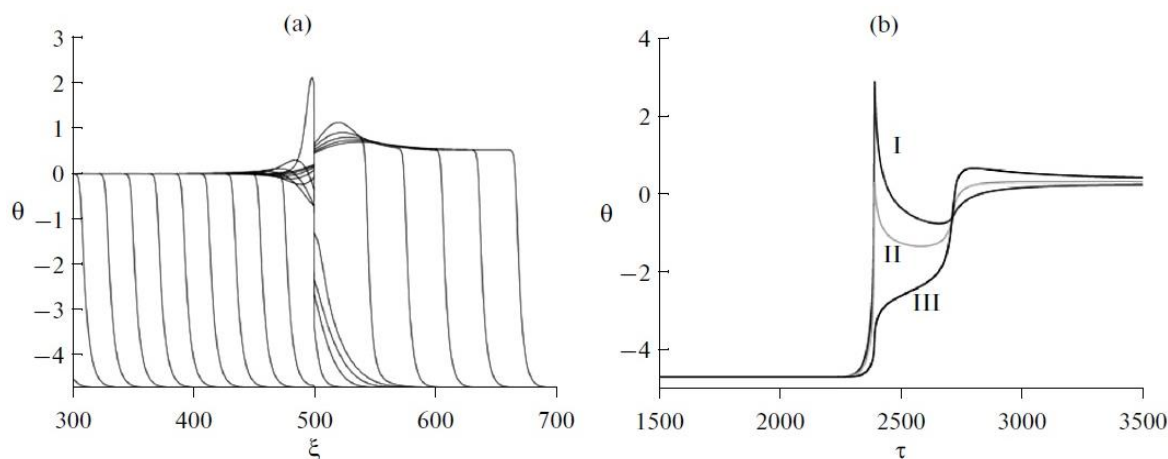


Fig. 3. (a) Time evolution of temperature profiles ahead of the gap (curve I), at the gap middle (curve II), and behind the gap (curve III); and (b) temperature profile at the interface:  $\Delta = 0.1$ ;  $b \approx 316$ .

If at least one reagent is able to melt at the interface below the combustion temperature and mutual dissolution happens faster than chemical reaction, the combustion reaction can be regarded as homogeneous. Interdiffusion at the interface can also affect the reaction kinetics and thus lead to formation of  $Ti_3SiC_2$  within the transition layer. It should also be noted that unsteady combustion at the interface may affect the thermophysical parameters of matter and kinetic parameters and hence the character of transient processes.

## Conclusions

The character of transient phenomena taking place during combustion of two-layer SHS systems depends on interrelation between thermal activities of constituent layers. In case of close contact, superadiabatic heating can be attained only in one of two adjacent systems. But in the presence of clearance gap, superadiabatic temperatures can be reached in both reactive layers. This may improve the conditions for heat/mass transfer between the layers and hence the quality of SHS joining. Our results may turn helpful for optimization of combustion in two-layer systems. Optimization of the clearance gap will be a subject of our forthcoming communication.

1. A.G. Strunina, A.N. Firsov, S.V. Kostin, Transition modes in the combustion of heterogeneous systems with solid phase products, *Combust. Explos. Shock Waves*, 1981, vol. 17, no. 5, pp. 500–505.
2. S.V. Kostin, A.G. Strunina, V.V. Barzykin, Influence of thermophysical parameters on the stability of a combustion wave on passing through an interface between gasless systems, *Combust. Explos. Shock Waves*, 1987, vol. 23, no. 6, pp. 715–720.
3. A.G. Strunina, V.I. Ermakov, E.A. Averson, Limiting conditions of ignition of gasless systems by a combustion, *Combust. Explos. Shock Waves*, 1979, vol. 15, no. 4, pp. 484–489.
4. A.G. Strunina, V.I. Ermakov, V.V. Barzykin, Influence of heat losses and thermophysical parameters on the ignition process of gasless systems of wave combustion, *Combust. Explos. Shock Waves*, 1978, vol. 14 no. 4, pp. 441–447.
5. S.G. Vadchenko, O.D. Boyarchenko, A.E. Sytshev, N.V. Sachkova, SHS joining in the Ti–Si–C system: Structure of transition layer, *Int. J. Self- Propag. High-Temp. Synth.*, 2013, vol. 22, no. 1, pp. 46–51.
6. Yu.M. Maksimov, A.I. Kirdyashkin, M.Kh. Ziatdinov, V.D. Kitler, Interphase convection in the contact interaction of metals under non-isothermal conditions, *Combust. Explos. Shock Waves*, 2000, vol. 36, no. 4, pp. 462–469.

7. A.I. Kirdyashkin, V.D. Kitler, V.G. Salamatov, R.A. Yusupov, Yu.M. Maksimov, Capillary hydrodynamic phenomena in gas free combustion, *Combust Explos. Shock Waves*, 2007, vol. 43, no. 6, pp. 645–653.
8. E.A. Averson, V.I. Rosenband, Approximate methods for calculating critical ignition conditions, *Combust. Explos. Shock Waves*, 1968, vol. 4, no. 4, pp. 299–303.
9. H.S. Carslaw, J.C. Jaeger, *Conduction of Heat in Solids*, Oxford (UK): Oxford University Press, 1986, pp. 164–165.
10. P.M. Krishenik, A.G. Merzhanov, K.G. Shkadinskii, Frontal transformation modes of structured energetic heterogeneous systems, *Combust. Explos. Shock Waves*, 2005, vol. 41, no. 2, pp. 164–173.

## SYNTHESIS OF NEW MIXED NIOBIUM–TUNGSTEN OXIDE BRONZES

M. K. Kotvanova\*<sup>a</sup> and I. A. Sologubova<sup>a</sup><sup>a</sup>Yugra State University, Khanty-Mansiysk, 628012 Russia

\*e-mail: kotvanova@mail.ru

DOI: 10.24411/9999-0014A-2019-10070

One of the promising areas in chemistry is the synthesis of materials with a given set of properties. The basis of such materials are various mixed metal oxides including oxide bronzes containing transition metal in different oxidation states. The structures of simplest tungsten bronzes are studied and well-known. These are octahedral structures with octahedra  $WO_6$  sharing corners to form a 3D framework with tunnels. Some of the tunnels can be occupied by alkali metal.

The great interest of researchers in oxide bronzes is due to the correct combination of mechanical, physical, and chemical properties. They have unusual electronic properties, chemical and thermal stability, and extreme corrosion resistance [1]. In addition, they are cheap and non-toxic. Recent studies have shown that oxide bronzes exhibit photothermal properties [2], and mixed tungsten bronzes are also promising thermoelectric materials which can play an important role in future power management [3].

At the same time, the practical application of these compounds is hampered by the problems of their synthesis. All currently known synthesis methods are extremely energy-intensive and time-consuming.

It is known SHS are distinguished by economics, simplicity of operation, and low energy requirements. In recent years, we have shown the possibility of producing oxide bronzes of titanium, molybdenum, and tungsten in the SHS mode using various exothermic additives, particularly copper oxide (II).

This work is devoted to the synthesis of mixed oxide bronzes in the K–Nb–W–O system. Oxide bronze  $K_{0.5}(NbW)_5O_{14}$  was prepared by SHS of stoichiometric mixture  $2WO_3:Nb_2O_5:KI:0.5CuO$  (Fig. 1). The initial substances were ground in an agate mortar until smooth and thoroughly mixed. The tablets measuring 1.5 cm were formed using ethanol as a binder. The SHS product was a dark blue substance. X-ray powder diffraction pattern for orthorhombic  $K_{0.5}(NbW)_5O_{14}$  is shown in Fig. 2 in comparison with our data for the hexagonal tungsten bronze  $K_{0.2}WO_3$  (Fig. 3) that we prepared earlier by SHS [4].

It is interesting that the similar phases (hexagonal bronze  $Cs_{0.32}WO_3$  and orthorhombic bronze  $Cs_{0.5}Nb_{2.5}W_{2.5}O_{14}$ ) were obtained by the authors [5] as a result of hydrothermal synthesis.

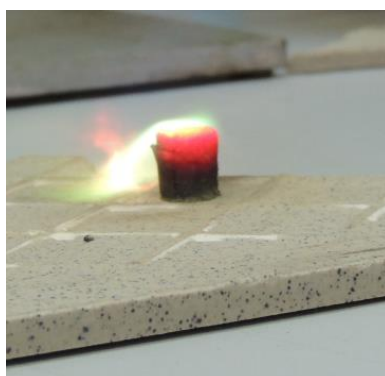


Fig. 1. Synthesis of  $K_{0.5}(NbW)_5O_{14}$ .

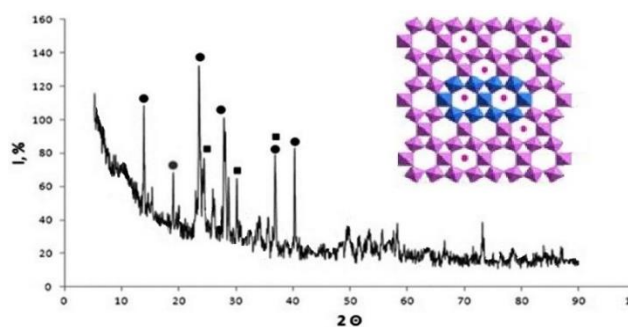


Fig. 2. X-Ray diffraction pattern of the sample  $K_{0.2}WO_3$  (SHS). ● -  $K_{0.2}WO_3$  ■ -  $WO_3$

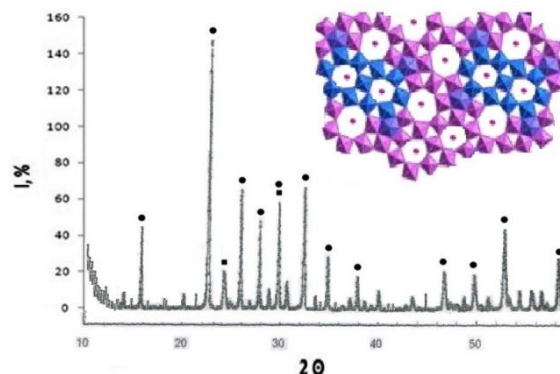


Fig. 3. X-Ray diffraction pattern of the sample  $K_{0.5}(NbW)_5O_{14}$  (SHS).

● -  $K_{0.5}(NbW)O_{14}$  ■ -  $WO_3$

Thus, new mixed niobium–tungsten oxide bronze was obtained. The addition of niobium leads to the structure transformation from hexagonal to orthorhombic.

1. M.K. Kotvanova, S.S. Pavlova, N.N. Efremova, Nanocrystals of oxide bronzes of titanium, molybdenum, tungsten as components of anti-corrosion coatings, *Rus. J. Chem. Chem. Technol.*, 2013, vol. 56, no. 9, pp.111–116.
2. P.Yu. Gulyaev, M.K. Kotvanova, A.I. Omel'chenko, Nanotechnologies of the treatment and production of complex transition metal oxides with high photothermal effect, *Inorg. Mater. Appl. Res.*, 2018, vol. 9, no. 3, pp. 540–545.
3. M.K. Kotvanova, S.S. Pavlova, E.N. Sobol, A.I. Omelchenko, P.Y. Gulyaev, Photothermal effects of laser heating iron oxide and oxide bronze nanoparticles in cartilaginous tissues, *Nanotechnol. Russ*, 2012, vol. 7, nos. 3–4, pp. 127–131.
4. M. Kotvanova, N. Blinova, P. Gulyaev, A. Dolmatov, S. Pavlova, Evaluation of combustion temperature and combustion speed of the process of SH-synthesis of titanium oxide bronze, *In Book Int. Symp. on Self-Propag. High-Temp. synth. SHS XIII*, 2015, pp. 160–161.
5. M.D. Soriano, E. Garcia-Gonzalez, P. Concepción, C.B. Rodella, J.M. L. Nieto, Self-organized transformation from hexagonal to orthorhombic bronze of Cs–Nb–W–O mixed oxides prepared hydrothermally, *Cryst. Growth Des.*, 2017, vol. 17, no. 12, pp. 6320–6331.

SYNTHESIS OF METAL OXIDE RADICALS IN ROTATING REACTOR  
WITH ALUMINOTHERMIC FLAME

G. I. Ksandopulo

Institute of Combustion Problems, Almaty, 050012 Kazakhstan  
e-mail: ksand@inbox.ru

DOI: 10.24411/9999-0014A-2019-10071

Due to high heat resistance, inorganic radicals (HP) have the ability to influence on high-temperature chemical processes, for example modifying agents that affecting on crystallization kinetics of various metal melts, causing a change in their physical and mechanical properties. A similar effect can be expected in polymerization processes of inorganic and organic systems. Intervention in recombination chain of organic radicals during combustion of liquid fuels may allow HP to extinguish the combustion in near-wall layer of rocket thrust chamber; radical reactions is also important for the treatment of cancerous growth. A free valence of HP is predisposed to change, catalyze, activate, or inhibit various chemical processes, as well as to create nonstoichiometric compounds. The synthesis of solid-phase radicals is carried out in a cylindrical reactor is rotating around an outer axle, is filled with a mixture of powders based on metal oxide. During combustion of mixture there is formed a centrifugal - accelerated flow of clusters from recovered metal [1–3]. Overtaking the front of combustion wave when being impact into fresh layers of reaction mixture, this flow creates an attacking impulse, which accelerates and broadens the front of combustion wave. The reaction is carried out at temperatures of 2800–3500 K, and its time does not exceed  $10^{-3}$  s. At the same time, an initiating energy is sufficiently large, both for formation of interatomic metallic bonds, and heteroatomic radical containing particles. An obvious requirement to conditions of radical synthesis is a high positive temperature gradient for heating of reaction mixture, as well as momentary cooling of the formed product. The forced effect of high-gradient heat at temperatures above 3000 K causes an appropriate degree of inequality in reaction medium, and its subsequent rapid cooling reduces the loss of free valence in acts of quadratic or other kind of death. Therefore, the achieving of maximum yield of radicals on concentration is a minimization of time interval between start and freezing of the reaction. In [1–4], there are presented fundamentals of self-propagating high-temperature synthesis (SHS) theory in oxide systems with mass transfer is caused by rotational forces effect on propagation of combustion wave. The aluminothermic reaction of SHS type is a source of the clusters:



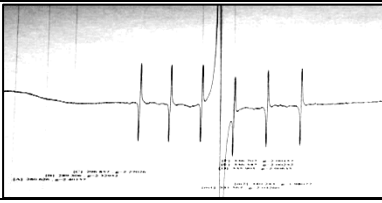
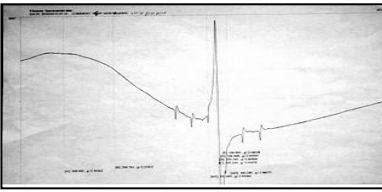
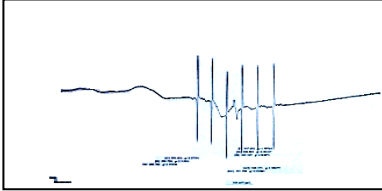
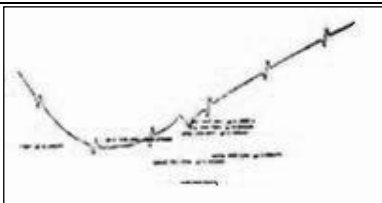
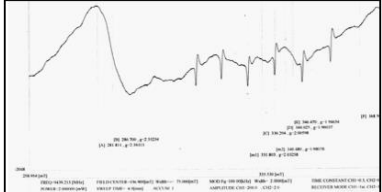
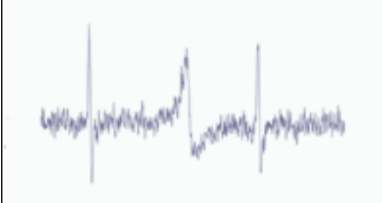
where  $\text{MeO}_3$  is metal oxide.

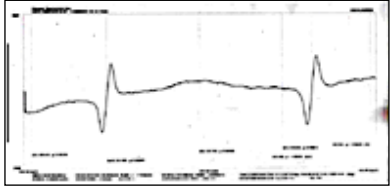
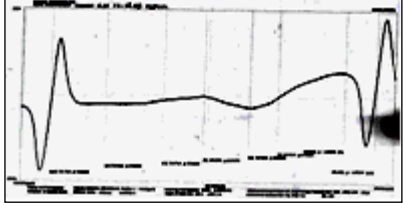
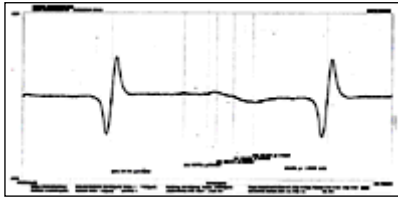
Synthesis products in two-layered systems stably contains inorganic radicals, in Table 1 there are presented results of X-ray diffraction analysis and EPR spectra for two types of attacked mixtures:  $\gamma\text{-Al}_2\text{O}_3$  и  $\text{B}_2\text{O}_3 + \text{Al}$ . Synthesis was carried out by clusters of metals that generated by the reaction (I) in mixtures based on tungsten, molybdenum, copper, nickel, cobalt and titanium. In order to prevent uncontrolled explosive combustion regimes, the initial mixtures were diluted with an inert additive  $\text{Al}_2\text{O}_3$ .

Due to the high thermal stability which was acquired during high-temperature synthesis, the synthesized metal oxide radicals can favorably influence to crystallization of metals structure and to improve the physicochemical properties of the alloys. Detailed studies of modifying abilities of the  $\text{Al}_{20}\text{B}_4\text{O}_{36}$  phase have been carried out. The signal magnitude is corresponding

to availability of free valence using EPR spectrum is proportional to the percentage of this chemical compound in probe. The silumin (brand AK12) (Si = 10.5% wt) has subjected to modification. The figure shows two images of cast structure of modified and unmodified silumin ingots. Their comparison shows that the introduction of modifier in the amount of 0.03% of the mass., leads to a radical change in the structure of the casting (Fig. 1).

Table 1. Investigation results of effectiveness of reaction mixture attack by clusters with different metals

| Attacked reaction mixture                | Element-attacked clusters  | X-ray phase analysis of obtained products            |  | ESR spectrum of obtained product   |  |
|--|--|--|--|--|--|
|  |  | Substance  | Weight content, %  |  |  |
| $\gamma$ -Al <sub>2</sub> O <sub>3</sub> | W  | CaAl <sub>4</sub> O <sub>7</sub>                     | 66,8   |    |  |
|  |  | Al <sub>2,427</sub> O <sub>3,64</sub>                | 18,4   |  |  |
|  |  | Al <sub>2,66</sub> O <sub>4</sub>                    | 11,7   |  |  |
|  |  | W  | 3,2  |  |  |
|  | Mo   | Al <sub>2</sub> O <sub>3</sub>                       | 73,4   |  |  |
|  |  | Al <sub>7,7</sub> Mo <sub>30</sub> Si <sub>3,3</sub> | 21,5   |  |  |
| Mo                                       |  | 5,1  |  |  |  |
| Cu                                       | Al <sub>2</sub> O <sub>3</sub>   | 74,8   |  |  |  |
|  | Al <sub>2,427</sub> O <sub>3,64</sub>  | 11,3   |  |  |  |
|  | Al <sub>2,66</sub> O <sub>4</sub>  | 8,3  |  |  |  |
|  | Cu   | 1,6  |  |  |  |
|  | SiO <sub>2</sub>   | 1,5  |  |  |  |
|  | Ca <sub>2,25</sub> (Si <sub>3</sub> O <sub>7,5</sub> (OH) <sub>1,5</sub> )(H <sub>2</sub> O) | 1,3  |  |  |  |
|  | Cu <sub>2</sub> O  | 1,2  |  |  |  |
| Ni                                       | Al <sub>2</sub> O <sub>3</sub>   | 57,2   |  |  |  |
|  | Al <sub>2,66</sub> O <sub>4</sub>  | 28,5   |  |  |  |
|  | SiO <sub>2</sub>   | 10,9   |  |  |  |
|  | Ni   | 3,5  |  |  |  |
| Co                                       | Al <sub>2</sub> O <sub>3</sub>   | 39,7   |  |  |  |
|  | Al <sub>2,427</sub> O <sub>3,64</sub>  | 34,5   |  |  |  |
|  | Al <sub>2,66</sub> O <sub>4</sub>  | 25,8   |  |  |  |
| B <sub>2</sub> O <sub>3</sub> + Al       | W  | Al <sub>2</sub> O <sub>3</sub>                       | 60,4   |  |  |
|  |  | Al <sub>20</sub> B <sub>4</sub> O <sub>36</sub>      | 30,3   |  |  |
|  |  | Al   | 3,3  |  |  |
|  |  | B(OH) <sub>3</sub> ***                               | 6,0  |  |  |

|    |  |      |  |
|----|--|------|--|
| Mo | SiO <sub>2</sub>                                       | 47,9 |  |
|    | B <sub>2</sub> Mo <sub>5</sub> Si                      | 24,6 |  |
|    | Mo   | 21,5 |  |
|    | Al <sub>3</sub> Mo                                     | 5,9  |  |
| Ti | Al <sub>2</sub> O <sub>3</sub>                         | 56,9 |  |
|    | Na <sub>2</sub> B <sub>6</sub> O <sub>10</sub>         | 11,4 |  |
|    | (TiN) <sub>0,88</sub>                                  | 7,2  |  |
|    | AlN  | 5,2  |  |
|    | AlTi <sub>3</sub> N                                    | 4,0  |  |
|    | Na <sub>1,22</sub> Al <sub>11</sub> O <sub>17,11</sub> | 6,7  |  |
|    | TiN  | 5,1  |  |
| Cu | Al   | 3,5  |  |
|    | Al <sub>2</sub> O <sub>3</sub>                         | 29,6 |  |
|    | SiO <sub>2</sub>                                       | 28,4 |  |
|    | Al   | 17,1 |  |
|    | Cu <sub>0,83</sub> Si <sub>0,17</sub>                  | 13,4 |  |
|    | Al <sub>2</sub> Cu                                     | 5,9  |  |
|    | Al <sub>20</sub> B <sub>4</sub> O <sub>36</sub>        | 3,4  |  |
| Cu | 2,2  |      |  |

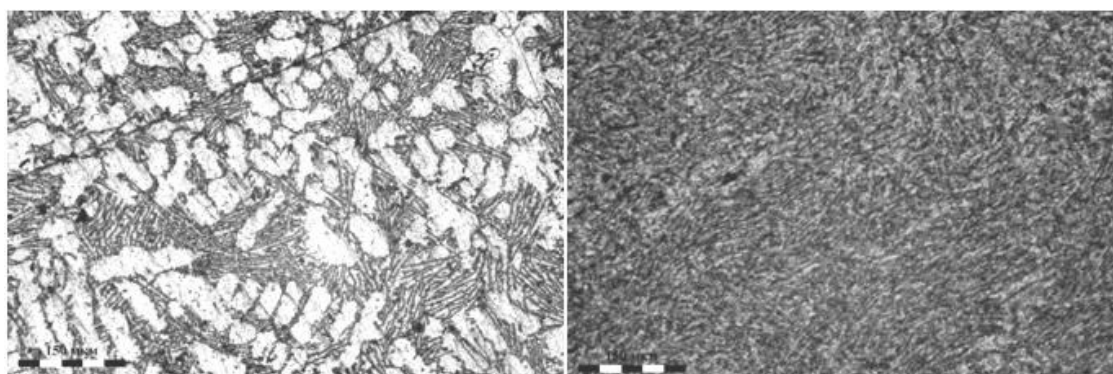


Fig. 1. Metallography of modified and non-modified silunim samples (line 150  $\mu\text{m}$ ).

The effect of this modifier cannot be explained by any of the accepted mechanisms. First of all, the syngony and crystal lattice parameters of modified corundum (trigonal:  $a = 0.467$  nm) and aluminum borate (orthorhombic:  $a = 0.769$  nm,  $b = 1.404$  nm,  $c = 0.567$  nm) do not correspond to those of the  $\alpha$ -phase of aluminum (cubic:  $a = 0.404$  nm) and  $\beta$ -phase silicon (cubic:  $a = 0.543$  nm). Consequently, in this case the Dankov principle is not fulfilled (the principle of the structural-dimensional correspondence between the nucleation centers of crystallization and the crystallizing phase). The modifying effect cannot be explained by the action of boron, which could pass into the melt by the reaction  $\text{B}_2\text{O}_3 + 2\text{Al} \rightarrow 2\text{B} + \text{Al}_2\text{O}_3$ , since boron is not an independent modifier in the Al–Si dual system.

It should be noted that the maximum boron content in melt due to modifier does not exceed 0.012% by mass. At the same time, the content of boron in the crystallization process is in solid solution.

Thus, the hypothesis of the modifying ability of ceramics in the Al–B–O system, which has a strong disequilibrium associated with free valence, has received a direct experimental confirmation.

The study of properties of multiphase substances that obtained under extremely non-equilibrium conditions by combustion method under centrifugal acceleration impact, it shows that such materials can be successfully used in many areas: metallurgy, catalysis, magnetism, effects on chemical processes of chain nature, increase in the burning rate of powders in the

production of explosives substances and mixed fuels; et al. Extensive possibilities in order to synthesize new materials based on high energy chemistry and create processes where the Arrhenius barrier reaches 1 mJ or more. By placing successively attacked layers in the reactor and increasing the rotational frequency up to 10 thousand rpm, it is possible to replace the attacking heavy metal clusters by light metal clusters, to use the attacking layers based on rare-earth elements.

- 1 G.I. Ksandopulo, SHS in conditions of rotation: thermal and concentration combustion limits for oxide systems taken as an example, *Int. J. Self-Propag. High-Temp. Synth.*, 2011, vol. 20, pp. 220–223.
- 2 G.I. Ksandopulo, Non-chain autoacceleration of SHS wave in conditions of rotation, *Int. J. Self-Propag. High-Temp. Synth.*, 2015, vol. 24, pp. 8–13.
- 3 A. Baideldonova, G. Ksandopulo, L. Mukhina, Initiation of the adiabatic wave of combustion for obtaining the substances with the free valence, *IOP Conf. Ser.: Mater. Sci. Eng.*, 2016, vol. 123.
- 4 G.I. Ksandopulo, A.N. Baideldinova, L.V. Mukhina, E.A. Ponamareva, Z.M. Azizov, Nanocarbon structures and other nontrivial substances in SHS products under centrifugal acceleration influence, Int. Symp. “Physics and chemistry of carbon materials and nanoengineering”, Int. Conf. “Nanoenergetic materials and nanoenergy”, Almaty, 2016, pp. 3–7.



## APPLICATION OF SHS-ELECTRODE MATERIALS IN PULSED ELECTROSPARK DEPOSITION TECHNOLOGY

A. E. Kudryashov\*<sup>a</sup> and E. A. Levashov<sup>a</sup>

<sup>a</sup>National University of Science and Technology MISiS, Moscow, 119049 Russia

\*e-mail: aekudr@yandex.ru

DOI: 10.24411/9999-0014A-2019-10072

The pulsed electrospark deposition (ESD) technology is widely used in different industries due to high adhesive properties of the deposited coatings and the fact that this technology allows local treatment of large-size items and is a relatively simple procedure that can be automated. Coating application is an environmentally friendly process characterized by low energy-output ratio, high profitability, and quick achievement of the breakeven point.

The range of practical application of the ESD technology can be broadened by developing novel compositions of electrode materials.

Metals and their alloys, graphite, and hard alloys (mainly those based on tungsten carbides of grades VK (WC–Co), TK (TiC–WC–Co), and TTK (TiC–WC–TaC–Co) that are produced using the traditional powder metallurgy technology) are conventionally used as electrode materials. Tungsten-free hard alloys of grades TN (TiC–Ni–Mo), KNT (Ti(CN)–Ni–Mo), LKTs (TiZr(CN)–Ni–Mo), etc. are less common [1, 2].

However, the conventional microcrystalline hard alloys do not always meet the requirements posed to electrode materials as they are characterized by high erosion resistance, low transfer efficiency, low hardness of coatings formed by these alloys, low heat and oxidation resistance of tungsten carbide, as well as the high coefficient of friction of the deposited coatings.

In this connection, there exists a demand for designing advanced electrode materials, including nanostructured hard alloys. Mastering the technology of self-propagating high-temperature synthesis (SHS) has opened up a fundamentally new approach to fabrication of electrodes for electrospark deposition.

Electrode materials forming multifunctional coatings (wear-, heat- and corrosion-resistant coatings, anti-friction coatings, coatings with enhanced hardness, etc.) on the surface of treated items are selected depending on a specific scientific-and-technological problem. By varying the frequency-energy modes of treatment, as well as the type of electrode materials (hard alloys, metals and their alloys), the ESD technology is successfully used for strengthening and repairing tools and machine components.

The objective of this study was to demonstrate application of SHS-electrode materials for the pulsed electrospark deposition technology.

The designed electrode materials can be subdivided into several groups. However, electrode materials modified with high-melting-point nanodispersed components are the most widely used ones [3].

Application of modified electrode materials becomes especially topical, since these materials improve properties of the deposited coatings (increase their thickness, continuity, microhardness, heat and wear resistance, as well as reduce their coefficient of friction) [3].

The Korona, Impuls, and Elitron equipment, as well as advanced high-frequency Alier-Metal setups, has been successfully employed for solving technical problems. The use of novel Alier-Metal high-frequency setups (with the pulse frequency ranging from 3000–3200 Hz to 50000 Hz) has significantly reduced roughness of the deposited coatings, making it possible to treat critical parts of specialized equipment. It is most reasonable to subject expensive small-batch

items (such as critical parts of aerospace and specialized equipment, large-sized dies for hot forging, and forming rollers) to electrospark treatment.

Electrospark strengthening of a pilot batch of flanges (made of VT 20 titanium alloy) with STIM-3BVn (TiC–Cr<sub>3</sub>C<sub>2</sub>–Ni–W<sup>nano</sup>) electrode materials was carried out to increase their service life (Fig. 1a). Bench tests conducted at the A. Lyulka Scientific and Technical Center of the Research and Production Association "Saturn" revealed that parts strengthened with SHS electrodes had undergone minimal wear. Tests of the parts strengthened with T15K6 alloy were stopped because of significant wear. STIM-3BVn electrode materials have been introduced into manufacturing of flanges employed in 117C aircraft engines and are supplied to a number of enterprises (PAO "Ufa Engine Industrial Association", Lytkarino Machine-Building Plant, and AO "Salyut Machine-Building Production Association.")

Technological recommendations for electrospark deposition of coatings using SHS electrodes onto pilot batches of advanced aircraft equipment parts made of titanium alloys have been developed in cooperation with the All-Russian Scientific Research Institute of Aviation Materials for OAO "Production Design Corporation Teploobmennik". The technology of electrospark treatment of dies was intended primarily for strengthening dies for hot-die forging as this is the most complex and expensive type of dies. The technology is successfully used for strengthening other types of dies: blanking, forming, drawing, bending, isothermal, as well as cold-forging dies.

Application of advanced modified hard-alloy electrodes and modern Alier-Metal equipment ensures that durability of die tooling is enhanced over twofold. In order to improve performance, solid lubricants (WSe<sub>2</sub>, MoS<sub>2</sub>, graphite) were applied onto coatings deposited by electrospark treatment. Durability of the drawing matrix used at the cold die-forging shop at the Likhachev Moscow Automotive Plant (AMO ZiL) treated using this technology increased more than 12-fold. The developed technology of electrospark strengthening of die tooling has undergone appraisal at such enterprises as PAO "Ufa Engine Industrial Association", S. Ordzhonikidze Plant (Podolsk, Russia), AO "Salyut Machine-Building Production Association", AMO ZiL, Turbine Blades Plant, a branch of OAO "Powder Machines" (St. Petersburg, Russia), Aircraft Production Association (Nizhny Novgorod, Russia), Plant of the Research Institute of Automation and Instrument-Building (NIIAP) (Moscow, Russia), AOOT "Kontur" (Novgorod, Russia), AO "Stupino Metallurgical Company", etc. At a number of enterprises, the developed technologies for die strengthening and SHS-electrode materials have been introduced into the technological process.

A hardening unit manufactured by Cobra company is used at ZAO "Sprint-RIM" (Moscow, Russia) to produce metal strap. The temperature of metal strap exposed to hardening is 960°C at the inlet and 20°C at the outlet of water-cooled plate. While in service, the plate surface undergoes severe wear. In order to increase the service life, the plate surface was subjected to ESD treatment with STIM-40NA (TiC–NiAl), STIM-40NAKNn (TiC–NiAl–NbC<sup>nano</sup>), and VK8 electrodes. ESD treatment enhanced plate durability more than tenfold.

Application of high-energy modes of ESD made it possible not only to strengthen the surface of forming rollers for copper wire production (up to fourfold) but also to restore their size after roller re-machining (ELKAT Enterprise, Moscow, Russia). Electrospark retreatment of the deposited coatings with carbon-containing materials was proposed to further enhance performance of the coatings. Retreatment reduces roughness of the surface layer and the size of structural components of the coating, increases the volume fraction of carbide phases, reduces and stabilizes the coefficient of friction at elevated loads and temperatures [4, 5].

SHS-electrode materials have been successfully used to treat cutting tools, parts of railway equipment, brick-making molds, drill bit casings and milling cutters for the construction industry, to strengthen valve ends of internal combustion engines for sport cars manufactured from titanium alloys, casings of sensors for oil wells (Fig. 1b), and to restore the size of various items.



Fig. 1. Strengthened items. A flange (a) and a sensor housing (b).

1. A.E. Gitlevich, V.V. Mikhailov, N.Y. Parkanskii, et al., *Electrospark Alloying of Metal Surfaces*, Chisinau: Shtiintsa, 1985, 195 p.
2. S.V. Nikolenko, A.D. Verkhoturov, *New Electrode Materials for Electrospark Alloying*, Vladivostok: Dal'nauka, 2005, 219 p.
3. E.A. Levashov, A.S. Rogachev, V.V. Kurbatkina, Yu.M. Maksimov, et al., *Advanced Materials and Technologies of Self-Propagating High-Temperature Synthesis*, Moscow: Mosk. Inst. Stali Splavov, 2011, 377 p.
4. A.E. Kudryashov, Zh.V. Ereemeeva, E.A. Levashov, V.Yu. Lopatin, et al., On application of carbon-containing electrode materials in technology of electrospark alloying: Part 1. Peculiarities of coating formation using electrospark treatment of titanium alloy OT4-1, *Surf. Eng. Appl. Electrochem.*, 2018, vol. 54, no 5, pp. 437–445.
5. A.E. Kudryashov, Zh.V. Ereemeeva, E.A. Levashov, V.Yu. Lopatin, et al., On the application of carbon-containing electrode materials in electrospark alloying technology. Part 2. Structure and properties of two-layer coatings. *Surf. Eng. Appl. Electrochem.*, vol. 54, no 6, pp. 535–545.

## FEATURES OF DEPOSITION, STRUCTURE AND PROPERTIES OF ELECTROSPARK COATINGS OF Cr–Al–B–Si, Mo–Si–B AND Zr–Si–B ON NICKEL ALLOY

**A. E. Kudryashov<sup>a</sup>, E. A. Levashov<sup>a</sup>, Ph. V. Kiryukhantsev-Korneev<sup>a</sup>, and A. N. Sheveiko<sup>a</sup>**

<sup>a</sup>National University of Science and Technology MISiS, Moscow, 119049 Russia

\*e-mail: aekudr@yandex.ru

DOI: 10.24411/9999-0014A-2019-10073

Metals and their alloys, graphite, and hard alloys (mostly those based on tungsten carbide) are conventionally used as electrode materials in the electrospark deposition technology. SHS-electrode materials based on titanium carbide and titanium diboride have recently started to be used [1]. Broadening of the range of practical application of the electrospark deposition technology is associated with the development of novel compositions of electrode materials. In this connection, it was decided to use SHS alloys based on the Cr–Al–B–Si, Mo–Si–B, and Zr–B–Si systems [2–4]. This study was aimed at investigating the features of formation, structure, composition, and properties of electrospark coatings deposited onto substrates made of refractory EP718-ID nickel alloy using heat-resistant SHS-electrode materials. The Cr–Al–Si–B, Mo–Si–B, and Zr–B–Si alloys fabricated by self-propagating high-temperature synthesis (SHS) were used as electrodes (anodes). The commonly used EP718-ID heat-resistant nickel alloy was applied as a substrate (cathode). This alloy is widely used in aircraft engine technology. The alloy composition was as follows: C ≤ 0.1 %; Cr ~ 14.0÷16.0 %; Ni ~ 43.0÷47.0 %; Fe ~ 22.0÷33.0 %; Mo ~ 4.0÷5.2 %; W ~ 2.5÷3.2 %; Nb ~ 0.8÷1.5 %; Ti ~ 1.9÷2.4 %; Al ~ 0.9÷1.4 %; Mn ~ 0.60 %; Si ~ 0.30 %; Zr ~ 0.02 %; Ce ~ 0.10 %; B ~ 0.008 %; S ~ 0.010 %; P ~ 0.015 %. The coatings were deposited using an Alier-Metal 303 setup. The applied three frequency-energy modes of electrospark treatment were characterized by current  $I = 120$  A and total pulse energy  $\Sigma E = 9.2$  kJ×min<sup>-1</sup> but differed in terms of pulse frequency and length (3200 Hz (20 μs), 1600 Hz (40 μs), and 800 Hz (80 μs)). The heat-resistance tests were conducted at a temperature of 700°C and exposure duration of 40 h (48 h for Mo–Si–B). The oxidation weight gain ( $\Delta m_s$ ) (changes in the sample weight due to oxidation per unit surface area) was determined using the following formula:

$$\Delta m_s = (m_1 - m_0)/S_0 \quad (1)$$

where  $m_0$  is the initial weight of the sample, g;  $m_1$  is the weight of the sample containing the oxidation products, g; and  $S_0$  is the area of the sample surface, m<sup>2</sup>.

The tribological properties of the coatings were determined in accordance with the international standards ASTM G 99-959 and DIN 50324 on a high-temperature tribometer (CSM Instruments) operating in the pin-on-disk mode. A ball made of Al<sub>2</sub>O<sub>3</sub> (6 mm in diameter) was used as a counter body. The coated samples were allowed to slide at a linear velocity of 10 cm/s under a load of 1 N. The temperature of the experiment was 500°C. The dependence between the coefficient of friction of the wearing pair and the path length of the counter pair (300 m) was plotted on a PC using the InstrumX software. The wear track profile and coating roughness (the arithmetic mean roughness value Ra) was evaluated using a Veeco WYKO NT1100 optical profilometer. The wear rate was calculated using the following formula:

$$W = (s \times L)/(N \times l) \quad (2)$$

where  $W$  is the wear rate, mm<sup>3</sup>·N<sup>-1</sup>·m<sup>-1</sup>;  $L$  is the perimeter of a circle, mm;  $s$  is the sectional area of the wear groove, mm<sup>2</sup>;  $N$  is the load, N; and  $l$  is the sliding distance, m.

### Cr–Al–B–Si system

The chemical and phase compositions of the applied electrode materials are listed in Table 1.

Table 1. The chemical and phase compositions of the Cr–Al–B–Si electrode materials.

| Electrode material | Content, % |      |      |      | Phase composition, %   |
|--------------------|------------|------|------|------|--|
|                    | Cr         | Al   | B    | Si   |  |
| Composition 1      | 69.4       | 8.1  | 12.0 | 10.5 | 65CrB + 27Cr(Si,Al) <sub>2</sub> + 8Cr <sub>5</sub> Si <sub>3</sub> B <sub>x</sub>   |
| Composition 2      | 65.8       | 16.2 | 12.0 | 6.0  | 35CrB + 26Cr <sub>5</sub> Si <sub>3</sub> + 39Cr <sub>4</sub> Al <sub>11</sub>   |
| Composition 3      | 63.4       | 21.6 | 12.0 | 3.0  | 15CrB + 24Cr <sub>5</sub> Si <sub>3</sub> + 57Cr <sub>4</sub> Al <sub>11</sub> + 4Cr <sub>5</sub> Si <sub>3</sub> B <sub>x</sub> |

It was found that application of the electrode with composition 1 (with the highest content of refractory CrB) caused weight loss on the kinetic curves showing the total weight gain of the cathode ( $\sum \Delta C_i$ ) after ESD for 3 min in all treatment regimes. For the electrodes with compositions 2 and 3, which have a much lower content of the boride phase, weight gain on the cathode (the substrate) was observed throughout the entire treatment for 10 min in all ESD regimes. At higher contents of low-melting phases Cr(Si,Al)<sub>2</sub>, Cr<sub>5</sub>Si<sub>3</sub>, and Cr<sub>4</sub>Al<sub>11</sub> (composition 3), coating formation became more vigorous as the amount of the melt in the discharge arc increased.

The high-frequency regime of coating treatment ( $f = 3200$  Hz), characterized by steady-state mass transfer and minimal roughness, was chosen to be optimal.

Table 2 lists the properties and composition of the deposited coatings. All the coatings are characterized by 100% continuity.

The coating deposited from the electrode with composition 1 had the minimal oxidation weight gain of 0.20 g/m<sup>2</sup> (the best heat resistance). The maximum oxidation weight gain values were observed for the coating deposited from the electrode with composition 3 and the uncoated sample (0.38 and 0.37 g/m<sup>2</sup>, respectively). It should be mentioned that when calculating this parameter, we did not take into account that the electrospark coating had a larger geometric surface area. The electrode with composition 1 was recommended to be used for treatment of items made of EP718-ID nickel alloy.

Table 2. Properties and composition of electrospark coatings.

| Electrode material | Thickness, $\mu\text{m}$ | Hardness*, GPa | Oxidation weight gain**, g/m <sup>2</sup> | Wear rate**, 10 <sup>-6</sup> mm <sup>3</sup> /(m $\times$ N) | Phase composition of ESD coatings**** (after 10 min)  |
|--------------------|--------------------------|----------------|---|---|---|
| Composition 1      | 15                       | 4.9            | 0.20                                      | 133   | Solid solution based on Ni, $\gamma$ -Al <sub>2</sub> O <sub>3</sub> , Cr <sub>2</sub> B  |
| Composition 2      | 20                       | 3.0            | 0.23                                      | 222   | Cr <sub>3</sub> Si, Cr, Fe <sub>3</sub> Si, Cr <sub>3</sub> B <sub>4</sub> , $\gamma$ -Al <sub>2</sub> O <sub>3</sub> , Fe <sub>3</sub> B                                   |
| Composition 3      | 25                       | 3.0            | 0.38                                      | 225   | Cr <sub>3</sub> Si, Cr, Fe <sub>3</sub> Si, $\gamma$ -Al <sub>2</sub> O <sub>3</sub> , Cr <sub>5</sub> Si <sub>3</sub> , Cr <sub>2</sub> N, Cr <sub>5</sub> Al <sub>8</sub> |

\*Hardness of EP718-ID nickel alloy was 1.4 GPa; \*\*Oxidation weight gain of EP718-ID nickel alloy was 0.37 g/m<sup>2</sup>; \*\*\*Wear rate of EP718-ID nickel alloy was 260 $\times$ 10<sup>-6</sup> mm<sup>3</sup>/(m $\times$ N); \*\*\*\*Phase composition of EP718-ID nickel alloy: Ni-based solid solution.

### Mo–Si–B system

The chemical and phase compositions of the applied electrode materials are listed in Table 3.

Cathode weight loss was observed during the entire treatment with the Mo-Si-B electrode materials. The properties and composition of the deposited coatings are summarized in Table 4. All the coatings had a 100% continuity. The minimal roughness ( $R_a$ ) was revealed for the coatings formed upon ESD treatment in the high-frequency regime.

It was found that the coatings deposited using the electrode materials with compositions 1–3 contained an amorphous phase. Weight loss was revealed upon oxidation of the coated

samples; the coatings oxidized using electrodes with compositions 1, 3, and 4 contained unoxidized spots. The electrodes with compositions 3 and 4 were recommended to be used to treat items made of EP718-ID nickel alloy.

Table 3. Chemical and phase compositions of Mo–Si–B electrode materials.

| Electrode material | Content, % |       |      | Phase composition of the electrodes, %                             |
|--------------------|------------|-------|------|--|
|                    | Mo         | Si    | B    |  |
| Composition 1      | 90.49      | 4.41  | 5.10 | 51 Mo <sub>2</sub> B + 2 MoB + 47 Mo <sub>5</sub> SiB <sub>2</sub> |
| Composition 2      | 74.12      | 21.7  | 4.18 | 57 MoSi <sub>2</sub> + 41% MoB + 2 Mo <sub>5</sub> Si <sub>3</sub> |
| Composition 3      | 90.61      | 5.31  | 4.08 | 96 Mo <sub>5</sub> SiB <sub>2</sub> + 2 Mo <sub>3</sub> Si + 2 Mo  |
| Composition 4      | 65.88      | 33.06 | 1.06 | 89 MoSi <sub>2</sub> + 9 MoB + 2 Mo <sub>5</sub> Si <sub>3</sub>   |

Table 4. Properties and composition of electrospark coatings.

| Electrode material | Thickness, μm | Hardness, GPa | Roughness R <sub>a</sub> , μm | Wear rate, 10 <sup>-6</sup> mm <sup>3</sup> /(m×N) | Phase composition of ESD coatings (after 10 min)                                     |
|--------------------|---------------|---------------|-------------------------------|--|--|
| Composition 1      | 35            | 4.4           | 6.26                          | 153  | Ni-based solid solution  |
| Composition 2      | 35            | 3.8           | 6.42                          | 169  | Ni-based solid solution, Mo-based solid solution                                     |
| Composition 3      | 45            | 3.8           | 8.76                          | 58   | solid solution based on Ni, Mo (Ni,Si) <sub>2</sub> , Cr <sub>3</sub> B <sub>4</sub> |
| Composition 6      | 45            | 3.2           | 8.05                          | 67   | Mo (Ni,Si) <sub>2</sub> , solid solution based on Ni, Cr <sub>3</sub> B <sub>4</sub> |

### Zr–Si–B system

Electrode material with composition 64.7 % Zr–20 % Si–15.3 % B (66 % B<sub>2</sub>–6% Si–26% ZrSi<sub>2</sub>–2 % ZrO<sub>2</sub>) was used for coating deposition. The coatings were deposited in various media: in air, argon, and under vacuum. Automated treatment was used to deposit coatings under vacuum. When coatings were deposited in air, the nickel alloy was pre-treated with carbon-carbon composite material (C-CCM) in order to produce a sublayer. Heat resistance tests of the samples were conducted at 900°C and exposure duration of 5 h. Thickness of the oxidized layer in the samples was determined by glow discharge optical emission spectroscopy (GD-OES) on a Profiler instrument (Horiba Jobin Yvon).

The maximum cathode weight gain was observed after treatment in argon. Treatment under vacuum also resulted in cathode weight gain. Electrospark deposition in air led to cathode weight loss. Cathode weight loss after pre-treatment of nickel alloy with C-CCM was less significant. Properties and composition of the coatings deposited onto EP718-ID nickel alloy are listed in Table 5. Exposure to high temperature led to formation of an oxide layer on the surface of the uncoated sample, which could be easily removed from the surface. Thickness of the deposited coatings was 20–25 μm, being much greater than depth of the oxidized layer. Therefore, it is fair to say that these coatings enhance heat resistance of nickel alloys.

Table 5. Properties and composition of electrospark coatings.

| Treatment medium | Roughness Ra, μm | Thickness of the oxidized layer*, μm | Phase composition of electrospark coatings (after 10 min)  |
|------------------|------------------|--------------------------------------|--|
| Vacuum           | 6.44             | 0.7                                  | Si, ZrB <sub>2</sub> , Ni, Ni <sub>(1-x)</sub> Si <sub>(x)</sub>   |
| Air              | 7.38             | 1.5                                  | Ni <sub>(1-x)</sub> Si <sub>(x)</sub> , ZrO <sub>2</sub> , Fe <sub>2</sub> Si, Ni <sub>4</sub> N                         |
| Argon            | 5.80             | 1.4                                  | Si, ZrB <sub>2</sub> , Ni, Ni <sub>(1-x)</sub> Si <sub>(x)</sub>   |
| Air (C-CCM + EM) | 6.01             | 0.9                                  | ZrB <sub>2</sub> , ZrC, Ni <sub>(1-x)</sub> Si <sub>(x)</sub> , ZrO <sub>2</sub> , Fe <sub>2</sub> Si, Ni <sub>4</sub> N |

\*Thickness of the oxidized layer of the EP718-ID alloy is 1 μm (without allowance for the oxidized layer that was removed).

It was impossible to measure the wear track depth when the load exerted by the counter body on the sample was minimal (1 N), since only some wear marks could be seen on the sample surface. When the load was increased to 5 N, the wear rate of the coated samples was approximately twofold lower than that for nickel alloy samples.

According to these findings, it is recommended that the Zr–Si–B electrode materials are deposited in argon or under vacuum for obtaining high-quality coatings.

This work was carried out with financial support from the Ministry of Education and Science of the Russian Federation in the framework of state assignment no.11.7172.2017/8.9.

1. E.A. Levashov, A.S. Rogachev, V.V. Kurbatkina, Yu.M. Maksimov, et al. *Advanced Materials and Technologies of Self-Propagating High-Temperature Synthesis*, Moscow: MISIS, 2011, 377 p.
2. Yu.S. Pogozev, A.Yu. Potanin, E.A. Levashov, D.Yu. Kovalev, The features of combustion and structure formation of ceramic materials in the Cr–Al–Si–B system, *Ceram. Intern.*, 2014, vol. 40, no. 10, pp. 16299–16308.
3. E.A. Levashov, Yu.S. Pogozev, A.Yu. Potanin, N.A. Kochetov, et al. Self-propagating high-temperature synthesis of advanced ceramics in the Mo–Si–B system: Kinetics and mechanism of combustion and structure formation, *Ceram. Intern.*, 2014, vol. 40, no 5, pp. 6541–6552.
4. Yu.S. Pogozev, I.V. Iatsyuk, A.Yu. Potanin, E.A. Levashov, et al. The kinetics and mechanism of combusted Zr–B–Si mixtures and structural features of ceramics based on zirconium boride and silicide, *Ceram. Intern.*, 2016, vol. 42, no 15, pp. 16758–1676.

## APPLICATION OF SHS-ELECTRODE MATERIALS IN METALLURGY

**A. E. Kudryashov<sup>\*a</sup>, A. V. Makarov<sup>b</sup>, N. I. Repnikov<sup>b</sup>, and E. M. Martynov<sup>b</sup>**<sup>a</sup>National University of Science and Technology MISiS, Moscow, 119049 Russia<sup>b</sup>A.A. Ugarov Stary Oskol Technological University, Branch of the National University of Science and Technology MISiS, Stary Oskol, 309516 Russia

\*e-mail: aekudr@yandex.ru

DOI: 10.24411/9999-0014A-2019-10074

Electrospark deposition is one of efficient technologies for enhancing the durability of forming rollers. VK (WC–Co) and TK (WC–TiC–Co) hard alloys, ferrochrome, high-chromium and high-carbon (1.0–2.0 % C) steels and alloys are used as electrode materials to strengthen the rollers [1]. Electrode materials of STIM grade (a Russian acronym for synthetic hard tool material) fabricated using the self-propagating high-temperature synthesis (SHS) are the most promising materials to strengthen forming rollers. Performance characteristics (hardness, heat and wear resistance) of coatings made of these materials are superior to those made of VK6 and T15K6 alloys [2].

Further enhancement of performance properties of the coatings deposited using the electrospark technology involves the application of SHS electrode materials modified with a nanodispersed component [3] and conduction of electrospark deposition via two stages. A barrier sublayer and a multifunctional protective coating are formed at the first and second stages, respectively.

This study aimed to demonstrate how SHS-electrode materials and the electrospark deposition technology are applied in metallurgy (forming rollers, rollers of a continuous billet casting machine).

When elaborating the technology for strengthening forming rollers, SPKhN-60 white cast iron samples were used as cathodes (substrates). STIM-40NAOKn (TiC–NiAl–ZrO<sub>2</sub><sup>nano</sup>) and STIM-11OKn (TiB<sub>2</sub>–NiAl + ZrO<sub>2</sub><sup>nano</sup>) alloys modified with a nanodispersed component were employed as electrode materials for production of the multi-functional layers.

Electrospark coatings were deposited in air on an Alier-Metal G53 setup.

Calculation of the Palatnik's criterion showed that the electrodes made of chromium and nickel are the optimal ones for sublayer deposition. The energy regime for treatment with metal electrodes was determined (0.175 J). The energy regime of 0.4 J was used for treatment using hard-alloy electrodes [2].

The cathode weight was increasing throughout the entire coating deposition duration (7 min) when the electrodes made of nickel and chromium were applied. Treatment of the samples without a sublayer and with a chromium sublayer with STIM-40NAOKn alloy led to cathode weight loss during 10 min. For the sample strengthened using a nickel sublayer, the cathode weight was increasing during the first 5 min. Application of the STIM-11OKn electrode caused cathode weight loss.

Electrospark treatment in the optimal energy regime gives rise to coatings characterized by high continuity (up to 100%), thickness up to 100 μm, and hardness up to 10.5 GPa.

Transmission electron microscopy examination revealed that grain size of the wear-resistant phases in the resulting layers was 10 nm.

Adhesion strength between the two-layer electrospark coatings and the white cast iron substrate is higher than 100 N.

It was found that preliminary deposition of a sublayer increases the content of refractory phases in the deposited coatings (TiC, Fe<sub>3</sub>(B,C), Fe<sub>23</sub>B<sub>6</sub>, Fe<sub>2</sub>B, Ti B<sub>2</sub>). The maximum content



of the refractory phases is observed in the coatings containing a nickel sublayer.

The coatings formed by the electrodes based on titanium diboride have higher heat resistance ( $T = 500^{\circ}\text{C}$ ) as compared to the coatings made of titanium carbide. Deposition of a nickel sublayer increases the heat resistance of STIM-11OKn coatings more than eightfold.

The application of two-layer coatings reduced wear rate fourfold as compared to that in non-strengthened white cast iron samples.

It was decided to test application of the electrospark deposition technology and STIM-11OKn and STIM-40NAOKn SHS-electrode materials for strengthening rollers of the continuous billet casting machine (CBCM).

Application of the electrode material based on titanium carbide ( $E = 0.4 \text{ J}$ ) was found to result in cathode weight gain, while treatment with an electrode based on titanium diboride caused cathode weight loss.

A set of studies of the structure, composition, and properties of the coatings deposited onto 20X13 steel was carried out.

No surface cracks were found after the coated samples had undergone 10 thermocycling rounds (exposure to  $T = 900^{\circ}\text{C}$  for 30 min, cooling at a rate of  $3^{\circ}\text{C/s}$ ).

The findings obtained in this study were used to elaborate the technology process for strengthening forming rollers.

The developed technology process was tested for forming rollers of a finisher stand no. 24 (roller diameter, 376.5 mm) using the facilities of the Oskol Electrometallurgical Plant JSC. The results of the tests showed that durability of the strengthened roll pass was eightfold higher than that of the uncoated roll pass.

1. A.E. Kudryashov, E.I. Zamulaeva, E.A. Levashov, O.S. Manakova, M.I. Petrzhik, Application of the electrospark deposition technology and modified SHS-electrode materials to enhance durability of forming rolls in a hot-rolling mill. Part 1. The features of coating formation on substrates made of SPKhN-60 white cast iron. Electron-assisted treatment of materials. *Elektron. Obrab. Mater.*, 2018, vol. 54, no. 5, pp. 43–55. (In Russ)
2. A.E. Kudryashov, O.N. Doronin, E.I. Zamulaeva, E.A. Levashov, N.V. Shvyndina, The prospects of application of electrode SHS materials and the electrospark deposition technology to strengthen forming rollers. *Chernye Met.*, 2013, no 10, p. 61–68. (In Russ)
3. A.E. Kudryashov, Yu.S. Pogochev, E.A. Levashov, Electrodes. Concise Encyclopedia of Self-Propagating High-Temperature Synthesis History, Theory, Technology, and Products, Eds I. Borovinskaya, A. Gromov, E. Levashov, Yu. Maksimov, A. Mukasyan, A. Rogachev, Elsevier, 2017, pp. 103–104.

## DEVELOPMENT OF FUNCTIONALLY GRADED WEAR-RESISTANT WC/a-C COATINGS BY A COMBINATION OF PULSED ARC EVAPORATION AND ELECTROSPARK DEPOSITION

K. A. Kuptsov<sup>\*a</sup>, A. N. Sheveyko<sup>a</sup>, D. A. Sidorenko<sup>a</sup>, and D. V. Shtansky<sup>a</sup><sup>a</sup>National University of Science and Technology MISiS, Moscow, 119049 Russia

\*e-mail: kuptsov.k@gmail.com

DOI: 10.24411/9999-0014A-2019-10075

Titanium alloys are widely used due to their unique combination of high strength-to-weight ratio, melting temperature and corrosion resistance. Their main disadvantages are low wear resistance and self-adhesive wear during friction. To overcome these drawbacks, they are coated by hard PVD coatings with low friction coefficient. However, small coatings thickness, typically below 10  $\mu\text{m}$ , is not sufficient to prevent substrate deformation under high contact loads. Herein we report on a new approach of two-layer WC/C coating deposition by a combination of pulsed arc evaporation (PAE) and electro-spark deposition (ESD) [1]. In such coatings, bottom ESD layer provides superior adhesion and stiffness due to high thickness ( $< 100 \mu\text{m}$ ), whereas top PAE layer possesses high mechanical and tribological properties. The structure, phase and chemical composition of the obtained two-layer coatings were studied by SEM, TEM, XRD, XPS, Raman spectroscopy, and GD-OES techniques. The coatings were also characterized in terms of their mechanical (hardness, Young's modulus, elastic recovery, adhesion strength, and resistance to cyclic impact load) and tribological (friction coefficient and wear rate) properties. In addition, in situ coating mechanical tests were carried out inside transmission electron microscope using Hysitron PI 95 PicoIndenter. For the ESD sublayer, a composite structure, in which carbide grains ( $\text{TiC}$  and  $\text{WC}_{1-x}$  with a cubic lattice of B1 type) were separated by layers of  $\alpha$ - and  $\beta$ -Ti phases, was observed. The upper PAE layer, deposited either in argon or in  $\text{C}_2\text{H}_4$ , consisted of tungsten carbide in the form of  $\text{W}_2\text{C}$  and cubic  $\text{WC}_{1-x}$  phases. Two-layer coatings obtained under optimal conditions demonstrated high hardness of 21 GPa, low coefficient of friction in the range of 0.15–0.18 at applied loads up to 10 N, enhanced wear resistance (wear rate  $< 1.4 \times 10^{-7} \text{ mm}^3/\text{Nm}$ ), and superior resistance to cyclic impact loads up to 1000 N for  $10^5$  cycles.

1. K.A. Kuptsov, A.N. Sheveyko, E.I. Zamulaeva, D.A. Sidorenko, D.V. Shtansky. Two-layer nanocomposite WC/a-C coatings produced by a combination of pulsed arc evaporation and electro-spark deposition in vacuum, *Mater. Des.*, 2019, vol. 167, 107645.

ADVANCED ULTRA-HIGH-TEMPERATURE COMPOSITES BASED ON  
SHS-SINGLE PHASE SOLID SOLUTION (Hf,Ta)B<sub>2</sub>V. V. Kurbatkina<sup>\*a</sup>, E. I. Patsera<sup>a</sup>, and E. A. Levashov<sup>a</sup><sup>a</sup>National University of Science and Technology MISIS, Moscow, 119049, Russia

\*e-mail: vvkurb@mail.ru

DOI: 10.24411/9999-0014A-2019-10076

Development of advanced composites for high-temperatures applications are important trend in materials science. Design of such materials will enable the creation of new types of energy-conversion engines, high-velocity transportation and aerospace vehicles [1–3].

Ones of the most prospective materials in this regard are composites based on HfB<sub>2</sub> ( $T_m = 3653$  K), ZrB<sub>2</sub> (3473 K), TaB<sub>2</sub> (3473 K), NbB<sub>2</sub> (3323 K) [4], which possess high strength, fracture toughness, resistance against the wear and thermal shock. Another important advantage of the boride composites is their high thermal conductivity, which ensures the efficient heat sink from the surface which contacts with the high-temperature oxidative gas. Solid solutions possess higher melting points as compared to the individual constituents. For example, single-phase carbide (Ta,Hf)C, containing 20% HfC, has the melting point of 4223 K. Non-linear dependence on the composition of the solid solution is characteristic for hardness, coefficient of thermal expansion (CTE), thermal conductivity. The combination of high thermal conductivity and low CTE defines the resistance of the material against thermal shocks [1–3].

Synthesis of single-phase compounds based on refractory borides is a relevant scientific and technological task. Various routes are known for the production of complex carbides and borides, including the heating of powder mixtures, carbon reduction of oxide mixture, solution precipitation, microwave synthesis, sol-gel synthesis, hot pressing, etc. SHS offers unique possibilities for the synthesis of UHTCs. Hybrid technologies SHS+HP, SHS+SPS and reactive HP and SPS are capable of producing the dense ultra-high temperature materials with unique structure and properties [3, 5, 6].

This work considers the problems of obtaining single-phase solid solutions based on hafnium and tantalum diborides (Hf,Ta)B<sub>2</sub> by the SHS method [7, 8].

In the Hf–Ta–B system, the phase formation mechanisms differ from the previously investigated Ta–Zr–B system [6], which is related to the contact melting which occurs in the Hf–B system at temperature 2153 K and B content  $\leq 0.8$  wt %. Contact melting occurs corresponding to the eutectic reaction:  $\beta\text{-Hf} + \text{HfB} \rightarrow \text{Liq}$  with the formation of a melt containing solid particles HfB +  $\beta\text{-Hf}$ . At temperature 2365 K, boron melts and nearly simultaneously the primary crystals of HfB<sub>2</sub> and TaB<sub>2</sub> are formed, followed by the melting of hafnium (2505 K) and active chemical interaction in melt following the formation of solid solution based on the tantalum and hafnium diborides [7, 8]. Due to the high melting temperature and high heat loss, the post-combustion zone is relatively narrow. Concentration homogenization takes place in the post-combustion zone. However, the high porosity of the synthesis products and low diffusion rates do not allow the formation of equilibrium phases to be completed. A significant difference in grain composition and size is retained in the synthesis products. However, the synthesized powders are successfully employed for the subsequent sintering by HP and SPS. Chemical uniformity is achieved during the sintering.

SHS powders in Hf–Ta–B systems were employed for the hot pressing and spark plasma sintering of dense composites with residual porosity below 2–3%. Two produced composites based on (Hf,Ta)B<sub>2</sub> possessed superior high hardness 60–70 GPa and elastic modulus 584 GPa.

The measured heat conductivity of the HfB<sub>2</sub>-based solid solutions (Hf,Ta)B<sub>2</sub> was 53 Wt/m·K, which is above the heat conductivity for TaB<sub>2</sub>, but below the heat conductivity of HfB<sub>2</sub>. Heat conductivity of two-phase specimen was 30 Wt/m·K. The measured values of heat conductivity are 10% higher for (HfTa)B<sub>2</sub> than for (Zr,Ta)B<sub>2</sub>, and are comparable to the ZrB<sub>2</sub>-25% SiC ceramic.

Refractory silicides are often used as the alloying additive for the betterment of the heat resistance of boride and carbide-based ceramics. In particular, in this work, Ti<sub>5</sub>Si<sub>3</sub> and TaSi<sub>2</sub> were added to the (HfTa)B<sub>2</sub> solid solution. SHS in the Hf–Ti–Ta–Si–B system was studied. Combustion temperature and velocity were measured, and the sequence of phase formation in the combustion front was investigated. Optimal conditions for the force SHS-pressing were established without the “chemical furnace” use, which allows the one-step production of dense Hf–Ti–Ta–Si–B ceramic with relative density 94–95%. Synthesized specimens consist of two complex solid solutions: (Hf,Ti,Ta)B<sub>2</sub> and (Hf,Ti,Ta)<sub>5</sub>Si<sub>3</sub>B. Diboride crystals with the size of 1–2 μm are embedded in the borosilicide matrix. Mechanical properties of such composites consisted of (Hf,Ti,Ta)B<sub>2</sub> and (Hf,Ti,Ta)<sub>5</sub>Si<sub>3</sub>B were studied. The microhardness of the (Hf,Ti,Ta)B<sub>2</sub> is almost three times higher as compared to the (Hf,Ti,Ta)<sub>5</sub>Si<sub>3</sub>B. In a similar fashion, elastic modulus for diboride solid solution was 3 times higher as compared with (Hf,Ti,Ta)<sub>5</sub>Si<sub>3</sub>B.

Specimens in system Hf–Ti–Ta–Si–B sintered by various techniques (HP, SPS, force SHS-pressing) have identical phase composition, which includes two complex solid solutions diboride-based (Hf,Ti,Ta)B<sub>2</sub> and borosilicide-based (Hf,Ti,Ta)<sub>5</sub>Si<sub>3</sub>B.

For the first time, the temperature dependencies of the heat capacity, thermal diffusivity, thermal conductivity, coefficient of thermal expansion were measured for the composites (Hf,Ti,Ta)B<sub>2</sub> + (Hf,Ti,Ta)<sub>5</sub>Si<sub>3</sub>B sintered by HP and SPS. Thermal conductivity for (initial mixture (Hf, Ta)B<sub>2</sub> + 35% Ti<sub>5</sub>Si<sub>3</sub>) ceramics produced by hot pressing at 1700°C was 24 Wt/m·K; for the same composition produced by SPS, the conductivity was 23 Wt/m·K. The CTE for the hot-pressed specimens at 600°C in the height direction was 14.5·10<sup>-6</sup> K<sup>-1</sup>, in the diameter direction – 7.0·10<sup>-6</sup> K<sup>-1</sup>. With an increase in the temperature till 900°C, these values increase up to 18.5 and 10.1·10<sup>-6</sup> K<sup>-1</sup>, correspondingly.

Oxidation mechanism for ceramics (Hf,Ti,Ta)<sub>5</sub>Si<sub>3</sub>B + (Hf,Ta,Ti)B<sub>2</sub> at 1100°C was studied. Mass change during oxidation was approximated as logarithmic functions for all specimens to reveal the common oxidation mechanism.

This work was conducted with the financial support of the Russian Ministry of Science and High Education in the framework of state assignment no. 11.1207.2017/ИЧ.

1. A. Paul, D.D. Jayaseelan, S. Venugopal, E. Zapata-Solvas, J. Binner, B. Vaidhyanathan, A. Heaton, P. Brown, W.E. Lee, *Amer. Ceram. Soc. Bull.*, 2012, vol. 91, no. 1, pp. 22–29.
2. E. Wuchina, E. Opila, M. Opeka, W. Fahrenholtz, I. Talmy, *Electrochem. Soc. Interface*, 2007, pp. 30–36.
3. R. Licheri, C. Musa, R. Orrù, G. Cao, D. Sciti, L. Silvestroni, *J. Alloys Compd.*, 2016, vol. 663, pp. 351–359.
4. H.O. Pierson, *Handbook of refractory carbides and nitrides*, 1996, pp. P8–P16.
5. E.A. Levashov, A.S. Mukasyan, A.S. Rogachev, D.V. Shtansky, *Int. Mater. Rev.*, 2017, vol. 62, no. 4, pp. 203–239.
6. V.V. Kurbatkina, E.I. Patsera, E.A. Levashov, A.N. Timofeev, *J. Europ. Ceram. Soc.*, 2018, vol. 38, pp. 1118–1127.
7. V.V. Kurbatkina, E.I. Patsera, E.A. Levashov, *Ceram. Int.*, 2019, vol. 45, pp. 4067–4075.
8. V.V. Kurbatkina, E.I. Patsera, D.V. Smirnov, E.A. Levashov, S. Vorotilo, A.N. Timofeev, *Ceram. Int.*, 2019, vol. 45, pp. 4076–4083.

## FABRICATION OF Al–AlN NANOCOMPOSITE BY POWDER METALLURGY METHOD USING AlN NANOPOWDER OF SHS-AZ BRAND

A. A. Kuzina<sup>a</sup>, A. P. Amosov<sup>\*b</sup>, D. A. Zakharov<sup>c</sup>, and Yu. V. Titova<sup>b</sup>

<sup>a</sup>Samara National Research University, Samara, 443086 Russia

<sup>b</sup>Samara State Technical University, Samara, 443100 Russia

<sup>c</sup>Joint-stock company Volgaburmash, Samara, 443004 Russia

\*e-mail: egundor@yandex.ru

DOI: 10.24411/9999-0014A-2019-10077

Dispersion-strengthened composites based on aluminum alloys, reinforced by ceramic particles of aluminum oxide and silicon carbide of the micron sizes from 1 to 50  $\mu\text{m}$ , are widely used for production of modern articles of the space and aviation industry. Currently, much attention is paid to the use of nanoscale (less than 0.1  $\mu\text{m}$ ) reinforcing particles, the introduction of which into the composites provides high strength characteristics of the composites with a low content of the dispersed phase, that allows to keep in such composite good ductility and workability of the aluminum matrix. Such nanocomposites are made by solid-phase methods of powder metallurgy and liquid-phase methods of casting. The liquid-phase methods differ in simplicity and profitability due to the possibility of using the existing low-cost foundry equipment and fabrication of castings of relatively large size and complex shape. Therefore, numerous attempts are being made to introduce nanoparticles of various refractory compounds ( $\text{Al}_2\text{O}_3$ , SiC, TiC,  $\text{Si}_3\text{N}_4$ , AlN, etc.) into the aluminum melt. However, nanoparticles are very active, oxidize at rather low temperatures, stick together in strong agglomerates, poorly wetted by liquid aluminum, therefore, their direct incorporation and uniform distribution in the aluminum melt are difficult. Variety of methods are used for introduction of such nanoparticles, for example, the introduction of particles by a jet of inert gas, the use of the semi-solid state of aluminum, the use of special methods of physical action on the melt, the use of the pressed briquettes of master nanopowder composites [1–8]. However, all these liquid-phase methods make it possible to introduce and distribute a relatively small amount of nanosized reinforcing phase in the matrix phase. The solid-phase methods, in contrast to liquid-phase methods, make it possible to introduce large volumes of the reinforcing phase, which can be poorly wetted by aluminum melt, to achieve a uniform distribution of the reinforcing particles over the matrix. The solid-phase methods of manufacturing the dispersion-hardened aluminum matrix composites include methods of powder metallurgy, mechanical alloying, friction with mixing, diffusion welding, etc. [2–4]. However, the use of these methods is limited by the high cost of the equipment and energy consumption of the process of manufacturing the components from the dispersion-hardened aluminum-matrix composites.

Currently, Al–AlN composites, reinforced by AlN nanoparticles, are promising for use in aerospace engineering at high temperatures up to 400–550°C [9]. But these composites have been studied less than Al– $\text{Al}_2\text{O}_3$  and Al–SiC composites, and, unlike the latter, they have not yet mastered industrial production technologies [4, 9]. Therefore, it is important to study and develop technologies for manufacturing the Al–AlN nanocomposites that are economically promising for industrial production. A review of the methods and properties of aluminum-matrix composite materials, discretely reinforced with AlN aluminum nitride nanoparticles, is presented in [10]. It follows from the review that the study of the possibility of using the achievements of a simple energy-saving powder technology based on the process of self-

propagating high-temperature synthesis (SHS) is of great interest for manufacturing the Al–AlN nanocomposites. The cost of nitrides nanopowders, obtained by the azide SHS technology, for their subsequent use in manufacturing the nanocomposites can be an order of magnitude less than the cost of similar nanopowders, produced by the method of plasma chemical synthesis [11]. As a result of our previous studies on the liquid-phase fabrication of Al–AlN nanocomposites using various methods of introducing a nanopowder of the SHS-Az brand of composition (AlN–35% Na<sub>3</sub>AlF<sub>6</sub>) into the melt of aluminum (or its alloys), it was possible to obtain cast Al–AlN nanocomposites with a nanoscale reinforcing phase AlN content of up to 7.7% [10–12].

This paper presents the results of studies of the possibility of fabrication of Al–AlN nanocomposite with a significantly higher content (up to 75% by weight) of AlN nanoparticles by a solid-phase powder metallurgy method using PA-4 aluminum powder and SHS-Az nanopowder (AlN–5% Na<sub>3</sub>AlF<sub>6</sub>).

The technological scheme for the fabrication of such aluminum-matrix composite hardened with AlN nanoparticles included the following powder metallurgy operations: mixing of the initial powders, one-side cold pressing of the powder mixture, and sintering in vacuum without a load. The following powders were used as the initial powders: aluminum powder PA-4 with average particle size of 70–80 μm and SHS-Az nanopowder (AlN–5% Na<sub>3</sub>AlF<sub>6</sub>) in the form of AlN nanofibers with diameter of 100–300 nm and length of 3 μm with an impurity 5% Na<sub>3</sub>AlF<sub>6</sub> halogen salt. This nanopowder was synthesized beforehand using the azide technology of SHS by burning a mixture of 20Al + (NH<sub>4</sub>)<sub>3</sub>AlF<sub>6</sub> + 6NaN<sub>3</sub> powders [13].

The preparation of the powder mixes Al–AlN was carried out by mechanical activation of the initial powders with the addition of 1% paraffin (as binding) and without the addition of paraffin in the planetary ball mill Fritsch Pulverisette 5 within 1 minute with speed of rotation of 250 rpm of hard-alloy grinding balls by diameter of 10 mm. The powder mixtures Al–AlN with the content of the disperse phase AlN of 5, 10, 15, 20, 25, 30, 50, and 75% were prepared. According to random samples taken from the prepared mixtures, the powder components are almost evenly distributed throughout the volume of the obtained powders. The maximum decrease in the average size of powder particles is observed in mixtures of Al–50% AlN and Al–75% AlN. The smallest average size of powder particles of 15–50 μm was obtained in mixture of Al–75% AlN. The maximum values of the specific surface and bulk density of the powders were obtained from mixtures of Al–50% AlN and Al–75% AlN, and were respectively 10.57 m<sup>2</sup>/g and 0.993 g/cm<sup>3</sup>; 13.73 m<sup>2</sup>/g and 0.995 g/cm<sup>3</sup>. The highest values of the mass fraction of the denser AlN phase in these powder mixtures explains the maximum values of the bulk mass and specific surface of the powder mixture Al–75% AlN. However, all the obtained Al–AlN powder mixtures did not have flowability, since the initial powders PA-4 and AlN–5% Na<sub>3</sub>AlF<sub>6</sub> are not flowable.

The compaction of the powder mixtures Al–AlN into briquettes was carried out with the PSU-50 press by uniaxial cold pressing with pressure of 200 and 300 MPa in the cylindrical die with the internal diameter of 16,5 mm. The height of briquettes was up to 4 mm, the weight was up to 2.5 g. The highest value of compact density was obtained for Al–50% AlN and Al–75% AlN mixtures, 2.86 g/cm<sup>3</sup> and 2.95 g/cm<sup>3</sup>, respectively, what is explained by the highest values of the mass fraction of the denser AlN phase in these powder mixtures.

The sintering of the obtained briquettes was carried out in the vacuum furnace of VKPGr model at temperatures of 580 and 650°C, the vacuum was 2·10<sup>-1</sup> mm of a mercury column, isothermal exposure time was 40 min.

At compaction of the powder mixtures Al–AlN without paraffin, the press tool (the punch and the die) previously was greased with Vaseline (thickness of lubricant did not exceed 1 mm). The use of the lubricant is explained by the need to reduce the energy and power parameters of pressing, as well as the prevention of possible welding and adhesion of aluminum to the press tool during the process of deforming powders, which can lead to the scratches on the surface of

the compacted samples. On the surface of the Al–AlN compacts without the addition of paraffin, the scratches were observed, that was a defect of processing. With increase in the content of the reinforcing AlN phase in samples prepared without the addition of paraffin, the number of scratches increased, that led to the distortion of the samples.

In Al–AlN samples prepared with the addition of paraffin, the minimum porosity was observed under a compaction pressure of 300 MPa. The maximum porosity in the compacted samples Al–AlN was observed at the AlN content of 50 and 75% and was 20 and 25%, respectively, that resulted in the increased brittleness of these samples and complicated their sintering.

After sintering in vacuum at temperature 650°C, almost all Al–AlN samples exhibited the shape distortion (warping of samples). The maximum porosity in Al–AlN samples was observed after sintering at 650°C with aluminum nitride content of 50 and 75% and was 18 and 23%, respectively, and after sintering at 580°C, it was 15 and 20%, respectively. Since the sintered Al–AlN samples containing 50 and 75% aluminum nitride were quite porous, further studies were carried out with sintered Al–AlN samples with aluminum nitride content up to 30%.

At sintering at temperature of 650°C, strong oxidation and exudation of aluminum from the studied samples were observed, that led to strong distortion of samples at this temperature. After sintering at smaller temperature of 580°C the samples Al–AlN with addition of paraffin, which were compacted under a pressure of 300 MPa, the external defects were not observed.

In Al–AlN samples (sintered at 580°C), the oxygen content was noticeably less than in samples sintered at 650°C, the element nitrogen was found in small mass fractions. This result can be explained by the fact that the liquid phase of aluminum does not appear at 580°C, the processes of oxidation of aluminum and aluminum nitride proceed, but not as intensively as at 650°C, and in the absence of the liquid phase, there is no Al exudation from the sample.

Minimal porosity after sintering was achieved in the sample Al–5% AlN and amounted to 4.5%; the maximum porosity was in the sample Al–75% AlN and amounted to 20%. Sintered Al–AlN samples with aluminum nitride content of 50 and 75% were obtained rather porous and brittle, therefore, the actual incorporation of AlN nanoparticles in this amount into aluminum by the solid-phase powder metallurgy method in the conditions under consideration is not possible. Figure 1 shows the microstructures of samples Al–5% AlN and Al–30% AlN obtained by sintering at temperature of 580°C.

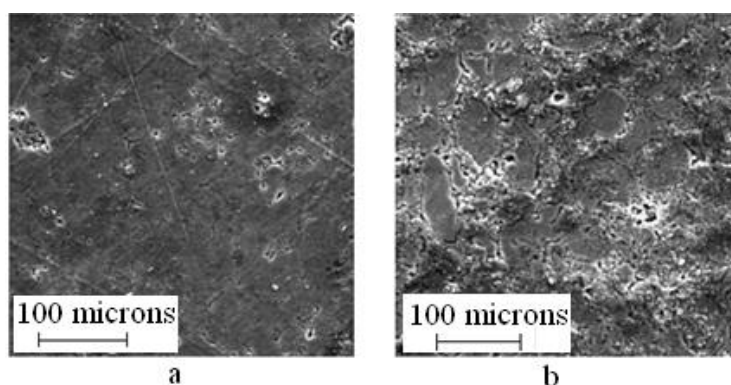


Fig. 1. Microstructure of Al–AlN samples after sintering at temperature of 580°C: (a) Al–5% AlN; (b) Al–30% AlN.

According to Fig. 1, the pores are observed in the fabricated samples, the presence of which is confirmed by the calculated values of the porosity of the sintered samples, studied by the hydrostatic weighing method.

The X-ray phase analysis of sintered Al–AlN samples containing aluminum nitride from 5

to 30% showed the actual phase composition of the composite materials under investigation, according to which three phases were found: free aluminum, aluminum oxide and aluminum nitride.

Thus, the use of solid-phase powder metallurgy technology made it possible to incorporate up to 30% (by weight) AlN nanoparticles, obtained by SHS azide technology, into aluminum-matrix composite.

1. S. Ray, Review synthesis of cast metal matrix particulate composites, *J. Mater. Sci.*, 1993, no. 28, pp. 5397–5413.
2. M.K. Surappa, Aluminum matrix composites: Challenges and opportunities, *Sadhana*, 2003, vol. 28, parts 1&2, pp. 319–334.
3. R.S. Rana, R. Purohit, S. Das, Review of recent studies in Al matrix composites, *Int. J. Sci. Eng. Res.*, 2012, vol. 3, no. 6, pp. 1–16.
4. C. Borgonovo, D. Apelian, Manufacture of aluminum nanocomposites: a critical review, *Mater. Sci. Forum*, 2011, vol. 678, pp. 1–22.
5. S.Ch. Tjong, Novel nanoparticle-reinforced metal matrix composites with enhanced mechanical properties, *Adv. Eng. Mater.*, 2007, vol. 9, no. 8, pp. 639–652.
6. F. He, Ceramic nanoparticles in metal matrix composites, *Ceramic Nanocomposites: A volume in Woodhead Publishing Series in Composites Science and Engineering*, 2013, pp. 185–207.
7. R. Casati, M. Vedani, Metal matrix composites reinforced by nano-particles - A Review, *Metals*, 2014, no. 4, pp. 65–83.
8. D. Zhou, F. Qiu, Q. Jiang, The nano-sized TiC particle reinforced Al–Cu matrix composite with superior tensile ductility, *Mater. Sci. Eng. A.*, 2015, vol. 622, pp. 189–193.
9. C. Borgonovo, D. Apelian, M.M. Makhlof, Aluminum nanocomposites for elevated temperature applications, *JOM*, 2011, vol. 63, no. 2, pp. 57–64.
10. A.P. Amosov, Y.V. Titova, I.Y. Timoshkin, A.A. Kuzina, Fabrication of Al–AlN nanocomposites, *Key Eng. Mater.*, 2016, vol. 684, pp. 302–309.
11. A.P. Amosov, Y.V. Titova, D.A. Maidan, A.A. Ermoshkin, I.Y. Timoshkin, Application of the nanopowder production of azide SHS technology for the reinforcement and modification of aluminum alloys, *Russ. J. Non-Ferr. Met.*, 2015, vol. 56, no. 2, pp. 222–228.
12. A.P. Amosov, Y.V. Titova, D.A. Maidan, E.I. Latukhin, Application of SHS auxiliary reaction of titanium carbide for introduction of AlN nanoparticles into aluminum melt, *J. Phys.: Conf. Ser.*, 2018, vol. 1115, is. 4, 042001.
13. Yu.V. Titova, A.P. Amosov, D.A. Maidan, A.V. Sholomova, A.V. Bolotskaya, SHS of ultrafine and nanosized powder of aluminum nitride using sodium azide and halide salt  $(\text{NH}_4)_3\text{AlF}_6$ , *SHS 2017. XIV Int. Symp. Self-Propag. High-Temp. Synth.: Book of Abstracts*, 2017, pp. 25–28.



SYNTHESIS OF METAL-LIKE REFRACTORY COMPOUNDS AND  
ULTRA-HIGH-TEMPERATURE MATERIALS IN MOLTEN SALTSS. A. Kuznetsov<sup>\*a</sup>, V. S. Dolmatov<sup>a</sup>, A. R. Dubrovskiy<sup>a</sup>, and Yu. V. Stulov<sup>a</sup><sup>a</sup>Tananaev Institute of Chemistry of the Federal Research Centre “Kola Science Centre of the Russian Academy of Sciences”, Apatity, 184209 Russia

\*e-mail: kuznet@chemy.kolasc.net.ru

DOI: 10.24411/9999-0014A-2019-10078

Extreme conditions of articles exploitation cause utilization of expensive refractory metals and their metal-like refractory compounds ensuring their adequate performance. The problem can be approached by depositing coatings on the surface of units and mechanisms, i.e. creating composite materials. In this case, the substrate material provides the strength and electric characteristics while the coatings realize the necessary surface properties.

Nowadays coatings of metal-like refractory compounds are used in aircraft, rocket space vehicle and mostly produced by CVD, PVD, SHS methods, plasma and detonation spraying. At the same time, using molten salts for deposition coatings is highly attractive. Molten salts provide the production of coatings by electrochemical synthesis, precise surface alloying, by employing the reaction of disproportionation and currentless transfer.

Electrochemical methods have the following advantages, as compared with other possible techniques of production of metal-like refractory compounds:

- (i) smooth coatings can be deposited even at surfaces of complicated geometry;
- (ii) single crystals, polycrystalline coatings and even ultra-disperse powders can be deposited depending on the parameters of the process;
- (iii) the composition of the deposit can be precisely controlled through process parameters;
- (iv) relatively low temperature of synthesis (down to 600°C), cheap and simple technological background and the cheap raw materials required make the process attractive from the economic point of view.

*Borides.* Process of electrochemical synthesis HfB<sub>2</sub> from the NaCl–KCl–NaF (5 wt %)–K<sub>2</sub>HfF<sub>6</sub> (5–15 wt %)–KBF<sub>4</sub> (5–10 wt %) molten system was studied in detail [1]. It was shown that the wave of electrochemical synthesis HfB<sub>2</sub> has a more positive potential than discharge potentials of boron and hafnium. Therefore, galvanostatic electrolysis is a convenient regime for deposition of hafnium diboride. Electrochemical synthesis HfB<sub>2</sub> was performed at the cathodic current density of 5–50 mA cm<sup>-2</sup> and temperature of 700–850°C. SEM micrograph of cross-section HfB<sub>2</sub> on a molybdenum substrate is presented in Fig. 1. As can be seen from Fig. 1 the coating had a column structure and microhardness determined on the cross-section was found 32±2 GPa [1].

Molybdenum can be used as a basic reactor material. However, molybdenum corrodes in contact with aggressive and water vapors at elevated temperatures. Therefore, low temperature oxidative stability of molybdenum substrates can be improved by siliciding in molten salts to produce a MoSi<sub>2</sub> layer followed by boronizing of the MoSi<sub>2</sub> phase.

Boronizing treatments were conducted in molten salts under inert gas atmosphere in the temperature range of 700–1000°C for 3–7 h. The oxidation resistance of the films was investigated by the weight change in an air-water (2.3 vol %) mixture at a temperature of 500°C for a period up to 700 h.

In non-current boronizing the MoSi<sub>2</sub> phase was transformed to the Mo<sub>5</sub>Si<sub>3</sub> phase, which became a major (content 10–30 wt %) phase after boronizing step performed in the range of 750–900°C and the matrix phase (> 60 wt %) above 950°C. The MoSi<sub>2</sub> phase was always present

in the films in the temperature range of 800–950°C after electrochemical synthesis. The main boride phases were MoB<sub>2</sub> and Mo<sub>2</sub>B<sub>5</sub>. The formation of the Mo<sub>5</sub>(BSi)<sub>3</sub> phase was only observed in electrochemical synthesis at 760°C. Pure MoB<sub>4</sub> was formed in the bulk MoSi<sub>2</sub> phase after electrochemical boronizing in the range of 760–840°C with a maximum content of ca. 15 wt % at 800°C. The presence of small amounts (12–15 wt. %) of the MoB<sub>4</sub> phase formed during boronizing of MoSi<sub>2</sub>/Mo films greatly improved the oxidation resistance of the molybdenum substrates. The weight gain observed was 6.5·10<sup>-4</sup> mg/cm<sup>2</sup>h. To provide the maximum protection, the duration of the boronizing step was adjusted to boronize an external MoSi<sub>2</sub> layer without boronizing the molybdenum substrate. No pest disintegration of the molybdenum substrate was observed in an air-water mixture at 500°C after 700 h.

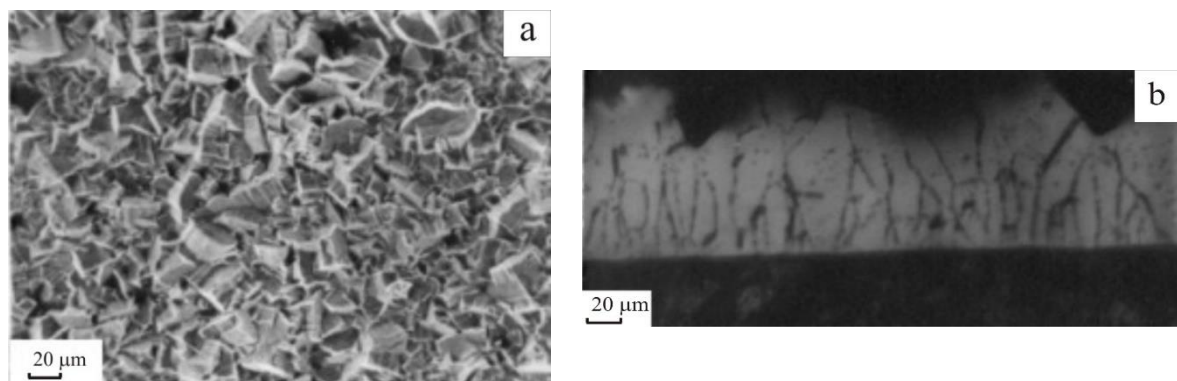
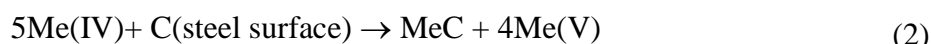


Fig. 1. Morphology (a) and cross-section of HfB<sub>2</sub> coating (b) on a molybdenum substrate obtained from the NaCl–KCl–NaF (5 wt %)-K<sub>2</sub>HfF<sub>6</sub> (5 wt %)-KBF<sub>4</sub> (5 wt %) melt; cathodic current density, 0.03 A cm<sup>-2</sup>; time of electrolysis 3 h; temperature 850°C.

**Carbides.** Synthesis of NbC and TaC coatings on the surface of carbon steels was carried out using currentless transfer from the molten salt NaCl–KCl–K<sub>2</sub>MeF<sub>7</sub>(30 wt %)-Me, where Me = Nb, Ta. Temperature of synthesis was 800–850°C with time of the process from 6 up to 24 h. The mechanism of formation, for example, for niobium carbide by currentless transfer can be described by the following reactions:



This process occurs due to the formation of lower oxidation states of niobium complexes, which formed owing to interaction of salt with own metal. The complexes of lower oxidation states are diffused to the steel substrate and disproportionate on its surface. The disproportionation (2) is accompanied by the formation of NbC and niobium complexes with higher oxidation state of +5. Nb(V) complexes again interact with niobium (1), the process forms cycle. The driving force of reaction (2) is energy of NbC formation.

The chromium carbide Cr<sub>7</sub>C<sub>3</sub> coatings were also synthesized by the currentless transfer method. As the melt, an equimolar NaCl–KCl mixture was used with the addition of 10 wt % CrCl<sub>3</sub> and the excess of metallic chromium. The melt was held for 2 h before the synthesis. The synthesis was realized at the temperature 850°C with time of the process 8 h.

The corrosion resistance of NbC, TaC, and Cr<sub>7</sub>C<sub>3</sub> carbides coatings was studied in concentrated HCl, H<sub>2</sub>SO<sub>4</sub>, and H<sub>3</sub>PO<sub>4</sub> acids at a 25°C during 48 h. The rate of corrosion was evaluated by the mass loss of the samples. The corrosion tests allowed to establish following rows of the chemical stability of samples with carbide coatings in HCl: Cr<sub>7</sub>C<sub>3</sub> > NbC > TaC; in H<sub>2</sub>SO<sub>4</sub>: TaC > Cr<sub>7</sub>C<sub>3</sub> > NbC; in H<sub>3</sub>PO<sub>4</sub>: Cr<sub>7</sub>C<sub>3</sub> > TaC > NbC. Of course, the quality of obtained

coatings affects the results to a certain degree. The wear resistance was evaluated also by the sample mass loss with the accuracy of 0.1 mg. The mass loss of a sample from hardened St.45 was  $35.2 \text{ mg cm}^{-2}$  and that of a coated with a  $\text{Cr}_7\text{C}_3$  –  $4.7 \text{ mg cm}^{-2}$ , NbC –  $2.9 \text{ mg cm}^{-2}$  and TaC –  $2.2 \text{ mg cm}^{-2}$  [2].

Due to the high wear and corrosion resistance  $\text{Cr}_7\text{C}_3$ , NbC, and TaC coatings on carbon steels can be applied in aggressive medium with the abrasive wear. Deposition of NbC coatings on parts of oil pumps increased their lifetime in several times. Tests carried out by LLC "Ecotech" showed that the coatings of  $\text{Cr}_7\text{C}_3$  or TaC on the knives for cutting rubber, made of St. 3, can improve their wear resistance and increase a tool lifetime in 2 (for  $\text{Cr}_7\text{C}_3$ )–2.5 (for TaC) times.

$\text{Mo}_2\text{C}$  coatings were obtained on Mo substrate at the temperature  $850^\circ\text{C}$  by electrochemical synthesis in an equimolar NaCl–KCl mixture containing 0.92 wt % of  $\text{Li}_2\text{CO}_3$ , 5 wt % of  $\text{Na}_2\text{MoO}_4$  at stoichiometric ratio  $\text{Mo/C} = 2:1$  and with a cathodic current density  $5\text{--}10 \text{ mA cm}^{-2}$ . The  $\text{Mo}_2\text{C}/\text{Mo}$  composition was tested as a catalyst for the water-gas shift reaction. The steady-state reaction rates for the  $\text{Mo}_2\text{C}/\text{Mo}$  composition were higher than those for the bulk  $\text{Mo}_2\text{C}$  and commercial Cu/ZnO/ $\text{Al}_2\text{O}_3$  catalysts over in the temperature range explored [3]. The catalytic activity remained constant during 5000 h on-stream. The coatings were also stable during the thermal cycling, while the activity of commercial catalysts tends to decrease with time. A novel microstructured reactor/heat-exchanger containing eight sections with a cross-section of 10 mm x 10 mm and a length of 100 mm has been designed and constructed. Each section of the reactor contains flat, goffered Mo plates and Mo wires with a diameter of 250  $\mu\text{m}$  and a length of 100 mm coated with a catalytic  $\text{Mo}_2\text{C}$  layer.

Silicides. Galvanostatic electrolysis of the melt NaCl–KCl–NaF (10 wt %)– $\text{K}_2\text{HfF}_6$  (5 wt %)– $\text{K}_2\text{SiF}_6$  (1.0 wt %) in contact with Si (anode) at temperature of  $750^\circ\text{C}$  and the cathodic current density of  $0.30 \text{ A cm}^{-2}$  led to the formation of hafnium silicide  $\text{HfSi}_2$ .

Electrochemical synthesis of tantalum silicides was performed in the NaCl–KCl–NaF (10 wt %)– $\text{K}_2\text{TaF}_7$  (3 wt %)– $\text{K}_2\text{SiF}_6$  (2 wt %) melt at temperature of  $750^\circ\text{C}$ . Tantalum silicides coatings on a silver substrate were synthesized by the galvanostatic electrolysis. The cathodic current density was varied from 30 up to  $50 \text{ mA cm}^{-2}$ . Parameters for electrodeposition of the  $\text{Ta}_5\text{Si}_3$  and  $\text{TaSi}_2$  coatings on a silver substrate were found.

Ultra-high-temperature Nb–Hf coatings. Articles based on graphite are widely used presently in aerospace techniques because of the unique properties of graphite. However, a drawback of graphite-based compositions is a low heat resistance in oxidizing atmosphere. It was shown that Nb–Hf coatings of  $\alpha + \beta$ -composition with a planar growing front and thickness of 20–40  $\mu\text{m}$  can be obtained from the NaCl–KCl–NaF (5 wt %)– $\text{K}_2\text{NbF}_7$  (1 wt %)– $\text{K}_2\text{HfF}_6$  (10 wt %) electrolyte [1]. It was found that niobium stabilized the low temperature monoclinic modification of  $\text{HfO}_2$ , which was formed during oxidation. The temperature of exploitation graphite articles can be increased up to  $2100^\circ\text{C}$  if to use niobium–hafnium protective coatings.

1. S.A. Kuznetsov. Electrodeposition of hafnium and hafnium-based coatings in molten salts, *Chem. Pap.*, 2012, vol. 66, no 5, pp. 513–518.
2. Yu.V Stulov, V.S. Dolmatov, A.R. Dubrovskiy, S.A. Kuznetsov, Electrochemical Methods for Obtaining Thin Films of the Refractory Metal Carbides in Molten salts, *Int. J. Electrochem. Sci.*, 2017, vol. 12, no. 6, pp. 5174–5184.
3. A.R. Dubrovskiy, O.V. Makarova, S.A. Kuznetsov, Effect of the Molybdenum Substrate Shape on  $\text{Mo}_2\text{C}$  Coating Electrodeposition, *Coatings*, 2018, vol. 8, no. 12, 442.

## FILTRATION COMBUSTION OF $\text{SiF}_4$ AND $\text{CaH}_2$ IN VERTICAL FLOW REACTOR

A. Yu. Lashkov<sup>\*a</sup>, A. D. Bulanov<sup>a,b</sup>, and O. Yu. Troshin<sup>a,b</sup>

<sup>a</sup>G.G. Devyatikh Institute of Chemistry of High-Purity Substances, Nizhny Novgorod, 603951 Russia

<sup>b</sup>National Research Lobachevsky State University, Nizhny Novgorod, 603950 Russia

\*e-mail: lashkov@ihps.nnov.ru

DOI: 10.24411/9999-0014A-2019-10079

Interaction of silicon tetrafluoride and calcium hydride for preparation of monosilane is one of the stages of fluoride-hydride technology for production of high-purity silicon, including monoisotopic silicon. Silicon is the main material of nanotechnologies [1] and quantum electronics [2]. De Pape showed [3] that formation of  $\text{SiH}_4$  occurs in the reaction of  $\text{SiF}_4$  and  $\text{CaH}_2$  at the temperature lower than  $300^\circ\text{C}$ . If the temperature is higher than  $300^\circ\text{C}$  then thermal decomposition of silane occurs. First experiments of interaction of these reagents took place in the vertical silica flow reactor (Fig. 1) and the initial temperature was  $180\text{--}200^\circ\text{C}$  [4]. We have defined that at this temperature the conversion of silicon tetrafluoride is 100%. We observed the planar reaction front propagating and change of solid phase color from light grey to brown after  $\text{SiF}_4$  flowing through the reactor with  $\text{CaH}_2$ . The temperature increased up to  $\approx 250^\circ\text{C}$  when the darkening zone of chromel-copel thermocouple, located inside reactor, was achieved. The temperature decreased when the reaction front passed through thermocouple. While comparing the literature data with the results of experiments we hypothesized that the reaction of silicon tetrafluoride with calcium hydride is the mode of filtration combustion. Next we replaced the silica flow reactor with stainless steel reactor (steel grade 12Kh18N10T) for filtration combustion (Fig. 2) due to starting of “Avogadro” project.

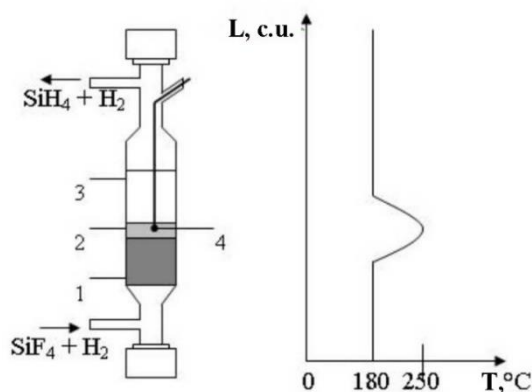


Fig. 1. Vertical silica flow reactor for preparing silane and temperature profile of process. 1 solid reaction products (brown); 2 reaction front (change colors); 3  $\text{CaH}_2$  (light grey); 4 thermocouple.

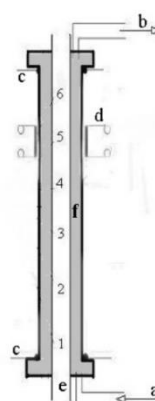


Fig. 2. Stainless steel reactor for filtration combustion of  $\text{SiF}_4$  and  $\text{CaH}_2$ . a input gases ( $\text{SiF}_4 + \text{H}_2$ ); b output gaseous products ( $\text{SiH}_4 + \text{H}_2$ ); c reactor heating; d resistive furnace; e stainless steel tube with thermocouples (1–6); f  $\text{CaH}_2$  powder.

Geometric parameters of stainless steel reactor are: the height ( $h$ ) is 120 cm, the diameter ( $d$ ) is 5 cm, the volume ( $V$ ) is  $2356\text{ cm}^3$ , the cross section ( $S$ ) is  $19\text{ cm}^2$ . The technique of experiment is as following. Hydrogen gas flows bottom-up with the rate of 120 ml/min. Then we loaded

into reactor  $\text{CaH}_2$  powder (the fraction is 0.6 mm, the bulk density is  $1.3 \text{ g/sm}^3$ ). Reactor and resistive furnace (Figs. 2c, 2d) preheating up 100 and  $150^\circ\text{C}$ , respectively. Then the gas mixture of  $\text{SiF}_4 + \text{H}_2$  is input. The gases flow rates: 200 ml/min is the reagent gas ( $\text{SiF}_4$ ) and 120 ml/min is the carrier gas ( $\text{H}_2$ ). Approximately after 10 min the temperature increase is observed at the location of resistive furnace (Fig. 3) indicating the starting of reaction. The counter-flow reaction is starting. Resistive furnace is “off” when temperature is the maximum on thermocouple 3. Counter wave motion is uniformly accelerated and the average rate is  $1.7 \times 10^{-4} \text{ m/s}$ . Reflection of combustion wave occurs when the counter front succeed to bottom flange. Then the co-flow reaction wave starts propagating. Co-flow motion is uniform with the front rate of  $6.7 \times 10^{-5} \text{ m/s}$ . The process is completed when the temperature maximum is attained on thermocouple 6. We have determined the basic kinetic parameters of this reaction in a counter wave in the vertical flow reactor: the reaction order is  $n = 1$ , the rate constant is  $k = 0.38 \pm 0.05 \text{ s}^{-1}$ , the activation energy is  $E_a = 17 \pm 2 \text{ kJ/mole}$  [5].

The thermogram in Fig. 3 shows the steady-state combustion at the above-mentioned temperatures of reactor and resistive furnace. There is a split reaction front if the reactor is heated above  $110^\circ\text{C}$  and the furnace is heated above  $170^\circ\text{C}$ . When the  $\text{CaH}_2$  powder of different dispersion is filled into the reactor, a standing combustion wave occurs [6].

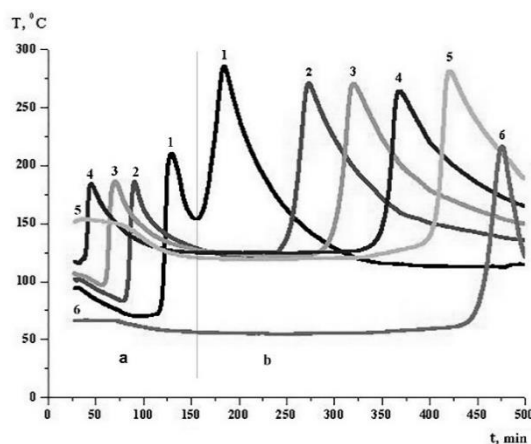


Fig. 3. Thermogram of filtration combustion of  $\text{SiF}_4$  and  $\text{CaH}_2$  in vertical flow reactor. *a* counter wave; *b* co-flow wave; 1–6 thermocouples.

1. O. Moutanabbir, S. Senz, Z. Zhang, U. Gösele, Synthesis of isotopically controlled metal-catalyzed silicon nanowires, *Nanotoday*, 2009, vol. 4, no. 5, pp. 393–398.
2. K. M. Itoh, An all-silicon linear chain NMR quantum computer, *Solid State Commun.*, 2005, vol. 133, no. 11, pp. 747–752.
3. R. De Pape, Reduction of silicon tetrafluoride and boron trifluoride by calcium hydride, *Ann. Chim.*, 1963, vol. 8, nos. 3–4, pp. 185–196.
4. G.G. Devyatikh, A.D. Bulanov, O.Yu. Troshin, V.V. Balabanov, D.A. Pryakhin, E.M. Dianov, Preparation of High-Purity Monoisotopic Silane:  $^{28}\text{SiH}_4$ ,  $^{29}\text{SiH}_4$ , and  $^{30}\text{SiH}_4$ , *Dokl. Chem.*, 2003, vol. 391, nos. 4–6, pp. 204–205.
5. A.Yu. Lashkov, A.D. Bulanov, O.Yu. Troshin, Filtration combustion of silicon tetrafluoride and calcium hydride for the preparation of monosilane, *Inorg. Mater.*, 2016, vol. 52, no. 9, pp. 915–918.
6. A.Yu. Lashkov, A.D. Bulanov, O.Yu. Troshin, Influence of technological parameters of  $\text{SiF}_4$  and  $\text{CaH}_2$  interaction on the nature of filtration combustion, *Russ. J. Appl. Chem.*, 2019, vol. 92, no. 4, (in print).

## COMBUSTION SYNTHESIS AND CONSOLIDATION OF (Zr/Hf)B<sub>2</sub>–(Zr/Hf)Si<sub>2</sub>–MoSi<sub>2</sub> POWDER CERAMICS FOR HIGH-TEMPERATURE PROTECTIVE COATINGS

**M. V. Lemesheva<sup>a</sup>, Yu. S. Pogozev<sup>a</sup>, A. Yu. Potanin<sup>a</sup>, S. I. Rupasov<sup>a</sup>, V. I. Vershinnikov<sup>b</sup>, and E. A. Levashov<sup>a</sup>**

<sup>a</sup>National University of Science and Technology MISIS, Moscow, 119049 Russia

<sup>b</sup>Merzhanov Institute of Structural Macrokinetics and Materials Science, Russian Academy of Sciences, Chernogolovka, Moscow, 142432 Russia

\*e-mail: lemesheva.margarita@yandex.ru

DOI: 10.24411/9999-0014A-2019-10080

Nowadays, superhigh-temperature ceramic materials that can be effectively used under severe thermal loads are of great importance in materials science research. Such materials must withstand extreme operating temperatures above 2000°C, resist erosion, evaporation and oxidation. The most Promising candidates for this kind of applications are diborides ZrB<sub>2</sub> and HfB<sub>2</sub>, which are characterized by high melting points (3246 and 3380°C) [1, 2], thermal conductivity (57.9 and 104 W/(m · K)) [1–3], hardness (21 and 28 GPa) [2, 4, 5], modulus of elasticity (450 and 480 GPa) [2], as well as a low coefficient of thermal expansion (5.9 and 6.3–7.15 × 10<sup>-6</sup> K<sup>-1</sup>) [3, 5, 6]. The use of pure ZrB<sub>2</sub> and HfB<sub>2</sub> ceramics is limited due to the evaporation of B<sub>2</sub>O<sub>3</sub> above 1100°C. The release of porous oxides ZrO<sub>2</sub> and HfO<sub>2</sub> occurs as a result, which leads to the penetrating oxidation of the material [7–9]. In order to improve heat resistance, SiC, MoSi<sub>2</sub>, ZrSi<sub>2</sub>, etc. are included into the ZrB<sub>2</sub> and HfB<sub>2</sub> ceramics. The presence of boron and silicon in ceramics leads to the formation of borosilicate glass during the oxidation process, which not only effectively resists high-temperature oxidation, but also has the effect of self-healing of defects and cracks [2, 7]. In addition, such additives have a positive effect on the compactibility of ceramics in the process of consolidation [10, 11]. Effective methods for producing such ceramics are self-propagating high-temperature synthesis and hot pressing (HP) [12, 13].

In the present work, composite powders with varying the concentration of the main elements (Zr, Hf, Mo, Si, B) were obtained by magnesium thermal reduction from oxides. The consolidation of the powders was carried out using the HP method in a graphite mold at a pressure of 30 MPa and a process temperature of 1200–1250°C. The microstructure and phase composition of the obtained powders and compact ceramics were studied by scanning electron microscopy, energy dispersive spectroscopy and X-ray phase analysis. Investigations of the fine structure were carried out on a transmission electron microscope. The granulometric composition of the powders was determined on a laser particle size analyzer. The density of the consolidated samples was measured by hydrostatic weighing and helium pycnometry. Residual porosity was calculated from the relative density values. Vickers hardness HV was measured on an automated hardness tester with a load of 10 kg.

The phase composition of the synthesized composite powders includes zirconium and hafnium diborides ZrB<sub>2</sub>/HfB<sub>2</sub>, silicides ZrSi<sub>2</sub>/HfSi<sub>2</sub>, ZrSi, and also MoSi<sub>2</sub>, with different ratio between them in dependence of the reactionary mixture composition. Synthesized SHS powders consists of polyhedral shape particles and characterized by a homogeneous, compositional, and finely dispersed structure (Fig. 1). The average particle size of the powders was 5–9 μm. Each powder particle is a microcomposite consisting of boride and silicide grains 1–2 and 2–4 μm in size, respectively.

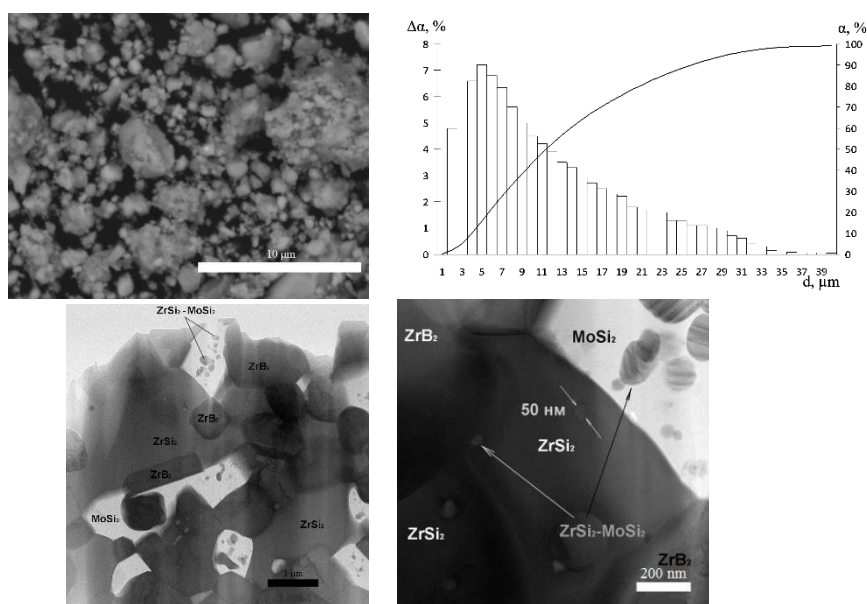


Fig. 1. Typical morphology, granulometric composition, and fine structure of SHS powders in the  $\text{Me}^{\text{IV}}\text{-Me}^{\text{VI}}\text{-B-Si}$  system.

The phase composition of the ceramic samples consolidated by HP is similar to powders and also represented by silicides and borides of transition metals. The microstructure of compact materials consisted of rectangular-shaped  $\text{ZrB}_2/\text{HfB}_2$  grains from 3 to 10  $\mu\text{m}$  in length and  $\text{ZrSi}_2/\text{HfSi}_2$  and  $\text{MoSi}_2$  inclusions in the form of large irregular-shaped grains. Compact ceramics had a low residual porosity of 1.1–1.7%, hardness of 11–12 GPa, thermal conductivity of 62–87  $\text{W}/(\text{m}\cdot\text{K})$  and specific oxidation rate of  $(1.3\text{--}2.9)\cdot 10^5 \text{ mg}/(\text{cm}^2\cdot\text{s})$ .

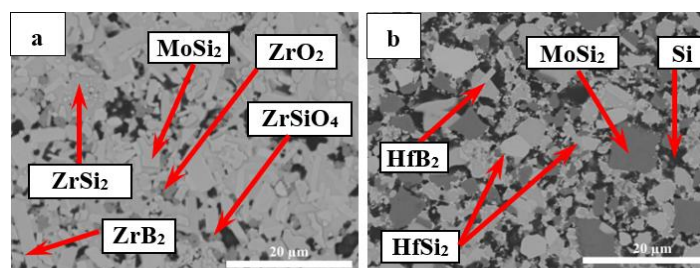


Fig. 2. Microstructure of compact samples obtained by hot pressing of SHS powders: (a)  $\text{ZrB}_2\text{-ZrSi}_2\text{-MoSi}_2$ ; (b)  $\text{HfB}_2\text{-HfSi}_2\text{-MoSi}_2$ .

Ceramic SHS powders were tested as precursors for the preparation of protective coatings on thermally loaded carbon-based structural elements operating in high-enthalpy oxidizing gas flows.

The reported study was funded by RFBR according to the research project no. 18-08-00269.

1. J.K. Sonber, T.S.R.Ch. Murthy, C. Subramanian, S. Kumar, R.K. Fotedar, A.K. Suri, Investigations on synthesis of  $\text{ZrB}_2$  and development of new composites with  $\text{HfB}_2$  and  $\text{TiSi}_2$ , *Int. J. Refract. Met. Hard Mater.*, 2011, vol. 29, no. 1, pp. 21–30.
2. M.M. Nasser, Comparison of  $\text{HfB}_2$  and  $\text{ZrB}_2$  behaviors for using in nuclear industry, *Ann. Nucl. Energy*, 2018, vol. 114, pp. 603–606.
3. M. Mallik, A. J. Kailath, K.K. Ray, R. Mitra. Electrical and thermophysical properties of  $\text{ZrB}_2$  and  $\text{HfB}_2$  based composites, *J. Europ. Ceram. Soc.*, 2012, vol. 32, pp. 2545–2555.

4. E.W. Neuman, G.E. Hilmas, W.G. Fahrenholtz, Processing, microstructure, and mechanical properties of zirconium diboride-boron carbide ceramics, *Ceram. Int.*, 2017, vol. 43, no. 9, pp. 6942–6948.
5. R. Tu, N. Li, Q. Li, S. Zhang, L. Zhang, T. Goto, Effect of microstructure on mechanical, electrical and thermal properties of B<sub>4</sub>C-HfB<sub>2</sub> composites prepared by arc melting, *J. Europ. Ceram. Soc.*, 2016, vol.36, pp. 3929–3937.
6. P. Wang, H. Li, J. Sun, R. Yuan, L. Zhang, Y. Zhang, T. Li, The effect of HfB<sub>2</sub> content on the oxidation and thermal shock resistance of SiC coating, *Surf. Coat. Technol.*, 2018, vol. 339, pp. 124–131.
7. T.A. Parthasarathy, R.A. Rapp, M.M. Opeka, R.J. Kerans, A model for the oxidation of ZrB<sub>2</sub>, HfB<sub>2</sub> and TiB<sub>2</sub>, *Acta Mater.*, 2007, vol. 55, pp. 5999–6010.
8. V.Z. Poilov, E.N. Pryamilova, Thermodynamics of oxidation of zirconium and hafnium borides, *Russ. J. Inorg. Chem.*, 2016, vol.61, no.1, 55-58
9. W. Zhang, Y. Zeng, L. Gbologah, X. XIONG, B. Huang, Preparation and oxidation property of ZrB<sub>2</sub>-MoSi<sub>2</sub>/SiC coating on carbon/carbon composites, *Trans. Nonferrous Met. Soc. China*, 2011, vol. 21, pp. 1538–1544.
10. D. Sciti, A. Balbo, A. Bellosi, Oxidation behaviour of a pressureless sintered HfB<sub>2</sub>-MoSi<sub>2</sub> composite, *J. Europ. Ceram. Soc.*, 2009, vol. 29, pp. 1809–1815.
11. S. Guo, Y. Kagaw, T. Nishimur, H. Tanaka, Pressureless sintering and physical properties of ZrB<sub>2</sub>-based composites with ZrSi<sub>2</sub> additive, *Scripta Mater.*, 2008, vol. 58, pp. 579–582.
12. A.S. Rogachev, A.S. Mukasyan, Combustion for Materials Synthesis, New York: Taylor and Francis, 2015.
13. S. Guo. Densification of ZrB<sub>2</sub>-based composites and their mechanical and physical properties: A review, *J. Europ. Ceram. Soc.*, 2009, vol. 29, pp. 995–1011.



## NON-ISOTHERMAL SYNTHESIS OF NANOLAMINATES

O. K. Lepakova<sup>a</sup>, N. I. Afanasyev<sup>\*a</sup>, A. M. Shulpekova<sup>a</sup>, and V. D. Kitler<sup>a</sup><sup>a</sup>Tomsk Scientific Center SB RAS, Tomsk, 634055 Russia

\*e-mail: af42@yandex.ru

DOI: 10.24411/9999-0014A-2019-10081

Creation of new materials and their production methods are one of the most important scientific and applied problems of physical materials science. At present, the obtaining of refractory high-strength materials possessing wear-resistance at elevated temperatures, high ductility at room temperature, and capable of operating under extreme conditions is an urgent problem.

MAX-materials are new materials and are of particular interest to develop refractory high-strength materials. These are ternary compounds that are described by the general formula  $M_{n+1}AX_n$ , where M is transition metal; A is the element of IIIA or IVA periodic group, X is carbon or nitrogen (or both) and, possibly, boron. A distinctive feature of these materials is the structure of hexagonal crystal lattices, in which the layers of atoms of the M and A elements alternate in a certain sequence, and carbon atoms (or nitrogen) are located in octahedral pores between atoms of the M element. The structure of their crystal lattices provides the unique combination of metal and ceramics properties. To obtain materials based on MAX-phases, various methods are used [1–5]. The basic method for the obtaining of materials based on MAX-phases is sintering which requires high power and time consumption. Self-propagating high-temperature synthesis (SHS) can be considered to be an alternative to sintering.

In this work, the phase composition, microstructure, and some properties of SHS materials based on MAX-phases ( $Nb_2AlC$ ,  $Nb_4AlC_3$ ) are studied. Powders of titanium (TPP8 grade, Avisma company, Berezniki), carbon (PM75 grade,  $< 0.033 \mu m$ ), niobium (TU 48-4-284-73,  $> 63$ ), aluminum (ASD4 grade), and amorphous boron were used for the preparation of reaction mixtures. The phase composition of synthesized materials was determined using a DRON-2 diffractometer ( $CoK_{\alpha}$  radiation). Optical (Axiovert 200M, Karl Zeiss) and scanning electron (SEM515, Philips) microscopes were used to study the microstructure. X-ray microanalysis (CAMEBAX MICROBEAM) was performed to determine the concentration of components.

In the Nb–Al–C system, two compounds with a layered structure,  $Nb_2AlC$  and  $Nb_4AlC_3$ , were detected [6, 7]. In these works,  $Nb_2AlC$  was obtained by hot isostatic pressing and  $Nb_4AlC_3$  was obtained by annealing  $Nb_2AlC$  at a temperature of  $1700^{\circ}C$ . The combustion of a  $2Nb + Al + C$  stoichiometric mixture proceeds in the spin mode. According to XRD analysis, the main phase in the synthesized product is  $Nb_2AlC$ ; NbC and niobium intermetallide are present. Figure 1 shows the structure of the break surface. Plate-shaped grains characteristic for MAX- phases are observed. Since the sample was not previously deformed, the layered structure of its grains was not detected. Since a mixture of  $2Nb + Al + C$  is low-exothermic, a high-quality product based on  $Nb_2AlC$  cannot be obtained by SHS without additional techniques.

The task of the study was to obtain a material with a nanolaminate structure in the four-component Nb–Al–C–N system (analogue to  $Ti_2AlN_{0.5}C_{0.5}$ ) in the combustion mode. The products of  $2Nb + Al + 0.5C$  obtained in the combustion mode at a nitrogen pressure of 60, 30, 15, and 4 atm were synthesized and analyzed. According to XRD analysis, multiphase products consisting of  $Al_2Nb_3C$ ,  $Nb_4N_{3.9}$ , and NbC are formed at a nitrogen pressures of 60, 30, and 15 atm (Fig. 2). And only at a nitrogen pressure of 4 atm, the XRD pattern of the synthesized product contains reflections of  $Nb_2AlC$ . The material with the MAX-phase  $Nb_2AlC$  was also obtained by the SHS method in a chemical furnace (Fig. 2d).

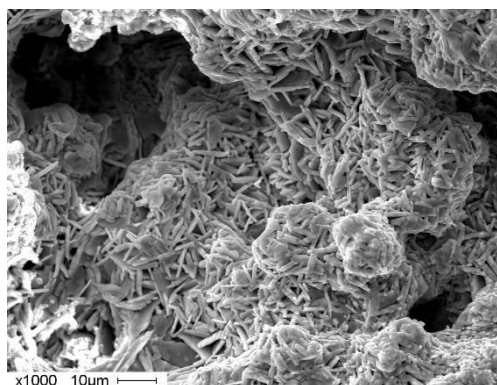


Fig. 1. Break structure in the SHS sample  $\text{Nb}_2\text{AlC}$ .

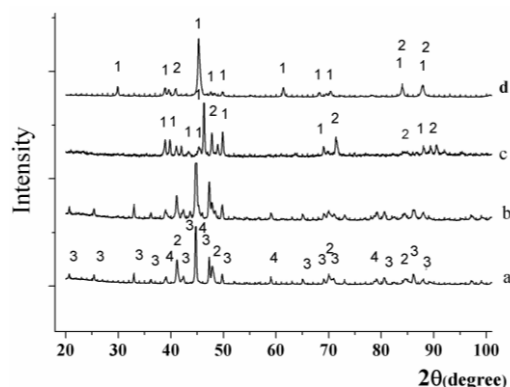


Fig. 2. XRD patterns of SHS products (Nb–Al–C system, Nb:Al:C = 2:1:1 molar ratio) synthesized under the nitrogen atmosphere at a pressure of (a) 60 atm; (b) 15 atm; (c) 4 atm; and (d) in a chemical furnace. 1  $\text{Nb}_2\text{AlC}$ ; 2  $\text{NbC}$ ; 3  $\text{Al}_2\text{Nb}_3\text{C}$ ; 4  $\text{NbC}_{0.5}$ .

Figure 3 shows the microstructure of the SHS products (Nb–Al–C system) obtained at nitrogen pressure of 60 and 4 atm. In Fig. 3a, plate-shaped crystals belong to the ternary  $\text{Al}_2\text{Nb}_3\text{C}$  compound, the round phases belong to  $\text{Nb}_4\text{N}_{3,9}$  and  $\text{NbC}$ . Figure 3b shows the microstructure of the sample synthesized at a pressure of 4 atm. Plate-shaped crystals typical for the samples with a nanolaminate structure are clearly observed.

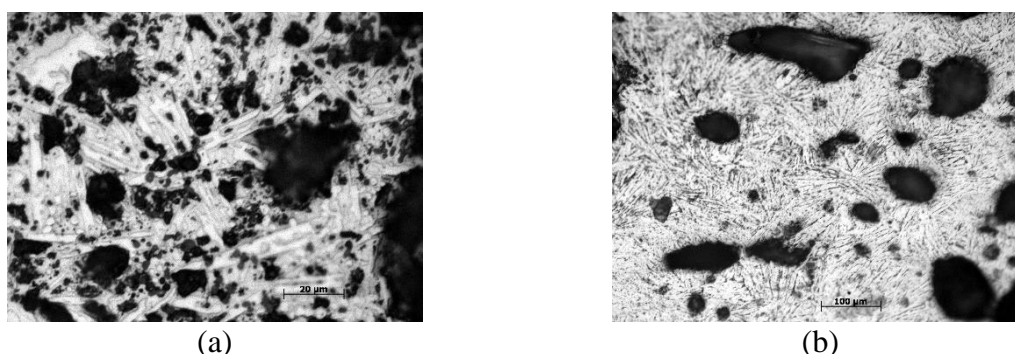


Fig. 3. Microstructures of the products (Nb–Al–C system) synthesized under the nitrogen atmosphere: (a) 60 atm, (b) 4 atm.

As already mentioned,  $\text{Nb}_4\text{AlC}_3$  MAX-phase was initially obtained by the high-temperature (1700°C) heat treatment of the  $\text{Nb}_2\text{AlC}$  MAX-phase [7]. Later, single-phase  $\text{Nb}_4\text{AlC}_3$  samples were synthesized by hot pressing and spark plasma sintering (SPS) [8, 9]. The microstructure and electrical, thermal and mechanical properties of synthesized  $\text{Nb}_4\text{AlC}_3$  MAX-phases were studied in these works. Excellent mechanical properties of  $\text{Nb}_4\text{AlC}_3$  at high temperatures were noted. The bending strength of  $\text{Nb}_4\text{AlC}_3$  (346 MPa) remains without worsening in the range from room temperature to 1400°C, the Young's modulus of  $\text{Nb}_4\text{AlC}_3$  can be maintained up to 1580°C that is much higher than that of  $\text{Nb}_2\text{AlC}$  (1400°C),  $\text{Ta}_4\text{AlC}_3$  (1200°C), and  $\text{Ta}_2\text{AlC}$  (1200°C), which indicates prospective using the MAX-phase ( $\text{Nb}_4\text{AlC}_3$ ) at high temperatures.

Considering the above, the studies were conducted to find the optimal conditions for obtaining the  $\text{Nb}_4\text{AlC}_3$  MAX-phase by the SHS method. As preliminary studies showed, the combustion of the  $4\text{Nb} + 1.2\text{Al} + 2.7\text{C}$  mixture developed in a spin mode. To increase the exothermicity of the mixture, a mixture of Ti + 2B powders was added to the initial mixture in an amount of 1, 5, and 10 wt % as an additional source of heat. Figure 4 shows the X-ray diffraction patterns of the SHS products based on  $\text{Nb}_4\text{AlC}_3$  and with the addition of Ti + 2B

powders. XRD analysis shows that the addition of 1 wt % Ti + 2B to the initial mixture during SHS forms a product consisting of  $\text{Nb}_4\text{AlC}_3$ , NbC, and a small amount of the intermetallic phase  $\text{NbAl}_3$ . The addition of a larger amount of Ti + 2B leads to a significant decrease in the MAX-phase of  $\text{Nb}_4\text{AlC}_3$  and the presence of niobium monoboride in the synthesized product. With the addition of 10 wt % Ti + 2B, the product consists of NbC,  $\text{NbAl}_3$ , and NbB.

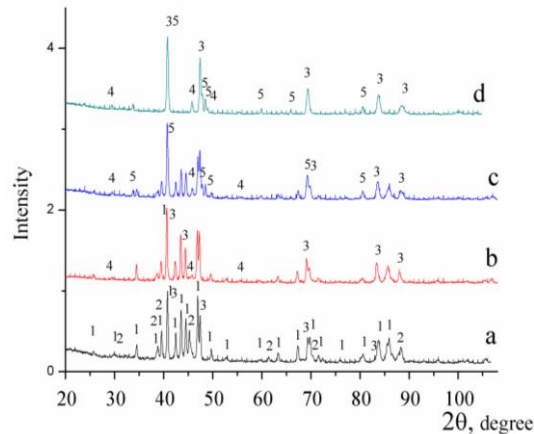


Fig. 4. XRD patterns of the SHS products (Nb–Al–C system, Nb:Al:C = 4:1.2:2.7 molar ratio) and with the addition of exothermic Ti + 2B powders, (a) Nb:Al:C = 4:1.2:2.7; (b) 1 wt % of Ti + 2B; (c) 5 wt % of Ti + 2B; (d) 10 wt % of Ti + 2B. 1  $\text{Nb}_4\text{AlC}_3$ ; 2  $\text{Nb}_2\text{AlC}$ ; 3 NbC; 4  $\text{NbAl}_3$ ; 5 NbB.

Currently, research is underway to develop and manufacture film heating elements. The electrical conductivity of polymer composite materials varies widely. This allows the use of the composition as a conductive material in electrical engineering. The requirements for electrically conductive composite materials can be met by selecting and optimizing the characteristics of the powder fillers used. It was previously shown that titanium carbosilicide ( $\text{Ti}_3\text{SiC}_2$ ) with high values of thermal and electrical conductivity can be used as a conductive material when creating film heaters. Studies have been conducted of the electrically conductive properties of the compounds, in which crushed SH-synthesis products based on  $\text{Nb}_2\text{AlC}$  and  $\text{Nb}_4\text{AlC}_3$  were used as electrically conductive fillers. Polymethylphenylsiloxane (PFMS) and its mixture with EDP epoxy resin were used as a binder in polymer compounds (Fig. 5).

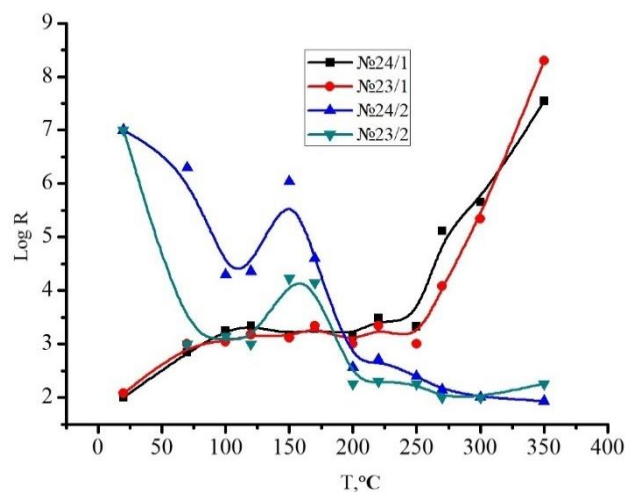


Fig. 5. The dependence of the electrical resistance of the coating on the heat treatment temperature with fillers: №23-based on  $\text{Nb}_4\text{AlC}_3$ , №24-based on  $\text{Nb}_2\text{AlC}$ . 1 PFMS, 2 PFMS + EDP.

A comparative analysis of the electrically conductive properties of coatings based on Nb<sub>2</sub>AlC and Nb<sub>4</sub>AlC<sub>3</sub> with coatings based on carbide and carborosilicide titanium showed that the electrical resistance of the latter is many times less.

Composite materials based on the MAX-phases, such as, Nb<sub>2</sub>AlC, Nb<sub>4</sub>AlC<sub>3</sub> were obtained by the method of self-propagating high-temperature synthesis. The SHS modes that ensure the maximum amount of, Nb<sub>2</sub>AlC and Nb<sub>4</sub>AlC<sub>3</sub> phases in the material were found. Composite polymer coatings based on Nb<sub>2</sub>AlC and Nb<sub>4</sub>AlC<sub>3</sub> can be used as film electric heating elements.

1. M.W. Barsoum, T. El-raghy, Synthesis and characterization of a remarkable ceramic: Ti<sub>3</sub>SiC<sub>2</sub>, *J. Am. Ceram. Soc.*, 1966, vol. 79, pp. 1953–1956.
2. T. Goto, T. Hirai, Chemically vapor deposited Ti<sub>3</sub>SiC<sub>2</sub>, *Mater. Res. Bull.*, 1987, vol. 22, pp. 1195–1201.
3. Z. Sun, Y. Zhang, Y. Zhou, Synthesis of Ti<sub>3</sub>SiC<sub>2</sub> powder by a solid-liquid reaction process, *Scr. Mater.*, 1999, vol. 41, no. 1, pp. 61–66.
4. Z. Sun, Y. Zhou, Fluctuation synthesis and characterization of Ti<sub>3</sub>SiC<sub>2</sub> powders, *J. Mater. Res. Innovat.*, 1999, pp. 227–231.
5. B.A. Goldin, P.V. Istomin, Yu.I. Ryabkov, Reduction solid-phase synthesis of titanium carborosilicide Ti<sub>3</sub>SiC<sub>2</sub>, *Inorg. Mater.*, 1997, vol. 33, pp. 691–693.
6. I. Salama, T. El-Raghy, M.W. Barsoum, Synthesis and mechanical properties of Nb<sub>2</sub>AlC and (Ti,Nb)<sub>2</sub>AlC, *J. Alloys Compd.*, 2002, vol. 347, pp. 271–278.
7. C. Hu, F. Li, J. Zhang, Nb<sub>4</sub>AlC<sub>3</sub>: A new compound belonging to the MAX phases, *Scripta Mater.*, 2007, vol. 57, pp. 893–896.
8. C.F. Hu, F.Z. Li, L.F. He, M.Y. Liu, J. Zhang, J.M. Wang, Y.W. Bao, J.Y. Wang, Y.C. Zhou, In situ reaction synthesis, electrical and thermal, and mechanical properties of Nb<sub>4</sub>AlC<sub>3</sub>, *J. Am. Ceram. Soc.*, 2008, vol. 91, pp. 2258–63.
9. C.F. Hu, Y. Sakka, H. Tanaka, T. Nishimura, S. Grasso, Low temperature thermal expansion, high temperature electrical conductivity, and mechanical properties of Nb<sub>4</sub>AlC<sub>3</sub> ceramic synthesized by spark plasma sintering, *J. Alloys Compd.*, 2009, vol. 487, pp. 675–81.

RECENT ADVANCES AND APPROACHES IN SHS OF  
HIGH-TEMPERATURE MATERIALS (OVERVIEW)

E. A. Levashov

National University of Science and Technology MISIS, Moscow, 119049 Russia  
e-mail: levashov@shs.misis.ru

DOI: 10.24411/9999-0014A-2019-10082

Development of next-generation spacecraft raises the problem of searching for materials resistant to high-enthalpy oxidative flows of gas containing abrasive particles. These materials are used in supersonic aerospace vehicles [1] with sharp leading edges and fairings, as well as in the critical section of nozzle clusters in solid propellant engines of spacecraft. Zirconium diboride  $ZrB_2$  is among promising materials: it is characterized by melting point  $> 3000^\circ C$  [2], high strength, fracture toughness, wear resistance, and thermal stability. High thermal conductivity ensuring rapid heat transfer away from the surface contacting the oxidative gas flow is an important advantage of  $ZrB_2$ -based composites. Elaboration of efficient methods for fabrication of erosion-resistant and ultrarefractory materials based on HfC ( $T_{melt} = 3900^\circ C$ ), TaC ( $3800^\circ C$ ), HfB<sub>2</sub> ( $3380^\circ C$ ),  $ZrB_2$  ( $3200^\circ C$ ), TaB<sub>2</sub> ( $3200^\circ C$ ), and NbB<sub>2</sub> ( $3050^\circ C$ ) is a topical problem. Solid solutions have a higher melting point than individual compounds. Thus, the melting point of single-phase carbide (Ta,Hf)C with 20% HfC dissolved in it is  $\sim 3950^\circ C$ . In addition to the high melting point, solid solutions are characterized by extreme correlations between hardness, coefficient of thermal expansion (CTE), or thermal conductivity and solid solution composition. A combination of high thermal conductivity and low CTE determines material's thermal shock resistance.

Therefore, synthesis of single-phase solid solutions (Ta,Zr)C, (Ta,Hf)C, (Ta,Zr)B<sub>2</sub>, and (Ta,Hf)B<sub>2</sub> is an independent task. These compounds can be fabricated using various methods: by heating a mixture of powders, reducing an oxide mixture by hydrogen, precipitating from solutions, by microwave synthesis, sol-gel synthesis, or SHS.

Elemental and magnesium-thermal SHS, hot pressing, and SPS were used to produce ultra-high temperature ceramics (UHTCs) based on the single-phase solid solutions of diborides (Ta,Zr)B<sub>2</sub>, (Ta,Hf)B<sub>2</sub> [3–7] and carbides (Ta,Zr)C, (Ta,Hf)C [8–11]. The kinetics and the mechanism of combustion and structure formation in the Ta–Zr–C, Ta–Hf–C, Zr–Ta–B, Hf–Ta–B, Mo–Si–B, Zr–B–Si, Zr–B–Si–C, and Ta–Si–C systems were studied. Mechanical activation (MA) or reaction mixtures was shown to play a crucial role in production of single-phase solid solutions (Ta,Hf)C and (Ta,Zr)C. For example, synthesis after MA of Ta–Hf–C mixtures gave rise to single-phase carbide (Ta,Hf)C with the lattice parameter  $a = 0.4487$  nm, which corresponded to 18 at % of dissolved HfC, while the content of HfO<sub>2</sub> impurity oxide was  $< 1\%$ . SHS powders of solid solutions are excellent raw materials for consolidation by such methods as HP, HIP, and SPS, which gave rise to materials with the relative density up to 98%.

It was explained [12] that the consolidation of powders of UHTCs such as  $ZrB_2$  [13],  $TiB_2$  [14],  $ZrB_2$ –ZrC–SiC [15] is made easier when using powders prepared by SHS, instead of other commercially available powders prepared by alternative methods. Mishra et al. [13] ascribed such peculiarity to the high defect concentration in SHS powders generated by the severe heating and cooling rate conditions in combustion wave.

To enhance the thermal shock, UHTCs were strengthened by whiskers/fibers of SiC<sub>f</sub> or C<sub>f</sub> [12]. In case of the HfB<sub>2</sub>–SiC<sub>f</sub> system, the best ceramic composition produced by SHS + SPS has a hardness (HV) = 21.6 GPa and fracture toughness ( $K_{Ic}$ ) = 6.2 MPa·m<sup>1/2</sup> [12]. However,

SiC fibers break into fragments at consolidation temperatures of 2000°C and higher; some silicides melt down. Therefore, the temperature of SPS should be around 1800°C or lower.

MoSi<sub>2</sub>, ZrSi<sub>2</sub>, and TaSi<sub>2</sub> silicides are fruitfully used as additives to diborides- and carbides-based composition in order to increase oxidation resistance [4, 16–20]. MoSi<sub>2</sub> is characterized by excellent oxidation resistance and can remain operable during 2000 h at 1923 K. Oxidation of ZrSi<sub>2</sub> gives rise to the ZrSiO<sub>4</sub>/SiO<sub>2</sub> glassy phase with an effect of self-healing of defects and cracks. SHS of heterophase powders ZrB<sub>2</sub>–MoSi<sub>2</sub>–ZrSi<sub>2</sub> and HfB<sub>2</sub>–MoSi<sub>2</sub>–HfSi<sub>2</sub> was employed to obtain UHTCs with 1–2 μm boride grains and 2–4 μm silicide grains. The kinetics and mechanism of high-temperature oxidation of dense heterophase ZrSi<sub>2</sub>–MoSi<sub>2</sub>–ZrB<sub>2</sub> ceramics at a temperature of 1650°C were studied [20]. The kinetic oxidation curve is described by the power-law function, which indicates that the evolutionary changes in the structure of the resulting oxide films significantly affect the course of the oxidation process. The oxidation mechanism involves formation of a multi-layered structure of heterogeneous oxide film, partial dissociation of the ZrSiO<sub>4</sub> phase, and formation of secondary MoB and Mo<sub>5</sub>Si<sub>3</sub> compounds. The influence of the content of ZrSi<sub>2</sub>, MoSi<sub>2</sub>, and ZrB<sub>2</sub> phases on the structural and morphological features of the formed oxide films and the efficiency of their protective action were studied. Silicon is reduced and zirconium is simultaneously oxidized to ZrO<sub>2</sub> in the ZrSi<sub>2</sub>–ZrSiO<sub>4</sub> system at temperatures above 1620°C in the absence of oxygen or in low-oxygen environment.

Vorotilo et al. [18] studied two schemes for fabricating the composite powders ZrB<sub>2</sub>–TaB<sub>2</sub>–TaSi<sub>2</sub> by SHS that are discussed in this study: (1) elemental synthesis in the Zr–Ta–B and Ta–Si mixtures followed by mixing of the combustion products, and (2) elemental synthesis in the Zr–Ta–Si–B mixture. The macrokinetic features of combustion of the Zr–Ta–Si–B mixtures, the mechanism of structure and phase formation in the combustion wave, and the structure and properties of the combustion products were discussed. Primary crystals of tantalum and zirconium diborides were formed in the preheating zone as a result of gas-phase mass transfer of boron onto the surface of metal particles. In the combustion zone, melting of Si–B eutectic and Zr particles took place, followed by the formation of borides and silicides of tantalum and zirconium. In the zones of post-combustion and secondary structure formation, zirconium diboride partially interacted with tantalum diboride and formed (Ta,Zr)B<sub>2</sub> solid solution. HP ceramics with the relative density of 98% fabricated using scheme 2 have a specific microgradient grain structure and significantly higher hardness and  $K_{1c}$  as compared to the similar composite prepared using scheme 1.

Investigation of the macrokinetic features of elemental synthesis in the Mo–Hf–Si–B mixtures, in particular the mechanisms of structure and phase formation in the combustion front as well as the structure and properties of consolidated ceramics, was carried out in [19]. Two routes were also used for fabrication of composite powders in the MoSi<sub>2</sub>–HfB<sub>2</sub>–MoB system:

(1) synthesis using Mo–Si–B and Hf–B mixtures followed by mixing of the combustion products and (2) synthesis using the four-component Mo–Hf–Si–B mixture. Although the particle size distribution and phase composition of SHS powders were similar for both routes, the structure and properties of both the composite SHS powders and hot-pressed ceramics differ considerably. Synthesis using the four-component Mo–Hf–Si–B mixture allows one to produce hierarchically ordered ceramics with improved hardness up to 17.6 GPa and  $K_{1c}$  up to 7.2 MPa m<sup>1/2</sup>.

The produced UHTCs exhibited high resistance against the impact of high-enthalpy oxidative gas flow. Sequences of chemical and structural transformations were investigated. At 3000°C, the rate of thermochemical corrosion of carbide-based UHTCs was 15–20% lower as compared to that of the basic composites, whereas the boride ceramics based on (Ta,Zr)B<sub>2</sub>, (Ta,Hf)B<sub>2</sub> demonstrated decomposition enthalpy up to 390 kJ/g, which is an order of magnitude higher than the enthalpy of analogous materials [7]. During firing tests, the

linear rate of thermochemical erosion of dense UHTCs of single-phase solid solution (Ta,Hf)C, (Ta,Zr)C produced by SPS and HP was lower than that of industrial analogues by 15–20% [9]. The hierarchically structured TaSi<sub>2</sub>–SiC ceramics reinforced with discrete SiC and Si<sub>3</sub>N<sub>4</sub> fibers were synthesized. The mechanism of formation of the TaSi<sub>2</sub> + SiC ceramics was revealed [21]. The microstructure becomes significantly finer-grained in the post-combustion zone as SiC nanocrystallites (20–40 nm in size) are formed inside the TaC, Ta<sub>5</sub>Si<sub>3</sub>, and TaSi<sub>2</sub> grains. Some SiC and TaSi<sub>2</sub> grains crystallize from silicon based melt, while crystallization of the remaining SiC and TaSi<sub>2</sub> grains occurs via the solid-phase transformation mechanism. The final product has a hierarchical two-level structure with high hardness of 19.1 GPa and fracture toughness  $K_{1c} = 6.7 \text{ MPa}\cdot\text{m}^{1/2}$ .

As an example of application, the TaSi<sub>2</sub> + SiC ceramic were applied in magnetron sputtering of high-temperature coatings [22]. Coatings consisted of the amorphous phase with the inclusion of nanoparticles of fcc solid solution Ta(Si,C,N), were characterized by hardness of 26 GPa, Young modulus of 268 GPa, thermal stability up to 800°C, and friction coefficient of 0.2 at 800°C in air. Low friction coefficient was caused by formation of a thin oxide layer consisting of TaSi<sub>x</sub>O<sub>y</sub> nanofibers in the contact zone.

This work was carried out with financial support from the Russian Science Foundation under project no. 19-19-00117.

1. A. Paul, D.D. Jayaseelan, S. Venugopal, E. Zapata-Solvas, et al., *Amer. Ceram. Soc. Bull.*, 2012, vol. 91, no. 1, pp. 22–29.
2. E. Wuchina, E. Opila, M. Opeka, W. Fahrenholtz, I. Talmy, *Electrochem. Soc. Interface*, 2007, pp. 30–36.
3. Concise Encyclopedia of Combustion Synthesis: History, Theory, Technology, and Products, ed. by I. Borovinskaya, A. Gromov, E. Levashov, Yu. Maksimov, A. Mukasyan, A. Rogachev, Elsevier, 2017, 466 p.
4. E.A. Levashov, A.S. Mukasyan, A.S. Rogachev, D.V. Shtansky, Self-propagating high-temperature synthesis of advanced materials and coatings, *Inter. Mater. Rev.*, 2017, vol. 62, no. 4, pp. 203–239.
5. V.V. Kurbatkina, E.I. Patsera, E.A. Levashov, A.N. Timofeev, Self-propagating high-temperature synthesis of refractory boride ceramics (Zr,Ta)B<sub>2</sub> with superior properties, *J. Europ. Ceram. Soc.*, 2018, vol. 38, pp. 1118–1127.
6. V.V. Kurbatkina, E.I. Patsera, E.A. Levashov, Combustion synthesis of ultra-high-temperature ceramics based on (Hf,Ta)B<sub>2</sub>. Part 1: The mechanisms of combustion and structure formation, *Ceram. Int.*, 2019, vol. 45, pp. 4067–4075.
7. V.V. Kurbatkina, E.I. Patsera, D.V. Smirnov, E.A. Levashov, S. Vorotilo, A.N. Timofeev, Combustion synthesis of ultra-high-temperature ceramics based on (Hf,Ta)B<sub>2</sub>. Part 2: Structure, mechanical and thermophysical properties of consolidated ceramics, *Ceram. Int.*, 2019, vol. 45, pp. 4076–4083.
8. V.V. Kurbatkina, E.I. Patsera, S. Vorotilo, E.A. Levashov, A.N. Timofeev, Conditions for fabricating single-phase (Ta,Zr)C carbide by SHS from mechanically activated reaction mixtures, *Ceram. Int.*, 2016, vol. 42, pp. 16491–16498.
9. V.V. Kurbatkina, E.I. Patsera, E.A. Levashov, A.N. Timofeev, Self-propagating high-temperature synthesis of single-phase binary tantalum-hafnium carbide (Ta,Hf)C and its consolidation by hot pressing and spark plasma sintering, *Ceram. Int.*, 2018, vol. 44, no. 4, pp. 4320–4329.
10. E.I. Patsera, E.A. Levashov, V.V. Kurbatkina, D.Yu. Kovalev, Production of ultra-high temperature carbide (Ta,Zr)C by self-propagating high-temperature synthesis of mechanically activated mixtures, *Ceram. Int.*, 2015, vol. 41, no. 7, pp. 8885–8893.

11. S.Vorotilo, K.Sidnov, I.Yu. Mosyagin, A.V. Khvan, E.A. Levashov, E.I. Patsera, I.A. Abrikosov, Ab-initio modeling and experimental investigation of the properties of ultra-high temperature solid solutions  $Ta_xZr_{1-x}C$ , *J. Alloys Compd.*, 2019, vol. 778, pp. 480–486.
12. C. Musa, R. Licheri, R. Orru, R. Marocco, G. Cao, *Ceramics in Modern Technologies*, 2019.
13. S.K. Mishra, S. Das, L.C. Pathak, Defect structures in zirconium diboride powder prepared by self-propagating high-temperature synthesis, *Mater. Sci. Eng. A*, 2004, vol. 364, pp. 249–255.
14. A.K. Khanra M.M. Godkhindi, L.C. Pathak, Comparative studies on sintering behavior of self-propagating high-temperature synthesized ultra-fine titanium diboride powder, *J. Am. Ceram. Soc.*, 2005, vol. 88, pp. 1619–1621.
15. R. Licheri, R. Orrù, C. Musa, G. Cao, Combination of SHS and SPS techniques for fabrication of fully dense  $ZrB_2$ - $ZrC$ - $SiC$  composites, *Mater. Lett.*, 2008, vol. 62, pp. 432–435.
16. Yu.S. Pogozhev, I.V. Yatsyuk, E.A. Levashov, A.V. Novikov, N.A. Kochetov, D.Yu. Kovalev, The kinetics and mechanism of combustion of the Zr-B-Si mixtures and the features of structure formation of ceramics based on zirconium boride and silicide, *Ceram. Int.*, 2016, vol. 42, pp. 16758–16765.
17. I.V. Yatsyuk, A.Yu. Potanin, E.A. Levashov, Combustion synthesis of high-temperature  $ZrB_2$ - $SiC$  ceramics, *J. Europ. Ceram. Soc.*, 2018, vol. 38, pp. 2792–2801.
18. S. Vorotilo, E.A. Levashov, M.I. Petrzhik, D.Yu. Kovalev, Combustion synthesis of  $ZrB_2$ - $TaB_2$ - $TaSi_2$  ceramics with microgradient grain structure and improved mechanical properties, *Ceram. Int.*, 2019, vol. 45, iss. 2, Part A, pp. 1503–1512.
19. S. Vorotilo, A.Yu. Potanin, Yu.S. Pogozhev, E.A. Levashov, N.A. Kochetov, D.Yu. Kovalev, Self-propagating high-temperature synthesis of advanced ceramics  $MoSi_2$ - $HfB_2$ - $MoB$ , *Ceram. Int.*, 2019, vol. 45, iss. 1, pp. 96–107.
20. A.N. Astapov, Yu.S. Pogozhev, M.V. Prokofiev, I.P. Lifanov, A.Yu. Potanin, E.A. Levashov, V.I. Vershinnikov, kinetics and mechanism of high-temperature oxidation of the heterophase  $ZrSi_2$ - $MoSi_2$ - $ZrB_2$  ceramics, *Ceram. Int.*, 2019, Vol. 79, vol. 45, iss. 5, 2019, pp. 6392–6404.
21. S. Vorotilo, E.A. Levashov, V.V. Kurbatkina, D.Yu. Kovalev, N.A. Kochetov, Self-propagating high-temperature synthesis of nanocomposite ceramics  $TaSi_2$ - $SiC$  with hierarchical structure and superior properties, *J. Europ. Ceram. Soc.*, 2018, vol. 38, no. 2, pp. 433–443.
22. A.V. Bondarev, S. Vorotilo, I.V. Shchetinin, E.A. Levashov, D.V. Shtansky, Fabrication of Ta-Si-C targets and their utilization for deposition of low friction wear resistant nanocomposite Si-Ta-C- (N) coatings intended for wide temperature range tribological applications, *Surf. Coat. Technol.*, 2019, vol. 359, pp. 342–353.



# SOLUTION COMBUSTION SYNTHESIS OF N-DOPED NiO/Ni@C COMPOSITE NANOMATERIALS AND ITS ELECTROCHEMICAL PERFORMANCE AS ANODE MATERIAL OF LITHIUM/SODIUM ION BATTERIES

Y. Y. Li<sup>a</sup>, C. X. Xu<sup>a,b</sup>, K. Y. Liu<sup>a</sup>, and P. W. Chen<sup>\*a</sup>

<sup>a</sup>School of Mechatronical Engineering, Beijing Institute of Technology, Beijing, 100081 China

<sup>b</sup>Aerospace Institute of Advanced Materials & Processing Technology, Beijing, 100074 China

\*e-mail: pwchen@bit.edu.cn

DOI: 10.24411/9999-0014A-2019-10083

Lithium-ion batteries are the most promising high-efficiency secondary batteries and the fastest-growing chemical energy storage power sources due to their high specific energy, low self-discharge, superior cycle performance, no memory effect and environmental protection. Porous carbon nanomaterials have high porosity, high specific surface area and good electron mobility. On the other hand, NiO has high lithium storage capacity ( $718 \text{ mAh}\cdot\text{g}^{-1}$ ), low cost, environmental protection and abundant reserves. Therefore, the composite of NiO and porous carbon has high potential to be a new material with superior electrochemical performance and high potential application as anode material.

Compared with the traditional combustion synthesis method, solution combustion synthesis features the advantages of spontaneous maintenance, fast reaction in milliseconds high controllability and atomic level mixing. Furthermore, solution combustion process produces a large amount of gas, leading to the formation of as-obtained porous nanomaterials with a loose, non-agglomerated, and high specific surface area structure.

In our study, N-doped NiO/Ni@C (Fig. 1) was synthesized through a one-step solution combustion process using  $\text{CO}_2$ , ethanol amine and nickel nitrate as carbon source, reaction solution and Ni source, respectively, with magnesium as combustion improver. The solution combustion experimental process is illustrated in Fig. 2. In addition, N-doped NiO@C composite nanomaterial was obtained via same process using hydrazine hydrate as reaction solution. The as-prepared composite nanomaterials with well-controlled NiO/Ni content exhibit a high specific surface area of  $245 \text{ m}^2\cdot\text{g}^{-1}$ , a high pore volume of  $1.85 \text{ m}^2\cdot\text{g}^{-1}$ , a well-structured pore structure, and a high content of 3.73 at % in-situ nitrogen doping. The anode made of NiO/Ni@C composite exhibit excellent capacities of  $791 \text{ mAh}\cdot\text{g}^{-1}$  at  $0.1 \text{ A}\cdot\text{g}^{-1}$  after 150 cycles in Li-ion battery and  $89 \text{ mAh}\cdot\text{g}^{-1}$  at  $0.1 \text{ A}\cdot\text{g}^{-1}$  after 150 cycles in Na-ion battery.

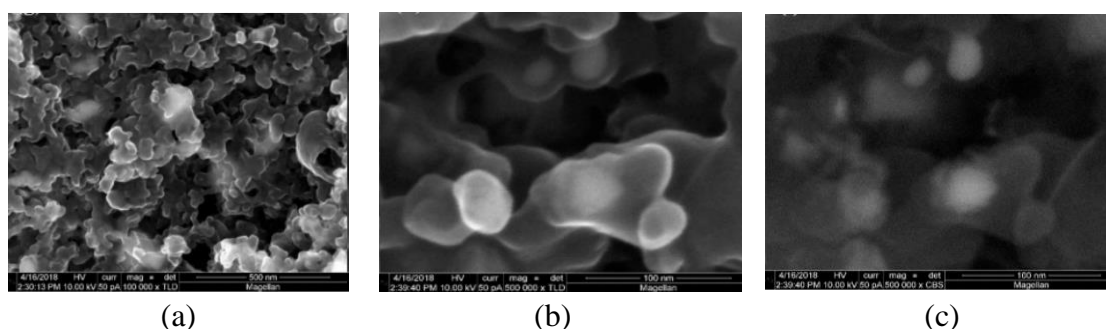


Fig. 1. SEM images (a, b) and back diffraction image (c) of NiO/Ni@C-0.375.

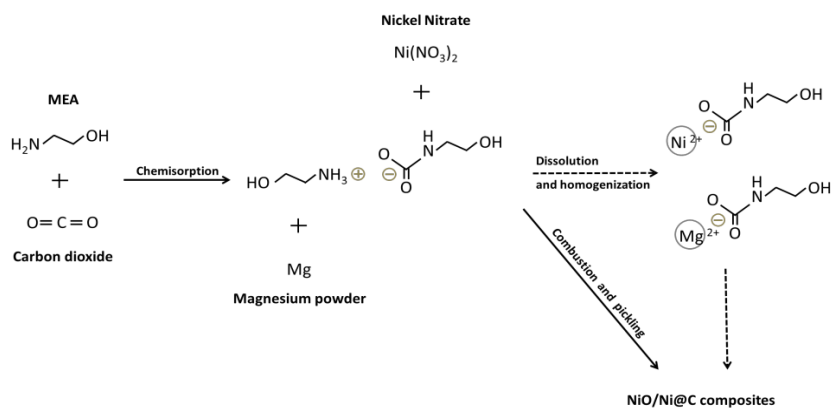


Fig. 2. Schematic of solution combustion synthesis of NiO/Ni@C composite nanomaterials.

Our research introduces an efficient, energy-saving and environmentally friendly solution combustion synthesis method, which can be modified into a non-combustion and flame-free pure cracking conversion process for a mild reaction condition and large-scale production.

## LASER TECHNOLOGY IN SYNTHESIS AND PROCESSING OF SHS DERIVED MAX MATERIALS

J. Lis<sup>\*a</sup>, P. Rutkowski<sup>a</sup>, D. Kata<sup>a</sup>, L. Chlubny<sup>a</sup>, and D. Sala<sup>b</sup>

<sup>a</sup>AGH University of Science and Technology in Krakow, Faculty of Materials Science and Ceramics, Krakow, 30-059 Poland

<sup>b</sup>AGH University of Science and Technology in Krakow, Faculty of Management, Krakow, 30-059 Poland  
\*e-mail: lis@agh.edu.pl

DOI: 10.24411/9999-0014A-2019-10084

Laser processing has contributed to almost all engineering areas that include mechanical, materials, industrial, aerospace, electrical and most recently biomedical engineering. Today, laser processing of ceramic becoming popular also, due to its flexible and customized manufacturing capabilities. The most interesting feature is to manufacture and shaping of new compounds difficult to obtain by conventional methods.

MAX phases are interesting group of layered ternary and quaternary materials which are combining properties typical for metals and ceramics [1–3]. Self-propagating high-temperature synthesis (SHS) is a versatile method used for the technology of obtaining a wide range of materials. It has been shown by the authors, that various MAX phase materials can be synthesized using SHS technique [4–8].

This paper concerns possibilities of continues work fiber laser application to MAX phases SHS synthesis and processing of polycrystalline MAXes prepared from SHS derived powders. In the first part of the research the laser apparatus was used to initiate of combustion of MAX phases in the Ti–Si–C system [9]. For that purpose, special prototype reaction chamber combined with laser scanner were used. The laser configuration allowed also the control of released temperature and monitor the reaction bed behavior. In combination with reaction bed thermal properties of differently packed material it allows to understand synthesis temperature rate. It was found that this technique, SHS initiated and controlled by laser beam, allows to obtain of MAX layers as well as products from the MAX phases in the form of 3D printed.

The second part of research concerns laser processing of hot-pressed  $Ti_3AlC_2$  and  $Ti_2AlC$  MAX phases prepared from SHS powders [10]. Both of materials were cut or welded in various laser condition such as laser power or processing speed rate. In case of  $Ti_3AlC_2$  MAX phase it was possible to obtain stable material joining. The titanium element was a major cause of material joining and secondary phases' recrystallization. Also, it was noticed that second type of laser processing instead of ablation process leads to filling cavity by the recrystallized material and results in  $Ti_3AlC_2$  material healing process.

Different situation during subtractive laser processing was in the case of  $Ti_2AlC$  material, which showed high porosity. During the surface laser modification, probably the generated pressure during laser machining allowed to fill the porous sides of the cut by recrystallized material. So, in this case, healing process was impossible at the expense of cut surfaces densification. The trial identification of recrystallized secondary phase in various heat affected zones (HAZ) as an effect of laser processing was made. The HAZ were examined. It was conducted in case of material welding, cutting and healing. The following analysis were made: optical microscopy, SEM, EDS, FIB.

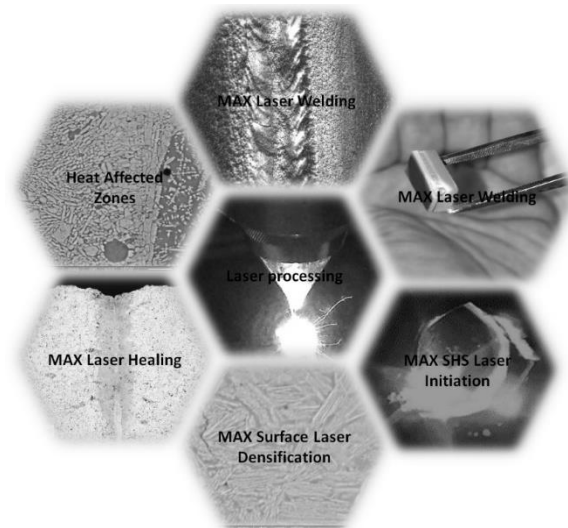


Fig. 1. MAX laser processing.

1. M.W. Barsoum, *Prog Solid St. Chem.*, 2000, vol. 28, pp. 201–281.
2. M.W. Barsoum, *MAX phases: properties of machinable ternary carbides and nitrides*, Wiley, 2013.
3. M. Radovic, M.W. Barsoum, *Am. Cer. Soc. Bull.*, 2013, vol. 92, no. 3, pp. 20–27.
4. J. Lis, R. Pampuch, L. Stobierski, *Int. J. Self-Propag. High-Temp. Synth.*, 1992, 1, 401.
5. L. Chlubny, J. Lis, K. Chabior, P. Chachlowska, C. Kapusta, *Arch. Metall. Mater.*, 2015, vol. 60, iss. 2, pp. 859–863.
6. L. Chlubny, J. Lis, M.M. Bucko, *Ceram. Eng. Sci. Proc.*, 2010, vol. 31, iss. 10, pp. 153–159.
7. L. Chlubny, J. Lis, M.M. Bućko, *Ceram. Eng. Sci. Proc.*, 2013, vol. 34, no. 10, pp. 265–271.
8. L. Chlubny, J. Lis, *Ceram. Trans.*, 2013, vol. 240, pp. 79–86.
9. P. Rutkowski, J. Huebner, D. Kata, J. Lis, A. Graboś, L. Chlubny, *Ceram. Int.*, 2018, vol. 44, no. 9, pp. 10883–10890.
10. P. Rutkowski, J. Huebner D. Kata, L. Chlubny, J. Lis, K. Witulska, *J. Therm. Anal. Calorim*, 2019.

## FABRICATION OF TiC–TiB<sub>2</sub> COMPOSITE CERAMIC BY SELF-PROPAGATING HIGH TEMPERATURE SYNTHESIS

**K. Y. Liu<sup>a</sup>, Y. Y. Li<sup>a</sup>, and P. W. Chen<sup>\*a</sup>**

<sup>a</sup>School of Mechatronical Engineering, Beijing Institute of Technology,  
Beijing, 100081 China  
<sup>\*</sup>e-mail: pwchen@bit.edu.cn

DOI: 10.24411/9999-0014A-2019-10085

TiC–TiB<sub>2</sub> composite ceramic is a potential structural material and has attracted tremendous attention in recent years. It exhibits excellent properties, including high hardness, high temperature oxidation resistance, thermal shock resistance, corrosion stability and so on. TiC–TiB<sub>2</sub> can be prepared by means of sintering process, hot isostatic pressing, and hot-pressed sintering. However, low production efficiency and high cost still exist for these conventional methods.

As a rapidly developed in-situ synthesis of materials technology, self-propagating high-temperature synthesis (SHS) has drawn much attention because of short reaction time, high production efficiency, and low cost.

In our study, TiC–TiB<sub>2</sub> composite ceramic was fabricated by SHS reaction of pre-compacted titanium and boron carbide mixture powder. The specimens were densified by rapid compression at the same time. XRD was employed to identify the phase compositions of ceramic materials. The microstructure of TiC–TiB<sub>2</sub> was observed by OM and SEM. The effects of synthesis conditions on the materials structure were investigated. The mechanical properties of TiC–TiB<sub>2</sub> composite ceramic were characterized.

## PRODUCED AND PROPERTIES OF UFP OF NICKEL FOR DIFFUSION WELDING OF HETEROGENEOUS MATERIALS

**A. V. Liushinskii**

JSC Ramenskoe Design Company, Ramenskoe, 140103 Russia  
e-mail: nilsvarka@yandex.ru

DOI: 10.24411/9999-0014A-2019-10086

The simplest most convenient method of intensifying the process of diffusion bonding and ensuring efficient operation of mechanical and thermal channels of activation is the use of interlayers which may play different functions during welding.

Interlayers are made of gold, silver, copper, nickel, aluminium and other metals in the form of wire, foil, powders, and films deposited on the surfaces to be bonded by electroplating or in the form of vacuum condensates. The type of interlayer is determined by the possibilities of technological production and depends on grade of welded materials, the welding conditions, the service conditions of resultant joints, etc.

A method has been developed of producing ultrafine powders (UFP) of metals characterized by high activity in compacting and sintering as a result of the developed free surfaces and the presence of a large number of crystal structure defects (dislocations, vacancies, etc.).

The author examined the effect of the dispersion and method of producing different powders on the quality of formation of the joint. He shows that the diffusion bonding parameters ensuring high-quality bonds decrease with an increase of the specific surface of powder and an increase of the distance of their state from thermodynamic equilibrium.

When using powder interlayers, especially those based on the UFP of nickel, produced by thermal dissociation of its format  $\text{Ni}(\text{COOH})_2 \cdot 2\text{H}_2\text{O}$ , in both the freely distributed form and the form of porous rolled strips, formation of both the physical contact and joints is made easier. This is one of the promising methods of a simultaneous reduction of the temperature and welding pressure and producing high-quality joints from dissimilar materials with the required mechanical properties without changing the initial electrophysical characteristics. To increase the mechanical strength of joints and special properties of sections as well as to reduce the thermal-strain effect on the welded components and the technological cycle of diffusion bonding, the author developed and examined two-component interlayers based on the most promising mixtures of UFPs of nickel, copper, and cobalt. Experiments into kinetics of thermal dissociation of mixtures were carried out in an inert gas atmosphere. The specific surface  $S_{\text{sp}}$  of metallic powders and porous rolled strips was measured by the method of thermal desorption of nitrogen. The microstructure of powders and strips was evaluated using a Stereoscan-150 electron microscope. Rolling of the UFPs into strips was carried out in special YUD-2200 rolling mill with horizontal rolls (diameter of 20 mm) and a stepped variation of the speed.

Mixtures of metallic powders (Ni + Co, Ni + Cu, Cu + Co) in different mass (%) ratios of the components (10 + 90, 25 + 75, 50 + 50, 75 + 25, 90 + 10) were produced by two method. The first method is mechanical mixing of formats, their homogenizing, and thermal dissociation (Fig. 1). The second method is preparation of the format of the given mixture with the required composition and its pyrolysis in which the organic salt dissociates into metal and gaseous products. Thermal dissociation of almost all mixtures is characterized by three endothermic effect, which were linked respectively with the processes of dehydration and subsequent dissociation of individual components – a mechanical mixture or a format of the mixture. The results show that the composition of powder mixtures affects the kinetic relationships of the process of dehydration and dissociation,  $S_{\text{sp}}$  of the particles and their form and dimensions.

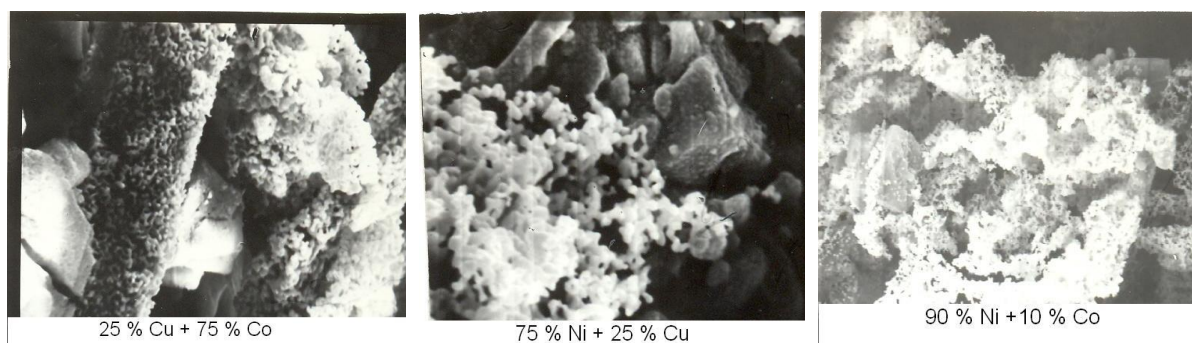


Fig. 1. Microstructure of UFPs.

The operation of depositing of the UFPs on welded surfaces is not efficient from the technological viewpoint (the layer thickness and mass are not uniform) and difficult to mechanise. The most suitable interlayer has to the form of porous strip produced by rolling the metallic UFPs. However, there are no results of systematic investigations into properties of the UFPs after their rolling into strip.

The author examined the dependence of the strength of the welded joint on the thickness and porosity of the rolled strip made of the UFP of nickel, and it was shown that it contained an extremum.

Diffusion bonding through powder interlayers is characterized by two simultaneous processes of forming the high-quality joints: sintering of the interlayer and its bonding to the surface of welded materials. Special attention will now be given to the features of volume shrinkage and the energy parameters of this process when sintering binary powder mixtures.

The kinetics of sintering under pressure (similar to welding) were examined on both specimens made of porous rolled strips produced from UFPs. The specimens were heated at a constant rate at 400–800°C in vacuum and were compressed after reaching the required temperature ( $P = 5\text{--}20$  MPa). The sintering time at the given temperature and pressure was varied from 5 to 30 min.

Sintering of the interlayer of one of the component, for example the UFP nickel, is accompanied by volume shrinkage of interlayer and takes place during a reduction of the free surface energy of the powder system as a result of reduction of the total area of the surface of inter particle pores. The interlayer made of a mixture of UFPs of two metals, capable of interaction with each other, together with the excess free energy also possesses an excess energy associated with the possibility of forming an alloy. Therefore, when sintering two-component powder interlayers two process should take place simultaneously: volume shrinkage of the interlayer and formation of the alloy.

The efficiency of joints produced by diffusion bonding through powder interlayers is determined by the strength of this interlayer and of its bond with the surface of the bonded materials. It is therefore interesting to examine the process taking place in the zone of contact of the interlayer with bonded surface and determine the mass transfer mechanisms taking place in this case with an allowance made from the phenomena detected when compacting the powder interlayer. In diffusion bonding through porous powder strips, potential active centers are represented by defects of the structure of UFP particles introduced in pyrolysis and formed during rolling as well as by surface roughness of the strip determined by the degree of development of the surface of the individual powder particles. An increase of the surface roughness of the strip increase the activity of the interlayer, which becomes evident at relatively low temperatures and is similar to the activity of the freely distributed UFP.

The result of examining interlayers based on mixtures of UFP of nickel, copper, and cobalt indicate it is possible to produce high-quality welded joints in dissimilar materials using parameters lower than those generally accepted. Positive results have been obtained when using the proposed interlayers for joining metallic materials (hard alloy + steel, hard alloy + hard

alloy, constant magnet + steel, titanium alloys + steels and other) and non-metallic materials (ceramics + sapphire, ceramics + piezoceramics and other).

1. A.V. Liushinskii, Functions of interlayers based on ultradisperse metal powders at diffusion bonding of heterogeneous materials, *IOP Conf. Ser.: Mater. Sci. Eng.*, 2018, vol. 447, 012034.
2. A.A. Uvarov, A.V. Liushinskii, et. al., A study of the structure of steel–titanium joints formed by diffusion welding with the use of ultrafine nickel, *Metal. Sci. Heat Treat.*, 2017, vol. 59, nos. 7–8, pp. 529–533.



## MECHANICAL AND ADHESIVE PROPERTIES OF TITANIUM DOPED Fe–Co–Ni BINDER FOR DIAMOND CUTTING TOOL

**P. A. Loginov<sup>\*a</sup>, D. A. Sidorenko<sup>a</sup>, and E. A. Levashov<sup>a</sup>**

<sup>a</sup>National University of Science and Technology MISiS, Moscow, 119049 Russia

<sup>\*</sup>e-mail: pavel.loginov.misis@list.ru

DOI: 10.24411/9999-0014A-2019-10087

Designing of new binder compositions for diamond cutting and grinding tools is a crucial task in modern building and mining industries. Cobalt is well-known as the most suitable material for binder because of its excellent compatibility at relatively low temperatures, high mechanical properties, and fine interaction and adhesion to diamond monocrystals [1]. Nevertheless, its high cost forces diamond tool producers to work on low-cobalt binders. One of them, based on Fe–Co–Ni alloys, prepared by means of mechanical alloying (MA) and hot pressing (HP) techniques, has a strong potential for using in the tools dealing with highly abrasive materials [2].

Fe–Co–Ni binders demonstrate a combination of high mechanical properties and wear resistance. But improving of their adhesion to diamond monocrystals is still a major challenge. The method, applied in this work, is addition of adhesion-active elements, such as titanium [3, 4]. In this case problem complexity involves the facts that Ti has low solubility with basic matrix components. This may tend to development of brittleness due to intermetallic compounds formation. Ti is usually present in the world market by powders with high average grain size (usually several dozens of  $\mu\text{m}$ ). This feature leads to reducing of contact surface of Ti with diamond if used in diamond tool. But this problem can be solved using MA method to produce multicomponent powder binders [5]. Processing in planetary ball mills with high energies allows to redistribute Ti homogeneously in the matrix via their dissolution in the crystal lattice of basic component (Fe).

Thus, this study addresses the fabrication of nanocrystalline Fe–Co–Ni–Ti alloy using two operations: MA and HP.

Carbonyl iron powder (OOO Sintez-PKZh, Russia), carbonyl nickel powder (AO Kola Mining and Metallurgical Company), and reduced cobalt powder (Nanjing Hanrui Cobalt Co Ltd, China) were used as the initial materials. The doping agent titanium (AO Polema, Russia) had average grain size of 28  $\mu\text{m}$ .

Powder mixtures were prepared using an Activator-2s planetary ball mills (PBM) (Russia) with carrier rotation speed of 694 rpm and centrifugal factor of 90 g. Duration of ball milling was varied in the range of 5–20 min. The jars were filled with argon to prevent oxidation of the charge mixture during treatment.

Compacted samples 10 × 10 cm in size were prepared from the powder mixtures by hot pressing (HP). The HP temperature was 950°C; pressure at the maximum temperature, 350 kg/cm<sup>2</sup>; exposure time, 3 min. These preforms were used to cut out samples to measure the ultimate bending strength, hardness, and porosity. Residual porosity of the compacted samples was determined by hydrostatic weighing on an analytical balance (A&D, Japan). Weights were measured with an accuracy of 10<sup>-4</sup> g.

The ultimate bending strength was measured using an LF-100 servo-hydraulic universal testing machine (Walter + bai, Switzerland) with an external digital controller (EDC). The ultimate bending strength values were determined using a DIONPro software enabling automated registration and statistical processing of the test results.

The Rockwell hardness was tested using a Wolpert Rockwell Hardness Tester (Wolpert 600 MRD, USA).

The friction coefficient and the reduced wear of the samples were determined using the rolling sliding wear test on an automated Tribometer machine (CSM Instruments, Switzerland) using the rod-on-disk scheme under the following conditions: the wear track radius, 6.8 mm; applied load, 2 N; the maximum speed, 10 cm/s; a ball 3 mm in diameter made of sintered  $\text{Al}_2\text{O}_3$  used as a counterbody; path, 214 m (5,000 cycles); air used as the medium. The fractographic examination of the wear tracks on the samples was carried out by optic profilometry using a WYKO NT1100 optical profiler (Veeco, USA).

X-ray powder diffraction (XRD) analysis was performed using an automated DRON 4-07 X-ray diffractometer with monochromated  $\text{CoK}\alpha$  radiation in the Bregg–Brentano geometry. A graphite monochromator was used to monochromatize radiation. Lattice parameters were measured with a relative error  $\Delta a/a = 10^{-4}$  nm.

The structure was studied by scanning electron microscopy on an S-3400N microscopy (Hitachi, Japan) equipped with a NORAN energy-dispersive X-ray spectrometer. Fine-structure features of the samples were studied by transmission electron microscopy using a JEOL JEM 2100 microscope. Samples  $5 \times 3 \mu\text{m}$  in size were prepared using a focused ion beam.

The challenge of using Ti as diamond to binder adhesion modifier is the relatively coarse grain size of the powders and consequently low surface area and probability of contact with diamond monocrystals.

The Ti-diamond surface area may be increased in the case of their uniform distribution in the binder. MA is a convenient method to solve this problem.

Fe–Co–Ni–Ti powder system demonstrated behavior at MA typical for the “ductile–ductile” systems. The powders were deformed after colliding with the grinding media and large composite granules were formed as a result of cold welding process. Thickness of the alternating layers varies between 1 and  $10 \mu\text{m}$ . Layer thickness decreases as the MA duration rises to 10 min; the homogeneous structure is formed after MA for 15 min (Fig. 1a). Further increase in duration of MA had no effect on the structure.

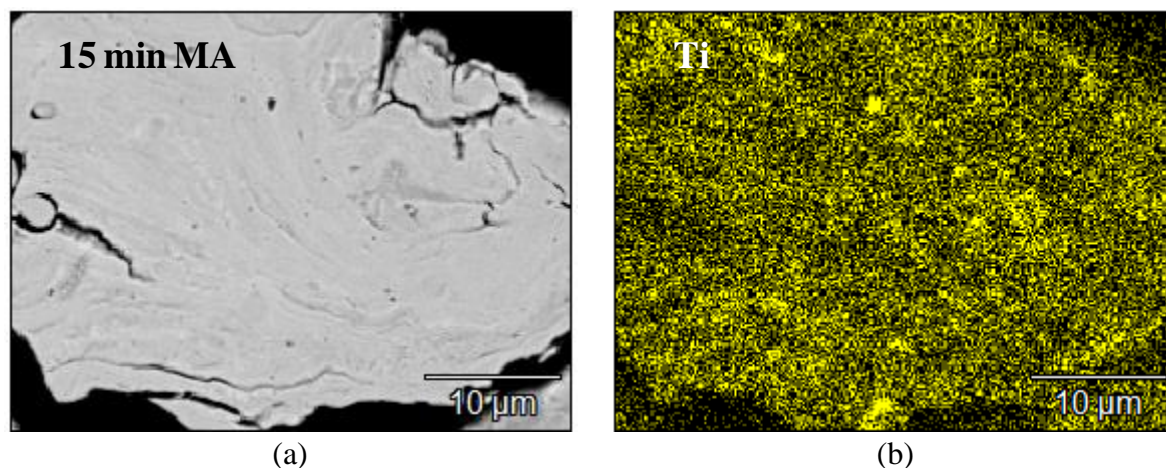


Fig. 1. Cross section image of Fe–Co–Ni–Ti binder after 15 min of MA (a) and titanium distribution (b).

The EDX analysis of obtained powder particles showed homogeneous distribution of Ti in the volume at this MA regime. According to XRD data all MA powder samples contained one phase – iron-based solid solution (bcc lattice).

The Fe–Co–Ni powder mixtures with addition of 0.5–5 mass % of Ti were prepared in PBM with MA duration for 15 min. They were used to obtain compact samples by means of hot pressing. The investigation of mechanical properties showed that 1% of Ti makes Fe–Co–Ni

binder 100 MPa stronger (up to 2000 MPa). The higher concentration of Ti leads to formation of brittle intermetallic phases  $\text{Fe}_2\text{Ti}$ , resulting in decreasing the strength.

The diamond containing bits with Fe–Co–Ni and Fe–Co–Ni–Ti binders were hot pressed at 950°C. After that the fracture surfaces were examined. The surface of diamond in Fe–Co–Ni bits was clean and didn't contain areas of adhered binder. In opposition to it, diamond surface in Fe–Co–Ni–Ti bits was covered with large amount of small metallic chips (Fig. 2).

In order to confirm the positive role of Ti on adhesion the thin lamella from diamond-binder interface was made by means of focused ion beam. Both EDX data and diffraction patterns made from the interface regions indicated the presence of thin (50 nm) but solid layer of TiC (Fig. 3).

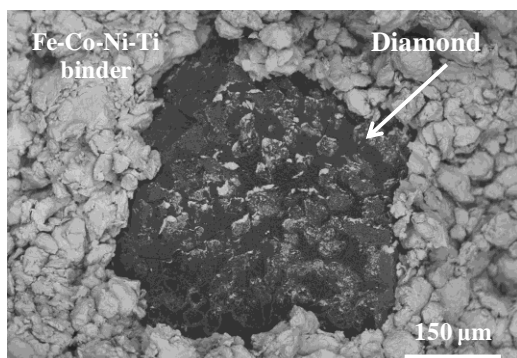


Fig. 2. Fracture surface of Fe–Co–Ni–Ti diamond composite.

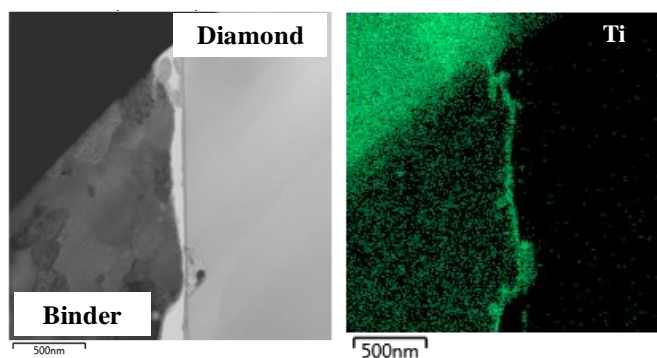


Fig. 3. TEM-image of diamond/binder interphase and titanium distribution.

An attempt to modify the Fe–Co–Ni binder for diamond cutting tool with adhesion active components (titanium) was made. It is shown that homogeneous distribution of Ti in Fe–Co–Ni matrix is possible by means of MA method using PBM, that ensures the highest possible contact areas of modifying agent with diamond. The best mechanical properties were found at samples containing 1% Ti. This composition was taken to produce diamond bits. The fracture surface analysis of the bits showed the presence of adhered metallic areas on diamond surface. The detailed investigation of diamond-binder interface proved formation of TiC layer, facilitating adhesion.

The authors gratefully acknowledge support from Russian Science Foundation (Project no. 17-79-20384).

1. F.A.C. Oliveira, C.A. Anjinho, A. Coelho, P.M. Amaral, M. Coelho, *Met. Powder Rep.*, 2017, vol. 72, no. 5, pp. 339–344.
2. P.A. Loginov, E.A. Levashov, V.V. Kurbatkina, A.A. Zaitsev, D.A. Sidorenko, *Powder Technol.*, 2015, vol. 276, pp. 166–174.
3. W. Tillmann, M. Ferreira, A. Steffen, K. Rüster, J. Möller, S. Bieder, M. Paulus, M. Tolan, *Diamond Relat. Mater.*, 2013, vol. 38, pp. 118–123.
4. R. Chang, J. Zang, Y. Wang, Y. Yu, J. Lu, X. Xu, *Diamond Relat. Mater.*, 2017, vol. 77, pp. 72–78.
5. P. Loginov, D. Sidorenko, M. Bychkova, M. Petrzhik, E. Levashov, *Met.*, 2017, vol. 7, 570.

STRUCTURE AND PROPERTIES OF ALLOYED COMPOSITES Al–TiC  
FABRICATED BY SHS METHODA. R. Lutz<sup>\*a</sup>, A. P. Amosov<sup>a</sup>, E. I. Latukhin<sup>a</sup>, A. D. Rybakov<sup>a</sup>, and S. I. Shipilov<sup>a</sup><sup>a</sup>Samara State Technical University, Samara, 443100 Russia

\*e-mail: alya\_luts@mail.ru

DOI: 10.24411/9999-0014A-2019-10088

Aluminum-matrix composites (AMCs), strengthened by the dispersed phase of titanium carbide (TiC), are now increasingly used as structural materials, and therefore, the development and implementation of methods to ensure a high level of their mechanical properties is an urgent task of modern materials science. Analysis of studies on this type of AMCs shows that the increase in strength was initially achieved primarily due to an increase in the dispersion of the reinforcing phase up to the nano-level [1–3].

Recently, however, the number of publications devoted to the alloying of aluminum-matrix composites has increased dramatically. Of the alloying elements, copper is most often used in an amount of 4–5% [4–7]. Thus, 4.5% Cu is added to the base of Al–10% TiC alloy which allows to increase the tensile strength from 118 to 147 MPa and hardness from 61 to 94 HV [5].

In a number of other studies, the hardening of complexly alloyed traditional aluminum alloys by the titanium carbide phase is analyzed [8, 9]. For example, the additive of 2, 4, 6, 8 or 10 wt % TiC to the base of 6061 alloy (the analog of alloy AD33 which contains Mg, Si, Fe, Cu, Cr, Zn, Ti, Mn) allows to increase density, hardness and strength by 7.8, 20, and 19.55%, respectively [9]. At the maximum content of TiC phase (10%), a strength value of 160 MPa and a relative elongation of 9% is achieved.

Many authors note the positive effect of alloying elements on the synthesis process and the morphology of the target phase of titanium carbide. For example, it was found that with an increase in the silicon content in the aluminum base, the TiC particle size significantly decreases, and this leads to an increase in the wear resistance of Al–TiC composites [10]. There is also a positive effect of alloying elements Mg, Zn, Sn on the microstructure and strength properties of Al–TiC composites at a high content of the ceramic phase (up to 50 wt %) [12].

Doping of the matrix alloy with 1% Mo allows to increase wettability due to the formation of a molybdenum shell around the titanium carbide particle, and as a result, there is a more uniform distribution of the particles over the body of the composite material and increased ductility [12]. On the basis of these data, it becomes obvious the positive effect of alloying elements on the structure and properties of AMCs.

A number of successful studies on the fabrication of Al–TiC composites through the use of the self-propagating high-temperature synthesis (SHS) method in the aluminum melt was also recently conducted in Samara State Technical University (SSTU). The essence of the method is to conduct an exothermic reaction of the synthesis of the TiC hardening phase particles from the mixture of titanium and carbon powders (Ti + C) directly in the aluminum melt. During the development of the technological process, it was possible to fabricate a composite with nano and ultrafine phase of titanium carbide, which allowed to increase the strength properties from 110 to 202 MPa at a relative elongation of about 4% [13].

Further direction for research in SSTU was determined to study the effect of alloying the aluminum base on the structure and properties of Al–TiC composites. On the basis of comprehensive analysis, the following elements were chosen as alloying additives:

(1) copper (5%) is a part of the solid solution, forms a phase  $\text{CuAl}_2$ , when cooled, contributing to the dispersion hardening of the alloy;

(2) manganese (2%) is a part of the solid solution, forms a phase  $\text{MnAl}_6$ , when cooled, contributing to grain boundary hardening;

(3) nickel (4%) forms the eutectic phase of  $\text{NiAl}_3$  of globular shape, positively affecting the ductility and fracture toughness of the alloy.

This paper presents the results of a study on the fabrication of alloyed composites (Al–5% Cu–2% Mn)–10% TiC and (Al–5% Cu–4% Ni)–10% TiC when using SHS method. The following starting materials were used in the research: aluminum ingot of A7 grade; titanium powder TPP-7 (purity 97.9%, initial particle size  $\leq 240 \mu\text{m}$ ); carbon technical P-701 (99.7%,  $\leq 0.15 \mu\text{m}$ ); copper powder PMS-1 (99.5%); manganese powder MN-95 (99.0%); nickel powder PNE-1 (99.5%).

In order to activate the SHS reaction, the halide salt  $\text{Na}_2\text{TiF}_6$  (99.0%) was added in a number of meltings in an amount of 5 wt % of the powder charge (Ti + C). The formation of matrix alloys of aluminum–copper–manganese and aluminum–copper–nickel was carried out according to the following scheme:

(1) heating the Al melt to a temperature of  $800^\circ\text{C}$ , the introduction of copper powder in aluminum foil in an amount of 5% of the melting mass into the Al melt, exposure for 30 min, active stirring;

(2) heating the Al–Cu melt to a temperature of  $850^\circ\text{C}$ , the introduction of the powder of manganese or nickel in an amount of 2 or 4% of the melting mass into the Al–Cu melt, holding for 30 min, active stirring;

(3) heating of the Al–Cu–Mn or Al–Cu–Ni melt to a temperature of  $900^\circ\text{C}$ , the introduction of batches of 6–8 g of SHS - charge (Ti + C) in aluminum foil into the melt, holding each batch of the charge under the melt level before the start of an active SHS reaction, accompanied by active spark and gas release (5–20 s), active stirring;

(4) exposure after the end of the SHS reaction from the last batch of charge for 5 min, pouring the composite melt into a steel chill to fabricate cast samples of the AMCs.

To determine the microstructure, the samples were etched with a solution of 50% HF + 50%  $\text{HNO}_3$  for 10–15 s. Metallographic analysis was performed using a JEOL JSM-6390A scanning electron microscope. Elemental chemical composition was determined by the method of micro-X-ray spectral analysis (MXRSA) on the same microscope using the attachment Jeol JED-2200. The hardness of the obtained samples was determined using a TSh-2M hardness tester according to GOST 9012-59, tensile tests were carried out on the tensile testing machine Inspekt 200 according to GOST 1497-84. The analysis of the microstructure of the fabricated AMCs samples showed that alloying additions of manganese or nickel in the presence of copper in both cases contributes to obtaining a homogeneous structure with uniformly distributed particles of titanium carbide in size of 80–500 nm. The maximum dispersion of the reinforcing phase (80–250 nm) is achieved with the addition of manganese and in the presence of  $\text{Na}_2\text{SiF}_6$  salt (Figs. 1, 2). MXRSA, conducted at the sites corresponding to the grain boundaries, confirmed the presence of manganese and nickel. Values of mechanical characteristics of the alloyed AMCs samples are given in Table 1.

The obtained results can be explained by the presence of lattice distortions due to the formation of a solid solution and obstacles in the form of particles of the second phase which significantly limits the possibility of sliding the dislocations and leads to additional strengthening. Thus, the simultaneous formation of solid solutions, secondary phases and highly dispersed reinforcing phase of titanium carbide, allows to achieve an increase in strength properties while maintaining a sufficient reserve of plasticity.

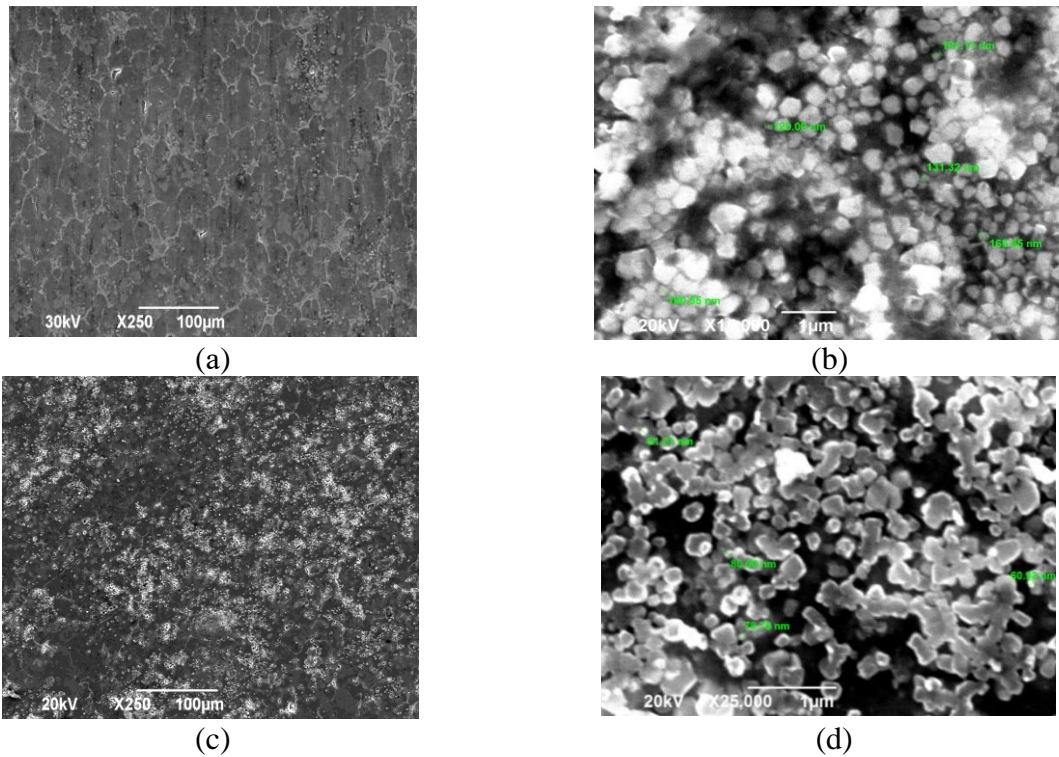


Fig. 1. (a, b) Microstructure of samples (Al-5% Cu-2% Mn)-10% TiC, (c, d) microstructure of samples (Al-5% Cu-2% Mn)-10% TiC (+ 5% Na<sub>2</sub>TiF<sub>6</sub>).

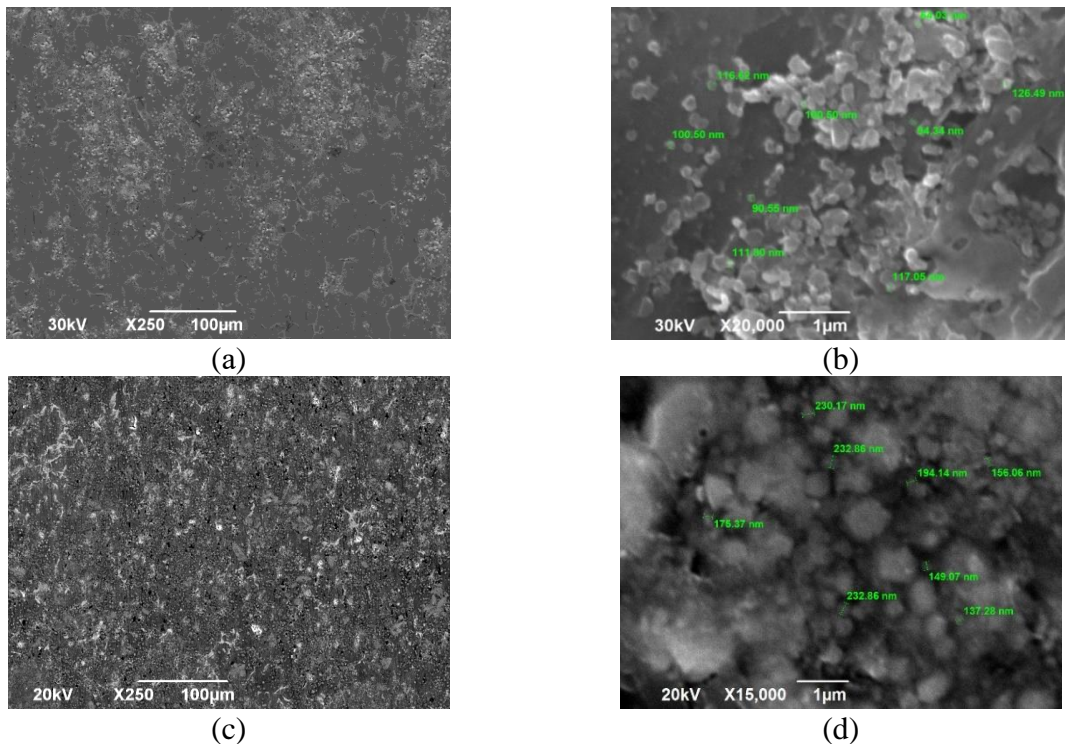


Fig. 2. (a, b) Microstructure of samples (Al-5% Cu-4% Ni)-10% TiC, (c, d) microstructure of samples (Al-5% Cu-4% Ni)-10% TiC (+ 5% Na<sub>2</sub>TiF<sub>6</sub>).

In general, the results of the study allow us to draw the following conclusions:

- (1) it is possible to obtain alloyed highly dispersed composites (Al-5% Cu-2% Mn)-10% TiC and (Al-5% Cu-4% Ni)-10% TiC when using SHS method in the melt;

(2) alloying the Al–10% TiC composite with copper–manganese or copper–nickel systems has a positive effect on its structure and properties, which makes the further research in this direction promising.

Table 1. Mechanical properties of aluminum-matrix composite samples\*.

| Aluminum-matrix composite  | $\sigma_{0.2}$ , MPa | $\sigma_u$ , MPa | $\delta$ , % | $\Psi$ , % | HB, MPa |
|--|----------------------|------------------|--------------|------------|---------|
| (Al–5% Cu)–10% TiC   | 74                   | 192              | 16.6         | 17.0       | 621     |
| (Al–5% Cu–2% Mn)–10% TiC   | 97                   | 188              | 8.6          | 13.3       | 960     |
| (Al–5% Cu–2% Mn)–10% TiC<br>(+ 5% Na <sub>2</sub> TiF <sub>6</sub> ) | 114                  | 213              | 6.6          | 7.3        | 970     |
| (Al–5% Cu–4% Ni)–10% TiC   | 102                  | 220              | 11.2         | 12         | 920     |
| (Al–5% Cu–4% Ni)–10% TiC<br>(+ 5% Na <sub>2</sub> TiF <sub>6</sub> ) | 118                  | 224              | 6.0          | 7          | 980     |

\* $\sigma_{0.2}$  is the yield strength;  $\sigma_u$  is the ultimate tensile strength;  $\delta$  is the percent elongation;  $\psi$  is the percent reduction in area; HB is the Brinell hardness.

1. P.H.C. Camargo, K.G. Satyanarayana, F. Wypych, Nanocomposites: synthesis, structure, properties and new application opportunities, *Mater. Res.*, 2009, vol.12, no. 1, pp. 1–39.
2. N. Selvakumar, M. Sivaraj, S. Muthuraman, Microstructure characterization and thermal properties of Al–TiC sintered nano composites, *Appl. Thermal Eng.*, 2016, vol. 107, pp. 625–632.
3. R. Casatti, M. Vedani, Metall matrix composites reinforced by nano-particles – a review, *Met.*, 2014, vol. 4, pp. 65–83.
4. Y.-H. Cho, J.-M. Lee, S.-H. Kim, Al–TiC composites fabricated by a thermally activated reaction process in an Al melt using Al–Ti–C–CuO powder mixtures, *Miner., Met. & Mater.*, 2014, vol. 45A, pp. 5667–5678.
5. A. Kumar, M.M. Maharapta, P. K. Jha, Fabrication and characterization of mechanical properties of Al–4.5% Cu/10TiC composite by in-situ method, *J. Miner. Mater. Charac. Eng.*, 2012, vol. 11, pp. 1075–1080.
6. B. Das, S. Roy, R. N. Rai, S.C. Saha, Development of an in-situ synthesized multi-component reinforced Al–4.5% Cu–TiC metal matrix composite by FAS technique – Optimization of process parameters, *Eng. Sci. Technol.*, 2015., vol. 19, no. 1, pp. 1–13.
7. D. Zhou, F. Qiu, Q. Jiang, The nano-sized TiC particle reinforced Al–Cu matrix composite with superior tensile ductility, *Mater. Sci. Eng.*, 2015, vol. A622, pp. 189–193.
8. S.V. Sujith, M.M. Mahapatra, R.S. Mulik, An investigation into fabrication and characterization of direct reaction synthesized Al–7079–TiC in situ metal matrix composites, *Arch. Civil Mechan. Eng.*, 2019, vol. 19, pp. 63–78.
9. M.S. Raviraj, C.M. Sharanprabhu, G.C. Mohankumar, Effect of TiC addition on fracture toughness of Al6061 alloy, *AIP Conf. Proc.*, 2018, vol. 1943, 020022.
10. M. Zhang, Y. Huo, L. Ma, B. Huang, Q. Hu, In situ TiC ceramic particles locally reinforced Al–Si matrix composites prepared by SHS-casting method from the Al–Si–Ti–C system, *Int. J. Appl. Ceram. Technol.* 2014, vol. 11, no. 4, pp. 723–731.
11. S. Shu, J. Lu, F. Qiu, Q. Xuan, Q. Jiang, Effects of alloy elements (Mg, Zn, Sn) on the microstructures and compression properties of high-volume-fraction TiC<sub>x</sub>/Al composites, *Scripta Mater.*, 2010, vol. 63, pp. 1209–1211.
12. Q. Wu, C. Yang, F. Xue, Effect of Mo addition on the microstructure and wear resistance of in situ TiC/Al composite, *Mat. & Design*, 2011, vol. 32, pp. 4999–5003.
13. A.P. Amosov, A.R. Lutz, A.A. Ermoshkin, Nanostructured aluminum matrix composites of Al–10%TiC obtained in situ by the method of SHS in the melt, *Key Eng. Mater.*, 2016, vol. 684, pp. 281–286.

## MA SHS AS A KINETIC PHENOMENON

N. Lyakhov<sup>a</sup>, T. Grigorieva<sup>a</sup>, and M. Korchagin<sup>a</sup><sup>a</sup>Institute of Solid State Chemistry and Mechanochemistry, Novosibirsk, Russia

DOI: 10.24411/9999-0014A-2019-10089

Mechanical activation is a rather complex process, which is not easy to investigate and to describe correctly. It depends on the type of mills applied, the milling procedure and regime and of course on mechanical properties of solid substances, which are the subject of mechanical activation (MA). The result of milling is a particle size distribution shifted to smaller dimensions. The result of MA we are waiting for, is an increased reactivity of solid reagents. Evidently, we never can “detach” the MA, if it exists, from a simple comminution that result in any milling technology. Let us note that in case of MA SHS we consider the MA as pretreatment of a (potentially) reactive mixture of reagents, sometimes very short, which do not change the chemical composition of starting materials involved in combustion, if any. In addition, we have to take into account that mechanical properties of mixtures under milling are very far from individual phases. That means the result of a separate MA is never equal to the preliminary treatment of reagent’s mixtures.

However, from kinetic point of view the mechanism of MA, which we understand as a highly increased reactivity, looks even more complicated! For reactions of the type  $A \text{ solid} + B \text{ solid} = (AB) \text{ solid}$ , it is always assumed that a limiting stage is the diffusion of one, or both components through the newly formed interphase layer of (AB) product. There is no other way to activate this process but to continue the MA until the reaction is finished. We have plenty of such solid + solid reactions, which we call mechanochemical.

Nevertheless, in many cases of SHS (exothermic) reactions we observe a significant increase of reactivity both for the ignition and for the combustion itself after preliminary MA. Same conclusions we can make from the so-called “thermal explosion” mode, when the heat evaluation gaps shift to lower temperatures with the increased time of preliminary activation. It is to note that even for simple systems like Ni + Al or Ti + Al the phase composition of reaction product do not correspond to the initial stoichiometry until some critical time of preliminary MA is reached (multiphase reactions). That means the mechanical activation results in some unusual processes before the reaction starts. Of course, there are mixing and comminution due to plastic deformation of one or both reagents, but not only. Mechanical activation of immiscible couples of metals, at least, shows that the more plastic metal can disappear from X-ray diffraction detection after few minutes of MA. Such is the case of Bi + Fe, where no new product appears while Bi reflections totally disappear because of MA.

Though we cannot eliminate diffusion as a rate determining process for solid + solid reactions, some other (coupled) phenomena should be taken into consideration for SHS reactions, such as heat evaluation, wetting and spreading of reagents over the fresh surface generated by milling, and the particle size. The overall model of MA SHS should incorporate all processes that provide formation of new and powerful diffusion sources which is proportional to the large contact surface formed at the very beginning of preliminary MA. Our presentation is an attempt to analyze the most valuable MA SHS experiments in order to formulate non-contradictory interpretation of this very interesting kinetic phenomenon.



COMBUSTION IN OILY COPPER WASTE–NiO–NH<sub>4</sub>NO<sub>3</sub> SYSTEM & SYNTHESIS OF Cu–Ni ALLOYH. A. Mahmoudi<sup>\*a,b</sup>, L. S. Abovyan<sup>c</sup>, V. V. Vardapetyan<sup>a</sup>, and S. L. Kharatyan<sup>a,c</sup><sup>a</sup>Yerevan State University, Yerevan, AM-0025 Armenia<sup>b</sup>National Iranian Copper Industries Company (NICICO), Kerman, Iran<sup>c</sup>A.B. Nalbandyan Institute of Chemical Physics NAS RA, Yerevan, 0014 Armenia

\*e-mail: mahmoody.h@gmail.com

DOI: 10.24411/9999-0014A-2019-10090

In the wiring industry at production of copper wires and cables about 0.6–0.7 wt % of copper is converted into waste representing mainly copper (I) oxide. Therewith, in all stages of rolling for decreasing the friction forces of moving details, as well as preventing the deep oxidation of metal hydrocarbon based mineral oils are used as lubricant. The copper waste used in this study consist of plate-like form particles with linear size up to 1.6 mm (0.4÷1.6 mm – 10 wt %) and thickness up to 0.25 mm and contains up to 15 wt % hydrocarbon based oil (hereinafter C<sub>n</sub>H<sub>m</sub>).

The possibility of copper (II) oxide reduction under the combustion mode has been shown for the first time in [1] by using combined organic reducers (polystyrene (PS), polyethylene (PE), urotropin, etc.). Then this approach was extended for reduction of other oxides (Cu<sub>2</sub>O, NiO, Co<sub>3</sub>O<sub>4</sub>) as well as joint reduction of CuO with NiO, NiO with Co<sub>3</sub>O<sub>4</sub> for production of metal powders and alloys [2, 3]. In [4] it was studied copper (I) oxide waste reduction after preliminary removing the oil, which is labour-intensive and expensive procedure. It was shown that complete reduction of copper from copper (I) oxide waste in the combustion mode is possible by using polystyrene + ammonium nitrate mixture (hereinafter PS + Nt). Recently complete reduction of copper from oily copper waste in the combustion mode was performed without preliminary cleaning stage in the presence of only ammonium nitrate in the initial mixture [5]. It was supposed that due to its hydrocarbonic nature, the oil can serve as combined reducer instead of polystyrene for reduction of copper oxide. Optimal conditions for obtaining copper powder from copper waste according to the content of oil and ammonium nitrate were determined.

In this work similar approach was applied for the joint reduction of oily copper (I) oxide waste and nickel oxide in the combustion mode targeting the preparation of composite powders and Cu–Ni alloys. To achieve this aim, combustion laws in the (Cu<sub>2</sub>O oily waste–NiO–Nt) system by using copper oxide (I) waste with different content of oil and at different ratio of metals oxides in initial mixture were investigated.

In the experiments, cylindrical pellets 20 mm in diameter and 45–50 mm height were prepared from initial mixtures (Cu<sub>2</sub>O oily waste + NiO + xNt) (mixture 1) and (Cu<sub>2</sub>O oily waste + 2NiO + xNt) (mixture 2) by using copper oxide waste with different content of oil. The main variables are x value and oil content in the waste. Thermocouple technique was used to measure the main combustion parameters: temperature ( $T_c$ ) and velocity ( $U_c$ ). After passing the combustion front and cooling-down the burned samples the lasts were examined by XRD analysis and scanning electron microscopy. Carbon content in the final product was determined using Leco SC-444 carbon/sulfur analyzer.

Combustion experiments were performed out in a wide range of parameter  $x$  ( $0 \leq x \leq 1$ ) for copper waste with 11 and 15 wt % content of oil. The reduction degree of metals was primarily estimated by the mass loss of samples after combustion. It was revealed that the lower limit of combustion is observed at significant decrease in Nt content in initial mixture. Thus, for the

mixture 1 with the waste containing 11 and 15 wt % oil, combustion limit appears at  $x = 0.2$  (Figs. 1a, 2a). It is obvious that increase in the parameter  $x$  leads to the increase both in combustion temperature and velocity, as well as mass loss of the samples ( $\Delta m$ ), which is associated with an increase in the portion of the strongly exothermic reaction  $C_nH_m$  (oil) + Nt in the total process.

According to the results of XRD analysis, at 11 wt % oil content, in the whole range of variation of the parameter  $x$  complete reduction of both metals does not take place (Fig. 1b). Combustion products, beside the reduced metals, contain also the oxides of corresponding metals, mainly NiO.

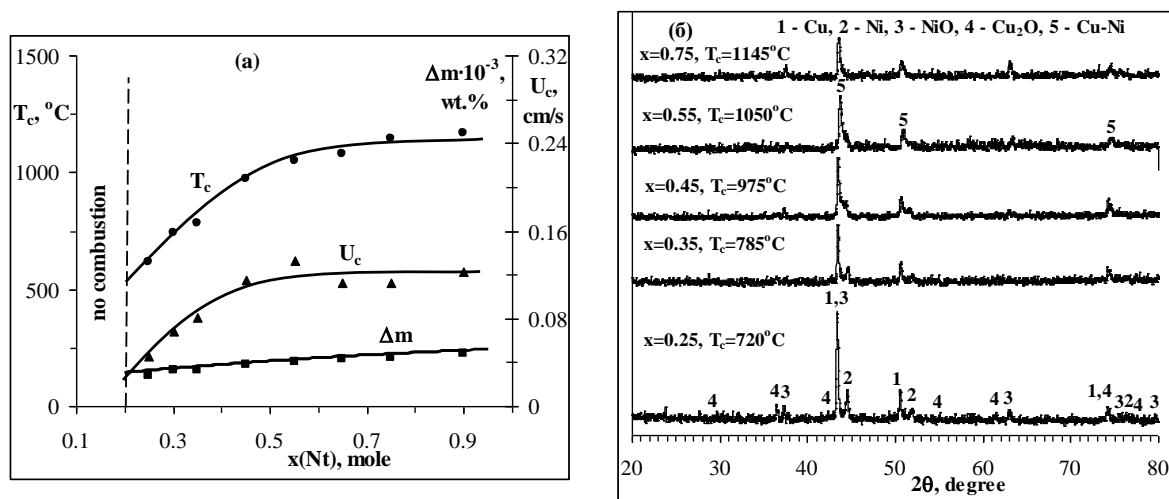


Fig.1. (a) Combustion temperature ( $T_c$ ), velocity ( $U_c$ ), and mass loss ( $\Delta m$ ) vs.  $x$  and (b) XRD patterns of combustion products for different  $x$  values. Mixture 1. 11 wt % oil content.

In the case of copper oxide waste containing 15 wt % oil (Fig. 2) for the mixture 1 at  $x > 0.3$  complete reduction of both metals was observed, with formation of monophasic product at  $x > 0.55$ , representing Cu–0.5Ni alloy containing 32 wt % Ni. The full reduction of metals and formation of solid solution (Cu–0.5Ni alloy) is due to the sufficient amount of reducing agent (oil) and relatively high combustion temperatures ensuring the formation of reduced copper in the smelted state which is seen in the microstructure (Fig. 3) of the fracture of combustion product for the mixture 1 at  $x = 0.75$ Nt.

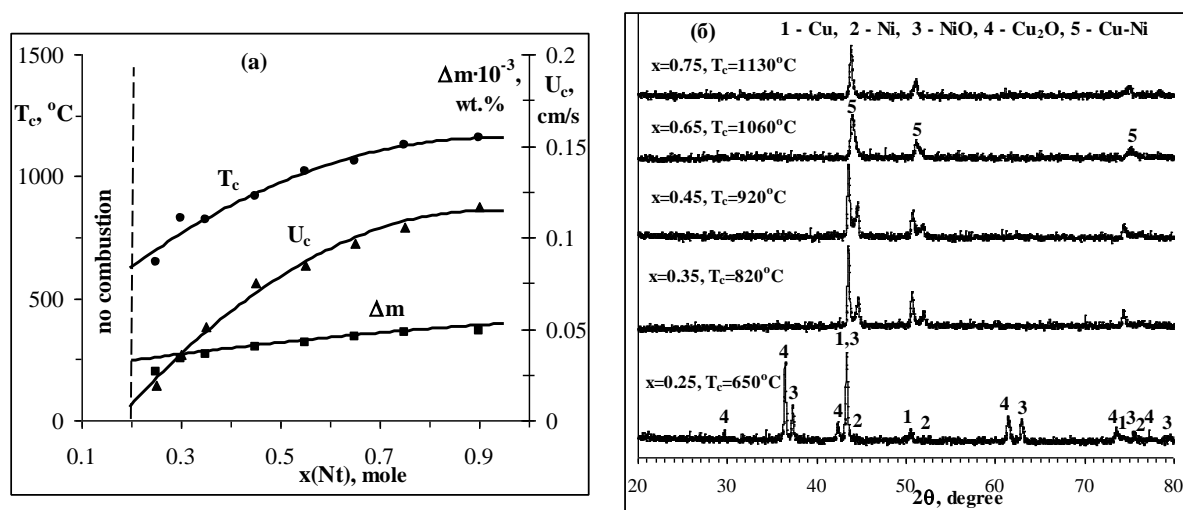


Fig. 2. (a) Combustion temperature ( $T_c$ ), velocity ( $U_c$ ), and mass loss ( $\Delta m$ ) vs.  $x$  and (b) XRD patterns of combustion products for different  $x$  values. Mixture 1. 15 wt % oil content.

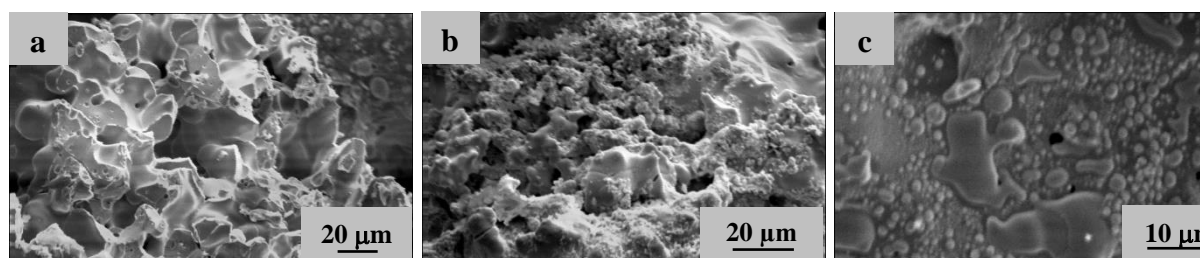


Fig. 3. Micrographs of the combustion product. Mixture 1. 15 wt % oil content.  $x = 0.75$ .

Similar studies were performed for the mixture 2 with the waste containing 11 and 15 wt % oil. In this case the lower limit of combustion by Nt content is observed at  $x = 0.25$ . According to XRD analysis results, at 11 wt % oil content, in the whole range of variation of the parameter  $x$  ( $0.3 \leq x \leq 1.2$ ) complete reduction of both metals and formation of monophase Cu–Ni alloy containing 48 wt % Ni does not take place. Combustion products, beside the reduced metals, contain also the oxides of corresponding metals.

In the case of copper oxide waste containing 15 wt % oil the complete reduction of both metals is observed in the interval  $0.6 < x \leq 0.9$  with formation of monophase Cu–Ni alloy at  $x = 0.9$ . At  $x > 0.9$  due to an excess of oxidizing agent, among the products of combustion unreduced oxides remain again.

Thus, the results obtained have showed the possibility of complete reduction of both metals and formation of Cu–Ni composite powder or Cu–Ni alloy under the combustion mode. Optimum conditions for obtaining Cu–Ni composite powder or Cu–Ni alloy were found out.

1. M.H. Yamukyan, Kh.V. Manukyan, S.L. Kharatyan, Copper oxide reduction by combined reducers under the combustion mode, *Chem. Eng. J.*, 2008, vol. 137, pp. 636–642.
2. S.L. Kharatyan, Metal Powders, in *Concise Encyclopedia of Self-Propagating High-Temperature Synthesis*, Ed. by I.P. Borovinskaya, A.A. Gromov, E.A. Levashov, Yu.M. Maksimov, A.S. Mukasyan, A.S. Rogachev, 2017, pp. 196–197.
3. L.S. Abovyan, A.S. Kharatyan, D.S. Eliazyan, S.L. Kharatyan, Preparation of Cu–Ni alloys by co-reduction of CuO and NiO oxides under the combustion mode, *Chem. J. Armenia*, 2017, vol. 70, no. 3, pp. 310–322 [in Russ.].
4. H.A. Mahmoudi, L.S. Abovyan, S.L. Kharatyan, SHS processing of copper waste into copper powder, *Chem. J. Armenia*, 2017, vol. 70, pp. 477–486.
5. H.A. Mahmoudi, L.S. Abovyan, V.V. Vardapetyan, S.L. Kharatyan, SHS processing of copper oxide oily waste into copper powder. Novel approach, *Book of abstracts of V Int. Conf. Current problems of chemical physics*, Yerevan, Armenia, 2018, pp. 164–165.

COMBUSTION OF TiO<sub>2</sub>/ZrO<sub>2</sub>-Ca THERMITE MIXTURES IN NITROGENYu. M. Maksimov<sup>a</sup>, A. N. Avramchik<sup>a</sup>, B. Sh. Braverman<sup>a</sup>, and A. M. Shulpekova<sup>a</sup>

<sup>a</sup>Tomsk Scientific Center of the Siberian Branch of the Russian Academy of Sciences,  
Tomsk, 634055 Russia  
e-mail: combustion2005@yandex.ru

DOI: 10.24411/9999-0014A-2019-10091

Titanium and zirconium nitrides are widely used in different industries due to their high melting point, acid resistance, etc. [1, 2]. There are different methods for obtaining nitrides: nitriding of metal powders during the heating in furnaces, nitriding of metal powders in the combustion mode, coal-thermal reduction of metal oxides in nitrogen, and others. One of the promising methods for the synthesis of nitrides is the reduction of metal oxides by calcium under nitrogen pressure in the combustion mode with the further chemical removal of calcium compounds [3, 4]. However, the reduction of refractory oxides is related with difficulties due to the kinetic deceleration of the process, which requires a search for ways to intensify it. To intensify the process, we proposed to add a mixture of calcium iodate and metal-reducing agent into the initial mixture. During thermal decomposition the iodate Ca(IO<sub>3</sub>)<sub>2</sub> produces CaO, oxygen, iodine, and CaI<sub>2</sub>. The latter exhibit high chemical activity that can be used to increase the heat-producing capability of the process, and also contributes to the acceleration of physicochemical transformations at low temperatures, which expands the temperature range of combustion.

Commercial calcium iodate is a partially hydrated substance. Therefore, physical and chemical processes were studied during its thermolysis. Thermal decomposition of Ca(IO<sub>3</sub>)<sub>2</sub>·H<sub>2</sub>O was studied using differential scanning calorimetry (DSC) under the argon atmosphere. Thermolysis was shown to involve three stages. The first stage (140–200°C) is the removal of crystalhydrate H<sub>2</sub>O. Polymorphic transformation takes place at 410°C; after reaching 520°C a two-stage melting process with the simultaneous decomposition of calcium iodate is observed. The data of X-ray diffraction of intermediate products obtained by the isothermal annealing of salt at temperatures of 300, 450, and 700°C are in good agreement with the DSC data. The kinetic parameters of the processes were calculated, namely, the activation energy, the preexponential factor, and the reaction order, which was first obtained for Ca(IO<sub>3</sub>)<sub>2</sub>·H<sub>2</sub>O. Thermodynamic calculations were carried out and combustion processes and products were experimentally studied in ZrO<sub>2</sub>-Ca-N<sub>2</sub> and TiO<sub>2</sub>-Ca-N<sub>2</sub> systems with dehydrated iodate and without calcium iodate. It was shown that with the excess of calcium from 10 to 70%, the calculated combustion temperature of the systems containing ZrO<sub>2</sub> was in the range of 1800–2900 K, depending on the nitrogen pressure (Fig.1), and 2250–3200 K for the systems containing TiO<sub>2</sub>. For the systems with ZrO<sub>2</sub>, the combustion temperature is limited to the CaO melting temperature and to the TiN melting temperature for the systems with TiO<sub>2</sub>. The activating ability of calcium iodate additives is most pronounced at relatively low reaction temperatures. To reduce combustion temperature, some amount of calcium was replaced by its nitride (Ca<sub>3</sub>N<sub>2</sub>) in the initial mixture. As a result, combustion was conducted at relatively low temperatures. Figure 2 shows the combustion temperature as a function of pressure for the composition, in which calcium is completely replaced by calcium nitride. Without the addition of iodate, the combustion of this composition is not possible. The measured temperatures are noticeably lower than the minimum combustion temperatures reached during the combustion of mixtures that do not contain calcium iodate. The products obtained by the combustion of compositions with calcium iodate and with or without calcium nitride after acid removal of calcium compounds are obtained in the form of powders with a size not exceeding 5 μm (Fig. 3).

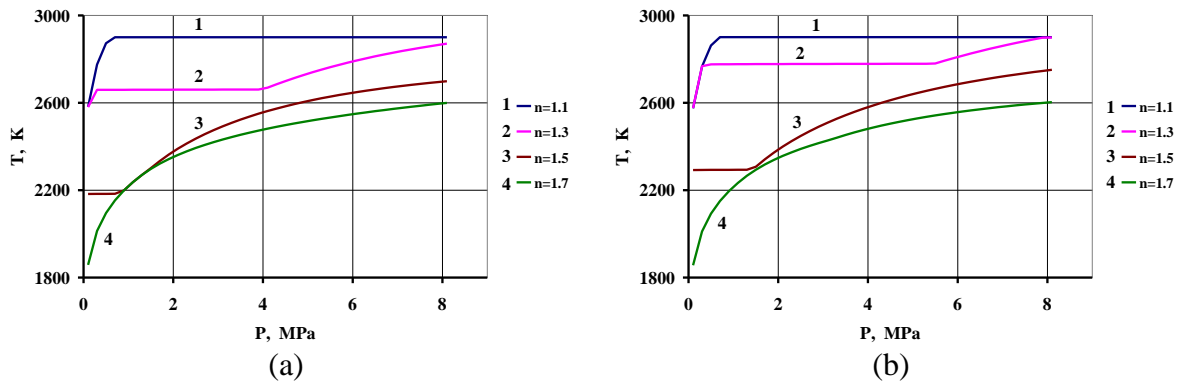


Fig. 1.  $T_{ad}$  as a function of nitrogen pressure: (a)  $ZrO_2$ -Ca- $N_2$  system, (b)  $ZrO_2$ -Ca- $N_2$  + 10%  $\{Ca(IO_3)_2 + 6Ca\}$  system,  $n = Ca/Ca_0$  is the ratio of calcium in the mixture to stoichiometric calcium. Plateau at 2900 K corresponds to melting CaO.

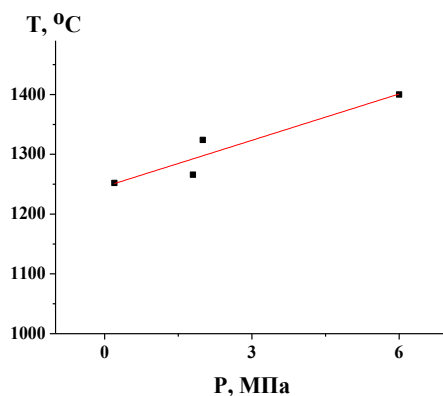


Fig. 2. Combustion temperature as a function of nitrogen pressure for the mixture with a composition: (32%)  $TiO_2$  + (10%)  $Ca(IO_3)_2$  + (58%) Ca.

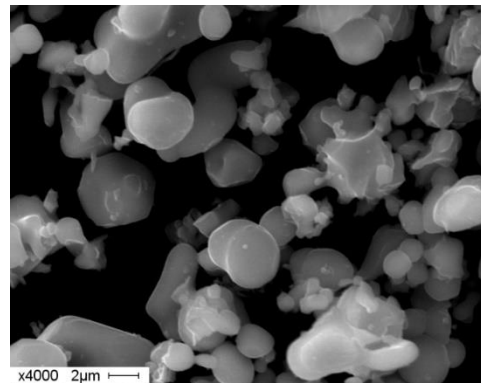


Fig. 3. SEM image of the combustion product at  $P_{N_2} = 4$  MPa for the mixture with a composition: (35%)  $TiO_2$  + (11%)  $Ca(IO_3)_2$  + (54%) Ca.

## Conclusions

1. The addition of calcium iodate to thermite mixtures  $TiO_2/ZrO_2$ -Ca expands the limits of combustion and reduces the minimum temperature of combustion.
2. Combustion products after chemical removal of calcium compounds are obtained in the form of powders with a size not exceeding 5 microns.

The work was carried out as a part of the state task for TSC SB RAS (no. 0365-2019-0005) and partially supported by RFBR (project no. 18-03-00875a).

1. G.V. Samsonov, Nitrides, Kiev: Naukova Dumka, 1969, 380 p.
2. A.A. Gromov, L.N. Chukhlomina, Nitride Ceramics: Combustion Synthesis, Properties and Applications, Wiley-VCH Verlag GmbH & Co. KGaA, 2015, 332 p.
3. A.N. Avramchik, B.Sh. Braverman, Yu.M. Maksimov, L.N. Chukhlomina, Calciothermic reduction of titanium dioxide and molybdenum trioxide under pressure of nitrogen gas, *Int. J. Self-Propag. High-Temp. Synth.*, 2017, vol. 26, no. 1, pp. 80–82.
4. B.Sh. Braverman, A.N. Avramchik, Yu.M. Maksimov, A.M. Shulpekov, Obtaining of vanadium nitrides during the combustion of vanadium oxide with calcium and calcium nitride in nitrogen, *J. Phys.: Conf. Ser.*, 2018, 1115, 042004.

## OBTAINING OF COMPOSITE MATERIALS BY SHOCK-WAVE TREATMENT AND SHS

A. Yu. Malakhov<sup>\*a</sup>, I. V. Saikov<sup>a</sup>, V. G. Salamatov<sup>a</sup>, and S. A. Seropyan<sup>a</sup><sup>a</sup>Merzhanov Institute of Structural Macrokinetics and Materials Science, Russian Academy of Sciences, Chernogolovka, Moscow, 142432 Russia

\*e-mail: sir.malahov2009@yandex.ru

DOI: 10.24411/9999-0014A-2019-10092

Cermet combine the properties of ceramics (high hardness, heat resistance) and metal (thermal conductivity, plasticity). It is widely used in aerospace and other fields of technology. The traditional method of obtaining cermet includes the following stages: a long high-temperature sintering of powder compositions to obtain ceramics (e.g., TiC and TiB<sub>2</sub>) and further sintering of metal powder (e.g., Ti, Ni, Al). Application of combustion synthesis [1] upon receipt of cermet powder systems is given much attention lately [2]. Interest is due to the possibility of the synthesis of materials in one stage and an external heat source due to the internal energy of the system. For some areas of engineering, as well as for individual tasks of the military-industrial complex (development of the armour material) prospectively the use of layered metal–ceramic composites. However, it is difficult to obtain because of the complexity of combining metal and ceramics in the same material. From this point of view seems promising Association or combination of two technologies: shock wave SHS-compacting materials and thermochemical synthesis to obtain composite materials. When this realization of synthesis of reactive powder mixtures is possible both at the stage of shock-wave treatment, and subsequent heat treatment and at rolling [3].

Study process shock wave loading was carried out on an example of powder systems Ti–B–Ni and Ti–C–Ni. The components of the reaction systems were titanium PTS powders with different particle sizes, boron B-99A, nickel PNE-1 and C carbon (T-800). Powder mixture composition of 90% (Ti + 2B) + 10% Ni ( $T_{ad} = 3144$  K) + 80% (Ti + C) + 20% Ni ( $T_{ad} = 2647$  K) for 2 h were mixed in a mixer "Turbula" type and molded in the form of cylinders with a diameter of 10 mm with a relative density of .,65. Mechanical activation of the green mixtures was carried out in a planetary ball mill AGO-2. The molded samples were placed in a metallic matrix (Fig. 1.a) with a pre-made blind holes (cells). The loading samples were throwing steel a planar flyer, which is accelerated by an explosive charge to velocities of 0.7; 1.0; 1.5 km/s according to the scheme indicated in Fig. 1b. Initiation detonation conducted from the center axis of the matrix thus provides the same loading conditions in all cells.

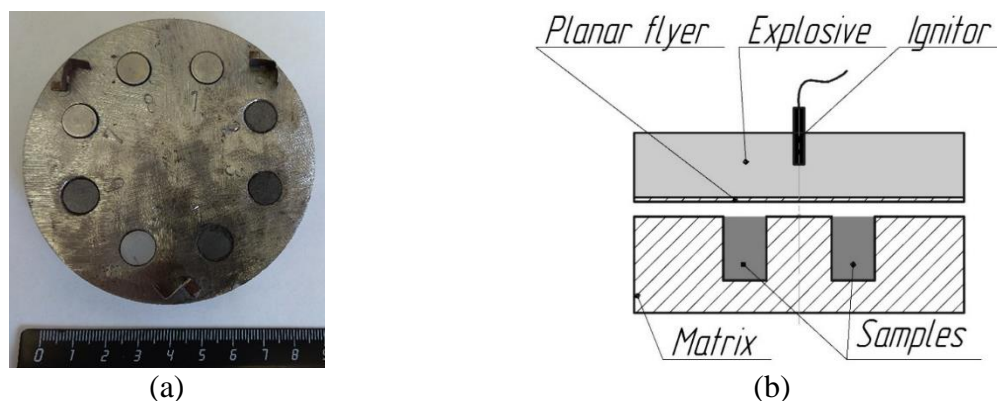


Fig. 1. Experimental scheme: (a) metal matrix with filled cells; (b) scheme of initiation the SHS by steel planar flyer.

The experiments investigated the effect on the initiation of the synthesis of the following factors: dispersion, density, mechanical pre-activation, throwing velocity a planar flyer.

After the shock wave loading depressurization assembly and removal of the cells were detected products. Samples were removed from the metal matrix and investigated by XRD, optical and electron microscopy. Because of experiments, it was determined that the rate of metallic a planar flyer of 1.5 km/s is achieved by stable high thermochemical synthesis SHS compositions. At speed of 1.0 km/s is required for mechanical activation of the initial synthesis mixture of powders and under the conditions of 0.7 km/s initiation SHS compositions occurs. Thus, in this study, conditions of shock wave loading under which passes thermochemical synthesis of mixtures of powders of 90% (Ti + 2B) + 10% Ni + 80% (Ti + C) + 20% Ni was determined and cermets TiB<sub>2</sub>-Ni and TiC-Ni were prepared.

The research was supported by the Russian Foundation for Basic Research (project no. 19-08-00754 A).

1. A. Levashov, A.S. Mukasyan, et. al., Self-propagating high-temperature synthesis of advanced materials and coatings, *Int. Mater. Rev.*, 2017, vol. 62, no. 4, pp. 203–239.
2. A.V. Istomin, V.E. Nadutkin, V.E. Grass, of Ti<sub>3</sub>SiC<sub>2</sub> -based ceramic matrix composites by a powder-free SHS technique, *Ceram. Int.*, 2013, no 39, pp. 3663–3667.
3. M.I. Alymov, L.B. Pervukhin, A.S. Rogachev, O.L. Pervukhina, I.V. Saikov, Combination of SHS and the shock-wave compaction for the production of composite materials, *Lett. Mater.*, 2014, no. 4, pp. 153–158.

## KINETIC FEATURES OF NICKEL OXIDE REDUCTION BY METHANE AT NON ISOTHERMAL CONDITIONS

S. Mamyán<sup>a</sup>, H. A. Chatilyan<sup>\*b</sup>, and S. L. Kharatyan<sup>a,b</sup><sup>a</sup>Yerevan State University, Yerevan, 0025 Armenia<sup>b</sup>A.B. Nalbandyan Institute of Chemical Physics NAS RA, Yerevan, 0014 Armenia

\*e-mail: hakob@ichph.sci.am

DOI: 10.24411/9999-0014A-2019-10093

In the work the results on the kinetics of NiO reduction by methane at non isothermal conditions based on *in situ* measurements of reaction rate, as well as on periodic measurements of sample weight loss during reduction are presented.

The experiments were carried out on high-speed scanning electrotermography setup [1, 2] at linear heating regime by using Ni wires 100 μm in diameter (NP-2 trademark, purity of 99.5%). The latters were preliminary oxidized in air ( $P = 1$  atm.,  $T = 1300^{\circ}\text{C}$ ,  $t = 150$  s) with formation of NiO layer on metal surface with a thickness of  $\sim 6$  μm. Then the oxidized wires were reduced by methane at  $T = 800\div 1050^{\circ}\text{C}$  and  $P_{\text{CH}_4} = 5\div 300$  torr; heating rates were varied between 1 to  $1000^{\circ}/\text{s}$ .

During the process the sample temperature,  $T$ , its electrical resistance,  $R(t)$ , and total electrical power applied,  $W(t)$ , for maintenance of linear heating regime with a given rate from  $T_0 = 800^{\circ}\text{C}$  up to reference temperature,  $1050^{\circ}\text{C}$  were continuously measured. The rate of heat release (in this particular case, heat absorption) due to NiO reduction by methane,  $W_r(t)$  was determined on the basis of non-stationary equation of thermal balance of metal wire with the environment as a difference of electrical powers, released on the wire at the first – reactive,  $W_1(t)$ , and the second – inert (after completion of the reduction reaction),  $W_2(t)$ , heatings with the same temperature-time history:  $W_r(t) = W_1(t) - W_2(t)$ . In Fig. 1 the reaction rate,  $W_r(t)$  (1), and conversion degree,  $\alpha$ , vs. time (solid line (2)) at linear heating (3) with  $V_h = 500^{\circ}/\text{s}$ , are presented, where

$$\alpha(t) = \frac{Q(t)}{Q_{\text{tot}}} = \frac{\int_0^t W_r(t) dt}{\int_0^{\infty} W_r(t) dt} = \frac{\int_0^t [W_1(t) - W_2(t)] dt}{\int_0^{\infty} [W_1(t) - W_2(t)] dt}$$

The points indicate conversion degree determined by periodic weighing the samples. Of special interest is a comparison of the kinetics of nickel oxide reduction by methane and hydrogen. As it follows from Fig. 1, in contrast to hydrogen reduction at  $T > 800^{\circ}\text{C}$  [3], the high-temperature reduction of NiO by methane is characterized by existence of a clearly marked induction period, followed by rapid acceleration of the process. As a result, the  $\alpha(t)$  curves have S-shaped form both at constant and linear heating regimes, which is specific for the topochemical reactions proceeding via the stages of nucleation and growth, and are described by well known Avrami equation:  $\alpha = 1 - \exp(-kt^n)$  [4].

In Figs. 2a–2c there are dependencies of reaction rate,  $W_r(t)$  vs. time at linear heating the sample with heating rates,  $V_h = 50, 100, \text{ and } 200^{\circ}/\text{s}$  and methane pressure,  $P_{\text{CH}_4} = 50$  torr. As it follows from the data presented, increasing the heating rate moves the reaction from the heating stage (non-isothermal interaction) to the isothermal region. Thus, at  $V_h = 50^{\circ}/\text{s}$ , the reduction



reaction occurs and finished at heating stage. At  $V_h = 100^\circ/\text{s}$  the reduction proceeds at transition from non-isothermal to isothermal period, while at  $V_h = 200^\circ/\text{s}$  the reaction completely occurs at reference temperature.

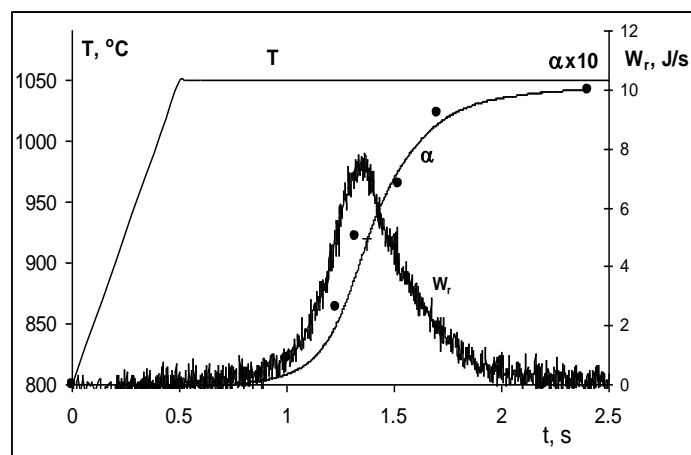


Fig. 1. Dependencies of temperature,  $T$ , reaction rate,  $W_r(t)$  and conversion degree,  $\alpha$  vs. time.

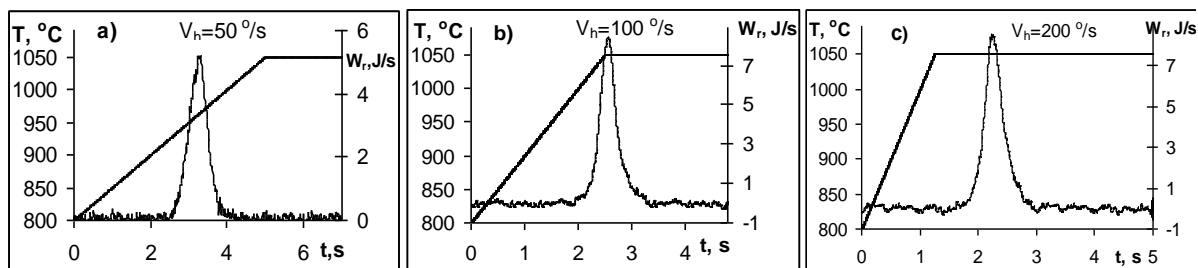


Fig. 2. Dependencies of temperature,  $T$ , and reaction rate,  $W_r(t)$ , vs. time at reduction of NiO by methane. Linear heating with (a)  $V_h = 50$ , (b) 100, and (c)  $200^\circ/\text{s}$ .  $P_{\text{CH}_4} = 50$  torr.

It was shown that the increase of methane pressure significantly reduces the induction period and moves the whole reduction process to the shorter time region (Figs. 3a–3c). At that, in the case of linear heating up to certain reference temperature, depending of methane pressure and heating rate the reduction occurs either at heating stage or fully at reference temperature, i.e. at isothermal conditions.

Based on data obtained at various heating rates and methane pressure, a heating rate ( $V_h$ )–methane pressure ( $P_{\text{CH}_4}$ ) diagram of reduction regimes was constructed (Fig. 4), according to the which at low heating rates and high pressures the reaction occurs mainly at heating stage. On the other hand, at high heating rates and low methane pressures, vice-versa, the process fully takes place at isothermal conditions.

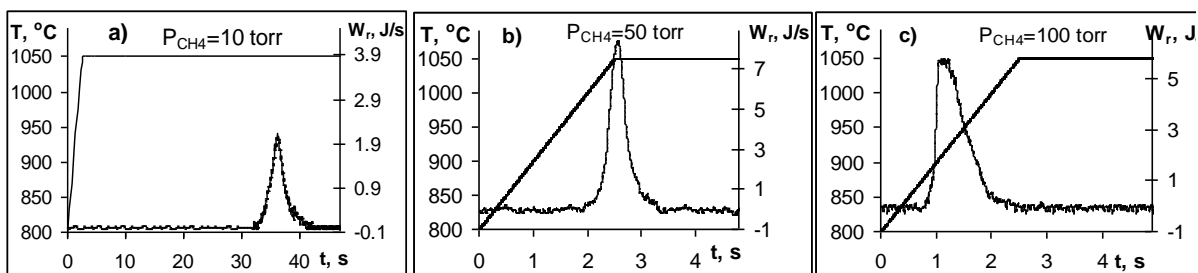


Fig. 3. Dependencies of temperature,  $T$ , and reaction rate,  $W_r(t)$ , vs. time at reduction of NiO by methane. Linear heating with  $V_h = 100^\circ/\text{s}$ : (a)  $P_{\text{CH}_4} = 10$ , (b) 50, and (c) 100 torr.

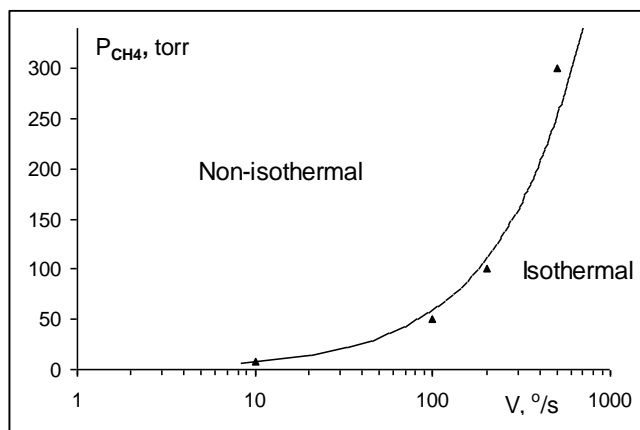


Fig. 4.  $P_{CH_4}$ – $V_h$  diagram of NiO reduction regimes by methane.

In parallel to the kinetic measurements, SEM studies of the samples at different stages of the process were performed to reveal the causes of the specific shape of the kinetic curves. It has been established, that in the induction period, before intensive chemical interaction, nickel nucleus are formed on the surface of the nickel oxide, which subsequently extend and grow in the volume of oxide, forming highly porous nickel layer. The S-shaped kinetic curve appearance and the presence of the induction period are caused just by the nucleation and their further growth processes.

This work was supported by the Committee of Science MES of RA (Research grant 18T-1D051).

1. S.L. Kharatyan, H.A. Chatilyan, L.H. Arakelyan, Kinetics of tungsten carbidization under non-isothermal conditions, *Mater. Res. Bull.*, 2008, vol. 43, is. 4, pp. 897–906.
2. S.L. Kharatyan, Electrothermography, Concise Encyclopedia of Self-Propagating High-Temperature Synthesis, 2017, pp. 107–109.
3. Kh.V. Manukyan, A.G. Avetisyan, Ch.E. Shuck, H.A. Chatilyan, S. Rouvimov, S.L. Kharatyan, A.S. Mukasyan, Nickel oxide reduction by hydrogen: kinetics and structural transformations, *J. Phys. Chem. C*, 2015, vol. 119, 16131–16138.
4. J.E. House, Principles of Chemical Kinetics, 2nd ed., Elsevier, 2007.

# MULTILAYER TiNbC COATINGS PRODUCED BY A COMBINATION OF PULSED ARC EVAPORATION AND ELECTRO-SPARK DEPOSITION IN VACUUM

O. S. Manakova<sup>\*a</sup>, K. A. Kuptsov<sup>a</sup>, A. N. Sheveyko<sup>a</sup>, D. V. Shtansky<sup>a</sup>,  
and D. A. Sidorenko<sup>a</sup>

<sup>a</sup>National University of Science and Technology MISIS, Moscow, 119049 Russia

\*e-mail: manakova@misis.ru

DOI: 10.24411/9999-0014A-2019-10094

Today, one of the promising ways to improve the performance of parts and components of various machines and mechanisms is to modify their surfaces. Protective coatings based on hard carbides, borides, nitrides, etc. are used to enhance mechanical properties, heat- and wear resistance. Developing surface with desired properties is possible not only by selecting the composition of the formed layers, but also by creating gradient and multilayer coatings [1].

Two-layer coatings based on double carbide (Ti, Nb)C were developed for the sequential treatment of the steel substrate by the combination of electric-spark deposition (ESD) and pulsed arc evaporation (PAE) methods. Composite dispersion-hardened materials based on (Ti, Nb)C carbide were used as electrode materials. To increase erosion of the electrodes and improve the quality of coatings, a metal binder based on Ni was introduced into the electrode material. In this work electrode materials based on Ti–Nb–C system with binder were produced by a combined force SHS-pressing technology. The electrode materials were heat treated in vacuum at a temperature of 900°C for 4 h [2].

Optimal regimes of surface treatment for each deposition method were established. Selection of the optimal regime of ESD layer deposition was conducted on the basis of kinetics of mass transfer, structure and properties studies. The criteria for selection of PAE layer deposition regimes were coatings growth rate and integrity of the electrodes.

It was found that the coatings with the best properties were formed in an argon atmosphere at a pressure of 0.3 Pa under optimal conditions.

The structure, phase and chemical composition of the obtained two-layer coatings were studied by SEM (Fig. 1), TEM, XRD, XPS, and Raman spectroscopy. The coatings were also characterized in terms of their mechanical and tribological properties. It was found that the main structural components of the ESD layer were carbide phases ((Ti, Nb)C and Fe<sub>2</sub>C) and intermetallic phases based on Fe, Ni, Co, Ti. The PAE layer contained mainly fcc-phase based on carbide (Ti, Nb)C with a strong texture in the (220) direction.

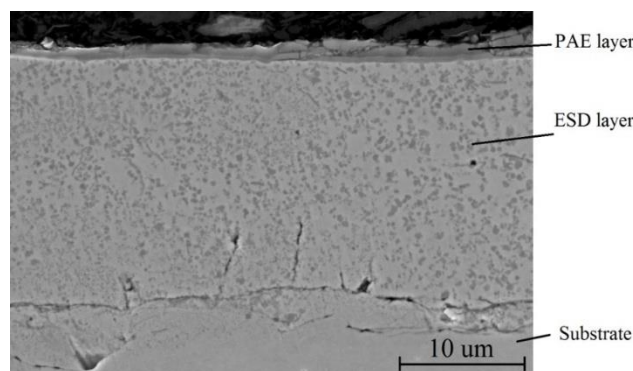


Fig. 1. The microstructure of the two-layer coatings based on double carbide (Ti, Nb)C.

The thickness of the formed two-layer coating was 21  $\mu\text{m}$ . Roughness did not exceed 3.0  $\mu\text{m}$ .

The two-layer coatings were successfully obtained by the ESD and PAE combined technology and were characterized by low friction coefficient in the range of 0.16–0.25 compared to the single layer ESD coatings characterized by high friction coefficient of 0.7–0.8.

1. Ph.V. Kiryukhantsev-Korneev, A.N. Sheveyko, N.V. Shvindina et al., *Ceram. Int.*, 2018, vol. 44, pp. 7637.
2. O.S. Manakova, V.V. Kurbatkina, E.A. Levashov, *Russ. J. Non-Ferr. Met.*, 2015, vol. 56, no. 4, pp. 486.

## THE ROLE OF MECHANOCHEMICAL TREATMENT IN THE DEVELOPMENT OF SH-SYNTHESIS AND OBTAINING COMPOSITION SYSTEMS OF DIFFERENT PURPOSES

Z. A. Mansurov<sup>\*a</sup>, N. N. Mofa<sup>a</sup>, B. S. Sadykov<sup>a</sup>, and A. Ye. Bakkara<sup>a</sup>

<sup>a</sup>Al-Farabi Kazakh National University, The Institute of Combustion Problems,  
Almaty, Kazakhstan

\*e-mail: zmansurov@kaznu.kz

DOI: 10.24411/9999-0014A-2019-10095

At the present, to prepare composite systems of different phase compositions with high mechanical characteristics and chemical resistance, technological combustion is widely used when, during exothermic reactions between powder components, the formation of the necessary products occurs in the mode of directional self-propagating high-temperature synthesis (SHS) [1, 2]. At the same time, much attention is paid to the process controllability and reproducibility of the final results according to the properties of the material obtained. Preliminary mechanochemical treatment (MCT) of the initial reagents used in charge mixtures for the SH-synthesis of various composites [3, 4] proved to be the most effective in terms of controlling the combustion process. Due to MCT of inorganic powder materials, not only their dispersiveness, but also the defect structure changes, mass transfer and mobility of the atomic structure get accelerated, there takes place disordering and rupture of interatomic bonds and a free-radical structure is formed. All this changes the reactivity of the materials being processed and expands the possibilities of obtaining composites in the SHS mode. By varying the pretreatment conditions, it is possible to purposefully regulate the phase and structure formation of materials during the SH-synthesis process. In this case, both individual components of the mixture, and mixtures of components are subjected to MCT. Initially, more attention was paid to the MCT of oxide systems, and then to the metal ones, which play the role of fuel in the SHS mixture [5].

In this report, several options for preparation of initial reagents (quartz and aluminum) in the MCT mode for their subsequent use as part of the SHS-charge mixture are considered. The change in the thermo-kinetic characteristics of the technological combustion and the formation of the phase composition of the synthesis products depending on the conditions of preparation of the initial reagents in the MCT were stated. We used aluminum powder of the PA-4 grade and quartz from the Kuskuduk deposit with a quartz content of 81.3 and 18.7% of microcline  $K(Si_3Al)O_8$ . The MCT was carried out in the presence of various organic modifying additives: carbon (graphite), butyl alcohol, polyvinyl alcohol, and stearic acid. During grinding, the amount of modifying additives introduced varied (3–20%), the grinding time was 20 min, according to the results of previous studies [4].

It is on quartz that all structural and radical transformations in the process of mechanochemical action are rather consistently studied. When an organic additive is introduced into dispersible quartz, the particle structure undergoes significant changes. The surface layer of a quartz particle is a multilayer formation with carbon structures of varying density with a thickness from 10 to 40 nm (Fig. 1). Carbonization of the quartz particle during MCT with butanol is due to destruction of the alcohol additive during processing.

The particles of the original aluminum powder are spherical in shape, with an average size of about 50  $\mu\text{m}$  (Fig. 2a). After MCT of aluminum with graphite and polyvinyl alcohol, the particles have a lamellar (scaly) shape of various thickness (Figs. 2b, 2c). Aluminum particles

treated in the presence of stearic acid, partially retain a spherical shape, they are encapsulated in a dense organic film (Fig. 2d) and are more dispersed than after treatment with graphite and polyvinyl alcohol.

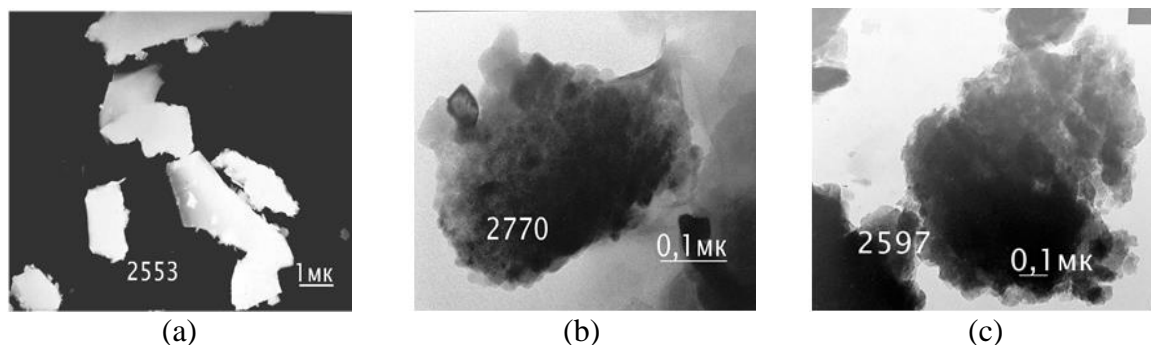


Fig. 1. Electron microscopic images of quartz in the original (a) and in modified with graphite (b) and butanol (c) state.

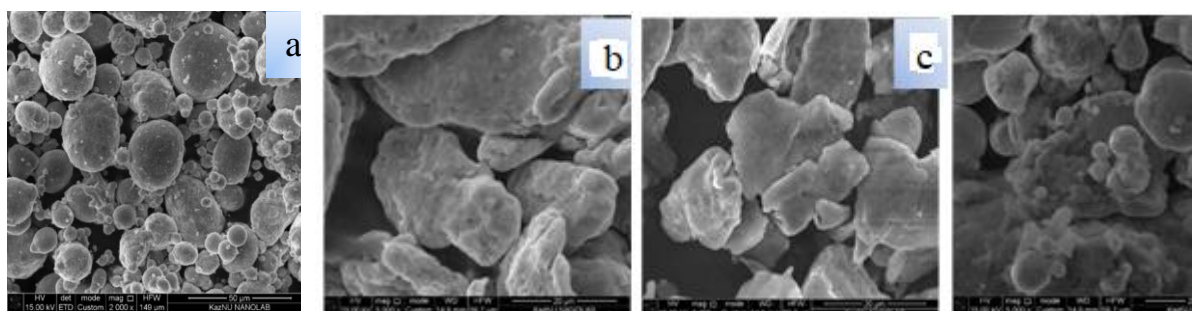


Fig. 2. Electron microscopic images of aluminum in the initial state (a) and after MCT with various modifying additives (b–d). (a) Al; (b) Al/C; (c) Al/(C<sub>2</sub>H<sub>3</sub>OH)<sub>n</sub>; (d) Al/C<sub>17</sub>H<sub>35</sub>COOH.

According to the results of the energy dispersive spectroscopy of the investigated aluminum powders, after MCT of aluminum with modifiers, the elemental composition of the surface layer changed. The amount of oxygen decreases, and the presence of carbon is registered, the content of which depends on the type of the modifying additive. The decrease in the content of oxygen is the result of reduction of aluminum in the surface oxide layer of the particles during the MCT process. The results of thermogravimetry, IR and EPR spectroscopy of activated and modified aluminum powder showed that during MCT there take place changes in the main spectra (new lines, frequency and strain bands are observed) and intensification of interaction processes with various components of the system. The surface of the particles is saturated with solid solutions of carbon-containing compounds. All this together should affect the activity of the processed powder. The use of such powder materials is effective, in particular, in the preparation of SHS composites with enhanced chemical and mechanical stability. So, MCT of quartz leads to the change of its maximum burning temperature with aluminum, i.e. (SiO<sub>2</sub> + 37.5% Al), induction ignition period, level and rate of temperature change at the post-process stage, when the phase composition of the synthesized material is actually formed (Fig. 3). Processing in a quartz mill in the presence of graphite and butyl alcohol results in a more pronounced time dependence of the maximum burning temperature.

MCT of aluminum also leads to a significant change in the thermokinetic characteristics of the combustion process (Fig. 4). The role of the modifying additive in this case is even more significant. There is a decrease in the induction period of ignition, an increase in speed and temperature at all stages of the combustion process. A distinctive feature of the combustion of such systems is a more stable, long-lasting and extensively developed combustion of the system, especially at the post-process stage.

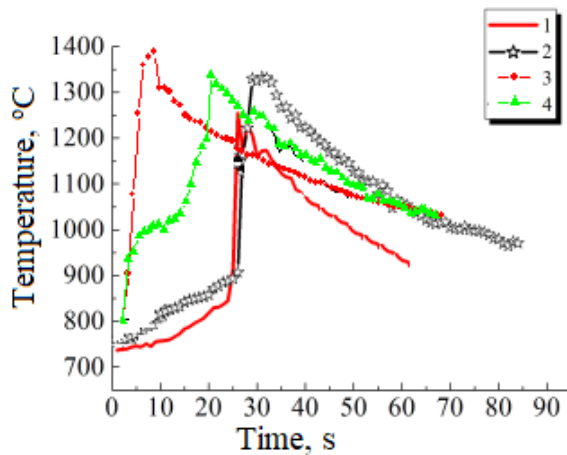


Fig. 3. Combustion thermograms for the system ( $\text{SiO}_2 + 37.5\% \text{ Al}$ ) with non activated quartz (1) and after MCT without a modifier (2) and with graphite (3) and butyl alcohol (4) for 20 min.

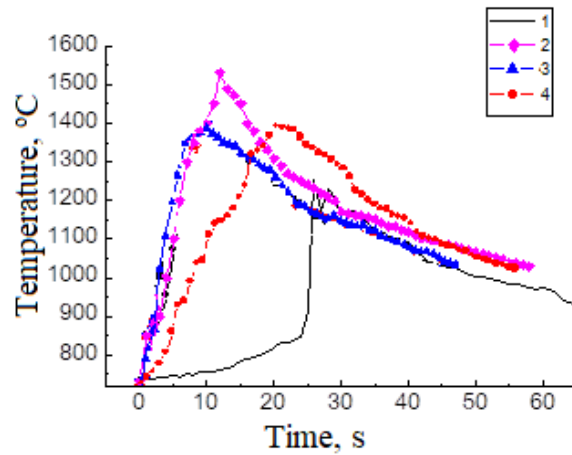


Fig. 4. Thermograms of combustion systems ( $\text{SiO}_2 + \text{Al}$ ) with Al in the initial state (1) and after 20 minutes of MCT with graphite (2), polyvinyl alcohol (3) and stearin (4).

The change in the reactivity of the system as a result of MCT affects not only the thermokinetic characteristics of the combustion process, but also the composition of the final synthesis product. Table 1 presents the data on the phase composition of SH-synthesis products of the system ( $\text{SiO}_2 + 37.5\% \text{ Al}$ ), depending on the state of the charge components after MCT of aluminum with modifying additives. Modification of the system contributes to the formation of aluminum nitride, iron and silicon disilicide, and the complex compound  $\text{FeAl}_3\text{Si}_2$ . The strength of the synthesized samples varies from 6.27 to 45.98 MPa. The high strength of the material is due to both the phase composition and the density of the samples. Modification of aluminum during MCT with stearic acid leads to formation of a finely porous structure due to burning out of its degradation products during MCT and in the process of SHS.

Table 1. Results of X-ray analysis of SHS samples depending on the conditions of mechanochemical treatment of aluminum with modifiers.

| Phases   | Phase content, % |      |      |      |      |      |      |
|--|------------------|------|------|------|------|------|------|
|  | Samples          |      |      |      |      |      |      |
|  | 1                | 2    | 3    | 4    | 5    | 6    | 7    |
| $\text{Al}_2\text{O}_3$                          | 43.6             | 67.9 | 77.2 | 65.8 | 61.5 | 65.3 | 51   |
| $\gamma\text{-Al}_2\text{O}_3$                   |                  |      |      | 3.1  | 10.5 |      |      |
| Si   | 14.9             | 15.8 | 9.8  | 25.8 | 25.3 | 17.5 | 21.9 |
| Al   | 10.2             | 2.0  |      | 1.5  |      | 5.0  | 11.7 |
| $\text{SiO}_2\text{-quartz}$                     | 29.9             | 4.1  | 1.2  | 2.8  | 2.7  | 8.0  | 4.2  |
| $\text{FeAl}_3\text{Si}_2$                       | 1.2              |      |      |      |      |      |      |
| AlN  |                  | 1.9  |      | 1.0  |      | 1.6  | 6.0  |
| $\text{FeSi}_2$                                  |                  | 0.6  | 1.2  |      |      | 0.7  | 0.5  |
| SiC- Moissanite 3C                               |                  | 2.1  | 7.8  |      |      |      |      |
| SiC-Moissanite 2H                                |                  |      | 2.8  |      |      |      |      |
| $\text{Al}_{4.59}\text{Si}_{1.41}\text{O}_{9.7}$ |                  | 3.4  |      |      |      | 1.8  | 4.6  |

1 – ( $\text{SiO}_2 + \text{Al}$ ), 2 – [ $\text{SiO}_2 + (\text{Al} + 5\% \text{ C})_{\text{MCT}}$ ]; 3 – [ $\text{SiO}_2 + (\text{Al} + 20\% \text{ C})_{\text{MCT}}$ ];  
 4 – [ $\text{SiO}_2 + (\text{Al} + 3\% (\text{C}_2\text{H}_3\text{OH})_n)_{\text{MCT}}$ ]; 5 – [ $\text{SiO}_2 + (\text{Al} + 20\% (\text{C}_2\text{H}_3\text{OH})_n)_{\text{MCT}}$ ];  
 6 – [ $\text{SiO}_2 + (\text{Al} + 3\% \text{C}_{17}\text{H}_{35}\text{COOH})_{\text{MCT}}$ ]; 7 – [ $\text{SiO}_2 + (\text{Al} + 10\% \text{C}_{17}\text{H}_{35}\text{COOH})_{\text{MCT}}$ ]

Thus, from the presented data it follows that by modifying the components of the mixture, one can purposefully influence the combustion process and the formation of a dense or porous

structure with ultradispersed phases that strengthen the material (the sample being synthesized). The presence of the modifier leads to a decrease in the induction period of the system ignition and an increase in the combustion rate. At the same time, in the composition of the charge, the amount of aluminum was lower than according to stoichiometry (37.5%), since the organic modifier is also present in the composites. The presence of carbon in the modifier during the synthesis process creates an inert atmosphere resulting in the interaction of aluminum with air nitrogen. The reactions of both carbide and nitrido formations are exothermic, this providing an increase in the combustion temperature.

1. A.G. Merzhanov, Self-propagating high-temperature synthesis, Physical chemistry: Modern problems, Ed. Y.M. Kolotyorkina, M.: Chemistry, 1983, pp. 5–44.
2. A.E. Levashov, A.S. Rogachev, V.I. Yukhvid, I.P. Borovinskaya, Physico-chemical and technological bases of self-propagating high-temperature synthesis, M.: BINOM, 1999, 176 p.
3. N.Z. Lyakhov, T.L. Talako, T.F. Grigorieva, The influence of mechanical activation on the phase and structure formation processes during self-propagating high-temperature synthesis, Novosibirsk: Parallel, 2008, 168 p.
4. Z.A. Mansurov, N.N. Mofa, Mechanochemical synthesis of composite materials, Almaty: Kazakh University, 2016, 376 p.
5. N.N. Mofa, B.S. Sadykov, A.Ye. Bakkara, Z.A. Mansurov, Features of the combustion of energy condensed systems with mechanically activated metallized composites, 7th Int. Conf. The space challenge of the XXI century, Sevastopol, 2015, pp. 61–63.



## CURRENT STATE AND FUTURE PROSPECTS OF SOLUTION COMBUSTION SYNTHESIS

**Kh. Manukyan**

Nuclear Science Laboratory, Department of Physics, University of Notre Dame,  
Notre Dame, IN 46556, USA  
e-mail: kmanukya@nd.edu

DOI: 10.24411/9999-0014A-2019-10096

Solution combustion synthesis (SCS) is a rapid method for energy-efficient preparation of a large variety of materials. The self-generated heat of synthesis provides a localized energy supply that eliminates or reduces the need for externally applied thermal processing. The synthesis of powdered materials by this method involves heating of homogeneous solutions containing metal nitrates and organic compounds. Rapid heating leads to evaporation of solvent and formation of a viscous gel. Further heating initiates a high-temperature self-sustaining reaction in the gels resulting in the formation of nanostructured simple and complex oxides. SCS provides a simple formation of high-quality multi-element compounds with complex crystal structures (perovskites, garnets, spinels, silicates, and phosphates).

This talk focuses on the analysis of new approaches and results in the field of SCS obtained during the last few years. Kinetics and thermodynamics of reactive solutions used in different chemical routes will be considered, and the role of process parameters will be discussed, focusing on the chemical mechanisms that are responsible for rapid self-sustained reactions. New approaches investigating the mechanism and kinetics of these reactions will be discussed. The relationships between processing conditions, structure, and morphology of products will be presented. The basic principles for controlling the composition, morphology, and structure of SCS-derived products, and routes to regulate the morphology and size of the nanoscale powders will also be reviewed.

Recent advances of SCS method in the preparation of actinide nanoscale materials, thin films as well as some complex multicomponent alloys which have high potentials for the use in advanced nuclear technologies or nuclear data measurements will be highlighted. Particular emphasis will be placed on tailoring the SCS to obtain non-oxide and non-metallic compounds with uniform morphology and structure. This presentation will also highlight several applications of SCS products, such as target materials for nuclear cross-section measurements as well as nanoscale magnetic materials. Recent results on examples of irradiation-induced modifications of the structure and properties of nanoscale materials will be presented. Emphasis will be placed on irradiation-induced changes in thin films and layered nanostructures. Some essential relationships linking the irradiation conditions, structural changes, and properties of materials will be outlined. Finally, the prospects of SCS for processing of nanoscale materials and its potential commercialization pathways will be summarized.

## SHS OF MACROPOROUS NiAl ALLOYS USED IN ADVANCED RADIANT BURNERS

A. Maznoy<sup>\*a</sup>, A. Kirdyashkin<sup>a</sup>, V. Kitler<sup>a</sup>, N. Pichugin<sup>a</sup>, and V. Salamatov<sup>b</sup><sup>a</sup>Tomsk Scientific Center of the Siberian Branch of the Russian Academy of Sciences, Tomsk, 634055 Russia<sup>b</sup>Merzhanov Institute of Structural Macrokinetics and Materials Science, Russian Academy of Sciences, Chernogolovka, Moscow, 142432 Russia

\*e-mail: maznoy\_a@mail.ru

DOI: 10.24411/9999-0014A-2019-10097

Since the first half of the 20th century, porous radiant burners have been successfully used for heating industrial premises and thermal processing and drying of materials. The key element of the radiant burner is a special gas permeable porous body – an emitter. The emitter takes part in heat exchange with a burning gas-air mixture, becomes red-hot, and emits the IR flux in accordance with the Stefan–Boltzmann law. Fursenko et al. [1] have demonstrated that depending on ignition conditions, the hollow cylindrical Ni–Al burners with the microchannels of less than the critical diameter can function both in the surface stabilized and internal combustion modes when the combustion zone stabilizes in the emitter internal cavity space. They have claimed that the radiation efficiency in the internal combustion mode is twice higher, up to 60% at a firing rate of 160 kW/m<sup>2</sup>. Maznoy et al. [2] have further found that in the internal combustion mode, the radiation efficiency of a cylindrical Ni–Al burner is close to the level of the highest possible radiant burner efficiency. To create reliable cylindrical burners, it is necessary to use materials that can endure thermo-mechanical stresses during a burner start-up without being destructed. Possible materials to be used are Ni–Al intermetallic alloys. The SHS reaction in the Ni + Al system starts at the melting point of Al and proceeds with a dissolution-precipitation mechanism, which is controlled by nickel diffusion in an aluminum melt. However, when both reagents melt, an abrupt increase in the reaction rate occurs. Rogachev et al. [3] have found that both reagents first melt in a Ni–Al combustion wave, and after that both liquids interact due to a very fast ( $t \sim 10^{-3}$  s) convective-reaction mixing, forming large drops of a melt. The size of the merged drops is 10–100 times larger than the size of the initial metal particles: there are about  $10^5$  particles of the initial reagents merged in one globule. This mechanism is called “reaction coalescence”. Kirdyashkin et al. [4] have further shown that capillary hydrodynamic phenomena such as the Marangoni convection and thermal-gradient or capillary driven filtration of melts take place in a combustion wave of melting systems. Under the reaction coalescence conditions, the combustion wave front looks like a multitude of randomly generated drops, the size of which determines the porous structure of synthesized intermetallic alloys. The motivation of the present work is to develop methods for controlling the reaction coalescence process along with the production of coarse porous B2 + L1<sub>2</sub> Ni–Al alloys. The main approach discussed in this paper is the use of a bifunctional additive. The first function of the additive is to form low-temperature eutectics with aluminum oxide, which is inevitably available on the surface of commercial aluminum powders. The second function is to decompose the additive in the combustion wave zone at the formation of gases, which increases the powders moveability and intensifies the reaction coalescence.

The reaction compositions of Ni + 13.5–31.5 wt % Al have been analyzed. Nickel powder PNK UT-1 and aluminum powder ASD-4 with a particle fewer than 10 μm in size have been used as the initial reagents. The powders have been thoroughly mixed using a Turbula mixer. Chemically pure powders CaO, CaF<sub>2</sub>, Ca(OH)<sub>2</sub>, CaCO<sub>3</sub> have been used as additives to Ni–Al

mixtures. The self-propagating high-temperature synthesis of porous Ni–Al alloys was carried out according to the following method (Fig. 1a). The pre-mixed blends of powders were laid inside a steel cylindrical shell (inner diameter of 38 mm, the height of 68 mm) and were exposed to the controlled vibroforming to the relative density in the range of  $\rho = 0.4\text{--}0.5$ . The shell with the powder mixture was located inside a hermetic reaction chamber equipped with programmable electrical heating. The chamber was vacuumized three times each time followed by filling with argon to the atmospheric pressure. The temperature  $T_0$  of the reaction medium preheating was set. To measure the maximum temperature  $T_M$  in the combustion wave, a tungsten–rhenium thermocouple of 200  $\mu\text{m}$  thick was installed in the center of the mixture. The combustion wave velocity was defined as  $U = \Delta t/l$ , where  $\Delta t$  was the passing time of the combustion wave between two K type thermocouples installed on the outer surface of the steel shell at a distance  $l$ . To visualize structural transformations in the SHS wave, high-speed imaging was employed using a Motion Pro X-3 camera (up to 10 000 fps). Since the thermocouple method is inertial, spectral pyrometry was additionally used to record instantaneous temperature values in the SHS wave. The dynamic monitoring of emission spectra was performed using an Ocean Optics HR4000 spectrometer according to the scheme shown in the Fig. 1b.

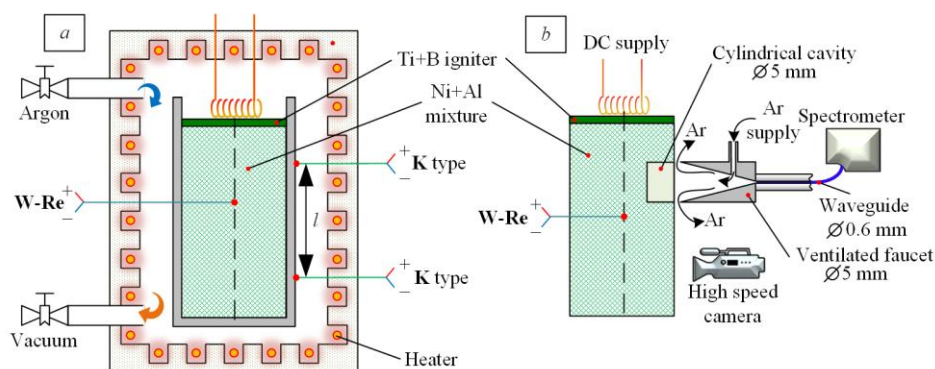


Fig. 1. The experimental scheme of porous materials synthesis (a); the scheme of spectral measurements and high-speed imaging during the SHS (b).

Let us consider the synthesis mechanism for coarse porous materials using an example of the reaction mixture Ni + 20 wt % Al with the relative density of  $\rho = 0.46$  and preheating value of  $T_0 = 200^\circ\text{C}$  (Table 1, Fig. 2).

The SHS in this mixture is realized with combustion velocities of more than 10 mm/s, and this produces materials with a fine porous and defective structure (Fig. 2a). It is possible to obtain coarse porous materials without defects by using CaO or CaF<sub>2</sub> additives (Figs. 4b, 4c). With these additives, a reduction of oxide films occurs on the surface of Al particles. The use of Ca(OH)<sub>2</sub> and CaCO<sub>3</sub> additives makes it possible to obtain coarse porous materials with an average diameter of Ni–Al elements up to 2 mm (Figs. 2d, 2e). From the high speed video filming data, it has been determined that in a combustion wave zone the decomposition of additives occurs with the formation of gases. The gases increase the mobility of the powder medium and form a fluidized bed. The formation of droplets in the combustion wave is stimulated not only by the reduced melt viscosity but also by the increased mobility of the powder particles of the fluidized bed. The thermocouple measurements have shown that the maximum temperature  $T_M$  in the combustion wave (about 1430°C) is consistent for both the mixture with additives and without additives, and this temperature is 40°C lower than the melting point of the alloy with this composition. The spectrometric measurements have shown that in the combustion wave region there are high-temperature scintillations of a short period ( $t < 50$  ms). Their temperature is 100–350°C higher than the solidus temperature, and this fact also increases the liquidus temperature (Fig. 3). It has been found that a planar front of the

combustion wave splits into many foci (Fig. 4), and everything seems to indicate that these superadiabatic scintillations correspond to the moments of melt droplets formation. Heat losses of a melt drop into the ambient, the temperature of which is lower than the solidus one, lead to rapid crystallization of the drop with its shape and size fixation. In such a way, the Ni–Al elements of a porous alloy are formed.

Table 1. The effect of an additive on the SHS parameters and the average size of skeleton elements of synthesized alloys  $D_E$ .

| # | Additive                | $U$ , mm/s     | $T_M$ , °C    | $D_E$ , $\mu\text{m}$ |
|---|-------------------------|----------------|---------------|-----------------------|
| 1 | no                      | $15.0 \pm 0.5$ |               | defects               |
| 2 | 2 % CaO                 | $7.8 \pm 0.3$  |               | $160 \pm 20$          |
| 3 | 2 % CaF <sub>2</sub>    | $3.6 \pm 0.2$  | $1430 \pm 10$ | $660 \pm 30$          |
| 4 | 2 % Ca(OH) <sub>2</sub> | $1.1 \pm 0.1$  |               | $1920 \pm 90$         |
| 5 | 2 % CaCO <sub>3</sub>   | $1.0 \pm 0.1$  |               | $1750 \pm 90$         |

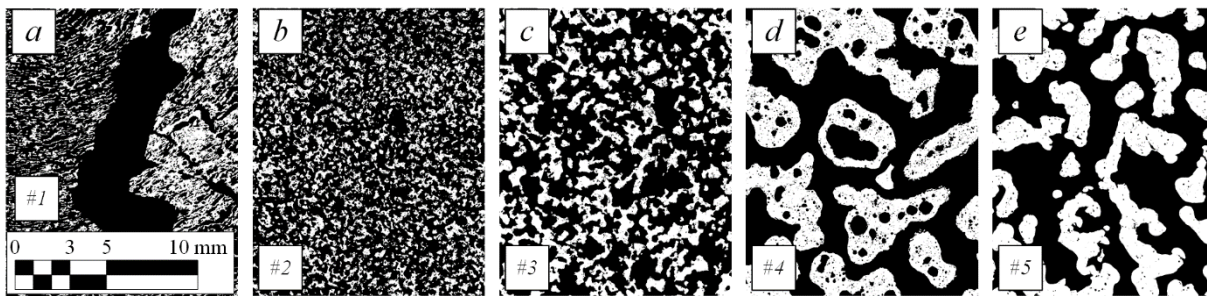


Fig. 2. Structures of Ni + 20 wt % Al alloys synthesized in accordance with Table 1.

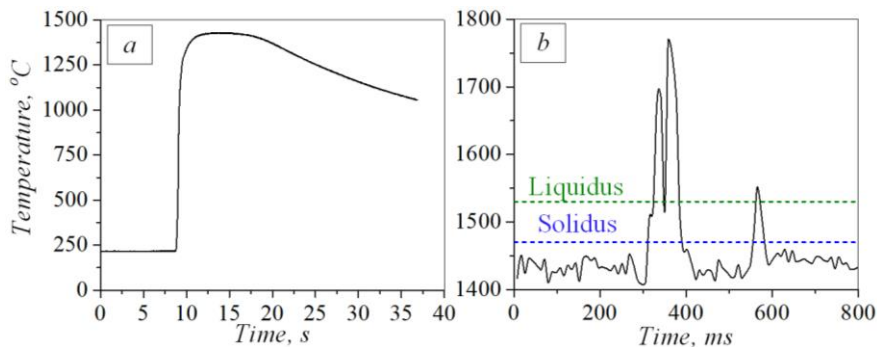


Fig. 3. Thermocouple measurements (part *a*) and spectrometric measurement data (part *b*). The reaction mixture of (Ni + 20 wt % Al) + 2 wt % CaCO<sub>3</sub>.



Fig. 4. Instantaneous time sequent photographs of the SHS process. The reaction mixture of (Ni + 20 wt % Al) + 2 wt % CaCO<sub>3</sub>.

Let us consider the effect of the initial synthesis conditions given in Table 2 on the average size of skeleton elements  $D_E$ . Without preheating the reaction mixture, the regulation range of the composition is 18–22 wt % Al, and it is 15–20 wt % Al with preheating (Fig. 5, #1, 2). Beyond these ranges, it is not possible to organize self-sustainable combustion, or the alloys are characterized by a substantially non-uniform porous structure. For a mixture with a given

chemical composition, the control of the SHS process is possible by varying the preheating temperature and relative density of the reaction mixture (Fig. 5, #3, 4).

The phase composition of the materials was determined by X-ray analysis using a Shimadzu XRD 600 diffractometer,  $\text{CuK}_\alpha$  radiation, PCPDFWIN and PDF+ databases. The synthesized alloys of  $(\text{Ni} + 13.5\text{--}14.5 \text{ wt \% Al}) + 2 \text{ wt \% CaCO}_3$  composition consist only of the  $\text{L}_{12} \text{Ni}_3\text{Al}$  phase. For the compositions  $(\text{Ni} + 24\text{--}31.5 \text{ wt \% Al}) + 2 \text{ wt \% CaCO}_3$ , the synthesized alloys are characterized only by the  $\text{B}_2 \text{NiAl}$  phase. The synthesized alloys of the  $\text{Ni} + 17\text{--}22 \text{ wt \% Al}$  composition mainly consist of a combination of the  $\text{B}_2 \text{NiAl}$  and  $\text{L}_{12} \text{Ni}_3\text{Al}$  phases. Some minor amounts of the  $\text{L}_{10}$  and  $7\text{R}$  martensite phases are also available. It has been established that at all ranges of  $\text{Ni} + 13.5\text{--}31.5 \text{ wt \% Al}$  compositions studied, the synthesis products are characterized by an equilibrium composition after an hour's  $1100^\circ\text{C}$  annealing.

Table 2. Considered synthesis conditions. By the example of 2 wt %  $\text{CaCO}_3$  additive.

| Variable parameters                   | # | Range   | Fixed parameters |            |        |
|---------------------------------------|---|---------|------------------|------------|--------|
|                                       |   |         | Al, wt.%         | $T_0$ , °C | $\rho$ |
| Aluminium concentration, wt %         | 1 | 13.5–25 |                  | 25         | 0.46   |
|                                       | 2 | 13.5–25 |                  | 250        | 0.46   |
| Sample initial temperature $T_0$ , °C | 3 | 25–350  | 20               |            | 0.46   |
| Sample relative density, $\rho$       | 4 | 0.4–0.5 | 20               | 25         |        |

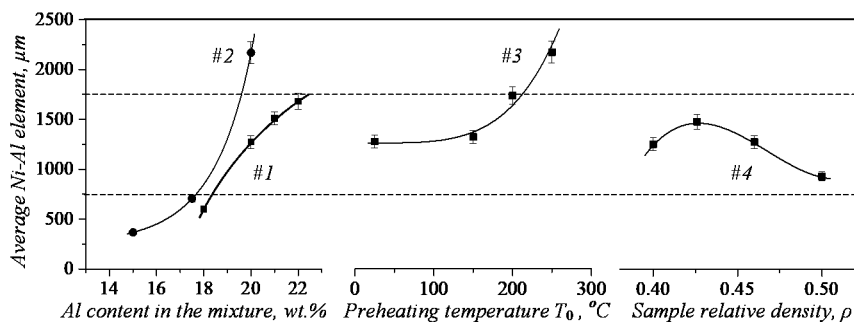


Fig. 5. Diameter dependence of average Ni–Al elements  $D_E$  in synthesized alloys on SHS conditions. The curves numbers correspond to Table 2.

The experiments have shown that the phase composition of cylindrical emitters has a significant impact on the performance properties of a radiant burner. Emitters of mono- $\text{B}_2$  composition and  $\text{B}_2 + \text{L}_{12}$  alloy can be destroyed when starting the burner using maximum power with a firing rate of  $500 \text{ kW/m}^2$ , and a temperature rise rate in the emitter being more than  $10^\circ\text{C}$  per second. The destructions are associated with cracks formation or porous emitter separation at the site of the weld joint. For trouble-free operation of  $\text{B}_2 + \text{L}_{12}$  emitters, it is necessary to perform a smooth start-up of the burner with the firing rate of about  $150\text{--}200 \text{ kW/m}^2$ , while the temperature rise rate is no more than  $5^\circ\text{C}$  per second. Our study has found that emitters made of mono  $\text{L}_{12} \text{Ni}_3\text{Al}$  could not be destroyed under any conditions of the burner start-up.

Thus, macro-porous Ni–Al intermetallic alloys have been successfully fabricated using self-propagating high-temperature synthesis. Testing the cylindrical radiant burners made by the SHS method has shown that the mono- $\text{L}_{12}$  alloy is characterized by increased robustness. It is also tolerant to any thermal gradients arising at the burner operation.

- 1 R. Fursenko, A. Maznoy, E. Odintsov, A. Kirdyashkin, S. Minaev, K. Sudarshan, Temperature and radiative characteristics of cylindrical porous Ni–Al burners, *Int. J. Heat Mass Transf.*, 2016, vol. 98, pp 277–284.
- 2 A. Maznoy, A. Kirdyashkin, S. Minaev, A. Markov, N. Pichugin, E. Yakovlev, A study on

- the effects of porous structure on the environmental and radiative characteristics of cylindrical Ni–Al burners, *Energy.*, 2018, vol. 160, pp. 399–409.
- 3 A.S. Rogachev, A. Varma, A.G. Merzhanov, The mechanism of self-propagating high-temperature synthesis of nickel aluminides, Part I: Formation of the product microstructure in a combustion wave, *Int. J. Self-Propag. High-Temp. Synth.*, 1993, vol. 2, pp. 25–38.
  - 4 A.I. Kirdyashkin, V.D. Kitler, V.G. Salamatov, R.A. Yusupov, Y.M. Maksimov, Capillary hydrodynamic phenomena in gas-free combustion, *Combust. Explos. Shock Waves.*, 2007, vol. 43, pp. 645–653.

## SYNTHESIS OF COMPOSITE MATERIALS IN THE Ti–Cr–B SYSTEM FROM MIXTURES BASED ON CALCIUM CHROMATES

P. A. Miloserdov<sup>\*a</sup>, V. A. Gorshkov<sup>a</sup>, O. M. Miloserdova<sup>a</sup>, and O. A. Golosova<sup>a</sup>

<sup>a</sup>Merzhanov Institute of Structural Macrokinetics and Materials Science, Russian Academy of Sciences, Chernogolovka, Moscow, 142432 Russia

\*e-mail: yu\_group@ism.ac.ru

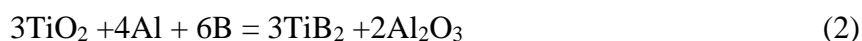
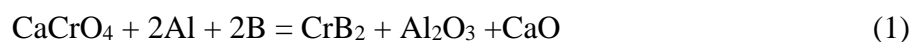
DOI: 10.24411/9999-0014A-2019-10098

Borides of titanium and chromium are used for the manufacture of heat-resistant, refractory and wear-resistant alloys and as the basis for cutting high-temperature materials, in cermets for nuclear engineering, for the manufacture of immersion thermocouple covers, etc. Chromium boride powder is used in various heat-resistant alloys of the type of boronite with significant loads and high temperatures, as well as to create wear-resistant surfacing alloys (BH-2, KBH). Borides of titanium and chromium have unlimited mutual solubility. The Ti–Cr–B system has a hardness higher than individual compounds and, more recently, has been intensively studied as a promising material for nuclear power engineering.

To create these materials, the most widely used methods are melting and high-temperature consolidation (sintering and hot pressing) from mixtures of metal powder and pure powders of boron or soot in vacuum at temperatures of 1800–2200°C. Ceramics based on chromium borides, especially CrB<sub>2</sub>, has unique properties: high hardness (20–22 GPa), high melting point (2200°C), high modulus of elasticity (211 GPa), good oxidation resistance, high thermal conductivity, low thermal coefficient expansion, high wear resistance and chemical inertness [1, 2].

The most promising way to obtain such materials is the one-step method of self-propagating high-temperature synthesis (SHS) [3]. One of the directions of this method is metallothermic SHS using initial mixtures consisting of metal oxides, a reducing metal (aluminum) and a non-metal (carbon, boron, silicon). The combustion temperatures of such mixtures exceed, as a rule, the melting points of the initial reagents and final products obtained in the combustion wave in a liquid-phase (cast) state. In early studies, the authors used initial mixtures containing chromic anhydride (CrO<sub>3</sub>), which is hygroscopic, thermally unstable, and toxic [4], which limits the practical implementation of the method.

To prepare a composite material, the following chemical conversion schemes were investigated:



The study of mixtures *I* depending on the boron content in the initial mixture showed that the mixtures are capable of burning; as a result, the cast target product consisting of a mixture of chromium borides (Cr<sub>3</sub>B<sub>4</sub>, CrB<sub>2</sub>) and aluminum is formed [5].

Thermodynamic analysis of mixtures *I* and *2* showed that with increasing  $\alpha$ , where  $\alpha = [M_2/(M_1 + M_2)] \times 100\%$ ,  $M_1$  is the mass of the mixture *I*, and  $M_2$  is the mass of the mixture *2*, the content of the “metallic” phase of products (*a*) increases. The combustion temperature gradually decreases from 2656 to 2590 K at  $\alpha = 80\%$ , then there is a sharp drop to 2450 K (Fig. 1).

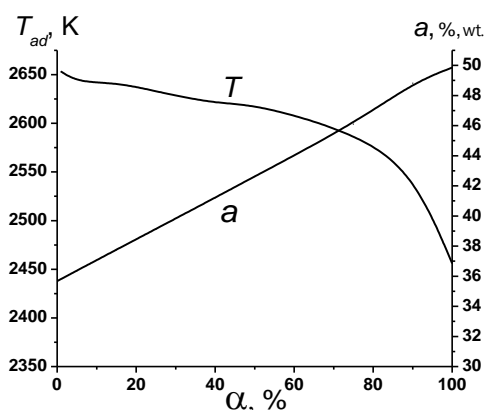


Fig. 1. The results of thermodynamic analysis of the system  $\text{CaCrO}_4 + \text{TiO}_2 + \text{Al} + \text{B}$ .

Experiments carried out using the reactor with  $V = 3.5$  l showed (Fig. 2) that the mixtures burn in the range of  $\alpha = 0$ –20%. With increasing  $\alpha$ , the burning rate decreases from 11 to 7 mm/s, the pressure increase in the reactor  $\Delta P$  also decreases from 13.5 to 8 atm. The yield of the target product decreases with increasing  $\alpha$  and the phase separation limit occurs at  $\alpha = 15\%$ .

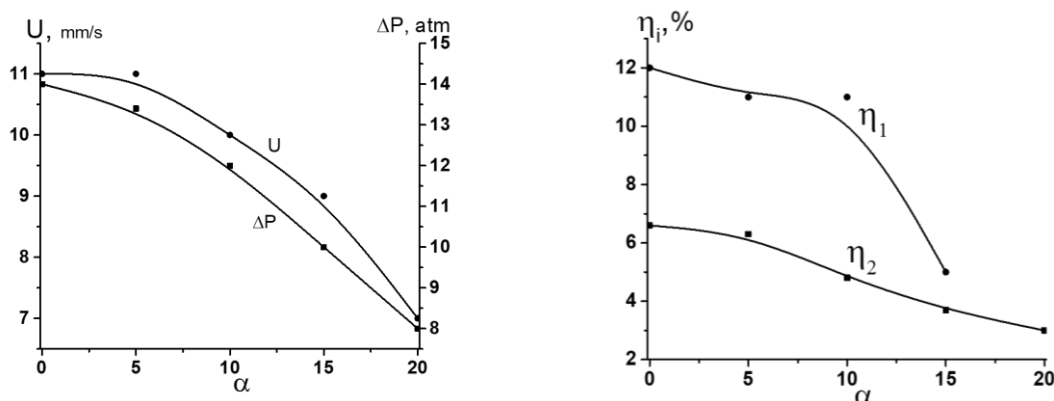


Fig. 2. The influence of  $\alpha$  on the burning rate  $U$  and the increase in pressure  $\Delta P$  in the reactor (a), on the yield of the target product  $\eta_1$  and the spread of combustion products  $\eta_2$ .

To extend the phase separation limit, the experiment was performed using the mixture with 20% highly exothermic  $\text{CaO}_2 + \text{Al}$  at  $\alpha = 20\%$ . As a result, the boride ingot with a diameter of 1 to 5 mm was poorly separated from oxide layer. Figure 3 shows that the product consists of titanium–chromium boride  $\text{Cr}_{0.5}\text{Ti}_{0.5}\text{B}_2$  and chromium borides  $\text{CrB}_2$  and  $\text{Cr}_3\text{B}_4$ .

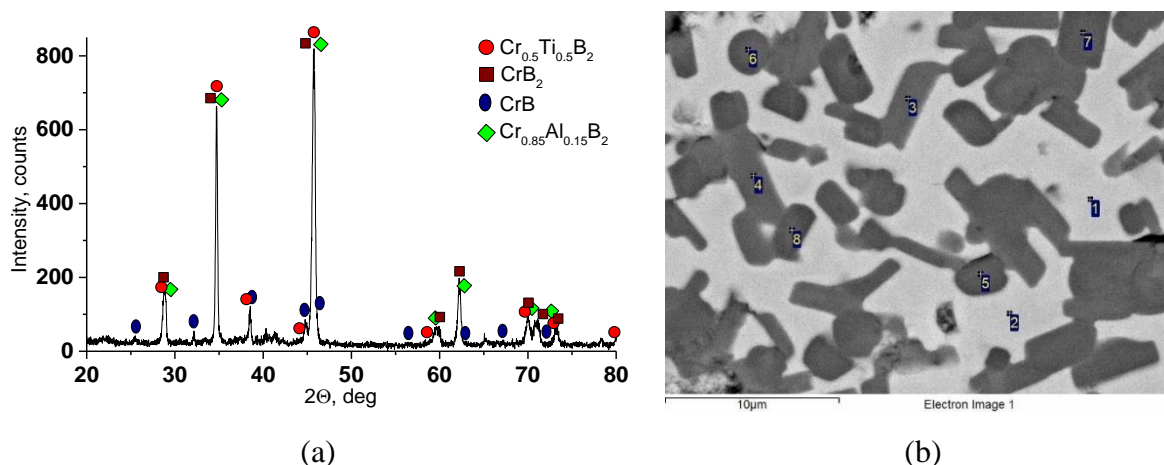


Fig. 3. (a) XRD pattern and (b) microstructure of the sample  $\text{CaCrO}_4 + \text{TiO}_2 + \text{Al} + \text{B}$ . EDS analysis data (wt %): 1 and 2 73 Cr, 3 Ti, 23 B, 1 Al; 3 and 4 33 Cr, 26 Ti, 40 B, 1 Al; 5–8 25 Cr, 36 Ti, 38.5 B, 0.5 Al.



## Conclusions

- (1) It is shown that replacing  $\text{CrO}_3$  in the initial mixture with slightly hygroscopic stable  $\text{CaCrO}_4$  allows to retain the high energy of the initial mixture and the ability of the mixture to burn, as well as to obtain cast refractory chromium borides.
- (2) The introduction of titanium oxide into the mixture leads to a noticeable decrease in the burning rate of the mixture and the yield of the target product.
- (3) The use of highly exothermic additives extends the limits of combustion and phase separation of the mixture. The prepared cast product consists of titanium–chromium boride and chromium borides.

The research was supported by the Russian Foundation for Basic Research (project no. 18-08-00804).

1. L.R. Jordan, A.J. Betts, K.L. Dahm, P.A. Dearnley, G.A. Wright, Corrosion and passivation mechanism of chromium diboride coatings on stainless steel, *Corros. Sci.*, 2005, vol. 47, iss. 5, pp. 1085–1096.
2. K. Iizumi, K. Kudaka, S. Odaka, Synthesis of chromium borides by solid-state reaction between chromium oxide (III) and amorphous boron powders, *J. Ceram. Soc. Jpn.*, 1998, vol. 106, no. 1237, pp. 931–934.
3. E.A. Levashov, A.S. Mukasyan, A.S. Rogachev, D.V. Shtansky, Self-propagating high-temperature synthesis of advanced materials and coatings, *Int. Mater. Rev.*, 2017, vol. 62, no. 4, pp. 203–239.
4. K. Salnikov, A. Zhitkovich, Genetic and epigenetic mechanisms in metal carcinogenesis and cocarcinogenesis: nickel, arsenic, and chromium, *Chem. Res. Toxicol.*, 2008, vol. 21, pp. 28–44.
5. P.A. Miloserdov, V.I. Yuxhvid, V.A. Gorshkov, T.I. Ignat'eva, V.N. Semenova, A.S. Shchukin, Combustion and autowave chemical transformations of a highly exothermic  $\text{CaCrO}_4/\text{Al/B}$  mixture, *Combust. Explos. Shock*, 2017, vol. 53, no 6, pp. 665–668.

## YESTERDAY, TODAY AND TOMORROW CHALLENGES FOR SHS

**Y. Miyamoto**

Joining and Welding Research Institute, Osaka University  
Mihogaok 1-1, Ibaraki City, Osaka 567-0047, Japan  
e-mail: yoshinari1027@yahoo.co.jp

DOI: 10.24411/9999-0014A-2019-10099

The SHS was born in 1967 on the earth of Russia from the great father Prof. A.G. Merzhanov and mother Prof. I.P. Borovinskaya. It was carefully grown mainly in a secret research town, Chernogorovka in the age of Soviet because of the great potential not only for science, but for industrial applications. The key issues are the very rapid and energy saving process releasing high thermal energy with high temperatures, and the productivity of numerous materials. Human history often gives hard lessons like the collapse of Soviet Union in 1991. For SHS, however it might open the more challenging future. The research and development power of SHS was released to the world through America, Poland, and Japan since early 1980's, then widely propagated to Korea, China, Europe, and other countries. The 1967 ~1970's may be called as the cradle age of SHS.

While, the 1980's ~1990's can be called as the rapidly growing and challenging age of SHS. This miracle and impressive SHS attracted attention from many ambitious scientists, engineers and entrepreneurs of the world. Various challenging approaches and analytic studies were promoted to understand and apply SHS. American researchers studied on the powder synthesis and the consolidation of advanced ceramics. In Poland, Prof. R. Pampuch and Prof. J. Lis succeeded in the combustion synthesis of unique ductile ceramics of  $Ti_3SiC_2$  that has much contributed to the current active R&D on MAX phases. In Japan, we succeeded in fabrication of high temperature dense ceramics of  $TiB_2$ ,  $TiC$ , and  $SiC$  by pressurized SHS in 1984.

Prof. O. Odawara invented a centrifugal thermite technique and formed alumina lining steel pipes in a period of seconds in 1983, of which technique was applied to practical uses in China. Various pressurizing techniques to SHS were developed not only for fabrication of dense materials or composite items, but for welding and lining metals, ceramics and intermetallics in Russia and in other countries.

The development of fine nitride ceramics was a world hot topic aiming to apply to ceramic engine and turbine parts, heat and wear resistant parts, electronic substrates and others in the growing age of SHS. Prof. Borovinskaya and our groups studied intensively the nitriding combustion synthesis of  $Si_3N_4$ , Sialon,  $AlN$ ,  $BN$ ,  $TiN$ ,  $NbN$  and others. The conversion of the desert sand of  $SiO_2$  to the unique high temperature ceramic of  $Si_2N_2O$  was our another challenge. Today, the commercial production of  $Si_3N_4$ ,  $AlN$  and other nitride powders by the SHS is growing in China.

In 1984, FGM (Functionally Graded Material) was proposed and developed in Japan. The FGM is the new tailored composite of different components such as a high temperature ceramic and a tough metal which are integrated with the graded interface relaxing the thermal stress. We demonstrated  $TiC/Ni$  and  $TiB_2/Ni$  FGMs by developing the SHS/HIP process. In order to realize the further potentiality of SHS, we challenged to develop the 3D-SHS printing and demonstrated some simple objects of  $NiAl$  intermetallic compounds in 2001. This unique 3D object can be formed by ejecting tiny molten Al droplets to the moving Ni powder bed on an X-Y-Z stage in the inert atmosphere under the CAD/CAM control.

The first international symposium on SHS was successfully organized in San Francisco, 1988 by Dr. J.B. Holt and Prof. Z.A. Munir. In 1992, the periodic issue of the international journal

on SHS has started. A Japanese text book entitled “Chemistry of Combustion Synthesis” was published in this year. Because no such a text book existed anywhere, it was translated into Russian and published.

The SHS has various advantages except a problem of difficult control. Unfortunately, SHS researchers cannot figure out yet the real answer to this difficulty.

Today, we are successfully producing fine and pure AlN powders by the controlled self-purification process of SHS. The AlN powders and fillers can be used to excellent heatsink substrates and sheet for electronic devices and LEDs, plasma and corrosion resistant parts of semiconductor manufacturing equipment, and phosphor materials.

In the 21<sup>st</sup> century, the energy and environmental issues will be more serious, while the space age should be full opened. The SHS is essentially energy saving, energy producing, self-controllable and environment-friendly process. In order to take advantage of SHS in the 21<sup>st</sup> century, we must further challenge to get more powerful abilities of precise analyzing and comprehensive understanding the very complex and delicate SHS using a modern tool of AI (Artificial Intelligence), and of fine and sophisticated control techniques for the stable and uniform combustion process. To stay on moon and Mars, it is necessary to construct space buildings, structures, and produce thermal energy using limited resources in vacuum and low gravity environment. The combination of SHS with AI and IoT (Internet of Things) may bring the new generation SHS which can act as a universal material and combustion science and technology in the space age. This is my dreaming of SHS on the earth.

## SH-SYNTHESIS OF CERAMIC MATERIALS BASED ON PRE-ACTIVATED AND MODIFIED SYSTEMS

**N. N. Mofa<sup>\*a</sup>, B. S. Sadykov<sup>a</sup>, G. Kaiypbek<sup>a</sup>, T. B. Osserov<sup>a</sup>, and D. Shaltykova<sup>a</sup>**

<sup>a</sup>Al-Farabi Kazakh National University, The Institute of Combustion Problems, Almaty, Kazakhstan

\*e-mail: nina.mofa@kaznu.kz

DOI: 10.24411/9999-0014A-2019-10100

One of the progressive ways to create materials both compact and with varying degrees of dispersion up to formation of nanostructured systems today is self-propagating high-temperature synthesis (SHS), or in other words - technological combustion [1]. The results of numerous experimental studies and theoretical calculations showed that the burning rate and temperature profile of the combustion wave during SHS are a function of many variables: the heating value of the mixture, the thermal conductivity of the combustion products, the volumetric heat release rate, the heat capacity of the products, the concentration of the initial substances and the reaction products, the diffusion coefficient of the reacting substance, activation energy of the reaction and its rate constant. With the help of various influences, it is possible to control the combustion process. The use of ultrasonic action [2] and mechanochemical treatment [3], which allow to change not only the dispersion, but also the energy state of the material, turned out to be effective.

Preliminary MCT in mechanical reactors (dynamic action mills) allows to achieve a high degree of dispersion of particles (up to 100 nm) and to change the structure, energy intensity and, consequently, reactivity of the material. When pre-activated systems are used in combustion processes, the task is to preserve the stored energy of the material for quite a long time, since it is well known that activated systems undergo aging, that is, a gradual relaxation of the energy stored in them. A real way to solve this problem is to modify the surface of particle with compounds that stabilize the energy state of the material, i.e. creating a capsule shell.

Another effective way to influence the structure and condition of various materials (liquid, amorphous, crystalline) is ultrasonic treatment (UST) of a different range of frequency, power and time, depending on the material and processing medium [4]. The main mechanisms for ultrasonic dispersion of powder materials in aqueous medium are cavitation and flows that occur in the working fluid during the collapse of cavitation cavities [5]. Erosion of the surface and destruction of particles under the influence of ultrasound leads to an increase in the chemical activity of their surface and accelerate the processes of interaction of particles of the material being processed with the processing medium. Thus, during UST, a mechanochemical effect is rendered on the material being processed. In both cases, there is a change in the structure, first of all, of the surface layers, the state and, consequently, the chemical activity of the material, which is then realized in various processes of synthesizing new materials for a specific purpose.

In this work, it is shown how, when using organic compounds containing bound water as well as carbon and ammonia groups as modifying additives during MCT, one can influence the thermokinetic characteristics of the technological combustion process (self-propagating high-temperature synthesis (SHS)), ensuring the completeness of the reaction between the main components of the reaction mixture. Mechanochemical and ultrasonic treatment of quartz, calcite (calcium carbonate) and wollastonite was carried out both individually and as a mixture of mineral powders.

Thus, MCT of a triple system including quartz, wollastonite and calcium carbonate, pre-activation and modification of components (a mixture of succinic acid with ammonia and polyvinyl alcohol) lead to a significant change in the thermokinetic characteristics of the combustion process (Fig. 1).

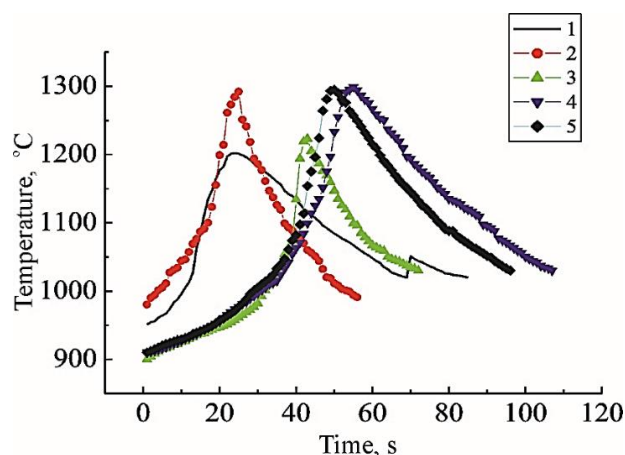


Fig. 1. Thermograms of the combustion system [(30%  $\text{CaCO}_3$  + 70%  $\text{SiO}_2$ ) + 5% wollastonite] (1) in the initial state, (2) after MCT and (3) modification with compound  $\text{C}_4\text{H}_6\text{O}_4$ , (4) with a mixture of 5%  $\text{C}_4\text{H}_6\text{O}_4$  + 5%  $\text{NH}_4\text{OH}$  and (5)  $(\text{C}_2\text{H}_3\text{OH})_n$ . MCT time was 20 min.

The modifiers used and the presence of calcium carbide in the charge after MCT enhance the role of gas-phase reactions in the combustion process of the activated system. Such conditions lead to the possibility of synthesis gas formation in the process of sample heating, which is actively involved in the combustion process, changing its thermokinetic characteristics. The result of these processes is a change in the strength of the SHS samples, which is determined by the phase composition of the synthesis products (Table 1).

Table 1. Phase composition of the combustion products of ( $\text{SiO}_2$  +  $\text{CaCO}_3$  + Al) system samples depending on the presence of wollastonite, modifier and conditions of MCT.

| Phases  | Phase content, % |      |      |      |      |      |      |
|---|------------------|------|------|------|------|------|------|
|   | Samples          |      |      |      |      |      |      |
|   | 1                | 2    | 3    | 4    | 5    | 6    | 7    |
| $\text{Al}_2\text{O}_3$                       | 42.7             | 20.8 | 32.8 | 30.7 | 32.8 | 37.3 | 30.4 |
| Si  | 20.3             | 10.3 | 12.1 | 13.2 | 17.7 | 11.8 | 10.5 |
| Al  | 7.8              | 11.1 | 5.7  | 11.6 | 8.2  | 3.5  | 9.6  |
| $\text{SiO}_2$                                | 9.2              | 3.4  | 1.9  | 1.5  | 10.6 | 1.1  | 4.5  |
| $\text{Ca}(\text{Al}_2\text{Si}_2\text{O}_8)$ |                  | 26.1 | 43.9 | 28.2 |      | 30.9 | 18.4 |
| $\text{Ca}_2\text{Al}(\text{AlSiO}_7)$        | 10.5             | 8.8  | 3.5  | 6.5  | 11.0 | 5.8  | 14.4 |
| CaO   | 5.8              |      |      |      |      |      | 1.0  |
| $\text{CaAl}_4\text{O}_7$                     |                  | 13.7 |      |      | 16.2 |      |      |
| $\text{Ca}_3\text{Si}_3\text{O}_9$            |                  |      |      |      |      |      | 5.7  |
| $\text{FeAl}_3\text{Si}_2$                    |                  | 5.7  |      | 6.7  | 3.5  | 7.2  | 5.3  |
| $\text{FeSi}_2$                               |                  |      |      | 1.5  |      | 2.3  |      |

1 (30%  $\text{CaCO}_3$  + 70%  $\text{SiO}_2$ ) + Al;  
2 (30%  $\text{CaCO}_3$  + 70%  $\text{SiO}_2$ )<sub>MCT 10 min</sub> + Al;  
3 [(30%  $\text{CaCO}_3$  + 70%  $\text{SiO}_2$ ) + 5% B\*]<sub>MCT 10 min</sub> + Al;  
4 [(30%  $\text{CaCO}_3$  + 70%  $\text{SiO}_2$ )<sub>MCT 10 min</sub> + (5% W + 5% SA\*\*)]<sub>MCT 20 min</sub> + Al;  
5 [(30%  $\text{CaCO}_3$  + 70%  $\text{SiO}_2$ )<sub>MCT 10 min</sub> + (5% W + 5% SA + 5% Ammonia)]<sub>MCT 20 min</sub> + Al;  
6 [(30%  $\text{CaCO}_3$  + 70%  $\text{SiO}_2$ )<sub>MCT 10 min</sub> + (5% W + 5% PVA\*\*\*\*)]<sub>MCT 20 min</sub> + Al;  
7 [(30%  $\text{CaCO}_3$  + 70%  $\text{SiO}_2$ )<sub>MCT 10 min</sub> + (10% W + 5% PVA\*\*\*\*)]<sub>MCT 20 min</sub> + Al;  
\*Wollastonite (W), \*\*Succinic acid (SA), \*\*\*Polyvinyl alcohol (PVA)

Activation and modification of the mixture components contribute to formation of anorthite and helenite in the combustion process. After modifying wollastonite with succinic acid and activating a mixture of quartz and marble, silicon is more completely realized in combustion reactions, wollastonite decomposes during the synthesis process, and decay products are involved in formation of anorthite, helenite, and  $\text{CaAl}_4\text{O}_7$ .

A comprehensive study of the technological combustion of systems containing wollastonite after ultrasonic treatment (UST) was also carried out. After ultrasonic treatment in aqueous solution in the presence of various modifying additives, highly dispersed particles and their aggregates are encapsulated in sufficiently dense polymer films [6]. Depending on the conditions of UST (time, frequency), the nature and level of structural changes are somewhat different, this being indicated in thermokinetic characteristics of the combustion process. Introduction of wollastonite modified during UST into the charge mixture ( $\text{SiO}_2 + \text{Al}$ ) in an amount of 10% contributes to a decrease in the induction period of the mixture ignition, an increase in the rate and temperature of combustion as well as a change in temperature at the post-process stage (Fig. 2).

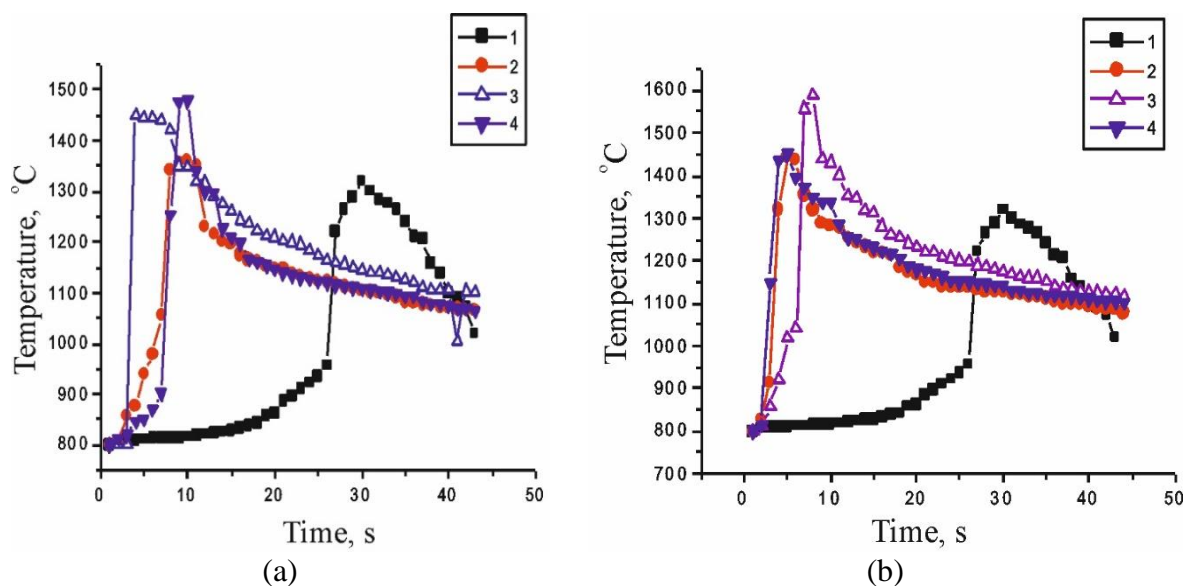


Fig. 2. Thermograms of the combustion system  $[(\text{SiO}_2 + 37.5\% \text{Al})]$  with 10% FW100 wollastonite (1) in the initial state and after ultrasonic treatment in water for (2) 20, (3) 40, and (4) 60 min at (a) a frequency of 40 kHz and (b) simultaneous exposure to 40 and 10 kHz.

The level of these characteristics varies with both the processing time and the frequency of ultrasound exposure. With introduction of various modifying additives into the medium of ultrasonic treatment of wollastonite, the general tendency to intensify the combustion process is preserved, only the parameters of the SH-synthesis process change somewhat.

One of the indicators of the quality of synthesized samples is the tensile strength. If for a synthesized sample of  $[\text{SiO}_2 + 37.5\% \text{Al}]$  system with quartz activated for 10 min in a planetary centrifugal mill the strength is 33 MPa, its values for SHS samples obtained with wollastonite modified at different conditions of UST vary significantly depending on the conditions of ultrasound modification. The measurement results are presented in Table 2. The highest strength was shown by samples containing wollastonite after ultrasonic treatment in water and in an aqueous solution of glycerin (73.15 MPa). In all cases, introduction of wollastonite into the charge after UST contributes to a more complete conversion of the initial components during the combustion of the samples [7]. The greatest amount of corundum and silicon is formed, when using wollastonite treated in water, an aqueous solution of polyvinyl alcohol and salicylic acid.

Table 2. Strength of SHS-samples [ $\text{SiO}_2 + 37.5\% \text{ Al}$ ] with 10% wollastonite modified under different conditions of UST depending on the frequency and time in different liquid media.

| Conditions of US-treatment |           | Strength of SHS-samples, MPa               |   |   |  |  |
|----------------------------|-----------|--|---|---|--|--|
| Frequency<br>$f$ , kHz     | Time, min | The medium of US-treatment of wollastonite |   |   |  |  |
|                            |           | $\text{H}_2\text{O}$                       | $\text{H}_2\text{O} + 5\% \text{ C}_3\text{H}_5(\text{OH})_3$ | $\text{H}_2\text{O} + 5\% \text{ H}_2\text{SiO}_3\text{nH}_2\text{O}$ | $\text{H}_2\text{O} + 5\% (\text{C}_2\text{H}_3\text{OH})_n$ | $\text{H}_2\text{O} + 5\% \text{ C}_9\text{H}_8\text{O}_4$ |
| 40                         | 20        | 41.8                                       | 50.16   | 25.08   | 20.9   | 62.70  |
|                            | 40        | 71.06                                      | 39.71   | 21.62   | 22.99  | 62.70  |
|                            | 60        | 62.70                                      | 41.80   | 18.81   | 35.53  | 52.25  |
| 100                        | 20        | 33.44                                      | 58.52   | 10.45   | 14.63  | 73.15  |
|                            | 40        | 31.35                                      | 12.54   | 16.75   | 33.44  | 62.70  |
|                            | 60        | 37.62                                      | 14.63   | 45.98   | 31.35  | 52.25  |
| 100 + 40                   | 20        | 41.80                                      | 18.81   | 52.25   | 39.71  | 73.15  |
|                            | 40        | 73.15                                      | 73.15   | 31.35   | 41.8   | 62.70  |
|                            | 60        | 29.26                                      | 20.90   | 27.17   | 20.9   | 62.70  |

The results of the studies clearly show that preliminary mechanochemical treatment both in dynamic mills and under ultrasonic action in liquid media is an effective way to influence the structure and the state of the material being processed, increases its reactivity, which is manifested in the changes in the thermokinetic characteristics of the combustion process (SHS mode), conversion of the reagents used, the phase composition of synthesis products and the properties of the material obtained.

1. A.E. Levashov, A.S. Rogachev, V.I. Yuxhvid, I.P. Borovinskaya, Physico-chemical and technological bases of self-propagating high-temperature synthesis, M.: BINOM, 1999, 176 p.
2. N.Z. Lyakhov, T.L. Talako, T.F. Grigorieva, The influence of mechanical activation on the phase and structure formation processes during self-propagating high-temperature synthesis, Novosibirsk: Parallel, 2008, 168 p.
3. O.V. Abramov, I.G. Kharbenko, S. Shvegla, Ultrasonic treatment of materials, M.: Mashinostroenie, 1984, 243 p.
4. A.E. Baranchikov, B.K. Ivanov, Yu.D. Tretyakov, Sonochemical synthesis of inorganic materials, *Adv. Chem.*, 2007, vol. 76, no. 2, pp. 147–168.
5. Z.A. Mansurov, N.N. Mofa, B.S. Sadykov, Zh.Zh. Sabaev, Ultrasonic treatment of wollastonite and obtaining SHS-composite systems, III Int. Sci. Conf. Modern Problems of Condensed Matter Physics, Nanotechnologies and Nanomaterials, 2014, Almaty, pp.18–20.
6. Z.A. Mansurov, N.N. Mofa, T.A. Shabanova, Hybride, nano-structured materials of special purpose on the basis of silicon dioxide, *Adv. Eng. Ceram. Compos.*, 2011, vol. 484, pp. 230–240.

## EVALUATION OF THE HOMOGENEITY OF POWDER COMPOSITIONS FOR SELF-PROPAGATING HIGH-TEMPERATURE SYNTHESIS USING SPECTRAL ANALYSIS METHODS

V. V. Mokrushin<sup>a</sup>, O. Yu. Zabrodina<sup>a</sup>, A. A. Potekhin<sup>a</sup>, I. A. Tsareva<sup>a</sup>,  
A. Yu. Postnikov<sup>a</sup>, M. V. Tsarev<sup>a</sup>, and P. G. Berezhko<sup>a</sup>

<sup>a</sup>Russian Federal Nuclear Center- All-Russian Research Institute for Experimental Physics,  
Sarov, 607188 Russia  
e-mail: mcr@dep19.vniief.ru

DOI: 10.24411/9999-0014A-2019-10101

One of the most important factors that has an effect on the self-propagating high-temperature synthesis (SHS) processes, as well as on the structure and properties of synthesis products, is the homogeneity of the initial charge mixture (see, for example, [1]). The approaches [2] for the evaluation of the homogeneity of the powder compositions for SHS using laser-induced breakdown spectroscopy (LIBS) and energy dispersive X-ray microanalysis (EDXMA), that allow to obtain and analyze spectra with the high level of locality, are proposed and tested in this paper.

Application of LIBS method with laser source of emission spectra excitation allows evaluating the homogeneity of elemental composition for SHS without determination of the concentration of separate charge mixture components [2]. For this purpose, it is calculated the ratio of arithmetical mean values of spectral lines intensities  $\bar{I}_{EI}$  of some chemical element chosen from the number of elements being part of charge mixture components, to the intensity of spectral lines of the comparison element  $\bar{I}_{Av}$ . As a rule, comparison element is the element which has the biggest mass fraction in the considered SHS composition. Under this approach we can evaluate the homogeneity of the charge mixture on the value of relative root-mean-square deviation  $V_{EI}$  of relative intensities of the chosen element spectral lines.

In the current paper we used the LIBS method to evaluate the macroheterogeneity of model powder SHS composition: Ti–Al at different times of components mixing in the hand mixer. In this case the comparison element was titanium, and we evaluated the macroheterogeneity of the mixture by analyzing spectral lines of aluminum in the samples, taken from the different portions of charge mixture volume. According to the suggested approach the analyses were done at different scales of the LIBS spectra excitation zone, specified by variation of the laser beam diameter  $D$  (see Fig. 1). The macroheterogeneity factor of charge mixture in that case was the variation coefficient  $V_{Al}$ , representing relative root-mean-square deviation of relative intensities of aluminum spectral lines, averaged on several LIBS spectra.

The obtained results (see Fig. 1) allowed to evaluate the scale zone of LIBS spectrum excitation, that corresponds to the beginning of the heterogeneous behavior manifestation of the studied mixture (laser beam diameter is less than 500  $\mu\text{m}$ ), as well as they clearly demonstrated the reduction of the SHS composition macroheterogeneity with the increase of the time of its components mixing.

The suggested approach for the evaluation of SHS composition homogeneity using spectral methods of analysis, consisting of the analysis of the dependence of some charge mixture component on the scale of the spectrum excitation zone, also allows determining the scale factors of homogeneity through numerical values of the «correlation radius» notion determined from the fractal theory [3]. This parameter characterizes the behavior of the heterogeneous systems properties while changing the consideration scale (sampling size or spectrum excitation zone), and corresponds to the transition from homogeneous behavior to the fractal behavior.



At scales bigger than  $\xi_1$ , heterogeneous systems behave as homogeneous systems, in the sense that their properties don't depend on sampling size, whereas at scales less than  $\xi_2$ , system properties depend a lot not only on the sampling size, but on its coordinates as well. As a rule, between  $\xi_2$  and  $\xi_1$  there is a zone of microinhomogeneous behavior, which is characterized by weak dependence on the consideration scale.

In the case of energy dispersive X-ray microanalysis application for the evaluation of the SHS composition homogeneity, the suggested approach [2] consists of the analysis of the dependence of any component content in surface and subsurface charge mixture layers on the scale of scanning zone. Thus concerning the studied model composition: Ti–Al, in the current paper we determined the homogeneity scale zones on the basis of the results for determination of the aluminum content in the surface and subsurface charge mixture layers, that were obtained at different growth ratio (see Fig. 2).

The obtained results (see Fig. 2) allowed to select the scale zones of energy dispersive X-ray spectrum excitation ( $\xi_1$  and  $\xi_2$ ), which correspond to homogeneous (more than  $\sim 430 \mu\text{m}$ ) and inhomogeneous (less than  $\sim 110 \mu\text{m}$ ) behavior of the studied SHS composition, as well as to the transition microinhomogeneous zone being between them. At the same time the comparison of the data, obtained by LIBS and EDXMA, allowed to conclude that the differences in the homogeneity of the studied composition samples, differing by various times of mixing in the hand mixer, appear only at scales less than  $500 \mu\text{m}$  (see Fig. 2), that is to say in the zones of microinhomogeneous and inhomogeneous behavior of the mixture (see Fig. 1).

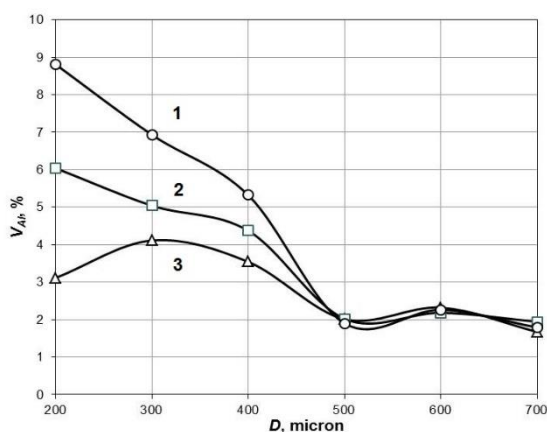


Fig. 1. Dependence of the macroheterogeneity variation coefficient of the SHS composition: Ti–Al on laser beam diameter, used while obtaining LIBS spectra, for the samples with different mixing time: 1 5 min; 2 10 min; 3 20 min.

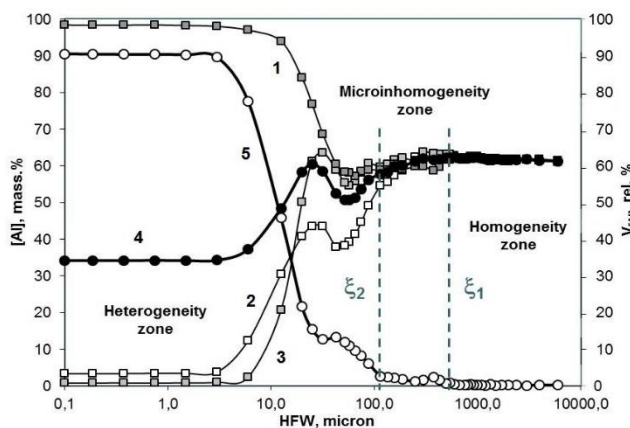


Fig. 2. Dependence of the aluminum content in the surface and subsurface layers of Ti–Al mixture (mixing time is 5 min), determined by EDXMA (the left axis), on the size of randomly selected scanning zone (Horizontal Field Width): 1 zone 1; 2 zone 2; 3 zone 3; 4 average value of [Al]; 5 variation coefficient  $V_{[Al]}$  (the right axis).

Thus, the approach to the evaluation of the powder SHS compositions homogeneity using laser-induced breakdown spectroscopy and energy dispersive X-ray microanalysis is proposed and tested in this work. With the example of studying of Ti–Al model mixture the work shows that the combination of the stated methods allows to combine the advantages of LIBS, characterizing the homogeneity of the chemical composition in the material volume, with the advantages of EDXMA, allowing to evaluate the homogeneity of the surface and subsurface layers of the charge mixture with the high level of discretization and locality, as well as to select the scale zones of the homogeneity.

1. A.G. Merzhanov, SHS development concept, as a domain of the scientific and technical progress. Chernogolovka: Territory, 2003.
2. I.M. Sokolov, *Phys. Success*, 1986, vol. 150, iss. 2, pp. 233–237.
3. V.V. Mokrushin, A.A. Potekhin, P.G. Berezhko, A.Yu. Postnikov, I.A. Tsareva, O.Yu. Yunchina, Technique of the determination of homogeneity factor for disperse material by spectral method and technique of the determination of homogeneity scale limits for disperse material by spectral method, *RF Patent 2646427*, priority of 24.01.2017; published on 05.03.2018, Bull. no. 7.

## REACTION SPARK PLASMA SINTERING OF BINARY AND HIGH-ENTROPY CARBIDES

D. O. Moskovskikh<sup>\*a</sup> and A. S. Mukasyan<sup>b</sup><sup>a</sup>National University of Science and Technology MISiS, Moscow, Russia<sup>b</sup>University of Notre Dame, Notre Dame, USA

\*e-mail: mos@misis.ru

DOI: 10.24411/9999-0014A-2019-10102

The work describes the production of bulk ceramic materials by spark plasma sintering (RSPS). The proposed method allows one to manufacture bulk ceramics based on SiC, B<sub>4</sub>C, HfC, Al<sub>2</sub>O<sub>3</sub>-SiC, and equiatomic Hf<sub>0.2</sub>Ta<sub>0.2</sub>Ti<sub>0.2</sub>Nb<sub>0.2</sub>Zr<sub>0.2</sub>C and Hf<sub>0.2</sub>Ta<sub>0.2</sub>Ti<sub>0.2</sub>Nb<sub>0.2</sub>Mo<sub>0.2</sub>C high-entropy ultra-high temperature carbides in one step. By short-term high-energy ball milling (HEBM) of mixtures of metal and carbon powders, we were able to produce nanostructured composite particles with elements mixed at the submicron level. The small size of the reagent particles and the large surface area of contact between them can significantly accelerate the reaction and the consolidation processes during the SPS, leading to the formation of low-porosity ceramics (< 5%) with fine (~ 5 μm) carbide grains and good mechanical properties. For example, optimization of HEBM + RSPS conditions allows rapid (less than 30 min of SPS) fabrication of B<sub>4</sub>C ceramics with porosity less than 2%, the hardness of ~ 35 GPa and fracture toughness of ~ 4.5 MPa m<sup>1/2</sup> as well as fabrication of SiC ceramics with a hardness of ~ 24 GPa and fracture toughness of ~ 5 MPa m<sup>1/2</sup>.

High-entropy ceramics were prepared in two steps. First, metallic high-entropy alloys Hf<sub>0.2</sub>Ta<sub>0.2</sub>Ti<sub>0.2</sub>Nb<sub>0.2</sub>Zr<sub>0.2</sub> and Hf<sub>0.2</sub>Ta<sub>0.2</sub>Ti<sub>0.2</sub>Nb<sub>0.2</sub>Mo<sub>0.2</sub> were produced by HEBM, then graphite powder was added to the alloy and mixture was milled for another 5 minutes. By the SPS of the resulting mixture, samples with the relative density up to 96%, hardness up to 33 GPa and Young modulus up to 570 GPa were produced. The composition Hf<sub>0.2</sub>Ta<sub>0.2</sub>Ti<sub>0.2</sub>Nb<sub>0.2</sub>Zr<sub>0.2</sub>C with the higher entropy-forming ability (100 (eV/atom)<sup>-1</sup>) was resistant against selective oxidation and formation of oxide phases during the sintering, whereas the composition Hf<sub>0.2</sub>Ta<sub>0.2</sub>Ti<sub>0.2</sub>Nb<sub>0.2</sub>Mo<sub>0.2</sub>C with lower entropy-forming ability (83 (eV/atom)<sup>-1</sup>) was prone to extensive formation of HfO<sub>2</sub> under the same processing conditions.

The RSPS method allows one to produce ceramics with at least comparable in properties with SPS counterparts, with greater energy efficiency and skipping the stage of the ceramic powder synthesis.

## ELIMINATION OF SURFACE DEFECTS OF SLM PRODUCTS DUE TO A SYNTHESIS OF NiAl INTERMETALLIC AT ELECTRO-SPARK DEPOSITION OF Al-CONTAINING PRECURSOR

S. K. Mukanov<sup>\*a</sup>, M. I. Petrzhik<sup>a</sup>, A. E. Kudryashov<sup>a</sup>, and E. A. Levashov<sup>a</sup>

<sup>a</sup>National University of Science and Technology MISiS, Moscow, 119049 Russia

<sup>\*</sup>e-mail: sam-mukanov@mail.ru

DOI: 10.24411/9999-0014A-2019-10103

Selective laser melting (SLM) is a kind of additive manufacturing, which consists in the obtaining parts of complex shape by layer-by-layer melting of a metal powder using a laser beam scanning [1]. A characteristic feature of SLM alloys is an increased surface roughness due to a formation of surface defects as pimples, microcracks, pores, etc. [2–5]. Pulsed electrospark deposition (ESD) is successfully used for surface modification to restore damaged or worn surfaces and working edges of the used parts due to simplicity and efficiency of the technology [6–8]. Thus, new prospects are opening up applying an electrospark modification of SLM parts to improve their roughness and geometry.

In this work, SLM parts based on alloys having in structure nickel aluminides which are prone to surface cracking at the production process [3, 4] were used. To develop the combined SLM + ESD technology it is necessary to tailor novel electrode materials and modes of ESD to secure a reactive formation of desired phases at modified surface layers free of all undesirable surface defects and having high performance properties.

The aim of the study is to apply electrospark deposition for surface modification of nickel-containing SLM parts using precursor-electrodes made of AK9 hypoeutectic aluminum alloy. The idea of the work is to create on the surface of SLM parts a modified layer formed by the local chemical interaction of the elements contained in both the precursor (Al) and SLM (Ni) products. It is expected that the precursor will locally melt at ESD, the molten near-eutectic Al–Si–Ni alloy will spread, interact with Ni of SLM substrate and fill in near-surface pores and cracks, leveling the surface relief and form reinforcing intermetallic phases during solidification.

An object of study was SLM alloy [1, 9, 10] Ni<sub>41</sub>Al<sub>41</sub>Cr<sub>14</sub>Co<sub>4</sub> with a dimension of 7 × 9 × 7 mm. To ensure the formation of low-melting drops at ESD process, a specially prepared precursor cut off from the AK9 alloy [11] was quenched from the melt to suppress the formation of primary crystals and coarse eutectics to obtain homogeneous structure cast rod.

ESD was performed on the ALIER-303 METAL experimental stand using high-frequency discharge mode ( $f = 3200$  Hz,  $I = 120$  A,  $\tau = 25$   $\mu$ s,  $U = 20$  V). The formation of the surface layers was carried out under protective atmosphere of argon by repeated scans of the precursor on the surface of conductive substrate in 120 s. Microstructure of the surface layer and its cross-section was studied using a S-3400N scanning electron microscope (SEM) ("Hitachi", Japan). To determine the surface roughness, a WYKO NT1100 (Veeco, USA) optical profiling system was used. X-ray diffraction analysis performed using a DRON-3 (Russia) diffractometer with monochrome Cu radiation was used to estimate the phase composition of samples. The study of hardness and Young's modulus near surface of polished cross-sections was carried by instrumented nanoindentation using a Nano-Hardness Tester (CSM Instruments, Switzerland).

Figures 1a and 1b show the morphology of the surface of SLM specimen. One can see defects in the form of microcracks and non-melted spherical particles of the original NiAl micropowder. In addition, there are areas containing Al and O in the ratio of 37:63 (Table 1, region 2), possibly based on aluminum oxide Al<sub>2</sub>O<sub>3</sub>.

After the electrospark modification with an aluminum contained precursor using high-frequency processing mode, a decrease in the width of surface cracks was observed, the presence of defects in the form of spherical particles was not detected (Figs. 1c, 1d). The thickness of the modified layer was 10.0–13.5  $\mu\text{m}$  as shown in Fig. 1c.

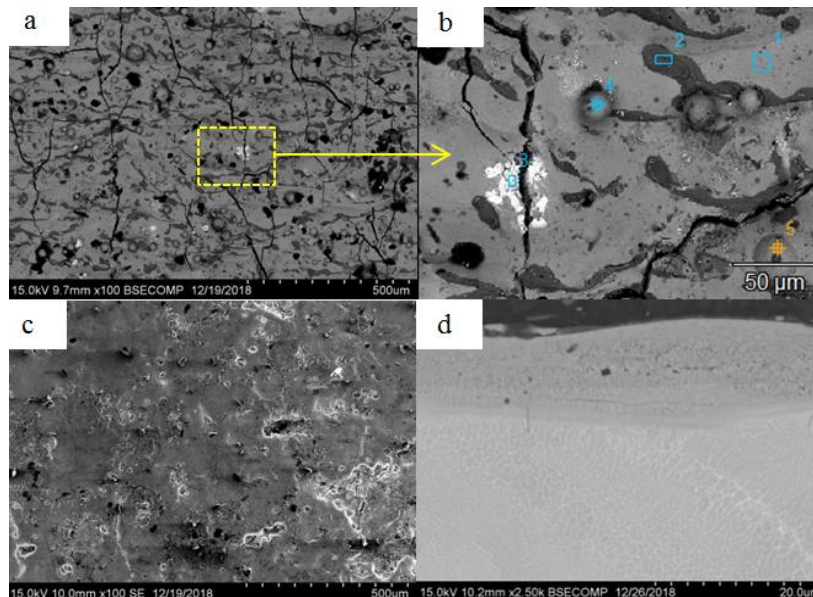


Fig. 1. The microstructure of the surface of the SLM sample: (a)  $\times 100$ ; (b)  $\times 500$ ; (c) the surface of the layer  $\times 100$ ; (d) cross-section  $\times 2500$ .

Table 1. The composition of the regions of the EDX for the SLM sample.

| Region of analysis | Content of elements, at % |      |      |     |      |      |
|--------------------|---------------------------|------|------|-----|------|------|
|                    | Ni                        | Al   | Cr   | Co  | Hf   | O    |
| 1 (matrix)         | 44.4                      | 41.9 | 7.4  | 6.3 | –    | –    |
| 2                  | –                         | 36.7 | –    | –   | 1.2  | 62.2 |
| 3                  | 18.6                      | 10.4 | 10.7 | 4.5 | 20.3 | 35.4 |
| 4                  | 37.2                      | 52.1 | 5.0  | 5.7 | –    | –    |
| 5                  | 34.3                      | 57.6 | 3.8  | 4.3 | –    | –    |

Figure 2 shows an image of a cross-section with a healed microcracks in an SLM sample subjected electrospark modification. EDX analysis showed that the concentration of elements in the composition of the surface layer (Table 2, spectrum 1) and the filled crack (Table 2, spectrum 2) are almost the same. The ratio of the atomic concentrations of Al to Ni is  $\sim 3$  and has the same ratio with the intermetallic compound  $\text{NiAl}_3$ , i.e. during ESD the synthesis of nickel aluminide with an excess of aluminum was done. ES processing leads to filling in surface cracks of the initial sample with Ni–Al–Si melt. The depth of filled in cracks reaches 34  $\mu\text{m}$ , and then the molten drop solidifies, having not enough time to completely fill in the microcrack.

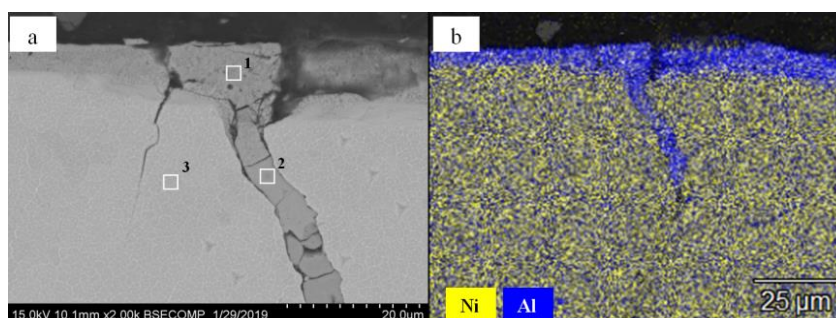


Fig. 2. (a) Image of the cross-section and (b) element map.

Table 2. Composition of the regions of the EDX for the ESD layer.

| Region of analysis | Content of elements, at % |      |     |     |     |
|--------------------|---------------------------|------|-----|-----|-----|
|                    | Al                        | Ni   | Si  | Cr  | Co  |
| 1                  | 61.8                      | 24.8 | 2.9 | 6.4 | 4.0 |
| 2                  | 67.8                      | 19.9 | 4.3 | 5.3 | 2.7 |
| 3                  | 41.3                      | 44.2 |     | 9.4 | 5.2 |

Studies of the original SLM sample by XRD analysis showed (Fig. 3a) that it consists of two phases: intermetallic NiAl and chromium-based solid solution [9]. It should be noted that both these phases have similar lattice periods, which gives a significant error in the analysis of the spectra [1, 9]. As can be seen in Table 3, ESD leads to the formation on the surface of 100% NiAl intermetallic (Fig. 3b). The spectra of the surface layer completely coincide and correspond to the NiAl phase with a cubic crystal system and lattice periods of 0.2879 nm, which is consistent with literature data of 0.2887 nm [12]. Additional phases which is characteristic of the substrate material were not detected.

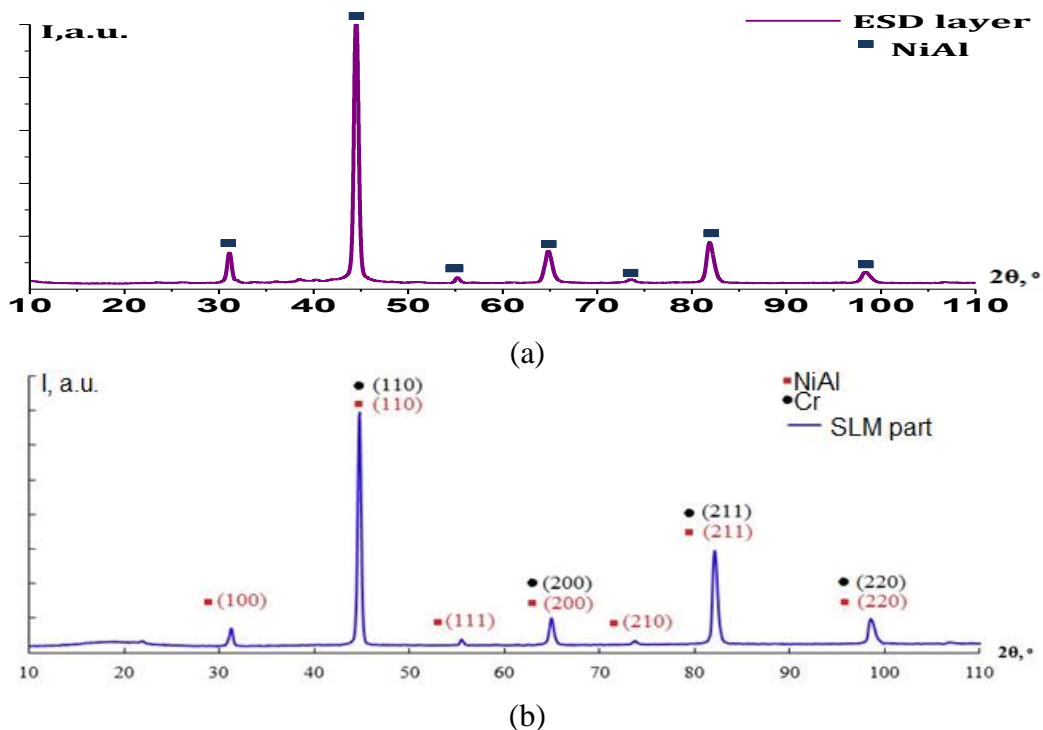


Fig. 3. X-ray diffraction spectra of samples: (a) SLM part; (b) ESD layer.

Table 3. Phase composition of the electrospark deposited layer.

| Phase | Structure type | Volume fraction, % | Weight fraction, % | Period, nm |
|-------|----------------|--------------------|--------------------|------------|
| NiAl  | cP2/1          | 100.0 ± 0.0        | 100.0 ± 0.0        | 0.2879     |

So, the hypothesis that during the ESD process a molten Al-enriched precursor would interact with an Ni-enriched SLM substrate resulting in reactive formation of NiAl intermetallic was confirmed.

The surface roughness of the SLM sample was  $R_a = 8.37 \pm 0.22 \mu\text{m}$ . ESD leads to a decrease in the surface roughness due to the filling of cracks (Fig. 2), which leads to the leveling of the surface and is  $R_a = 3.41 \pm 0.13 \mu\text{m}$  (Fig. 4). The 2D profiles shown in Fig. 4c clearly show how irregularities in the form of depressions are present on the sample surface along the baseline. the synthesis of Al-containing precursor leads to a decrease in such irregularities.

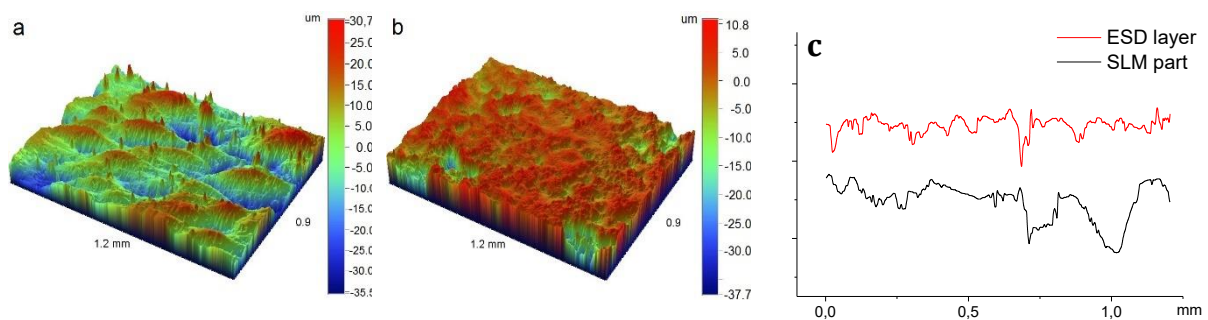


Fig. 4. Topography of the sample surface: (a) SLM part; (b) ESD layer; (c) 2D profilogram.

The study of mechanical properties was carried out in several areas of the SLM sample and the modified surface layer. The test showed that during the ESD stimulated synthesis of NiAl intermetallic a harder surface layer was formed. Its hardness value was  $10.9 \pm 0.5$  GPa, whereas the hardness of the original SLM alloy was  $6.2 \pm 0.2$  GPa.

Thus, the possibility of using ESD for surface modification of nickel-containing SLM parts was tested. A modified layer based on nickel aluminide was obtained by electrospark deposition of a rapidly quenched Al-containing precursor on the defective surface of an SLM part from nickel alloy. This work demonstrates that ESD allows to improve the surface quality of SLM products by means reducing the surface roughness and filling the microcracks, as well as increase the surface strength.

The reported study was funded by Russian Foundation for Basic Research (RFBR) and Bulgarian National Science Fund (BNSF) according to the research project no. 19-58-18022.

1. Yu.Yu. Kaplanskii, A.A. Zaitsev, E.A. Levashov, P.A. Loginov, Zh.A. Sentyurina, NiAl based alloy produced by HIP and SLM of pre-alloyed spherical powders. Evolution of the structure and mechanical behavior at high temperatures, *Mater. Sci. Eng. A*, 2018, vol. 717, pp. 48–59.
2. P.D. Enrique, E. Marzbanrad, Y. Mahmoodkhani, Z. Jiao, E. Toyserkani, N.Y. Zhou, Surface modification of binder-jet additive manufactured Inconel 625 via electrospark deposition, *Surf. Coat. Technol.*, 2019, vol. 362, pp. 141–149.
3. L.N. Carter, Ch. Martin, Ph.J. Withers, M.M. Attallah, The influence of the laser scan strategy on grain structure and cracking behaviour in SLM powder-bed fabricated nickel superalloy, *J. Alloys Compd.*, 2014, vol. 615, pp. 338–347.
4. Ch. Qiu, Ch. Panwisawas, M. Ward, et al, On the role of melt flow into the surface structure and porosity development during selective laser melting, *Acta Mater.*, 2015, vol. 96, pp. 72–79.
5. M. Leary, Surface roughness optimization for selective laser melting (SLM): Accommodating relevant and irrelevant surfaces, *Laser Addit. Manuf. Mater. Des. Technol.*, 2017, pp. 99–118.
6. A.E. Kudryashov, E.A. Levashov, L.B. Aksenov, V.M. Petrov, Use of electric spark alloying technology and promising nanostructured electrode materials for improving the life of punching equipment, *Metallurgist*, 2010, vol. 54, nos. 7–8, pp. 514–522.
7. E.A. Levashov, E.I. Zamulaeva, A.E. Kudryashov, M. Petrzhik, et al, Materials science and technological aspects of electrospark deposition of nanostructured WC–Co coatings onto titanium substrates, *Plasm. Proc. Polym.*, 2007, vol. 4, pp. 293–300.
8. A.E. Kudryashov, D.N. Lebedev, A.Yu. Potanin, E.A. Levashov, Structure and properties of coatings produced by pulsed electrospark deposition on nickel alloy using Mo–Si–B electrodes, *Surf. Coat. Technol.*, 2018, vol. 335, pp. 104–117.

9. A.A. Zaitsev, Z.A. Sentyurina, E.A. Levashov, Yu.S. Pogozhev, V.N. Sanin, P.A. Loginov, M.I. Petrzhek, Structure and properties of NiAl–Cr(Co,Hf) alloys prepared by centrifugal SHS casting. Part 1 – Room temperature investigations, *Mater. Sci. Eng. A*, 2017, vol. 690, pp. 463–472.
10. A.A. Zaitsev, Z.A. Sentyurina, E.A. Levashov, Yu.S. Pogozhev, V.N. Sanin, D.A. Sidorenko, Structure and properties of NiAl–Cr(Co,Hf) alloys prepared by centrifugal SHS casting followed by vacuum induction remelting. Part 2–Evolution of the structure and mechanical behavior at high temperature, *Mater. Sci. Eng. A*, 2017, vol. 690, pp. 473–481.
11. GOST 1583-93, Aluminium casting alloys. Specifications, M. Izd. Stand., 2003, 24 p.
12. D.B. Miracle, R. Darolia, NiAl and its alloys, *Intermet. Compd.*, 1995, vol. 2, pp. 55–74.



## SHS CERAMICS: HISTORY AND RECENT ADVANCES

A. S. Mukasyan

University of Notre Dame, Notre Dame, Indiana, 46556 USA  
National University of Science and Technology MISiS, Moscow, 119049 Russia  
e-mail: amoukasi@nd.edu

DOI: 10.24411/9999-0014A-2019-10104

The fundamental paradigm for self-propagating high-temperature synthesis (SHS) of ceramics consists of exothermic self-sustained reactions that, without any external heat sources, lead to formation of non-metallic inorganic solid materials comprising metal and non-metal atoms primarily held by ionic and covalent bonds. The term ‘ceramics’ comes from Greek word ‘Keramos’, which is related to an old Sanskrit root meaning “to burn”. Thus, SHS of ceramics is probably the closest technology to the root meaning of the term, since it uses combustion, i.e. ‘burning’, for both synthesis and consolidation of the materials.

History of the SHS is overviewed in many publications (c.f. [1–3]). No doubt that, while having predecessors, including works by N.N. Beketov and H. Goldschmidt, only after thorough fundamental research initiated by A.G. Merzhanov and co-workers, this approach became the widely recognized technology for synthesis of almost any type of compounds, and ceramics were among the first materials fabricated by SHS method. Statistical analysis of publications shows that the CS method for fabrication of materials attracts attention of more and more researchers and engineers, currently scientists in 117 countries are involved in the CS field and number of related publications increases exponentially (Fig. 1).

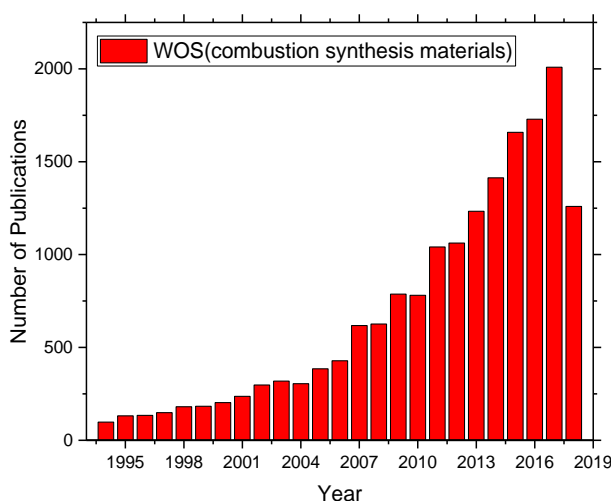


Fig. 1. Dynamic of the citations in the field of combustion synthesis of materials.

Conventional reaction sintering (RS) method for ceramic fabrication also involves synthesis and consolidation. However, in the latter case external heat source (e.g. furnace) is used to assist these processes. Moreover, during RS one has to avoid conditions (e.g. local overheating), which may lead to the “uncontrollable” events associated with self-sustained interactions. Thus, SHS can be considered as a limiting route of RS, when preheating conditions lead to local self-initiation of the reaction followed by its propagation along the media.

Advantages and disadvantages of RS and SHS are as follows. On the one hand, during RS, one may essentially independently vary processing parameters, such as temperature, pressure

and time, which, by trial-and-error strategy, allows optimization of the conditions for fabrication of materials with desired microstructure and thus properties. However, the SR is long (hours) and energy consuming method, which requires an expensive and complicated equipment. On the other hand, rapid (seconds), energy saving SHS method needs simple equipment. Nevertheless, all parameters of SHS process are strongly correlated and it is impossible to change one of them keeping the others unaffected. Thus, the issue of process controllability becomes critical. After years of research, we now may confidently state, that based on the fundamental knowledge of the mechanism for self-sustained heterogeneous reactions, one may control the SHS process. Indeed, many examples demonstrate the durability of SHS for controlling of the microstructure and properties of the materials (c.f. [4–7]). This is an important nowadays conclusion.

All systems, which lead to the SHS of ceramics, can be subdivided into two main classes:

- reactive solid powder mixtures in inert or reactive gaseous atmosphere – heterogeneous SHS;
- reactive aqueous solutions in inert or reactive gaseous atmosphere – solution combustion synthesis (SCS).

Heterogeneous SHS can be sub-divided into several groups. First group involves solid-solid systems in which compounds are produced from the elements. Examples of ceramics which are produced by SHS include, carbides (metal: TiC, ZrC, HfC, NbC, TaC and nonmetal: SiC, B<sub>4</sub>C) and borides (TiB, TiB<sub>2</sub>, ZrB, ZrB<sub>2</sub>, NbB, NbB<sub>2</sub>, TaB<sub>2</sub> etc.). Contribution of V. Shkiro, who is one of the co-founder of the solid flame discovery, in investigation of the combustion mechanism in Ti–C system is difficult to overestimate. These works led to the development of technology for fabrication of the SHS/TiC-based polishing pastes, which found wide commercial applications. Titanium boride was one of the first compound synthesized by combustion method. Powder of TiB<sub>2</sub> also was produced on industrial level by SHS method.

Second group consists of solid-gas systems and permits SHS of oxides, nitrides and hydride-based ceramics. It is worth noting that, because of their extremely high exothermicity, the SHS of oxides by gas-solid reactions is probably not effective approach. Solution combustion synthesis is typically used to fabricate different nano-sized oxide powders. However, we want to outline works by M. Nersesyan on developing of continuous SHS-based technology for production of ferrites, which found industrial application. Special case is SHS of nitride-based ceramics, including metallic nitride (TiN, ZrN, HfN, TaN, and AlN etc.), nonmetallic nitrides (Si<sub>3</sub>N<sub>4</sub>, h-BN, c-BN etc.) and oxinitides (AlONs, SiAlONs etc.) [8]. An important concept of infiltration combustion has been established based on pioneering experimental works on metal combustion in nitrogen by I. Borovinskaya, Yu. Volodin, A. Pityulin, V. Loryan and theoretical studies by A. Aldushin. SHS-based technology for nitriding of ferrovanadium alloy developed by M. Ziatdinov found wide industrial application. Contributions of V. Martinenko and V. Prokudina in establishing of SHS technologies for production of silicon and aluminum nitrides should be outlined. Industrial production of silicon nitride had history on the SHS production plant in Spain.

Third group of SHS systems involves so-called thermite type of reaction systems that include stage during which one element (typically Mg, Al or C) reduce metal (e.g. TiO<sub>2</sub>) or nonmetal (B<sub>2</sub>O<sub>3</sub>) oxides to produce elements (e.g. Ti and B), which may be followed by reaction between the elements to produced ceramics (e.g. TiB<sub>2</sub> or BN). In our opinion, this approach is preferable for fabrication of fine non-oxide ceramic powders by using combustion-based technology. The necessity of additional chemical leaching of MgO from combustion product does not make this method too complex. However, as it was shown in works by S. Mamyán, this method requires detailed optimization of the composition for the initial reactive powder mixture. The extremely high exothermicity of some thermite systems allows one to produce large corundum crystals when using Al as a reducing element.

Forth group of SHS systems includes so-called displacement reactions, in which one element displaces another from a compound. It is worth noting that thermite reactions represent a specific type of displacement reactions, but historically they made a separate class of combustion system. Metathesis self-sustained reactions that sometimes called double replacement or double decomposition reactions, which involves the exchange of bonds between two chemical compounds, also belong to this group of SHS systems. On the best of our knowledge, metathesis systems were brought to SHS field by I. Parkin from University College London and, as it will be shown in this presentation, currently such reactions are widely used to fabricate different type of bulk SHS ceramics, including borides, nitrides and carbides.

Solution combustion synthesis (SCS) involves propagation of self-sustained exothermic reactions along an aqueous or sol-gel homogeneous media. SCS allows for the synthesis of nanoscale materials and coatings (cf. [7]). It provides easy formation of high-quality multi-element compounds with complex crystal structures, such as perovskites, garnets, spinels, silicates, and phosphates. SCS also permits for efficient doping of materials, even with a trace amount of elements. Additional details on the historical achievements in SHS field can be found in the Concise Encyclopedia of Self-Propagating High-Temperature Synthesis [9].

Recent works in the SHS field demonstrate new capabilities of SHS approach. We will focus on the following novel directions:

- Fabrication of 1D, 2D, and 3D nanopowder (Fig. 2, see also review [6]);
- Direct production of bulk ceramics by combination of SHS and spark plasma sintering (Fig. 3, see review also [5, 10]);
- SHS of non-equilibrium phases;
- High entropy ceramics by SHS;
- Nano-sized materials synthesized by combination of mechanical activation and SHS processes [6–8];
- Ultra-high temperature ceramics [10];
- Ceramics by SHS and shock wave [11];
- SCS ceramics, including, inorganic phosphorous, functional ceramics, electro- and magnetic- ceramics, coatings and bio ceramics [8].

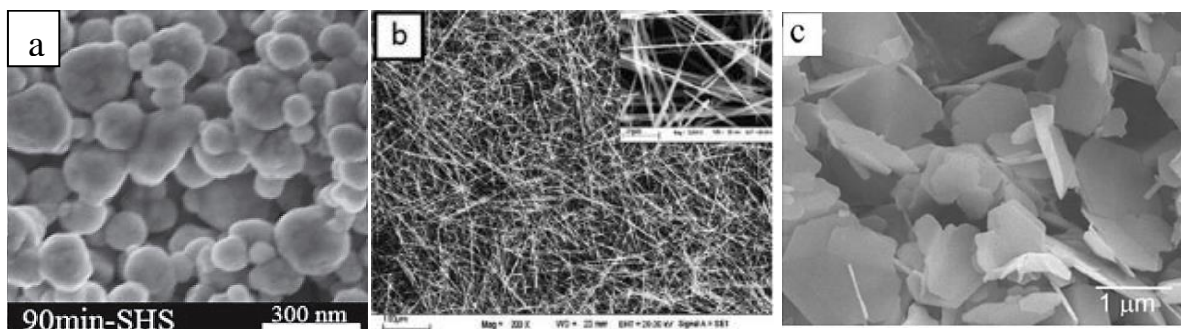


Fig. 2. Typical microstructure of SHS nanopowder: (a) 3D-SiC; (b) 1D-Si<sub>3</sub>N<sub>4</sub>; (c) 2D-BN.

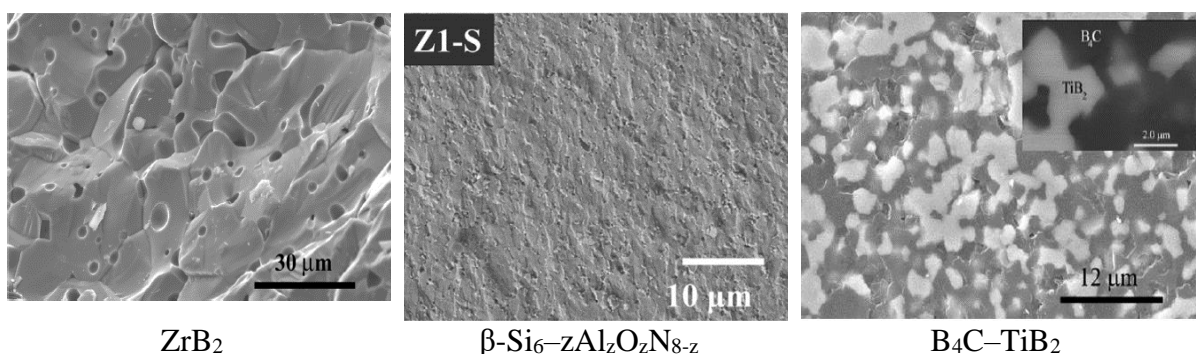


Fig. 3. Typical microstructure of SHS bulk ceramics.

It is concluded that combustion-based methods allow fabrication of a wide variety of ceramics: powders, bulk materials, coatings and net shape articles. Nanomaterials of any dimensions can be also produced through self-sustained reactions. Several advantages of the approach can be outlined. The unique conditions of the combustion approaches (e.g. high temperatures, rapid self-heating and cooling) facilitate formation of non-equilibrium phases. Other specific feature of SHS is its ability to produce multi element compounds with complex crystal structures. In addition, the SHS permits scale of materials production. Indeed, increasing the amount of reactive mixture leads to more adiabatic conditions and thus more steady-state combustion regime. Finally, the SHS allows continuous schemes for processing of different ceramics.

However, several limitations of SHS should to be resolved, before this method can be widely implemented in large-scale production of advanced ceramics. The main issues are related to the uniformity of the morphology and microstructure for the produced materials and controllability of SHS process. In this regards it is important that many recent works showed that by investigating the mechanisms of the combustion reactions and structural transformations, which occur during SHS, one might establish effective ways to control the structure of the ceramic materials. Indeed, during the last decade, CS direction made several significant steps ahead in finding new routes of material synthesis. From completely not controlled thermal explosion by heating in furnace, to precisely controlled steady state self-propagating mode. From agglomerates with non-uniform microstructures, to super fine (less than 10 nm) nanoparticles. From powders to thin films and 1D and 2D crystals. From porous bulk materials to pore-free nanostructured net-shape articles.

This work was supported by the Department of Energy, National Nuclear Security Administration; under the award number DE-NA0002377 as part of the Predictive Science Academic Alliance Program II. We acknowledge the financial support of the Ministry of Science and Higher Education of the Russian Federation in the framework of Increase Competitiveness Program of NUST «MISiS» (no. K2-2017-083), implemented by a governmental decree dated 16 the of March 2013, N 211.

1. A.G. Merzhanov, 40 years of SHS: A Lucky Star of Scientific Discovery, Bentham Science Publisher, Brussel, Belgium, 2012, pp. 1–104.
2. V. Hlavacek, Combustion synthesis: A historical perspective, Amer, *Ceram. Soc. Bull.*, 1991, vol. 70, no. 2, pp. 240–243.
3. A.G. Merzhanov, History and recent development in SHS, *Ceram. Int.*, 1995, vol. 21, no. 5, pp. 371–379.
4. A.S. Rogachev, A.S. Mukasyan, Combustion for Material Synthesis, CRC Press, Taylor and Francis, 2015, pp.1–398.
5. E.A. Levashov, A.S. Mukasyan, A.S. Rogachev, D.V. Shtansky, *Int. Mater. Rev.*, 2017, vol. 62, no. 4, pp. 203–239.
6. H.H. Nersisyan, J.H. Lee, J.R. Ding, K.S. Kim, K. Manukyan, A.S. Mukasyan, Combustion synthesis of zero-, one-, two- and three-dimensional nanostructures: Current trends and future perspectives, *Prog. Ener. Combust. Sci.*, 2017, vol. 63, pp. 79–118.
7. A. Varma, A.S. Mukasyan, A.S. Rogachev. K. Manukyan, *Chem. Rev.*, 2016, vol. 116, pp. 14493–14586.
8. A.A. Gromov, L. Chukhlomina, Nitride Ceramics: Combustion Synthesis and Applications, Wiley, VCH, 2014, pp.1–234.
9. I. Borovinskaya, A. Gromov, E. Levashov, A.S. Mukasyan, A. Rogachev, Concise Encyclopedia of Self-Propagating High-Temperature Synthesis, 1-st Edition, Editors: Elsevier, Amsterdam, Netherlands, 2017.

10. R. Orrù, G. Cao, Comparison of reactive and non-reactive spark plasma sintering routes for the fabrication of monolithic and composite ultra high temperature ceramics (UHTC), *Mater.*, 2013, vol. 6, pp. 1566–1583.
11. M.T. Beason, J.M. Pauls, I.E. Gunduz, S. Rouvimov, K.V. Manukyan, K. Matous, S.F. Son, A.S. Mukasyan, Shock-induced reaction synthesis of cubic boron nitride, *APL*, 2018, vol. 112, no. 17, 171903.

## THE EXCLUSIVE ROLE OF THE INITIATION TEMPERATURE IN THE START OF NANOSCALE SOLID-STATE REACTIONS

V. G. Myagkov

Kirensky Institute of Physics, Federal Research Center KSC SB RAS,  
Krasnoyarsk, 660036 Russia  
e-mail: miagkov@iph.krasn.ru

DOI: 10.24411/9999-0014A-2019-10105

Control and predictability of the synthesis of new materials is one of the most fundamental challenges in material science. The prediction of the phases in binary systems that will be formed during the thin-film solid-state reaction has been a subject of numerous studies, and different empirical rules have been developed for predicting first phase formation. Studies of solid-state reactions in nanolayers showed three fundamental features that strongly distinguish them from bulk powders:

(i) Formation of only the first phase at the film reagent interface at a certain temperature called the initiation (formation) temperature  $T_{in}$ . As the annealing temperature is increased, other phases can occur and form the phase sequence.

(ii) The threshold of the reaction, characterized by intense intermixing at the interface and formation of compounds, arises at temperatures above initiation (formation) temperature  $T_{in}$ . The values of  $T_{in}$  in the first phase can be about room temperature or even at cryogenic temperatures.

(iii) Migration of the dominant diffusing species through the interface during first phase formation.

The formation of only the first phase among equilibrium phases, low initiation temperatures, and migration of the dominant diffusing species are unique, unexplained features of solid-state reactions in nanofilms. From the above results it follows that the first phase and its initiation temperature  $T_{in}$  are control characteristics of the thin-film solid-state reactions. The initiation temperatures  $T_{in}$  of the first phase for most bilayers (multilayers) lie below 400°C. However, many thin-film reactions are initiated near room temperature and even at cryogenic temperatures. At such low temperatures, diffusion is extremely small and cannot provide the transfer of atoms in the solid state. This suggests an alternative view, in which chemical interactions rather than diffusion ones take place, plays a crucial role in the initiation and kinetics of interphase reactions in the solid state [1–3].

Previously, it was shown that the initiation temperatures  $T_{in}$  are close or coincide with the solid-state transformation temperatures  $T_k$  of the reagent-based binary system, such as order-disorder transitions, the superionic transition, the spinodal decomposition and others [1–3]. In particular, initiation temperatures  $T_{in}(\text{Cu}/\text{Au})$ ,  $T_{in}(\text{Pd}/\text{Fe})$ ,  $T_{in}(\text{Co}/\text{Pt})$ ,  $T_{in}(\text{Ni}/\text{Fe})$ , and  $T_{in}(\text{Cu}/\text{Fe})$  of reactions in the Cu/Au, Pd/Fe, Co/Pt, Ni/Fe, and Cu/Fe bilayers coincide with the minimum temperature of the order-disorder phase transition in Cu–Au, Pd–Fe, Co–Pt and the eutectoid decomposition temperature in the Fe–Ni, Cu–Fe binary systems, respectively. Martensitic transitions are not diffusion transformations; however, they also satisfy ( $T_{in} = T_k$ ) equality. It is well established that the ordered B2 alloys, such as NiTi, AuCd, NiAl have reversible low-temperature martensitic transformations, in which the high-temperature austenite B2-phase develops into a low-temperature martensitic phase through a complex process of the formation of intermediate phases. We have shown earlier that the initiation temperatures  $T_{in}(\text{Ti}/\text{Ni}) < 150^\circ\text{C}$ ,  $T_{in}(\text{Ni}/\text{Al}) \sim 180^\circ\text{C}$ ,  $T_{in}(\text{Cd}/\text{Au}) = 67^\circ\text{C}$  in Ti/Ni, Ni/Al, Cd/Au bilayers, respectively [1–3]. These temperatures are close or coincide with reverse martensitic

transformation starting temperatures  $A_s(\text{B2-TiNi}) \sim 100^\circ\text{C}$ ,  $A_s(\text{B2-NiAl}) \sim 180^\circ\text{C}$ ,  $A_s(\text{B2-CdAu}) = 67^\circ\text{C}$ . As mentioned above, with increasing of the temperature of the bilayer above  $T_{\text{in}}$  leads to the beginning of intermixing of the reagents and first phase synthesis on the interface and consequently physical characteristics of the film samples, such as electrical resistance, magnetization, transparency, heat release begins radically change. Obviously, the start temperature of these changes is the reaction initiation temperature  $T_{\text{in}}$ . In most cases the energetic properties of thermite nanocomposites were investigated by differential thermal analysis (DTA), thermogravimetric analysis (TGA), and differential scanning calorimetry (DSC). In this case the initiation temperature  $T_{\text{in}}$  is the temperature at which heat release starts.

The one important characteristic of reactive multilayer films is the ignition temperature  $T_{\text{ig}}$  which can be defined as a minimum temperature of onset of a self-sustaining reaction for given experiment. As known, the self-sustaining regime of reaction arises then the rate of heat generation  $Q_{\text{reaction}}$  overcomes the rate of heat losses  $Q_{\text{loss}}$  ( $Q_{\text{reaction}} > Q_{\text{loss}}$ ). Unlike  $T_{\text{ig}}$  the initiation temperature  $T_{\text{in}}$  is start temperature of reaction at which the rate of heat generation  $Q_{\text{reaction}}$  less than the rate of heat losses  $Q_{\text{loss}}$  ( $Q_{\text{reaction}} < Q_{\text{loss}}$ ) and so always the initiation temperature  $T_{\text{in}}$  is less than the ignition temperature  $T_{\text{ig}}$  ( $T_{\text{in}} < T_{\text{ig}}$ ). As discussed above the initiation temperature  $T_{\text{in}}$  is threshold temperature: no reaction below  $T_{\text{in}}$  and reaction initiate just the temperature of sample overcomes  $T_{\text{in}}$ . Thus, the initiation temperature  $T_{\text{in}}$  is fundamental temperature for given reaction couple. In contrast to  $T_{\text{in}}$ , the ignition temperature  $T_{\text{ig}}$  is a kinetic quantity that depends on the heating rate and the rate of heat loss.

In contrast to the universally accepted diffusion mechanism, the above clearly demonstrates that the same chemical interactions underlie and control both the thin-film solid-state reactions and corresponding solid-state transformations [1–3]. Under the impact of chemical interactions above the initiation temperature  $T > T_{\text{in}}$  the chemical bonds in the reactants are broken. the reacting atoms are transfer through of the reaction product layer and the synthesis of new compounds are occurring. This proves that there is no reaction below  $T_{\text{in}}$ . The equality  $T_{\text{in}} = T_{\text{k}}$  indicates that low-temperature solid-state thin-film reactions in A/B bilayers occur only in A–B binary systems, which have corresponding low-temperature solid-state transformations. Therefore, the study of reactions in A/B bilayers with different layer ratios is a study of the A–B phase diagram.

1. V.G. Myagkov, L.E. Bykova, A.A. Matsynin, M.N. Volochaev, V.S. Zhigalov, I.A. Tambasov, Yu.L. Mikhlin, D.A. Velikanov, G.N. Bondarenko, Solid state synthesis of  $\text{Mn}_5\text{Ge}_3$  in Ge/Ag/Mn trilayers: Structural and magnetic studies, *J. Solid State Chem.*, 2017, vol. 246, pp. 379–387.
2. V. Myagkov, O. Bayukov, Yu. Mikhlin, V. Zhigalov, L. Bykova, G. Bondarenko, Long-range chemical interactions in solid-state reactions: effect of an inert ag interlayer on the formation of L10-FePd in epitaxial Pd(001)/Ag(001)/Fe(001) and Fe(001)/Ag(001)/Pd(001) trilayers, *Phil. Mag.*, 2014, vol. 94, no 23, pp. 2595–2622.
3. V.G. Myagkov, V.C. Zhigalov, L.E. Bykova, G.N. Bondarenko, Long-range chemical interaction in solid-state synthesis: chemical interaction between Ni and Fe in epitaxial Ni(001)/Ag(001)/Fe(001) trilayers, *Int. J. Self-Propag. High-Temp. Synth.*, 2009, vol. 18, no. 2, pp. 117–124.

## THE INITIATION TEMPERATURES IN NANOTHERMITE REACTIONS

V. G. Myagkov

Kirensky Institute of Physics, Federal Research Center KSC SB RAS,  
Krasnoyarsk, 660036 Russia  
e-mail: miagkov@iph.krasn.ru

DOI: 10.24411/9999-0014A-2019-10106

Over the past decade, investigations focused on the nanoenergetic materials, such as reactive multilayer thin films and nanostructured reactive mixtures. Thermite mixtures belong to a wide class of energetic materials that comprise a metal fuel (e.g. Al, Mg, or B) and an oxidizer (e.g.  $\text{Fe}_2\text{O}_3$ ,  $\text{MoO}_3$ ,  $\text{CuO}$ ,  $\text{Bi}_2\text{O}_3$ , or  $\text{WO}_3$ ). These mixtures react with a lot of heat release; therefore, the thermite reactions often occur in a self-sustaining mode. In recent years, there has been an increasing interest in nanothermites (superthermites) where the particle size is reduced to a few nanometers. Studies of nanothermite combustion are mainly aimed at measuring the combustion wave velocity, burning temperature, delay time, and their dependences on density, morphology, and composition of the reaction mixture. Despite the intense investigations of thermite reactions, their general regularities and mechanisms remain unclear. Currently, the classical nanothermite Goldschmidt reaction  $\text{Fe}_2\text{O}_3 + 2\text{Al} = \text{Al}_2\text{O}_3 + 2\text{Fe}$  and other Al-based reactions are well studied.

In this work, we extend the existing concepts of the first phase and its initiation temperature  $T_{\text{in}}$  which describe the initial stage of solid-state reactions in nanofilms onto thermite reactions and demonstrate that in all Al-based nanothermite mixtures the synthesis of the  $\text{Al}_2\text{O}_3$  phase starts at the same initiation temperature  $T_{\text{in}} \sim 510^\circ\text{C}$ . These results open up a way for understanding the exclusive role of the initiation temperature  $T_{\text{in}}$  in the solid-state reactions at the nanoscale.

The enthalpy of formation of the first phase is a good measure of the free energy variation during the solid-state interaction; therefore, the heats of formation were used in several initial models to predict the first phase and phase sequence formation. Pretorius et. al. [1] proposed an effective model for the enthalpy of formation, which was successfully used for predicting the first phase formation in many binary systems.

As mentioned above, an increase in the temperature of the bilayer above  $T_{\text{in}}$  leads to the beginning of intermixing of the reagents and first phase synthesis on the interface and consequently physical characteristics of the film samples, such as electrical resistance, magnetization, transparency, and heat release, begin to radically change. Obviously, the start temperature of these changes is the reaction initiation temperature  $T_{\text{in}}$ . In most cases the energetic properties of thermite nanocomposites were investigated by differential thermal analysis (DTA), thermogravimetric analysis (TGA), and differential scanning calorimetry (DSC). In this case the initiation temperature  $T_{\text{in}}$  is the temperature at which heat release starts. An important characteristic of the DSC curves is also the exothermic peak temperature, which, unlike the initiation temperature  $T_{\text{in}}$ , depends on the heat removal conditions from the reaction zone. It is important to note that the contaminants that form on the reagent interface during various methods of sample preparation (especially for chemically produced samples) can form thin barrier layers that slightly change the initiation temperature  $T_{\text{in}}$  but do not suppress the reaction. An error in finding the exact value of the initiation temperature  $T_{\text{in}}$  can also follow from the certain inaccuracy in determining  $T_{\text{in}}$  from DTA, TGA, and DSC plots. To find the exact  $T_{\text{in}}$  value, low heating rates are required. Therefore, we referred only to the studies in which the heat release curves were obtained at minimum heating rates (5, 10 or  $20^\circ\text{C}/\text{min}$ ).



The main results of the work based on an analysis of more than 60 papers presented in the literature and our papers are summarized in the schematic diagram in Fig. 1. showing the initiation temperature  $T_{in} \sim 510^\circ\text{C}$  of the  $\text{Al}_2\text{O}_3$  phase in  $\text{Al}/\text{Fe}_2\text{O}_3$ ,  $\text{Al}/\text{Co}_3\text{O}_4$ ,  $\text{Al}/\text{NiO}$ ,  $\text{Al}/\text{MnO}_2$ ,  $\text{Al}/\text{Bi}_2\text{O}_3$ ,  $\text{Al}/\text{CuO}$ ,  $\text{Al}/\text{MoO}_3$  nanothermite reactions and oxidation of Al nanomaterials.

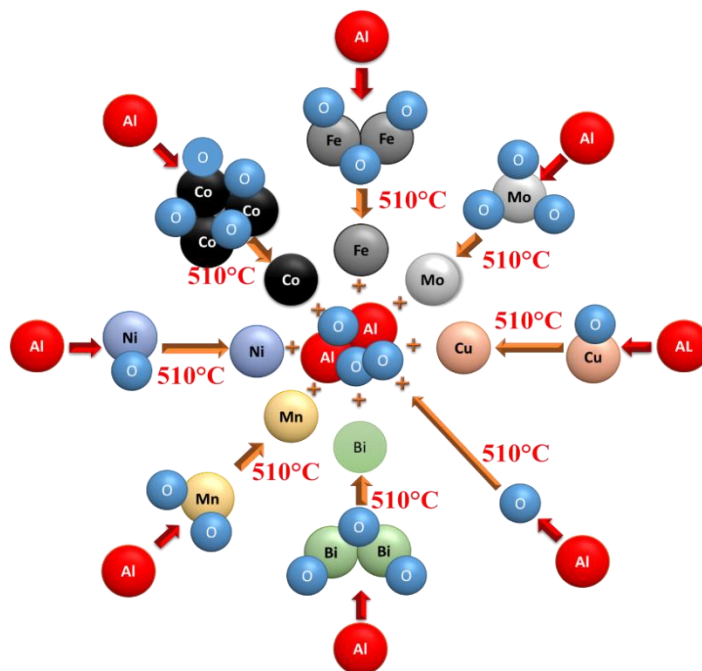


Fig. 1. The schematic illustration of the initiation temperature  $T_{in} \sim 510^\circ\text{C}$  for the Al-based nanothermite reactions with  $\text{Fe}_2\text{O}_3$ ,  $\text{Co}_3\text{O}_4$ ,  $\text{NiO}$ ,  $\text{MnO}_2$ ,  $\text{Bi}_2\text{O}_3$ ,  $\text{CuO}$ ,  $\text{MoO}_3$  oxidizers and the oxidation of Al nanomaterials. The initiation temperature  $T_{in} \sim 510^\circ\text{C}$  is characteristic of the leading  $\text{Al}_2\text{O}_3$  phase (first phase), which has a high negative enthalpy of formation ( $\Delta H_f = -1676 \text{ kJ/mol}$ ) and is the driving force of all the Al-based nanothermite reactions.

These results suggest the following reaction mechanism: below the initiation temperature  $T_{in} < \sim 510^\circ\text{C}$ , Al and O atoms remain chemically neutral. At  $T_{in} > \sim 510^\circ\text{C}$ , strong chemical interactions occur between Al and O atoms that break old chemical bonds causing the directed atomic migration to the reaction zone and the synthesis of  $\text{Al}_2\text{O}_3$  regardless of the system they exist in. Therefore, the initiation temperature  $T_{in} \sim 510^\circ\text{C}$  is a universal parameter of all Al-based nanothermite reactions.

The main concepts of this study are the first phase and its initiation temperature  $T_{in}$ , which describe thin-film solid-state reactions and were extended onto nanothermite reactions. The paper results prove that all Al-based nanothermite reactions have the same initiation temperature and they only start higher  $T_{in} > \sim 510^\circ\text{C}$ . Analysis presented in the literature and our papers of Zr-, Mg-, and In-based nanothermite reactions show the same initiation temperatures  $\sim 250$ ,  $\sim 450$ , and  $\sim 180^\circ\text{C}$ , respectively. Finally, these findings predict that nanothermite reactions based on other fuels (e.g. Ti and B) must have their own initiation temperatures. This approach can be widely applicable in the study of the multicomponent thin-film solid-state reactions.

1. R. Pretorius, C.C. Theron, A. Vantomme, J.W. Mayer, Compound phase formation in thin film structures, *Crit. Rev. Solid State Mater. Sci.*, 1999, vol. 24, pp. 1–62.

## REACTIVE ROUNDED Ti/Al COMPOSITE POWDERS PRODUCED BY HIGH-ENERGY BALL MILLING FOR SELECTIVE LASER MELTING TECHNOLOGY

**A. A. Nepapushev<sup>a</sup>, D. O. Moskovskikh<sup>a</sup>, V. S. Buinevich<sup>a</sup>, S. G. Vadchenko<sup>b</sup>,  
and A. S. Rogachev<sup>b</sup>**

<sup>a</sup>Center of Functional Nano-Ceramics, National University of Science and Technology MISiS, Moscow, 119049, Russia

<sup>b</sup>Merzhanov Institute of Structural Macrokinetics and Materials Science, Russian Academy of Sciences, Chernogolovka, Moscow, 142432, Russia

DOI: 10.24411/9999-0014A-2019-10107

The modern additive manufacturing (AM) is an efficient way to produce complex-shape [1], functionally-graded [2] or non-standard parts [3] for various engineering applications. Currently, the AM is not confined to the rapid printing of prototypes but allows to produce real-scale fully functional parts. For example, selective laser sintering (SLS) was initially developed for the production of polymer prototypes by the point-by-point scanning technique. Afterward, due to the application of more potent heat sources, this approach was widened to include metallic and ceramic powders. Porous parts fabricated by SLS are now widely employed in biomedicine.

Currently, pure metals are rarely used in the AM due to their low mechanical properties and resistance towards oxidation and corrosion. Application of pre-alloyed Ti, Ni, and Fe-based powders increases significantly the properties of produced parts. A new perspective direction for the development of AM lies in the application of reactive composite precursor powders. In this approach, a mixture of components with a relatively low melting point is used as the feedstock, and the mixture reacts during the SLS or SLM to form a more refractory compound. If the reaction is exothermic, the heat produced by the reaction is added to that produced by the laser heating. This widens the possibilities of SLM and allows to produce more refractory materials and products. However, the production of the composite reactive particles with the required spherical shape is a complicated problem due to the difference in the mechanical properties of the reagents and impossibility of application of the different atomization methods. This problem can be solved using the mechanical structuring methods, for example, high-energy ball milling (HEBM), but it necessitates the optimization of the mechanical treatment regime for the production of spherical powders.

In this work, we investigated the possibility of the production of reactive composite powders in the Ti–Al system with various morphology especially with rounded particles with high flowability, which is important for use in SLM technology, by HEBM. This system is interesting because the exothermic reaction in it can be initiated at the relatively low temperature of 650–700°C, moreover, this temperature can be further decreased by using mechanical activation. For the HEBM initial Ti and Al in the chosen compositions were loaded in the jars along with the milling bodies. HEBM treatment was performed using an Activator 2S device in the following conditions: working volume of the vial of 250 ml, ball to mixture mass ratio of 20:1, the rotation speed of the planetary disc of 200 rpm. 2-mm and 6-mm steel balls were used as the milling bodies. HEBM was conducted in the argon atmosphere (4 atm).

During our previous studies of the influence of HEBM regime on the structure and properties of various powder mixtures [4, 5] we discovered that high-velocity milling does not allow to produce spherical particles. Therefore, in this study, we decreased the disc rotation speed to transition from the dynamic impact and attrition regime to a “softer” regime, characterized by

rolling of balls against one another and the vial walls. As a result, the treatment of Ti + Al mixture at disc rotation velocity of 200 rpm and  $K = 1.0$  using balls with varied diameter leads to a considerable change in the morphology of produced powders (Fig. 1). After 60-min activation, the particles shape becomes more rounded. This process is largely influenced by the diameter of the milling bodies. If 6-mm balls are used, the treated powders have a size of 300–400  $\mu\text{m}$  (Fig. 1a); a decrease in the balls size to 2 mm leads to the formation of particles with a size of 100–150  $\mu\text{m}$ . Two fractions of powders can be observed: the first fraction consists of relatively coarse and rounded particles, while the second fraction is comprised of finer (30–50  $\mu\text{m}$ ) and irregularly shaped particles (Fig. 1b). The increase in the HEBM duration to 120 min leads to the formation of more pronounced layered structure and more spherical shape of particles (Fig. 2). More detailed study of the internal structure of the powders revealed their composite structure, in which the titanium (Figs. 2c, 2d, bright phase) is embedded in the aluminum matrix (Figs. 2c, 2d, dark phase). Therefore, the adjustment of the HEBM regime, in particular of the disc rotation velocity, allows one to influence to a great extent the morphology of produced composite powders.

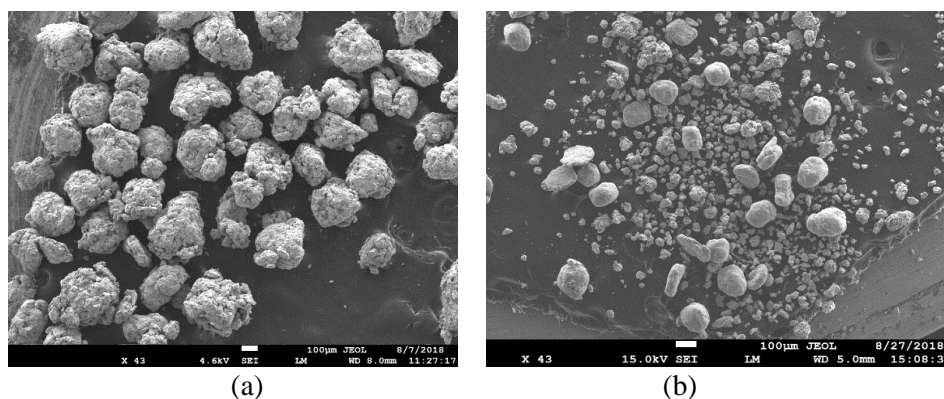


Fig. 1. Ti + Al powder after 60 min of HEBM: (a) 6-mm balls; (b) 2-mm balls.

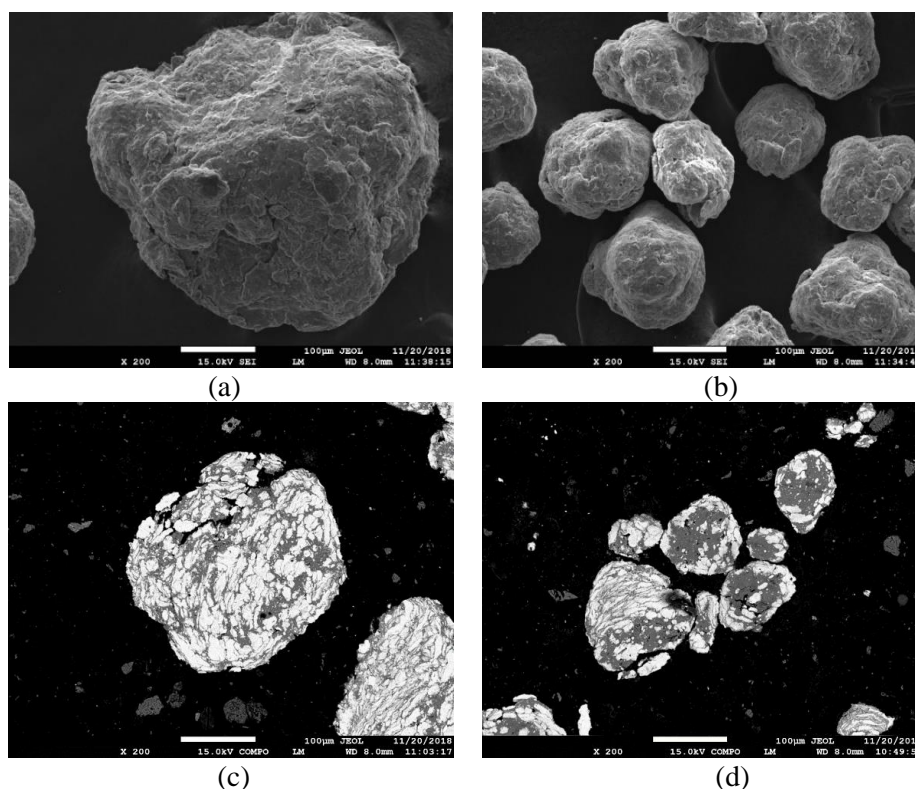


Fig. 2. Ti + Al powder after 120 min of HEBM: (a) 6-mm balls; (b) 2-mm balls and (c–d) corresponding cross-sections.

Powder flowability is important for the AM since it defines whether the deposited powder layers will be uniform and reproducible. In this work, the flowability was determined by the direct measurement of the time needed for the 50 g of powder to flow through a funnel with a diameter of 2.54 mm (Table 1). For the mixtures treated using 6-mm balls, an increase in the treatment duration to 120 min leads to the improved flowability due to the more spherical shape of the powders as compared to 60-min treatment. In the case of the mixtures treated using 2-mm balls, the flowability decreases after 120 min, which might be related to a decrease in the particles size and an increase in their specific surface. The Ti + Al mixture prepared in a mortar does not flow (no flowability).

Table 1. Flowability of Ti + Al powder after HEBM treatment.

| Treatment duration | 2-mm balls    | 6-mm balls |
|--------------------|---------------|------------|
| 0 min              | Does not flow |            |
| 60 min             | 56.7 s        | 87,5 s     |
| 120 min            | 61.7 s        | 81.25 s    |

In mixtures after 60 and 120 min of HEBM were initiated the reactions, the ignition temperature of the treated mixture is 640–650°C, which is near to the melting temperature of Al. The microstructure of the powders after 60-min HEBM at 200 rpm and subsequent combustion synthesis was investigated. The morphology and size of the particles after the SHS coincide with the composite particles produced by HEBM. EDS results show that the conversion was incomplete, and the reaction resulted in the formation of a composite comprised of Ti and TiAl<sub>3</sub>.

Thus, for mixtures of elementary Ti and Al powders regimes of high energy ball milling in a planetary mill, that allow obtaining rounded reactive composite particles of Ti/Al, were found. The produced powders are characterized by flowability sufficient for the application in the SLS and SLM processes. In the produced composite powders, the combustion is initiated at ~ 660°C and Ti–TiAl<sub>3</sub> composite is formed as a result of combustion.

This work was supported by the Ministry of Science and Higher Education of the Russian Federation in the framework of the Federal Target Program “Research and Development on Priority Directions of the Scientific and Production Complex of Russia for 2014-2020”, agreement no. 14.587.21.0051, project RFMEFI58718X0051.

1. X. Ren, H. Shao, T. Lin, H. Zheng, *Mater. Des.*, 2016, vol.101, pp. 80–87.
2. A. Levy, A. Miriyev, A. Elliott, S.S. Babu, N. Frage, *Mater. Des.*, 2017, vol. 118, pp. 198–203.
3. R. Liu, Z. Wang, T. Sparks, F. Liou, J. Newkirk, *Laser Add. Manufact.: Mater., Des., Technol., Appl.*, 2017, pp. 351–371.
4. A.S. Rogachev, D.O. Moskovskikh, A.A. Nepapushev, T.A. Sviridova, S.G. Vadchenko, S.A. Rogachev, A.S. Mukasyan, *Powder Technol.*, 2015, vol. 274, pp. 44–52.
5. A.S. Rogachev, N.F. Shkodich, S.G. Vadchenko, F. Baras, D.Y. Kovalev, S. Rouvimov, A.A. Nepapushev, A.S. Mukasyan, *J. Alloys Compd.*, 2013, vol. 577, pp. 600–605.

## MORPHOLOGICAL DIVERSITY OF METAL NITRIDES CRYSTALS: SYNTHESIS, CHARACTERIZATION AND THEORETICAL MODELING

H. H. Nersisyan\*, W. B. Kim, and J. H. Lee

<sup>a</sup>RASOM, Chungnam National University, 99 Daehak-ro, Yuseong-gu,  
Daejeon, 34134 Republic of Korea

<sup>b</sup>Graduate School of Materials Science and Engineering, Chungnam National University, 99  
Daehak-ro, Yuseong-gu, Daejeon, 34134 Republic of Korea  
\*e-mail: haykrasom@hotmail.com

DOI: 10.24411/9999-0014A-2019-10108

Among the nitrides, aluminum nitride (AlN), gallium nitride (GaN), and silicon nitride (Si<sub>3</sub>N<sub>4</sub>) have been identified as a key members of the group III–IV nitrides family. The most remarkable properties exhibited by metal nitrides are their high thermal conductivity (AlN: 150–200 Wm<sup>-1</sup>K<sup>-1</sup>; Si<sub>3</sub>N<sub>4</sub>: 10–43 Wm<sup>-1</sup>K<sup>-1</sup>; GaN: 130 Wm<sup>-1</sup>K<sup>-1</sup>), highest band gap (AlN: 6.2 eV; Si<sub>3</sub>N<sub>4</sub>: 5.0 eV; GaN: 3.4 eV), small electron affinity (AlN: 1.9; GaN: 4.1; Si<sub>3</sub>N<sub>4</sub>: 0.9–3.2 eV), strong piezoelectricity (AlN: 4.81 pm/V; Si<sub>3</sub>N<sub>4</sub>: 3.1 pm/V; GaN: 15 pm/V), high surface acoustic wave (SAW) velocity (AlN: 5760 m/s; GaN: 3690 m/s), high chemical resistance, and high melting point (> 2500°C). They are ideal materials for applications in microelectrochemical systems (MEMS), surface acoustic waves (SAWs), optoelectronic devices such as light emitting diodes (LED), field emitters, flexible pulse-wave sensors, and ultraviolet nanolasers. The metal nitrides exist in various morphological forms such as nanoparticles, nanowires, nanotubes, nanorods, nanobelts, nanosheets, thin films, and dendritic structures such as sectored plates, stellar, and fern-like dendrites, six and multifold symmetry crystals, and this make nitride materials unique for a broad application. Four main topics are covered in this keynote lecture: (1) general synthesis, fabrication and classification as zero-dimensional (0D), one dimensional (1D), two-dimensional (2D) and three-dimensional (3D) nano- and microstructures of metal nitrides; (2) nucleation and growth of nitride crystals; (3) computer simulation of growth processes based on density functional theory (DFT) and phase field (PF) modeling approaches; (4) metal nitride application and micro-devices. Our lecture also provides a perspective on future research relevant to metal nitride micro- and nanostructures. In the beginning of the lecture, we will address to the morphological diversity of metal nitride nano- and microstructures and the synthesis of these materials through various chemical and physical methods. We will place a particular focus on the various synthesis approaches, involving direct nitridation, combustion synthesis (SHS), chemical vapour deposition (CVD), physical vapor deposition (PVD), and reactive sputtering. The structural development of micro- and nanostructures upon the process temperature, reaction mixture composition, type of additives, presence of a catalyst, and the type of substrate will be highlighted. For illustration, the several morphological fragments of AlN, Si<sub>3</sub>N<sub>4</sub>, and GaN crystals fabricated by different synthesis methods are shown in Fig. 1a. Figure 1a (1–3) demonstrate 6-fold symmetry dendritic crystals of AlN prepared by SHS technique [1, 2]. Figure 1a (4–6) shows combustion synthesized-Si<sub>3</sub>N<sub>4</sub> branched structures consisted of some long and slender prisms. These structures have a central junction from which the columnar crystals radiate in c-axis direction forming branched microstructures. Figure 1a (7–9) shows GaN columnar crystals grown by metal organic vapour phase epitaxy (MOVPE) [3, 4]. The growth mechanism of metal nitride micro- and nanostructures will be discussed based on synthesis methods and the vapor-solid (VS) and vapor-liquid-solid (VLS) growth mechanisms. Moreover, the preferable crystallographic directions in which the crystals grow will be highlighted.

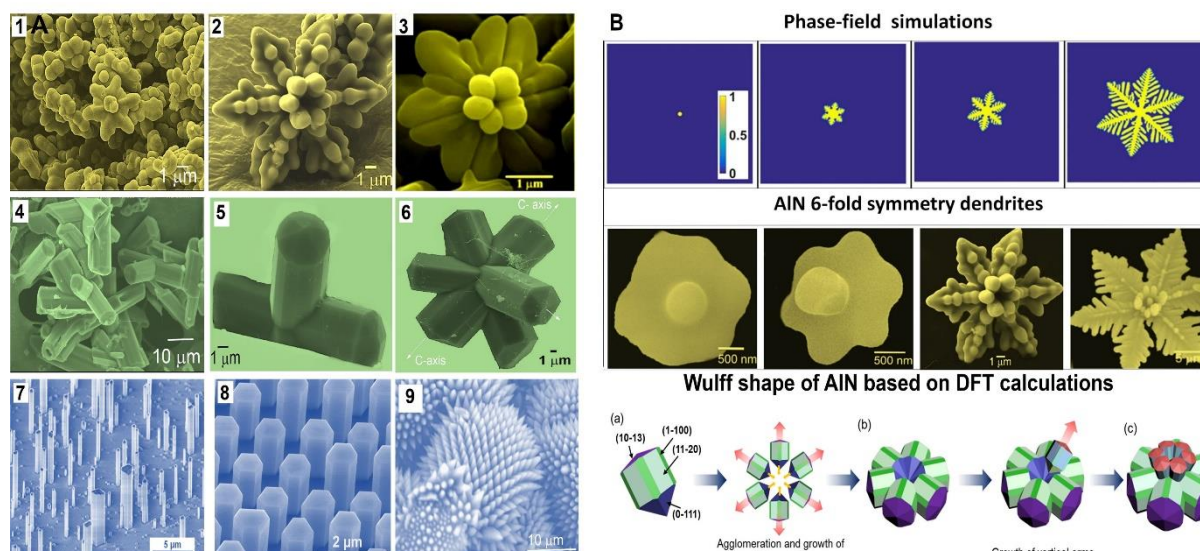


Fig. 1. (a) SEM morphology of AlN (1–3), Si<sub>3</sub>N<sub>4</sub> (4–6), and GaN (7–9) structures. (b) AlN crystals: phase-field, DFT calculations and experiments.

The growth mechanism of metal nitride micro- and nanostructures will be discussed based on synthesis methods and the vapor-solid (VS) and vapor-liquid-solid (VLS) growth mechanisms. Moreover, the preferable crystallographic directions in which the crystals grow will be highlighted.

We will also discuss the growth process of nitride structures based on two well-known computational models: quantum-mechanical calculations based on density-functional theory (DFT) and Wulff constructions, used for the prediction of equilibrium shapes of metal nanostructures, and (2) phase-field models for solving interface problems and predicting the solidification dynamics. Figure 1b shows the shape of 6-fold symmetry crystals of AlN obtained by the experiments and validated by phase field and DFT simulations. All results are well-agreed with each other's.

Finally, we will briefly discuss the application and microelectronic devices based of metal nitride micro- and nanostructures. Lastly but not least, some issues that need to be clarified in the near future will be also discussed.

This research was supported by Basic Science Research Program through the National Research Foundation of Korea (NRF) funded by the Ministry of Education (NRF-2016R1D1A1B03936187).

1. H.H. Nersisyan, J.H. Lee, J.R. Ding, K.S. Kim, K.V. Manukyan, A.S. Mukasyan, Combustion synthesis of zero-, one-, two- and three-dimensional nanostructures: Current trends and future perspectives, *Prog. Energy Combust. Sci.*, 2017, vol. 63, pp. 79–118.
2. H.H. Nersisyan, S.H. Lee, J.H. Choi, B.U. Yoo, J.H. Lee, Single-step combustion process for the synthesis of 1-D, 2-D, and 3-D hierarchically grown AlN structures, *Combust. Flame*, 2017, vol. 185, pp. 210–219.
3. M. Nami, I.E. Stricklin, K.M. DaVico, et. al., Carrier dynamics and electro optical characterization of high performance GaN/InGaN core-shell nanowire light-emitting diodes, *Sci. Rep.*, 2018, vol. 8, pp. 501–507.
4. T. Kente, S.D. Mhlanga, Gallium nitride nanostructures: Synthesis, characterization and applications, *J. Cryst. Growth.*, 2016. vol. 444. pp. 55–72.

## STRUCTURE AND PHASE COMPOSITION OF Nb–Si–C-BASED COMPOSITES PREPARED BY SHS METHOD

R. M. Nikonova<sup>\*a</sup>, N. S. Larionova<sup>a</sup>, V. I. Lad'yanov<sup>a</sup>, B. E. Pushkarev<sup>a</sup>,  
and A. V. Panteleyeva<sup>b</sup>

<sup>a</sup>Udmurt Federal Research Center, Ural Branch, Russian Academy of Sciences,  
Izhevsk, 426067 Russia

<sup>b</sup>Udmurt State University, Izhevsk, 426034 Russia

\*e-mail: rozamuz@udman.ru

DOI: 10.24411/9999-0014A-2019-10109

Modern heat-resistant alloys (HRAs) applied in manufacturing shoulder-blades of gas-turbine engines are only able to endure temperatures up to 1100–1150°C, which is 80–85% of their melting temperature [1]. Usually nickel alloys are used as heat-resistant alloys. Additional doping of nickel with high-melting elements results in an increased density of the material and makes the alloys costly. As an alternative Nb–Si-based composite materials [1–5], which have lower density and high melting temperatures in comparison with Ni-HRA, are considered promising. Rotor shoulder-blades from NbSi-based materials will endure the temperature up to 1350°C, which is 200–250°C higher than the temperatures in case of Ni-HRA [1]. It is assumed that high heat resistance of Nb–Si materials can be achieved at the expense of the combined strengthening of Ni–Si-based materials by intermetallides  $Nb_xSi_y$  and carbide NbC. With account of high melting temperature ( $\sim 2500^\circ\text{C}$ ) and low density ( $\sim 7 \text{ g/cm}^3$ ),  $Nb_5Si_3$  is the best variant of all the other silicides [1].

Nb–Si-based ceramic materials are mainly produced by hybrid spark plasma sintering of powders, vacuum arc melting, and by precision investment casting [5–7]. A promising technique for preparation of alloys is self-propagating high-temperature synthesis (SHS). It seems highly attractive due to its simplicity, low energy consumption, and high purity of combustion products.

The Nb–Si–C alloy described in this paper was prepared by SHS. The sample was synthesized from the mixture of  $Nb_2O_5 + SiC +$  aluminum–magnesium powder (AMP) in Ar atmosphere ( $P_{Ar} = 80 \text{ atm}$ ). For better wetting and hence reactivity cryolite was added. To increase exothermicity potassium perchlorate was introduced.

To determine phase composition, a DRON-6 diffractometer with  $FeK_\alpha$  radiation and a MISA software package were used. Neophot-21 optical microscope, Philips SEM-515 scanning electron microscope equipped with a Genesis 2000 XMS energy-dispersive X-ray microanalysis system, and FEI Inspect S50 scanning electron microscope were used to study the microstructure of sample. Quantitative chemical analysis to measure the content of Si, Mg, and Al was performed by atomic-emission spectroscopy using a Spectroflame Modula S scanning ICP spectrometer. To measure carbon content, the sample was placed in an Exan carbon analyzer where it was combusted in oxygen flux.

XRD pattern of obtained sample is seen in Fig. 1 to contain two basic phases  $Nb_5Si_3$  and NbC, and a small amount of  $NbSi_2$ .

Figure 2 shows the SEM images of fracture and grinding face. It can be seen that the alloy obtained was represented by a dense uniform structure with a grain size of 5–20  $\mu\text{m}$  (Fig. 2).

Spot analysis of the sample surface confirmed that the composite mainly consisted of intermetallide  $Nb_5Si_3$ , carbide phase NbC, and a small amount of intermetallide  $NbSi_2$  (Fig. 3).

Thus, the results obtained evidence the possibility of using SHS to prepare the composite Nb–Si–C strengthened by the combination of intermetallides  $Nb_5Si_3$ ,  $NbSi_2$ , and carbide NbC.

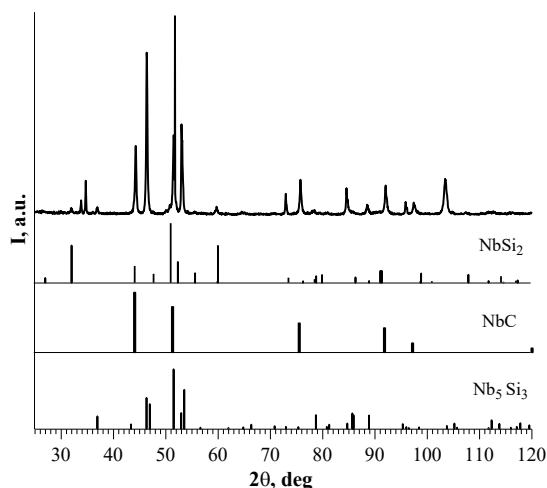


Fig.1. X-ray diffraction pattern of obtained Nb-Si-C composite.

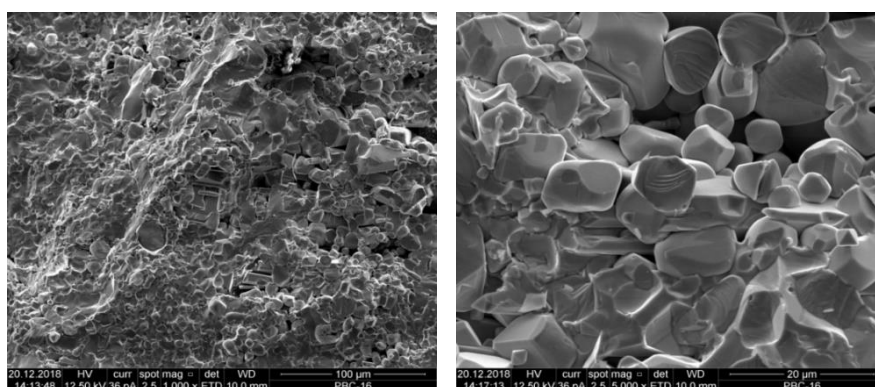
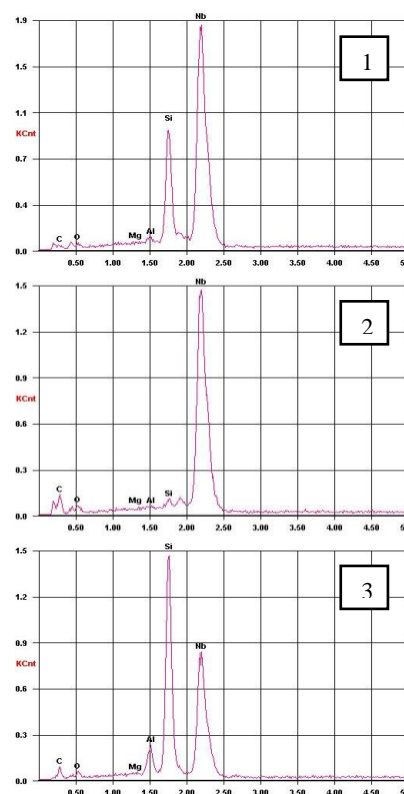
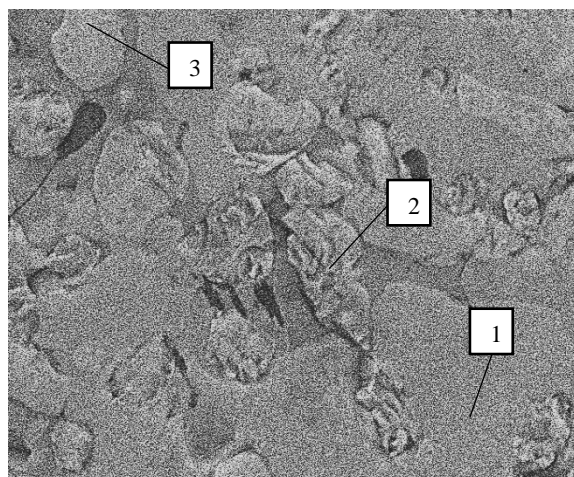


Fig. 2. Destruction surface of the alloy. Scanning electron microscopy.



| № | Content of elements, wt % |      |      |      |       |       | Estimated Phase                 |
|---|---------------------------|------|------|------|-------|-------|---------------------------------|
|   | C                         | O    | Mg   | Al   | Si    | Nb    |                                 |
| 1 | 4.04                      | 1.62 | 0    | 0.66 | 15.38 | 78.30 | Nb <sub>5</sub> Si <sub>3</sub> |
| 2 | 18.34                     | 2.87 | 0    | 0.11 | 0.80  | 77.88 | NbC                             |
| 3 | 14.19                     | 2.26 | 0.22 | 3.44 | 30.3  | 49.59 | NbSi <sub>2</sub> ,<br>NbC      |

Fig. 3. General view of the sample surface and energy spectra obtained from different sites. × 2500



1. Ye.N. Kablov, I.L. Svetlov, I.Yu. Yefimochkin, High-temperature Nb–Si composite materials, *Bull. MSTU named after N.E. Bauman, Ser. Mashinostroyenie*, 2011, pp. 164–173.
2. M.I. Karpov, V.P. Korzhov, D.V. Rohorov, Natural and artificial composite materials: niobium-based heat-resistant alloys, *Bull. TSU*, 2013, vol.18, iss. 4, pp. 1805–1806.
3. R. Tanaka, A. Kasama, M. Fujikura, I. Iwanaga, H. Tanak, Y. Matsumura, Research and development of niobium-based superalloys for hot components of gas turbines, *Proc. Int. Gas Turbine Congress*, 2003, pp. 1–5.
4. F. Gang, M. Heilmaier, Influence of directional solidification on the creep properties of a binary NbSi eutectic alloy, *JOM*, 2014, vol. 66, no. 9, pp. 1908–1913.
5. I.L. Svetlov, High-temperature Nb–Si-composites, *Materialovedenie*, 2010, nos. 9–10, pp. 18–38.
6. I.Yu. Yefimochkin, N.A. Kuzmina, *Trudy VIAM*, 2018, no. 11, pp. 54–63.
7. A.P. Amosov, I.P. Borovinskaya, A.G. Merzhanov, Powder technology of self-propagating high-temperature synthesis of materials: Textbook, M.: Mashinostroyenie, 2007. 567 p.

## SHS IN A MELT OF Al–TiC(B) COMPOSITES

**R. M. Nikonova<sup>\*a</sup>, A. V. Panteleyeva<sup>b</sup>, and V. I. Lad'yanov<sup>a</sup>**<sup>a</sup>Udmurt Federal Research Center, Ural Branch, Russian Academy of Sciences, Izhevsk, 426067 Russia<sup>b</sup>Udmurt State University, Izhevsk, 426034 Russia

\*e-mail: rozamuz@udman.ru

DOI: 10.24411/9999-0014A-2019-10110

There has been much research in recent years focused on the development of aluminium matrix composites because of their high specific strength, modulus of elasticity, wear resistance, hardness, etc. Especially popular are aluminium matrix composites with such ceramic strengthening phases as SiC, Al<sub>2</sub>O<sub>3</sub>, TiB<sub>2</sub>, and TiC. Titanium carbide for example attracts the researchers' attention with its high hardness and modulus of flexibility, low density and uniform distribution of TiC particles in an aluminium matrix at the expense of good wettability by liquid aluminium. Apart from being a strengthening phase TiC serves also as a center of crystallization in aluminium, thus assisting grain refinement in a composite alloy [1–5].

A promising method of composites preparation is self-propagating high-temperature synthesis (SHS) [6–8]. A SHS method in melt, which is an *in situ* method, is a SHS variant that combines a traditional casting practice and self-propagating high-temperature synthesis. During the process of SHS in melt strengthening phases are synthesized from initial components or their compounds directly in melt.

Apart from the benefit of one-stage preparation of composites, this provides their thermal stability, tight contact, and good adhesion between the matrix and the strengthening phase. Among the advantages of the method there are low energy consumption and manufacturing cost, high productivity, possibility of controlling structure and properties of a product synthesized [6].

The purpose of the present research is modification of aluminium alloy by titanium carbide and titanium diboride using SHS in melt.

The research objects were pure aluminium and Al–TiC and Al–TiB obtained by SHS in melt. For better wetting and hence reactivity 1 g of cryolite was added.

Quantitative distribution of introduced elements was determined on a GDA-650HR spectrometer using glow discharge method, which also provided metallographic etching of the samples. The sample microstructure was studied using a Philips SEM-515 scanning electron microscope (SEM) equipped with a Genesis 2000 XMS energy-dispersive X-ray spectroscopy (EDS). Phase composition was determined using a Dron-6 diffractometer with CoK<sub>α</sub> radiation. Microhardness was measured using a PMT-3 tester under a load of 100 g.

According to EDS results the composite Al–TiC contained up to 4% titanium and 0.9% carbon; the composite Al–TiB contained up to 12% titanium and 2.8% boron. XRD analysis (Fig.1) demonstrated the presence of titanium carbide in the Al–TiC alloy apart from pure aluminium in quantity of ~ 3.5%. This evidences the formation of TiC during SHS. In the Al–TiB sample, two strengthening phases, Al<sub>3</sub>Ti and TiB<sub>2</sub>, (4% of each phase) were distinguished. The XRD pattern also contains a carbon line, which can be attributed to the method of alloys preparation (graphite heater was used). As we see from the surface analysis (see Fig. 2) the grain size in aluminium matrix in case of Al–TiC (Figs. 2c, 2d) is 20–35 μm; the size of inclusions is no more than 20 μm. In case of Al–TiB (Figs. 2e, 2f) the grain size is 10–20 μm. Keeping in mind the grain size of 70 μm in initial aluminium we can state a 2–3 times decrease in grain size in Al–TiC and 3–5 times in Al–TiB.

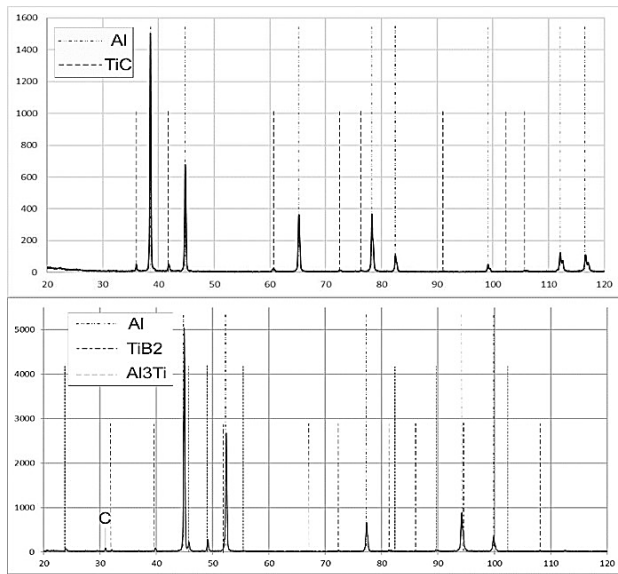


Fig. 1. XRD pattern of composite Al–TiC and Al–TiB.

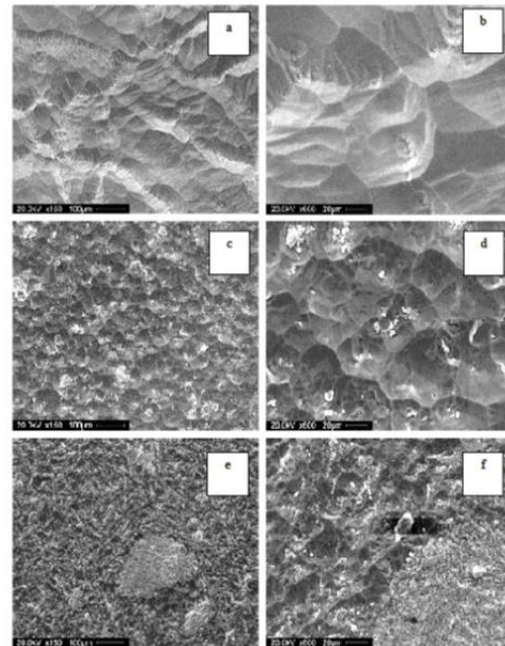


Fig. 2. Surface of (a, b) Al, (c, d) Al–TiC, and (e, f) Al–TiB after etching. (a, b, c)  $\times 150$ , (d, e, f)  $\times 600$ .

The superposition of concentration maps obtained by SEM and EDS (Fig. 3) demonstrated (a) in case of Al–TiC the presence of titanium carbide on dark areas of aluminium; (b) in case of Al–TiB fairly uniform distribution of boron, with occasional inclusions of titanium, aluminium and boron ascribed to  $\text{TiB}_2$  of aluminium matrix. Based on the results from [9], needle-like elements represent  $\text{Al}_3\text{Ti}$ -phase.

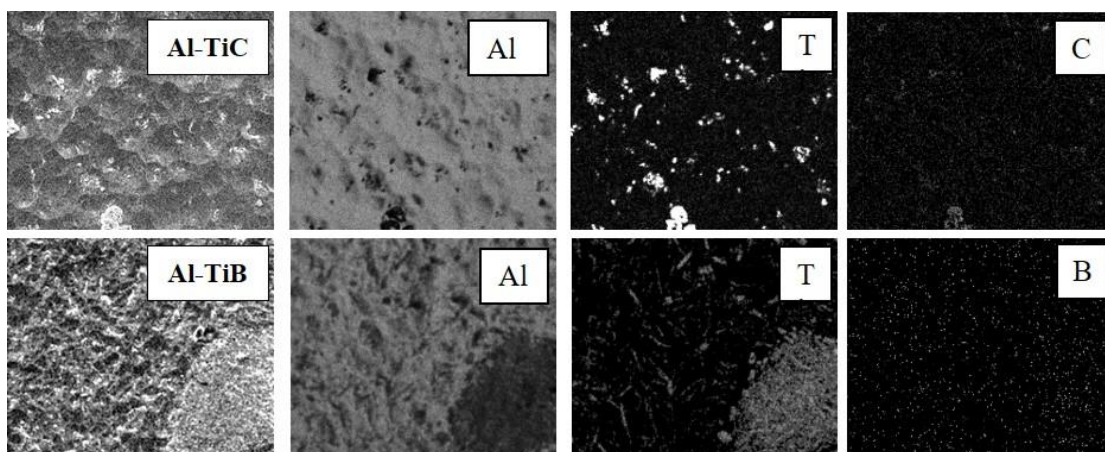


Fig. 3. Concentration maps for (a) Al–TiC and (b) Al–TiB.

Figure 4 shows that the formation of TiC in the composite Al–TiC and  $\text{Al}_3\text{Ti}$  and  $\text{TiB}_2$  in Al–TiB results in the increased microhardness of metal. For pure aluminium it is  $75 \text{ kgf/mm}^2$ , and for Al–TiC it makes up  $116 \text{ kgf/mm}^2$ . In Al–TiB an increase in microhardness makes up as much as 98%. Such a difference in microhardness of the composites is attributed to a two times bigger content of the strengthening phase in Al–TiB as compared to Al–TiC.

Thus, by means of SHS in melt composites Al–TiC and Al TiB were obtained. XRD analysis, SEM, and EDS demonstrated that an “in situ” technology applied lead to the formation of TiC,  $\text{Al}_3\text{Ti}$ , and  $\text{TiB}_2$  phases that modified aluminium. It was also shown that SHS in the presence of the additives (Ti + C) (Ti + B) made it possible to decrease grain size from 70 to 20–10  $\mu\text{m}$  and to increase microhardness by 55–98 %.

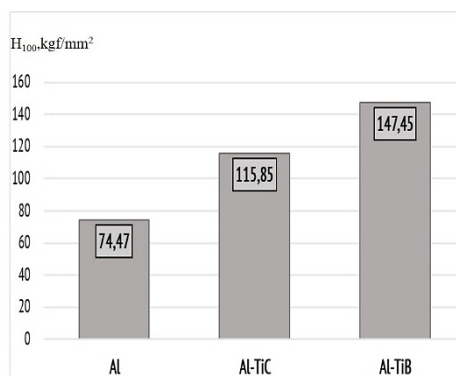


Fig. 4. Microhardness for Al, Al–TiC, and Al–TiB.

1. L. Xiangfa, W. Zhenqing, Z. Zuogui, B. Xiufang, The relationship between microstructures and refining performances of Al–Ti–C master alloys, *Mater. Sci. Eng. A*, 2002, vol. 332, iss. 1–2, pp. 70–74.
2. M.K. Premkumar, M.G. Chu, Al–TiC particulate composite produced by a liquid state in situ process, *Mater. Sci. Eng. A*, 1995, vol. 202, iss. 1–2, pp. 172–178.
3. Y. Birol, Grain refining efficiently of Al–Ti–C alloys, *J. Alloys Compd.*, 2006, vol. 422, iss. 1–2, pp. 128–131.
4. H. Ding, X. Liu, L. Yu, G. Zhao, The influence of forming processes on the distribution and morphologies of TiC in Al–Ti–C master alloys, *Scripta Mater.*, 2007, vol. 57, iss. 7, pp. 575–578.
5. R.S. Mikheyev, I.Ye. Kalashnikov, L.I. Kobeleva, T.A. Chernyshova, Razrabotka kompozitsionnykh materialov sistemy Al–Ti–TiC, *Fizika i khimiya obrabotki materialov*, 2009, no. 3, pp. 85–90.
6. A.R. Luts, A.G. Makarenko, Samorasprostranyayushchiysya vysokotemperaturnyy sintez alyuminiyevykh splavov, Samara: Mashinostroyeniye, SamGTU, 2008. 175 p.
7. Ye.G. Kandalova, V.I. Nikitin, A.T. Makarenko, et al., In situ technology of Al-TiC composite preparation, *Bull. SamSTU: Tech. Sci.*, 2005, no. 32, pp. 95–101.
8. Information package of International Conference “SVS-50” on the occasion of 50<sup>th</sup> anniversary of scientific invention of self-propagating high-temperature synthesis (SHS), Chernogolovka, ISMAN, 2017, 241 p.
9. E.A. Popova, A.V. Dolmatov, L.Ye. Bodrova, et al, Analysis of modifying ability of different types of Al–Ti and Al–Ti–C alloys, *Melts*, 2009, no. 5, pp. 3–9.

ADVANCED COMBUSTION SYNTHESIS FOR HIGH PERFORMANCE  
MATERIALS AND POWER SYSTEMS DEVELOPMENTS

O. Odawara

PROSAP Inc., Tokyo, 153-0064 Japan  
Professor Emeritus, Tokyo Institute of Technology  
e-mail: odawara@justsap-me.org

DOI: 10.24411/9999-0014A-2019-10111

Combustion synthesis has been successfully applied to geothermal energy developments [1] and *in-situ* resource utilization in space exploration [2] by establishing the optimum process control parameters under centrifugal force, low gravity, and high vacuum conditions. The potentials of the combustion synthesis technologies even in other extreme environments such as underwater and disaster-stricken areas are improved more flexibly and efficiently by combining the process characteristics with effective external additions and steep gradient in temperature and pressure formed during spontaneous propagation of exothermic reaction. In view of recent technological developments on energy storage, transport, and conversion, the combustion synthesis technologies to provide high performance materials and rapid high-temperature environments are widely expanded in practical approaches with much precise controllability.

The R&Ds on effective utilizations of resources, functional materials development and exergy loss minimization have advanced the combustion synthesis technologies as highly operable ones and made great progress toward the fields such as “Al–H<sub>2</sub>O” reactions, “catalytic recuperative coupling” reactions and “heat-to-electricity” conversions.

**Al–H<sub>2</sub>O reactions:** Researches on Al–H<sub>2</sub>O reaction have been much attractive in the field of not only propellants and explosives but also H<sub>2</sub> extraction/storage and ultra-low density transparent materials of AlOOH-based aerogels. With increasing the particle sizes of Al powders and lowering the reaction temperatures, the products synthesized by exothermic reactions of Al and H<sub>2</sub>O are in the order of Al<sub>2</sub>O<sub>3</sub> ( $2\text{Al} + 3\text{H}_2\text{O} = \text{Al}_2\text{O}_3 + 3\text{H}_2$ ), AlOOH ( $2\text{Al} + 4\text{H}_2\text{O} = 2\text{AlOOH} + 3\text{H}_2$ ), and Al(OH)<sub>3</sub> ( $2\text{Al} + 6\text{H}_2\text{O} = 2\text{Al(OH)}_3 + 3\text{H}_2$ ).

**Catalytic recuperative coupling reactions:** The exothermic reaction of CO<sub>2</sub> and H<sub>2</sub> generates CH<sub>4</sub> and H<sub>2</sub>O over efficient catalysts, which is called a “Sabatier reaction”. Further utilizations of the CH<sub>4</sub> are not only in the exothermic reaction of CH<sub>4</sub>–O<sub>2</sub> but also for endothermic treatments of steam reforming, thermal pyrolysis and dry reforming. The recycle with self-supply of such as H<sub>2</sub>, H<sub>2</sub>O and syngas from CO<sub>2</sub> can be systemized in the closed-loop of the catalytic recuperative coupling reactions formed by inducing these exothermic and endothermic processes adjacently.

**Heat-to-electricity conversions:** Concept of heat-to-electricity conversion has been proposed and developed in various fields aided with “waste-heat” of thermo-photovoltaic energy conversion, acoustic-to-electric power conversion, thermo-electric tube, etc. The combustion synthesis technologies can provide a high-temperature environment with simple processes, with which the system related with energy conversion of heat-to-electricity would be effectively combined.

In recent years, the developments of supercritical CO<sub>2</sub> (s-CO<sub>2</sub>) cycle have been actively investigated for efficient power generation improvements. As the s-CO<sub>2</sub> undergoes large changes in density with small changes in pressure or temperature, to use s-CO<sub>2</sub> as the working fluid can reveal high efficiency for powering turbines and less work to convert heat to electricity regardless of the source of heat. The density of s-CO<sub>2</sub> is about half of H<sub>2</sub>O, so the compressing

is easier than steam. The energy saving feature of s-CO<sub>2</sub> greatly contributes to the turbine's overall efficiency. With the s-CO<sub>2</sub> as the working fluid, the generating plant can function with a smaller compressor and turbine, and the high fluid density of the s-CO<sub>2</sub> can attain the compact and highly efficient system with simple single-casing body. The closed-loop geothermal power cycle with the s-CO<sub>2</sub> has been also proposed to produce a few MWe with some existing non-productive geothermal wells. If such a closed-loop system for single-well is established, it is possible to eliminate thermal fatigue and corrosion associated in the case of steam system.

The present work mainly focuses on a closed-loop s-CO<sub>2</sub> geothermal power generation formed at the single-well with the downward and upward flowing lines set concentrically. As a principle, the system starts by injecting CO<sub>2</sub> at supercritical conditions into an insulated pipe that is placed inside the well. The fluid then flows down until it reaches the heat exchanging part at the geothermal reservoir for absorbing the heat from the environment. Due to the fact that the higher the fluid temperature, the smaller the density, the temperature, and pressure of fluid are different at flowing lines downward and upward. The main principal of the system concerned with this power generation is the large variation of density with relatively small variations in pressure and temperature of the s-CO<sub>2</sub>, which results in a "thermo-siphoning effect" to the heat transport process of CO<sub>2</sub>. The flow of CO<sub>2</sub> as a working fluid is ideally maintained in a supercritical state throughout the cycle. With decreasing the density of the s-CO<sub>2</sub> with increasing the temperature where buoyancy forces come into play, the dense s-CO<sub>2</sub> at high temperature pushes out the less dense hot s-CO<sub>2</sub> to the surface. The pressure and temperature differences between the hot and cold sides of the cycle can then be exploited to generate electricity.

In the present work, the upward s-CO<sub>2</sub> flow is amplified with the reduction of the density of upward s-CO<sub>2</sub> flow with setting of the heat reservoir around the surface area of the concentric single-well as shown in Fig. 1. For keeping the temperature high around the surface area formed around the heat reservoir, the combustion synthesis technologies are applied with the combinations of such as the Al-H<sub>2</sub>O reactions and catalytic recuperative coupling processes. The noticed approach of the present work is also in the utilization of dry ice as injection source. The downstream flow of dry ice is carried out undisturbed by the side wall of the pipe as the "Leidenfrost" effect which makes dry ice surface separate from the hot pipe wall. To inject CO<sub>2</sub> source as dry ice to the geothermal well can make the maximum s-CO<sub>2</sub> temperature difference with keeping s-CO<sub>2</sub> in the high temperature and high pressure around the geothermal reservoir. Since the density of s-CO<sub>2</sub> changes more drastically when increasing the temperature from its critical temperature than the case of the pressure changes from the critical pressure, the present approaches would play an important role in its thermosiphoning effect. The R&Ds of the combustion synthesis technologies proceeded in consideration of the effects involved in the phase change of CO<sub>2</sub> from dry ice to s-CO<sub>2</sub>, Leidenfrost levitation and catalytic combustion of recuperative coupling would be applicable in extreme environments utilizations toward improvements of sustainable human activities.

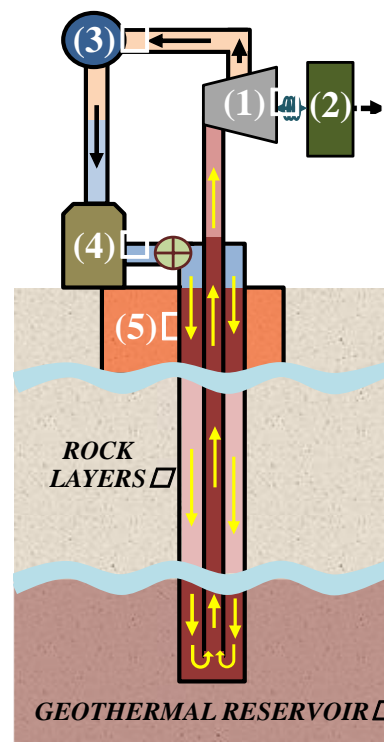


Fig. 1 Schematic of a closed-loop s-CO<sub>2</sub> geothermal energy system.

- (1) turbine; (2) generator;  
 (3) compressor pump;  
 (4) injection control; (5) heat storage.

1. O. Odawara, T. Fujita, A.V. Gubarevich, H. Wada, Thermite-related technologies for developments in extreme geothermal environments, *Int. J. Self-Propag. High-Temp. Synth.*, 2018, vol. 27, no. 4, pp. 228–235.
2. O. Odawara, Combustion synthesis technology for a sustainable settlement overnight, *Eurasian Chem. Tech. J.*, 2018, vol. 20, no. 1, pp. 3–16.

FORMATION OF STRUCTURE OF SHS- AND MA-POWDERS  $Ti_3SiC_2$  BY SPS

 S. A. Oglezneva<sup>\*a</sup>, T. L. Talako<sup>b</sup>, A. A. Smetkin<sup>a</sup>, A. I. Letsko<sup>b</sup>, and M. N. Kachenjuk<sup>a</sup>
<sup>a</sup>Perm National Research Polytechnic University, Perm, 614990 Russia

<sup>b</sup>O.V. Roman Powder Metallurgy Institute, Minsk, 220005 Belarus

\*e-mail: osa@pm.pstu.ac.ru

DOI: 10.24411/9999-0014A-2019-10112

The development of effective methods for producing composites based on MAX-phases is an urgent task in materials science. Many researchers have shown that with the help of reaction sintering, SHS method it is possible to obtain composites with different MAX-phase content [1–4]. The aim of the present work was a comparative analysis of consolidation composition of Ti–SiC–C upon SPS of the mechanically activated (MA) powder mixtures and the powders obtained by SHS.

For consolidation, (1) mechanically activated mixture of powders of titanium, silicon carbide, and carbon in a molar ratio of 3Ti:1.25SiC:0.75C, which was obtained by processing in a planetary mill and (2) the reaction mixture of titanium, silicon carbide and carbon in a molar ratio of 5Ti:2SiC:1C, which was crushed after after SHS sinters, containing 75% of  $Ti_3SiC_2$ , 10 % TiC, and 15%  $Ti_xSi_y$  were used. The average particle size of MA and SHS powders was 20 and 1.5  $\mu m$ , respectively. Consolidation of powders was carried out by SPS using Dr. Sinter SPS-1050b plant (SPS Syntex Inc.) at temperatures of 1100, 1200, 1300 and 1400°C, holding time for 5 min, and under a pressure of 30 MPa. XRD analysis of consolidated powders is shown in Table 1.

Table 1. Phase composition of samples after SPS of MA and SHS-powders.

| Method of processing mixtures | $T_{SPS}$ , °C | $Ti_3SiC_2$ | TiC | $Ti_xSi_y$ | Ti | SiC |
|-------------------------------|----------------|-------------|-----|------------|----|-----|
| MA                            | 1100           | 28          | 52  | --         | 10 | 10  |
| SHS                           |                | 33          | 54  | 13         | -- | --  |
| MA                            | 1200           | 45          | 55  | --         | -- | --  |
| SHS                           |                | 6           | 66  | 28         | -- | --  |
| MA                            | 1300           | 82          | 18  | --         | -- | --  |
| SHS                           |                | 8           | 68  | 24         | -- | --  |
| MA                            | 1400           | 80          | 20  | --         | -- | --  |
| SHS                           |                | 12          | 84  | 4          | -- | --  |

From the presented data it follows that the greatest number of  $Ti_3SiC_2$  phase (82%) was obtained during consolidation at  $T = 1300^\circ C$  of MA mixture. This is due to the fact that the process of formation of  $Ti_3SiC_2$  occurs at such a temperature  $T = 1300^\circ C$  due to the interaction of intermediate phases  $Ti_xSi_y$  with TiC formed at lower temperatures. At temperatures of 1100 and 1200°C diffusion processes are limited by temperature and time parameters, so the composites are preferred phases of titanium carbides and silicides. At a higher temperature  $T = 1400^\circ C$  the content of  $Ti_3SiC_2$  is slightly reduced due to the decomposition of titanium silicon carbide on titanium carbide and silicon, partially evaporating in a vacuum.

With the consolidation of the milled powders obtained by SHS method, the degradation  $Ti_3SiC_2$ -phase to carbide and the silicides of titanium, due to its dispersion in the initial state and probably the presence of impurities. Already at  $T = 1100^\circ C$   $Ti_3SiC_2$  decomposition occurs,



its share decreases from 75 to 33%. Further temperature rise even more dramatically reduces the content of  $Ti_3SiC_2$  to 12% at 1400°C.

Figure 1 shows the dependence of the shrinkage of MA and SHS powders on the sintering temperature (up to 1400°C). The nature of their compaction differs significantly from each other. MA powder is compacted almost monotonously throughout the temperature range. The formation of titanium silicon carbide starts at temperatures above 1100°C and is accompanied by a slowing of the shrinkage due to the fact that the resulting  $Ti_3SiC_2$  has a large volume.

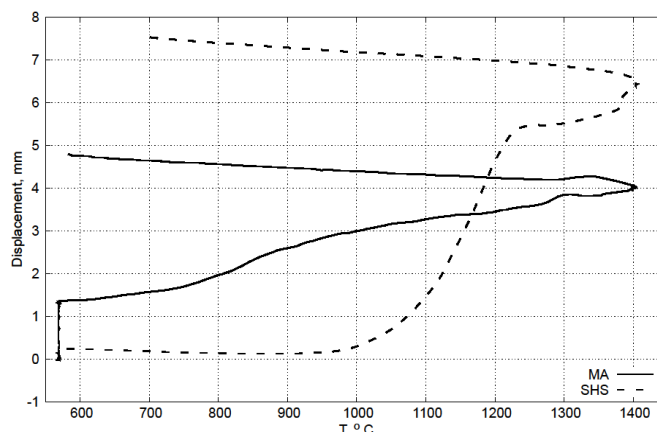


Fig. 1. Shrinkage dependence on the sintering temperature of MA and SHS powders.

SHS powders due to their high dispersion are actively consolidated, starting with  $T = 900^\circ\text{C}$  up to the holding temperature  $T = 1200^\circ\text{C}$ . Intensive shrinkage of briquettes from SHS powders can be connected, including, with the change in the phase composition during the decomposition of  $Ti_3SiC_2$ . Above the temperature of 1200°C, there is an inhibition of the process of shrinkage, associated with the two simultaneously occurring processes - decomposition of  $Ti_3SiC_2$  leading to a decrease in the volume of the sample and synthesis of  $Ti_3SiC_2$  from silicides and carbides of titanium leading to an increase in sample volume. The quantity of  $Ti_3SiC_2$  with an increase in the temperature from 1200 to 1400°C increases from 6 to 12%, Table. The density of  $Ti_3SiC_2/TiC$  composites based on MA powders consolidated at 1400°C is 4.5 g/cm<sup>3</sup>, and  $TiC/Ti_3SiC_2$  composites based on SHS powders is 4.8 g/cm<sup>3</sup>.

Thus, SPS of MA powders at temperatures of 1300 and 1400°C makes it possible to form a  $Ti_3SiC_2/TiC$  composite material due to reaction sintering, while the  $Ti_3SiC_2$  phase is thermally stable. In SPS of highly dispersed SHS powders occurring reversible processes of decomposition-synthesis  $Ti_3SiC_2$ -phase.

The work is executed at financial support of Russian Foundation for Basic Research and Belarusian Republican Foundation for Fundamental Research, grants no. 18-58-00031 Bel\_a and T18P-101.

1. Z.M. Sun, Progress in research and development on MAX phases: a family of layered ternary compounds, *Int. Mater. Rev.*, 2011, vol. 56, p. 143–166.
2. H. Hashimoto, Z. M. Sun, S. Tada, Morphological evolution during reaction sintering of Ti, SiC and C powder blend, *J. Alloys Compd.*, 2007, vol. 441, nos. 1–2, pp.174–180.
3. M. A. El Saeed, F.A. Deorsola, R. M. Rashad, Optimization of the  $Ti_3SiC_2$  MAX phase synthesis, *Int. J. Refr. Met. Hard Mater.*, 2012, no. 35, pp. 127–131.
4. L. Chlubny, et al., Processing and properties of MAX phases-based materials using SHS technique, *Arch. Metall. Mater.*, 2015, vol. 60, no. 2, pp.859–863.

## EXOTHERMIC HYDROGENATION KINETICS OF MG WITH CATALYTIC DISSOCIATION OF MOLECULAR HYDROGEN

M. Ohyanagi<sup>\*a</sup>, Y. Shimizu<sup>a</sup>, M. Otowaki<sup>a</sup>, and K. Shirai<sup>a</sup><sup>a</sup>Department of Materials Chemistry, Ryukoku University, Ohtsu, 520-2194 Japan

\*e-mail: ohyanagi@rins.ryukoku.ac.jp

DOI: 10.24411/9999-0014A-2019-10113

Most of materials synthesis with highly exothermic reaction of reactants is classified as combustion synthesis. The combination of melting of one reactant and dissolution of the other by the heat release from combustion wave front sustains the self-propagation of reaction. The apparent activation energy of combustion synthesis is calculated by the propagation velocity and maximum combustion temperature[1, 2]. However, in view point of the microscopic phenomenon for momentary time, the contact and diffusion of one reactant to the other before the melting in the combustion wave front initiate the exothermic reaction, leading subsequent both of the ignition and the combustion. When one of the reactant is gaseous, the reaction with the other solid reactant must initiate first by reaction-controlled step and then immediately occur with the diffusion-controlled step between gas and solid in the initial stage of combustion synthesis, often followed by the melting, because the most of gas-solid reaction becomes very fast at the surface of solid just after the ignition and the gas is consumed there so that the reaction rate is controlled by diffusion of gas in the boundary layer between gas and solid [3]. In case of the less exothermic combustion between gas and solid, the uniform heating of whole reactants often leads this kind of combustion regime, that is, the volume combustion. The criteria between the reaction-controlled step at the surface of solid and the diffusion-controlled step in the boundary layer between gas and solid is if the reaction rate of product or the consumption rate of reactant gas strongly depends on the temperature for the reaction. In the volume combustion synthesis, the apparent activation energy is not capable to calculate from the both of propagating velocity and the maximum combustion temperature. The activation energy for the volume combustion has to be calculated by the Arrhenius plot of reaction kinetic constant.

The exothermic reaction of Mg and hydrogen molecule takes place reversibly with reaction heat of 75.9 kJ/mol at 293 K [4]. The adiabatic temperature for the hydrogenation is 1255 K. The rate-determined step to form MgH<sub>2</sub> from Mg + H<sub>2</sub> is considered to be a dissociation-adsorption of molecular hydrogen, not diffusion of H into Mg. The dissociation-adsorption of molecular hydrogen also accelerates by the catalyst such as metal oxides [5]. The initial stage of hydrogenation of Mg using catalytic Nb<sub>2</sub>O<sub>5</sub> and TiO was kinetically analyzed by the consumption of hydrogen gas from a decrease in hydrogen pressure in given volume using Sieverts method as shown in Fig. 1 with assumption of the rate-determining step of the dissociation-adsorption of molecular hydrogen as a first order reaction at the temperature below 313 K for Nb<sub>2</sub>O<sub>5</sub> catalyst and 423 K for TiO catalyst. The lower activation energies for the catalysts compared to the value for Mg without catalyst, 72–97 kJ/mol [6] were calculated to be 45 and 31 kJ/mol in the lower temperature range, respectively. However, as shown in Fig. 2 the hydrogen pressure for the hydrogenation of Mg with Nb<sub>2</sub>O<sub>5</sub> catalyst abruptly decreased in time at 303 K to 323 K, that is, the consumption rate of hydrogen intensively increased in the transient temperature range, just like ignition and combustion of Mg and molecular hydrogen. As the consumption rate of hydrogen is almost equal or slightly increase at the several initial temperatures, in other words, did not depend on the temperature so much, the rate constant was calculated based on a diffusion-controlled mechanism in the boundary layer (apparent first order reaction) for the combustion-type hydrogenation above the transient temperature which

gives abrupt consumption of hydrogen gas. The apparent activation energies for the catalysts were calculated to be nearly equal to be zero above 313 K for  $\text{Nb}_2\text{O}_5$  and 423 K for  $\text{TiO}$ , respectively.

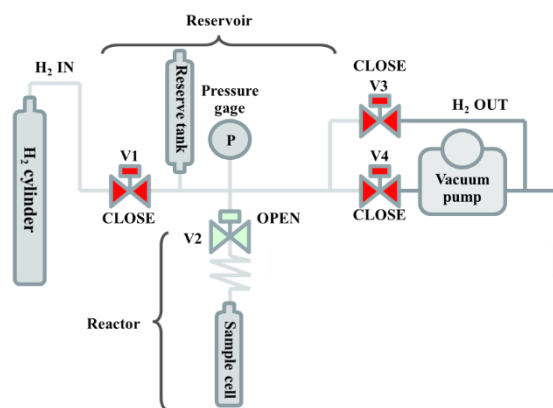


Fig. 1. Illustration of pressure-composition-temperature measurement apparatus (Sieverts method); The pressure was recorded against time. Under the initial steady pressure, the time which the pressure started to decrease was defined as  $t = 0$ .

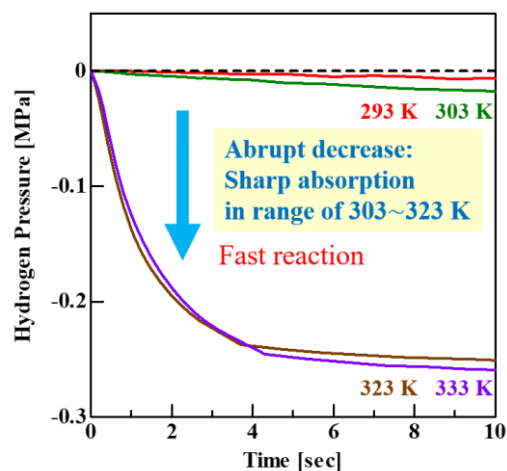


Fig. 2. A decrease of hydrogen pressure for the hydrogenation of Mg (dehydrogenated from  $\text{MgH}_2$  at 623 K for 2h in vacuo) with 10 wt %  $\text{Nb}_2\text{O}_5$  catalyst at the given temperature.

1. C.-L. Yeh, C.-Y. Ke, Combustion synthesis of FeAl-based composites from thermite and intermetallic reactions, *Cryst.*, 2019, vol. 9, no. 3, p.127.
2. C. L. Yeh, W.H. Chen, Preparation of niobium borides  $\text{NbB}$  and  $\text{NbB}_2$  by self-propagating combustion synthesis, *J. Alloys Compd.*, 2006, vol. 420, no. 1, p. 111.
3. G. Bruce, Clean coal engineering technology, 2ed, Chapter 4, 2017, 195 p.
4. J.M.W. Chase, et al., *J. Phys. Chem. Ref. Data*, 1985, vol. 14, no.1.
5. A. Borgschulte, J. H. Rector, B. Dam, R. Griessen, A. Zuttel, The role of niobium oxide as a surface catalyst for hydrogen absorption, *J. Catal.*, 2005, vol. 235, no. 2, p. 353.
6. M. Pozzo, D. Alfè, Hydrogen dissociation and diffusion on transition metal (= Ti, Zr, V, Fe, Ru, Co, Rh, Ni, Pd, Cu, Ag)-doped  $\text{Mg}(0001)$  surfaces, *Int. J. Hydrogen Energy*, 2009, vol. 34, no. 4, p. 1922.

## CAPACITOR GRADE POWDERS FROM SCRAP OF TANTALUM CAPACITORS PRODUCTS

V. M. Orlov<sup>a</sup>, T. Yu. Prokhorova<sup>\*a</sup>, and E. N. Kiselev<sup>a</sup>

<sup>a</sup>Tananaev Institute of Chemistry - Subdivision of the Federal Research Centre “Kola Science Centre of the Russian Academy of Sciences”, Apatity, 184209 Russia

\*e-mail: tantal@chemy.kolasc.net.ru

DOI: 10.24411/9999-0014A-2019-10114

Regeneration of tantalum from secondary sources of raw materials provides up to 10% of world demand for tantalum (in the USA - up to 25%) [1]. Capacitor scrap makes up about 20% of the amount of recycled tantalum returning to the market [2]. This scrap is an anode, rejected at different stages of the manufacture of capacitors. trimming tantalum wire used as a lead, a snap-out of compact metal and its waste during its manufacture.

Some methods of using scrap provide for a full processing cycle ending with the production of tantalum compounds and their subsequent reduction to metal [3–6]. Direct use of sintered anodes scrap by hydrogenation, grinding, dehydrogenation followed by agglomeration and deoxidation didn't ensure the high quality of the powder [7]. The possibility of processing the anodes of electrolytic and oxide-semiconductor capacitors into high-quality capacitor powder without the use of refining electron-beam remelting is shown in [8, 9]. Schematic diagrams for processing various types of scrap from the production of tantalum capacitors to produce conditioned capacitor grade powder with a specific charge of 5500–8400 CV/g were proposed in [10].

It was of interest to consider the possibility of using high-purity tantalum scrap to produce capacitor powders with a specific charge of 100000 CV/g.

Waste capacitor powder, rejected sintered anodes, scrap of wire used as lead were used as a raw material. The metal was oxidized in a muffle furnace at 800°C for 4 h. The resulting pentoxide was analyzed for the content of metallic impurities by atomic emission spectroscopy with photographic recording of the spectrum. The reduction was carried out with magnesium vapor at a temperature of 830°C and a residual pressure of argon in the reactor for 5–6 h. The apparatus and method of reduction are given in [11].

Data on the content of impurities in Ta<sub>2</sub>O<sub>5</sub> obtained from various types of scrap is shown in the Table 1. It can be seen that the samples differ mainly in the content of niobium. Depending on the type of waste, the specific surface area of Ta<sub>2</sub>O<sub>5</sub> ranged from 0.3 to 1.9 m<sup>2</sup>·g<sup>-1</sup>, which affected the characteristics of the obtained tantalum powder. The dependence of the specific surface of tantalum powder on the specific surface of pentoxide is shown in Fig. 1a. Since the powders obtained by the reduction of the tantalum oxide compounds with magnesium vapors have the mesoporous structure [11], the value of their surface area is determined by the surface area of the pores (Fig. 1b). At the same time at least 50% of the surface falls on pores with a diameter of less than 10 nm.

Table 1. Impurity content in Ta<sub>2</sub>O<sub>5</sub>.

| No. | Scrap type | Impurity content, % |          |          |         |         |
|-----|------------|---------------------|----------|----------|---------|---------|
|     |            | Fe                  | Ni       | Cr       | Nb      | Si      |
| 1   | Powder     | 0.0017              | < 0.0003 | < 0.0003 | 0.045   | < 0.001 |
| 2   | Cuttings   | 0.0018              | 0.0002   | < 0.0003 | 0.300   | 0.002   |
| 3   | Wire       | 0.0012              | 0.0010   | < 0.0003 | < 0.004 | < 0.002 |

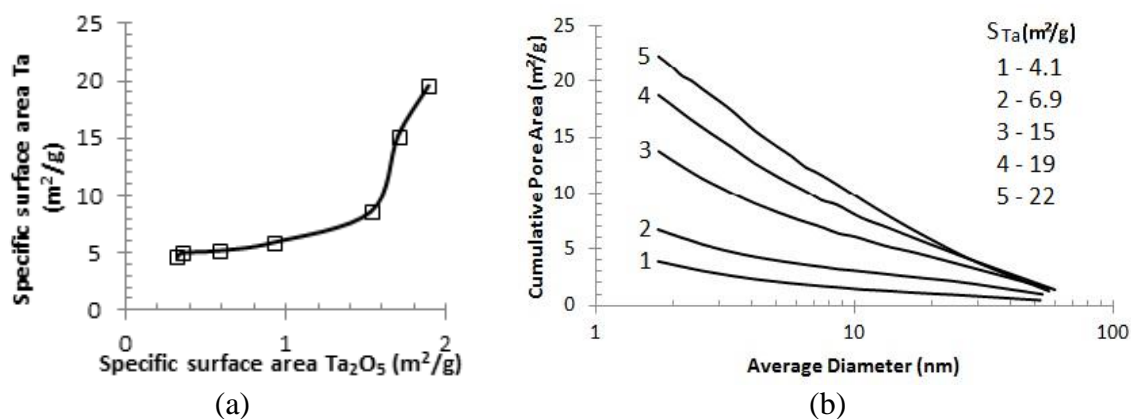


Fig. 1. (a) Dependence of the specific surface of the Ta powder on the specific surface of  $Ta_2O_5$  and (b) cumulative distribution curves of the pore area in the Ta powders with different surfaces.

The SEM images of tantalum powders obtained from precursors with different characteristics presented in Fig. 2 give an idea of the morphology of the particles. It is seen that they have the same appearance and similar sizes. If the precursor was pentoxide which was obtained by burning a compact metal (wire, cuttings) Ta powders had a smaller surface area. This affected the characteristics of the anodes made from them (Table 2). The specific surface area of the used powder ( $S$ ), temperature ( $T$ ), and the duration of sintering of the anodes ( $\tau$ ), their diameter shrinkage ( $\Delta d/d$ ), specific charge ( $Q$ ) and leakage current ( $I$ ) are shown in Table 2; anodizing voltage is 16 V.

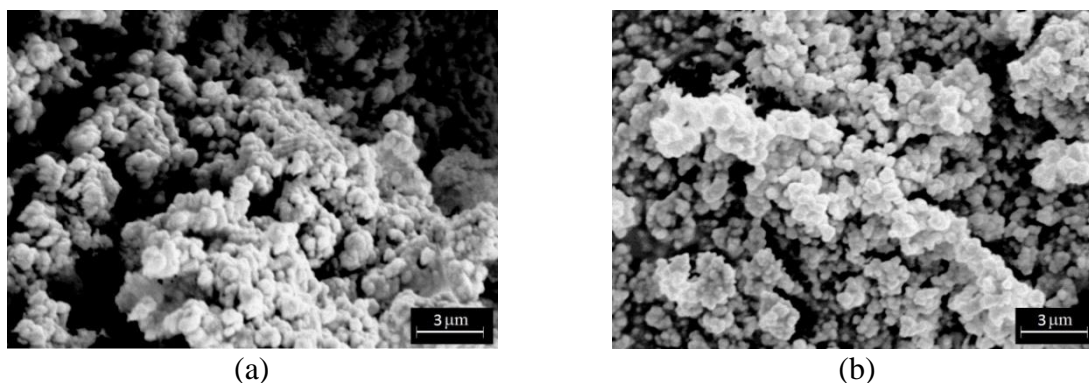


Fig. 2. The SEM images of tantalum powder particles with specific surface area,  $m^2/g$ : (a) 14, (b) 4.5.  $Ta_2O_5$  obtained by burning of: (a) powder, (b) compact metal.

Table 2. Characteristics of the anodes.

| No. | Scrap type | $S, m^2/g$ | $T, ^\circ C /$<br>$\tau, min$ | $\Delta d/d, g/cm^3$ | $tg\delta, \%$ | $Q, CV/g$ | $I, A/C$ |
|-----|------------|------------|--------------------------------|----------------------|----------------|-----------|----------|
| 1   | Powder     | 14         | 1250 / 15                      | 8.5                  | 47             | 148700    | 0.001    |
|     |            |            | 1300 / 20                      | 19                   | 22             | 94200     | 0.001    |
| 2   | Cuttings   | 5.2        | 1300 / 20                      | 8.9                  | 46             | 138300    | 0.001    |
| 3   | Wire       | 4.6        | 1300 / 20                      | 8.0                  | 47             | 125600    | 0.0008   |

The use of powders with a lower specific surface area makes it possible to raise the sintering temperature of the anodes without a significant decrease in the specific charge. Despite the higher nickel content in the pentoxide, the lowest leakage current was observed in the anodes made from the powder obtained from the recycling of waste wire. Thus, some types of tantalum

scrap can be used as a raw material without the use of deep chemical processing or refining electron beam remelting and for the production of magnesium thermal capacitor powders with a specific charge of more than 100000 CV/g.

1. G.A. Kolobov, V.S. Panov, N.N. Rakova, technologies of secondary refractory rare metals (review), *Russ. J. Non-Ferr. Met.*, 2014, vol. 55, no. 2, pp. 141–147
2. P. Stratton, J. Anderson, R. Baylis, The changing face of tantalum, *T.I.C. Bull.*, 2018, no. 172, pp. 16–21.
3. K. Mineta, T.H. Okabe, Development of recycling process for tantalum from capacitor scraps, *J. Phys. Chem. Solids*, 2005, vol. 66, nos. 2–4, pp. 318–321.
4. K. Mineta, T.H. Okabe, Recycling process for tantalum from capacitor scraps and chlorination by utilizing chloride wastes, *Shigen-to-Sozai*, 2005, vol. 121, pp. 284–290.
5. J.D. Lessard, L.N. Shekhter, D.G. Gribbin, Yu. Blagoveshchensky, L.F. McHugh, A new technology platform for the production of electronic grade tantalum nanopowders from tantalum scrap sources, *Int. J. Refract. Met. Hard Mater.*, 2015, no. 48, pp. 408–413.
6. V.M. Chumarev, V.V. Berezko, A.A. Shtin, et al, Tekhnologiya pererabotki vtorichnogo tantalovogo syr'ya, *Tsvet. Met.*, 2006, no. 3, pp. 52–54.
7. J. Smokovich, C.F. Hafner, Method for the production of tantalum powder using reclaimed scrap as source material, *Pat. 7981191 US*, 2006.
8. V.M. Orlov, V.V. Sukhorukov, E.S. Matychenko, Pererabotka skrapa tantalovykh kondensatorov, *Tsvet. Metall.*, 2005, no. 6, pp. 10–14.
9. V.M. Orlov, E.N. Kiselev, Sposob pererabotki skrapa anodov tantalovykh oksidno-poluprovodnikovoykh kondensatorov, *Pat. 2480529 RU*, 2013.
10. V.M. Orlov, E.N. Kiselev, Polucheniye kondensatornykh poroshkov iz otkhodov proizvodstva tantalovykh kondensatorov, *Khimich. Tekhnol.*, 2013, no. 11, pp. 682–687.
11. V.M. Orlov, M.V. Kryzhanov, Production of tantalum powders by the magnesium reduction of tantalates, *Russ. Metall. (Met.)*, 2015, no. 7, pp. 590–593.

COMBINATION OF SHS AND SPS PROCESSING ROUTES FOR  
ADVANCED CERAMICSR. Orrù<sup>\*a</sup>, G. Tallarita<sup>a</sup>, R. Licheri<sup>a</sup>, and G. Cao<sup>a</sup>

<sup>a</sup>Dipartimento di Ingegneria Meccanica, Chimica e dei Materiali, Unità di Ricerca del  
Consorzio Interuniversitario Nazionale per la Scienza e Tecnologia dei Materiali (INSTM),  
Università di Cagliari, Via Marengo 2, 09123 Cagliari, Italy  
<sup>\*</sup>e-mail: roberto.orrù@dimcm.unica.it

DOI: 10.24411/9999-0014A-2019-10115

The fabrication of fully dense components is well known to represent a difficult target to achieve for various refractory ceramic systems, particularly if the starting powders are produced by conventional (furnace or solution) methods while pressure-less or standard hot-pressing (HP) techniques are employed to consolidate them. For instance, when considering members of the materials family generally referred to as ultra-high temperature ceramics (UHTCs) based transition metal borides and carbides, powders have to be usually exposed for hours to temperature above 2000°C in order to reach reasonable densification levels. Therefore, it is apparent that more convenient synthesis/consolidation routes should be considered to fully exploit the unique combination of chemico-physical and mechanical properties of UHTCs (melting temperature exceeding 3000°C, high hardness, chemical inertness, good thermal and electrical conductivities, neutron and selective solar energy absorption capabilities, etc.) which makes them so attractive in the aerospace, nuclear, solar energy, and other industrial fields. In this context, the efficient spark plasma sintering (SPS), where the die/powders/punches ensemble is fastly heated by an electric current flowing through it, is often found to require less severe temperature/time conditions for powders consolidation with respect to standard HP [1]. Moreover, significant beneficial effects are reported in the literature when the self-propagating high-temperature synthesis (SHS) technique was adopted for the preparation of powders to be subsequently consolidated via SPS. The latter statement is supported by the several highly dense ceramics, including various UHTCs, as well as metallic, and composite systems, successfully fabricated through the SHS-SPS route. Alternatively, the synthesis reaction and the consolidation of the resulting product can be carried out concurrently, according to the reactive SPS (R-SPS) method. Various monophasic ( $ZrB_2$ ,  $HfB_2$ ,  $TaB_2$ ,  $TiB_2$ ,  $ZrC$ ,  $HfC$ ,  $TaC$ ), binary ( $ZrB_2-SiC$ ,  $HfB_2-SiC$ ,  $TaB_2-SiC$ ) and ternary ( $ZrB_2-ZrC-SiC$ ,  $HfB_2-HfC-SiC$ ,  $TaB_2-TaC-SiC$ ) ultra-refractory ceramic systems have been produced either by R-SPS or SHS-SPS.

Because of the strong exothermic nature of the reactions typically involved for synthesizing UHTCs, the studies conducted so far evidenced that the intrinsic potential of the R-SPS method is often hampered by various negative features accompanying the sudden occurrence of combustion synthesis events, which make the process quite difficult to control, albeit the product densification could be correspondingly facilitated. It should be noted in this regard that the combustion synthesis regime could be suppressed during the R-SPS process, if the heating rate is adequately lowered [2].

The R-SPS and SHS-SPS procedures have been both recently considered for the fabrication of some high entropy borides (HEBs), an emerging class of UHTCs. HEBs belong to the more general family of high-entropy alloys, where metallic elements are combined in near equimolar ratios to provide a single crystalline solid-solution characterized by maximum configurational entropy. The method originally proposed in the literature to produce massive HEBs was based on the consolidation of the ceramic constituents ( $ZrB_2$ ,  $HfB_2$ ,  $TaB_2$ , etc.) combined in equimolar

ratio, after being subjected for 6 h to high energy ball milling [3]. Since such an intense mechanical treatment prolongs markedly the total processing time and the contamination of the resulting powders from milling media becomes unavoidable, more suitable fabrication strategies should be proposed.

In this context, the use of the R-SPS process for the preparation of HEBs, with the synthesis reaction evolving under the combustion regime, was attempted for the case of  $(\text{Hf}_{0.2}\text{Mo}_{0.2}\text{Ta}_{0.2}\text{Nb}_{0.2}\text{Ti}_{0.2})\text{B}_2$ . Specifically, when the elemental reactants (Hf, Mo, Ta, Nb, Ti, and B) were processed by SPS for 20 min at 1950°C, with a heating rate of 200°C/min and the mechanical pressure switched from 20 to 70 MPa immediately after the combustion synthesis event, a 91.5 % dense material was obtained. However, as evidenced in Figs. 1a, 1b, the resulting material display some large pores (approximately up to 15  $\mu\text{m}$  sized) and the elemental distribution, particularly niobium, was not uniform across the sample. These negative features could be likely associated with the occurrence of the rapid combustion synthesis reaction, since the gases correspondingly liberated because of the presence of impurities or volatile species, are not able to freely escape from the die/punches tool, so that the resulting product microstructures become inhomogeneous with the presence of relatively large pores.

According to the SHS-SPS technique, the same elemental precursors were also reacted in few seconds by SHS using free standing pellets. The resulting product was composed of the desired  $(\text{Hf}_{0.2}\text{Mo}_{0.2}\text{Ta}_{0.2}\text{Nb}_{0.2}\text{Ti}_{0.2})\text{B}_2$  phase for approximately 96 wt %, with minor amounts of  $(\text{Ta}_{0.5}\text{Ti}_{0.5})\text{B}_2$ ,  $(\text{Hf}_{0.5}\text{Ti}_{0.5})\text{B}_2$ , and  $\text{HfB}_2$ , as well as traces of  $\text{HfO}_2$  [4]. Furthermore, when the corresponding powders were processed for 20 min at 1950°C by SPS under an applied pressure of 20 MPa, the full conversion to the single phase HEB was accomplished. In addition, the final product was about 92.5% dense, very similarly to consolidation levels achieved by Gild et al. for the same system [3]. From the SEM micrograph and the corresponding EDX elemental mapping shown in Figs. 1c and 1d, respectively, it can be deduced not only that a good densification level is reached but also that the species composition is very uniform across the material.

Similar results are also recently obtained for other HEB systems, to demonstrate that the use of the SHS-SPS approach could provide a useful contribution for the development of this new class of ultrarefractory ceramics.

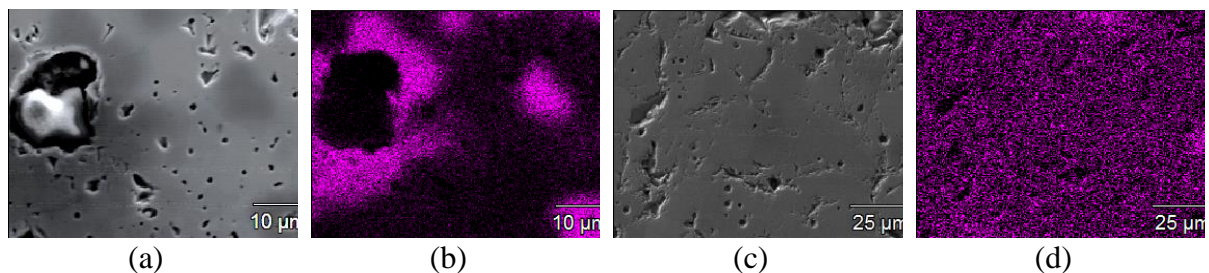


Fig. 1. SEM micrographs and related niobium EDX maps of the HEB sample produced by (a, b) R-SPS and (c, d) SHS-SPS.

This research was supported by the Regione Autonoma della Sardegna (Italy), Fondo di Sviluppo e Coesione 2014-2020, (project ARCHIMEDES - A new family of reinforced ultrahigh-temperature metal diborides for advanced applications, Cod. RAS: RASSR88309, Cod. CUP: F76C18000980002). One of the authors (G.T.) performed her activity in the framework of the International PhD in Innovation Sciences and Technologies at the University of Cagliari, Italy.

1. R. Orrù, R. Licheri, A.M. Locci, A. Cincotti, G. Cao, Consolidation/synthesis of materials by electric current activated/assisted sintering, *Mater. Sci. Eng. R*, 2009, vol. 63, nos. 4–6, pp. 127–287.



2. R. Licheri, C. Musa, R. Orrù, G. Cao, Influence of the heating rate on the in-situ synthesis and consolidation of  $ZrB_2$  by reactive spark plasma sintering, *J. Eur. Ceram. Soc.*, 2015, vol. 35, no. 4, pp. 1129–1137.
3. J. Gild, Y. Zhang, T. Harrington, S. Jiang, T. Hu, M.C. Quinn, W.M. Mellor, N. Zhou, K. Vecchio, J. Luo, High-entropy metal diborides: a new class of high-entropy materials and a new type of ultrahigh temperature ceramics, *Sci. Rep.*, 2016, vol. 6, pp. 37946.
4. G. Tallarita, R. Licheri, S. Garroni, R. Orrù, G. Cao, Novel processing route for the fabrication of bulk high-entropy metal diborides, *Scripta Mater.*, 2019, vol. 158, pp. 100–104.

## HEAT-RESISTANT PHOSPHATE MATERIALS IN SELF-PROPAGATING EXOTHERMIC SYNTHESIS MODE

Ch. G. Pak<sup>a</sup>, V. M. Batrashov<sup>\*a</sup>, G. A. Koshkin<sup>a</sup>, and K. V. Sokolova<sup>a</sup><sup>a</sup>Penza State University, Penza, 440026 Russia<sup>\*</sup>e-mail: shift150887@mail.ru

DOI: 10.24411/9999-0014A-2019-10116

The most time-consuming and energy-intensive operation of modern production of heat-resistant materials with application temperatures of up to 1700°C is the use of materials drying and firing processes. In addition, the manufacturing technology of such materials provides for a limited range of products. The self-propagating exothermic synthesis of heat-resistant materials allows to avoid unnecessary energy consumption, as well as to obtain products with enhanced physicomechanical and heat-resistant properties of various geometric shapes and sizes [1]. The technology is based on conducting an exothermic reaction between dispersed aluminum and phosphate binder [2]. The filler in this system can serve as refractory and refractory powders, including industrial waste. The production technology of heat-resistant materials in the exothermic reaction mode can be represented by the following scheme:  $X + Y + Z = N$ , where X is liquid phosphate binders system; Y is metal or alloy of metals or their mixture; Z is refractory filler of aluminosilicate composition, alumina, high alumina oxides, fibers, mixtures of oxides; N is synthesis product.

At present, self-hardening heat-resistant materials of aluminophosphate, aluminochromophosphate, aluminomagnesium phosphate, aluminosilicophosphate, magnesium phosphate composition with average density of 400–1000 kg/m<sup>3</sup>, application temperature above 1770°C [3] have been obtained by self-propagating exothermic synthesis.

Controlling the formation of physicomechanical and heat-resistant properties of materials is possible by controlling the process of structure formation of materials, which in turn can be achieved in several ways [4]:

- change in the reaction exotherm (change in the ratio of the liquid and solid phases of the original system, the use of phosphate binders of varying degrees of substitution, the controlled amount and dispersion of aluminum powder, the use of heating and cooling of the initial mixture);
- synthesis of materials in a limited formwork under gas pressure or in vacuum;
- material formation by layered synthesis.

The possibility of material formation by layer-by-layer synthesis opens up an interesting direction for the development of heat-resistant phosphate materials—obtaining materials of varying density. Figure 1 shows the main types of heat-resistant materials of variable density.

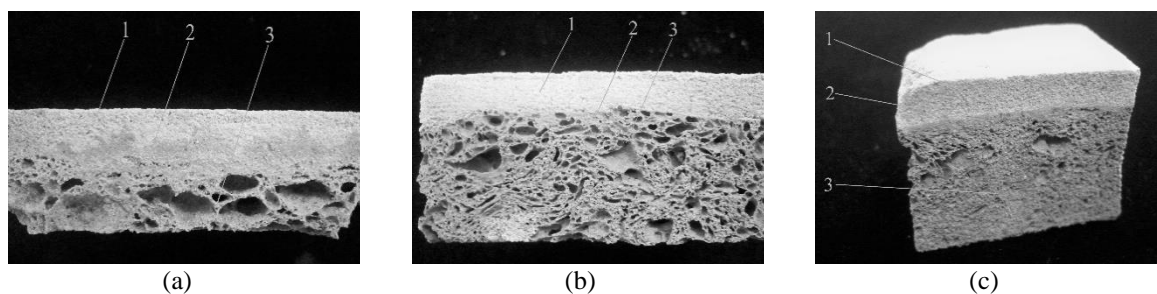


Fig. 1. Phosphate heat-resistant material of variable density: (a) aluminum powder PAP-1 is represented as the aluminum component; (b) modified aluminum powder POS-15 is presented as an aluminum component; (c) as an aluminum component, PA-4 aluminum powder is presented.

A feature of the materials obtained is the process of obtaining products in the mode of self-propagating exothermic synthesis. In the macrostructural analysis of the obtained materials, 3 zones are clearly visible: 1 zone is pressed phosphate material with a spherical aluminosilicate filler; 2 zone is intermediate structure; 3 zone is cellular phosphate heat-resistant material.

1. A.G. Merzhanov, Self-propagating high-temperature synthesis of refractory compounds, *Bull. USSR Acad. Sci.*, 1976, no. 10.
2. A.N. Abyzov, Obtaining heat-insulating heat-resistant phosphate materials by the method of self-propagating synthesis, Heat-resistant materials and concrete, Chelyabinsk, UralNIIstromproekt, 1978.
3. V.A. Abyzov, A.N. Abyzov, Cellular heat-resistant concretes based on phosphate binders and aggregates from aluminum production and processing wastes, *Refract. Tech. Ceram.*, 2015, nos. 4–5, pp. 69–73.
4. V.A. Grachev, A.Y. Rozen, C.G. Pak, V.M. Batrashov, SHS technology for development of high-temperature thermal insulation composite, *J. Ind. Pollut. Control*, 2017, vol. 33, no. 1, pp. 824–833.

## PRODUCTION OF ULTRA-REFRACTORY CARBIDES OF VARIOUS STOICHIOMETRIES IN THE SYSTEMS Ta–Zr–C, Ta–Hf–C BY SHS

E. I. Patsera<sup>a</sup>, S. A. Vorotilo<sup>a</sup>, V. V. Kurbatkina<sup>a</sup>, and E. A. Levashov<sup>a</sup>

<sup>a</sup>NUST MISiS, Moscow, 119049 Russia

DOI: 10.24411/9999-0014A-2019-10117

The development of aerospace technologies dictates the increased demands towards the crucial heat-loaded parts, which must effectively endure temperatures above 2500°C. The solution to this problem is possible via the creation of novel heat-resistant materials; hence the relevance of the development of materials based on the ultra-high temperature carbides with melting points above 4000°C (for example, 4125°C for (Ta,Hf)C with 20% HfC) [1]. Unfortunately, the high melting points of tantalum, zirconium, and hafnium carbides impede the sintering of powder materials and parts [2, 3]. The primary goal of this work was to produce the single-phase  $Ta_{(1-x)}Me_xC$  (Me = Zr, Hf,  $x = 10, 30, 50\%$ ) solid solutions by the means of self-propagating high-temperature synthesis, to sinter them and to characterize the structure and properties of produced ceramics. Mechanical activation (MA) was conducted in air using AIR-0.015 and Aktivator-4M planetary ball mills (PBM) for 5, 10, and 15 min at balls-to-mixture ratio 20:1. The following PBM schemes were used:

scheme 1: simultaneous loading of all components in jars and MA;

scheme 2: two-stage MA: first the mixture of tantalum and carbon black is activated, then either Zr or Hf is added and the activation continues for extra 5 min.

When mixtures are milled in ordinary ball mills for 4 h, no noticeable refinement of metallic particles occurs, but they are uniformly covered in carbon black. Microstructural investigation of MA mixtures Ta–Zr–C revealed the formation of layered composite powders consisting of Ta, Zr, and C layers. Size and structure of layered particles depend on the employed scheme of MA (Fig. 1). Microstructural analysis of the mixtures activated using various MA schemes demonstrated that scheme 1 leads to the intense milling of Zr, whose particles become significantly smaller than for Ta. After 10 min of MA using scheme 1, medial size of composite particles is 100–300  $\mu\text{m}$ , layers of tantalum and zirconium are  $25 \div 40$  and  $1 \div 2$   $\mu\text{m}$  wide.

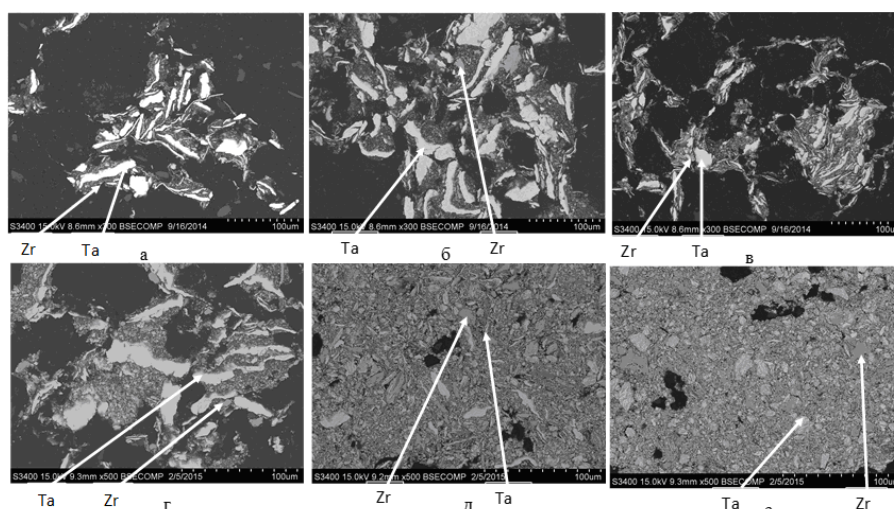


Fig. 1. Microstructure of reactive composite particles in Ta–Zr–C mixture, activated according to two schemes: Scheme 1:  $\tau = 5$  (a), 10 (b), 15 min (c); Scheme 2:  $\tau = 5$  (d), 10 (e), 15 min (f).

MA mixtures Ta–Hf–C, prepared in PBM AIR, were characterized by uneven mixing and insufficient energy accumulation due to the low planetary acceleration of the mill (25 g). Therefore, a more powerful Aktivator 4M with the planetary acceleration up to 120 g for used for MA of Ta–Hf–C mixtures. 10-min MA leads to the formation of 10–150  $\mu\text{m}$  granules comprised of alternating 0.5–2  $\mu\text{m}$  wide Ta and Hf layers, with C being located both within the granules and on their surface.

Similarly to Ta–Zr–C, phase composition of MA mixtures Ta–Hf–C prepared according to scheme 1 for 5, 10, and 15 min in air did not change. Increase in MA duration over 10 min increased the flammability of the mixtures considerably; therefore, MA durations below 10 min were used.

Prolongation of MA decreased the coherent scattering areas (CSAs) and increased the crystal lattice microdeformation of Ta, which signifies an efficient accumulation of excess energy in form of crystal lattice defects.

Products of combustion of Ta–Zr–C MA mixtures were obtained in the form of porous sinter cake ( $\Pi = 40\%$ ), and consisted of single-phase (Ta,Zr)C solution with a grains size of 1–10  $\mu\text{m}$  (Fig. 2). Low density of sinter cakes facilitates their milling into micron powders. Increase in ZrC content in solid solution led to higher value of its lattice parameter.

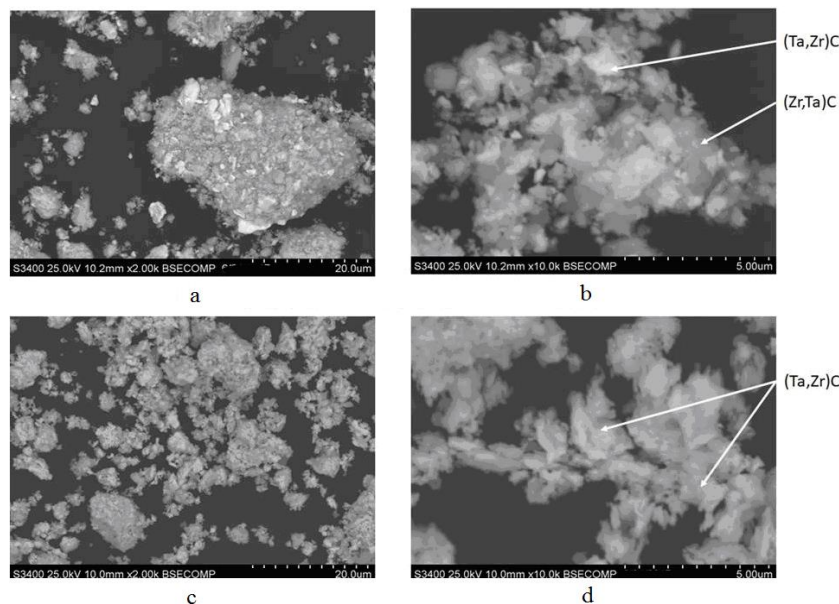


Fig. 2. Structure of combustion products with the composition 70% TaC–30% ZrC, produced using the mixtures after (a, b) ball milling and (c, d) after MA.

In case of Ta–Zr–C system, the particles size distribution of produced powders was somewhat dependent on the Zr content in the reactive mixture. Largest particles size (up to 10  $\mu\text{m}$ ) was characteristic for powders produced from combustion products 90% TaC–10% ZrC, whereas the finest powders (up to 3  $\mu\text{m}$ ) were produced from 50% TaC–50% ZrC combustion products.

Products of combustion of MA mixtures Ta–Hf–C were characterized by high residual porosity ( $\Pi = 50\%$ ) and grains size of 1–5  $\mu\text{m}$  (Fig. 3). Ball milling of sinter cake yielded 1–3  $\mu\text{m}$  powders.

Sintering of the produced powders was conducted using hot pressing or spark plasma sintering at 2100  $^{\circ}\text{C}$ . Depending on the composition of solid solution, the density of produced ceramics was 93–95%. No noticeable grain coarsening occurred. Size of residual pores did not exceed 1  $\mu\text{m}$ .

Nanoindentation of sintered ceramics revealed that their hardness and elastic moduli were fairly similar regardless of sintering technique (Table 1).

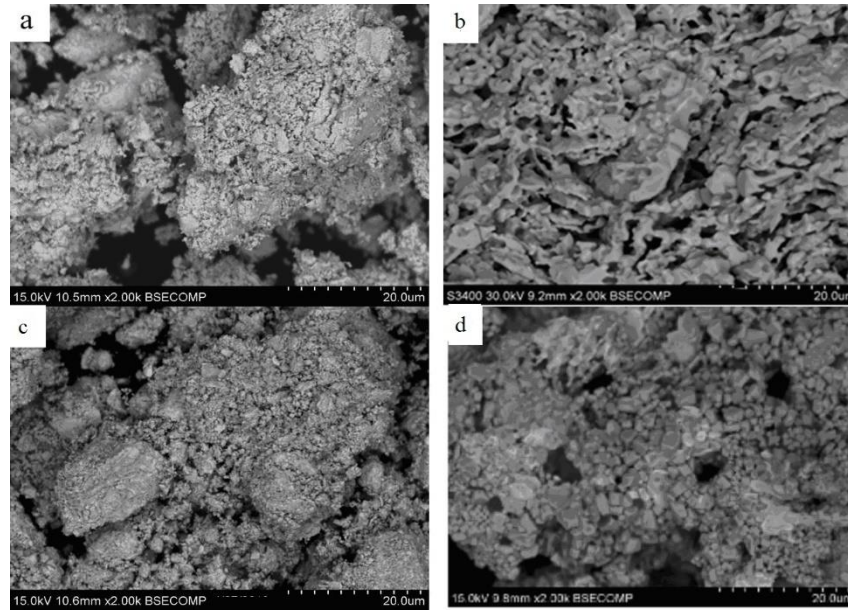


Fig. 3. Microstructure of the combustion products with composition: (a) TaC–10% HfC, (b) TaC–20% HfC, (c) TaC–30% HfC, (d) TaC–50% HfC.

Table 1. Mechanical properties of solid solutions measured by nanoindentation.

| Composition | Hardness, GPa | Young modulus, GPa |
|-------------|---------------|--------------------|
| TaC–20% ZrC | 32.2          | 520                |
| TaC–30% ZrC | 30.6          | 451                |
| TaC–50% ZrC | 38.8          | 582                |
| TaC–20% HfC | 27.4          | 484                |

This work was financially supported by Russian Science Foundation in the framework of project no. 17-79-10173 «Self-propagating high-temperature synthesis of single-phase ultra-refractory carbides with various compositions in the Ta–(Zr, Hf)–C system».

1. S.A. Ghaffari, M.A. Faghihi-Sani, F. Golestani-Fard, M. Nojabayy, Diffusion and solid solution formation between the binary carbides of TaC, HfC, and ZrC, *Int. J. Refract. Met. Hard Mater.*, 2013, vol. 41, pp. 180–184.
2. V.V. Kurbatkina, E.I. Patsera, S.A. Vorotilo, E.A. Levashov, A.N. Timofeev, Conditions for fabricating single-phase (Ta, Zr)C carbide by SHS from mechanically activated reaction mixtures, *Ceram. Int.*, 2016, vol. 42, no. 15, pp. 16491–16498.
3. V.V. Kurbatkina, E.I. Patsera, E.A. Levashov, S. Vorotilo, SHS processing and consolidation of Ta–Ti–C, Ta–Zr–C and Ta–Hf–C carbides for ultra-high-temperatures application, *Adv. Eng. Mater.*, 2018, 20.

# CHEVREL PHASE COMPOUND NANOMATERIALS SYNTHESIS VIA ULTRA-FAST SELF-PROPAGATING HIGH TEMPERATURE SYNTHESIS REACTION

M. Pawar and P. Gouma

The Ohio State University, Columbus, Ohio, 43210 USA

DOI: 10.24411/9999-0014A-2019-10118

Chevrel phase compounds with ( $M_xMo_6S_8$ : M Ternary metal cation) formula have been extensively explored as a catalyst material due to the ability of Mo atoms reduced oxidation state. Chevrel Phase with its R-3 symmetry has preferential channels for ion transport. Synthesis of Chevrel phase compound in nano configuration has been a road block for exploration of these material category for exploration of wide spectrum of applications regarding functional nanomaterials. Electrospinning is a facile way to produce nanofibers of Chevrel phase compounds followed by ultra-fast self-propagating high temperature synthesis (SHS) heat-treatment to obtain Chevrel phase nanofibers. Nanofibrous material provides high aspect ratio with high surface area makes it excellent candidate for catalyst in hydrodesulfurization and emerging field of battery science as a cathode material for better ion transport. This research study focuses on synthesis of nanopowders and nanofibers of Chevrel phase compounds via self-propagating high temperature synthesis reaction. Also nanofabrication of Chevrel phase ( $Cu_2Mo_6S_8$ ) nanofibers with electrospinning and SHS heat-treatment provided with complete material characterization (XRD, SEM, TEM, Raman, Chronoamperometry) is presented. It is very difficult to produce Chevrel phase compounds with nanoconfiguration via SHS synthesis reaction. Hence optimized process parameters were explored in order to utilize fast synthesis method which would otherwise take more than 40 h in order to synthesize 100% Chevrel phase compounds. As synthesized Chevrel phase compounds are explored as catalytic material and their efficiency with complete characterization will be presented.



Fig. 1. As pressed pellet (left), punch and die (right).

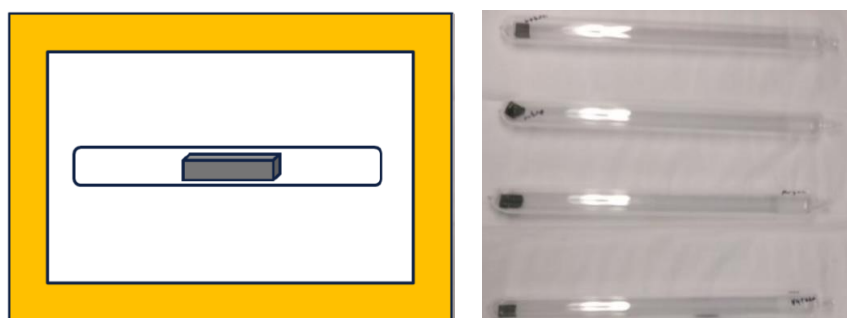


Fig. 2. Schematic diagram of synthesis, sample encapsulated in glass ampoules (right).

Optical micrograph of a cross-section of as synthesized circular pellet at 1000°C and 6-h holding time. Three distinguished layers are being observed and labeled in Fig. 3. Core looks dark in color with second layer having silver-like appearance. Outermost layer looks grey in color.

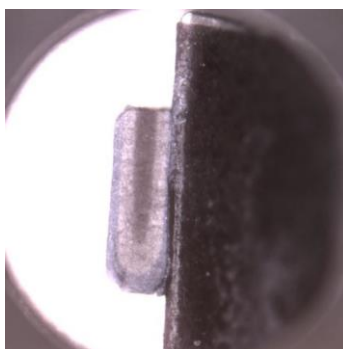


Fig. 3. Optical micrograph of cross-section of pellet heat-treated at 1000°C for 6 h.

Figure 4 represents SEM micrograph of region having MoS<sub>2</sub> rod and polyhedral Chevrel phase clusters. For elemental mapping does not show any presence of Cu in rod like structure. Rod like structure has high Mo and S content. Due to absence of Cu and high content of Mo as well as S rod like structure should be MoS<sub>2</sub>.

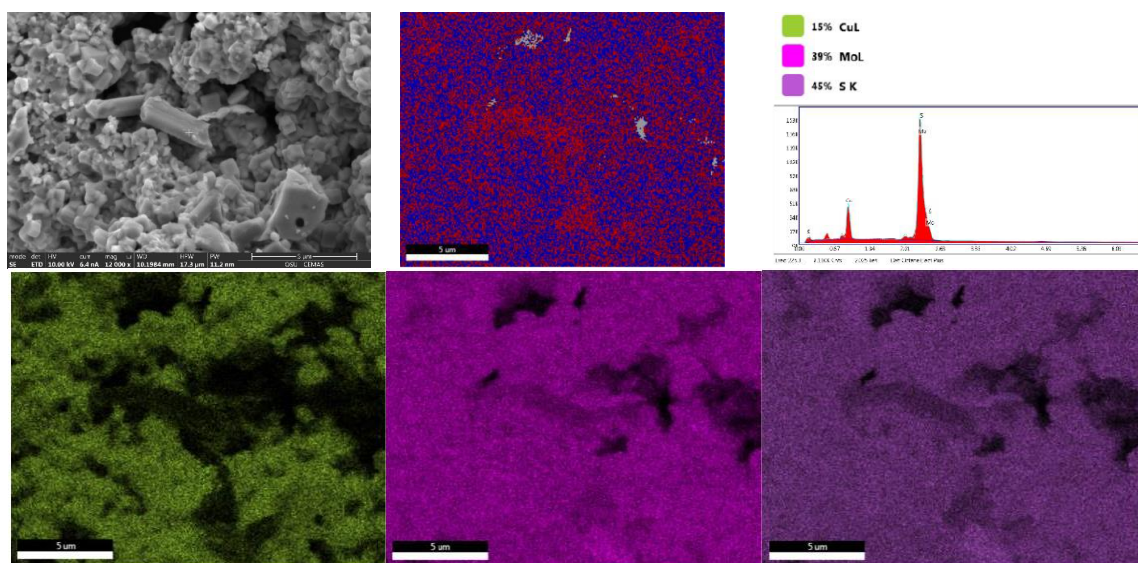


Fig. 4. SEM and EDS images.



## CONSOLIDATION OF SHS DERIVED SiC BASED COMPOSITES

Z. Pędzich<sup>\*a</sup>, K. Wojteczko<sup>a</sup>, A. Wojteczko<sup>a</sup>, A. Gubernat<sup>a</sup>, and M. M. Bućko<sup>a</sup><sup>a</sup>AGH University of Science and Technology, Kraków, Poland

\*e-mail: pedzich@agh.edu.pl

DOI: 10.24411/9999-0014A-2019-10119

HS synthesis could be a useful method of homogeneous incorporation of minority phases into ceramic matrix. The aim of presented studies was to check the possibility of incorporation phases containing yttrium or chromium into silicon carbide polycrystalline material. The scheme of experimental procedure was as follows: in the first step SHS synthesis of silicon carbide was conducted starting from elemental silicon and graphite powders mixed with suitable oxide additive ( $Y_2O_3$  or  $Cr_2O_3$ ) in the amount of 5% in each case. Substrates were compacted and heated up to  $1550^\circ C$  when SHS reaction started. The phase composition of porous products achieved during synthesis were examined by XRD method. Results confirmed proper stoichiometry of starting mixture. Whole silicon and carbon reacted and there was no free elemental silicon or carbon detected in products (see Figs. 1a, 1b).

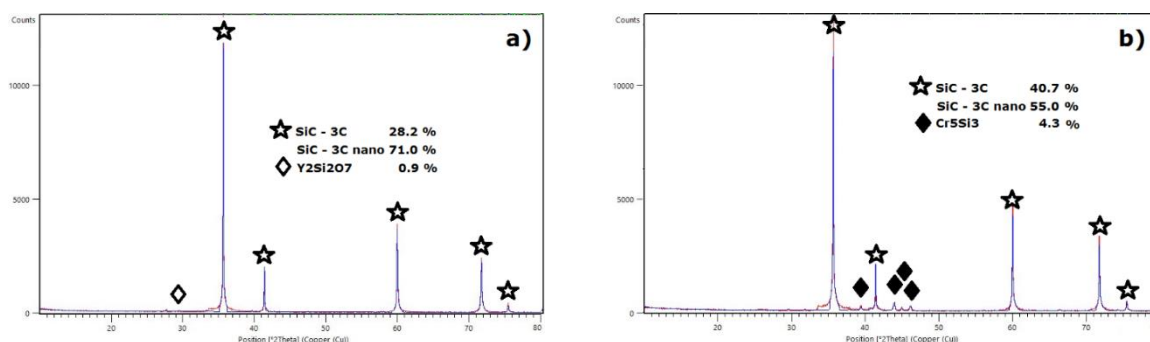


Fig. 1. The phase composition of powders after SHS synthesis: (a) powder containing yttria in the starting mixture; (b) powder containing chromia in the starting mixture.

Yttria included into reacting mixture transformed into yttriasilicate phase ( $Y_2Si_2O_7$ ) (Fig. 1a). What is worth to noticed silicon carbide produced in SHS reaction was composed of two moissanite phases. The typical coarse grains 3C type phase and the nanometric one. Rietveld procedure applied for calculations distinctly indicated the presence of the majority of this nanometric 3C type phase. Powder achieved in the presence of chromia (Fig. 1b) also was composed of two SiC 3C type crystallites differ in size. The amount of nanometric one was slightly less than in powder contained yttria additive. The whole oxygen was removed from the system and chromium was present only in the  $Cr_5Si_3$  phase. Powders achieved in SHS procedure were consequently milled and consolidated by hot-pressing. Conditions of HP procedure was as follows: the graphite stamps, argon atmosphere,  $2150^\circ C$  maximum temperature with 45 min of soaking time. Heating rate was  $15^\circ C/min$  and applied pressure was 25 MPa. After consolidation materials were examined for their phase composition and microstructural observation were conducted by means of SEM technique.

Figures 2a and 2b show phase composition of sintered materials. In both cases HP process caused significant changes in SiC phase composition. In both cases nano SiC phase disappeared what is obvious because of the highest diffusional activity of nano grains during sintering. Surprisingly, the structure of 3C type was detected as a dominant phase not 6H structure type usually typical for sintered SiC bodies. Such phase composition of sintered bodies could be

caused by the presence of external pressure during sintering and by the presence of nanograins of phases contain yttrium or chromium in the starting powder. The most important statements were that finally both, yttrium and chromium were present in sintered bodies as carbide phases and that reduction conditions during HP process led to free carbon appearance.

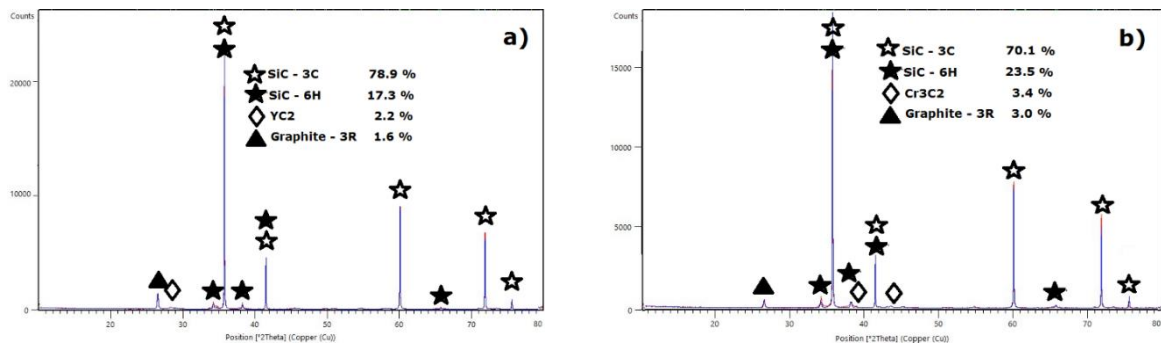


Fig. 2. The phase composition of HP bodies: (a) the sample containing yttria in the starting mixture; (b) the sample containing chromia in the starting mixture.

Figures 3a and 3b show morphology of carbide inclusions in sintered bodies. In both cases observed carbide grains were not so fine, rather in micro- than nanometric size. The inclusions size is bigger than yttria and chromia starting powders. It fact suggests that SHS process non preserved the system against agglomeration of phases dispersed in SiC matrix.

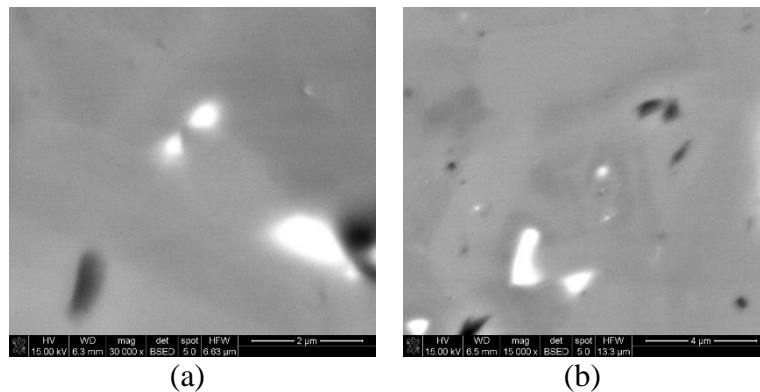


Fig. 3. Carbide inclusions in sintered bodies: (a) yttrium carbide YC<sub>2</sub> and (b) chromium carbide Cr<sub>3</sub>C<sub>2</sub>.

## APPLICATION OF HARDMETAL ELECTRODE MATERIALS IN PULSED ELECTROSPARK DEPOSITION TECHNOLOGY

**T. G. Penyashki<sup>\*a</sup>, M. I. Petrzhik<sup>b</sup>, and A. E. Kudryashov<sup>b</sup>**

<sup>a</sup>ISSAPP "N. Pushkarov" - Agricultural Academy, Sofia, 1331 Bulgaria

<sup>b</sup>National University of Science and Technology MISiS, Moscow, 119049 Russia

\*e-mail: tpenyashki@abv.bg

DOI: 10.24411/9999-0014A-2019-10120

Electrospark deposition (ESD) technology is widely used in various industries due to the excellent performance and high adhesion of the formed coatings, the possibility of local processing of large products, the relative ease of implementation and automation capabilities. The coating process is environmentally friendly and low energy consumption. Traditionally, metals and their alloys, graphite, as well as WC-containing hard alloys of VK (WC–Co), TK (TiC–WC–Co), TTK (TiC–WC–TaC–Co) grades, obtained by powder metallurgy technology, are used as electrode materials in ESD technology.

However, microcrystalline WC-containing hard alloys do not always meet the requirements for electrode materials, due to their high erosion resistance, low transfer coefficient, and high cost. In this connection, there is an urgent need to create economical electrode materials from tungsten-free hard alloys. The aim of the work is to demonstrate the advantages of tungsten-free electrode materials compared to standard hard metal alloys.

Currently, non-tungsten electrode materials have been developed, which are successfully used in many industries. Depending on the technical problem to be solved, electrode materials are selected that form multifunctional coatings on the surface of the processed products: wear-resistant, heat-resistant, corrosion-resistant, antifriction, with increased hardness, etc. To improve the performance properties of coatings, additives affecting erosion resistance are introduced into the materials. The compositions of electrode materials used to strengthen the cutting tool of high-speed steel HS6-5-2 are shown in Table 1 [1].

**Table 1. Compositions of tungsten-free electrode materials for hardening the cutting tool.**

| Grade of electrode materials | Composition   |
|------------------------------|---|
| TNM10                        | TiC + 10% Ni + Mo   |
| TN10                         | TiN + 10% Ni + Cr   |
| KNT16                        | TiCN + 16% Ni + Mo  |
| TNM20                        | TiN + 20% Ni + Cr   |
| TC                           | TiC + 14% Ni, Mo + 1% Cu, B, Al <sub>2</sub> O <sub>3</sub>       |
| TN                           | TiN + 14% Ni, Cr + 1% Cu, B, Al <sub>2</sub> O <sub>3</sub>       |
| TC-TN                        | TiC + TiN + 12% Ni, Mo + 1% Cu, B, Al <sub>2</sub> O <sub>3</sub> |

It is found that the resource of tools hardened with tungsten-free alloys (countersinks, cutters) more than 2.5 times exceeds the resource of non-hardened tools and 1.2–1.5 times the resource of tools treated with WC–Co electrodes. The best properties have the coating formed with TC–TN electrode.

To strengthen the rolling rolls made of white cast iron SPKhN-60 by the ESD the tungsten-free electrodes manufactured by technology SHS were tested [2]. The compositions of the studied electrode materials are given in Table 2.

Table 2. The compositions of electrode materials for strengthening rolling rolls.

| No. | Grade of electrode materials | Composition                 |
|-----|------------------------------|-----------------------------|
| 1   | SHIM *- 40HA                 | TiC-40 % NiAl               |
| 2   | SHIM - 9/20A                 | TiB-20 % Al                 |
| 3   | SHIM - 11                    | TiB <sub>2</sub> -40 % NiAl |
| 4   | SHIM - 20H                   | TiC-20 % Ni                 |
| 5   | SHIM - 2/40HM                | TiC-40 % (Mo-70% Ni)        |
| 6   | BK6                          | WC-6 % Co                   |
| 7   | T15K6                        | 15 % TiC-79 % WC-6 % Co     |

\*Russian alloy grade “SHIM” (synthetic hard instrumental material).

Coatings deposited using SHS-electrode materials SHIM-11 and SHIM-40HA were characterized by higher performance properties (heat resistance, wear resistance) compared with coatings of deposited with tungsten-containing electrodes.

During industrial test at Oskol Electrometallurgical Plant it was established that electrospark deposition with SHS-electrode SHIM-40HA increases the resistance of the mill rolls more than 2 times. These materials were recommended for electrospark treatment of rolling rolls made of white cast iron in order to increase their operating time.

A new promising direction of development of electrospark alloying technology is the selection and application of metallic glass-forming precursor electrode materials, which form at ESD nanostructured coatings with high performance properties [3–6].

Developing this approach, the metallic glass (MG) containing surface layer has been formed on the metallic (Fe-based and Ti-based) substrates using glass forming precursors-electrodes having both high and low Glass Forming Ability (GFA). High GFA electrodes like Fe<sub>61</sub>Co<sub>7</sub>Zr<sub>10</sub>Mo<sub>5</sub>W<sub>2</sub>B<sub>15</sub> and Fe<sub>48</sub>Cr<sub>15</sub>Mo<sub>14</sub>Y<sub>2</sub>C<sub>15</sub>B<sub>6</sub> had pronounced supercooled liquid range (about 60 and 38 K, respectively). However, industrial amorphous Fe<sub>78</sub>Mo<sub>2</sub>B<sub>20</sub> ribbon with lower GFA also was successfully applied as a precursor-electrode at ESD to form nanocrystalline and metallic glass contained layer on titanium substrate. In this case, supercooled liquid range is missing and GFA is much lower comparing to the best glass formers [6]. So, it was found that the efficiency of heat removal of motionless substrate at ESD is comparable with that at quenching the melt by spinning on a rotating drum (cooling rate of about 1,000,000 K/s).

Surface glass formation is accompanied by hardening of the crystalline metal substrate. It is achieved through a rapid local melting and solidification due to increasing of carbon and boron concentration and quenching stresses at near surface layers. This ensures high hardness (more than 15 GPa) and wear resistance (by three orders of magnitude) [3, 6]. Further development of this approach is associated with a reasonable selection for specific applications the certain couples "MG precursor-crystal substrate" as well as modes of electro spark deposition.

The present work includes studies funded by the Bulgarian National Science Fund (BNSF) of the Ministry of Education and Science under the project “Research and Development of New Wear-Resistant Coatings Using Compositional and Nano Materials” and by BNSF and Russian Foundation for Basic Research (RFBR) under the project no. 19-58-18022.

1. T. Penyashki, G. Kostadinov, M. Kandeveva, Examination of the wear of non-tungsten electrospark coatings on high speed steel, *Agricultural Eng.*, 2017, vol. 49, pp. 1–7.
2. A.E. Kudryashov, O.N. Doronin, E.I. Zamulaeva, et al, Prospects of application of electrode SHS-materials and technology of electrospark alloying for strengthening of rolling rolls, *Chernye Met.*, 2013, no. 10, pp. 61–68 (in Russ.).
3. M.I. Petrzhik, P.V. Vakaev, T.R. Chueva, et al, From bulk metallic glasses to amorphous metallic coatings, *J. Metastable Nanocryst. Mater.*, 2005, vol. 24–25, pp. 101–104.

4. E.A. Levashov, A.E. Kudryashov, E.I. Zamulaeva, et al, New classes of electrode materials for electrospark deposition, Proc. Int. conf. "Materials Science of refractory compounds: achievements and problems", 2008, Kiev, Ukraine, NASU, p. 162 (in Russ.).
5. A.V. Kolomeichenko, I.S. Kuznetsov, T.G. Penyashki, et al, On making problem of amorphous and nanocrystalline structures in electrical discharge coatings, *Remont, Vosstanovlenie, Modernizatsiya (Repair, Reconditioning, Modernization)*, 2015, no. 5, p. 33 (in Russ.).
6. M. Petrzhik, V Molokanov, E. Levashov, On conditions of bulk and surface glass formation of metallic alloys, *J. Alloys Compd.*, 2017, vol. 707, pp. 68–72.

## RARE EARTH OXIDES TRANSPARENT CERAMICS BASED ON THE SHS-DERIVED POWDERS

**D. A. Permin<sup>\*a</sup>, S. S. Balabanov<sup>a</sup>, E. M. Gavrishchuk<sup>a</sup>, A. V. Novikova<sup>a</sup>,  
Ye. E. Rostokina<sup>a</sup>, S. V. Filofeev<sup>a</sup>, and V. A. Koshkin<sup>a</sup>**

<sup>a</sup>G.G. Devyatikh Institute of Chemistry of High-Purity Substances, Russian Academy of Sciences, Nizhny Novgorod, 603951 Russia

\*e-mail: permin@ihps.nnov.ru

DOI: 10.24411/9999-0014A-2019-10121

Rare-earth metal sesquioxides (RE<sub>2</sub>O<sub>3</sub>) are promising laser-host and magneto-optical materials by virtue of their high optical and thermal properties. Transparent RE<sub>2</sub>O<sub>3</sub> materials are possible to obtain both in the form of single crystals and ceramics. At that the ceramic approach offers several advantages compared to single crystal growth such as controlling the material composition, increasing the aperture of the optical elements and fabrication of gradient-doped samples. Fabrication of optical ceramics requires using fine powders (with an average particle size from 100 to 200 nm) with a low agglomeration degree. The first requirement stems from the high sinterability of such powders, and the second one is that powder particles should be uniformly packed before sintering. The presence of agglomerates in powders leads to the formation of large pores, which act as light scattering centers.

At present, RE<sub>2</sub>O<sub>3</sub> optical ceramics are produced using powders prepared by precipitation from solution, laser sublimation, spray pyrolysis, and self-propagating high-temperature synthesis (SHS, combustion synthesis, propellant synthesis). The last method appears to be the most promising because of its high performance, and good reproducibility of the characteristics of powders.

The present report is devoted to the development of self-propagating high-temperature synthesis (SHS) of nanocrystalline rare earth (Y, Sc, Lu, Dy, Ho, Tb) oxides powders, their sintering to transparent ceramic samples and investigating basic optical properties of the prepared materials.

The main parameter determining final SHS-powder properties is a precursor composition. So, the work was focused on the effect of the fuel type and its ratio to oxidizer (metal nitrate) on the combustion process parameters and product characteristics. To estimate the influence of SHS-precursors compositions on the reaction parameters thermodynamic analysis was performed. It was shown that the synthesis should be provided in a slight excess of the oxidizer. The decomposition of SHS-precursors was studied using thermal analysis. Comparison of thermogravimetry and differential scanning calorimetry data for separate oxidant and fuels as well as reaction mixtures indicates that the initiation of chemical reactions underlying SHS is associated with the thermal destruction of the oxidant.

The obtained powders of different rare earth oxides are very similar in morphology. By the data of electron microscopy all the powders had a sponge-like structure, consisting of particles combined in “soft” agglomerates up to ~ 50 μm in size. Summarizing the results of particle size distribution measurements by the light scattering method it was revealed that glycine-nitrate combustion is a universal approach to produce low agglomeration degree RE<sub>2</sub>O<sub>3</sub> powders, although acetate-nitrate and citrate-nitrate precursors are also acceptable for preparing Y<sub>2</sub>O<sub>3</sub> and Lu<sub>2</sub>O<sub>3</sub> powders for example.

Based on the SHS derived powders two groups of materials were fabricated. The first group is laser active yttrium, lutetium and scandium oxides doped with ytterbium; the second one is magneto-optical terbium, holmium and dysprosium oxides ceramics for Faraday isolators (FI).

It was revealed that  $\text{La}_2\text{O}_3$  serves as an effective dopant to achieve highly transparent  $\text{Y}_2\text{O}_3$  and  $\text{Lu}_2\text{O}_3$  ceramics by vacuum sintering. Free-running lasing was observed on  $\text{Yb}:(\text{Y}_{0.9}\text{La}_{0.1})_2\text{O}_3$  with slope-efficiency 36% and average power 8 W; on  $\text{Yb}:(\text{Lu}_{0.7}\text{Y}_{0.25}\text{La}_{0.05})_2\text{O}_3$  with slope-efficiency 20% and average power 2 W. Transparent scandium oxide was prepared by hot pressing of SHS-powders with LiF sintering aid, laser generation was shown on  $\text{Yb}:\text{Sc}_2\text{O}_3$  with slope-efficiency 25% and average power 1.5 W.

Novel magneto-optical materials based on terbium, holmium, and dysprosium oxides were obtained. Holmium and dysprosium oxides transparent samples were vacuum sintered with the  $\text{La}_2\text{O}_3$  aid at temperatures of 1750–1800°C. The Verdet constant values of the  $\text{Ho}_2\text{O}_3$  and  $\text{Dy}_2\text{O}_3$  optical ceramics are 1.3 and 2 times higher compared to terbium-gallium garnet (TGG is the most commonly used FI material) which makes them perspective materials for magneto-optical media of Faraday isolators and rotators. Transparent ceramics of  $\text{Tb}_2\text{O}_3$  was obtained by hot-pressing at 1500–1550°C for 3 h under a pressure of 50 MPa. The value of Verdet constant of  $\text{Tb}_2\text{O}_3$  material is substantially higher compared to TGG (3.5 times higher), which makes it very promising for Faraday devices and further investigation of its properties is of great interest.

This study was financially supported by the Russian Foundation for Basic Research within the framework of the scientific project no. 16–33–60153 mol\_a\_dk and Russian Science Foundation within the framework of the scientific project no. 18-13-00355.

## SHOCK COMPACTION AND SINTERING OF Ni POWDERS: INFLUENCE OF $Y_2O_3$ -CoO CONTAINING OXIDE FILMS

O. L. Pervukhina<sup>\*a</sup> and A. S. Shishkina<sup>a</sup>

<sup>a</sup>Merzhnov Institute of Structural Macrokinetics and Materials Science, Russian Academy of Sciences, Chernogolovka, Moscow, 142432 Russia

\*e-mail: opervukhina@mail.ru

DOI: 10.24411/9999-0014A-2019-10122

In this work, we explored the influence of oxide nanofilms deposited onto the surface of Ni particles on the shock consolidation of Ni powders followed by their sintering. In our experiments, we used two Ni powders: the particles of one were covered with an  $Y_2O_3$  film with a nominal thickness of 7 nm while those in the other, with an  $Y_2O_3$ -CoO film (Y/Co = 23/13 by wt) of the same thickness (7 nm).

Shock compaction in cylindrical geometry was carried out at two detonation velocities: 3000 and 4500 m/s. For the sake of comparison, the recovery ampoules were filled with pure,  $Y_2O_3$ -clad, and  $Y_2O_3$ -CoO-clad Ni powders in a layer-by-layer mode. Calculations of the loading parameters were carried out according to the method [1]. After shock compaction, the samples were extracted from the ampoule, cut into separate specimens, and then sintered at 875°C. The process of sintering was accompanied by some heat release in an identified reaction. The microstructure of compacts was characterized by optical microscopy, SEM, and XRD.

Shock compression did not destroy the deposited nanofilms but led to dense packing of powder particles accompanied by their deformation and surface activation, on retention of overall powder structure (Fig. 1). Note that shock compression also markedly decreased the sintering temperature (much below the melting point).

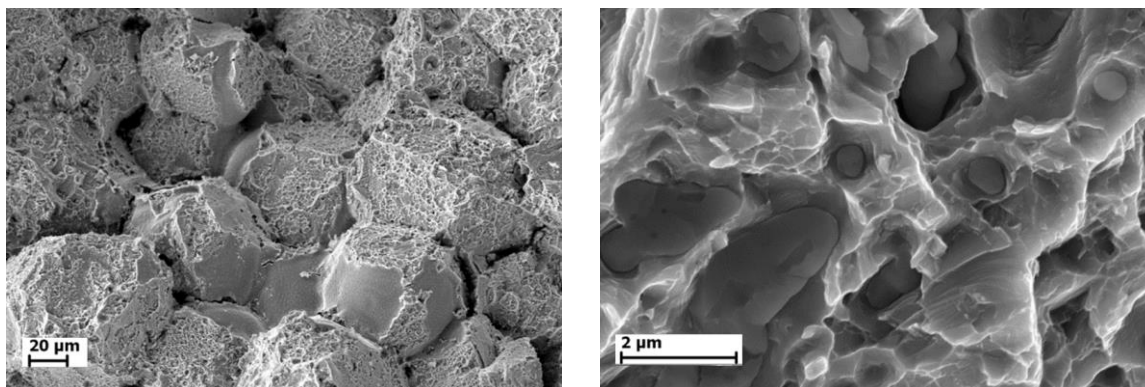


Fig. 1. Fragments of the compact Ni particles with deposited  $Y_2O_3$ -CoO film.

In compacts of pure Ni, we observed the presence of W and Mo in the particles bulk and the contact surface, as well as some amount of Fe (Fig. 2). Tentatively, this can be associated with sample overheating. In compacts of  $Y_2O_3$ -clad Ni particles, no new phases and steel components were detected. Hence the  $Y_2O_3$  film prevents the diffusion of the elements into the particle bulk and facilitates strong bonding during shock compaction and subsequent sintering. For compacts of  $Y_2O_3$ -CoO-clad Ni particles, some interaction with a graphite base was noticed thus suggesting that in some surface areas the oxide film was absent.

Shock-consolidated Ni may find its use in some high-temperature applications requiring high corrosion/oxidation resistance.



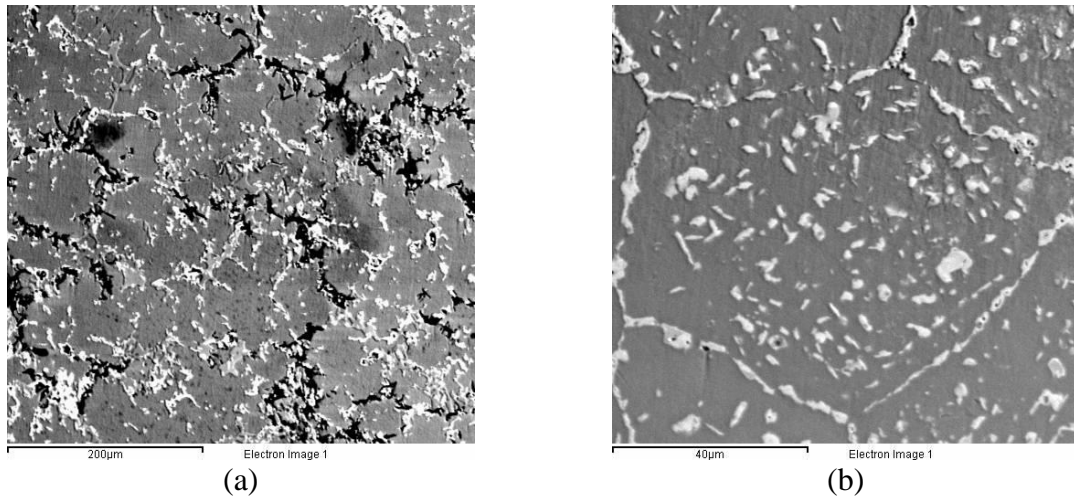


Fig. 2. Microstructure of (a) compact pure Ni particles and (b) compact Ni particles with deposited  $Y_2O_3$  film (b).

1. V.D. Rogozin, *Vzryvnaya obrabotka poroshkovykh materialov*, Volgograd: RPK Politekhnik, 2002, 135 p.

## INVESTIGATION OF THE EFFECT OF METAL POWDERS ON THE SURFACE OF THE TARGET SUBJECTED TO HIGH ENERGY TREATMENT

**E. V. Petrov\*<sup>a</sup> and V. S. Trofimov<sup>a</sup>**

<sup>a</sup>Merzhanov Institute of Structural Macrokinetics and Materials Science, Russian Academy of Sciences, Chernogolovka, Moscow, 142432 Russia

\*e-mail: petrov@ism.ac.ru

DOI: 10.24411/9999-0014A-2019-10123

The investigation of structural and phase transformations caused by the high-energy interaction of metal particles with the surface of the target is of interest for solving both applied and fundamental problems. The first type of problems involves research concerning the hardening and deposition of wear-resistant coatings on the surface of structural materials using explosive treatment [1, 2]. The formation of coatings on metals and alloys requires a temperature above 1000 K that is necessary either for the formation of the compound or for the creation of strong bond between a coating and a material. This requirement restricts the creation of coatings from refractory powders, since high temperature heating leads to undesirable physicochemical and structural changes in the product. The second type of problems involves the investigation of the interaction of powder particles with the surface of the target [3, 4]. During the interaction of detonation with powder particles in an explosive wave for explosive spraying of wear-resistant coatings, the entrainment of particles takes place due to rigid collision of molecules of detonation products with powder particles.

When a flux of particles of different dispersity, accelerated by explosion energy up to a velocity of 1–3 km/s, interacts with the surface of the target, their material can penetrate into the target at a depth that is hundreds of times larger than the size of the initial particles and affects the material structure of the sample under study. The interaction of the flux of particles with the sample stops most of the particles in the near-surface zone and forms a coating on the surface of the sample. Shock-wave loading and the impact of high-velocity particles improve physical and mechanical properties of the surface and the entire volume of the materials processed. Despite the fact that the nature of this effect has not yet been explained, the research method can simulate quite exactly the effect of space debris on aircrafts in space.

The purpose of this work is to investigate the effect of the flux of particles on the surface of the target subjected to high-energy treatment.

Steel samples (St3 grade) with a diameter of 20 mm and a height of 30 mm were selected as a steel target; the shape of the samples was chosen to simplify the experiments. The tungsten powder with a particle size of 10–16  $\mu\text{m}$  was used. The scheme of the experiment was as follows: a cylindrical sample was placed in a guiding channel, on top of which a ring containing a powder with a bulk density of 3 g was located. Cylindrically shaped bulk hexogen with a detonator was used as an explosive and placed on the ring. The ratio of the length to the diameter of the explosive was chosen to be equal to three to provide the stationary detonation process. The experimental procedure for the impact of a high-velocity flux of particles with a steel target is given in [5]. During the detonation process, shock wave and explosion products accelerated the powder and together with it affected the sample under study.

After loading, the samples were cut along the loading axis to obtain thin sections for the analysis of the results obtained.

The SEM images of the near-surface zone of the samples subjected to the high-velocity flux of powder particles show the formation of a coating (Fig. 1a) with a thickness from 10  $\mu\text{m}$  to

50  $\mu\text{m}$ . The obtained coatings formed by powder particles are nonuniformly distributed over the surface of the target, not solid, and contain cavities (Fig. 1b). This indicates that the unmelted powder particles interact with the surface of the samples and the coating consists of sintered particles. These experimental results are in good agreement with the theoretical calculations of the time during which the particles of powders are exposed to detonation and the particle temperatures attained during a high-velocity impact with the target.

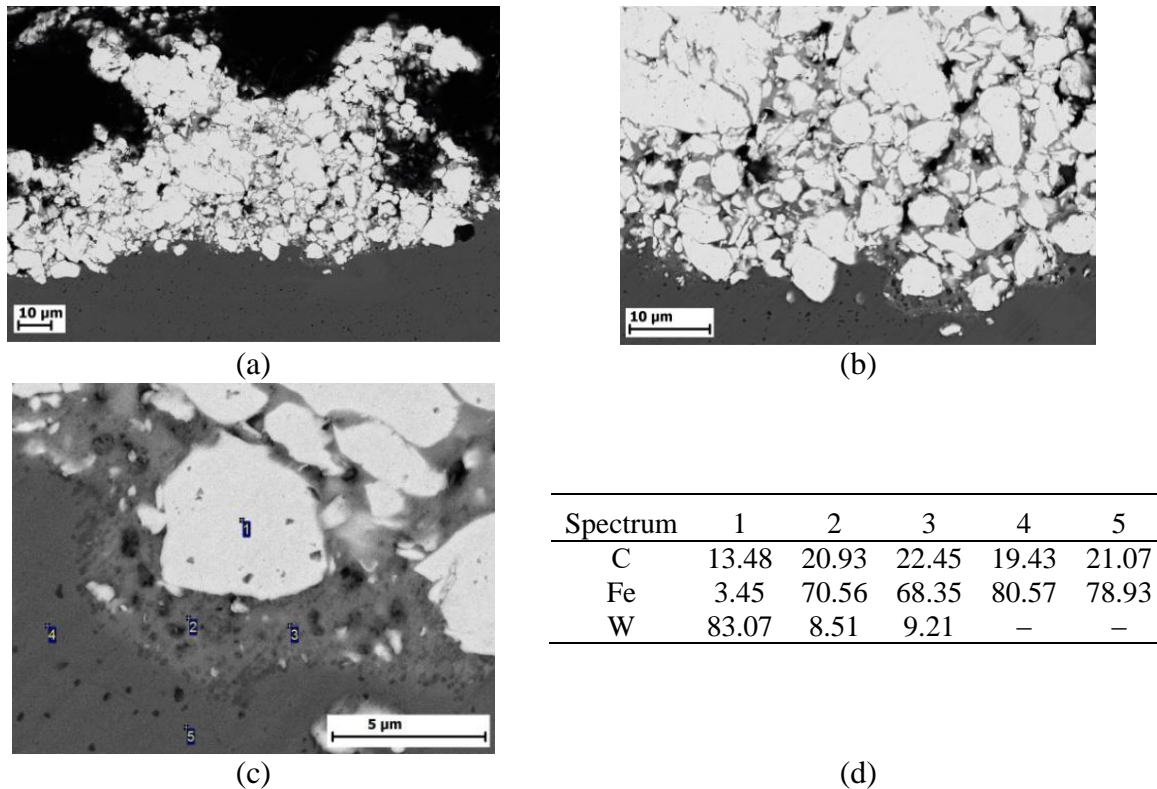


Fig. 1. SEM images of (a, b) coating formed from tungsten particles, (c) transition zone, and (d) energy-dispersive analysis of the near-surface zone corresponding to (c) (wt %).

The study of the sample-coating interface revealed the transition zones (Fig. 1c) consisting of particles of tungsten, iron, and their intermetallic compound. The impact of tungsten powder particles with steel (St3) produces the maximum energy release which brings the system in a metastable state. The temperature in the active zone exceeds the temperature of peritectoid reaction at 1060°C in the Fe–W system. Under these temperature conditions, the polymorphic transformation of iron takes place with the formation of austenite and the dissolution of tungsten carbide in austenite. When cooled, the austenite solution is oversaturated with tungsten and stabilizes. As a result, the supercooled cellular austenite with tungsten carbide mesh along grain boundaries is formed in the steel structure, which is identical to the structure of cast high-speed steel with complex carbide eutectic.

After analyzing the high-velocity interaction of the flux of particles with the surface of the target, it is of interest to investigate this process using high-speed video and color pyrometry for the processing of obtained data, as well as to record the mass velocity profile and the time of shock wave propagation in the sample.

The project was supported by the Russian Foundation for Basic Research (project no. 19-08-00553).

1. Yu.S. Usherenko, S.M. Usherenko, J. Yazdani, Composite materials for steel cutting and concrete crushing, *Procedia Eng.*, 2017, no. 172, pp. 1198–1203.

2. M.K. Valyuzhenich, A.L. Krivchenko, A.M. Shterenberg, Modification of the surface of titanium alloy by explosion plasma spraying coatings, *Deformatsiya i Razrusheniye Materialov*, 2008, no. 5, pp. 44–47.
3. Q. Chengzhi, C. Jianjie, Physical mechanism of super-deep penetration of solid microparticles into solid targets, *J. Mechan. Behav. Mater.*, 2014, vol. 23, nos. 1–2, pp. 21–26.
4. A.I. Kretelev, Modeling the process of entrainment of powder particles by explosive shock waves, *Vestnik Samara State Technical University Series of Physical and Mathematical Sciences*, 2014, vol. 35, no. 2, pp. 125–129.
5. R.G. Kirsanov, E.V. Petrov, A.L. Krivchenko, Features of the hardness distribution of tool steels by volume depending on the angle of incidence of the particle flow, *Deformatsiya i Razrusheniye Materialov*, 2010, no. 6, pp. 43–46.

## REACTIVE PHASE FORMATION BY ELECTROSPARK DEPOSITION

M. I. Petrzhik<sup>\*a</sup>, A. E. Kudryashov<sup>a</sup>, and E. I. Zamulaeva<sup>a</sup><sup>a</sup>National University of Science and Technology MISiS, Moscow, 119049 Russia

\*e-mail: petrzhik@shs.misis.ru

DOI: 10.24411/9999-0014A-2019-10124

The traditional task of ESD is to strengthen the surface layers of metal conductive substrates by transferring the refractory and high-strength phases contained in the precursor electrode. An example of such electrodes produced by SHS technology can be unique refractory carbides or laminate MAX phases [1]. With such solid-phase mass transfer, an important parameter of the process is the erosion ability of the electrode, and the formed coatings usually have an increased roughness.

On the contrary, the reactive phase formation takes place if the conditions for local melting are created during the electrospark deposition, in which the electrode and substrate components are actively mixed, culminating in the synthesis of new phases that were not in the system. This is possible with a strong chemical interaction of low-melting (near-eutectic) electrodes with the substrate components. Reasonably selected pairs of "glass-forming precursor–crystalline substrate" were successfully used to obtain coatings contained metallic mixed (metallic glass and nanocrystals) structure with superior properties [2, 3].

Due to the characteristic of eutectics ability to spread (fluidity) electrical discharge machining improves the quality and reduces the surface roughness. This was used to improve the surface quality of additive manufacturing products [4]. This was achieved with the help of ESD, as in the process of reactive electrospark deposition, three fast-flowing phenomena are observed: (1) plasma smoothing of protrusions, (2) filling in cavities and microcracks with a low-melting near-eutectic melt, which is formed during the rapid local melting of the precursor electrode under the conditions of a pulsed electric spark discharge, followed by (3) local reaction synthesis of wear-resistant intermetallic compounds during the chemical interaction of the melt with the substrate.

The reported study was partially funded by Russian Foundation for Basic Research (RFBR) and Bulgarian National Science Fund (BNSF) according to the research project no. 19-58-18022.

1. E.I. Zamulaeva, E.A. Levashov, T.A. Sviridova, N.V. Shvyndina, M.I. Petrzhik, Pulsed electrospark deposition of MAX phase Cr<sub>2</sub>AlC based coatings on titanium alloy, *Surf. Coat. Technol.*, 2013, vol. 235, pp. 454–460.
2. M.I. Petrzhik, P.V. Vakaev, T.R. Chueva, T.A. Sviridova, V.V. Molokanov, Yu.K. Kovneristy, E.A. Levashov, From bulk metallic glasses to amorphous metallic coatings, *J. Metastable Nanocryst. Mater.*, 2005, vol. 24–25, pp. 101–104.
3. M. Petrzhik, V. Molokanov, E. Levashov, On conditions of bulk and surface glass formation of metallic alloys, *J. Alloys Compd.*, 2017, vol. 707, pp. 68–72.
4. S.K. Mukanov, M.I. Petrzhik, A.E. Kudryashov, E.A. Levashov, Elimination of surface defects of SLM products due to a synthesis of NiAl intermetallic at electro-spark deposition of Al-containing precursor, Presented at this Symposium.

## HIERARCHICALLY-STRUCTURED HIGH-TEMPERATURE ZrB<sub>2</sub>–MoB–MoSi<sub>2</sub> CERAMICS PRODUCED BY DIFFERENT SHS ROUTES AND SUBSEQUENT HP

**Yu. S. Pogozhev<sup>a\*</sup>, M. V. Lemesheva<sup>a</sup>, A. Yu. Potanin<sup>a</sup>, S. I. Rupasov<sup>a</sup>,  
V. I. Vershinnikov<sup>b</sup>, and E. A. Levashov<sup>a</sup>**

<sup>a</sup>National University of Science and Technology MISiS, Moscow, 119049 Russia

<sup>b</sup>Merzhanov Institute of Structural Macrokinetics and Materials Science, Russian Academy of Sciences, Chernogolovka, 142432 Russia

\*e-mail: yspogozhev@mail.ru

DOI: 10.24411/9999-0014A-2019-10125

The creation of new generation of power-generating units, high-temperature internal combustion engines, supersonic aircrafts, and reusable space vehicles greatly increases the interest to high-temperature ceramic materials used to manufacture thermal protection systems for gliders and air flow ducts in propulsion systems [1]. Such high-temperature ceramics is crucial for aerospace engineering, chemical and metallurgical facilities [2].

At present time, the choice of structural materials to be used in aerospace industry under high-temperature oxidation conditions is limited to SiC- and Si<sub>3</sub>N<sub>4</sub>-based composites, oxide ceramics, superalloys based on Ni, Cr, Fe, and carbon–carbon composites with protective SiC coatings. The temperature range of application of SiC- and Si<sub>3</sub>N<sub>4</sub>-based composites is limited to 1600°C. However, they exhibit low stability to thermal cycling, low resistance against water vapor-induced corrosion, a strong decrease of oxidation resistance at presence of cations of alkali and alkaline earth metals salts, and deterioration of mechanical properties upon intensive oxidation [3]. The operational temperature of superalloys is lower than 1000°C. They cannot be used at higher temperatures due to low creep and oxidation resistance. Carbon based materials possess excellent mechanical properties in a wide temperature range, but above 600°C they undergo to rapid oxidation.

Currently, the next generation of high-temperature hierarchically structured ceramics with high oxidation resistance and excellent mechanical properties at elevated temperatures is being developed. Refractory transition metal disilicides and molybdenum disilicide MoSi<sub>2</sub>, in particular, are widely used as basis of such high-temperature ceramics. MoSi<sub>2</sub> is characterized by excellent resistance to high-temperature oxidation up to 1600°C [4, 5] and less susceptible than SiC to deterioration upon exposure to water vapor and alkali metal cations. However, MoSi<sub>2</sub> possess poor mechanical properties: low plasticity at temperatures less than 1000°C, low strength, and creep resistance at temperatures greater 1250°C, and also characterized by low oxidation resistance in the range of 500–700°C due to oxide layer destruction (peeling phenomena) [6]. That's why the single-phase MoSi<sub>2</sub> material cannot be used as a high-temperature structural material for specified purposes. Alloying of MoSi<sub>2</sub>-based composites with transition metal borides, like MoB, HfB<sub>2</sub>, and ZrB<sub>2</sub>, prevents the intense oxidation at low temperature range and also increase hardness and strength of the composite and improve its creep resistance and thermal cycling stability [7–9]. In [9], it was shown that the composition 90% MoSi<sub>2</sub>–10% MoB (at %) has the best resistance to high-temperature oxidation. Further improvement of the performance characteristics of MoSi<sub>2</sub>-based ceramics is possible when doping with HfB<sub>2</sub> and ZrB<sub>2</sub> borides, which have similar mechanical and thermophysical properties [10, 11]. However, from an economic point of view, the most appropriate use is ZrB<sub>2</sub>.

Self-propagating high-temperature synthesis (SHS) is an effective way of obtaining MoSi<sub>2</sub>–MoB–ZrB<sub>2</sub> ceramics from both elemental powders and less expensive oxide raw materials

[12–14]. To obtain similar high-density ceramics are mainly used methods of hot pressing (HP) and spark plasma sintering (SPS), as well as the hybrid technologies SHS + HP (reactive HP) and SHS + SPS (reactive SPS) [15, 16]. However, the use of hybrid methods is associated with some problems related to significant differences in the melting points of the initial components and the necessity of high purity elemental powders application. The technology of forced SHS-pressing is devoid of these drawbacks and allows to obtain similar ceramics with a hierarchical structure and level of residual porosity of 1.5–3.0%. However, this does not always satisfy the requirements for such materials. To obtain high-density  $\text{MoSi}_2\text{--MoB--ZrB}_2$  ceramics, it is advisable to use a combined two-stage method, when the heterophase SHS-powders obtained at the 1st stage is consolidated using the HP or SPS methods on the 2<sup>nd</sup> stage. SHS-powders have improved sinterability compared to powders obtained by traditional methods. The increased concentration of defects in SHS powders is a consequence of extreme heating and cooling rates ( $2000\text{--}20000\text{ K}\cdot\text{min}^{-1}$ ) during the combustion wave propagation [17]. Two different SHS routes can be used to produce SHS-powders of  $\text{MoSi}_2\text{--MoB--ZrB}_2$  ceramics: direct synthesis from elemental powders and magnesiothermic reduction of oxide raw.

The present study suggests a complex technology for the production of high-density  $\text{MoSi}_2\text{--MoB--ZrB}_2$  ceramics, which includes two stages: 1) synthesis of heterophase SHS-powders using both above mentioned SHS routes; 2) consolidation of SHS-powders by HP technology.

Experimental studies of the combustion process kinetics were carried out during direct elemental synthesis of the heterophase SHS powders. Unconventional dependences of combustion temperature ( $T_c$ ) of the reactionary mixtures on the initial temperature ( $T_0$ ) of the SHS-process were observed. The increase in  $T_0$  from 25 to 450°C leads to a proportional reduction of combustion temperature ( $T_c$ ) by 80–130°C in dependence of the mixture composition. Probably this is due to the zirconium oxidation with an increase in  $T_0$ , as evidenced by the self-heating of the mixture before the initiation of combustion. At the same time combustion rate ( $U_c$ ) of the mixture calculated for the formation of 40%  $\text{ZrB}_2$  monotonically increases from 1 to 3 cm/s as the  $T_0$  increases. The  $U_c(T_0)$  dependence for the reactionary mixture calculated for the formation of 20%  $\text{ZrB}_2$  has an extreme nature. With an increase in  $T_0$  to 140°C, the  $U_c$  increases by more than 2 times, and further growth of  $T_0$  leads to its slight decrease. Apparently, this is due to changes in the combustion mechanism or the transition of chemical reactions of  $\text{MoSi}_2$  and  $\text{ZrB}_2$  formation occurring in this heterogeneous system from the merge mode to the separated mode [18]. The amount of heat released as a result of chemical reactions in the elemental reactionary mixture containing the greatest amount of zirconium and boron is 1654 J/g.

Heterophase SHS powders obtained by both SHS routes (direct elemental synthesis and magnesiothermic reduction) are characterized by homogeneous and fine structure (Fig. 1a).

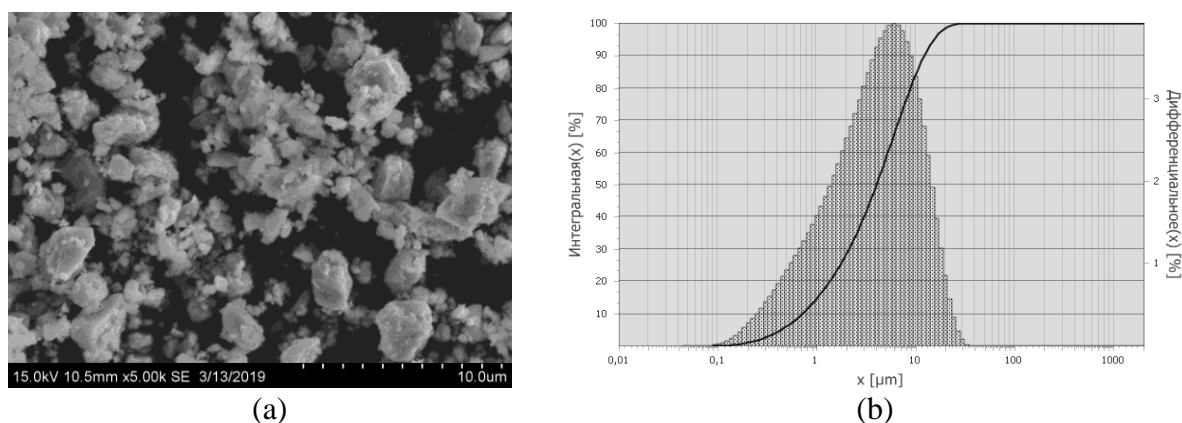


Fig. 1. (a) Typical structure of the SHS powders in  $\text{MoSi}_2\text{--MoB--ZrB}_2$  obtained by direct elemental synthesis and (b) its fractional composition.

Particles of the resulting composite SHS powders have polyhedral shape closed to spherical shape, and consist of 50–70%  $\text{MoSi}_2$ , 20–40%  $\text{ZrB}_2$ , and 5–10%  $\text{MoB}$  in dependence of the initial mixture composition. Also there is a small amount of  $\text{ZrO}_2$  in powders composition less than 1%. Differential curves of granulometric composition of the obtained powders are similar for both SHS routes and demonstrate normal particle size distribution with only one maximum. The average particles size of the obtained SHS powders is about 5  $\mu\text{m}$  with a maximum size less than 25  $\mu\text{m}$ .

Consolidated ceramic samples by HP using obtained heterophase SHS powders have homogeneous dense structure (Fig. 2).

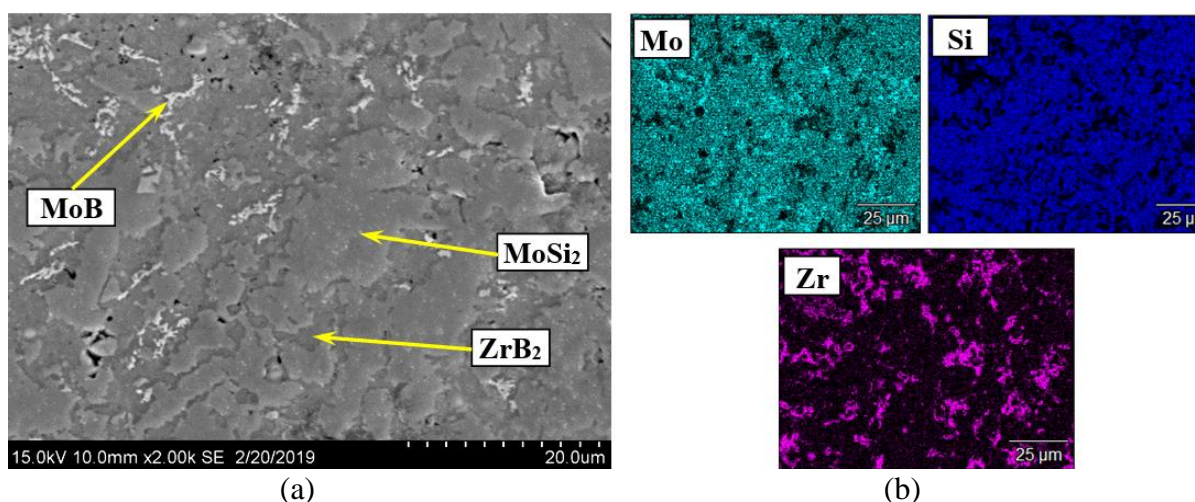


Fig. 2. (a) Microstructure of the  $\text{MoSi}_2$ – $\text{MoB}$ – $\text{ZrB}_2$  ceramic samples obtained by HP and (b) corresponding element distribution maps.

The phase composition of hot-pressed samples is almost identical to the phase composition of SHS-powders. The structure of compact ceramics is represented by a two-phase matrix consisting of  $\text{MoSi}_2$  and  $\text{ZrSi}_2$  grains. Light-gray  $\text{MoB}$  inclusions are located on the grain boundaries. Elements distribution maps demonstrate a high uniformity of Mo, Si, and Zr distribution over the samples volume. The relative density of the obtained ceramic samples is 98.9–99.3%, and their thermal conductivity varies in the range of 32–36  $\text{W}/(\text{m}\cdot\text{K})$  in dependence of the  $\text{ZrB}_2$  content.

Heterophase  $\text{MoSi}_2$ – $\text{MoB}$ – $\text{ZrB}_2$  ceramics is a promising structural material for the creation of heat-loaded structural elements for aerospace engineering.

The research was carried out under the financial support of the Russian Science Foundation in the framework of project no. 19-19-00117.

1. J. Cotton, Ultra-high-temperature ceramics, *Adv. Mater. Processes*, 2010, vol. 168, pp. 26–28.
2. N.P. Bansal, J. Lamon, *Ceramic Matrix Composites: Materials, Modeling and Technology*, Wiley, 2014, 694 p.
3. N.S. Jacobson, E.J. Opila, D.S. Fox, J.L. Smialek, Oxidation and corrosion of silicon based ceramics and composites, *High Temp. Corros. Prot. Mater.*, Trans Tech Publications, Switzerland, 1997, pp. 817–832.
4. A.T. Chaharsoughi, G.H. Borhani, R. Tahmasebi, Structural characterization of  $\text{MoSi}_2$  synthesized by high-energy mechanical milling followed by annealing heat treatment, *J. Alloy. Compd.*, 2011, vol. 509, pp. 2617–2620.
5. G. Cabouro, S.L. Gallet, S. Chevalier, E. Gaffet, Y. Grin, F. Bernard, Dense  $\text{MoSi}_2$  produced by reactive flash sintering: control of Mo/Si agglomerates prepared by high-energy ball



- milling, *Powder Technol.*, 2011, vol. 208, pp. 526–531.
6. S. Knittel, S. Mathieu, M. Vilasi, The oxidation behaviour of uniaxial hot pressed MoSi<sub>2</sub> in air from 400 to 1400°C, *Intermetallics*, 2011, vol. 19, pp. 1207–1215.
  7. D. Sciti, L. Silvestroni, L. Mercatelli, J.-L. Sans, Elisa Sani. Suitability of ultra-refractory diboride ceramics as absorbers for solar energy applications, *Sol. Energy Mater. Sol. Cells*, 2013, vol. 109, pp. 8–16.
  8. D. Sciti, L. Silvestroni, M. Nygren, Spark plasma sintering of Zr- and Hf-borides with decreasing amounts of MoSi<sub>2</sub> as sintering aid, *J. Eur. Ceram. Soc.*, 2008, vol. 28, no. 6, pp. 1287–1296.
  9. A.Yu. Potanin, Yu.S. Pogozhev, E.A. Levashov, A.V. Novikov, N.V. Shvindina, T.A. Sviridova, Kinetics and oxidation mechanism of MoSi<sub>2</sub>–MoB ceramics in the 600–1200°C temperature range, *Ceram. Int.*, 2017, vol. 43, no. 13, pp. 10478–10486.
  10. W.G. Fahrenholtz, E.J. Wuchina, W.E. Lee, Y. Zhou, Ultrahigh temperature ceramics: materials for extreme environment applications, Hoboken, New Jersey: Wiley & Sons Inc, 2014.
  11. S. Vorotilo, A.Yu. Potanin, Yu.S. Pogozhev, E.A. Levashov, N.A. Kochetov, D.Yu. Kovalev, Self-propagating high-temperature synthesis of advanced ceramics MoSi<sub>2</sub>–HfB<sub>2</sub>–MoB, *Ceram. Int.*, 2019, vol. 45, pp. 96–107.
  12. I.P. Borovinskaya, A.A. Gromov, E.A. Levashov, Y.M. Maksimov, A.S. Mukasyan, A.S. Rogachev, Concise encyclopedia of self-propagating high-temperature synthesis: History, theory, technology, and products, Elsevier, 2017.
  13. I.V. Iatsyuk, Yu.S. Pogozhev, E.A. Levashov, A.V. Novikov, N.A. Kochetov, D.Yu. Kovalev, Combustion synthesis of high-temperature ZrB<sub>2</sub>–SiC ceramics, *J. Eur. Ceram. Soc.*, 2018, vol. 38, iss. 7, pp. 2792–2801.
  14. Yu.S. Pogozhev, I.V. Iatsyuk, A.Yu. Potanin, E.A. Levashov, A.V. Novikov, N.A. Kochetov, D.Yu. Kovalev, The kinetics and mechanism of combusted Zr–B–Si mixtures and the structural features of ceramics based on zirconium boride and silicide, *Ceram. Int.*, 2016, vol. 42, iss. 15, pp. 16758–16765.
  15. R. Licheri, R. Orrù, C. Musa, G. Cao, Combination of SHS and SPS techniques for fabrication of fully dense ZrB<sub>2</sub>–ZrC–SiC composites, *Mater. Lett.*, 2008, vol. 62, iss. 3, pp. 432–435.
  16. P. Hu, K. Gui, W. Hong, X. Zhang, Preparation of ZrB<sub>2</sub>–SiC ceramics by single-step and optimized two-step hot pressing using nanosized ZrB<sub>2</sub> powders, *Mater. Lett.*, 2017, vol. 200, pp. 14–17.
  17. S.K. Mishra, S. Das, L.C. Pathak, Defect structures in zirconium diboride powder prepared by self-propagating high-temperature synthesis, *Mat. Sci. Eng. A*, 2004, vol. 364, pp. 249–255.
  18. E.A. Levashov, Yu.S. Pogozhev, A.Yu. Potanin, N.A. Kochetov, D.Yu. Kovalev, N.V. Shvindina, T.A. Sviridova, Self-propagating high-temperature synthesis of advanced ceramics in the Mo–Si–B system: kinetics and mechanism of combustion and structure formation, *Ceram. Int.*, 2014, vol. 40, no. 5, pp. 6541–6552.

## MILLION-ATOM MOLECULAR DYNAMICS SIMULATIONS OF EXPLOSIVE CRYSTALLIZATION IN AMORPHOUS CuTi THIN FILMS

**O. Politano<sup>\*a</sup>, S. A. Rogachev<sup>b</sup>, F. Baras<sup>a</sup>, and A. S. Rogachev<sup>b</sup>**<sup>a</sup>Laboratoire Interdisciplinaire Carnot de Bourgogne, UMR 6303 CNRS-Université de Bourgogne Franche-Comté, Dijon, France.<sup>b</sup>Merzhanov Institute of Structural Macrokinetics and Materials Science, Russian Academy of Sciences, Chernogolovka, Russia<sup>\*</sup>e-mail: olivier.politano@u-bourgogne.fr

DOI: 10.24411/9999-0014A-2019-10126

Metallic glasses produced by fast quenching of melts possess very interesting physicochemical properties (e.g. high Young modulus, corrosion resistance, specific electric and magnetic properties), which make them attractive materials for various applications [1]. They are metastable at room temperature and can spontaneously transform into a crystalline solid by an exothermic process, named devitrification. During the transformation of a restricted amorphous domain, the local temperature increases and accelerates the crystallization process in adjacent regions. When the heat release is large enough, the local initiating amorphous-to-crystalline transformation becomes self-sustained and self-accelerating.

The very first observations of spontaneous self-propagating crystallization wave (i.e. “explosive crystallization”) were done in layers of amorphous antimony [2]. In recent years, one can notice a renewed interest on this process due to its promising application for the production of thin film polycrystalline solar cells or optical data storage [3, 4]. Beyond semiconductors and dielectrics systems, explosive crystallization was also experimentally characterized in metallic Cu–Ti, Fe–B, and Fe–Si–B glasses [5–7]. Among them, the Cu<sub>50</sub>Ti<sub>50</sub> glass is a perfect candidate to study theoretically the “explosive crystallization” process as it transforms into the crystalline phase CuTi of the same chemical composition, without the appearance of any other stable or metastable phase.

In this work, we explored the processes of devitrification and explosive crystallization in the CuTi metallic glass by molecular dynamic simulations using LAMMPS [8]. The simulation box contains one to two million atoms interacting through the EAM potential developed by Zhou et al. [9]. Two types of systems were considered [10]. The first one was obtained by first heating a  $\gamma$ -CuTi single crystal above its melting temperature. Then, a fast quenching (cooling rate  $\sim 10^{13}$  K/s) of the metallic melt down to the ambient temperature allowed us to obtain a metastable metallic CuTi glass. This sample was then reheated to 675 K and the spontaneous formation of the crystalline phase was monitored (see Fig. 1). In such systems, it was shown that the nucleation of primary crystalline clusters occurs homogeneously due to spontaneous fluctuations of atomic structure. We observed that most of the clusters larger than 50–100 atoms ( $\sim 8$ –10 nm in diameter) will grow into steady crystalline grains. The spontaneous nucleation and growth of many crystalline grains observed leads to a local increase of temperature, which is the initial step to observe a thermal explosion. A second type of simulations concerns self-propagating front of crystallization in very long sample (see Fig. 2). This geometry was inspired by our pioneering work on SHS into Ni–Al system by molecular dynamics [11]. The reaction was initiated locally by heating one extremity (10 nm) of the glassy sample. The devitrification starts and propagates across the whole sample accompanied by a thermal wave (see Fig. 3). Due to the exothermic devitrification, temperature rises in the reactive front up to 665–714 K. The thickness of the preheated zone is about 20 nm and the thickness of the amorphous-to-crystalline transition zone is about 1 nm. The velocity of the front was  $\sim 40$  m/s.

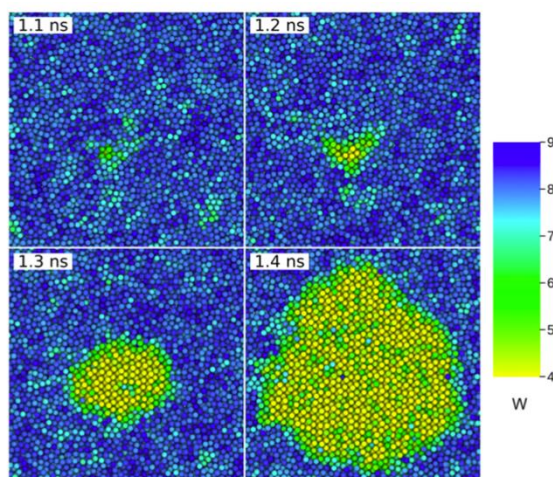


Fig. 1. Spontaneous homogeneous nucleation and growth of crystallite (cross section of the simulated box). The color-bar represents an ordering parameter ( $W$ ). Blue (dark grey) indicates atoms in an amorphous state, yellow (light grey) crystallized atoms; intermediate colors indicate partially ordered clusters.

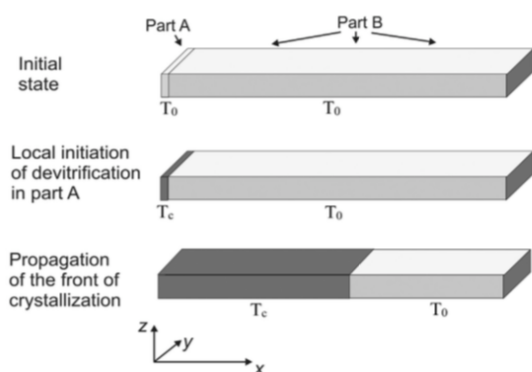


Fig. 2. Schematic representation of MD simulated sample for studying self-propagating explosive crystallization.

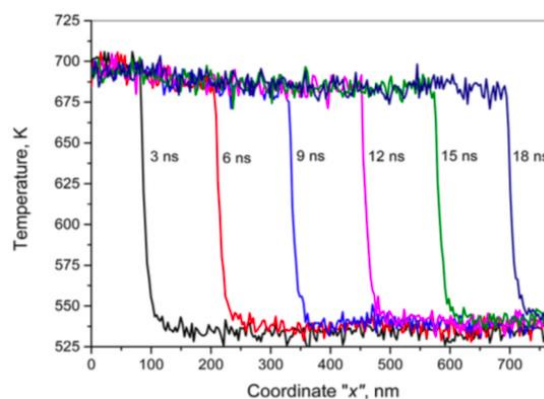


Fig. 3. Temperatures profiles of propagating waves during explosive crystallization along the  $x$  coordinate at successive times.

As we will show during the talk, molecular dynamics allowed us to model short-time atomic processes occurring during explosive crystallization. In particular, we studied the nucleation and growth of crystalline clusters and grains, which are difficult to characterize by experimental approaches. The simulated results will be compared with the available experimental data on macroscopic behavior of the explosive crystallization waves.

This work was financially supported by the Russian Science Foundation (grant no. 16-13-10431). The use of computational facilities at the Computing Center of the University of Bourgogne. PSIUN-CCUB. is gratefully acknowledged.

1. A.I. Greer, Metallic glasses, *Sci.*, 1995, vol. 267, pp. 1947–1953.
2. G. Gore, On a peculiar phenomenon in the electro-deposition of antimony, *Philos. Magaz.*, 1855, vol. 9, pp. 73–74.
3. M.A. Green, J. Zhao, A. Wang, S.R. Wenham, Progress and outlook for high-efficiency crystalline silicon solar cells, *Sol. Energy Mater. Sol. Cells*, 2001, vol. 65, pp. 9–16.
4. C.E. Wickersham, G. Bajor, J.E. Greene, Optical information storage using explosive crystallization in amorphous films, *J. Vac. Sci. Technol. A*, 1983, vol. 1, pp. 1857–1860.

5. A.S. Rogachev, S.G. Vadchenko, A.S. Shchukin, I.D. Kovalev, A.S. Aronin, Self-propagating crystallization waves in the TiCu amorphous alloy, *JETP Lett.*, 2016, vol. 104, no. 10, pp. 726–729.
6. A.S. Rogachev, S.G. Vadchenko, A.S. Aronin, S. Rouvimov, A.A. Nepapushev, I.D. Kovalev, F. Baras, O. Politano, S.A. Rogachev, A.S. Mukasyan, Self-propagating waves of crystallization in metallic glasses, *Appl. Phys. Lett.*, 2017, vol. 111, pp. 1–6.
7. A.S. Rogachev, S.G. Vadchenko, A.S. Aronin, A.S. Shchukin, D.Yu. Kovalev, A.A. Nepapushev, S. Rouvimov, A.S. Mukasyan, Self-sustained exothermal waves in amorphous and nanocrystalline films: A comparative study, *J. Alloys Compd.*, 2018, vol. 749, pp. 44–51.
8. S. Plimpton, Fast parallel algorithms for short-range molecular dynamics, *J. Comput. Phys.*, 1995, vol. 117, no. 1, pp. 1–19.
9. X.W. Zhou, R.A. Johnson, H.N.G. Wadley, Misfit-energy-increasing dislocations in vapor-deposited CoFe/NiFe multilayers, *Phys. Rev. B*, 2004, vol. 69, pp. 1–10.
10. S.A. Rogachev, O. Politano, F. Baras, A.S. Rogachev, Explosive crystallization in amorphous CuTi thin films: a molecular dynamics study, *J. Non-Cryst. Solids*, 2019, vol. 505, pp. 202–210.
11. O. Politano, F. Baras, Molecular dynamics simulations of self-propagating reactions in Ni–Al multilayer nanofoils, *J. Alloys Compd.*, 2015, vol. 652, pp. 25–29.

## STRUCTURE FORMATION AT CONSECUTIVE PORTION PACKING OF MONODISPERSED GRANULES IN SQUARE MATRICES WITH SMOOTH AND PROFILED BOTTOM

M. A. Ponomarev\*<sup>a</sup> and V. E. Loryan<sup>a</sup>

<sup>a</sup>Merzhanov Institute of Structural Macrokinetics and Materials Science, Russian Academy of Sciences, Chernogolovka, Moscow, 142432 Russia  
\*e-mail: map@ism.ac.ru

DOI: 10.24411/9999-0014A-2019-10127

The spatial arrangement of the components in the initial powder reaction mixtures significantly affects the course of SHS and characteristics of the synthesis product – microstructure, density distribution, and pore morphology in the final product [1]. When solving the problem of formation of a certain macro- and microstructure in the synthesis product [1, 2], it is advisable to use powder systems with the components and corresponding reaction cells located in the mixture volume as regularly as possible [3, 4]. In connection with the earlier studies of structural ordering of the components in the model heterogeneous systems [5–7], in this paper we study specific features of structured billets formation in successive compaction of monodispersed granules depending on the nature of the initial distribution of the mixture in the matrix volume and the state of the pressing punches surface. The investigation results are relevant for preparation of composite materials by the SHS method from the mixtures with one of the components consisting of large spherical particles [5, 6].

The compaction regularities of the backfills of the model system of large steel granules in matrix molds with a square cross section (side of the square  $L = 14.2$  mm) are investigated. A consecutive portion compaction was used. The density of the filling was taken as the ratio of the total mass of all portions of the granules, at each stage of the portion compaction, to the total volume occupied by them in the matrix between the planes of the upper and lower punch. The granules were calibrated balls of monodispersed composition ( $d = 1$  mm), which allowed simulating the compaction of multicomponent SHS mixtures including narrow fractions of large spherical particles – metal, composite, mechanoactivated and clad ones – along with fine components [1, 5, 6].

The peculiarities of structural ordering in the model system using different ways of filling the original portions of the granules into the matrix were considered. They can be practically used for pressing long billets for the subsequent obtaining of the items by SHS. To achieve a preset uneven distribution of the granules in the cross section of the mold during the portion loading we used special inserts into the matrix – dies. Four different cases of each portion distribution by the cross-section of the matrix before the compaction procedure are considered: (1) the filling components fill the matrix corners; (2) the filling is located near the middle section of the side walls of the matrix; (3) the filling is in the central part of the matrix; (4) the filling is evenly distributed throughout the matrix. The ratio of openings areas in the dies ( $S_i$ ) for the granules to the total cross-section area of the matrix ( $S$ ) were:  $S_1/S = 21.5\%$ ;  $S_2/S = 22\%$ ;  $S_3/S = 17\%$ ;  $S_4/S = 18.5\%$ . During the compaction with the punch, redistribution of the granules in the mold volume occurred.

The lower fixed punches with the ends of two types were used as the base of the matrix: (1) with a smooth polished surface; (2) with a surface evenly covered with holes (196 ones) obtained by drilling with a spiral drill of 1 mm in diameter with a sharpening angle of  $135^\circ$  to a depth of 0.8 mm. The position of the centers of the holes corresponded to the nodes of a

regular cubic lattice of the size 14 by 14. Pre-filling of the holes with steel balls gave a profiled matrix bottom, covered with a monolayer of balls, which corresponded to one layer of cubic, octahedral and rhombohedral packing [4].

Structure formation peculiarities of multilayered compacts at consecutive portion compaction of the fillings was studied; the number of granules in the portions ( $\delta N_0$ ) could vary (for small fillings:  $\delta N_0 = 5$  for  $N = 196-725$ ,  $\delta N_0 = 10$  when  $N = 725-2200$ ; for large fillings:  $\delta N_0 = 196$  odd monolayers and  $\delta N_0 = 169$  for even monolayers). The number of the balls in the compacts ( $N$ ) reached 2200. Low compaction pressure ( $P = 1$  MPa) did not allow the granules to deform significantly. The filling density increased due to the movement of the granules in the volume ( $V_c$ ) limited by the matrix walls and the planes of the punches. With embedding the punch we measured the height of the compacted layer of granules with a micrometer. The distance between the upper punch and the plane corresponding to the position of the lower point of the granule in the first monolayer was taken as the height ( $H$ ) of the compact. The relative density of the samples ( $\rho_0$ ) was defined as  $\rho_0 = \rho/\rho_s$  (where  $\rho_s$  is the density of the granules;  $\rho$  is the density of the compact – the ratio of the granules mass to the volume they occupy of the height  $H$ :  $\rho = (\rho_s \cdot V_b \cdot N)/V_c$ , where  $V_b$  is the spherical granule volume), and calculated by the formula  $\rho_0 = \pi d^3 \cdot N / (6H \cdot L^2)$ .

Figures 1–4 demonstrate the packing density of the granules in the matrices with smooth and profiled bottom as well as their structure changes (observed upper monolayers) with an increasing height of the compacts. The plots of experimental dependences  $\rho_0 = f(N)$  have a number of density maxima – from 5 to 10 (Figs. 1, 3).

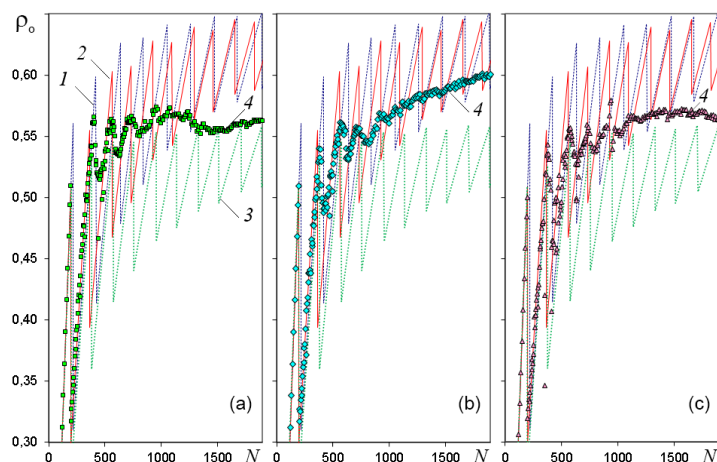


Fig. 1. Dependences of the relative density of compacts on the number of balls (the matrix with the profiled bottom,  $\delta N_0 = 5-10$ ): (a) the filling is evenly distributed; (b) the filling in the center; (c) the filling is in the corners of the matrix; 1–3 the calculated density of the structures at consecutive packing of the balls in the tetrahedral (1), octahedral (2) and rhombohedral (3) packaging; 4 experimental plots.

For the compacts in the matrices with the profiled bottom when small backfills were used,  $\delta N_0 = 5-10$  after 6–7 density maxima, we observed smoothing of the dependencies, and the extremes became fuzzy (Figs. 1a, 1b and Fig. 3a). In the photo of the upper layer of the compacts, it is seen that with the growth of  $N$ , the number and area of the fragments with octahedral packing decreases, and with tetrahedral – increases. On the experimental curves (Figs. 1a, 1b, 3a), we observe a shift in the density extremums along the  $x$ -axis from the respective calculated values of the density of octahedral packing (curves 2) in the direction of the density extremums of tetrahedral packing (curves 1). After 6–7 density maximums, the number of ordered fragments decreases, and the structure becomes disordered. The decrease in ordering is apparently connected with the increase in the spread of granules from one monolayer in the coordinate arrangement in the direction of the matrix axis, that is, the gradual

degeneration of the layer-by-layer structure of the compact. This phenomenon is facilitated by the formation of stable fragments of rhombohedral packing near the walls along the perimeter of the matrix. The distance between the granule centers in the rhombohedral packing is greater than in the tetrahedral and octahedral, so the punch, resting on the granules near the walls, exerts force on the granules remote from the walls, which is not enough to align their position in the transverse plane and the formation of fragments of octahedral and tetrahedral packing.

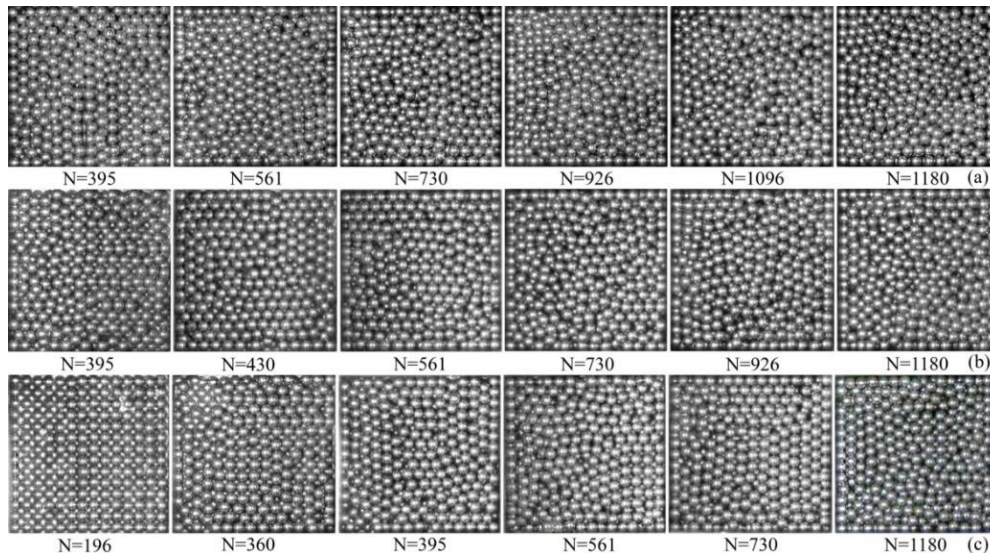


Fig. 2. The upper monolayer of granules (the matrix with the profiled bottom,  $\delta N_0 = 5-10$ ): (a) the filling is evenly distributed; (b) the filling is in the center; (c) the filling is in the corners of the matrix.

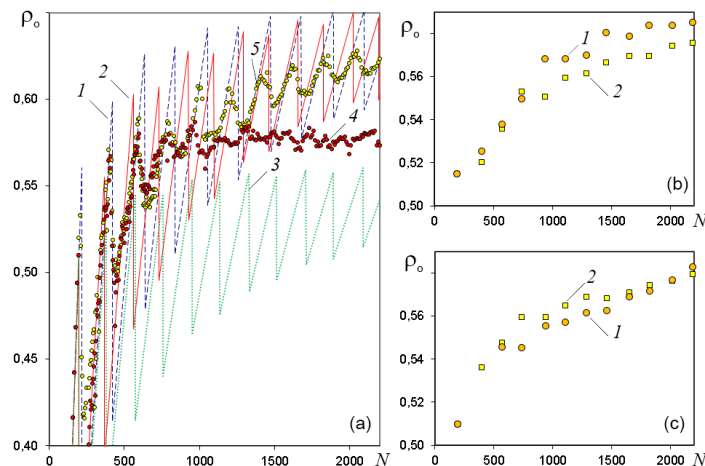


Fig. 3. Dependences of the relative density of compacts on the number of balls: (a) the filling is at the walls of the matrix ( $\delta N_0 = 5-10$ ), 1–3 the calculated density of the structures (in the matrix) at consecutive packing of the balls in the tetrahedron (1), octahedral (2) and rhombohedral (3) packaging, 4, 5 experimental plots (4 smooth bottom, 5 profiled); (b, c) large filling  $\delta N_0 = 169-196$ , matrix with smooth (b) and profiled (c) bottom: 1 filling at the walls of the matrix; 2 filling in the center.

In the matrices with the smooth bottom, clear density maximums were observed for all the values of  $N$  (Fig. 3), mainly, there were fragments of the tetrahedral packing (Fig. 4). The average density was higher than that in the case of granule compacting in the matrix with the profiled bottom. In the case of large backfills (Figs. 3b, 3c), the relative density of the compacts is comparable to the result at small  $\delta N_0$ .

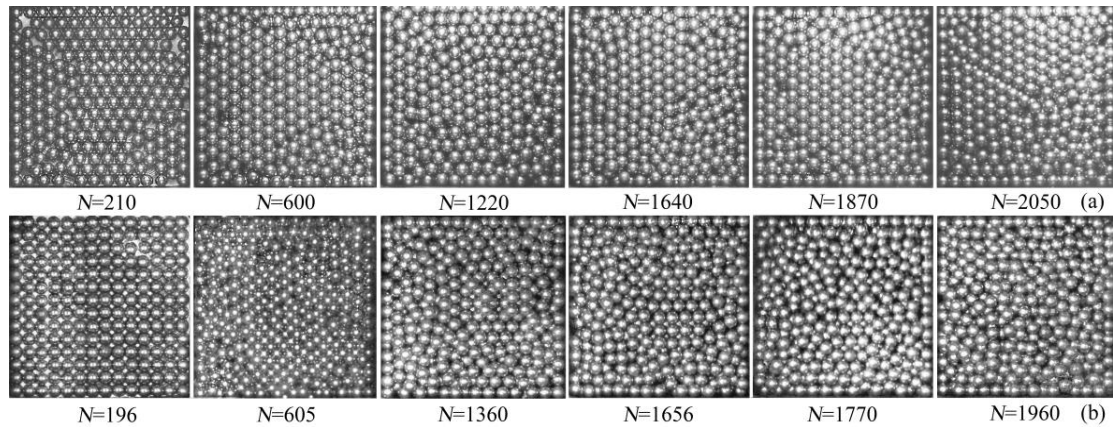


Fig. 4. The upper monolayer of granules (filling at the walls of the matrix  $\delta N_0 = 5-10$ ): (a) matrix with smooth bottom; (b) with profiled bottom.

Thus, the consecutive portion pressing of non-deformable spherical granules into the square matrix with the bottom shaped as a monolayer of octahedral packing granules ( $L/d = 14$ ) does not result in the stable formation of the structure with extensive fragments of octahedral or tetrahedral packing for more than 6–7 monolayers of the granules. In the square matrix with the smooth bottom there was a steady formation of extensive fragments of tetrahedral packing, on the boundaries of which there were elements of octahedral packing. A thin wall layer of the granules with rhombohedral packing along the perimeter of the matrix can prevent compaction and formation of fragments of denser and more stable packing – octahedral and tetrahedral. The obtained results can be useful in the formation of homogeneous compact billets from multicomponent mixtures for the production of composite materials by the SHS method.

1. M.A. Ponomarev, V.E. Loryan, A.S. Shchukin, A.G. Merzhanov, SHS in preliminary structured compacts: II. Ti–2B and Ti–Al blends, *Int. J. Self-Propag. High-Temp. Synth.*, 2013, vol. 22, no. 4, pp. 202–209.
2. N.A. Kochetov, A.S. Rogachev, A.N. Emel'yanov, et al, Microstructure of heterogeneous mixtures for gasless combustion, *Combust. Explos. Shock Waves*, 2004, vol. 40, no. 5, pp. 564–570.
3. M.A. Ponomarev, V.E. Loryan, A.G. Merzhanov, Uniaxial compression of Ti, B, and T–B powders: structurization in case of spherical Ti particles, *Int. J. Self-Propag. High-Temp. Synth.*, 2012, vol. 21, no. 1, pp. 51–54.
4. M.A. Ponomarev, V.E. Loryan, Self-ordering of balls in compressed thin layers, *Int. J. Self-Prop. High-Temp. Synth.*, 2016, vol. 25, no. 1, pp 43–49.
5. M.A. Ponomarev, V.E. Loryan, Synthesis of porous composite materials via combustion of a mixture of titanium, VT6 alloy, and amorphous boron powders, *Inorg. Mater.*, 2018, vol. 54, no. 8, pp. 772–778.
6. M.A. Ponomarev, V.E. Loryan, Sintez kompozicionnogo materiala v sisteme Al–Ti–B pri gorenii poroshkov titana. bora i plakirovanny`x alyuminiem granul splava VT6 [Synthesis of composite material in Al–Ti–B system during combustion of titanium and boron powders and aluminum-clad granules of VT6 alloy], *Perspek. Mater.*, 2019, no. 3, pp. 62 – 73.



## SYNTHESIS OF POROUS MATERIAL FROM MIXTURES OF BORON, TITANIUM, AND NICKEL-CLAD ALUMINUM COMPOSITE POWDERS (NPA75-80)

M. A. Ponomarev\*<sup>a</sup> and V. E. Loryan<sup>a</sup>

<sup>a</sup>Merzhanov Institute of Structural Macrokinetics and Materials Science, Russian Academy of Sciences, Chernogolovka, Moscow, 142432 Russia  
\*e-mail: map@ism.ac.ru

DOI: 10.24411/9999-0014A-2019-10128

The aim of the study was to synthesize a porous composite material in one technological stage by the SHS method in Al–Ni–Ti–B system. The initial billets were samples layer-by-layer compacted from model mixtures consisting of titanium and boron powders, and composite Al–Ni granules, in which spherical aluminum particles were clad with nickel layer. In the previously studied powder mixtures of Ti–Al, Ni–Al, Ti–B containing large particles of the components, the initial heating of the billets up to 800–1000°C was required to initiate the combustion [1, 2]. In the model system under consideration, synthesis of Al–Ni–Ti–B is possible without preheating, since the chemical reaction between titanium and boron powders, being a “chemical ovens” toward more inert clad granules [3], is able to heat the granules and provide their chemical reaction [2]. Melting and spreading of the melt of the metal components contributes to the appearance of numerous pores of different sizes and morphology in the product. The stage nature of the synthesis is characterized by rapid appearance of boride matrix with subsequent filling of its pores with the melt of intermetallic compounds formed during the reaction in the granules, which leads to the appearance of the synthesis product with the microstructure close to the composite one [3].

Model mixtures of (Al + Ni) + (Ti + 2B) were used in the experiments. They included:

- amorphous boron (99.8 wt %, particle size  $d_b = 0.2\text{--}6\ \mu\text{m}$ );
- titanium powder Ti(d1), grade PTS (average particle size  $d_{d1} \approx 120\ \mu\text{m}$ ; the content of chemical impurities in titanium: 0.08 wt % N, 0.05 wt % C, 0.35 wt % H, 0.4 wt % Fe + Ni, 0.10 wt % Si, 0.004 wt % Cl);
- composite clad powders with a size of 40–160  $\mu\text{m}$  made by hydrogen reduction under pressure in autoclaves, with the following compositions: (1) (Al + Ni(75)) aluminum covered with nickel NPA75 (25 wt % Al and 75 wt % Ni); (2) (Al + Ni(80)) aluminum covered with nickel NPA80 (20 wt % Al and 80 wt % Ni). The clad granules had an average diameter of  $d_1 = 100 \pm 60\ \mu\text{m}$ ,  $d_2 = 100 \pm 60\ \mu\text{m}$  and a coating thickness of 10–20  $\mu\text{m}$ . The particle morphology is shown in Fig.1.

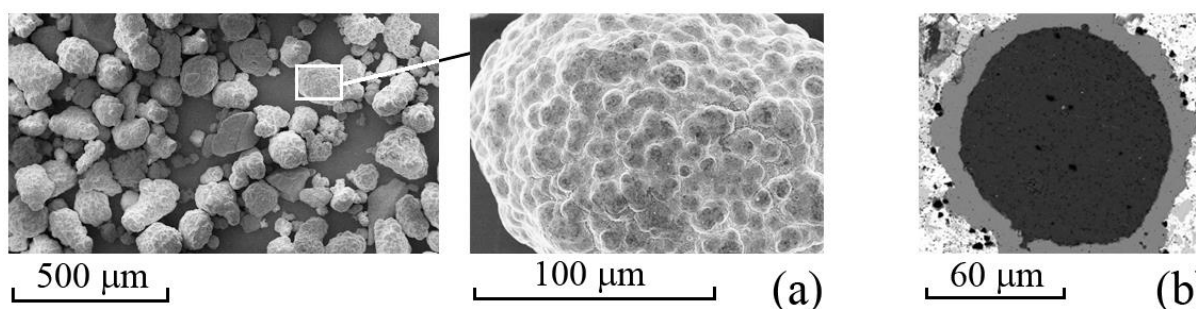


Fig. 1. Shape and morphology of clad granules of NPA75 powder (a); cross-section (Wood's alloy) (b).

A mixture of  $\text{Ti}(d_1) + 2\text{B}$  (69 wt % Ti and 31 wt % B based on the final product of  $\text{TiB}_2$ ) was prepared. Mixtures of  $a(\text{Al} + \text{Ni}(75)) + (1-a)(\text{Ti}(d_1) + 2\text{B})$  and  $a(\text{Al} + \text{Ni}(80)) + (1-a)(\text{Ti}(d_1) + 2\text{B})$  were made from  $\text{Ti}(d_1) + 2\text{B}$  and (Al + Ni) clad particles ( $a$  is the mass fraction of clad particle in the mixture, the variation interval  $a = 0-0.8$ ). When filling the cylindrical quartz moulds with the reaction mixtures, a consecutive portion compaction was used (quartz moulds length of 43mm, internal diameter of  $D = 4-4.4$  mm, external diameter of  $D_o = 7.8$  mm,  $D/d_1 \sim 40$ ,  $D/d_2 \sim 40$ ) [4]. The compaction of each layer of the mixture was due to the pulse obtained from the striker of  $m = 684$  g, falling from  $h = 43$  mm. The height of the layers was 1200–1400  $\mu\text{m}$ . The billet contained 19–23 layers.

The synthesis was carried out in argon atmosphere (at 1 atm). The quartz mould and the plugs on its ends eliminated the sample resizing. The temperature in the synthesis wave was measured with a tungsten–rhenium thermocouples (type A, diameter of the seal with a protective layer of 0.25–0.35 mm) and sent by a temperature recorder QMBox 4050-8-1 to the computer ASUS–A52J. The burning rate was determined due to the shooting of the process with a camera Sony HDR–CX130E. Electron microscopic study was performed using SEM LEO 1450 VP, Carl Zeiss.

The synthesis in  $a(\text{Al} + \text{Ni}(75)) + (1-a)(\text{Ti}(d_1) + 2\text{B})$  samples proceeded in the combustion mode at  $a = 0-0.5$ , at the initial temperature  $T_0 = 20^\circ\text{C}$ . At  $a = 1$  combustion did not occur, that is, the clad granules themselves could not react in the combustion mode. The average combustion rate ( $u$ ) was  $\sim 3$  cm/s at  $a = 0.4$ . The temperature profile in the combustion wave  $T_b = f(t)$  is shown in Fig. 2.

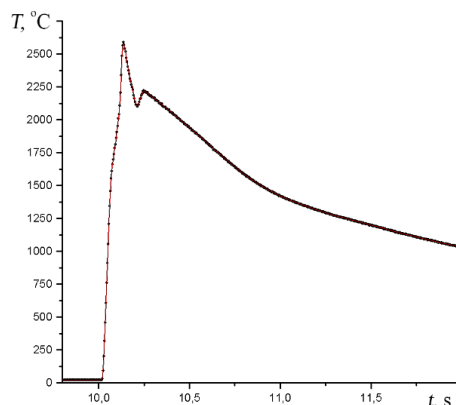


Fig. 2. Thermogram of  $a(\text{Al} + \text{Ni}(75)) + (1-a)(\text{Ti}(d_1) + 2\text{B})$  sample combustion at  $a = 0.4$ .

In thermograms, there are two temperature maxima (at  $a = 0.4$ ), which are associated with the staging of the synthesis process. Melting in the warm-up zone of the most low-melting components of this mixture - first aluminum, and then nickel leads, first of all, to the beginning of a chemical reaction inside the clad granules. Upon reaching the melting point of titanium, a fast and strongly exothermic reaction begins between titanium and boron. Between the clad particles (Al + Ni), the interlayers of the  $\text{Ti}(d_1) + 2\text{B}$  mixture have a thickness of 100–200  $\mu\text{m}$ , which is sufficient for the synthesis in them with a high combustion rate [4]. The first maximum of temperature (at  $T_b = 2580^\circ\text{C}$ ) in the thermogram is associated with this reaction. The second temperature maximum (at  $T_b = 2220^\circ\text{C}$ ) is associated with the reaction in the clad granules. In this case, the melt of nickel and its aluminides penetrates into the boride layer that has arisen around the granules. The product of synthesis has a developed porous structure and the open porosity of  $\sim 45-48\%$ , the density of 2.6–2.8  $\text{g}/\text{cm}^3$  (Fig. 3). Three types of the pore size are distinguished (Fig. 3):

- pores of round-shape of medium size ( $\sim 100-160$   $\mu\text{m}$  in diameter), connected with each other by capillaries (diameter of  $\sim 10-30$   $\mu\text{m}$ ), arising at the site of the clad granules after melt spread into the pores of the boride matrix, and irregularly shaped pores ( $\sim 10-120$   $\mu\text{m}$ ), which appeared

at the site of  $Ti(d_1)$  particles after melting and spreading of the melt into the surrounding boron [5, 6];

- small pores of round shape with a size of  $\sim 1\text{--}5\ \mu\text{m}$ , arising from the interaction of the fine fraction of titanium powder  $Ti(d_1)$  with boron; small pores are partially or completely filled with nickel and nickel aluminide at the stage of their spreading;
- pores of submicron size ( $< 1\ \mu\text{m}$ ), which appeared during phase formation.

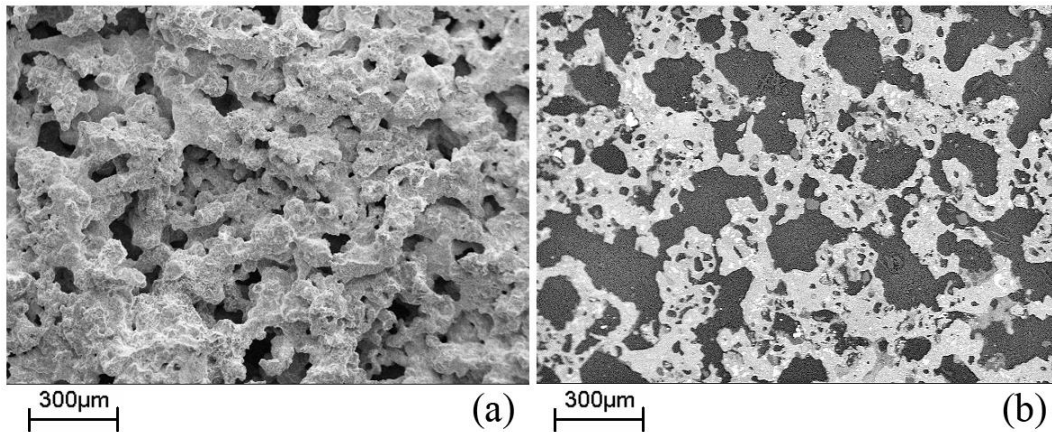


Fig. 3. Macrostructure of synthesis product ( $a = 0.4$ ): (a) cleavage, (b) section.

The microstructure of the product of synthesis around rounded pores is mainly fine-grained (Figs. 4b, 4c). On the inner surface of the pores, the matrix structure of titanium diboride crystallites is well distinguishable (Fig. 4a).

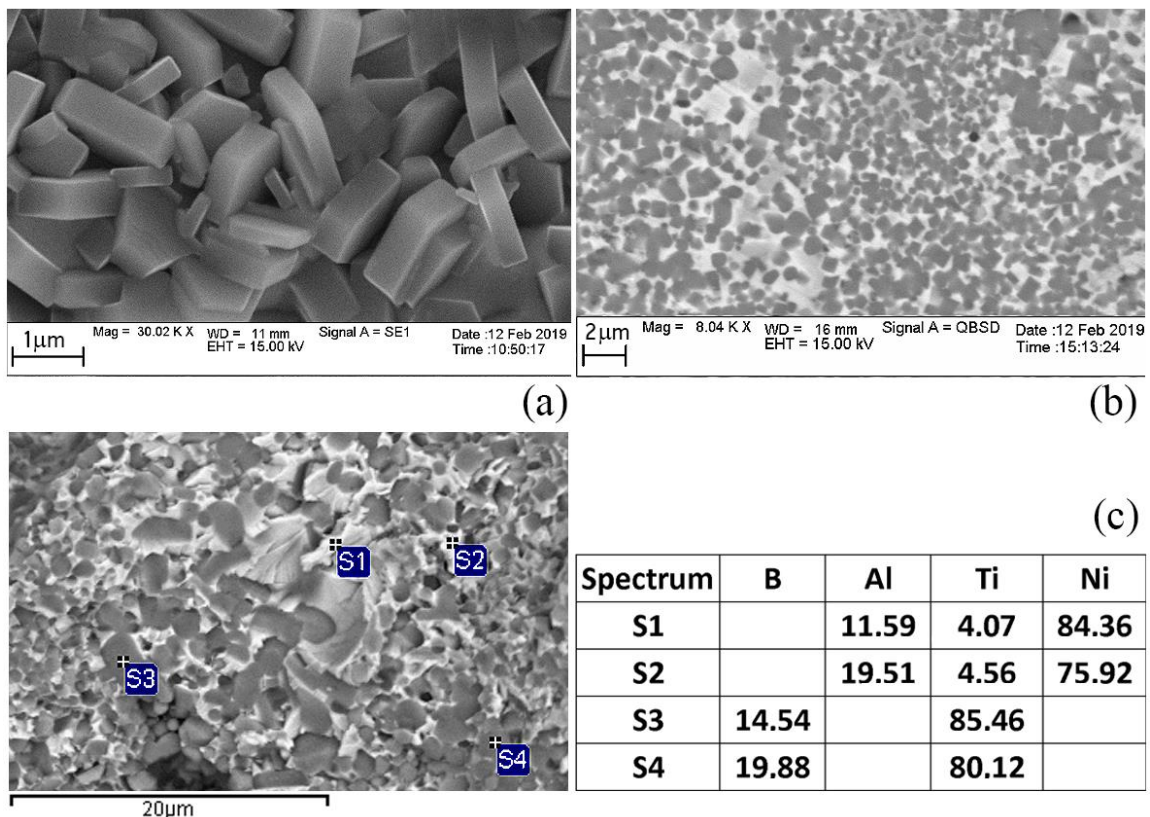


Fig. 4. (a) Image of crystals on the surface of the pores, (b) microstructure (polished section) and (c) composition in points (wt %) in the boride matrix and intermetallic interlayers (cleavage structure) ( $a = 0.4$ ).

The main phases found in the synthesis product are  $TiB_2$ ,  $Ni_3Al$ ,  $NiAl$ , and a small amount of  $Ni_2B$  and  $Ni_2B$  phases. The phase composition and distribution of elements in the synthesized product reflect the stages of the processes occurring in the combustion wave. Areas with the dark gray phase correspond to the increased content of boron and titanium (Fig. 4c, points S3 and S4) and  $TiB_2$  phase (according to XRD data). In the lighter areas (0.5–1.5  $\mu m$ ) around the grains of the dark gray phase, the increased nickel and aluminum content (points S1 and S2) is recorded, which corresponds to nickel aluminides (according to XRD data,  $Ni_3Al$  and  $NiAl$ ).

Thus, the material having a developed porous structure and the composite structure of the solid phase according to the type of interpenetrating frameworks - ceramic (fine-grained) and intermetallic is synthesized into one technological stage.

1. M.A. Ponomarev, V.E. Loryan, N.A. Kochetov, A.G. Merzhanov, SHS in preliminary structured compacts: I. Ni–Al blends, *Int. J. Self-Propag. High-Temp. Synth.*, 2013, vol. 22, no. 4, pp. 193–201.
2. M.A. Ponomarev, V.E. Loryan, A.S. Shchukin, A.G. Merzhanov, SHS in preliminary structured compacts: II. Ti–2B and Ti–Al blends, *Int. J. Self-Propag. High-Temp. Synth.*, 2013, vol. 22, no. 4, pp. 202–209.
3. A.G. Merzhanov, Thermally coupled SHS reactions, *Int. J. Self-Propag. High-Temp. Synth.*, 2011, vol. 20, no. 1, pp. 61–63.
4. M.A. Ponomarev, V.A. Shcherbakov, A.S. Shteinberg, Zakonomernosti goreniya tonkikh sloev poroshkovoï smesi titan–bor [Combustion patterns of thin layers of Ti–B powder mixture], *Dokl. Akad. Nauk: Proceed. Russ. Acad. Sci.*, 1995, vol. 340, no. 5, pp. 642–645.
5. M.A. Ponomarev, V.E. Loryan, Synthesis of porous composite materials via combustion of a mixture of titanium, VT6 alloy, and amorphous boron powders, *Inorg. Mater.*, 2018, vol. 54, no. 8, pp. 772–778.
6. M.A. Ponomarev, V.E. Loryan, Sintez kompozitsionnogo materiala v sisteme Al–Ti–B pri gorenii poroshkov titana, bora i plakirovannykh alyuminiem granul splava VT6, [Synthesis of composite material in Al–Ti–B system during combustion of titanium and boron powders and aluminum-clad granules of VT6 alloy], *Perspek. Mater.*, 2019, no. 3, pp. 62–73.

## ANTIBACTERIAL PROPERTIES OF TiCaPCON COATING DOPED WITH Pt AND Fe DEPOSITED USING SHS TARGETS

V. A. Ponomarev<sup>\*a</sup>, A. N. Sheveyko<sup>a</sup>, S. G. Ignatov<sup>b</sup>, J. Polčák<sup>c</sup>, and D. V. Shtansky<sup>a</sup>

<sup>a</sup>National University of Science and Technology MISiS, Moscow, 119049 Russia

<sup>b</sup>State Research Center for Applied Microbiology and Biotechnology, Obolensk, 142279 Russia

<sup>c</sup>Brno University of Technology, Brno, 616 69 Czech Republic

\*e-mail: ponomarev.viktor1993@yandex.ru

DOI: 10.24411/9999-0014A-2019-10129

Increasing the number of antibiotic-resistant bacteria requires the development of biocompatible antibacterial materials. In this report, we studied the effect of Pt, Fe nanoparticles and their combinations distributed on the surface of the TiCaPCON bioactive coating on the antibacterial properties of the material, taking into account factors contributing to the death of bacteria: the release of bactericidal ions into the biological environment, the formation of reactive oxygen forms and the formation of microgalvanic pairs between the nanoparticles and the surrounding matrix.

Coating TiCaPCON was precipitated on a silicon wafer by magnetron sputtering of composite SHS-target TiC–CaO–Ti<sub>3</sub>PO(*x*). Pt, Fe particles and their combinations were obtained by implantation of metal ions into the TiCaPCON coating. The formation of metal nanoparticles on the surface was due to their limited solubility in the crystal lattice of the coating. To change the size and distribution of nanoparticles on the surface, some samples were annealed at a temperature of 700° C for 1 h. Thus, samples with particles: Pt, Fe, P<sub>an</sub>, Fe, (Pt + Fe), P<sub>an</sub> + Fe (Pt + Fe) were obtained and investigated.

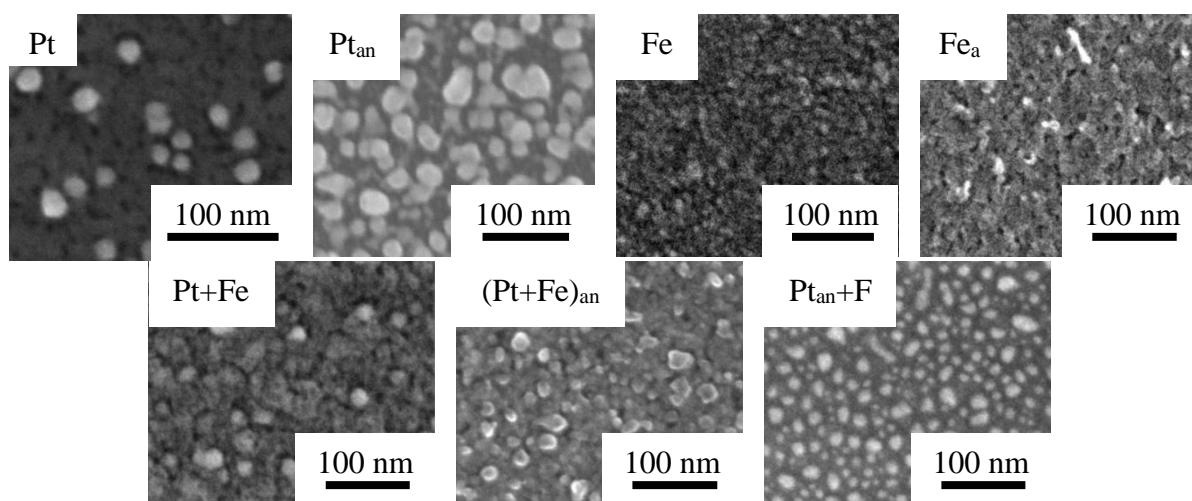


Fig. 1. SEM surface images of TiCaPCON films after different surface treatments. (a) Pt ion implantation (II), (b) Pt II + annealing, (c) Fe II, (d) Fe II + annealing, (e) subsequent Pt and Fe II, (f) subsequent Pt and Fe II + annealing, (g) Pt II + annealing + Fe II.

Investigation by SEM showed (Fig. 1) that the size of the spherical Pt particles is in the range of 15–30 nm. After annealing, the density of Pt particles increased significantly. Separate inclusions of Fe particles of 5–7 nm size were observed in the sample implanted with Fe, but the particles were not formed. After annealing, the growth of formless Fe particles was

observed. In other samples the size of nanoparticles was 3–20 nm. The charge distribution map on the sample surface was obtained by AFM using a Kelvin probe. It is shown that a potential difference of 5–30 mV is formed between the Ptan nanoparticles and the matrix when the samples are immersed in a physiological solution (FR). The maximum potential difference was observed in the sample  $(\text{Pt} + \text{Fe})_{\text{an}} - 50\text{--}60$  mV. This indicates the possibility of microgalvanic currents on the surface of the sample. It was found that the polarity of nanoparticles with respect to the matrix changes during incubation in saline solution. The concentration of reactive oxygen species was determined by fluorescence spectrophotometry. The concentration of PT, Fe ions was determined by inductively coupled plasma mass spectrometry. The paper discusses the influence of various parameters on the antibacterial characteristics of coatings. The action of Pt and Fe nanoparticles against eight types of different bacteria was studied, as well as the effect of ions of these metals on the overall antibacterial activity.

# APPLICATION OF SHS FOR PRODUCTION OF COMPOSITE CERAMIC CATHODES FOR PVD OF HIGH-TEMPERATURE PROTECTIVE Mo– (Hf/Zr)–Si–B COATINGS

A. Yu. Potanin<sup>\*a</sup>, Ph. V. Kiryukhantsev-Korneev<sup>a</sup>, S. I. Rupasov<sup>a</sup>, Yu. S. Pogozhev<sup>a</sup>,  
and E. A. Levashov<sup>a</sup>

<sup>a</sup>National University of Science and Technology MISIS, Moscow, Russia

\*e-mail: a.potanin@inbox.ru

DOI: 10.24411/9999-0014A-2019-10130

This work is supposed to carry out experimental studies on obtaining high-temperature ceramic materials based on borides and silicides of transition refractory metals of the IV–VI groups of the Periodic Elements Table by self-propagating high-temperature synthesis (SHS) technology [1]. Also, the mechanisms of the phase and structure formation, as well as the stages of reactions during the ceramics synthesis in the Mo–Si–B, Mo–Hf–Si–B, and Mo–Zr–Si–B systems were studied. The high-temperature ceramic experimental samples, including target-cathodes were produced by the hybrid SHS + HP technology. The coatings were deposited by direct current magnetron sputtering. The structure, element and phase composition of coatings were studied by means of scanning and transmission electron microscopy, X-ray diffraction, X-ray photoelectron spectroscopy, energy-dispersive spectroscopy, and glow discharge optical emission spectroscopy. To evaluate their oxidation resistance, the coatings were annealed in air in the temperature range of 500–1600°C during different time slots between 10 min and 5 h. The complex materials researches that establish the relationship between the composition and the structure of ceramic materials, the parameters of sputtering and the properties of coatings were carried out.

The dense composite ceramic cathodes characterized by high hardness and low residual porosity were produced by hot pressing of SHS powders. Phase composition and structure were investigated. The final composition of the reaction products consists of HfB<sub>2</sub>/ZrB<sub>2</sub>, MoSi<sub>2</sub>, and MoB phases. The microstructure of the HP specimen in Mo–Hf–Si–B system is presented in Fig. 1. In the obtained ceramic, MoSi<sub>2</sub> (≤ 10 μm), MoB (2–10 μm), and HfB<sub>2</sub> (≤ 1 μm) grains are present. All phases have comparable size and are randomly distributed in the structure. These compositions are advanced for high-temperature application in oxidizing condition because of formation of strong oxide films SiO<sub>2</sub>–HfO<sub>2</sub>–B<sub>2</sub>O<sub>3</sub> along with the complex oxide HfSiO<sub>4</sub>, which serve as an effective diffusion barrier and reduce the oxidation rate.

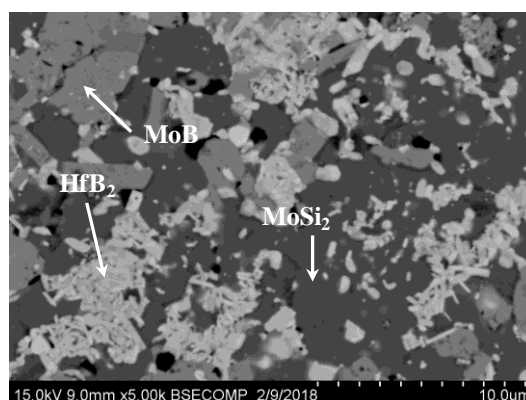


Fig. 1. Microstructure of the composite ceramic cathode fabricated by hot pressing of SHS powder in Mo–Hf–Si–B system.

Hard Mo–(Hf,Zr)–Si–B–(N) films were deposited by magnetron sputtering of SHS-targets in Ar + N<sub>2</sub> (0, 10, 15, 25, and 100% N<sub>2</sub>). According to XRD results, the MoSi<sub>2</sub> hexagonal phase was the main structural component of all studied samples (Fig. 2). Certain lines were close or overlapped on the lines from the Al<sub>2</sub>O<sub>3</sub> substrate, but reflections at angles  $2\theta = 22.2^\circ$ ,  $41.7^\circ$ , and  $45.5^\circ$  evidenced the presence of the h-MoSi<sub>2</sub> phase. The MoSiB coating had a pronounced texture in the (100) direction.

It was established that single-layer MoSiB coatings possess a hardness of 27 GPa, elasticity modulus of 390 GPa, and elastic recovery of 48%. They can also resist oxidation up at  $T = 1200$  and  $1500^\circ\text{C}$  (Fig. 3), which is caused by the formation of the SiO<sub>2</sub>-based protective film on their surface. The MoSi<sub>2</sub> coatings can have hardness comparable to the hardness of MoSiB coatings, but they are somewhat worse than them in regards to oxidation resistance [2].

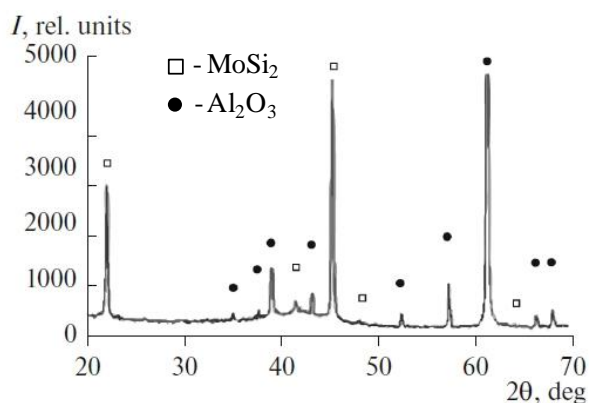


Fig. 2. X-ray diffraction pattern of coating MoSiB.

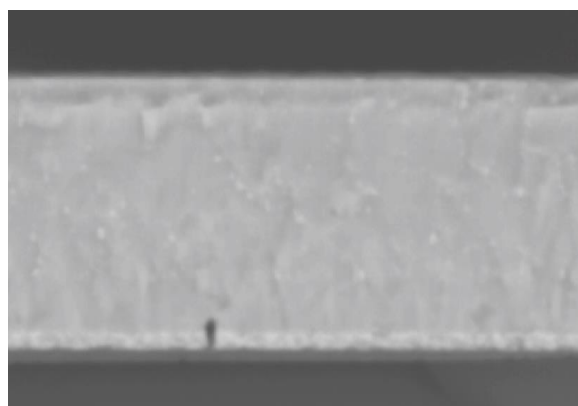


Fig. 3. SEM data for MoSiB coating after annealing at  $T = 1200^\circ\text{C}$  for 1 h.

The reported study was funded by RFBR according to the research project no. 18-08-00269.

1. E.A. Levashov, A.S. Mukasyan, A.S. Rogachev, D.V. Shtansky, Self-propagating high-temperature synthesis of advanced materials and coatings, *Int. Mater. Rev.*, 2017, vol. 62, no. 4, pp. 203–239.
2. Ph.V. Kiryukhantsev-Korneev, A.Yu. Potanin, Structure, mechanical properties, and oxidation resistance of MoSi<sub>2</sub>, MoSiB, and MoSiB/SiBC coatings, *Russ. J. Non-Ferr. Met.*, 2018, vol. 59, pp. 698–708.



## THE KINETICS AND MECHANISMS OF HIGH-TEMPERATURE OXIDATION OF HEAT-RESISTANT MoSi<sub>2</sub>–MoB–HfB<sub>2</sub> CERAMICS PRODUCED BY HYBRID SHS + HP TECHNOLOGY

A. Yu. Potanin<sup>\*a</sup>, S. Vorotilo<sup>a</sup>, Yu. S. Pogozhev<sup>a</sup>, P. V. Loginov<sup>a</sup>, and E. A. Levashov<sup>a</sup>

<sup>a</sup>National University of Science and Technology MISIS, Moscow, Russia

\*e-mail: a.potanin@inbox.ru

DOI: 10.24411/9999-0014A-2019-10131

Transition metals silicide composites are prospective as high-temperature oxidation and corrosion-resistant structural materials and coatings. They can withstand the mechanical loads at temperatures up to 1700–2000°C in aggressive environments [1]. Among these materials, MoSi<sub>2</sub>-based composites attract special interest. In particular, they are applied as the heating elements in high-temperature industrial furnaces and exhaust systems of internal combustion engines [2].

The high-temperature oxidation resistance of MoSi<sub>2</sub> is based on the formation of glassy SiO<sub>2</sub>-based protective film, which is nearly impermeable to gasses. However, at the temperatures above 1800°C the formation and evaporation mono-oxide SiO causes the degradation of the SiO<sub>2</sub> film and drastically decreases the oxidation resistance of MoSi<sub>2</sub>.

Alloying by borides TiB<sub>2</sub>, ZrB<sub>2</sub>, MoB, HfB<sub>2</sub> allows one to enhance the performance of MoSi<sub>2</sub>-based materials and optimize the protective properties of the oxide films [3, 4]. Formation of a protective borosilicate glass layer (B–SiO<sub>2</sub>) contributes to efficient healing of microcracks and pores that inevitably emerge in the protective layer during its operation.

The goal of this work was to investigate the influence of the composition and microstructure of the ceramics MoSi<sub>2</sub>–MoB–HfB<sub>2</sub> produced by hybrid SHS + HP technology on the thermal conductivity, mechanisms and kinetics of oxidation in furnace static conditions at 1200 and 1650°C. In the investigated Mo–Hf–Si–B system, the composition of the combustion products was calculated according to the equation (100 – X)(90MoSi<sub>2</sub> + 10MoB) + X·HfB<sub>2</sub>, where X = 0 and 34 at %. Reaction mixtures were prepared using the elemental powders of Mo, Hf, Si, and B. The raw SHS powders were produced according to two schemes: (1) products of the combustion of reaction mixtures Mo–Si–B (X = 0) and Hf + 2B were milled and mixed in a ball mill with HfB<sub>2</sub> concentration of 34 at %; (2) products of the combustion of Mo–Hf–Si–B mixture (X = 34%) were ball milled until the micron-sized MoSi<sub>2</sub>–MoB–HfB<sub>2</sub> composite powders were produced. Dense ceramics were produced by hot pressing (HP) of the SHS powders using the DSP-515 SA installation («Dr. Fritsch», Germany) in vacuum at temperature of 1600°C, heating rate of 10 °C/min, pressure of 35 MPa and dwelling time of 10 min.

Figure 1 shows the microstructure of the HP specimens. In the X0 ceramic, MoSi<sub>2</sub> (≤15 μm) and MoB (5–10 μm) grains are present. X34(1) ceramic (Fig. 1b) in addition to MoSi<sub>2</sub> and MoB contains faceted HfB<sub>2</sub> grains (4–10 μm) and a small number of HfSiO<sub>4</sub> inclusions (≤ 4 μm). In both X0 and X34(1) ceramics, all phases have comparable size and are randomly distributed in the structure; hence these ceramics are denoted as single-level structures (SLS). X34(2) ceramic has a two-level structure (TLS) (Fig. 1c), relatively large MoSi<sub>2</sub> grains (≤ 10 μm) are surrounded by the 2–4 μm wide HfB<sub>2</sub> layers, which are comprised of elongated HfB<sub>2</sub> grains with diameter of ~ 0.3 μm and length of 0.5–1 μm. MoB grains (≤ 3 μm) are also present in the structure, usually in conjunction with HfB<sub>2</sub> grains. This is related to the stages of crystallization in the combustion front of Mo–Hf–Si–B mixture: the most refractory HfB<sub>2</sub> forms first, followed by crystallization of MoB on the surface of HfB<sub>2</sub> [5].

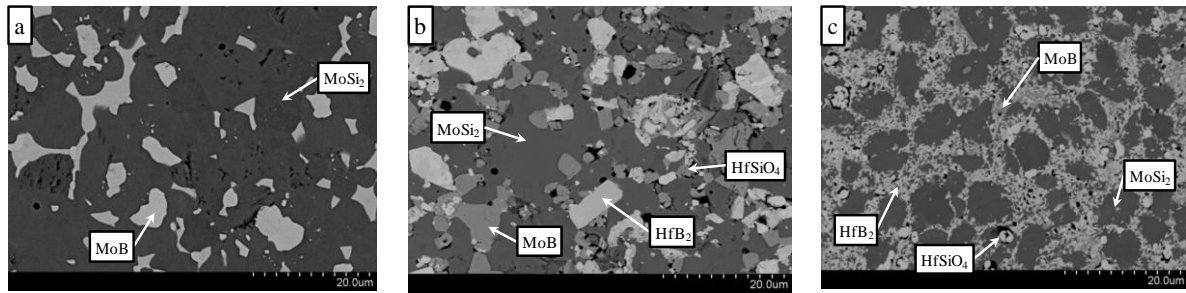


Fig. 1. Microstructure of the HP specimens: (a) X0, (b) X34(I), and (c) X34(2).

Addition of hafnium diboride leads to the increase of mass change during the oxidation at 1200°C due to the formation of  $\text{HfO}_2$  and  $\text{HfSiO}_4$ , which are denser than  $\text{SiO}_2$ . Oxidation of SLS and TLS ceramics produced two-layered oxide films. In the case of SLS ceramic,  $\text{SiO}_2$ -based oxide film was comprised of top 9–12  $\mu\text{m}$  wide Hf-doped amorphous silica layer and bottom 3–5  $\mu\text{m}$  crystalline  $\alpha\text{-SiO}_2$  layer (Fig. 2b). In the case of TLS ceramic, top layer consisted of crystalline  $\alpha\text{-SiO}_2$ , whereas the bottom layer was formed by  $\text{HfSiO}_4$  grains (Fig. 2c).

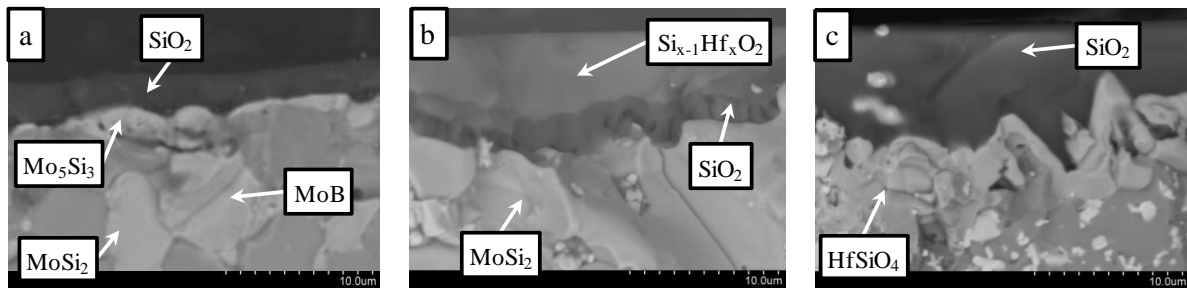


Fig. 2. SEM images of the fractures of specimens (a) X0, (b) X34(I), and (c) X34(2) oxidized at 1200°C during 30 h.

Figure 3a shows the microstructure of fracture of surface region of X34(I) specimen oxidized at 1650°C during 0.5 h. On the surface of sample, a one-layered  $\text{SiO}_2$ -based 8–10  $\mu\text{m}$  thick film formed, containing fine Hf–Si–O precipitates. These inclusions were investigated by TEM (Fig. 3b). Elongated dark-grey precipitates are distributed homogeneously in the  $\text{SiO}_2$  matrix and have the length of 300–400 nm and width of 100–200 nm. By the electron diffraction pattern and energy dispersive X-ray spectrometry analysis, these precipitates were identified as  $\text{HfSiO}_4$  with body-centered tetragonal lattice. HRTEM (Fig. 3c) demonstrated that the submicron precipitates have no subgrains and are defect-free.

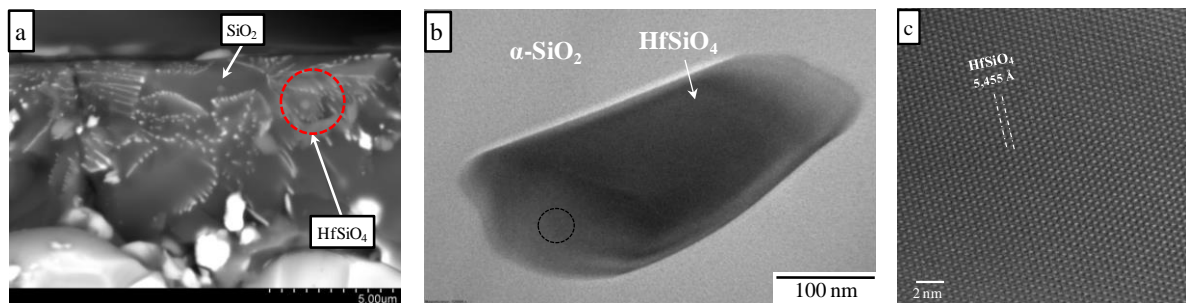


Fig. 3. (a) SEM image of the near-surface zone of fractured specimen X34(I) oxidized at 1650°C during 0.5 h. (b) TEM and (c) HRTEM images of the  $\text{HfSiO}_4$  precipitate.

Understanding and control of the phase and structure formation of oxide films in single-level structured and two-level structured ceramics open new avenues for the optimization of the

composition and structure of ceramics in regards to the intended working conditions. Application of SHS is particularly promising in this regard since it allows one to produce a wide spectrum of ceramics with similar phase composition but drastically different microstructures and properties.

The reported study was funded by RFBR and Moscow city Government according to the research project no. 19-38-70013.

1. S.P. Tantry, S.K. Ramasesha, J.S. Lee, T. Yano, U. Ramamurty, Effect of double reinforcements on elevated-temperature strength and toughness of molybdenum disilicide, *J. Am. Ceram. Soc.*, 2004, vol. 87, pp. 626–632.
2. A.K. Vasudévan, J.J. Petrovic, A comparative overview of molybdenum disilicide composites, *Mater. Sci. Eng. A*, 1992, vol. 155, pp. 1–17.
3. J. Cook, A. Khan, E. Lee, R. Mahapatra, Oxidation of MoSi<sub>2</sub>-based composites, *Mater. Sci. Eng. A*, 1992, vol. 155, pp. 183–198.
4. A.Yu. Potanin, Yu.S. Pogochev, E.A. Levashov, A.V. Novikov, N.V. Shvindina, T.A. Sviridova, Kinetics and oxidation mechanism of MoSi<sub>2</sub>–MoB ceramics in the 600–1200°C temperature range, *Ceram. Int*, 2017, vol. 43, pp. 10478–10486.
5. S. Vorotilo, A.Yu. Potanin, Yu.S. Pogochev, E.A. Levashov, N.A. Kochetov, D.Yu. Kovalev, Self-propagating high-temperature synthesis of advanced ceramics MoSi<sub>2</sub>–HfB<sub>2</sub>–MoB, *Ceram. Int.*, 2019, vol. 45, pp. 96–107.

## SELF-PROPAGATING HIGH-TEMPERATURE SYNTHESIS OF METAL MATRIX COMPOSITE POWDERS FROM MECHANOACTIVATED POWDER MIXTURES

**G. A. Pribytkov<sup>\*a</sup>, A. V. Baranovskii<sup>a,b</sup>, M. G. Krinitsyn<sup>a,b</sup>, V. V. Korzhova<sup>a</sup>, and E. N. Korosteleva<sup>a,b</sup>**

<sup>a</sup>Institute of Strength Physics and Materials Science, SB, RAS, Tomsk, 634055 Russia

<sup>b</sup>National Research Tomsk Polytechnic University, Tomsk, 634050 Russia

\*e-mail: gapribyt@mail.ru

DOI: 10.24411/9999-0014A-2019-10132

Mechanical activation (MA) of reaction mixtures on the basis of metal powders is usually used to promote combustion reaction. When there is a metal excess in metal – nonmetal powder mixtures SHS products represent metal matrix composites (MMC). MMC structure corresponds disperse particles of hard compounds (carbide, boride, silicide) imbedded into metal matrix (binder). Disperse compound particles serve as strengthening phase in the composite. Less is size of the particles more is the strengthening effect. The most often titanium carbide is used as a strengthening phase in the SHS metal matrix composites. Due to high negative enthalpy of TiC it is possible to get high volume fraction of the metal matrix in the SHS composite. It is known, that the more is concentration of inert metal matrix powder in reactive mixture the more is a dispersion of TiC particles in SHS composite. A size of TiC particles varies from 10 to 1  $\mu\text{m}$  [1–4] depending of the metal binder concentration in the reaction mixtures. Representative structures of the composites synthesized from powder mixtures with high content of metal binder powder are shown in Fig 1.

SHS TiC + Me binder powders are used for cladding and spraying of wear resistant coatings [4, 5]. The powders can be easy produced by crashing of porous SHS cakes and screening out granules of required size. To get more fine carbide phase in SHS metal matrix composite a processing of reaction powder mixtures of titanium, carbon and metal matrix in high energy planetary mills is used. As a result, concentration limits of wave mode SHS extend and the combustion temperature goes down. However, damping effect of metal matrix powder resists MA of titanium and carbon powders. That is why we failed to get considerable effect of MA on metal binder concentration for Ti + C + cast iron and Ti + C + high speed steel (HSS) powder mixtures. The same damping effect of the metal binder prevents disintegration of TiC particles in the granules. A single positive impact of a processing SHS metal matrix powder in high energy planetary mills is formation rounded shape of the MMC granules (Fig. 2a). The rounded shape of the granules is needed to promote a steady powder delivery to plasma spray or to cladding pool.

Another way to get TiC + Me matrix composite powders with submicron carbide inclusions is intensive processing powder mixture of fine carbide and metal matrix. If metal matrix powder is ductile enough composite granules are formed by impregnation of carbide particle into metal matrix powder. We produced TiC + 50 vol % Ti binder composite powder via three steps route: SHS of TiC + 25 vol % Ti binder powder from titanium and black carbon powder mixtures  $\rightarrow$  intensive processing of SHS powder in planetary mill (MA) to get submicron size powder (Fig. 2b)  $\rightarrow$  blending of Ti powder with MA treated SHS composite powder and at last MA retreatment of TiC + Ti powder mixture. The TiC + 50 vol % Ti binder composite powders (Fig. 2c) were used for cladding and sputtering of wear resistance coatings and in additive technologies.

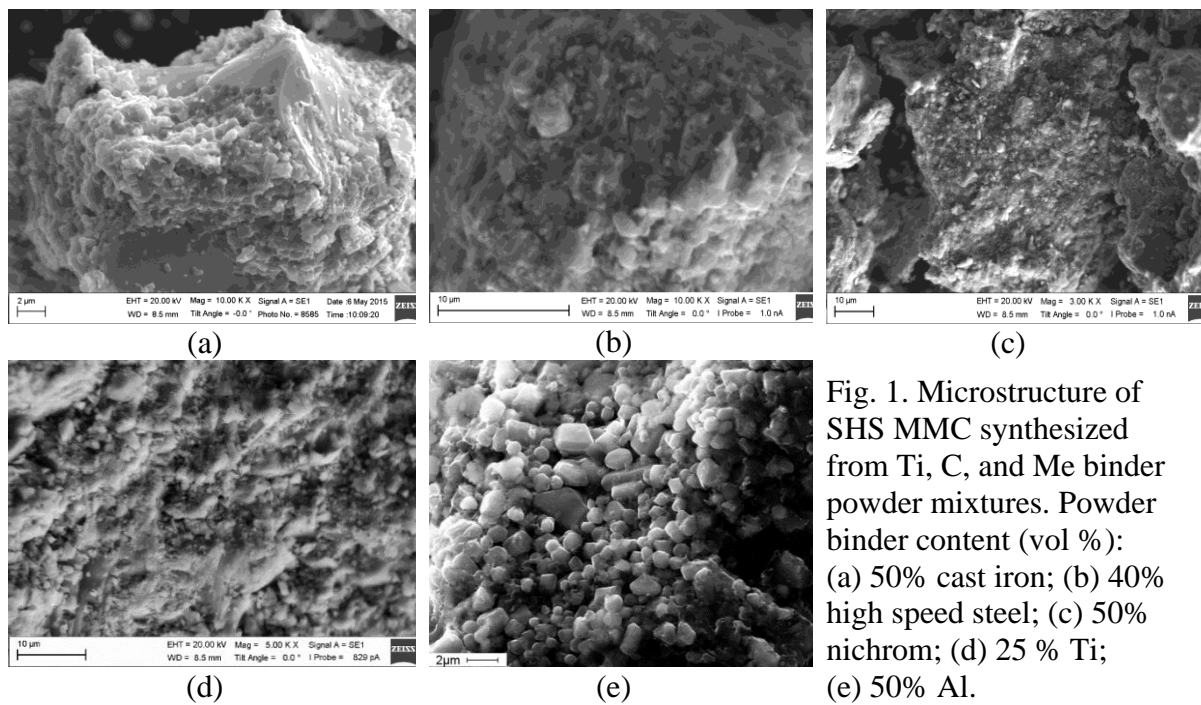


Fig. 1. Microstructure of SHS MMC synthesized from Ti, C, and Me binder powder mixtures. Powder binder content (vol %): (a) 50% cast iron; (b) 40% high speed steel; (c) 50% nichrom; (d) 25 % Ti; (e) 50% Al.

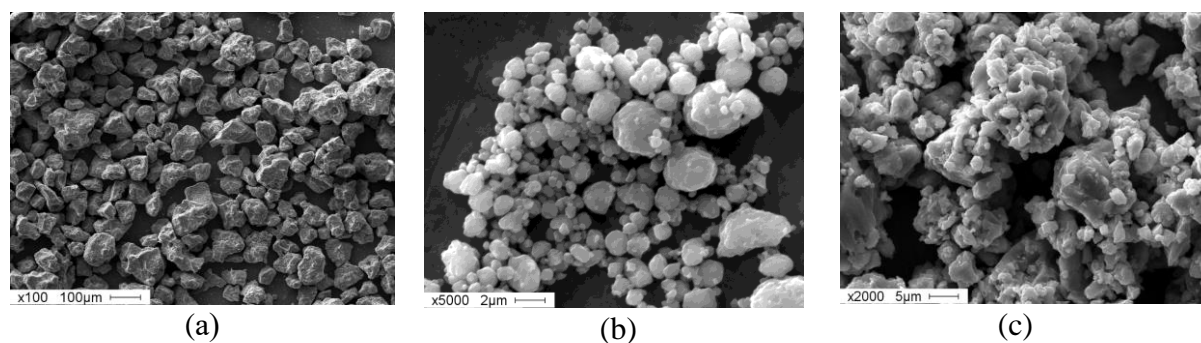


Fig. 2. Effect of planetary mill processing on morphology of SHS metal matrix composites. (a) TiC + 50 vol % HSS; (b) TiC + 25 vol % Ti; (c) TiC + 50 vol % Ti.

The research was performed within the frame of the Fundamental Research Program of the State Academies of Sciences for 2013-2020, line of research III.23.

1. E.N. Korosteleva, G.A. Pribytkov, M.G. Krinitcyn, A.V. Baranovskii, V.V. Korzhova, V.E. Strel'nitskij, Fabrication of «TiC-HSS steel binder» composite powders by self-propagating high temperature synthesis, *Key Eng. Mater.*, 2016, vol. 712, pp. 195–199.
2. G.A. Pribytkov, I.A. Firsina, V.V. Korzhova, M.G. Krinitcyn, A.V. Baranovskiy, SHS of «TiC–NiCrBSi binder» composite powders, *J. Phys. Conf. Ser.*, 2018, vol. 1115, 042056.
3. G.A. Pribytkov, A.V. Baranovskiy, V.V. Korzhova, M.G. Krinitcyn, An investigation of SHS products in titanium, carbon (black carbon) and aluminum powder mixtures, *J. Phys. Conf. Ser.*, 2018, vol. 1115, 042055.
4. M. Krinitcyn, G. Pribytkov, V. Korzhova, I. Firsina, Structure and properties of composite coatings prepared by electron beam melting with "titanium carbide-titanium binder", *Surf. Coat. Technol.*, 2019, vol. 358, pp. 706–714.
5. G.A. Pribytkov, V.I. Kalita, D.I. Komlev, V.V. Korzhova, A.A. Radyuk, A.V. Baranovsky, A.Yu. Ivannikov, M.G. Krinitcyn, A.B. Mikhailova, Structure and wear resistance of plasma coatings sputtered using TiC + HSS binder composite powder, *Inorg. Mater.: Appl. Res.*, 2018, vol. 9, no. 3, pp. 442–450.

## SYNTHESIS AND APPLICATION OF SHS COMPOSITE POWDERS OF THE TITANIUM BORIDE–TITANIUM SYSTEM

G. A. Pribytkov<sup>a</sup>, M. G. Krinitcyn<sup>\*a,b</sup>, V. V. Korzhova<sup>a</sup>, and I. A. Firsina<sup>a</sup><sup>a</sup>Institute of Strength Physics and Materials Science, SB, RAS, Tomsk, 634055 Russia<sup>b</sup>National Research Tomsk Polytechnic University, Tomsk, 634050 Russia

\*e-mail: krinmax@gmail.com

DOI: 10.24411/9999-0014A-2019-10133

Metal matrix composites (MMCs) "dispersed hardener–metal matrix (binder)" have a unique combination of hardness and toughness, which provides them with widespread use as bulk materials and coatings on parts working under conditions of intense wear. The use of titanium as a binder allows obtaining materials with high specific strength. Solid particles of refractory compounds usually act as a hardener: TiN, TiC, TiB, TiB<sub>2</sub> [1–10]. Of particular interest as a dispersed hardening phase in titanium matrix composites are TiC and TiB compounds bordering on solid solutions based on titanium on double equilibrium diagrams, which ensures good compatibility of the hardening phase with the titanium matrix. These compounds have excellent thermodynamic and chemical stability, high hardness (about 30 GPa), as well as close thermal expansion coefficients  $\alpha$ : Ti =  $8.2 \times 10^{-6}/^{\circ}\text{C}$ ; TiB =  $7.2 \times 10^{-6}/^{\circ}\text{C}$ ; TiC =  $7.9 \times 10^{-6}/^{\circ}\text{C}$  [3–7].

The properties of the MMCs depend not only on the properties of the elements of the composition but also on the structure, the main characteristics of which are: volume fraction, average size, and morphology of solid particles of the strengthening phase. Inclusions with rounded particles (TiC) increase the hardness and wear resistance of composites under dry friction. Phases that form non-axial inclusions (for instance whiskers of TiB) increase the creep resistance [8]. Different methods for producing composite materials can significantly change the morphology and distribution of solid particles in the structure of metal-matrix composites.

It is of interest to use powder obtained from synthesis products in powder mixtures of titanium and boron, and for an additive during surfacing, instead of mechanical mixtures, and an electron beam as a heat source. In this regard, the purpose of this work was to find out the possibility of using SHS composite powders TiB + Ti for electron beam surfacing of coatings and compare the structure and properties of the obtained coatings with previously published results on coatings obtained by laser welding and melting.

Composite powder was obtained from the SHS specs synthesized in the layer-by-layer burning mode of cylindrical compacts with a diameter of 35 mm from powder mixtures of titanium TPP-8 (99.5%, < 160  $\mu\text{m}$ ) and boron amorphous technical grade "A" (93%) in two reaction media (argon and air). The pressing pressure of the reaction mixtures was selected to achieve an initial porosity of the compacts of 40–45%. The burning was initiated by heating the molybdenum helix that ignites the pellet. The synthesis was carried out in two modes: in a sealed reactor in an argon atmosphere with an overpressure of about 0.5 atm followed by slow cooling in the reactor and in the air with rapid cooling in water. Compounds with the estimated content of the titanium bond from 20 to 60 vol % were synthesized with the measurement of the maximum combustion temperatures by the thermocouple method. To measure the temperature, junctions of tungsten–rhenium thermocouples with a diameter of thermoelectrodes of 100  $\mu\text{m}$  were placed in holes drilled in compacts. Porous SHS specimens obtained by synthesis in argon were crushed and a fraction of 56–200  $\mu\text{m}$  necessary for surfacing was selected by sieving.

Electron beam coatings from composite powders were deposited on a 4-mm titanium VT1-0 substrate in a vacuum using a setup consisting of an electron source, a scanning electron

beam control system, a powder feeder, and a manipulator for moving the substrate relative to the scanning electron beam [11]. Structural studies of the products of synthesis and deposited coatings were carried out using the equipment of the Nanotech Center for Collective Use of the Institute of Strength Physics and Materials Science, SB, RAS by optical metallography (AXIOVERT-200MAT, Zeiss, Germany), scanning electron microscopy (EVO 50, Zeiss, Germany), and X-ray diffraction analysis (DRON-3 diffractometer, Bourevestnik, Russia). ASTM database was used for XRD data decoding.

X-ray phase analysis showed that for all the formulations studied by us, the synthesis products are multiphase. According to the estimated content of phases by the sum of the areas under the peaks, the main phase in the synthesis products is titanium monoboride (ASTM 5-700). Also in the products of synthesis other phases were identified. During air synthesis, a significant portion of titanium is consumed in reactions with atmospheric gases to form titanium dioxide and the  $TiN_{0.3}$  phase (ASTM 41-1352), which is isomorphic to hexagonal  $\alpha$ -Ti, therefore, this phase is a solid solution of nitrogen in titanium. In products synthesized in argon, titanium dioxide  $TiO$  (ASTM 9-240) is formed instead of titanium dioxide (ASTM 21-1276), and its content increases with increasing titanium content in the reaction mixtures. The phase  $TiN_{0.3}$  was not detected in the synthesis products in argon. Titanium diboride is also present in all products of the synthesis (ASTM 35-741). Due to the formation of these side phases (non-target), the content of unbound titanium, forming a metal binder, is reduced compared to the target values. In composites synthesized in air, almost all titanium, not participating in the formation of monoboride, goes into side phases. The morphology (Figs. 1a, 1c) and microstructure (Figs. 1b, 1d) of composite powders synthesized in argon depend on the composition of the reaction mixtures.

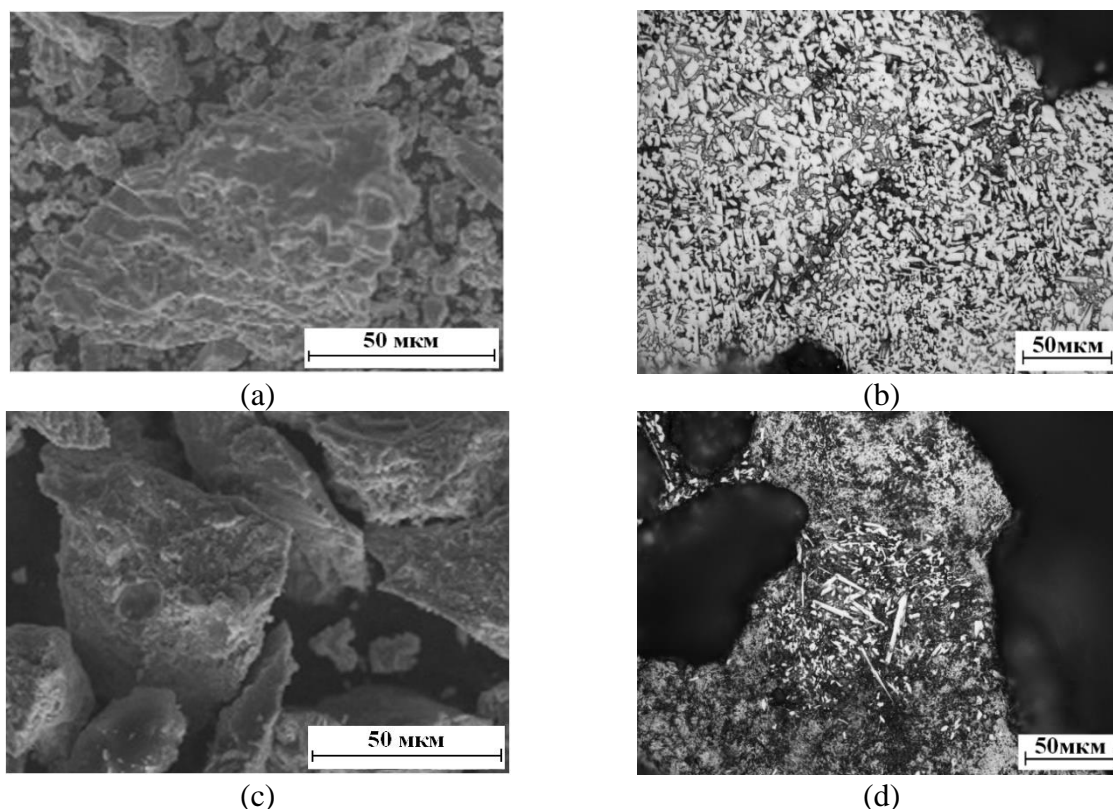


Fig. 1. (a, c) Morphology and (b, d) microstructure of SHS powders synthesized in argon. The content of the titanium ligament (vol %): (a, b) 20%; (c, d) 50%.

The SHS product containing 20% of the binder is very brittle, therefore, when crushing, many small fragments are formed (Fig. 1a). This is due to the brittleness of  $TiB$ , which occupies

80% of the volume in the SHS product. Due to the limited volume of the titanium ligament, the growth of boride whiskers in the melt during the synthesis process takes place in cramped conditions. Therefore, the microstructure of the SHS product consists of relatively small randomly oriented boride whiskers (Fig. 1b). The SHS product with 50 vol % titanium binder has considerable plasticity; therefore, when crushing the SHS cakes, few small fragments are formed among the fragmentation granules (Fig. 1c). It is difficult to interpret the microstructure of the SHS granules of the TiB + 50% Ti product using optical micrographs (Fig. 1d), since according to the results of X-ray diffraction analysis, in addition to the target phases (titanium and titanium monoboride) it contains titanium diboride (22.4%) and titanium oxide. The structure of the granules is highly heterogeneous (perhaps due to insufficient homogeneity of the reaction mixture), and the size of TiB whiskers in the areas where they occur is much larger than in the SHS product with 20% titanium binder. Composite powders of two compositions with calculated titanium binder content of 20 and 50 vol % were synthesized in argon for electron-beam surfacing. Therefore, the main phase in the deposited coatings is titanium (ASTM 5-682). Titanium monoboride is the second phase in coatings. The content of individual phases in surfacing with mixtures with titanium binder content in SHS powders of 20 and 50% is different, despite the identical elemental composition of the mixtures. This difference does not qualitatively affect the microstructure of the deposited coatings (Fig. 2).

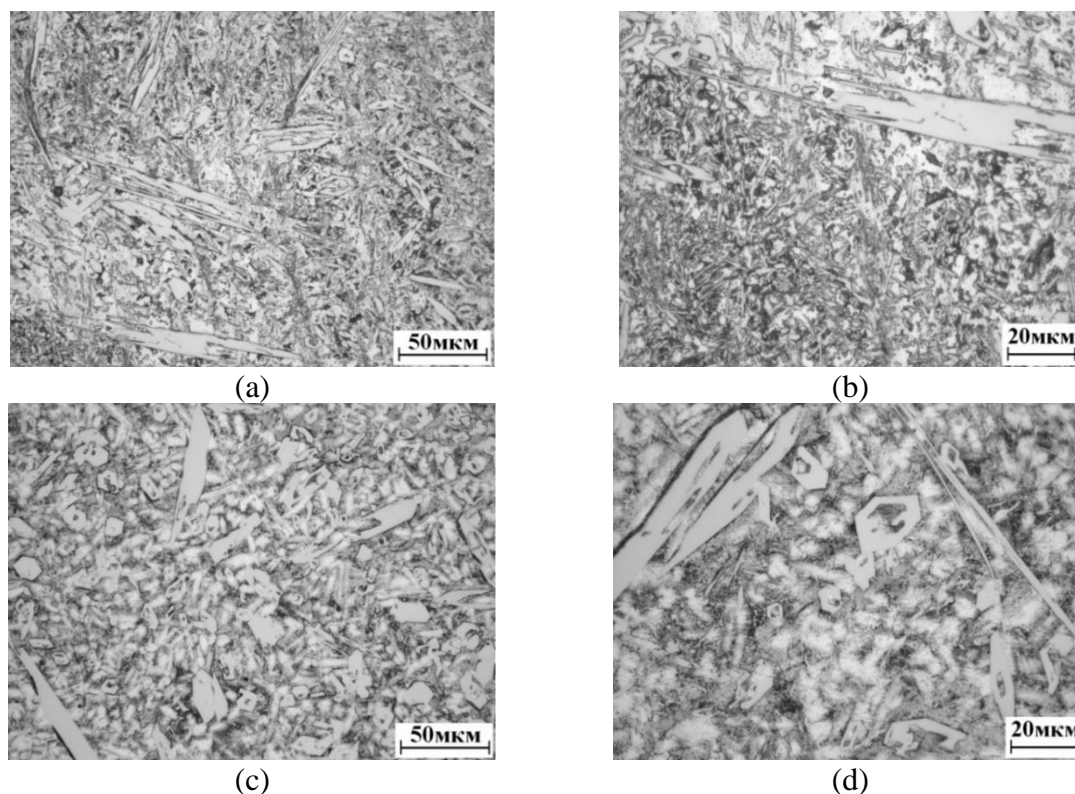


Fig. 2. Structure of the deposited coatings: (a, b) TiB + Ti (20 → 80)%;  
(c, d) TiB + Ti (50 → 80)%.

In the structure of the coatings, the coarse needle-like inclusions of the primary titanium monoboride stand out against the background of the etched ligament, which is a dispersed TiB + Ti eutectic. Fine TiB whiskers in the structure of the eutectic are not resolved because of the small increase. The volume fraction of primary borides is visually larger in surfacing with a mixture with composite powder TiB + 20% Ti than in surfacing with a mixture with powder TiB + 50% Ti, which is consistent with the results of X-ray diffraction analysis.



This work was supported by the Russian Science Foundation (Grant no. 17-19-01425).

1. J.Q. Qi, H.W. Wang, C.M. Zou, W.Q. Wei, Z.J. Wei, Temperature dependence of fracture behavior of in situ synthesized TiC/Ti-alloy matrix composite, *Mater. Sci. Eng. A*, 2011, vol. 528, nos. 25–26, pp. 7669–7673.
2. G. Rasool, S. Mridha, M.M. Stack, Mapping wear mechanisms of TiC/Ti composite coatings, *Wear*, 2015, vol. 328, pp. 498–508.
3. S.C. Tjong, Z.Y. Ma, Microstructural and mechanical characteristics of in situ metal matrix composites, *Mater. Sci. Eng.: R*, 2010, vol. 29, nos. 3–4, pp. 49–113.
4. J. Zhang, W. Ke, W. Ji, Z. Fan, W. Wang, Z. Fu, Microstructure and properties of in situ titanium boride (TiB)/titanium (Ti) composites, *Mater. Sci. Eng. A*, 2000, vol. 648, pp. 158–163.
5. H. Attar, L. Löber, A. Funk, M. Calin, L.C. Zhang, K.G. Prashanth, J. Eckert, Mechanical behavior of porous commercially pure Ti and Ti–TiB composite materials manufactured by selective laser melting, *Mater. Sci. Eng. A*, 2015, vol. 625, pp. 350–356.
6. S.S. Sahay, K.S. Ravichandran, R. Atri, B. Chen, J. Rubin, Evolution of microstructure and phases in in situ processed Ti–TiB composites containing high volume fractions of TiB whiskers, *J. Mater. Res.*, 1999, vol. 14, no. 11, pp. 4214–4223.
7. F. Ma, T. Wang, P. Liu, W. Li, X. Liu, X. Chen, W. Lu, Mechanical properties and strengthening effects of in situ (TiB+ TiC)/Ti-1100 composite at elevated temperatures, *Mater. Sci. Eng. A*, 2016, vol. 654, pp. 352–358.
8. S. Li, K. Kondoh, H. Imai, B. Chen, L. Jia, J. Umeda, Y. Fu, Strengthening behavior of in situ-synthesized (TiC–TiB)/Ti composites by powder metallurgy and hot extrusion, *Mater. Design*, 2016, vol. 95, pp. 127–132.
9. V. Imayev, R. Gaisin, E. Gaisina, R. Imayev, H.J. Fecht, F. Pyczak, Effect of hot forging on microstructure and tensile properties of Ti–TiB based composites produced by casting, *Mater. Sci. Eng. A*, 2014, vol. 609, pp. 34–41.
10. V.M. Imayev, R.A. Gaisin, R.M. Imayev, Effect of boron additions and processing on microstructure and mechanical properties of a titanium alloy Ti–6.5 Al–3.3 Mo–0.3 Si, *Mater. Sci. Eng. A*, 2015, vol. 641, pp. 71–83.
11. M. Krinitcyn, G. Pribytkov, V. Korzhova, I. Firsina, Structure and properties of composite coatings prepared by electron beam melting with “titanium carbide–titanium binder”, *Surf. Coat. Technol.*, 2019, vol. 358, pp. 706–714.

## 2D DISCRETE MODEL OF THE MULTICOMPONENT SHS PROCESS

**V. G. Prokof'ev<sup>a,b</sup>**<sup>a</sup>Tomsk State University, Tomsk, 634050 Russia<sup>b</sup>Tomsk Scientific Centre, Tomsk, 634021 Russia

e-mail: pvg@ftf.tsu.ru

DOI: 10.24411/9999-0014A-2019-10134

Theoretical study on formation of the macrostructure of products in the wave of heterogeneous combustion of gas-free systems is an important part of the targeted combustion synthesis of materials. Combustion synthesis of inorganic materials or SHS includes heterogeneous exothermic reactions. However, most theoretical concepts of high-temperature synthesis are based on homogeneous approximation.

In [1], an analytical review of modern heterogeneous models of combustion of SHS systems was reported. The authors compare the simulation results with known experimental data. A two-dimensional model of the combustion of a heterogeneous "fuel-inert component" system, represented as a set of square cells of the same size with a uniform and stochastic distribution of fuel in cells, was proposed in [2]. The reaction rate was described by a step function of temperature. The thermophysical properties of all cells were considered to be constant. The heat transfer between the cells was determined according to Newton's law, which implied the presence of an air gap at the cell boundaries. The model of the stochastic spatial structure was developed in [3], where the concentration and thermal limits of the propagation of the combustion wave were investigated. The significant role of fluctuations in the spatial distribution of reagents was revealed for the limit of propagation of the combustion wave, and the behavior of the system under critical conditions was explained based on the percolation theory. The effect of cell-particle sizes on the transition of combustion from the quasi-homogeneous to heterogeneous relay mode was considered for the "fuel-inert component" system in [4]. The microstructure of products was experimentally studied during the transition from the stationary (quasi-homogeneous) to scintillation (relay) combustion mode with an increase in the particle size of the Ni–Al mixture [5].

In multicomponent SHS systems, several thermally-coupled highly and slightly exothermic reactions that differ in both kinetics and thermal effects can occur simultaneously. A.G. Merzhanov proposed to call the first type reactions the donor, and the second one the acceptor. This method of forming a mixture of reactive components in the form of a layered composition in order to synthesize material using a slightly exothermic or endothermic mixture is called a "chemical oven".

In the paper, a two-dimensional discrete model of combustion of a multicomponent gas-free mixture consisting of two types of reaction cells, donor (DC) and acceptor (AC), such as Ni + Al and Ti + Al is proposed and numerically investigated. Granular mixtures, particles of one reagent coated with a layer of another one, can be analogous to cells. The ratio of DC and AC volumes was constant and assumed to be 1:1 in all calculations, which was related to the chosen spatial distribution of cells in the model. All cells have a square shape and one size, determining the heterogeneous system scale that is one of the main parameters of the problem. The adjacent boundary conditions of heat transfer are set at the boundaries between the cells. The rate of exothermic reaction is determined by the Arrhenius temperature dependence. Both regular system elements with a uniform distribution of cells and irregular ones with a random distribution of system elements are considered (Fig. 1).

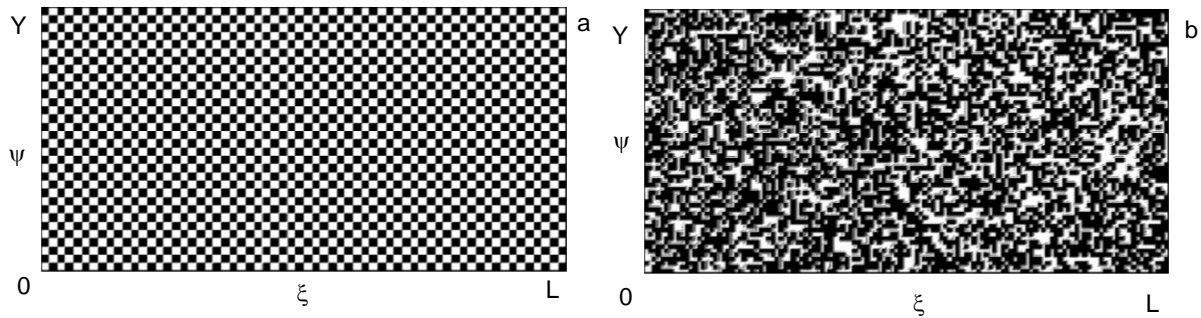


Fig. 1 Scheme of the sample with (a) regular and (b) irregular volume generating the cells.

The mathematical model of the combustion of a multicomponent gas-free mixture includes the dimensionless heat conduction equation and the equation of chemical kinetics:

$$\frac{\partial \theta}{\partial \tau} = S_{i,j} \frac{\partial}{\partial \xi} \left( \Lambda_{i,j} \frac{\partial \theta}{\partial \xi} \right) + S_{i,j} \frac{\partial}{\partial \psi} \left( \Lambda_{i,j} \frac{\partial \theta}{\partial \psi} \right) + \Omega_{i,j} W_{i,j}(\theta, \eta) \quad (1)$$

$$\frac{\partial \eta}{\partial \tau} = \Gamma_{i,j} W_{i,j}(\theta, \eta) \quad (2)$$

$$W_{i,j}(\theta, \eta) = \exp \left( \frac{\sigma_{i,j} \theta}{1 + \text{Ar} \theta} \right) \quad (3)$$

All cells have a square shape with a side  $d = \xi_i - \xi_{i-1}$  or  $d = \psi_j - \psi_{j-1}$ , where  $d$  is the characteristic cell size which determines the heterogeneous scale of the system. Scale variables are determined by the composition of the DC donor cell. The known stoichiometric Ni–Al SHS mixture was chosen as the donor mixture. Parameters with subscripts ( $i, j$ ) are determined according to the type of the cell as follows:  $S_{i,j} = 1$ ,  $\Lambda_{i,j} = 1$ ,  $\Omega_{i,j} = 1$ ,  $\Gamma_{i,j} = 1$ , and  $\sigma_{i,j} = 1$  for DC cells and  $S_{i,j} = S_A$ ,  $\Lambda_{i,j} = \Lambda_A$ ,  $\Omega_{i,j} = \Omega_A$ ,  $\Gamma_{i,j} = \gamma_A$ , and  $\sigma_{i,j} = \sigma_A$  for AC cells. The parameters of the composition of acceptor cells were varied. The above-mentioned system is complemented by boundary conditions at the outer edges of the rectangular sample and by initial conditions.

$$\tau \leq \tau_{\text{ign}} : \theta(0, \psi, \tau) = 0, \tau > \tau_{\text{ign}} : \frac{\partial \theta(0, \psi, \tau)}{\partial \xi} = 0; \frac{\partial \theta(L, \psi, \tau)}{\partial \xi} = 0; \quad (4)$$

$$\frac{\partial \theta(\xi, 0, \tau)}{\partial \psi} - \text{Bi}[\theta(\xi, 0, \tau) - \theta_0] = 0; \quad (5)$$

$$\frac{\partial \theta(\xi, Y, \tau)}{\partial \psi} + \text{Bi}[\theta(\xi, Y, \tau) - \theta_0] = 0; \quad (6)$$

$$\theta(\xi, \psi, 0) = \theta_0; \eta(\xi, \psi, 0) = 0. \quad (7)$$

where  $i$  and  $j$  are the cell numbers along the axes  $\xi$  and  $\psi$ , respectively.

The mathematical formulation of the problem (1)–(7) uses dimensionless variables and parameters as follows:  $\gamma_D = \frac{c_D R T_*^2}{Q_D E_D}$ ,  $\gamma_A = \frac{K_A(T_*)}{K_D(T_*)} \gamma_D$ ,  $\text{Ar} = \frac{R T_*}{E_D}$ ,  $\theta = \frac{(T - T_*) E_D}{R T_*^2}$ ,  $\theta_0 = -\frac{1}{\gamma_D}$ ,

$$\Lambda_A = \frac{\lambda_A}{\lambda_D}, \quad S_A = \frac{c_D \rho_D}{c_A \rho_A}, \quad \xi = \frac{x}{x_*}, \quad \psi = \frac{y}{y_*}, \quad t_* = \frac{c_D R T_*^2}{Q_D E_D K_D(T_*)}, \quad x_* = \sqrt{\frac{\lambda_D t_*}{c_D \rho_D}}, \quad \sigma_A = \frac{E_A}{E_D},$$

$$\text{Bi} = \frac{\alpha x_*}{\lambda_D}, \quad \tau = \frac{t}{t_*}, \quad \tau_{\text{ign}} = \frac{t_{\text{ign}}}{t_*}, \quad L = \frac{L_0}{x_*}, \quad Y = \frac{Y_0}{y_*}, \quad d = \frac{d_0}{x_*}, \quad \Omega_A = \frac{Q_A K_A(T_*) c_D}{Q_D K_D(T_*) c_A}.$$

One of the goals of the numerical solution of equations (1)–(7) was to determine the average combustion rate of the system under adiabatic conditions at  $Bi = 0$ , depending on the scale of heterogeneity  $d$  (Fig. 2). The combustion rate was determined as the ratio between the linear dimension of the system  $L$  and the time of complete combustion of all cells in the volume. The scale of heterogeneity  $d$  can significantly affect the combustion rate of the system (Fig. 2, curve 2). For this curve, the relative parameters of the acceptor mixture were chosen close to the Co + Ti system that was the main composition of the acceptor mixture. With a small cell size  $d = 4$ , the combustion front is uniform and the temperature pulsations are insignificant. Combustion of systems with large cells is accompanied by high temperature pulsations along the front line, which leads to a decrease in the propagation velocity of the combustion wave with an increase in the scale of heterogeneity by 30%. With the increase in the scale of heterogeneity, the maximum combustion temperature of a DC cell increases from  $\theta_{\max} = 0.15$  at  $d = 4$  to  $\theta_{\max} = 1.28$  at  $d = 32$ . This effect is explained by a significant difference in the heat-conducting properties of AC and DC. In the classical theory of gas-free combustion of homogeneous systems, the stationary combustion rate, as a rule, is higher than the average non-stationary combustion rate. A possible (hypothetical) change in the properties of acceptor AC cells with respect to the basic composition of DC changes the dependence  $U(d)$  (Fig. 2, curve 1). A decrease in the activation energy ( $\sigma_A = 0.5$ ) and an increase in the thermal conductivity coefficient ( $\Lambda_A = 0.46$ ) result in equalizing the combustion rates of AC and DC and leveling the effect of the cell size on the combustion rate of the heterogeneous system.

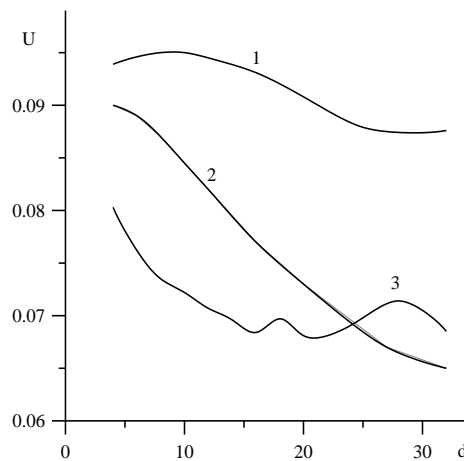


Fig. 2. Combustion rate as a function of the scale of heterogeneity for the regular (1, 2) and irregular (3) systems: 1  $\sigma_A = 0.5$ ,  $\Lambda_A = 0.8$ ,  $S_A = 0.5$ ,  $\Omega_A = 0.68$ ,  $\theta_0 = -6$ ,  $Ar = 0.1$ ,  $L = 512$ ,  $Y = 128$ ; 2, 3  $\sigma_A = 0.92$ ,  $\Lambda_A = 0.46$ ,  $S_A = 0.6$ ,  $\Omega_A = 0.68$ ,  $\theta_0 = -6$ ,  $Ar = 0.1$ ,  $L = 512$ ,  $Y = 128$ .

To set the random volume distribution of particles, the Random procedure in the Delphi7 compiler was used. For each set of parameters, 20 packings with a random volume distribution of initial composition AC and DC particles were generated and the average combustion rate was calculated with respect to the number of generations (Fig. 2, curve 3). In the case of a random distribution of cells, clusters can be formed from weakly reacting acceptor AC cells which overlap the sample across its entire width  $Y$  for sufficiently large cells. With such generating the cells, the combustion rate drops sharply when the combustion wave passes through the cluster.

The combustion rate of an ordered system is higher than that of a system with a random arrangement of elements in the region with a small heterogeneity scale  $d \leq 20$  (Fig. 2). During the combustion of a system with large cells  $d > 20$ , the effect of fluctuations in the spatial distribution of the parameters of the donor and acceptor mixtures increases, which leads to the occurrence of maxima and minima on the  $U(d)$  curve. However, the size of the cell becomes

comparable to the width of the sample, and the calculated combustion rates of the regular and irregular systems are close. It is worth noting that in [2] the average combustion rate of a regular system with the presence of inert particles far from the concentration limit of combustion is 2 and more times higher than that of a disordered (random) system.

Numerical simulation of the gas-free combustion of SHS systems with a cellular structure has established the dependence of the average combustion rate on the size of a cell. The dependence is determined by the ratio of thermophysical and formal kinetic characteristics of donor and acceptor mixtures. The combustion rate of a system with a random distribution of cells is lower than that of a structurally-ordered system with the same ratio of system components. The thermal limit of propagation of a combustion wave weakly depends on the size of cells: the region of stable combustion under conditions of an external heat sink expands with increasing the size of cells.

The research was supported by the Russian Foundation for Basic Research, (project no. 19-03-00081).

1. A.S. Rogachev, A.S. Mukasyan, Experimental verification of discrete models of combustion of microheterogeneous compositions which form condensed combustion products (review), *Combust. Explos. Shock Waves*, 2015, vol. 51, no. 1, pp. 66–76.
2. P.S. Grinchuk, O.S. Rabinovich, Percolating phase transition during the combustion of heterogeneous mixtures, *Combust. Explos. Shock Waves*, 2004, vol. 40, no. 4, pp. 41–53.
3. P.S. Grinchuk, Combustion of heterogeneous systems with a stochastic spatial structure near the limits of propagation, *J. Eng. Phys. Thermophys.*, 2013, vol. 86, no. 4, pp. 819–831.
4. P.M. Krishenik, S.A. Rogachev, K.G. Shkadinsky, Unsteady transformations in thin two-component films: a model taking into account random particle size distribution, *Int. J. Self-Propag. High-Temp. Synth.*, 2012, vol. 21, no. 2, pp. 75–82.
5. J.M. Pauls, C.E. Shuck, A.S. Rogachev, A.S. Mykasyan, Micro-heterogeneous regimes for gasless combustion of composite materials, *Combust. Sci. Technol.*, 2010, vol. 182, no. 8, pp. 1009–1028.

## EFFECT OF THERMOCAPILLARY FLOW OF MELT ON COMBUSTION OF A BINARY GASLESS MIXTURE

V. G. Prokof'ev<sup>\*a,b</sup>, A. I. Kirdyashkin<sup>a</sup>, V. D. Kitler<sup>a</sup>, and O. V. Lapshin<sup>a</sup><sup>a</sup>Tomsk Scientific Centre, Tomsk, 634021 Russia<sup>b</sup>Tomsk State University, Tomsk, 634050 Russia

\*e-mail: pvg@ftf.tsu.ru

DOI: 10.24411/9999-0014A-2019-10135

The combustion of gasless powder mixtures is accompanied by the melting and convective flow of one or several components of a heterogeneous system in the matrix of refractory components and reaction products. The capillary flow of the melt is due to the action of surface tension forces in a porous medium. The first time, an experimental study of the capillary flow of a liquid metal and its effect on the combustion of gas-free systems was considered in [1] using the example of a powder mixture of titanium with carbon. In [2], approximate analytical estimates were obtained of the effect of capillary spreading on the propagation of a combustion wave in gas-free systems within the framework of the model of reactionary cells. The effect of the dispersion of reagents on the transition of the combustion regime from diffusion to capillary was considered in [3, 4]. In [5], the "anomalous" dependences of the burning rate on the size of titanium particles were obtained for powder systems Ti + Si and Ti + Fe, indicating that along with diffusion and capillary mass exchange, there is a convective mixing mechanism of the system components. An experimental study of powder mixtures by methods of high-speed video and dynamic pyrometry in [6] showed an "anomalous" increase in the burning rate with increasing size of aluminum particles. The authors explained this effect by the transition from the diffusion to hydrodynamic combustion regime with the development of convective aluminum melt flows. The effect of Marangoni capillary convection on the combustion of oxide systems and the separation of the metal and oxide phases was considered in [7]. An analytical and numerical study of the effect of thermocapillary convection on heat transfer in a gasless combustion wave with a meltable reagent for the inertialess flow of the liquid phase is considered in [8].

In this paper, we consider a model of combustion of a binary mixture, one of the components which is a low-melting metal. The synthesis reaction scheme can be represented as  $(1 - \nu)A(\text{solid}) + \nu B(\text{solid, liquid}) = P(\text{solid})$ , where  $\nu$  is the mass (stoichiometric) concentration B in the reaction product P.

The main goal of solving the problem was to calculate the burning rate of the A + B binary mixture (Fig. 1), as the main integral characteristic of high-temperature synthesis. Plots of  $U(\alpha)$  are non-monotonic. The maximum burning rate shifts towards mixtures with excess B as a result of the influence of thermocapillary convection. The burning rate of the stoichiometric mixture ( $\alpha = 1$ ) is lower than for a non-stoichiometric mixture with an excess melting component  $\alpha = 1.1$  (Fig. 1, curves 2, 3). The effect appears at a relatively high rate of thermocapillary melt flow  $\omega$ . However, the calculated burning temperature of the stoichiometric mixture was always higher than the burning temperature of the mixture of non-stoichiometric composition and practically did not depend on the rate of convective flow. Similar "anomalous" dependences of the burning rate on the size of aluminum and titanium particles were obtained experimentally for Ni + 31.5% Al and (FeO + 20% Al) +  $m\text{Al}_2\text{O}_3$  systems in [6] and the Ti + 37% Si mixture in [5]. The maximum value of concentration B in the heating zone was about 70% higher than the initial concentration of this component. Then component B is consumed in a chemical reaction and its concentration drops.

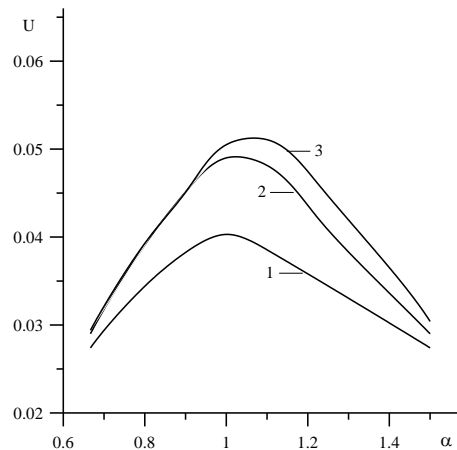


Fig. 1. The dependence of the burning rate on the coefficient of excess  $\alpha$  of component B and on the scale of the flow velocity  $\omega$ : 1  $\omega = 0$ , 2  $\omega = 0.6$ , 3  $\omega = 0.8$ .

Thus, it is shown that it is possible in principle to burn mixtures with an excess of the low-melting component at a higher rate than when burning a mixture of stoichiometric composition.

The research was supported by the Russian Foundation for Basic Research, (project no. 19-03-00081).

1. V.M. Shkiro, I.P. Borovinskaya, Capillary flow of liquid metal during combustion of titanium mixtures with carbon, *Combust. Expl. Shock Waves*, 1976, vol. 12, no. 6, pp. 828–831.
2. E.A. Nekrasov, Yu.M. Maksimov, M.Kh. Ziatdinov, A.S. Shteinberg, Effect of capillary spreading on combustion-wave propagation in gas-free system, *Combust. Expl. Shock Waves*, 1978, vol. 14, no. 5, pp. 575–581.
3. A.I. Kyrdyashkin, Yu.M. Maksimov, A.G. Merzhanov, Effects of capillary flow on combustion in a gas-free system, *Combust. Expl. Shock Waves*, 1981, vol. 17, no. 6, pp. 591–595.
4. A.I. Kyrdyashkin, O.K. Lepakova, Yu.M. Maksimov, A.T. Pak, Structural transformations of powder mixture components in a gasless combustion wave, *Combust. Expl. Shock Waves*, 1989, vol. 25, no. 6, pp. 718–723.
5. Yu.M. Maksimov, A.I. Kyrdyashkin, M.Kh. Ziatdinov, V.D. Kitler, Interphase convection in the contact interaction of metals under nonisothermal conditions, *Combust. Expl. Shock Waves*, 2000, vol. 36, no. 4, pp. 462–469.
6. A.I. Kyrdyashkin, V.D. Kitler, V.G. Salamatov, R.A. Yusupov, Yu.M. Maksimov, Capillary hydrodynamic phenomena in gas-free combustion, *Combust. Expl. Shock Waves*, 2007, vol. 43, no. 6, pp. 645–653.
7. A.I. Kyrdyashkin, V.D. Kitler, V.G. Salamatov, R.A. Yusupov, Specific features of structural dynamics of high-temperature metallothermic processes with the FeO–Al–Al<sub>2</sub>O<sub>3</sub> system as an example, *Combust. Expl. Shock Waves*, 2008, vol. 44, no. 1, pp. 71–75.
8. V.G. Prokof'ev, V.K. Smolyakov, Thermocapillary convection in gasless combustion wave, *Combust. Expl. Shock Wave*, 2019, vol. 55, no. 1.

## SELF-SUSTAINING REACTIONS AT NANOSCALE

**J. A. Puszynski**

South Dakota School of Mines and Technology,  
501 E Saint Joseph St., Rapid City, SD 57701, USA

DOI: 10.24411/9999-0014A-2019-10136

During the past two decades, a significant effort has been on investigation of reaction front propagation and the rate of energy release in heterogeneous systems consisting of fuel and oxidizer reactants having significantly shorter diffusion distances needed to complete the reaction. Substantial size reduction of each reactant powder (e.g. from micro- to nano-size), formation of composite structures by mechanical milling or mixing oxidizer and fuel in a solution leads to significant increases of the reaction front propagation. For example, the scaling-down the sizes of reactants to the nano-scale has allowed for several capabilities and applications that were not previously possible with conventional micro-sized thermite mixtures. A significant size reduction of reactant powders increases number of contact points between fuel and oxidizer particles. As a consequence of this significant reduction of size, new issues such as dispersion and mixing of reactants, safety, and surface functionalization of fuel particles in order to minimize potential undesired reactions with oxygen and water vapor must be addressed.

A main focus of this presentation will be on the review of the current state-of-the-art in the area of self-sustaining reactions at nanoscale, including reactions between nano-sized powders, mechano-activated composite structures, and solution combustion of novel nanopowders. In addition, some challenges associated with processing and safety of self-sustaining reaction at nanoscale will be addressed as well.



## HIGH ENERGY BALL MILLING OF SHS MIXTURES: MECHANISMS AND OPPORTUNITIES

A. S. Rogachev<sup>\*a</sup>, S. G. Vadchenko<sup>a</sup>, N. A. Nepapushev<sup>b</sup>, and D. O. Moskovskikh<sup>b</sup>

<sup>a</sup>Merzhanov Institute of Structural Macrokinetics and Materials Science, Russian Academy of Sciences, Chernogolovka, Moscow, 142432 Russia

<sup>b</sup>National University of Science and Technology MISiS, Moscow, 119049 Russia

\*e-mail: rogachev@ism.ac.ru

DOI: 10.24411/9999-0014A-2019-10137

Experimental, theoretical, and applied results in the field of mechanical activation of reactive powder mixtures by means of arrested high-energy ball milling (HEBM) and materials synthesis using activated mixtures are considered in the overview. Influence of regimes of activation on combustion temperature and velocity, self-ignition temperature, reaction energy of activation, as well as microstructure and atomic structure of the reactive compositions are discussed. Special attention is paid to revealing structural transformations that result in increasing chemical activity of the powder mixtures. Some examples of practical application of the reviewed processes are presented.

It is known that HEBM allows expanding limits of combustion synthesis in low-exothermal systems, e.g., Si–C, B–C, etc. The HEBM process can be used also for mechanical alloying of high entropy alloys (HEA), such as CoCrFeNiMn, AlCoCrFeNi, etc., and ceramic-metal composites [1]. However, processes inside the milling vials and structural transformations that result in increasing chemical activity of the powder mixtures and alloying of multicomponent materials, have not been adequately studied up to now. Thus, three general aspects of the problem should be outlined: (i) kinematics and dynamics of milling bodies inside the mill jar; (ii) structural transformations in reactive mixtures caused by HEBM and resulting to increase reactivity, and (iii) application of HEBM for materials synthesis.

Using specially designed technique of high-speed video recording and images treatment, we studied in-situ dynamics of the balls motion during high energy ball milling, including balls trajectories and velocities (Fig. 1).

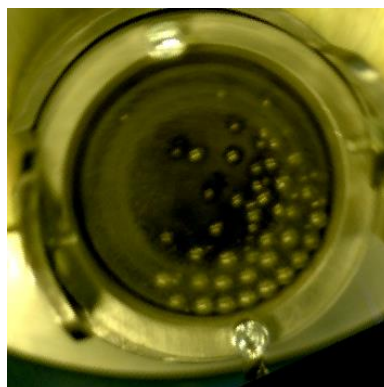


Fig. 1. High-speed video frame of the movement of balls during HEBM.

The results proved that multiple shear deformations due to friction play a major role in the mechanical activation, as compared to impacts of the balls.

Another important aspect concerns the transformations induced by HEBM in reactive powder mixtures to produce new phase (i.e. mechanical alloying) or to enhance their reactivity.

SEM and TEM study of micro- and nano-structural transformations proved leading role of shear deformations and sliding friction in the activation effect (Fig. 2). Influence of regimes of activation on combustion temperature and velocity, self-ignition temperature, reaction energy of activation, as well as microstructure and atomic structure of the reactive compositions are discussed (Fig. 3).

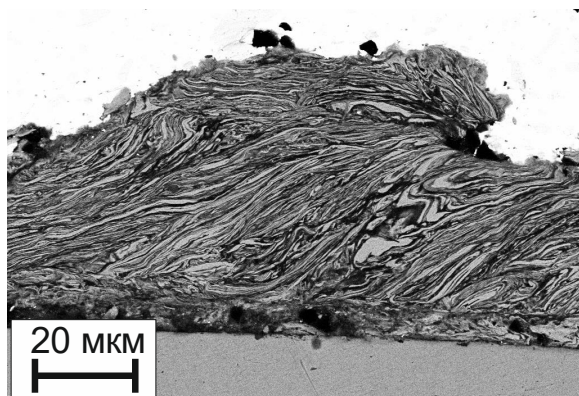


Fig. 2. Microstructure of the Ni + Al reactive mixture after 5 min of HEBM: the layer stuck on the surface of milling ball [2].

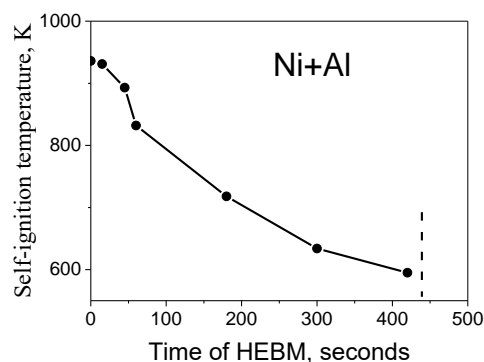


Fig. 3. Dependence of self-ignition temperature on duration of HEBM [3].

Finally, examples of application of HEBM conjugated with SHS, hot pressing and spark plasma sintering for obtaining consolidated ceramics, ceramic-metal composites and multicomponent alloys are presented. It is shown that HEBM + SHS + SPS technique provides exciting opportunities for production of advanced materials.

This work is supported by Ministry of Science and Higher Education of the Russian Federation in the framework of the Federal Target Program “Research and Development on Priority Directions of the Scientific and Production Complex of Russia for 2014–2020”, agreement no. 14.587.21.0051, project RFMEFI58718X0051, in the frames of International Russian-French PHC Kolmogorov "RECIPES" (no. 41144SG).

1. I.P. Borovinskaya, A.A. Gromov, E.A. Levachov, Y.M. Maksimov, A.S. Mukasyan, A.S. Rogachev, Concise Encyclopedia of Self-Propagating High-Temperature Synthesis: History, Theory, Technology, and Products, Elsevier Pbl., 2011.
2. A.S. Rogachev, N.F. Shkodich, S.G. Vadchenko, F. Baras, R. Chassagnon, N.V. Sachkova, O.D. Boyarchenko, Reactivity of mechanically activated powder blends: Role of micro and nano structures, *Int. J. Self-Propag. High-Temp. Synth.*, 2013, vol. 22, pp. 210–216.
3. A.S. Rogachev, N.F. Shkodich, S.G. Vadchenko, F. Baras, D.Yu. Kovalev, S. Rouvimov, A.A. Nepapushev, A.S. Mukasyan, Influence of the high energy ball milling on structure and reactivity of the Ni + Al powder mixture, *J. Alloys Compd.*, 2013, vol. 577, pp. 600–605.

## MOLECULAR DYNAMICS SIMULATION OF REFRACTORY COMPOUNDS AND METHODS OF THEIR SYNTHESIS

**S. A. Rogachev**

Merzhanov Institute of Structural Macrokinetics and Materials Science, Russian Academy of Sciences, Chernogolovka, Moscow, 142432 Russia  
e-mail: RogachevSA@gmail.com

DOI: 10.24411/9999-0014A-2019-10138

With increasing computing power, the use of molecular dynamics methods to predict the properties of materials is becoming more common. This approach is also applicable to the investigation of the properties of refractory materials. For the analysis of the properties of any materials, the first-principle (ab-initio) modeling method is the most applicable. However, this method has a big weakness, which is a high computational complexity (systems containing more than a thousand atoms are difficult to calculate). Classical molecular dynamics simulation to determine the melting point uses a large number of atoms, therefore, for an ab-initio modeling, it is necessary to develop a new approach. The developed method is a modification of the two-phase method. The idea of a two-phase method consists in the equilibrium coexistence of a solid and a liquid phase of a substance. To do this, we create a sample consisting of half of the melt, and half of the crystal structure. Then we set a certain initial temperature and observe the evolution of the system under isoenthalpic ensemble. Depending on what the initial temperature was chosen, the system can go either to a completely liquid state, or to a completely crystalline state, or reach the phase equilibrium of the liquid and the crystal structure. In this process, the temperature will vary from the initial to some certain value. This certain value will be the melting point. The number of atoms, available in ab-initio modeling, is a small statistical selection, but its increase will lead to computational difficulties. Therefore, it was proposed to increase not the number of atoms in the system, but the number of model experiments with slightly different initial temperatures. In this case, since the system is extremely small, the result of evolution in a two-phase system is either a completely liquid phase or a completely solid phase. In this case, the initial temperature is taken as the melting point, at which out of 12 numerical experiments, 6 ends in the solid phase, and 6 in the liquid phase. The approximate error in calculating the temperature in this way is about 50 K. By this method, using the VASP software package and using the PAW potentials, the melting points were calculated for pure metals such as Fe (1850 K), Pd (1850 K), Ti (1950 K), Pt (2050 K), Zr (2150 K), Mo (2900 K), Ta (3300 K), W (3700 K), and also for titanium and tantalum carbides. The results obtained are in good agreement with the experimental data. In the future we plan to apply this approach for a wide range of materials. Due to the smallness of the systems it is difficult to predict methods of synthesis, using the ab-initio simulation. Therefore, it is necessary to develop EAM and MEAM potentials for carrying out molecular-dynamic calculations in a large system. The MEAM interaction potential for the Ta-C system was developed. For interaction between atoms of the same type, MEAM potentials were taken from the literature. The main difficulty was the development of the interaction potential for atoms of different types. To do this, using the VASP software package, calculations such as the cohesive energy of tantalum carbide in a cubic face-centered lattice, the heat of formation, the equilibrium distance between atoms in the crystal lattice, and the elastic modulus were carried out from first principles. The tantalum carbide melting point calculated using this MEAM potential differs from the experimental value, but it makes it possible to investigate various methods of synthesis. In the future we plan to develop MEAM potentials for Hf, Ta, C, N systems.

This work was supported by the Russian Foundation for Basic Research (no. 18-33-00641).

## THE ROLE OF MICROWAVES IN THE IGNITION OF LOW-EXOTHERMIC SYSTEMS: THE CASE OF Ni–Ti INTERMETALLICS

R. Rosa<sup>\*a</sup>, L. Trombi<sup>b</sup>, C. Milioli<sup>c</sup>, F. Cugini<sup>d</sup>, A. Casagrande<sup>e</sup>, C. Leonelli<sup>c</sup>, and P. Veronesi<sup>c</sup>

<sup>a</sup>Dipartimento di Scienze e Metodi dell'Ingegneria, Università degli Studi di Modena e Reggio Emilia, via Amendola 2, 42100 Reggio Emilia, Italy

<sup>b</sup>Zare, via IV novembre 37A, 42022, Boretto, Reggio Emilia, Italy

<sup>c</sup>Dipartimento di Ingegneria "Enzo Ferrari", Università degli Studi di Modena e Reggio Emilia, via Vivarelli 10, 41125 Modena, Italy

<sup>d</sup>Dipartimento di Scienze Matematiche, Fisiche e Informatiche, Università degli Studi di Parma, Parco Area delle Scienze 7/A, 43124 Parma, Italy

<sup>e</sup>Dipartimento di Ingegneria Industriale, Alma Mater Studiorum, Università di Bologna, viale Risorgimento 4, 40136 Bologna, Italy

\*e-mail: roberto.rosa@unimore.it

DOI: 10.24411/9999-0014A-2019-10139

NiTi-based intermetallics are widely used in many high technological fields such as aerospace, automotive and biomedical ones, mainly due to the following characteristics: superelasticity, shape memory, high recovery force, wear resistance, relatively low Young's modulus and high biocompatibility [1].

Combustion synthesis (CS) approach typically represents the most advantageous production technique for intermetallics-based materials, thanks to the low production time, energy saving, simplicity of the experimental apparatus and the possibility of precise porosity control. However, although production of Ni–Ti intermetallics has been investigated by CS experiments performed both under self-propagating high-temperature synthesis (SHS) regime of combustion and thermal explosion (TE) one, the low exothermic character of near equiatomic mixtures of Ni and Ti powders contributed to reduce CS technique advantages for this particular reactive system [2], due to the necessity of the starting mixture to be pre-heated. Particularly, in order to synthesize intermetallic NiTi with an effective SHS approach, the ignition must occur at a later stage and with a different energy source than the one used to preheat the entire sample homogeneously. On the contrary, when ignition is carried out in the same way as homogeneous preheating, combustion is carried out under TE regime.

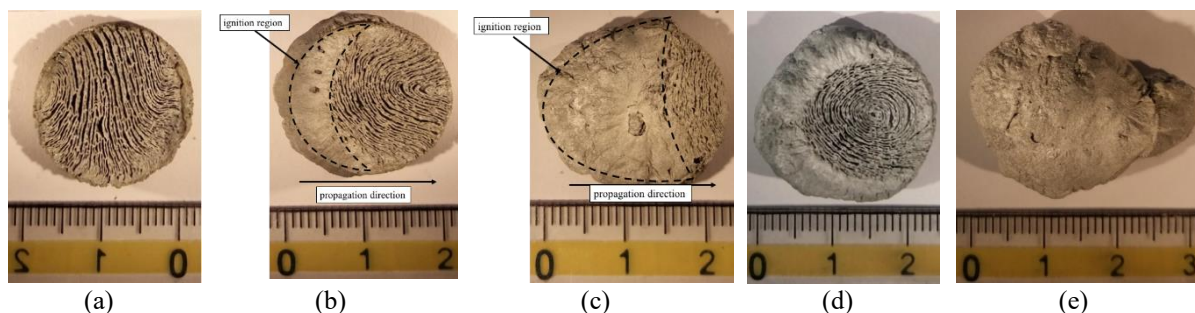


Fig. 1. Examples of NiTi-based intermetallic specimens synthesized by direct interaction of microwaves with the reactive Ni + Ti powders mixture. The combustion regime moved from a real SHS (a), through intermediate combustion ways (b–d) to a complete TE one (e).

The aim of this work is to demonstrate how the use of microwave (MW) energy as a source of ignition can overcome these latter limitations. Particularly, the use of scientific single mode applicators will demonstrate the high versatility offered by realizing direct interaction of the

electromagnetic field with the reactive specimen. The extension of the specimen volume which shows the ignition conditions can be modified by changing the impedance matching effectiveness, thus shifting the combustion synthesis mode from a pure SHS to a regime closer to a TE [3]. Moreover, the effect of positioning the sample into regions of predominant electric or magnetic field and the effect of the incident microwave frequency, on the realizable combustion regime will be presented and discussed. Some macrographs of the samples prepared by changing the electromagnetic field disposition inside the microwave cavity are reported in Fig. 1.

1. J.M. Jani, M. Leary, A. Subic, M.A. Gibson, A review of shape memory alloy research, applications and opportunities, *Mater. Design*, 2014, vol. 56, pp. 1078–1113.
2. C.L. Yeh, and W.Y. Sung, Synthesis of NiTi intermetallics by self-propagating combustion, *J. Alloys Compds.*, 2004, vol. 376, pp. 79–88.
3. R. Rosa, L. Trombi, A. Casagrande, F. Cugini, C. Leonelli, P. Veronesi, On the versatility and distinctiveness arising from the use of microwave energy for the ignition of low exothermic Ni–Ti intermetallics combustion synthesis, *Mater. Chem. Phys.*, 2019, submitted.

## SOLUTION COMBUSTION SYNTHESIS OF NANOSTRUCTURED METASTABLE NITRIDES AND INTERMETALLICS

**S. I. Roslyakov<sup>\*a</sup>, A. S. Mukasyan<sup>a,b</sup>, and Kh. V. Manukyan<sup>c</sup>**<sup>a</sup>National University of Science and Technology MISiS, Moscow, 119049 Russia<sup>b</sup>Department of Chemical and Biomolecular Engineering, University of Notre Dame, Notre Dame, IN 46556, USA<sup>c</sup>Nuclear Science Laboratory, Department of Physics, University of Notre Dame, Notre Dame, IN 46556, USA

\*e-mail: roslyakov.si@misis.ru

DOI: 10.24411/9999-0014A-2019-10140

Solution combustion synthesis (SCS) has attracted considerable attention of scientists from around the world for versatile synthesis of a variety of nanoscale materials [1–5]. SCS is based on generic idea of using exothermic self-sustained combustion reactions, which can be initiated in water solutions of oxidizer (typically metal nitrates) and organic fuel (glycine, urea, citric acid, etc.). One of the unique advantages of SCS is the ability to prepare high-quality multi-element compounds with complex crystal structures, such as garnets, perovskites, spinels, silicates, phosphates, and others [4, 6]. The mixing of reactants at the molecular level enables efficient doping of materials, even with a trace amount of elements. Proper selection of fuel and optimization of the process allow for avoidance of secondary calcination step and prepare materials in one technological stage. Finally, the process can be performed in continuous schemes providing high throughput synthesis of nanoscale materials [3]. A limitation of SCS is related to the relatively low level of control over the morphological uniformity of the fabricated materials. The rapid increase in temperature leads to spontaneous nucleation, growth, and agglomeration of the products' particles [1, 5]. The most critical role in determining the morphology of the final products is played by maximum temperature and gas release. Another limitation of synthesis related to chemical nature of the mixture is preparation of predominantly oxide materials. Indeed, it is well-known the high temperature decomposition of metal nitrates leads to the formation of corresponding metal oxides [7, 8].

Several works demonstrate utilization of sulfur-containing organic compounds to produce metals sulfides. Currently, the preparation nanoscale metals and alloys is one of the active direction of SCS research. It was found that under certain conditions (typically excess of fuel) the intermediate gaseous combustion products have a reduction (typically hydrogen-based) nature and thus allow reduction of metal oxides to form metals (Ni, Cu, Co, Pt etc.) or alloys (NiCu, NiCo etc.) during SCS. In our recent works we reported the use of time-resolved X-ray diffraction, high-speed infrared imaging, and thermal analysis with mass spectrometry to reveal the metal formation mechanism during the SCS [9]. Tailoring the synthesis conditions also permitted to achieve highly dispersed supported metallic catalysts with particle sizes below 5 nm [10].

These promising results suggest that by understanding the fundamentals of combustion in reactive solutions we will be able to synthesize other compounds including nitrides, intermetallics, carbides, and others, thus significantly widening the spectrum of SCS materials. For example, one can expect that rich amount of carbon and nitrogen in organic fuels could create favorable conditions for carbonization or nitridation of metals. However, attempts to produce carbides or nitrides were not successful yet. In the above context, it is difficult to overestimate the importance of the research targeting routes for spreading the application of SCS to produce wide variety of non-oxide-based compounds.

In this work, we apply thermal analysis, mass- and FTIR spectroscopy and rapid combustion diagnostic techniques to produce new non-oxide phases and establish the mechanism of the ceramic ( $\epsilon$ -Fe<sub>3</sub>N) and intermetallic (NiAl) formation during SCS. Here, we report for the first time one step solution combustion synthesis of the nitride and intermetallic by self-sustained reactions of gels containing metal nitrates (Fe(NO<sub>3</sub>)<sub>3</sub>, Al(NO<sub>3</sub>)<sub>3</sub>) and fuels (C<sub>6</sub>H<sub>12</sub>N<sub>4</sub>, C<sub>2</sub>H<sub>5</sub>NO<sub>2</sub>) in an inert atmosphere. It is also important that the short process durations (seconds), high-reaction temperatures ( $\sim$  900 K) and rapid cooling rates ( $\sim$  20 K/s) permit formation of metastable  $\epsilon$ -Fe<sub>3</sub>N phase. The obtained results indicate that the exothermic high-temperature decomposition of a coordinating compound formed due to the interaction between Fe(NO<sub>3</sub>)<sub>3</sub> and C<sub>6</sub>H<sub>12</sub>N<sub>4</sub> in the reaction front leads to the formation of nanoscale  $\epsilon$ -Fe<sub>3</sub>N particles with sizes of 5–15 nm. The SCS conditions permit well preservation of crystalline nanoparticles of metastable  $\epsilon$ -Fe<sub>3</sub>N phase, which possess a good magnetic behavior (Fig. 1).

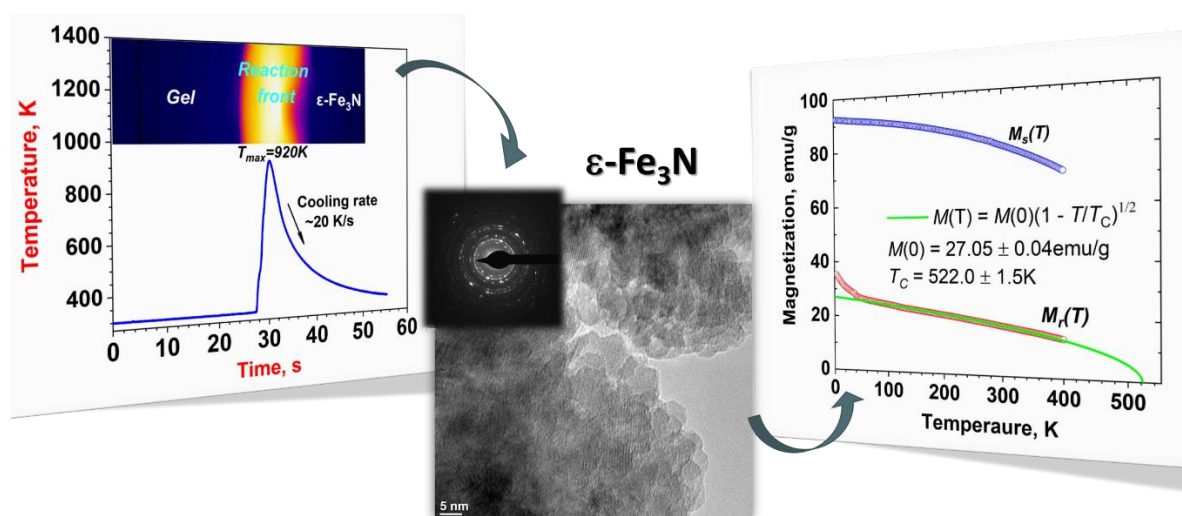


Fig. 1. A single step combustion method in iron nitrate (Fe(NO<sub>3</sub>)<sub>3</sub>) and hexamethylenetetramine (C<sub>6</sub>H<sub>12</sub>N<sub>4</sub>) gels.

The research was supported by the Russian Foundation for Basic Research (project no. 18-03-00306).

1. A. Varma, A.S. Mukasyan, A.S. Rogachev, K.V. Manukyan, Solution Combustion Synthesis of Nanoscale Materials, *Chem. Rev.*, 2016, vol. 116, pp. 14493–14586.
2. X. Yu, J. Smith, N. Zhou, L. Zeng, et al, Spray-combustion synthesis: Efficient solution route to high-performance oxide transistors, *Proc. Natl. Acad. Sci.*, 2015, vol. 112, pp. 3217– 3222.
3. K.C. Patil, S.T. Aruna, T. Mimani, Combustion Synthesis: An Update, *Curr. Opin. Solid State Mater. Sci.*, 2002, vol. 6, pp. 507–512.
4. W. Wen, J-C. Yao, C-C. Jiang, , J-M. Wu, Solution-combustion synthesis of nanomaterials for lithium storage, *Int. J. Self-Propag. High-Temp. Synth.*, 2017, vol. 26, pp. 187–198.
5. H.H. Nersisyan, J.H. Lee, J.R. Ding, K.S. Kim, K.V. Manukyan, A.S. Mukasyan, Combustion synthesis of zero-, one-, two- and three-dimensional nanostructures: Current trends and future perspectives, *Prog. Energy Combust. Sci.*, 2017, vol. 63, pp. 79–118.
6. A. Pendashteh, M.S. Rahmanifar, et al, Facile synthesis of nanostructured CuCO<sub>2</sub>O<sub>4</sub> as a novel electrode material for high-rate supercapacitors, *Chem. Commun.* 2014, vol. 50, pp. 1972–1975.
7. A.S. Mukasyan, P. Epstein, P. Dinka, Solution combustion synthesis of nanomaterials, *Proc. Combust. Inst.*, 2007, vol. 31, pp. 1789–1795.
8. K. Deshpande, A. Mukasyan, A. Varma, Direct synthesis of iron oxide nanopowders by the

- combustion approach: reaction mechanism and properties, *Chem. Mater.*, 2004, vol. 16, pp. 4896–4904.
9. K.V. Manukyan, A. Cross, S. Roslyakov, et al, Solution combustion synthesis of nanocrystalline metallic materials: mechanistic studies, *J. Phys. Chem. C*, 2013, vol. 117, pp. 24417–24427.
  10. A. Cross, S. Roslyakov, K.V. Manukyan, et al, In situ preparation of highly stable Ni-based supported catalysts by solution combustion synthesis, *J. Phys. Chem. C*, 2014, vol. 118, pp. 26191–26198.



## ENERGY INTENSITY OF SOLID FUEL SYSTEMS WITH MECHANICALLY ACTIVATED ALUMINUM

**B. S. Sadykov<sup>\*a</sup>, A. Ye. Bakkara<sup>a</sup>, L. Galfetti<sup>a</sup>, K. S. Zhamanbalinova<sup>a</sup>, N. Meirbekov<sup>a</sup>,  
and N. N. Mofa<sup>a</sup>**

<sup>a</sup>Al-Farabi Kazakh National University, The Institute of Combustion Problems,  
Almaty, Kazakhstan

\*e-mail: sadykoff\_baha@mail.ru

DOI: 10.24411/9999-0014A-2019-10141

Aluminum is widely used in energy-intensive systems for various purposes, both in hydrogen energy and in technological combustion processes in the synthesis of various composite materials [1]. In the rocket-engine area, aluminum is used mainly to improve the gravimetric and volumetric specific impulse of solid-fuel rocket motors or to increase the regression rate of hybrid fuels [2]. In both cases, the reactivity of the aluminum powder plays a key role, which is related with the processes occurring in the combustion chamber. Micrometric aluminum is the most commonly used in space power plants with a high metal content (for example, 97.7% by weight of aluminum of grade PA4, dispersion of 50  $\mu\text{m}$ ) and low toxicity. However, its low reactivity is due to the presence of an oxide film on the surface of the particles, which reduces the specific impulse and burning rate in solid-fuel motors [3]. To increase the activity, different methods are used: chemical activation, mechanical and mechanochemical treatment (MCT) [4]. It is known that addition of metal powders to solid rocket fuel leads to an increase in system performance due to high energy per unit mass.

Studies on the MCT of aluminum were carried out on the powder grade PA4. Figure 1 presents the electron microscopic image, the energy dispersion spectrum, and the mass fraction of the elements of the original aluminum powder. From the presented picture it follows that the particles of Al have a spherical shape. According to the particle size analysis, the average particle size is about 50  $\mu\text{m}$ .

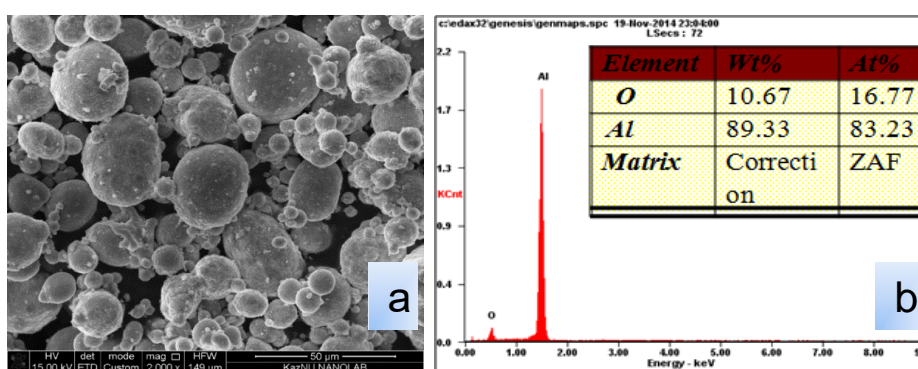


Fig. 1. Characteristics of the original aluminum powder of grade PA4: (a) electron microscopic image; (b) energy dispersive spectrum and mass fraction of elements.

From the results of energy dispersive analysis of the initial powder, it follows that the amount of aluminum metal is 89.33 wt %, and that of oxygen is 10.67 wt %. The presence of oxygen atoms indicates the presence of a sufficiently dense layer of oxide film on the surface of particles. Powder particles are gray in color with metallic luster and do not contain foreign inclusions.

Mechanochemical treatment of aluminum was carried out with graphite (C), stearic acid ( $C_{17}H_{35}COOH$ ), and polyvinyl alcohol ( $(C_2H_3OH)_n$ ) with different amounts of the modifying additive (from 3 to 20%). The processing time was 20 minutes. The choice of the optimal time of MCT was determined by the results of previous studies [5]. In order to prevent aluminum particles from oxidizing with oxygen of the air after MCT and to estimate the changes actually associated with the mechanical action, the samples of the dispersed mixture were passivated with hexane ( $C_6H_{14}$ ).

Studies have been conducted on the effect of mechanochemical treatment (MCT) of aluminum powder on the mechanism of combustion of solid fuels and the structure of combustion. Measurements were made of the burning rate and the visualization of the burning process using a high-speed video camera. To study the effect of MCT on the ballistic properties, we used the standard formulation: AP/Al/HTPB: 68%/18%/14%. The fuels were distinguished by organic additives during the mechanochemical synthesis of aluminum powders. The MCT of metal aluminum was carried out for 20 min with the ratio of powder to grinding balls 1/4 Mp/Mb. Graphite, stearic acid and polyvinyl alcohol were used as modifiers. During processing, the amount of modifying additives varied from 3 to 20%, as well as the presence of silicon oxide ( $SiO_2$ ) in an amount of from 5 to 20%.

The measurement of the steady-state burning rate was performed using samples of  $4 \times 4 \times 30$  mm. They were burned in a nitrogen atmosphere in a bomb with windows. As can be seen from in Fig. 2, the base fuel containing aluminum in the initial state with a particle size of  $50 \mu m$  has a low burning rate and a high pressure exponent ( $n = 0.5572$ ). When replaced with aluminum treated with 3% graphite, an increase in the burning rate by 22% and a decrease in the pressure exponent ( $n = 0.456$ ) are observed. The obtained data indicate the fact of the combustion process stabilization.

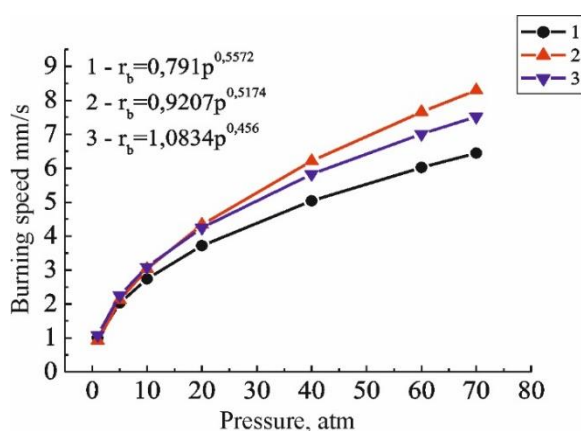


Fig. 2. Change of the burning rate of AP/HTPB/ $Al_x$  fuels with non-activated aluminum and after MCT of composites: 1 Al initial; 2 [Al + 3% C]<sub>MCT</sub>; 3 [Al + 20% C]<sub>MCT</sub>.

Compositions based on PA/HTPB/(Al +  $C_{17}H_{35}COOH$  +  $SiO_2$ ) demonstrated the best result in burning rate and exponential pressure (Fig. 3). At present, stearic acid is used for the passivation of aluminum powders on an industrial scale [6]. Firstly, stearic acid is hydrophobic, secondly, with MCT, it fills cracks in the oxide film on the surface of aluminum particles and, thirdly, increases the chemical resistance of aluminum in relation to other fuel components, thereby increasing the shelf life of solid fuel. Aluminum particles in solid rocket fuels are initially localized between large oxidizer particles. When the melting point reaches  $660^\circ C$ , the aluminum particles become liquid, but they are still in the bulk of the oxide film, i.e. in an isolated state. The melting point of aluminum oxide is three times higher than the melting point of aluminum. In our case, as in the opinion of Price [7], liquid aluminum can leak due to cracks in the oxide shell formed during the MCT and filled with stearic acid, which can facilitate the

ignition of particles. Perhaps the subsequent agglomeration of particles may occur in the heating zone adjacent to the burning surface layer.

After introduction of the mechanically activated composite (Al + 3% C<sub>17</sub>H<sub>35</sub>COOH + 5% SiO<sub>2</sub>) into solid fuel, there is a good increase in the burning rate by 13.5% at 5 atm and by 15.9% at 40 atm. The use of powder (Al + 3% C<sub>17</sub>H<sub>35</sub>COOH + 20% SiO<sub>2</sub>) caused only minor changes in the burning rate as compared to (Al + 3% C<sub>17</sub>H<sub>35</sub>COOH + 5% SiO<sub>2</sub>) within  $\Delta r_b = 17.6\%$  in the considered pressure range. The content of active aluminum, which was determined by the volumetric method, was no more than  $\sim 85.1\%$  in the system. A possible factor of this result is that the active combustible system is fully composite [Al + 3% C<sub>17</sub>H<sub>35</sub>COOH + 20% SiO<sub>2</sub>].

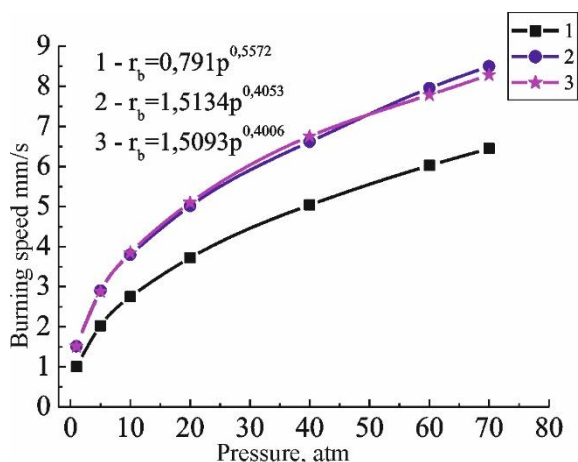


Fig. 3. Change of burning rate of fuels PA/HTPB/Al<sub>x</sub> with non-activated aluminum and after MCT of composites: 1 Al initial; 2 [Al + 3 % C<sub>17</sub>H<sub>35</sub>COOH + 5 % SiO<sub>2</sub>]<sub>MCT</sub>; 3 [Al + 3 % C<sub>17</sub>H<sub>35</sub>COOH + 10 % SiO<sub>2</sub>]<sub>MCT</sub>.

Mechanically activated aluminum-based powders with a modifier were prepared using a centrifugal mill. After MCT of powders, the morphology of the particles, the metal content in the composite, and its reactivity were studied. The final effect depends on the activation modifier and promoter. Solid additives (silicon dioxide) contributed to finer grinding of aluminum powder and loosening of its surface oxide layer, which led to more effective activation, as well as an increase in the reactivity of the composite. Formulations of powders of aluminum with polyvinyl alcohol after MCT of the burning composition occurs with an explosive effect. Such systems can be used in other energy compositions such as: gas generators, explosives, thermite compositions to obtain porous ceramics.

1. Z.A. Mansurov, N.N. Mofa, Mechanochemical synthesis of composite materials, Almaty: Kazak University, 2016, 376 p.
2. C.C. Koch, J.D. Whittenberger, Mechanical milling, alloying of intermetallics, *Intermetallics*, 1996, vol. 4, no 5, pp. 339–355.
3. C. Suryanarayana, Mechanical alloying and milling, *Progress in Mater. Sci.*, 2001, vol. 46, no. 1-2, pp. 181–184.
4. E. Gaffet, F. Bernard, J-C. Nierce, F. Charlot, C. Gras, G. Le Caer, Some recent developments in mechanical activation and mechanosynthesis, *Journ. Mater. Chem.*, 1999, vol. 9, pp. 305–314.
5. Z.A. Mansurov, N.N. Mofa, B.S. Sadykov, Zh.Zh. Sabaev, A.Ye. Bakkara, Mechanochemical treatment, structural features, properties and reactivity of SHS systems based on natural materials. Part 3: The influence of mechanochemical processing and modification of oxide materials on technological combustion, *Eng. Phys. J.*, 2014, vol. 87, no. 5, pp. 1000–1008.

6. A. Gromov, A. Ilyin, V. An, F. Faubert, C. de Izarra, A. Espagnacq, L. Brunet, Characterization of aluminum powders. 1: Parameters of reactivity of aluminium powders, *Propellants, Explosives, Pirotechnics*, 2002, vol. 27, iss. 6, pp. 361–364.
7. E.W. Price, R.K. Sigman, J.R. Sambamurthi, C.J. Park, Behavior of aluminum in solid propellant combustion, *AFOSR-TR-82-0964*, *Georgia Inst. of technology*, 1982, vol.4, pp. 1344–1351.

## SHOCK-WAVE TREATMENT OF REACTIVE POWDERS

I. V. Saikov<sup>\*a</sup>, S. G. Vadchenko<sup>a</sup>, I. D. Kovalev<sup>a</sup>, and M. I. Alymov<sup>a</sup>

<sup>a</sup>Merzhanov Institute of Structural Macrokinetics and Materials Science, Russian Academy of Sciences, Chernogolovka, Moscow, 142432 Russia  
\*e-mail: revan.84@mail.ru

DOI: 10.24411/9999-0014A-2019-10142

At the moment, there is an increased interest in research aimed at identifying the main laws of the interaction of metals with a polytetrafluoroethylene (PTFE) polymer matrix under shock-wave loading of powder mixtures. Mixtures of PTFE with metals are widely used in pyrotechnics due to the high temperatures developed during their combustion [1–7]. At the same time, in some cases, a high density of energy-releasing composites is needed, which can be achieved using high-density metals such as tungsten as a filler [8–10]. Unlike well-studied reactions of PTFE with aluminum and magnesium, there is practically no information about the kinetics of the reaction of interaction with other metals, ignition, combustion, and detonation of mixtures with PTFE in open sources. Analysis of literature data shows that the main direction in the development of reaction materials is the search for activating additives (including aluminum and titanium, referred to in this work) and the definition of criteria for reliable initiation. In this work, an important aspect is additionally taken into account concerning not only the fact of shock-wave initiation, but also the features of the exothermic reaction (the ratio of liquid, solid and gaseous products), which strongly affect the characteristics of the reactive material.

The research aims to identify the main patterns of interaction of metal powders with a polymer matrix during combustion and shock-wave loading of the reactive materials [11, 12]. The features of ignition and gas evolution, as well as the conditions of shock-wave initiation were investigated. It is shown that the structure of the formed products and the amount of the melt depend on the heating rate, and in the samples pressed from mechanically activated powders, the amount of melt is less than from non-activated ones. Experiments have shown that compositions that form a large volume of gaseous products while simultaneously forming a melt are completely sprayed (W–Ti–PTFE), or form a highly porous structure. The heating rate has little effect on the ignition temperature, but it has a strong effect on the amount of melt produced: as the heating rate increases, the amount of the liquid phase increases. The high degree of homogeneity of the mixture, achieved by mechanical activation, also does not contribute to the consolidation of particles of combustion products. Since tungsten and aluminum practically do not contain impurity gases, gas evolution is mainly due to the destruction and gasification of the PTFE flowing in the combustion wave front. It is characteristic that the burning rate decreases with increasing sample density. This is due to the fact that with an increase in the density, the thermal conductivity of the sample increases, the destruction of the PTFE begins in the heating zone at a temperature of about 300°C and the released gases loosen the sample. This leads to instability of burning, which is observed in the form of a sequence of depressions and inflammations. The same factors lead to an anomalous dependence of the burning rate on the calculated adiabatic temperature – compositions with a higher combustion temperature burn at a lower speed. It is shown that there are two limiting values of the liquid/gaseous and liquid/solid product ratios, which determine the preservation of the product with a porous structure, or its expansion and deposition on the reactor parts. Saving the sample shape is impossible both in the presence of high concentrations of the liquid and gas phases in the combustion zone (composition 72W–18PTFE–10Al), and with a low

concentration of the liquid phase and large gas evolution (composition 64W–16PTFE–20Al). In the first case, the gas not only loosens the heating zone, but also breaks the melt in the combustion zone. In the second case, the melt is not enough for sintering and the formation of a frame of the resulting products, and they are sprayed. In this case, the rate of gas evolution is not a defining characteristic. So the composition of 72W–18PTFE–10Al has a burning rate and gas evolution is less than that of other compositions, but at the same time there is a destruction of the sample and the spraying of products. Experiments on determination of gas evolution and burning rate of the reaction materials showed that with an increase in the concentration of aluminum in the mixture from 5 to 10 wt % the combustion mode, the structure of the resulting products, and the completeness of combustion change dramatically. Therefore, for practical use, the optimal concentration of aluminum, taking into account the scale factor, is about 5 wt % [12]. The essential role of “activating” additives (Al, Ti, B) in initiating, passing a chemical reaction in a powder mixture and the final phase formation was experimentally shown. Tungsten-based systems (W–Al–PTFE, W–Ti–PTFE, W–Hf–PTFE) proved to be difficult to initiate under shock-wave loading. In this case, the additive metal (Al, Hf) reacted quite actively with fluorine from Teflon to form fluorides  $\text{AlF}_3$  and  $\text{HfF}_4$ . The most fully react are Ni–Al, Ni–Al–PTFE MA, Ti–B–PTFE, Hf–B–PTFE. It is important to note that the two systems Ti–B–PTFE and Hf–B–PTFE are most advantageous in terms of energy release, their adiabatic combustion temperatures are 2920°C and 3280°C, respectively. Thus, the systems based on metals (titanium and hafnium) with additions of boron and PTFE are the most promising from the point of view of the attained synthesis temperature, initiation by shock-wave action, and completeness of the reaction passage for the application of the reactive material.

1. N.A. Imkhovik, A.V. Svidinsky, A.S. Smirnov, V.B. Yashin, Foreign investigations of new high-density reactive materials for different advanced munitions, *Gorenie i Vzryv [Combustion and Explosion]*, 2017, vol. 10, no. 1, pp. 93–101.
2. J. Huang, X. Fang, S. Wu, L. Yang, Z. Yu, Y. Li, Mechanical response and shear-induced initiation properties of PTFE/Al/MoO<sub>3</sub> reactive composites, *Mater.*, 2018, vol. 11, no 7, pp. 1200.
3. W. Xiong, X. Zhang, M. Tan, C. Liu, X. Wu, The energy release characteristics of shock-induced chemical reaction of Al/Ni composites, *J. Phys. Chem. C*, 2016, vol. 120, no. 43, pp. 24551–24559.
4. S. M. Peiris, Enhancing energy in future conventional munitions using reactive materials, *AIP Conf. Proceedings*, 2018, vol. 1979, pp. 020002
5. F. Zhang, Some issues for blast from a structural reactive material solid, *Shock Waves*, 2018, vol. 28, no. 4, pp. 693–707.
6. X. Liu, H. Ren, Preparation and quasi-static mechanical properties of a reactive material, *Beijing Ligong Daxue Xuebao/Transaction of Beijing Institute of Technology*, 2016, vol. 36, no. 4, pp. 365–369.
7. Guo, H. Wu, Y. Cao, F. Huang, Progress in the study of mechanical response properties of multi-functional energetic structural materials, *Binggong Xuebao/Acta Armamentarii*, 2012, vol. 33, pp. 337–345.
8. Y. Li, Z. Wang, C. Jiang, H. Niu, Experimental study on impact-induced reaction characteristics of PTFE/Ti composites enhanced by W particles, *Mater.*, 2017, vol. 10, no. 2, pp. 175.
9. J. Zhou, Y. He, C.T. Wang, Investigation on impact initiation characteristics of fluoropolymer-matrix reactive materials, *Propellants, Explosives, Pyrotechnics*, 2017, vol. 42, no. 6, pp. 603–615.
10. D.L. Hastings, L. D. Edward, Reactive structural materials: preparation and characterization, *Adv. Eng. Mater.*, 2017, vol. 20, no. 3, pp. 1700631.
11. I.V. Saikov, M.I. Alymov, S.G. Vadchenko, I.D. Kovalev, Investigation of shock-wave

- initiation in metal-teflon powder mixtures, *Lett. Mater.*, 2017, vol. 7, no. 4. pp. 465–468.
12. I.V. Saikov, M.I. Alymov, S.G. Vadchenko, P.Yu. Gulyaev, Shock-wave synthesis in powder mixtures, *J. Phys.: Conf. Ser.*, 2018, vol. 1115. pp. 042012.
  13. S.G. Vadchenko, I.S. Gordopolova, I.D. Kovalev, I.V. Saikov, M.I. Alymov, Gas release during combustion of W–Teflon–Al mixtures, *Int. J. Self-Propag. High-Temp. Synth.*, 2019, vol. 28, no. 1, pp. 64–67.

## TEMPERATURE MEASUREMENTS OF THE COMBUSTION WAVE BY DYNAMIC SPECTROMETRY

V. G. Salamatov<sup>\*a</sup>, A. I. Kirdyashkin<sup>b</sup>, and V. D. Kitler<sup>b</sup><sup>a</sup>Merzhanov Institute of Structural Macrokinetics and Materials Science, Russian Academy of Sciences, Chernogolovka, Moscow, 142432 Russia<sup>b</sup>Tomsk Scientific Center, Siberian Branch, Russian Academy of Sciences, Tomsk, 634055 Russia

\*e-mail: Salamvit@yandex.ru

DOI: 10.24411/9999-0014A-2019-10143

Temperature measurements are of importance to understand the kinetics of chemical conversions in a reaction wave of rapid high-temperature combustion [1]. Optical pyrometry methods are the most promising for solving this problem. Spectral pyrometry (thermal spectrum thermometry) [2, 3] of heated materials is a method that does not require, in contrast to brightness and color pyrometry, experimental and model concepts of the emissivity factor for the object under study. The latter is achieved by observing the distribution of the radiation intensity of a heated body in a wide range of wavelengths to identify the interval where the profile of the thermal spectrum is described by the Planck function. This work provides the temperature measurements of the SHS reaction wave for mixtures with a composition  $(1 - x)(\text{Ni} + 30 \text{ wt } \% \text{ Al}) + x\text{CaCO}_3$ , where  $x$  is the mass of the gasifying additive using dynamic spectrometry [3]. The processes were monitored using high speed video recording (Motion ProX-3), the frame frequency was up to  $10.000 \text{ s}^{-1}$ , and by dynamic monitoring of emission spectra (HR 4000-Ocean Optics spectrometer, range of wavelengths is  $200 \div 1100 \text{ nm}$ , optical resolution is  $0.2 \text{ nm}$ ). The gasifying additive is shown to form a porous drop structure of the reaction product. Here, according to the analysis of the high-speed video data and the dynamic spectrometry of combustion, the formation of drops is accompanied by bright flashes, the temperature of which is  $200 \div 400 \text{ K}$  higher than the relatively homogeneous temperature in the zone of the reaction wave. The addition of  $\text{CaCO}_3$  to the initial mixture destructs oxide films on the surface of the particles, which, in turn, decreases the surface tension of melts and creates conditions for the formation of drops in the heating zone. During the formation of drops, a gap is formed between them and the initial mixture. The gap prevents the transfer of heat from the heated drop of the initial mixture, which leads to its overheating and decrease in melt viscosity. The movement of drops on the surface is accompanied by their merging or sticking to each other. The latter leads to the formation of chains of drops stuck together. Increasing the initial density of the samples leads to the formation of a foamed structure of the product. The structure is formed in a narrow zone adjacent to the combustion front. As in the first case, reaction sources (drops) are formed in the front, move within the voids formed by the merging of the initial particles into drops and combine into small agglomerates. The high initial density explains the homogeneous, along the entire length of the front, temperature of the sample, and also the restriction of the free movement and growth of drops.

This work was supported by RFBR (project no. 19-03-00081 A).

1. E.A. Levashov, A.S. Mukasyan, et. al., Self-propagating high-temperature synthesis of advanced materials and coatings, *Int. Mater. Rev.*, 2017, vol. 62, no. 4, pp. 203–239.
2. A.N. Magunov, Spectral pyrometry (review), *J. Instrum. Exp. Tech.*, 2009, vol. 52, no 4, pp. 451–472.
3. V.G. Salamatov, A.I. Kirdyashkin, et. al., Combustion of composite Ni–Al fibers, *J. Phys.: Conf. Ser.*, 2018, vol. 1115, 042033.



## CENTRIFUGAL ASSISTED SHS SURFACING OF CoCrFeNiMnAl<sub>x</sub> HIGH ENTROPY ALLOY ON Ti ALLOY SUBSTRATE

V. N. Sanin<sup>\*a</sup>, D. M. Ikornikov<sup>a</sup>, O. A. Golosova<sup>a</sup>, D. E. Andreev<sup>a</sup>, and V. I. Yuxhvid<sup>a</sup>

<sup>a</sup>Merzhanov Institute of Structural Macrokinetics and Materials Science, Russian Academy of Sciences, Chernogolovka, Moscow, 142432 Russia

\*e-mail: svn@ism.ac.ru

DOI: 10.24411/9999-0014A-2019-10144

High-entropy alloys (HEAs) are newly developed multicomponent alloys wherein the configurational entropy (CE) is higher than the fusion entropy of most common metals [1]. These alloys draw increasing scientific interest, especially regarding the fundamental aspects of massive solid-solution (SS) phases and the basic role of CE therein [2–5]. These efforts are well motivated, as the HEA concept was originally based on CE maximization (i.e., by increasing the number of equiatomically proportioned alloying elements). However, this strategy has led so far to only a few successful single-phase alloys [6–9] and the role of CE in these successful cases is being debated. Instead, most of the investigated alloys pertaining to this class develop complex, multiphase microstructures and low tensile ductility, providing limited prospects for future applications. Even for the present success stories such as Co<sub>20</sub>Cr<sub>20</sub>Fe<sub>20</sub>Mn<sub>20</sub>Ni<sub>20</sub>, the most promising HEA with a highly stable and ductile single-phase SS, the specific composition tolerance window, the weak high-temperature behavior, and the expensive alloying (e.g., Ni) are still pending challenges. Considering that the overall applicability of a new material class is strongly linked to the versatility of the properties it can deliver in exchange for the practical and economical complexities created by its bulk processing, the above-mentioned difficulties and uncertainties call for a critical assessment of the versatility versus complexity balance in HEA.

The main aim of this work is to provide such an analysis as well as new perspectives to improve on the aforementioned limiting aspects of apply properties. Thus, in what follows, taking the reported Co<sub>20</sub>Cr<sub>20</sub>Fe<sub>20</sub>Mn<sub>20</sub>Ni<sub>20</sub> alloy as the starting point, we investigate the possibility of forming the coating in-situ SHS (SHS-surfacing) of HEAs Co<sub>20</sub>Cr<sub>20</sub>Fe<sub>20</sub>Mn<sub>20</sub>Ni<sub>20</sub> on a metal substrate (Ti alloy).

The compositional design, centrifugal casting (SHS processing routes), and microstructure/property relations of synthesized HEA/Ti substrate composite will be pointed out. The HEA surfacing on Ti alloy substrate was carried out by a relatively new method called the SHS surfacing, which is one of the technological directions of metallothermic SHS (SHS metallurgy) [10]. This is a low-energy consuming technique due to the use of internal energy released in high-caloric combustion reactions. Recently, cast high-entropy transition metal alloys were first prepared [11]. The use of highly exothermic SHS compounds of the thermite type makes it possible to produce melts of combustion products (at temperature above 2500°C) and, as a consequence, to obtain cast products (ingots). Cast coatings can be formed directly during synthesis process (*in-situ* SHS) on a metal plate (substrate) placed in the bottom part of refractory mold (Fig. 1).

However, the surfacing on substrates consisting of active metals will inevitably lead to the formation of not only a mechanical connection between the layers but also the formation of new structural components based on active metal and alloy components. That is why in the frame of this work special attention was paid to the study of the area of section of the formed layer material consisting of titanium alloy VT20 (Russian trademark) and cast HEA.

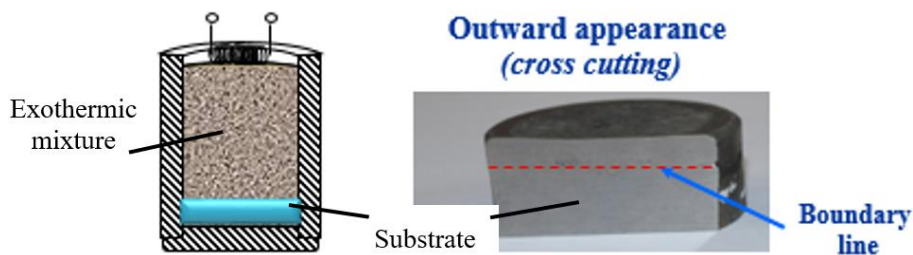


Fig. 1. (a) Schema of initial sample and (b) outward appearance of sample after SHS surfacing (cross cutting).

Figure 2 and 3 shows the structure of transition zone between deposited coating layer and Ti substrate. Analysis of the microstructure of the deposited layer (Figs. 2a, 2b) revealed three zones where the base material (Ti) gradient distributed over the height of the deposited layer. Figure 2c shows that the hardness of coating is higher by 3 times than that of substrate.

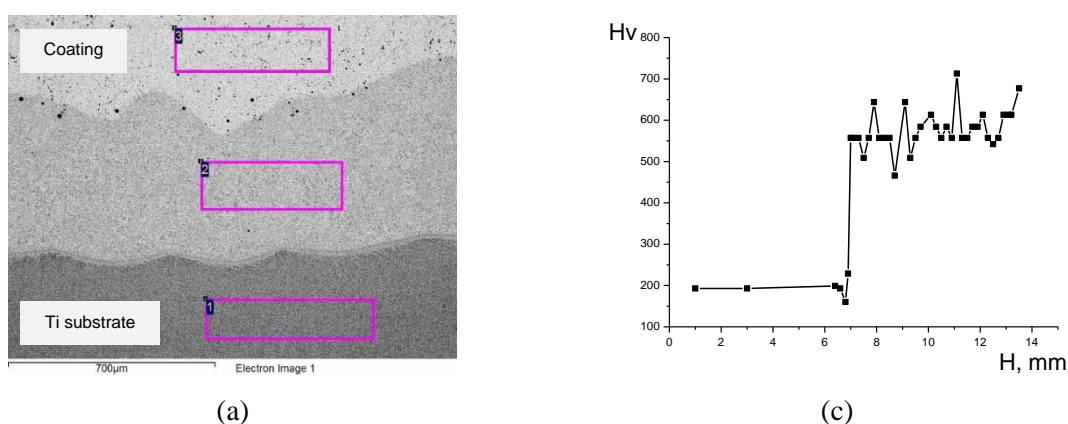


Fig. 2. (a) SEM image of coating/Ti substrate composite, (b) EDS data of transition zone, and (c) dependence of microhardness on height of coating.

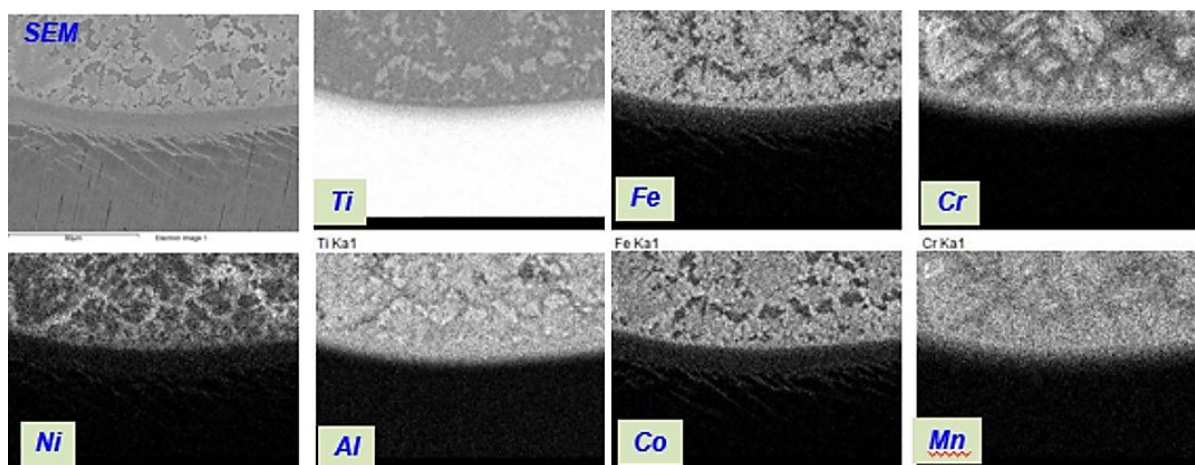


Fig. 3. EDX maps of boundary layer of the SHS coating.

The analysis of the obtained data allows drawing a conclusion about the prospects of the materials under investigation and the method of their production for the formation of volumetric

materials and coating of them. The production of metallic composite materials based on the new principle of formation of polymetallic alloys can significantly expand the basis for the creation of new materials and facilitate the creation of new technological models.

The research was supported by the Russian Foundation for Basic Research, (project no. 19-08-01108).

1. B. Cantor, et al, Microstructural development in equiatomic multicomponent alloys, *Mater. Sci. Eng. A*, 2004, vol. 375, pp. 213–218.
2. F. Otto, et al, Relative effects of enthalpy and entropy on the phase stability of equiatomic high-entropy alloys, *Acta Mater.*, 2013, vol. 61, pp. 2628–2638.
3. J.W. Yeh, et al, Nanostructured high-entropy alloys with multiple principal elements: novel alloy design concepts and outcomes, *Adv. Eng. Mater.*, 2004, vol. 6, pp. 299–303.
4. Y. Zhang, et al, Microstructures and properties of high-entropy alloys, *Prog. Mater. Sci.*, 2014, vol. 61, pp. 1–93.
5. J.W. Yeh, Alloy design strategies on high-entropy alloys, *JOM*, 2013, vol. 65, pp. 1759–1771.
6. D.B. Miracle, et al, Exploration and development of high entropy alloys for structural applications, *Entropy*, 2014, vol. 16, pp. 494–525.
7. J. W. Yeh, Recent progress in high-entropy alloys, *Europ. J. Cont.*, 2006, vol. 31, no. 6, pp. 633–648.
8. M.J. Yao, K.G. Pradeep, C.C. Tasan, D. Raabe, A novel, single phase, non-equiatomic FeMnNiCoCr high-entropy alloy with exceptional phase stability and tensile ductility, *Scripta Mater.*, 2014, vol. 72–73, pp. 5–8.
9. B. Gludovatz, A. Hohenwarter, D. Catoor, E.H. Chang, E.P. George, R.O. Ritchie, A fracture-resistant high-entropy alloy for cryogenic applications, *Sci.*, 2014, 345.
10. V.N. Sanin, D.M. Ikornikov, D.E. Andreev, V.I. Yuxhvid, Centrifugal SHS metallurgy of nickel aluminide based eutectic alloys, *Russ. J. Non-Ferr. Met.*, 2014, vol. 55, no. 6, pp. 613–619.
11. V.N. Sanin, V.I. Yuxhvid, D.M. Ikornikov, D.E. Andreev, N.V. Sachkova, M.I. Alymov, SHS metallurgy of high-entropy transition metal alloys, *Dokl. Phys. Chem.*, 2016, vol. 470, part 2, pp. 145–149.

## CENTRIFUGAL CASTING–SHS PROCESS OF THE CAST CoCrFeNiMn-TYPE HIGH-ENTROPY ALLOY HARDENED BY THERMOMECHANICAL TREATMENT AND THE INTRODUCTION OF SILICON–BORIDE HARDENERS

V. N. Sanin<sup>\*a</sup>, D. M. Ikornikov<sup>a</sup>, O. A. Golosova<sup>a</sup>, D. E. Andreev<sup>a</sup>, V. I. Yuxhvid<sup>a</sup>, and S. V. Zharebtsov<sup>b</sup>

<sup>a</sup>Merzhanov Institute of Structural Macrokinetics and Materials Science, Russian Academy of Sciences, Chernogolovka, Moscow, 142432 Russia

<sup>b</sup>Belgorod State University, Belgorod, 308015 Russia

\*e-mail: svn@ism.ac.ru

DOI: 10.24411/9999-0014A-2019-10145

Conventional alloy design over the past centuries has been obliged by the concept of one or two prevalent base elements. As a breakthrough of this restriction, the concept of high-entropy alloys (HEAs) containing multiple principal elements has drawn great attention over the last 13 years due to the numerous opportunities for investigations in the huge unexplored compositional space of multicomponent alloys [1–6]. A large number of studies in this field have been motivated by the original HEA concept, which suggested that achieving maximized configurational entropy using equiatomic ratios of multiple principal elements could stabilize singlephase massive solid-solution phases [3]. However, an increasing number of studies have revealed that formation of single-phase solid solutions in HEAs shows weak dependence on maximization of the configurational entropy through equiatomic ratios of elements [2] and it was even found that maximum entropy is not the most essential parameter when designing multicomponent alloys with superior properties [4–8]. These findings encouraged efforts to relax the unnecessary restrictions on both the equiatomic ratio of multiple principal elements as well as the formation of single-phase solid solutions. In this context, non-equiatomic HEAs with single-, dual-, or multiphase structure have recently been proposed to explore the flexibility of HEA design and overcome the limitations of the original HEA design concept [9]. Also, deviation from the equimolar composition rule facilitates identification of compositions which allow the often-brittle intermetallic phases to be avoided. Thermodynamic investigations of non-equiatomic HEAs showed that the configurational entropy curve of these alloys is rather flat, indicating that a wide range of compositions alongside the equiatomic configuration assume similar entropy values. As compared with conventional alloys with one or two principal elements plus minor alloying components, as well as equiatomic HEAs with equimolar ratios of all alloy elements, non-equiatomic HEAs greatly expand the compositional space that can be probed. Indeed, recent studies have revealed that outstanding mechanical properties exceeding those of equiatomic HEAs can be achieved by non-equiatomic alloys [7, 9, 10]. As one of the possible pathways, a novel type of transformation-induced plasticity-assisted dualphase (TRIP-DP) HEA was developed [4]. The two constituent phases in the alloy, i.e., the face-centered cubic (FCC) matrix and the hexagonal close-packed (HCP) phase, are compositionally equivalent and thus can both be referred to as high-entropy phases [4]. This leads to a significantly improved strength– ductility combination compared with corresponding equiatomic HEAs, mainly due to the combination of massive solid-solution strengthening and the TRIP effect [11]. The above-mentioned findings clearly indicate that expanding the HEA design concept to nonequiatomic compositions has great potential for pursuing more compositional opportunities for design of novel materials with exceptional properties. For transition-metal HEAs, vacuum induction furnace is used to melt and cast various HEAs. In as-

cast condition, the multiple principal elements are typically not homogeneously distributed in the bulk HEAs with their coarse dendritic microstructure owing to liquid segregation, although X-ray diffraction (XRD) analysis may suggest single- or dual-phase structures. Therefore, to obtain high-quality alloys with a controlled microstructure and the level of mechanical properties we have to use the post-processing thermo-mechanical treatment and controlled introduction of various modifying or strengthening additives during casting process.

Processing routes are not only decisive for the grain size and phase fraction corresponding to a targeted specific composition but are also critical with respect to the compositional homogeneity state, which also has significant effects on the mechanical behavior. To obtain from cast alloys the samples with different compositional homogeneity various processing routes are applied including hot-rolling, homogenization, cold rolling, and recrystallization annealing etc.

Today, the most studied alloys belonging to this HEAs group are the alloys in the Co–Cr–Fe–Ni–Mn system. The equiatomic Co–Cr–Fe–Ni–Mn alloy have a single-phase structure of a disordered substitution solid solution on the basis of a face-centered cubic *fcc* lattice. The multicomponent high-entropy *fcc* alloys Co–Cr–Fe–Ni–Mn exhibited high ductility at room and cryogenic temperatures [12] and record breaking fracture toughness at cryogenic temperatures; but the yield strength of the alloy was rather low (HEAs). There have been many efforts to improve the properties of the CoCrFeNiMn alloy. It was found that the highest strength can be attained in the alloys with a *fcc* matrix strengthened with the particles of some another compound. However, the design of dispersion strengthened HEAs with optimal properties requires additional efforts.

In frame of the work, we will provide some recent results of various strong and ductile Al, C-containing CoCrFeNiMn-type high-entropy alloys hardened by thermo-mechanical treatment and the introduction of silicon-boride hardeners. The compositional design, centrifugal casting–SHS processing routes, and microstructure/property relations will be pointed out. With comparison of the conventional multistage vacuum casting processes the relatedly new technique which is called the SHS-technology of high temperature melts or the metalothermic SHS [13], is promising route to produce cast HEAs. This is a low-energy consuming technique due to the use of internal energy released in high-caloric combustion reactions. Recently, cast high-entropy transition metal alloys were first prepared [14]. The use of highly exothermic SHS compounds of the thermite type makes it possible to produce melts of combustion products (at temperature above 2500°C) and, as a consequence, to obtain cast products (ingots). The synthesis was carried out using powdered SHS systems containing oxides of target elements (NiO, Cr<sub>2</sub>O<sub>3</sub>, Fe<sub>2</sub>O<sub>3</sub>, Co<sub>3</sub>O<sub>4</sub>, MnO<sub>2</sub>), reduced metal (Al) and alloy additives (C, silicon–boride hardeners (Ti(Cr)–B–Si)). The experiments were carried out using a centrifugal SHS machine [13] under the influence of an overload of 10 to 80 g, which in turn is a powerful tool for controlling the combustion processes and the formation of synthesis products [13, 14]. The effect of overload in the combustion stage makes it possible to suppress the spread of products during combustion, to realize intensive mixing of the melt over the combustion front and to obtain a high conversion of the initial mixture in the combustion front. At the stage of gravitational separation and cooling, the effect of overloading makes it possible to realize the high yield of the metallic phase in the ingot (close to the calculated one), to remove the gaseous products from it and to facilitate the equalization of the chemical composition by the HEA ingot volume, which was very important for the synthesis of polymetallic alloys. The general scheme of the process for the synthesis of cast alloys was described in [14]. Figure 1 illustrates XRD pattern and microstructure of SHS-produced CoCrFeNiMn alloy without additives.

The XRD pattern contains only *fcc* phase with lattice parameter  $a = 3.588$  nm. XRD and EBSD data show strong crystallographic texture typical of the cast materials. The alloy has coarse structure with a grain size of 250–400 μm. The grain boundaries are often curved, and the shape of the grains is irregular. SEM and TEM studies revealed no second phases.

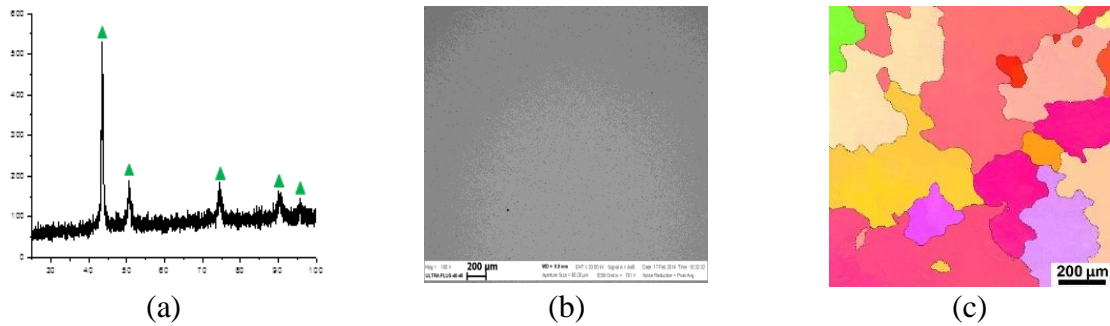


Fig. 1. (a) XRD pattern ( $\blacktriangle$  FCC ( $Im\bar{3}m$ )), (b) SEM image, and (c) EBSD map of crystallographic orientations of as-cast CoCrFeNiMn alloy.

The introduction of 0.2 wt % carbon into alloy does not have a noticeable effect on the phase composition formation but significantly increases the hardness of the alloy. The introduction of silicon–boride hardeners Ti(Cr)–B–Si affects the phase composition. The introduction of Al into composition of alloy markedly reduces the density of the alloy. The formation of intermetallic phase NiAl is observed at high concentrations of Al and it promotes to a sharp decrease in plasticity.

The synthesized  $Al_{3.4}Co_{0.7}Co_{22.3}Cr_{19.7}Fe_{22.9}Ni_{22.4}Mn_{8.6}$  alloy was subjected to thermomechanical treatment (cold rolling and following annealing). Mechanical properties of treated samples—yield strength ( $\sigma_{0.2}$ ), ultimate tensile strength ( $\sigma_{UTS}$ ), uniform elongation ( $\epsilon_u$ ), and elongation to fracture ( $\epsilon_f$ )—are given in Table 1.

Table 1. Tensile properties of  $Al_{3.4}Co_{0.7}Co_{22.35}Cr_{19.7}Fe_{22.9}Ni_{22.4}Mn_{8.6}$  alloy.

|             | $\sigma_{0.2}$ ,<br>MPa | $\sigma_{UTS}$ ,<br>MPa | $\epsilon_u$ ,<br>% | $\epsilon_f$ ,<br>% |                     | $\sigma_{0.2}$ ,<br>MPa | $\sigma_{UTS}$ ,<br>MPa | $\epsilon_u$ ,<br>% | $\epsilon_f$ ,<br>% |
|-------------|-------------------------|-------------------------|---------------------|---------------------|---------------------|-------------------------|-------------------------|---------------------|---------------------|
| As-cast     | 210                     | 455                     | 74                  | 80                  | Annealing at 700°C  | 870                     | 1060                    | 13                  | 24                  |
| 20% rolling | 545                     | 650                     | 18                  | 25                  | Annealing at 800°C  | 610                     | 925                     | 25                  | 38                  |
| 40% rolling | 945                     | 980                     | 3.7                 | 7                   | Annealing at 900°C  | 530                     | 875                     | 27                  | 41                  |
| 60% rolling | 965                     | 1140                    | 2.3                 | 5.4                 | 80% rolling         | 435                     | 820                     | 36                  | 44                  |
| 80% rolling | 1310                    | 1500                    | 1.3                 | 6.5                 | Annealing at 1100°C | 320                     | 760                     | 40                  | 47                  |

The stress–strain curves of the annealed  $Al_{3.4}Co_{0.7}Co_{22.35}Cr_{19.7}Fe_{22.9}Ni_{22.4}Mn_{8.6}$  alloy demonstrate (Fig. 2) that mechanical properties of the alloy can be further tailored by annealing treatment. Apparently, the alloy becomes softer and more ductile with increasing annealing temperature. For example, after annealing at 700°C the alloy still retains high strength: the yield strength and ultimate tensile strength are 870 and 1060 MPa, respectively, at a reasonable ductility of 13 and 25%. An increase in the annealing temperature up to 900°C decreases the material strength, especially the yield strength (530 MPa).

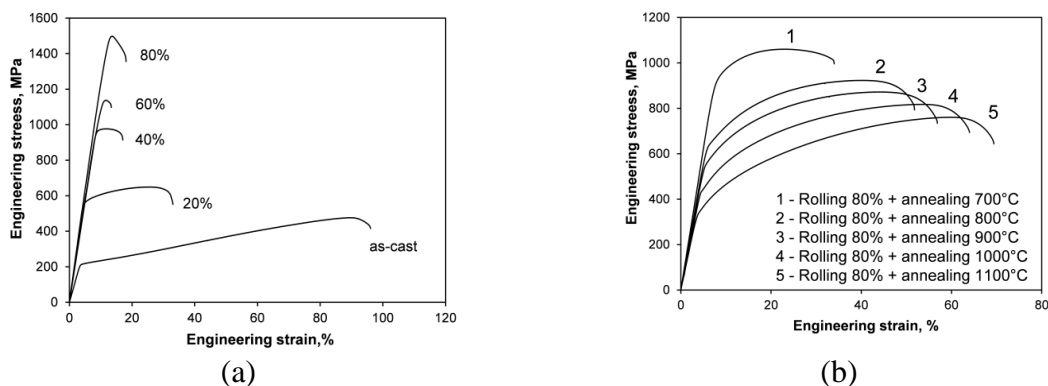


Fig. 2. Tensile stress–strain curves of  $Al_{3.4}Co_{0.7}Co_{22.35}Cr_{19.7}Fe_{22.9}Ni_{22.4}Mn_{8.6}$  after: (a) cold rolling with different thickness reductions and (b) after subsequent annealing at 700–1100°C for 1 h.

Thus, cast CoCrFeNiMn-type high-entropy alloy hardened with different additive components can be fabricated by centrifugal SHS metallurgy in optimized conditions. The analysis of the obtained data allows drawing a conclusion about the prospects of the materials under investigation and the method of their production for the formation of volumetric nanostructured materials. The production of metallic composite materials based on the new principle of formation of polymetallic alloys can significantly expand the basis for the creation of new materials and facilitate the creation of new technological models.

The research was supported by the Russian Foundation for Basic Research, (project no. 19-08-01108).

1. B. Cantor, et al, Microstructural development in equiatomic multicomponent alloys, *Mater. Sci. Eng. A*, 2004, vol. 375, pp. 213–218.
2. F. Otto, et al, Relative effects of enthalpy and entropy on the phase stability of equiatomic high-entropy alloys, *Acta Mater.*, 2013, vol. 61, pp. 2628–2638.
3. J.W. Yeh, et al, Nanostructured high-entropy alloys with multiple principal elements: novel alloy design concepts and outcomes, *Adv. Eng. Mater.*, 2004, vol. 6, pp. 299–303.
4. Y. Zhang, et al, Microstructures and properties of high-entropy alloys, *Prog. Mater. Sci.*, 2014, vol. 61, pp. 1–93.
5. J.W. Yeh, Alloy design strategies on high-entropy alloys, *JOM*, 2013, vol. 65, pp. 1759–1771.
6. D.B. Miracle, et al, Exploration and development of high entropy alloys for structural applications, *Entropy*, 2014, vol. 16, pp. 494–525.
7. J. W. Yeh, Recent progress in high-entropy alloys, *Europ. J. Cont.*, 2006, vol. 31, no. 6, pp. 633–648.
8. O.N. Senkov, G.B. Wilks, J.M. Scott, D.B. Miracle, Mechanical properties of Nb<sub>25</sub>Mo<sub>25</sub>Ta<sub>25</sub>W<sub>25</sub> and V<sub>20</sub>Nb<sub>20</sub>Mo<sub>20</sub>Ta<sub>20</sub>W<sub>20</sub> refractory high entropy alloys, *Intermetallics*, 2011, vol. 19, pp. 698–706.
9. M.J. Yao, K.G. Pradeep, C.C. Tasan, D. Raabe, A novel, single phase, non-equiatomic FeMnNiCoCr high-entropy alloy with exceptional phase stability and tensile ductility, *Scripta Mater.*, 2014, vol. 72–73, pp. 5–8.
10. K.G. Pradeep, C.C. Tasan, M.J. Yao, Y. Deng, H. Springer, D. Raabe, Nonequiatomic high entropy alloys: approach towards rapid alloy screening and property-oriented design, *Mater. Sci. Eng. A*, 2015, vol. 648, pp. 183–192.
11. Z. Li, C.C. Tasan, K.G. Pradeep, D. Raabe, A TRIP-assisted dual-phase high-entropy alloy: grain size and phase fraction effects on deformation behavior, *Acta Mater.*, 2017, vol. 131, pp. 323–335.
12. B. Gludovatz, A. Hohenwarter, D. Catoor, E.H. Chang, E.P. George, R.O. Ritchie, A fracture-resistant high-entropy alloy for cryogenic applications, *Sci.*, 2014, 345.
13. V.N. Sanin, D.M. Ikornikov, D.E. Andreev, V.I. Yuxhvid, Centrifugal SHS metallurgy of nickel aluminide based eutectic alloys, *Russ. J. Non-Ferr. Met.*, 2014, vol. 55, no. 6, pp. 613–619.
14. V.N. Sanin, V.I. Yuxhvid, D.M. Ikornikov, D.E. Andreev, N.V. Sachkova, M.I. Alymov, SHS metallurgy of high-entropy transition metal alloys, *Dokl. Phys. Chem.*, 2016, vol. 470, part 2, pp. 145–149.

## COMBINED METHOD OF PRODUCING AN ALLOY OF IMMISCIBLE ELEMENTS $\text{Cu}_{70}\text{Fe}_{30}$ WITH SUBMICRON STRUCTURAL COMPONENTS

**V. V. Sanin<sup>\*a</sup>, M. R. Filonov<sup>a</sup>, Yu. A. Anikin<sup>a</sup>, E. V. Kosticina<sup>a</sup>, V. I. Yuxhvid<sup>b</sup>, and D. M. Ikornikov<sup>b</sup>**

<sup>a</sup>National University of Science and Technology MISiS, Moscow, 119049 Russia

<sup>b</sup>Merzhanov Institute of Structural Macrokinetics and Materials Science, Russian Academy of Sciences, Chernogolovka, Moscow, 142432 Russia

\*e-mail: sanin@misis.ru

DOI: 10.24411/9999-0014A-2019-10146

Limited-solubility (LS) alloys have long been impossible to produce in a liquid or solid state by conventional metallurgical methods. The main technological difficulties metallurgists encounter when making such alloys are the significant difference in the unit mass and melting points, as well as a strong tendency to delamination in liquid or solid state in a wide range of temperatures and concentrations.

Copper–iron alloys can be classified as LS alloys [1, 2]. Their phase composition is quite simple, as it contains pure components. This makes such alloys interesting [1]. An optimal production technology can produce a final product that combines the properties of the pure components in a proportion suitable for this or that application. For instance, in Cu–Fe alloys, diamagnetic copper shows high electrical and thermal conductivity, while ferromagnetic iron is stronger than copper. A specifically tailored alloy structure will produce either a highly conductive product like copper with the strength of iron; or a hard-magnetic material with the ductility of copper alloys [1].

In this paper, reaching the necessary operating properties of Cu–Fe alloys is associated with a specific dispersion, in which the iron (Fe) components must be uniformly distributed throughout the entire copper (Cu) matrix while being ellipsoid in shape and 70 to 200 nm in size.

Previously published papers [3] compare the morphological and mechanical properties of the produced  $\text{Cu}_{70}\text{Fe}_{30}$  alloy. An alloy produced conventionally by VI melting had a dispersed structure; however, the distribution of Fe particles in the Cu matrix was uneven. On the other hand, similarly composed SHS alloys were characterized by a uniform distribution of the structural components while matching the pre-configured particle size; however, the presence of gases ( $\text{O}_2 = 0.046$ ;  $\text{N}_2 = 0.0021$  wt %) affected the quality of the machined products.

To attain the goals, the research team has successfully tested a new combined method that consists of multiple steps:

(I) to produce cast-charge materials (CCM) of  $\text{Cu}_{70}\text{Fe}_{30}$  by SHS;

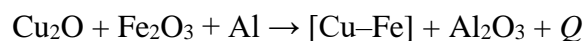
(II) to optimize the CCM remaking parameters;

(III) to carry out single-step VIM for producing a long rod;

(IV) to carry out machining and heat treatment, which includes drawing.

The studied alloy was  $\text{Cu}_{70}\text{Fe}_{30}$ . We performed a series of experiments to produce a  $\text{Cu}_{70}\text{Fe}_{30}$  alloy by SHS metallurgy, then optimized the synthesis conditions and studied how overloading would affect the process parameters.

Chemically, the synthesis could be represented as follows:



where the component weights are selected based on the calculated mass balance of the specified



mixture components, as well as on the actual composition analysis.

$\text{Cu}_{70}\text{Fe}_{30}$  alloy were synthesized under various experimental configurations. Figure 1a shows how overloading affected the main macrokinetic parameters of the synthesis process. Figure 1b illustrates the overall view of alloys prepared under different overloads. At low overloads of  $< 15$  g, the shape of alloys is different. The incomplete separation of phases in such specimens made it difficult to identify the metal phase (the target product) from the oxide phase (aluminum oxide); as a result, the ingots were inconsistently top-coated with corundum. Unlike the specimens synthesized at  $< 30$ g, the ingots produced under 50g looked solid and did not have explicit macrostructural defects.

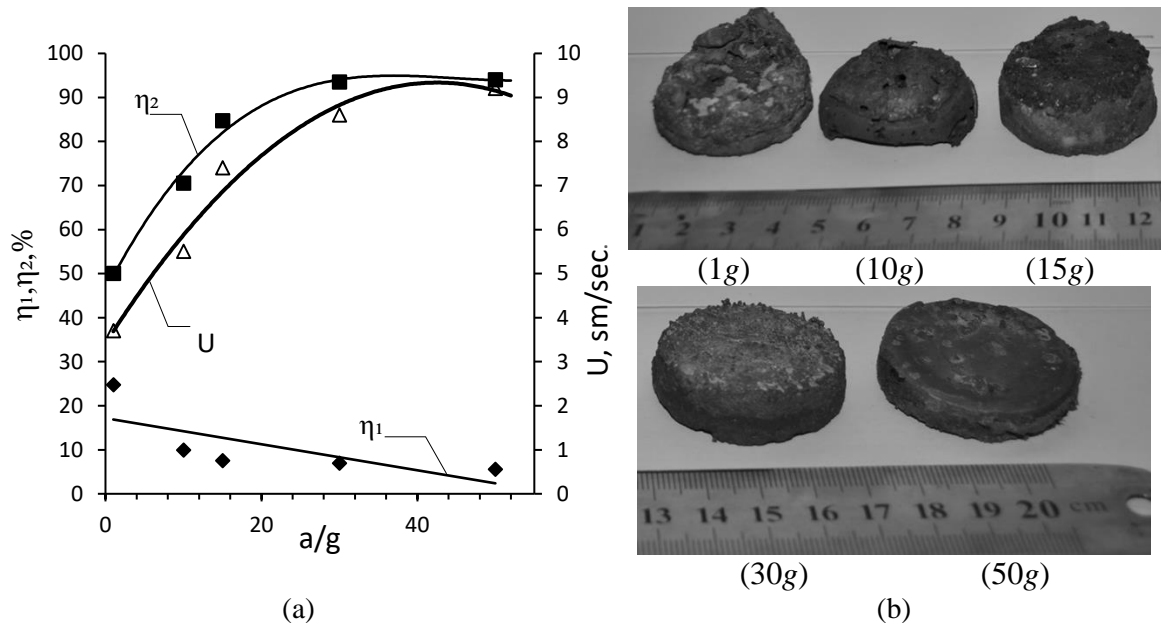


Fig. 1. (a) Dependence of overload ( $n = a/g$ ) on burning rate ( $U$ ), scatter of the mixture ( $\eta_1$ ), and complete yield of the metal phase into the ingot ( $\eta_2$ ); (b) overall view of the samples obtained at various values of overload.

Figure 2 shows that the alloy has a dispersed structure with a uniform distribution of drop-shaped iron (Fe) particles in the copper (Cu) matrix (direct “emulsion”). In [3], the microstructural analysis was presented in detail. It is shown that the  $\text{Cu}_{70}\text{Fe}_{30}$  SHS alloy is represented by a multimodal hierarchical structure with three levels. Level 1 (Figs. 2b, 2c) is where drop-shaped iron particles (direct emulsion), sized 10 to 30  $\mu\text{m}$  on average, are evenly distributed in the copper matrix throughout the specimen. Level 2 (Fig. 3c) releases copper (reverse emulsion) inside the drop-shaped iron particles; the particle size ranges from 200 to 400 nm. Level 3 generates nanoscale iron formations in the copper matrix with a size of 20 to 30 nm. (Fig. 3d). Note that the latter are also observed in the copper particles that are produced at Level 2 (Fig. 3e).

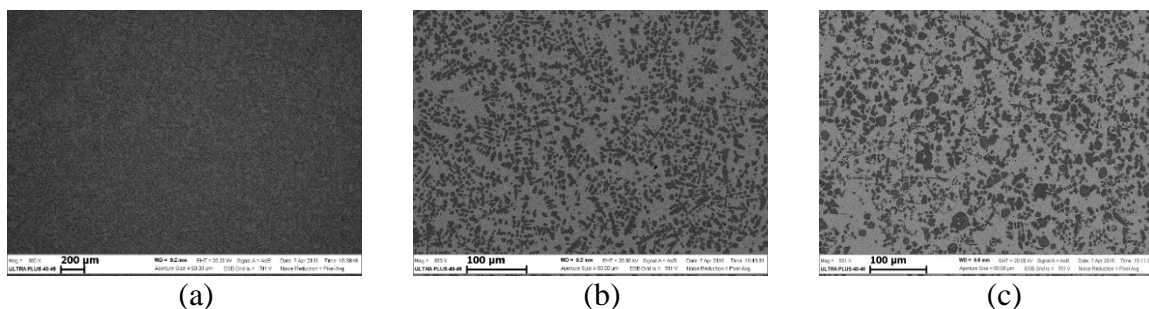


Fig. 2. Microstructure of alloy  $\text{Cu}_{70}\text{Fe}_{30}$  obtained by the method of SHS metallurgy: (a, b) transverse and (b) longitudinal section.

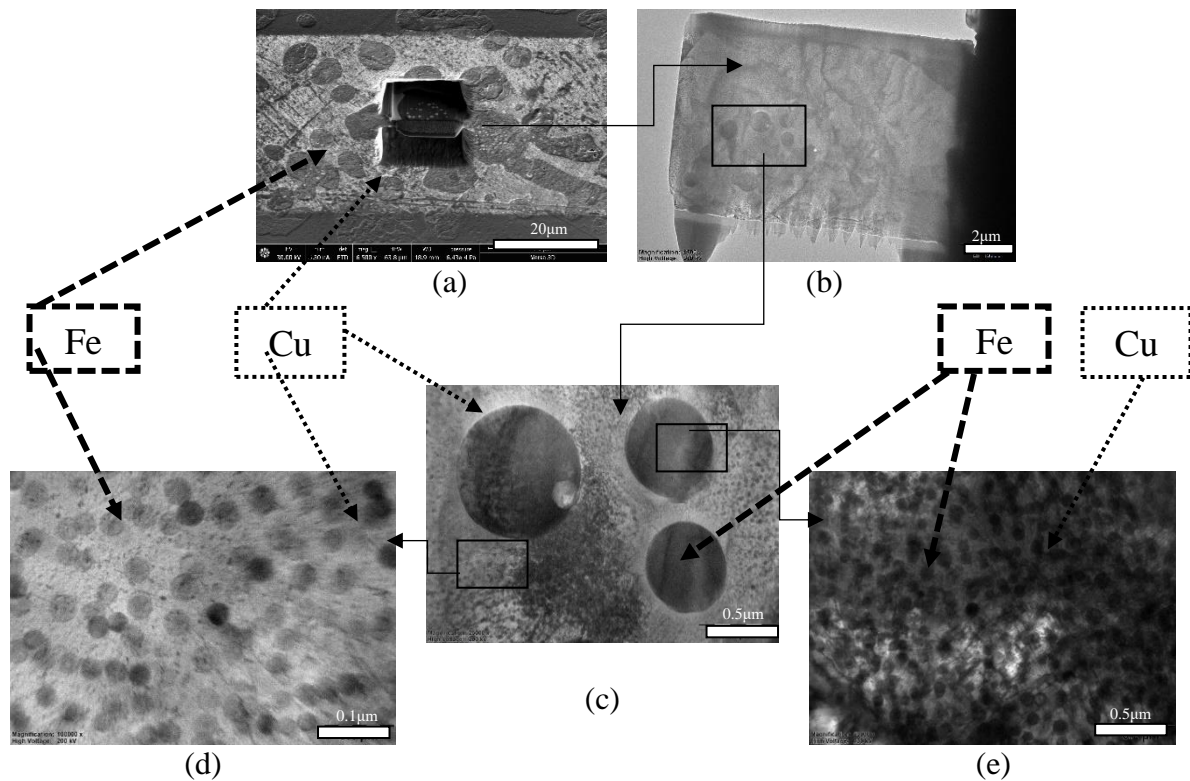


Fig. 3. (a) SEM and (b–e) TEM images of structure of the SHS-alloy of  $\text{Cu}_{70}\text{Fe}_{30}$ .

This could be due to the specifics of SHS metallurgy. SHS mixture burns at  $\sim 2500^\circ\text{C}$ . This melting temperature (unattainable in vacuum furnaces) improves the mutual solubility of Cu and Fe. At the crystallization stage, as the melt cools down, and the solubility limit drops; copper is released as dispersed nanoscale particles.

The next step was to use SHS ingots with uniform alloy component distribution for a single-stage remelting of the  $\text{Cu}_{70}\text{Fe}_{30}$  alloy so as to remove gases, then cast it into long rods. However, it was important to retain the original SHS alloy structure or at least to closely reproduce the earlier evenly distributed fine-grained structure (Fig. 4).

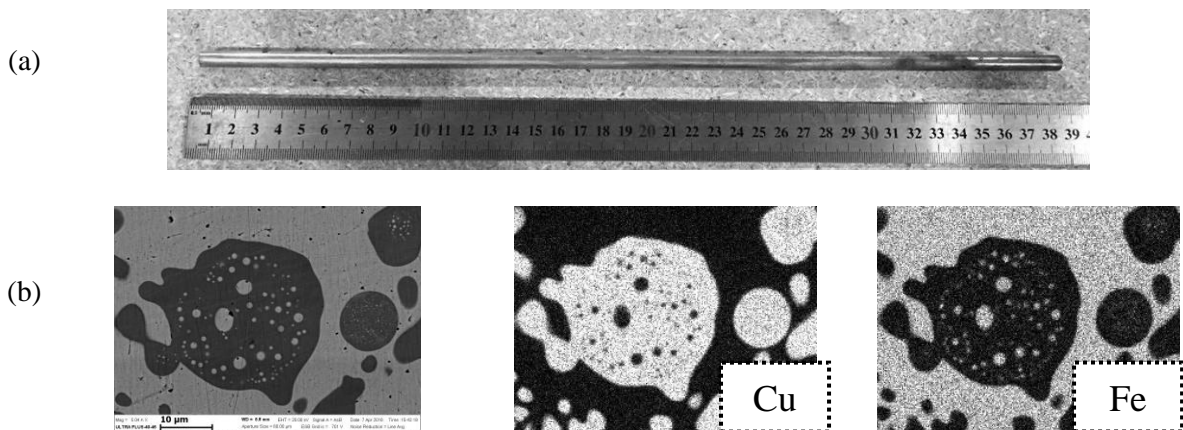


Fig. 4. (a) Overall view of a lengthy rod made of  $\text{Cu}_{70}\text{Fe}_{30}$  alloy obtained from a remelted SHS alloy; (b) element distribution map.

This required optimizing the melting parameters on the basis of the alloy structural parameters sensitive to VIM. To optimize the temperature and time settings of VIM, it seemed necessary to analyze the alloy structure and near-solidus and near-liquidus temperatures. To that end, the research team used a high-temperature unit for research into the viscosity of metallic melts (HTV) [3, 4].

At the final stage, the researchers studied the production of lengthy products from the obtained long rods. The rod was single-drawn to produce longitudinal structurally ordered components. The initial cast rod was drawn through a spinneret along a rectilinear trajectory from 6 mm to 1.7 mm with  $\varepsilon = 92\%$ . Figure 5 shows the overall view and microstructure.

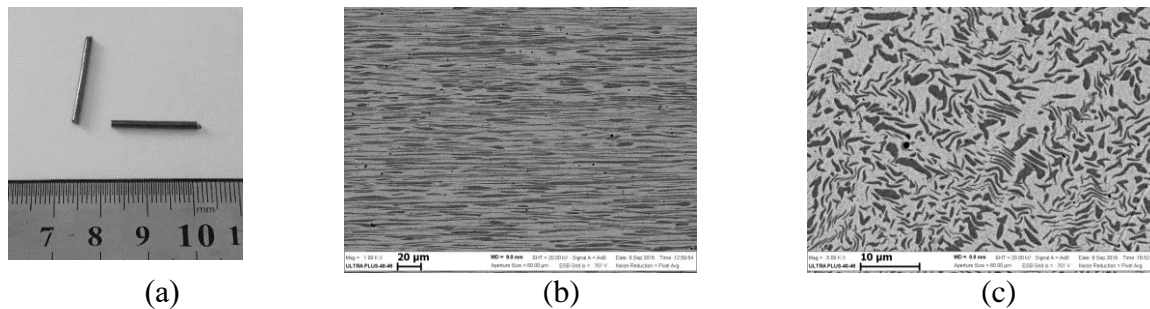


Fig. 5. (a) Overall view and (b, c) microstructure of the wire specimens: (b) longitudinal and (c) transverse section.

Analysis of the microstructural data collected from a cut along the rod axis, see Figure 5, shows that such structurally ordered materials could well be used for further studies into their magnetism. Iron structural components consist of a multitude of nanoscale iron and copper particles, which forms the early identified multimodal structure that was obtained in the workpiece SHS and retained in remelting, machining, and thermal treatment.

1. X. Yang, C. Jiang, J. Zou, X. Wang, Preparation and characterization of CuFe alloy ribbons, *J. Rare Met. Mater. Eng.*, 2015, vol. 44, iss. 12, pp. 2949–2953
2. T. Mittlera, T. Gresha, M. Feistlea, M. Krinningera, U. Hofmannb, J. Riedleb, R. Gollea, W. Volk, Fabrication and processing of metallurgically bonded copper bimetal sheets, *J. Mater. Proc. Tech.*, 2019, vol. 263, pp. 33–41.
3. V.V. Sanin, M.R. Filonov, V.I. Yuhvid, Y.A. Anikin, Structural investigation of 70Cu/30Fe based cast alloy obtained by combined use of centrifugal casting-SHS process and forging, *J. MATEC Web Conf.*, 2017, vol. 129, pp. 1–4.
4. M.R. Filonov, Yu.A. Anikin, Yu.B. Levi, Fundamentals for production of amorphous and nanocrystalline alloys by melt spinning technique, Moscow: Izd. MISiS, 2006, 327 p.

## SHS BORON-CONTAINING LIGATURES, INTRODUCTION INTO THE MELT AND THE RESEARCH OF INFLUENCE ON THE PROPERTIES OF THE RESULTING ALUMINUM-MATRIX COMPOSITES

V. V. Sanin<sup>\*a</sup>, M. R. Filonov<sup>a</sup>, Yu. A. Anikin<sup>a</sup>, V. I. Yuxhvid<sup>b</sup>, and D. M. Ikornikov<sup>b</sup><sup>a</sup>National University of Science and Technology MISiS, Moscow, 119049 Russia<sup>b</sup>Merzhanov Institute of Structural Macrokinetics and Materials Science, Russian Academy of Sciences, Chernogolovka, Moscow, 142432 Russia

\*e-mail: sanin@misis.ru

DOI: 10.24411/9999-0014A-2019-10147

Production of strong, durable, and thermally stable materials is one of the most important challenges of the today's metallurgy and material science. What makes aluminum matrix composite materials (AMC) so interesting is their unique properties, which combine low weight, high strength, high stiffness and modulus of elastic, low thermal expansion, and good wear resistance. This is what makes AMC promising and important materials that find use in many industries [1]. Of special interest are Al-based materials alloyed with boron and heavy metals (W, Mo) [1, 2]. Such alloying systems could feature a long-needed set of properties, including the structural properties of Al-based materials and radiation protection necessary for low-power nuclear plants used in aerospace, as well as for the space-based and terrestrial wireless electronics protections, which must feature specific weight and size.

The main challenge of making composites is to ensure the effective interaction of matrices and strengthening phases. In particular, direct injection of refractory particles (especially nanoscale ones) in an aluminum melt is nearly impossible due to their agglomeration and flotation caused by poor wettability in liquid metal. This challenge could be addressed by pre-made ligatures. Of importance is the way of synthesis of ligature, which helps optimize the phase composition of the strengthening phase particles.

To obtain ligatures of controlled phase composition, this research used self-propagating high-temperature synthesis. SHS can be used to make inorganic compounds of various classes (carbides, borides, nitrides, hydrides, silicides, oxides, intermetallics, and phosphides) as individual compounds or more complex ones [3]. With respect to light alloys, SHS ligatures consisting of individual crystallites of the target refractory phase are apparently feasible and promising. Agglomeration could be prevented by producing particles of refractory compounds separated with a thin matrix-alloy layer that melts while the ligature is being injected. Cast modified ligatures were synthesized (with a controlled alloying level and components) by front burning involving various active components injected directly into the source exothermic formulations. The burning of such formulations helps attain a temperature needed for melting the combustion products or producing cast synthesized ingots.

For this research, three boron-containing ligature systems were selected: (1) Co–B–Al, (2) Ni–B–Al, and (3) W–B–Al. Macrostructural analysis of the SHS-produced ingots for all the three systems revealed that defect-free ingots were formed at overloads above 30 to 40 g, depending on the system. Ingots synthesized at low overloads (below 30g) had gaseous (Fig. 1) and nonmetallic (aluminum oxide) inclusions, which was why ingots were further synthesized at  $\pm 50g$ . Analysis of microstructure of SHS ingot confirmed the presence of all the target elements. Figure 2 shows SEM images of W–B–Al ligature; apparently, the target alloy has quite a dense structure without gaseous porous inclusions, which is important for the subsequent melting of the ligatures and Al by VIM. The morphology of the boride-phase ( $W_2B_5$ ) particles is clearly faceted, which is typical of most boride materials.

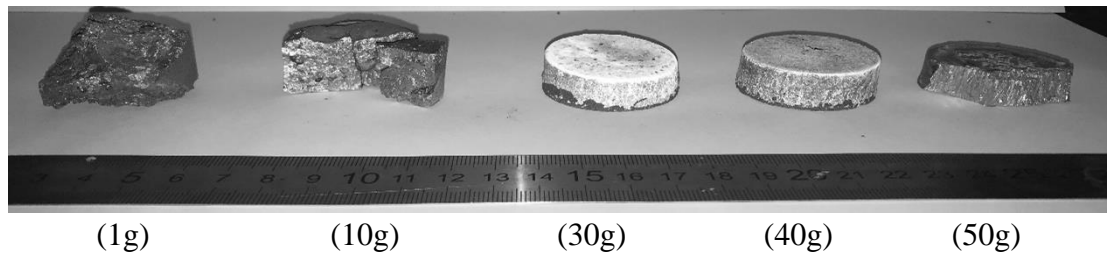


Fig.1. Overall view of the cast samples of the W–B–Al ligature of the system after removal from the mold at different values of overload.

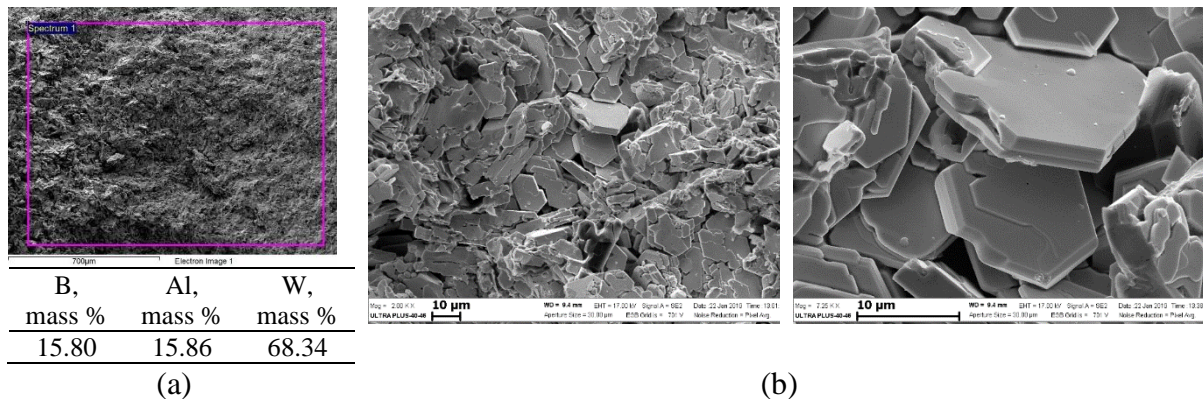


Fig. 2. (a) EDS data and (b) SEM images of the synthesized SHS-alloy modifying ligature for the W–B–Al system.

Injection of synthesized modifiers (SHS ligatures) in the aluminum melt was done in a Leybold-Heraeus vacuum furnace that can control the temperature and time of fusing. Pure aluminum (A99) was molten in vacuum as follows: heat to 700°C, cure for 5 min (during the 3rd minute, release Ar to 0.02 MPa), then inject a configured dose of the alloying formulation (SHS ligature) via a dispenser into the resulting melt.

Figure 3 presents the results of EDS analysis of melted AMC. Figure 3a demonstrates a zonal localization of higher Ni concentrations. Zonal inclusions have a mesh structure and are relatively uniformly distributed throughout the alloy. Unlike Ni, boron is distributed evenly regardless of the zonal Ni concentrations. Figure 3b shows that in the Al–Co–B alloying system, the post-fusing distribution is even for all the target elements, no zonal localization of boron or cobalt. EDS analysis data of the third system (Figure 3c) show that both tungsten and boron are evenly distributed throughout the alloy.

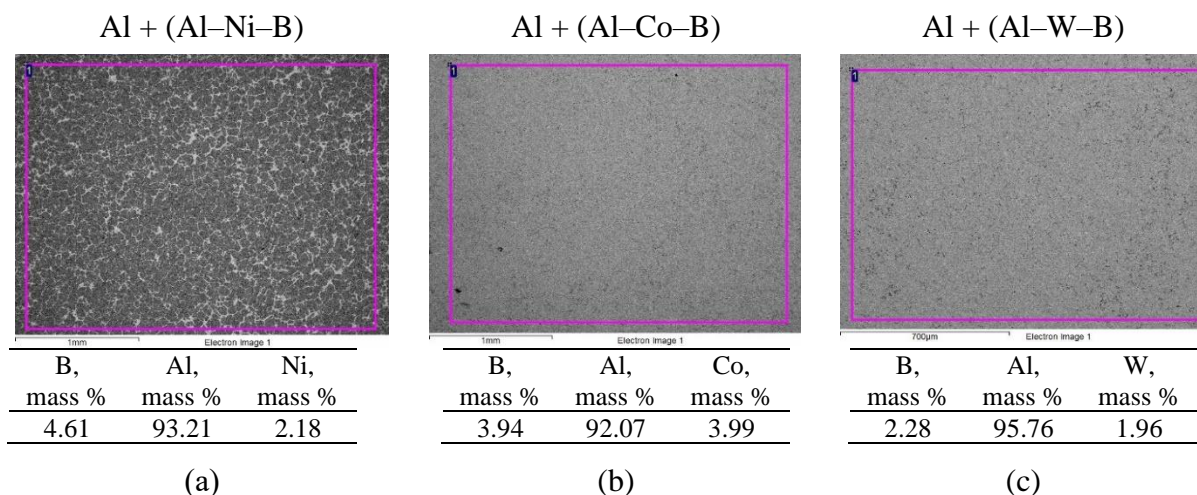


Fig. 3. EDS data of melted AMC.

Mechanical tests of cast rods of AMC modified with boron-containing alloying formulations were carried out (see Table 1).

Experimental data obtain for all the three systems during the reported study period represent the first positive experience of producing modified Al alloys by sequential combination of SHS (to synthesize cast boron-based ligatures) ensued by the injection of the synthesized alloying formulations during the VIM process.

Table 1. Mechanical properties of Al–Co–B, Al–Ni–B, and Al–W–B samples.

| Sample  | Yield strength, MPa | Maximum load, kN | Tensile strength, MPa | Relative extension, % | Impact energy, J | Impact strength, KCU, J/cm <sup>2</sup> | Hardness, HV |
|---------|---------------------|------------------|-----------------------|-----------------------|------------------|---|--------------|
| Al–Co–B | 64.90               | 2.51             | 127.75                | 16.67                 | 20.92            | 16.67                                   | 38.0         |
| Al–Ni–B | 45.76               | 1.93             | 98.19                 | 33.33                 | 74.70            | 33.33                                   | 42.0         |
| Al–W–B  | 52.51               | –                | 97.47                 | 28.91                 | –                | 46                                      | –            |

The reported study was funded by RFBR according to the research project no. 18-38-00932.

1. L. Klein, B. von Bartenwerffer, M.S. Killian, P. Schmuki, S. Virtanen, The effect of grain boundaries on high temperature oxidation of new  $\gamma$ '-strengthened Co–Al–W–B superalloys, *J. Corros. Sci.*, 2014, no. 9, pp. 29–33.
2. H. Ahmoum, M. Boughrara, M. Kerouad, Electronic and magnetic properties of Al doped (w-BN) with intrinsic vacancy, *J. Superlattices Microstruct.*, 2019, no. 1, pp. 186–190.
3. V.N. Sanin, D.M. Ikornikov, V.I. Yuxhvid, E.A. Levashov, Centrifugal SHS metallurgy of cast alloys based on nickel aluminide, high boron alloy, *Tsvet. Met.*, 2014, no. 11, pp. 83–88.

## INTEGRATED PROCESS SHS-REMELTING-PREP FLOW SHEET PRODUCTION OF NiAl–Fe COMPOSITE MICROGRANULES FOR THE ADDITIVE TECHNOLOGY

V. V. Sanin<sup>\*a</sup>, M. R. Filonov<sup>a</sup>, E. A. Levashov<sup>a</sup>, V. I. Yukhvid<sup>b</sup>, Zh. A. Sentyurina<sup>c</sup>,  
and A. I. Logacheva<sup>c</sup>

<sup>a</sup>National University of Science and Technology MISiS, Moscow, 119049 Russia

<sup>b</sup>Merzhanov Institute of Structural Macrokinetics and Materials Science, Russian Academy of Sciences, Chernogolovka, Moscow, 142432 Russia

<sup>c</sup>JSC Kompozit, Korolev, 141070 Russia.

\*e-mail: sanin@misis.ru

DOI: 10.24411/9999-0014A-2019-10148

Granular metallurgy is one of the most effective ways to make products of brittle and hard-to-machine materials. Making products of a complex shape by AT requires a source powder, where microgranules have regular spherical shape and regulated and rather narrow particle-size distribution. One urgent problem of today is the need to develop brand-new technologies for the production of microgranules (powders) and metal-powder compositions in Russia, tailored to address its environmental and energy-saving challenges. The alloyed intermetallic NiAl is a promising basis for lightweight high-temperature structural materials for use in aerospace industries. Earlier papers [1, 2] described the difficulties and problems of making electrodes from complex-alloyed intermetallic (CompoNiAl) alloys by combining SHS and VIM methods.

This paper proposes a brand-new combined sequential method for making composite (CompoNiAl) spherical microgranules. The proposed process consists of the following steps: (1) synthesis of CompoNiAl intermetallic alloy of a regulated chemical composition by the centrifugal SHS method; (2) machining of synthesized SHS materials (CCM) by vacuum induction melting or inert medium melting, then casting in special tube mold tube to make a shell; (3) centrifugally spraying (PREP) of produced steel-shell electrode to make spherical composite microgranules. This method can produce composite intermetallic microgranules consisting of remelted alloy and shell material (Fe, Ni, etc.). The research team originally ran a series of experiments to optimize the synthesis of the multicomponent intermetallic alloy CompoNiAl by SHS metallurgy [1, 3]. The high gravity of the centrifugal unit would scatter the combustion products during such synthesis, intensify the separation of metal phase (the alloy) from oxide phase (corundum), and facilitate the homogenization of the alloy, producing a finer-grained structure. Figure 1 shows experimental ingots produced under various overloads (from 1 to 300 g).

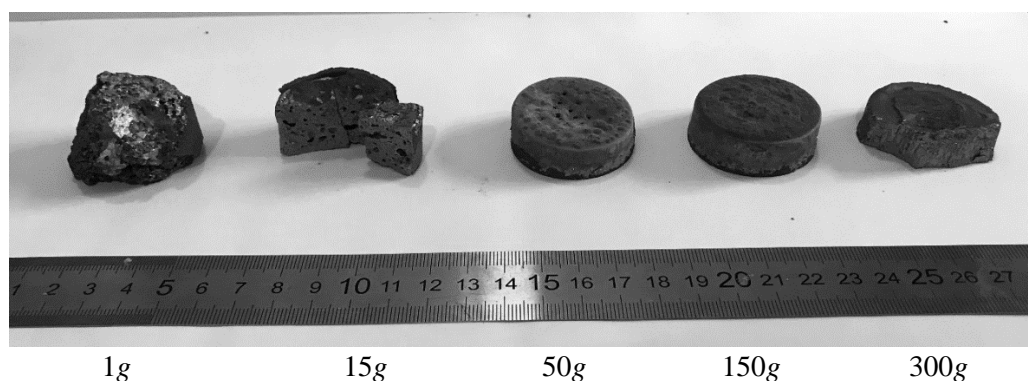


Fig. 1. Overall view of samples obtained under various overloads (g).

Ingots synthesized at 150 to 300 g had no visible inclusions or residual porosity. All the specimen produced at the specified overload looked solid-cased and had two pronounced layers: target alloy and oxide layer ( $\text{Al}_2\text{O}_3$ ).

We preliminarily studied the two-phase area of the synthesized SHS alloy and identified its melting point. To that end, we adjusted the attenuation decrement (the logarithm of the preceding-to-previous amplitude ratio) of the HTV machine [3, 4]. This method is suitable for study of phase transitions, construction of various functions, and for analyze of influence of heating parameters and exposures on the coagulation and dissolution of the strengthening phases. The next step was to use vacuum induction melting (VIM) of the SHS-produced CompoNiAl workpieces for casting in steel tubes of various diameters.

Melt and cast of the alloy in the molds of various diameters were carried out (Fig. 2). The optimal option was to use a cylindrical mold with 6 mm thick walls. Raising the mold wall thickness to 6 mm produced defect-free, holistic, layered electrodes from the intermetallic alloy in a steel shell without any chemical impact or “blurring” the inner wall (Fig. 2c). CompoNiAl does not chemically react with the steel tube mold. The alloy is retained due to friction as well as due to the fact that CompoNiAl and steel tube are close in the coefficient of thermal expansion (CTE). The integrity, lack of inner pores and cavities in the produced layered electrode are confirmed by ultrasonic testing (Fig. 3).

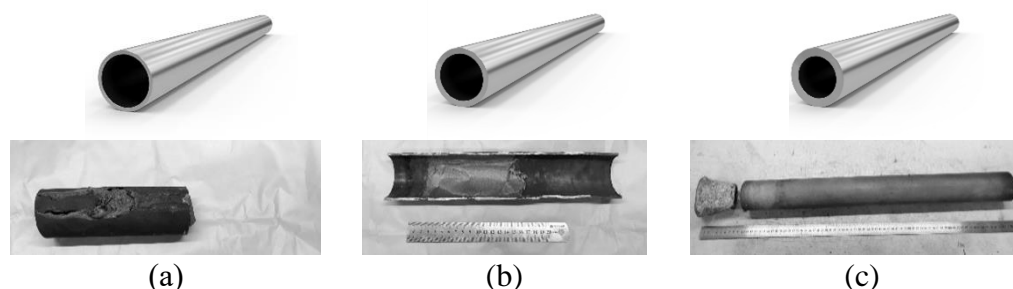


Fig. 2. Experimental samples of pipe-molds with different wall thicknesses: (a) 3 mm, (b) 5 mm, and (c) 6 mm.

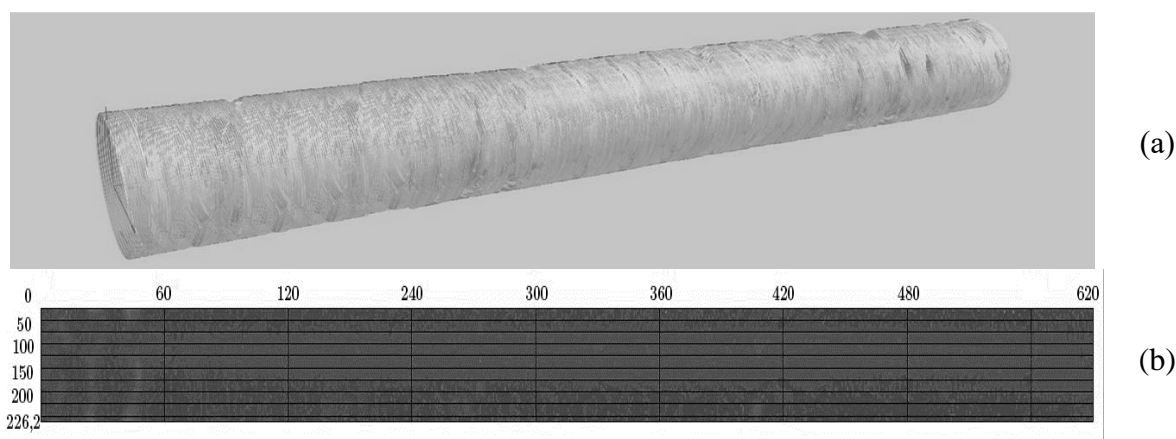


Fig. 3. Analysis of the UT: (a) 3D visualization of the integrity of the inner part of the layered electrode (alloy CompoNiAl); (b) analysis of the integrity of the shell (steel pipe)

The final stage of the work is the approbation of sputtering of the obtained CompoNiAl + Fe layered electrode, obtaining and studying the final product in the form of spherical composite microgranules.

During the plasma rotating electrode process (PREP), under the action of centrifugal forces, the melt in the film moves from the center to the periphery of the consumable electrode, then accumulates on the edge with a Fe-shell and fuses with it. Thus, the compositions are mixed



with the formation of a composite microgranule.

The image of composite microgranules obtained is presented in Fig. 4b. Most microgranules have a spherical shape. There are no satellite particles on the surface of the granules, which is one of the advantages of PREP. Also microcrystals contain no crystallization defects (pores).

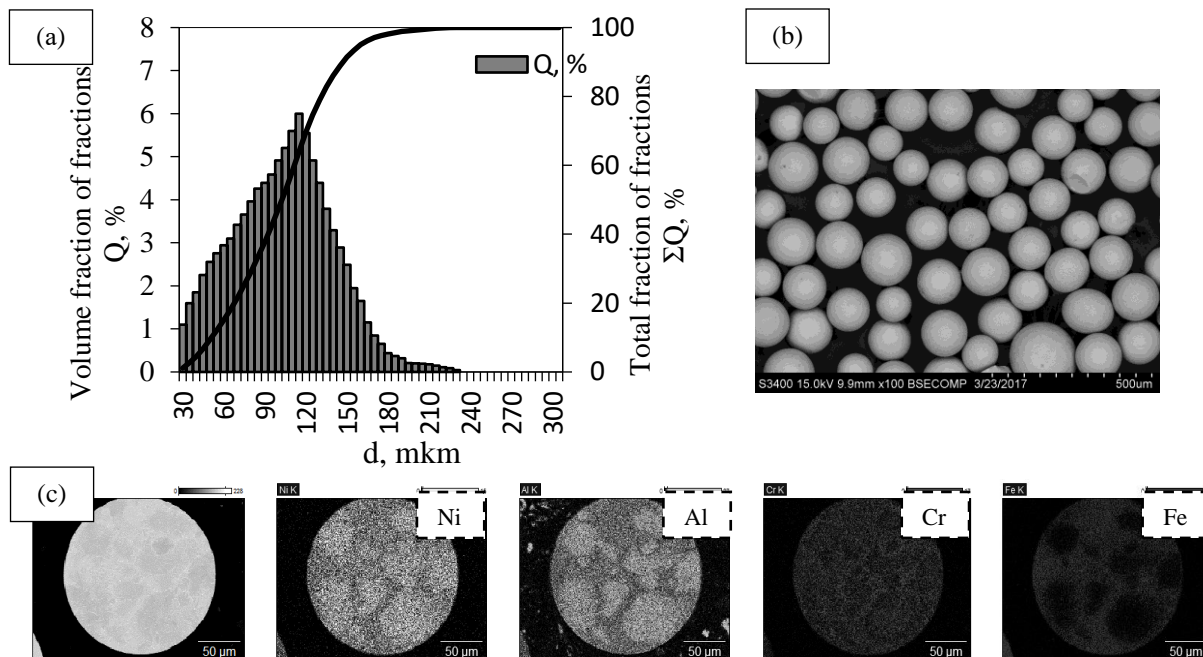


Fig. 4. (a) Fractional composition of composite microgranules; (b) SEM image of microgranules; (c) microgranule component distribution map.

Particle-size distribution is shown in Fig. 4a. The proposed method was able to produce microgranules of different size. Most of the composite microgranules are within 50 to 150 μm, which suits the needs of AT products. Figure 4c shows the structural component distribution maps. The basis here is the dendritic NiAl grains distributed across the entire microgranule with an average dendritic-branch size of 2 to 15 μm. Fe and Co are distributed throughout a microgranule.

1. Yu.S. Pogozhev, V.N. Sanin, D.M. Ikornikov, D.E. Andreev, V.I. Yuxhvid, E.A. Levashov, Zh.A. Sentyurina, A.I. Logacheva, A.N. Timofeev, NiAl-based electrodes by combined use of centrifugal SHS and induction remelting, *Int. J. Self-Propag. High-Temp. Synth.*, 2016, vol. 25, no. 3, pp. 186–199.
2. A.A. Zaitsev, Zh.A. Sentyurina, E.A. Levashov, Yu. S. Pogozhev, V.N. Sanin, P.A. Loginov, M.I. Petrzhik, Structure and properties of NiAl–Cr(Co,Hf) alloys prepared by centrifugal SHS casting, *J. Mater. Sci. Eng. A*, 2017, pp. 463–472.
3. V.V. Sanin, Yu.A. Anikin, V.I. Yuxhvid, M.R. Filonov, Structural heredity of alloys produced by centrifugal SHS: influence of remelting temperature, *Int. J. Self-Propag. High-Temp. Synth.*, 2015, vol. 24, no. 4, pp. 210–214.
4. M.R. Filonov, Yu.A. Anikin, Yu.B. Levin, Fundamentals for production of amorphous and nanocrystalline alloys by melt spinning technique, Moscow: Izd. MISiS, 2006, 327 p.

## SOLUTION COMBUSTION SYNTHESIS OF DOPED $\text{Ca}_2\text{AlMnO}_5$ AS A NEW OXYGEN STORAGE MATERIAL

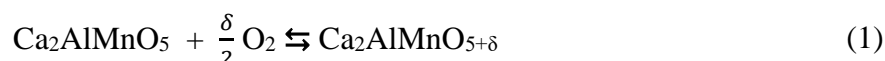
A. Sato, G. Saito, K. Abe, T. Nomura, and T. Akiyama

Center for Advanced Research of Energy and Materials, Hokkaido University,  
Kita 13 Nishi 8 kita-ku, Sapporo, 060-8628 Japan

\*e-mail: vr38dett@live.jp

DOI: 10.24411/9999-0014A-2019-10149

Oxygen is used in many fields such as steelmaking, garbage incinerator, welding, rocket fuel, etc. Although cryogenic separation from air is a mainstream of the current oxygen production method, PSA (Pressure Swing Adsorption) process using an oxygen storage material (OSM) as a more energy saving method attracts attention. As the OSM,  $\text{Ca}_2\text{AlMnO}_5$  (CAMO) is promising because oxygen storage/release performance is high [1]. As shown in Fig.1, CAMO has a brownmillerite-type structure whose chemical composition is expressed as  $\text{A}_2\text{B}_2\text{O}_5$  in which oxygen vacancies of the perovskite structure  $\text{ABO}_3$  are ordered [2]. The B site has a composition in which Al and Mn occupy orderly at a ratio of 1:1.  $\text{AlO}_4$  tetrahedral layer and  $\text{MnO}_6$  octahedral layer are alternately arranged, but when oxygen is occluded, the  $\text{AlO}_4$  tetrahedron partially oxidizes and changes to  $\text{AlO}_6$  octahedron. The following reaction occurs in the CAMO during oxygen adsorption/desorption:



The above reversible absorption/desorption reaction is induced by temperature and pressure changes. However, CAMO has problems such as lowering the operating temperature range, reducing hysteresis, increasing the speed of adsorption and desorption. Improvement of properties can be expected by doping Ca and Mn sites in CAMO with trace elements, but it is still in the theoretical stage and not verified experimentally [3]. Therefore, in order to improve the properties, we attempted to dope La into the Ca site of CAMO. Doping of trivalent La into bivalent Ca will cause the lattice size change due to the change in the valence of Mn and the difference of the ion radii between La and Ca (1.12 and 1.17 Å, respectively). In this study, we investigated the effects of La doping into Ca sites in CAMO on the oxygen storage characteristics.

We tried to synthesize CAMO by solution combustion synthesis. Solution combustion synthesis (SCS) is a combustion synthesis process based on a highly exothermic, self-sustaining reaction generated by heating a solution mixture of aqueous metal salts and fuels such as urea, citric acid, and glycine. This approach has been used to synthesize a variety of compounds including binary and complex oxides, such as ferrites, spinels, and perovskites [4–6]. This

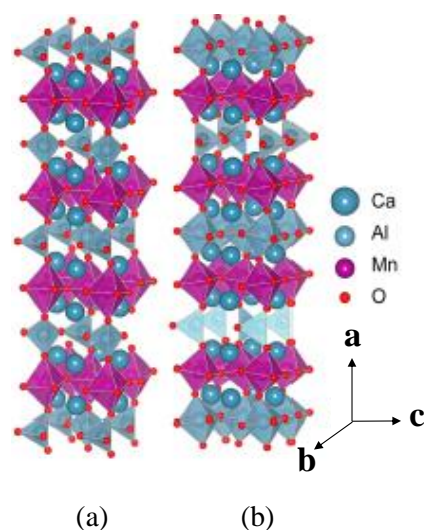


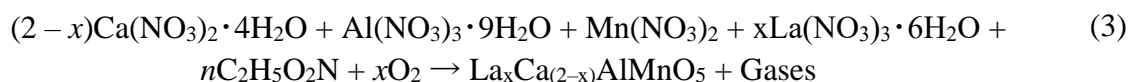
Fig. 1. Schematic illustration of the crystal structures of (a) Brownmillerite-type  $\text{Ca}_2\text{AlMnO}_5$  and (b) its fully oxygenated form  $\text{Ca}_2\text{AlMnO}_{5+\delta}$  [1].

method not only yields nanosized products exhibiting large specific surface areas but also enables uniform (homogeneous) doping of trace amounts of various elements in a single step. The characteristics (including the purity, structure and size) of the SCS oxide powders are typically determined by several synthetic parameters, such as the species of fuel and oxidizer reactants, the fuel-to-oxidizer ratio, and the subsequent sintering treatment after SCS [7]. In addition, in this experiment by SCS, the synthesis time is also very short, about 1 min.

Precursors of  $\text{La}_x\text{Ca}_{(2-x)}\text{AlMnO}_5$  were prepared by a solution combustion synthesis (SCS) method. Reagents of  $\text{Ca}(\text{NO}_3)_2 \cdot 4\text{H}_2\text{O}$  (99.0%),  $\text{Al}(\text{NO}_3)_3 \cdot 9\text{H}_2\text{O}$  (99.9%),  $\text{Mn}(\text{NO}_3)_2$  (50.0% aqueous solution),  $\text{La}(\text{NO}_3)_3 \cdot 6\text{H}_2\text{O}$  (99.9%) and glycine (99.0%) were used as raw materials. Glycine was charged as a fuel for the SCS. As an index for determining the amount of glycine to be added, the fuel ratio  $\Phi$  was defined by the following formula.

$$\Phi = \frac{\text{total valency of fuel}}{\text{total valency of oxidizer}} \quad (2)$$

In this reaction the relationship between  $\Phi$  and  $n$  is  $\Phi = n/5$ . Here,  $\Phi = 1$  means a stoichiometric sample in Eq. (2),  $\Phi < 1$  means a sample with a small amount of fuel (= reducing agent), and  $\Phi > 1$  means a fuel excess condition. The fuel ratio of all samples was set to  $\Phi = 1$  [8]. The SCS reaction of  $\text{La}_x\text{Ca}_{(2-x)}\text{AlMnO}_5$  is expressed by the following equation.



The reagents were weighed according to the eq. (3) and 10 ml of distilled water was added to them. They were stirred and dried at  $90^\circ\text{C}$  for 4 h to obtain a gel-like sample. This gel-like sample was put in a cylindrical reaction vessel preheated to  $400^\circ\text{C}$  to carry out the SCS. A schematic diagram of the SCS equipment used in this experiment is shown in Fig. 2.

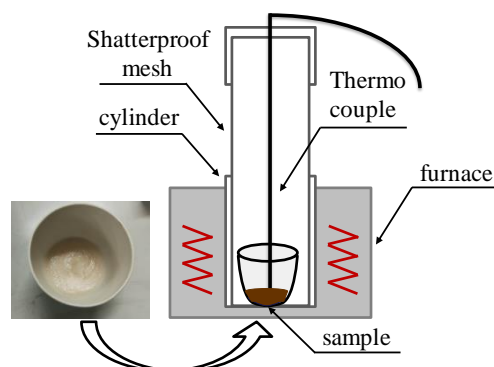


Fig. 2. Schematic illustration of the solution combustion synthesis.

The obtained sample was annealed at  $1250^\circ\text{C}$  in air for 12 h and then annealed again at the same temperature and time under an Ar atmosphere to remove excess oxygen in the sample. Phase identification of the obtained product was conducted by XRD, and oxygen adsorption/desorption of the SCS samples was examined by TG-DSC.

Figure 3 shows the XRD patterns of the SCSed  $\text{La}_x\text{Ca}_{(2-x)}\text{AlMnO}_5$ . The main peaks of all the SCSed samples corresponded to those of the brown mirror light structure. That meant substitution of La to the Ca-site maintained the CAMO structure. The peaks of perovskite-type impurity phases were observed when La was excessively doped ( $x \geq 0.1$ ). In addition, as the amount of La added increases, the peak of CAMO weakens, and the peak of the perovskite-type impurity phase appears more notably. The simple perovskite phase other than the CAMO phase occurred at  $x \geq 0.1$  and did not occur at  $x \leq 0.05$ .

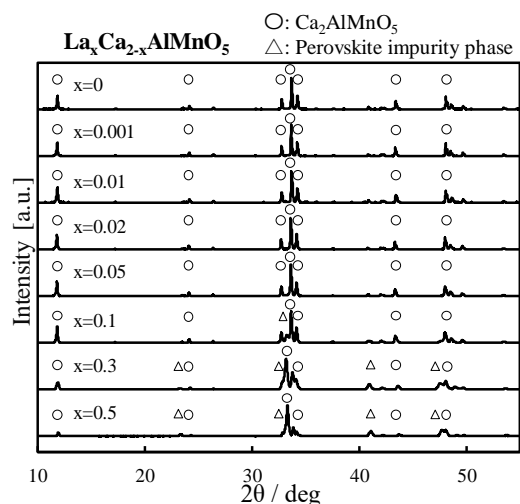
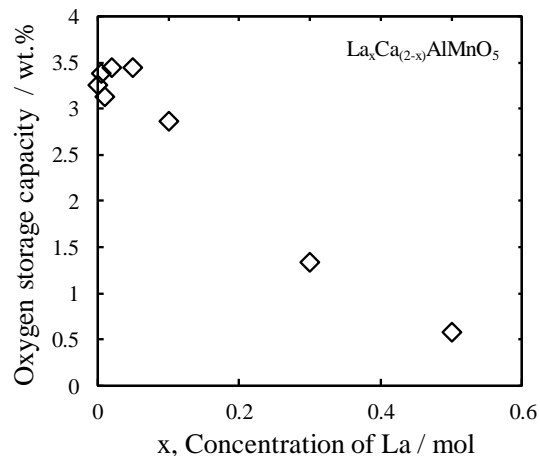

 Fig. 3. XRD patterns of  $\text{La}_x\text{Ca}_{(2-x)}\text{AlMnO}_5$ .


Fig. 4. Relationship between the amount of La doped and the oxygen storage amount

Figure 4 shows the maximum oxygen storage amounts of the La-doped CAMO. The oxygen storage amounts were evaluated based on the thermogravimetric change of the samples. The amount of stored oxygen was slightly increased up to  $x \leq 0.05$ . On the other hand, when  $x \geq 0.1$ , the storage amount of oxygen was greatly reduced with the addition amount of La. The decrease in the oxygen storage amount was due to the perovskite impurity phase. Figure 5 shows the relationship between the amount of La doped and the lattice volume of the SCSed CAMO. The lattice volume was calculated based on the XRD data. There was two different tendencies in the change of the lattice volume; the lattice volume increased with larger amount of doped La at  $x < 0.10$  but decreased at  $x \geq 0.10$ . At  $x < 0.10$ , the doped La increased the lattice constant; the ion radii of La and Ca are 1.7 and 1.12 Å, respectively. On the other hand, the lattice shrank with the larger amount of doped La at the range of  $x \geq 0.1$ . A perovskite impurity phase was generated at  $x \geq 0.1$ , resulting in the decrease in lattice constant.

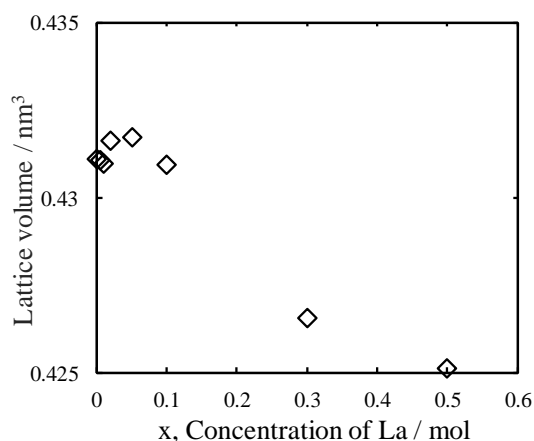


Fig. 5. Relationship between the amount of La doped and lattice volume.

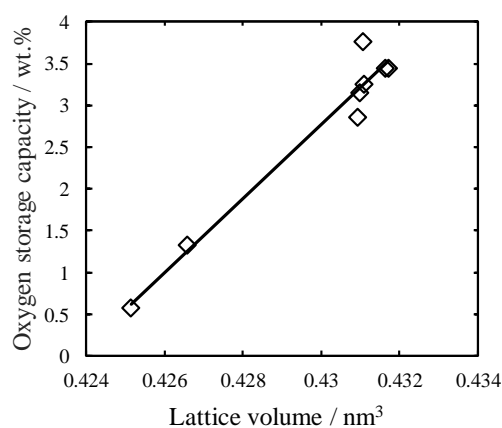


Fig. 6. Relationship between the lattice volume and the oxygen storage amount.

La-doped CAMO was successfully synthesized by SCS. Although the oxygen storage capacity decreased when La doped was too much, the oxygen storage capacity increased with an appropriate amount of La doped. When it was La doped too much, a perovskite impurity phase was generated and the oxygen storage characteristics were degraded. Increase in lattice volume by appropriate amount of La doped led to increase in oxygen storage capacity (Fig. 6).

1. T. Motohashi, Y. Hirano, Y. Masubuchi, K. Oshima, T. Setoyama, S. Kikkawa, *Chem. Mater.*, 2010, vol. 22, 3192.
2. A.J. Wright, H.M. Palmer, P.A. Anderson, G. Greaves, *Chem. Mater.*, 2002, vol. 12, pp. 978–982.
3. A. Ling, R. Zhang, H. Jia, *ACS Appl. Mater. Interface*, 2015, vol. 7, pp. 14518–14527.
4. G. Xanthopoulou, *Adv. Sci. Technol.*, 2011, vol. 63, pp. 287–96.
5. A. Mukasyan, P. Dinka, *J. Self-Propag. High-Temp. Synth.*, 2007, vol. 16, pp. 23–35.
6. S.T. Aruna, A. Mukasyan, *Curr. Opin. Solid State Mater. Sci.*, 2008, vol. 12, pp. 44–50.
7. A. Zhu, A. Nobuta, I. Nakatsugawa, T. Akiyama, *Int. J. Hydrogen Energy*, 2013, vol. 38, pp. 13238–13248.
8. T. Nomura, C. Zhu, N. Sheng, R. Murai, T. Akiyama, *J. Alloys Compds*, 2015, vol. 645, pp. 900–905.

**THE STUDY OF HIGH-ENTROPY CERAMICS  $\text{Hf}_{0.2}\text{Ta}_{0.2}\text{Ti}_{0.2}\text{Nb}_{0.2}\text{Mo}_{0.2}\text{C}$   
AND  $\text{Hf}_{0.2}\text{Ta}_{0.2}\text{Ti}_{0.2}\text{Nb}_{0.2}\text{Zr}_{0.2}\text{C}$  OBTAINED BY SHS  
AND SPARK PLASMA SINTERING****A. Sedegov<sup>\*a</sup>, S. Vorotilo<sup>a</sup>, V. Tsybulin<sup>a</sup>, K. Kuskov<sup>a</sup>, D. Moscovskikh<sup>a</sup>,  
S. Vadchenko<sup>b</sup>, and A. Mukasyan<sup>a,c</sup>**<sup>a</sup>National University of Science and Technology MISiS, Moscow, 119049 Russia<sup>b</sup>Merzhanov Institute of Structural Macrokinetics and Materials Science, Russian Academy of Sciences, Chernogolovka, Moscow, 142432 Russia<sup>c</sup>University of Notre Dame, Notre Dame, IN 46556 USA

\*e-mail: a.sedegoff@gmail.com

DOI: 10.24411/9999-0014A-2019-10150

Conventionally, the majority of alloys are based on one main constituent element. For the increase of properties and performance, they are alloyed by alloying elements which enhance the alloy's strength, corrosion resistance and other properties. Thus, the families of alloys are made. However, the number of elements is limited; therefore, the number of alloys which could be developed on the base of one or two main constituent elements is finite. However, what if one is to go outside the classical definition and increase the number of constituent elements? This conception was first suggested in 1995 [1], and these materials were later branded as high-entropy alloys [2].

High-entropy materials by definition contain five or more main constituent elements with the concentration between 5 and 35% [3]. The currently available data in the areas of physical metallurgy and binary and ternary diagram suggests that such multicomponent alloys might contain dozens of phases and intermetallics, which are usually brittle and have limited applicability. However, in contrary to these expectations that the increased entropy in these alloys leads to the formation of solid solutions with a relatively simple structure, thus diminishing the content of unwanted phases or eliminating them. These peculiar features, related to high entropy, are of the utmost importance for the development and applications of the high-entropy alloys.

During the last years of investigation of high-entropy materials, more than 300 compositions with wide functionality were developed on the basis on non-ferrous and refractory metals. Currently, the hottest topic is the development of high-entropy alloys (HEA) for high-temperature applications, which require high phase stability upon heating up to 1800°C, oxidation resistance and high-temperature strength.

Due to their unique multi-component compositions, HEAs might possess a complex of outstanding properties, including high strength and hardness, unmatched high-temperature strength, good structural stability, and corrosion resistance. The close interest in the development of these materials is driven by the demand for the materials with increased operating temperature from the aerospace industry.

Equimolar composition  $\text{HfTaTiZrNbMo}$  was investigated in [4] and demonstrated the high mechanical properties at room temperature and 1200°C. Xueliang Yan et al. in their recent article [5] synthesized a high-entropy with the composition  $(\text{Hf}_{0.2}\text{Zr}_{0.2}\text{Ta}_{0.2}\text{Nb}_{0.2}\text{Ti}_{0.2})\text{C}$  from the monocarbides, which were mixed in a mill and consolidated by spark plasma sintering at 2000°C. The produced material is characterized by high thermal conductivity, thermal diffusivity, and the coefficient of thermal expansion, which was compared to the initial monocarbides. In various articles dedicated to the investigation of HEAs, the samples are usually produced by arc melting. However, this production route often leads to the formation

of a dendritic structure, leading to the degradation of mechanical properties. To retain the fine-grain structure, which is most beneficial for mechanical properties, the powder metallurgy route is most perspective, since it ensures the homogeneity of material. Also, as a new class of high-entropy, Jian Luo et al. [6] described the ultra-high-temperature diboride ceramic based on the Hf–Ta–Ti–Nb–Mo–Zr system. In our work, a high-entropy alloy Hf–Ta–Ti–Nb–Mo–Zr and the related high-entropy carbide were produced by high-energy ball milling and spark plasma sintering.

The majority of high-entropy materials are produced by vacuum arc melting, which requires high energy expenditures. In this work, high-entropy materials were produced by various routes, which involve the mixing of metal powders and carbon, subsequent synthesis, and sintering.

For the obtain of high-entropy ceramics (HEC-1 corresponds to the composition  $(\text{Hf}_{0,2}\text{Ta}_{0,2}\text{Ti}_{0,2}\text{Zr}_{0,2}\text{Nb}_{0,2}\text{Mo}_{0,2})\text{C}$ ; HEC-2 corresponds to the composition  $(\text{Hf}_{0,2}\text{Ta}_{0,2}\text{Ti}_{0,2}\text{Zr}_{0,2}\text{Nb}_{0,2}\text{Zr}_{0,2})\text{C}$ ), the mixture of powders were treated in the planetary ball mill Activator-2S (Russia). High-energy ball milling (HEBM) was organized according by the following scheme: milling of the mixture of metals during 90 min (+ 5 min with hexane to ensure the unloading the powder from the surface of jars and balls), then milling of pre-milled metal powders with graphite for 5 min i.e mechanical activation (MA) of reaction mixtures.

After MA, self-propagating high-temperature synthesis of powders was carried out. It can be seen in Fig. 1 that after MA of metals and carbon powder, a mixture without a crystalline structure is obtained (the black line for the two mixtures is similar). And as a result of the SHS, a material with an FCC lattice is formed. First-stage HEBM produced amorphous powders, which did not react with the carbon during the second stage of HEBM. Then the high entropy carbide was synthesized in the lab reactor in an argon atmosphere. Combustion temperature and rate were measured during the synthesis. Combustion rate was 4.17 and 7.69 mm/s for HEC-1 and HEC-2, respectively.

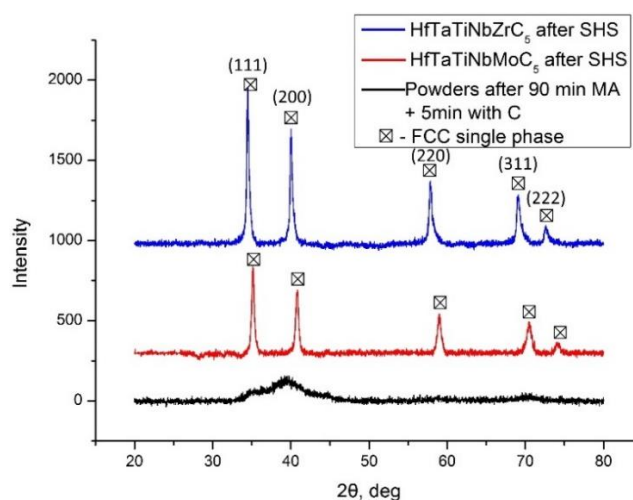


Fig. 1. XRD patterns for powders after HEBM and combustion synthesis.

Sintering of the powders produced by combustion synthesis (90-min milling of metals, 5-min milling of mixture of metals and graphite and subsequent combustion synthesis in lab reactor) was conducted on the hot pressing installation Dr. Fritsch DSP 515 (Germany) and spark plasma sintering installation SPS Labox 650 (Japan) in a graphite matrix in vacuum at temperatures 1800 °C, pressure 50 MPa, dwelling time 5 min.

Figure 2 presents the results of the SEM of sintered powder samples. Where there is clearly visible the presence of other phases and the difference in the size of the grains during hot pressing and the SPS method. The EDS analysis (Figs. 2b, 2d, 2h, 2f) showed that the light areas are more saturated with heavy metals such as hafnium and tantalum, and the black

inclusions in the grains are iron left after processing in steel drums. In general, it is clear that all elements are evenly distributed over the entire area, which makes it possible to call this material - high entropy ceramic.

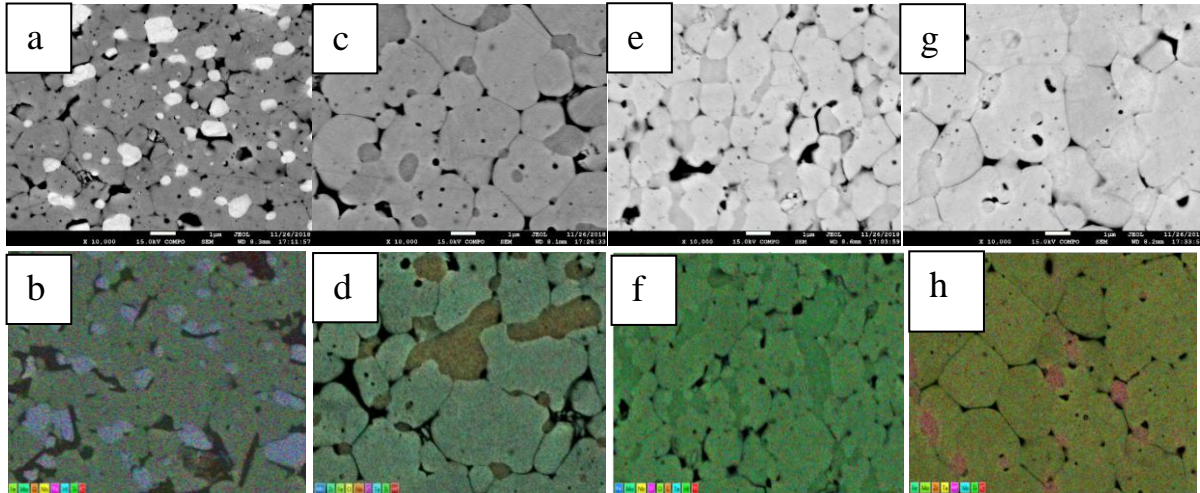


Fig. 2. SEM and EDS maps of ceramics: HEC-1, hot-pressed at 1800°C (a, b); HEC-1 SPSed at 1800°C (c, d); HEC-2 hot-pressed at 1800°C (e, f); HEC-2 SPSed at 1800°C (g, h).

The results of hardness measurements are presented in Table 1. It is important to note that the material sintered by the SPS method has a higher hardness compared with hot-pressed.

Table 1. Hardness test result.

| Material | Method of sintering  | Hardness, GPa |
|----------|----------------------|---------------|
| HEC-1    | Hot pressing 1800° C | 15.95         |
| HEC-1    | SPS 1800° C          | 22.62         |
| HEC-2    | Hot pressing 1800° C | 18.58         |
| HEC-2    | SPS 1800° C          | 20.53         |

This work was conducted with the financial support of the Russian Science Foundation (grant no. 18-79-10215).

1. K.H. Huang, J.W. Yeh, A study on multicomponent alloy systems containing equal-mole elements M.S. thesis. Hsinchu: National Tsing Hua University, 1996.
2. J.W. Yeh, S.K. Chen, S.J. Lin, J.Y. Gan, T.S. Chin, T.T. Shun, C.H. Tsau, S.Y. Chang, Nanostructured high-entropy alloys with multiple principal elements: novel alloy design concepts and outcomes, *Adv Eng Mater.*, 2004, vol. 6, pp. 299–303
3. Y. Zhang, T.T. Zuo, Z. Tang, et al, *Prog. Mater. Sci.*, 2014, vol. 61, pp. 1–93.
4. C.-C. Juan, M.-H. Tsai, C.-W. Tsai, C.-M. Lin, *Intermetallics*, 2015, vol. 62, 7683.
5. X. Yan, L. Constantin, J.-F. Silvain, et al, Hf<sub>0.2</sub>Zr<sub>0.2</sub>Ta<sub>0.2</sub>Nb<sub>0.2</sub>Ti<sub>0.2</sub>C high-entropy ceramics with low thermal conductivity, *J. Am. Ceram. Soc.*, 2018, vol. 101, no. 10, pp. 4486–4491.
6. J. Luo, J. Gild, T. Harrington, et al, High-entropy metal diborides: a new class of ultra-high temperature ceramics, in *Ultra-High Temperature Ceramics: Materials for Extreme Environment Applications IV*, Jon Binner, The University of Birmingham, Edgbaston, United Kingdom Bill Lee, Imperial College, London, United Kingdom Eds, ECI Symposium Series, 2017.



## PEROVSKITE-LIKE MATRIX FOR IMMOBILIZATION OF HIGH-LEVEL RADIOACTIVE WASTE PRODUCED BY SHS METHOD

A. O. Semenov<sup>\*a</sup>, M. S. Kuznetsov<sup>a</sup>, and O. Yu. Dolmatov<sup>a</sup>

National Research Tomsk Polytechnic University, Tomsk, 634050 Russia

\*e-mail: semenov\_ao@tpu.ru

DOI: 10.24411/9999-0014A-2019-10151

Active evolution of nuclear programs leads to the accumulation of high-level radioactive waste (HLW) [1]. The necessity of isolation of the most long-lived and biologically hazardous radionuclides from the environment for a long time and decreasing of the storage sites service life lead to the development of innovative technologies and creation of perspective materials for immobilization of waste and subsequent storage during the time for reduction of radioactivity to acceptable level. The growing necessity to isolate the most long lived and biologically hazardous radionuclides coupled with a shorter storage sites service life require new innovative technologies and materials for waste immobilization and further storage within the period of time needed for radioactivity reduction to acceptable levels for radioactive decay. Currently the most frequently used technology for the radioactive waste disposal is radionuclides vitrifying into aluminophosphate or borosilicate glasses [2]. Meanwhile, vitreous matrix materials are not an ideal solution in terms of time and storage conditions. Glass cannot ensure stable and safe HLW storage during several thousand years due to its chemical instability and tendency to spontaneous crystallization. Alternative materials for immobilization are crystalline matrices which are synthetic analogues of naturally occurring geologically stable minerals. Such minerals compounds (perovskite, monazite, zirconolite, pyrochlore, etc.) are able to reliably hold/contain highly active fractions of radioactive waste for a long time [3]. The application of these matrixes is complicated by the lack of industrial manufacturing techniques. One of the alternative methods of matrix production is self-propagating high-temperature synthesis (SHS). The advantages of SHS are the possibility of obtaining materials with desired properties, high purity of the final product, low energy consumption and the ability to control all the stages of the synthesis process [4]. The present paper shows experimental studies of perovskite-like matrix production by SHS-mode. A mixture of industrially manufactured powders of neodymium and aluminum oxides was added to nickel and aluminum powders following the stoichiometric ratio:



where  $\text{Nd}_2\text{O}_3$  was a simulator of the trivalent actinide fractions of radioactive waste because of the ionic radius of Nd is similar to different isotopes of actinides.

Reagents powders were mixed/prepared in an Erweka cubic mixer. The initial batch was pressed using a hydraulic laboratory press PGL-12 into cylindrical samples with a diameter of 25 mm and a height of 12–15 mm, but under/with different pressures: 15, 20, 25, 30, and 40 MPa to obtain samples with different densities. The synthesis was conducted under residual pressure (300 Pa) on an experimental installation for pyrometric studies of the SHS process which included a SHS-reactor.

We prepared a series of laboratory experiments on varying the content of the  $\text{Nd}_2\text{O}_3$ – $\text{Al}_2\text{O}_3$  additive from 10 to 40 wt % in the basic mixture of Ni–Al system and pressing pressure of 10–30 MPa to study the effect of density of the batch components and the dilution ratio on synthesis and phase composition of the immobilization matrix.

During the heating process a burning wave was initiated at the edges of samples and propagated over the entire sample volume if initial samples had a system density of 4.8–5.2 g/cm<sup>3</sup> (10–30 MPa) and a dilution ratio no higher than 30 wt % as well as initial temperature of 650–700 K (depending on the preparation conditions of the initial mixture). We observed local combustion areas without further wave generation followed by synthesis attenuation when the batch of Ni-Al was diluted by more than 30 wt % of Nd<sub>2</sub>O<sub>3</sub>–Al<sub>2</sub>O<sub>3</sub> regardless of the density of the mixture due to excessive dilution as well as energy consumption of the neodymium aluminate synthesis reaction.

Thermomechanical destruction of samples is observed when the density of the system is higher than 5.27 g/cm<sup>3</sup> (pressing pressure of 40 MPa) due to the non-stationarity of the combustion wave propagation. It can be explained by excessive density of the initial mixture which leads to a significant growth in the specific energy yield of reactions occurring in a unit volume of the sample.

On the next stage of research, the synthesized samples were subjected to XRD analysis to study the composition. The results of after synthesis phase formation for different percentages of the additive are summarized in Table 1.

Table 1. Results of XRD analysis.

| No. | P, MPa | Additive content<br>Nd <sub>2</sub> O <sub>3</sub> +Al <sub>2</sub> O <sub>3</sub> ,<br>x, wt % | Phase formation, wt %.         |                                |                                 |                    |      |                    |
|-----|--------|---|--------------------------------|--------------------------------|---------------------------------|--------------------|------|--------------------|
|     |        |   | Nd <sub>2</sub> O <sub>3</sub> | Al <sub>2</sub> O <sub>3</sub> | Ni <sub>2</sub> Al <sub>3</sub> | Al <sub>3</sub> Ni | NiAl | NdAlO <sub>3</sub> |
| 1   | 10     | 10  | 1.2                            | 8.3                            | 32.4                            | 21.1               | 21.2 | 15.7               |
| 2   | 20     | 10  | 2.3                            | 7.2                            | 35.2                            | 16.2               | 23.4 | 15.6               |
| 3   | 30     | 10  | 2.6                            | 4.5                            | 31.7                            | 1.1                | 33.5 | 26.6               |
| 4   | 10     | 20  | 8.3                            | 7.4                            | 27.3                            | 16.2               | 24.3 | 16.5               |
| 5   | 20     | 20  | 2.8                            | 6.6                            | 31.7                            | 15.6               | 25.4 | 17.9               |
| 6   | 30     | 20  | 4.9                            | 2.7                            | 27.2                            | -                  | 27.2 | 37.9               |
| 7   | 10     | 30  | 13.8                           | 12.6                           | 19.9                            | 22.2               | 15.4 | 16.1               |
| 8   | 20     | 30  | 8.1                            | 7.1                            | 26.2                            | 14.3               | 19.6 | 24.7               |
| 9   | 30     | 30  | 2.8                            | 4.7                            | 26.8                            | -                  | 24.2 | 41.5               |

According to Table 1, all samples with different synthesis conditions contained neodymium aluminate phases NdAlO<sub>3</sub> from 15 to 44 wt %. The maximum perovskite content was obtained in the sample with 30 wt % additives and the pressing pressure of 30 MPa which equaled the density of 5.15 g/cm<sup>3</sup>. Under a pressing pressure of 10–20 MPa, the phases of unreacted reagents in Nd<sub>2</sub>O<sub>3</sub> equaled to 1.2–13.86 wt %; Al<sub>2</sub>O<sub>3</sub> 6.6–12.6 wt %. The proportion of unreacted products at the same density increases with the growth of the initial mixture dilution by the Nd<sub>2</sub>O<sub>3</sub>–Al<sub>2</sub>O<sub>3</sub> system. However, if the applied pressing pressure rises, the number of unreacted diluent phases reduces with the perovskite phase formation. Thus, for example, when the additive value is  $x = 10$  wt % and the pressing pressure rises from 10 to 30 MPa, the synthesized neodymium aluminate phase in the sample increases by 9 wt %; at  $x = 20$  wt % and  $x = 30$  wt % by 21% and by 25 wt % respectively. This fact is explained by the combustion growth temperature during the synthesis process. In addition, the change in the degree of dilution also affects the formation of the nickel aluminide NiAl phase: Ni<sub>2</sub>Al<sub>3</sub> and NiAl<sub>3</sub> phase formation grows whereas NiAl phase with dilution decreases.

The content of Ni<sub>2</sub>Al<sub>3</sub> and NiAl<sub>3</sub> phases can lead to an increase in the strength characteristics of the matrix material due to the distortion of their crystal lattices compared to NiAl.

The further stage of the experiments intends to determine the leaching rates of the samples during the simulation of long-term storage in geological formations. The obtained samples were placed in the central channel №2 of the IRT-T nuclear research reactor for irradiation by the fast neutron flux ( $\Phi = 10^{14}$  n/cm<sup>2</sup>·s and a set of maximum fluencies ( $9.2 \cdot 10^{19}$  n/cm<sup>2</sup>). Fast

neutrons emit energy during elastic collisions, which cause numerous atomic displacements. Irradiation acts similarly to recoil nuclei and simulates radiation damage/impact from  $\alpha$ -particles and behavior of recoil nuclei in crystal structures. This fluence corresponds approximately to 20000 years of storage.

The leachability of the samples was tested at 90°C and is based on the IAEA MCC-1 static test for monolithic samples with a known geometric surface.

Figure 1 represents/shows the rates of samples leaching under  $P = 30$  MPa and with different dilution ratios.

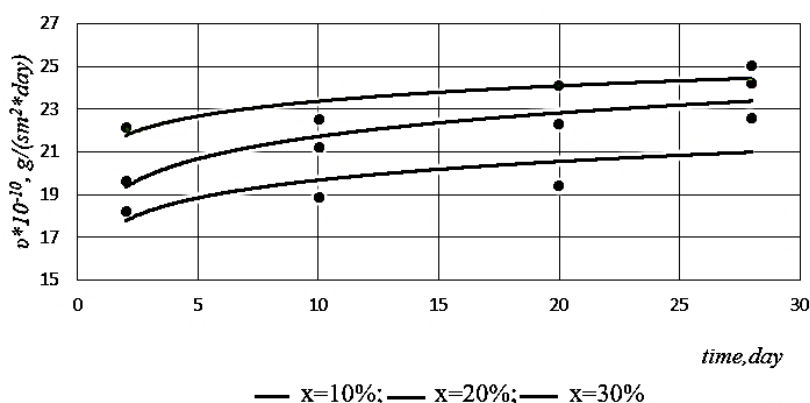


Fig. 1. Leaching rate of the simulator after irradiation in the nuclear core in IRT-T reactor.

Values of average leaching rates for all samples are  $(1.98\text{--}2.34) \cdot 10^{-9}$  g/(cm<sup>2</sup>·day) and do not exceed the requirements of  $10^{-7}$  g/(cm<sup>2</sup>·day), which is  $10^4$  times lower than the known values for borosilicate and phosphate glasses.

Thus, the material can be used as the immobilizing matrix for actinide fraction of radioactive waste.

1. J. Zhang, Nuclear Fuel Reprocessing and Waste Management (Modern Nuclear Energy Analysis Methods Book 2), Singapore: World Scientific Publishing Company, 2018, 308 p.
2. K.D. Kok, Nuclear Engineering Handbook (Mechanical and Aerospace Engineering Series 60), Boca Raton: CRC Press, 2016, 1000 p.
3. R.E. Masterson, Nuclear Engineering Fundamentals: A Practical Perspective, Boca Raton: CRC Press, 2017, 987 p.
4. E.A. Levashov, A.S. Mukasyan, A.S. Rogachev, D.V. Shtansky, Self-propagating high-temperature synthesis of advanced materials and coatings, Int. Mater. Rev., 2017, vol. 62, pp. 203–239.

## THERMALLY COUPLED PROCESSES IN A COMPOSITE GRANULAR MIXTURE (Ni + Al)–(Ti + C)

B. S. Seplyarskii<sup>\*a</sup>, R. A. Kochetkov<sup>a</sup>, T. G. Lisina<sup>a</sup>, and N. I. Abzalov<sup>a</sup><sup>a</sup>Merzhanov Institute of Structural Macrokinetics and Materials Science, Russian Academy of Sciences, Chernogolovka, Moscow, 142432 Russia

\*e-mail: numenor@list.ru

DOI: 10.24411/9999-0014A-2019-10152

As is known, practical implementation of thermally coupled SHS reactions [1] encounters the problem of scaling associated with non-uniform warmup/ignition, evolution of impurity gases [2], and separation of combustion products. A best way to go about solving the problem may turn the use of granulated green compositions [3–5].

In this work, we explored coflow combustion of composite (Ni + Al)–(Ti + C) granules in which rapidly burning Ti–C granules played the role of donor while slowly burning Ni–Al granules, the role of acceptor.

Commercial powders of Ti (PTM-1 brand), carbon black (P-308), Al (ASD-4), and Ni (PNE-1) were used as reagents. Preparation of granules, experimental setup, and measurement procedure were described in detail elsewhere [3]. The content of donor Ti + C mixtures in composite granules was 46 wt %.

In the absence of gas flow, the burning velocity of composite mixtures (12.5 mm/s) is much higher than that of acceptor ones (3 mm/s). In view of this, we assumed that, within the combustion front, the Ni + Al granules behaved as an inert additive. To check the validity of this assumption, in control experiments we replaced them by the inert Al<sub>2</sub>O<sub>3</sub> granules of the same size and weight ratio, i.e. 54% Al<sub>2</sub>O<sub>3</sub> to 46% (Ti + C). Such a mixture could not be ignited altogether, thus implying that, in the 54% (Ni + Al)–46% (Ti + C) mixture, the Ni + Al granules ignited within the combustion front. This was verified in the experiments conducted in the combustion geometry shown in Fig. 1. In this case, a column of Ti + C granules (black) was separated by a 3-mm layer of Ni + Al granules (grey). After ignition at the top, the combustion wave propagated through the Ni + Al barrier without delay but at strong deceleration accompanied by a marked decrease in visual luminosity (see Fig. 1b). The layers emittance equalized in 5 s after the end of wave propagation (Fig. 1c), this time period being shorter than the time required for sample cooling down to room temperature. It is clear that, in uniform donor–acceptor mixtures, the time required for temperature equilibration should be several times shorter and, above all, depend only on granular size.

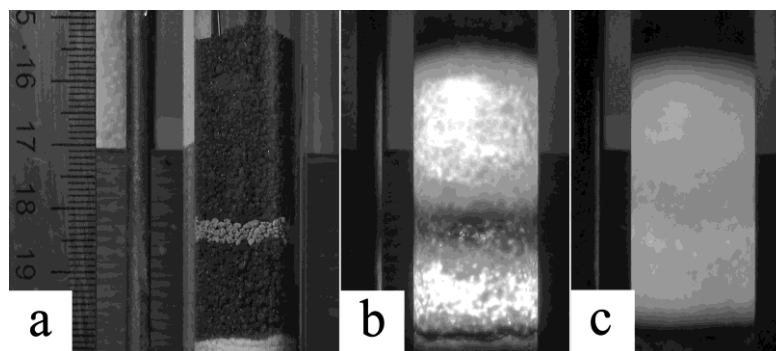


Fig. 1. Propagation of combustion front through a column of Ti + C granules (black) with a 3-mm interlayer of Ni + Al granules (grey): (a) green structure, (b) just after the end of wave propagation, and (c) afterglow in 5 s afterwards (without gas flow).

It is worth noting that the products formed upon combustion of granulated composite mixtures did not sinter and could be manually separated (by color) into individual grains probably due to the fact that TiC is not wetted with NiAl.

In the theory of filtration combustion [6], burning velocity  $U_f$  is represented as a linear function of gas flow rate  $Q$  through sample sectional area  $s$  as  $U_f = U_0 + c_g \rho_g Q / s c_s \rho_s$ , where  $U_0$  is burning velocity at  $Q = 0$ ,  $c_g$  and  $c_s$  are heat capacity of gas and of porous solid, respectively,  $\rho_g$  and  $\rho_s$  are gas density and the bulk density of granulated sample. In calculations, we assumed that  $s = 2 \text{ cm}^2$ ;  $\rho_s$  and  $c_s$  are  $0.8 \text{ g/cm}^3$  and  $560 \text{ J/(kg}\cdot\text{K)}$  for Ti + C granules; and  $1.7 \text{ g/cm}^3$  and  $590 \text{ J/(kg}\cdot\text{K)}$  for Ni + Al ones. Table 1 presents the measured ( $U$ ) and calculated ( $U_f$ ) burning velocities in constituent and composite granules for different  $Q$ .

As follows from Table 1, the measured ( $U$ ) values for Ti + C granules grow faster with increasing  $Q$  than the calculated ( $U_f$ ) ones. This is indicative of the involvement of reactive gas in the process of granules igniting from the surface [7]. For Ni + Al granules, the calculated values better agree with the measured ones (cf. Table 1).

Table 1. Measured ( $U$ ) and calculated ( $U_f$ ) burning velocities in constituent and composite granules at different  $Q$ .

| Ni + Al<br>$T_{\text{ad}} = 1912 \text{ K}^b$ |               |                 | Ti + C<br>$T_{\text{ad}} = 3290 \text{ K}^b$ |               |                 | 54% (Ni + Al)–46% (Ti + C) <sup>a</sup><br>$T_{\text{ad}} = 2518 \text{ K}^b$ |               |              |
|---|---------------|-----------------|--|---------------|-----------------|---|---------------|--------------|
| $Q$ ,<br>L/h                                  | $U$ ,<br>mm/s | $U_f$ ,<br>mm/s | $Q$ ,<br>L/h                                 | $U$ ,<br>mm/s | $U_f$ ,<br>mm/s | $Q$ ,<br>L/h  | $U$ ,<br>mm/s | $U_f$ , mm/s |
| 0   | 3             | 3               | 0  | 22            | 22              | 0   | 12.5          | 12.5         |
| 630 (Ar)                                      | 4.5           | 3.8             | 750 (Ar)                                     | 25            | 24              | 720 (Ar)  | 16.8          | 15.7         |
| 220 (N <sub>2</sub> )                         | 3             | 3.3             | 200 (N <sub>2</sub> )                        | 23            | 22.8            | 200 (N <sub>2</sub> )   | 15.5          | 13           |
| 700 (N <sub>2</sub> )                         | 6.2           | 4.2             | 650 (N <sub>2</sub> )                        | 36            | 24.5            | 720 (N <sub>2</sub> )   | 24            | 14.4         |
| 1000 (N <sub>2</sub> )                        | 8             | 4.7             | 1050 (N <sub>2</sub> )                       | 45            | 26.1            | 1100 (N <sub>2</sub> )  | 28.5          | 15.4         |

<sup>a</sup>Weight percentage. <sup>b</sup>TERMO software ([www.ism.ac.ru/thermo](http://www.ism.ac.ru/thermo))

In case of composite 54% (Ni + Al)–46% (Ti + C) granules in Ar, the gain in  $U$  was low even for  $Q = 600$ – $700$  l/h, in full agreement with theoretically predicted  $U_f$  values (see Table 1). The combustion products formed in Ar retained their shape, were brittle, and easily disintegrated into individual grains. This finding looks unexpected in view of the fact that (a)  $T_{\text{ad}}$  for composite granules (2518 K) is markedly higher than the melting point of NiAl (1912 K) and (b) the presence of the liquid phase facilitates sample shrinkage [7, 8].

In principle, the  $U(Q)$  function for composite granules at  $Q < 1100$  l/h can be approximated by a straight line steeper than it follows from the filtration combustion theory. It could be assumed that, for high  $Q$ , heat exchange between donor and acceptor granules might take place behind the combustion wave, so that the Ni + Al granules would ignite and burn after passage of the visible combustion front. However, thorough inspection of still frames of combustion in granulated (Ni + Al)–(Ti + C) mixtures did not show any signs for formation of a double-front combustion mode at any  $Q$ .

The formation of brittle product in combustion of 54% (Ni + Al)–46% (Ti + C) mixtures in the presence of nitrogen flow can be explained by the formation of titanium nitride on the surface of Ti + C granules, thus preventing their sintering. Our XRD results confirm that the combustion product contains TiC and NiAl. The absence of nitride and carbonitride phases can be ascribed to low sensitivity of the method.

1. A.G. Merzhanov, Thermally coupled processes of self-propagating high-temperature synthesis, *Dokl. Phys. Chem.*, 2010, vol. 434, pp. 159–162.
2. S.G. Vadchenko, N.T. Balikhina, V.L. Kvanin, Combustion of hollow cylinders, *Combust.*

- Explos. Shock Waves*, 2004, vol. 38, no. 4, pp. 425–429.
3. B.S. Seplyarskii, A.G. Tarasov, R.A. Kochetkov, Experimental investigation of combustion of a gasless pelletized mixture of Ti + 0.5C in argon and nitrogen coflows, *Combust. Explos. Shock Waves*, 2013, vol. 49, no. 5.
  4. A.A. Samboruk, E.A. Kuznets, A.G. Makarenko, A.R. Samboruk, Fabrication of TiC by SHS from granulated green mixtures, *Vestn. SamGTU, Tekh. Nauki*, 2008, vol. 21, no. 1, pp. 124–129.
  5. B.S. Braverman, Y.M. Maksimov, Y.V. Tsybul'nik, Possibility of nitriding industrial ferroalloys in a nitrogen-containing gas flow, *Combust. Explos. Shock Waves*, 2012, vol. 48, no. 6, pp. 734–735.
  6. A.G. Merzhanov, A.S. Mukasyan, S.V. Postnikov, Hydraulic effect in processes of gasless combustion, *Dokl. Ros. Akad. Nauk*, 1995, vol. 343, no. 3, pp. 340–342.
  7. B.S. Seplyarskii, R.A. Kochetkov, A study of the characteristics of the combustion of Ti + xC ( $x > 0.5$ ) powder and granular compositions in a gas coflow, *Russ. J. Phys. Chem. B*, 2017, vol.11, no. 5, pp. 798–807.
  8. O.V. Lapshin, V.G. Prokof'ev, V.K. Smolyakov, Combustion of granulated gasless mixtures in a flow of inert gas, *Int. J. Self-Propag. High-Temp. Synth.*, 2018, vol. 27, no. 1, pp. 14–17.

## THE IMPLEMENTATION OF THE CONVECTIVE MODE OF COMBUSTION FOR GRANULAR MIXTURES OF Ti + xC

**B. S. Seplyarskii<sup>\*a</sup>, R. A. Kochetkov<sup>a</sup>, T. G. Lisina<sup>a</sup>, and M. I. Alymov<sup>a</sup>**

<sup>a</sup>Merzhanov Institute of Structural Macrokinetics and Materials Science, Russian Academy of Sciences, Chernogolovka, Moscow, 142432 Russia

\*e-mail: seplb1@mail.ru

DOI: 10.24411/9999-0014A-2019-10153

The occurrence of convection-driven coflow combustion of Ti + xC ( $0.5 \leq x \leq 1$ ) granules at a nitrogen pressure drop of 1–2 atm was established in [1, 2]. By saying convection-driven combustion, we mean a mode of fast burning in a coflow of reactive gas. Hereafter, the term conduction-driven combustion will refer to a mode with burning velocity described by the theory of filtration combustion [3]. To date, the existing numerical models [4, 5] give no answer to the question which conditions are needed for the onset of transition between these modes. In this work, we attempted to fill this gap using coflow combustion of granulated Ti + xC mixtures ( $x = 0.5, 0.75, 1.0$ ) as an example.

Burning velocity  $u$  is found as  $u = d/t$ , where  $d$  is mean granule size (1 mm) and  $t$  is the time required for ignition of a granule. A magnitude of  $t$  can be determined using well-known expressions for warmup of a semi-infinite body [6] at kind III boundary conditions:

$$\frac{T_{\text{ig}} - T_0}{T_{\text{g}} - T_0} = 1 - \varphi(\omega)$$

where  $T_{\text{g}}$  is combustion temperature of granules,  $T_0$  is the initial temperature,  $T_{\text{ig}}$  is the temperature of granule surface at the moment of its ignition,  $\varphi(\omega) = \exp(\omega^2)(1 - \text{erf } \omega)$  is additional error function, and  $\omega(T_{\text{g}}, T_0, T_{\text{ig}}) = \alpha^*(Q) \sqrt{at} / \lambda$ . Here  $\alpha^*(Q)$  is the coefficient of interphase heat exchange at volume rate  $Q$  of gas flow. For Ti + C granule material thermal conductivity  $\lambda$  is equal 1 W/(m·K), and thermal diffusivity  $a$  is  $10^{-2}$  cm<sup>2</sup>/s.

We obtain:

$$u_c(Q) = d[\alpha_h^*(Q)/\omega(T_{\text{g}}, T_0, T_{\text{ig}}) \lambda]^2/a \quad (1)$$

We assume that  $T_{\text{ig}} = 1155$  K ( $\alpha \rightarrow \beta$  transition in Ti) in case of nitrogen flow and 1933 K (Ti melting point) in case of argon flow [1, 2]. As follows from (2), in order to calculate the  $u(Q)$  function, we have to know the dependence of  $\alpha^*$  on  $Q$ .

As is known, in case of porous media, the expression for the interphase heat exchange coefficient  $\alpha$  can be represented in the form [9]:

$$\alpha(Q) = \rho_g Q c_g \text{Pr}^{-2/3} (1 - \varepsilon)^{-1} \Psi(\varepsilon) / 4s \quad (2)$$

where  $\Psi(\varepsilon) = 0.508 - 0.56(1 - \varepsilon)$  for  $\varepsilon < 0.4$  and  $\Psi(\varepsilon) = 1 - 1.164(1 - \varepsilon)^{2/3}$  for  $\varepsilon > 0.4$ ; Pr stands for Prandtl number,  $0 < \varepsilon < 1$  indicates the extent of open porosity,  $\rho_g$  stands for gas density,  $c_g$  is heat capacity of gas,  $s$  is sectional area of sample (2 cm<sup>2</sup>). It can be assumed [2] that Pr = 0.8 for nitrogen and 0.6 for Ar,  $\varepsilon = 0.5$ .

The results obtained for  $Q = 800$  l/h nitrogen flow  $\alpha = 262$  W/(m<sup>2</sup>·K). It is smaller than semi-

empirical  $\alpha^* = 2711 \text{ W}/(\text{m}^2 \cdot \text{K})$  taken from [2] by a factor of 10.4, which can be associated with a rough surface of reactive Ti–C granules and irregular packing of reactive and inert mixtures [10, 11]. Assuming that the ratio  $\alpha^*/\alpha = 10.4$  holds true for other  $Q$ , the  $\alpha^*$  values for others  $Q$  were obtained simply by scaling-up on a factor of 10.4.

Given that a convection-driven combustion mode can also be realized in Ar flow, we have to use appropriate values of  $\alpha_{\text{Ar}}^*$ . For this to be done, the  $\alpha_{\text{Ar}}(Q)$  magnitudes derived from (2) were multiplied by 10.4.

Since expression (2) contains no thermophysical parameters, the results obtained for mixtures with  $x = 1.0$  can be expected applicable to those with  $x = 0.5$  and  $0.75$ . The values of  $T_g$ ,  $T_0$ , and  $T_{\text{ig}}$  used in calculating  $\omega(T_g, T_0, T_{\text{ig}})$  are given in Table 1, along with resultant values of  $\omega$  and  $u$ .

Table 1. Calculated values of  $\omega$  and  $u$  for combustion of Ti +  $x$ C mixtures in a CvC mode.

|                | $T_0$ ,<br>K | $T_{\text{ig}}$ ,<br>K | Ti + C                 |                        | Ti + 0.75C             |                        | Ti + 0.5C |                       |
|----------------|--------------|------------------------|------------------------|------------------------|------------------------|------------------------|-----------|-----------------------|
|                |              |                        | $T_g = 3300 \text{ K}$ | $T_g = 3100 \text{ K}$ | $T_g = 3100 \text{ K}$ | $T_g = 2600 \text{ K}$ |           |                       |
|                |              |                        | $\omega$               | $u$ , mm/s             | $\omega$               | $u$ , mm/s             | $\omega$  | $u$ , mm/s            |
| N <sub>2</sub> | 300          | 1155                   | 0.35                   | $9 \cdot 10^{-5} Q^2$  | 0.38                   | $8 \cdot 10^{-5} Q^2$  | 0.51      | $4 \cdot 10^{-5} Q^2$ |
| Ar             | 300          | 1933                   | 0.90                   | $8 \cdot 10^{-6} Q^2$  | 1.03                   | $6 \cdot 10^{-6} Q^2$  | 1.71      | $2 \cdot 10^{-6} Q^2$ |

Figure 1 shows burning velocity  $u$  vs.  $Q$  (nitrogen coflow, convective-driven mode) for  $T_{\text{ig}} = 1155 \text{ K}$  and different  $T_g$ . Straight lines show burning velocities  $u_f$  predicted by filtration combustion theory [3] (nitrogen coflow, conduction-driven mode) for mixtures with  $x = 1$  (2), 0.75 (4), and 0.5 (6): data points at  $Q = 0$  correspond to those measured in [2]. The points of intersection in Fig. 1 define a theoretical boundary at which the mode transition may take place. In case of Ar flow, the factors at  $Q^2$  (see Table 1) are one order of magnitude smaller compared to those in nitrogen flow, whereas the calculated  $u_f$  values are close to those observed for combustion in nitrogen. Thus, a point of possible intersection is far above  $Q = 1100 \text{ l/h}$ . Therefore, realization of a convective-driven mode in Ar in conditions [2] is impossible.

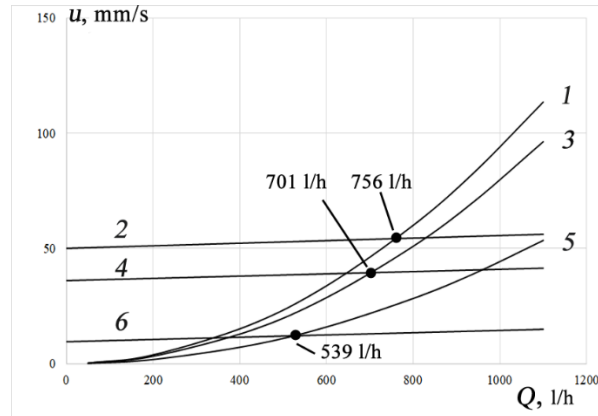


Fig. 1. Burning velocity  $u$  vs.  $Q$  (nitrogen coflow, convective-driven mode):  $T_0 = 300 \text{ K}$ ,  $T_{\text{ig}} = 1155 \text{ K}$ , and  $T_g = 3300$  (1), 3100 (3), and 2600 K (5). Straight lines show burning velocities  $u_f$  predicted by filtration combustion theory for mixtures with  $x = 1$  (2), 0.75 (4), and 0.5 (6): the magnitudes at  $Q = 0$  correspond to those measured in [2].

Figure 2 presents the calculated  $u$  values as a function of  $z = T_g - T_{\text{ig}}$  for convective-driven modes at several  $Q$ . All dependences are well approximated by exponentials whose pre-exponential factor grows with increasing  $Q$ .

Experimental verification of the above calculation was done by using the experimental setup described in [3]. We estimated an experimental boundary value of 732 l/h, while the calculated intersection point is at 779 l/h.



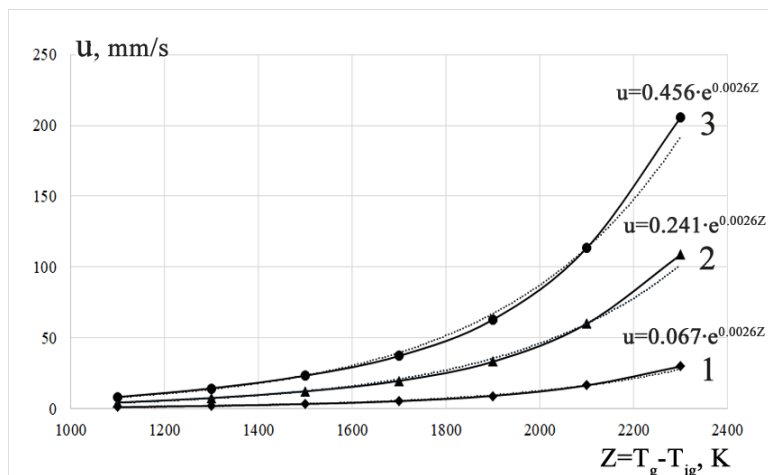


Fig. 2. Calculated  $u$  values as a function of  $z = T_g - T_{ig}$  at  $Q = 420$  (1), 800 (2), and 1100 l/h.

Key factors responsible for the onset of transition from conduction-driven to convection-driven coflow combustion in granulated  $Ti + xC$  ( $0.5 \leq x \leq 1$ ) mixtures are (a) volume rate  $Q$  of gas flow, (b) difference between the ignition and combustion temperatures for granules, and (c) burning velocity at  $Q = 0$ . The measured  $Q$  values at the points of transition from conduction-driven to convection-driven combustion well agree with theoretical predictions for  $Ti + 0.5C$  mixture.

1. B.S. Seplyarskii, A.G. Tarasov, R.A. Kochetkov, Experimental investigation of combustion of a gasless pelletized mixture of  $Ti + 0.5C$  in argon and nitrogen coflows, *Combust. Explos. Shock Waves*, 2013, vol. 49, no. 5, pp. 555–562.
2. B.S. Seplyarskii, R.A. Kochetkov, A study of the characteristics of the combustion of  $Ti + xC$  ( $x > 0.5$ ) powder and granular compositions in a gas coflow, *Russ. J. Phys. Chem. B*, 2017, vol. 11, no. 5, pp. 798–807.
3. A.G. Merzhanov, A.S. Mukasyan, S.V. Postnikov, Hydraulic effect in processes of gasless combustion, *Dokl. Akad. Nauk*, 1995, vol. 343, no. 3, pp. 340–342.
4. A.P. Aldushin, Heat transfer and convection combustion regimes of porous systems with filtration of heat carrier, *Combust. Explos. Shock Waves*, 1990, vol. 26, no. 2, pp. 180–187.
5. O.V. Lapshin, V.G. Prokof'ev, V.K. Smolyakov, Combustion of granulated gasless mixtures in a flow of inert gas, *Int. J. Self-Propag. High-Temp. Synth.*, 2018, vol. 27, no. 1, pp. 14–17.
6. L.K. Gusachenko, V.E. Zarko, A.D. Rychkov, N.Yu. Shokina, Filtration combustion of an energetic material in a co-current flow of its combustion products: Critical combustion conditions, *Combust. Explos. Shock Waves*, 2003, vol. 39, no. 6, pp. 694–700.

## NI–AL BASED REACTIVE MATERIAL: MECHANICAL PROPERTIES AND FEATURES OF COMBUSTION

S. A. Seropyan<sup>\*a</sup>, I. V. Saikov<sup>a</sup>, V. G. Salamatov<sup>a</sup>, M. I. Alymov<sup>a</sup>, A. V. Dolmatov<sup>b</sup>, and P. Yu. Gulyaev<sup>b</sup>

<sup>a</sup>Merzhanov Institute of Structural Macrokinetics and Materials Science Russian Academy of Sciences, Chernogolovka, 142432 Russia

<sup>b</sup>Yugra State University, Khanty-Mansiysk, 628012 Russia

\*e-mail: stepan.seropyan@mail.ru

DOI: 10.24411/9999-0014A-2019-10154

Reactive materials are a class of energetic materials characterized by high energy intensity, low sensitivity under normal conditions, and the ability for intense chemical reaction under high-speed impact and heating conditions. Reactive materials are typically compressed powder [1–3].

The creation of structural reactive materials that combining a required set of physico-mechanical characteristics and high energy release are associated with a number of physico-chemical limitations and technological difficulties [4–6]. Such research, as a rule, are purely experimental and are distinguished by the complexity of studying fast-acting physicochemical processes directly in the process of explosive loading of the reaction mixture, which is characterized by high rates of deformation, pressures, and temperatures. The current problem is the development of consolidation methods that would preserve the ability to achieve sufficient structural strength of the material as a whole.

The studies were carried out with a powder mixture of Ni–Al of the composition Ni + 31.5 wt % Al, the reagents of which were Ni powders (grade PNE-1) and Al (grade ASD-4). Mixing of powders of a given composition was carried out in a Turbula type mixer for 4 h. Green mixture was molded in the form of parallelepipeds, including with reinforcing inserts (boron fibers (diameter of 140  $\mu\text{m}$ ) or tungsten wires (diameter of 300  $\mu\text{m}$ )). Samples (20  $\times$  5  $\times$  5 mm) with reinforcing inserts were prepared as follows: the green mixture for one sample was divided into 5 equal parts, which were poured into the mold. Then the reinforcing elements in the amount of 5 (tungsten) or 6 (boron fiber) were placed between these layers. The obtained composites were subjected to one-side pressing to a relative density of 0.7–0.8.

In separate experiments, a mixture of  $(1 - x)(\text{Ni} + 31.5 \text{ wt } \% \text{ Al}) + x\text{Tf}$  was used as a charge between reinforcing elements, where  $x$  is wt % of Teflon (Tf). The amount of Teflon varied in the range of 1–25 wt %. The relative density of the resulting composites was 0.83–0.99.

The effect of heat treatment on the strength characteristics of composites was investigated. The samples were heated in a furnace in an atmosphere of air. The exposure time of the samples varied from 1 to 4 h, and the temperature changed from 300 to 550°C.

Tests to determine the strength of samples with three-point bending conducted on the equipment Instron 1195 according to GOST 25282-93. The combustion was initiated from the lateral end by a heated electric wire in air at normal pressure. After initiation, a self-sustaining reaction wave propagated along the sample (with an average burning rate of 60–100 mm/s). The burning of composites takes place in a non-stationary mode and is characterized by the presence of reaction foci (average size of 400  $\mu\text{m}$ ), which randomly move in front of the front. Investigation has shown that reinforcement of samples with boron fibers or tungsten wires increases the strength of the reactive materials. Boron fibers increase the strength by 1.6 times compared to non-reinforced samples. Reinforcing tungsten wire increases the strength of 3.8 times compared with non-reinforced. The cause for this effect is due to the redistribution of the

load from the matrix to the reinforcement inserts. It is necessary to note the problem of insufficient adhesion of the fiber with the matrix, as a result of which their entire resource is not used. For reinforced samples, the number of fibers is an important parameter. Adding Teflon allows for a higher density. Reinforcement with boron fibers increases strength by 2 times at 1 wt % Tf. A further increase in the content of Teflon leads to a decrease in strength. The reinforcement of composites with a high content of Teflon does not lead to a significant increase in strength.

Heat treatment of unreinforced samples increases strength: at 300°C and 3 h, by 1.3 times; at 400°C and 4 h, by 3.7 times; at 500°C and 1 h, by 5.7 times; at 550°C and 3 h, by 6.3 times. Heat treatment of the samples reinforced with boron fibers made it possible to increase the strength under the following conditions: at 400°C and 2 h, by 1.6 times; at 500°C and 1 h, by 3 times. The samples reinforced with tungsten fibers after heat treatment: increased strength: at 400°C and 3 h, by 1.8 times. After heat treatment in air, the samples increase their mass by 0.5÷5.5%. With an increase in temperature and exposure time, the increase in mass linearly increases.

1. N.A. Imkhovik, A.V. Svidinsky, A.S. Smirnov, V.B. Yashin, Foreign investigations of new high-density reactive materials for different advanced munitions, *Gorenie i Vzryv (Moskva) – Combustion and Explosion*, 2017, vol. 10, no. 1, pp. 93–101.
2. I.V. Saikov, M.I. Alymov, S.G. Vadchenko, I.D. Kovalev, Investigation of shock-wave initiation in metal- teflon powder mixtures, *Lett. Mater.*, 2017, vol. 7, no. 4, pp. 465–468.
3. I.V. Saikov, M.I. Alymov, S.G. Vadchenko, P.Yu. Gulyaev, Shock-wave synthesis in powder mixtures, *J. Phys.: Conf. Ser.*, 2018, vol. 1115, p. 042012.
4. J. Wu, X. Fang, Z. Gao, H. Wang, J. Huang, S. Wu, Y. Li, Investigation on mechanical properties and reaction characteristics of Al-PTFE composites with different al particle size, *Adv. Mater. Sci. Eng.*, 2018, vol. 2018 p. 2767563.
5. D.L. Hastings, E.L. Dreizin, Reactive structural materials: Preparation and characterization, *Adv. Eng. Mater.*, 2017, vol. 20, no. 3, p. 1700631.
6. F. Zhang, Some issues for blast from a structural reactive material solid, *Shock Waves*, vol. 28, no. 4, pp. 693–707.

EXOTHERMIC SYNTHESIS AND CONSOLIDATION OF  
Ta<sub>4</sub>ZrC<sub>5</sub> COMPOSITEV. A. Shcherbakov<sup>\*a</sup>, A. N. Gryadunov<sup>a</sup>, S. G. Vadchenko<sup>a</sup>, and M. I. Alymov<sup>a</sup><sup>a</sup>Merzhanov Institute of Structural Macrokinetics and Materials Science Russian Academy of Sciences, Chernogolovka, 142432 Russia

\*e-mail: vladimir@ism.ac.ru

DOI: 10.24411/9999-0014A-2019-10155

An ultra-high temperature (UHT) composite with melting point of 4000°C, synthesized on the basis of the TaC–ZrC system [1], is interesting for use in an aerospace industry for production products having a long service life at high temperature under conditions of erosion wear.

The composites were obtained by multistage methods, including synthesis of refractory TaC and ZrC compounds, grinding to micron particle size, next synthesis of complex carbides (Ta<sub>4</sub>ZrC<sub>5</sub>), their re-grinding and subsequent sintering or hot pressing. In order to reduce the sintering temperature, single-phase nanocrystalline powders of complex carbides were prepared by the sol-gel method [2]. Powder of single-phase composites Ta<sub>4</sub>ZrC<sub>5</sub> was obtained by self-propagating high-temperature synthesis (SHS) using a mixture of tantalum, zirconium and soot powders mechanically activated for 5 min in a ball mill [3]. After grinding the SHS product was consolidated by electrospark sintering. The disadvantages of described above methods for producing ultra-high temperature composite materials are multistage process, high energy costs, low productivity.

An effective method combining exothermic synthesis in the electrothermal explosion (ETE) mode and consolidation of a hot product under quasi-isostatic compression has developed at ISMAN [4]. This paper presents experimental results on production of Ta<sub>4</sub>ZrC<sub>5</sub> ultra-high temperature composite by exothermic synthesis and consolidation in one technological stage. It allowed exclude intermediate stages of preparation and grinding the refractory compounds. The aim of this work is to study the possibility of preparation of Ta<sub>4</sub>ZrC<sub>5</sub> single-phase UHT composite by one-stage technique combining ETE of tantalum, zirconium, and carbon black powders mixture and consolidation of the final product in conditions of quasi-isostatic compression.

The exothermic synthesis of the UHT composite was carried out according to the scheme:



Reaction mixtures were prepared from tantalum (TAM brand), zirconium (PCRK-1 brand), and carbon black (P 804-T brand) powders. The mixture was mixed in a planetary activator AGO-2C at acceleration of 90 g. Mechanical activation of powders was carried out in two stages. The first one produced an activated mixture of tantalum and zirconium powders for 0 to 30 min. On the second, carbon black was added into the resulting mixture of activated metal powders, the obtained mixture was mixed for four min.

Cylindrical samples with a height  $h = 12$  mm and a diameter  $d = 15$  mm were pressed from the prepared mixture to a relative density of 0.5. The test sample was placed in a reaction mold. The laboratory set-up for synthesis of a UHT composite by the ETE under pressure is described in detail in [4]. In the experiments, the sample was compressed at pressure of 100 MPa and heated with Joule heat until the exothermic interaction of the reagents in the thermal explosion mode.

The microstructure of the composites was studied using an autoemission scanning electron microscope of ultra-high resolution Zeiss Ultra plus. The phase composition of SHS-composites was studied with the diffractometer "DRON-3", using monochromatic  $\text{CrK}\alpha$  radiation, the computer program "Crystallographica Search Match" and the base for diffraction data Power Diffraction File (PDF-2, ICDD, USA, Release 2011). For the study, the sections of synthesized samples were used.

Figure 1 shows the microstructure of the composite obtained by the ETE under pressure of the non-activated mixture. It is seen that the composite has a heterogeneous microstructure. It consists of tantalum carbide (light phase) and solid solution based on zirconium carbide (gray phase). The particle size of the TaC is changed in the range of 20–100  $\mu\text{m}$ ; of the solid solution ( $\text{Zr,TaC}$ ), in the range of 10–15  $\mu\text{m}$ . It is important to note that the macropores (up to 10  $\mu\text{m}$ ) are in the center of coarse TaC particles. Formation of macropores is associated with the mechanism of high-temperature formation of TaC particles during ETE.

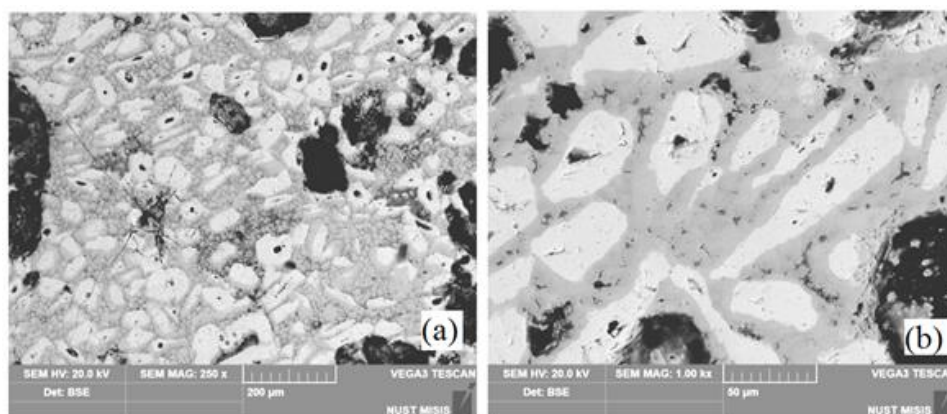


Fig. 1. SEM images of the  $\text{Ta}_4\text{ZrC}_5$  composite prepared with using non-activated reactant mixture.

The results obtained are consistent with the data of microstructural analysis of the synthesized composite. The results of the XRD analysis of the UHT composite obtained by ETE of non-activated mixture of tantalum, zirconium, and carbon black powders are presented in Fig. 2 (curve 1). It is seen that the final product contains TaC and a solid solution based on ( $\text{Zr,TaC}$ ). The diffraction peaks of the solid solution are shifted relative to the position of the peaks of the phase ZrC.

To reduce the effect of particle size, the powder mixture had been subjected to mechanical activation in the planetary ball mill AGO-2. Activated mixing of tantalum and zirconium powders was carried out for 10 to 30 min.

Figure 3 shows the XRD patterns of mechanically activated powder mixture. It is seen that after 10 min of activated mixing the diffraction peaks of zirconium completely disappeared. For tantalum, on the contrary, after 30 min of activated mixing, the peaks did not disappear, despite the fact that their intensity decreased significantly. This indicates a significant reduction of particles and destruction of crystal lattices of zirconium and tantalum as a result of the formation of defects.

Figure 4 shows the microstructure of the composite prepared with using the mixture mechanically activated in two-stage mixing of tantalum, zirconium, and carbon black powders (the first stage: 20 min without carbon black, the second one: 4 min after the addition of carbon black). It is seen that the single-phase composite  $\text{Ta}_4\text{ZrC}_5$  with a particle size of 2–3  $\mu\text{m}$  was formed during the ETE. The single-phase composition of the composite  $\text{Ta}_4\text{ZrC}_5$  is confirmed by the results of XRD analysis (Fig. 3, curve 2).

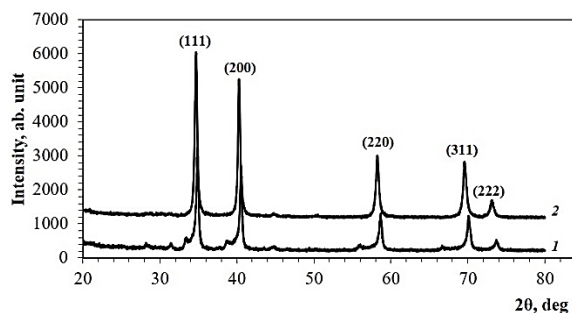


Fig. 2. XRD patterns of the composites obtained using 1 non-activated and 2 activated reactant mixture.

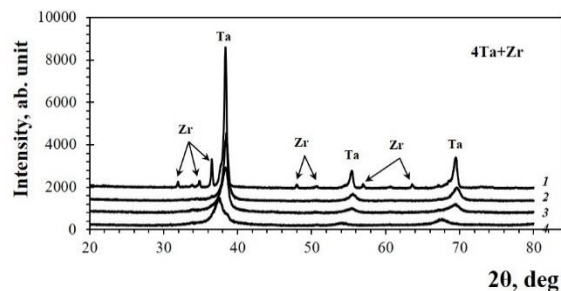


Fig. 3. XRD patterns of the 4Ta+Zr powder mixtures obtained by mechanical activation for 0 (1), 10 (2), 20 (3), and 30 (4) min.

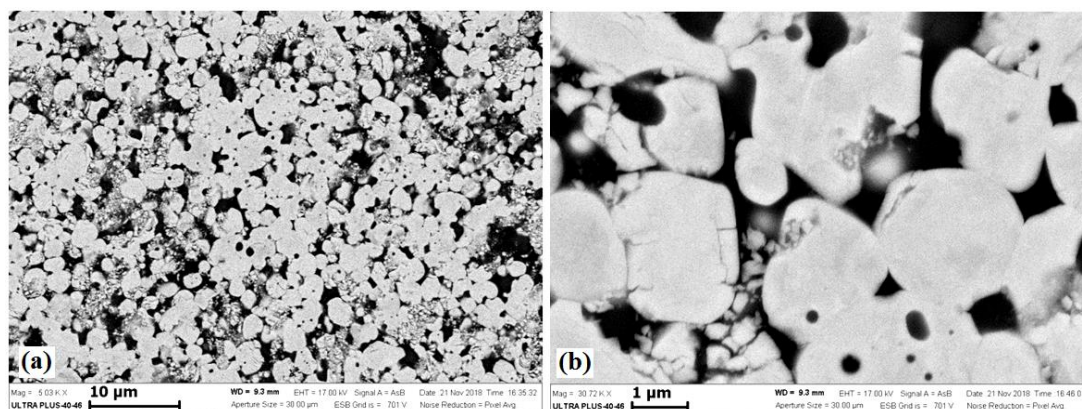


Fig. 4. SEM images of the  $Ta_4ZrC_5$  composites obtained with using activated reactant mixture.

Thus, it was developed the efficient single-stage method combining the exothermic synthesis in a mode of electrothermal explosion (ETE) and consolidation of a hot product in terms quasi-isostatic compression. The dense  $Ta_4ZrC_5$  UHT composite was prepared by this technique. The condition for the synthesis of a single-phase composite is the use of a mixture of tantalum, zirconium and carbon powders, mechanically activated in two stages: the first stage produces an activated mixture of tantalum and zirconium powders for 20 min, the second stage includes carbon black and mixing for 4 min. The  $Ta_4ZrC_5$  single-phase composite with a particle size of 2–3  $\mu m$  was formed under a pressure of 100 MPa in during few seconds. The residual porosity of the ultra-melting composite is 8–10%.

The work was supported by the Russian Foundation for Basic Research (project no.19-08-01085 A) using the equipment of the Center of Shared Serves of ISMAN.

1. C. Agte, H. Alterthum, Systems of high-melting carbides: Contributions to the problem carbon fusion, *Tech. Phys.*, 1930, vol. 11, no. 6, pp.182–191.
2. E.P. Simonenko, N.Ah. Ignatov, N.P. Simonenko, et al, Synthesis of highly dispersed super-refractory carbides of tantalum-zirconium  $Ta_4ZrC_5$  and tantalum-hafnium  $Ta_4ZrC_5$  via sol-gel technique, *Zhurn. Neorgan. Chem.*, 2011, vol. 56, no. 11, pp. 1763–1769.
3. E.I. Patsera, E.A. Levashov, V.V. Kurbatkina, et al, Production of ultra-high temperature carbide (Ta,Zr)C by self-propagating high-temperature synthesis of mechanically activated mixtures, *Ceram. Int.*, 2015, vol. 41, no. 7, pp. 8885–8893.
4. V.A. Shcherbakov, A.V. Shcherbakov, M.I. Alymov, V.Yu. Barinov, I.D. Kovalev, et al, The preparation of the  $TaB_2-CrB$  composites by electro-thermal explosion under pressure, *Fundam. Res.*, 2018, no. 2, pp. 39–45.

## BEHAVIOURS OF ELECTROTHERMAL EXPLOSION OF TITANIUM–CARBON BLACK MIXTURE UNDER QUASI-ISOSTATIC COMPRESSION

V. A. Shcherbakov\*<sup>a</sup> and A. V. Shcherbakov<sup>a</sup>

<sup>a</sup>Merzhanov Institute of Structural Macrokinetics and Materials Science Russian Academy of Sciences, Chernogolovka, 142432 Russia  
\*e-mail: vladimir@ism.ac.ru

DOI: 10.24411/9999-0014A-2019-10156

Electrothermal explosion (ETE) of heterogeneous condensed systems under quasi-isostatic compression is an effective method for producing ceramic composites [1, 2]. The method includes Joule heating of the reaction heterogeneous mixture of metal and non-metal powders to the ignition temperature and pressing the hot synthesis product. The combined electrochemical heating source allows control of the thermal synthesis and consolidation regime to produce composites with minimal residual porosity. The search for optimal conditions of exothermic synthesis to obtain composites with minimal residual porosity, submicron microstructure and high physical and mechanical characteristics stimulated the study of regularities and mechanism of fast exothermic interaction.

In the present work the results of experimental diagnostics of thermal modes of ETE of titanium and carbon black mixture under conditions quasi-isostatic compression summarizes. Studying of the ETE behavior of a heterogeneous mixture under pressure is based on the measurement of thermal and electrical parameters in conditions of subcritical and supercritical heating. This temperature was measured using a tungsten–rhenium thermocouple in the center

of the sample. This technique under pressure is described in [3]. ETE thermograms obtained at different pressures of quasi-isostatic compression are shown in Fig. 1. Sharp bends in ETE thermograms separate the stages of pre-heating ( $T_0 < T < T_{\text{ign}}$ ), thermal explosion ( $T_{\text{ign}} < T < T_{\text{max}}$ ) and post-process ( $T_{\text{max}} < T < T_s$ ) occurring at cooling of the final product (Fig. 1). Increasing the pressure from 8 to 96 MPa leads to decrease in ignition time from 3.1 to 1.2 s, and in maximum temperature of the thermal explosion  $T_{\text{max}}$  from 3000 to 2500 K. The ignition temperature  $T_{\text{ign}}$  reaches the maximum value of 700 K at pressures of 24 MPa, and the abnormally low value of 400 K at 8 MPa.

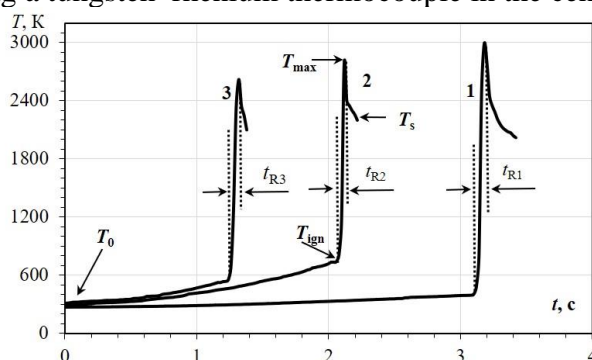


Fig. 1. ETE thermograms of titanium and carbon black mixture obtained at  $U = 9$  V and  $P = 8$  (1), 48 (2), 96 (3) MPa.

The dependencies of the electric current force  $I$  on the time obtained at the ETE of titanium and carbon black mixture at different quasi-isostatic compression pressures are shown in Fig. 2. It is seen that at the stage of thermal explosion, the electrical parameters, like the thermal parameters changed sharply (curves 1–3). The value of the electric current  $I_{\text{ign}}$  and  $I_{\text{max}}$  are achieved at  $T_{\text{ign}}$  and  $T_{\text{ign}}$ , respectively. Dotted lines drawn through the characteristic points  $I_{\text{ign}}$  and  $I_{\text{max}}$  separate the stages of the pre-heating ( $I_0 < I < I_{\text{ign}}$ ), thermal explosion

( $I_{\text{ign}} < I < I_{\text{max}}$ ) and cooling ( $I_{\text{max}} < I < I_s$ ). In extrapolation, the dotted lines intersect at the point at which the change in the electric current  $\Delta I \approx 0$ .

The decrease in electrical resistance is due to the increase in the number of contacts between the particles, as the particles of titanium and soot during cold pressing are poorly deformed due to the high stiffness. At high pressure, electrical contacts are formed in the sample, including almost all the particles of the mixture, and at low pressure – only a small fraction of the particles.

Ratio of the times of exothermic interaction and the change in the electric current at the stage of a thermal explosion is criterion to determine a thermal regime of ETE. In the case of a homogeneous heating mode, the ratio of the time of exothermic interaction and the change in the electric current is close to one, and in the case of inhomogeneous heating, the time of exothermic interaction is much less than the time of the change in the electric current force.

Figure 3 shows the ETE thermograms of the titanium and carbon black mixture at quasi-isostatic compression pressure of 48 MPa and various electrical voltages. It is seen that the parameters of the ETE depend on the magnitude of the applied electric voltage  $U$ . In subcritical conditions ( $U = 3$  V), the sample temperature increases smoothly to a temperature of 1600 K (Fig. 3, curve 1). Stable ignition of the mixture was carried out at  $U > 4$  V.

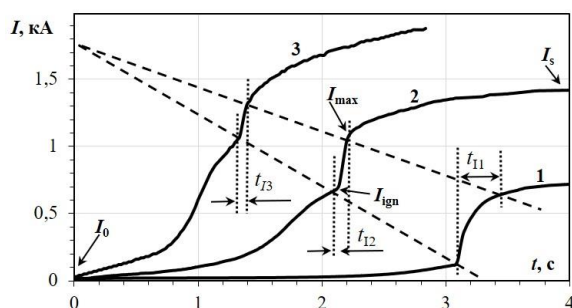


Fig. 2. Dependencies of electric current force on time, obtained at ETE of titanium and carbon black mixture at  $U = 9$  V and  $P = 8$  (1), 48 (2), 96 (3) MPa.

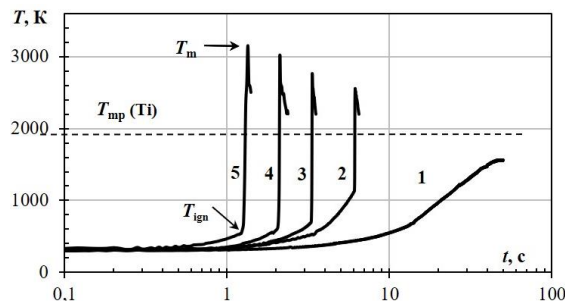


Fig. 3. ETE thermograms of titanium and carbon black mixture obtained at  $P = 48$  MPa and  $U$  (V): 1 3; 2 4; 3 6; 4 9; and 5 11.

In supercritical conditions ( $U > 4$  V) at the stage of thermal explosion the ETE temperature increased abruptly. The characteristic points in the thermograms are ignition temperature ( $T_{\text{ign}}$ ), ignition time ( $t_{\text{ign}}$ ), as well as the maximum temperature of the ETE ( $T_m$ ) and the reaction time ( $t_m$ ). At  $T_m$  the reagents mixture is complete transformed into the final product. The ignition time and reaction time correspond to the duration of the temperature rise in the range  $T_o < T < T_{\text{ign}}$ , and  $T_{\text{ign}} < T < T_m$ , respectively. As the electric voltage increases,  $t_{\text{ign}}$  and  $T_{\text{ign}}$  decrease, and  $T_m$  increases.

Changing the parameters of ETE is associated with the interaction of reagents at the stage of preheating and the formation of the final product. The heat released at this stage is removed from the sample to the environment. Therefore, the decrease in  $T_m$  is due to a decrease in the chemical energy reserve in the sample, and the increase in the ignition temperature of the  $t_{\text{ign}}$  reaction mixture is due to an increase in the concentration of thermal ballast. The melting point of titanium is in the area of linear temperature increase. It is important to note that when  $T < T_{\text{mp}}$  and  $T > T_{\text{mp}}$ ,  $dT/dt \approx 60000$  K/c. Therefore, the melting of titanium does not influence on the power of chemical heat release.

The dependences of electric current force on time are shown in Fig. 4. In subcritical conditions ( $U = 3$  V) for 50 s of heating curve 1 gradually increases. In supercritical conditions ( $U > 4$  V) at the stage of thermal explosion electrical parameters like thermal ones change abruptly (curves 2–5). Parameters  $I_{\text{ign}}$  and  $I_m$  correspond to the values of the electric current force when the ignition temperature ( $T_{\text{ign}}$ ) and the maximum temperature of the ETE ( $T_m$ ) are achieved, respectively.



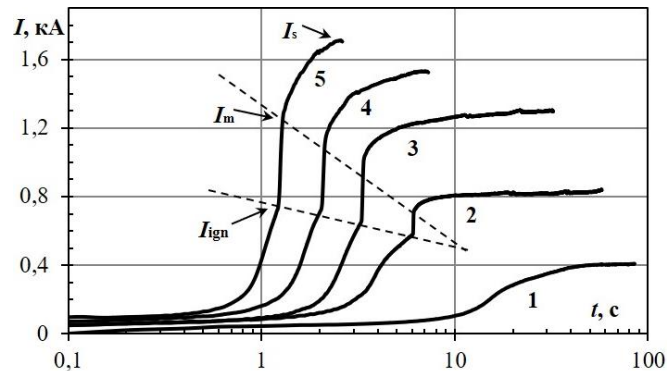


Fig. 4. Dependencies of electric current force on time, obtained at ETE of titanium and carbon black mixture at  $P = 48$  MPa and  $U$  (V): 1 3; 2 4; 3 6; 4 9; and 5 11.

Thus, the results obtained showed that the measurement of thermal and electrical parameters allows to determine the separate stage of ETV, but also the modes of homogeneous or inhomogeneous heating of the test sample.

1. V.A. Shcherbakov, V.T. Tilopa, A.V. Shcherbakov, Preparation of composite materials based on fused titanium carbide by the electro-thermal explosion under pressure, *Compos. Nanostruct.*, 2016, vol. 8, no. 1, pp. 70–80.
2. V.T. Telepa, V.A. Shcherbakov, A.V. Shcherbakov, Production of composite TiC–30 weight % Fe by electrothermal explosion under pressure, *Mater. Lett.*, 2016, vol. 6, no. 4, pp. 286–289.
3. V.A. Scherbakov, A.V. Shcherbakov, S.A. Bostandzhiyan, Electrothermal explosion of titanium and carbon black mixture under quasi-isostatic compression. Part I - Thermal and electrical parameters, *Combust. Shock Wave*, 2019, no. 1, pp. 83–91.

## THE METASTABLE PHASE COMPOSITION OF FeTiB FILMS PRODUCED BY MAGNETRON SPUTTERING

E. N. Sheftel<sup>\*a</sup>, Ph. V. Kiryukhantsev-Korneev<sup>b</sup>, V. A. Tedzhetov<sup>a</sup>, E. V. Harin<sup>a</sup>, and G. Sh. Usmanova<sup>a</sup>

<sup>a</sup>Baikov Institute of Metallurgy and Materials Science, RAS, Moscow, 119334 Russia

<sup>b</sup>National University of Science and Technology MISiS, Moscow, 119049 Russia

\*e-mail: velmurad@yandex.ru

DOI: 10.24411/9999-0014A-2019-10157

The paper presents the results of the complex study of nanocrystalline Fe<sub>97.8-54.5</sub>Ti<sub>0-16.6</sub>B<sub>0-28.9</sub>O<sub>0-3.8</sub> films. The films were deposited on glass and metal substrates by magnetron DC sputtering [1] of composite targets: Fe target & SHS TiB/TiB<sub>2</sub> chips, Fe target and hot-pressed TiB<sub>2</sub> chips, or SHS TiB target & Fe chips. The sputtering was performed in Ar atmosphere. The films were annealed in vacuum at temperatures of 200–500°C. The chemical composition and structure of the as-deposited and annealed films were studied using SEM, EDS, GDOES, XRD, and TEM methods. Magnetic properties were studied by the VSM method. Mechanical properties were measured by nanoindentation under loads of 1–5 mN.

The phase composition of the films depends on the concentration of C<sub>B</sub> and C<sub>Ti</sub>, their ratio C<sub>B</sub>/C<sub>Ti</sub> and the type of boride ceramic used in the target (Fig. 1):

- (a) (C<sub>B</sub>/C<sub>Ti</sub> ~ 2) single phase – bcc solid solution α-Fe(Ti,B);
- (b) (C<sub>B</sub>/C<sub>Ti</sub> < 2) two-phase – α-Fe (main phase) + α-Ti/Fe<sub>2</sub>B/FeTi/TiB<sub>2</sub> (additional phases), target with SHS chips;
- (c) (C<sub>B</sub>/C<sub>Ti</sub> < 2) four-phase – α-Fe + α-Ti + Fe<sub>2</sub>B + Ti<sub>2</sub>B<sub>5</sub>, a target with hot-pressed chips;
- (d) (C<sub>B</sub> + C<sub>Ti</sub> > 19) XRD amorphous phase.

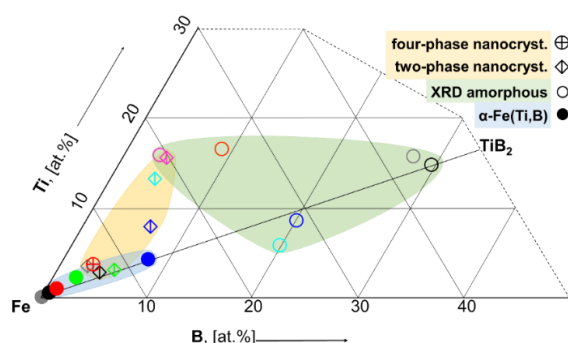


Fig. 1. Chemical compositions of studied as-deposited films.

The formation of a solid solution in nanocrystalline films (a, b, and c) is confirmed by XRD data (the lattice parameter of the bcc phase is higher than that of pure Fe). In single-phase (a) and multiphase (b, c) as-deposited films, with increasing Ti and B content, the lattice parameter of the bcc phase increases (Fig. 2a), and the bcc grain size decreases (Fig. 2b). According to the TEM results, XRD amorphous films (d) have a nanocrystalline structure with a grain size less than 1.6 nm.

The films with a nanocrystalline structure (a, b, c) are strong ferromagnets with a saturation induction in the range of 0.95–2.13 T, depending on the chemical composition. The magnitude of the coercive field of studied films (3–52 Oe) characterizes them as soft magnetic materials. Films with X-ray amorphous structure are superparamagnetic.

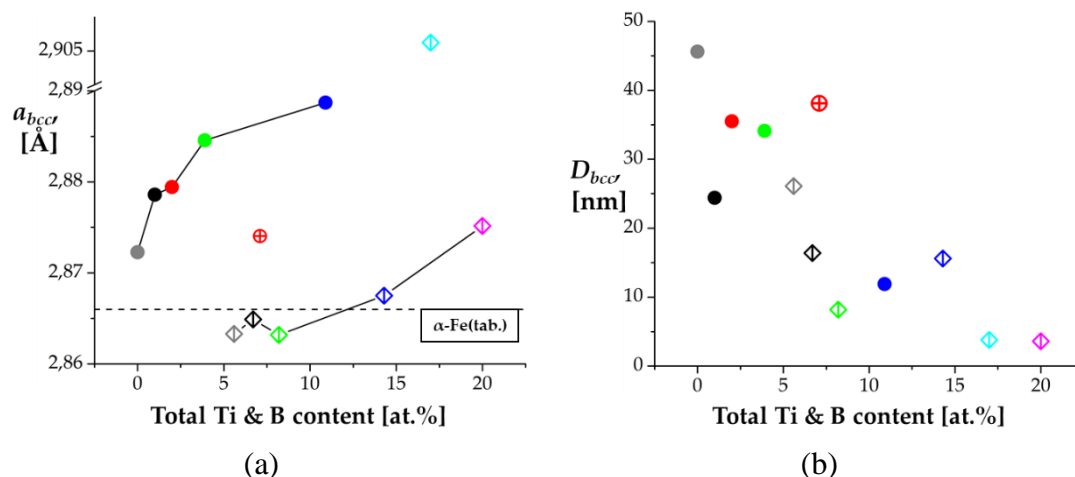


Fig. 2. Lattice parameter (a) and grain size (b) of the bcc phase as functions of the total Ti and B contents in as-deposited films.

The single-phase as-deposited films (a) have high hardness (12.8÷21.7 GPa) in combination with a low modulus of elasticity (159÷221 GPa) and high elastic recovery (> 55%), which allows predicting high resistance to plastic deformation [2].

The data obtained in this work testifies to the prospects of using SHS boride ceramics as a material for a sputtered target for producing Fe–Ti–B films.

The research was supported by the Russian Foundation for Basic Research, (project no. 18-03-00502).

1. E.N. Sheftel, V.A. Tedzhetov, E.V. Harin, et al., *Phys. Status Solidi C.*, 2016, vol. 13, nos. 10–12, pp. 965–971.
2. A. Leyland, A. Matthews, *Wear*, 2000, vol. 246, pp. 1–11.

## FORMATION OF TiC/C LAYER ON Ti ALLOYS BY A SIMULTANEOUS ELECTRO-SPARK AND ARC EVAPORATION TREATMENT WITH GRAPHITE ELECTRODE

A. N. Sheveyko<sup>\*a</sup>, K. A. Kuptsov<sup>a</sup>, A. E. Kudryashov<sup>a</sup>, and D. V. Shtansky<sup>a</sup>

<sup>a</sup>National University of Science and Technology MISiS, Moscow, 119049 Russia

\*e-mail: sheveyko@mail.ru

DOI: 10.24411/9999-0014A-2019-10158

A new technology combining pulsed arc evaporation (PAE) and electric-spark deposition (ESD) in vacuum was developed and used for two-layer wear-resistant Ti–TiC/a-C coating deposition on Ti. Both processes were carried out together in a single vacuum process using the same graphite electrode. In such a process, part of the electrical impulses is realized in the spark discharge due to electrodes contact leading to graphite transfer into the crater of titanium melt, which, in turn, results in carbide formation. Another part of the pulses causes the arc discharge initiation leading to carbon transfer to the substrate surface with the formation of a carbon coating. The structure, elemental and phase composition of the coatings were studied by means of X-ray diffraction, scanning and transmission electron microscopy, X-ray photoelectron spectroscopy, energy dispersive X-ray spectroscopy, glow discharge optical emission spectroscopy, and Raman spectroscopy. The ESD layer, more than 100  $\mu\text{m}$  thick, was consisted of  $\alpha$ -Ti ( $\sim 50\%$ ),  $\text{TiC}_x$ , and a small amount of free carbon. The PAE layer 10–15  $\mu\text{m}$  thick was characterized by a nanocomposite, nearly amorphous structure, in which disordered  $\text{TiC}_x$  crystallites 3–5 nm in size were dispersed in an amorphous carbon matrix with 30% of  $\text{sp}^3$ -hybridized bonds. The ESD layer had a hardness of approximately 15 GPa. The two-layer coating demonstrated a superior tribological performance ( $\text{CoF} < 0.2$ , wear rate  $< 5 \times 10^{-7} \text{ mm}^3/\text{Nm}$ ), which was attributed to a combination of high toughness and thickness of the ESD layer, which prevented the substrate from plastic deformation, and to low friction coefficient of the top PAE layer due to nearly amorphous structure with large amount of free carbon in graphite state acting as a solid lubricant.

The authors gratefully acknowledge the financial support from the Russian Scientific Foundation (agreement No. 15-19-00203-II).

# EVOLUTION OF THE STRUCTURAL CONDITION OF REACTION POWDER MIXTURES OF THE Ti–Ni SYSTEM UNDER MECHANICAL ACTIVATION. THEORETICAL ESTIMATES BASED ON EXPERIMENTAL STUDIES

**O. A. Shkoda and O. V. Lapshin**

Tomsk Scientific Center, Siberian Branch, Russian Academy of Sciences,  
Tomsk, 634055 Russia  
e-mail: ovlap@mail.ru, O.Shkoda@dsm.tsc.ru

DOI: 10.24411/9999-0014A-2019-10159

An experimental study of the mechanical activation process (MA) of a powder mixture of nickel and titanium was carried out. It is revealed that the MA time has a significant impact on the physico-chemical and structural transformations of the crushed mixture. The reason for this effect is a change in the composition and structure of the layered agglomerates arising during the MA from the components of the mixture. The method of the inverse problem is used to estimate the kinetic constant characterizing the growth rate of the interfacial surface in agglomerates during the mechanical treatment of the powder mixture. Theoretical calculations of the layer thickness and the size of the interfacial surface in the agglomerate are carried out. Mechanical activation is the effective method of stimulation of chemical reactions, allowing to expand the possibilities of synthesis of inorganic materials [1]. For example, with the help of MA it is possible to synthesize low-energy compositions, which in traditional conditions of the organization of synthesis practically do not burn. To date, the main part of the experimental studies is devoted to the study of combustion characteristics and phase composition in the pre-MA condensed systems [2–5]. Much less work is paid to the study of the features arising in the reaction mixture at the first stage of mechanosynthesis during the preliminary MA.

As shown in [6, 7], the mechanical activation changes the morphology and microstructure of the initial powders, brittle substances are mainly crushed, and in the presence of plastic materials, layered agglomerates of various sizes are formed. Sizes can vary from a few nanometers to millimeters, depending on the composition and time of the MA. There is a constant breaking of the initial and already agglomerated particles and simultaneous connection of the newly formed surfaces into a layered agglomerate. The process of breaking and formation of new agglomerates during MA is carried out constantly.

In the layered agglomerates formed in this way, consisting of crushed initial reagents, their contact area increases and a high concentration of non-equilibrium defects and internal stresses is created. Also, there is a destruction of oxide layers and adsorbed films on powder particles, which are a diffusion barrier to interaction. Thus, the preliminary MA of the initial powders leads to a significant change in the structure of the powder mixture to the accumulation of the energy supplied and determines the nature of the subsequent combustion at the second stage of mechanosynthesis.

In this paper, we study the regularities of the formation of the internal structure of layered agglomerates formed during MA in the Ti–Ni system. The experiments used powders of titanium PTEM 1 and Nickel grade PNE 1. Mechanical activation of powder mixture of Ti–55.06 mass % Ni (stoichiometry TiNi) was performed in a planetary mill M-3 with a power density of 45 g in the environment of argon. The weight ratio of the powder to the weight of balls was 1:5. Duration was from 1 to 9 min. The total time of mechanical activation was collected in discrete periods of 30 s, between which there was a cooling period of 5 min. The

structure and composition of the studied activated powder mixtures and combustion products were investigated by scanning electron microscopy (Philips SEM515) and optical metallography (Axiovert200m). Figure 1 shows the agglomerate formed after 2 min of MA. It can be seen that the agglomerate consists of sticking smaller pieces and layers.

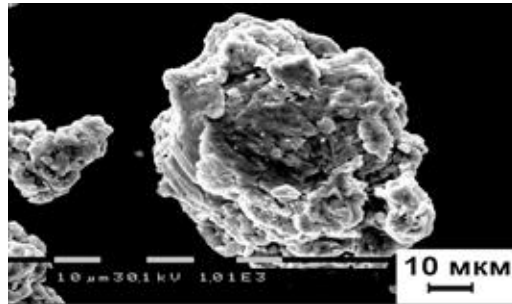


Fig.1 Microphotography of appearance of layered agglomerate formed during MA.

Figure 2 shows the SEM images of the cross section of agglomerates after 2 min (a) and 3 min (b) of MA, respectively. Layers of light color belong to nickel, dark layers belong to titanium. With a further increase in the time of MA agglomerates constantly change their size and structure. To study the internal structure of the agglomerate, metallographic sections of layered agglomerates were made, on which a sequence of layers of titanium and Nickel powders is clearly visible.

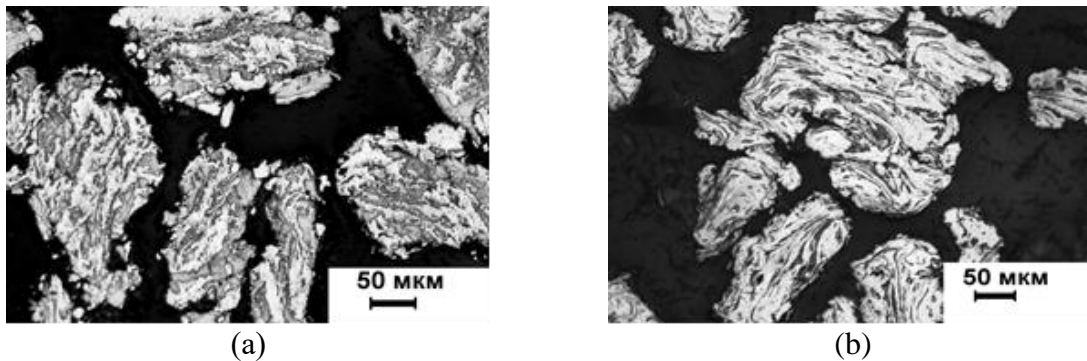


Fig. 2. Microphotography of sections of layered agglomerates formed after 2 min (a) and 3 min (b) of MA.

The thickness of the layers in the agglomerate, as well as the size of the agglomerate itself, undergo changes throughout the MA: in general dynamics, they are thinned, which contributes to the creation of a more developed interfacial surface in the agglomerate. Moreover, the differences in the layer structure of the agglomerate in the presented images are quite noticeable, although the difference between them is only 1 min of MA time.

An important aspect in experimental studies is the knowledge of effective kinetic constants that allow using the developed mathematical models to obtain preliminary prognostic estimates. In [8] a mathematical model describing the formation of layered structure in the agglomerates in the milling conditions of a binary mixture in energozatratno mill. There is also obtained the ratio, which is performed for small machining times, which determines the dependence of the thickness of the total layer, including two adjacent layers  $d$  of dissimilar components in the structure of the agglomerate, on the time of mechanical activation.

$$d = \frac{2}{K\mu_{0Ti}\mu_{0Ni}t^2} \quad (1)$$

where  $K = kW/V$  is the kinetic constant;  $W$  is the power of the energy-stressed mill;  $V$  is the volume of the crushed mixture;  $k$  is the coefficient depending on the physical and chemical

properties of the components involved in grinding and agglomeration;  $t$  is the time;  $\mu_{0Ti}$  and  $\mu_{0Ni}$  are the initial volume fractions of Ti and Ni components in the mechanically activated mixture. The inverse of the parameter  $d$  determines the specific interfacial surface in the agglomerate  $S = 1/d$ .

The straightening of the method of least squares of the experimental results allowed to calculate the part of the relation (1) parameter  $K = 0.263$  ( $\mu\text{m min}^2$ ) for  $\mu_{0Ti} = 0.62$  and  $\mu_{0Ni} = 0.38$ . The experimental study of the dynamics of the thickness of the layers of agglomerates in the conditions of mechanical activation of the powder mixture of titanium and nickel. It is revealed that with the increase of MA time there is a predominant decrease in the width of the layers of titanium and nickel in the agglomerate, the developed interfacial surface is formed in it.

The kinetic constant determining the formation of a layered structure in an agglomerate at MA in the Ti–Ni system is estimated. It is shown that the theoretical calculations of the dynamics of quantities  $d$  and  $S$  in the process of MA at the qualitative level correspond to the results of experiments carried out using the kinetic constant found.

1. T.F. Grigor'eva, A.P. Barinova, N.Z. Lyakhov, Mechanical-Chemical Synthesis in Metal Systems [in Russian], Parallel', Novosibirsk, 2008.
2. O.A. Shkoda, L.G. Raskolenko, *Int. J. Self-Propag. High-Temp. Synth.*, 2010, vol. 19, no. 2, pp. 128.
3. M.A. Korchagin, T.F. Grigor'eva, B.B. Bokhonov, et al, *Fiz. Gor. Vzryva*, 2003, vol. 39, no. 1, pp. 51–68.
4. E.A. Levashov, V.V. Kurbatkina, K.V. Kolesnichenko, *Izv. Vyssh. Uchebn. Zaved., Tsvetn. Metall.*, 2000, no. 6, pp. 61–67.
5. V.K. Smolyakov, V.I. Itin, N.N. Golobokov, et al, *Fiz. Gor. Vzryva*, 2005, vol. 41, no. 5, pp. 92–99.
6. N.G. Kasatskii, O. A. Shkoda, *Fiz. Khim. Obrab. Mater.*, 2012, no. 5, pp. 71.
7. E.G. Avvakumov, Mechanical Methods for Activation of Chemical Properties [in Russian], Nauka, Novosibirsk, 1986.
8. O.V. Lapshin, V.K. Smolyakov, *Khim, Fiz. Mezosk.*, 2013, vol. 15, no. 2, pp. 272–278.

## STRUCTURAL EVOLUTION AND MAGNETIC PROPERTIES OF HIGH ENTROPY CuCrFeTiNi ALLOYS PREPARED BY MECHANICAL ALLOYING AND SPS

**N. F. Shkodich<sup>\*a,b</sup>, M. Spasova<sup>c</sup>, M. Farle<sup>c</sup>, D. Yu. Kovalev<sup>a</sup>, A. A. Nepapushev<sup>b</sup>, K. V. Kuskov<sup>b</sup>, Yu. S. Vergunova<sup>b</sup>, Yu. B. Scheck<sup>a</sup>, and A. S. Rogachev<sup>a,b</sup>**

<sup>a</sup>Merzhanov Institute of Structural Macrokinetics and Materials Science, Russian Academy of Sciences, Chernogolovka, Moscow, 142432 Russia

<sup>b</sup>Center of Functional Nano-Ceramics, National University of Science and Technology MISIS, Moscow, 119049 Russia

<sup>c</sup>Faculty of Physics and Center of Nanointegration (CENIDE), University of Duisburg-Essen, Duisburg, 47057 Germany

\*e-mail: n.f.shkodich@mail.ru

DOI: 10.24411/9999-0014A-2019-10160

A novel approach to the fabrication of a new class of alloys—also known as high-entropy alloys (HEAs)—was developed by Yeh et al. [1–3]. The HEAs containing at least 5 components in equiatomic or nearly equiatomic amounts (ranging between 5 and 35 at %) are attractive in terms of hardness, wear resistance, high-temperature strength, corrosion resistance, low-temperature ductility, glass forming ability, super-plasticity, and some magnetic properties [4, 5]. These HEA are stabilized by the increase of the mixing entropy which is thought to suppress the formation of metallic phases and thus favors the formation of simple solid solutions with a fcc or bcc or bcc + fcc structure.

HEAs have been fabricated by several methods, including arc melting and casting, mechanical alloying, and laser cladding [6–8]. Among these, especially promising seems to be high-energy ball milling (HEBM) in planetary ball mills that can yield stable microstructures and nanocrystalline alloys of better homogeneity compared to other non-equilibrium processes. In this communication, we report the first preparation of CuCrFeTiNi HEA particles by high-energy ball milling (HEBM) and spark plasma sintering (SPS) and provide a structural and magnetic characterization. The powder of equiatomic CuCrFeTiNi high-entropy alloy was prepared by short-term HEBM. Our XRD, SEM, and EDX results showed that a bcc CuCrFeTiNi solid solution with refined microstructure of nanosized grains (~ 6 nm) could be obtained starting from 30 min of HEBM. Produced HEA powders were studied by DSC and showed a thermal stability of up to 500°C. The as-milled HEA powder was subsequently consolidated by spark plasma sintering at 700°C, and the bcc and fcc phases were found to coexist in consolidated HEA. The kinetics and structural transformations upon heating to 1000°C were studied by high-temperature X-ray diffraction (HTXRD) (Fig. 1).

The Vickers hardness of the HEA CuCrFeTiNi alloy (milled for  $t = 180$  min) consolidated by SPS was markedly higher (7.7 GPa) than that of SPS-produced ones without HEBM (2.1 GPa). Electrical resistance of consolidated CuCrFeTiNi alloys was  $10^{-6}$  Ω m. The influence of HEBM duration on the magnetic properties of HEA powders were determined at different temperatures. The HEA powder formed after 180 min of HEBM exhibited paramagnetic behavior at room temperature with a small ferromagnetic contribution at low fields: small hysteresis is observed at 5 K and 300 K with a coercive field of around 16 kA/m. Above 100 K, the inverse susceptibility of HEA powder ( $t = 240$  min) shows the linear response to increasing temperature typical of paramagnets. A Curie temperature  $T_C = 50$  K was measured.



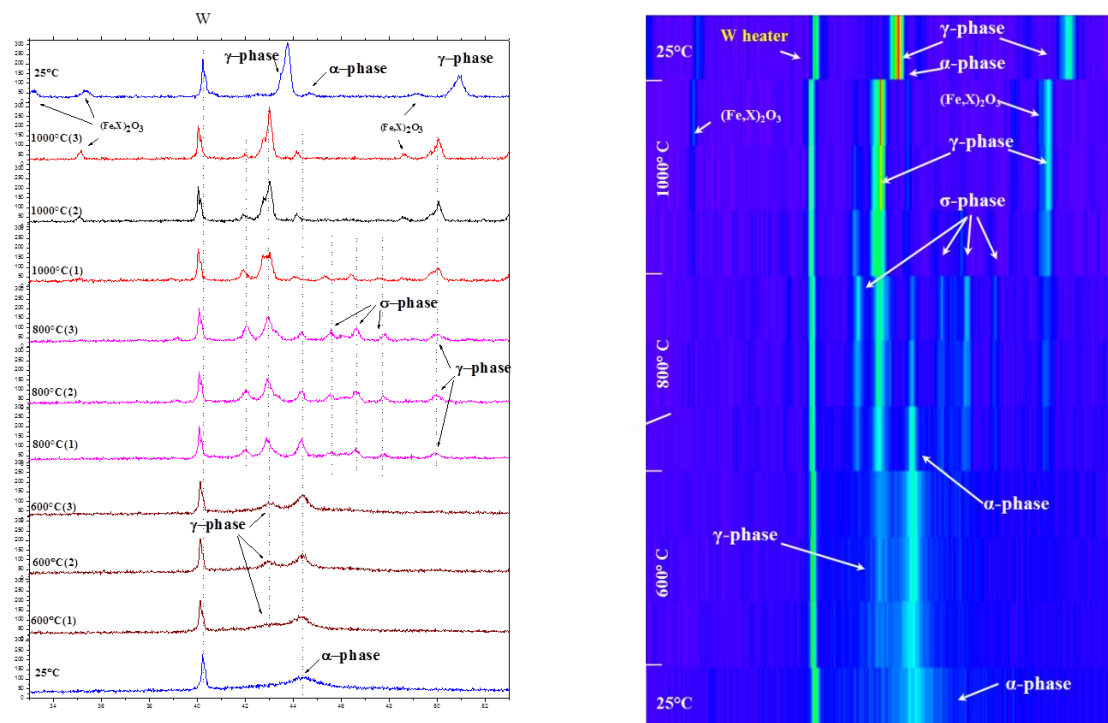


Fig. 1. High-temperature XRD for CuCrFeTiNi powder mixtures milled for 180 min.

We thank M. Acet and U. Wiedwald for helpful discussions and G.V. Trusov., and I. D. Kovalev for their kind help in experiments. This work was financially supported by Russian Foundation for Basic Research through grant 18-53-15006.

1. P.-K. Huang, J.-W. Yeh, T.-T. Shun, S.-K. Chen, Multi-principal-element alloys with improved oxidation and wear resistance for thermal spray coating, *Adv. Eng. Mater.*, 2004, vol. 6, pp. 74–78.
2. J.-W. Yeh, S.-K. Chen, J.-W. Gan, S.-J. Lin, T.-S. Chin, T.-T. Shun, C.-H. Tsau, S.-Y. Chang, Formation of simple crystal structures in Cu–Co–Ni–Cr–Al–Fe–Ti–V alloys with multiprincipal metallic elements, *Metall. Mater. Trans. A*, 2004, vol. 35, pp. 2533–2536.
3. J.-W. Yeh, S.-K. Chen, S.-J. Lin, J.-Y. Gan, T.-S. Chin, T.-T. Shun, C.-H. Tsau, S.-Y. Chang, Nanostructured high-entropy alloys with multiple principal elements: Novel alloy design concepts and outcomes, *Adv. Eng. Mater.*, 2004, vol. 6, pp. 299–303.
4. B. Cantor, I.T.H. Chang, P. Knight, A.J.B. Vincent, Microstructural development in equiatomic multicomponent alloys, *Mater. Sci. Eng. A*, 2004, vol. 375–377, pp. 213–218.
5. D.B. Miracle, O.N. Senkov, A critical review of high-entropy alloys and related concepts, *Acta Mater.*, 2017, vol. 122, pp. 448–511.
6. G.A. Baglyuk, M.V. Marich, A.A. Mamonova, A.N. Gripachevskii, Features of structurization during sintering of compacts from a multicomponent Ti–Cr–Fe–Ni–Cu charge, *Powder Metall. Met. Ceram.*, 2016, vol. 54, nos. 9–10, pp. 543–547.
7. J. Lua, B. Wang, X. Qiu, Zh. Peng, M. Ma, Microstructure evolution and properties of CrCuFeNiTi high-entropy alloy coating by plasma cladding on Q235, *Surf. Coat. Technol.*, 2017, vol. 328, pp. 313–318.
8. K. Sobiyyi, M. Bodunrin, E. Akinlabi & B. Obadele, Microstructure and Tribological Behaviour of CrCuFeNiTi High Entropy Alloys, *MATEC Web Conf.*, 2016, vol. 82, 02007.

## SHS IN SURFACE ENGINEERING

**D. V. Shtansky**

National University of Science and Technology MISiS, Moscow, 119049 Russia  
e-mail: shtansky@shs.misis.ru

DOI: 10.24411/9999-0014A-2019-10161

Utilization of SHS in surface engineering is rapidly growing field. The heat released during SHS is useful in terms of providing high adhesion strength between coating and substrate. The surface treatment process which combines SHS and coating deposition is referred as SHS coating. The process can be subdivided according to the method of coating deposition, type of precursor materials, type of external heat source to initiate combustion reaction, as well as the densification method used for synthesized products [1].

In the field of surface engineering, SHS is frequently combined with other methods such as centrifugation, microwave and induction heating, laser cladding, sol-gel, concentrated solar energy treatment, high velocity oxy-fuel thermal spraying, reactive and atmospheric plasma spraying, plasma transferred arc overlay welding, and electroless plating. Various metallic, ceramics, metal matrix composite, steel matrix composite, and ceramic matrix composite coatings were fabricated. There are two main routes of coating deposition which may be classified as SHS: (i) a mixture of exothermically reactive powders or a cold pressed product is applied to the substrate surface as a precursor and then ignited by an external energy source and (ii) SHS-derived powders, targets or electrodes were fabricated separately and then used in coating deposition technologies such as plasma spraying, magnetron and ion sputtering, electro-spark deposition, and electroless plating. The first route is often referred to as an in situ or single step process because both processes, namely SHS and coating deposition, occur simultaneously.

The possibilities of various physical vapor deposition (PVD) technologies can be extended through the application of SHS targets and electrodes. Coatings with an improved combination of properties can also be produced through non-vacuum methods, for example by pulsed electrospark deposition (ESD), using SHS electrodes. The method utilizes an exothermic reaction initiated by an electric discharge within an inter-electrode space. Recently, a new cost-efficient technology that combines pulsed arc evaporation (PAE) and ESD in vacuum to fabricate two-layer coatings in a single technological run using the same electrode was developed (Fig. 1). Two-layer PAE/ESD coatings have several advantages over their single-layer counterparts: the ESA sublayer is expected to provide excellent adhesion (due to local melting and mixing of deposited and substrate materials in an erosion hole), high coating thickness (up to 100  $\mu\text{m}$ ) and enhanced toughness, whereas the upper thinner layer (up to 10  $\mu\text{m}$ ) obtained by PAE method provides better mechanical and tribological characteristics due to the absence of substrate material.

Herein after a brief introduction in the field of SHS in surface engineering we consider most recent successful examples of SHS target utilization for depositing advanced coatings for various tribological and medical applications:

- (a) Low friction wear resistant nanocomposite Si-Ta-C-(N) coatings intended for wide temperature range tribological applications (Fig. 2) [3];
- (b) Ti-C-Ni-Al, Ti-C-Ni-Fe, and Ti-C-Ni-Al/Ti-C-Ni-Fe coatings produced by magnetron sputtering, ESD, and a combined two-step process [4];
- (c) Biodegradable polycaprolactone (PCL) nanofibers coated with bioactive TiCaPCON film [5];

- (d) B-doped TiCaPCON films [6];  
 (e) Ag, Pt, Zn, and Fe nanoparticle-decorated antibacterial TiCaPCON films (Fig. 3) [7];  
 (f) Antibiotic-loaded TiCaPCON-Ag films [8].

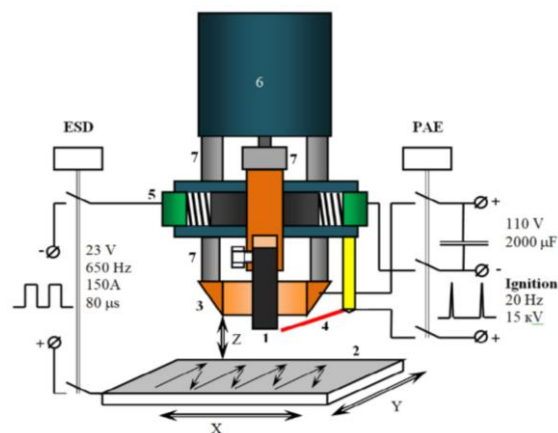


Fig. 1. Scheme of ESD/PAE unit. 1 electrode, 2 substrate, 3 circular anode, 4 ignition electrode, 5 brush assembly, 6 electric motor, 7 insulating ceramics [2].

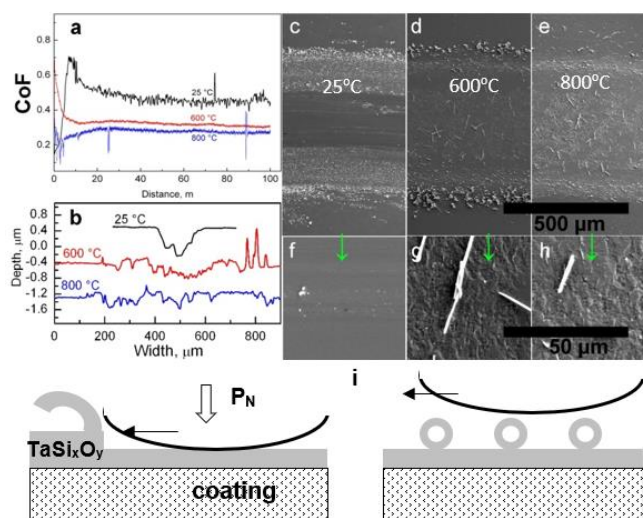


Fig. 2. Friction coefficients of Ta–Si–C–N coatings at different temperatures (a), wear track profiles after the tests (b), SEM images of wear tracks after the tests, and the schematics of the possible wear mechanism involving microfibers (i) [3].

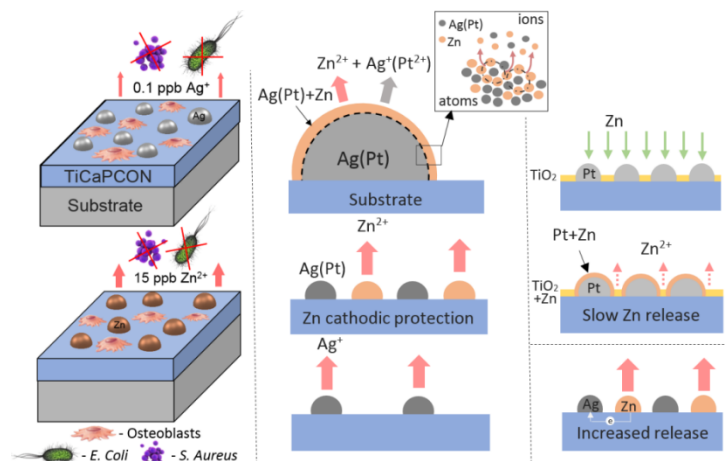


Fig. 3. Scheme of Ag, Pt, and Zn nanoparticles on the surface of TiCaPCON film, the mechanisms of their dissolution, ion release, and effects on bacteria and cells [7].

The work was supported by the Russian Science Foundation (Agreement no. 15-19-00203-II) in the part of tribological coatings and the Ministry of Education and Science of the Russian Federation (Increased Competitiveness Program of NUST “MISiS” no. K2-2018-012) in the part of biological films.

1. E.A. Levashov, A.S. Mukasyan, A.S. Rogachev, D.V. Shtansky, *Int. Mater. Rev.*, 2017, vol. 62, no. 4, pp. 203–239.
2. K.A. Kuptsov, A.N. Sheveyko, E.I. Zamulaeva, D.A. Sidorenko, D.V. Shtansky, *Mater. Design*, 2019, vol. 167, 107645.
3. A.V. Bondarev, S. Vorotilo, I.V. Shchetinin, E.A. Levashov, D.V. Shtansky, *Surf. Coat. Technol.*, 2019, vol. 359, pp. 342–353.
4. Ph.V. Kiryukhantsev-Korneev, A.N. Sheveyko, N.V. Shvindina, E.A. Levashov, D.V. Shtansky, *Ceram. Int.*, 2018, vol. 44, pp. 7637–7646.
5. A. Manakhov, E. Permykova, S. Ershov, A. Sheveyko, J. Polcak, N. Gloushankova, L. Zajickova, D. Shtansky, *Appl. Surf. Sci.*, 2019, vol. 479, pp. 796–802.
6. V.A. Ponomarev, A.N. Sheveiko, I.V. Sukhorukova, N.V. Shvindina, A.M. Manakhov, I.Y. Zhitnyak, N.A. Gloushankova, N.K. Fursova, S.G. Ignatov, E.S. Permyakova, J. Polčak, D.V. Shtansky, *Appl. Surf. Sci.*, 2019, vol. 465, pp. 486–497.
7. V.A. Ponomarev, I.V. Sukhorukova, A.N. Sheveyko, E.S. Permyakova, A.M. Manakhov, S.G. Ignatov, N.A. Gloushankova, I.Y. Zhitnyak, O.I. Lebedev, J. Polčak, A.M. Kozmin, D.V. Shtansky, *ACS Appl. Mater. Interfaces*, 2018, vol. 10, pp. 24406–24420.
8. I.V. Sukhorukova, A.N. Sheveyko, A. Manakhov, I.Y. Zhitnyak, N.A. Gloushankova, E.A. Denisenko, S. Yu. Filippovich, S.G. Ignatov, D.V. Shtansky, *Mater. Sci. Eng. C*, 2018, vol. 90, pp. 289–299.

## SELF-PROPAGATING HIGH-TEMPERATURE SYNTHESIS OF HEAT-RESISTANT ELECTRICALLY CONDUCTIVE COATINGS BASED ON Ni–Al AND Ti–Al–C SYSTEM COMPOUNDS

A. M. Shulpekov<sup>\*a</sup>, R. M. Gabbasov<sup>a</sup>, and O. K. Lepakova<sup>a</sup>

Tomsk Scientific center SB RAS, Tomsk, 634055 Russia

<sup>\*</sup>e-mail: shulp@yandex.ru

DOI: 10.24411/9999-0014A-2019-10162

Compounds formed in the Ni–Al and Ti–Al–C systems have high heat resistance, oxidation resistance, hardness and electrical conductivity [1, 2]. Coatings of these materials are used as heat-resistant protective layers [3]. Traditionally, such coatings are produced by the method of air-plasma spraying [4]. The method requires the use of a large amount of energy to create a plasma and to provide a high temperature for melting the coating components. In this paper, we have proposed a method for obtaining a coating, which consists in applying a mixture of powders of the initial components to the substrate. Heating a portion of the powder layer leads to an exothermic synthesis reaction of compounds with increasing temperature. Further, the reaction spreads over the surface in the form of a combustion wave. Thus, the energy costs are insignificant and are only needed to initiate the process. This process is the essence of obtaining materials by the method of self-propagating high-temperature synthesis (SHS). The aim of the work is to study the effect of the layer thickness on the temperature and speed of propagation of the combustion wave, the structure and electrical conductivity of the coating. To obtain a coating based on aluminum nickelides, a mixture of powders of nickel PNC1-UT1 and aluminum grade ASD-4 was prepared in a ratio of 31.5 wt % Al and 68.5 wt % Ni. And to obtain coatings based on the MAX phases of Ti<sub>2</sub>AlC, Ti<sub>3</sub>AlC<sub>2</sub>, powders of titanium PTX with a particle size of less than 40 μm, aluminum (ASD-4), carbon black (PM-15) were used in a ratio of 70 wt % Ti, 20 wt % Al and 10 wt % carbon black. The powders were previously annealed in vacuum at 200°C. A mixture of powders in the form of a suspension in isopropyl alcohol was applied onto a ceramic plate VK-1 through a stencil with a thickness of 0.3 to 2 mm and a width of 20 mm. The coating was dried in air at room temperature for 24 h. Previously, thermocouples of the T-type or WRe 5/20 brand were fixed on the ceramic plate at a distance of 10–35 mm from each other. To record thermograms, thermocouples were connected to an ADC and a personal computer. The propagation velocity was determined from the delay of the signal from two thermocouples (Fig. 1). The initiation of the reaction was carried out using an electric helix heated by an electric current. The phase composition of the synthesis products was determined on a portable tabletop X-ray device RIKOR (CoK<sub>α</sub> radiation) provided by Tomsk common use center SB RAS. Microstructural studies were performed on an optical microscope (Axiovert 200M, Karl Zeiss). The electrical resistance of the coatings was measured using a F-410 milliohm meter with a measurement range of  $1 \times 10^{-2}$ – $1 \times 10^7 \Omega$ . In separate experiments, the temperature of the combustion wave was measured by spectral pyrometry using a CCD spectrometer (HR 4000, Ocean Optics) (200–1100 nm, frequency 220 Hz, the duration of signal accumulation in a single spectrum  $4.5 \times 10^{-3}$  s) [5]. The experimental results show that after initiating the reaction, a burning wave with a front about 5 mm wide runs through the sample. The burning wave profile is shown in Fig. 2a. The temperature in the wave of combustion is much lower than that of cylindrical samples of similar composition. This is due to the large heat sink for flat specimens. The wave propagation velocity (5–10 mm/s) is close to the velocity of the combustion wave front of cylindrical samples of similar composition.

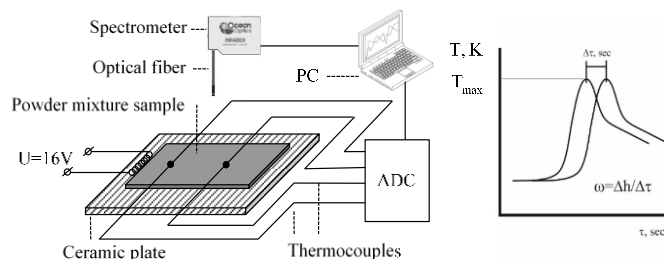


Fig. 1. Experimental setup.

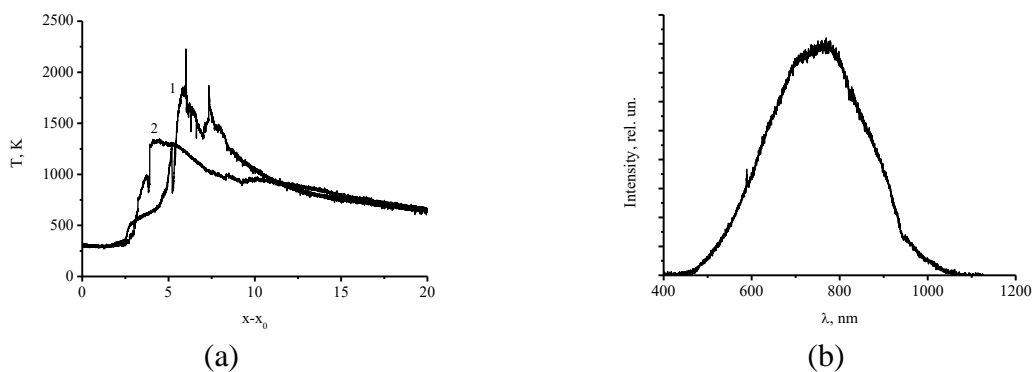


Fig. 2. (a) Combustion wave profile and (b) the emission spectrum from the combustion wave (for Ni–Al): 1 Ti–Al–C system, 2 Ni–Al.

For samples of composition 2Ti–Al–C, the temperature of the combustion wave front is higher than for samples of Ni–Al. This is also consistent with the data obtained for cylindrical samples. The emission spectrum from the combustion wave, shown in Fig. 2b, is close in shape to the spectrum of the thermal radiation of a heated body; the characteristic emission bands of the ions of the components of the initial mixture are not observed. The brightness temperature calculated from the emission spectra at 200–300°C above the temperature measured by a thermocouple. This may be due to the effect of radiation from the oxidation products of the powders, since the experiment was conducted in air.

With a coating thickness of less than 200 μm, the front does not spread, and with a thickness of more than 1500 μm, the ceramic substrate is destroyed due to thermal shock. With an increase in the thickness of the coating as NiAl, the velocity of the combustion wave front and the maximum temperature increase (Fig. 3a). This is due to the fact that the amount of heat released in the combustion wave increases. Heat losses are proportional to the sample area and, when its diameter changes, increase to a lesser degree than heat generation. Consequently, the energy of the system increases and, as a result, the temperature and speed of propagation of the front. In layered systems, the sample thickness is analogous to the diameter for cylindrical samples and the observed patterns are similar.

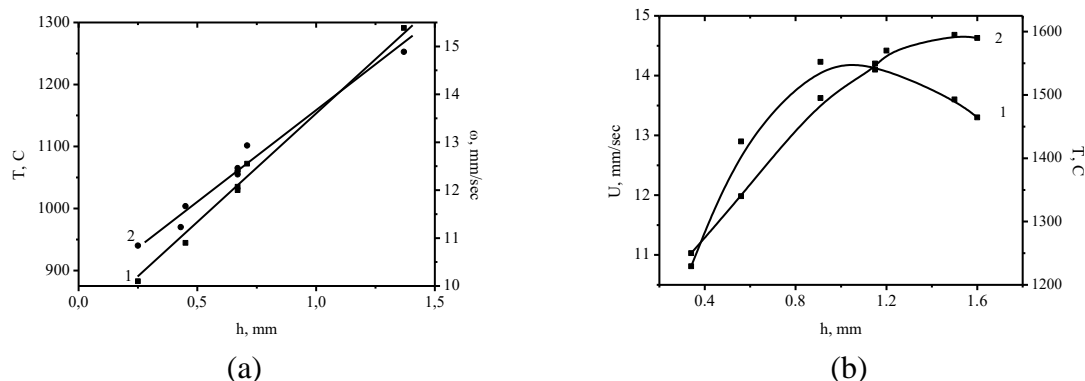


Fig. 3. The velocity of propagation of the front (curve 1) and the maximum temperature (curve 2) of Ni–Al (a) and Ti–Al–C (b) coatings of various thickness.

It can be seen in Fig. 3a that a similar regularity is observed for the Ti–Al–C system, but with a large layer thickness, the curve tends to saturation. This pattern is consistent with theoretical ideas about the processes of the combustion wave.

In addition, the propagation velocity of the front and its temperature largely depend on the relative density of the samples and the initial temperature. The use of metal substrates (Cu, Al, Fe, Ti) leads to an increase in the velocity of propagation of the front.

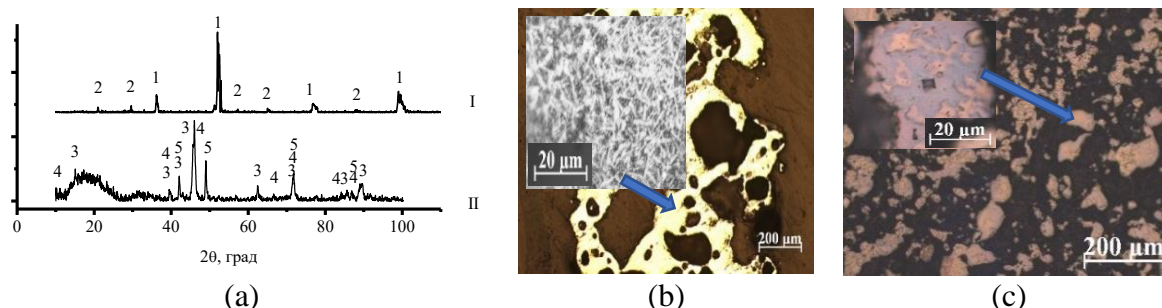


Fig. 4. (a) XRD patterns: I NiAl, II  $Ti_2AlC$  and the microstructure of the coating  $Ti_2AlC$  (b), and Ni–Al (c). Phases are designated: 1 NiAl, 2  $Ni_3Al$ , 3  $Ti_2AlC$ , 4  $Ti_3AlC_2$ , 5 TiC.

The Ni–Al coating contains NiAl and  $Ni_3Al$  phases (Fig. 4a). The predominant phase is NiAl. Nevertheless, the presence of the  $Ni_3Al$  phase indicates a significant lack of response in the combustion wave. This is due to the fact that the temperature in the combustion wave is much lower than for samples in the form of a cylinder. Increasing the thickness of the coating increases the concentration of the target phase NiAl. This is due to the increase in temperature in the combustion wave and the intensification of processes. The coating based on the Ti–Al–C system consists of the phases  $Ti_2AlC$ ,  $Ti_3AlC_2$ , TiC. With an increase in the thickness of the powder mixture, the content of  $Ti_2AlC$  relative to  $Ti_3AlC_2$  increases. The high content of titanium carbide indicates a significant failure in the system. Figure 4b shows a micrograph of the  $Ti_2AlC$  coating site. It can be seen that the coating consists of small rounded particles, often hollow, fused together. With a larger magnification, it can be seen that the particles consist mainly of needle-like crystals of MAX phases. Ni–Al coating consists of rounded solid particles fused with each other. At high magnification, it can be seen that the particles consist of two phases NiAl and  $Ni_3Al$  distributed in each other. The electrical resistance of the coating is  $2\text{--}8 \times 10^{-2} \Omega$ . This coincides with the resistance value for cylindrical samples obtained by the SHS method. This is due to the fact that the coating consists of many small particles fused with each other. It should be noted that the electrical resistance decreases with increasing coating thickness, which indicates that the resistivity of the coating material remains constant.

Thus, the effect of the thickness of the powder layer, its relative density and the initial temperature of the mixture on the front propagation velocity and the maximum temperature of the reaction wave for the layered powder mixtures of Ni–Al and Ti–Al–C during the SHS process is studied. A coating was obtained on the basis of the target heat-resistant phases — NiAl,  $Ni_3Al$  or  $Ti_2AlC$ ,  $Ti_3AlC_2$  with an optimum thickness of 200–1200  $\mu\text{m}$  and an electrical resistance of  $2\text{--}8 \times 10^{-2} \Omega$ . The coating can be used as protective layers or film electric heaters.

1. Y. Yang, H. Wu, Microstructure and microhardness of tempered Ni–Al alloyed layer, *J. Mater. Sci. Technol.*, 2012, vol. 28, no. 10, pp. 937–40.
2. B.A. Grinberg, M.A. Ivanov, Intermetallides  $Ni_3Al$  and TiAl: microstructure, deformation behavior, Ekaterinburg: UrO RAN, 2002, 360 p.
3. A. Hasuy, O. Morigaki, Surfacing and spraying M.: Mechanical Engineering, 1985, 240 p.
4. O.A. Rubtsova, I.D. Kuchumova, V.S. Miller, Structural studies of nickeline coatings, 16th AllRus. Sci.-Techn. Conf., Novosibirsk: Publishing house of the NSTU, 2015, p. 675-78.
5. A.N. Magunov, Spectral Pyrometry (Review), *Prib. Tekh. Eksp.*, 2009, vol. 4, p. 5.

## MODIFYING OF THE STAINLESS STEEL POROUS SURFACE BY NANOSTRUCTURED ALUMINA

V. V. Shustov<sup>\*a</sup>, V. A. Zelensky<sup>a</sup>, and A. B. Ankudinov<sup>a</sup><sup>a</sup>Baikov Institute of Metallurgy and Materials Science, Russian Academy of Sciences, Moscow, 119334 Russia\*e-mail: [\\_Nemo\\_73@mail.ru](mailto:_Nemo_73@mail.ru)

DOI: 10.24411/9999-0014A-2019-10163

A number of experiments were carried out to modify the inner surface in order to create nanostructures on carriers that do not have a highly developed inner surface but have high permeability values. On samples made of X18H10T stainless steel powder the nanostructure was formed by impregnating a porous carrier with solutions of salts and their subsequent thermal decomposition.

The process of production a porous sample consisted in compacting a mixture of stainless steel powder (with an average particle size of 10–20  $\mu\text{m}$ ) and a pore former (particle size of 250–320  $\mu\text{m}$ ) with a single-sided pressure of 400 MPa in a cylindrical matrix. Burnout of the pore former and sintering at 700°C result to the formation of a porous structure in the material, which was characterized by a bimodal pore size distribution.

Figure 1 shows the image of the fracture surface of a sintered sample obtained with a raster electron microscope. In Fig. 1 b, for clarity, some large pores in the sample are circled in white, the size of which is about 200  $\mu\text{m}$ , and the presence of channels that are visible as black spots can also be noticed. These channels can connect pores throughout the sample volume, having outlets into the space of separate pores (in the figure such outlets are marked with arrows). When determining the pore sizes in permeable materials, it should be understood that it is the size and number of such channels that determine such functional characteristics as filtration fineness and permeability of the material.

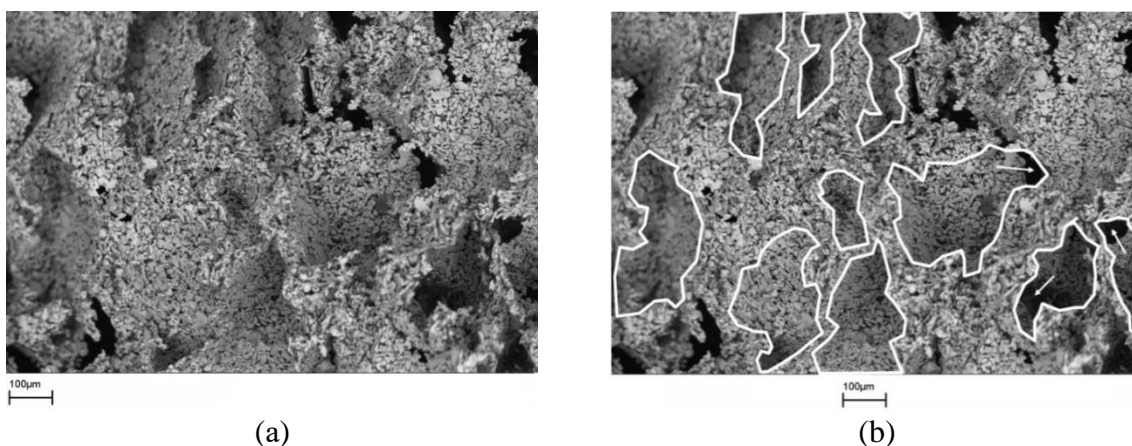


Fig. 1. Micrograph of the fracture of the stainless steel sample: (a) general view, (b) with the selection of macropores.

Modifying the surface of a porous carrier with aluminum oxide was carried out by impregnating it with an aqueous solution of an aluminum nitrate salt  $\text{Al}(\text{NO}_3)_3 \cdot 9\text{H}_2\text{O}$ . The porous sample was impregnated with solutions of salts of different concentrations from 0.5 to 1.5 mol/l. Full impregnation of the sample was achieved by immersing the pre-evacuated sample into the solution. It is known that aluminum nitrate  $\text{Al}(\text{NO}_3)_3$  undergoes hydrolysis,



when dissolved in water. The process of hydrolysis proceeds in three stages with the formation of intermediate compounds and ends with the appearance of aluminum hydroxide  $\text{Al}(\text{OH})_3$  and nitric acid  $\text{HNO}_3$  in solution. As a result of drying and subsequent annealing, decomposition of the remaining salt and aluminum hydroxide to an oxide occurs, and nitric acid also decomposes. Annealing was carried out at a temperature of  $450^\circ\text{C}$  for 60 min in a flowing argon atmosphere.

The structure of the obtained material was studied using scanning electron microscopy. Pores of about  $10\ \mu\text{m}$  in size are also present in the material, due to the fact that stainless steel powder with a particle size of  $10\text{--}20\ \mu\text{m}$  was used. The sintering mode led to the growth of necks between the particles, while the porosity value slightly changed as compared to compressed powder compact. Figure 2 clearly shows how a structure resembling a smooth thin film was formed on the surface of a porous carrier.

X-ray microanalysis showed the presence of aluminum and oxygen, with the aluminum content on the surface of the carrier particles being less than 1 wt % (Fig. 3, spectra S1, S2, S4), which can be explained by the nanometer thickness of the film formed on the surface of stainless steel. More voluminous aluminum oxide clusters were also found, which on SEM images in reflected electrons were seen as a translucent material located in the voids of the base material made of stainless steel (Fig. 4). Thus, the authors succeeded in creating a nanostructure on the surface of a material from stainless steel powders with a porous structure — a thin film of aluminum oxide. Such material is planned to be used for the manufacture of a catalytic cell in an ethanol catalysis unit.

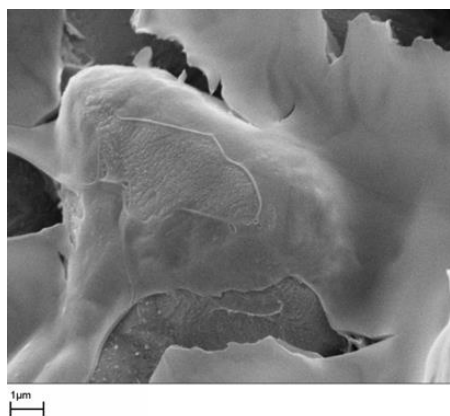
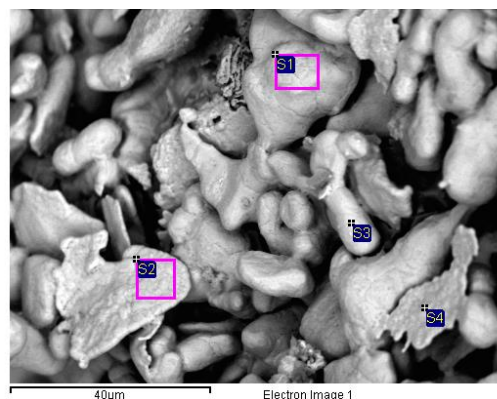


Fig. 2. Micrograph of the sample after the application of aluminum oxide.



| Spectrum | C   | O    | Al   | Cr   | Fe   | Ni   |
|----------|-----|------|------|------|------|------|
| S1       | 4.8 | 10.1 | 0.65 | 17.3 | 55.4 | 11.8 |
| S2       | 5.2 | 9.5  | 0.67 | 17.0 | 56.4 | 11.2 |
| S3       |     | 7.5  |      | 18.4 | 62.0 | 12.1 |
| S4       | 7.0 | 12.8 | 0.69 | 15.2 | 53.6 | 10.8 |

Fig.3. X-ray microanalysis of a stainless steel sample after the application of alumina.

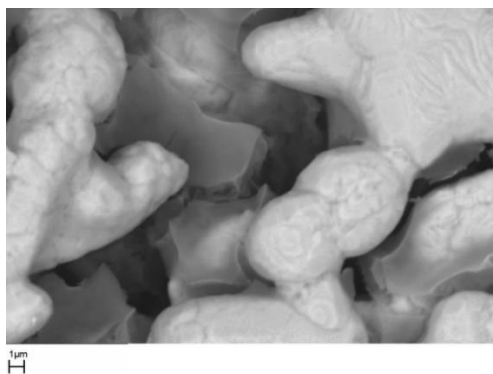


Fig. 4. SEM image of a porous stainless steel material coated with aluminum oxide.

The research was supported by the Russian Foundation for Basic Research (project no. 17-03-00867) with the involvement of state assignment number 075-00746-19-00.

## HYBRID POWDER BINDERS FOR EXTRA WEAR RESISTANT DIAMOND CUTTING TOOLS

**D. A. Sidorenko<sup>\*a</sup>, P. A. Loginov<sup>a</sup>, and E. A. Levashov<sup>a</sup>**

<sup>a</sup>National University of Science and Technology MISiS,  
Moscow, 119049 Russia  
<sup>\*</sup>e-mail: d.sidorenko@misis.ru

DOI: 10.24411/9999-0014A-2019-10164

Diamond tools are widely used to machine the most difficult-to-work-with materials, such as natural stone, reinforced concrete, asphalt and steels. The tool is a composite material with diamond grains incorporated into the metal, ceramic, or polymer binder. A promising way to design enhanced metal binders is mechanical alloying of elemental powders with simultaneous nanoparticle reinforcement.

We have proposed a new way of advanced binder design, which involved hybrid reinforcement with different types of nanoparticles. The various nanoparticles (MWCNT, h-BN, WC) and their combinations were incorporated into metallic matrices and their mechanical properties were experimentally determined. Nanoparticles pattern of distribution in binders (intracrystalline or intercrystalline) was studied using transmission electron microscope (Fig. 1). In-situ tests were carried out to study the effect of various nanoparticles on the deformation and fracture mechanisms of the composite materials under compression and tension conditions in a transmission electron microscope.

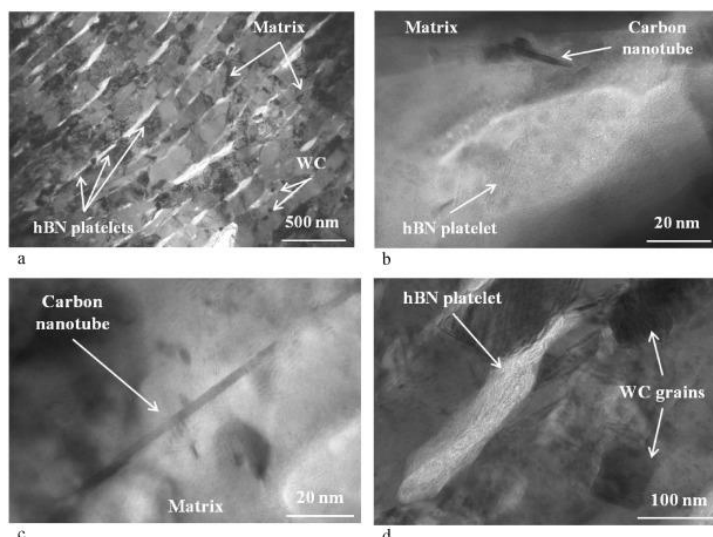


Fig. 1 Microstructure of hot pressed model sample [80%Cu–20%Ni]–0.1%hBN + 0.1%MWCNT + 0.69% WC (a) and images of hBN (b), CNT (c) and WC nanoparticles (d).

It was shown that the strong positive effect of the proposed combined nanoreinforcement was caused not by accumulation of mechanical effects, but rather by combination of different structure controlling effects, namely, grain size reducing due to carbon nanotubes introduction, mechanical reinforcement because of tungsten carbide, and lubricating properties of h-BN particles.

This work was supported by the Russian Science Foundation (grant no. 17-79-20384).

## SHS METALLURGY OF THE HARD ALLOY ON THE BASIS OF TUNGSTEN CARBIDE WITH THE NICKEL BOND

S. L. Silyakov<sup>\*a</sup>, V. I. Yuxhvid<sup>a</sup>, N. Yu. Khomenko<sup>a</sup>, T. I. Ignat'eva<sup>a</sup>,  
and N. V. Sachkova<sup>a</sup>

<sup>a</sup>Merzhanov Institute of Structural Macrokinetics and Materials Science, Russian Academy of Sciences, Chernogolovka, Moscow, 142432 Russia

\*e-mail: ssl@ism.ac.ru

DOI: 10.24411/9999-0014A-2019-10165

It is the most expedient to choose surfacing materials based on carbide–tungsten for protection and restitution of mechanisms details and junctions for the purpose of their resistance to all types of intensive wear under operating conditions. A relit is most often applicable as a reinforcing component phase of the surfacing carbide–tungsten materials. Often the cast relit is used in combination with cobalt and nickel bonds [1–4]. And in hard-facing alloys mainly cobalt is used as a cementing phase. However, its high cost forces to replace it with other metals, first in properties, particularly nickel. Comparative tests for two alloys WC–C and WC–Ni show advantage of the first in durability, hardness and wear resistances in comparison with the alloy with a nickel bond [5, 6]. However, in some cases manufacture of at mechanism details or while coating by means of flame spraying or high-velocity oxygen fuel spraying (HVOF), etc WC–Ni alloys are out of the competition. In this case mechanisms details are capable to resist to collateral influence of wear and corrosion.

Powder metallurgy remains the main traditional way of receiving surfacing materials based on carbide–tungsten [5]. As a result, this technique provides synthesis of tungsten carbide (WC), relit (WC–W<sub>2</sub>C) and alloys with a nickel bond on their basis. Due to the need for new approaches to receiving carbide–tungsten coverings, various ways of synthesis of carbide–tungsten surfacing materials on a nickel basis are offered [6–10].

In the present article we demonstrate the results on synthesis of a cast carbide–tungsten material by self-propagating high-temperature synthesis with a 15% nickel bond with use of the exothermic mixture of a thermite type.

The initial composition and the optimal ratios between the components of the exothermic mixture of a thermite type WO<sub>3</sub>:Al:Ca:C=0.705:0.090:0.164:0.041 are received during the research work [11]. This ratio provides synthesis of the cast carbide–tungsten material with the content of the fixed carbon 2.1 wt % at the minimum impurity content. For further researches the initial composition of the exothermic mixture WO<sub>3</sub>/Al/Ca/C is complemented with a mixture NiO:Al=0.806:0.194 which after combustion becomes a nickel source.

As components of the initial high-exothermic mixtures of a thermite type we use pure-grade powders of the tungsten oxide (VI) and nikel (II), aluminum powder (ASD-1 brand) calcium granules (CAS 7440–70–2, 99.1% activity) and graphite (GMZ, grain size 90/63 μm). Before mixing, these components are dried. The synthesis is carried out in a constant pressure bomb. In all experiments, the exothermic mixture is burned in graphite glasses with 20 mm in internal diameter and 60 mm in height. The exothermic mixtures weighing 30 g are poured out into the glasses at filling density of 1.98–2.00 g/cm<sup>3</sup>. The ignition is conducted using a tungsten helix. The mixtures combustion is carried out in a technical nitrogen atmosphere at initial gas pressure of 5.0 MPa.

In the experiments the relative weight loss ( $\eta_1$ ) and the relative yield of the metal-ceramic phase in the ingot ( $\eta_2$ ) are fixed and calculated by formulas:  $\eta_1 = [(m_1 - m_2)/m_1] \times 100\%$ ;

$\eta_2 = m_3/m_1$ , where  $m_1$  is a weight of the initial mixture,  $m_2$  is a weight of the combustion products,  $m_3$  is a weight of the ingot of the metal-ceramic carbide–tungsten material.

During the experiments video filming is carried out, at the same time the concentration limit and the burning rate ( $u$ ) are determined. The burning rate is calculated as an average burning rate between four basic points by a formula:  $u_i = H_i/t_i$ , where  $H_i$  is height of the exothermic mixture layer,  $t_i$  is time of combustion of mixture layer.

The synthesis products are explored by methods of classical chemical and X-ray analysis. The microstructure of the cast materials is studied using Zeiss Ultra plus- a high-resolution field-emission scanning electron microscope. The calculation of the adiabatic combustion temperatures is carried out using the "Thermo" program.

The experimental research of the process of the exothermic mixture combustion [ $\alpha(\text{WO}_3/\text{Al}/\text{Ca}/\text{C}) + (100 - \alpha)(\text{NiO}/\text{Al})$ ] shows that the combustion temperatures realized during synthesis are sufficient for synthesis of cast combustion products. It is recorded that at the mixture combustion  $\text{WO}_3/\text{Al}/\text{Ca}/\text{NiO}/\text{C}$  the synthesis process proceeds at any  $\alpha$  ratio. With increasing share (NiO/Al) in the initial mixture the values of the burning rate ( $u$ ) and the relative yield of the metal-ceramic phase in the ingot ( $\eta_2$ ) increase on the initial part, and then the curves come for saturation, Fig. 1. Simultaneously the relative weight loss ( $\eta_1$ ) monotonically decreases.

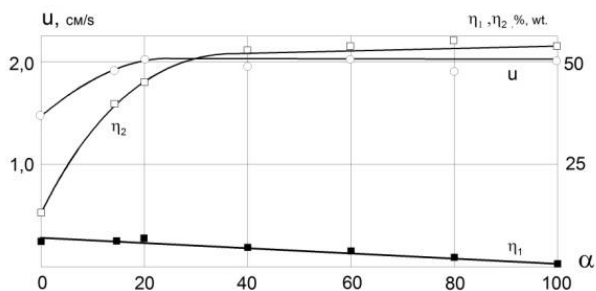


Fig. 1. Influence of the mixture share (NiO/Al) in the initial exothermic mixture [ $\alpha(\text{WO}_3/\text{Al}/\text{Ca}/\text{C}) + (100 - \alpha)(\text{NiO}/\text{Al})$ ] on the burning rate ( $u$ ), the relative weight loss at combustion of the initial mixture ( $\eta_1$ ) and the relative yield of the metal-ceramic phase in the ingot ( $\eta_2$ ).  $P_0 = 5$  MPa.

The study of the chemical composition of the cast metal-ceramic products in a range  $5 \leq \alpha \leq 25$  wt % of NiO/Al content in the mixture  $\text{WO}_3/\text{Al}/\text{Ca}/\text{NiO}/\text{C}$  reveals a linear increase in nickel content in the synthesized carbide–tungsten ingot with  $\alpha$  increase, Fig. 2. Increase in a share of NiO/Al provides increase in nickel content in cast products from 5 to 24 wt %. At the same time, we observe a negative linear increase of the impurity aluminum in the cast ingot with the general carbon drop in the synthesized ingots. To achieve the research goal the mixture 85( $\text{WO}_3/\text{Al}/\text{Ca}/\text{C}$ ) + 15(NiO/Al) is chosen with the fixed carbon content of 2.3 wt %. The ingot is formed on the basis of phases:  $\text{W}_2\text{C}$ , W,  $\text{Ni}_2\text{W}_4\text{C}$ ,  $\text{Ni}_3\text{W}_9\text{C}_4$ .

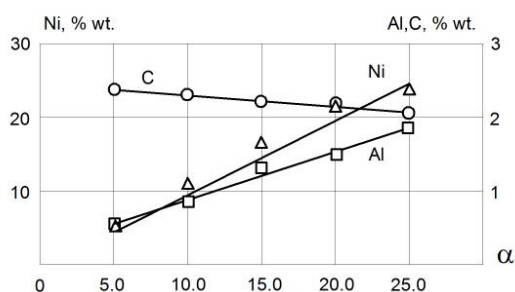


Fig. 2. Influence of the mixture share (NiO/Al) in the initial exothermic mixture [ $\alpha(\text{WO}_3/\text{Al}/\text{Ca}/\text{C}) + (100 - \alpha)(\text{NiO}/\text{Al})$ ] on the chemical composition of the metal-ceramic ingot.  $P_0 = 5$  MPa.

The most universal method of increasing of the fixed carbon content in the carbide–tungsten ingot is introduction of its excess content into the initial exothermic mixture of a thermite type 85( $\text{WO}_3/\text{Al}/\text{Ca}/\text{C}$ ) + 15(NiO/Al). In the experiments this approach provides an effective increase in the fixed carbon content to 4.2 wt %, Fig. 3. However, due to partial participation

of the carbon (graphite) in a recovery stage along with aluminum and calcium the content of the impurity aluminum also increases.

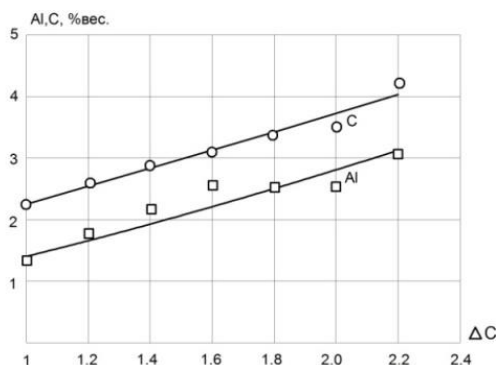


Fig. 3. Influence of the excess carbon content ( $\Delta C$ ) in the initial mixture  $WO_3/Al/Ca/C/NiO$  on the chemical composition of the metal-ceramic ingot.  $\Delta C_0 = WO_3:Al:Ca:C:NiO = 0.599:0.106:0.139:0.035:0.121$ .  $P_0 = 5.0$  MPa.

Graphite introduction considerably influences a synthesis process speed. With increase in carbon share in the initial exothermic mixture of a thermite type the burning rate and the relative weight loss at combustion of the initial mixture ( $\eta_1$ ) fall, Fig. 4. The concentration limit of combustion is recorded at nine fold increase of the graphite content in the initial mixture.

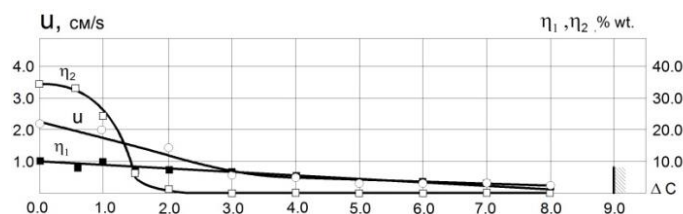


Fig. 4. Influence of the excess carbon content ( $\Delta C$ ) in the initial mixture  $WO_3/Al/Ca/C/NiO$  on the burning rate ( $u$ ), the relative weight loss at combustion of the initial mixture ( $\eta_1$ ) and the relative yield of the metal-ceramic phase in the ingot ( $\eta_2$ ).  $\Delta C_0 = WO_3:Al:Ca:C:NiO = 0.599:0.106:0.139:0.035:0.121$ .  $P_0 = 5.0$  MPa.

At  $\Delta C = 9.0$  the exothermic mixture ignites, and the further process of combustion fades. The area of synthesis of the cast carbide-tungsten products at introduction of excess carbon is limited by double excess. At  $\Delta C > 2.0$  only sintered cermet materials are synthesized. The analysis of influence of excess carbon content ( $\Delta C$ ) in the initial mixture on combustion characteristics ( $\eta_1$ ,  $\eta_2$ ) and chemical composition of the synthesized cast metal-ceramic carbide-tungsten materials allows to choose the composition with  $\Delta C = 1.8$  which is perspective for further researches, Fig. 3. Unfortunately, the cast material contains impurity aluminum (2.5 wt %) and is formed on the basis of four phases  $WC$ ,  $W_2C$ ,  $Ni_3W_{10}C_{3,4}$ ,  $AlNi_3$ .

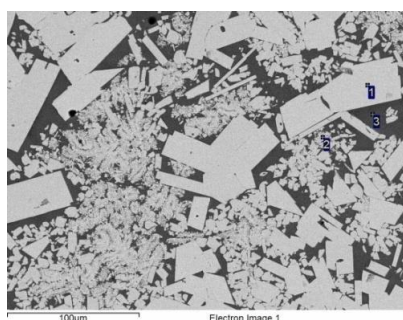
Impurity aluminium reduction in the cast carbide-tungsten material is carried out by its share decrease in the initial mixture composition  $WO_3/Al/Ca/C/NiO$ , Table 1.

Table 1. Influence of aluminum deficiency in the initial mixture  $WO_3:NiO:Al:Ca:C = 0.579:0.113:0.106:0.135:0.067$  on the chemical composition of the cast carbide-tungsten materials and the synthesis parameters.

| $\Delta Al$  | -2.5%    | -5%      | -7.5%    | -10%     | -15%     |
|--|----------|----------|----------|----------|----------|
| Al share in the initial mixture $WO_3/NiO/Al/Ca/C$ , % wt. | 10.04    | 9.81     | 9.57     | 9.34     | 8.87     |
| $\eta_1$   | 11.37    | 12.46    | 9.52     | 7.36     | 6.05     |
| $\eta_2$   | 46.9     | 46.76    | 47.32    | 47.45    | 45.32    |
| Al content in the ingot, % wt.                             | 1.28     | 0.58     | 0.53     | 0.47     | 0.46     |
| C content in the ingot, %wt.                               | 3.21     | 3.48     | 3.95     | 3.42     | 3.24     |
| Ni content in the ingot, % wt.                             | 15.80    | 18.60    | 17.50    | 16.20    | 16.00    |
| W content in the ingot, % wt.                              | the rest | the rest | the rest | the rest | the rest |

Thus, aluminium deficiency of 7.5 wt % in the initial exothermic mixture brings to impurity aluminium decrease to 0.53%, in the ingot at the satisfactory values of the relative weight loss at combustion of the initial mixture ( $\eta_1$ ) and relative yield of the cast carbide–tungsten material in the ingot ( $\eta_2$ ). In the ingot we also find the impurity content of calcium and free carbon which is according to the chemical analysis is  $C_{fr} = 0.219$  wt %,  $Ca = 0.1$  wt %. The synthesized material is formed on the basis of three main phases: WC,  $W_2C$ ,  $Ni_3W_{10}C_{3.4}$ , preferential of which is the phase WC.

The detailed analysis of a microstructure of the synthesized material is given in Fig. 5. The microstructure of the cross section at increase X1000 is presented as large WC grains of rectangular and triangular forms about 100  $\mu m$  in size. The fine grains of  $W_2C$  of 1–2  $\mu m$  in size are grouped in the area of 20–50  $\mu m$  and located in a bond of Ni–W–C. The element composition in weight percentage is presented in the table in Fig. 5. The excessive carbon content is caused by imperfection of a cleaning technique of the micro section sample from diamond paste after grinding.



| No | C    | Al   | Ni    | W     |
|----|------|------|-------|-------|
| 1  | 9.35 | 0.49 | 0.09  | 90.07 |
| 2  | 5.6  | 0.94 | 14.87 | 78.58 |
| 3  | 2.58 | 6.32 | 74.54 | 16.55 |

Fig. 5. Microstructure and EDS data of the cast carbide–tungsten material with a nickel bond.

This work is financially supported by the Russian Foundation for Basic Research (project no. 17-08-00903).

1. A.P. Zhudra, *Automatic welding*, 2014, nos. 6–7, pp. 66–72.
2. A.I. Som, *Automatic welding*, 2004, no. 10, pp. 49–53.
3. A.P. Zhudra, A.P. Voronchuk, *Automatic welding*, 2012, no. 1, pp. 39–44.
4. G.A. Vorob'eva, E.E. Skladnev, V.K. Erofeev, A.A. Ustinov, *Design steel and alloys*, Poly. SPb, 2013, 440 p.
5. V.S. Panov, A.M. Chuvilin, *Technology and properties of sintered hard alloys and their products: Textbook for universities*, Moscow, MISIS, 2001, 432 p.
6. A.S. Kurlov, A.I. Gusev, *Physics and chemistry of tungsten carbides*, Moscow, Fizmatlit, 2013, 272 p.
7. E. Taheri-Nassaj, S.H. Mirhosseini, An in situ WC–Ni composite fabricated by the SHS method, *J. Mater. Proc. Technol.*, 2003, vol. 142, iss. 2, pp. 422–426.
8. A.V. Laptev, A.I. Tolochin, L.F. Ochkas, *Powder metallurgy*, 2003, no. 11/12, pp. 84–95.
9. A.I. Tolochin, A.V. Laptev, I.Yu. Okun, M.S. Kovalchenko, Composite WC–35% Ni produced from ultrafine WC + NiO powders. I. Density and structure, *Powder Metall. Met. Ceram.*, 2011, vol. 50, nos. 5–6, pp. 83–94.
10. M. Sakaki, A. Karimzadeh Behnami, M.Sh. Bafghi, An investigation of the fabrication of tungsten carbide–alumina composite powder from  $WO_3$ , Al and C reactants through microwave-assisted SHS process, *Int. J. Refrac. Met. Hard Mater.*, 2014, vol. 44, pp. 142–147.
11. S.L. Silyakov, V.I. Yuxhvid, Chemical, phase, and structural transformations in the combustion of mixtures with tungsten oxide with aluminum, *Russ. J. Phys. Chem. B*, 2019, vol. 13, no. 1, pp. 96–100.

## FEATURES OF GRAIN STRUCTURE AT SHS EXTRUSION FOR MATERIAL BASED ON TiC + Co

L. S. Stelmakh<sup>\*a</sup>, A. M. Stolin<sup>a</sup>, and P. M. Bazhin<sup>a</sup>

<sup>a</sup>Merzhanov Institute of Structural Macrokinetics and Materials Science, Russian Academy of Sciences, Chernogolovka, Moscow, 142432 Russia

\*e-mail: stelm@ism.ac.ru

DOI: 10.24411/9999-0014A-2019-10166

In recent years, a promising direction in the field of materials science of metal-ceramic materials for various purposes is the study of the possibilities of refinement of the grain structure under conditions of combining combustion processes with high-temperature shear deformation of combustion products, which is implemented in the conditions of SHS-extrusion [1, 2]. This method provides very wide possibilities for controlling the process characteristics by parameters and deformation modes and, accordingly, by the structure of materials. In recent years, a large number of studies have been devoted to studying the effect of high-temperature shear deformation and heating conditions on the structure and properties of metal-ceramic materials during SHS extrusion. However, theoretical models explaining the patterns of formation and subsequent evolution of the structure of materials during hot deformation are not sufficiently developed. In the present work, based on modeling the thermal conditions of SHS extrusion, theoretical and experimental studies of grinding the grain structure during SHS extrusion and studying the features of the formed structure of alloys based on titanium carbide with a cobalt bond depending on temperature and degree of deformation were carried out. A mathematical model of the thermal conditions of the SHS extrusion process was developed earlier [3]. This model allows us to explore the temperature fields in the sample material in a cylindrical mold, heat insulator and extruded rod depending on various technological parameters of the process (combustion temperature, delay time, press plunger speed, heating temperature of various equipment zones, etc.) and predict the length of extruded rods. Since grain growth depends exponentially on temperature, information on temperature fields during the synthesis, pressing, and molding of a material can be very useful in obtaining a compact quality material. The grain growth kinetics in the final product of the synthesis reaction is investigated depending on the temperature, which according to [4] is described by the following equation:

$$\frac{dD}{dt} = \frac{k_0 \exp(-E/RT)}{D^h}$$

where  $D = D(r, z, t)$  is the flowing size (diameter) of the combustion product grain, which is a function of two coordinates  $r$  and  $z$  and time  $t$ ,  $k_0$  is a predictor,  $E$  is the activation energy of grain growth,  $R$  is the universal gas constant,  $T$  is the temperature,  $h$  is the exponent, the largest close to unity.

It is assumed that when the material passes from the chamber to the caliber through the profiling matrix, the grain size decreases according to the law [5], depending on the degree of deformation:

$$D_\varepsilon = \frac{D}{A^{1/3}(\varepsilon/\varepsilon_{cr})^{2/3}}$$

where  $\varepsilon$  is the degree of deformation,  $\varepsilon = (r_0^2 - r_1^2)/r_0^2$ ,  $r_0$  and  $r_1$  are radiuses of the sample and the rod after extrusion, respectively,  $\varepsilon_{cr}$  is the critical strain under which the nucleation of



recrystallization occurs ( $\varepsilon_{cr} = 0.1$  [5]),  $A$  is the coefficient of shape of the area of the original grain boundaries ( $4\pi/3\langle A \rangle/6$ ). In numerical calculations, data for the composition of TiC (70%) + Co (30%) were used. The calculations showed that the distribution of grain size in the material located in the chamber and located above the hole of the profiling matrix is uneven in height of the mold (Fig. 1).

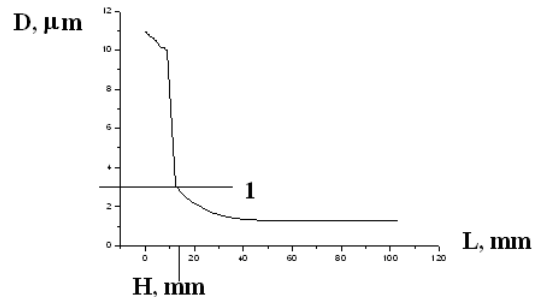


Fig. 1. Grain size distribution ( $D$ ) in the chamber (from 0 to  $H$ ) and the rod (from  $H$  to  $L$ ). Direct 1 separates the chamber and the extruded rod.

Before the hole of the profiling matrix in the chamber, the average grain size is  $11 \mu\text{m}$ , and when it leaves the chamber, it is crushed: when the material passes from the chamber to the caliber through the profiling matrix, the grain size changes from  $7.7$  to  $3 \mu\text{m}$ . Then, for most of the core, the grain size is smaller than  $3 \mu\text{m}$ , and starting from  $21 \text{ mm}$  and to the end, it is uniform both in length and radius and is less than  $2 \mu\text{m}$ .

Figure 2 shows the distribution of grain sizes along the length of the extruded rod and along the radius, which is uniform throughout the volume of the material.

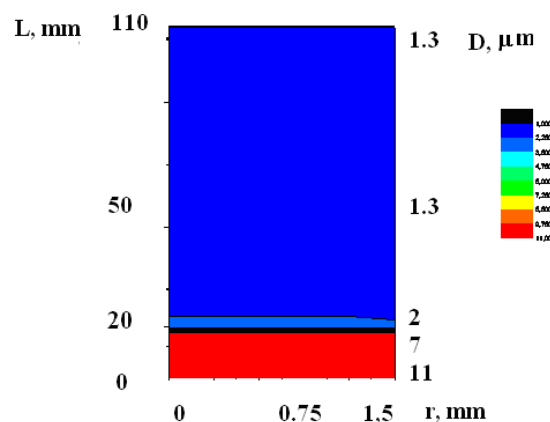


Fig. 2. Grain size distribution in the rod: hole diameter is  $3 \text{ mm}$ . The length of the rod is  $102 \text{ mm}$ .

This is confirmed by experimental data (Fig. 3). To study the grain sizes of titanium carbide, 3 types of samples were obtained, the microstructure of which is shown in Fig. 3: (a) press residue, (b) and (c) images taken from the middle and edge of an extruded rod  $3 \text{ mm}$  in diameter. The press residue after SHS extrusion is a material that has been solidly compacted, but not extruded. Under the action of normal stresses, the material compacted and, due to the applied external pressure, the average grain size of titanium carbide decreased to  $3.8 \mu\text{m}$ . The sizes of the largest grains also decreased to  $7.4 \mu\text{m}$ . The average grain size in the extruded rod decreased to  $2 \mu\text{m}$ . Due to normal and radial stresses, the material under extrusion underwent high degrees of deformation ( $0.99$ ), which led to a significant refinement of grains. It should be noted that the grain size in the samples (Figs. 3b, 3c) is almost identical, which indicates their uniform distribution along the length of the rod. Moreover, the distribution of grain sizes in the rod is uniform.

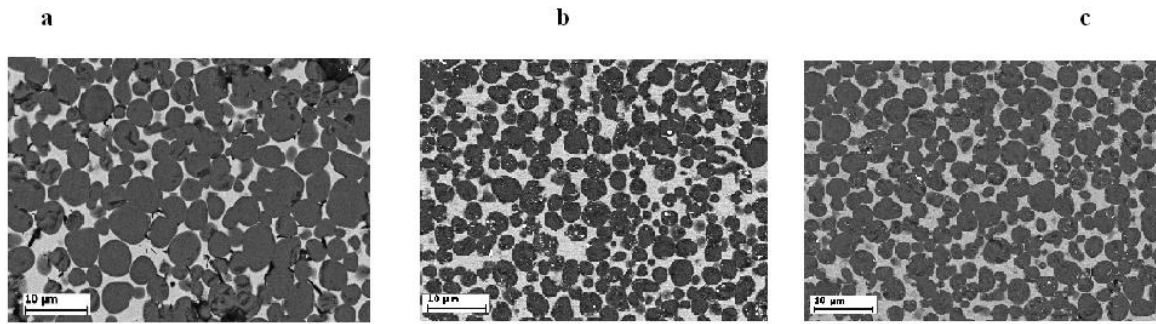


Fig. 3. Characteristic microstructure of the obtained samples: (a) press residue, (b) middle of the extruded rod, (c) edge (bottom) of the extruded rod.

#### Conclusions:

The proposed mathematical model of thermal regimes of SHS extrusion can be used to predict the pattern of grain distribution in an extruded rod.

It is theoretically and experimentally shown that with SHS extrusion, combining the action of shear deformations and pressure, the refinement of grain is realized due to the action of tensile stresses and shear deformations.

It was established that at the exit from the chamber the grain size along the length of the rod varies from 7.7 to 3  $\mu\text{m}$ . Further, on the most part of the rod, a uniform distribution of grains over the material volume is realized, and this part of the rod has an average grain size of 2  $\mu\text{m}$ .

1. A.M. Stolin, P.M. Bazhin, Receiving multifunctional products from composite and ceramic materials in the mode of combustion and high-temperature deformation (SHS-extrusion), *Theoret. Found. Chem. Technol.*, 2014, vol. 48, no. 6, pp. 1–13.
2. V.E. Ovcharenko, O.V. Lapshin, V.A. Chudinov, E.G. Kolobova, The evolution of the grain structure of an intermetallic compound during the extrusion of an intermetallic compound during its high-temperature synthesis under pressure, *Phys. Mesomech.*, 2005, pp. 65–68.
3. A. M. Stolin, L.S. Stel'makh, Mathematical modeling of SHS compaction/ Extrusion: An Autoreview, *Int. J. Self-Propag. High-Temp. Synth.*, 2008, vol. 13, no. 1, pp. 53–70.
4. R. Kana, Physical metallurgy. Phase transformations. Metallography, M.: Peace, 1968, 490 p.
5. M.A. Shtremel, V. I. Lizunov, V.V. Shkatov, Grain conversion during primary recrystallization, *Metallography and heat treatment of metals*, 1984, no. 6, pp. 2–5.

PRODUCTION OF COMPOSITE CERAMIC MATERIALS AND  
PRODUCTS BY COMBINED USE OF SHS AND HIGH-TEMPERATURE  
SHEAR DEFORMATION

**A. M. Stolin**

Merzhanov Institute of Structural Macrokinetics and Materials Science, Russian Academy  
of Sciences, Chernogolovka, Moscow, 142432 Russia  
\*e-mail: amstolin@ism.ac.ru

DOI: 10.24411/9999-0014A-2019-10167

In laboratory of Plastic Deformation Materials (ISMAN), a new scientific direction has been developed: SHS in conditions of shear high-temperature deformation. Combination of SHS process and high-temperature synthesis makes it possible to produce materials and products based on refractory compounds.

The report presents the results of development of the SHS-extrusion process to obtain long products from brittle and hardly deformed powders of refractory inorganic compounds. Experimental studies of rheological behavior of SHS materials and their ability to plastic deformation at high temperatures are discussed. Structure and properties of extruded SHS materials are presented. The main aspects of mathematical modeling of SHS-extrusion and pressing are considered. Examples of practical application of the developed SHS extrusion method for producing long products from new multifunctional materials — composite ceramic materials with nanoscale structural elements, materials based on MAX phase of the titanium–aluminum carbon system, materials based on intermetallic compounds — are given.

FILTRATION COMBUSTION OF TITANIUM–ALUMINUM–NITROGEN  
TERNARY SYSTEM IN FLOW-TYPE REACTORI. A. Studenikin<sup>\*a</sup>, A. V. Linde<sup>a</sup>, A. A. Kondakov<sup>a</sup>, and V. V. Grachev<sup>a</sup><sup>a</sup>Merzhanov Institute of Structural Macrokinetics and Materials Science, Russian Academy of Sciences, Chernogolovka, Moscow, 142432 Russia

\*e-mail: studenikin@ism.ac.ru

DOI: 10.24411/9999-0014A-2019-10168

Combustion in titanium–aluminum–nitrogen system is the interesting object for investigations from the fundamental combustion science point of view as well as from technological point of view because of the opportunity of valuable combustion products obtaining such as binary nitrides of titanium and aluminum, complex ternary nitrides, MAX-phases. The varied regimes of combustion in this system are determined by the competition of parallel reactions, melting of reagents and intermediate phases in the combustion wave, changes of porosity and medium permeability, accordingly, the changes of gas reagent flow and extent of nitridation.

Earlier the combustion of mixtures based on Ti, Al, TiAl, and TiN at nitrogen pressure from 0.1 to 5 MPa with natural gas flow was investigated [1–4]. Depending on the initial conditions (initial mixture composition, gas pressure, thermal-vacuum treatment of initial mixture) different combustion modes (surface, layer-by-layer, spin, multipoint, 2- and 3-stages of front propagation) were observed. As a rule, the phase composition of combustion products consisted of TiN and AlN, intermetallics and ternary compounds (MAX-phases, complex nitrides). Efforts to obtain both monophasic Ti<sub>2</sub>AlN and TiN–AlN composite have been unsuccessful. On the one hand, it can be explained, that the formation of binary nitrides is preferable from the thermodynamic point of view. On the other hand, generated heat of combustion is sufficient for melting of components. Formed liquid phase decreases medium permeability and blocks supply of nitrogen in reaction zone fixing system in all forms of intermediate states.

Experimental study of filtration combustion modes in nitrogen coflow was carried out in [5–7] by the example of titanium–carbon system. It was revealed that forced flow of gas is a powerful controlling factor, which can influence on the mode of combustion wave propagation and phase composition of reaction products.

The aim of this work was investigation of filtration combustion in titanium–aluminum–nitrogen system in flow-type reactor at variation of composition of the initial solid-state reagents mixture, gas mixture composition (nitrogen–argon), value of gas flow and its flow direction (coflow or counter flow) in relation to the direction of combustion front propagation. Three following stages can be separated in this research:

1. Development, fabrication, and setup of experimental stand. Experimental procedure was tested by the combustion of Ti + TiN mixtures in coflow nitrogen. Simultaneously the titanium nitride as one of the initial component for the subsequent experiments was produced.
2. Investigation of coflow and counter flow modes of combustion of Ti + Al + TiN mixtures both in pure nitrogen and in mix with argon to research the opportunity of obtaining MAX-phases.
3. Experimental study of hydrodynamic instability of filtration combustion front with formation of «finger» [8].

The experimental stand consists of:

- vertical steel tube reactor with cooling jacket and five thermal couple ports, reaction camera diameter is 44 mm and its height is 290 mm;
- system of gas feeding into reactor from balloon through gas-pressure reducer;

- gas venting system from reactor through the filter-refrigerant into vacuum pump 2NVR-5DM;
- flowmeter Bronkhorst EL-Flow on entering the reactor and pressure sensors MC2000 on entering and exit from the reactor;
- data acquisition system based on ADC QMLab and IBM PC.

The initial reagents were titanium powder of PTS trademark, aluminum powder of ASD-1 trademark, titanium nitride powder obtained in preliminary experiments and nitrogen (extra pure grade 99.995 wt %). Powder reagents were mixed in cylindrical vessel on the rolls without milling. Gas supply was performed through upper gate and gas extraction through bottom gate. To realize coflow mode the powder mixture was ignited at the top of reaction camera, and for counter flow – at its bottom. At pure nitrogen coflow combustion of Ti +  $x$ TiN mixture (where  $x$  is from 50 to 70 wt %) plane front of filtration combustion was observed. Combustion velocity was from 1.2 to 2.6 mm/s and increased linearly with increasing of gas flow from 20 to 25.5 l/min and decreasing of dilution ratio  $x$  from 70 to 50 wt %. The obtained sintered product can be divided in two parts: a near-wall multiphase layer containing TiN, Ti, and TiN<sub>0.3</sub>, and a central part containing only TiN. Product quantity of near-wall multiphase layer decreased proportionally from 27 to 5.2 wt % with increasing nitrogen flow and decreasing dilution ratio. Sintered product cleared from external layer was easily milled in the pounder to powder with particles size closed to particles size of initial powder-reagents. Content of nitrogen in monophasic product reached 21.5 wt % (stoichiometric value for TiN is 22 wt %). Obtained titanium nitride powder was used for preparation of Ti + Al + TiN mixtures. Combustion products of Ti + Al + TiN mixtures in coflow of pure nitrogen (Table 1) mainly represent binary nitrides and formation of ternary phases is inconsiderable.

Table 1.

| Mixture composition | Initial gas flow, l/min | Product type  | Total weight gain, % | Product phase composition |   | $U_{\text{comb}}^{\text{mid}}$ , mm/s | $T_{\text{comb}}^{\text{max}}$ , °C | Cake height shrinkage, % |
|---------------------|-------------------------|---|----------------------|---------------------------|---|---------------------------------------|-------------------------------------|--------------------------|
|                     |                         |   |                      | Major phases              | Secondary phases  |                                       |                                     |                          |
| 2Ti+Al+2TiN         | 15.15                   | porous cake: grey near-wall layer + yellow central part | 13.08                | TiN                       | AlN   | 1.99                                  | 2256                                | 0.76                     |
| 1.5Ti+Al+0.5TiN     | 20                      | melted macroporous sponge                               | 14.32                | TiN                       | Ti <sub>2</sub> AlN, Ti <sub>4</sub> AlN <sub>3</sub> , AlN | -                                     | -                                   | 7.66                     |

Changes in gas flow direction on counter mode and gas composition on nitrogen + argon mixture lead to an increase in the ternary phase content in combustion products (Table 2). In this case, combustion velocity increased and temperature decreased in comparison with coflow combustion for the same mixture compositions. There was an essential shrinkage of product by two times compared with the initial height. Sintered product was a grey hard-milled fine porous sponge with a metallic luster on the shear.

At combustion of Ti + Al + TiN mixtures in nitrogen–argon gas coflow a hydrodynamic instability of propagation of plane front was revealed. It was earlier predicted theoretically [7]. The instability of plane front leads to combustion mode with formation of «finger», when inside of porous cylinder a gas channel forms (see Fig. 1). Experimental results and conditions of finger formation are presented in Table 3. Finger propagation velocity after formation was about 1 mm/s. Further on the half-way its velocity increased to ~ 2 mm/s and in the end of process increased to ~ 3 mm/s. Accordingly, gas flow through reactor increased proportionally to finger motion and in the end of process it exceeded start value about in three times.

Table 2.

| Mixture composition | Initial gas flow, l/min | Gas composition, vol. % |    | Total weight gain, % | Product phase composition                                    |                               | $U_{\text{comb}}^{\text{mid}}$ , mm/s | $T_{\text{comb}}^{\text{max}}$ , °C | Cake height shrinkage, % |
|---------------------|-------------------------|-------------------------|----|----------------------|--|-------------------------------|---------------------------------------|-------------------------------------|--------------------------|
|                     |                         | N <sub>2</sub>          | Ar |                      | Major phases   | Secondary phases              |                                       |                                     |                          |
| 2Ti+Al              | 11.68                   | 50                      | 50 | 5.39                 | Ti <sub>3</sub> AlN, Ti <sub>3</sub> Al                      | Ti <sub>2</sub> AlN           | 2.36                                  | 1536                                | 49.8                     |
| 2Ti+Al              | 11.35                   | 63                      | 37 | 5.33                 | Ti <sub>3</sub> AlN, Ti <sub>3</sub> Al, Ti <sub>2</sub> AlN | TiN                           | 3.77                                  | 1382                                | 57.8                     |
| 1.5Ti+Al+0.5TiN     | 11.8                    | 50                      | 50 | 5.09                 | Ti <sub>2</sub> AlN  | TiAl, TiN, Ti <sub>3</sub> Al | 2.08                                  | 1580                                | 41.5                     |
| 1.5Ti+Al+0.5TiN     | 11.35                   | 63                      | 37 | 5.36                 | Ti <sub>2</sub> AlN  | TiAl, TiN, Ti <sub>3</sub> Al | 2.31                                  | 1484                                | 51.1                     |

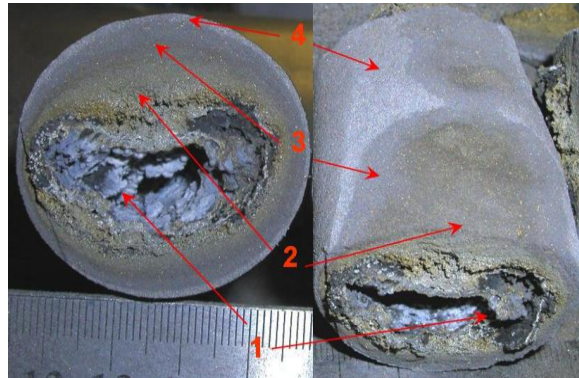


Fig. 1. Cross section of sample burned with «finger» formation.

Table 3.

| Mixture composition | Gas composition, vol. % |     | Initial gas flow, l/min | Product type                         | Total weight gain, % | Product phase composition  |                  |
|---------------------|-------------------------|-----|-------------------------|--------------------------------------|----------------------|--|------------------|
|                     | N <sub>2</sub>          | Ar  |                         |                                      |                      | Major phases   | Secondary phases |
| Ti + Al             | 100                     | 0   | 10.14                   | melted cake                          | 5.11                 | TiAl, Ti <sub>2</sub> AlN  | TiN              |
| Ti + Al             | 98.5                    | 1.5 | 10.07                   | melted cake                          | 4.42                 | TiAl, Ti <sub>2</sub> AlN  |                  |
| Ti + Al             | 63                      | 37  | 11.3                    | melted cake with formation of finger | 4.07                 | multilayer: TiN, Ti <sub>2</sub> AlN, TiAl <sub>3</sub> , AlN, Ti <sub>3</sub> Al, TiAl <sub>3</sub> , Ti, Al; |                  |
| Ti + Al             | 34                      | 66  | 12.3                    | doesn't burn                         | -                    |  |                  |
| 1.5Ti+Al+0.5TiN     | 50                      | 50  | 11.6                    | melted cake with formation of finger | 4.91                 | multilayer: TiN, Ti <sub>2</sub> AlN, TiAl <sub>3</sub> , AlN, Ti <sub>3</sub> Al, TiAl <sub>3</sub> , Ti, Al; |                  |
| 1.5Ti+Al+0.5TiN     | 50                      | 50  | 5.8                     | doesn't burn                         | -                    |  |                  |

For all cases of finger formation sintered material is essentially inhomogeneous on phase composition in cross section (Fig. 1): melted layer covered finger surface (1) consists of mainly TiN and Ti<sub>2</sub>AlN, to a less extent TiAl<sub>3</sub> and AlN. The second golden-grey porous layer mainly consists of TiAl, Ti<sub>3</sub>Al and TiN. The third dark-grey porous layer (3) consists of TiAl<sub>3</sub>, Ti<sub>3</sub>Al,

unreacted Ti, Al and initial TiN. In the fourth light-grey thin layer near the reactor wall were mainly phases of the initial TiN, Ti and Al and to a less extent  $TiAl_3$  and  $Ti_3Al$  intermetallics.

As a result of carried out research we can draw next conclusions:

1. Experimental stand based on flow-type reactor was made and started up. It was equipped with temperature and pressure gages, flowmeter, computer data acquisition system. This experimental stand enables to carry out investigations of filtration combustion modes both in coflow and in counter flow of gas mixtures with different composition.
2. At combustion of Ti + Al + TiN mixtures in coflow of pure nitrogen the combustion products consist mainly of binary nitrides and formation of ternary phases is inconsiderable.
3. Formation of ternary compounds such as MAX-phase ( $Ti_2AlN$ ) and complex nitride ( $Ti_3AlN$ ) was observed at combustion of Ti + Al + TiN mixtures in counter flow of gas mixture of nitrogen with argon.
4. For the first time at filtration combustion of SHS-systems in the forced flow of gas reagent, the theoretically predicted hydrodynamic instability of plane front propagation was experimentally revealed. Evolution of instability leads to initiation of combustion modes with finger formation when a gas channel appears inside of porous solid material. Finger formation was observed only for coflow mode of Ti + Al + TiN mixtures combustion in nitrogen-argon gas mixture.

1. A.A. Kondakov, A.V. Linde, I.A. Studenikin, V.V. Grachev, Devyataya Vserossiyskaya s mezhdunarodnym uchastiem Shkola-seminar po strukturnoy makrokinetike dlya molodykh uchennykh [IX School-Seminar on Structural Macrokinetics for Younger Researchers], Chernogolovka, ISMAN, 2011, pp. 101–103.
2. A.A. Kondakov, V.V. Grachev, Desyataya Vserossiyskaya s mezhdunarodnym uchastiem Shkola-seminar po strukturnoy makrokinetike dlya molodykh uchennykh [X School-Seminar on Structural Macrokinetics for Younger Researchers], Chernogolovka, ISMAN, 2012, pp. 167–169.
3. S.I. Kolesnikov, A.A. Kondakov, P.A. Miloserdov, I.M. Novickij, M.A. Bardin, Determination of the optimum conditions of synthesis in a triple system of Ti–Al–N for products containing the highest number of MAX–phases, *Bashkir Chem. J.*, 2012, vol. 19, no. 4, pp. 162–165.
4. A.A. Kondakov, V.V. Grachev, Modes of Filtration Combustion of Titanium–Aluminum – Nitrogen ternary system, Proceedings of the Third Conference on Filtration Combustion, Chernogolovka, 2013, pp. 35–38.
5. B.S. Seplyarsky, S.V. Kostin, G.B. Brauer, Dynamic combustion regimes of the Ti-(Ti+0.5C) layered system in a concurrent nitrogen flow, *Combust. Explos. Shock Waves*, 2008, vol. 44, no. 6, pp. 655–661.
6. B.S. Seplyarsky, G.B. Brauer, A.G. Tarasov, Combustion of the gasless system Ti + 0.5C in a nitrogen coflow, *Combust. Explos. Shock Waves*, 2011, vol. 47, no. 3, pp. 294–301.
7. B.S. Seplyarsky, A.G. Tarasov, R.A. Kochetkov, I.D. Kovalev, Combustion behavior of a Ti + TiC mixture in a nitrogen coflow, *Combust. Explos. Shock Waves*, 2014, vol. 50, no. 3, pp. 300–305.
8. A.P. Aldushin, T.P. Ivleva, Simulation of the hydrodynamic instability of a filtration combustion wave in a porous medium, *Combust. Explos. Shock Waves*, 2015, vol. 51, no. 1, pp. 107–115.

## HIGH THERMOELECTRIC PERFORMANCE OF p-BiSbTe COMPOUNDS PREPARED BY ULTRA-FAST THERMALLY INDUCED REACTION

**X. Su<sup>\*a</sup>, Y. Yan<sup>a</sup>, and X. Tang<sup>a</sup>**

<sup>a</sup>State Key Laboratory of Advanced Technology for Materials Synthesis and Processing, Wuhan University of Technology, Wuhan, 430070 China

\*e-mail: [suxianli@whut.edu.cn](mailto:suxianli@whut.edu.cn)

DOI: 10.24411/9999-0014A-2019-10169

The traditional zone melting (ZM) method for the fabrication of state of the art Bi<sub>2</sub>Te<sub>3</sub>-based thermoelectric materials has long been considered a time and energy intensive process. Herein, a combustion synthesis known as the thermally induced flash synthesis (TIFS) is employed to synthesize high performance p-type BiSbTe alloys within 20 min compared to tens of hours for the ZM samples. The thermodynamic parameters and phase transformation mechanism during the TIFS process were systematically studied for the first time. TIFS combined with plasma activated sintering (PAS) results in a single-phase homogeneous material with excellent repeatability, high thermoelectric performance (maximum  $ZT \sim 1.2$  at 373 K) and robust mechanical properties in a very short time of less than 20 min. The technologically relevant average  $ZT$  value of TIFS-PAS fabricated Bi<sub>0.5</sub>Sb<sub>1.5</sub>Te<sub>3</sub> from 298 K to 523 K is 0.86, about a 46% improvement over the ZM sample. The compressive and bending strength of TIFS-PAS Bi<sub>0.5</sub>Sb<sub>1.5</sub>Te<sub>3</sub> are also improved by about 5 fold compared with those of the ZM samples. Thermoelectric power generation modules assembled using the TIFS-based high performance n and p type materials show the largest thermoelectric conversion efficiency of 5.2% when subjected to a temperature gradient of 250 K, representing about 42% enhancement compared with the commercial ZM-based module. Because of the simplicity and scalability of the process and short synthesis time, the TIFS-PAS technology provides a new and efficient way for large-scale, economical fabrication of Bi<sub>2</sub>Te<sub>3</sub>-based thermoelectrics.



## PUBLISHER SUPPORTS TRANSFER FROM RESEARCH TO APPLICATION

**R. Suchentrunk**

Senior Manager Aerospace and Automotive (retired)  
Editor Thin Films and Plasmatechnology (Eugen G. Leuze Verlag)  
Am Feldl 17, D 85658 Egming  
e-mail: richard.suchentrunk@t-online.de

DOI: 10.24411/9999-0014A-2019-10170

There is a strong need for transferring scientific results into industrial application. Many data bases are available worldwide, most of them peer reviewed and so guaranteeing a high quality level. But especially for small and medium enterprises the preparation of “high quality” publications is time consuming and difficult. Additionally, they must observe constantly the technical state of the art, but there are not so many journals available, which provide technical information on a “not peer reviewed” level. The trade journal “Galvanotechnik”, published by Eugen G. Leuze Verlag, Bad Saulgau, Germany, closes this gap. It provides scientific and technical information in the areas

- Electroplating
- Thin films and plasma technology
- Energy technology
- Medical technology
- Environmental engineering

in English as well as in German language. The journal is existing more than hundred years now and the readers are coming from industry as well as from research institutes. The presentation will give a short overview on the activities of Eugen G. Leuze Verlag, a world-wide leading publisher (not only) in the electroplating area. The program of the publishing house includes technical and scientific journals, reference books with various topics of surface technology and a big supply of school- and textbooks, dictionaries, annuals and lexica. Three trade journals for Electroplaters, Surface Coaters and Electronic Specialists (Galvanotechnik, PLUS, JEPT) provide detailed information in a broad field of surface technology. Additionally a website is available with information about archived articles, new publications, important events, actual news from industry, jobs e.g. As a summary examples for the close and long time cooperation between Leuze Verlag and the Scientific-Educational Center of SHS/Department of Powder Metallurgy and Functional Coatings of the National University of Science and Technology MISIS will be presented. This includes publications in journals and books as well as joint projects and activities.

## COMBUSTION SYNTHESIS AND STRUCTURE FORMATION IN Ni–Al–C SYSTEM

A. E. Sytshev<sup>\*a</sup>, N. A. Kochetov<sup>a</sup>, A. S. Shchukin<sup>a</sup>, M. L. Busurina<sup>a</sup>, and A. V. Aborkin<sup>b</sup>

<sup>a</sup>Merzhanov Institute of Structural Macrokinetics and Materials Science, Russian Academy of Sciences, Chernogolovka, Moscow, 142432 Russia

<sup>b</sup>Vladimir State University named after Alexander and Nikolay Stoletovs, Vladimir, Russia

\*e-mail: sytshev@ism.ac.ru

DOI: 10.24411/9999-0014A-2019-10171

Ni–Al intermetallics have a significant drawback due to insufficient ductility especially at the room temperature. Mechanical properties, such as strength, modulus of elasticity, viscosity can vary significantly even when very small amounts of carbon are added. The small presence of carbon in the Ni–Al alloy leads to an increase in strength by 30%. Carbon is a promising solid lubricant due to its excellent tribological properties. It is proved that graphene as a solid lubricant not only causes low wear but provides easy shearing and thus results in reduced friction. The formation of a chemical bond between carbon components and matrix, which strongly affects the mechanical properties of the material, can vary depending on the conditions for obtaining the material. The presence of the melt greatly accelerates the process of mutual diffusion of the reaction components and increases the contact area due to the capillary spreading of the melt over the carbon. The formation of a melt in the Ni–Al system is easily realized during SHS process. The most important stage in the preparation of the reactive blends can also be mechanical activation (MA), the parameters of which ultimately affect the kinetics of solid-phase combustion (sintering). The peculiarities of the formation of the structure of intermetallic Ni–Al alloys modified by carbon components in the mode of self-propagating high-temperature synthesis (SHS) and spark plasma sintering (SPS), and the influence on the structure of preliminary MA are investigated in this study. SHS experiments in the Ni–Al–C system showed the possibility of obtaining a material using carbon components in the combustion regime. The reaction mixture was prepared from ASD-1 aluminum powders of about 20  $\mu\text{m}$  in size, containing about 99.7% Al, and a metallic carbonyl nickel grade PNA (not less than 99.9 wt %) of about 10  $\mu\text{m}$  in size for NiAl production. In a mixture of Ni and Al powders, carbon (0–6 wt %) was added in the form of carbon black. The reaction mixture was exposed to MA for 1 min on the ATO-2 attritor. Cylindrical samples with a diameter of 1 cm were pressed from activated mixtures by cold pressing. The combustion velocity is noticeably decreased with increasing of the soot content. XRD analysis of the synthesized material showed only the presence of the NiAl phase. NiAl diffraction lines are shifted to smaller angles with an increase in the carbon content in the initial charge, which indicates an increase in the cell parameters. Due to the low amount of soot in the starting mixture (2–6 wt %), carbon was not detected in the synthesized product. The microstructural studies showed that as a result of the synthesis, a close-packed intermetallic matrix based on NiAl with a grain size of about 5–10  $\mu\text{m}$  was formed. Carbon is predominantly located along the boundaries of intermetallic NiAl grains and forms a continuous multilayer graphene-like film on the surface with a thickness of about 66 nm (Fig. 1).

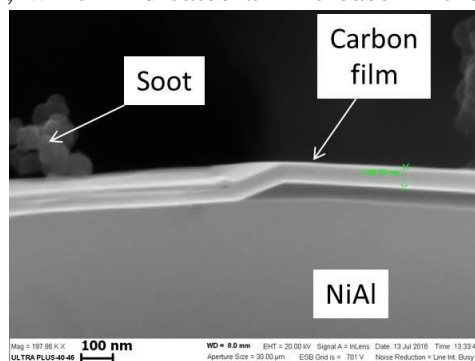


Fig.1. Cross section of NiAl/C composite.

It can be assumed that the formation of multilayer carbon nanofilms is occurred as a result of allotropic conversion of carbon black to graphite only at the point of direct contact of the Ni–Al melt with soot. Figure 2 shows the graphite film on the surface of NiAl grain after complete solidification of the melt. The film has a specific morphology of smooth surface areas separated from each other by out of plane faceted wrinkles. The structure at the joint between the wrinkles is more complicated, but the faceted structure is still evident. The graphitic nanofilm is wrinkled due to its thermal expansion coefficient mismatch with NiAl intermetallic.

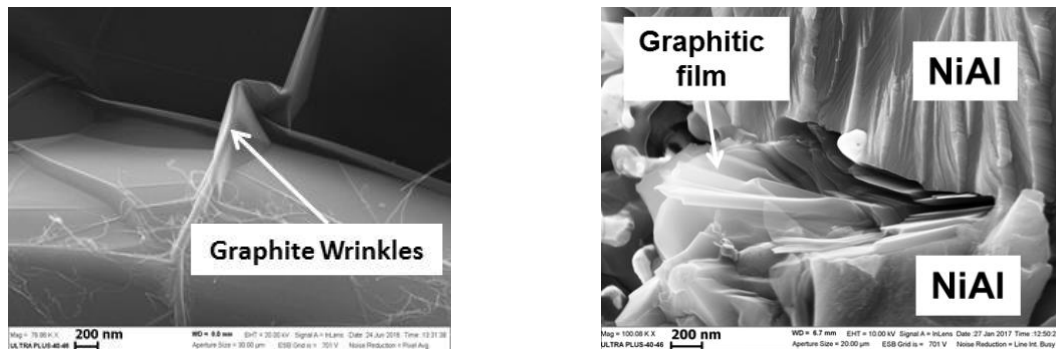


Fig. 2. The view of graphite film on the surface of NiAl grains.

It is known that if the carbon concentration in the solid exceeds the limit of solubility at a given temperature, it is possible to segregate excess of carbon to the surface to form graphene-like structure. A well-known example of this approach is segregation on the Ni surface. The solubility of carbon in nickel increases with increasing temperature. Therefore, it is possible to create an excess concentration of carbon in Ni as a result of cooling the metal saturated with carbon at high temperature. The mechanism of carbon film formation during SHS can be associated with dissolution of carbon (soot, graphite, carbon nanotubes) in the Ni–Al melt at the combustion temperature that is followed by the growth as graphite films on the melt surface during cooling down.

Spark plasma sintering (SPS) experiments in the Ni–Al–C (2 and 4 wt % C) system are also showed the possibility of synthesizing dense material with 2D carbon film. SHS product shows similar microstructures of NiAl intermetallic with different carbon content. NiAl grains have regular shape with the size about 20  $\mu\text{m}$ .

Ni and Al particles are melted in contact with a carbon during SHS to saturate with carbon at a concentration correspond to the binary phase diagram of metal–carbon. Upon cooling, as the solubility of carbon in the Ni–Al melt decreased, the excess carbon formed on top of the Ni–Al melt as well as other sites within the melt. The solubility of carbon in Ni–Al melts increases with increasing combustion temperature. It is possible to create an excess concentration of carbon in Ni–Al melt as a result of cooling the melt saturated with carbon at high temperature.

According to the tribological tests (Fig. 3), the friction coefficient of NiAl–C composite is about 0.5. The friction coefficient of the sample with 2 wt % C increases sharply on the sliding distance of 0–25 m to 0.75. Microstructural analysis showed (Figs. 4, 5) that tribological test resulted to formation of noticeable friction grooves. EDA analysis of the friction surface shows the presence of elements contained in the composition of the counterbody – iron Fe and oxygen O, which indicates their transfer. It is observed that metal oxides and carbon components are present in different regions in the wear track. Thus, visual analysis of friction surfaces, peculiarities of changes in the chemical composition of the friction surface, and the layer on the counterbody indicate the adhesion-abrasive wear mechanism of the contact pair.

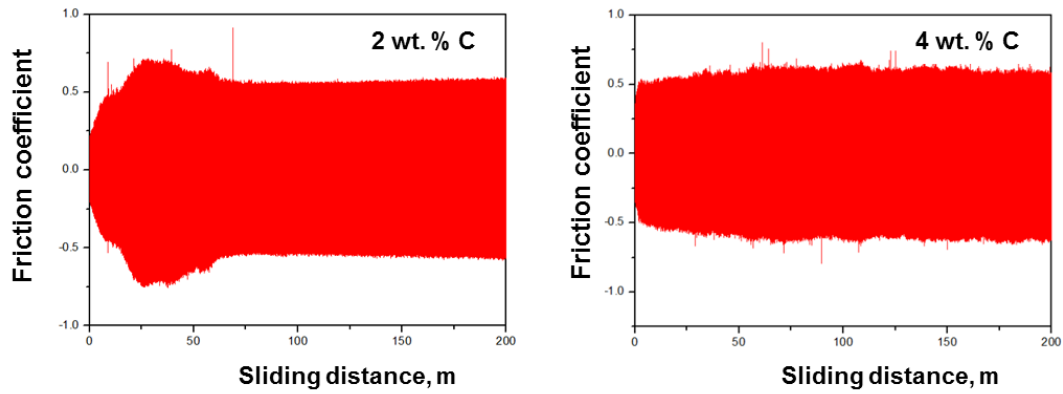


Fig. 3. Tribological test of Ni–Al–C (2 and 4 wt % C samples).

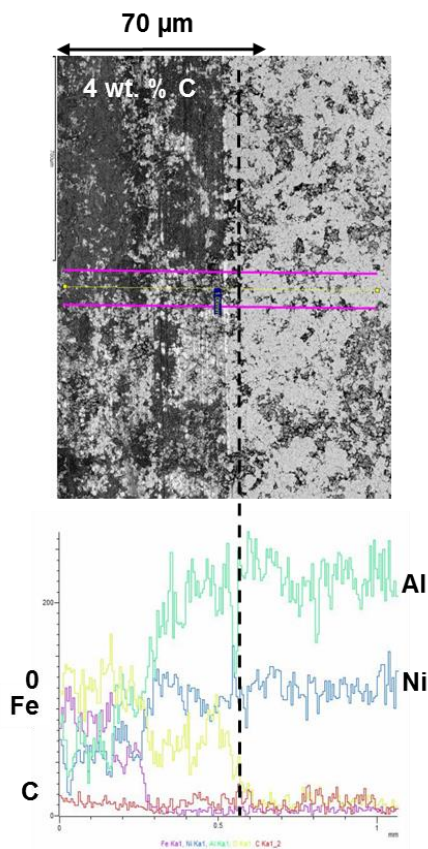


Fig. 4. Microstructure and concentration profiles of elements in the friction area of Ni–Al–C (2 wt % C).

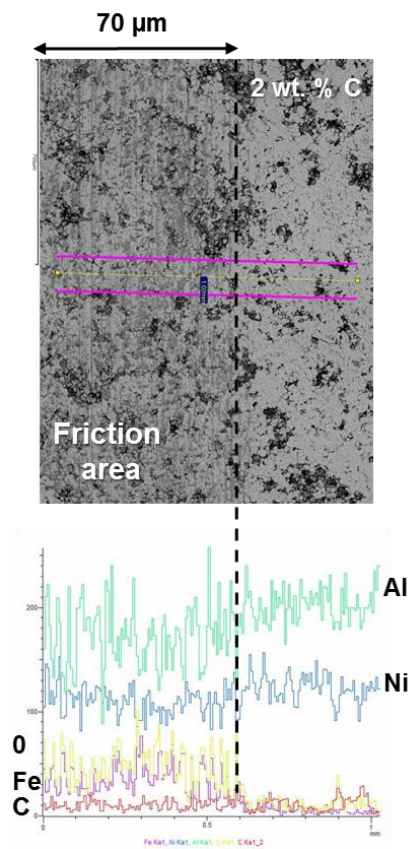


Fig. 5. Microstructure and concentration profiles of elements in the friction area of Ni–Al–C (4 wt % C).

The work was supported by the Russian Foundation for Basic Research (project no. 18–08–00181\18).

1. A.M.M. Ibrahim, X. Shi, A. Zhang, K. Yang, W. Zhai, Tribological characteristics of NiAl matrix composites with 1.5 wt % graphene at elevated temperatures: an experimental and theoretical study, *Tribology Transactions*, 2015, vol. 58, no. 6, pp. 1076–1083.
2. C. Julius, H.N. Schuster, The Ternary System Ni–Al–C, *Monatsh Chem.*, 1982, pp. 113–163.
3. V.K. Portnoi, A.V. Leonov, A.V. Logachev, A.N. Streletskii, V.A. Popov, Mechanical alloying as method for introducing carbon in Ni<sub>3</sub>Al intermetallide, *Phys. Met. Metall.*, 2012, vol. 113, no. 12, pp. 1169–1181.

## SHS SYNTHESIS OF THERMOELECTRIC MATERIALS: THERMODYNAMIC CRITERION FOR COMBUSTION SYNTHESIS

**X. Tang<sup>\*a</sup>, X. Su<sup>a</sup>, and Y. Yan<sup>a</sup>**

<sup>a</sup>State Key Laboratory of Advanced Technology for Materials Synthesis and Processing,  
Wuhan University of Technology, Wuhan, 430070 China

\*e-mail: tangxf@whut.edu.cn

DOI: 10.24411/9999-0014A-2019-10172

Here we report compound thermoelectric materials ( $\text{Bi}_2\text{Te}_3$ ,  $\text{Bi}_2\text{Se}_3$ ,  $\text{Cu}_2\text{Se}$ ,  $\text{Cu}_2\text{SnSe}_3$ , half-Heusler alloys, lead chalcogenides, skutterudites, and magnesium silicides) with thermoelectric properties comparable with materials prepared by the traditional routes of synthesis can be synthesized at a minimal cost and on the time scale of seconds using the self-propagating high temperature synthesis method. Moreover, we found that the criterion often quoted in the literature as the necessary precondition for combustion synthesis,  $T_{\text{ad}} \geq 1800 \text{ K}$ , is not universal and certainly not applicable to thermoelectric compound semiconductors. Instead, we offer new empirically-based criterion, which covers all materials synthesized by self-propagating high temperature synthesis, including the high temperature refractory compounds for which the  $T_{\text{ad}} \geq 1800 \text{ K}$  criterion was originally developed. Our work opens a new avenue for ultra-fast, low cost, mass production fabrication of efficient thermoelectric materials and the new criterion greatly broadens the scope of materials that can be successfully synthesized by self-propagating high temperature synthesis.

## PECULIARITIES OF TECHNOLOGICAL PARAMETERS OF SHS-ELECTRICAL ROLLING

**G. Tavadze<sup>\*a</sup>, T. Namicheishvili<sup>a</sup>, G. Oniashvili<sup>a</sup>, A. Tutberidze<sup>a</sup>, Z. Aslamazashvili<sup>a</sup>, and G. Zakharov<sup>a</sup>**

<sup>a</sup>F. Tavadze Metallurgy and Materials Science Institute, Tbilisi, 0186 Georgia

\*e-mail: tavadzeg@gmail.com

DOI: 10.24411/9999-0014A-2019-10173

The production of composite materials by self-propagating high-temperature synthesis (SHS) method gave possibility to develop the technology for production of compact composite materials and products [1]. The method is characterized by technological advantages, in particular, high productivity, low energy expenses, high quality of the product, and ecological purity. The main idea of the technology involves in direct compaction of SHS products down to non-porous state just after the arrival of synthesis front. As a result of the application of the method, the instrumental and construction materials are fabricated [2]. We should mention that the geometry of the material obtained by proposed technology is limited, because the synthesis front has certain velocity, which means that there is time interval necessary to move the synthesis front in the whole sample. As a result, the initial part of sample, where the synthesis front passed earlier, starts cooling and there is temperature gradient in the sample, which leads to non-homogenous of properties. In the cases, when the synthesis of material takes more than 10–12 s, badly compacted, porous defected sample are obtained. Therefore, when obtaining samples by mentioned technology, the geometric sizes are restricted. Proposed SHS-electrical rolling innovation technology enables to obtain the product with no limitation in length. The width of product is limited according to the width of rolls. The technology provides the realization of the process in non-stop regime, which is achieved by joining two technologies: energy consuming SHS and electrical rolling. The main principle of the technology is following: the container filled with pre-compacted chasm is delivered to the rolls of special rolling installation and the monor snatching provides the electric contact between container and rolls. During the process electric energy is delivered in the heart of deformation area with the use of contact and the heat, generated in the initial section of deformation heart, initiates the SHS process. As a result, the front of synthesis is created, which starts displacement with distinct speed in the sample located in container. Just after the described process, the rolls instantly start rotation with the set speed to ensure the motion of material. This speed should be equal to the speed of propagation of synthesis front. The synthesized product in hot plastic condition is delivered to the rolls in nonstop regime, simultaneously, providing the current in deformation zone in order to compensate the energy losses. As a result, by using the innovation SHS-electrical rolling technology we obtain long dimensional metal-ceramic product (Fig.1).

In both SHS and electrical rolling technology, the high quality (nonporous or low porosity < 2%) of materials and product is directly depended on the liquid phase content just after the passing of synthesis front in the sample. The more content of liquid phase provides the higher quality of material. The content of liquid phase itself depends on synthesis parameters: speed and temperature of synthesis. The higher the speed and temperature of synthesis we have, higher the content of liquid phase is formed. The speed and the temperature of synthesis depend on the  $\Delta\rho$  relative density of sample formed from initial chasm, this means it depends on the pressure of formation of the sample. Figure 2 describes the dependence of synthesis speed and temperatures on pressures of sample formation in Ti–Cr–C–X18H15, Ti–B, and Ti–B–Me systems relevantly.

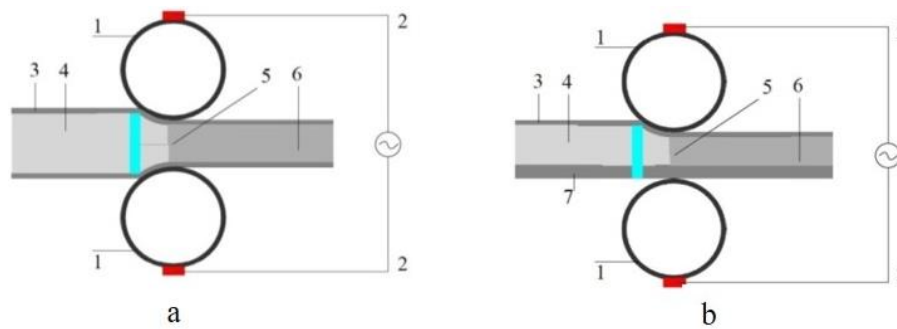


Fig. 1. (a) Production of composite material by SHS-electrical rolling; (b) Production of gradient material by SHS-electrical rolling; 1 rolls, 2 heating electric contacts, 3 container, 4 briquette of chasm, 5 synthesis (combustion) front, 6 rolled sample, 7 metal support.

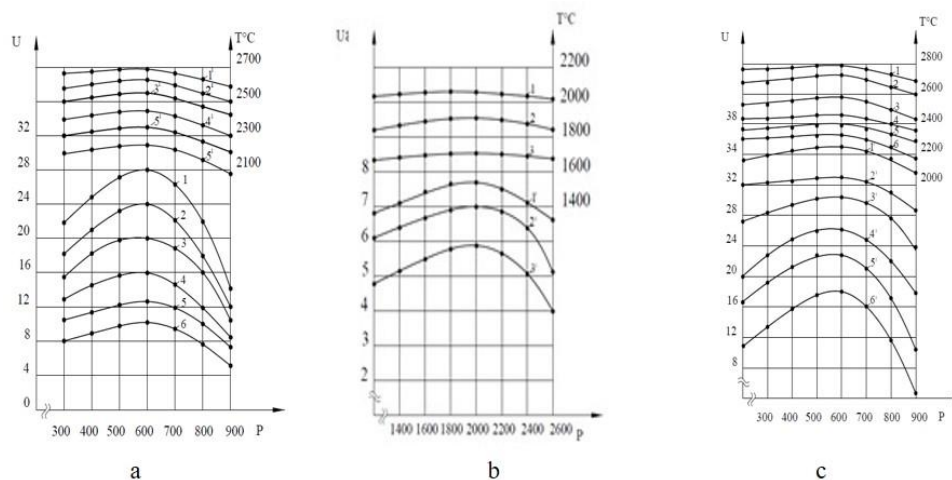


Fig. 2. (a) Curves (1–6) of synthesis temperature and curves (1<sup>l</sup>–6<sup>l</sup>) of synthesis speeds in Ti–Cr–C–18H15 system, depending on formation pressure of sample; (b) Curves (1–3) of synthesis temperature and curves (1<sup>l</sup>–3<sup>l</sup>) of synthesis speeds in Ti–B system, depending on formation pressure of sample; (c) Curves (1–6) of synthesis temperature and curves (1<sup>l</sup>–6<sup>l</sup>) of synthesis speeds in Ti–B–Me (Me = Cu, X18H15) system, depending on formation pressure of sample.

Therefore, based on the above presented curves, we say that the optimal pressures in Ti–Cr–C–Steel X18H15, Ti–B, and Ti–B–Me systems are established. Their values are defined as 50–70 MPa, 180–220 MPa, and 45–70 MPa. In order to obtain well compacted high quality materials, in addition to the synthesis parameters, it is important to determine technological, so called compaction parameters and their optimal values. These are time and pressure values and is depended on synthesis parameters and are determined experimentally. These parameters are: time of holding the pressing  $\tau_h$ , time of pressing  $\tau_p$ , preliminary pressing value  $P_{pr}$  and final pressing value  $P_f$ .  $P_{pr}$  preliminary pressure is the pressure value where we have initiation and realization of the synthesis process. The right selection of this value ensures the realization of the synthesis process in optimal conditions. Based on the analysis of experimental results, can be concluded, that the  $P_{pr}$  must be the right value in order to provide densification, which ensures the maximum velocity and temperature of the synthesis. Accordingly, the optimal values of  $P_{pr}$  preliminary pressure are 500–700 kg/cm<sup>2</sup>, 1800–2200 kg/cm<sup>2</sup>, and 450–700 kg/cm<sup>2</sup> respectively for the Ti–Cr–C–X18H15, Ti–B, and Ti–B–Me systems (Fig. 2). The other technological parameters as  $\tau_p$ ,  $\tau_h$ ,  $P_f$  are different from the similar compaction parameters due to the peculiarities of SHS-electrical rolling. The peculiarity is expressed in the limitation of final sample formation time and is defined by the time necessary for tensing the

sample between the rolls. Therefore, it is necessary to have maximal content of liquid phase for the final compaction.  $\tau_h$  is the time interval from the initiation of SHS process before starting the pressing of the sample.

Experiments showed that minimal value of  $\tau_h$  is 1 s. It is one of the important parameters of technological process. If the  $\tau_h$  exceeds the optimal value, which means the delay of pressing and because of the heat losses sample gets colder and accordingly reduces the liquid phase. As a result, the obtained sample is porous and low quality. If  $\tau_h$  is less than the optimal value, we have the rolling of semi-synthesized sample.

The analysis of above presented curve (Fig. 2) determines the optimal time intervals for pressing  $\tau_h$ , so that the materials should have maximal density, strength and hardness values. Therefore, the optimal pressing time intervals for Ti–Cr–C–X18H15, Ti–B, and Ti–B–Me can be no more than 3, 7, and 3 s respectively.

The time of pressing  $\tau_p$ , during the electrical rolling, is directly depended on the rolling speed, which itself is depended on the velocity of synthesis process. The real value of  $\tau_p$  is usually 1–2 s proceeding from the technological processes. This value is not sufficient for obtaining desired strength, density and hardness of the material. Therefore, for the compensating  $\tau_p$  time, the final pressing  $P_f$  is used, which means the high 65–68% tensing value applied during the rolling.

$P_f$  final pressing value is the value for the final compaction of the synthesized material. The right selection of this value provides the fabrication materials with the lowest porosity. As described above, the  $P_f$  value is selected in a way to obtain lowest porosity (highest density), high strength and high hardness in whole material. In our experimental studies the optimal value of tensing is the rolls is 65–68%

After determining the optimal compaction regimes for the production of materials in Ti–Cr–C–X18H15, Ti–B, and Ti–B–Me systems, the pilot samples were prepared, which are presented in Fig. 3.



Fig. 4. Samples obtained by SHS-electrical rolling.

### Conclusions:

1. The peculiarities of SHS-electric rolling were studied;
2. The optimal technological values of SHS-electrical rolling were defined;
3. Pilot samples were produced based on the optimal technological parameters of SHS-electrical rolling.

1. A.G. Merzhanov, I.P. Borovinskaya, The self-extending high-temperature synthesis in chemistry and technology of refractory connections, 1979, pp. 223–227.
2. G.Sh. Oniashvili, Z.G. Aslamazashvili, G.V. Zakharov, G.F. Tavadze, M.N. Chikhradze, T.A. Dzigrashvili, A. Berner, SHS of fine-grained ceramics containing carbides, nitrides, and borides, *Int. J. Self-Propag. High-Temp. Synth.*, 2013, vol. 22, no. 4, pp. 185–188.
3. Z.G. Aslamazashvili, A.N. Pityulin, A.S. Rogachyov, A.G. Merzhanov, G.Sh. Oniashvili, F.N. Tavadze, Development, receiving and properties of okalinostoyky tool STIM-3V alloy, Pre-print “ОИХФ АН СССР”, Chernogolovka, 1985, 102 p.



## SHS OF CERAMIC NITRIDE–CARBIDE NANOPOWDER COMPOSITIONS OF $\text{Si}_3\text{N}_4$ – $\text{SiC}$ AND $\text{AlN}$ – $\text{SiC}$ WITH THE USE OF SODIUM AZIDE AND HALIDE SALTS

Yu. V. Titova\*<sup>a</sup>, A. P. Amosov<sup>a</sup>, D. A. Maidan<sup>a</sup>, G. S. Belova<sup>a</sup>, and I. A. Uvarova<sup>a</sup>

<sup>a</sup>Samara State Technical University, Samara, 443100 Russia

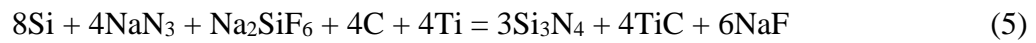
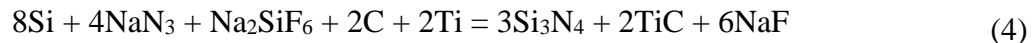
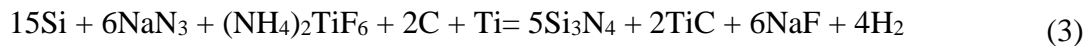
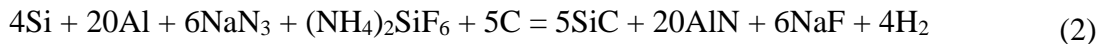
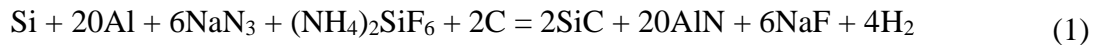
\*e-mail: titova600@mail.ru

DOI: 10.24411/9999-0014A-2019-10174

Powders of refractory nitride ( $\text{AlN}$ ,  $\text{Si}_3\text{N}_4$ ) and carbide ( $\text{SiC}$ ,  $\text{TiC}$ ) compounds are widely used for the manufacture of non-oxide structural ceramics with low weight, high hardness, wear resistance, heat resistance, corrosion resistance [1, 2]. Traditionally, such ceramics are produced by reaction sintering or hot pressing of powders. But single-phase ceramics from individual refractory compounds can be badly sintered, poorly processed, be too brittle, have a large coefficient of friction, etc. To solve these problems, several approaches are used. First, composite ceramics of several phases are used [1–3]. For example, the addition of titanium carbide particles to silicon nitride increases the hardness and fracture toughness due to the higher hardness of  $\text{TiC}$  compared to  $\text{Si}_3\text{N}_4$  and due to stresses arising because of the different thermal expansion coefficients resulting in the curvature of cracks caused by internal stresses. The hardness of  $\text{Si}_3\text{N}_4$ –5%  $\text{TiC}$  composites is 17 HPa, the fracture toughness is  $6.5 \text{ MPa m}^{1/2}$  [4]. Such composites are used for the production of cutting tools and wear-resistant parts, as well as ceramics with improved thermal conductivity and electrical conductivity [5]. To obtain dense ceramics with high dielectric properties,  $\text{SiC}$  is added to  $\text{AlN}$  [6]. The  $\text{AlN}$ – $\text{SiC}$  composition has an increased bending strength with an increase in the  $\text{SiC}$  content, and the maximum bending strength is observed in the  $\text{AlN}$ –30%  $\text{SiC}$  composite containing  $\beta$ - $\text{SiC}$  fibers [7]. Secondly, the transition to nanostructured ceramics is used, since it has been repeatedly shown that the reduction of the powder size, the transition to nanopowders and the manufacture of nanostructured ceramics can significantly improve its properties [8, 9]. But traditional methods of sintering can no longer be used here, as they lead to the consolidation of nanopowders and increase their size. A modern alternative to this traditional method is, for example, the spark plasma sintering (SPS) method, which is most widely used for sintering nanopowders. Third, both approaches are used simultaneously, i.e. nanostructured ceramic composites. A study on  $\text{Si}_3\text{N}_4$ / $\text{SiC}$  nanocomposites reported improved bending strength [10]. It should be noted that if a component is introduced into the initial mixture of ceramic powders in the form of large particles or agglomerates of small particles, the compaction of the composite and its strength after sintering deteriorate [3]. To obtain high strength of the composite, it is necessary that the particles of all components are very small and evenly distributed over the volume of the composite [3]. It is also necessary to take into account that very small particles of the components can be uniformly distributed in the volume of the composite not by mechanical mixing of the powders, but by chemical synthesis of these particles in the volume of the composite in the implementation of in-situ processes [3].

One of the promising in-situ processes is the process of self-propagating high-temperature synthesis (SHS) of a wide variety of refractory compounds, including nitrides and carbides [11, 12]. The process of SHS is attractive due to its simplicity and efficiency, and provides great opportunities for regulating the dispersion and structure of the synthesized ceramic powders, bringing them to the nanoscale level. In particular, in the synthesis of nitrides, such capabilities are realized in the azide SHS process, referred to as SHS-Az, in which as a nitriding reagent is

used not nitrogen gas, but sodium azide powder  $\text{NaN}_3$ , as well as halide salts. The successful experience of application of the process of azide SHS to obtain nanopowders of nitride compositions  $\text{TiN-BN}$ ,  $\text{AlN-BN}$ ,  $\text{Si}_3\text{N}_4\text{-TiN}$  using precursors – halide salts of both nitrated elements [13]. The aim of this work is to study the possibility of obtaining ceramic nitride-carbide nanopowder compositions  $\text{Si}_3\text{N}_4\text{-TiC}$  and  $\text{AlN-SiC}$  by azide SHS. The compositions of initial powder mixtures for the preparation of single-phase powders  $\text{AlN}$ ,  $\text{Si}_3\text{N}_4$ ,  $\text{SiC}$  and  $\text{TiC}$  by the azide SHS technology are known [12], from the analysis of which the following equations of chemical reactions can be proposed for the synthesis of target compositions  $\text{Si}_3\text{N}_4\text{-TiC}$  and  $\text{AlN-SiC}$ :



The phase composition of the synthesized products was determined on the Dron-3 diffractometer. X-ray spectra were measured using Cu-radiation. The quantitative phase analysis was performed by the full-profile analysis method (Rietveld method) using the program PDXL 1.8.1.0 using the open crystallographic database (COD). The results of the X-ray phase analysis of the products are given in Tables 1 and 2. Table 1 shows that in combustion of mixtures (1) and (2) it is possible to synthesize the target composition  $\text{AlN-SiC}$ , but the reaction products also include water-insoluble admixtures of  $\text{Na}_3\text{AlF}_6$  and free Si. Moreover, the share of the by-product  $\text{Na}_3\text{AlF}_6$  increases with increasing carbon content in the initial mixture that can be explained by decrease in combustion temperature. Table 2 shows that in combustion of mixtures (3)–(5) it was also possible to synthesize the target composition  $\text{Si}_3\text{N}_4\text{-TiC}$ . The byproducts of these reactions are: free silicon and silicon carbide, but their total content does not exceed 6 wt %.

Table 1. The ratio of phases in the washed combustion products for  $\text{AlN-SiC}$  synthesis.

| The composition of the starting mixture                                      | Composition of combustion products, wt % |     |                           |     |
|--|--|-----|---------------------------|-----|
|  | AlN                                      | SiC | $\text{Na}_3\text{AlF}_6$ | Si  |
| $\text{Si}+20\text{Al}+6\text{NaN}_3+(\text{NH}_4)_2\text{SiF}_6+2\text{C}$  | 90.3                                     | 1.3 | 7.7                       | 0.7 |
| $4\text{Si}+20\text{Al}+6\text{NaN}_3+(\text{NH}_4)_2\text{SiF}_6+5\text{C}$ | 81.0                                     | 2.6 | 15.5                      | 0.9 |

Table 2. The ratio of phases in the washed combustion products for  $\text{Si}_3\text{N}_4\text{-TiC}$  synthesis.

| The composition of the starting mixture                                 | Composition of combustion products, wt % |                                |      |      |     |
|---|--|--------------------------------|------|------|-----|
|   | $\beta\text{-Si}_3\text{N}_4$            | $\alpha\text{-Si}_3\text{N}_4$ | TiC  | Si   | SiC |
| $15\text{Si}+6\text{NaN}_3+(\text{NH}_4)_2\text{TiF}_6+\text{C}$        | 63.5                                     | 28.4                           | 5.66 | 2.44 | –   |
| $8\text{Si}+4\text{NaN}_3+\text{Na}_2\text{SiF}_6+2\text{C}+2\text{Ti}$ | 37.7                                     | 38.2                           | 20.3 | 2.3  | 1.5 |
| $8\text{Si}+4\text{NaN}_3+\text{Na}_2\text{SiF}_6+4\text{C}+4\text{Ti}$ | 35.6                                     | 26.6                           | 31.9 | 1.9  | 4.0 |

The study of the surface topography and morphology of the particles of the synthesized compositions was carried out on a scanning electron microscope JSM-6390A Jeol with the prefix Jeol JED-2200. The results are presented in Figs. 1 and 2. From the presented photos, taking into account the results of the energy dispersion analysis, it is clear that the photos of powders before the operation of water washing in distilled water contain mainly sodium fluoride crystals. Analyzing the photos of powders after washing, it can be concluded that aluminum nitride and silicon carbide are synthesized in the form of equiaxial micro-sized particles.

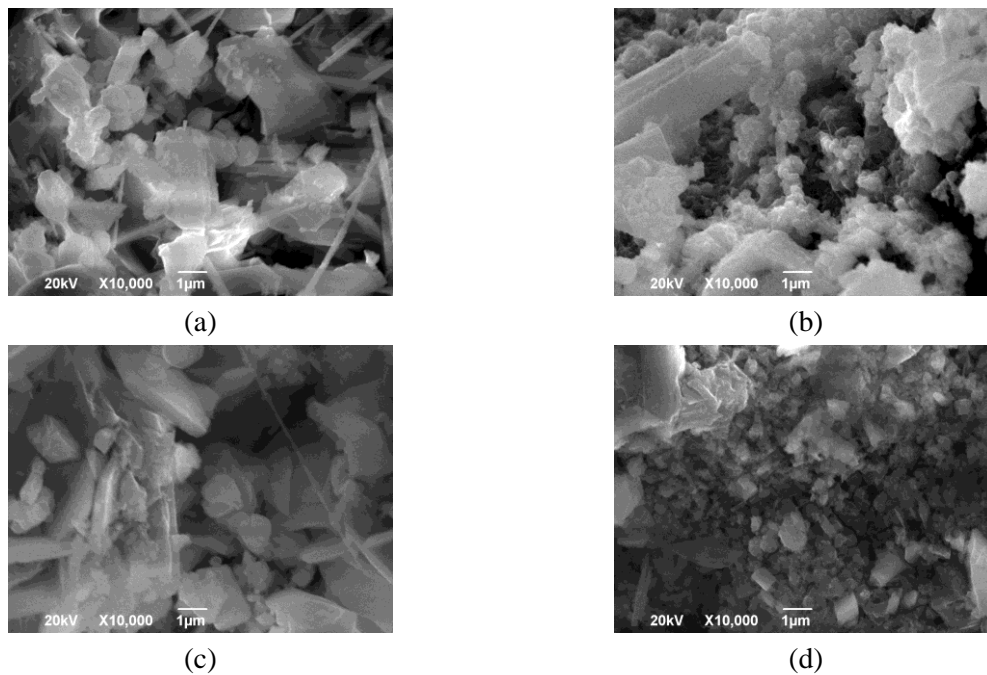


Fig. 1. Morphology of particles of combustion products of mixtures  $\text{Si} + 20\text{Al} + 6\text{NaN}_3 + (\text{NH}_4)_2\text{SiF}_6 + 2\text{C}$  (a, b) and  $4\text{Si} + 20\text{Al} + 6\text{NaN}_3 + (\text{NH}_4)_2\text{SiF}_6 + 5\text{C}$  (c, d) before and after water washing.

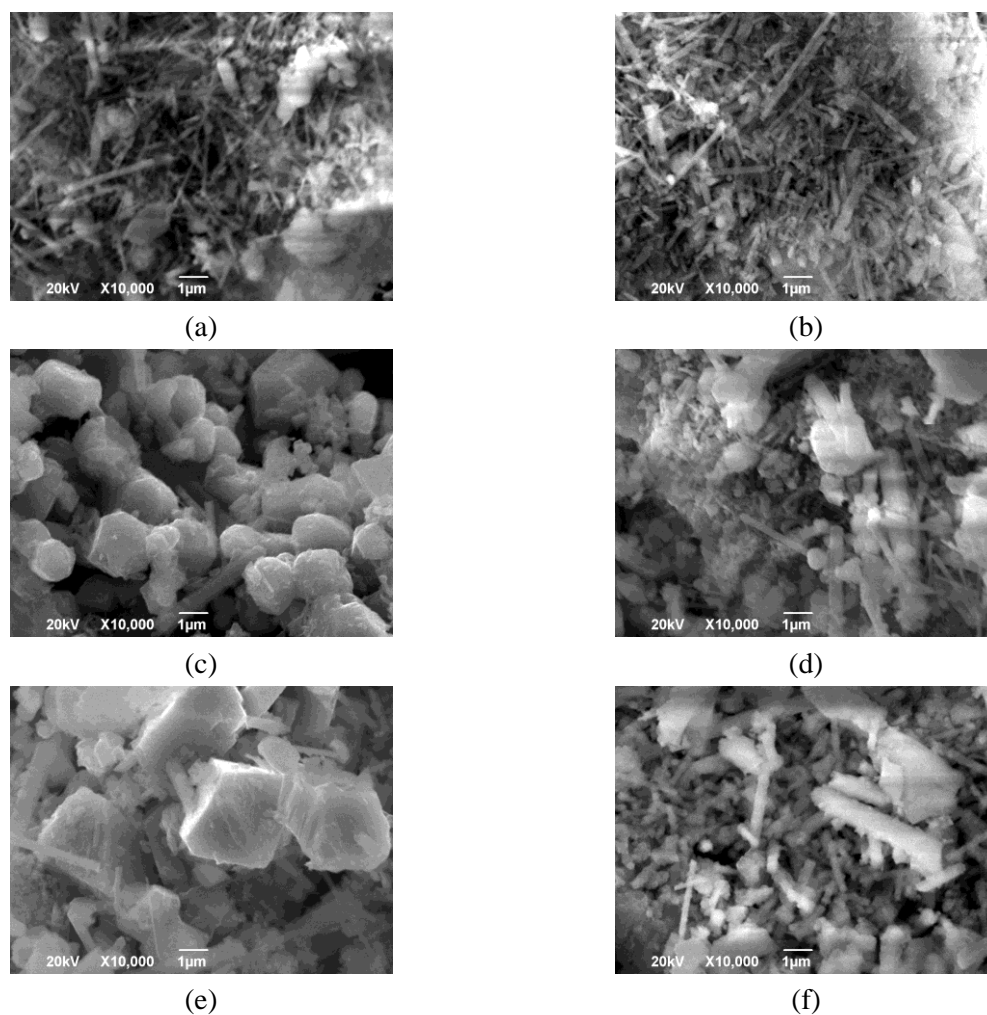


Fig. 2. Morphology of particles of combustion products of mixtures  $15\text{Si} + 6\text{NaN}_3 + (\text{NH}_4)_2\text{TiF}_6 + \text{C}$  (a, b),  $8\text{Si} + 4\text{NaN}_3 + \text{Na}_2\text{SiF}_6 + 2\text{C} + 2\text{Ti}$  (c, d),  $8\text{Si} + 4\text{NaN}_3 + \text{Na}_2\text{SiF}_6 + 4\text{C} + 4\text{Ti}$  (e, f) before and after water washing.

Thus, the method of azide SHS made it possible to obtain promising ceramic nitride-carbide powder compositions  $\text{Si}_3\text{N}_4\text{-TiC}$  and  $\text{AlN-SiC}$  in one stage using precursors – halide salts of elements to be nitrated and carbided.

The synthesized composite powders  $\text{Si}_3\text{N}_4\text{-TiC}$  and  $\text{AlN-SiC}$  are promising for use in sintering the corresponding composite ceramic materials with increased properties, lower brittleness, good machinability, lower sintering temperatures compared to single-phase ceramic materials made of nitrides or carbides. Additional studies are required to obtain nanoscale powder compositions  $\text{Si}_3\text{N}_4\text{-TiC}$  and  $\text{AlN-SiC}$ .

1. B. Basu, K. Balani, *Advanced Structural Ceramics*, Hoboken (NJ): Wiley, 2011.
2. B. Basu, M. Kalin, *Tribology of ceramics and composites: a materials science perspective*, Hoboken, New Jersey: John Wiley & Sons, Inc., 2011.
3. G.-J. Zhang, J.-F. Yang, M. Ando, T. Ohji, Nonoxide-boron nitride composites, *J. Eur. Ceram. Soc.*, 2002, vol. 22, no. 14, pp. 2551–2554.
4. G. Zheng, J. Zhao, Y. Zhou, Zh. Gao, Preparation and characterization of  $\text{Si}_3\text{N}_4/\text{TiCN}$  composite ceramic tool material, *Adv. Mater. Res.*, 2011, vol. 152–153, pp. 500–503.
5. V.A. Izhevskiy, L.A. Genova, J.C. Bressiani, Investigation of the Chemical Interaction in the  $\text{TiC-Si}_3\text{N}_4$  System, *Mat. Res.*, 1999, vol. 2, no. 4, pp. 271–277.
6. L. Qiao, H.P. Zhou, H. Xue, S.H. Wang, Effect of  $\text{Y}_2\text{O}_3$  on low temperature sintering and thermal conductivity of AlN ceramics, *J. Eur. Ceram. Soc.*, 2003, vol. 23, no. 1, pp. 61–67.
7. J.-F. Li, M. Asano, Y. Kobayashi, A. Kawasaki, R. Watanabe, Mechanical Properties of AlN-SiC Ceramic Composites Synthesized by Pressureless Sintering and Post-HIP Treatment, *J. Jap. Soc. Powder Powder Met.*, 1995, vol. 42, no. 12, pp. 1452–1456.
8. Y.M., Komura, A. Yamakawa, Microstructure and tribological properties of nano-sized  $\text{Si}_3\text{N}_4$ , *Scr. Mater.*, 2001, vol. 44, pp. 1517–1521.
9. P. Palmero, Structural ceramic nanocomposites: a review of properties and powders synthesis methods, *Nanomater.*, 2015, vol. 5, no. 2, pp. 656–696.
10. M. Poorteman, P. Descamps, F. Cambier, Silicon nitride/silicon carbide nanocomposite obtained by nitridation of SiC: fabrication and high temperature properties, *J. Eur. Ceram. Soc.*, 2003, vol. 23, no. 13, pp. 2361–2366.
11. A.P. Amosov, I.P. Borovinskaya, A.G. Merzhanov, A.E. Sytchev, Principles and methods for regulation of dispersed structure of SHS powders: From monocrystallites to nanoparticles, *Int. J. Self-Propag. High-Temp. Synth.*, 2005, vol. 14, no. 1, pp. 165–186.
12. G.V. Bichurov, Halides in SHS azide technology of nitrides obtaining, *Nitride Ceramics: Combustion synthesis, properties, and applications*, Eds. A.A. Gromov, L.N. Chukhlomina. Weinheim: Wiley-VCH Verlag GmbH & Co. KGaA, 2015, pp. 229–263.
13. A.P. Amosov, G.V. Bichurov, L.A. Kondrat'eva, I.A. Kerson, Nitride nanopowders by azide SHS technology, *Int. J. Self-Propag. High-Temper. Synth.*, 2017, vol. 26, no. 1, pp. 11–21.

## SHS OF BN NANOPOWDER USING BORON-CONTAINING COMPOUNDS AND SODIUM AZIDE

**Yu. V. Titova<sup>\*a</sup>, A. P. Amosov<sup>a</sup>, D. A. Maidan<sup>a</sup>, D. R. Safaeva<sup>a</sup>, M. V. Suslov<sup>a</sup>,  
and D. V. Ostroukhov<sup>a</sup>**

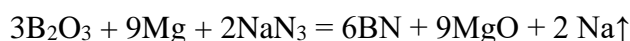
<sup>a</sup>Samara State Technical University, Samara, 443100 Russia

<sup>\*</sup>e-mail: titova600@mail.ru

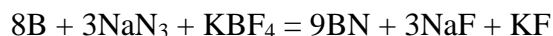
DOI: 10.24411/9999-0014A-2019-10175

Hexagonal boron nitride (BN) has a unique set of properties and a wide range of applications, which led to the creation of a large number of methods to obtain it [1]. However, the known methods for producing BN are based on long-term heating to high temperatures, are energy-intensive and expensive, and therefore energy-saving technologies based on the SHS process represent an effective alternative to traditional technologies for producing hexagonal BN [1]. The first SHS technologies were based on nitriding the pure boron powder or its chemical compounds by gaseous nitrogen during their combustion in the SHS reactor in a nitrogen atmosphere [1–3]. However, for nitriding the pure boron, it is necessary to create very high nitrogen pressures of 10–500 MPa, which greatly complicates the design of the SHS reactor and the technology for obtaining BN, or significantly dilute the initial boron powder with the final product BN. In the case of nitriding the chemical compounds (B<sub>2</sub>O<sub>3</sub>, KBF<sub>4</sub>), a metal-reducer (most often magnesium Mg) is added to the charge, which lowers the required nitrogen pressure in the reactor to an average of 5 MPa, but also leads to the formation of by-products along with the target product BN, which have to be separated by subsequent acid washing, which also complicates the SHS technology.

Then, methods of azide SHS with the use of solid nitriding reagent–sodium azide NaN<sub>3</sub> instead of gaseous nitrogen were used to obtain hexagonal BN [4–7]. In the case of nitriding the boron oxide B<sub>2</sub>O<sub>3</sub>, a metal-reducer Mg or Ca was used [4]:



The combustion process took place at atmospheric nitrogen pressure of 0.1 MPa with the formation of 90–95% BN and 5 to 10% of MgO or CaO impurities that are removed by subsequent acid washing. The disadvantage of the method was also the formation of fire-hazardous atomic sodium. Powders of pure boron and boron-containing halide salts KBF<sub>4</sub> or NH<sub>4</sub>BF<sub>4</sub> were used as initial reagents at Samara State Technical University [5–7]:



The SHS process took place at a nitrogen pressure in the reactor of 5 MPa with the formation of 97–98.5% BN and 1.5–3% NaF and KF impurities easily removed by subsequent water washing. In this paper, an attempt is made to replace the KBF<sub>4</sub> or NH<sub>4</sub>BF<sub>4</sub> salt with cheaper and available boron-containing compounds: boric anhydride B<sub>2</sub>O<sub>3</sub> and boric acid H<sub>3</sub>BO<sub>3</sub>.

The aim of this work is to study the possibility of obtaining and determining the conditions for the synthesis of boron nitride powder by SHS from the systems "boric acid–sodium azide", "boric anhydride–sodium azide" with the addition of amorphous boron. The process of obtaining boron nitride from these systems consisted in the following sequence of operations. The powders of the initial components, taken in the desired ratio, were mixed manually in a porcelain mortar for 10 minutes. The resulting mixture was poured into a tracing paper cup to

form a sample with a diameter of 30 mm and a height of 45 mm, and then placed in a constant pressure reactor. The samples were burned in a nitrogen atmosphere at a pressure of 4 MPa, and the temperatures and combustion rates of the studied systems were recorded. Table 1 presents the results of experimental studies of the temperature and combustion rate of mixtures intended for the synthesis of boron nitride.

Table 1. The results of experimental studies of the temperature and combustion rate of mixtures intended for the synthesis of boron nitride.

| Initial mixture   | Combustion temperature, °C | Combustion rate, cm/s |
|---|----------------------------|-----------------------|
| 8B + B <sub>2</sub> O <sub>3</sub> + 6NaN <sub>3</sub>    | 2497                       | 1.4                   |
| 16B + B <sub>2</sub> O <sub>3</sub> + 6N                  | 2944                       | 1.6                   |
| 16B + 2H <sub>3</sub> BO <sub>3</sub> + 6NaN <sub>3</sub> | 2563                       | 1.4                   |
| 17B + H <sub>3</sub> BO <sub>3</sub> + 6NaN <sub>3</sub>  | 2877                       | 1.7                   |

It can be seen from the presented results that with an increase in the boron content in the initial mixture, the temperature and combustion rate increase. The phase composition of the synthesized products was determined on the Dron-2 X-ray diffractometer. X-ray spectra were measured using Cu-radiation. The results of the X-ray phase analysis of the products are shown in Figs. 1, 2.

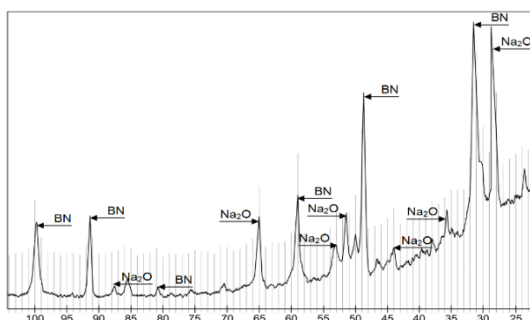


Fig. 1. XRD pattern of the products of combustion of the mixture 8B + B<sub>2</sub>O<sub>3</sub> + 6NaN<sub>3</sub>.

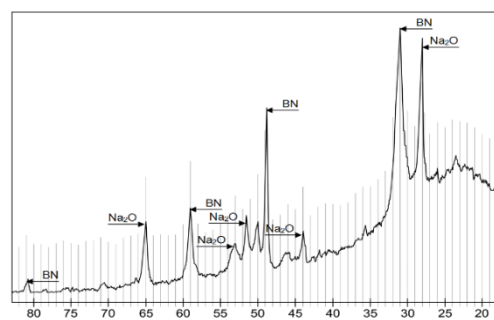
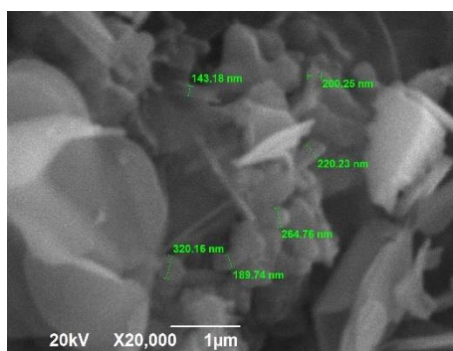
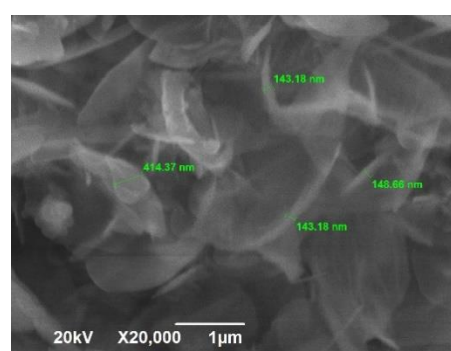


Fig. 2. XRD pattern of the products of combustion of the mixture 16B + B<sub>2</sub>O<sub>3</sub> + 6NaN<sub>3</sub>.

It can be seen from the presented XRD patterns that the combustion products of the mixtures 8B + B<sub>2</sub>O<sub>3</sub> + 6NaN<sub>3</sub> and 16B + B<sub>2</sub>O<sub>3</sub> + 6NaN<sub>3</sub> consist of two phases: target is boron nitride (BN) and side is sodium oxide (Na<sub>2</sub>O). With an increase in the content of boron in the initial mixture, the amount of sodium oxide is slightly reduced. The study of the surface topography and morphology of reaction product particles was carried out using the Jeol scanning electron microscope JSM-6390A with the prefix Jeol JED-2200. The results are presented in Figs. 3 and 4.



(a)



(b)

Fig. 3. SEM image of particles of combustion products of mixtures 8B + B<sub>2</sub>O<sub>3</sub> + 6NaN<sub>3</sub> (a) and 16B + B<sub>2</sub>O<sub>3</sub> + 6NaN<sub>3</sub> (b).

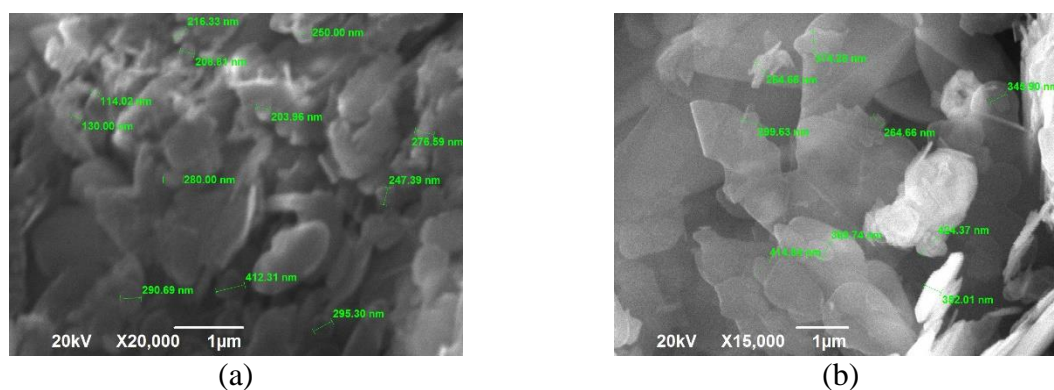


Fig. 4. SEM image of particles of combustion products of mixtures 16B + 2H<sub>3</sub>BO<sub>3</sub> + 6NaN<sub>3</sub> (a) and 17B + H<sub>3</sub>BO<sub>3</sub> + 6NaN<sub>3</sub> (b).

Comparing the photos presented in Fig. 3 and taking into account the results of XRD analysis presented below, we can conclude that the combustion of mixtures of 8B + B<sub>2</sub>O<sub>3</sub> + 6NaN<sub>3</sub> and 16B + B<sub>2</sub>O<sub>3</sub> + 6NaN<sub>3</sub> formed particles of lamellar and irregular shape of boron nitride and sodium oxide. The size of boron nitride particles varies in the range from 150 to 400 nm. The particle size of BN increases with the boron content rise.

Figure 5 shows the XRD pattern of combustion products of mixture 17B + H<sub>3</sub>BO<sub>3</sub> + 6NaN<sub>3</sub>. It can be seen from the XRD pattern that the products of combustion of the mixture 17B + H<sub>3</sub>BO<sub>3</sub> + 6NaN<sub>3</sub> consists of two phases: the task is boron nitride (BN) and side is sodium oxide (Na<sub>2</sub>O). Moreover, the yield of the target product is slightly lower than in systems using boron oxide as a starting component.

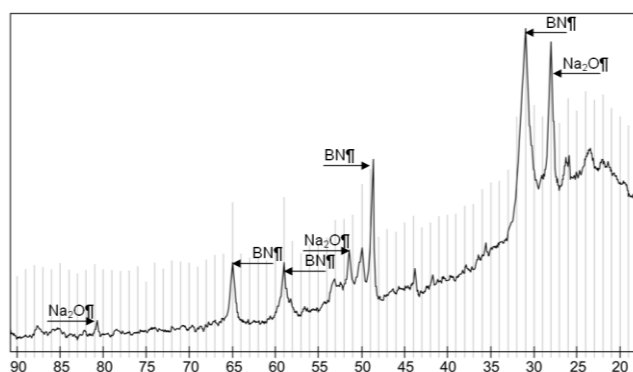


Fig. 5. XRD pattern of the products of combustion of the mixture 17B + H<sub>3</sub>BO<sub>3</sub> + 6NaN<sub>3</sub>.

Comparing the photos presented in Fig. 4 and taking into account the results of X-ray phase analysis presented below, it can be concluded that the combustion of mixtures of 16B + 2H<sub>3</sub>BO<sub>3</sub> + 6NaN<sub>3</sub> and 17B + H<sub>3</sub>BO<sub>3</sub> + 6NaN<sub>3</sub> formed particles of lamellar and irregular shape of boron nitride and sodium oxide. The size of boron nitride particles varies in the range from 150 to 450 nm. The particle size of BN synthesized from boric acid systems is larger than that of boron oxide systems.

Thus, the experiments conducted to obtain micro- and nanopowders of target boron nitride by SHS using boron-containing compounds and sodium azide led to the following results. It was found that the synthesized boron nitride has lamellar and irregular particles ranging in size from 150 to 450 nm. The final products contain sodium oxide along with the target boron nitride. The addition of boron to the initial charge increases the yield of the target product, but the particle size increases.

The authors express their gratitude to the company ETIMADEN-Etiproducts Ltd. for the donation of samples of boric acid H<sub>3</sub>BO<sub>3</sub> ULSPOWDER and boron oxide B<sub>2</sub>O<sub>3</sub> POROUS.

1. A.S. Mukasyan, Combustion Synthesis of Boron Nitride Ceramics: Fundamentals and Applications, Nitride Ceramics: Combustion Synthesis, Properties, and Applications, Ed. by A.A. Gromov and L.N. Chukhlomina, Weinheim: Wiley-VCH, 2015, pp. 49–74.
2. I.P. Borovinskaya, T.I. Ignat'eva, V.I. Vershinnikov, G.G. Khurtina, N.V. Sachkova, Preparation of ultrafine boron nitride powders by self-propagating high-temperature synthesis, *Inorg. Mater.*, 2003, vol. 39, no. 6, pp. 588–593.
3. G.F. Tavadze, A.S. Shteinberg, Production of Advanced Materials by Methods of Self-Propagating High-Temperature Synthesis, Springer, 2013.
4. US Patent 4459363, J.B. Holt, Synthesis of refractory materials, Jul. 10, 1984.
5. A.P. Amosov, G.V. Bichurov, N.F. Bolshova, V.M. Erin, A.G. Makarenko, Y.M. Markov, Azides as reagents in SHS processes, *Int. J. Self-Propag. High-Temp. Synth.*, 1992, vol. 1, no. 2, pp. 239–245.
6. G.V. Bichurov, The use of halides in SHS azide technology, *Int. J. Self-Propag. High-Temp. Synth.*, 2000, vol. 9, no. 2, pp. 247–268.
7. G.V. Bichurov, Halides in SHS Azide Technology of Nitrides Obtaining, Nitride Ceramics: Combustion Synthesis, Properties, and Applications, Ed. by A.A. Gromov and L.N. Chukhlomina, Weinheim: Wiley-VCH, 2015, pp. 229–263.



MICROWAVE ASSISTED COMBUSTION SYNTHESIS OF  $\text{AlFe}_2\text{B}_2$ **L. Trombi<sup>\*a</sup>, F. Cugini<sup>b</sup>, R. Rosa<sup>c</sup>, P. Veronesi<sup>c</sup>, M. Solzi<sup>b</sup>, and C. Leonelli<sup>b</sup>**<sup>a</sup>Zare, Via IV Novembre, 37A, 42022, Boretto, Italy<sup>b</sup>Dipartimento di Fisica e Scienze della Terra “Macedonio Melloni”, Università degli Studi di Parma, Parco Area delle Scienze 7/A, 43124, Parma<sup>c</sup>Dipartimento d’Ingegneria “Enzo Ferrari”, Università degli Studi di Modena e Reggio Emilia, Via P. Vivarelli 10, 41125, Modena, Italy

\*e-mail: l.trombi@zare.it

DOI: 10.24411/9999-0014A-2019-10176

Magnetocaloric materials are a new class of multifunctional materials appropriate for thermal management applications (e.g. magnetic refrigeration) that exhibit significant “caloric” effects: they experience temperature changes under isothermal or adiabatic variations of a magnetic field [1]. Many of these materials contain rare, toxic or strategically limited elements: these materials include Gd,  $\text{Gd}_5(\text{GeSi})_4$ , FeRh, MnAs, FeMnAsP and  $(\text{La}((\text{FeCo})\text{Si}(\text{H}))_{13})$  [1].

A promising system is  $\text{AlFe}_2\text{B}_2$ , lightweight and composed of earth-abundant, easy recyclable and safe elements [2]. It has a simple two-dimensional layered structure with a magnetic transition near room temperature, the order of which is presently under debate [1].

Arc furnace melting (in vacuum or in Argon atmosphere) is the most used synthesis technique, but with a strong tendency to segregation and to produce byproducts. Hence, multiple re-meltings, longtime/high temperature annealings and HCl etching are required [1, 2], in order to obtain only  $\text{AlFe}_2\text{B}_2$ .

In this work we discover a new simpler and low-cost route to synthesize  $\text{AlFe}_2\text{B}_2$  through microwave assisted combustion synthesis (MACS/MASHS).

The aim of this study is to understand what are the most suitable parameters to obtain a bulk sample in which the reaction yield which is maximized, namely, maximize the amount of  $\text{AlFe}_2\text{B}_2$  phase, minimizing the byproducts (such as different types of Fe-aluminides, and Al/Fe-borides).

Samples were made using a single mode MW applicator (power: 300mW). We synthesized specimens with different application field mode (E or H), cold forming pressure, weights and with or without SiC susceptors (within mixed with elemental metal powders or outside). The samples were studied by XRD, SEM, and Magnetic VSM measurements.

The results show a high percentage of magneto-caloric phase already after MACS synthesis and a magneto-caloric effect with a similar magnitude to the state of the art (specimens mainly produced via arc melting, several re-melting, annealing and HCl etching).

Finally, the MACS route is able to achieve quickly and easily the magneto-caloric phase  $\text{AlFe}_2\text{B}_2$ .

1. X. Tan, et al, Magnetocaloric effect in  $\text{AlFe}_2\text{B}_2$ : Toward magnetic refrigerants from earth-abundant elements, *J. Am. Chem. Soc.*, 2013, vol. 135, pp. 9553–9557.
2. L.H. Lewis, et al, Developing magnetofunctionality: Coupled structural and magnetic phase transition in  $\text{AlFe}_2\text{B}_2$ , *J. Alloys Compd.*, 2015, vol. 650, pp. 482–488.

## METAL FOAMS FABRICATED BY SPRAY SOLUTION COMBUSTION SYNTHESIS AND SPARK PLASMA SINTERING

**G. V. Trusov<sup>\*a,b</sup>, A. B. Tarasov<sup>c</sup>, D. O. Moskovskih<sup>b</sup>, A. S. Rogachev<sup>a,b</sup>,  
and A. S. Mukasyan<sup>d</sup>**

<sup>a</sup>Merzhanov Institute of Structural Macrokinetics and Materials Science, Russian Academy of Sciences, Chernogolovka, Russia

<sup>b</sup>National University of Science and Technology MISIS, Moscow, Russia

<sup>c</sup>Lomonosov Moscow State University, Moscow, Russia

<sup>d</sup>University of Notre Dame, USA

\*e-mail: german.v.trusov@gmail.com

DOI: 10.24411/9999-0014A-2019-10177

Nickel are most demanded oxide materials for scientific and industrial applications. They are widely used in different forms and modifications as catalysts, magnetic materials, for medical purposes [1]. Although many different approaches are developed to obtain nickel with required properties, any new technique allowing a direct synthesis of single-phase materials still attracts a big attention. As it has been shown recently, a "solution combustion" technique is one of the most promising candidate for nickel production with controllable properties [2]. The method is based on the usage of highly exothermic self-sustained redox reactions between metal nitrates and organic "fuels", which are mixed on a molecular level in aqueous solution. Heating of reaction solution leads to water evaporation and formation of a homogeneous reactive mixture, followed by reaction initiation with rapid heat release. The intensive adiabatic self-heating of the environment and appearance of a great amount of gaseous products facilitates the formation of oxide nanocrystalline aggregates. The further development of the method requires to overcome aggregation of resulted nanoparticles.

In present work, we have developed the solution combustion reaction in the individual micron-size droplets of ultrasonic-generated aerosols using an oxidizer and fuel, namely nickel nitrate and glycine. An aqueous reaction solution was nebulized in a preheated to 800°C quartz tube furnace to produce gray powder depending on preparation temperature and aerosol flow velocity. Phase composition, morphology and optical properties of resulted powders were studied by XRD, SEM, TEM and BET techniques. The magnetic powder obtained at high temperatures or low flow velocity was found to be a well crystalline single-phase nickel. Powder consisted of non-aggregated hollow micron-sized spheres with a complex internal structure. All products demonstrated high values of specific surface area. A spray solution combustion synthesis (SSCS) approach allows fabrication of hollow metal (Ni) spheres with a unique morphology (Fig. 1). The outer diameters of the spheres range from 0.5 to 5  $\mu\text{m}$  with average wall thicknesses of  $\sim 20$  nm. The most important feature is that the shell consists of Ni nanoparticles and amorphous areas forming a porous skeleton. Such morphological features play an important role during spark plasma sintering of such particles: this "active" porous nano-shell allows rapid transfer of the matter to make strong necks between the spheres, while sintering of the shell itself leads to the formation of rigid pore-free surfaces. Rapid (15 min) low temperature (763 K) spark plasma sintering (SPS) treatment of these particles leads to the fabrication of high porous (up to 93%) cellular materials with relatively high mechanical properties (reduced elastic modulus  $E/\rho = 5.7$  GPa and  $E/\rho^2 = 81.6$  GPa) and thermal conductivity 70 times smaller than for bulk Ni. Thus, it is demonstrated that the combination of SSCS and SPS methods can be considered as a novel technological approach for fabrication of metallic foams [3].

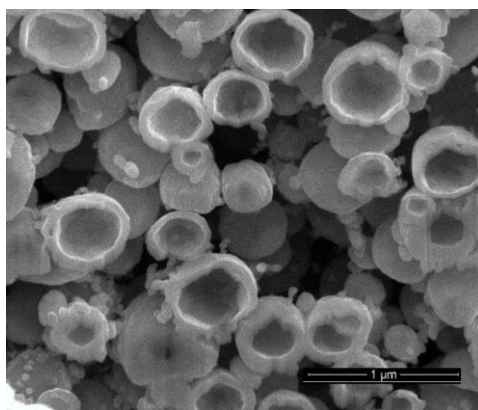


Fig. 1. SEM image of the sintered nickel microspheres by spark plasma sintering (SPS) without pressure.

Finally, it is worth noting that SSCS allows fabrication a variety of hollow spherical particles with different non-oxide compositions including Cu, Co, NiCu, NiFe, NiCoCu and etc. It implies that the composition of metallic high porous cellular materials produced by hybrid SSCS + SPS approach can be significantly expanded.

1. S.T. Aruna, A.S. Mukasyan, Combustion synthesis and nanomaterials, *Curr. Opin. Solid State Mater. Sci.*, 2008, vol. 12, no. 3, pp. 44–50.
2. K. Manukyan, A. Cross, S. Roslyakov, S. Rouvimov, A. Rogachev, E.E. Wolf, A. Mukasyan, Solution combustion synthesis of nano-crystalline metallic materials: mechanistic studies, *J. Phys. Chem. C*, 2013, vol. 117, no. 46, pp. 24417–24427.
3. G.V. Trusov, A.B. Tarasov, D.O. Moskovskikh, A.S. Rogachev, A.S. Mukasyan, High porous cellular materials by spray solution combustion synthesis and spark plasma sintering, *J. Alloys Compd.*, 2019, vol. 779, pp. 557–565.

## APPLICATION OF RESISTOMETRY AND IMPEDANCE SPECTROSCOPY METHODS TO STUDY MIXING OF POWDER MIXTURES FOR SHS

**M. V. Tsarev<sup>\*a</sup>, V. V. Mokrushin<sup>a</sup>, K. V. Korshunov<sup>a</sup>, A. M. Shapovalov<sup>a</sup>,  
A. Yu. Postnikov<sup>a</sup>, I. A. Tsareva<sup>a</sup>, O. Yu. Zabrodina<sup>a</sup>, D. G. Ivanov<sup>a</sup>,  
Ye. V. Zabavin<sup>a</sup>, and A. Ye. Kanunov<sup>a</sup>**

<sup>a</sup>Russian Federal Nuclear Center - All-Russian Research Institute for Experimental Physics (RFNC-VNIIEF), Sarov, 607188 Russia

\*e-mail: tsarev@dep19.vniief.ru

DOI: 10.24411/9999-0014A-2019-10178

This paper presents the investigation results of the processes occurring when mixing the two-component model powder mixture: fuel-oxidizer in a ball-mill. The fuel making part of composition for self-propagating high-temperature synthesis (SHS) is a metal powder with a particle size  $< 10 \mu\text{m}$ , which conducts well the electric current. The oxidizer manifests dielectric properties and its particles are mostly nano-sized. The treatment of the initial components was fulfilled in a ball-mill in inert medium during 50 h with sampling at different mixing stages. The selected samples were investigated by resistometry [1–6] and impedance spectroscopy [6–9] methods for powder materials that enable obtaining data about the structure of compositions for SHS and their components particle surface state.

As shown earlier in works [5, 6] using resistometry the mixing the components of the studied model mixture in a ball-mill provokes first increase and then decrease of its active resistance measured at a constant current. This is due to the fact that at the initial mixing stages the smaller oxidizer particles «envelop» the larger fuel particles because of redistribution of components against each other. As a result, the mixture resistance increases due to «shielding» of the contacts between the metal particles with the layers of nonconducting oxidizer. With further mixing the solid particles of the oxidizer begin to be «pressed» into the surface of the more plastic fuel particles under impact of the balls, therefore the contact surface between the metal particles begins to increase, and the mixture resistance decreases. Besides another factor also contributing to the resistance decrease is accumulation of mechanochemical reactions products with metallic conductivity on the fuel particles' surface.

In the present work the composition for SHS under study was analyzed with impedance spectroscopy method using measuring techniques described in [6, 8] for better understanding the processes occurring during mixing. By analogy with resistometry [1–6], the composition impedance ( $Z$ ) was measured at an alternating current (AC) in the process of the powder sample stage compression, and the relationship of complex resistance on AC frequency ( $\omega$ ) was obtained at each fixed relative density ( $\vartheta$ ) value. The powder stage compression was fulfilled using a specially developed contact device [9] that is part of the automated complex created on the basis of BDS40 dielectric spectrometer. Each sample probe measuring result was a set of hodographs of impedance obtained at different compression densities, each of which is a dependence of the impedance reactive component ( $Z''$ ) on its active component ( $Z'$ ).

According to the theoretical simulation results fulfilled in the work [7], the hodograph of impedance of the mixture under study should be a semicircle with its center located on the abscissa axis. With increase of the sample density the diameter of semicircle should decrease and lead to shifting of the right (low-frequency) hodograph component to the left. The segment cut off on this axis by the left (high-frequency) hodograph component should be constant for all density values. The obtained data showed that exactly this type of hodograph is

typical for the mixture under study with mixing of components up to 15 h (see Figs. 1a–1c). At the same time with further mixing the type of hodographs changes fundamentally, and they are straight almost parallel to the ordinate axis, which «go» to the positive value domain  $Z''$  with increase in the AC frequency (see Fig. 1d).

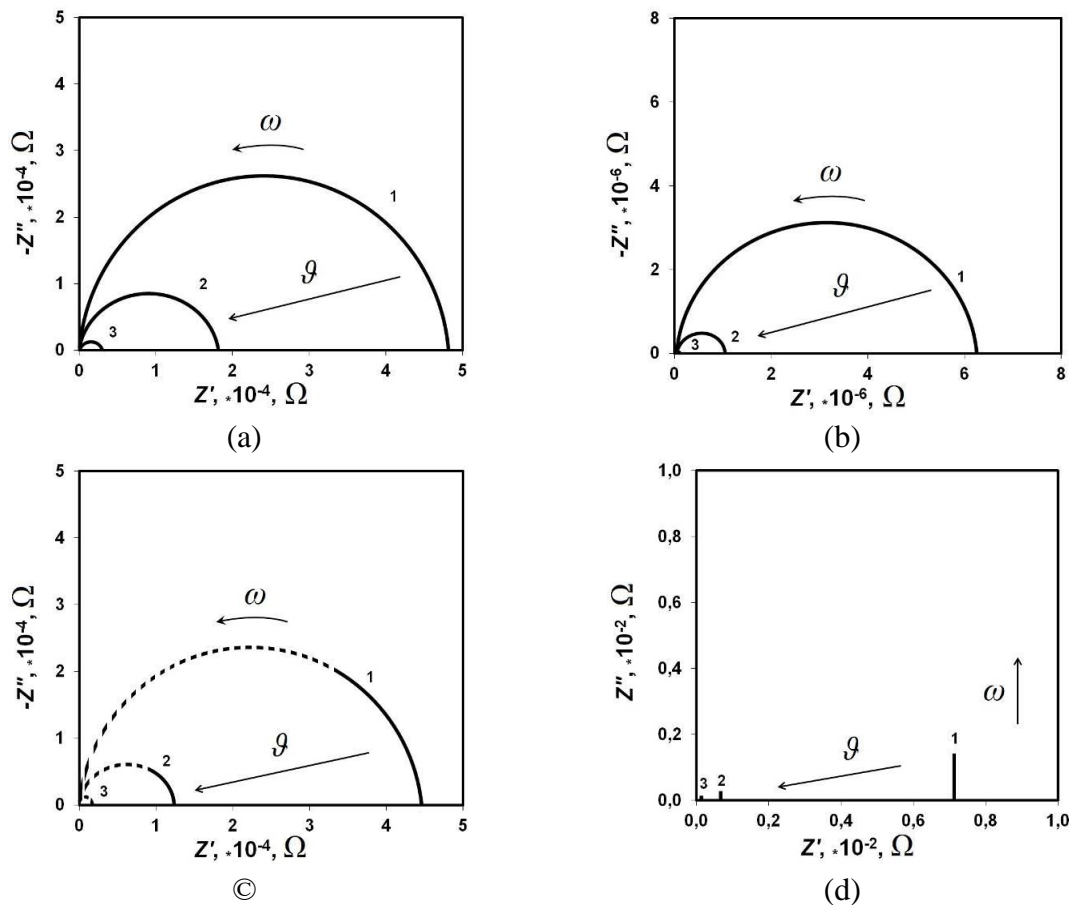


Fig. 1. Experimental hodographs of impedance of powder mixture for SHS at different density ( $\rho$ ) values: 1 0.50 rel. units; 2 0.55 rel. units; 3 0.60 rel. units; mixing time: 0.5 h (a); 3 h (b); 15 h, dotted line – extrapolation (c); 50 h (d).

It is known that the first hodograph type (Figs. 1a–1c) corresponds to the mixture conductive structure where the contact between the fuel particles is realized through the oxidizer «layers» («globular» structure [3, 7, 10]). The second type of hodograph (Fig. 1d) corresponds to the conductive structure characterized by the presence of percolation cluster permeating the entire volume of the sample that is formed by the contacting fuel particles and the mechanochemical reactions conductive products located on their surface («frame» structure [3, 7, 10]).

The equivalent electric circuits given in Fig. 2 [10] were used to describe the hodographs obtained in this work. In case of «globular» structure (Fig. 2a) the equivalent circuit included two active resistances ( $R_1$ ;  $R_2$ ) and capacity ( $C$ ).  $R_1$  corresponds to the fuel particle resistance;  $R_2$  corresponds to the oxidizer «layers» resistance, and  $C$  characterizes capacity generated between adjacent fuel particles, which surface plays the role of capacitor plates [10]. In case of «frame» structure (Fig. 2b) the equivalent circuit included an active resistance ( $R_1$ ) and inductance ( $L$ ) characterizing the conductive properties of the percolation cluster [10]. The measurement data processing enabled obtaining numerical values of parameters of equivalent circuits given in Fig. 2 and evaluating contribution of  $R_1$  and  $R_2$  to the complex resistance of the mixture (see Fig. 3).

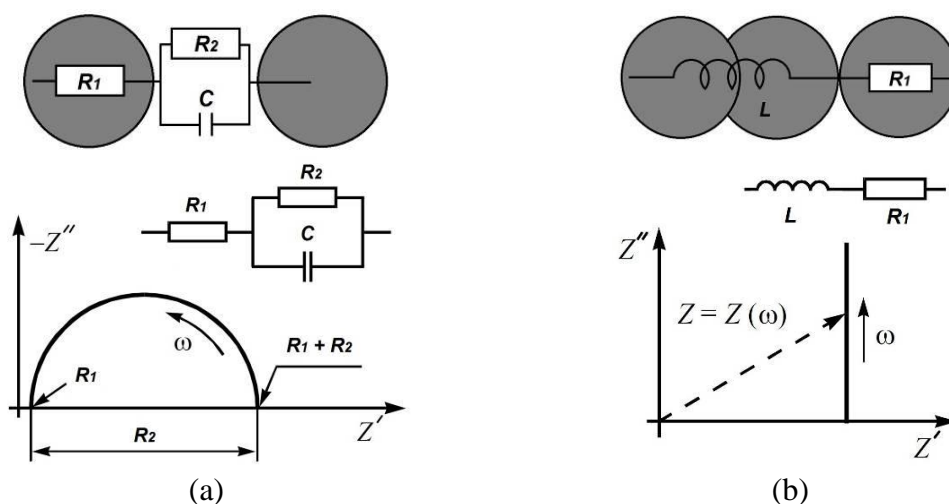


Fig. 2. Impedance hodographs and equivalent electric circuits of «globular» (a) and «frame» (b) structures.

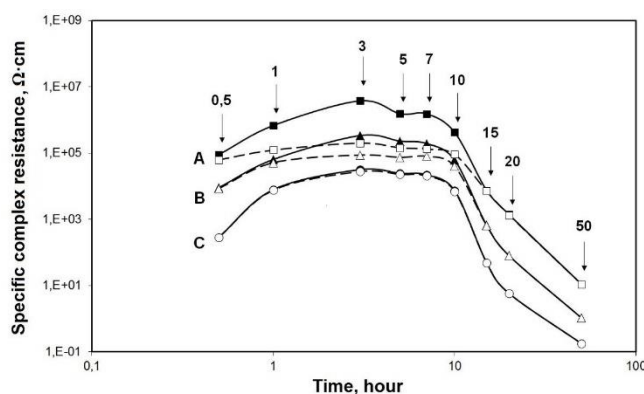


Fig. 3. Dependence of specific complex resistance of powder mixture for SHS on the logarithm of the mixing time at different density ( $\rho$ ) values (A 0.50 rel. units; B 0.55 rel. units; C 0.60 rel. units) and different AC frequencies (dark signs – 10 Hz; light signs – 100 kHz); mixing time (h) is indicated above arrows.

Figure 3 shows the complex resistance values of mixture pass through maximum during mixing that is in a good agreement with the data obtained using resistometry method [5, 6]. It follows also from Fig. 3 that at the initial stage of component mixing this parameter is almost independent of the flowing current frequency. This indicates that its value is generally determined by the resistance of the metal contacts between the fuel particles that come in contact in the entire powder sample volume. The resistance of the oxidizer «layers» makes a significant contribution to the mixture specific complex resistance value when mixing from 1 up to 10 h. The «layers» isolate the fuel particles from each other and determine the presence of capacity element in the scheme in Fig. 2a. A and B curves in Fig. 3 show the difference between the specific complex resistance measured at 10 Hz and the one measured at 100 kHz becomes the greatest in case of 3-h mixing. This indicates that the maximum degree of the metal particle surface shielding with the fuel «layers» is achieved. The specific complex resistance ceases again depending on the current frequency when mixing more than 15 h. At this stage its value is determined by the resistance of the contacts generated between the adjacent fuel particles through the conducting «films» consisting of the mechanochemical reaction products, which provoke the appearance of inductance element in the scheme in Fig. 2b. The amount of these products increases with ball-mill processing time, and for long mixing times (~ 50 h) the mixture specific complex resistance reaches the values typical for compact metals.

Thus, the present work shows that the dependence of the specific complex resistance of the studied two-component mixture for SHS on the ball-mill mixing time passes through the maximum. The impedance spectroscopy method enabled setting component mixing time intervals, at which a significant contribution to the mixture complex resistance value is consistently made by: resistance of metal contacts between the fuel particles, resistance of the oxidizer non-conducting «layers» and resistance of mechanochemical reaction products accumulated on the fuel particles' surface. The obtained data indicate that in the mixture under study the transition from the «globular» to the «frame» conductive structure occurs after ~ 15-h mixing.

The authors are grateful to A.A. Potanin, P.G. Berezhko, I.V. Dudorov, A.A. Potehkin, D.V. Chulkov, and M.V. Pospelov for their support and interest in this work.

1. V.V. Mokrushin, Generalized conductivity of powders under load: Patterns of behavior, *Dokl. Akad. Nauk*, 1997, vol. 357, no. 3, pp. 332–334 [Dokl. Phys. (Engl. Transl.), 1997, vol. 42, no. 11, pp. 586–589].
2. A.N. Emel'yanov, V.M. Shkiro, A.S. Rogachev, V.I. Rubtsov, Electric and thermal conductivity of titanium-based powder mixtures for SHS, *Izv. Vyssh. Uchebn. Zaved., Tsvet. Metall.*, 2002, no. 2, pp. 67–70.
3. N.A. Kochetov, A.S. Rogachev, A.N. Emel'yanov, E.V. Illarionova, V.M. Shkiro, Microstructure of heterogeneous mixtures for gasless combustion, *Fiz. Goreniya Vzryva*, 2004, vol. 40, no. 5, pp. 74–80 [Combust. Explos. Shock Waves (Engl. Transl.), 2004, vol. 40, no. 5, pp. 564–570].
4. M.V. Tsarev, V.V. Mokrushin, Effect of granulometric properties of metallic scandium powder on its conductivity, *Technical Physics*, 2007, vol. 52, no. 3, pp. 369–375.
5. V.V. Mokrushin, M.V. Tsarev, Resistivity measurements for characterization of SHS powders, *Int. J. Self-Propag. High-Temp. Synth.*, 2007, vol. 16, no. 2, pp. 96–104.
6. V.V. Mokrushin, M.V. Tsarev, K.V. Korshunov, A.Yu. Postnikov, I.A. Tsareva, Resistometry and impedance spectroscopy for characterization of powders used in SHS reactions. *Int. J. Self-Propag. High-Temp. Synth.*, 2014, vol. 23, no. 1, pp. 26–35.
7. V.V. Mokrushin, M.V. Tsarev, Ye.V. Zabavin, Complex conductivity of matrix two-phase systems in the presence of contact areas between inclusions, Proceedings of RFNC-VNIIEF, Sarov: RFNC-VNIIEF IPK, 2014, no. 19, part 1, pp. 284–297.
8. K.V. Korshunov, M.V. Tsarev, V.V. Mokrushin, A.M. Shapovalov, E.V. Zabavin, Application of impedance spectroscopy to study oxidized powders of titanium hydride, *J. Alloys Compd.*, 2015, vol. 645, pp. 140–143.
9. A.M. Shapvalov, V.V. Mokrushin, K.V. Korshunov, M.V. Tsarev, I.V. Dudorov, V.V. Gorelov, Ye.V. Zabavin, Contact device to determine electrical resistance of powder material during its compression, RF Patent 2546994, priority of 06.11.2013; published on 10.04.2015, Bull. № 10.
10. N.A. Poklonsky, N.I. Gorbachuk, Foundations of composite impedance spectroscopy, Minsk: BSU, 2005.

## Ni–Cr–Al–Mg CATALYSTS PREPARED BY SOLUTION COMBUSTION SYNTHESIS FOR CATALYTIC REFORMING OF METHANE INTO SYNTHESIS GAS

S. A. Tungatarova<sup>\*a,b</sup>, G. Xanthopoulou<sup>c</sup>, G. N. Kaumenova<sup>a,b</sup>,  
and T. S. Baizhumanova<sup>a,b</sup>

<sup>a</sup>JSC D.V. Sokolsky Institute of Fuel, Catalysis and Electrochemistry,  
Almaty, 050010 Kazakhstan

<sup>b</sup>Al-Farabi Kazakh National University, Almaty, 050040 Kazakhstan

<sup>c</sup>Institute of Nanoscience and Nanotechnology, NCSR Demokritos, Athens, 15341 Greece

\*e-mail: tungatarova58@mail.ru

DOI: 10.24411/9999-0014A-2019-10179

Preparation of catalysts by solution combustion synthesis is one of the new directions in catalysis. Solution combustion is based on an exothermic redox reaction between soluble salts with organic fuel in an aqueous solution. The effectiveness of this method lies in the simplicity and ease of preparation of catalysts, short reaction time and relatively low cost, and hence the efficiency of the process. The solution combustion method is used in various industries, especially for the preparation of ceramic materials, catalysts, pigments and alloys [1].

Methane is a major component of natural gas. In the future, the conversion of methane to hydrogen and synthesis gas (CO and H<sub>2</sub>) using heterogeneous catalysts may play an important role in the production of liquid fuels and chemicals. It is known that catalysts based on Ni–Al–Mg exhibit very high activity and selectivity in the partial oxidation reaction [2].

Metal nitrates as the oxidizing agents and glycine as the fuel were used for synthesis of the Ni–Cr–Al–Mg catalysts. The catalysts were prepared by solution combustion synthesis. Nitrate to fuel ratio equal to 1.10 ml of distilled water heated to 80°C was added to the initial mixture of active ingredients for the preparation of catalysts. The resulting mixture was mixed until homogeneous state. The catalysts were placed in a muffle furnace, which was previously heated to 500°C. Figure 1 shows the temperature–time profile of the volumetric mode of combustion for the Ni–Cr–Al–Mg system.

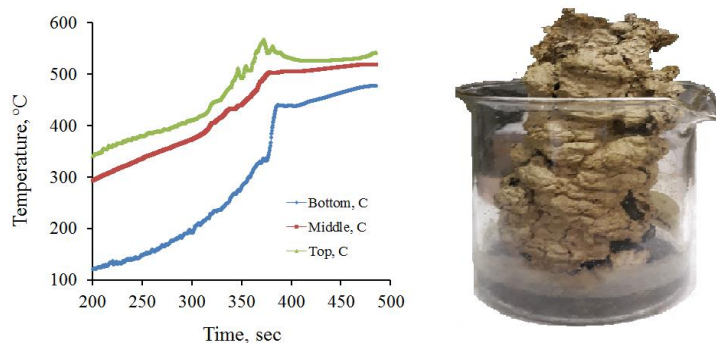


Fig. 1. Temperature–time profile of the volumetric mode of combustion of the Ni–Cr–Al–Mg system.

From the figure it can be seen that evaporation of water followed by gel formation occurred up to 300 s. The combustion temperatures in the lower, middle, and upper parts differed in temperature. At about 375 s, the temperature rose quickly and gas formation was observed. After completion of the preparation process, the beaker with the obtained catalyst was removed



from the muffle furnace and cooled at room temperature. The content of nickel and chromium in the catalysts varied from 5 to 35%.

Figure 2 shows the electron microscopic images of the 25% Ni(NO<sub>3</sub>)<sub>2</sub> + 5% Cr(NO<sub>3</sub>)<sub>3</sub> + 10% Al(NO<sub>3</sub>)<sub>3</sub> + 10% Mg(NO<sub>3</sub>)<sub>2</sub> + 50% glycine catalysts.

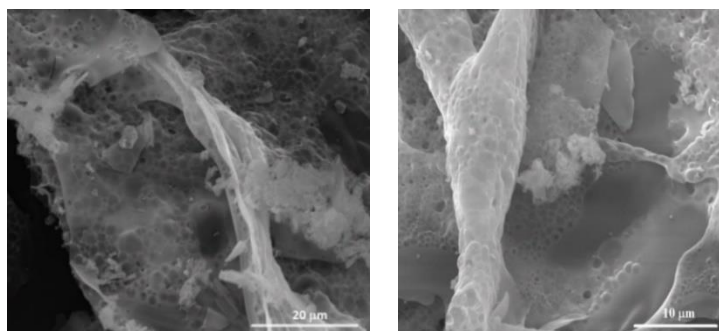


Fig. 2. SEM images of the 25% Ni(NO<sub>3</sub>)<sub>2</sub> + 5% Cr(NO<sub>3</sub>)<sub>3</sub> + 10% Al(NO<sub>3</sub>)<sub>3</sub> + 10% Mg(NO<sub>3</sub>)<sub>2</sub> + 50% glycine catalyst.

The figure shows that the catalyst is nanoscale. Small bubbles are visible at a magnification, and nanopores are formed during combustion. The activity of catalysts was investigated on a flow catalytic installation with a tubular quartz reactor. In the course of experiment, the influence of space velocity on yield of products, as well as the ratio of initial gases to process parameters, was determined. The composition of the initial reaction mixture: 34% CH<sub>4</sub>:17% O<sub>2</sub>:49% Ar. It has been shown that the Ni–Cr–Al–Mg catalysts with different contents of Ni and Cr are active in the partial oxidation of methane. Figure 3a shows the effect of space velocity on methane conversion in the temperature range from 600 to 900°C. The highest results (methane conversion up to 98% and CH<sub>4</sub>/O<sub>2</sub> ratio = 2) were obtained at GHSV = 2500 h<sup>-1</sup>. Figure 3b shows the effect of nickel content in catalyst composition on methane conversion in the temperature range from 600 to 900°C at GHSV = 2500 h<sup>-1</sup>. The best catalytic characteristics were observed for the 25% Ni(NO<sub>3</sub>)<sub>2</sub> + 5% Cr(NO<sub>3</sub>)<sub>3</sub> + 10% Al(NO<sub>3</sub>)<sub>3</sub> + 10% Mg(NO<sub>3</sub>)<sub>2</sub> + 50% glycine sample on which high CH<sub>4</sub> conversion (up to 98%) values were obtained.

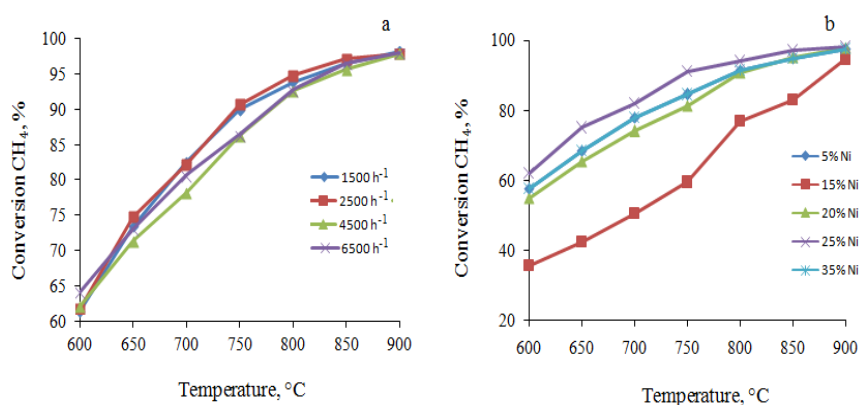


Fig. 3. Methane conversion on the 25% Ni(NO<sub>3</sub>)<sub>2</sub> + 5% Cr(NO<sub>3</sub>)<sub>3</sub> + 10% Al(NO<sub>3</sub>)<sub>3</sub> + 10% Mg(NO<sub>3</sub>)<sub>2</sub> + 50% glycine catalysts at various space velocities (a) and influence the composition of catalyst on conversion of methane at 600–900°C.

High selectivity for H<sub>2</sub> (up to 92.4%) and CO (up to 99.5%) (Fig. 4) was achieved under optimal conditions for the conversion of methane to synthesis gas on the 25% Ni(NO<sub>3</sub>)<sub>2</sub> + 5% Cr(NO<sub>3</sub>)<sub>3</sub> + 10% Al(NO<sub>3</sub>)<sub>3</sub> + 10% Mg(NO<sub>3</sub>)<sub>2</sub> + 50% glycine catalyst, and the ratio of reaction products varied in the range of H<sub>2</sub>/CO = 1.49÷1.87 at 600–900°C.

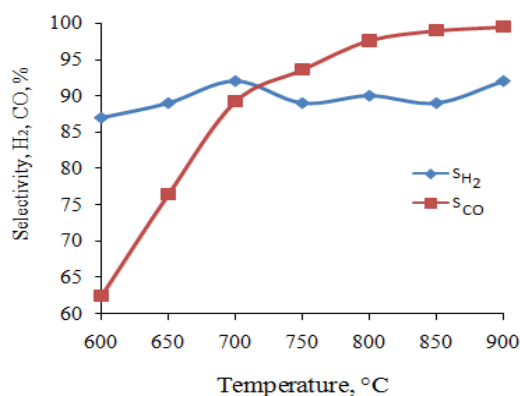


Fig. 4. Effect of process temperature on hydrogen and CO selectivity on the 25% Ni(NO<sub>3</sub>)<sub>2</sub> + 5% Cr(NO<sub>3</sub>)<sub>3</sub> + 10% Al(NO<sub>3</sub>)<sub>3</sub> + 10% Mg(NO<sub>3</sub>)<sub>2</sub> + 50% glycine catalyst.

The study of catalyst on a transmission electron microscope showed that semitransparent plates with small dense particles of 8–10 nm in size are present in the original samples recorded at low magnification. The microdiffraction pattern is represented by reflexes arranged in rings and can be attributed to a mixture of phases of NiO (JCPDS, 4-825), MgO (JCPDS, 4-829), MgNiO<sub>2</sub> (JCPDS, 24-712), CrO (JCPDS, 8-254). Dense aggregates composed of particles ranging in size from 1 to 5 nm are present on spent catalysts recorded at low magnification. In addition, elastic carbon nanotubes with a diameter from 1 to 2.5 nm are present in the samples.

The work was supported by the Ministry of Education and Science of the Republic of Kazakhstan (AP05132348).

1. S. Specchia, G. Ercolino, S. Karimi, C. Italiano, A. Vita, Solution combustion synthesis for preparation of structured catalysts: A mini-review on process intensification for energy applications and pollution control, *Int. J. Self-Propag. High-Temp. Synth.*, 2017, vol. 26, no. 3, pp. 166–186.
2. H. Messaoudi, S. Thomas, A. Djaidja, S. Slyemi, R. Chebout, S. Barama, F. Benaliouche, Hydrogen production over partial oxidation of methane using Ni Mg Al spinel catalysts: A kinetic approach, *C. R. Chim.*, 2017, vol. 20, no. 7, pp. 738–746.

## FABRICATION OF ALUMINUM-CERAMIC SKELETON COMPOSITES BASED ON TITANIUM ALUMINIDE CARBIDE USING SHS PROCESS

E. R. Umerov<sup>a</sup>, A. P. Amosov<sup>\*a</sup>, E. I. Latukhin<sup>a</sup>, P. E. Kichaev<sup>a</sup>, and V. A. Novikov<sup>a</sup>

<sup>a</sup>Samara State Technical University, Samara, 443100 Russia

\*e-mail: egundor@yandex.ru

DOI: 10.24411/9999-0014A-2019-10180

As you know, the use of ceramic materials is limited by their brittleness. A new type of ceramic materials, so-called MAX-phases, occupies an intermediate position between metals and traditional ceramic materials, and the MAX-phases are less brittle compared to traditional ceramic materials [1]. Composite materials consisting of MAX-phases and metals will be even less brittle and able to provide increased strength, so the production of ceramic-metal composites (cermets) based on MAX-phase skeletons is an urgent task [2–6]. Studies of the possibility of obtaining and properties of the composites based on such MAX-phases as titanium silicide carbide ( $\text{Ti}_3\text{SiC}_2$ ) and titanium aluminide carbide ( $\text{Ti}_3\text{AlC}_2$ ) are the most numerous. However, the methods of powder metallurgy for producing such composites (pressing followed by sintering, hot pressing and infiltration) are complex and energy-intensive, so it is very attractive to use the method of self-propagating high-temperature synthesis (SHS) with simple technological equipment and low energy consumption, which can contribute to the creation of economically justified production of skeleton ceramic-metal composites based on MAX phases.

The application of the SHS process by burning in air was investigated for a single-stage fabrication of Cu– $\text{Ti}_3\text{SiC}_2$  ceramic-metal composite [3]. The location of a briquette of a metal powder of copper between two adjacent charge briquettes for the synthesis of  $\text{Ti}_3\text{SiC}_2$  with subsequent burning of this charge briquettes made it possible to synthesize porous skeletons of MAX-phase  $\text{Ti}_3\text{SiC}_2$ , and simultaneously to use a large heat effect of SHS to melt the copper and infiltrate these porous skeletons of  $\text{Ti}_3\text{SiC}_2$  by the Cu melt. However, as a result of the burning of these briquettes, a relatively small amount of copper was melted, which was not enough to completely fill the porous skeletons of the MAX-phase  $\text{Ti}_3\text{SiC}_2$  formed on the site of the charge briquettes. Also, it was found that the presence of the Cu melt prevents the formation of MAX-phase of titanium silicide carbide, reducing its amount or completely destroying it due to deintercalation silicon from  $\text{Ti}_3\text{SiC}_2$  and dissolving it in the molten copper. It was necessary to carry out separate ignition of charge briquettes with ignition delay of the second briquette after ignition of the first briquette, so that the infiltration by the molten metal began later and less prevented the formation of the MAX-phase  $\text{Ti}_3\text{SiC}_2$  from the initial reagents.

To obtain aluminum–ceramic composite, it is advisable to use a MAX-phases of titanium aluminide carbide  $\text{Ti}_3\text{AlC}_2$  and  $\text{Ti}_2\text{AlC}$  instead of MAX-phase of titanium silicide carbide  $\text{Ti}_3\text{SiC}_2$ , in order to avoid the destruction of MAX-phase at the expense of deintercalation of Al atoms from the MAX-phase. In the study of the reaction activity between the copper matrix and  $\text{Ti}_3\text{AlC}_2$ , it is shown that at temperatures above 950°C the rate of aluminum deintercalation from  $\text{Ti}_3\text{AlC}_2$  into copper increases sharply, followed by partial filling of the liberated layers of Al in  $\text{Ti}_3\text{AlC}_2$  with copper atoms [4]. Obviously, the deintercalation of aluminum atoms from the MAX-phase  $\text{Ti}_3\text{AlC}_2$  into metallic aluminum will be significantly less than into metallic copper or absent altogether. The paper [5] considered a single-stage technology for the fabrication of aluminum-ceramic skeleton composites by combining the processes of SHS of a porous skeleton of MAX-phase  $\text{Ti}_2\text{AlC}$  and its infiltration under pressure by aluminum melt (SHS-pressing method). The influence of infiltration pressure on the distribution of aluminum

over the MAX-phase skeleton, on the mechanism of formation of the composite composition depending on the infiltration pressure was studied. In this paper we investigate the possibility of fabrication of aluminum-ceramic composites based on titanium aluminide carbide with the use of SHS process of porous skeleton MAX-phases  $Ti_3AlC_2$  and  $Ti_2AlC$  with subsequent thermocapillary infiltration them with aluminum melt without application of pressure. that greatly simplifies the technology of producing such composites.

Synthesis of porous cylindrical briquettes of MAX-phases with a diameter of 23 mm and a height of about 10 mm was carried out from charge briquettes, which were the mixtures of powder materials with a ratio of components:  $2Ti + 2Al + 1C$  for  $Ti_2AlC$  and  $3Ti + 2Al + 2C$  for  $Ti_3AlC_2$ . (To ensure the synthesis of the maximum amount of the MAX-phase of titanium aluminide carbide. it is necessary to feed a double amount of aluminum powder into the SHS charge [6].) Taking into account the stages of formation of MAX-phase of titanium aluminide carbide [7], a pause of 7–9 s was maintained upon completion of the combustion of charge briquettes in the air ensuring the completion of the process of formation of the MAX-phase in the sample, after which the hot sample was immersed in the aluminum melt with a temperature of  $850^\circ C$ . (The experiment showed that exposure of more than 8–9 s in air leads to overcooling of the sample and complication of infiltration. Supercooling dramatically worsens the wettability of the MAX-phase by aluminum melt, which reduces not only the completeness of the impregnation, but also the strength of the composite.) The relatively high heat capacity of the aluminum melt leads to rapid cooling of the submerged porous sample to a melt temperature of  $850^\circ C$ , when the MAX phase is no longer formed, but begins to disintegrate due to interaction with the liquid aluminum. Therefore, after 10–15 s, the impregnated sample was removed from the melt and continued to cool in the air.

The microstructure and distribution of the chemical elements of  $Ti_3AlC_2$ -Al composite sample are shown in Figs. 1 and 2. Multidirectional MAX-phase plates with an average length of 10–20  $\mu m$  are clearly distinguishable in Fig. 1a. It follows from Figs. 1b and 2 that the dark relatively homogeneous regions are aluminum and its intermetallic, since the darker and homogeneous right side is saturated with aluminum, and the left, lighter and layered, corresponds approximately to the ratio of elements in the MAX-phase  $Ti_3AlC_2$ . The interfacial layer with a size of 1  $\mu m$  or more has not been detected, which indicates a low activity of the chemical interaction between  $Ti_3AlC_2$  and Al. Visually, other phases (carbides, oxides) are practically not observed, which indicates a successfully fabricated composite with a low content of impurities.

The samples of composites were machined to give a disc shape with parallel planes. which allows to carry out tests on the compression strength on a technical complex Instron Bluehill 3. Graphs of the compression load with a compression rate of 2 mm/min on the absolute deformation of the samples are shown in Fig. 3.

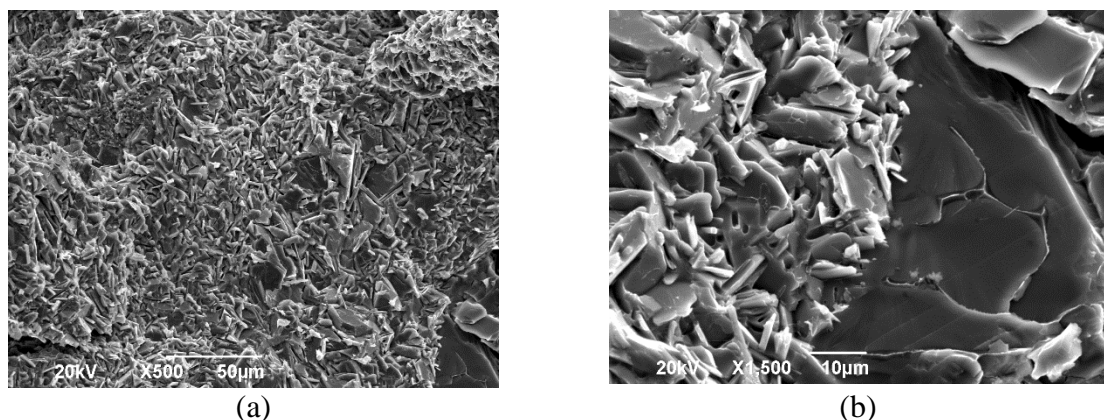


Fig. 1. Characteristic microstructure of fracture surface of  $Ti_3AlC_2$ -Al composite.

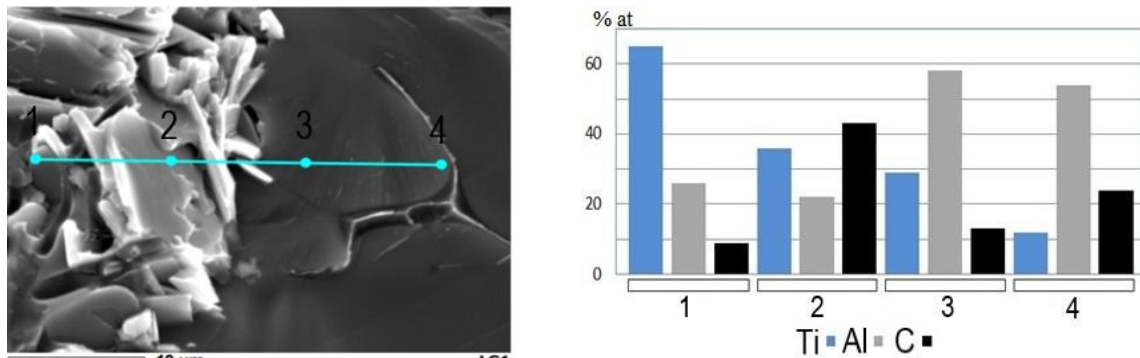


Fig. 2. Distribution of chemical elements by points on line of  $Ti_3AlC_2-Al$  sample.

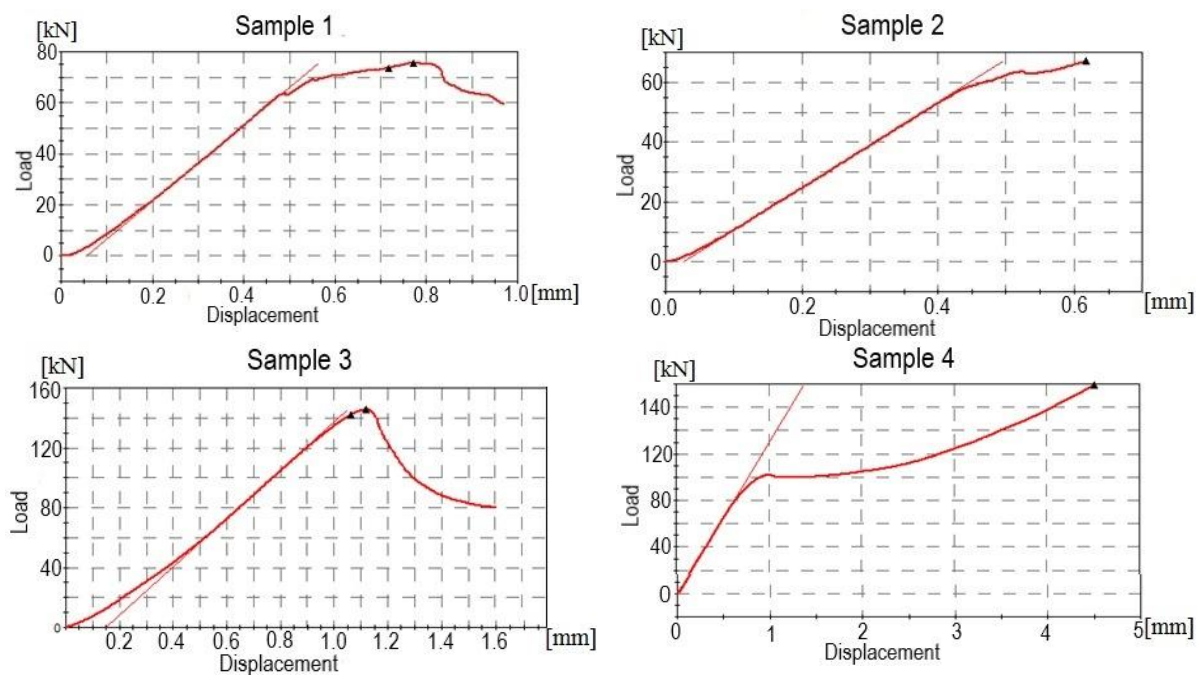


Fig. 3. The loading curves of the composite samples: 1  $Ti_2AlC-Al$ , a delay time of 7 s; 2 and 3  $Ti_3AlC_2-Al$ , 8.5 s; 4  $Ti_3AlC_2-Al$ , 8 s.

The delay time of the sample in the caption under Fig. 3 indicates the time from the end of the combustion of the charge briquette in air to immersion into the aluminum melt in the fabrication of the sample. Samples with corresponding numbers after the compression test are shown in Fig. 4.

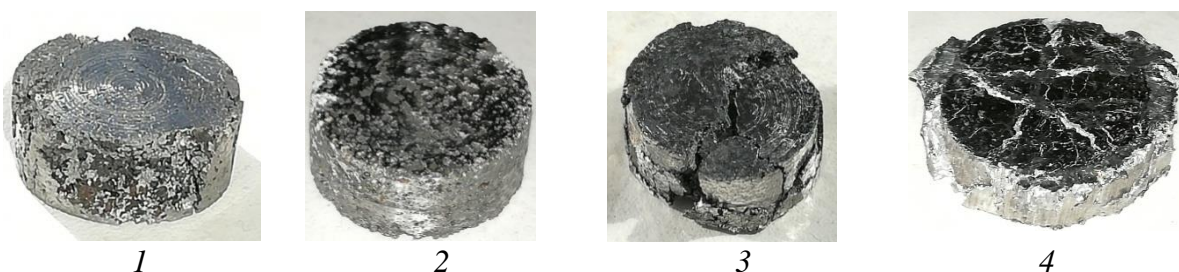


Fig. 4. Appearance of composite samples after compression tests.

The photos of samples 1 and 2 show that they are porous and have dark areas, non-impregnated with aluminum. Porosity is not visible on samples 3 and 4, these samples are completely impregnated. The results of the study of the fracture surface of sample 3 were presented in Figs. 1 and 2.

Processing of the compression test results shown in Fig. 3, shows that samples 1 and 2 have the lowest values of compression strength (219 and 180 MPa, respectively) and the lowest values of deformation before failure (6.2 and 5.8%), due to the presence of residual porosity in these samples. Samples 3 and 4 have significantly higher values of compression strength (457 and 280 MPa) and deformation before failure (11.2 and 10.0%) due to a more complete impregnation with aluminum. The type of load-displacement curves indicates that the deviation from the linear portion of the elastic deformation is associated with the destruction of the ceramic skeleton in the composite. This destruction can have both the character of brittle failure with the separation of the composite into parts with a sharp drop in the load resistance (sample 3) and ductile failure with an increase in the compression load resistance due to the metal component of the composite (sample 4). Therefore, the completeness of the impregnation with aluminum plays a crucial role in ensuring the strength of the skeleton aluminum-ceramic composite on the basis of titanium aluminide carbide, fabricated by the method of capillary impregnation.

Thus, the samples of aluminum-ceramic composites  $\text{Ti}_3\text{AlC}_2\text{-Al}$  and  $\text{Ti}_2\text{AlC-Al}$  are fabricated by the method of capillary impregnation when immersed in aluminum melt of the hot porous skeletons of MAX-phases of titanium aluminide carbide  $\text{Ti}_3\text{AlC}_2$  and  $\text{Ti}_2\text{AlC}$  synthesized just before this by the SHS method in combustion of powder charges in the air. It is shown that the impregnation of the skeleton of the MAX-phases of these samples with aluminum melt can be complete even without the application of excess pressure, which greatly simplifies the technology of manufacturing skeleton aluminum-ceramic composites based on titanium aluminide carbide in the application of the SHS process.

1. M.W. Barsoum, MAX Phases. Properties of Machinable Ternary Carbides and Nitrides, Weinheim: Wiley-VCH, 2013.
2. S.A. Oglezneva, M.N. Kachenjukm, N.D. Ogleznev, Investigation into the structure formation and properties of materials in the copper-titanium disilicide system, *Russ. J. Non-Ferr. Met.*, 2017, vol. 58, no. 6, pp. 649–55.
3. A.P. Amosov, E.I. Latukhin, A.M. Ryabov, E.R. Umerov, V.A. Novikov, Application of SHS process for fabrication of copper-titanium silicon carbide composite ( $\text{Cu-Ti}_3\text{SiC}_2$ ), *J. Phys.: Conf. Ser.*, 2018, vol. 1115, is. 4, article no. 042003.
4. J. Zhang, J.Y. Wang, Y.C. Zhou, Structure stability of  $\text{Ti}_3\text{AlC}_2$  in Cu and microstructure evolution of  $\text{Cu-Ti}_3\text{AlC}_2$  composites, *Acta Mater.*, 2007, vol. 55, pp. 4381–4390.
5. A.F. Fedotov, A.P. Amosov, E.I. Latukhin, V.A. Novikov, Fabrication of aluminum-ceramic skeleton composites based on the  $\text{Ti}_2\text{AlC}$  MAX phase by SHS compaction, *Russ. J. Non-Ferr. Met.*, 2016, vol. 57, no. 1, pp. 33–40.
6. A.F. Fedotov, A.P. Amosov, E.I. Latukhin, A.A. Ermoshkin, D.M. Davydov, The influence of gasifying additives on phase composition of combustion products at self-propagating high-temperature synthesis of MAX-phases in  $\text{Ti-C-Al}$  system, *Izvestia of Samara Scientific Center of the Russian Academy of Sciences*, 2014, vol. 16, no. 6, pp. 50–55.
7. P.M. Bazhin, D.Yu. Kovalev, M.A. Luginina, Combustion of  $\text{Ti-Al-C}$  compacts in air and helium: A TRXRD study, *Int. J. Self-Propag. High-Temp. Synth.*, 2016, vol. 25, no. 1, pp. 30–34.

## MAGNETIC PROPERTIES OF POWDER Fe–30Cr–(8–16)Co ALLOYS OBTAINED BY LOW-TEMPERATURE SINTERING

A. S. Ustyukhin<sup>a</sup>, V. A. Zelenskii<sup>a</sup>, I. M. Milyaev<sup>a</sup>, M. I. Alymov<sup>b</sup>, and S. F. Zabelin<sup>c</sup>

<sup>a</sup>Baikov Institute of Metallurgy and Materials Science, Russian Academy of Sciences, Moscow, 119991 Russia

<sup>b</sup>Merzhanov Institute of Structural Macrokinetics and Materials Science, Russian Academy of Sciences, Chernogolovka, 142432 Russia

<sup>c</sup>Transbaikal State University, Chita, 672039 Russia

\*e-mail: fcbneo@yandex.ru

DOI: 10.24411/9999-0014A-2019-10181

In conventional production of magnetic alloys in the Fe–Cr–Co system by powder metallurgy methods, the sintering temperature of compacts is high (about 1400°C) [1–3]. It is well known that magnets of the Fe–Cr–Co system lose strongly in magnetic hysteresis properties if the nonmagnetic  $\gamma$ -phase is present in their structure. According to Fe–Cr–Co phase diagrams the presence of the  $\gamma$ -phase in material depends on Cr and Co content and also sintering temperature. Sintered at a conventional temperature of the order of 1400°C, the powder low-cobalt and high-cobalt magnets do not have the  $\gamma$ -phase in their composition. In the previous work [4], it was shown that for magnetic materials with a low and moderate cobalt content (8–16 wt %), the use of a lower sintering temperature (down to 1150°C) is possible, producing dense compacts with practically no nonmagnetic  $\gamma$ -phase precipitation after quenching.

In present work, sintering of Fe–30Cr–8Co, Fe–30Cr–12Co, and Fe–30Cr–16Co powder alloys was carried out at 1100°C. Magnetic hysteresis properties of materials obtained in this way are given. The green compacts had a relative density of ~75–80%, while with increasing cobalt content, the density of the compacts decreased somewhat, probably because of the low bulk density of the cobalt powder. The results of measurements of the density of sintered specimens are shown in Table 1. It is seen that all 3 alloys have a good density for this low-temperature sintering conditions. Specimens of the Fe–30Cr–8Co, Fe–30Cr–12Co, and Fe–30Cr–16Co alloys were heat-treated under several conditions and their magnetic properties were measured. A magnetic field in the course of thermomagnetic treatment was applied along the easy magnetization axis coinciding with the axis of a cylindrical specimen. The results of measurements of the magnetic hysteresis properties of sintered specimens are shown in Table 2.

Table 1. Density of sintered Fe–Cr–Co samples.

| Alloy        | Sintering temperature, °C | Relative density, % |
|--------------|---------------------------|---------------------|
| Fe–30Cr–8Co  | 1100                      | 94.5                |
| Fe–30Cr–12Co |                           | 93.5                |
| Fe–30Cr–16Co |                           | 93.5                |

Table 2. Magnetic hysteresis properties of sintered Fe–Cr–Co samples.

| Alloy        | Sintering temperature, °C | $B_r$ , T | $H_{cB}$ , kA/m | $(BH)_{max}$ , kJ/m <sup>3</sup> |
|--------------|---------------------------|-----------|-----------------|----------------------------------|
| Fe–30Cr–8Co  | 1100                      | 1.18–1.19 | 40.7–40.8       | 27.6–27.8                        |
| Fe–30Cr–12Co |                           | 0.86–0.88 | 22.7–23.8       | 7.4–8.0                          |
| Fe–30Cr–16Co |                           | 0.06–0.12 | 6.7–7.7         | 0.1–0.3                          |

It is seen that the magnetic properties strongly decreased with the increase of Co content and tends to zero for Fe–30Cr–16Co alloy. Magnetic properties of Fe–30Cr–8Co alloy are good and meet the standards for low-cobalt Fe–Cr–Co cast alloys.

The X-ray powder diffraction analysis of the samples has shown differences for each alloy after thermomagnetic treatment (Fig. 1).

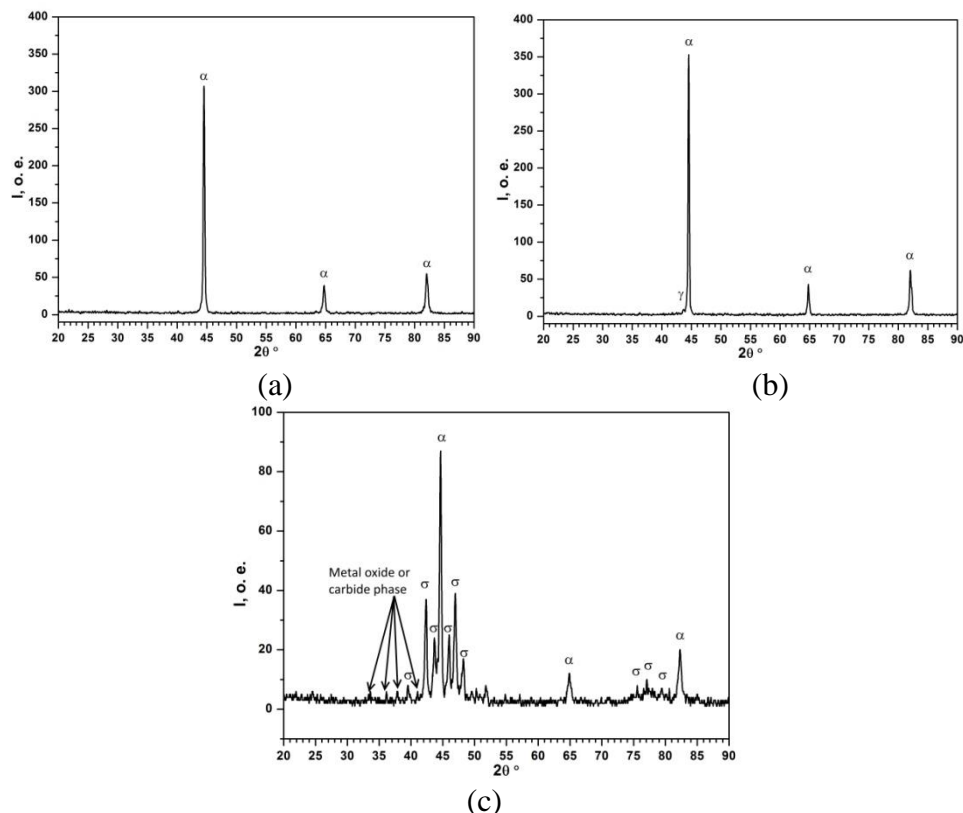


Fig. 1. X-ray powder diffraction patterns of Fe–30Cr–8Co (a), Fe–30Cr–12Co (b), and Fe–30Cr–16Co (c) samples after thermomagnetic treatment.

The X-ray diffraction pattern of the Fe–30Cr–8Co alloy (Fig. 1a) sintered at 1100°C shows the presence of the  $\alpha$ -phase only. The X-ray diffraction pattern of the Fe–30Cr–12Co alloy (Fig. 1b) sintered at 1100°C shows traces of the presence of the  $\gamma$ -phase, what explains the decrease of magnetic properties. The X-ray diffraction pattern of the Fe–30Cr–16Co alloy (Fig. 1c) sintered at 1100°C is completely different. It shows the presence of the  $\alpha$ -phase and tetragonal intermetallic phase FeCr ( $\sigma$ -phase), which is also undesirable for obtaining good magnetic properties. Also, in Fe–30Cr–16Co sample weak traces of some metal oxide or metal carbide phase were discovered, however, accurately identify the phase is not possible due to the small number of diffraction maximums and their low intensity.

Summarizing, Fe–30Cr–12Co and Fe–30Cr–16Co powder alloys don't have good magnetic properties despite the fact that they have good density after low-temperature sintering and almost no traces of the  $\gamma$ -phase presence after quenching. It is known that alloying additives could significantly increase magnetic hysteresis properties of Fe–Cr–Co alloys, but in this case phase composition after thermomagnetic treatment may be determined by inhomogeneity of the  $\alpha$ -phase itself due to low diffusion coefficient during sintering at 1100°C. As for Fe–30Cr–8Co alloy good magnetic properties can be obtained after low-temperature sintering even without alloying additives.

The research was supported by the Russian Foundation for Basic Research (project no. 18-03-00666-a).



1. M.L. Green, R.C. Sherwood, C.C. Wong, *J. Appl. Phys.*, 1982, vol. 53, no. 3, pp. 2398–2400.
2. A.A. Shatsov, *Met. Sci. Heat Treat.*, 2004, vol. 46, pp. 152–155.
3. M.I. Alymov, A.B. Ankudinov, V.A. Zelenskii, I.M. Milyaev, V.S. Yusupov, A.S. Ustyukhin, *Fiz. Khim. Obrab. Mater.*, 2011, no. 3, pp. 34–38.
4. A.S. Ustyukhin, A.B. Ankudinov, V.A. Zelenskii, I.M. Milyaev, A.A. Ashmarin, M.I. Alymov, *Dokl. Phys. Chem.*, 2018, Vol. 482, Part 2, pp. 140–144.

## SYNTHESIS OF SHS MEMBRANES BASED ON MICA-LIKE STRUCTURE MATERIALS FOR LIQUID AND GAS FILTRATION

V. I. Uvarov<sup>a</sup>, A. R. Kachin<sup>a</sup>, V. E. Loryan<sup>a</sup>, V. S. Shustov<sup>a</sup>, and M. V. Tsodikov<sup>b</sup>

<sup>a</sup>Merzhanov Institute of Structural Macrokinetics and Materials Science, RAS, Chernogolovka, 142432 Russia

<sup>b</sup>Topchiev Institute of Petrochemical Synthesis, RAS, Moscow, 119991 Russia  
e-mail: uvar@ism.ac.ru; kachin@ism.ac.ru

DOI: 10.24411/9999-0014A-2019-10182

Man-made burden on the environment can lead to irreversible changes in the composition of natural water. In particular, surface and underground water sources are contaminated by substances of anthropogenic origin - heavy metal ions, nitrates, volatile organochlorine compounds, herbicides, pesticides, radionuclides, etc. [1, 2]. Therefore, the research aimed at purification of drinking water, in particular development of filter technologies using various materials, is relevant.

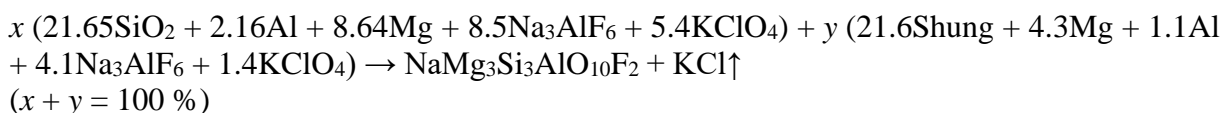
The process of self-propagating high-temperature synthesis (SHS) of materials, including porous, is energetically advantageous, since the heating of the charge, the synthesis and sintering of the final materials is not due to external heating, but due to the release of heat during chemical reactions between the components of the charge, which provides the possibility of propagation of the combustion wave.

A comparative analysis of characteristics of filters manufactured in different countries shows the expected advantages of SHS filters, especially multiple application after regeneration. It is impossible for the filters produced by traditional methods [3, 4].

Fluorophlogopite is known to have mica-like structure and a high ion-exchange capacity. It can be used for binding and preservation of heavy metal ions due to heterovalent replacement of Na<sup>+</sup> ion by metal ions determining water hardness (Ca<sup>+</sup>, Mg<sup>+</sup>, Sr<sup>2+</sup>, Ba<sup>2+</sup>). It is possible to obtain porous material based on fluorophlogopite by the SHS method. Filters based on fluorophlogopite can be used for fine purification of air and process gases from aggressive dispersed micro-impurities and radioactive aerosols.

The aim of this study is to create highly efficient, corrosion-resistant SHS membranes for purification of liquids and gases both in industrial plants and for small installations that allow regulating the salt composition of water that is necessary for providing active human activity during its consumption.

**Experimental methods.** Quartz sand (SiO<sub>2</sub>), Karelian schungite, aluminum PAD-1 (GOST 6058-73), and magnesium MPF-3 (GOST 6001-79) were used as initial elements in the experiments. Recycled cryolite Na<sub>3</sub>AlF<sub>6</sub> was used as a source of fluorine, potassium perchlorate KClO<sub>4</sub> (TU 6-09-3801-76) – as an oxygen source. Some amounts (up to 15%) of iron and chromium oxides were introduced into the mixture as catalytically active additives. The quartz sand and schungite were crushed into powder of less than 150 and 50 μm in ball drums. The particle size was measured using a MicroSizer 201 analyzer. The mixtures which can react in the SHS mode were used. The initial mixture composition was estimated by the following chemical scheme:



The initial billets of 40 mm in diameter and ~ 5 mm in height were sintered in the furnace at  $T = 930^{\circ}\text{C}$  in the air of atmospheric pressure. The temperature was being raised during 1 h. The exposure time at  $930^{\circ}\text{C}$  was 10 min. The phase composition of the product was determined with  $\text{CuK}\alpha$  radiation diffractometer DRON-3M. Metallographic studies were performed using an optical microscope Axiovert 200 MAT. The quantitative elemental composition of the phases was carried out using a Zeiss Ultra Plus high-resolution SEM with INCA 350 Oxford Instruments X-ray microanalysis system.

The porosity of the synthesized material was determined in accordance with GOST 2409-80. The size of the open pores of the synthesized material was determined according to GOST 26849-86. The concentration of chemical elements in tap water before and after filtration was determined by the atomic absorption method.

**Experimental results.** The appearance of the synthesized sample is shown in Fig. 1. The main phases of the synthesized material are those of spinel and fluorophlogopite in approximately equal mass fractions (Fig. 2). At the same time, the presence of unidentified lines indicates a more complex composition of the material.



Fig. 1. Appearance of the synthesized sample.

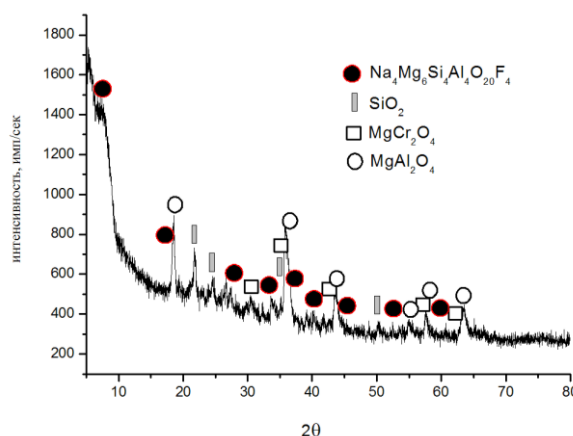


Fig. 2. Phase composition of the synthesized material.

Figure 3 demonstrates the fracture structure (3a) typical of mica-like structure materials and the porosity of the synthesized sample (3b). According to the analysis, the material porosity is 60 %, the open porosity is 45%. The measured value of open pores (according to GOST 26849-86) in the synthesized material is 1–3  $\mu\text{m}$ . The sample bending strength is 5.5–6 MPa.

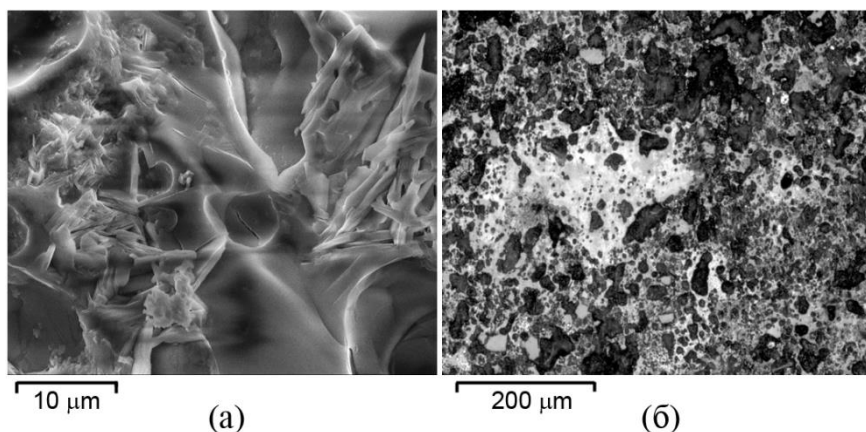


Fig. 3. Synthesized material structure.

Membranes with mica-like structure were obtained by the direct synthesis. Their pore size was 1–3.5  $\mu\text{m}$ , porosity > 60%, open porosity was up to 45%. It was established that the bending strength of the obtained samples was 5.5–6 MPa. the specific surface area was 1.203  $\text{m}^2/\text{g}$ .

As a result of the work, laboratory devices were developed and experiments in water purification were carried out. Table 1 demonstrates the content of metal ions in the water before and after its filtration through the synthesized membrane. The results prove that the obtained sample of the filter purifies the tap water rather efficiently from the high content of heavy metal ions and reduces the water hardness by 30%.

Table 1. Content of Mg and Ca ions in the water before and after filtration.

| Chemical element | Concentration of chemical element in tap water, mg/l |   |
|------------------|--|---|
|                  | Before filtration                                    | After filtration through the synthesized filter |
| Mg               | 23.706   | 16.856  |
|                  |  | 16.343  |
|                  |  | 15.963  |
|                  |  | 63.276  |
| Ca               | 81.350   | 62.735  |
|                  |  | 63.186  |

### Conclusions

Membranes with mica-like structure were obtained by the direct synthesis. Their pore size was 1–3.5  $\mu\text{m}$ , porosity > 60%, open porosity was up to 45%. It was established that the bending strength of the obtained samples was 5.5–6 MPa, the specific surface area was 1.203  $\text{m}^2/\text{g}$ .

Multiple regeneration of filters can be carried out by a reverse pulsed flow of the purified water, washing with solvent or high-temperature annealing. The investigation results can be used for development of production technologies of porous mica-crystalline filters for fine purification of water and technological gases from dispersed micro-impurities.

1. V.I. Mironenko, K.V. Mironenko, K.L. Reznikov, S.P. Kofanov, A.P. Krotov, V.D. Goncharov, The impact of man-made factors on the environment of the Altai Territory, Barnaul: Altai, 1996, pp. 25–28.
2. V.Ya. Varshavsky, G.I. Nikoladze, Yu.A. Rakhmanin, L.S. Skvortsov, A.B. Tseskis, ed. by L.S. Skvortsov, Installations (Filters) for Drinking Water Purification, Moscow: Center Moskva, 1996. 97 p.
3. S.G. Tresvyatski, M.A. Parkhomenko, A.D. Kondratenko, Study on microcrystalline materials of mica-like structure, *Inorg. Mater.*, 1965, vol. 1, no. 4, pp. 449–59.
4. I.P. Borovinskaya, A.G. Merzhanov, V.I. Uvarov, Capillary-porous SHS-materials for liquid and gas filtration, *Nauka proizvodstvu*, 2001, no. 10, pp. 28–32.

## CLAD POWDERS BY COMBINED USE OF METAL REDUCTION AND HIGH-ENERGY BALL MILLING IN SALT SOLUTIONS: THEIR PREPARATION AND IGNITION

S. G. Vadchenko

Merzhanov Institute of Structural Macrokinetics and Materials Science, Russian Academy of Sciences, Chernogolovka, Moscow, 142432 Russia  
e-mail: vadchenko@ism.ac.ru

DOI: 10.24411/9999-0014A-2019-10183

The cladding (plating) of metal powders with other metals can be performed in several ways [1, 2]. The process of cladding is normally carried out in mills or vibratory machines from a mixture of basic and cladding metals. Usually the clad layers obtained via metal reduction from aqueous solution of salts exhibit weak adhesion to the surface of basic powder.

This work aimed at elaboration of a new method for fabrication of clad powders by combined use of metal reduction and high-energy ball milling (HEBM). The latter affords for formation of composite powders with a fine laminate structure of individual particulates showing elevated reactivity. If constituent metals are capable of reacting with heat release, such composite powders can be used as green mixtures for SHS production of materials or fabrication of items by sintering. In this work, Cu–Ti and Ni–Al clad particle were obtained by deposition of Ni and Cu onto Ti and Al powders from aqueous solution of their chlorides, sulfates, and nitrates. The reduction of metals takes place during HEBM and can be facilitated by reductants, such as glycine, hydrazine sulfate, and sodium hyposulfite. Thus, prepared clad powders were characterized by SEM and XRD.

Figure 1 shows the deposits of Cu (bright) on Al (a) and Ti (b) powder particles formed at the initial stages of milling the Al–CuSO<sub>4</sub>·5H<sub>2</sub>O and Ti–CuSO<sub>4</sub>·5H<sub>2</sub>O mixtures. Copper is deposited in the form of small particles with a size of below 0.2 μm.

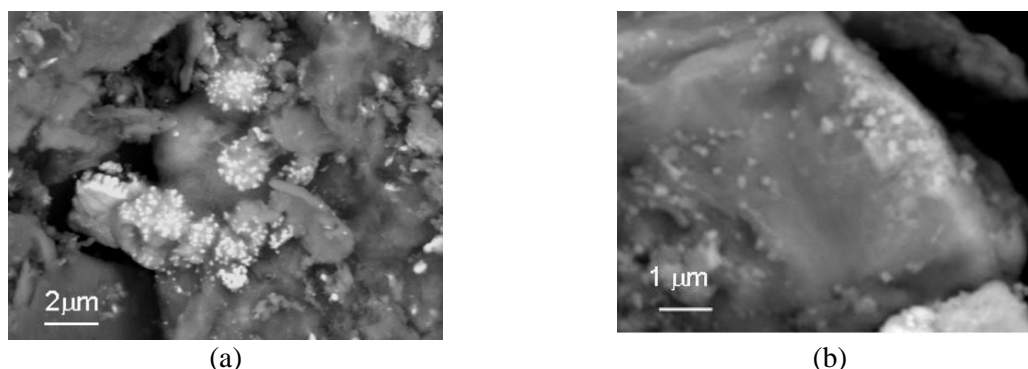


Fig. 1. SEM images showing the deposits of Cu (bright) on Al (a) and Ti (b) powder particles.

Figure 2 presents the temperature profiles of thermal explosion in Ti–Al pellets prepared from different mixtures. The ignition profiles for the pellets prepared from composite particles obtained in the combined process markedly differ from those prepared from unprocessed and milled Ni–Al mixtures (Fig.2). The onset of temperature rise for the mixture of Al with the Ni reduced from NiSO<sub>4</sub>·7H<sub>2</sub>O (curve 1) is by 200–300°C lower than that for unprocessed Ni–Al mixture (curve 6). The former is seen to proceed in two stages due to the melting of excessive Al.

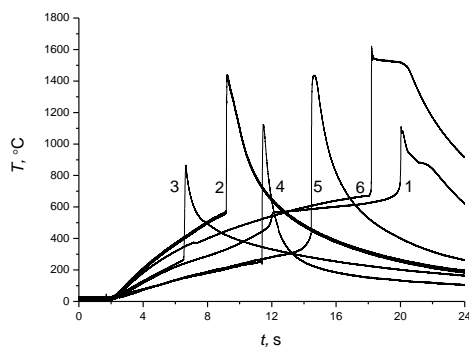


Fig. 2. Thermograms of thermal explosion in Ti–Al pellets prepared from: (1) mixture of Al with the Ni reduced from  $\text{NiSO}_4 \cdot 7\text{H}_2\text{O}$ ; (2) mixture of Ni and Al nanopowders; (3) fine fraction of Ni–Al mixture milled in water; (4) Ni–Al nanofoils; and (5) milled Ni–Al mixture; and (6) unprocessed Ni–Al mixture.

This research was financially supported by the Russian Foundation for Basic Research (project no. 18-03-00438).

1. A.G. Meilakh, Steel production from nickel-plated iron powder, *Steel in Translation*, 2014, vol. 44, no. 2, pp. 162–165.
2. Yu.V. Kontsevoi, A.V. Dolmatov, E.A. Pastukhov, T.F. Grigor'eva, Mechanical plating of Fe–Al and Fe–Cu systems under dynamic loading, *Poroshk. Metall. Funkts. Pokr.*, 2015, no. 1, pp. 8–11.

## EXPERIMENTAL 2D MODEL OF HETEROGENEOUS COMBUSTION

S. G. Vadchenko<sup>\*a</sup>, E. V. Suvorova<sup>a</sup>, and A. S. Rogachev<sup>a</sup>

<sup>a</sup>Merzhanov Institute of Structural Macrokinetics and Materials Science, Russian Academy of Sciences, Chernogolovka, Moscow, 142432 Russia  
\*e-mail: vadchenko@ism.ac.ru

DOI: 10.24411/9999-0014A-2019-10184

Theoretical models of heterogeneous combustion, based on relay-race or quasi-homogeneous heat transfer [1–5], need pictorial interpretation with experimental models. Existing simple models [6] cannot consider porosity or dilution of the mixture by inert addition. Here, we suggest two-dimensional (2D) experimental model of heterogeneous combustion. Macroscopic samples are built of small cylindrical pellets that imitate powder particles of real mixtures. The model allows close or loose packing, modelling inert additions and percolation combustion mechanism. This model also allows to change heat- and mass-transfer conditions on the “side” boundaries of the sample by means of placing various inert pellets along the perimeter. The pellets can be placed vertically or horizontally in one or several layers. Some examples of the packing of pellets are shown in Fig. 1.

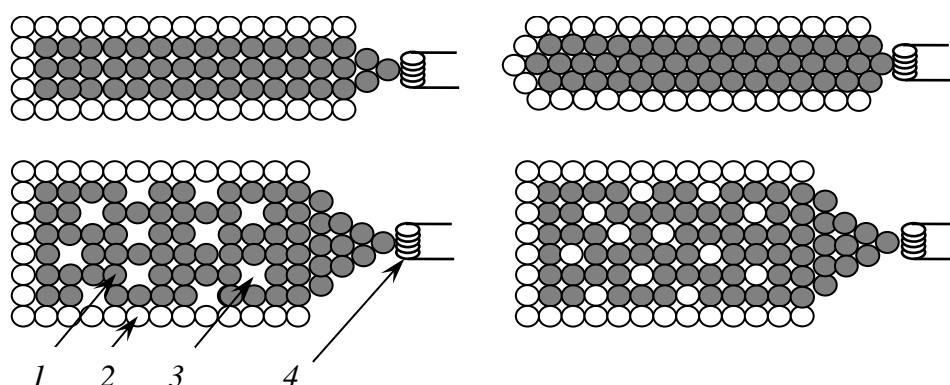


Fig. 1. Schematics of close and loose packing of the pellets. 1 reactive pellet, 2 inert pellet, 3 pore, 4 igniting coil.

The reactive pellets with diameter  $d = 1$  mm and height  $h = 1.3$  mm were cold-pressed from Hf powder (HFN-1). Density of the pellets was  $7.073 \pm 0.005$  g/cm<sup>3</sup>, which corresponds to 0.536 theoretical density (bulk Hf). Burned pellets were used as inert ones. All experiments were made in air, and the combustion process was video-recorded at 50 fps. Photosensor with slit collimator was used for recording transient of combustion between pellets.

Selected video-frames of the process are presented in Fig. 2 for different packings. The combustion front was almost flat in closed samples, i.e., when side layers were made of inert pellets (Figs. 2a, 2b) and got curved in the open samples with reactive side layers (Figs. 2c, 2d). This can be caused by gas filtration difficulties and heat transfer into inert pellets. After some transition unsteady combustion taking place immediately after initiation, a steady-state regime of combustion appeared (Fig. 3). This effect was observed even for one row of the pellets. Average values of combustion velocity were measured for the steady regime along the central axis of the sample after formation of the cone-like front.

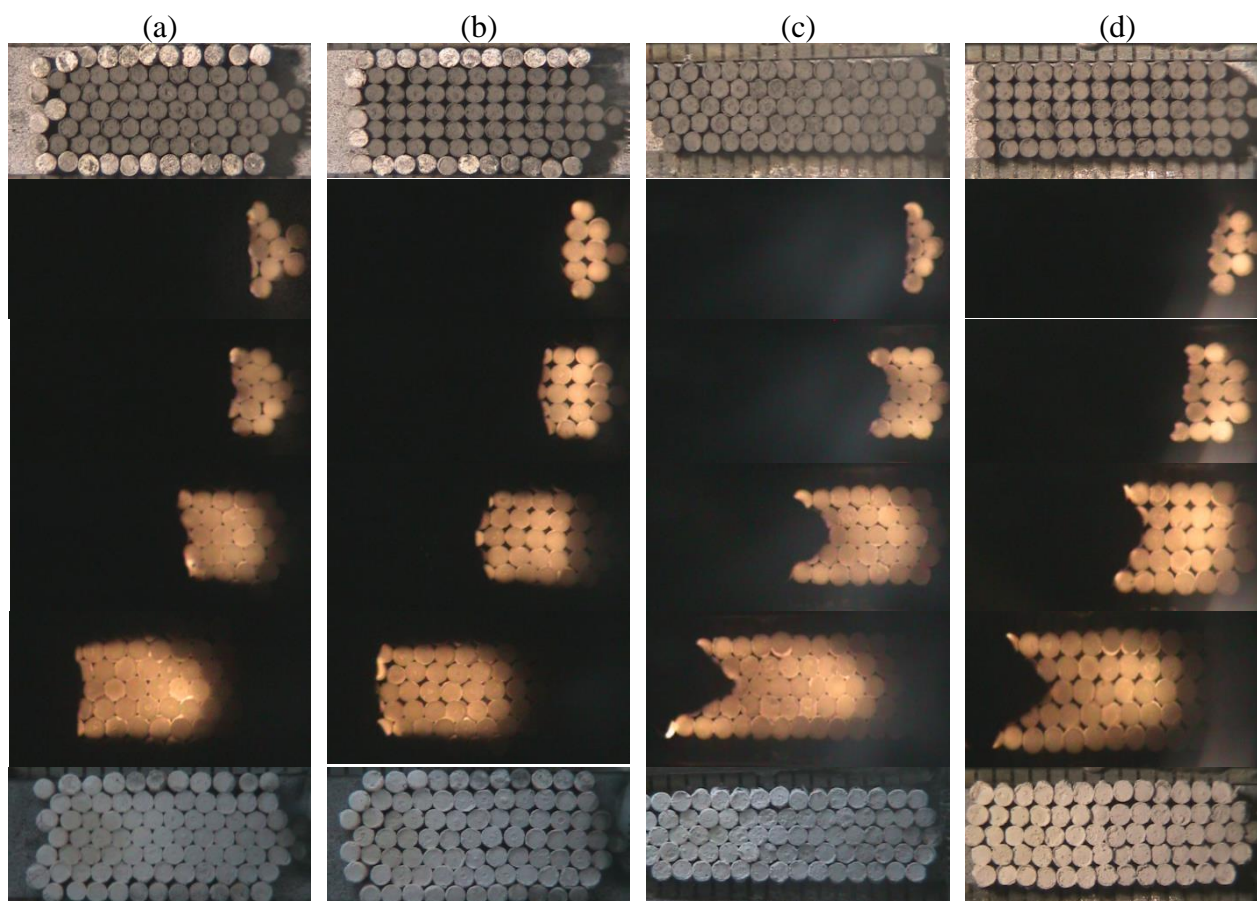


Fig. 2. Initial samples, frames of video recordings ( $\Delta t = 2$  s) and burned samples for different types of packing.

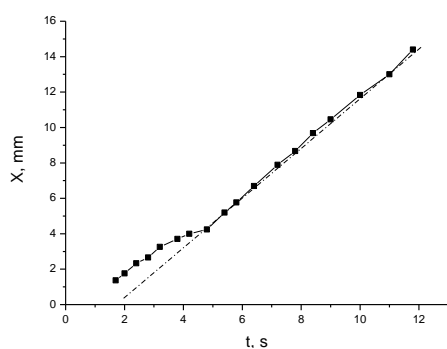


Fig. 3. Coordinate of the combustion front as function of time for one row of the pellets.

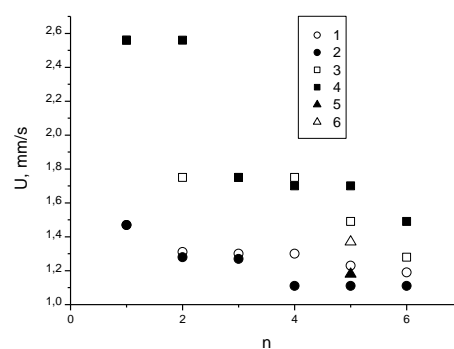


Fig. 4. Dependences of combustion velocity on the sample structure: 1 closed sample, close packed; 2 closed, square packed; 3 open sample, close packed; 4 open, square packed; 5 closed, close packed, with inert dilution; 6 closed, square packed, with pores.

Figure 4 demonstrates that dilution and porosity result in decreasing of combustion velocity (points 5 and 6), as compared to non-diluted and “pore-free” samples. Transition of the combustion front from one pellet to another generally may include up to 3 stages: flash in the end of the first pellet burning, depression, and second flash in the beginning of the next pellet burning. In some cases, not all stages were observed, depending on contacts between pellets that are influenced by packing type and external stress. Signals of the photosensor for one row of the pellets are shown in Fig. 5. Vertical lines indicate contact boundaries of pellets. In the



first case (Fig. 5a), two flashes of the transition process can be observed near the pellet contacts. Intermediate oscillations of the brightness appear due to self-oscillating combustion mode, which forms only if  $h/d > 1$ , and don't appear when  $h/d < 1$ . The oscillations can be due to cracking of the pellet induced by oxidation reaction. After burning, the samples height increased by 4 – 6%, resulting in stresses, bending of pellets and shifts of the rows. In the second case (Fig. 5b), only two stages, flash and depression, were observed.

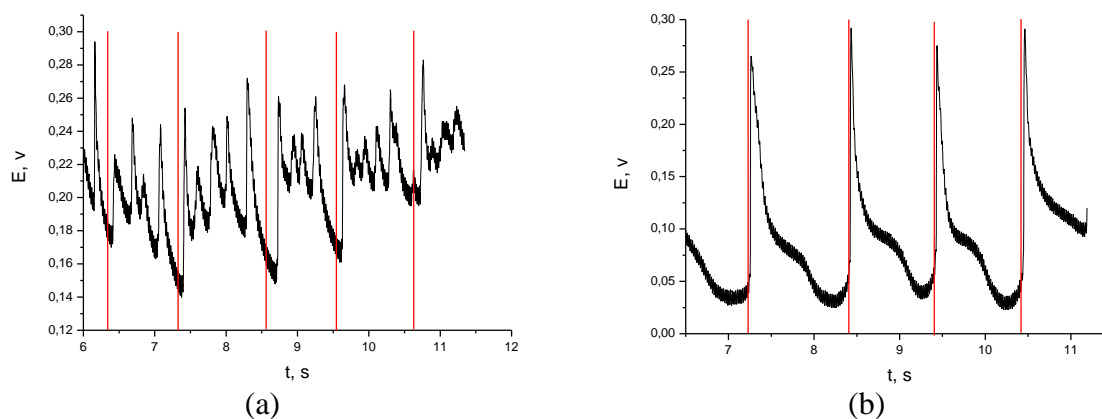


Fig. 5. Brightness signal from photosensor: (a)  $h = 1.2\text{--}1.4$  mm; (b)  $h = 0.5\text{--}0.6$  mm.

## Conclusion

Experimental model allows pictorial imitation of heterogeneous combustion, including porosity, dilution, and packing density of the combustible mixture. Combustion propagating velocity can be controlled by controlling height of the pellets, which can be used in delay elements and initiators. Such models may be useful for imitation of industrial and forest fires.

1. A.G. Merzhanov, *Dokl. Academ. Nauk*, 1997, no. 4, pp. 505–507.
2. I.A. Filimonov, *Fizika gorenia i vzryva*, 1998, vol. 34, no. 3, pp. 69–71.
3. A.G. Merzhanov, A.S. Rogachev, *Russ. J. Phys. Chem.*, 2000, vol. 74, pp. S20–S27.
4. P.M. Krishenik, A.G. Merzhanov, K.G. Shkadinskii, *Fizika gorenia i vzryva*, 2002, vol. 38, no. 3, pp. 70–79.
5. A.S. Mukasyan, A.S. Rogachev, *Prog. Energy Combust. Sci.*, 2008, vol. 34, pp. 377–416.
6. S.G. Vadchenko, A.G. Merzhanov, *Dokl. Russ. Academ. Nauk*, 1997, vol. 352, no. 4, pp. 487–489.

## SYNTHESIS OF THE $Ti_2AlC$ AND $Ti_3AlC_2$ MAX PHASE WITH A REDUCTION STEP VIA COMBUSTION OF A $TiO_2 + Mg + Al + C$ MIXTURE

V. I. Vershinnikov\*<sup>a</sup> and D. Yu. Kovalev<sup>a</sup>

<sup>a</sup>Merzhanov Institute of Structural Macrokinetics and Materials Science, Russian Academy of Sciences, Chernogolovka, 142432 Russia

\*e-mail: [vervi@ism.ac.ru](mailto:vervi@ism.ac.ru)

DOI: 10.24411/9999-0014A-2019-10185

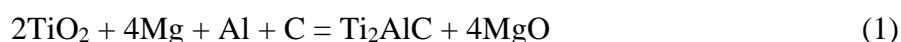
The last decade has seen increasing interest in the synthesis and characterization of MAX phases—ternary compounds with a hexagonal close-packed structure and the general formula  $M_{n+1}AX_n$ , where M is a transition metal, A is a group IIIA or IVA *p*-block element (for example, Si, Ge, Al, S, Sn, and others), X is carbon or nitrogen, and  $n = 1-4$ . The MAX phases have a layered crystal structure in which  $[M_{n+1}X_n]$  carbide or nitride slabs are sandwiched between monolayers of group IIIA or IVA elements. Their layered crystal structure leads to a laminate structure of grains, with layer thicknesses of up to several tens of nanometers. Materials based on the MAX phases combine properties of ceramics and metals. Like ceramics, they have low density and high elastic moduli, heat resistance, and high-temperature strength. Like metals, they have appreciable electrical and thermal conductivity and offer high fracture toughness and thermal stability. To date, about 70 compounds of the MAX family have been reported. The best studied MAX phases, which are of practical interest, are the titanium-based MAX phases:  $Ti_2AlC$  and  $Ti_3AlC_2$ . Such compounds are typically prepared from elemental mixtures by hot isostatic pressing (HIP) [1], spark plasma sintering (SPS) [2], and self-propagating high-temperature synthesis (SHS) [3, 4]. Despite the diversity of synthesis processes, almost all of them use oxygen-free compounds as starting materials. Li et al. [5] prepared the  $Ti_2AlC$  and  $Ti_3AlC_2$  phases using a titanium oxide, aluminum, and graphite. The MAX phases  $Ti_2AlC$  and  $Ti_3AlC_2$  were synthesized by heating a mixture of the starting materials to a temperature of 1500°C, followed by isothermal holding for 2 h.

### EXPERIMENTAL

In our experiments, we used the following powders: magnesium (98.5–99.5% purity, particle size under 250  $\mu m$ ), commercial  $TiO_2$  (grade 1, Russian Federation State Purity Standard TU 1715-347-00545484-94), aluminum (99.5% purity, particle size under 5  $\mu m$ ), carbon black (P804-T, specific surface area  $S = 12 \text{ m}^2/\text{g}$ ), and graphite ( $S = 3.6 \text{ m}^2/\text{g}$ ). MAX phases were isolated from intermediate products ( $Ti_2AlC$  MgO and  $Ti_3AlC_2$  MgO) using dilute hydrochloric acid (1:3). Mixing was performed in tumbling mills. We used samples with a loose bulk density. A starting mixture weighing 250 g was poured into a graphite boat. Combustion was initiated on the top surface of the samples using a tungsten coil. The combustion process was run in an SVS-8 reactor under an argon atmosphere at a pressure  $P = 4 \text{ MPa}$ .

### RESULTS AND DISCUSSION

$Ti_2AlC$  MAX phases were synthesized in the combustion regime in an argon atmosphere under a pressure of 3 MPa according to the reaction scheme:



After chemical leaching in hydrochloric acid, the powder consisted of  $Ti_2AlC$ ,  $MgAl_2O_4$ , and TiC (Table 1, run 1). The formation of  $MgAl_2O_4$  (spinel) points to deficiency of the reducing agent (magnesium) in the starting mixture. As a result, some of the aluminum reduces

the titanium dioxide to give titanium metal and  $\text{Al}_2\text{O}_3$ . This leads to the formation of  $\text{MgO}\cdot\text{Al}_2\text{O}_3$ .

Table 1 presents the ratio of the starting materials and the phase composition of the powder after acid enrichment of the  $\text{Ti}_2\text{AlC}\cdot\text{MgO}$  and  $\text{Ti}_3\text{AlC}_2\cdot\text{MgO}$  intermediate product in hydrochloric acid.

Table 1. Ratio of the starting materials and phase composition of the powder after acid enrichment of the  $\text{Ti}_2\text{AlC}\cdot\text{MgO}$  and  $\text{Ti}_3\text{AlC}_2$  intermediate product in hydrochloric acid.

| Composition, wt % |      |     |     | Phase composition of the powder, wt % |                         |     |                           | Run no. |
|-------------------|------|-----|-----|---------------------------------------|-------------------------|-----|---------------------------|---------|
| $\text{TiO}_2$    | Mg   | Al  | C   | $\text{Ti}_2\text{AlC}$               | $\text{Ti}_3\text{AlC}$ | TiC | $\text{MgAl}_2\text{O}_4$ |         |
| 54.2              | 32.6 | 9.2 | 4   | 28                                    | 0                       | 55  | 17                        | 1       |
| 50.9              | 36.7 | 5.6 | 3.8 | 90                                    | 0                       | 10  | 0                         | 2       |
| 50.5              | 36.4 | 9.3 | 3.8 | 80                                    | 0                       | 13  | 7                         | 3       |
| 49.4              | 38.6 | 8.4 | 3.6 | 93                                    | 0                       | 7   | 0                         | 4       |
| 48.6              | 39.5 | 8.3 | 3.6 | 87                                    | 0                       | 13  | 0                         | 5       |
| 49.6              | 38.8 | 8.4 | 3.2 | 96                                    | 0                       | 4   | 0                         | 6       |
| 49.1              | 38.3 | 8.3 | 4.3 | 11                                    | 86                      | 3   | 0                         | 7       |
| 48.9              | 38.2 | 8.3 | 4.6 | 4.6                                   | 89.4                    | 6   | 0                         | 8       |

Increasing the magnesium content of the starting mixture to  $\text{Mg}_{\text{ex}} = 20\%$  leads to complete magnesium reduction of the titanium dioxide and the formation of the MAX phase  $\text{Ti}_2\text{AlC}$  and titanium carbide (Table 1, run 2). The addition of 10% excess of aluminum to this starting mixture led to an increase in the percentages of  $\text{MgAl}_2\text{O}_4$  (spinel) and titanium carbide in the  $\text{Ti}_2\text{AlC}$  powder (Table 1, run 3). Increasing the excess of magnesium in the starting mixture to 30% led to a decrease in the percentage of titanium carbide in the final product. After leaching, the powder consisted of the MAX phase  $\text{Ti}_2\text{AlC}$  and a small amount (7%) of titanium carbide (Table 1, run 4). Increasing the excess of magnesium in the starting mixture to 35% leads to an increase in the percentage of titanium carbide in the powder of the MAX phase  $\text{Ti}_2\text{AlC}$ . In subsequent investigation, we used 30% excess of magnesium (Table 1, run 4) in the starting mixture. We studied the effect of carbon black deficiency on the formation of the MAX phase  $\text{Ti}_2\text{AlC}$  and the titanium carbide content of the powder. Reducing the carbon black content of the starting mixture by 10 wt % leads to a decrease in the titanium carbide content of the powder by 4% (Table 1, run 6). A 20% carbon black deficiency leads to a sharp increase in titanium carbide content and a decrease in the content of the MAX phase  $\text{Ti}_2\text{AlC}$  in the powder. Figure 1a shows the X-ray diffraction pattern of the  $\text{Ti}_2\text{AlC}$  powder (Table 1, run 6) and Figure 1b shows its micrograph. It is seen from the X-ray diffraction pattern that the powder consists of two phases:  $\text{Ti}_2\text{AlC}$  and TiC.

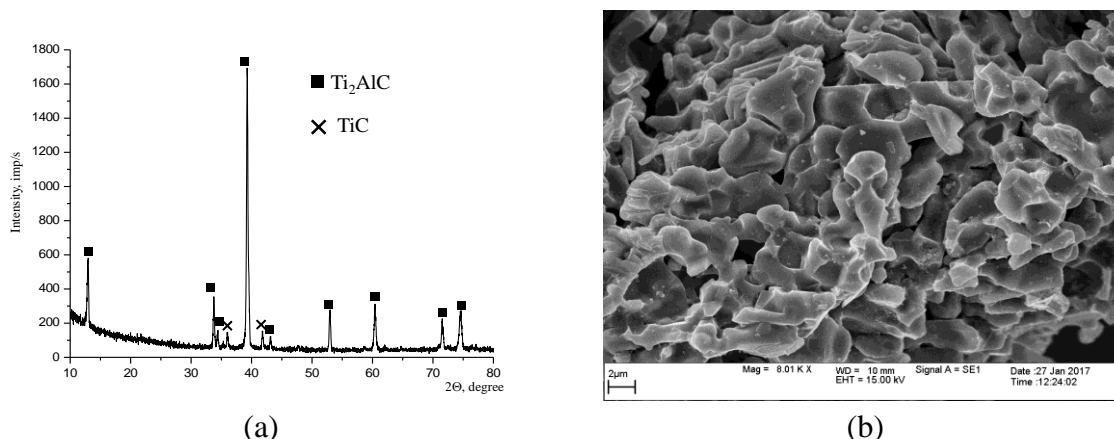


Fig. 1. (a) X-ray diffraction pattern and (b) micrograph of the  $\text{Ti}_2\text{AlC}$  powder (Table 1, run 6:  $\text{Mg}_{\text{ex}} = 30\%$ ,  $\text{C}_{\text{def}} = 10\%$ ,  $P_{\text{Ar}} = 3$  MPa, loose bulk density of the starting mixture).

Increasing the excess of carbon black in the starting mixture to 20% created conditions for the formation of a mixture of the MAX phases  $Ti_2AlC$  and  $Ti_3AlC_2$  and titanium carbide (Table 1, run 7). The X-ray diffraction pattern of this powder is presented in Fig. 2.

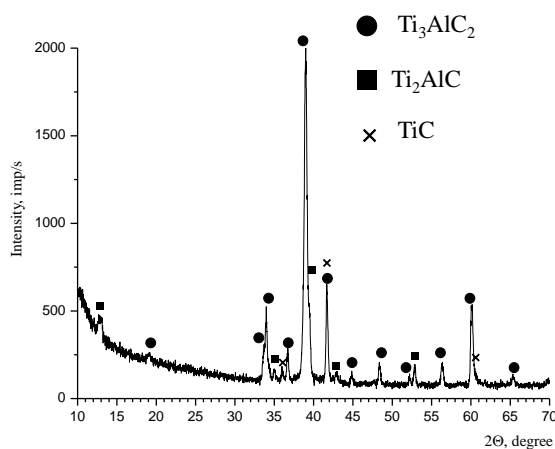


Fig. 2. X-ray diffraction pattern of the  $Ti_2AlC + Ti_3AlC_2 + TiC$  powder (Table 1, run 7:  $Mg_{ex} = 30\%$ ,  $C_{ex} = 20\%$ ,  $P_{Ar} = 3$  MPa, loose bulk density of the starting mixture).

A further increase in the excess black carbon to 35% led to the formation of the powder consisting of the  $Ti_3AlC_2$  phase and some amount of  $Ti_2AlC$  and titanium carbide (ex. 8, Table 1).

Figure 3 demonstrates X-ray diffraction pattern and SEM image of the powder at 30% excess of carbon black in the mixture. MAX phase particles are thin plates of 70 nm or more in thickness.

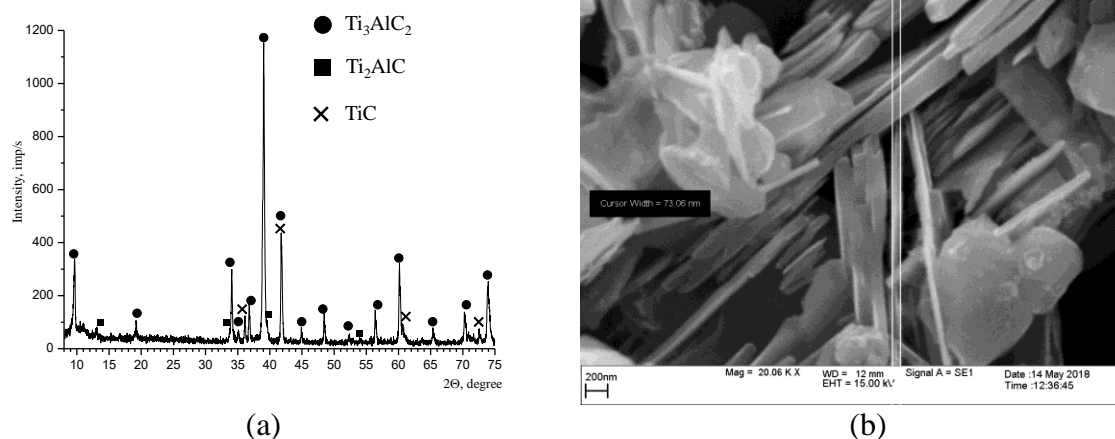


Fig. 3. (a) X-ray diffraction pattern and (b) micrograph of the powder (Table 1, run 8):  $C_{ex} = 30\%$ ,  $P_{Ar} = 3$  MPa, loose bulk density of the starting mixture.

## CONCLUSIONS

It follows from the present results that the MAX phase  $Ti_2AlC$  can be prepared by SHS with a reduction step. In this process, an excess of magnesium helps to minimize the percentage of  $MgAl_2O_4$  (spinel), and carbon deficiency in the starting mixture leads to a decrease in the percentage of titanium carbide in the final product. An excess of carbon black in the starting mixture leads to the formation of a mixture of the MAX phases  $Ti_2AlC$  and  $Ti_3AlC_2$ .

1. Y. Bai, X. He, Y. Li, C. Zhu, S. Zhang, Rapid synthesis of bulk  $Ti_2AlC$  by selfpropagating high temperature combustion synthesis with a pseudo-hot isostatic pressing process, *J. Mater. Res.*, 2009, vol. 24, no. 8, pp. 2528–2535.
2. W.B. Zhou, B.C. Mei, J.Q. Zhu, X.L. Hong, Rapid synthesis of  $Ti_2AlC$  by spark plasma sintering technique, *J. Mater. Lett.*, 2005, vol. 59, no. 1, pp. 131–134.
4. M. Łopacín'ski, J. Puszynski, J. Lis, Synthesis of ternary titanium aluminum carbides using self-propagating high temperature synthesis technique, *J. Am. Ceram. Soc.*, 2004, vol. 84, no. 12, pp. 3051–3053.
5. P.M. Bazhin, D.Yu. Kovalev, M.A. Luginina, O.A. Averichev, Combustion of Ti–Al–C compacts in air and helium: a TRXRD study, *Int. J. Self-Propag. High-Temp. Synth.*, 2016, vol. 25, no. 1, pp. 30–34.
6. C. Li, S. Kota, C. Hu, M.W. Barsoum, On the synthesis of low-cost, titanium-based MAXenes, *J. Ceram. Sci. Technol.*, 2016, vol. 7, no. 3, pp. 301–306.

## HYBRID SURFACE ENGINEERING TECHNOLOGIES FOR SELF-ADAPTIVE FRICTION AND WEAR BEHAVIOR IN EXTREME ENVIRONMENTS

**A. A. Voevodin**

Department of Materials Science and Engineering, the University of North Texas,  
Denton, TX 76203, USA  
e-mail: andrey.voevodin@unt.edu

DOI: 10.24411/9999-0014A-2019-10186

Self-adaptive low friction and wear resistant coatings, which can re-arrange their structure and chemistry in a response to changes in environment temperature and humidity are of a practical importance for aerospace, automotive and tool industry applications to help reliable operation under cycles of extreme temperatures, mechanical loads and environments. Surface engineering approaches to provide self-adaptive friction and wear behavior were a subject of intensive research. This includes development of hard, abrasion and oxidation resistance ceramic-based coatings with embedded soft and low friction solid lubricants made of graphite and diamond-like carbon (DLC), transition metal dichalcogenides, soft metals and easy to shear oxides. Other approaches include the development of protective coating compositions with the use of transition metals which can react with environment to form low shear moduli oxides at elevated temperatures in air. The resulted self-adaptive coatings have a capability of solid lubricant release as well as self-adjustment of surface chemistry and microstructure in response to temperature and environment variations. These coatings were coined “chameleon” to reflect their ability to self-adjust their surface to operating environments to maintain low friction and wear. The realization of self-adaptive coatings relies on hybrid surface engineering technologies, since hard and oxidation resistance ceramics normally require high temperature and energy parameters for their synthesis, while the inclusions of solid lubricants (temperature and oxidation sensitive) are normally need be processed at reduced temperatures and energies to retain lubricating properties. A review of hybrid surface engineering technologies is presented with a focus on self-adaptive friction and wear protective coatings for extreme environment applications.

### ***Hybrid of magnetron sputtering and pulsed laser deposition***

This versatile hybrid physical vapor deposition (PVD) method was used to explore and produce a number of nanocomposite coatings made of hard nano-crystalline carbide, nitride and oxide matrices ( $ZrO_2$ ,  $Al_2O_3$ , TiCN, CrN, etc.). These had embedded nano-sized inclusions of solid lubricants ( $MoS_2$ ,  $WS_2$ , DLC, Ag, Au) and transition metals capable to form low shear modulus oxide for adaptive lubrication in variable humidity and temperatures up to  $1000^\circ C$  [1, 2]. The stored lubricant materials released from nanophase reservoirs facilitate chemistry and structure change of mechanical interfaces to continuously reduce friction and wear in environment cycles (Fig. 1a). Coating compositions were modified to form contact tribofilms made of defected double oxides (e.g. Magnéli phases) as well as ternary oxides, where interlayered metallic and ionic bonding along specific crystallographic orientations provides sliding friction reduction and adaptive lubrication in the challenging mid-temperature regime of  $500\text{--}700^\circ C$ , allowing to keep friction coefficient stable over the broad temperature range (Fig. 1b). The nanocomposite “chameleon” structures were also sandwiched between diffusion barrier nitride layers for extended operations and adding temperature cycling capability. In addition, coating nanostructure designs, texture and orientation control were also shown to provide a thermal management functionality, using thermal conductivity anisotropy and phase transitions in tribological contacts [1].

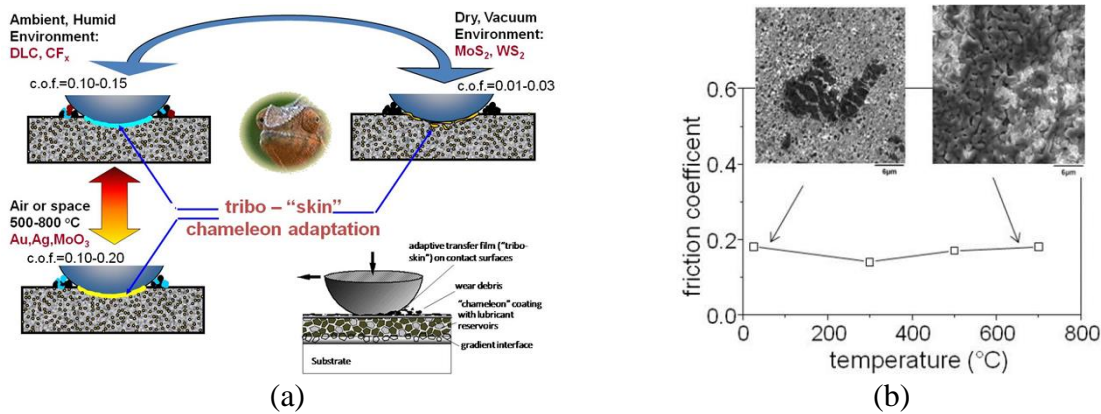


Fig. 1. (a) A design concept of multi-environment self-adaptation for chameleon tribological coating. (b) Performance of a broad temperature range YSZ–Mo–Au–MoS<sub>2</sub> chameleon coating with insets showing a dominance of MoS<sub>2</sub> lubrication at low temperature and MoO<sub>3</sub> lubrication at high temperature [1, 2].

### *Laser texturing of ceramic surfaces with burnished application of composite solid lubricants*

This approach uses laser processing to form micron-sized reservoirs on the surface of hard wear resistant ceramics followed with an application of self-adaptive chameleon compositions to fill these reservoirs and provide solid lubricant replenishment in friction contacts. One example is laser processing of a functionally gradient Ti–TiC–TiC/DLC coatings with laser cut tracks along wear paths filled with MoS<sub>2</sub> [3]. Another example is laser machining of arrays of micrometer sized dimple reservoirs on the surface of TiCN coatings, which are filled with chameleon solid lubricants based on MoS<sub>2</sub> and graphite applied by burnishing (Fig. 2a) [4]. Such hybrid processed surfaces exhibited environmental adaptation with friction coefficients of 0.15 in humid air and 0.02 in dry or vacuum conditions, while wear life was increased by at least one order of magnitude. The laser-processed micro-reservoirs also helped to renew lubricant supply in multiple cycling between humid air and dry nitrogen, evidenced by repeated change from hexagonal MoS<sub>2</sub> to graphitic carbon in the wear track with each dry/humid environment cycle (Fig. 2b).

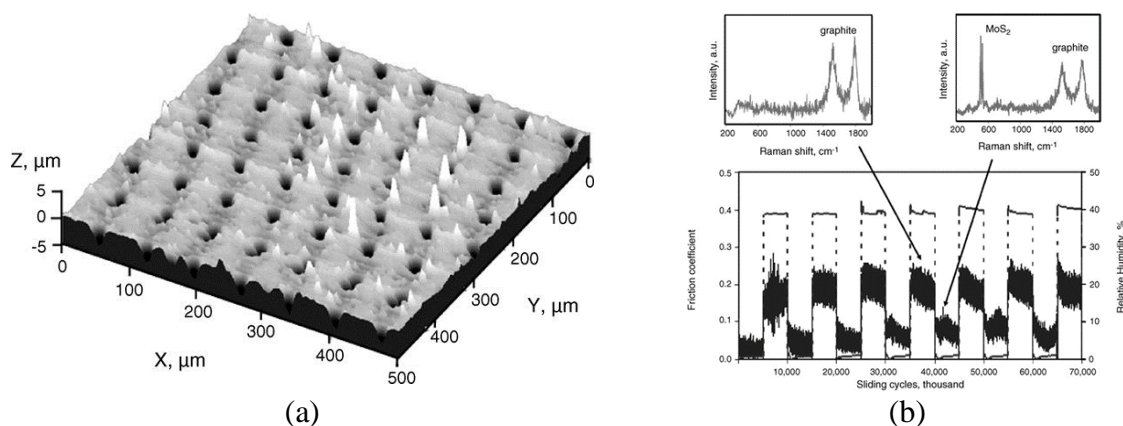


Fig. 2. (a) Laser textured TiCN surface before applying a top burnished chameleon MoS<sub>2</sub>/graphite/Sb<sub>2</sub>O<sub>3</sub> and (b) variation of the friction coefficient (solid line) in sliding tests a cycled environment humidity (dotted line). Insets show Raman spectra taken from wear tracks [4].

### *Cold spray deposited metal matrix coatings with addition of hard carbide phase*

This approach allows fabrication of relatively thick coatings with adaptive lubrication by using metal matrices capable to form low shear strength binary and ternary oxides. As an example, tribological properties of cold sprayed Ni–WC metal matrix composite coatings were

investigated under dry sliding conditions from room temperature to 400°C, including thermal cycling to explore their temperature adaptive friction and wear behavior [5]. The adaptive tribo-oxide formation mechanisms were used to control friction and wear, where both friction coefficients and wear rates were reduced by easy to shear NiO and NiWO<sub>4</sub> oxide formations on sliding contact surfaces. The coating also exhibits low friction behavior during thermal cycling by restoring the lubricious oxides inside the wear track at 400°C temperature intervals [5].

***Duplex technology combining plasma electrolytic oxidation (PEO) with burnished nanocomposite adaptive solid lubricant***

Plasma electrolytic oxidation (PEO) is an attractive technology for improving wear resistance, temperature and corrosive environment protection of aluminum and titanium alloys [6]. PEO results in the hard and well-adhered ceramic coatings which morphology is graded from a dense region near the substrate interface to a porous outside region (Fig. 3a). Such properties provide PEO as an ideal underlying layer for the application of solid lubricants, which can be entrapped in outside reservoirs for the self-adaptive lubrication. In one example, a PEO produced Al–Si–O surface was over-coated with a MoS<sub>2</sub>/Sb<sub>2</sub>O<sub>3</sub>/C chameleon layer (Fig. 3b) for self-adaptive friction behavior and fretting wear reduction [7]. The tests demonstrated low friction coefficients in multiple environments (Fig. 3c) and also considerable reduction in a critical amplitude for the stick-slip transition for fatigue wear mitigation of aluminum and titanium alloy substrates.

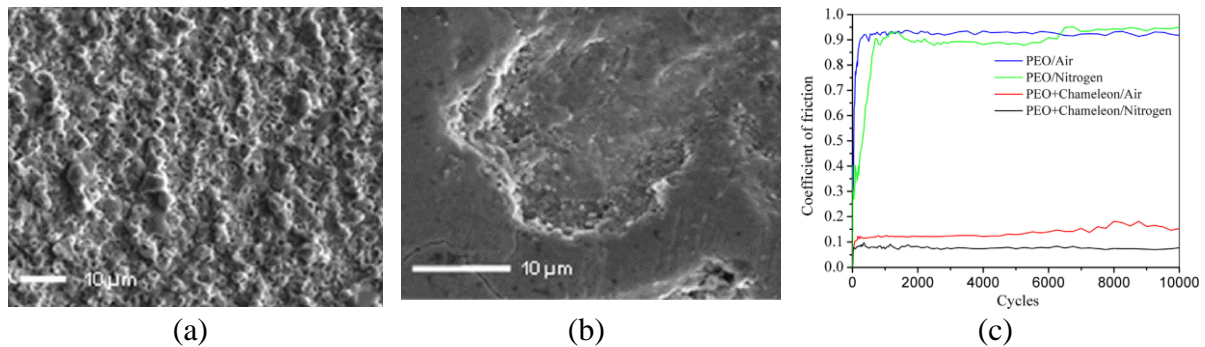


Fig. 3. Surface topography (a) Al–Si–O PEO coating and (b) PEO/chameleon duplex coating. Coefficient of friction evolution of PEO and PEO/chameleon coatings against steel in fretting wear with about 1.6 GPa contact pressures and 100 µm stroke amplitude [7].

***Self-propagating high temperature synthesis (SHS) of sputtering targets and electro spark deposition (ESD) electrodes for surface engineering of tribological coatings***

SHS is versatile technology allowing for the synthesis of complex composition ceramic materials leading to virtually unlimited combinations of hard oxide, borides, nitrides and carbides [8], which makes it attractive for engineering adaptive wear protective surfaces. SHS was used extensively to manufacture a number multicomponent targets for hybrid magnetron sputtering and ion beam depositions, including for the hybrid PVD growth of self-adaptive low friction and wear coatings, such as TiAlSiCN/MoSeC [9], TiCrBN/WSe<sub>x</sub> [10] and other.

SHS was also widely used for fabrication of electrodes for ESD processes, which produce hard, low wear and oxidation resistant protective coatings with an excellent adhesion to metal alloy substrates due to metallurgical and chemical mixing of deposited electrode material with substrate surfaces in spark discharges. Nanostructured ESD electrodes made of cemented carbides (WC, TiC) and Ni matrices provide adaptive tribological coatings, capable for easy to shear oxide formations, and additions of refractory nano-powders (ZrO<sub>2</sub>, Al<sub>2</sub>O<sub>3</sub>, NbC, Si<sub>3</sub>N<sub>4</sub>, W, Mo, WC, WC–Co, and diamond) into SHS powders lead to further improvements of wear and friction reducing ESD coatings [8, 11].



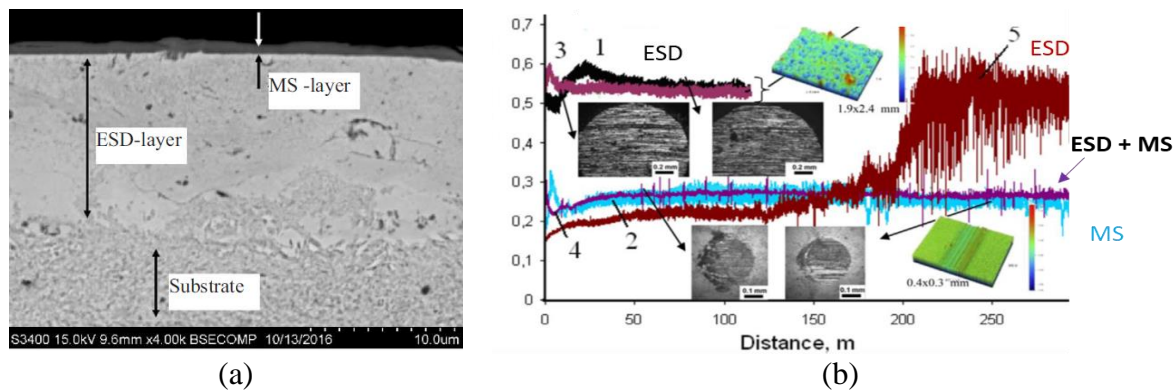


Fig. 4. ESD + MS duplex coating cross section and results of sliding friction tests against steel counterparts for coatings prepared by ESD, magnetron sputtering, and duplex MS-ESD [12].

Exothermic SHS reactions can be initiated by electric discharges within an inter-electrode space to provide coatings with high density, mechanical strength and adhesion [8]. The ESD technology was also combined with magnetron sputtering (MS). In this duplex MS-ESD technology an underlying relatively thick Ti–C–Ni–Fe layer is obtained by ESD for load support and high toughness, whereas a top Ti–C–Ni–Al layer is fabricated by sputtering to improve coating wear, corrosion resistance, and provide a stable and low friction coefficient behavior (Fig. 4) [12].

1. A.A. Voevodin, C. Muratore, S.M. Aouadi, Hard coatings with high temperature adaptive lubrication and contact thermal management: review, *Surf. Coat. Technol.*, 2014, vol. 257, pp. 247–265.
2. A.A. Voevodin, C. Muratore, J.S. Zabinski, Chameleon or smart solid lubricating coatings, in Q.J.Wang and Y.-W.Chung (Eds.) *Encyclopedia of Tribology*, Springer, 2012, pp. 347–354.
3. A.A. Voevodin, J. Bultman, J.S. Zabinski, Investigation into a 3-dimensional processing of tribological coatings, *Surf. Coat. Technol.* 1998, vol. 107, pp. 12–19.
4. A.A. Voevodin, J.S. Zabinski, Laser surface texturing for adaptive solid lubrication, *Wear*, 2006, vol. 261, pp. 1285–1292.
5. T. Torgerson, M. Harris, S. Alidokht, T. Scharf, S.M. Aouadi, R.R. Chromik, J.S. Zabinski, A.A. Voevodin, Room and elevated temperature sliding wear behavior of cold sprayed Ni–WC composite coatings, *Surf. Coat. Technol.*, 2018, vol. 350, pp. 146–145.
6. A.L. Yerokhin, X. Nie, A. Leyland, A. Matthews, S.J. Dowey, Plasma electrolysis for surface engineering, *Surf. Coat. Technol.*, 1999, vol. 122, pp. 73–93.
7. Y.-F. Liu, T. Liskiewicz, A.L. Yerokhin, A. Korenyi-Both, J.S. Zabinski, M. Lin, A. Matthews, A.A. Voevodin, Fretting wear behavior of duplex PEO/chameleon coating on Al alloy, *Surf. Coat. Technol.*, 2018, vol. 352, pp. 238–246.
8. E.A. Levashov, A.S. Mukasyan, A.S. Rogachev, D.V. Shtansky, Self-propagating high-temperature synthesis of advanced materials and coatings, *Int. Mater. Rev.*, 2017, vol. 62, pp. 203–239.
9. A.V. Bondarev, Ph.V. Kiryukhantsev-Korneev, A.N. Sheveiko, D.V. Shtansky, Structure, tribological and electrochemical properties of low friction TiAlSiCN/MoSeC coatings, *Appl. Surf. Sci.*, 2015, vol. 327, pp. 253–261.
10. D.V. Shtansky, A.N. Sheveiko, D.I. Sorokin, L.C. Lev, N. Mavrin, Ph.V. Kiryukhantsev-Korneev, Structure and properties of multi-component and multilayer TiCrBN/WSe<sub>x</sub>

coatings deposited by sputtering of TiCrB and WSe<sub>2</sub> targets, *Surf. Coat. Technol.*, 2008, vol. 202, pp. 5953–5961.

11. E.A. Levashov, A.E. Kudryashov, P.V. Vakaev, Prospects of nanodispersive powder applications in surface engineering technologies, in: A.A. Voevodin, D.V. Shtansky, E.A. Levashov, J.J. Moore (Eds.), *Nanostructured thin films and nanodispersion strengthened coatings*, Kluwer, 2004, pp. 231–240.
12. P.V. Kiryukhantsev-Korneev, A.N. Sheveyko, N.V. Shvindina, E.A. Levashov, D.V. Shtansky, Comparative study of Ti–C–Ni–Al, Ti–C–Ni–Fe, and Ti–C–Ni–Al/Ti–C–Ni–Fe coatings produced by magnetron sputtering, electro-spark deposition, and a combined two-step process, *Ceram. Int.*, 2018, vol. 44, pp. 7637–7646.

## SYNTHESIS AND CHARACTERIZATION OF BN/Pt AND BN/Au NANOHYBRIDS AS PERSPECTIVE CATALYSTS

I. N. Volkov<sup>\*a</sup>, A. M. Kovalkii<sup>a</sup>, and D. V. Shtansky<sup>a</sup><sup>a</sup>National University of Science and Technology MISiS, Moscow, 119049 Russia

\*e-mail: ilia.volkov@outlook.com

DOI: 10.24411/9999-0014A-2019-10187

For several years BN nanostructures attracted a great attention from material science community as perspective material for various applications in catalysis, drug delivery, tribology and structural materials. Such a wide range of applications is associated with its unique combination of physical and chemical properties, such as low specific density, high thermal stability, oxidation resistance, excellent dispersion stability and transparency, enhanced adsorbing capacity, and a wide band gap [1]. Here we report synthesis and characterization of BN/Pt and BN/Au nano hybrids as perspective catalysts.

Hexagonal BN (h-BN) nanoparticles were synthesized by CVD method using FeO, MgO, SnO, H<sub>3</sub>BO<sub>3</sub>, and B precursors and various Ar and NH<sub>3</sub> gas flow rates. The synthesis temperature was 1200–1300°C [2]. BN/Au hybrids were synthesized by chemical deposition method from gold chloride acid solution in polyethylene glycol. BN/Pt hybrids were obtained by chemical deposition from platinum hydrochloric acid solution flowed by reduction in hydrogen flow at  $T = 350^{\circ}\text{C}$ .

Nanohybrids were analyzed by scanning and transmission electron microscopy using JSM7600F and JEM 2100 instruments (Jeol Ltd.).

The synthesized BN particles had external dimension 80–150 nm. Immobilized agents had average size less than 10 nm (Figs. 1, 2).

Catalytic properties of BN/Au and BN/Pt systems were investigated toward carbon monoxide (CO) oxidation. The best results were obtained for the BN/Pt catalyst: the onset and full conversion temperatures were 154 and 184°C, respectively.

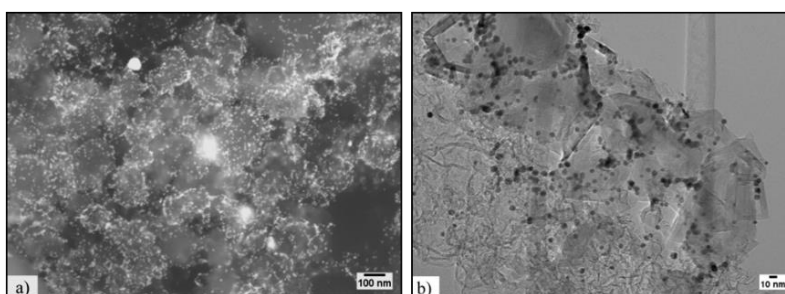


Fig. 1. SEM (a) and TEM (b) images of BN/Au hybrid nanoparticles.

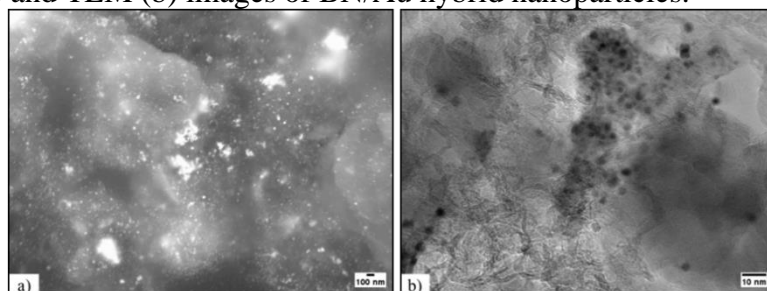


Fig. 2. SEM (a) and TEM (b) images of BN/Pt hybrid nanoparticles.

The work was supported by the Russian Science Foundation (Project no. 18-58-53034).

1. D.V. Shtansky, K.L. Firestein, D.V. Golberg, Fabrication and application of BN nanoparticles, nanosheets and their nanohybrids, *Nanoscale*, 2018, vol. 10, pp. 17477–17493.
2. A.M. Kovalskii, A.T. Matveev, O.I. Lebedev, I.V. Sukhorukova, K.L. Firestein, A.E. Steinman, D.V. Shtansky, D. Golberg, Growth of spherical boron oxynitride nanoparticles with smooth and petalled surfaces during a chemical vapour deposition process, *Crystengcomm.*, 2016, vol. 18, pp. 6689–6699.

## SHS OF SOLID SOLUTIONS IN Ta–Zr–C SYSTEM: MACROKINETIC FEATURES, PHASE/STRUCTURE FORMATION, AND PHASE STABILITY

S. Vorotilo<sup>\*a</sup>, E. A. Levashov<sup>a</sup>, K. Sidnov<sup>a</sup>, and E. I. Patsera<sup>a</sup>

<sup>a</sup>National University of Science and Technology MISiS, Moscow, 119049 Russia

\*e-mail: s.vorotilo@misis.ru

DOI: 10.24411/9999-0014A-2019-10188

Two approaches were used for the preparation of the reaction mixtures Ta–Zr–C: mechanical activation (MA) in a planetary ball mill (PBM) and mixing in a ball mill. The composition of reaction mixtures was calculated for the formation of solid solutions TaC–10, 30, and 50 at % ZrC. MA of the Ta–Zr–C mixtures was performed in the PBM AIR-0.015. MA was carried out in the air atmosphere during 5, 10, and 15 min. PBM was equipped with the steel jars and balls, while ball mill was equipped with hard-metal jar and balls. In the case of ball milling of reaction mixtures during 4 h, a macro-homogeneous mixture is formed with a uniform distribution of carbon black on the surface of the metal particles. Metal particles retain their size and form. During the MA of Ta–Zr–C mixtures, intense plastic deformation of the metal particles takes place. Zirconium particles are drastically reduced in size. Formation of composite granules (100–300 μm) takes place, which are comprised of layers of tantalum (25–40 μm), zirconium (1–2 μm), and carbon black.

Although the increase in the MA duration for Ta–Zr–C mixtures led to the accumulation of excess energy in the form of defects of crystal lattice of Ta, increase in the MA duration over 15 min MA is not viable due to emergence of the carbide phases during the MA and substantial increase of inflammability of the MA mixtures. The dependence of heat release on the MA duration was investigated using the mixtures TaC–50% ZrC. When the mixture was prepared in ball mill (MA duration was 0 min) the heat release ( $Q$ ) was equal to 70 kJ/mol; after 5, 10, and 15 min of MA  $Q = 70, 75,$  and 74 kJ/mol, correspondingly.

MA mixtures activated during the 10 min demonstrated the highest reaction activity and were subsequently used for the synthesis of the single-phase solid solutions specimens. However, for the investigation of the macrokinetic parameters and the mechanisms of the structure and phase formation in the combustion wave, it is expedient to use the mixtures prepared in a ball mill because the green specimens prepared from MA mixtures disintegrate during the combustion. For the Ta–Zr–C system, the highest combustion velocity (up to 1.17 cm/s) and combustion temperature (up to 2890°C) were measured for the TaC–10% ZrC mixture. Effective activation energies for the mixtures TaC–10, 30, and 50% ZrC were estimated to be 206, 194, and 213 kJ/mol correspondingly, which is close to the data reported in the literature for the SHS of TaC. The thermograms of combustion for all the measured specimens were characterized by a single peak; combustion occurred in the stationary regime.

To elucidate the mechanisms of the structure and phase formation, the techniques of time-resolved XRD (TRXRD) and quenched combustion front (QCF) were applied for the mixtures TaC–10, 30, and 50% ZrC. TRXRD demonstrated that for the mixtures TaC–10, 30, and 50% ZrC the sequence of phase formation in the combustion front was similar. After 1 s after the beginning of the analysis, the decrease in the intensity of the peaks of initial reagents and emergence of peaks of TaC and ZrC were observed. After 2 s, the peaks of initial reagents vanished, while the intensity of the peaks of TaC and ZrC increased. After 3 s, the displacement of the peaks of TaC and ZrC was observed, suggesting the formation of solid solution (Ta,Zr)C.

Combustion fronts were quenched in a copper wedge. In all the investigated Ta–Zr–C mixtures, in the pre-heating zone, the agglomerates of highly dispersed TaC particles were formed. These agglomerated were located in the close proximity with the Zr particles which retained their initial morphology, suggesting that in the pre-heating zone the formation of TaC occurs via the gas-transport mechanism by Boudoir-Bell reaction. However, while in the case of TaC–10% ZrC and TaC–30% ZrC, TaC in the pre-heating zone formed porous “fractal-like” aggregates, in the case of TaC–50% ZrC the TaC particles in the pre-heating zone had equiaxial shape with a size of up to 500 nm and were distributed uniformly on the surface of tantalum particles.

In the combustion zone, zirconium melted, and tantalum partially dissolved into it. For the mixtures TaC–10, 30% ZrC in the combustion zone the zirconium and tantalum carbides formed nanostructured ring structures (rings width was up to 100 nm, diameter was up to 400–600 nm). The formation of these structures was evidently caused by the capillary spreading of the local micro-volumes of zirconium-based melt on the surface of carbon black with the subsequent crystallization of carbides. Simultaneously, in the located nearby relatively large Ta particles (up to 20  $\mu\text{m}$ ), diffusion layers were formed with a gradient of C concentration. Evidently, in the case of Ta particles which did not interact with the zirconium melt, TaC is formed via the gas-phase mechanism. In the case of TaC–50% ZrC mixture, in the combustion zone, equiaxial carbide grains (up to 0.7  $\mu\text{m}$ ) were present instead of ring-shaped structures, suggesting that the formation of the ZrC occurs via the dissolution of C in the volume of Zr melt and precipitation of ZrC grains from the oversaturated solution instead of capillary spreading of the Zr melt.

In the case of SHS of Ta–Zr–C mixtures prepared in a ball mill, the formation of single-phase solid solution did not occur due to the relatively high heterogeneity of the reaction mixture. Single-phase carbide solid solutions TaC–10, 30, and 50% ZrC were produced by the MA-SHS corresponding to the following optimized regimes: (1) preparation of the mixture with 1.5 wt % excess C over the stoichiometry; (2) 10 min of MA in PBM AIR in the air atmosphere; (3) SHS of MA mixtures in the “sand mold” with the reaction mixture to “chemical oven” ratio of 1:1.5. The synthesized SHS products were characterized by the porosity of 50%. Ball-milling of the SHS products produced the powders of single-phase carbide solid solutions with the grains size up to 10  $\mu\text{m}$  for the subsequent sintering.

This work was carried out with financial support from the Russian Science Foundation in the framework of project no. 19-19-00117.

# ULTRAFINE-GRAINED BORON CARBIDE CERAMICS FABRICATED VIA ULTRAFAST SHS-QP SINTERING ASSISTED BY HIGH-ENERGY BALL MILLING

W. Wang<sup>\*a</sup>, Z. Zhang<sup>b</sup>, Z. Fu<sup>a</sup>, H. Wang<sup>a</sup>, J. Zhang<sup>a</sup>, and W. Ji<sup>a</sup>

<sup>a</sup>State Key Laboratory of Advanced Technology for Materials Synthesis and Processing, Wuhan University of Technology, Wuhan 430070, China

<sup>b</sup>College of Materials Science and Engineering, Hebei University of Engineering, Handan 056038, China

\*e-mail: wangwm@hotmail.com

DOI: 10.24411/9999-0014A-2019-10189

Boron carbide ( $B_4C$ ) is a structural material with outstanding physical and chemical properties, including high melting point, good wear resistance, excellent chemical stability and good neutron absorption capability [1, 2]. The combined low density ( $2.52 \text{ g/cm}^3$ ) and high hardness properties of  $B_4C$  make it distinct from other structural materials. Researchers aim to fabricate dense  $B_4C$  ceramics with a fine-grained structure because these characteristics maintain the excellent properties of  $B_4C$  materials [3, 4]. However, due to the low self-diffusion coefficient results from the strong covalent bonding, low plasticity and high resistance to grain boundary sliding, high sintering temperature ( $> 2100^\circ\text{C}$ ) and long holding time ( $> 40 \text{ min}$ ) are necessary to obtain dense  $B_4C$  ceramics using mainstream pressureless or hot-pressing sintering. High sintering temperature, long holding time and slow heating rate not only lead to considerable time and energy cost but also serious grain growth. Therefore, fabrication of dense  $B_4C$  with fine-grained microstructure is considerably difficult.

In this paper, ultrafine-grained boron carbide ceramics with ultrahigh hardness were fabricated via a unique combination of high-energy ball milling and self-propagating high-temperature synthesis plus quick pressing (SHS/QP) method (Fig.1a).

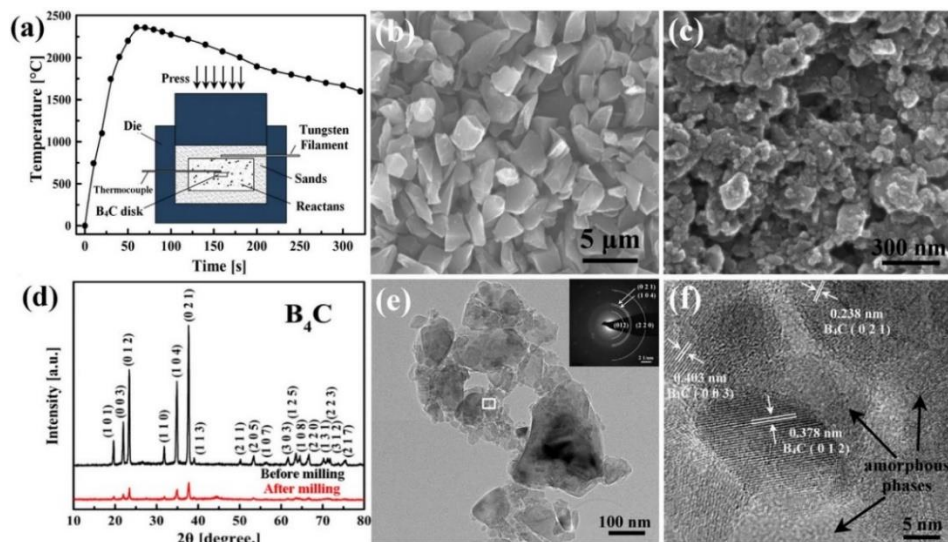


Fig. 1. (a) Schematic representation of the SHS/QP process and temperature curve versus time during the SHS/QP process. (b)–(f) Characteristics of  $B_4C$  powders before and after milling. (b) SEM image of commercial  $B_4C$  powders. (c) SEM image of milled  $B_4C$  powders. (d) XRD patterns of  $B_4C$  powders before and after milling. (e) TEM image with SAED pattern of milled powders. (f) HRTEM image of the white rectangle in (e).

Ultrafine powders obtained by milling possess a disordered character (Figs. 2b–2f). During the SHS/QP, the tiny particles in the milled powders are integrated into neighbouring large particles to form ceramic grains, most of the grain sizes in the ceramics cluster range from 100 to 400 nm, and only approximately 2.2% grains with a size less than 100 nm are found, as shown in Fig. 2c. The average grain size of the ceramics is approximately 290 nm.

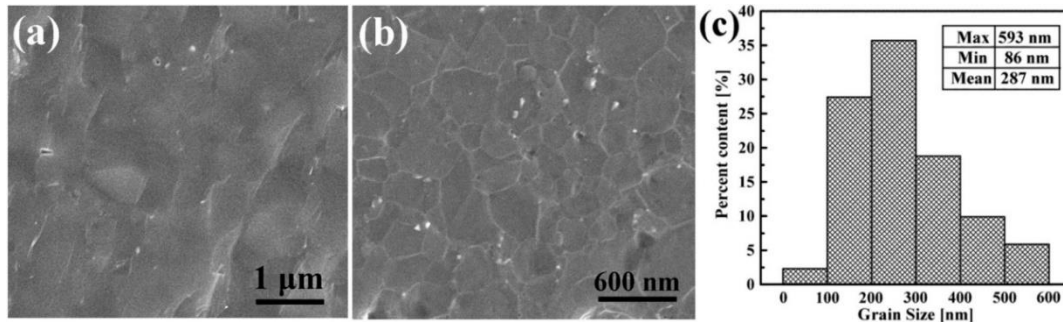


Fig. 2. Microstructure and grain size distribution of  $B_4C$  ceramics. (a) SEM image of fracture surface. (b) SEM image of polished and etched surface. (c) statistical chart of grain size distribution.

After SHS/QP, a few amorphous areas and high-density defects were still observed in ceramics (Fig. 3). The ceramics possess high relative density (approximately 99.2%) and ultrafine grain, but with a weak degree of crystallinity which weakens hardness. Heat treatment can improve crystallinity while maintaining the ultrafine grain of the  $B_4C$  ceramics, thereby increasing the hardness of the ceramics from 31 GPa to 40 GPa (Table 1).

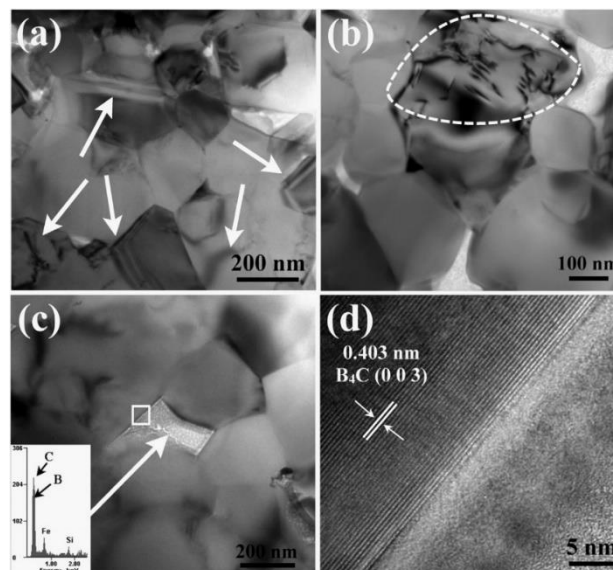


Fig. 3. TEM images with EDS of  $B_4C$  ceramics. (a) ordinary dislocations. (b) high-density short dislocations. (c) amorphous region. (d) HRTEM image of the white rectangle in (c).

Table 1. Characteristics of  $B_4C$  ceramics.

| $B_4C$ samples          | Before heat treatment | After heat treatment |
|-------------------------|-----------------------|----------------------|
| Relative density (%)    | $99.2 \pm 0.4$        | $99.1 \pm 0.5$       |
| Average grain size (nm) | 287                   | 294                  |
| Vickers hardness (GPa)  | $31.3 \pm 1.6$        | $39.8 \pm 1.3$       |



1. A.K. Suri, C. Subramanian, J.K. Sonber, T.S.R.C. Murthy, Synthesis and consolidation of boron carbide: a review, *Int. Mater. Rev.*, 2010, vol. 55, pp. 4–40.
2. V. Domnich, S. Reynaud, R.A. Haber, M. Chhowalla, Boron carbide: structure, properties, and stability under stress, *J. Am. Ceram. Soc.*, 2011, vol. 94, pp. 3605–3628.
3. Z. Liu, D. Wang, J. Li, Q. Huang, S. Ran, Densification of high-strength  $B_4C$ – $TiB_2$  composites fabricated by pulsed electric current sintering of  $TiC$ – $B$  mixture, *Scr. Mater.*, 2017, vol. 135, pp. 15–18.
4. Z. Zhang, X. Du, Z. Li, W. Wang, J. Zhang, Z. Fu, Microstructures and mechanical properties of  $B_4C$ – $SiC$  intergranular/intragranular nanocomposite ceramics fabricated from  $B_4C$ ,  $Si$ , and graphite powders, *J. Eur. Ceram. Soc.*, 2014, vol. 34, pp. 2153–2161.

PIONEER RESEARCH AND BREAKTHROUGHS CPI IN THE FIELD OF SHS CATALYSTS, PIGMENTS AND TPS FOR SPACE APPLICATION THAT INITIATED NEW COMBUSTION SYNTHESIS RESEARCH DIRECTIONS IN THE WORLD

G. Xanthopoulou<sup>\*a</sup> and G. Ksandopulo<sup>b</sup>

<sup>a</sup>Institute of Nanoscience and Nanotechnology, NCSR “Demokritos”,  
Agia Paraskevi Attikis 15310, Greece

<sup>b</sup>Institute of Combustion Problems, Almaty, 050012 Republic of Kazakhstan

\*e-mail: g.xanthopoulou@inn.demokritos.gr

DOI: 10.24411/9999-0014A-2019-10190

- *Pioneering studies on the mechanisms of structural formation during combustion synthesis of catalysts.* Study of combustion wave structure of SHS systems was performed [1]. Conditions for “freezing” combustion wave were found. Mechanism of reactions and structure formation in different zones of combustions were discovered. For the first time clearly showed that, unlike the short-term processes in the combustion front (i.e. in the zone of chemical interaction), a slower process of the cooling and crystallization process (i.e. following the combustion front) is the main determinant of practical importance for physical properties of the target SHS products (this finding creates the basis for developing qualitatively new and effective SHS methods).
- *For the first time in the world detailed SHS catalysts production technology developed.* Now at more than 50 countries researchers follow those studies. Such interest to SHS catalyst can be explained by high activity of catalysts prepared by this methods and advantages of SHS method in comparison with traditional methods of preparation of catalysts. The main differences of SHS method for catalysts production in comparison with other methods of preparation of catalysts are: very high heating and cooling rates:  $10^3$ – $10^6$ °C/s, very short completion times, of the order of minutes which leads to formation of high defect structure responsible for high activity of SHS catalysts. Method is attractive for industrial production: much lower energy consumption than traditional production methods, much lower energy costs, possibility for “just-in-time” manufacturing, high productivity, cheap catalysts, relatively simple process - easily adaptable to industrial scale, controlled physico-chemical properties of the products, large range of new materials which can be used in catalysis, it has wide diapason of structural forms of products - from granules of different size to blocks of honeycomb structure and different geometric forms. SHS catalysts have low surface area (usually 0.5–5 m<sup>2</sup>) because of high combustion temperatures. The high specific catalytic activity at such low surface areas is related to both the SHS materials unique composition as well as their very high atomic defect concentration resulting from the SHS process conditions. Influence of initial batch composition, particle size of each material in the initial batch, binder concentration, pressure, drying conditions, preheating temperature and speed, initiation combustion conditions, velocity of combustion, temperature of combustion, time of cooling on the chemical composition, structure, physical properties and activity in different catalytic processes studied. The SHS method is being developed for the production of a new class of active catalyst materials based on metals, alloys, metal oxides, borides, carbides and spinels for various applications [2, 3]. In the case of heterogeneous spinel catalysts, it is well known that local distortions of the primary crystalline lattice act as active catalytic centers. The nature and extent of such distortions depends on the atomic radii of the lattice ions, the type and

parameters of the crystalline lattice and atomic bonds, the size and dispersion of the crystallites, the size and nature of the dopant ions etc. It was found that functionally significant, changes in the crystal lattice parameters of the active components of a spinel catalyst are usually caused by introducing various modifying additives, which increase the number of defects. For a particular catalyst and chemical process, there appears to exist an optimum amount of lattice distortion that gives high catalytic activity. The results indicate that, it may be possible to predict or “tune” the activity of a catalytic system for a particular process, by appropriate “design” of the crystal lattice. This could be done by adding specific ions which are known to produce the needed amount of distortion. SHS appear to be ideal techniques for this, since the materials synthesised by combustion synthesis are often metastable and the atomic lattice remains distorted after synthesis due to the rapid heating and cooling rates. This has become clear during studies of the mechanisms of spinel formation in the combustion wave, secondary structure formation in the process of further reaction of components and final structure formation in the process of cooling and is particularly noticeable in the formation of intermediate and non-stoichiometric compounds. The influence of the existence of distorted atomic lattice on catalytic activity has been studied for a number of spinel systems. By comparing the published data for SHS catalysts for various processes, it was possible to confirm the above conclusion and develop predictive criteria for the composition and atomic crystal structure giving the highest catalytic activity. Specifically, the trend of crystal lattice spacing was found to correlate with the trend of the length of the bonds of organic substances which must be adsorbed, broken on the catalyst surface and recombined with others for the synthesis of the reaction product. As a result, it is possible to “tune” the lattice spacing for maximum catalytic activity by doping the material with ions of appropriate radii, thereby distorting the crystal lattice by the correct amount. Very active SHS catalysts were developed for different processes. *Development of SHS catalysts for dehydrodimerization of methane.* The SHS method has been used to produce a range of active manganese-based catalysts for the oxidative dehydrodimerization of methane (for the production of ethylene). In the best case found, ethylene yield was found to reach about 26% at a selectivity of 85% and methane conversion of 30.2%. Some ethane, propene, propane and hydrogen were also obtained. The catalytic activity was found to be enhanced by careful control of SHS conditions and various post-synthesis treatments of the materials [4, 5]. The scheme of reactions during SHS discovered, supplemented by X-ray photoelectron spectroscopy measurements and by electron paramagnetic resonance (EPR), allowed for elucidation of the formation of the various products that appear in the synthesized material. *Development of SHS catalysts for hydrogenation of olefins.* SHS catalyst on the base of Ni–Al alloys were produced and studied in the hydrogenation of olefins with double and triple bonds. Influence of composition and different synthesis parameters on the physico-chemical characteristics studied and found out, that SHS catalysts are more active than Ni–Raney. *Development of SHS catalysts for diesel fuel, petrol pyrolysis and dehydrogenation.* Chemical gases and liquids, such as ethene, ethane, propene, propane, benzene and toluene, are usually industrially produced from petrol (gasoline) or diesel. It was found, that increased porosity increases the yield of liquid products and coke but decreases the yield of ethane and other olefines. Coke formation is a serious problem with catalysts with small pores. Coke tends to clog the entrance to small pores thereby quickly decreasing catalytic activity. SHS method offer simple way to regulate pores size and obtain low surface area catalysts with high specific activity. The substitution of Mg by Co in the Mg–Al–O spinel system deforms the structure changing slightly the crystal lattice parameters, depending on the amount of Co in the lattice, which can result in a significant number of lattice defects. The incorporation of Co in the spinel lattice resulted also in improved conversion efficiency. The sum of the ethene and propene yield was reaching 62 vol %. When Co was increased even further in the starting materials, excess oxide of Co appeared in the SHS product which changed the overall function of the catalyst to that of dehydrogenation

with a  $H_2$  yield of up to 80%. Such enhanced hydrogen yield suppresses the possibility of ethene production, but this catalyst is very good for dehydrogenation process. The catalytic activity of a mixed spinel material 0.6%  $CoAl_2O_4/99.4\%$   $MgAl_2O_4$  was also compared with that of a commercial catalyst ( $KVO_3$  on a mullite/ corundum carrier) used in the production of ethene. The relative yield of ethene on the Co-containing spinel SHS catalysts was measured to be 38 vol % as compared to 28 vol % for the  $KVO_3$  catalyst. Furthermore, the coke accumulation on the SHS catalyst was on average 3.7 times lower than on the commercial catalysts [6]. *Development of SHS catalyst for methane reforming to synthesis gas.* Co-based catalysts were developed and their activity studied in partial oxidation of methane to synthesis gas. Two section reactor was build and kinetic of oxidation was studied. *Development of SHS catalyst for partial oxidation of methane to methanol.* Optimization of catalyst composition and conditions of process and study influence of these parameters on the yield of product were studied. *Development and study of SHS catalysts for deep methane and CO oxidation.* Those processes are very important in industry as it is directly applicable to the purification of exhaust gases from a large spectrum of industries, vehicles, catalytic heat generators etc. The efficiency of catalytic oxidation in exhaust gases can be enhanced if finely comminuted catalysts are dispersed on carriers with very high surface area in contact with the gas flow. The SHS materials studied include various compositions based on the systems Al–Mn–Mg–O, Mg–Cr–O, Mg–Al–O, Mg–Cr–Al–O and Cu–Cr–O with and without the addition of Cerium oxide and an epoxide additive as catalysts and as catalysts on SHS carriers. It is evident from the results that the most active catalysts for this process are those containing chromium and especially manganese (100% conversion of methane) and Cu–Cr–O catalysts for CO oxidation (they are as active as catalysts on the base of noble metals).

- *Development (for the first time) of SHS carriers of honeycomb structure by extrusion with further SHS.* Honeycomb-shaped blocks were manufactured by extrusion of the green powders and in-situ SHS and were found to satisfy most of the carrier requirements for mechanical properties, surface and to have good thermal stability. Influence of number of parameters were studied for optimisation of extrusion process, drying and SHS method parameters for receiving good quality carriers.
- *For the first time in the world the SHS pigments production technology developed and color regulation mechanism determined.* The above method for predicting and “tuning” the functionality of various spinels made by SHS is also applicable for spinel pigments. By the addition of appropriate dopants, it is possible to produce almost any colour and hue of the spinel-based pigments, as confirmed from the results of many years’ work on colour formation in SHS materials [7]. For the first time color formation mechanism in SHS pigments determined. It was found that the major factors responsible for formation of colour in specific spinel pigments, were the type of ion (Co, Ni, Mn, Cr, Fe, Cd, Cu etc.), atomic size and structure of the dopant and the lattice position in which it enters, which decides the size and type of lattice distortion. The ionic radius of the dopant metal ion was found to be correlated to the wavelength of the reflected light from each pigment, i.e. the colour of the pigment. For example, in the system Co–M–O (where M is the metal ion), the wavelength of the reflected light was found to decrease monotonically with increasing ionic radius of dopant metal ion. It is expected that the above predictive process would be applicable to all types of functional spinels produced by SHS and SCS with ordered structure and composition. The spinel structure is fairly empty and flexible in the accommodation of non-stoichiometry, which is characterized by an excess of cations, located both tetrahedral and octahedral sites. Thus, cations in the spinel structure can be substituted by many other cations to give multicomponent system, whose properties can be regulated by proper selection of the cations, appropriate adjustment of composition and structure, lattice parameters. For the first time were synthesised SHS pigments at about 1000 hues of colors. Studied their characteristics as pigments and characteristics of plastics, paints, ceramic, porcelaine,

cosmetics with those pigments. All characteristics were also checked in different plants. Full animal positive tests (2 years animals study) were done for SHS pigments application in cosmetic. Catalogue of 1000 pigments hues was prepared. Catalogues of tiles with SHS pigments and glaze (tiles and glaze of each plant we work with) were also made for each plant. It was found that those pigments can be used in industry (documents-tests from ceramic, plastic, oil and emulsion paint, porcelain plants from Russia and Kazakhstan were received). Production of these pigments started in 1991 in the industrial scale.

- *Basic theoretical studies of interaction of SHS pigments with glazes.* Investigating of physico-chemical properties of glazes of different composition with SHS pigments on the base of vanadium system. Segregation phenomenon during combustion in this layer discovered. It was found that intermediate compositions of SHS and non-equilibrium conditions of crystallization produce mable effect in thing layers. Developed new low temperature melted glazes for high speed production of ceramic tiles [8]. Those glazes used in Uralsk plant.
  - *Recycling and exploitation of solid industrial wastes and rare materials by SHS – production of ceramic products.* Industrial wasted of metallurgical, power plants, chemical plants production of Kazakhstan were studied and used for production ceramic tiles, wollastonite pigments and catalysts. For example, chromate concentrate was used for pyrolysis of diesel fuel. The elaborated SHS method of immobilization of radioactive and chemically dangerous components spread in grounds was developed [9].
  - *Refractories-TPS for Tupolev planes.* Refractories on the base of Mg–Al–O spinel + MgO were developed according to Tupolev construction buro requerements and produced 200 tiles.
  - *Thermal protection systems based on SHS ceramics for the “Buran Space Shuttle”.* the development of heat-insulation shield of high-temperature heating block for heating to temperatures 1900–2000°C was performed. At about 300 tiles with required characteristics (working temperature 2500°C, with density 0.5 g/cm<sup>3</sup>) were developed produced by SHS for “Buran” shuttle (USSR period) and placed on it, reactive bonding of high temperature ceramic (> 2500°C) also was studied [10].
1. G. Gladoun-Xanthopoulou, V. Sergienko, G. Ksandopulo, The combustion wave structure of SHS-systems based on the Compounds of iron and manganese oxides, *Int. J. Self-Propag. High-Temp. Synth.*, 1997, vol. 6, no. 4, pp. 399–404
  2. G. Xanthopoulou, I. Orynbeikova, G.I. Ksandopoulo, E. Grigorian, A. Merzhanov, I. Borovinskaya, M. Nersesian, Reception method of catalysts for the synthesis of organic substances, Patent N 1729028 (USSR), 1991.
  3. G. Gladoun-Xanthopoulou, Self-propagation high-temperature synthesis of catalysts and supports, *Int. J. Self-Propag. High-Temp. Synth.*, 1994, vol. 3, no. 1, pp. 51–58.
  4. G.I. Ksandopulo, G. Gladoun-Xanthopoulou, Z. Leiman, N. Yakubova, N. Sebyraeva, Batch for the catalysts reception for synthesis of ethylene, Patent N1805578 (USSR), 1992.
  5. G. Xanthopoulou, Oxidative dehydrodimerization of methane using lead and samarium based catalysts made by self-propagating high-temperature synthesis, *Appl. Catal. A General*, 1999, vol. 185, pp. L185–L192.
  6. G. Xanthopoulou, Oxide catalysts for pyrolysis of diesel fuel made by self-propagating high-temperature synthesis. Part I: cobalt-modified Mg–Al spinel catalysts, *Appl. Catal. A General*, 1999, vol. 182, no. 2, pp. 285–295.
  7. G. Xanthopoulou, SHS pigments, *Amer. Cer. Soc Bull.*, 1998, vol. 77, pp. 87–96.
  8. G. Gladoun-Xanthopoulou, T. Chernoglazova, G. Ksandopulo, Interaction of SHS-pigments with glazes in films on the carrier, *Int. J. Self-Propag. High-Temp. Synth.*, 1997, vol. 6, no. 1, pp. 71–76.

9. G. Gladoun-Xanthopoulou, V.D. Gladoun, L. Astapenkova, Investigation of chromate concentrates as resources for high temperature synthesis of catalysts, *J. Compl. Utilisation Mineral Resour.*, Alma-Ata, 1990, no. 10, pp. 49–53.
10. G. Gladoun-Xanthopoulou, E. Baymouhamedov, A. Sherinhanov, SHS high-temperature light refractories, *J. Eng. Phys. Thermophys.*, 1993, vol. 65, no. 4, pp. 1024–1025.

DENDRIC 3-DIMENTIONAL STRUCTURE COMBUSTION, FLAME  
BIFURCATION IN REPETITIVE EXTINCTION-IGNITION DYNAMICS,  
LIQUID PHASE SINTERING - A NEW COMPREHENSIVE REACTION  
MECHANISM FOR SCS IN CONDITIONS OF NANO-SCALE  
HETEROGENEITY

**G. Xanthopoulou<sup>\*a</sup>, O. Thoda<sup>a</sup>, S. Roslyakov<sup>b</sup>, E. Levashov<sup>b</sup>, and G. Vekinis<sup>a</sup>**

<sup>a</sup>Institute of Nanoscience and Nanotechnology, NCSR “Demokritos”,  
Agia Paraskevi Attikis 15310, Greece

<sup>b</sup>National University of Science and Technology MISIS, Moscow, 119049 Russia  
<sup>\*</sup>e-mail: g.xanthopoulou@inn.demokritos.gr

DOI: 10.24411/9999-0014A-2019-10191

The synthesis of nanomaterials and the assembly of nanostructures in complexes to become functional is one of the most critical aspects of nanoscience. Thus, it is necessary to develop reliable methods which will be able to produce accurately nanostructures with the desired characteristics such as morphology, stoichiometry and phase purity. A common problem with all techniques in the production of nanomaterials is the formation of clumps. If aggregation occurs, the properties of the material are determined by the size of the agglomerates and not by the size of the nanoparticles. Solution Combustion Synthesis (SCS) is an efficient approach to deliver materials with desirable properties directly in the nanoscale. Nevertheless, it is a very sensitive method and there are many parameters that influence the final materials' properties and microstructure. Here they are:

1. Changing the oxidizer/reducer ratio affects the generated heat from the combustion, thus the cooling time change also. On the other hand, there is a specific time for the formation of metal as well as for its oxidation. Consequently, the maximum in the metal content can be attributed to the initial increase of time for metal formation, while after exceeding critical amount there is enough time for metal oxidation as well [1].

2. At the excess (over stoichiometric concentration) of fuel, the carbon originated from fuel is employed to the soot oxidation reaction lead to rising combustion temperature and resulted in reduction of metal content in the SCS product because of quick oxidation. At the same time, in this conditions carbon is the major element that reduces metal oxide for the production of metal, and not hydrogen as it was in the case of stoichiometric conditions. Thermogravimetric analysis showed that for fuel concentration greater than the stoichiometric ratio between metal nitrate and fuel, the decomposition product (soot) reacts partially during combustion but most of soot oxidation takes place after SCS is completed. This leads to increased sintering and aggregation processes, changing the open shape of the pores to “bottle neck”, changing the ratio between nanomicro and macro pores and consequently changing adsorption–desorption process and catalytic activity.

3. Ratio oxidizer/fuel affects porous structure of nanomaterial and the form of pores. For example, regarding the shape of the hysteresis loops, the adsorption/desorption isotherms of samples with 50 and 125% glycine correspond to type B, suggesting the existence of large number of cylindrical and slit-shape pores with all open sides. On the other hand, the type of loop in samples with 75 and 100% glycine are type C indicating that the pores have a predominately wedge shape. The pore shape affects the adsorption–desorption process during catalysis influencing the exhibited activity of catalysts.

4. It was determined that if crystallites of metal and metal oxide grow, the nanomaterials' surface area reduces accordingly. Usually crystallite size increase with increasing of combustion temperature. But in some cases, by increasing the percentage of fuel (from 50 to 100%) the size of the crystallites is reduced. That can be justified by the increase of the generated gases (CO and CO<sub>2</sub>) as the quantity of carbon increases, leading to quicker cooling rates that result in smaller crystallites. Nanomaterials with smaller crystallites have higher volume of nanopores and higher porosity which lead to enhanced specific surface area.

5. It appears that when the slow heating mode is applied, the metal content in the final nanomaterials is reduced. Moreover, the metal crystallites are also reduced in comparison with quick mode. That can be explained as in the case of slow heating, a big part of the metal nitrate is already decomposed in metal oxide, before the time the mixture reaches its ignition point. As a result, there is less quantity of nitrate available to react and participate in the SCS, leading to less nickel concentration in the final products. Moreover, the lessened quantity of nitrate that participates in the SCS reduces the heat that is emitted from the exothermic reaction. Consequently, there is less sintering process taking place that justifies the reduction in the size of metal crystallites.

6. Dynamic XRD measurements indicate that after the formation of metal, its concentration starts to decrease with time, while the concentration of MeO increases. That explains the reason that the time in the furnace after SCS finalized leads to increasing of MeO/Me phase ratio. By increasing the time in the furnace, the crystallites of both metal and metal oxide are increasing as well due to the sintering process that takes place.

7. Precursor concentration in solvent and nanomaterials room temperature aging on the growth morphology and surface characteristics of Me–MeO nanopowders produced by dendrites combustion during SCS were studied. TEM results highlighted that nanomaterials microstructure is modified by changing the reactants' concentration in water. Thus, the concentration of the initial mixture Me(NO<sub>3</sub>)<sub>2</sub>, fuel in water plays a significant role for the nanomaterials. Aging has an influence on the local monolayer capacities. In the case of fresh nanomaterial and aged nanomaterial the local monolayer changes 2–3 times. Therefore, the monolayer capacity and the time of its maximum is a function of aging time. For the first time, room temperature aging of oxide nanomaterials was investigated, as room temperature aging is new phenomenon for nanomaterials.

8. By comparing the XPS spectrum intensities, it can be clearly seen that by increasingly adding water the concentration of surface oxidized states has increased considerably (it is important for catalyst activity). The reason of changing activity is that MeO structure can result in bridging oxygen structure. These bridging structures can cause problem of adsorption of the hydrogen on the catalyst surface and as consequence to reduce its activity.

9. For the first time it was found that the initial concentration of nitrates in the aqueous solution affects the characteristics and properties of nanomaterials including their final composition, crystallite size and parameters of crystal lattice, pores size distribution and surface area. In addition, the relative amount of water in the initial aqueous solution appears to have a substantial effect on their catalytic activity. The underlying mechanism for this effect appears to be the prolonged persistence and delayed decomposition of hydrates that form during the early preheating stages of SCS. This is especially significant for structure-sensitive catalytic reactions. This work shows for the first time, that compounds, such as hydrates, which form in solution appear to persist even after all the water has evaporated and influence the physico-chemical properties of the products formed during later stages. This apparent "memory effect" exists even during the later sintering stages and may explain many of the difficulties reported in repeating synthesis results since the strength of the initial aqueous solution is generally not taken into consideration during analysis of catalytic synthesis.

10. The dendrites growth conditions appears to be the main factor that is responsible for the observed changes in the crystallite size of the samples, as their structure depends on the



concentration of metal nitrate and fuel in the water. Various dendrites structure indicates that the combustion takes place in different conditions during SCS and the heat distribution during cooling is also affected. IR high speed camera demonstrates combustion in dendrites (Fig. 1). New combustion type is discovered: combustion in dendrites. The more developed the structure of dendrites is, the combustion temperature is lower, the cooling velocity is higher and the size of crystallites is smaller.



Fig. 1. Photograph of the sample during SCS, taken using an IR camera.

The structure and properties of the hydrates in the aqueous electrolyte solutions with different concentrations (i.e., when water quantity changes) depend on the substitution and ion implantation and the method of formation of hydrates and other ion complexes in the initial matrix of water. This is a possible reason for the observed influence of water quantity on the structure of the final product during SCS. The underlying mechanism for this effect appears to be the prolonged persistence and delayed decomposition of hydrates that form during the early preheating stages of SCS. This is especially significant for structure-sensitive catalytic reactions, such as catalysis in the liquid phase. [2].

10. The pretreatment influences the metal nitrate-fuel complexes that are formed in the precursor solution in the form of dendrites, which play a key role in the SCS reaction mechanism and the formation of metal. It appears that when these dendrites exist (with pretreatment) the reaction takes place in lower velocity as it is yielded through their complicated structure and thus, there is less time available for the oxidation of nickel. The existence of dendrites led to the inhibition of the oxygen diffusion on the foam-like structure, due to the resulting denser structure (lower height of dendrites in the final product). In accordance, the oxidation of fuel is not complete, yielding carbon and carbon monoxide which reduce metal oxide to metal. This “double thermal treatment” led to the occurrence of sintering process and the increase of crystallite size. Larger crystallites have less surface energy and as a result they tend to agglomerate less, leading to enhanced specific surface area [3].

11. Widening of NMR spectra peaks observed may be connected with glycine-nickel nitrate complex dendritic formation. During SCS, the dendrites formed consist mainly of Ni, but surface of pores is oxidized because of lower heat loss, lower speed of cooling after reaction which gives sufficient time for oxidation of the inside surface of the pores.

12. The three-dimensional percolation-like network and hierarchical structure of nano-composites on the basis of metal oxides and metals obtained by combustion in solutions provides a distinct possibility of increasing the selectivity and activity of such catalysts [4].

13. It was found by temperature profile measurements during SCS that the reactions take place mainly within the gel where the concentration of components is higher. In the gas phase, above the SCS solution, the exothermic effects detected mainly concern hydrogen formation. In samples with (stoichiometric ratio) two waves occurred during combustion: hydrogen formation takes place in first wave followed by reduction of metaloxide in the second wave together with metal oxidation. When hydrogen is formed in the gas phase, a combustion wave

propagates from the top to the bottom of the reactor while the second combustion wave is initiated at the bottom (within the gel) – first by reduction of Me and then by partial Me oxidation, because of the higher temperature developed.

14. In heterogeneous reactions the initial reagents are received from volume to the interface surface where there is a reaction, and the products are removed in the volume, thus there is macroscopic movement of substances. The reaction takes place, and then inhibited its products, they are removed into another phase and the reaction is again able to start, etc. The reason for such chemical oscillations can be considered as heterogeneity or, at least, a stationary support outside the spatial heterogeneity of the system (the generated complexes of nickel nitrate and glycine). They showed that if in a closed system is observed self-accelerating reactions, in the corresponding open system there is a region with three steady states. A further change of parameter around this stationary state lead to originating of the stable oscillations (Fig. 2).

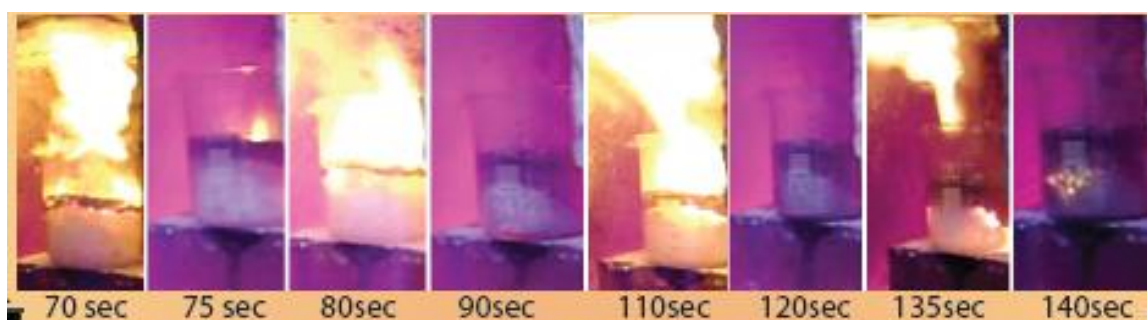


Fig. 2. Oscillations during SCS.

This is evidence of the flame bifurcation in repetitive extinction-ignition dynamics in nonequilibrium thermodynamics and synergetics — change of steady-state operation of the system.

15. The main shrinkage is in the process of liquid-phase sintering due to the contraction and rearrangement of particles under the action of capillary forces of the liquid phase and transfer of the material particles through the liquid phase. The greatest part of the densification is achieved in the process of retraction and rearrangement of solid particles. At liquid-phase sintering of systems with reacting components, an effective densification is achieved with smaller quantities of the liquid phase due to the additional, but slower shrinkage due to recrystallization through the liquid phase and the dispersion larger particles with the penetration of the melt in the grain boundary, adjustment and coalescence due to dissolution and deposition.

Understanding the interrelationships between the processing parameters and the ensuing structure has allowed a degree of optimization of the properties of the new nanomaterials. Due to increasing attention of researchers to SCS and other approaches in order to synthesize nanomaterials, this research will play a significant role in for nanomaterials studies.

1. O. Thoda, G. Xanthopoulou, G. Vekinis, A. Chroneos, Parametric optimisation of Solution Combustion Synthesis catalysts and their application for the aqueous hydrogenation of maleic acid, *Catal. Lett.*, 2018, vol. 148, pp. 764–778.
2. G. Xanthopoulou, O. Thoda, E.D. Metaxa, G. Vekinis, A. Chroneos, Influence of atomic structure on the nano-nickel-based catalysts activity produced by solution combustion synthesis in the hydrogenation of maleic acid, *J. Catal.*, 2017, vol. 348, pp. 9–21.
3. O. Thoda, G. Xanthopoulou, G. Vekinis, A. Chroneos, The Effect of the Precursor Solution's Pretreatment on the Properties and Microstructure of the SCS Final Nanomaterials, *Adv. Eng. Mater.*, 2018, vol. 20, 1800047.
4. G. Xanthopoulou, O. Thoda, S. Roslyakov, A. Steinman, D. Kovalev, E. Levashov, G. Vekinis, A. Sytshev, A. Chroneos, Solution combustion synthesis of nano-catalysts with a hierarchical structure, *J. Catal.*, 2018, vol. 364, pp. 112–124.

# ONE-STEP ULTRA-RAPID FABRICATION OF BULK THERMOELECTRIC MATERIALS VIA SELF-PROPAGATING HIGH-TEMPERATURE SYNTHESIS COMBINED WITH IN-SITU QUICK PRESSING

**Y. Yan<sup>\*a</sup>, T. Hu<sup>a</sup>, X. Su<sup>a</sup>, W. Liu<sup>a</sup>, and X. Tang<sup>a</sup>**

<sup>a</sup>State Key Laboratory of Advanced Technology for Materials Synthesis and Processing,  
Wuhan University of Technology, Wuhan, 430070 China  
<sup>\*</sup>e-mail: yanyonggao@whut.edu.cn

DOI: 10.24411/9999-0014A-2019-10192

Cu<sub>2</sub>Se is a promising material for high temperature thermoelectric energy conversion due to its unique combination of excellent electronic properties and low thermal conductivity owing to its ionic liquid characteristic at high temperature. The conventional fabrication of bulk thermoelectric materials usually involves time and energy consuming steps including melting, annealing and sintering et al, which restricts the large-scale application. In this paper, fully dense single-phase bulk Cu<sub>2</sub>Se material was prepared by the combination of self-propagating high-temperature synthesis (SHS) with in-situ quick pressing (QP) for the first time. This new approach shortens the duration of the synthesis from days to hours compared to conventional preparation methods. SHS-QP technique is an ultra-fast preparation method, which utilizes the heat released by the SHS reaction and an external applied pressure to achieve the synthesis and densification of materials in one-step. The ultra-fast process of the SHS-QP technique enables the fabrication of single-phase Cu<sub>2</sub>Se bulk materials with relative density of over 98% and with precise control over the stoichiometry owing to the ability to suppress the Se vapor during the reaction. The SHS-QP prepared Cu<sub>2</sub>Se samples exhibit excellent thermoelectric figure of merit,  $ZT \sim 1.46$  at 900 K, which is comparable to those of Cu<sub>2</sub>Se materials prepared by conventional methods. This study opens a new avenue for the ultra-fast and low-cost fabrication of Cu<sub>2</sub>Se thermoelectric materials.

## SOLID SOLUTION PRECIPITATION MECHANISM AND MICROSTRUCTURE EVOLUTION OF $\text{Al}_2\text{O}_3/\text{ZrO}_2$ NANOCOMPOSITE CERAMICS

Y. Yu<sup>a</sup>, Y. Zheng<sup>\*a</sup>, W. Yu<sup>a</sup>, X. Su<sup>a</sup>, B. Liu<sup>a</sup>, and F. Lin<sup>a</sup>

<sup>a</sup>National Key Laboratory of Science and Technology for National Defence on Advanced Composites in Special Environments, Center for Composite Materials and Structures, Harbin Institute of Technology, Harbin 150080, P.R. China

\*e-mail: zhengyt@hit.edu.cn

DOI: 10.24411/9999-0014A-2019-10193

In recent years, in order to improve the performance of ZTA ceramics, materials researchers have begun to use nano- $\text{ZrO}_2$  powders and nano- $\text{Al}_2\text{O}_3$  powders as raw materials to prepare high-performance ZTA nanocomposite ceramics [1–4]. The dispersion and uniform mixing of nano-powders of this method become very important. In order to obtain the nano-powders that meet the requirements, a liquid phase preparation process, such as a coprecipitation method [1, 3, 4], a sol-gel method [2], etc., is generally used to prepare nano-composite powders. These methods enable in-situ mixing of nano-powders such as  $\text{ZrO}_2$ ,  $\text{Al}_2\text{O}_3$ , and stabilizers in the raw material preparation stage. However, nano-powders are still very active, difficult to disperse, easy to agglomerate, high cost of preparation and easy to pollute, and there are still some problems such as grain growth in the later stage of sintering. In order to solve these problems, this paper began to explore the use of solid phase transition method to obtain nanocomposite structures. The basic idea of the phase change method is to prepare a metastable intermediate phase, which undergoes a phase change during the sintering process, such as amorphous crystallization or solid solution precipitation, and a high-density fine and uniform nanostructure can be obtained. Based on our previous research basis [5–6], the high-energy metastable solid solution powder (SSP) was prepared by combustion synthesis assisted water cooling. After hot-pressing sintering (HPS), the nano- $\text{ZrO}_2$  toughened  $\text{Al}_2\text{O}_3$  nanocomposite ceramics were obtained. This method not only reduces the cost, but also improves the mechanical properties of the  $\text{Al}_2\text{O}_3/\text{ZrO}_2$  nanocomposite ceramics (AZNC). The preparation method of the nanocomposite ceramics is not only suitable for ZTA, but also suitable for other oxides, and can even be extended to the preparation of carbide and nitride nano-ceramics. Figure 1a shows the backscattered electron (BSE) image of the cross section for solid solution powders. The inside of the powder is gray but does not exhibit the contrast of black and white phase (black- $\text{Al}_2\text{O}_3$  phase and white- $\text{ZrO}_2$  phase), indicating that  $\text{Al}_2\text{O}_3$  and  $\text{ZrO}_2$  are dissolved together, corresponding to the energy dispersive spectrometry (EDS) spectrum in Fig. 1b.

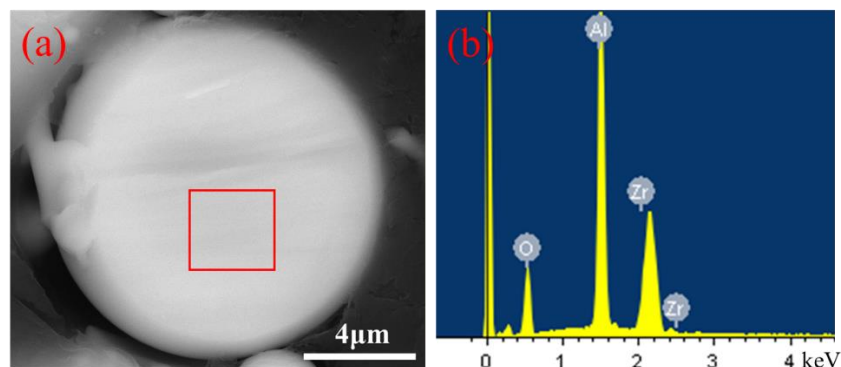


Fig. 1. (a) The BSE photograph of microstructure of solid solution cross section, and (b) EDS spectrum of the red box area in (a) graph.

After the SSP was subjected to HPS, the AZNC can be obtained. During the sintering process, the powder was decomposed to precipitate the  $\text{Al}_2\text{O}_3$  and  $\text{ZrO}_2$  nanocrystals, and the grains grown in the later stage to form nanocomposite ceramics. Based on the phase field model, it is widely used in the simulation of phase transformation of solidification and solid phase transformation. The phase field model of AZNC can describe the continuous precipitation process in the solid solution and the evolution of the microstructure of the material. Figure 2a shows the results of the phase field simulation (white  $\text{ZrO}_2$  phase and black  $\text{Al}_2\text{O}_3$  phase), and  $\text{ZrO}_2$  was present in the  $\text{Al}_2\text{O}_3$  group in the form of nanoparticles. In the figure, a small amount of  $\text{ZrO}_2$  particles began to merge and grow. The microstructure of the Scanning Electron Microscope (SEM) of the AZNC is shown in Fig. 2b, in which a large amount of nano- $\text{ZrO}_2$  particles and a small amount of micro- $\text{ZrO}_2$  particles are present, corresponding to the phase field simulation results. In short, it is feasible to prepare nanocomposite ceramics by solid solution precipitation, which is necessary to improve its mechanical properties. It provides theoretical guidance for the preparation of various oxides, nitrides, carbide-based nanoceramics, nano-cermets and nano-alloys.

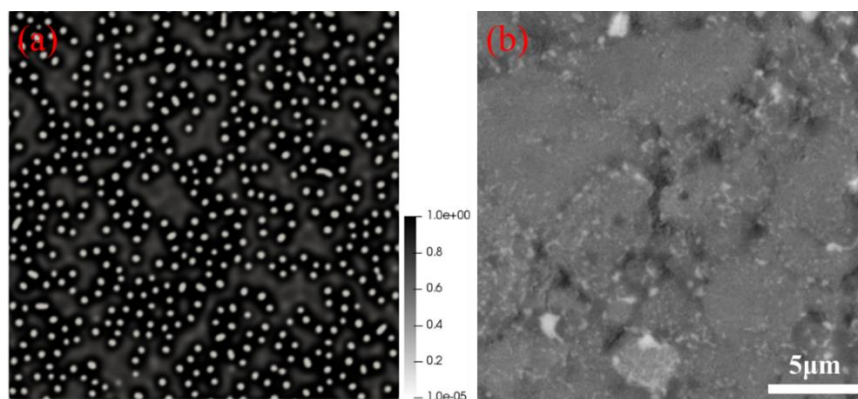


Fig. 2. (a) Microstructure of the AZNC under high temperature phase field simulation and (b) The SEM image of microstructure of AZNC.

1. L. Gao, H.Z. Wang, J.S. Hong, et al, SiC– $\text{ZrO}_2(3\text{Y})$ – $\text{Al}_2\text{O}_3$  nanocomposites superfaster densified by spark plasma sintering, *Nanostruct. Mater.*, 1999, vol. 11, no. 1, pp. 43–49.
2. D. Sarkar, S. Adak, M. C. Chu, et al, Influence of  $\text{ZrO}_2$  on the thermo-mechanical response of nano-ZTA, *Ceram. Int.*, 2007, vol. 33, no. 2, pp. 255–261.
3. B. Wang, Preparation of  $\text{Al}_2\text{O}_3/\text{ZrO}_2(\text{Y}_2\text{O}_3)$  powders and composite ceramics with eutectic composition, Doctoral dissertation, Harbin Institute of Technology, China, 2015, 53–59.
4. H. Lin, Mechanical and wear properties of  $\text{MgO} + \text{Y-TZP}/\text{Al}_2\text{O}_3$  composites, Doctoral dissertation, South China University of Technology, China, 2010, 40–52.
5. W. Yu, Y. Zheng, Y. Yu, et al, The reaction mechanism analysis and mechanical properties of large-size  $\text{Al}_2\text{O}_3/\text{ZrO}_2$ , eutectic ceramics prepared by a novel combustion synthesis, *Ceram. Int.*, 2018, vol. 44, no. 11, pp. 12987–12995.
6. J. Pan, Y. Zheng, Y. Zheng, et al, Solidification mechanism and microstructure evolution of  $\text{Al}_2\text{O}_3$ – $\text{ZrO}_2$  ceramic coating prepared by combustion synthesis and thermal explosion spraying, *Ceram. Int.*, 2017, vol. 43, no. 5, pp. 4037–4041.

## PRODUCTION OF METALS AND ALLOYS THROUGH VACUUM METALLOTHERMIC PROCESS

**O. Yucel<sup>\*a</sup>, K. C. Tasyurek<sup>a</sup>, M. Bugdayci<sup>b</sup>, and A. Turan<sup>b</sup>**

<sup>a</sup>Istanbul Technical University, Metallurgy and Material Engineering Department, Chemical and Metallurgical Engineering Faculty, Istanbul, 34469 Turkey

<sup>b</sup>Yalova University, Chemical and Process Engineering Department, Faculty of Engineering, Yalova, 77200 Turkey

\*e-mail: yucel@itu.edu.tr

DOI: 10.24411/9999-0014A-2019-10194

Mg is a silver grey metal and the consumption of magnesium in many fields, such as aircrafts, rockets and automobile industry, is expected to increase rapidly for the next decade, because magnesium has the lowest density as 1.738 g/cm<sup>3</sup> in all structural metals and its strength/density ratio is very high. Sr has 2.63 g/cm<sup>3</sup> density it has also a place around the light materials and a candidate material for grain refinement of magnesium. Ca has 1.55 g/cm<sup>3</sup> density it has also a place around the light materials. Its physical and chemical properties are very similar to its heavier homologues: elements like strontium and barium. It is the fifth-most abundant element on earth.

The world's demand for magnesium is increasing by about 10% per year. However, the mechanical properties and processing performances of the developed-magnesium alloys such as AZ series alloys still not enough for some important parts in transportation, aeronautical, and helicopter parts. In order to improve this properties a lot of processes were investigated in the world, grain refinement is an alternative method for this studies. Recent results indicated that Sr element which has been widely used in industrial practice especially for the modification of Al-Si alloys, was potential effective additions of grain refinement for magnesium alloys. However adding pure Sr to Mg alloys causes burning loss. Thus, using Mg–Sr master alloys is effective way to alloying Mg. Xiang-guo et al. applied melt-leaching-reduction (MLR) process alloying Mg with Sr in order to avoid burning loss and they produced Mg–Sr alloys. Vacuum metalothermic process is the main production method for magnesium in last decades. This process reduction is highly endothermic and it needs vacuum. Also Strontium and Ca reduction is possible by this method from their oxides. This method is an alternative process to MLR technique. In MLR technique metallic Sr used as strontium source which was produced from SrO. Mg–Sr alloy can produce via vacuum metalothermic process which is a one step process to obtain desired alloy and has advantage to MLR technique because SrO used as Sr source.

In silicothermic Mg production route, Pidgeon process is inefficient when the Mg source is MgO due to the reaction product which is in the form of MgO.SiO<sub>2</sub>. The formation of that compound stops the reduction. To avoid MgO.SiO<sub>2</sub> formation, SiO<sub>2</sub> activity must be decreased with some additives. In this case CaO is the most suitable additive which is provided by using calcined dolomite as reactant. The reduction of Mg from MgO becomes easier and the reduction efficiency of Mg increases in accordance with the formation of CaO.SiO<sub>2</sub> structure in reaction products. Because of that reason, in industrial silicothermic process calcined dolomite is used as a raw material instead of MgO.

In the present study, experimental sets were developed to understand the effects of reductants type on the vacuum metalothermic process of calcined dolomite. In the first set, the change of Mg recovery was investigated with the increase in charge (reactant) weights in the case FeSi (100% stoichiometric) was used as reductant. Two different retorts were used in this experimental set. The experiment with 50 g charge weight was carried out in 1 liter (l) retort,

others (2000 g, 3000 g, and 5000 g charges) were executed in 10 liter retort at 1250°C under 1 mbar. In all experiments process durations were 6 hours (Fig. 1a). In the second experimental set, effects of Si, FeSi, and Al reductants were examined. The experiments were conducted in 1 liter retort. Effect of process duration on Mg recovery was investigated for 60, 120, 180, 240, and 300 min (Fig. 1b).

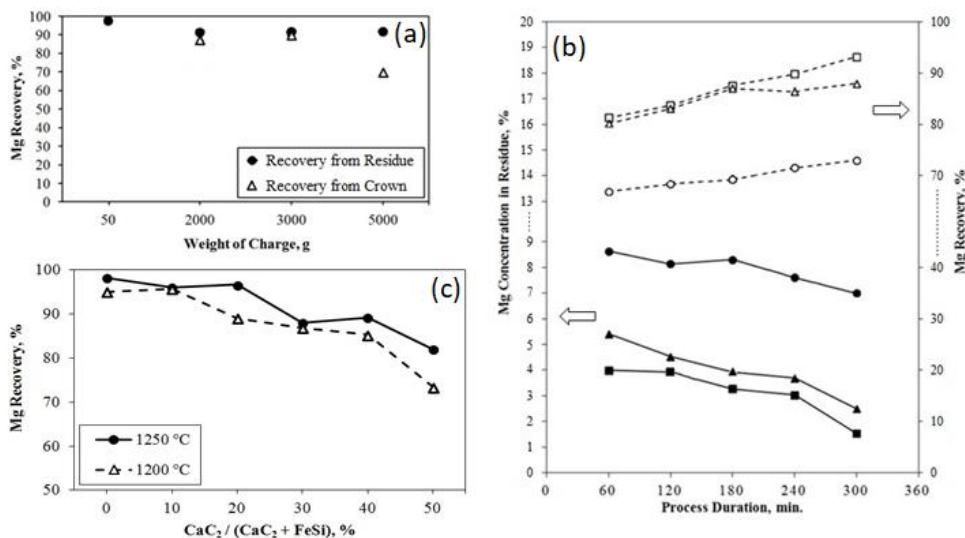


Fig. 1. (a) Mg recovery calculated from both residue and crown with the increase in charge weight. 50 g experiment was carried out in 1 liter retort, others in 10 liter retort (1250°C, 1 mbar and 6 h), (b) Mg amounts in residues and Mg recovery ratios for Si, FeSi, and Al reductants with increasing process duration (2.5% CaF<sub>2</sub> addition at 1200°C, 50 g, 1 liter, 1 mbar). Reductants are Si (□, ■), Al (△, ▲), and FeSi (○, ●), (c) The change of Mg recovery calculated from residue with increasing CaC<sub>2</sub> addition ratios at different temperatures.

In the first group experimental set, effect of charge amount was investigated on magnesium recovery. 2000 g and 3000 g charge amounts respectively presented the highest recovery rates which were calculated from residue. The highest Mg recovery was detected from the charge amount of 50 g as 98%. In this experiment, crown Mg efficiency cannot be calculated, because crown Mg amount was not enough to carry out analyses. On the other hand, the highest Mg recovery calculated from crown was determined as 90% for the experiment which was conducted with 3000 g charge amount Fig. 1a. When the difference is evaluated between the Mg recovery rates calculated from residue and crown for the same conditions (such as reactant weight of 50 g) show that Mg was highly reduced, but the conditions were not enough to collect in the form of crown in a high recovery ratio. It was understood that increasing charge weight firstly affected Mg reduction rate negatively, but it had a positive effect on the collected Mg amount in condensation zone. Mg recovery, calculated from residue, decreased from 98% to 90% whereas Mg recovery, calculated from crown, increased from 90 to 92% when charge amount increased from 2000 to 3000 g. According to the results, reduction duration must be extended with increasing amount of charge. In the second experimental set, effects of Si, FeSi, and Al reductants were examined. The experiments were conducted in 1 liter retort. Effect of process duration on Mg recovery was investigated for 60, 120, 180, 240, and 300 min (Fig. 1b). In the third experimental set, 100% stoichiometric 50 g mixtures were prepared. Stoichiometric amount of the reducing agent was calculated through sum of the oxides in the calcined dolomite which are MgO, FeO and SiO<sub>2</sub>. The mixture stoichiometric ratios were changed from 100% FeSi–0% CaC<sub>2</sub> to 50% FeSi–50% CaC<sub>2</sub> with 10% intervals. The change of Mg recovery with increasing CaC<sub>2</sub> addition ratio in FeSi was carried out at 1200 and 1250°C under 1 mbar vacuum

atmosphere for 6 h (Fig. 1c). In the last experimental set, the experiments were conducted with increasing  $\text{CaC}_2$  addition and in different volumes of retorts as 1 and 10 l.

Strontium oxide with Al, BaO, CaO, and  $\text{CaC}_2$  subjected to reduction process under an average process pressure of 2 mbar, at 1050, 1100, 1150, and 1200°C temperatures for 60, 120, 180, and 240 min (in 1 liter retort). During SrO vacuum aluminothermic reduction, high amount of Sr-aluminate structure obtained. In order to eliminate this structure some functional additive added to green mixture such as BaO, CaO, and  $\text{CaC}_2$ . Addition BaO is essential for high efficiency of strontium reduction. Temperature must be above of 1150°C, 1250°C is enough. The maximum recoveries were observed as 96.89% with addition of 300% stoichiometric Al and BaO for 240 min and 96.87% with addition of 300% stoichiometric Al and BaO for 240 min. Sr recovery increases with increasing experiment time. Sr recovery increases with increasing stoichiometric ratio of Al and BaO (Fig. 2a). In the CaO addition set, effect of time was examined in constant temperature 1250°C. Rising duration of experiment exponentially increase the efficiency of Sr up to 360 min, after this value, it is not changed. The highest Sr recovery detected at 1250°C for 480 min in experiment with 77.43%. Figure 2b presents effect of CaO addition on the Sr recovery at ranging durations.

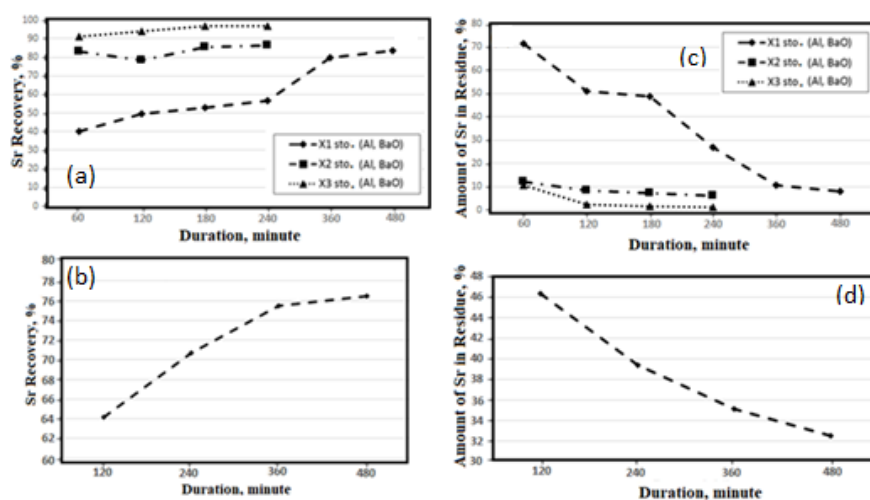


Fig. 2. (a) Effect of BaO addition on Sr recovery (1 liter retort, 1250°C, 1 mbar), (b) Effect of CaO addition on Sr recovery (1 liter retort, 1250°C, 1 mbar), (c) Amount of Sr in residue with BaO addition (1 liter retort, 1250°C, 1 mbar), (d) Amount of Sr in residue with CaO addition (1 liter retort, 1250°C, 1 mbar).

In Mg–Sr alloying study, combine metallothermic reduction of calcined dolomite and SrO production conditions alter to MLR process were investigated. In experiments % 100 stoichiometric mixtures prepared for Mg reduction from calcined dolomite, than (weight %2.5, %5, %7.5, %10) stoichiometric SrO mixtures were added to charge. In the first group of Mg and Sr reduction experiments, FeSi used as a reductant in order to reduce calcined dolomite. In the second experimental set Al used as a main reductant to reduce calcine dolomite. For SrO reduction, Al used as reductant for all experiments. In the experimental set using the FeSi reductant to reduce magnesium, the highest Mg recovery was determined at 1250°C, with the 5% Sr addition with 79.3%, the highest Sr recovery was in the 2.5% Sr mixture addition experiment, at 1250°C, with 63.5%. In the experimental set using the Al reductant to reduce magnesium, the highest Mg recovery was determined at 1250°C, with the 2.5% Sr addition with 89.8%, the highest Sr recovery was in the 7.5% Sr mixture addition experiment, at 1250°C, with 78.6%.

In the last experimental set, metallic calcium production by the metallothermic process in a vacuum atmosphere were investigated. In this experimental set authors aimed evaluation of



magnesium production slag as a raw material for the production of metallic calcium. Conventionally, in metallic Ca production, limestone is used as Ca source. In that process there is a calcination step in order to obtain CaO. In this study, it is also aimed to decreasing of energy consumption required for calcination, decreasing of CO<sub>2</sub> emission and decreasing disposal Mg production slag. In the experiments, Al powder is the only reductant used for metallothermic calcium production. The effects of Al stoichiometry, time variances, and temperature changes were investigated. The experiments were carried out at 1200, 1250, and 1300°C, and with 100, 125, and 150% Al stoichiometry to produce metallic calcium from the residue of metallic magnesium production. According to the experimental results, the highest recovery rate parameters for the reduction of calcium are 150% stoichiometric Al for 480 min at 1300°C, with 72% recovery (Fig. 3).

These reduction system were thermodynamically modelled by using FactSage 6.4 software. Table 1 was plotted to understand the change of the reduction conditions of Mg from pure MgO and calcine dolomite by Si, Al and CaC<sub>2</sub> under 1 bar and 1 mbar pressures respectively. According to the thermodynamical investigations, the formation temperatures of the reactions are very high under 1 bar atmosphere pressure. In the condition which the reduction temperatures with others are higher than Al, these are 2143, 1789, and 1847°C for Si, FeSi, and CaC<sub>2</sub> respectively for 1 bar. According to Fact Sage 6.4 software, the reaction beginning temperatures are 850°C for Al, 1155°C for FeSi, 1200°C for CaC<sub>2</sub>, and 1325°C for Si under 1 mbar pressure. Table 2 presents minimum reduction temperature of SrO production. According to calculation, the reduction of Sr with Si, Al, FeSi, and CaC<sub>2</sub> at 1536, 996, 1618, and 1312°C is possible at atmospheric pressure of 1 mbar, so Al is a better choice for reduction. These values are 2654, 1884, 3050, and 2102°C for Si and Al respectively in vacuum-free atmospheric conditions. Due to the high temperature requirement in Sr production, it is necessary to use vacuum in this process. Table 3 gives reduction temperatures of MgO and CaO with the Al reductant from Mg production slag, and it can be clearly seen that CaO reduction starts at 1298°C.

Table 1. Minimum reduction temperatures of MgO alone and in calcined dolomite for different reductant.

| Reductant        | Minimum Reduction Temp. (°C) |        |        |        |
|------------------|------------------------------|--------|--------|--------|
|                  | MgO                          |        | Dolime |        |
|                  | 1 bar                        | 1 mbar | 1 bar  | 1 mbar |
| Si               | 2143                         | 1325   | 2489   | 1318   |
| Al               | 1475                         | 850    | 1427   | 842    |
| FeSi             | 1789                         | 1155   | 1870   | 1098   |
| CaC <sub>2</sub> | 1847                         | 1200   | 1828   | 1191   |

Table 2. Minimum reduction temperatures of SrO for different reductant.

| Reductant        | Minimum Reduction Temp. (°C) |        |
|------------------|------------------------------|--------|
|                  | 1 bar                        | 1 mbar |
| Si               | 2654                         | 1536   |
| Al               | 1884                         | 996    |
| FeSi             | 3050                         | 1618   |
| CaC <sub>2</sub> | 2102                         | 1312   |

Table 3. Minimum reduction temperatures of CaO and MgO in Mg production slag for Al reductant.

|     | Minimum Reduction Temp. (°C) |        |
|-----|------------------------------|--------|
|     | 1 bar                        | 1 mbar |
| CaO | 2332                         | 1298   |
| MgO | 1481                         | 838    |

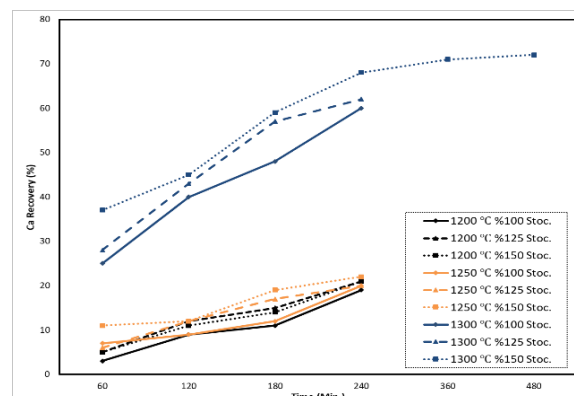


Fig. 3. Ca recovery ratios for different temperatures and reductant stoichiometry.

1. K.C. Taşyürek, M. Buğdaycı, O. Yücel, Reduction conditions of metallic calcium from magnesium production residues, *Met.*, 2018, vol. 8, no. 6, pp. 383.
2. M. Yang, F. Pan, L. Cheng, Effects of minor Sr on as-cast microstructure and mechanical properties of ZA84 magnesium alloy, *J Mater Eng Perform.*, 2010, vol. 19, no. 7, pp. 1043.
3. M. Yang, F. Pan, L. Cheng, A. Tang, Effects of Al–10Sr master alloys on grain refinement of AZ31 magnesium alloy, *Transact. Nonferr. Met. Soc. China*, 2008, vol. 18, iss. 1, pp. 52–58.
4. M. Aljarrah, M. Medraj, Thermodynamic modelling of the Mg–Ca, Mg–Sr, Ca–Sr, and Mg–Ca–Sr systems using the modified quasichemical model, 2008, vol. 32, pp. 240–251.

SHS METALLURGY OF COMPOSITE MATERIALS  
BASED ON REFRACTORY METALSV. I. Yukhvid<sup>\*a</sup>, D. E. Andreev<sup>a</sup>, Yu. S. Vdovin<sup>a</sup>, S. L. Silyakov<sup>a</sup>, N. V. Sachkova<sup>a</sup>,  
and I. D. Kovalev<sup>a</sup><sup>a</sup>Merzhanov Institute of Structural Macrokinetics and Materials Science, Russian Academy of  
Sciences, Chernogolovka, Moscow, 142432 Russia  
\*e-mail: yukh@ism.ac.ru

DOI: 10.24411/9999-0014A-2019-10195

Refractory metals (W, Mo, and Nb) and related composite materials (CMs) are widely used in engineering. Thus, tungsten carbides are the basis of hard alloys for steel processing and oil industry, fabrication of surfacing materials for protective coatings [1]. CMs based on Nb–Si and Mo–Si [2, 3] have great potential for implementation in the aircraft engine industry. The melting points of cast Nb–Si- and Mo–Si-based CMs exceed 1750 and 1950°C, respectively. These cast CMs can have a higher operating temperature than nickel superalloys. Niobium–silicide and molybdenum–silicide CMs are currently being developed for hot section turbines for both aircraft engines and ground turbines. Due to the high melting point, CMs based on W, Mo, and Nb are most often produced by powder metallurgy methods. In this paper, the possibility of obtaining cast CMs based on W, Mo, and Nb by SHS metallurgy was considered.

In experiments, the burning velocity ( $u$ ), the relative mass loss during combustion ( $\eta_1$ ), and the relative yield of the “metal” phase into the ingot ( $\eta_2$ ) were determined:  $u = h/t$ ,  $\eta_1 = [(m_1 - m_2)/m_1] \times 100\%$ ,  $\eta_2 = (m_3/m_1) \times 100\%$ , where  $m_1$  is the weight of the starting mixture,  $m_2$  is the weight of the combustion products,  $m_3$  is the weight of the desired product “metal ingot”, (wt %). Metal ingot were investigated by analytical chemistry, XRD analysis, and electron microscopy.

**SHS-metallurgy of W–C–Ni.** Powders  $\text{WO}_3$ , NiO, Al, granules of Ca and graphite were used as components of the initial mixtures for the production of cast CMs with different ratios of W–C and Ni. 30-g prepared mixtures were placed in graphite shells with an internal diameter of 20 mm and a height of 60 mm and were compacted. The synthesis was carried out in a laboratory reactor under a nitrogen ( $P$ ) pressure of 5 MPa. The ratio of  $\text{WO}_3/\text{Al}/\text{Ca}/\text{C}$  (0.71/0.09/0.16/0.04) and NiO/Al (0.81/0.19), ( $\alpha$ ) in the initial mixture was varied. The optimal ratio of reagents in the composition 1 was determined in previous experiments [4]. The composition 2 was calculated from the stoichiometric equation  $3\text{NiO} + 2\text{Al} \rightarrow 3\text{Ni} + \text{Al}_2\text{O}_3$ . The calculated adiabatic combustion temperature of the mixture at  $P = 5$  MPa (“Thermo” program) in the range  $0 < \alpha < 1$  is above 3000 K, which significantly exceeds the liquidus temperature of the WC–Ni alloy.

In experimental studies, it was shown, that the mixture burns in the entire range  $\alpha$ . Cast combustion products are divided into 2 layers (metal and oxide). The loss of the mixture during combustion does not exceed 5% (Fig. 1). According to XRD data in Fig. 2, cast CM contains WC,  $\text{W}_2\text{C}$ ,  $\text{Ni}_3\text{W}_{10}\text{C}_{3,4}$ , and  $\text{Ni}_3\text{Al}$  aluminide. EDS data and SEM image presented in Fig. 3 show that WC and  $\text{W}_2\text{C}$  are formed as plates,  $\text{Ni}_3\text{W}_{10}\text{C}_{3,4}$  is lace-shaped grains, and nickel aluminide ( $\text{Ni}_3\text{Al}$ ) forms the intergranular boundaries.

**SHS-metallurgy of Mo–Si–B.** Mo–Si–B was synthesized using a mixture consisting of high exothermic mixture  $\text{MoO}_3/\text{Al}/\text{Si}/\text{B}$  (71.6/26.5/1.4/0.5) and low exothermic mixture Mo/Si/B (96.2/2.8/1.0). 20-g prepared mixtures were placed in quartz shells with an internal diameter of 25 mm and a height of 70 mm and were compacted. According to thermodynamic calculation

in a wide range of ratios of compositions ( $\alpha$ ), the combustion temperature exceeds 3000 K. The combustion products contain a significant amount of gaseous products (metal vapor and suboxides). In order to suppress the sputtering of the mixture during combustion, experiments were carried out in centrifugal plants under the influence of gravity ( $a/g$ ) of 1–400 g. Experiments showed that combustion products are formed as a two-layer ingot: the bottom layer was Mo–Si–B (target product) and the upper layer was  $\text{Al}_2\text{O}_3$  (slag product). The value of  $\alpha$  was varied from 0 to 40% wt,  $a/g$  was 1 to 400.

It was found that  $u$  and  $\eta_1$  decrease, and  $\eta_2$  increases with increasing  $\alpha$  from 0 to 40% wt (Fig. 4) and reaches 50 % of the calculated value. At  $\alpha > 60\%$ , the completeness of the target product yield into the ingot decreases sharply and at  $\alpha = 70$  reaches zero (the limit of gravitational separation is reached). At  $\alpha = 80\%$  combustion is stopped (reached limit of combustion). According to XRD analysis, cast Mo–Si–B contains 3 phases: Mo,  $\text{Mo}_5\text{SiB}_2$ , and  $\text{Mo}_3\text{Si}$  (Fig. 5). Figure 6 shows that coarse grains of Mo–Si solution are surrounded by Mo–Si–Al. Inclusions of Mo–Si–B–Al take place in the boundary bulk.

**SHS-metallurgy of Nb–Si–Hf–Ti.**  $\text{Nb}_2\text{O}_5$ , Al, Si, Hf,  $\text{HfAl}_3$ , and Ti mixtures were used for the synthesis of cast Nb/Si/Hf/Ti. The prepared mixtures were placed in quartz shells (15 g) or graphite molds (100 g) and were compacted. The experiments were carried out under artificial gravity (1–500 g). Combustion of mixtures of  $\text{Nb}_2\text{O}_5$ , Al, Si, Hf (powder),  $\text{HfAl}_3$  (granules), and Ti in a centrifugal setup proceeds differently. In the first case, combustion proceeds in an explosive mode with a complete release of the mixture from the reaction form; in the second case, in a stationary mode at a velocity of 0.8–1.5 cm/s and with small losses of mixture during combustion. In the main series of experiments,  $\text{HfAl}_3$  granules of the following fractions were used: 0–40, 40–100, 100–160, and 160–300  $\mu\text{m}$ . Granules were manufactured from ingots  $\text{HfAl}_3$  obtained by SHS-metallurgy. In experiments, it was shown that with an increase in the  $a/g$  from 50 to 500, the burning velocity of mixture and the completeness of output of alloy into ingot increase from 0.8 to 1.5 cm/s and from 70 to 100 % wt, respectively. The spread of the mixture does not exceed 10 wt % and slightly reduced (Fig. 7). The Hf content in CM decreases markedly, Ti increases. The content of all other target elements in the alloy varies slightly. Figure 8 shows that XRD pattern of CM produced using a large amount of  $\text{HfAl}_3$  particles contains 3 phases: Nb (base),  $\text{Nb}_5\text{Si}_3$ , and a small amount of  $\text{Nb}_3\text{Si}$ . No phases based on Hf, Ti, and Al were detected. Microstructure of Nb–Si–Hf–Ti is presented in Fig. 9.

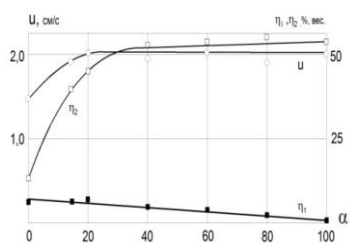


Fig. 1. Effect of  $\alpha$  on  $u$ ,  $\eta_1$ , and  $\eta_2$ .

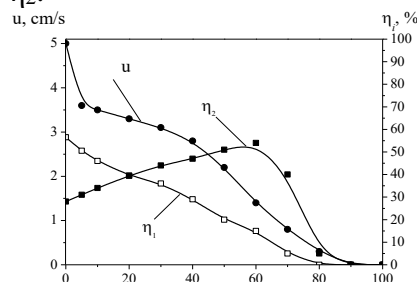


Fig. 4. Effect of  $\alpha$  on  $u$ ,  $\eta_1$ , and  $\eta_2$ .  $a/g = 40$ .

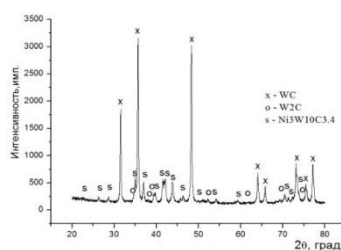


Fig. 2. XRD pattern of W/C/Ni/Al.

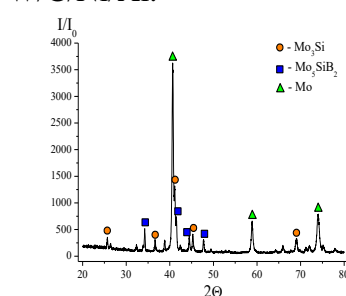


Fig. 5. XRD pattern of Mo/Si/B.

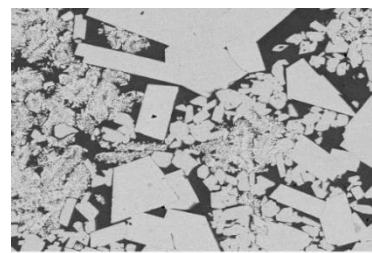


Fig. 3. Microstructure of W/C/Ni/Al.

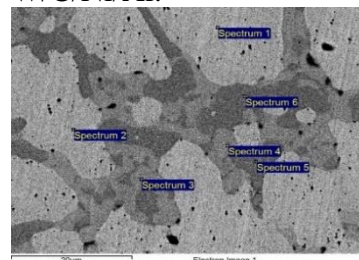


Fig. 6. Microstructure of Mo/Si/B.

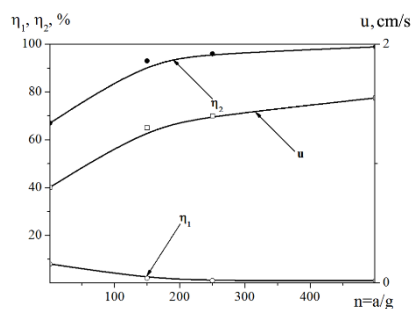


Fig. 7. Effect of  $a/g$  on  $u$ ,  $\eta_1$ , and  $\eta_2$ .

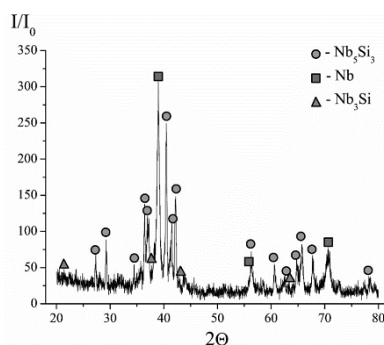


Fig. 8. XRD pattern of Nb/Si/Hf/Ti.

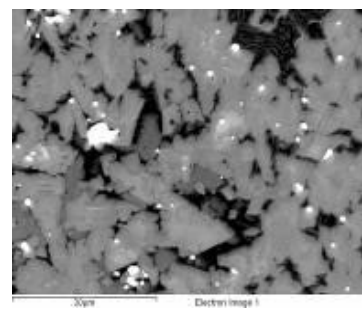


Fig. 9. Microstructure of Nb/Si/Hf/Ti.

Two scheme of chemical stage of transformation of compounds  $\text{Nb}_2\text{O}_5/\text{Al}/\text{Si}/\text{Hf}/\text{Ti}$  and  $\text{Nb}_2\text{O}_5/\text{Al}/\text{Si}/\text{HfAl}_3/\text{Ti}$  in the combustion wave was suggested from the analysis of experimental results.

(1) For  $\text{Nb}_2\text{O}_5/\text{Al}/\text{Si}/\text{Hf}/\text{Ti}$  mixture, the leading stage determining the combustion mode and regularities is  $\text{Nb}_2\text{O}_5/\text{Hf} \rightarrow \text{Nb}-\text{HfO}_2$ . All other stages:  $\text{Nb}_2\text{O}_5/\text{Al} \rightarrow \text{Nb}-\text{Al}_2\text{O}_3$ ,  $\text{Nb}_2\text{O}_5/\text{Ti} \rightarrow \text{Nb}-\text{Ti}_2\text{O}_3$ , etc. are in spatial mode. Due to the high activity of hafnium, combustion occurs in an explosive mode and is accompanied by the release of combustion products from the reaction form ("champagne effect").

(2) The stage  $\text{Nb}_2\text{O}_5/\text{Al} \rightarrow \text{Nb}-\text{Al}_2\text{O}_3$  is the leading stage when you replace Hf on  $\text{HfAl}_3$ . All other stages,  $\text{Nb}_2\text{O}_5/\text{HfAl}_3 \rightarrow \text{Nb}-\text{HfO}_2-\text{Al}_2\text{O}_3$ ,  $\text{Nb}_2\text{O}_5/\text{Ti} \rightarrow \text{Nb}-\text{Ti}_2\text{O}_3$ , etc. are carried out spatial mode in with the leading stage. Due to the lower activity of Al and  $\text{HfAl}_3$  than hafnium, combustion occurs stationary at a velocity of 0.8–1.5 cm/s and small losses of the mixture during combustion, which leads to the increase in the content of Hf in CM.

The study was supported by the Russian Foundation for Basic Research (project no. 18-08-00228).

1. A.P. Zhudra, Surfacing materials based on tungsten carbides, *Automatic Welding*, 2014, nos. 6–7, pp. 69–74.
2. S. Drawin, J.F. Justin, Advanced lightweight silicide and nitride based materials for turbo-engine applications, *J. AerospaceLab*, 2011, no. 3, pp. 1–13.
3. R.A. Gaisin, V.M. Imayev, R.A. Shaimardanov, R.M. Imayev, Structure and properties of Mo–9Si–8B alloy fabricated by casting, *Inorg. Mater. Appl. Res.*, 2017, vol. 8, no. 5, pp 750–754.
4. S.L. Silyakov, V.I. Yuxhvid, Chemical, phase and structural transformations during combustion of mixtures based on tungsten oxide with aluminum, *Chem. Phys.*, 2019, vol. 38, no. 1, pp. 49–54.

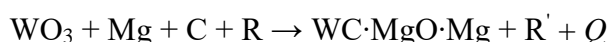
## NEAR-NANO AND COARSE-GRAIN WC POWDERS OBTAINED BY THE SHS AND CEMENTED CARBIDES ON THEIR BASIS

A. A. Zaitsev<sup>\*a</sup>, E. A. Levashov<sup>a</sup>, V. I. Vershinnikov<sup>b</sup>, I. Konyashin<sup>a,c</sup>, and E. I. Patsera<sup>a</sup><sup>a</sup>National University of Science and Technology MISiS, Moscow, 119049 Russia<sup>b</sup>Merzhanov Institute of Structural Macrokinetics and Materials Science, Russian Academy of Sciences, Chernogolovka, Moscow, 142432 Russia<sup>c</sup>Element Six GmbH, Burghaun, 36151 Germany

\*e-mail: aazaitsev@bk.ru

DOI: 10.24411/9999-0014A-2019-10196

Tungsten carbide (WC) is a chemical compound used for many applications due to its unique combination of physical and chemical properties. In particular, WC is mainly employed in cutting and drilling tools in the form of cemented tungsten carbide. The properties of cemented carbides depend primarily on binder content and grain size of WC. Methods for producing WC are quite diverse. WC is usually fabricated on a large scale either by the direct carburization of tungsten oxides or the carburization of tungsten metal powders. Such methods as the rapid carburization process, thermochemical precursor reduction, vapor phase reaction process, mechano-chemical synthesis, and high energy milling are also used to obtain near-nano or nano-WC powders [1–6]. WC powders can also be produced by self-propagating high-temperature synthesis (SHS). This method is now employed for the fabrication of different refractory compounds [7, 8]. The reaction of elemental synthesis of WC:  $W + C = WC$  is characterized by a relatively low heat effect ( $\Delta H = -40.6$  kJ/mol, the calculated adiabatic flame temperature  $\sim 1083$  K [9]), which makes it difficult to produce WC in the combustion mode without adding heat to the system (e.g., by passing electric current [10, 11] or by employing induction heating [12, 13] of tungsten–carbon mixtures). Reactions involving the reduction stage with tungsten compounds (oxides, halides, etc.) used for the SHS synthesis instead of tungsten and highly active metals used as reducing agents, show promise for producing WC powders. In the present study magnesium is used as a reducing agent so SHS reaction can be summarized as follow:



where R is a regulating additive, Q is the thermal effect, and R' is other products of the reaction. In the general case R' is a result of interaction  $Mg + C + R$ .

The morphology of the near-nano and medium-coarse WC powders obtained by the SHS is shown in Fig. 1.

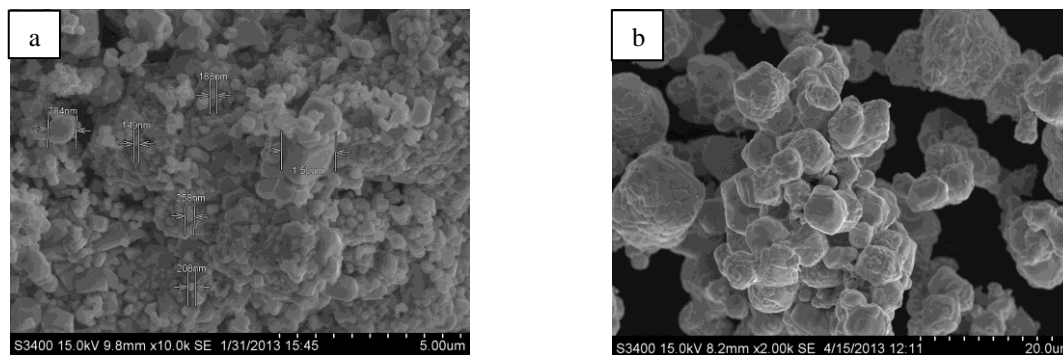


Fig. 1. Morphology of the near-nano (a) and medium-coarse WC powder (b) obtained by the SHS method.

The near-nano WC powder (Fig. 1a) is uniform and does not comprise abnormally coarse WC grains; the mean grains size was found to be about 200 nm. The chemical analysis showed that the synthesized near-nano tungsten carbide contained 6.13 wt %  $C_{\text{bound}}$ , 0.08 wt %  $C_{\text{free}}$ , and 0.08 wt % oxygen. The coarse-grain WC powder (Fig. 1b) is nearly stoichiometric and consists of sintered round-shaped agglomerates with the average grain size of up to 16  $\mu\text{m}$  and containing only traces of magnesium and oxygen. The agglomerates comprise WC single-crystals of roughly 1  $\mu\text{m}$  to 8  $\mu\text{m}$  in size.

The microstructure of the submicron grade with 5 wt % Co made of near-nano WC powder obtained by the SHS method and the standard submicron grade is similar with slightly coarser WC grains in the grade made of SHS WC powder (Fig. 2a). The mechanical properties of the submicron WC–5% Co grade made of near-nano WC powder obtained by the SHS method and its wear-resistance ( $\text{TRS} = 2130 \text{ MPa}$ ,  $K_{\text{IC}} = 9.5 \text{ MPa}\cdot\text{m}^{1/2}$ ,  $\text{HV}_{30} = 18.1 \text{ GPa}$ ,  $\text{Wear} = 9.1 \cdot 10^{-6} \text{ mm/rev}$ ) are comparable with those of the standard ultrafine grade, except for the TRS, which is slightly lower for the grade of SHS WC powder. The microstructure of the medium-coarse WC–6 wt % Co cemented carbide made of medium-coarse WC powder obtained by the SHS method and its properties ( $\text{TRS} = 1900 \text{ MPa}$ ,  $K_{\text{IC}} = 13.5 \text{ MPa}\cdot\text{m}^{1/2}$ ,  $\text{HV}_{30} = 13.1 \text{ GPa}$ ) are comparable with those of the standard medium-coarse grade for percussive drilling (Fig. 2b).

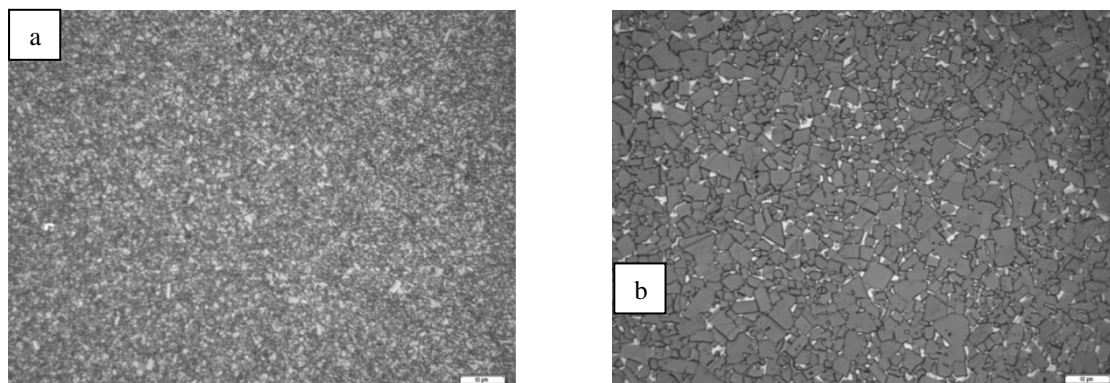


Fig. 2. The microstructure of the submicron (a) and coarse-grain (b) WC–6 wt % Co cemented carbide made from the near-nano and coarse WC powder obtained by SHS.

Results of laboratory performance tests on percussive drilling of the medium-coarse WC–6% Co grade obtained from both the SHS WC powder indicate that its wear-resistance is very similar to that of the standard grade for percussive drilling produced from the conventionally fabricated WC powder. Thus, it is established that high-quality WC–Co cemented carbides with different WC grain sizes varying from submicron to medium-coarse can be produced from the WC powders fabricated by the SHS method.

1. W.D. Schubert, A. Bock, B. Lux, General aspects and limits of conventional ultrafine WC powder manufacture and hard metal production, *Int. J. Refract. Met. Hard Mater.*, 1995, vol. 13, pp 281–296.
2. P. Seegopaul, L.E. McCandlish, F.M. Shinneman, Production capability and powder processing methods for nanostructured WC–Co powder, *Int. J. Refract. Met. Hard Mater.*, 1997, vol. 15, pp 133–138.
3. F.F.P. Medeiros, S.A. Oliviera, C.P. Souza, A.G.P. Silva, U.U. Gomes, J.F. Souza, Synthesis of tungsten carbide through gas–solid reaction at low temperatures, *Mater. Sci. Eng. A*, 2001, vol. 315, pp. 58–62.
4. F.L. Zhang, C.Y. Wang, M. Zhu, Nanostructured WC/Co composite powder prepared by high energy ball milling, *Scr. Mater.*, 2003, vol. 49, pp. 1123–1128.

5. S. Kim, S.H. Han, J.K. Park, H.E. Kim, Variation of WC grain shape with carbon content in the WC–Co alloys during liquid-phase sintering, *Scr. Mater.*, 2003, vol. 48, pp. 635–639.
6. J.C. Kim, B.K. Kim, Synthesis of nanosized tungsten carbide powder by the chemical vapor condensation process, *Scr. Mater.*, 2004, vol. 50, pp. 969–972.
7. L. Guanghua, L. Jiangtao, C. Kexin, Combustion synthesis of refractory and hard materials: a review, *Int. J. Refract. Met. Hard Mater.*, 2013, vol. 39, pp. 90–102.
8. A.G. Merzhanov, History and recent developments in SHS: a review, *Ceram. Int.*, 1995, vol. 21, pp. 371–379.
9. E.A. Levashov, A.S. Rogachev, V.I. Yuxhvid, I.P. Borovinskaia, Fiziko-khimicheskiye i tekhnologicheskiye osnovy samorasprostranyayushchegosya vysokotemperaturnogo sinteza (Physico-chemical and Technological Bases of Self-propagating Hightemperature Synthesis), BINOM, Moscow, 1999. (In Russ.).
10. G. Jiang, H. Zhuang, W. Li, Combustion synthesis of tungsten carbides under electric field. I. Field activated combustion synthesis, *Ceram. Int.*, 2004, vol. 30, pp. 185–190.
11. G. Jiang, H. Zhuang, W. Li, Synthesis of tungsten carbide–cobalt composites by the field-activated combustion synthesis method, *J. Alloys Compd.*, 2005, vol. 387, pp. 90–96.
12. H.C. Kim, I.J. Shon, J.K. Yoon, S.K. Lee, Z.A. Munir, One step synthesis and densification of ultra-fine WC by high-frequency induction combustion, *Int. J. Refract. Met. Hard Mater.*, 2006, vol. 24, pp. 202–209.
13. H.C. Kim, D.Y. Oh, I.J. Shon, Synthesis of WC and dense WC– $x$  vol % Co hard materials by high-frequency induction heated combustion method, *Int. J. Refract. Met. Hard Mater.*, 2004, vol. 22, pp. 41–49.



W–Ag NANOCOMPOSITE PREPARATION BY COMBINING  
SCS AND SHSM. K. Zakaryan<sup>\*a,b</sup>, A. A. Baldryan<sup>a</sup>, and S. L. Kharatyan<sup>a,b</sup><sup>a</sup>A.B. Nalbandyan Institute of Chemical Physics NAS RA, Yerevan, 0014 Armenia<sup>b</sup>Yerevan State University, Yerevan, 0025 Armenia

\*e-mail: zakaryan526219@gmail.com

DOI: 10.24411/9999-0014A-2019-10197

In recent years, tungsten (W)-based heavy alloys have received increased use in both commercial and industrial spheres. Most heavy alloys consist of W particles embedded in matrix of other metals or their alloys such as iron, nickel, silver or copper. In particular, W–Ag alloys may tend to replace as heat dissipation materials in the microelectronic devices that are prone to failure at high operating temperatures, as diverter plates in fusion reactors. They combine the arc erosion and welding resistance of tungsten with the excellent thermal and electrical conductivities of silver. The composite's thermal expansion coefficient can be adjusted by changing its composition to match those of ceramic materials used as substrates in semiconductor devices. The tungsten-silver composite may have various contents of silver, generally from 25 to 50% by weight [1]. In these cases, the W–Ag composite may be used in heat sinks and microwave absorbers in microelectronic devices. Powder metallurgy is the technique utilized to manufacture this material, but due to the mutual insolubility of W and Ag and to the poor wet ability of liquid Ag on W, sintering cannot easily produce dense and homogeneous structures [2, 3].

As there is no alloying between the silver and tungsten the properties of the composites depend on direct proportion their composition, the size, morphology, and distribution of phases within the composite, with finer particles giving improved performance [4].

In this work we report a new pathway for the preparation of Ag–W composite nanopowder/pseudoalloy by energy-saving combustion synthesis (CS) method. It is well known that the selection of the starting materials can highly contribute to enhancing the structure and properties of the final products. Regarding to that, fine precursor representing silver + tungsten oxide, was prepared by solution combustion synthesis (SCS) method using ammonium paratungstate ((NH<sub>4</sub>)<sub>10</sub>(H<sub>2</sub>W<sub>12</sub>O<sub>42</sub>)·4H<sub>2</sub>O) (APT) and silver nitrate (AgNO<sub>3</sub>) in the presence of citric acid (C<sub>6</sub>H<sub>8</sub>O<sub>7</sub>) as a reducer and ammonium nitrate (NH<sub>4</sub>NO<sub>3</sub>) as an auxiliary oxidizing agent to increase the reaction enthalpy. The solution prepared was heated on electrical heater for evaporation of water, after a viscous liquid is formed which is autoignited at ~ 150 °C accompanied by release of gas and smoke ( $T_{\max} \sim 600^{\circ}\text{C}$ ) (Fig. 1a). As a result, the initial reaction media being in the liquid state allows mixing the reactants on the molecular level, thus promoting the formation of nanocomposite with homogeneous composition and uniform distribution of phases (Fig. 1b).

Thus, the suggested approach of Ag:W = 1:1 composite powder preparation comprises the obtaining of homogeneous and nanostructured WO<sub>3</sub>–Ag precursor by SCS method and subsequent reduction of WO<sub>3</sub> by conventional SHS with applying reaction's coupling approach [5].

Thermodynamic calculations were carried out to reveal the possibility of combustion in Ag–WO<sub>3</sub>–yMg–xC system and for determining optimal conditions for complete reduction, aimed to obtain W–Ag pseudoalloy.

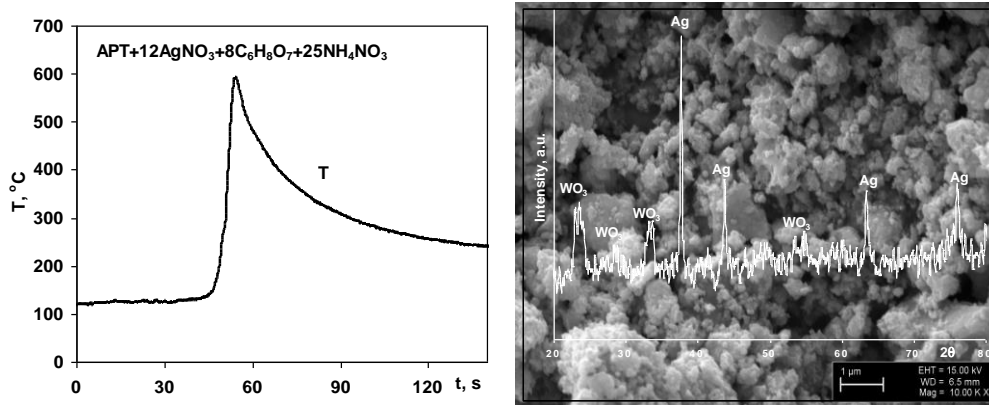


Fig. 1. Combustion temperature profile of the SCS reaction (a) and XRD and SEM analyses results of obtained precursor (b).

In Fig. 2, the formation area for tungsten–silver bimetallic system was clearly marked depending on carbon and magnesium amounts. According to these results, the joint and complete reduction of silver and tungsten is attainable at magnesium and carbon amounts of  $y = 1.5$ – $2$  moles and  $x = 0.5$ – $1.2$  moles, respectively, within the temperature interval  $1500$ – $2200^\circ\text{C}$ . Based on the results of thermodynamic calculations, experiments on magnesiocarbothermal reduction were carried out with the amount of magnesium corresponding to the low-temperature part of the optimal region ( $y = 1.5$  mol) (Fig. 2). To find out optimum composition for preparing W–Ag composite material, the effect of carbon amount on the behaviour of combustion parameters (temperature and velocity), phase composition and morphology of product, a series of experiments were performed with changing carbon amount (Fig. 3). As it can be seen in Fig. 2, at  $x > 6.25$  mol combustion limit was observed. All the products were exposed to XRD analyses, according to which  $\text{WO}_3 + \text{Ag} + 1.5\text{Mg} + 1.2\text{C}$  composition (see Fig. 2) was selected as optimum for preparing W–Ag pseudoalloy. Byproduct magnesia was removed by acid treatment with hydrochloric acid ( $\omega = 10\%$ ). The product after acid leaching represents W–Ag nanocomposite material.

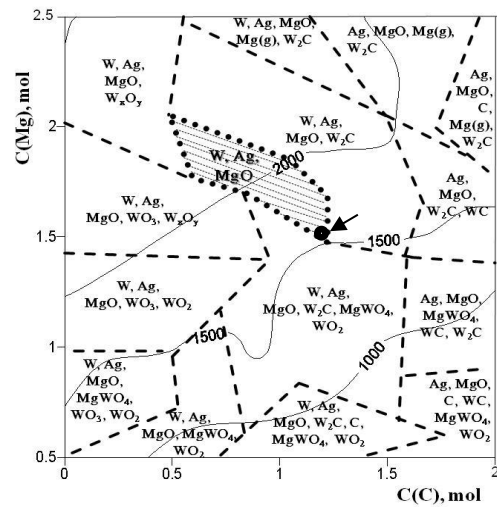


Fig. 2. Thermodynamic analysis results for the  $\text{WO}_3$ –Ag– $y\text{Mg}$ – $x\text{C}$  system,  $P = 0.5$  MPa.

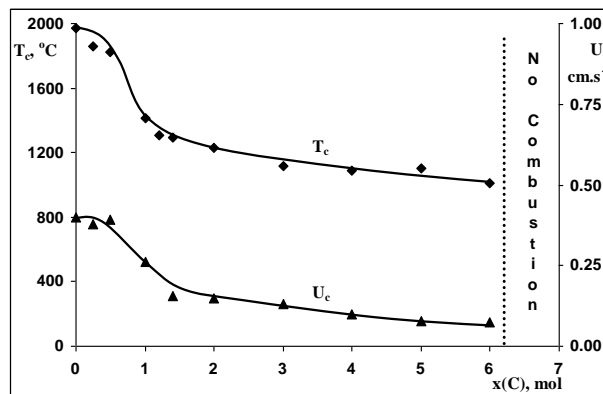


Fig. 3. Combustion temperature and velocity vs. carbon amount for the the  $\text{WO}_3$ –Ag– $1.5\text{Mg}$ – $x\text{C}$  system,  $P = 0.5$  MPa.

This work was supported by the Committee of Science MES of RA (Research grant 18A-1d12).

1. Sh.M. Azhar, M. Es-saheb, Homogenous silver–tungsten composite production for electrical contacts, *Res. J. Appl. Sci. Eng. Tech.*, 2015, vol. 9, no. 8, pp. 549–560.
2. F.A. da Costa, A.G.P. da Silva, F.A. Filho, U.U. Gomes, F.A. Vieira, Synthesis of a nanocrystalline composite W–25 wt % Ag powder by high energy milling, *Powder Technol.*, 2008, vol. 188, pp. 30–33.
3. F.A. da Costa, A.G.P. da Silva, F.A. Filho, U.U. Gomes, Solid state sintering of a W–25 wt % Ag powder prepared by high energy milling, *Int. J. Refract. Metals Hard Mater.*, 2008, vol. 26, pp. 318–323.
4. D. Stone, J. Liu, D.P. Singh, C. Muratore, A.A. Voevodin, S. Mishra, C. Rebholz, Q. Geb, S.M. Aouadia, Layered atomic structures of double oxides for low shear strength at high temperatures, *Scripta Mater.*, 2010, vol. 62, pp. 735–738.
5. S.L. Kharatyan, A.G. Merzhanov, Coupled SHS reactions as a useful tool for synthesis of materials: an overview, *Int. J. SHS*, 2012, vol. 21, no 1, pp. 59–73.

JOINT REDUCTION OF NiO + WO<sub>3</sub> OXIDES BY COMBINED Mg/C REDUCER. SYNERGETIC EFFECTM. K. Zakaryan<sup>\*a,b</sup>, Kh. T. Nazaretyan<sup>a</sup>, S. V. Aydinyan<sup>a,c</sup>, and S. L. Kharatyan<sup>a,b</sup><sup>a</sup>A.B. Nalbandyan Institute of Chemical Physics NAS RA, Yerevan, 0014 Armenia<sup>b</sup>Yerevan State University, Yerevan, 0025 Armenia<sup>c</sup>Tallinn University of Technology, Tallinn, 19086 Estonia

\*e-mail: zakaryan526219@gmail.com

DOI: 10.24411/9999-0014A-2019-10198

It is known that nickel–tungsten alloys possess high hardness and good wear resistance. This makes such alloys suitable for the production of turbine blades, hot forging dies, friction materials for brake assemblies, substitutes for chromium coatings, repair materials (without dismantling) for steam generators of nuclear power plants, decorative jackets, and bearings. It is already reported that tungsten-nickel alloys might be obtained by joint reduction of their oxides under heating in a hydrogen atmosphere or by carbon monoxide [1, 2].

However, it is well known that refractory metal containing alloys are difficult to prepare by conventional methods due to large differences in melting points and limited mutual solubility. Hence, the development of new preparation methods of Ni–W composite materials with tailored physicomechanical properties and full bulk density are in the focus of modern research.

In our previous work [3], we performed joint reduction of nickel/tungsten oxides by energy saving combustion synthesis method using Mg + C mixture as combined reducer. The using of such reducing mixture allows to control the reaction temperature in a wide range and to synthesize Ni–W composite powders in a controllable combustion mode.

In this work the mechanism and kinetics of tungsten and nickel oxides joint reduction by Mg + C combined reducer was studied utilizing high-speed temperature scanner (HSTS). The latter provides an advanced opportunity to disclose the stepwise nature of complex reactions in the multicomponent systems at high heating rates,  $V_h$  (up to  $10^4 \cdot \text{min}^{-1}$ ) and  $T_{\text{max}} = 1300^\circ\text{C}$ .

Firstly, binary (NiO–Mg) and ternary (NiO–Mg–C, NiO–WO<sub>3</sub>–Mg) systems were studied at the same conditions, considering only magnesiothermic or magnesio-carbothermic reduction reactions. The rest systems (WO<sub>3</sub>–Mg–C and WO<sub>3</sub>–Mg) were studied in [4].

It is worthy to note, that kinetic parameters and reaction pathway for the reduction processes of nickel oxide with simultaneous utilization of magnesium and carbon were established in the work [5] via DTA/DTG technique (“Derivatograph Q1500” MOM, Hungary;  $V_h = 5\text{--}20^\circ\text{C} \cdot \text{min}^{-1}$ ).

**NiO–Mg binary system**

The exothermic interaction in the NiO + Mg system starts immediately after the magnesium melting ( $T_o = 680^\circ\text{C}$ ,  $T_{\text{max}} = 1300^\circ\text{C}$ ) under  $V_h = 300^\circ\text{C} \cdot \text{min}^{-1}$  heating rate conditions. According to XRD analyses results the full reduction of nickel oxide takes place at  $1200^\circ\text{C}$  (Fig. 1a).

**NiO–Mg–C ternary system**

The reduction process in the  $2\text{NiO} + \text{Mg} + \text{C}$  reaction at  $V_h = 300^\circ\text{C} \cdot \text{min}^{-1}$  heating rate conditions also starts later than magnesium melting ( $T_o = 720^\circ\text{C}$ ,  $T_{\text{max}} = 1270^\circ\text{C}$ ). It should be noted, that in this case, the full reduction of nickel oxide proceeds at incomparably low  $800^\circ\text{C}$  temperature (Fig. 1b). Note that, according to XRD analyses results, the complete reduction of nickel oxide by carbon takes place at  $1035^\circ\text{C}$ .

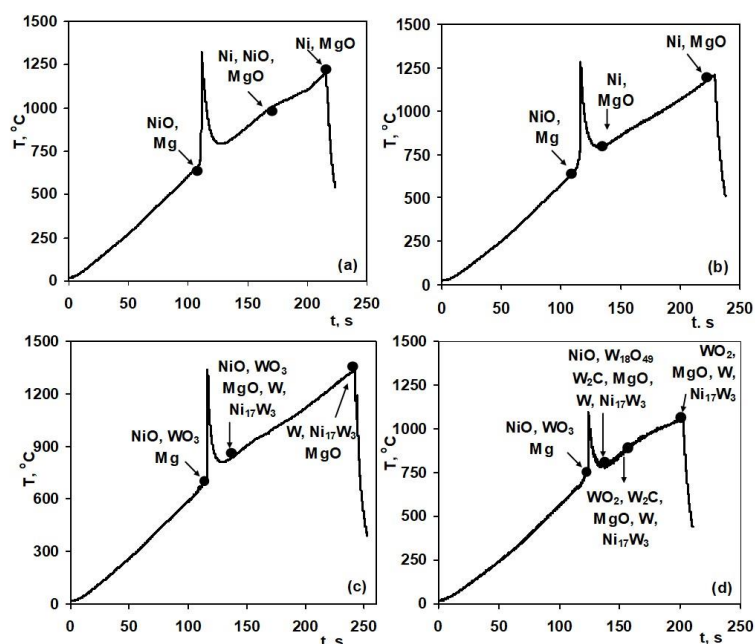


Fig. 1. Heating thermograms with the results of XRD analyses for NiO + Mg (a), 2NiO + Mg + C (b), NiO + WO<sub>3</sub> + 4Mg (c), NiO + WO<sub>3</sub> + 2.5Mg + 1.5C (d) mixtures,  $V_h = 300^\circ\text{C}\cdot\text{min}^{-1}$ .

### NiO–WO<sub>3</sub>–Mg–C quaternary system

Experiments performed with the quaternary NiO + WO<sub>3</sub> + 2.5Mg + 1.5C mixture showed that the combined reduction process starts also after magnesium melting. On the other hand, unlike low heating rates [4] at high heating rates the reduction stages are not separated (Fig. 1d). The intense interaction starts at 750°C with 1100°C maximum temperature. It's worthy to note that as it was shown in [3], NiO + WO<sub>3</sub> + 1.8Mg + 2.2C mixture was chosen as optimum for joint and complete reduction of NiO and WO<sub>3</sub> in combustion mode. At that the main products formed are Ni<sub>17</sub>W<sub>3</sub> and W metal.

Experiments performed at various heating rates ( $V_h = 100\text{--}1200^\circ\text{C}\cdot\text{min}^{-1}$ ) allow to calculate the kinetic parameters (effective values of activation energy) for the magnesiothermal reduction stage for the NiO + Mg, 2NiO + Mg + C, WO<sub>3</sub> + NiO + 4Mg and NiO + WO<sub>3</sub> + 2.5Mg + 1.5C reactions (Table) using the Kissinger method [5].

Table. The values of activation energies for magnesiothermic reduction reactions of oxides.

| Reaction   | Activation energy, $\text{kJ}\cdot\text{mol}^{-1}$ | Reference   |
|--|--|-------------|
| WO <sub>3</sub> + Mg   | 106  | [3]         |
| WO <sub>3</sub> + Mg + C<br>(for WO <sub>3</sub> + Mg stage)                   | 92   | [3]         |
| NiO + Mg   | 175  | [this work] |
| NiO + Mg + C<br>(for NiO + Mg stage)   | 185  | [this work] |
| WO <sub>3</sub> + NiO + 4Mg  | 139  | [this work] |
| NiO + WO <sub>3</sub> + 2.5Mg + 1.5C<br>(for NiO + WO <sub>3</sub> + Mg stage) | 198  | [this work] |

It was revealed that the reduction of oxides by combined reducer (Mg + C) proceeds at lower temperature compared to the separate binary mixtures, which evidences about the particular synergetic effect in the ternary (2NiO + Mg + C, WO<sub>3</sub> + Mg + C) and quaternary (NiO + WO<sub>3</sub> + Mg + C) mixtures. Thus, full reduction of nickel by the reaction NiO + C is observed at 1035°C, in a mixture of NiO + Mg, at 1200°C, and in the case of 2NiO + Mg + C, at 800°C.

This work was supported by the Committee of Science MES of RA (Research grants 18A-1d12 and 18T-1D051), and the Estonian Research Council grant PSG220 (S. Aydinyan).

1. Kh.K. Khan, M. Mehmood, M. ul Hassan, J. Ahmad, Z. Iqbal, T. Muddasser, gas nitriding of electrodeposited Ni–W Alloys, *Met. Sci. Heat Treat.*, 2011, vol. 53, nos. 1–2, pp. 87–90.
2. P. Indyka, E. Beltowska-Lehman, L. Tarkowski, A. Bigos, E. García-Lecina, Structure characterization of nanocrystalline Ni–W alloys obtained by electrodeposition, *J. Alloys Compd.*, 2014 vol. 590, pp. 75–79.
3. M. Zakaryan, S. Aydinyan, S. Kharatyan, Combustion synthesis and consolidation of Ni–W nanocomposite material, *Ceram. Mod. Tech.*, 2018, <https://doi.org/10.29272/cmt.2018.0007>
4. S.V. Aydinyan, Kh.T. Nazaretyan, A.G. Zargaryan, M.E. Tumanyan, S.L. Kharatyan, Reduction mechanism of  $WO_3 + CuO$  mixture by combined Mg/C reducer, Non-isothermal conditions-high heating rates, *J. Therm. Anal. Calorim.*, 2018, vol. 133, no. 1, pp. 261–269.
5. M.K. Zakaryan, O.M. Niazyan, S.V. Aydinyan, S.L. Kharatyan, DTA/TG Study of NiO Reduction by Mg + C Combined Reducer, *Chem J. Armenia*, 2018, vol. 71, no. 4, pp. 473–485.
6. H.E. Kissinger, Reaction kinetics in differential thermal analysis, *Anal Chem.*, 1957, vol. 29, pp. 1702–1706.

## COMPARISON OF THE INFLUENCE OF VIBRATION AND CENTRIFUGAL FORCES FOR THE FORMATION OF HARD ALLOYS

G. Zakharov<sup>\*a</sup>, Z. Aslamazashvili<sup>a</sup>, G. Tavadze<sup>a</sup>, G. Oniashvili<sup>a</sup>, T. Batsikadze<sup>a</sup>,  
and D. Kvashkvadze<sup>a</sup>

<sup>a</sup>F. Tavadze Metallurgy and Materials Science Institute, Tbilisi, 0186 Georgia  
\*e-mail: algar@mail.ru

DOI: 10.24411/9999-0014A-2019-10199

During self-propagating high-temperature synthesis (SHS) external influences, such as pressure, ultrasound, centrifugal force, etc. have significant effect on structure and physical and mechanical characteristics when forming a target product [1–5]. These can be achieved by applying SHS-compaction and SHS-metallurgy [6, 7]. In SHS processes at the minimum "critical" sizes of a reactionary form (internal diameter and length) synthesis of exothermic chasm does not proceed that is the well-known fact. The minimum critical internal diameter of a reactionary form to be in repartitions is 8–12mm, which depends on structure, density, and methods of impact on exothermic mixture during synthesis of target material. These technological disadvantages can be overcome by the SHS-extrusion method. One of the most important process parameters of SHS extrusion is delay-time pressing. At small delay time expression is practically not observed, material does not succeed to be synthesized completely. At large time delay material loses the plastic properties and there is an obstruction of a matrix. It should be noted that an optimum interval of time delay is very narrow and defined as 4.5–6.5 s [8]. Search for new technology solutions for synthesis of materials and receiving samples with a critical internal diameter of a reactionary form is a topical task.

For comparison of quality of the received cast solid alloy experiments were conducted in the high-pressure reactor and in the laboratory centrifugal machine.

Samples were obtained from the solid alloy developed after studying multicomponent system: NiO–Cr<sub>2</sub>O<sub>3</sub>–Co<sub>3</sub>O<sub>4</sub>–WO<sub>3</sub>–TiO<sub>2</sub>–MoO<sub>3</sub>–B<sub>2</sub>O<sub>3</sub>–Nb–Zr–C –Al.

By using the laboratory centrifugal machine the prepared exothermic mixture was placed in a graphite glass in which placed a graphite form-building element with an internal diameter of 18 mm and with the height of sample of 45 mm. The limitation of height of a sample was connected to design of the centrifugal machine which did not allow receiving a sample more than 45 mm in length. At the established rotation speed of 2000 rpm the exothermic mixture/chasm was initiated. Figure 1 shows samples of various geometrical form with height of 45 mm which are dense and pore-free.



Fig. 1. The cast samples with various geometrical form with height of 45 mm received by laboratory centrifugal machine.

In the high pressure reactor samples with diameter  $\sim D = 15$  mm and 110 mm in length were obtained. Researches were directed to receiving dense material from solid alloy by vibrations and with the changing frequency and amplitude. Frequency of vibrations was ranging from 50 up to 100 Hz, amplitudes was 0.1 and 0.2 mm. For experiments the vibration device shown in Fig. 2 (general view (a) and the drawing in 3D format (b)) was designed. Necessary frequency of vibrations was carried out by means of the developed electronic device (Frequency Generator), the scheme is presented in Fig. 3.



Fig. 2. Vibration installation: interior (a), drawing in 3D (b). 1 graphite adapter, 2 quartz forming tube, 3 graphite form, 4 protective glass, 5 vibrating table.

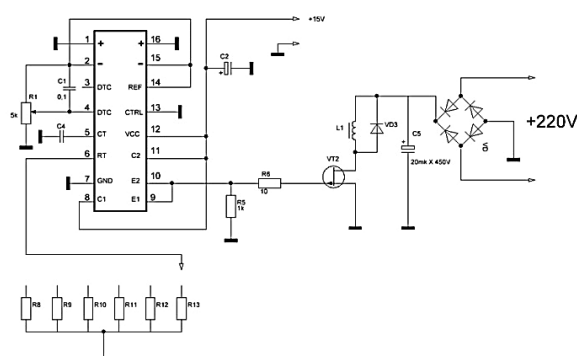


Fig. 3. Principal scheme of electronic installation (Frequency Generator).

Chasm components are preliminary dried, dosed and mixed. Chasm in weight of 250 g was loaded into a graphite form of the vibration device which was then placed in a high-pressure reactor. The initiating spiral was fixed on conductor cables, and brought into contact with exothermic chasm. It must be note that the scheme was assembled so that the mechanism of the vibration device starts just after the initiation of exothermic mixture and burning of an electric spiral. The general scheme of the vibration device placed in high pressure reactor and connection of electronic device is presented in Fig. 4.

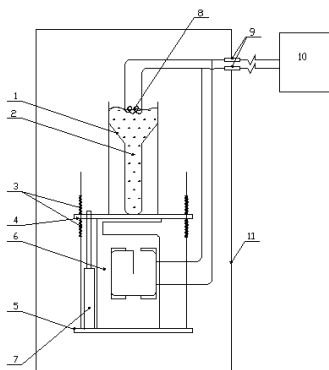


Fig 4. Scheme of the vibration installation placed in high pressure reactor  
1 graphite form, 2 chasm, 3 mechanism of vertical shift of a vibration table from 0.1 to 0.2 mm providing the required amplitudes of fluctuations of the formed sample, 4 vibration table, 5 clamp, 6 transformator, 7 shock rod, 8 initiating spiral, 9 conductor cables, 10 internal contour of high pressure reactor, 11 frequency generator.



Experiments were made in the atmosphere of nitrogen under a pressure of 30 atm. The received samples are presented in Fig. 5.



Fig. 5. The samples received in the high-pressure reactor as a result of vibration:  
 1 amplitude of fluctuations is 0.1 mm, frequency is 50 Hz;  
 2 amplitude of fluctuations is 0.2 mm, frequency is 100 Hz;  
 3 amplitude of fluctuations is 0.2 mm, frequency is 50 Hz;  
 4 amplitude of fluctuations is 0.1 mm, frequency is 100 Hz.

It is visible that with increase in frequency and amplitude of fluctuations the porosity of material is considerably reduced.

The analysis of the received results showed that synthesis of materials with a critical internal diameter and length with more than 45 mm can be realized by increasing the length of the reactionary camera of the centrifugal machine. For realization of the task, it is planned to be developed (modernization) of the laboratory centrifugal machine. Realization of a task of receiving pore-free materials in high pressure reactor demands to improve a design and the electronic system of the vibration device.

On the basis of the received experimental results was outlined tendency for obtaining the optimistic final results. For the solution of set tasks research works will be continued. The result will be achieved after development of new devices. It will allow to synthesize materials and products with a critical internal diameter of a reactionary form and not less than 110 mm in length under conditions of centrifugal force and in high pressure reactor.

1. L. Kecskes, B. Butler, G. Oniashvili, Z. Aslamazashvili, G. Zakharov, A. Peikrishvili, Effect of titanium–aluminum ratio on the thermal explosion processing of TiAl–TiB<sub>0.6</sub> layered composites, *Mater. Manufact. Proc.*, 2011, vol. 26, no. 9, pp. 1157–1163.
2. V. Klubovich, M. Kulak, B. Hina, Ultrasound in processes of the self-extending high-temperature synthesis, Monograph. Minsk, BNTU, 2006, 279 p.
3. G. Jishkariani, G. Jandieri, D. Sakhvadze, G. Tavadze, G. Zakharov, G. Oniashvili, Z. Aslamazishvili, Ecological problems related to mining-metallurgical industries and innovatory, Energy-efficient ways of solving them, *Eng.*, 2012, vol. 4, no. 2, pp. 83–89.
4. V. Yukhvid, A. Kachin, G. Zakharov, Centrifugal SHS-surfacing of the refractory inorganic materials, *Int. J. Self-Propag. High-Temp. Synth.*, 1994, vol. 3, no. 4, p. 321–332.
5. A. Chirakadze, Z. Buachidze, A. Gigineishvili, P. Kervalishvili, G. Zakharov, G. Oniashvili, Combined processing of waste organic polymers and manganese bearing waste/low grade ores into fuels and low-carbon manganese alloys, *Int. J. Global Warming*, 2016, vol. 10, no. 1/2/3, pp. 242–262.
6. Z. Aslamazashvili, G. Oniashvili, G. Zakharov, et al, Some peculiarities of phase formation in Ti–Cr–C–Me system by SHS, *Sci. Technol.*, 2014, vol. 715, no. 1, pp. 45–51.
7. G. Oniashvili, G. Tavadze, G. Zakharov, Z. Aslamazashvili, Self-propagating high-temperature synthesis of ferroalloys, LAP LAMBERT Academic Publishing, International Book Market Service Ltd, 2018.
8. P. Bazhin, A. Savelyev, A. Stolin, A. Aborkin, Receiving ceramic materials on the basis of TiC–W<sub>2</sub>C–Co by the SVS-extrusion method, *New Refract. Mater.*, 2017, no. 1, pp. 21–24.

## METALLOTHERMIC SHS OF ALLOYED COMPOSITES BASED ON Co

**K. V. Zakharov<sup>\*a</sup>, D. E. Andreev<sup>a</sup>, V. I. Yuxhvid<sup>a</sup>, N. V. Sachkova<sup>a</sup>,  
and N. Yu. Khomenko<sup>a</sup>**

<sup>a</sup>Merzhanov Institute of Structural Macrokinetics and Materials Science, Russian Academy of Sciences, Chernogolovka, Moscow, 142432 Russia

\*e-mail: zakharov@ism.ac.ru

DOI: 10.24411/9999-0014A-2019-10200

This work is aimed at the synthesis via gravity-assisted metallothemic SHS of cast alloyed composites based on cobalt: hard alloys (Co–Cr–Ti–C, etc.), refractory alloys (Co–Al–Mo, etc.). In addition to solving the fundamental problem associated with obtaining new cobalt-based composites with unique properties, the task of developing the foundations of high-tech, high-performance manufacturing technologies will be solved. The materials being developed can be used in metalworking (stamping), for solving problems of the aerospace complex (refractory materials). Earlier, the authors showed that the methods and approaches of metallothemic SHS can be effectively used to produce superalloys based on nickel and titanium, niobium silicides, as well as hard alloys and FGM based on titanium carbides and chromium. It was found that the autowave (frontal) chemical transformation of the initial mixture into final products occurs in the combustion wave. The target product of autowave synthesis is refractory material (RM), and a side product is the oxide phase (metal oxide of the reducing agent). High combustion temperature leads to gas formation and dispersion of the melt at atmospheric pressure [1, 2]. Increased pressure and centrifugal action allow to suppress the spread, therefore, SHS-metallurgy is carried out in reactors under gas pressure or, most often, in centrifugal installations. Optimization of the composition of the initial mixtures, the level of overload allowed to obtain composites (CM) with a high level of properties necessary for use in industry. At the initial stage of research, highly exothermic mixtures capable of burning were developed for the synthesis of the material and the production of composite materials based on Co–Cr–Mo–Nb–Ti–C with dispersion/dispersion hardening TiC/Ti + C, respectively; waves of combustion, experimental studies have been carried out in centrifugal installations, the influence of burning velocity and overload on the formation of chemical and phase composition, macro- and microstructure of cast products of combustion determined optimal synthesis conditions. It was found that in the case of dispersed alloying with titanium carbide (TiC), the burning velocity, combustion temperature and, as a result, the formation of a cermet grade decrease. In turn, in the case of dispersion alloying, when Ti and C are introduced into the exothermic mixture, the combustion process in the form of titanium powder (PTOM) and soot undergoes the following changes: in the beginning, there is a significant variation in the reaction products due to the formation of metal suboxides and carbon black interaction with the resulting oxygen decomposition results of the starting oxides. In addition, the expansion of the limits of combustion and phase separation was revealed.

The research was supported by the Russian Foundation for Basic Research, no. 19-03-00088.

1. M.I. Alymov, V.I. Yuxhvid, D.E. Andreev, V.N. Sanin, Chemical transformations of multicomponent thermite-type mixtures in combustion waves, *Dokl. Phys. Chem.*, 2015, vol. 460, iss. 1, pp. 6–9.
2. D.E. Andreev, V.I. Yuxhvid, D.M. Ikornikov, V.N. Sanin, T.I. Ignat'eva, Gravity-assisted metallothemic SHS of titanium aluminide with Al–Ca mixture as a reducing agent, *Int. J. Self-Propag. High-Temp. Synth.*, 2018, vol. 27, iss. 2, pp. 89–91.

SELF-PROPAGATING HIGH-TEMPERATURE SYNTHESIS OF  $\alpha$ - $\text{Si}_3\text{N}_4$   
WITH PARTICIPATION OF SODIUM HALOGENIDESV. V. Zakorzhevsky<sup>\*a</sup>, N. I. Mukhina<sup>a</sup>, and I. D. Kovalev<sup>a</sup><sup>a</sup>Merzhanov Institute of Structural Macrokinetics and Materials Science, Russian Academy of Sciences, Chernogolovka, Moscow, 142432 Russia

\*e-mail: zakvl@ism.ac.ru

DOI: 10.24411/9999-0014A-2019-10201

Ceramic materials from silicon nitride are widely used for the production of structural and functional ceramics operating under extreme conditions of high temperatures and mechanical loads. The strength properties of ceramics depend on the characteristics of the initial powders of silicon nitride. One of the important parameters affecting the properties of ceramics is the size and shape of particles. To obtain ceramics by hot pressing and slip casting, it is preferable to use powders with equiaxial particles.

Generally, silicon nitride powder is obtained by furnace method [1–3] and by synthesis and decomposition of silicon diimide [4]. Grinding and classification operations are performed to obtain equiaxed particles.

During the synthesis of the alpha phase of silicon nitride in the combustion mode, silicon nitride particles are formed in the form of filamentous crystals. Such a microstructure is formed due to realization of gas-phase mechanism of structure formation [5, 6]. Since the elongated silicon nitride particles are formed as a result of gas-phase reactions, it is necessary to create synthesis conditions that prevent the realization of the gas-phase mechanism of structure formation in order to obtain equiaxed particles. The paper presents the results of studies on the effect of sodium halide additives on the microstructure and phase composition of silicon nitride.

In the study of the effect of sodium fluoride on the microstructure and synthesis parameters of  $\text{Si}_3\text{N}_4$ , it was found that with the introduction of 24 wt % Si and 1 wt % NaF into the reaction mixture, the synthesis product is formed in the form of conglomerates which consist of particles of equiaxed shape of 0.3–3  $\mu\text{m}$  in size (Fig. 1). Combustion temperature was 1713°C. The alpha phase content increased from 97 to 98 wt %. By increasing the additive NaF to 3 wt %, the combustion temperature was 1773°C. The alpha phase content in the synthesis product was significantly decreased from 97 to 91 wt %. The synthesis product consisted of conglomerates formed by mainly equiaxial particles 0.5–3  $\mu\text{m}$  in size with a predominance of particles larger than 1  $\mu\text{m}$  in size (Fig. 2). The analysis carried out by the method of energy-dispersive scattering showed the presence of fluorine and sodium atoms in samples of  $\text{Si}_3\text{N}_4$  in an amount of 0.7–1.3 wt %. The calculation of the equilibrium composition with sodium fluoride for the synthesis conditions showed the formation of  $\text{Si}_3\text{N}_4$ , Si-liquid, Na-gas, SiF,  $\text{Na}_2\text{SiO}_3$ -liquid. Sodium silicate is formed as a film on the surface of silicon particles when NaF interacts with a silicon oxide film by the reaction  $\text{Si} + \text{SiO}_2 + \text{NaF} = \text{Na}_2\text{SiO}_3 + \text{SiF}$ . The film NaF,  $\text{Na}_2\text{SiO}_3$  apparently prevents the gasification of silicon and, accordingly, the implementation of the gas-phase mechanism of structure formation. Nitriding occurs in the diffusion mode. Sodium silicate is also as a sintering additive.

When using a green mixture with 1 and 3 wt % sodium chloride, combustion temperature varied from 1615 to 1785°C for 24 and 26 wt % Si respectively. The microstructure of both samples is represented by particles of equiaxial and elongated shape (Figs. 3, 4). The content of the alpha phase increased by 2 wt %. Compared with the initial mixture, X-ray phase analysis showed that the NaCl phase is present only in the surface layer of the cake.

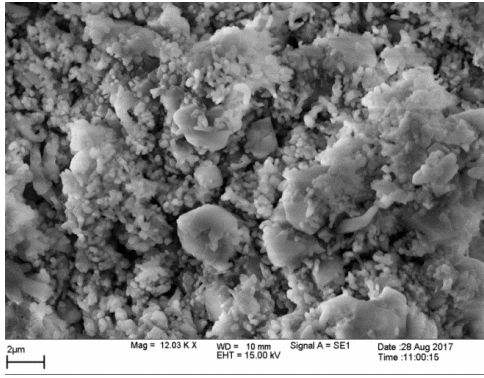


Fig. 1. Microstructure of  $\text{Si}_3\text{N}_4$ . 24 wt % Si, 1 wt % NaF.  $T_{\text{comb}} = 1713^\circ\text{C}$ .

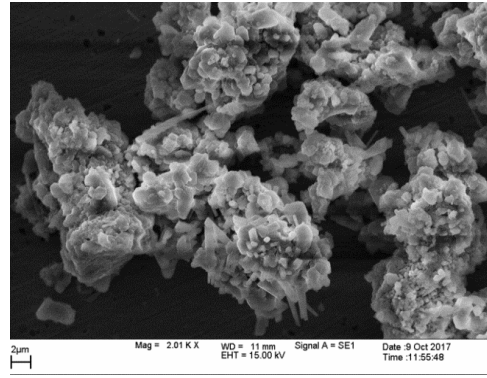


Fig. 2. Microstructure of  $\text{Si}_3\text{N}_4$ . 26 wt % Si, 3 wt % NaF.  $T_{\text{comb}} = 1773^\circ\text{C}$ .

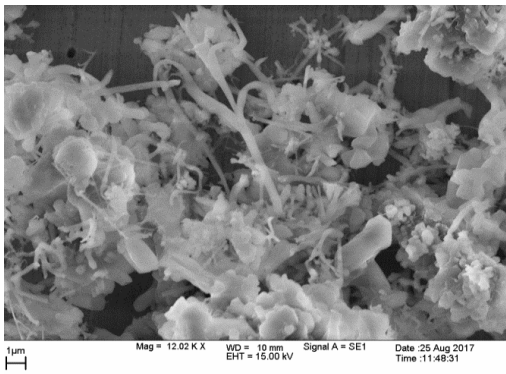


Fig. 3. Microstructure of  $\text{Si}_3\text{N}_4$ . 24 wt % Si, 1 wt % NaF.  $T_{\text{comb}} = 1615^\circ\text{C}$ .

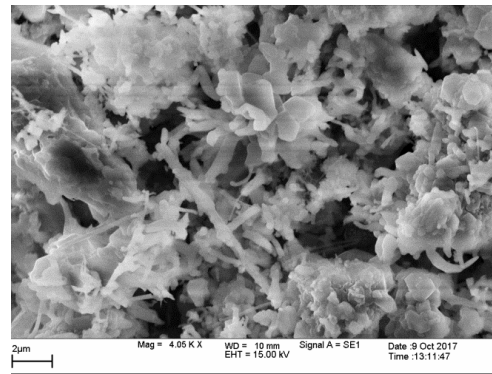


Fig. 4. Microstructure of  $\text{Si}_3\text{N}_4$ . 26 wt % Si, 3 wt % NaF.  $T_{\text{comb}} = 1785^\circ\text{C}$ .

The formation of filamentary crystals of  $\text{Si}_3\text{N}_4$  indicates the realization of the gas-phase mechanism of structure formation. The calculation of the equilibrium composition with sodium chloride for the synthesis conditions showed the presence of Na-gas, SiCl, SiO, Si-liquid, which promote to the partial realization of the gas-phase mechanism of structure formation, by reaction  $\text{SiCl} + \text{Na-gas} + \text{N}_2 = \text{Si}_3\text{N}_4 + \text{NaCl}$ . It was found that with the use of 3 wt % NaCl additives, the alpha phase content does not decrease at  $T_{\text{comb}} = 1785^\circ\text{C}$ , as compared to NaF. This can be explained by the fact that when using NaCl, volatile silicon suboxide (SiO) is formed in the combustion wave, which evaporates from the reaction zone, thereby not participating in the phase transition, unlike NaF, which forms the liquid phase of sodium silicate.

Samples of silicon nitride obtained with the participation of sodium fluoride were crushed with ceramic balls in water for 1 h to destroy the conglomerates and remove sodium fluoride. Silicon nitride was separated from the NaF solution using a vacuum filter and washed with distilled water. After drying, the silicon nitride was deagglomerated in a jet mill. The final product is a powder with equiaxed particle shape, polydisperse distribution. The average particle diameter  $d_{50}$  was 1.2–1.5  $\mu\text{m}$ . The specific surface area was 5–6  $\text{m}^2/\text{g}$ .

1. A. Atkinson, A.J. Moulson, E.W. Roberts, Nitridation of high purity silicon, *J. Am. Ceram. Soc.*, 1976, vol. 59, no. 3, pp. 285–289.
2. S.C. Zhang, W.R. Cannon, Preparation of silicon nitride from silica, *J. Am. Ceram. Soc.*, 1984, vol. 67, no. 10, pp. 691–695.
3. M. Ekelund, B. Forslund, J. Zheng, Control of particle size in  $\text{Si}_3\text{N}_4$  powders prepared by high-pressure carbothermal nitridation, *J. Mater. Sci.*, 1996, vol. 21, no. 21, pp. 5749.
4. T. Yamada, Preparation and evaluation of sinterable silicon nitride powder by imide decomposition method, *Am. Ceram. Soc. Bull.*, 1993, vol. 72, no. 5, pp. 99–106.

5. V.V. Zakorzhevsky, I.P. Borovinskaya, Some regularities of  $\alpha$ -Si<sub>3</sub>N<sub>4</sub> synthesis in a commercial SHS reactor, *Int. J. Self-Propag. High-Temp. Synth.*, 2000, vol. 9, no. 2, pp. 171–191.
6. V.V. Zakorzhevskii, I. P. Borovinskaya, Combustion synthesis of silicon nitride using ultrafine silicon powders, *Powder Metall. Met. Ceram.*, 2009, vol. 48, nos. 7–8, pp. 375–380.

## STRUCTURE AND PROPERTIES OF ANTIBACTERIAL YET BIOCOMPATIBLE Ag-DOPED MULTICOMPONENT COATINGS OBTAINED BY PULSED ELECTROSPARK DEPOSITION USING SHS-ELECTRODES

**E. I. Zamulaeva<sup>\*a</sup>, A. Yu. Potanin<sup>a</sup>, A. N. Sheveyko<sup>a</sup>, N. A. Gloushankova<sup>b</sup>, N. V. Shvindina<sup>a</sup>, S. G. Ignatov<sup>c</sup>, E. A. Levashov<sup>a</sup>, and D. V. Shtansky<sup>a</sup>**

<sup>a</sup>National University of Science and Technology MISIS, Moscow, 119049 Russia

<sup>b</sup>N. N. Blokhin Medical Research Center of Oncology of Ministry of Health, Moscow, 115478 Russia

<sup>c</sup>State Research Center for Applied Microbiology and Biotechnology, Obolensk, 142279 Russia

\*e-mail: zamulaeva@gmail.com

DOI: 10.24411/9999-0014A-2019-10202

Bone and joint degenerative and inflammatory problems affect millions of people worldwide, and the development of antibacterial yet biocompatible surfaces is a challenge that the biological community has been facing for many years, but the “materials of dream” have not been developed yet. Although the bulk properties of metallic materials in healthcare applications have been more or less optimized, the poor interfacial bonding between their surface and the surrounding tissue, as well as the occurrence of implant-related microbial infections remains a serious problem in reconstructive surgery. Surface engineering is an effective tool to impart desirable chemical, biological, and mechanical characteristics to the surface without compromising material bulk properties. For example, changing the chemical composition and surface roughness of metal implants can significantly improve their osteoconductive and osteoinductive characteristics. Another important task is imparting antibacterial characteristics to a surface in order to reduce the risk of microbial contamination when integrating the implant into living tissue. Self-propagating high-temperature synthesis (SHS) has become a “hot” and a rapidly developing topic in surface engineering. The most notable progress has been made in the field of SHS-produced targets and electrodes, which are widely used for deposition of various types of coatings. The aim of this work is to obtain antibacterial yet biocompatible coatings using pulsed electrospark deposition (PED). For this purpose new composite electrodes were fabricated from reaction mixtures Ti–C–20%Fe–10%Ca<sub>3</sub>(PO<sub>4</sub>)<sub>2</sub>–3.4%Mg–X%Ag with different amount of antibacterial component (X = 0, 0.5, 1.0, 1.5, and 2.0 at % Ag) using SHS method. Figure 1 represents the microstructure of the synthesized electrodes.

During the pulsed electrospark deposition (PED) the electrodes with a high Ag content demonstrated an enhanced mass transfer (77%) but reduced material erosion. The PED coatings mainly consisted of spherical TiC<sub>x</sub> grains evenly distributed in the Ti-based matrix and oxide inclusions. The Ag particles were homogeneously distributed through the coating thickness and their amount increased when the Ag content in electrode was raised. The Ag-doped PED coatings are characterized by a relatively high hardness (> 11 GPa) and an increased surface roughness ( $R_a > 4.5 \mu\text{m}$ ). Regardless of the method of Ag introducing into the coatings (PED using Ag-containing electrode or Ag<sup>+</sup> ion implantation into an Ag-free PED coating), the material with a small amount of Ag ( $\leq 1$  at %) demonstrated a high antibacterial effect against both gram-positive *S. aureus* and gram-negative *E. coli* bacteria. Although small Ag concentrations had a negative effect on the adhesion of osteoblast cells, at the optimal Ag content ( $\leq 0.7$  at %), the number of cells on the coating surfaces noticeably increased with time

and were not statistically significantly different from that in controls after 3–5 days. Thus, the PED is a promising technology that allows for implementation of a relatively simple, cost-effective, and scalable approach to obtaining biocompatible yet bactericide materials with a rough surface in a single technological run.

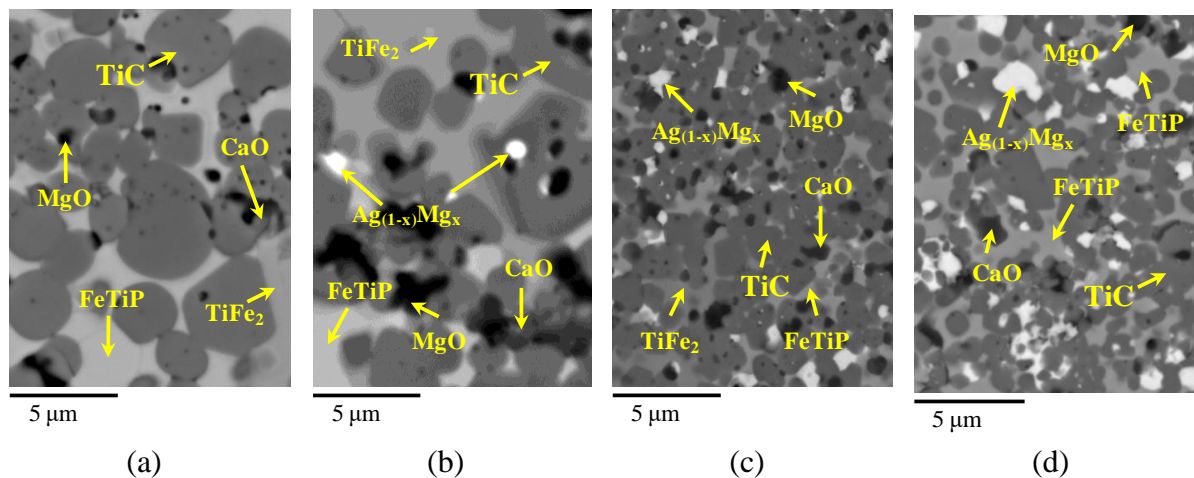


Fig. 1. Back-scattered electron SEM images of electrodes:  $X = 0$  (a);  $0.5$  (b);  $1$  (c); and  $2$  (d) at %.

1. E.I. Zamulaeva, A.N. Sheveyko, A.Y. Potanin, I.Y. Zhitnyak, N.A. Gloushankova, I.V. Sukhorukova, N.V. Shvindina, S.G. Ignatovc, E.A. Levashov, D.V. Shtansky, Comparative investigation of antibacterial yet biocompatible Ag-doped multicomponent coatings obtained by pulsed electrospark deposition and its combination with ion implantation, *Ceram. Int.*, 2018, vol. 44, pp. 3765–3774.

## HARD-MAGNETIC MATERIAL FROM A MECHANOACTIVATED SPHERICAL POWDER OF THE ALLOY 25XK15ЮБ

V. A. Zelensky<sup>\*a</sup>, V. S. Shustov<sup>a</sup>, A. B. Ankudinov<sup>a</sup>, I. M. Milyaev<sup>a</sup>, and M. I. Alymov<sup>b</sup>

<sup>a</sup>Baikov Institute of Metallurgy and Materials Science, Russian Academy of Sciences, Moscow, 119991 Russia

<sup>b</sup>Merzhanov Institute of Structural Macrokinetics and Materials Science, Russian Academy of Sciences, Chernogolovka, Moscow, 142432 Russia

\*e-mail: zelensky55@bk.ru

DOI: 10.24411/9999-0014A-2019-10203

The hard-magnetic single-phase alloys of the Fe–Cr–Co system occupy a well-deserved place among hard-magnetic materials due to their high mechanical properties with a sufficiently high level of magnetic hysteresis properties (residual induction  $B_r$ , coercive force  $H_{cB}$ , maximum energy  $(BH)_{max}$ ) [1, 2]. The production of magnets is carried out by casting or powder metallurgy. In the case of powder manufacture, in some cases it is more economically advantageous to give up the use of elemental powders, and to use powders of alloys with the required chemical composition. In the present work the alloy powder obtained by spraying the melt of a given composition with a stream of gas is selected as the starting material for the manufacture of samples of a hard-magnetic material. The cooling of the particles after spraying was performed at high speeds, which often leads to high hardness of the powder due to quenching. The use of such powders for the manufacture of details by powder metallurgy methods is associated with a many of difficulties. In particular, the compaction of such powders is complicated due to the spherical shape of the particles and the high strength of the powder due to quenching [3]. In this paper, an effective method for preparing the initial charge is proposed, which allows forming defect-free powder compacts and obtaining high-quality hard-magnetic material.

Spherical powder of 25XK15ЮБ alloy with an average particle size of about 20  $\mu\text{m}$  was used. Its chemical composition is presented in Table 1.

Table 1. Chemical composition (wt %) of 25XK15ЮБ powder.

| Fe   | C     | Cr   | Co   | V    | Al   | Si   | Nb   | S      | P    | O <sub>2</sub> | N <sub>2</sub> |
|------|-------|------|------|------|------|------|------|--------|------|----------------|----------------|
| base | 0.053 | 24.9 | 15.1 | 0.88 | 0.58 | 0.68 | 0.81 | 0.0074 | 0.03 | 0.47           | 0.23           |

Pressing a spherical powder in the state of delivery, despite the high pressure (up to 600 MPa) and the use of a split matrix, makes it impossible to obtain samples without defects. Pressings are stratified, and pieces of compacts are disintegrated into powder with a weak touch. To increase the compressibility of the powder, various methods were used: annealing of powder at a temperature above the recrystallization temperature; used plasticizer; the powder was mechanically activated in a planetary mill using balls of different sizes. However, the annealing did not improve the pressing - the same separation of compacts was observed as on the original powder. The introduction of a plasticizer (polyvinyl alcohol was used) made it possible to obtain high-quality compacts and, after sintering, to obtain defect-free samples of a hard magnetic-alloy. However, the magnetic hysteresis characteristics (especially the maximum energy product) at the same time turned out to be unsatisfactory.

Mechanical activation of the charge was performed on a planetary mill Pulverizette-7 at a speed of 500 rpm. 10 g of powder and 70 g of steel balls with a diameter of 3 or 5 mm were taken for filling, the time was varied and was 20, 40, and 80 min. After mechanical activation,



the powders were pressed. Analysis of the quality of compacts shows that the use of 5-mm balls for mechanical activation is preferable. Grinding with 3 mm balls for 20 min as well as on the powder without grinding makes it impossible to get defect-free pressing. The results of the experiments are presented in Table 2, where the magnetic hysteresis characteristics of the sintered samples are also presented. As can be seen, their values have acceptable values for technical use and are comparable with the properties of hard-magnetic materials obtained by casting methods and powder metallurgy using elemental powders [4–6].

Table 2. Properties of compacts and magnetic hysteresis characteristics of sintered samples.

| Grinding time, min               | 20             |              | 40           |      | 80   |      |
|----------------------------------|----------------|--------------|--------------|------|------|------|
| Diameter of balls, mm            | 3              | 5            | 3            | 5    | 3    | 5    |
| Quality of pressing              | unsatisfactory | satisfactory | satisfactory | good | good | good |
| $B_r$ , T                        | -              | 1.185        | 1.23         | 1.25 | 1.21 | 1.18 |
| $H_{cB}$ , kA/m                  | -              | 42.4         | 43.0         | 42.7 | 43.0 | 43.1 |
| $(BH)_{max}$ , kJ/m <sup>3</sup> | -              | 27.6         | 30.6         | 31.7 | 30.7 | 31.8 |

Figure 1 shows the hysteresis curve of a hard-magnetic material synthesized from a powder, processed for 80 min with 5-mm balls. The density of obtained material is about 99%. Figure 2 shows the SEM images of spherical particles of the initial powder and the powder after grinding for 40 min with balls with a diameter of 5 mm. It is clearly seen that grinding leads to coarsening of powders due to cold welding and a drastic change in the shape of particles compared with the original spherical powder. The scatter of particles in size becomes significantly smaller in comparison with the original spheres, where the diameter of the main mass of particles lies in the range from 2 to 20  $\mu\text{m}$ . The fact that there are no small particles (less than 10  $\mu\text{m}$ ) in the treated powders also indicates that cold welding took place during grinding, during which small spherical particles become part of large ones.

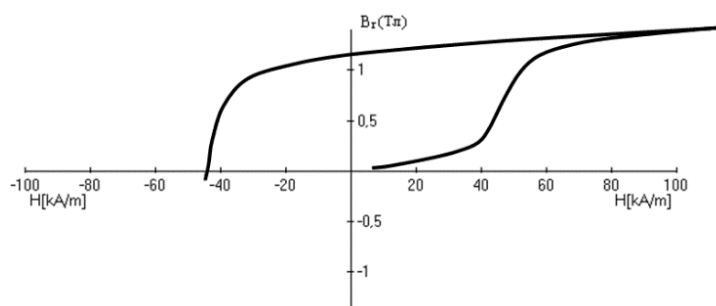


Fig. 1. Hysteresis curve of a sample from mechanically activated powder treated for 80 min using 5-mm balls.

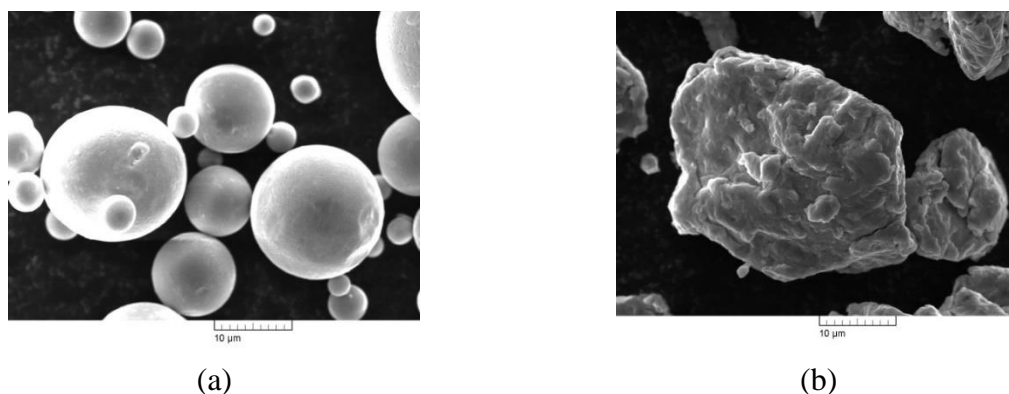


Fig. 2. Powders: (a) initial spherical; (b) grinding for 40 min with balls  $\varnothing$  5 mm.

Thus, it has been shown that the rational method of preparing a charge from spherical powder, obtained by the method of melt sputtering with a gas jet, is the mechanical activation procedure. Materials synthesized from mechanically activated mixtures have high magnetic properties that ensures their technical application. The best result of magnetic hysteresis characteristics was obtained during mechanical activation for 80 min:  $B_r = 1.18$  T;  $H_{cB} = 43.1$  kA/m;  $(BH)_{\max} = 31.8$  kJ/m<sup>3</sup>.

This work was supported by the Russian Foundation for Basic Research, grant no. 18-03-00666 with the involvement of state assignment number 075-00746-19-00.

1. H. Kaneko, M. Homma, K. Nakamura, New ductile permanent magnet of Fe–Cr–Co system, *AIP Conf. Proc.*, 1972, no. 5, pp. 1088–1092.
2. H. Kaneko, M. Homma, M. Okada, T. Fukunada, Fe–Cr–Co permanent magnet alloys containing Nb and Al, *IEEE Transact. Magnet.*, 1975, vol. 11, no. 5, pp. 1440–1442.
3. O.S. Nichiporenko, YU.I. Nayda, A.B. Medvedovskiy, *Raspylennyye metallicheskiye poroshki*, Kiyev: Naukova dumka, 1980, 240 p.
4. A.V. Korznikov, S.V. Dmitriev, G.F. Korznikova, S.V. Gladkovskii, A.I. Potekaev, The Effect of the heat treatment regime on the structure and physical-mechanical properties of a 23X15KT hard magnetic alloy, *Russ. Phys. J.*, 2015, vol. 57, no. 10, pp. 1308–1312.
5. I.M. Milyayev, M.I. Alymov, V.S. Yusupov, A.B. Ankudinov, V.A. Zelenskiy, A.I. Milyayev, Vliyaniye kremniya i molibdena na magnitnyye gisteresisnyye svoystva magnitotverdogo poroshkovogo splava 22KH15KA, *Izvestiya vysshikh uchebnykh zavedeniy. Poroshkovaya metallurgiya i funktsionalnyye pokrytiya*, 2011, no. 4, pp. 54–57.
6. Yu.V. Sudenkov, V.M. Sarnatskii, I.V. Smirnov, Orientation magnetic phase transition induced by shock loading of the Fe–Cr–Co alloy, *Phys. Solid State*, 2017, vol. 59, no. 2, pp. 287–291.

## SOLID-STATE REACTIONS IN Al-BASED MULTILAYER NANOSYSTEMS

S. M. Zharkov<sup>\*a,b</sup>, R. R. Altunin<sup>b</sup>, and E. T. Moiseenko<sup>b</sup><sup>a</sup>Kirensky Institute of Physics, Federal Research Center KSC SB RAS,  
Krasnoyarsk, 660036 Russia<sup>b</sup>Siberian Federal University, Krasnoyarsk, 660041 Russia  
\*e-mail: zharkov@iph.krasn.ru

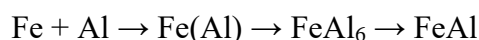
DOI: 10.24411/9999-0014A-2019-10204

The aim of this study was to establish a sequence of phases formed during the solid-state reaction in Al/Cu and Al/Fe bilayer nanosystems. The investigations were carried out by *in situ* electron diffraction, which allowed us to examine the phase composition variation directly during the solid-state reaction.

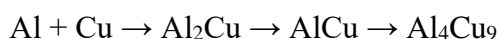
The Al/Cu and Al/Fe bilayer nanosystems were obtained by the method of electron beam evaporation in high vacuum with the help of a high vacuum installation MED-020 (Bal-Tec). The base vacuum was  $5 \times 10^{-5}$  Pa. The bilayer films with the thickness of 40–60 nm were obtained by the successive deposition of layers onto a substrate.

The microstructure and elemental composition of the nanosystems were examined by a JEOL JEM-2100 transmission electron microscope. The phase composition of the investigated samples was determined from electron diffraction patterns. The solid state reactions in Al/Cu and Al/Fe were initiated by thermal heating. The heating was performed directly in the JEM-2100 column using a Gatan heating holder. This method was successfully used to study the solid state reactions in Al/Pt [1], Cu/Au and Fe/Pd [2] bilayer nanosystems.

The solid-state reaction between Al and Fe nanolayers was detected at a temperature  $\approx 100^\circ\text{C}$ . The reaction starts from the formation of Fe(Al) – the solid solution of Al in  $\alpha$ -Fe. This is accompanied by the increase of the  $\alpha$ -Fe lattice constant (see Fig. 1). At  $\approx 400^\circ\text{C}$  there begins the formation of a FeAl<sub>6</sub> phase and at  $\approx 480^\circ\text{C}$  the formation of FeAl phase stars (Fig. 2), which corresponds to the atomic proportion of Fe and Al in the Al/Fe bilayer nanosystem under investigation (Al:Fe  $\approx 50:50$  at %). So, the following phase sequence was observed during the solid-state reaction in the Al/Fe nanosystem:



The beginning of the solid-state reaction between Al and Cu nanolayers was detected at  $\approx 90^\circ\text{C}$ . The reaction starts from the formation of Al<sub>2</sub>Cu phase, in accordance with the prediction of the effective heat of the formation rule [3]. The following phase sequence was observed during the solid-state reaction in the Al/Cu bilayer nanosystem:



The electron diffraction patterns obtained in the process of heating of the Al/Cu nanosystem were analyzed to determine the quantitative content of the phases formed during the solid-state reaction in the Al/Cu bilayer nanosystem (see Fig. 3).

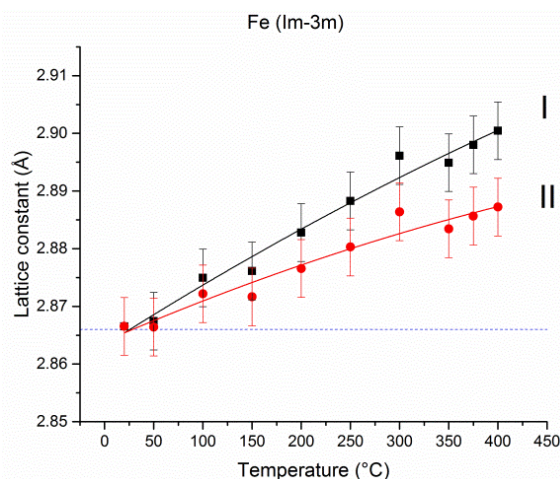


Fig. 1. The changing of  $\alpha$ -Fe lattice constant during the heating of Al/Fe (curve I – the experimental data; curve II – the data without contribution of thermal expansion).

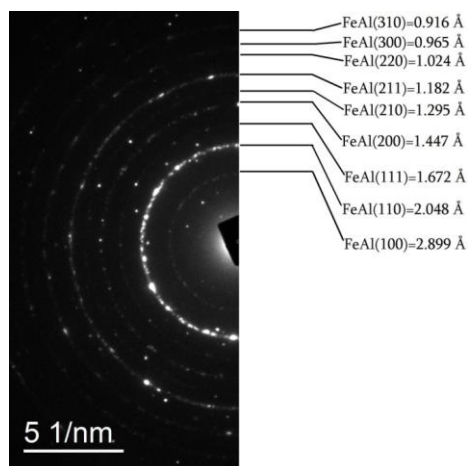


Fig. 2. Electron diffraction pattern obtained from Al/Fe at heating up to 650°C.

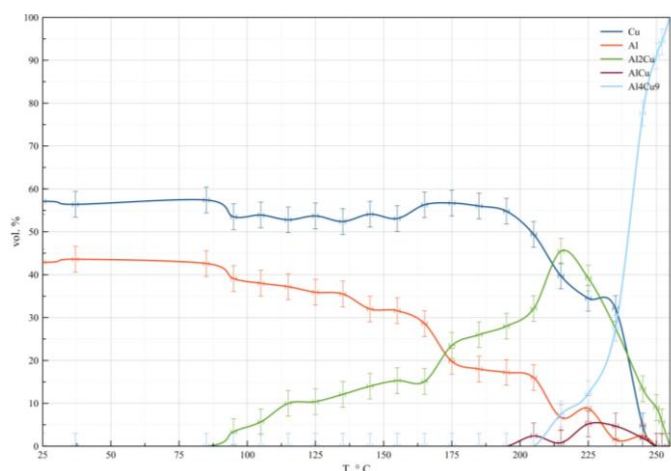


Fig. 3. Variation in the phase composition during the solid-state reaction in the Al/Cu bilayer nanosystem (vol %).

The investigation of the Al/Cu nanosystem was conducted under the financial support of the Russian Science Foundation (project no. 18-13-00080) and the investigation of the Al/Fe nanosystem was supported by the Russian Foundation for Basic Research (project no.18-03-01173).

1. R.R. Altunin, E.T. Moiseenko, S.M. Zharkov, Structural phase transformations in Al/Pt bilayer thin films during the solid-state reaction, *Phys. Solid State*, 2018, vol. 60, no. 7, pp. 1413–1418.
2. S.M. Zharkov, E.T. Moiseenko, R.R. Altunin, L1<sub>0</sub> ordered phase formation at solid state reactions in Cu/Au and Fe/Pd thin films, *J. Solid State Chem.*, 2019, vol. 269, pp. 36–42.
3. R. Pretorius, A.M. Vredenberg, F.W. Saris, R. de Reus, Prediction of phase formation sequence and phase stability in binary metal-aluminum thin-film systems using the effective heat of formation rule, *J. Appl. Phys.*, 1991, vol. 70, no. 7, pp. 3636–3646.

## COMBUSTION SYNTHESIS OF COMPOSITION ALLOYS

M. Kh. Ziatdinov

Tomsk State University, Tomsk, 634050 Russia

\*e-mail: ziatdinovm@mail.ru

DOI: 10.24411/9999-0014A-2019-10205

We are presenting research findings in the development of a specialized SHS technology for composite ferrous alloys for steel melting and blast furnace iron-making. To resolve the principle goal of creating metallurgical production lines we developed a new approach to practical implementation of the SHS method — a metallurgical SHS process. The metallurgical version of SHS is based on using different metallurgical alloys as the main raw stock; those include dust-type wastes of ferrite alloys production. In this case, the process of synthesis by combustion is implemented via exothermic exchange reactions. Here, composite materials form; they are based on inorganic compositions bound with iron and/or an alloy based on iron. It has been shown that depending on the aggregate state of source reagents, metallurgical SHS processes can be gasless, gas-absorbing or gas-yielding. Combustion modes for these processes largely differ. To arrange for metallurgical SHS process in weakly exothermic systems, we can use different versions of the thermal bonding principle. We have investigated self-propagating high-temperature synthesis of nitrated ferrovandium and ferrochrome. It has been shown that the phase composition of the source alloy has strong impact on the consistent behaviors of the combustion flow and the combustion mechanism of ferrovandium (if combustion is taking place in nitrogen atmosphere). In the course of nitrating  $\sigma$ -(Fe-V), process activation takes place; the activation is related to the transformation of the intermetallide into  $\alpha$ -solid solution when the phase transition temperature is reached ( $\sim 1200^\circ\text{C}$ ). The composition structure of ferrovandium nitride products is formed by the confluence of solid-liquid droplet-particles that consist of molten Fe and solid vanadium nitride. A 3-phase mechanism of ferrochrome interaction with nitrogen facilitates the achievement of a high degree of nitrating. We have shown that the combustion rates of ferrochrome (and chrome) during nitrating in coflow filtration mode increase as the nitrogen flow rate is increased. Here, the degree of ferrochrome nitrating during forced filtration (4.7–7.5% N) is much less than that during non-forced filtration (8.8–14.2% N).

It is shown that consistent patterns in the combustion of ferrosilicium in nitrogen are rather similar to those of metal silicon. As the concentration of silicon in initial ferrosilicium is increased, the intensity of its interaction with nitrogen increases as well, resulting in a significant growth of the combustion rate. The concentration of nitrogen in the combustion products here increases as well. In the entire investigated range of initial parameters (nitrogen pressure, powder fineness, burden mix), the main phase in the combustion products is  $\beta$ - $\text{Si}_3\text{N}_4$ . No considerable amounts of  $\alpha$ - $\text{Si}_3\text{N}_4$  have been observed. In practical applications, the use of FS75 and FS90 grade ferrosilicium is optimal for producing fire-resistant materials, while FS65 and FS75 (being the purest alloy grades) are optimal for obtaining alloying steel compositions. Introducing iron into the Ti-B ( $T_{\text{ad}} = 3190 \text{ K}$ ) system significantly narrows down the concentration limits of combustion. (Fe-B) + Ti mixture with 16.9% B alloy burns in a narrow range of Ti:B concentrations close to 0.86. When a ferroboration-titanium mixture burns, an increase in the initial temperature significantly expands the synthesis concentration limits. In all the cases, an increase in the initial temperature leads to a significant increase in the combustion rate. Heating up to  $T_0 \geq 300^\circ\text{C}$  allows for involving mixtures with more coarse titanium powders ( $r_{\text{av.Ti}} \geq 0.4 \text{ mm}$ ) into the SHS process. The synthesis is implemented in a

wide range of B:Ti ratios. By burning such mixtures, we can obtain alloys with 6–14% B and 30–60% Ti. Specialized industrial equipment has been built: a series of SHS reactors with the operation volume of 0.06, 0.15, and 0.3 m<sup>3</sup> for the serial production of manufacturing items based on hard-melting inorganic compositions (nitrides, borides, silicides, etc.) for metallurgical applications. Industrial SHS production of composite materials based on oxygenless compositions has been set up.

OBTAINING CARBON-CONTAINING COMPOSITES BASED ON  
ILMENITE AND CHROME CONCENTRATE BY SHSS. Tolendiuly<sup>\*a</sup>, S. M. Fomenko<sup>a</sup>, A. Akishev<sup>a</sup>, N. Rakhym<sup>a</sup>, and D. Kashkynbai<sup>a</sup><sup>a</sup>The Institute of Combustion Problems, Almaty, 050012 Kazakhstan

\*e-mail: sanat\_tolendiuly@mail.ru

DOI: 10.24411/9999-0014A-2019-10206

The creation of new materials and technologies for their production is one of the most important scientific and applied problems of physical materials science. The particular interest presents the new class of materials MAX-phase. These are ternary compounds that correspond to the general formula  $M_n + 1AX_n$ , where M is a transition metal; A is an element IIIA or IVA of the periodic group of elements, X is carbon or nitrogen. The structural features of their crystal lattices determine the unique combination of the properties of metal and ceramics in such materials. To obtain materials based on MAX phases, various methods are used. The main method of obtaining materials based on MAX phases is sintering, which requires a lot of energy and time. An alternative to sintering is self-propagating high temperature synthesis (SHS) [1]. Such compounds can be present in the carbon-containing refractories and give them the unique properties [2, 3].

Carbonaceous refractory materials have high thermal conductivity, good chemical resistance in contact with metal melts, slag and lining applied for the substructure domain electro thermal furnaces, smelting units for nonferrous metals. The general approach to the synthesis of carbon-containing refractory materials is to conduct aluminothermic solid-phase combustion of metal oxides in the mode of SHS in the presence of carbon. SHS products are a composite material of refractory compounds: aluminum oxide, metal carbide, carbon [4–8].

In this work, the phase composition, microstructure and some properties of SHS materials based on ilmenite and chromite concentrates were studied.

The following reagents taken to get carbonaceous refractory materials: aluminum powder PA-4 (99% purity), ilmenite concentrate, chromite concentrate, carbon in the form of electrode graphite (purity 95%), and silica powder (purity 98, 5%). Silica sol and 15% of  $MgSO_4$  aqueous solution were used as a cohesive. The silica sol prepared by hydrolyzing ethyl silicate brand ES-40 with a weak solution of sulfuric acid.

A number of laboratory experiments was carried out to determine the optimal ratio of initial components for the production of carbon-containing composite materials with desired properties. The temperature during the SHS process recorded using a high-precision pyrometer Raytek 3I.

A mixture of the green components thoroughly mixed in an agate mortar to obtain a homogeneous structure. Then, the samples were pressed in a tablet form using a hydraulic press with a 30 kN force to obtain dense samples, which then left on a special table for natural drying at room temperature of 18–22°C for 24 h. Next, the samples placed in a muffle furnace preheated to 950°C to initiate SH-synthesis. The temperature during the SHS process was about 1200°C.

The phase composition of the obtained materials was determined using X-ray phase analysis on a Dron-4M diffractometer using cobalt Ka-radiation. The completeness of the reaction was determined by the phase composition of the products of synthesis. X-ray phase analysis of synthesized carbon-containing samples from the ilmenite concentrate showed that the final product consists mainly of aluminum oxide and contains a small amount of useful silicon

carbide phase. It found that when an aqueous solution of magnesium sulfate used as a cohesive during SH-synthesis, an undesirable intermetallic phase of  $\text{Fe}_x\text{Si}_y\text{Ti}$  formed. The maximum amount of silicon carbide phase formed (the  $\text{Fe}_x\text{Si}_y\text{Ti}$  phase is not formed) when carbon content was 40–45%, the ilmenite concentrate was 30–32% by weight in sample.

X-ray phase analysis of synthesized carbon-containing chromite concentrate-based composites showed that the final combustion product consists mainly of spinel, pentachrome trisilicide and contains a small amount of useful silicon carbide, forsterite and aluminum oxide. When an aqueous solution of magnesium sulfate used as a cohesive during SH-synthesis, double  $\text{Cr}_x\text{Si}_y\text{C}_z$  carbide formed, which can be identified as the MAX phase. MAX phase is very important for imparting useful properties to the composite. The optimum content of components was to yield the maximum output  $\text{Cr}_x\text{Si}_y\text{C}_z$  phase: carbon 33%, chromium 35% by weight. It established that a silica sol does not form such phase during SH-synthesis when used it as a cohesive.

The morphology (Fig. 1) of the synthesized samples based on ilmenite concentrate analyzed using a Quanta 200i 3D scanning electron microscope. Figure 1a shows a sample based on ilmenite concentrate with silica sol, where it can be seen that the sample has a dense structure (with small pores) with particle sizes ranging from 0.8 to 3  $\mu\text{m}$  and have a fibrous form. According to Fig. 1b, the sample based on the ilmenite concentrate with magnesium sulfate was loose with numerous micropores whose particle size is in the range of from 3 to 10  $\mu\text{m}$ .

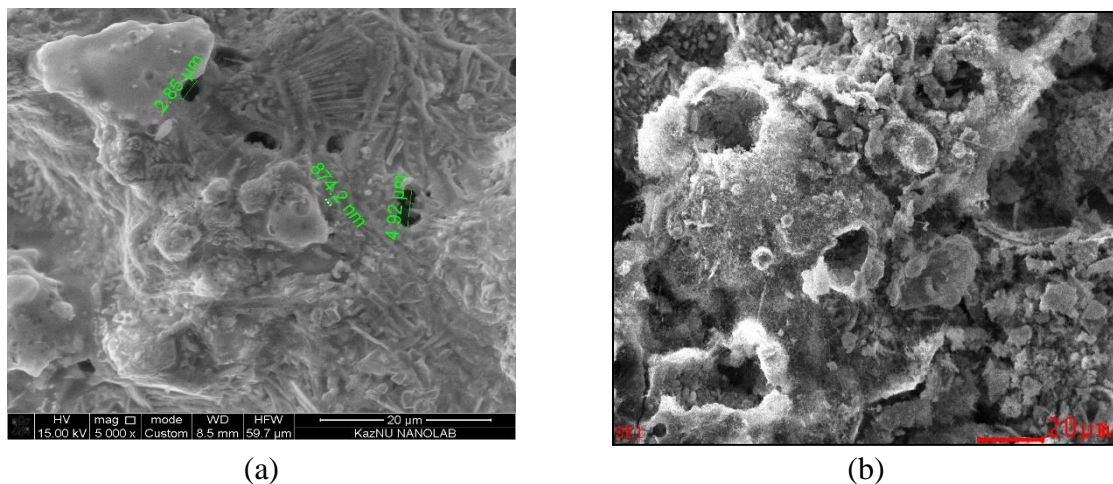


Fig. 1. Images of samples based on ilmenite concentrate with: (a) silica sol; (b) magnesium sulfate.

Figure 2a shows a sample based on chromite concentrate with magnesium sulphate, where it can be seen that the sample has a porous structure (with small pores) with particle sizes ranging from 1 to 3  $\mu\text{m}$  and have a fibrous form. According to Fig. 2b, a sample based on a chromite concentrate with a silica sol has a loose structure with numerous micropores whose particle sizes are in the range of 4 to 10  $\mu\text{m}$ .

Mechanical properties of the samples were determined by using a testing machine YES 2000 Type. The strength characteristics of the samples vary depending on the carbon content in the initial mixture. It is established that samples containing carbon about 40–45% by weight showed the best result of 5–8 MPa. Further studies have shown that the mechanical compressive strength decreases when trying to increase the carbon content in the mixture.

Carbon containing composite materials based on ilmenite and chromite concentrates were obtained by self-propagating high-temperature synthesis. The optimal conditions for the SH-synthesis of carbon-containing composites based on ilmenite and chromite concentrates with various cohesive were selected experimentally, providing the maximum content of titanium, silicon, chromium carbides and MAX-phase analogs in the material.



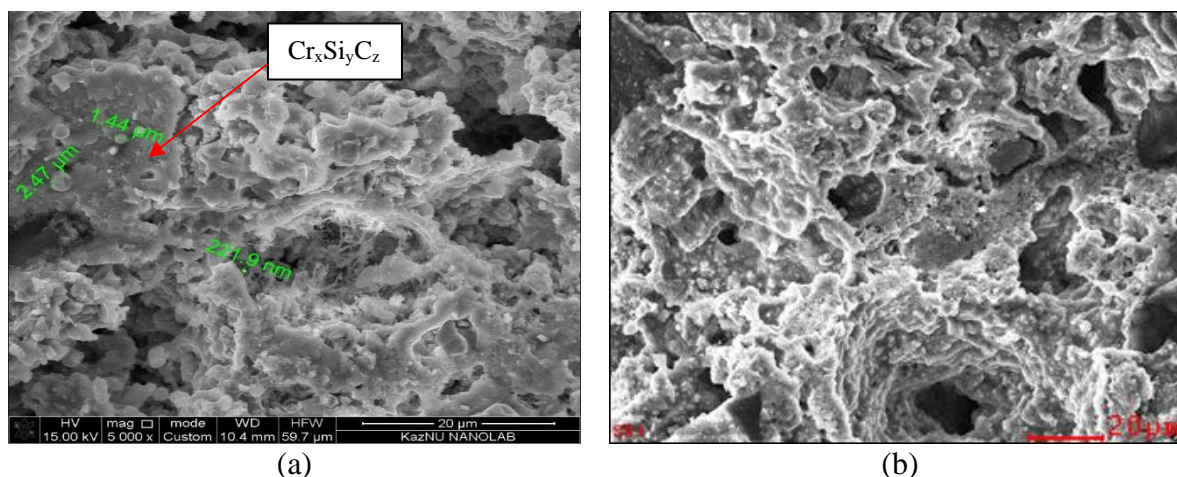


Fig. 2. Images of samples based on a chromite concentrate with: (a) magnesium sulfate; (b) silica sol.

1. V.L. Radishevsky, O.K. Lepakova, N.I. Afanasyev, Synthesis, structure and properties of the MAX phases  $Ti_3SiC_2$  and  $Nb_2AlC$ , *Tomsk State University Bull. Chem.*, 2015, no. 1, pp. 33–38.
2. V.E. Vaganov, N.V. Kamanina, Effect of carbon-containing nanostructures on the optical and physical properties of materials, including liquid crystals, *Liquid crystals and their practical use*, 2010, vol. 32, no. 2, pp. 5–24.
3. G.P. Fetisov, V.M. Karpman, V.S. Matyunin, et. al., *Materials science and technology of metals*, M.: Higher school, 2001, 370 p.
4. K.K. Strelov, P.S. Mamykin, *Refractory technology* 4th edition, Moscow, Metallurgy, 1988, 528 p.
5. V.E. Vaganov, Structure formation during sintering of powder materials of the system iron-carbon nanotubes (nanofibres), *Mater. Sci.*, 2011, no. 2, pp. 53–56.
6. Z.A. Mansurov, S.M. Fomenko, Carbonaceous refractory materials on SHS-technology, *Adv. Sci. Technol. Mater. Res.*, 2014, vol. 88, pp. 112–128.
7. S.M. Fomenko, A.Kh. Akishev, S. Tolendiuly, Study of intrastructural stresses under the influence of uneven heat loads, XVII International Conference of Refractors and Metallurgists, 2019.
8. A.Kh. Akishev, S.M. Fomenko, S. Tolendiuly, D.T. Kashkynbai, N.T. Rakhym, Intrastructural temperature stress is a major factor in the destruction of the refractories of metallurgical furnaces, *Combust. Plasma Chem.*, 2019, vol. 17, pp. 33–39,

## APPLICATION OF MICROVAWE RADIATION IN HETEROGENEOUS CATALYSIS

A. Zurnachyan<sup>a</sup>, D. Davtyan<sup>a</sup>, E. Karakhanov<sup>b</sup>, A. Akopyan<sup>b</sup>, and R. Mnatsakanyan<sup>a</sup><sup>a</sup>A.B. Nalbandyan Institute of Chemical Physics, NAS RA, Yerevan, Republic of Armenia<sup>b</sup>Lomonosov Moscow State University, Moscow, Russia

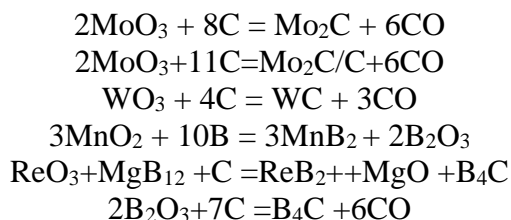
e-mail: rmnats@rambler.ru

DOI: 10.24411/9999-0014A-2019-10207

Microwave radiation (MWR) was used both for the synthesis of heterogeneous catalysts and for carrying out catalytic reactions. In recent years, MWR has been widely used in materials science due to the advantages [1] that it possesses, compared to traditional synthesis methods, rapid and homogeneous heating of the entire volume of the reaction mixture, rapid cooling of synthesis products, the possibility of obtaining nanoparticles with a narrow particle diameter distribution. The activation of catalytic reactions using MWR has the following advantages: a sharp reduction in the reaction time [2], an increase in the conversion and selectivity of the reaction in one direction, a decrease in the reaction temperature. It is natural to expect that with large-scale production all these factors will lead to greater energy economy and environmentally friendly processes. The main requirement for the use of MWR in chemical processes is the absorption ability of reagents to radiation. From this point of view, transition metals oxides, some modifications of carbon absorb MWR well and are good raw materials for the synthesis of carbides and borides to which the presented work is devoted.

The following compounds were synthesized and tested as catalysts: carbides Mo<sub>2</sub>C, 80% Mo<sub>2</sub>C/C, WC, 80% WC/C B<sub>4</sub>C, borides MnB<sub>2</sub>, ReB<sub>2</sub>.

The following reactions were used for the synthesis:



The carbon source was Vulcan XC-72 R (Cabot. Corp.), which absorbs MWR very well and thus serves not only as a carbon source, but also as an effective heater for the reaction mixture. The source of MWR was a household microwave oven with a frequency of 2.45 GHz and an output power of 900W (Electrolux). The synthesis was carried out in a quartz reactor in a stream of nitrogen or helium. The reaction temperature was measured using an Hi Temp 1800 infrared thermometer (Dostmann Electr.). The synthesis of carbides and borides usually lasted 5–20 min. X-ray phase analysis (Fig. 1) showed almost 100% conversion of the starting compounds. The broadening of the diffraction lines made it possible to estimate the size of the crystals using the Scherrer equation. Their catalytic activity in model and applied reactions was investigated.

The catalytic decomposition of hydrazine [3] was investigated in an autoclave with microwave heating in the presence of Mo<sub>2</sub>C or WC catalysts. The results are compared with conventional heating (Fig. 2) in a water bath. It can be seen that at the same temperature at MWR, the conversion of hydrazine is much higher. The synthesized catalysts were tested [4] in the reaction of catalytic hydrogenation of a series of alkenes-cyclohexene, octene-1, decene-1, and hexadecene-1 under autoclave conditions. Table 1 shows the alkenes conversion values in the presence of molybdenum carbide.

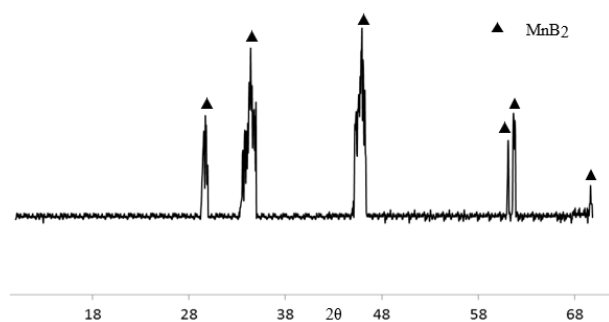
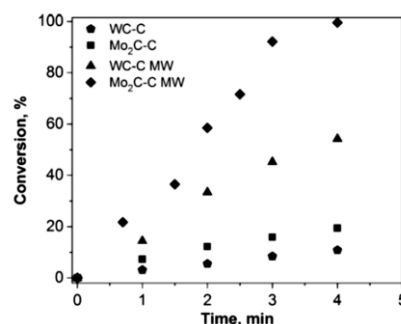
Fig. 1. XRD diffractogram of MnB<sub>2</sub>.

Fig. 2. Conversion of hydrous hydrazine.

Table 1. Alkenes conversion in the presence of Mo<sub>2</sub>C catalyst. Hydrogenation conditions: 2 h, 300°C,  $p(\text{H}_2) = 40$  atm,  $m(\text{catalyst}) = 50$  mg.

| Substrate    | Conversion, (40 atm H <sub>2</sub> ) % | Conversion, (30 atm H <sub>2</sub> ) % |
|--------------|--|--|
| Cyclohexene  | 40                                     | 66                                     |
| Octen-1      | 2                                      | 10                                     |
| Hexadecene-1 | 2                                      | 15                                     |
| Decene-1     | 8                                      | 26                                     |

Since cyclohexene is an effective substrate, further studies of the synthesized catalysts were tested with it. Table 3 compares the catalytic activities of the resulting systems.

Table 3. Effect of catalyst composition on cyclohexene hydrogenation. Hydrogenation conditions: 2 h, 300°C,  $p(\text{H}_2) = 40$  atm,  $m(\text{catalyst}) = 50$  mg.

| No | Catalyst                               | Conversion, % | Note   |
|----|--|---------------|--|
| 1  | Mo <sub>2</sub> C                      | 68            | activated by H <sub>2</sub>                  |
| 2  | Mo <sub>2</sub> C                      | 75            | activated by H <sub>2</sub> /CH <sub>4</sub> |
| 3  | WC                                     | 53            | activated by H <sub>2</sub>                  |
| 4  | WC                                     | 59            | activated by H <sub>2</sub> /CH <sub>4</sub> |
| 5  | WC                                     | 26            | commercial                                   |
| 6  | WB                                     | 13            | activated by H <sub>2</sub>                  |
| 7  | MnB <sub>2</sub>                       | 21            | activated by H <sub>2</sub>                  |
| 8  | Mn <sub>0.16</sub> W <sub>0.84</sub> B | 6             | activated by H <sub>2</sub>                  |
| 9  | ReB <sub>2</sub>                       | 16            | activated by H <sub>2</sub>                  |

The effects of temperature, hydrogen pressure, catalyst mass, and contact time on the catalytic conversion of cyclohexene were also studied.

Thus, the possibility of using molybdenum and tungsten carbides synthesized by the method of microwave radiation as catalysts for the process of hydrogenation of alkenes has been shown.

1. S. Horikoshi, N. Serpone, Role of microwaves in heterogeneous catalytic systems, *Catal. Sci. Technol.*, 2014, no. 4, pp. 1197.
2. I. Bilecka, M. Niederberger, Microwave chemistry for inorganic nanomaterials synthesis, *Nanoscale*, 2010, no. 2, pp. 1358–1374.
3. R. Mnatsakanyan, A. R. Zurnachyan, V. A. Matyshak, K. V. Manukyan, Al. S. Mukasyan, Microwave-assisted synthesis of carbon-supported carbides catalysts for hydrous hydrazine decomposition, *J. Phys. Chem. Solids*, 2016, vol. 96–97, pp. 115–120.
4. A.V. Akopyan, P.D. Polykarpov, O.I. Forofontova, I.S. Levin, R.A. Mnatsakanyan, D.A. Davtyan, A.R. Zurnachyan, A.V. Anisimov, E.A. Karakhanov, Hydrogenation of alkenes on molybdenum and tungsten carbides, *Chimicheskaya Tekhnologiya*, 2019, vol. 20, no. 6. (in Russ.)

## Author Index

### A

Abdulkarimova R. G., 1  
Abe K., 4, 7, 408  
Abedi M., 10  
Abkaryan A. K., 102  
Aborkin A. V., 464  
Abovyan L. S., 247  
Abzalov N. I., 418  
Afanasyev N. I., 223  
Akishev A., 565  
Akiyama T., 4, 7, 408  
Akopdzhanyan T. G., 12  
Akopyan A., 568  
Altunin R. R., 561  
Alymov M. I., 13, 122, 387, 421, 424, 493, 558  
Amirkhanyan N., 15  
Amosov A. P., 17, 211, 242, 471, 475, 489  
Andreev D. E., 22, 25, 140, 391, 394, 537  
Anikin Yu. A., 398, 402  
Ankudinov A. B., 446, 558  
Antonyuk M. N., 59  
Aouadi S. M., 27  
Aslamazashvili Z., 30, 33, 468, 549  
Astapov A. N., 36  
Avdeenko E. N., 40  
Avramchik A. N., 250  
Aydinyan S. V., 546

### B

Baideldinova A. N., 42  
Baizhumanova T. S., 486  
Bakkara A. Ye., 45, 259, 383  
Balabanov S. S., 332  
Baldryan A. A., 543  
Baranovskiy A. V., 362  
Baras F., 49, 344  
Batrashov V. M., 320  
Batsikadze T., 549  
Bazhin P. M., 52, 454  
Belova G. S., 471  
Benzeşik K., 54  
Berbentsev V. D., 122  
Berezhko P. G., 278

Bernard E., 82  
Bernard F., 124  
Bondarev A. V., 12, 58, 59  
Borshch V. N., 61  
Braverman B. Sh., 250  
Bučko M. M., 327  
Bugakov V. I., 122  
Bugdayci M., 64, 99, 532  
Buinevich V. S., 67, 296  
Bulanov A. D., 218  
Busurina M. L., 69, 464  
Bykova L. E., 72

### C

Cai X., 74, 112  
Cao G., 317  
Casagrande A., 378  
Chan K.-Y., 78  
Chatilyan H. A., 254  
Chen P. W., 80, 231, 235  
Chikhradze M., 30, 33  
Chintersingh K. L., 85  
Chizhikov A. P., 52  
Chlubny L., 233  
Chuev I. I., 187  
Cinarli U., 99  
Cugini F., 378, 479

### D

Davtyan D., 568  
Dement'eva I. M., 61  
Derin B., 158  
Dine S., 82, 84  
Dirras G., 84  
Dolmatov A. V., 424  
Dolmatov O. Yu., 415  
Dolmatov V. S., 215  
Dreizin E. L., 85  
Du J., 88  
Dubrovskiy A. R., 215  
Dyachkova L. N., 92

**E**

Eremeeva Zh. V., 96  
Ergul T., 99

**F**

Fadeev T. V., 102  
Farle M., 438  
Fedorov S. V., 105  
Fellenberg R., 109  
Feng P., 74, 112, 146  
Filimonov V. Yu., 116  
Filofeev S. V., 332  
Filonov M. R., 398, 402, 405  
Firsina I. A., 364  
Fomenko S. M., 565  
Fourmont A., 49  
Fu Z., 517

**G**

Gabbasov R. M., 119, 169, 443  
Galfetti L., 383  
Galiev F. F., 122  
Gao X., 80  
Gavrishchuk E. M., 332  
Gilev V. G., 126  
Gloushankova N. A., 556  
Golodok R. P., 129  
Golosova O. A., 134, 269, 391, 394  
Gorshkov V. A., 134, 136, 269  
Gotman I., 139  
Gouma P., 325  
Grachev V. V., 458  
Gradoboev A. V., 116  
Grigoriev E. G., 129  
Grigorieva T., 246  
Grisolia C., 82  
Gryadunov A. N., 69  
Gubernat A., 327  
Guda S. A., 187  
Gulyaev P. Yu., 424  
Gulyutin A. V., 122  
Gutmanas E. Y., 139

**H**

Harin E. V., 432  
Hastings D., 85  
Herlin N., 82  
Ho C.-K., 78

Homenko N. Yu., 136  
Hu T., 529

**I**

Ignat'eva T. I., 450  
Ignatov S. G., 355, 556  
Ikornikov D. M., 25, 140, 391, 394,  
398, 402  
Ilyushenko A. Ph., 92, 144  
Ivanov D. G., 482  
Ivanov S. G., 116

**J**

Ji W., 517  
Jiao X., 112, 146

**K**

Kachenyuk M. N., 126, 310  
Kachin A. R., 496  
Kaiypbek G., 274  
Kamunur K., 1  
Kamynina O. K., 13, 150  
Kanunov A. Ye., 482  
Kaplanskii Yu. Yu., 153  
Kapustin R. D., 156  
Karakhanov E., 568  
Karpov A. V., 69  
Kashkynbai D., 565  
Kata D., 233  
Kaumenova G. N., 486  
Kaya F., 158  
Kentheswaran V., 84  
Ketegenov T. A., 160  
Khaptakhanova P. A., 162  
Kharatyan S. L., 15, 247, 254, 543, 546  
Khomenko N. Yu., 25, 187, 450  
Kichaev P. E., 489  
Kim W. B., 299  
Kirakosyan H., 165  
Kirdyashkin A., 264  
Kirdyashkin A. I., 169, 372, 390  
Kiryukhantsev-Korneev Ph. V., 173,  
174, 175, 202, 357, 432  
Kiselev E. N., 314  
Kitler V., 264  
Kitler V. D., 119, 223, 372, 390  
Kochetkov R. A., 418, 421  
Kochetov N. A., 12, 464  
Kolosov V. N., 178, 182

Kondakov A. A., 12, 458  
 Konovalikhin S. V., 122, 187  
 Konstantinov A. S., 52  
 Konyashin I., 40, 540  
 Korchaguin M., 246  
 Korosteleva E. N., 362  
 Korotitskiy A. V., 153  
 Korshunov K. V., 482  
 Korzhova V. V., 362, 364  
 Koshkin G. A., 320  
 Koshkin V. A., 332  
 Kosticina E. V., 398  
 Kostin S. V., 189  
 Kotvanova M. K., 193  
 Kovalev D. Yu., 69, 187, 438, 504  
 Kovalev I. D., 387, 537, 553  
 Kovalkii A. M., 513  
 Kozlova A., 174  
 Kozlova A. P., 12  
 Kozlova N. S., 174  
 Kozochkin M. P., 105  
 Krinitcyn M. G., 362, 364  
 Krishenik P. M., 189  
 Ksandopulo G., 520  
 Ksandopulo G. I., 42, 195  
 Kudryashov A. E., 199, 202, 206, 282, 329, 339, 434  
 Kuptsov K. A., 208, 257, 434  
 Kurbatkina V. V., 209, 322  
 Kurkin T. S., 162  
 Kurniawan A., 4  
 Kuskov K., 412  
 Kuskov K. V., 438  
 Kuzina A. A., 17, 211  
 Kuznechik O. O., 129  
 Kuznetsov M. S., 415  
 Kuznetsov S. A., 215  
 Kvaskhvadze D., 549  
 Kveglis L. I., 102

## L

Lad'yanov V. I., 301, 304  
 Lam W. Y., 78  
 Lapshin O. V., 372, 435  
 Larionova N. S., 301  
 Lashkov A. Yu., 218  
 Latukhin E. I., 17, 242, 489  
 Le Gallet S., 49, 124  
 Lee J. H., 299  
 Lemesheva M. V., 220, 340  
 Leonelli C., 378, 479

Lepakova O. K., 223, 443  
 Letsko A. I., 144, 310  
 Levashov E. A., 36, 40, 59, 153, 174, 175, 199, 202, 209, 220, 227, 239, 282, 322, 340, 357, 359, 405, 449, 515, 525, 540, 556  
 Li C.-Y. V., 78  
 Li Y. Y., 231, 235  
 Li Z., 112  
 Licheri R., 317  
 Lifanov I. P., 36  
 Lin F., 530  
 Linde A. V., 458  
 Lis J., 233  
 Lisina T. G., 418, 421  
 Liu B., 530  
 Liu K. Y., 80, 231, 235  
 Liu W., 529  
 Liushinskii A. V., 236  
 Lizunov A. I., 96  
 Logacheva A. I., 405  
 Loginov P. A., 153, 239, 449  
 Loginov P. V., 359  
 Loginova M. V., 116  
 Loryan V. E., 347, 351, 496  
 Luts A. R., 17  
 Lutz A. R., 242  
 Lyakhov N., 246

## M

Mahmoudi H. A., 247  
 Maidan D. A., 17, 471, 475  
 Makarov A. V., 206  
 Maksimov Yu. M., 250  
 Malakhov A. Yu., 252  
 Mamyran S., 254  
 Manakova O. S., 257  
 Mansurov Z. A., 45, 259  
 Manukyan Kh., 263  
 Manukyan Kh. V., 15, 380  
 Martynov E. M., 206  
 Matsynin A. A., 72  
 Maznoy A., 264  
 Meirbekov N., 383  
 Mikaberidze G., 33  
 Milioli C., 378  
 Miloserdov P. A., 134, 136, 269  
 Miloserdova O. M., 134, 269  
 Milyaev I. M., 493, 558  
 Min Htet Swe, 105  
 Miroshnichenko M. N., 178, 182

Mishunin D. Y., 96  
 Miyamoto Y., 272  
 Mnatsakanyan R., 568  
 Mofa N. N., 45, 259, 274, 383  
 Moiseenko E. T., 561  
 Mokrushin V. V., 278, 482  
 Moscovskikh D., 412  
 Moskovskikh D. O., 10, 67, 281, 296, 375, 480  
 Mukanov S. K., 282  
 Mukasyan A. S., 10, 67, 281, 287, 380, 412, 480  
 Mukhina L. V., 42  
 Mukhina N. I., 553  
 Mursalat M., 85  
 Myagkov V. G., 72, 292, 294  
 Myakisheva L. V., 96  
 Myasnikov A. Yu., 116

## N

Namicheishvili T., 468  
 Nazaretyan K., 165  
 Nazaretyan Kh. T., 546  
 Negodyaev A. Z., 116  
 Nemtsev I. V., 102  
 Nepapushev A., 49  
 Nepapushev A. A., 67, 96, 296, 438  
 Nepapushev N. A., 375  
 Nersisyan H. H., 299  
 Nikonova R. M., 301, 304  
 Nomura T., 4, 408  
 Novikov V. A., 489  
 Novikova A. V., 332

## O

Odawara O., 307  
 Oglezneva S. A., 126, 310  
 Ohyanagi M., 312  
 Okinaka N., 7  
 Oniashvili G., 30, 33, 468, 549  
 Orlov V. M., 182, 314  
 Orrù R., 317  
 Osserov T. B., 274  
 Ostroukhov D. V., 475  
 Otowaki M., 312

## P

Pak Ch. G., 320  
 Panov V. S., 96

Panteleyeva A. V., 301, 304  
 Parnitsky N. M., 92  
 Patsera E. I., 153, 209, 322, 515, 540  
 Pawar M., 325  
 Pędzich Z., 327  
 Penyashki T. G., 329  
 Permin D. A., 332  
 Pervukhina O. L., 334  
 Petrov E. V., 336  
 Petrzhik M. I., 282, 329, 339  
 Pichugin N., 264  
 Poberezhny S. V., 129  
 Pogozhev Yu. S., 36, 220, 340, 357, 359  
 Polčák J., 355  
 Polcar T., 58, 59  
 Politano O., 49, 344  
 Ponomarev M. A., 347, 351  
 Ponomarev V. A., 355  
 Postnikov A. Yu., 278, 482  
 Potanin A. Yu., 36, 220, 340, 357, 359, 556  
 Potekhin A. A., 278  
 Pribytkov G. A., 362, 364  
 Prokhorova T. Yu., 178, 314  
 Prokof'ev V. G., 368, 372  
 Prokofiev M. V., 36  
 Prokopets A. D., 52  
 Pushkarev B. E., 301  
 Puszynski J. A., 374

## Q

Qin B., 78

## R

Rakhym N., 565  
 Repnikov N. I., 206  
 Rogachev A. S., 49, 67, 296, 344, 375, 438, 480, 501  
 Rogachev S. A., 189, 344, 377  
 Rosa R., 378, 479  
 Roslyakov S., 525  
 Roslyakov S. I., 380  
 Rostokina Ye. E., 332  
 Rupasov S. I., 12, 220, 340, 357  
 Rutkowski P., 233  
 Rybakov A. D., 242

## S

Sachkova N. V., 69, 122, 136, 450, 537

Sadykov B. S., 45, 259, 274, 383  
 Safaeva D. R., 475  
 Saikov I. V., 122, 252, 387, 424  
 Saito G., 408  
 Sala D., 233  
 Salamatov V., 264  
 Salamatov V. G., 150, 252, 390, 424  
 Sanada M., 4  
 Sang C., 112  
 Sanin V. N., 140, 391, 394  
 Sanin V. V., 398, 402, 405  
 Sato A., 408  
 Savich V. V., 129  
 Scheck Yu. B., 438  
 Schoenitz M., 85  
 Sedegov A., 49, 412  
 Seidualiyeva A. J., 1  
 Semenov A. O., 415  
 Sentyurina Zh. A., 153, 405  
 Seplyarskii B. S., 418, 421  
 Seropyan S. A., 252, 424  
 Shaltykova D., 274  
 Shapovalov A. M., 482  
 Sharafutdinov M. R., 116  
 Shcherbakov A. V., 429  
 Shcherbakov V. A., 69, 429  
 Shchukin A. S., 150, 464  
 Sheftel E. N., 432  
 Sheveiko A. N., 202  
 Sheveyko A. N., 59, 208, 257, 355, 434, 556  
 Shimizu Y., 312  
 Shipilov S. I., 242  
 Shirai K., 312  
 Shishkina A. S., 334  
 Shkoda O. A., 435  
 Shkodich N. F., 438  
 Shtansky D. V., 59, 208, 257, 355, 434, 440, 513, 556  
 Shulpekov A. M., 119, 223, 250, 443  
 Shustov V. S., 496, 558  
 Shustov V. V., 446  
 Shvindina N. V., 175, 556  
 Sidnov K., 515  
 Sidorenko D. A., 40, 96, 208, 239, 257, 449  
 Silyakov S. L., 187, 450, 537  
 Sitnikov A. A., 116  
 Smetkin A. A., 126, 310  
 Sobachkin A. V., 116  
 Sokolova K. V., 320

Sologubova I. A., 193  
 Solzi M., 479  
 Spasova M., 438  
 Stelmakh L. S., 454  
 Stolin A. M., 52, 454, 457  
 Studenikin I. A., 458  
 Stulov Yu. V., 215  
 Su X., 462, 467, 529, 530  
 Suchentrunk R., 463  
 Sultanova Z. L., 45  
 Suslov M. V., 475  
 Suvorova E. V., 501  
 Sviridova T. A., 175  
 Sytshev A. E., 69, 189, 464

## T

Talako T. L., 144, 310  
 Tallarita G., 317  
 Tang X., 462, 467, 529  
 Tarasov A. B., 480  
 Taskaev S. Yu., 162  
 Tasyurek K. C., 532  
 Tavadze G., 30, 33, 468, 549  
 Tedzhetov V. A., 432  
 Thein Htoo Maung, 105  
 Thoda O., 525  
 Titova Yu. V., 17, 211, 471, 475  
 Tolendiuly S., 42, 565  
 Tolochko B. P., 116  
 Trofimov V. S., 336  
 Trombi L., 378, 479  
 Troshin O. Yu., 218  
 Trusov G. V., 67, 480  
 Tsarev M. V., 278, 482  
 Tsareva I. A., 278, 482  
 Tsodikov M. V., 496  
 Tsybulin V., 412  
 Tungatarova S. A., 486  
 Turan A., 54, 64, 99, 532  
 Tutberidze A., 468

## U

Umerov E. R., 489  
 Usmanova G. Sh., 432  
 Uspenskii S. A., 162  
 Ustyukhin A. S., 493  
 Uvarov V. I., 496  
 Uvarova I. A., 471



**V**

Vadchenko S., 49, 412  
Vadchenko S. G., 150, 296, 375, 387,  
499, 501  
Valluri S. K., 85  
Vardapetyan V. V., 247  
Vdovin Yu. S., 22, 537  
Vekinis G., 525  
Vergunova Yu. S., 438  
Veronesi P., 378, 479  
Vershinnikov V. I., 220, 340, 504, 540  
Vityaz P. A., 144  
Voevodin A. A., 508  
Volkov I. N., 513  
Volochnaev M. N., 102  
Voronetskaya L. Ya., 92  
Vorotilo S., 96, 359, 412, 515  
Vorotilo S. A., 322  
Voskanyan A. A., 78  
Vrel D., 82, 84

**W**

Wang H., 517  
Wang L., 78  
Wang W., 517  
Wojteczko A., 327  
Wojteczko K., 327

**X**

Xanthopoulou G., 486, 520, 525  
Xu C. X., 80, 231

**Y**

Yakovlev V. I., 116  
Yan Y., 462, 467, 529  
Yu W., 530  
Yu Y., 530  
Yucel O., 532  
Yücel O., 54  
Yukhvid V. I., 22, 25, 136, 140, 391,  
394, 398, 402, 405, 450, 537

**Z**

Zabavin Ye. V., 482  
Zabelin S. F., 493  
Zabrodina O. Yu., 278, 482  
Zaitsev A. A., 40, 540  
Zakaryan M. K., 543, 546  
Zakharov D. A., 211  
Zakharov G., 30, 33, 468, 549  
Zakharov K. V., 25  
Zakorzhevsky V. V., 553  
Zamulaeva E. I., 339, 556  
Zeer G. M., 102  
Zelenetskii A. N., 162  
Zelenskii V. A., 493  
Zelensky V. A., 446, 558  
Zhamanbalinova K. S., 383  
Zhang J., 517  
Zhang Z., 517  
Zharkov S. M., 561  
Zheng Y., 530  
Zherebtsov S. V., 394  
Zhigalov V. S., 72  
Ziatdinov M. Kh., 563  
Zurnachyan A., 568

# **Self-Propagating High-Temperature Synthesis**

## **Самораспространяющийся Высокотемпературный Синтез**

Компьютерная верстка *О. А. Голосова*  
Дизайн обложки *О. В. Амелина*

ISBN 978-5-6040595-4-8



9 785604 059548